Proceedings of:

The Twenty-second Annual Meeting

The American Society for Precision Engineering

October 14-19, 2007
The Fairmont Dallas Hotel
Dallas, Texas

The American Society for Precision Engineering (ASPE) is a multidisciplinary professional and technical society concerned with research and development, design, manufacture and measurement of high accuracy components and systems. ASPE activities encompass relevant aspects of mechanical, electronic, optical and production engineering, physics, chemistry, and computer and materials science. Membership is open to anyone interested in any aspect of precision engineering.

Founded in 1986, ASPE provides a new focus for a diverse but important community. Other professional organizations have covered aspects of precision engineering, always as a sideline to their principal goals. ASPE is based on the core of generic concepts necessary to achieve precision in any application; independent of discipline, ASPE intends to be the focus for precision technology — and to represent all facets from research to application.

ASPE — The American Society for Precision Engineering
301 Glenwood Avenue, Suite 205, Raleigh, NC 27603
P.O. Box 10826, Raleigh, NC 27605
Telephone: (919) 839-8444 Fax (919) 839-8039
http://www.aspe.net

Preface

This book comprises the proceedings of the 2007 Annual Meeting. The contributions reflect the authors' opinions and are published as presented to ASPE, without change. Their inclusion in this publication does not necessarily constitute endorsement by the ASPE, or its editorial staff.

Individual readers of this book and nonprofit libraries acting for them are permitted to make fair use of the material contained in this book to be used in teaching or research; provided they copy said paper in total, as written by the author. Permission is granted to quote excerpts from the scientific or technical works in this book with proper acknowledgment of the source to include: The author's name, the book name, and the ASPE tag line. Reproduction of figures and tables is likewise permitted from the contents of this book, provided that the same acknowledgment of the same source and content is permitted.

Any other type reproduction, systematic copying or multiple reproduction of any material in this book is expressly prohibited except with the written permission of the ASPE editorial staff, addressed to the Society's headquarters.

ISBN 978-1-887706-44-5

2007

American Society for Precision Engineering
301 Glenwood Avenue, Suite 205
Raleigh, NC 27603

Printed in the United States of America

Welcome Note

Welcome to Dallas for the Twenty-second Annual Meeting of The American Society for Precision Engineering. The growth and success of the Society reflects the increasing importance of precision engineering in a wide variety of fields, from manufacturing to microelectronics to basic science. The Society serves as a focus for precision engineers across all of these fields. The Annual Meeting has evolved into a premier international forum for the exchange of ideas and presentation of research results relating to precision engineering, metrology, controls, and system integration. Precision engineers and scientists from private industry, government laboratories, and universities meet to learn about the latest developments and to exchange ideas about the future directions of these technologies.

This year's meeting continues the tradition of offering two full days of tutorials presented by some of the foremost precision engineers and scientists in the world. The technical sessions and poster presentations offer the latest research results in the areas of ultraprecision machining, metrology, controls, precision grinding, micro-positioning, material processing, design, precision transducers, surface profilometry, and error compensation. The commercial exhibits will provide attendees with the opportunity to view and discuss the latest precision engineering equipment, products, and services that are commercially available.

The conference organizing committee is proud to present the program for the Twenty-second Annual Meeting of the ASPE. We welcome your participation and your feedback on how to make next year's meeting even better.

2007 Organizing & Technical Program Committee

Alex Sohn
North Carolina State University, Conference Chair

Luis A. Aguirre, 3M Company
Jones B. Arnold, BWXT Y12, L.L.C.
Eberhard Bamberg, University of Utah
Eric S. Buice, University of North Carolina at Charlotte
Keith Carlisle, Lawrence Livermore National Laboratory
John M. Casstevens, Dallas Optical Systems, Inc.
Thomas Mclendon Crawford, University of South Carolina
Timothy M. Dalrymple, Zygo Corporation
Thomas A. Dow, North Carolina State University
Craig Richard Forest, Massachusetts Institute of Technology
Kenneth P. Garrard, North Carolina State University
Anthony E. Gee, University College, London
David D. Gill, Sandia National Laboratories
Byron R. Knapp, Olympic Precision, Inc.
Oscar M. Lechuga, Fresnel Technologies, Inc.
Don A. Lucca, Oklahoma State University
Eric R. Marsh, The Pennsylvania State University
Jerald Lee Overcash, University of North Carolina at Charlotte
Burak O. Ozdoganlar, Carnegie Mellon University
Senajith Bandara Rekawa, Lawrence Berkeley National Laboratory
Jeffrey W. Roblee, AMETEK Precitech, Inc.
Tony L. Schmitz, University of Florida
Deming Shu, Argonne National Laboratory
Mark A. Stocker, Corning, Inc.
Pradeep K. Subrahmanyan, RAPT Industries, Inc.
Yazid F. Tohme, Moore Nanotechnology Systems, LLC
Hans-Jochen Trost, MicroFab Technologies, Inc.
Bobby C. Van Winkle, Alcon Laboratories, Inc.
Allen Y. Yi, The Ohio State University

2007 Scholarship Recipients

Mr. Abdallah H. Alkhaleel, University of Nebraska-Lincoln
R.V. Jones Memorial Scholarship

Mr. Nicholas Jay Ferrell, The Ohio State University

Mr. Nathan A. Mauntler, University of Florida

2007 Annual Meeting
Contents

Preface ii

Welcome Note iii

Organizing Committee – 2007 Scholarship Recipient iv

Table of Contents v

Program vi

Keynote Address vii

Technical Exhibitors viii

Sustaining Corporate Sponsors ix

Corporate Sponsors x

Lifetime Achievement Award 1

Technical Paper Index 2-10

Technical Papers 13-492

Author Index. 493-496

Program

2007 ASPE Annual Meeting

Time	Sun., Oct. 14	Mon., Oct. 15	Tues., Oct. 16	Wed., Oct. 17	Thurs., Oct. 18	Fri., Oct. 19
8:00	Registration		Early Coffee and Registration			
9:00	Tutorials	Tutorials	Technical Session I	Technical Session III	Technical Session VI	Technical Tour #1
10:00			Break	Break	Break	
11:00			Technical Session II	Technical Session IV	Technical Session VII	
12:00			Lunch and Committee Meetings	Awards Lunch and Business Meeting	Lunch and Open Forum	
1:00						
2:00	Tutorials	Tutorials	Commercial Session	Technical Session V	Technical Session VIII	
3:00			Break	Break	Technical Tour #2	
4:00			Poster Session	Poster Session		
5:00			Hospitality Hour	Hospitality Hour		
6:00		Welcome Reception		Open Evening		
7:00		Keynote Address	Dinner Banquet at American Airlines Museum			
8:00						
9:00						

Exhibit Open Hours

Keynote Address

C. T. "Tom" Burbage
Lockheed Martin Aeronautics Company

Monday, October 15, 7:00 p.m.
Session Chair: Alex Sohn, North Carolina State University

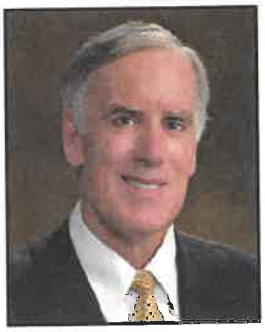

C. T. "Tom" Burbage

Tom Burbage is the Executive Vice President and General Manager, Joint Strike Fighter Program Integration. He is responsible for developing and implementing the multi-national F-35 Production and Global Sustainment elements of the JSF Program. He was the Executive Vice President and General Manager, Joint Strike Fighter from August of 2000 until assuming his current assignment in November 0f 2004.

Mr. Burbage joined Lockheed Martin in 1980 in the business development branch and later became manager of business development for U.S. government programs at the Lockheed California Company operations in Burbank, California. In December 1987, he was appointed vice president for Washington operations and coordinated the company's relationships with the Department of Defense and the U.S. Congress, as well as the embassies of foreign governments. He restructured and streamlined the Washington Operations group and recorded the highest annual performance in the Congressional budget cycle in the history of LM Aeronautics. He then moved to Marietta, Georgia, in 1990 as vice president for Business Development and Product Support at Aeronautical Systems. During his tenure, LM Aero launched several new initiatives including C-130J, C-27J, C-5AMP and RERP.

After receiving a bachelor's degree in aerospace engineering from the U.S. Naval Academy in 1969, Mr. Burbage served on active duty in the United States Navy until 1980, achieving the rank of lieutenant commander. After completing the U.S. Navy Test Pilot School in 1975, he accumulated more than 3,000 hours in 38 different types of military aircraft. On October 31, 1994, he retired from the Navy Reserves as a captain. Mr. Burbage also holds master's degrees in aeronautical systems and business administration.

F-35 – A Product of Precision Engineering

F-35 is a 5th generation fighter with mission requirements generated by three U. S. Military services and eight International partners. Its stealthy design dictated a higher level of external surface smoothness than legacy aircraft which required increased precision in tooling and detail part fabrication. In addition, parts, components and systems are designed and produced by a global supply chain which also demanded precision in design and manufacturing to insure assembly ease and accuracy. When we reach rate production, we will be moving parts throughout the world with multiple sources of major subassemblies feeding multiple Final Assembly lines overlayed by a Performance Based Logistics Sustainment environment. Also, with affordability being a pillar of the program, product cost was a driver in design and manufacturing. In order to meet all of these requirements we use:

- *A common digital database shared among all partners and subcontractors*
- *Automated processes for part fabrication*
  - *Auto drillers*
  - *Auto machining*
  - *Laser control*
  - *Automated Fiber Placement*
  - *Precision milling machine*
  - *Laser ultrasonic inspection*
- *Automated aircraft finishing*
- *Automated precision assembly*
- *Moving Line Assembly Process*
- *Electronic Mate and Assembly System (EMAS)*

The result of using these increased precision tools and processes has already been shown in the design, fabrication and assembly of the first F-35 aircraft.

- *Part quality is significantly improved over legacy programs*
- *Part non conformances are greatly reduced over legacy programs*
- *Major assembly span time is significantly reduced over legacy programs*
- *Affordability of part fabrication and assembly is significantly improved*

Cooperating Sponsors

Elsevier Science, Inc.

Technical Exhibitors

4D Technology Corporation

Aerotech, Inc.

AMETEK Precitech, Inc.

Bal-tec

Center for Precision Metrology—
University of North Carolina at Charlotte

Chardon Tool

CMPC Surface Finishes

Contour Fine Tooling, Inc.

CoorsTek, Inc,

Fabreeka International, Inc.

Heidenhain Corporation

Lion Precision

Machine Dynamics Research Laboratory —
The Pennsylvania State University

MicroFab Technologies, Inc.

MOOG, Inc.

Moore Nanotech Systems

Moore Tool Company, Inc.

New Way Air Bearings, Inc.

Olympic Precision, Inc.

Philips Applied Technologies

Precision Engineering Center —
North Carolina State University

Precision MicroDynamics, Inc.

Professional Instruments Company, Inc.

Queensgate Instruments, Ltd.

The Precision Alliance

Third Wave Systems, Inc.

Trust Automation

Veeco Instruments, Inc.

Commercial Session

Tuesday, October 16, 1:30 - 3:00 p.m.

Session Co-Chairs: John Casstevens (Dallas Optical Systems, Inc.) and Jerald L. Overcash (University of North Carolina at Charlotte)

The Commercial Session will take place early in the week on Tuesday afternoon. This is a special session where companies and participants are free to open discussions on a less-formal basis and to promote interaction on a variety of topics. In the first part of this session, company representatives are invited to make brief presentations (five minutes) on new products associated with precision engineering. This provides participants with the opportunity to receive timely information on new technologies that have been commercialized into products and services, as well as information on advances that can be expected in the near future.

ASPE 2007 Sustaining Corporate Sponsors

3M Company
St. Paul, MN 55144
Phone: (651) 737-3790
www.mmm.com

ADCOLE Corporation
669 Forest Street
Marlborough, MA 01752
Phone: (508) 485-9100
Fax: (508) 481-6142
www.adcole.com

Aerotech, Inc.
101 Zeta Drive
Pittsburgh, PA 15238-2897
Phone: (412) 963-7470
Fax: (412) 963-7459
www.aerotech.com

AMETEK Precitech, Inc.
44 Blackbrook Road
Keene, NH 03431
Phone: (603) 357-2511
Fax: (603) 358-6174
www.precitech.com

Chardon Tool
115 Parker Ct.
Chardon, OH 44024
Phone: (440) 286-6440
Fax: (440) 286-7165
www.chardontool.com

Corning Tropel Corporation
60 O'Connor Road
Fairport, NY 14450
Phone: (585) 388-3500
Toll-free: (888) 4-TROPEL
www.tropel.com

Equilibria
472 Amherst Street, Suite 25
Nashua, NH 03063-1204
Phone: (603) 880-7722
www.eqlib.com

Fabreeka International, Inc.
P.O. Box 210
1023 Turnpike Street
Stoughton, MA 02072
Phone: (781) 341-3655
Toll-free: (800)-322-7352
www.fabreeka.com

Lion Precision
563 Shoreview Park Road
St. Paul, MN 55126-7014
Phone: (651) 484-6544
Fax: (651) 484-6824
www.lionprecision.com

Mitutoyo America Corporation*
945 Corporate Boulevard
Aurora, IL 60504-9102
Phone: (630) 723-3619
Fax: (630) 978-6471
www.mitutoyo.com

Moore Tool Company, Inc.
800 Union Avenue
Bridgeport, CT 06607-0088
Phone: (203) 366-3224
Fax: (203) 366-5694
www.mooretool.com

New Way Precision, Inc.
4009-I Market Street
Aston, PA 19014
Phone: (610) 494-6700
Fax: (610) 494-0911
Toll-Free: (800) 394-1046
www.newwaybearings.com

Philips Applied Technologies
1140 Ringwood Court
MS16
San Jose, CA 95131-1706
Phone: (408) 991-2261
www.apptech.philips.com

Professional Instruments Company
7800 Powell Road
Hopkins, MN 55343
Phone: (952) 933-1222
Fax: (952) 933-3315
www.airbearings.com

Queensgate Instruments, Ltd.
Woodland Road
Torquay Devon TQ2 7AY
United Kingdom
Phone: 44-1803-407710
Fax: 44-1803-407699
www.nanopositioning.com

Trust Automation
143 Suburban Road, Bldg. 100
San Luis Obispo, CA 93401
Phone: (805) 544-0761
Fax: (805) 544-4621
www.trustautomation.com

Zygo Corporation

Zygo Corporation
Laurel Brook Road
Middlefield, CT 06455-0448
Phone: (860) 347-8506
Fax: (860) 347-8372
Toll-free: (800) ZYGO-NOW
www.zygo.com

ASPE 2007 Corporate Sponsors

Center for Precision Metrology – University of North Carolina at Charlotte
Charlotte, NC 28223-0001
Contact: Gregory W. Caskey
(704) 687-8499

Contour Fine Tooling, Inc.
Marlborough, NH 03455
Contact: Jeffrey Tomlin
(603) 876-4908

Corning Inc.
Corning, NY 14831
Contact: John Thomas
(607) 974-3842

Cranfield Precision, Div. of Landis Lund
Division of Cinetic Landis Grinding, Ltd.
Cranfield, Bedford MK43 OJR,
United Kingdom
Contact: Edric M. E. Brown
+44-1234-754222

euspen
Cranfield University Campus
Bedford, MK43 OAL, United Kingdom
+44-1234-754024

Nano Corporation
Tokyo 144-0042, Japan
Contact: Akira Hayashi
+81-3-5735-6631

Reflexite Precision Technology Ctr.
West Henrietta, NY 14586
Contact: Mr. Steven M. Scott
(585) 272-0290

Seagate Technology
Scotts Valley, CA 95066
Contact: Robert M. Pelstring
(831) 439-3697

Singulus Mastering B.V.
5657 EN Eindhoven, The Netherlands
Contact: Guido Dalessi
+31 40 7501 400

Taylor Hobson, Ltd.
Leicester LE4 9JQ, United Kingdom
Contact: Daniel I. Mansfield
+44-116-2763771, Ext. 2126

Veeco Instruments, Inc.
Tucson, AZ 85706-7123
Contact: Geoffrey Anderson
(520) 741-1044

2007 ASPE Lifetime Achievement Award

E. Clayton Teague

Clayton earned B.S. and M.S. degrees in physics from the Georgia Institute of Technology and a PhD, also in physics, from the University of North Texas. His doctoral work was completed at the National Bureau of Standards (now the National Institute of Standards and Technology), which Clayton joined in 1972. Clayton's PhD thesis on metal-vacuum-metal electron tunneling was ground-breaking work, demonstrating for the first time several basic phenomena that underlie the present widespread use of scanning tunneling microscopes. His thesis provided some important physical concepts that lead to the realization of atomic resolution via the Scanning Tunneling Microscope for which G. Binnig and H. Rohrer received the 1986 Nobel Prize.

At NBS/NIST, Clayton made major contributions to surface microtopography measurement, including the development of a new series of sinusoidal profile roughness artifacts, available today as NIST Standard Reference Materials. He also developed new experimental and theoretical techniques for the measurement of surface roughness using light scattering. Clayton's long interest in, and deep understanding of, the fundamental concepts that underlie the design of precision instruments culminated in the building of the NIST Molecular Measuring Machine. This machine has demonstrated the ability to image atoms and to reposition and measure coordinate positions to nanometer-scale uncertainties over areas of square centimeters - a combination of capabilities achieved by few other instruments in the world.

During his years at NBS/NIST, Clayton assumed positions of increasing technical leadership and responsibility, serving as Group Leader in Nanoscale Metrology and subsequently as Chief of the Manufacturing Metrology Division in the Manufacturing Engineering Laboratory. His technical efforts in nanoscale science and technology, precision engineering and surface metrology have resulted in more than 70 authored or coauthored papers, over 75 invited talks, and 12 keynote lectures.

In 2003, Clayton Teague was appointed as the Director of the National Nanotechnology Coordination Office (NNCO). The NNCO provides technical and administrative support to the Nanoscale Science Engineering and Technology Subcommittee and serves as the point of contact on Federal nanotechnology activities for regional, state and local nanotechnology initiatives, government organizations, academia, industry, professional societies and others.

Clayton Teague is a Charter Member of ASPE and played a leading role in the founding of the Society in 1985. He served as first Chairman of the Board of Directors and later served a term as President. He was instrumental in the development of ASPE's Annual Meeting tutorial series and for many years taught a highly-successful, very well attended tutorial on the basic concepts of precision instrument design. For ten years Clayton was Editor-in-Chief of the international journal Nanotechnology. *For this service, and for his technical contributions to the field of nanotechnology, he was elected a Fellow of the UK Institute of Physics. Among his many awards are US Department of Commerce Gold and Silver Medals and the DOC/NIST Allen V. Astin Measurement Science Award. In addition, Clayton received the Kilby International Award from the Kilby Awards Foundation, and an IR-100 Industrial Research and Development Award.*

Technical and Poster Sessions Index

The technical program of the 2007 ASPE Annual Meeting contain 123 papers on precision engineering advances. Papers that lent themselves to significant verbal interaction, concise but important discoveries, or strongly visual or tactile subjects have been selected for the poster presentation. Authors will be in attendance to discuss their work on Tuesday, October 16, and Wednesday, October 17, from 3:30 to 5:00 p.m.

Session I
Machine Design I

Tuesday, October 16, 2007, 8:30 am - 10:00 am

Session Chair: Keith Carlisle (Lawrence Livermore National Laboratory) and Eberhard Bamberg (University of Utah)

1. ***Water Hydrostatic Bearings for Precision Machine Tools and Industrial Machinery (Invited Paper)***
   Slocum, A. H. (Massachusetts Institute of Technology) . . . . . *page 13*
2. ***Comparing the Thermo-mechanical-behavior of Machine Tool Frame Designs Using a FDMFEA Simulation Approach***
   Mayr, J.; Weikert, S.; Wegener, K. (Swiss Federal Institute of Technology . . . . . *page 17*
3. ***Instrumented Crank Slider Mechanism for Validation of a Combined Finite Element Wear Model***
   Mauntler, N. A.; Kim, N.-H.; Sawyer, W. G.; Schmitz, T. L. (University of Florida) . . . . . *page 21*
4. ***Prediction and Control of Acoustically Induced Vibrations of High-precision Equipment***
   Roozen, N. B.; Vervoordeldonk, M. J. (Philips Applied Technologies). . . . . . *page 24*

Session II
Machining

Tuesday, October 16, 2007, 10:30 am - 12:00 pm

Session Chair: Deming Shu (Argonne National Laboratory) and Eric S. Buice (University of North Carolina at Charlotte)

1. ***A Novel Micromilling Technology Based on Single-point Tool Tip Geometry***
   Bamberg, E.; Heamawatanachai, S. (University of Utah) . . . . . *page 28*
2. ***A Novel Method for the On-center Turning of Tightly Toleranced Micro Arrays***
   Gill, D. D.; Hsu, A.; Keeler, G. A.; Sweatt, W. C. (Sandia National Laboratories) . . . . . *page 32*
3. ***Micro Electrical Discharge Machining Using a 5-DOF Controlled Maglev Actuator***
   Zhang, X.; Shinshi, T.; Endo, H.; Shimokohbe, A. (Tokyo Institute of Technology); and Imai, Y.; Miyake, H.; Nakagawa, T. (Mitsubishi Electric Corporation) . . . . . *page 36*
4. ***Study of Gap Control and Electrostatic Force in Nano Electro Machining***
   Alkhaleel, A. H.; Sundaram, M. M.; Rajurkar, K. P. (University of Nebraska-Lincoln); and Malshe, A. (University of Arkansas) . . . . . *page 40*

Session III

Metrology I

Wednesday, October 17, 2007, 8:30 am - 10:00 am

Session Chair: Hans-Jochen Trost (MicroFab Technologies, Inc.) and Eric R. Marsh (The Pennsylvania State University)

1. ***NIST Standard Bullets and Casings Project***
   Song, J.-F. J.; Vorburger, T. V.; Ballou, S.; Renegar, T. B.; Ma, L.; Whitenton, E. P.; Kelley, D.; Clary, R.; Zheng, A. (National Institute of Standards and Technology); and Ols, M. (Bureau of Alcohol, Tobacco, Firearms and Explosives (ATF)) ..... page 44
2. ***CMM Dynamic Error Analysis, Control and Compensation***
   Chang, D. W.; Spence, A. D. (McMaster University) ..... page 48
3. ***Direct Measurement of Spindle Error Motion with 10-picometer Resolution Using Regular Crystalline Lattice and Scanning Tunneling Microscope***
   Aketagawa, M.; Patamaporn, C. (Nagaoka University of Technology); and Okuyama, E. (Akita University) ..... page 52
4. ***High Resolution Computed Tomography for Metrology***
   Lehmann, D. K.; Brockdorf, K. (phoenix\|x-ray Systems + Services Inc.); and Neuber, D. (phoenix\|x-ray Systems + Services GmbH) ..... page 56

Session IV

Optics Fabrication

Wednesday, October 17, 2007, 10:30 am - 12:00 pm

Session Chair: Jeffrey W. Roblee (AMETEK Precitech, Inc.) and Tony L. Schmitz (University of Florida)

1. ***Optical Effect of Surface Finish by Single Point Diamond Machining***
   Li, L.; Collins, Jr., S. A.; Yi, A. Y. (The Ohio State University) ..... page 61
2. ***Development of Large Ultra-precision Diamond Turning Machine for Making Next Generation Hard X-Ray Telescopes***
   Namba, Y.; Shimomura, T.; Shimizu, T. (Chubu University); and Kunieda, H.; Ogasaka, Y.; Yamashita, K. (Nagoya University) ..... page 65
3. ***Rapid Manufacturing of Fast Aspheres***
   Subrahmanyan, P. K.; Gardopee, G. (RAPT Industries, Inc.) ..... page 69
4. ***Manufacture and Metrology of 300 mm Silicon Wafers With Ultra-low Thickness Variation***
   Hall, C.; Tricard, M.; Dumas, P. R. (QED Technologies, International) ..... page 73

Session V

Metrology II

Wednesday, October 17, 2007, 1:30 pm - 3:00 pm

Session Chair: David D. Gill (Sandia National Laboratories) and Mark A. Stocker (Cranfield Precision)

1. ***Tribology and Corrosion Evaluation Using White-light Interferometry***
   Novak, E. L.; Blewett, N. R.; Stout, T. (Veeco Instruments, Inc.) ..... page 77
2. ***Intelligent Shape Sensor***
   Merritt, J.; Mostafavi, M. T. (University of North Carolina at Charlotte); and Sayeh, M. (Southern Illinois University Carbondale) ..... page 81
3. ***First and Second Order Periodic Error Measurement Under Non-constant Velocity Conditions***
   Kim, H. S.; Schmitz, T. L. (University of Florida); and Chu, D. C. K.; Lee, H. (Agilent Technolgies, Inc.) ..... page 85
4. ***Roundness Measurements Using the NIST Fiber Probe***
   Muralikrishnan, B.; Stone Jr., J. A.; Stoup, J. R. (National Institute of Standards and Technology) ..... page 89

Session VI

Novel Systems

Thursday, October 18, 2007, 8:30 am - 10:00 am

Session Chair: Thomas M. Crawford (University of South Carolina) and Anthony A. Gee (University College, London)

1. ***Spatial and Temporal Measurements of the Field of a Magnetic Recording Head Using a Contact Read/Write Tester (Invited Paper)***
   Gokemeijer, N. J.; Kaka, S.; Langzettel, A. K. (Seagate Technology, LLC) . . . . . page 93
2. ***Plasmon Resonance Enhanced Scanning Near-field Optical Microscope Probes for Single Fluorescent Molecule Observations***
   Sugimoto, S.; Morii, H.; Nagato, K.; Tsuchiya, K.; Hamaguchi, T.; Nakao, M. (The University of Tokyo) . . . . . page 97
3. ***Design of an Injection-molded Impedance Cell for Measuring the Dielectric Constant and Conductivity of Liquids and Gases Across Adjustable Nanometer Electrode Gaps***
   Ma, H.; Slocum, A. H. (Massachusetts Institute of Technology) . . . . . page 101
4. ***Pinpoint Synthesis of Tungsten Oxide Nanowires Using Heat Controlling Layer***
   Kojima, Y.; Nagato, K.; Moritani, H.; Nakao, M. (The University of Tokyo); and Kasuya, K. (Hitachi, Ltd.) . . . . . page 105

Session VII

Biomedical Instrumentation

Thursday, October 18, 2007, 10:30 am - 12:00 pm

Session Chair: Craig R. Forest (Massachusetts Institute of Technology) and Yazid Tohme (Moore Tool Company, Inc.)

1. ***Squirt-guns, Syringes and Science: Precise Jet Delivery of Liquid Drug Using Servo-controlled Linear Lorentz-force Actuators (Invited Paper)***
   Taberner, A. J.; Hogan, N. C.; Hunter, I. W. (Massachusetts Institute of Technology) . . . . . page 109
2. ***The Design and Dynamic Characterication of a Precision Three-axis, Micro-scale Fast Scanning Stage for Two-photon Endomicroscopy***
   Chen, S.-C.; Culpepper, M. L.; Choi, H.; So, P. T. (Massachusetts Institute of Technology) . . . . . page 111
3. ***A Combined Scanned Probe and Confocal Microcope System for Live Cell Spectroscopic Imaging***
   Elliott, K. E.; Smith, S. T.; Elliott, G.; Moyer, P. J. (University of North Carolina at Charlotte) . . . . . page 115
4. ***Fabrication Methods for Polymer MEMS***
   Ferrell, N. J.; Gallego, D.; Woodard, J. A.; Hansford, D. J. (The Ohio State University) . . . . . page 119

Session VIII

Machine Design II

Thursday, October 18, 2007, 1:30 pm - 3:00 pm

Session Chair: Thomas A. Dow (Noth Carolina State University) and Lius A. Aguirre (3M Company)

1. ***Hybrid Electromagnetic Air Bearing Systems***
   van Beek, A.; Spronck, J. W.; Langen, H. H.; van Ostayen, R. A. J.; Munnig Schmidt, R.-H. (Delft University of Technology) . . . . . page 123
2. ***Hybrid Bi-directional Flexure Joints***
   Lee, V.; Ziegert, J. C. (Clemson University) . . . . . page 127
3. ***Model-based Subnano-positioning Control***
   van Hulzen, J.; van Eijk, J.; Van den Hof, P. M. J. (Delft University of Technology) . . . . . page 131
4. ***A High-speed Air Bearing Spindle***
   Delhaes, G. M. J.; van Beek, A.; van Ostayen, R. A. J.; Munnig Schmidt, R.-H. (Delft University of Technology) . . . . . page 135

Poster Sessions

Tuesday, October 16, 2007, 3:30 pm - 5:00 pm

Wednesday, October 17, 2007, 3:30 pm - 5:00 pm

Session Chair: Byron R. Knapp (Olympic Precision, Inc.) and Senajith B. Rekawa (Lawrence Berkeley National Laboratory)

BIOMEDICAL

Biomedical

1. ***Design and Fabrication of an Operating Room Computer Assisted Orthopaedic Hip Surgery Artifact***
   Dagalakis, N. G.; Kim, Y. S.; Sawyer, D. S.; Shakarji, C. M. (National Institute of Standards and Technology) . . . . . *page 139*
2. ***Single-chromosome Chip Which Extends, Fixes DNA Fibers and Analyzes the Gene***
   Horiuchi, H.; Nakao, M. (The University of Tokyo); and Kaneko, S. (Tokyo Dental College) . . . . . *page 143*
3. ***Combination of Mechanical Micromachining and Glass Bonding to Fabricate Robust Micro Structures for Painless Drug Delivery***
   Wu, K.-H.; Gatzen, H. H. (University of Hannover); and Adams, H.-A. (Hannover Medical School) . . . . . *page 147*

EQUIPMENT, MACHINES & INSTRUMENTS

Analysis & Modeling

1. ***Modeling Magnetic Fields for Precision Magnetic Actuators That Use Non-periodic Magnet Arrays***
   Golda, D.; Culpepper, M. L. (Massachusetts Institute of Technology) . . . . . *page 151*
2. ***In-process Diameter Control in Precision Cylindrical Grinding***
   Moerlein, A.; Deakyne, T. R.; Marsh, E. R. (The Pennsylvania State University); and Vallance, R. R. (The George Washington University) . . . . . *page 155*
3. ***Analytical Representation of Nanoscale Parasitic Motion in Flexure-based One DOF Translation Mechanism***
   Patil, C. B.; Sreenivasan, S. V.; Longoria, R. G. (The University of Texas at Austin) . . . . . *page 159*
4. ***Evaluation of Machine Tool Concepts Under Friction Influences***
   Weikert, S.; Bossoni, S.; Wegener, K. (Swiss Federal Institute of Technology (ETHZ)) . . . . . *page 163*

Controls

1. ***Sub-microkelvin Precision Thermal Control System Using Model Predictive Algorithm for Laser Interferometer Space Antenna Ground Verification Facility***
   Higuchi, S.; DeBra, D. B.; Rock, S. (Stanford University) . . . . . *page 167*
2. ***Integrated Design of High-performance Servomechanisms Using a Disturbance Observer***
   Kim, M.-S.; Sung, C.-M.; Chung, S.-C. (Hanyang University) . . . . . *page 171*
3. ***Adaptive Repetitive Control of Piezoelectric Actuators for Nano-precision Motion Control***
   Lin, C.-Y.; Tsao, T.-C. (University of California - Los Angeles) . . . . . *page 175*
4. ***Simple and Practical Control Method for Ultra-precision Positioning — Application to a Ballscrew Mechanism***
   Sato, K.; Maeda, G. J. (Tokyo Institute of Technology) . . . . . *page 179*
5. ***Integrated Tuning of Bi-axial Servomechanisms for Precise Motion Control***
   Sung, C.-M.; Chung, S.-C. (Hanyang University) and Kim, K.-D. (Small Business Corporation) . . . . . *page 183*

Design & Testing

1. ***A Versatile, Long-range, Positioning System for Mechanical Probe Studies***
   Buice, E. S.; Smith, S. T.; Hocken, R. J. (University of North Carolina at Charlotte); and Trumper, D. L.; Otten, D. (Massachusetts Institute of Technology) . . . . . *page 187*
2. ***Synthesis of Multi-degree-of-freedom Precision Flexure Concepts Via Freedom and Constraint Topologies***
   Hopkins, J. B.; Culpepper, M. L. (Massachusetts Institute of Technology) . . . . . *page 191*

3. ***A Design Process for the Creation of Precision Flexure Conceps Via the Use of Freedom and Constraint Topology***
Hopkins, J. B.; Culpepper, M. L. (Massachusetts Institute of Technology) . . . . . *page 195*

4. ***Optimization of Diamond Micro-drilling Processes in Glass Machining***
Kim, H.-H.; Chung, S.-C. (Hanyang University) . . . . . *page 199*

5. ***Development of a Design Tool Supporting Conceptual Design of Machine Tools — Application to Multi-axis Machine Tools —***
Mishima, N. (Advanced Manufacturing Research Institute (AIST)) . . . . . *page 203*

6. ***Modeling and Self-calibration of Laser Tracker System Using Planar Constraints***
Ouyang, J.; Yan, Y.-G.; Liang, Z. (Henan Polytechnic University); and Liu, W.; Qu, X. (Tianjin University) . . . . . *page 207*

7. ***Recent Developments and Upgrades In-progress of a Precision Six Degree-of-freedom Magnetically Suspended Measuring Instrument***
Overcash, J. L.; Stroup, C. G.; Hocken, R. J. (University of North Carolina at Charlotte) . . . . . *page 211*

8. ***Development of Ultra-light Ultra-flat Robot Applying Monolithic Spiral Joint Mechanism***
Sai, R.; Hiramoto, T.; Sakaki, Y.; Tsuda, N. (Tokai University) . . . . . *page 215*

9. ***80mm Displacement Flexure Stage With Sub-micrometric Deviation From Straight Line***
Villar, F.; Geneves, G. (Laboratoire National de Métrologie et d'Essais - LNE); and David, J. (École Nationale Supérieure d'Arts at Métiers - ENSAM) . . . . . *page 219*

Mechatronics

1. ***Sub-pico Liter Dispensing Mechanism With Precise Optical Gap Detector***
Aoyama, H.; Ekko, T.; Adachihara, Y.; Fuchiwaki, O. (University of Electro-Communications-Tokyo); Misaki, D. (Shizuoka Institute of Science & Technology); Irie, Y.; Dejima, S.; Kato, Y. (Applied Micro Systems Inc.); and Usuda, T. (National Institute of Advanced Industrial Science & Technology) . . . . . *page 223*

2. ***Calibration of a Robust 2 DOF Path Monitoring Tool for Industrial Robots and Machine Tools Based on Parallel Kinematics***
Batzies, E.; Kreutzer, M.; Zirn, O. (Giessen University of Applied Sciences); and Leucht, D.; Welker, V. (Philipps-Universität Marburg) . . . . . *page 227*

3. ***An Advanced NURBS Interpolator for Mechanical-coupled Linear Servo Systems***
Cheng, C.-W. (Industrial Technology Research Institute); and Yang, C.-H.; Tsai, M.-C. (National Cheng Kung University) . . . . . *page 232*

4. ***Development of Small Vibratory Crusher for Sample-return Mission***
Furutani, K.; Tagata, Y. (Toyota Technological Institute) . . . . . *page 236*

5. ***Fabrication of a New Position Surveying System for the Underground Pipes Using Two Pairs of Rotary Encoders***
Hamano, T.; Shino, A.; Kato, S. (Nippon Institute of Technology); and Ono, M. (Tokyo Metropolitan College of Technology) . . . . . *page 240*

6. ***Fabrication of a Microrobot Movable in Freely Held Pig's Small Intestine***
Kato, S.; Gakuhari, A.; Hamano, T. (Nippon Institute of Technology); and Ono, M.; Kuniyoshi, Y. (Tokyo Metropolitan College of Industrial Technology) . . . . . *page 244*

7. ***Development of a Laser-guided Deep-hole Grinding Tool: Performance Test***
Katsuki, A.; Park, H. K.; Onikura, H.; Sajima, T.; Nakanishi, T. (Kyushu University); and Murakami, H. (Fukuoka Industrial Technology Center) . . . . . *page 248*

8. ***DSP-based Precision Motion Controller for Iron-core Linear Motors***
Kim, S.-C.; Chung, S.-C. (Hanyang University); and Kim, K.-D. (Small Business Corporation) . . . . . *page 252*

9. ***Planar Motor Based on the Principle of Ultrasonic Wave Using PZT***
Lee, C.-W.; Song, J.-Y.; Ha, T.-H. (Korea Institute of Machinery & Materials) . . . . . *page 256*

10. ***3D Model Reconstruction With Non-contact Rotation Mechanism Using Micro Robots***
Misaki, D.; Oguri, A.; Zhu, N. (Shizuoka Institute of Science and Technology); and Fuchiwaki, O.; Aoyama, H. (University of Electro-Communications) . . . . . *page 260*

11. ***Proposal of a Snake Type In-pipe Mobile Robot Corresponding to the Different Diameters***
Ono, M.; Ito, S.; Ikeda, S. (Tokyo Metropolitan College of Technology); and Kato, S. (Nippon Institute of Technology) . . . . . *page 264*

12. ***Design and Optimization of an Active Aerostatic Thrust Bearing***
van Ostayen, R. A. J.; van Beek, A.; Munnig-Schmidt, R.-H. (Delft University of Technology) . . . . . *page 268*

MEMS, LIGA & Nanotechnology

1. ***Development of Micro Mechanical Parts Utilized Extra Fine Wires***
Honda, S. (Tokyo Metropolitan University) . . . . . *page 272*
2. ***Development of 2-DOF Deflection Mirror With Closed Loop Control***
Kuijpers, T. A. A.; van Lierop, D.; Nellissen, T. A. J. M.; Soemers, H. M. J. R.; Rankers, A. M. (Philips Applied Technologies) . . . . . *page 276*
3. ***Fabrication of a 50nm Level Master With a Spiral Pattern for Optical Storage Memory Using E-beam Lithography***
Oh, S.-H.; Jeong, M.-Y. (Pusan National University); and Je, T.-J.; Yoo, Y.-E.; Choi, D.-S. (Korea Institute of Machinery & Materials) . . . . . *page 279*
4. ***Precise Micromolding of Patterned Silicone Layers for Formation of Plating Instant-masks***
Zhang, G. (Echemics) . . . . . *page 283*

Novel Systems

1. ***Fast Long Range Actuator (FLORA)***
Chen, Q.; Dow, T. A.; Garrard, K. P.; Sohn, A. (North Carolina State University) . . . . . *page 287*
2. ***On a Bearingless Linear Motor Capable of Self-magnetic Levitation***
Kim, W.-Y.; Kim, S.-J.; Lee, J.-M. (Korea Institute of Science and Technology); Chung, S.-C. (Hanyang University); and Kim, S. J. (Nano Motion Technology Co.) . . . . . *page 291*
3. ***Design of a Precision Specimen Exchange Robot-arm System for a Hard X-ray Nanoprobe Instrument***
Shu, D.; Maser, J.; Holt, M.; Winarski, R.; Preissner, C.; Lai, B.; Vogt, S.; Stephenson, G. B. (Argonne National Laboratory) . . . . . *page 295*
4. ***Photocatalytic Nano-imprinting Using Direct Near-field Oxidation***
Sugiue, Y.; Morii, H.; Nagato, K.; Tsuchiya, K.; Hamaguchi, T.; Nakao, M. (The University of Tokyo) . . . . . *page 299*

METROLOGY

Form & Geometry

1. ***A Study on Surface Material Measures for Areal Surface Texture Measuring Instruments***
Nemoto, K.; Yanagi, K.; Aketagawa, M.; Kanda, D.; Sakurai, T. (Nagaoka University of Technology); Yoshida, I. (Japan Science and Technology Agency); and Uchidate, M. (Iwate University) . . . . . *page 303*

Instrumentation, Design & Testing

1. ***Microlens Characterization Using Contact Profilometry and Point-spread Function Measurement***
Forest, C. R.; Saez, M. A.; Hunter, I. W. (Massachusetts Institute of Technology) . . . . . *page 307*
2. ***The Use of Magnetic Recording for Nanoscale Metrology***
Heaton, R. J.; Crawford, T. M. (University of South Carolina) . . . . . *page 310*
3. ***Novel High-bandwidth Active Parasitic Motion Compensation for Sub-nm Planarity in AFM and Profiler Applications***
Jordan, S. (PI (Physik Instrumente) L.P.); and Marth, H. (Physik Instrumente (PI) GmbH & Co. KG) . . . . . *page 314*
4. ***Surface Profile Measurement by Tandem Type Sequential Two-point Method—Improvement of Spatial Resolution Without Approximation —***
Kamiya, K.; Nomura, T. (Toyama Prefectural University); and Tashiro, H. (Toyama University) . . . . . *page 317*
5. ***Basic Study for Development of Measurement System for Micro Cylinder***
Ogura, I.; Okazaki, Y. (National Institute of Advanced Industrial Science and Technology) . . . . . *page 321*
6. ***Development of a Calibration Device for Atomic Force Microscope***
Suzuki, Y.; Honda, S. (Tokyo Metropolitan University) . . . . . *page 324*

Measurement Uncertainty

1. ***Uncertainty Analysis of a Laser Calibration System for Kinematic Accuracy Assessment of Machine Tools***
Castro, H. F. F. (Universidade Federal da Bahia) . . . . . *page 328*

2. ***Including the Uncertainty of CMM Measurements and Stitching Algorithms in the Uncertainty Analysis of Fiducial Based Machining***
Chopra, D.; Woody, B. A.; Smith, K. S. (University of North Carolina at Charlotte) . . . . . page 332

3. ***Studies on Reproducibility and Accurate Measurement of Moisture Content of Wood Samples Using an Electric Moisture Meter***
Okai, R. (University of Education at Winneba) . . . . . page 336

4. ***Uncertainty in Measurements of Dimensional Changes from an Interferometric Dilatometer***
Ren, D.; Miller, J. A.; Lawton, K. M. (University of North Carolina at Charlotte) . . . . . page 340

5. ***Design and Evaluation of Bulk-Micromachined Silicon Artifacts for Hybrid Dimensional Calibration***
Shilling, K. M.; Claudet, A. A.; Luck, D. L.; Tran, H. D. (Sandia National Laboratories) . . . . . page 344

Surface & Subsurface

1. ***Advanced Applications for Stylus Profilometers***
Bullaro, M.; Novak, E. L. (Veeco Instruments, Inc.) . . . . . page 348

2. ***The Effect of 3D Anisotropic Rough Surface on Friction in Precision Hydraulic Assemblies***
Manesh, K. K.; Ramamoorthy, B.; Singaperumal, M. (Indian Institute of Technology Madras) . . . . . page 351

3. ***Characterization and Selection of Surface Texture Measurement Instruments and Manufacturing Processes for a Function***
Peruru, H.; Raja, J. (University of North Carolina at Charlotte) . . . . . page 355

4. ***Development of Straightness Measuring Machine for Long Parts Using In-situ Self Calibration Laser Differential Auto-collimation — Influences of Probe Assemble Error —***
Uda, Y.; Shimada, S. (Osaka Electro-Communication University); and Go, Y. (Nagase Integrex Co., Ltd.) . . . . . page 359

OPTICS

Optical Fabrication

1. ***Millimeter-scale Reflecting Optics Fabricated Using Elliptical Vibration-assisted Machining (EVAM)***
Brehl, D. E.; Dow, T. A.; Garrard, K. P.; Sohn, A. (North Carolina State University) . . . . . page 363

2. ***Laser Micromachining in Silica Glass with Absorbent Slurry***
Kono, I.; Sugita, N.; Mitsuishi, M. (The University of Tokyo) . . . . . page 367

3. ***Characterization of Errors Affecting Surface Generation in Fast Tool Servo (FTS) Machining***
Kwok, T. C.; Cheung, C.-F.; To, S.; Lee, W.-B. (Hong Kong Polytechnic University) . . . . . page 371

Optics / Interferometry

1. ***Optically Balanced, Multi-pass Displacement Interferometry for Picometer Stability Testing***
Ellis, J. D.; Spronck, J. W.; Munnig Schmidt, R.-H. (Delft University of Technology); and Hatzigeorgopoulos, J. H. (TNO Science and Industry) . . . . . page 375

2. ***Ultra-precise and Wide-range Displacement Measurement Using Phase Modulation Homodyne Interferometer and Tunable Laser Diodes***
Ishige, M.; Kawasugi, M.; Hoshino, Y.; Aketagawa, M. (Nagaoka University of Technology) . . . . . page 379

PROCESSES

Grinding

1. ***Development and Slicing Performance of High Accuracy Multi-wire Saw: Effect of Table Feed Accuracy and Thermal Deformation of Frame on Slicing Accuracy***
Abe, Y.; Hamasaki, T. (Toyo Advanced Technologies Co., Ltd.); and Ishikawa, K.-I.; Suwabe, H. (Kanazawa Institute of Technology) . . . . . page 382

2. ***Concept for Distinction Between the Circumferential and Sidewall Effects During the Dicing of Single Crystal Silicon***
Cvetkovic, S.; Gatzen, H. H. (University of Hannover) . . . . . page 386

3. ***Use of Varying Work-piece Distance to Study the Effects on Machine Stiffness in Plunge Grinding***
Deakyne, T. R.; Marsh, E. R. (The Pennsylvania State University) . . . . . page 390

4. ***Investigation on High Depth of Cut of Ultra-smoothness Grinding of Al_2O_3-TiC Ceramic***
Yamamoto, Y.; Yasui, H.; Tanaka, Y.; Sakamoto, R.; Matsuda, K.; Yoshimura, T.; Miyamoto, K. (Kumamoto University) . . . . page 394

5. ***Selection of Optimal Machining Parameters in Diamond Core Drilling Processes***
Yoon, K.-W.; Chung, S.-C. (Hanyang University) . . . . page 398

Machining

1. ***Chatter in Turning With Process Damping***
Eynian, M.; Altintas, Y. (The University of British Columbia); and Onozuka, H. (Hitachi, Ltd.) . . . . page 402

2. ***Precision Machining of Glass Lens Mold With Minute Structures***
Fujii, T.; Ishida, T.; Takeuchi, Y. (Osaka University); and Hirano, M.; Shibukawa, T. (JTEKT Corporation) . . . . page 406

3. ***Study on Improvement of Accuracy in End Mill Machining***
Iso, S.; Toida, N.; Ikeda, N.; Kobayashi, Y.; Shirai, K. (Nihon University) and Tozawa, K. (Nissan Motor Co., Ltd.) . . . . page 410

4 ***Temperature and Stress Analysis in Micro-cutting of TI-6AL-4V and AL7050-T6 With Advantedge***
Lu, D.; Li, J. F. (Shandong University); Rong, Y. (Worcester Polytechnic Institute); and Grevstad, A.; Usui, S. (Third Wave Systems) . . . . page 414

5. ***Fixturing for Ultraprecision Machining of Spherical Parts***
Rhorer, R. L. (National Institute of Standards and Technology) . . . . page 418

6. ***Shrinking Lead Times with Micro Technology ****
Richmond, L. A. (Makino) . . . . page 420

7. ***Precision Drilling of CFRP (Carbon Fiber Reinforced Plastics) with Coated Tools***
Sakamoto, S.; Kajiwara, Y.; Yasui, H. (Kumamoto University) . . . . page 421

8. ***Effect of Drill Shapes on the Drill-out of CFRP (Carbon Fiber Reinforced Plastics)***
Sakamoto, S.; Kajiwara, Y.; Yasui, H. (Kumamoto University) . . . . page 425

9. ***Rake Angle Variation in Diamond Turning***
Sohn, A. (North Carolina State University) . . . . page 429

10. ***Micro Drilling for Printed Circuit Boards — Influence of Run-out of Micro Drilling on Hole Quality —***
Watanabe, H.; Tsuzaka, H. (Union Tool Co.); and Masuda, M. (Niigata University) . . . . page 433

11. ***Quantifying the Stability Uncertainty in a Milling Model***
Zapata-Ramos, R. E.; Schmitz, T. L. (University of Florida); and Abbas, A. E.; Yang, L. (University of Illinois, Urbana-Champagne) . . . . page 437

Manufacturing

1. ***The Critical Speeds of a Machine Tool Spindle-bearing System With the High Stiffness Hydrostatic Journal Bearings***
Chen, Y. S.; Cheng, Y. D.; Chiou, C. C. (Yuan-Ze University) . . . . page 441

2. ***Cost-effective Wire-cut EDM System for Precision Mold Manufacturing***
Kim, H.-G.; Kim, H.-H.; Yoon, K.-W.; Chung, S.-C. (Hanyang University); and Song, I.-H. (Ajou University) . . . . page 445

3. ***Selection of Optimal Cutting Conditions in Micro-endmilling Processes***
Lee, K.-J.; Lee, W.-S.; and Chung, S.-C. (Hanyang University); and Kim, K.-D. (Small Business Corporation) . . . . page 449

4. ***Self-unbalance-correction Technique for Production Process of Precision High-speed Rotors***
Nagato, K.; Hamaguchi, T.; Ide, T.; Tsuchiya, K.; Nakao, M. (The University of Tokyo); and Ohno, N. (Konicaminolta Business Technologies, Ltd.) . . . . page 453

5. ***Sharing of CAE Data to Fabricate Precision Parts in Injection Molding and Die Casting Processes***
Song, I.-H. (Ajou University); and Kim, H.-G.; Chung, S.-C. (Hanyang University) . . . . page 457

6. ***New Laser Micro-fabrication for Creating Surface Functions***
Wakabayashi, M.; Ikeno, J.-I.; Shibutani, H.; Suzuki, A. (Saitama University) . . . . page 461

**Extended Abstract unavailable at press time*

Non-conventional

1. ***A Piezoactuated Tool Feed Mechanism for Micro EDM***
   Rao, M.; Vasa, N. J.; Singaperumal, M. (Indian Institute of Technology Madras) . . . . . *page 465*

Polishing, Lapping & ECM

1. ***Investigation of the Impact on Process Quality When Utilizing Different Pads During Chemical Mechanical Polishing of MEMS***
   Cvetkovic, S.; Gatzen, H. H. (University of Hannover) . . . . . *page 469*
2. ***Development of Superabrasive Stone for Mechanochemical Superfinishing***
   Higuchi, M.; Yamaguchi, T.; Sugimoto, T. (Kansai University); Shimada, S. (Osaka Electro-Communication University); and Matsumori, N.; Ogura, H. (Mizuho Co., Ltd.) . . . . . *page 473*
3. ***Development of Polishing Simulator for Optical Elements***
   Ishibashi, H.; Ishida, T.; Takeuchi, Y. (Osaka University) . . . . . *page 477*
4. ***Influence of Polisher Surface Structure on Polisher Life in Ultra-smoothness Polishing of NiP Plated Aluminum Magnetic Disk Substrate***
   Yamaguchi, K.; Yasui, H.; Otsuka, S.; Nagata, T.; Kusaba, K. (Kumamoto University) . . . . . *page 481*

Replication

1. ***Nano-Scale Mechanics of Front-side Contamination in Photonic Device Fabrication Using Imprint Lithography***
   Singhal, S.; Sreenivasan, S. V. (The University of Texas at Austin) . . . . . *page 485*
2. ***Micro Molding of Metallic Glass Structured Components***
   Suzuki, H.; Kawano, T.; Mukohata, D.; Yamamoto, Y.; Nakamoto, K.; Shibasaka, T. (Kobe University); and Moriwaki, T. (Setsunan University) . . . . . *page 489*

Technical Papers

WATER HYDROSTATIC BEARINGS FOR PRECISION MACHINE TOOLS AND INDUSTRIAL MACHINERY

Alexander H. Slocum
Department of Mechanical Engineering
Massachusetts Institute of Technology
Cambridge, MA, USA 02139

ABSTRACT

Hydrostatic bearings have been used for many years to provide precision and long life in machine tools and industrial machines. Oil is typically used for ease of pumping and its inherent lubricity in case of pressure loss. In many applications, such as grinding of ceramics, high speed spindles, and industrial applications, such as paper machinery, water would be the preferred working fluid. A great challenge is flora and fauna readily grow in water, and can cause inlet flow restrictors to clog which results in bearing failure. Surface self compensation or constant pressure supply (gear pumps) overcomes this problem, and ceramic bearing surfaces provide very long life.

INTRODUCTION

Hydrostatic bearings have a number of advantages over sliding contact or rolling element bearings [1], and their design principles are well known [2, 3] because they are based on a simple pressure divider circuit model shown in Figure 1 for the flow into and out of the bearing pocket. In this model, a constant pressure supply feeds inlet restrictors such as orifices or capillaries. The flow enters the pockets and exits the lands as shown in Figure 2. Nominally the inlet flow resistance is equal to the pocket outlet flow resistance for good performance.

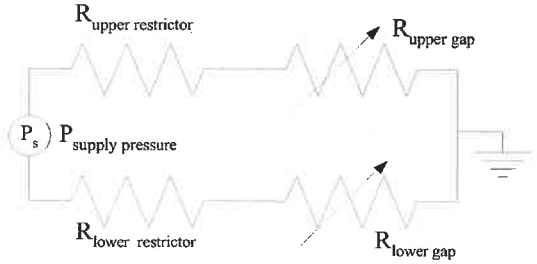

FIGURE 1. Circuit model for a hydrostatic bearing with pressure supply and inlet restrictor

Compensation Methods

There are a number of ways of achieving an inlet flow resistance including fixed and active compensation methods. Fixed compensation methods include orifices, capillaries, slots, grooves, and porous structures which can be modeled as shown in Figure 1. Each has its own merits ranging from low cost to greater efficiency. However, when used with water, all may suffer from things growing in the water. In particular, all systems will have piping, and there will be corners where there is a zero velocity point at which gunk deposits and builds up until it breaks loose and travels downstream to clog even the biggest orifice. A clogged orifice leads to failure, because if one pocket's flow is shut off, the others will keep applying force and contact and failure will likely result.

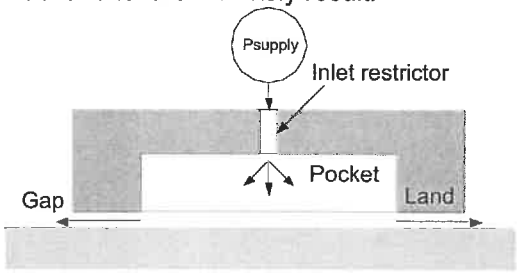

FIGURE 2. Conventional external inlet restrictor

Active compensation can change resistance in response to loads placed on the bearings. This concept can be used in a feedback mode to obtain "infinite stiffness" using a diaphragm which is available as a commercially produced modular restrictor unit [4].

Between infinite and constant stiffness is self compensation, where the stiffness is always good even if the gap varies from that which was assumed during the design and manufacturing process. First shown perhaps in a US patent [5] and available commercially [6], self compensation brings the supply pressure directly to the surfaces of each side of an opposed pad preloaded hydrostatic bearing where it flows across a land region which acts to restrict the flow according to the geometry and the gap. As shown in Figure 3, the flow is collected in a collector groove which is then connected either by an internal manifold or

external piping to the pocket on the opposite side. Figure 4 shows how the stiffness is good even if there is significant manufacturing error in the gap, as compared to the effect of manufacturing errors on a fixed compensation system shown in Figure 5.

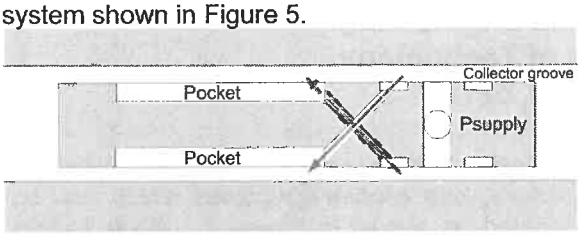

FIGURE 3. Principle of self compensation.

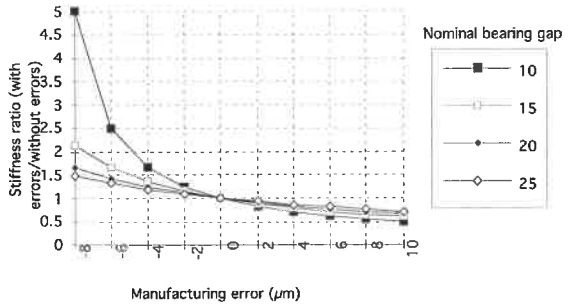

FIGURE 4. Manufacturing error effect on stiffness for a self compensated bearing.

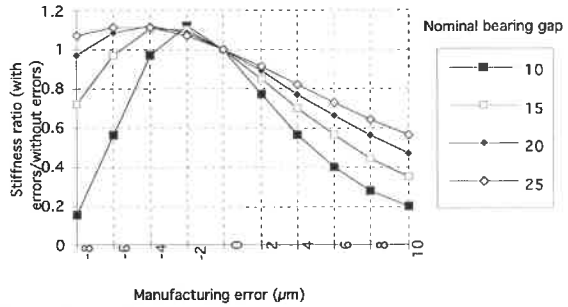

FIGURE 5. Manufacturing error effect on stiffness for a self compensated bearing.

Applications

The principle of self compensation has been used in many machines with oil as the working fluid, but for applications such as grinding ceramics, water is the preferred working fluid because any oil contamination of the water-based grinding fluid can be too detrimental to the parts and process. This is particularly true for semiconductor applications.

However, water as the working hydrostatic fluid poses some very unique challenges, the most basic of which is the pressure supply which must typically supply tens of atmospheres of pressure. Centrifugal pumps are often inefficient and cause heating of the water. Piston pumps are efficient but the pressure pulsations can cause vibrations in the machine unless they are filtered with accumulators and stubs [7].

Another issue is water in a small gap between the bearing rail and the carriage. Metal on metal is very bad in this case. Plastics are too soft and prone to scratching from abrasive particles that may wash through the system. Ceramic on metal or ceramic on ceramic is ideal.

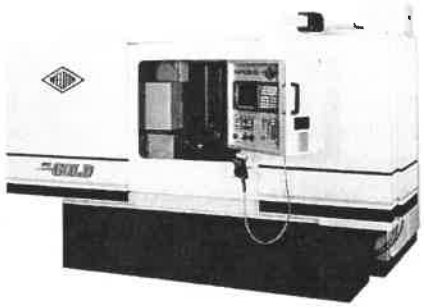

FIGURE 6. Weldon's 1632 Gold grinder used a modular design with either roller bearings or self compensated water hydrostatic bearings.

The hydrostatic pads can be made from ceramic, such as zirconia, and should the fluid pressure be lost, the zirconia merely polishes the metal rail. A punch grinder, shown in Figure 6 was made with this design. Initially the bearing fluid was the same as the cutting fluid, but for grinding metal, the swarf contained long metal chips which could pass through the filter, and the chips could collect in the plumbing that connected the compensators and pockets. The solution was to install collection gutters and keep the fluid separate.

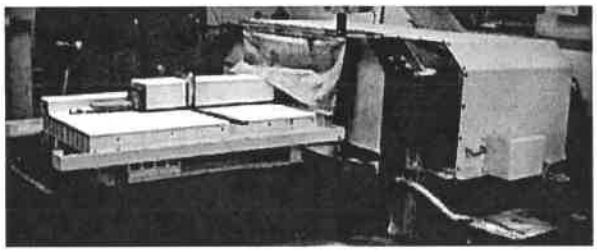

FIGURE 7. MIT/CoorsTek alumina grinder with self compensated water hydrostatic bearings.

Allowing the bearing fluid to flow freely into the same collection troughs as for the grinding fluid saves considerable cost. For grinding of ceramics were the grinding residue is not stringy, this is feasible. However, to prevent the surfaces from eroding, they must all be ceramic.

Such a machine was designed and built from alumina in cooperation with CoorsTek and is shown in Figure 7 [8]. This particular machine has a decade of two shifts per day production at CoorsTek, has never had to be rebuilt, and still grinds with submicron precision. The machine is used mostly to grind the ends of ceramic beams square, and is thus called the *End Grinder.*

Conventional wisdom used to assume that an all ceramic machine would be too expensive, vibrate too much, be too brittle, and would have thermal problems. These were addressed by:

- *Cost:* Standard sections were used and bonded together
- *Vibration:* The large hydrostatic bearings acted as squeeze film dampers. In addition, the machine structure had a large flat bottom and when mounted on rubber pads on a concrete slab, the concrete and rubber act like a constrained layer damper.
- *Brittleness:* In 10 years of operation by even novice machinists who have often crashed it, it has never lost accuracy because ceramics do not suffer from plastic deformations, and large bonded sections are immensely strong. A corner was chipped when a forklift ran into it however.
- *Thermal:* The machine sits inside a coolant tank and is bathed by coolant: a variant of the coolant shower technique favored by Bryan and LLNL [9].

The Weldon 1632 Gold grinder and the MIT/CoorsTek End Grinder both use a boxway design where the carriage wraps around the rail. This requires ceramic bearing pads to use external tubes, as shown in Figure 8, to connect the compensators to the pockets. The external tubing does require some time to install, but it can be easily taken apart and cleaned if needed.

Water hydrostatic bearing based machine tools can also be made using a single small gear pump per pocket. Preload can be provided with an opposed pad, or with the magnetic attraction force from an inclined linear electric motor used to actuate the axis [10, 11]. Such an all-alumina research machine was built at MIT in cooperation with Okamoto Corp. and the Japan Defense University and is shown in Figure 9. Note the use of two cable carriers to help balance cable forces on the carriage.

Active compensation can also be used to control bearing gap by varying pressure to the pocket. With feedback from an appropriate sensor, such as an impedance probe measuring, which is not affected by liquids, against an appropriate metal target, or a laser interferometer, the carriage position and orientation can be actively controlled [12] to overcome manufacturing errors or static applied loads. Manufacturing errors includes the expansion of the structure when the hydrostatic pressure is applied. The bearing rails and bearings can be mounted to balance hydrostatic forces [13] which reduces gap error. In this type of design, the hydrostatic pockets are on opposite sides of a block of material, so external plumbing is not required and if self compensation is used, the compensator can be connected to the pocket by cross-drilling as shown in Figure 2.

FIGURE 8. External tubes to connect compensators to pockets.

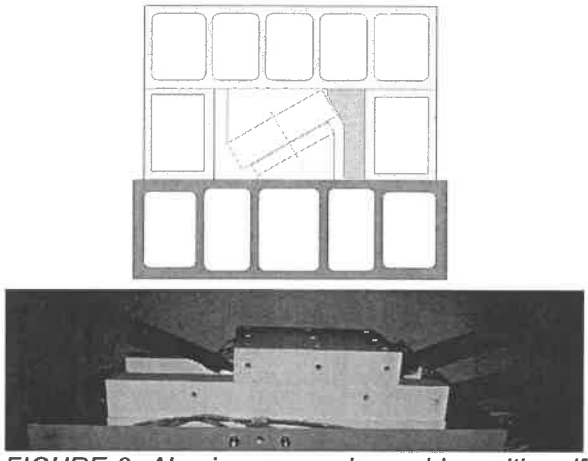

FIGURE 9. Alumina research machine with self compensated water hydrostatic bearings preloaded by an inclined permanent magnet linear electric motor.

Thus far, problems have not occurred with clogging when there is a large diameter (>4 mm) simple connection between the compensation region or pump and the pocket. Any flora or fauna buildup in a corner of the connection that eventually breaks free is digested in the pocket by the motion of the bearing, which is another reason for using a ceramic bearing.

Surface Self Compensation

The ideal hydrostatic bearing could be cast (or as-fired) or very simply machined. This desire led to the concept of surface self compensation where the compensator is integral with the

bearing surface. Topologically, a groove must be cut on the bearing surface to connect the compensator to a pocket opposite, and this implies a round bearing. This design lends itself to spindles as shown in Figure 10 [14].

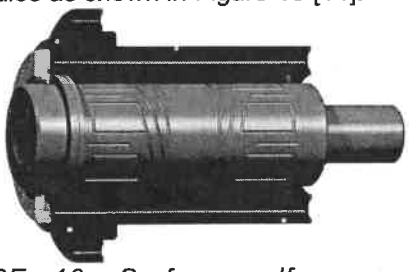

FIGURE 10. Surface self compensated hydrostatic spindle

Machining the grooves on the surface of the shaft is straightforward and not expensive; however, they can be made even less costly by casting on the inside of a bore, and hence the concept of the HydroBushing was created as shown in Figure 11 [15]. The HydroBushing can be sand cast for large bushings or investment cast after 3D printing for small bushings. Ceramic HydroBushings can also be easily made. Surface self compensation can also be applied to a rotary/axial bearing as shown in Figure 12. This design is used in Precitech's production HydroRound table and achieves a hydrostatic averaging effect of over 50 [16].

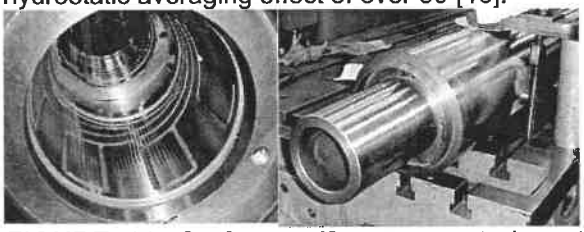

FIGURE 11. Surface self compensated cast HydroBushing

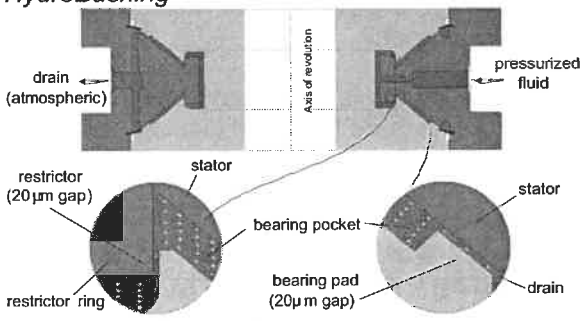

FIGURE 12. Surface self compensated rotary/axial bearing: the HydroRound.

CONCLUSIONS

It is predicted that low cost micropump fed hydrostatic pockets and self compensated (e.g., surface) hydrostatic bearings combined with judicious use of ceramic elements can lead to a new generation of ultra precision machine tools and industrial machines which currently use lubricants (from oil to water) in their processes, so a little extra fluid flowing will not be an issue.

ACKNOWLEDGEMENTS

This paper describes work done over a number of years with a number of people including (in alpha order). M. Basaran, C. Brünnner, R. Cortesi, D. Devitt, D. Davies, H. Gaub, L. Hale, A.J., Hart, M. Kotilainen, J. Moore, R. Maas, G. Rothenhofer, P. Scagnetti, J. Sihler, K. Wasson. Resources were provided by many different companies and agencies including Aesop, Cranfield Precision, CoorsTek, Jung, NewWay Bearings, ONR, NIST ATP, NSF, Okamoto, Moore Tool, Precitech, Royal Society, Weldon. Thanks to all for many wonderful/memorable hydrostatic times!

REFERENCES

[1] M. Weck, Handbook of Machine Tools, Vols. 1 and 2, John Wiley & Sons, New York, 1984.

[2] Slocum, A.H., Precision Machine Design, SME, Dearborn, MI, 1995

[3] Stansfield, F., Hydrostatic Bearings for Machine Tools, Machinery Publishing Co., Ltd. London, 1970

[4] www.hyprostakik.de

[5] US patent from 1940s

[6] http://www.zollern.de/centix/en/gleitlager/produktueberblick/hydrostatik.html

[7] Taco viersma

[8] Slocum, A.H., Scagnetti, P.E., Kane, N.R., Brünnner, C., "Design of Self Compensated Water-Hydrostatic Bearings", Precis. Eng., Vol. 17, No. 3, 1995, pp 173-185.

[9] Bryan, J., et al., "An Order of Magnitude Improvement in Thermal Stability with Use of Liquid Shower on a General Purpose Measuring Machine," SME Precis. Eng. Workshop Technical Paper IQ82-936, St. Paul, MN, June 1982

[10] Slocum, A., Basaran, M., Cortesi, R., Hart, A.J., "Linear Motion Carriage with Bearings Preloaded by Inclined Iron Core Linear Electric Motor", Precis. Eng., 27 (2003) 382-394

[11] US Patent 6,150,740

[12] van der Wielen, A.M., Schellekens, P.H.J., Jaartsveld, F.T.M., "Accurate Tool Height Control by Bearing Gap Adjustment", Annals of the CIRP, 51(1/200), 351-354.

[13] ibid

[14] US Patent 5,700,092

[15] Kotilainen, M., Slocum, A. "Manufacturing of Cast Monolithic Hydrostatic Journal Bearings", Precis. Eng., Vol. 25 2001, pp. 235-244.

[16] Kane, N. R. , Sihler, J., Slocum, A.H., "A hydrostatic rotary bearing with angled surface self-compensation", Precis. Eng., V 27, No. 2, 2003, pp 125-139.

COMPARING THE THERMO-MACHANICAL-BEHAVIOR OF MACHINE TOOL FRAME DESIGNS USING A FDM-FEA SIMULATION APPROACH

Josef Mayr[1], Sascha Weikert[1] and Konrad Wegener[1]
[1]Institute of Machine Tools and Manufacturing
Swiss Federal Institute of Technology
Zurich, Switzerland

ABSTRACT

This is a presentation of an alternative way for simulating the thermo-mechanical behavior of machine tools. The approach combines the advantages of the finite difference method (FDM) and the finite element analysis (FEA). In the first step the transient 3-D-temperature distribution at discrete points of time during the simulated period is calculated using the FDM. In the second step the thermally induced deformations are calculated using the FEA. The temperature distribution at the discrete time points calculated via FDM is used as temperature field for the FEA. An example illustrates the use of the combined finite difference element method (FDEM) for comparing two different concepts of machine tool frames of a laser engraving machine. The advantages of the approach for simulating several load cases are shown. With a standard PC it takes less then five minutes to calculate the thermo-mechanical behavior of a machine tool frame over 24 hours simulation time.

INTRODUCTION

The thermo-elastic deformations of machine tools caused by internal and external heat sources can contribute more than 50% to the overall geometrical inaccuracies of the work piece [1,2]. Thus, to handle thermal effects on machine tools is the capital importance on the way to more accurate works peaces. Having the control over thermally-induced deformations of machine tools plays a critical role in high accurate machining. After construction of the prototype it is often recognized that the accuracies defined in product requirement specifications cannot be maintained due to thermal influences. The consequence of implementation of design modifications is the incurrence of high costs in time and money. Therefore thermal simulation of machine tools moves increasingly into the foreground of research activities.

In the recent years several simulation models based on FEA have been developed to calculate the thermal behavior of entire machine tools or of components of machine tools [3,4,5]. Other authors developed a hybrid model based on the two computational methods FEA and FDM to compute the behavior of a headstock. Several components of the headstock were modeled by FEA using tetrahedral elements. The axial-symmetric components were modeled by FDM using ring elements, which render in a natural way the geometry and the phenomena that occur in the assemblies [6].

FDM is often used to solve temperature and fluid fields in numerical simulation with the advantages that the models can easily be established and programmed, and the calculation speed is high. But it is difficult to use the FDM for calculating stress problems. The FEA is well investigated and usually used to solve stress problems, but it is difficult to solve heat and mass transfer problems using FEA [7].

FDEM

The idea of the FDEM is to combine the advantages of the FDM and the FEA. In the first step the transient temperature distribution is calculated by solving the heat transfer problem using the FDM. The results are the temperature distribution in the model at discrete time points. In the second step the thermally induced deformations at these discrete time points are calculated using the FEA. The temperature distribution at the discrete time points of the earlier FDM is used as temperature field for the FEA. Thus the FDEM can be seen as a serial simulation tool. FIGURE 1 shows the schematic of the FDEM.

Calculating the transient temperature distribution at discrete time points using the FDM, the calculation time-step size can not be chosen arbitrarily. The maximum calculation time-step for a 1-D transient problem is restricted by a stability criteria [9,10,11].

$$\Delta t = \frac{l^2}{a} Fo \leq \frac{l^2}{2\alpha(1+Bi)} \qquad (1)$$

For the stability criteria the Biot number (Bi) is part of the denominator. Thus, when Bi is large,

Δt must be chosen unnecessarily small for stability reasons, resulting in a substantial increase in computation time. A more efficient way to calculate the transient heat transfer problems is to use numerical integration methods to solve the difference equations. Those solvers (e.g. the ODE-solver in the software package of Matlab/Simulink) are able to diversify the time-steps by given accurate criteria. This is a very efficient way because these solvers are able to handle much greater time-steps than the maximum time-step given by the stability criteria.

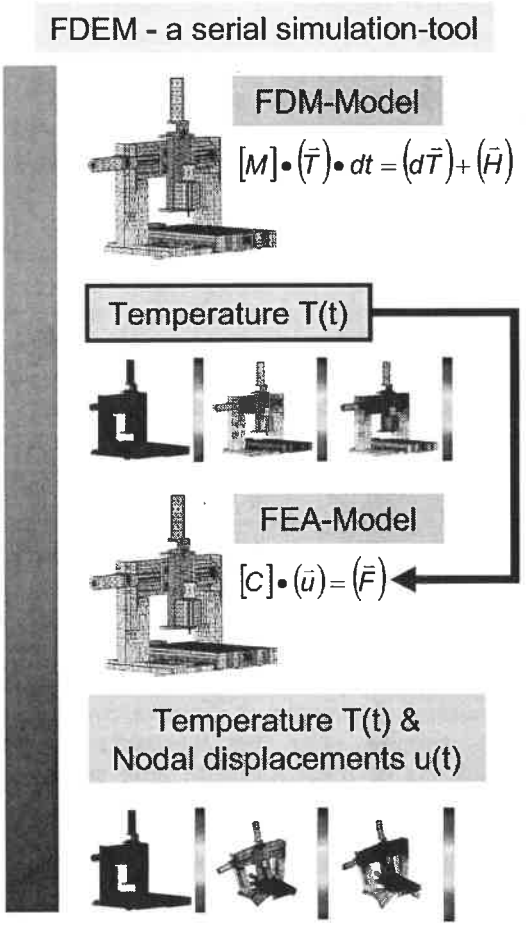

FIGURE 1. Schematic of the FDEM

FDEM-MODEL OF A MACHINE TOOL FRAME

The thermo-mechanical-behavior of two different welded machine tool frames for a laser engraving machine are compared using the FDEM approach. For the FDM models brick elements with six boundary areas are used. Every element has one temperature-node set to the centre of the elements. For the FEA models the same mesh of brick elements is used. Thus the element temperatures calculated with the FDM can directly be assigned to the FEA elements. For the FEA eight node brick elements with linear shape functions are used. FIGURE 2 shows the models of the two welded machine tool frames.

In this study, the former machine tool frame design is called "old design" and the enhanced machine tool frame design is called "new design".

The "old design" is characterized by having one column on the left side. The right hand side column is just a single plate of 8mm. The stiffener of the left hand side column is a kind of spinal column. The sheet thicknesses used for the column stiffener and the feed stiffener elements on the frame are 10mm. The sheet thicknesses of the other elements are 8mm. No background sheet is used thus the design is open on the bottom side.

The "new design" is characterized by two columns to get a symmetric construction. The columns are a light-weight design with closed profiles and the stiffener elements are arranged in a comb-structure. The sheet thicknesses are 5mm, 6mm and 8mm. For the stiffener of the feeds 10mm sheets are used. The table is also a closed profile with an 8mm sheet at the bottom side.

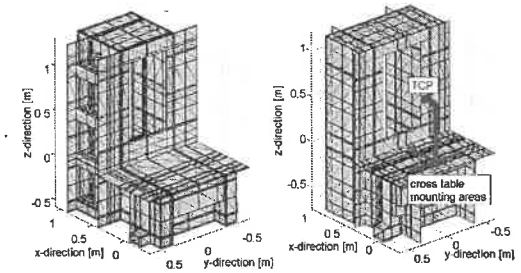

FIGURE 2. Model of the welded machine tool frames: left hand side "old design"; right hand side "new design" with the geometrical model for the calculation of the TCP-displacements caused by deformations of the table

For the simulations the thermo-mechanical behavior of the parts attached on the frames (e.g. the cross table) is not considered. For the calculation of the tool centre point (TCP) displacements relative to the work piece, mechanical parts attached to the frame are represented by rigid kinematic models. To some nodes of the substructure of the cross table (red in FIGURE 2) as well as to some nodes of the plane for the Z guide rails a rigid coordinate frame is attached and moved together with these nodes. The displacement is then

represented by the relative displacement of the coordinate points of the TCP in the respective frames. For the TCP-position the middle of the x-y strokes and the maximum work piece height is chosen.

The convective boundary conditions for the horizontal, vertical and inclined sheets are calculated with equations form the VDI-Wärme-atlas [8]. The following assumptions are made:

- boundary conditions are calculated with a assumed temperature of the sheet, which is due to small temperature intervals sufficient accurate.
- boundary conditions are set to be constant during the simulation.
- convective boundary conditions at the sheet edges are taken to be the same as on the flat sides.
- There are no temperatures fixed on the surfaces.
- The radiation term is neglected.

NUMERICAL SIMULATION

The thermo-mechanical behaviors of the two different machine tool frames are compared with each other by the simulation of the displacements for three different thermal load cases:

- heating up of "workspace region".
- heating up of "right hand side column".
- change of "ambient temperature".

During the simulations "workspace region" and "right hand side column" only the concerned surfaces, shown on FIGURE 3, are assumed to be loaded with higher ambient temperatures. During the simulation "ambient temperature" all areas are subject to higher ambient temperatures.

During the simulated time a temperature profile outside the loaded areas was assumed. It was found that the time constants of both frames are nearly identical. Thus just the steady state results need to be compared.

A second simulation was done with the ambient temperature profile shown in FIGURE 5 (black curve). This ambient temperature profile represents a possible room temperature profile in a workshop over a time period of one day. In this study this case is called "ambient temperature variation". The assumed ambient temperature profile:

- 0-6 h: linear rise from 20 to 25°C
- 6-12 h: steady state at 25°C
- 10-18 h: linear fall from 25 to 20°C
- 18-24 h: steady state at 20°C

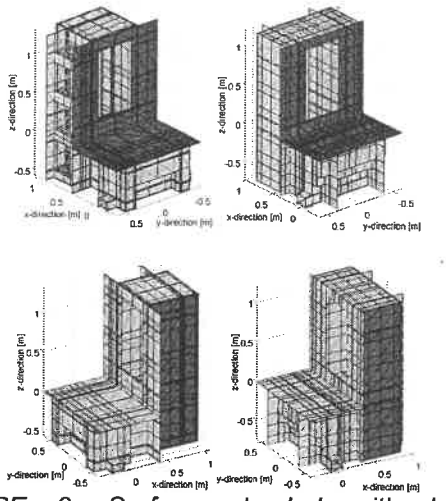

FIGURE 3. Surfaces loaded with higher temperature, left hand side: "old design, right hand side: "new design", top: work space region, bottom: right hand side column

RESULTS AND DICUSSION

In TABLE 1 the translatory and the rotatory TCP-displacements in steady state of the simulations "workspace region", "right hand side column" and "ambient temperature" are listed.

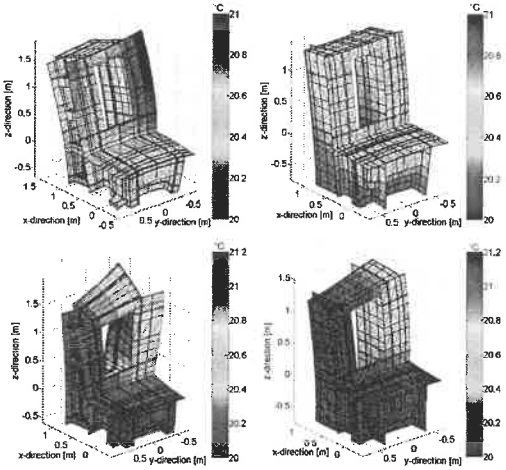

FIGURE 4. Simulation results: Temperature distribution and thermally induced deformations, left hand side: "old design", right hand side: "new design", top: work space region, bottom: right hand side column

In FIGURE 4 the machine tool frames under thermal loads in steady state are shown for the cases "workspace region" and "right hand side column". The thermally induced deformations are shown by plotting the machine tool frames with a deformation scale factor of 1000. The temperature distributions are given according to the colorbars.

TABLE 1. Comparison of the steady state: translatory TCP-displacements in μm

	dx	dy	dz
workspace region			
"old design"	18.3	6.0	8.8
"new design"	7.7	2.7	4.3
right hand side column			
"old design"	1.7	7.5	3.0
"new design"	1.2	4.2	1.4
ambient temperature			
"old design"	86.9	20.7	49.6
"new design"	50.4	21.2	34.8

rotatory TCP-displacements in μm/m

	dA	dB	dC
workspace region			
"old design"	-1.7	14.1	-2.8
"new design"	-0.3	5.4	-1.5
right hand side column			
"old design"	-4.7	2.6	-3.0
"new design"	-3.5	0.8	0.5
ambient temperature			
"old design"	2.0	40.7	-5.6
"new design"	0.2	10.7	0.1

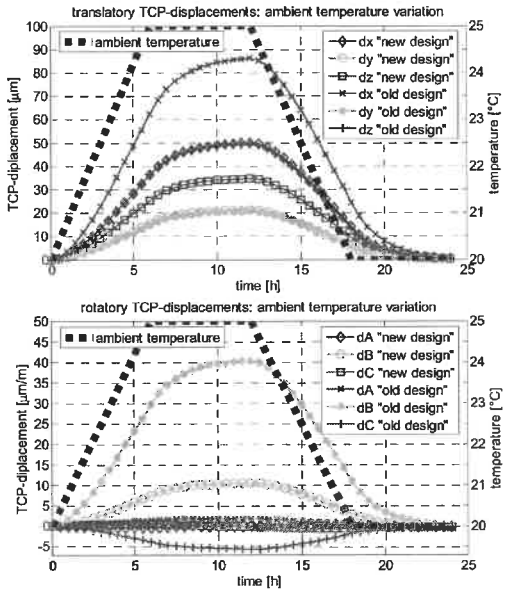

FIGURE 5. Comparison of the resulting TCP-displacements top: translatory-, bottom: rotatory TCP-displacements

It can be shown that in all simulated cases in steady state the thermally induced deformations are smaller with the "new design". The reasons for this behavior are the higher mechanical stiffness of the new design and the larger area of convection. The calculation time of a simulation over 24 hours time is less than 5 minutes (e.g. workspace region: 3min 45sec).

In FIGURE 5 the time-depend TCP-displacements are show. It can be seen that the machine tool frame is thermally fast and follows the ambient temperature profile only with little delay. After 12 hours the steady state values are nearly reached. Also after 24 hours the initial position is nearly reached again.

ACKNOWLEDGEMENT:
The authors like to thank BBT for financial support.

REFERENCES

[1] Bryan J. International Status of Thermal Error Research. Annals of the CIRP. 1990, 39/2. 645-656

[2] Weck M, McKeown P, Bonse R, Herbst U. Reduction and Compensation of Thermal Errors in Machine Tools. Annals of the CIRP. 1995, 44/2. 589-598

[3] Wu C-H, Kung Y-T. Thermal analyses for the feed drive system of a CNC machine centre. Int. Jour. of Machine Tools & Manufacture. 2003, 43. 1521-1528

[4] Kim J-J, Jeong Y H, Cho D-W. Thermal behavior of machine tool equipped with linear motors. Int. Jour. of Machine Tools & Manufacture. 2004, 44. 749-758

[5] Huo D, Cheng K, Webb D, Wardle F. A Novel FEA Model for the Integral Analysis of a Machine Tool and Machining Processes. Key Engineering Materials. 2004, 257-258. 45-50

[6] Jedrzejewski J, Kowal Z, Kwasny W, Modrzycki W. Hybrid Model of High Speed Machining Centre Headstock. Annals of the CIRP. 2004, 53/1. 285-288

[7] Xue X, Tian J, Xui G. Numerical Simulation of Thermal Stress in Castings Using FDM/FEM Integrated Method. Material Science Forum 2005, 490-491. 85-90

[8] VDI-Gesellschaft für Verfahrenstechnik und Chemieingenieurswesen. VDI-Wärmeatlas, 10. Auflage. Springer Verlag Berlin Heidelberg New York. 2006

[9] Croft D R, Lilley D G. Heat transfer Calculation using Finite Differences Equations. Applied Science Publisher LTD London. 1977

[10] Dusinberre G M, Obert E F. Heat Transfer Calculation by Finite Differences. International Textbook Company, Scranton, Pennsylvania. 1961

[11] Baehr H D, Stephan K. Wärme und Stoffübertragung, 4. Auflage, Springer Verlag Berlin Heidelberg New York. 2003

INSTRUMENTED CRANK SLIDER MECHANISM FOR VALIDATION OF A COMBINED FINITE ELEMENT WEAR MODEL

Nathan A. Mauntler[1], Nam-Ho Kim[1], W. Gregory Sawyer[1] and Tony L. Schmitz[1]
[1]Department of Mechanical and Aerospace Engineering
University of Florida
Gainesville, Florida, United States

INTRODUCTION

Software currently being produced at the University of Florida is incorporates traditional wear models into finite element analyses. This Coupled Evolution Wear Model (CEWM) uses the finite element method and generic material wear rates to continuously update contact pressures and geometry. This software package can be used to predict wear evolution, degradation of precision motion, and ultimately the end of a joint's useful life. Whereas traditional wear models do not account for changes in load profile due to changes in geometry, the CEWM iteratively updates material loss, shape, and pressure distributions to more realistically predict how a joint wears. This model has already been adapted and validated for several scenarios including a block on ring and the human knee [1,2]. Ultimately this software package will be available to designers in order to predict the influence of wear on the performance of moving parts over the course of their useful lives.

Recently the CEWM has been adapted to model a crank slider mechanism, where the integrity of the joint between the crank and connector rod can influence the ability to accurately control the location of a follower link. In order to validate the CEWM in this scenario, a crank slider tribometer is used to run controlled wear tests at the crank-connector rod joint (Fig. 1).

MECHANICAL DESIGN

The design of the tribometer is centered around the isolating friction, wear, and error motions to the joint of interest as much as possible.

Motion Generation

Motion of the crank slider is driven by a high-stiffness block spindle powered by a ¾ HP DC motor. This motor is elevated to the same height as the follower joint to minimize out-of-plane moments. A flywheel with 0.0847 kg-m^2 mass moment of inertia can be attached to the spindle to help maintain a constant velocity.

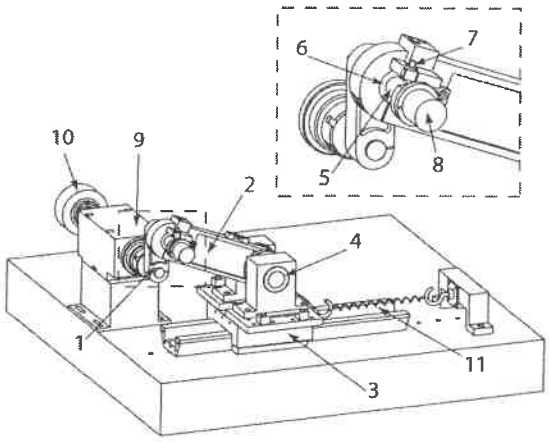

FIGURE 1. Crank slider tribometer (1) Crank arm (2) Follower arm (3) Slide (4) Thrust bushing (5) Instrumented pin (6) Bushing (7) Capacitance probe (8) Slip ring (9) Spindle (10) Encoder (11) Loading spring

The crank and follower arm are both machined from aluminum and pocketed to reduce weight. The crank is clamped to the spindle shaft at one end and to an instrumented pin at the other end. The pin is then free to rotate within a wearing bushing which is clamped in the follower arm. The follower arm is then constrained to in-plane rotations by two thrust air bushings. These bushings are mounted in pillow blocks which are in turn bolted to a dovetail air bearing stage. Both the thrust bushings and dovetail slide are constructed from porous carbon air bearings to minimize error motions while maintaining a high level of joint stiffness. All of the structural components of the tribometer are bolted to a granite plate.

Instrumentation

Forces transmitted through the joint of interest are measured via a load cell built into a steel pin (Fig. 2). Two full-bridge arrays of strain gages mounted to a necked-down portion of the pin monitor transverse loads while cancelling out bending stresses. The necked portion of the pin, along with a hollow cross section, also serve to

localize the strain to the region where the gages are attached. A milled face allows repeatable orientation of the pin with respect to the crank arm. A slip ring mounted to the free end of the pin allows power and signals to be transmitted to and from the strain gages. The load cell is dead-weight calibrated, has a full scale capacity of 400 N and a resolution of 2 N.

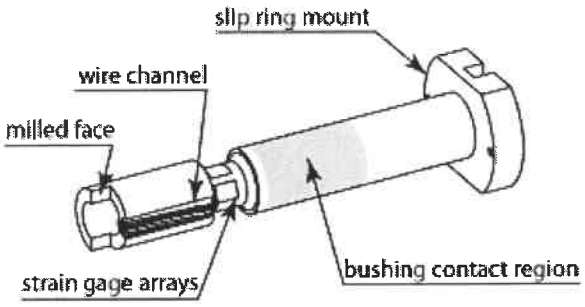

FIGURE 2. The pin at the joint of interest also serves as a load cell to measure transverse loads during testing.

Simultaneously, two orthogonally mounted capacitance probes monitor the position of the pin relative to bushing (Fig. 3). These probes are clamped to the follower arm and are electrically insulated by polymer bushings. Additionally, the pin, as the target, is electrically grounded.

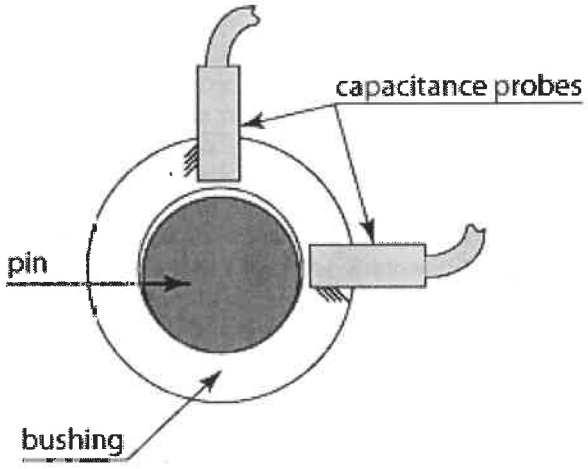

FIGURE 3. Orthogonally mounted capacitance probes monitor the position of the pin with respect to the bushing.

Additionally, the angular position of the crank is measured by a hollow shaft incremental encoder attached to the spindle shaft.

Load Profile

In addition to the inertial load of the slide and follower arm, the load profile seen by the pin-bushing joint can be adjusted in two ways. First, a spring can be added to the air bearing stage to provide a positional dependence to the load profile. Also, up to 10 kg of additional mass can be added to the stage. Adding mass to the stage influences the load profile as a function of both acceleration and position.

DATA ACQUISITION

Data from the load cell, capacitance probe, and encoder are collected simultaneously as waveforms. Typically, a packet of data is acquired once per revolution at a pre-specified sampling rate, depending on the crank speed. For each channel, the maximum value, minimum value, and root mean square of the data are then recorded to show broad trends over many cycles at a glance (Fig. 4).

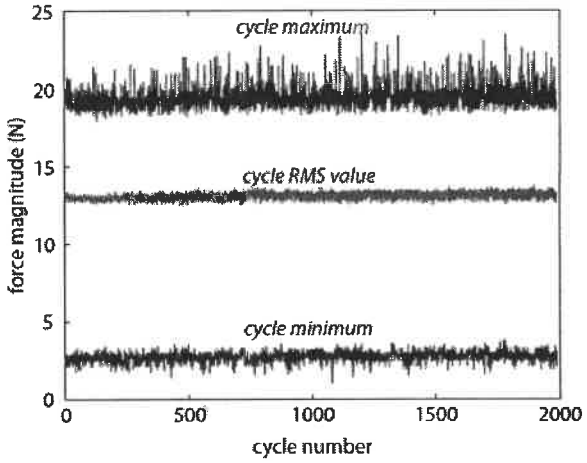

FIGURE 4. Force magnitude extrema plotted as a function of cycle number. Variations in the cycle maximum force value can be seen to increase as the test progresses.

Additionally, whole cycles of data from each channel are periodically saved. Force and displacement signals can then be plotted against the crank position to observe the evolution of the force profile and bushing geometry (Fig. 5). This also allows events observed in the force data to be directly correlated to events in the displacement data.

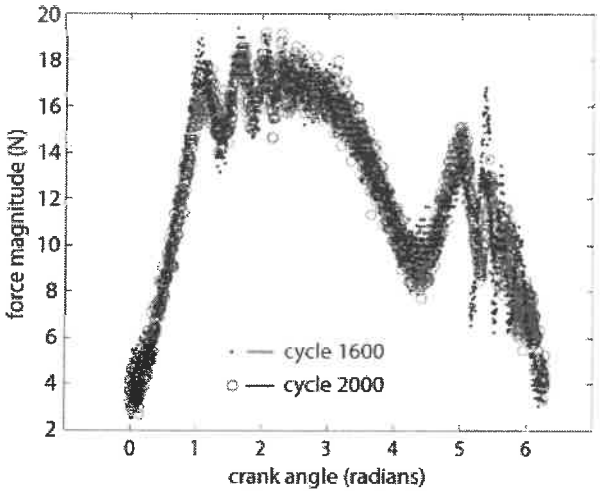

FIGURE 5. Force magnitude data from two cycles. The load profile can be seen to evolve in the severity of the dynamic forces.

FUTURE WORK

In the near future, whole tests will be run in which bushings are worn from their original state until the range capacity of the capacitance probes have been met. The results from these tests will then be compared to CEWM simulations using the same initial conditions.

REFERENCES

[1] Bei, Y. et al. The Relationship Between Contact Pressure, Insert Thickness, and Mild Wear in Total Knee Replacement. Computer Modeling in Engineering and Science. 2004; 6: 145-152.

[2] Kim, N.H. et al. Finite Element Analysis and Validation of Metal/Metal Wear in Oscillatory Contacts. Wear. 2005; 258: 1787-1793.

PREDICTION AND CONTROL OF ACOUSTICALLY INDUCED VIBRATIONS OF HIGH-PRECISION EQUIPMENT

N.B. Roozen[1,2], and M.J. Vervoordeldonk[1]
[1]Department of Mechatronics
Philips Applied Technologies
High Tech Campus 7, 5656 AE Eindhoven, The Netherlands
[2]Department of Mechanical Engineering
Eindhoven University of Technology
P.O. Box 513, 5600 MB Eindhoven, The Netherlands

ABSTRACT

With the accuracy of metrology frame applications entering the nanometer-range, the necessity arises to tackle all types of disturbances. In the process of estimating the relative importance of the different types of disturbances on the machine accuracy, also called dynamic error budgeting, acoustic excitation has gained more importance, mainly because of the tightening of the performance requirements as well as the relatively high noise levels of air-conditioning systems in clean room. To estimate the dynamic error budget claimed by acoustic excitation already in the design phase of the machine, there is a clear need to predict this type of excitation in the design stage. This paper presents an efficient numerical procedure to predict the errors due to acoustic excitation and introduces an active structural damping concept to control acoustically induced vibrations.

To validate the numerical procedure, tests were done on a relatively simple structure consisting of a cantilever beam and a base plate that represents the typical structural dynamics of a practical high-precision mechatronic system. The sensitivity of this structure to diffuse acoustic sound field excitation, typical for the sound fields in clean rooms, was predicted and measured. The simulations agree reasonably well with the measurements in a reverberant room.

The level of metrology frame vibrations caused by internal or external sources, such as acoustically induced vibrations, is to a large extend determined by the (lack of) structural damping. This lack of damping is typical for metrology frames. Designing for stiffness, so as to achieve nanometer accuracy, inevitably implies a low intrinsic structural damping. In order to solve this dilemma, an alternative approach for the creation of active damping in the structure is proposed. The approach will be referred to as ASD - Active Structural Damping. The effectiveness of the ASD approach is demonstrated by simulation and experimental results on a cantilever beam and a base plate subjected to acoustic excitation.

NUMERICAL SIMULATION PROCEDURE

High precision equipment in clean rooms are subjected to relatively high acoustic noise levels. The acoustic noise spectrum of clean room air-conditioning systems usually dominates at frequencies around the 125 Hz 1/3rd octave band, reaching levels of up to 85 dB [1]. For many high precision mechatronic applications this implies that both the rigid body motion and the first internal resonance of a machine are excited significantly.

The nature of the acoustic noise in clean rooms is such that the acoustic sound fields are impinging random from all directions, called a diffuse sound field. In this section we will postulate an expression for the determination of the acoustic sensitivity of structures due to a diffuse sound field. The expression will be applied in the next section "Simulations and experiments".

For linear systems there exists a relationship between the sound radiated by a vibrating mechanical system and the reciprocal problem, i.e. a mechanical system excited by sound. Following Cremer, Heckl and Petersson [2] the following relation can be derived

$$\frac{|v'|^2}{|p'|^2} = \frac{8\pi}{k^2\rho^2 c}\frac{P_{rad}}{|F|^2} \qquad (1)$$

where $|v'|^2$ is the structural velocity response squared at a certain point A of the structure due to a diffuse acoustic sound field with a (spatially averaged) sound pressure level $|p'|^2$ (the sound incidence case), whereas P_{rad} is the acoustic sound

power which is radiated by a force F acting on the same point A (the sound radiation case).

Relationship 1 can be used to determine the sensitivity of a structure to a diffuse acoustic field, expressed mathematically as $|v'|^2/|p'|^2$, simply by performing a reciprocal numerical experiment in which a mechanical force F acts upon the structure (at the point where we want to know the structural response due to the acoustic excitation) and determine the acoustic power P_{rad} radiated by the structure. In other words, the response of a structure may be determined from its radiation (and vice versa), provided a point force is employed and the incident sound field is random i.e., all directions of incidence are equally probable. For the interested reader reference is made to Roozen [3], [4] who used a similar approach.

Equation 1 will be used in the following section to calculate the sensitivity of structures due to acoustic excitation.

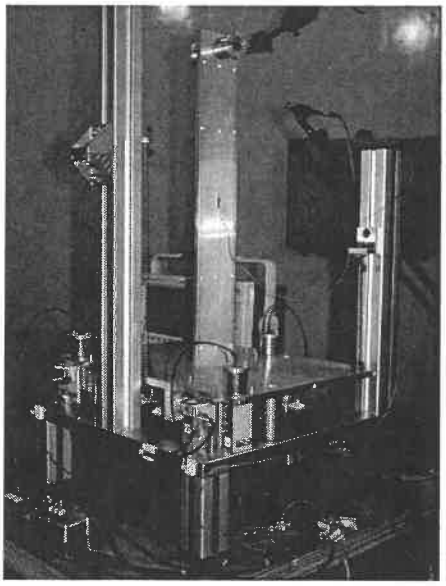

FIGURE 1. Experimental set-up subjected to diffuse acoustic field in a reverberant room

SIMULATIONS AND EXPERIMENTS

A relatively simple structure consisting of a cantilever beam and a base plate is investigated. The structural dynamics of this test set-up is typical for high-precision mechatronic systems in terms of its eigenfrequencies; the base plate is suspended with springs, as shown in Figure 1, resulting in suspension eigenfrequencies at around 1 Hz, whilst the first structural mode is at about 40 Hz, which is a mode for which the beam deforms relative to the base plate. Furthermore, the system is equipped with the standard components for active damping, as will be discussed in the next section. During the experiments discussed in this section, however, the active damping system is not activated.

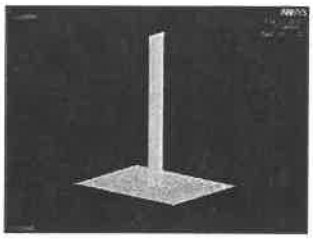

FIGURE 2. Finite element model of base plate and cantilever beam

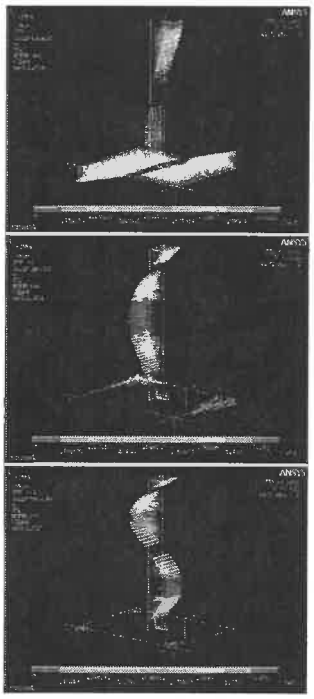

FIGURE 3. Finite element model results showing the first three cantilever bending modes

A finite element model of the base-plate and cantilever beam was made, as shown in Figure 2. The first three (non-suspension) structural modes, including the already mentioned 40 Hz bending mode of the beam relative to the base plate, are shown in Figure 3. The numerical model predicts structural resonances at 43 Hz, 186 Hz and at 536 Hz. These three internal structural resonances as well as the six suspension modes with eigenfrequencies smaller than 1 Hz are used as a modal base for the description of the structural behavior of the mechanical system

under investigation. A specific point of interest is the vibration of the tip of the cantilever beam. During the experiments a geophone mounted at the tip of the cantilever beam is used to measure the acoustically induced vibrations in a reverberant chamber test. For this reason, we are specifically interested in the structural dynamics at that point.

The test set-up was excited by a diffuse acoustic field in a reverberant room as shown in Figure 1. The reverberant room has a net volume of approximately 300 m^3.

Figure 4 compares the measured transferfunction from microphone pressure to geophone velocity with the numerically predicted result for the diffuse sound field excitation. The cumulative power spectra of the squared velocity over the squared acoustic pressure is given in Figure 5. Though the cumulative spectra look similar, there is a difference in the level of the measured and predicted cumulative power spectra, especially around the 60 Hz resonance. The reason for this discrepancy is most probably due to the rather difficult type of measurement in the reverberant room. Above 80 Hz the acoustic mode density of the room is sufficiently high for the acoustic field to be diffuse. Below this frequency the measurements are unreliable, causing this discrepancy. It can be noted that above 80 Hz, the measurements and simulations agree reasonably well.

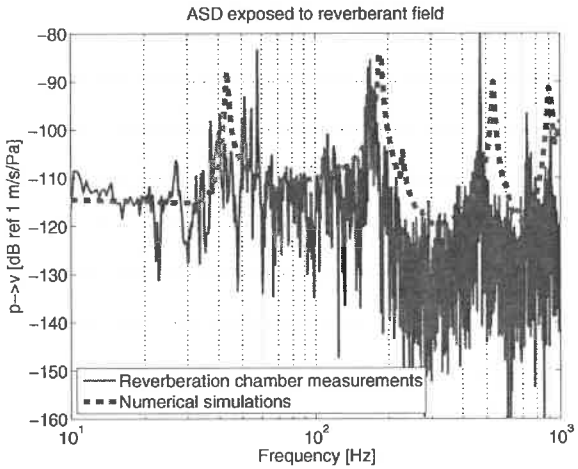

FIGURE 4. Measured and predicted transfer function from microphone pressure to geophone velocity, tip cantilever beam, reverberant field

ACTIVE STRUCTURAL DAMPING

The control of acoustically induced vibrations in high precision equipment can be done effectively

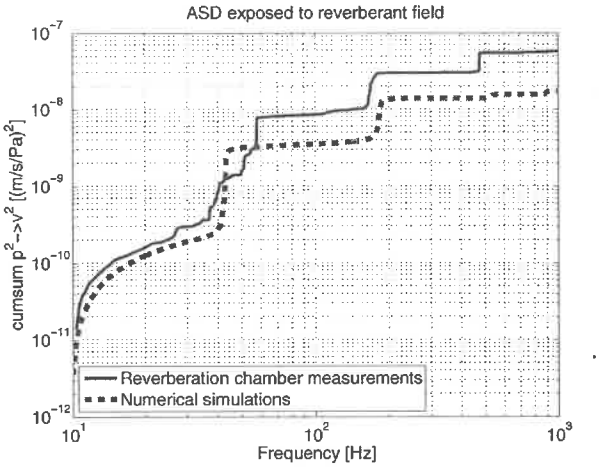

FIGURE 5. Cumulative sum of geophone velocity squared over pressure squared, reverberant field

by damping the structural resonances. "Sky hook damping" is a widely accepted method to damp suspension modes of a mechanical system in an active manner. However, in the tuning process of the sky hook damping the internal structural modes, which are the modes specifically excited by acoustic excitation rather than the suspension modes, generally show up in the open loop as parasitic dynamics. Fortunately, from a controller point of view this implies that those parasitic structural modes are both 'controllable' and 'observable'. The active structural damping (ASD) approach presented in this paper utilizes the presence of 'parasitic dynamics', and turns this into an advantage by creating active damping for those modes. Key is the implementation of a controller that uses the controllability and observability of the internal structural modes, so as to damp those modes. Furthermore it was found that an addition of a phase lag in the controller can significantly increase the achievable damping of the internal structural modes.

An extensive discussion of the ASD approach is beyond the scope of this paper. In this paper the major conclusions will be presented, with reference to [5] for a more detailed discussion.

The proposed method was tested by means of the test rig as shown in Figure 6. The test rig is equipped with the standard components for active suspension damping. The base plate houses 6 Lorentz actuators and 6 geophones for velocity measurements. For the initial measurements the first structural mode around 43 Hz is defined

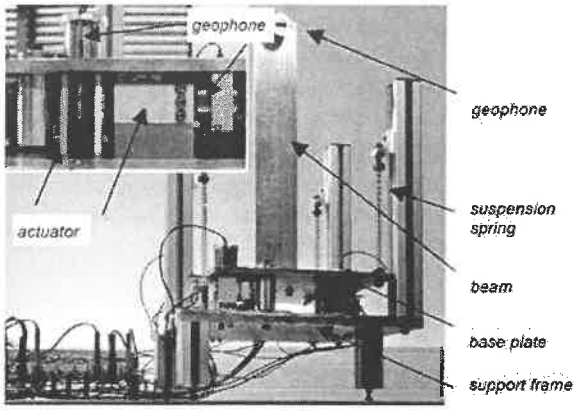

FIGURE 6. Experimental set-up. The beam height is 0.5 meter. Inset: detail of two collocated actuator-sensor pairs

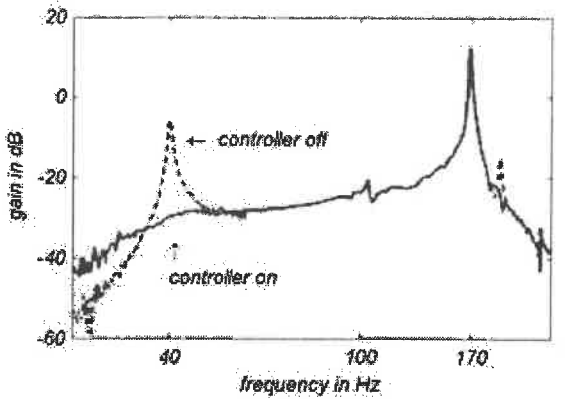

FIGURE 7. Frequency response function from excitation voltage loudspeaker to beam-tip velocity. Dotted line: controller off, solid line: controller (low pass) on. Note: y-axis with arbitrary scale.

as the relevant structural mode, and one, vertical oriented actuator-sensor pair on a corner of the base plate will be used to dampen this structural mode. Applying DVF (direct velocity feedback), using a standard controller implementation without additional phase lag, resulted in 15% critical damping. This is confirmed with a model of the fitted plant. By adding a low pass filter to create phase lag, a relative damping of up to 39% critical was reached with manual loop shaping of the plant model. The effectiveness of the active damping is illustrated with a measurement of the following frequency response function. The system is excited by means of a nearby placed loudspeaker and the resulting velocity of the top of the beam is measured (using an additional geophone, not used by the controller). The reference signal for the measurement is the input signal of the loudspeaker. In Figure 7 the frequency response function from 'excitation voltage' to measured velocity is shown, with and without feedback. The influence of the feedback loop with extra phase lag in the controller on the 40 Hz mode is clearly visible. A more detailed discussion about the controller implementation can be found in [5].

CONCLUSIONS

A numerical procedure to predict the disturbances due to acoustic excitation of machinery is presented. The procedure appears to be a numerically efficient way (both in terms of CPU and in terms of disk usage) to predict the structural response due to diffuse sound field excitation. The procedure was validated on a relatively simple structure consisting of a cantilever beam and a base plate that represents the typical structural dynamics of a practical high-precision mechatronic system. The correspondence between experiments in a reverberant room and the numerical predictions were satisfactory.

By means of the ASD Active Vibration Damping concept, employing an additional phase lag in the controller, the acoustically induced vibrations can be controlled effectively.

REFERENCES

[1] Gendreau M. Effect of acoustic noise on optical tools. In: SPIE Conference on Current Developments in Vibration Control for Optomechanical Systems, Denver, Colorado; 1999. .

[2] Cremer L, Heckl M, Petersson BAT. Structure-borne sound. Springer; 2005.

[3] Roozen NB, Verhaar BT, Rijs RMG. Acoustic excitation of mechatronic systems. In: 12th International Congress on Sound and Vibration, Lisabon. IIAV; 2005. .

[4] Roozen NB, Verhaar BT, Vervoordeldonk MJ. Acoustic excitation of mechatronic systems by diffuse acoustic sound fields; Numerical predictions and measurements. In: Proceedings of ISMA 2006, Leuven, Belgium; 2006. .

[5] Vervoordeldonk MJ, van Eijk J, Roozen NB. Active Structural Damping in high-precision equipment. In: Proceedings of ISMA 2006, Leuven, Belgium; 2006. .

A NOVEL MICROMILLING TECHNOLOGY BASED ON SINGLE-POINT TOOL TIP GEOMETRY

Eberhard Bamberg, Sumet Heamawatanachai
Precision Design Laboratory, Department of Mechanical Engineering
University of Utah
Salt Lake City, UT, USA

INTRODUCTION

To machine increasingly smaller features with defined geometry tools such as end mills, manufacturing the tool becomes increasingly more difficult. This is due to the complex geometry of end mills which typically involve two or more helical flutes on the outside diameter of the tool. The flutes, which are difficult to make to begin with, reduce the stress carrying cross section of the end mill, thereby increasing the likelihood of tool breakage, especially for very small tool diameters of 0.2 mm and less [1]. Also, it has been observed that micro end mills are prone to chip clogging, which then leads to breakage of the tool [2]. The novel micromilling technique presented in this paper has elements similar to ultrasonic face milling [3], yet its cutting mechanism is based on a single-point tool-material interaction, which is very different from anything existing. The reduced stresses from single-point tools compared to standard cylindrical tools has been shown in diamond turning to enable ductile material removal of otherwise brittle materials such as silicon [4-5]. This greatly increases the surface quality to the mirror-type surface finish that diamond turning is known for.

CUTTING MODULE

This novel micromilling technology is based on single-point diamond tip milling which can be used to machine microsized features into a wide range of materials ranging from polymers, through metals to glass. The unique characteristic of this technology is that the cutting velocity is not created by rotating the tool tip about its axis of rotation. Instead, the cutting motion is generated by actuating the tool tip on a recirculating, microscopic trajectory at high frequencies. This allows a standard 3-axis setup to generate the macroscopic motion required for the tool path while at the microscopic level, the cutting motion and the tool tip path are being generated by the tool itself. As a result, truly three-dimensional part geometries at the micron level with exceptional surface finish and part accuracy can be created.

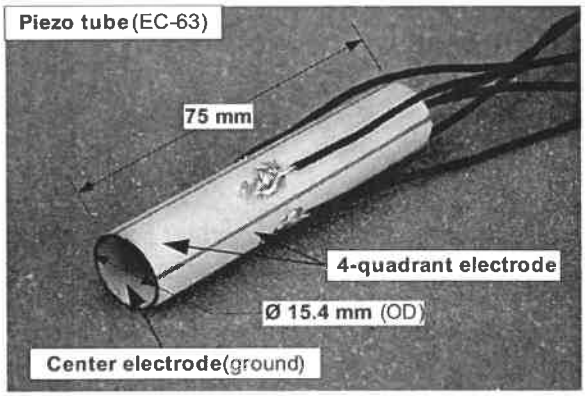

FIGURE 1. The ceramic piezo tube scanner (PZT) with four electrodes on the outside surface and the center ground on the inside surface.

The microscopic motion of the tool tip is achieved by a 75 mm long piezo tube scanner (PZT) shown in FIGURE 1.) and is made from EC-63 ceramics with an outer diameter of 15.4 mm and a wall thickness of 0.79 mm with four external electrodes. By energizing the four electrodes with time-varying voltages that range between 0 and -1000 V, periodic bending of the free end of the tube is achieved. If the voltages are sinusoidal with a phase lag of 90 degrees between adjacent electrodes, the resulting periodic bending creates a planar, orbiting motion with a maximum radius of 35 μm that is perpendicular to the PZT's axis.

The concept of the voltage generation is shown in FIGURE 2.) and consists of a National Instruments DAQ card (PXI-6040E) and four high-voltage piezo amplifiers (PI E-507.00) which amplify the 0 - 10 V analog waveforms by a factor of minus 100 to produce the 0 to -1000 V used to drive the PZT.

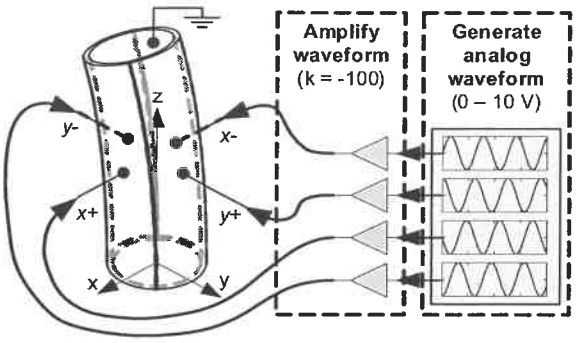

FIGURE 2. The PZT is actuated by analog voltages that vary from 0 to -1000 V.

Since the orbiting motion is planar, the machined surface is flat, making this cutting mode the equivalent of a miniaturized fly cutter, whose tool tip offset from the axis of rotation can be varied during cutting simply by varying the amplitude of the driving voltages (FIGURE 3.).

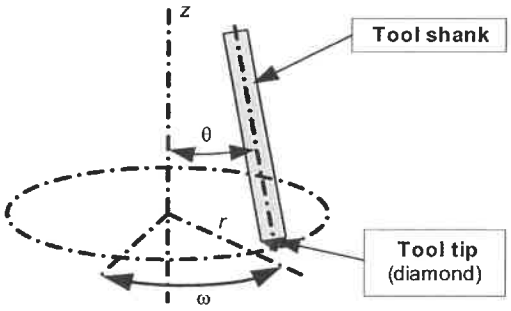

FIGURE 3. The cyclic bending of the PZT generates a planar, orbital motion similar to a fly cutter.

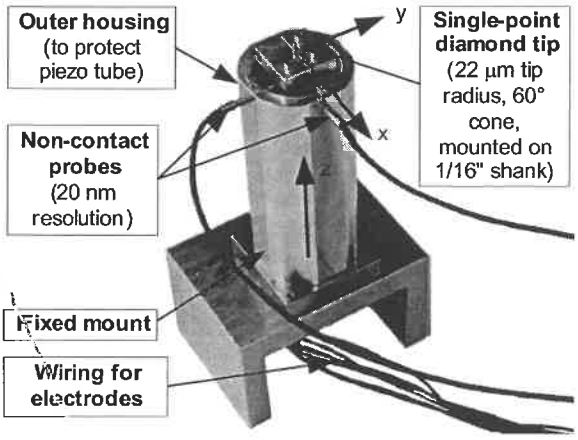
Outer housing (to protect piezo tube)
Non-contact probes (20 nm resolution)
Fixed mount
Wiring for electrodes
y
x
Single-point diamond tip (22 µm tip radius, 60° cone, mounted on 1/16" shank)

FIGURE 4. The cutting module prototype consists of the PZT, a housing to protect the tube, a clamp to hold the tool shank, and non-contact probes to monitor the cutting motion.

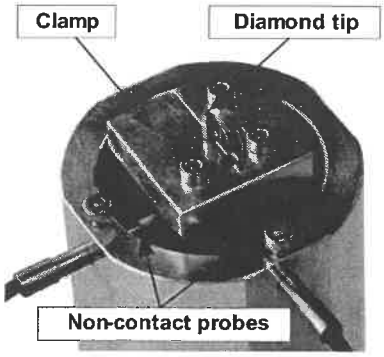

FIGURE 5. A clamp holding the tool shank is mounted to the free end of the PZT.

TOOL PATHS

While applying properly timed sinusoidal voltages creates cyclic bending that will result in a circular orbiting motion of the free end (FIGURE 3.), other modes of actuation are possible as well. For example, the magnitude of the x- and y voltages can be varied as shown in EQ. (1), resulting in different amplitudes in both directions. This would lead to an elliptical tool path as shown in FIGURE 6.).

$$x+ = V_{1x}\sin(\omega t) \qquad \text{EQ. (1)}$$
$$x- = V_{1x}\sin(\omega t + \pi)$$
$$y+ = V_{1y}\cos(\omega t)$$
$$y- = V_{1y}\cos(\omega t + \pi)$$

Even more complex tool paths can be generated if the length of the tube is manipulated as well. For example, the length of the tube can be shortened or lengthened by applying the same voltage to all four electrodes. This causes the tool to change its position in the z-axis (the height). Overlaying such a voltage on top of the primary voltage then causes orbiting of the tool tip while simultaneously allowing its height to be changed. The voltage that is applied to manipulate the

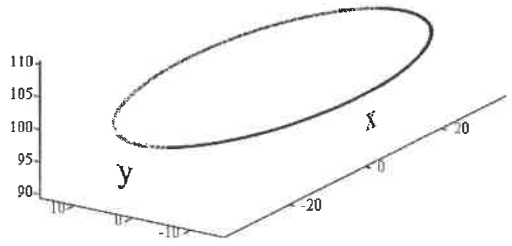

FIGURE 6. Plane, elliptic motion as a result of voltages shown in EQ. (1).

length of the PZT tube is referred to as the secondary voltage V_2.

$$
\begin{aligned}
x+ &= V_1 \sin(\omega t) + V_2 \cos(\omega t + \varphi) \qquad \text{EQ. (2)} \\
x- &= V_1 \sin(\omega t + \pi) + V_2 \cos(\omega t + \varphi) \\
y+ &= V_1 \cos(\omega t) + V_2 \cos(\omega t + \varphi) \\
y- &= V_1 \cos(\omega t + \pi) + V_2 \cos(\omega t + \varphi)
\end{aligned}
$$

The sinusoidal secondary voltage V_2 in EQ. (2) causes a tilt of the orbiting motion. The orientation is determined by the phase lag φ. For φ=0, the tilt will be about the y-axis while φ=90° results in tilt about the x-axis (FIGURE 7.).

The resulting tilted motion allows tapered surfaces to be machined without the need for tilting the work piece (or the spindle) or the use of a tapered end mill. The tilt angle is easily adjustable by varying the magnitude of the secondary voltage while the orientation of the tilt with respect to the z-axis is easily adjusted by the phase lag φ in the secondary voltages V_2.

CONTROL

The analog voltages that drive the PZT are generated with a National Instruments card that is controlled by LabVIEW. The card used for the prototype only has two analog channels which produce two sinusoidal waveforms with a 90° phase. These voltages drive the x+ and y+ electrodes. To generate the voltages required to power the x- and y- electrodes, a separate circuit with op-amps was used to invert the voltages, thereby creating the required 180° phase between the positive and negative electrodes such that the x-axis electrodes are driven by the same voltage but with a 180° phase lag. The LabVIEW control VI is shown in FIGURE 8.) and

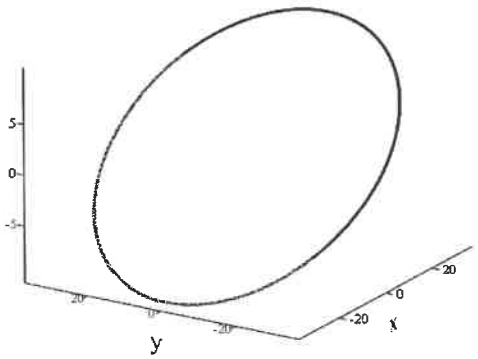

FIGURE 7. Orbiting motion tilted about the x-y plane as a result of voltages shown in EQ. (2).

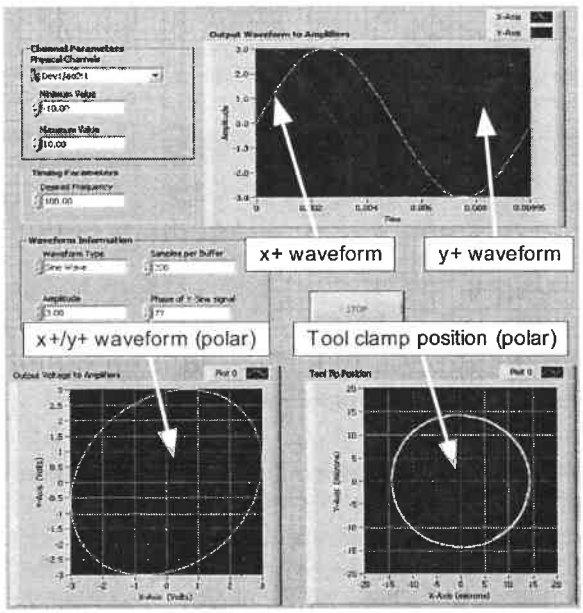

FIGURE 8. LabVIEW VI showing the two sinusoidal waveforms for the two positive electrodes and the resulting motion of the tool clamp.

illustrates the two sinusoidal waveforms that generate the driving voltage for the two positive PZT electrodes, x+ and y+. Also shown is the circular motion of the tool clamp as measured by the non-contact probes.

From FIGURE 8.) it is interesting to note, that the polar plots of the x+/y+ waveform and the resulting tool motion don't match. While the tool motion is clearly circular, the driving voltage to generate this motion is shaped like an oval with a phase of 77° between the two waveforms. This is most likely the result of manufacturing and assembly tolerances but also due to variations in material properties of the PZT itself.

MACHINING EXPERIMENTS

To demonstrate the machining ability of the prototype, the cutting module was mounted on a 3-axis micro-EDM machine (Optimation Profile 24P) that is equipped with an x-y stage that is driven by piezoelectric linear motors and encoders with a resolution of 100 nm. Five different materials in the form of flat stock were machined. These were: acrylic (polycarbonate), pure copper, stainless steel (304), titanium-alloy (Ti-6Al-4V), and glass. A 2-1/2-D tool path was programmed to machine a microfluidic-type feature with outer dimensions of 450 x 450 microns. This feature milled into stainless steel to a depth of

15 μm is shown in FIGURE 9.) with a surface roughness of 0.138 μm R_a. The same feature machined in pure glass is shown in FIGURE 10.) with a comparable surface finish. Both features were machined at a feed rate of 5 μm/s, a depth of cut of 5 μm and a 10 μm step over between passes.

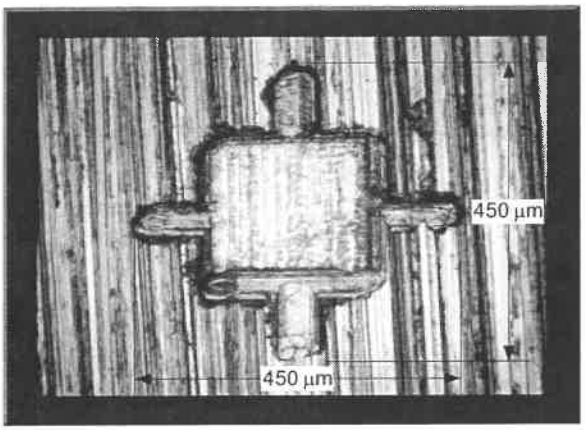

FIGURE 9. Intensity plot of microfluidic feature of size 450 x 450 μm in stainless steel.

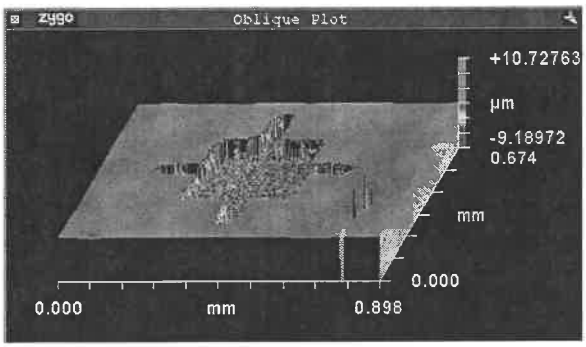

FIGURE 10. 3D view of microfluidic feature machined into glass. The surface roughness was measured as 0.184 μm.

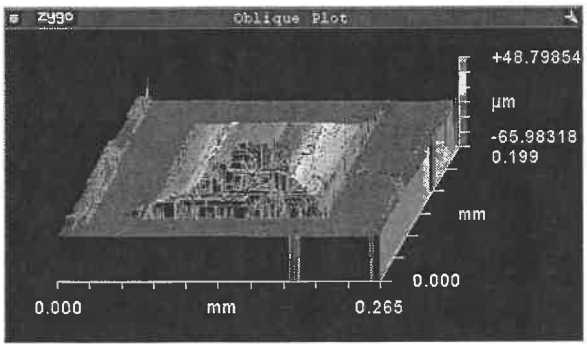

FIGURE 11. 100x100 μm pyramid with a height of 107 μm milled into pure copper. The Ra surface roughness of the machined bottom is 0.294 μm.

This was followed by a 3-dimensional tool path that cut a 100 x 100 micron pyramid with a total height of 100 microns in pure copper. FIGURE 11.) depicts a white light interferometer scan of the feature. The top surface (shown in red) is the material surface. The bottom of the pyramid is milled to a depth of 107 μm. The excellent R_a surface finish of less than 0.294 μm and the detailed shape of the pyramid are clearly visible.

CONCLUSIONS

This novel micromilling technique is based on single-point diamond tips that are actuated at the microlevel by a piezo tube scanner. The resulting tool tip paths, which are used to generate the cutting motion, have a maximum amplitude of 35 microns and a maximum frequency of 200 Hz. By actuating the tool tip on its own, recirculating tool paths, the cutting speed is decoupled from the feed speed, making this the equivalent of a miniature fly cutter. Machining experiments with ductile and brittle materials were conducted and the machined features showed excellent surface roughness and part accuracies. As a novel micromilling technique, this tool is intended for the prototyping of small parts in typically difficult to machine materials.

ACKNOWLEDGMENTS

The authors would like acknowledge the financial support by the University of Utah Seed Program.

REFERENCES

[1] I. Tansel, O. Rodriguez, M. Trjillo, E. Paz, W. Li, "Micro-end-milling - I. Wear and Breakage", International Journal of Machine Tool and Manufacture, 38 (1998), pp. 1419-1436.

[2] W. Koenig, K. Kutzner, U. Schehl, "Tool monitoring of small drills with acoustic emission", International Journal of Machine Tool and Manufacture, 32 (1992), pp. 487-493.

[3] Z.J. Pei, P.M. Ferreira, "An experimental investigation of rotary ultrasonic face milling", International Journal of Machine Tool and Manufacture, 39 (1999), pp. 1327-1344.

[4] P.S. Pizani, R. Jasinevecius, J.G. Duduch, A.J.V. Porto, "Ductile and brittle modes in single-point-diamond-turning of silicon probed by Raman scattering, Journal of Materials Science Letters, 18 (1999), pp. 1185-1187.

[5] J.A. Patten, W. Gao, "Extreme negative angle technique for single point diamond nano-cutting of silicon", Precision Engineering, 25 (2001), pp. 165-167.

A NOVEL METHOD FOR THE ON-CENTER TURNING OF TIGHTLY TOLERANCED MICRO ARRAYS

David D. Gill[1], Alan Hsu[2], Gordon A. Keeler[2], William C. Sweatt[3]
[1]Mesoscale Manufacturing and Systems Development
[2]RF / Optoelectronics
[3]Applied Photonic Microsystems
Sandia National Laboratories
Albuquerque, NM USA

ABSTRACT
Sandia National Laboratories has developed a means of manufacturing high precision aspheric lenslet arrays turned on-center. An innovative chucking and indexing mechanism was designed and implemented which allows the part to be indexed in two orthogonal directions parallel to the spindle face. This system was designed to meet a need for center to center positioning of 2μm and form error of λ/10. The part utilizes scribed orthogonal sets of grooves that locate the part on the chuck. The averaging of the grooves increases the repeatability of the system. The part is moved an integral number of grooves across the chuck by means of a vacuum chuck on a tool post that is mated to the part and holds the part while the chuck repositions to receive the part. The current setup is designed to create as many as 169 lenslets distributed over a 3mm square area while holding a true position tolerance of 1μm for all lenslets.

INTRODUCTION
An R&D project at Sandia National Laboratories has a need for the manufacture of high precision micro arrays. The arrays are to be used in a complex optical assembly that is integrated with high speed optoelectronics. The micro lenslets are hyperbolic aspheres with an aperture of 220μm and are in an array with 250μm pitch spacing. A larger array of optics is also required for the backside and these optics are 910μm diameter and are positioned on a 1mm pitch spacing. Performance requirements for the array required that the radial true position tolerance for each lenslet be 2μm, the axial position tolerance be ±1μm, and the form tolerance be λ/10 for 1550nm light. The system required as many as 169 optics in a 3mm x 3mm area and also included total internal reflection (TIR) rooftop prisms to be cut in alignment with the arrayed aspheres. It was also required that a positioning system be integrated into the arrays so that they could be aligned with other optical arrays on the backside and with the optoelectronics package as well.

Evaluation of the requirements revealed that single point diamond turning (SPDT) was the preferred manufacturing method to meet the demanding requirements. Other potential manufacturing methods included diamond milling which would have required significant development to meet the form requirements, and grayscale lithography which was incapable of achieving the significant sag of the larger lenses and had form accuracy no better than ±1%. In order to meet the demanding requirements using SPDT, the Zia fixture system was developed.

THE ZIA FIXTURE SYSTEM
The Zia fixture system is shown in Figure 1 and is named after the Zia sun symbol found in historic Native American art and on the New Mexico state flag. The Zia fixture allows a part to be moved around the chuck in precise 250μm increments. Each time the part is repositioned, a new aspherical lenslet can be turned on-center.

The Zia Fixture
The Zia fixture contains a circular vacuum chuck system surrounded by 4 pillars with Vee grooves. Two of the sets of Vee grooves are horizontal and the other two sets are vertical which causes the fixture to look like the zia symbol. The vacuum chuck was designed using the foundational principles of precision chucks with a series of 75μm wide lands separated by 300μm wide grooves. The groove width was designed to allow adequate vacuum area while minimizing deflection of the 1mm thick plastic substrates. The land width is chosen to allow adequate support while minimizing the area on which dust and contaminants may gather which

would prevent intimate part contact with the vacuum chuck.

The 4 square pillars surrounding the vacuum chuck each have 9 grooves scribed into the top. These grooves are cut with the machine spindle in "C-Axis servo" mode at 0°, 90°, 180°, and 270°. The parallel grooves have a 250µm pitch to match the required pitch spacing of the lenslets. These grooves help to ensure that the optic will move in 250µm increments. While the positioning of the array is not kinematically determinant, it relies on the principle of averaging to achieve highly repeatable positioning of the polymer optics. The vee grooves on the towers are cut so that the optic will contact the vee grooves approximately 1µm above the vacuum chuck. This is done to ensure that the optic is well positioned before it is pulled into contact with the vacuum chuck (which deflects the part as much as 1µm). The lands of the vacuum chuck, the lands on the vee grooves, and the outer diamond turned surface are all cut to the same height. This allows the same fixture to be used when the parts have the Zia grooves machined into them as is used for machining the optical arrays. It also allows other projects to utilize the machine without having to remove and re-fabricate the chuck.

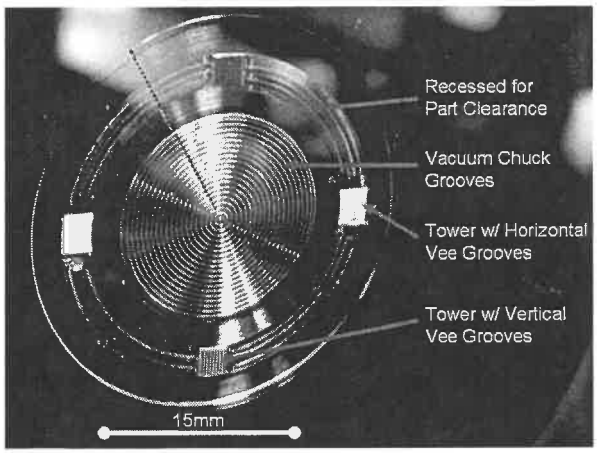

FIGURE 1. *The Zia fixture is shown with labels indicating the vacuum grooves and the horizontal and vertical positioning grooves.*

The Zia Part

The Zia part consists of aspheres cut into a 1mm thick disc of Zeonex E48R optical polymer. This disc is prepared by facing the backside of the part and cutting a circular recess into the part. This recess is the face that will contact the vacuum chuck. The raised ring around the recess has 24 vee grooves cut into it that will mate with the vee grooves of the chuck (having a pitch of 250µm). The recess is of sufficient diameter to allow the part to be moved as much as ±1.5mm in the vertical and horizontal directions. The 24 vee grooves in the part are also of sufficient number and sufficient length to allow the same range of motion.

There are two sets of aspheres that must be fabricated for this application. The first is an array of 16 aspheres in 4 rows of 4 lenslets. These small aspheres are 220µm diameter with a sag of 18.9µm. The system also requires large aspheres of 910µm diameter and 228µm sag. These large aspheres are cut in a 1x2 array. The two types of aspherical arrays are shown in Figure 2 with a penny for scale.

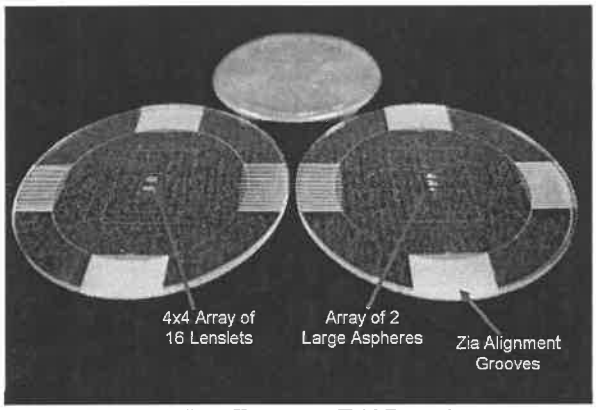

FIGURE 2. *The Zeonex E48R polymer parts are shown with a penny after the two types of lenslet arrays were machined into the top surfaces. The 4x4 array of smaller lenslets are 220µm diameter and the 1x2 array of larger lenslets are 910µm diameter. The Zia alignment grooves were used to move the part around the vacuum chuck in precise 250µm increments allowing each lens to be machined on-center.*

Using the Zia Fixture to Create Lenslet Arrays

The machining of an array of lenslets requires the use of the Zia fixture, the Zia polymer part, and an auxiliary vacuum chuck mounted by the tool posts. The auxiliary vacuum chuck is shown in Figure 3 where it is labeled as tool #5. It is mounted on a spring-loaded precision slideway so that it has some compliance in the axial direction of the machine spindle.

Initially, the part must be prepared by machining the faces to be parallel, adding the recessed portion on the back of the part, and putting in the

vee grooves of the Zia system In addition, features are added that are later used for dicing the part, assembling the system, and aligning the optics. The part back is machined with a large radius tool and a 90° included angle vee tool. Once the back is completed, the polymer part is flipped over and mounted on the vacuum chuck. In this process, a specific set of part grooves and corresponding fixture grooves must be utilized so that the part is correctly positioned with respect to location features machined into the back of the part. This is done using a high-magnification camera looking at the chuck through the part.

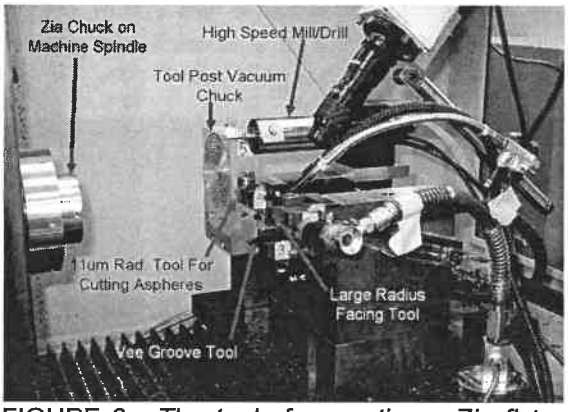
Zia Chuck on Machine Spindle
High Speed Mill/Drill
Tool Post Vacuum Chuck
11um Rad Tool For Cutting Aspheres
Large Radius Facing Tool
Vee Groove Tool

FIGURE 3. *The tools for creating a Zia fixture and part are shown in the machine. The part is passed from the Zia chuck on the machine spindle to the tool post vacuum chuck and back to displace the part in 250μm increments around the chuck. This allows the array's lenslets to be turned on-center.*

Once the part is in position, the spindle is set to free-running mode and an aspheric lenslet is machined into the part using a small radius diamond tool. Next, the spindle is returned to C-axis mode and positioned to 0°. The machine moves the spindle so that it is in position near the auxiliary vacuum chuck and slowly moves into contact with the auxiliary chuck. The vacuum on the auxiliary chuck is turned on, the vacuum for the spindle chuck is turned off, and the spindle is moved away from the part which is now positioned on the auxiliary chuck. The spindle is moved in the plane orthogonal to the spindle axis in increments of 250μm, and the spindle is moved back into contact with the part and the auxiliary vacuum chuck. The vacuum settings are reversed and the spindle chuck moves away with the part positioned in integer multiples of 250μm from its previous location. The spindle is returned to free-running mode and a new lenslet is machined.

Performance of the Zia Fixturing Method

The Zia fixturing system has shown good results for as much as has been measured. Measurements of the lens centers have shown the lenses to all have axial displacements of less than 2μm for a field of 16 lenslets spaced over a 1.5mm x 1mm area. The center-to-center position for the lenses has not yet been fully quantified, but will be reported in the oral presentation. An initial check of center-to-center spacing using an optical gaging system showed the array's desired 250μm spacing to have been met with an error of less than the ±1.5μm uncertainty of the measurement system.

During the machining of the arrays, the part can be moved off of center by as much as 2.1mm for machining at the extremes of the array. There was concern that this eccentric motion of the part would lead to excessive vibration during machining. However, the use of a low-mass part, a high stiffness air-bearing spindle, and a relatively massive chuck have prevented the part's eccentric motion from inducing substantial error in the part. A white-light interferometry image is shown in Figure 4(A) in which the form of the part is shown to be good with only a small center artifact remaining from tool centering. Outside of the center artifact, this lenslet measured a 250nm P-V form error, Figure 4(C) across the 200μm diameter of the lenslet. This form error was measured without removing tilt because the tilt of the lenslets with respect to each other is important to the performance of the system. This lens is representative of the lenslets produced thus far.

CONCLUSIONS

Zia, a novel manufacturing method, has been developed for the on-center turning of arrays of aspheric micro-lenses. The system allows the lenslets to be accurately machined on 250μm centers. The part is positioned in 4 sets of matching, orthogonal vee grooves machined into the fixture and polymer part. These grooves rely upon the principal of averaging to achieve accurate, repeatable positioning. Initial tests have shown the optics produced by the zia system to be positioned axially within 1μm of each other and radially to within the ±1.5μm uncertainty of the optical gaging system. Interferometry of the lenslets has shown the general form of the lenslets to have 250nm PV

error with a small remaining center artifact. Additional measurements of system capability will be presented in the oral presentation.

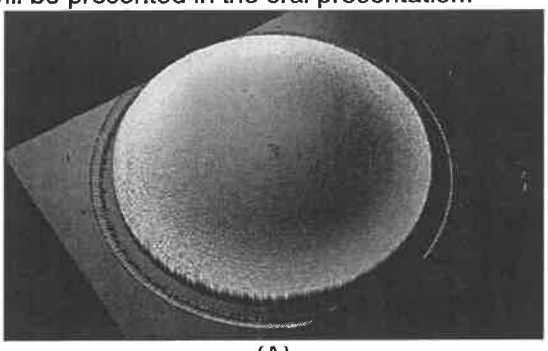

(A)

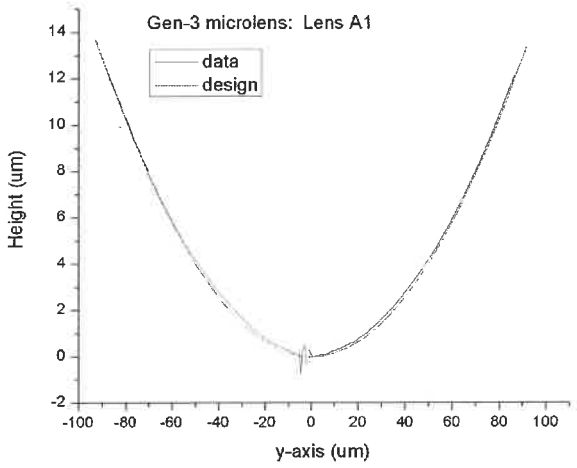

(B)

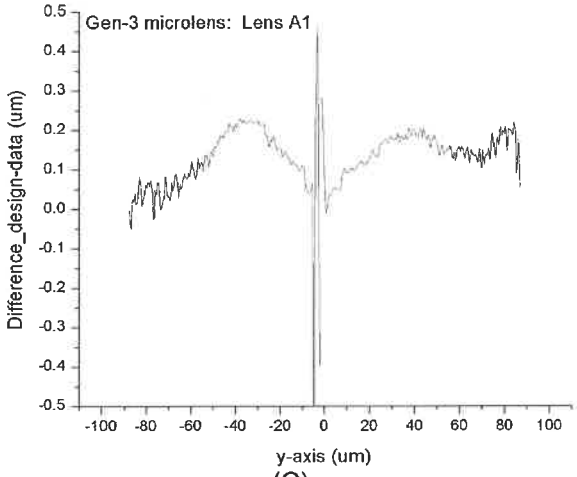

(C)

FIGURE 4. *White light interferometry measurements of a lenslet(A) from an array fabricated using the Zia system. A comparison of the measurement to the design data(B) show a form error of 250nm P-V (C) outside of a center artifact remaining on the lenslet.*

ACKNOWLEDGEMENTS

Sandia is a multiprogram laboratory operated by Sandia Corporation, a Lockheed Martin Company, for the United States Department of Energy's National Nuclear Security Administration under contract DE-AC04-94AL85000. The authors acknowledge the support of the National Information Assurance Research Laboratory in this work. The authors also wish to thank several colleagues for their teamwork in this project and in the continuing improvement of the Zia fixturing system. These colleagues are Darwin K. Serkland, Sayan D. Mukherjee, and Kent M. Geib, all of Sandia National Laboratories, RF/Optoelectronics organization.

MICRO ELECTRICAL DISCHARGE MACHINING USING A 5-DOF CONTROLLED MAGLEV ACTUATOR

Zhang X.[1], Shinshi T.[1], Endo H.[1], Shimokohbe A.[1]
Imai Y.[2], Miyake H.[2], and Nakagawa T.[2]
[1] Precision and Intelligence Laboratory
Tokyo Institute of Technology
Yokohama, Kanagawa Prefecture, Japan
[2] Advanced Technology R&D Center
Mitsubishi Electric Corporation
Amagasaki, Hyogo Prefecture, Japan

ABSTRACT
This paper describes a 5-DOF controlled maglev actuator to realize a high-speed micro electrical discharge machining (EDM). The actuator is sufficiently compact to be attached to conventional electrical discharge machines. It possesses a submicron and micro-radian positioning resolution, bandwidths greater than 100Hz in the 5-DOF directions, and a positioning stroke of 2mm in the thrust direction. Using this actuator, multi directional holes can be machined, and the machining speed can be improved.

KEYWORDS
Electrical discharge machining, Positioning
Maglev local actuator,

INTRODUCTION
In electrical discharge machining (EDM), the machining speed and accuracy are limited by the probability and efficiency of the electrical discharge. To improve the machining speed and accuracy, a combination of a conventional electrical discharge machine and a high-speed, high-precision local actuator, which can speedily re-position the electrode to obtain a stable electrical discharge, was proposed, as shown in Fig. 1 [1-3]. For this actuator, a positioning stroke of a few millimeters for rapid retraction of the electrode in at least one direction of motion is also necessary, in order to remove debris from around the electrode when holes with high aspect ratio are machined.

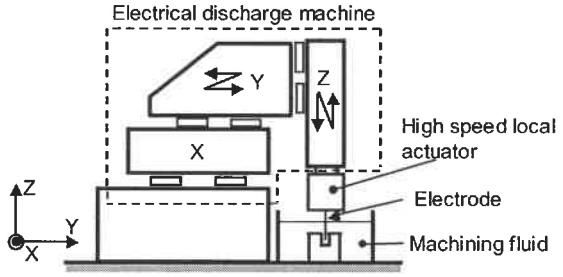

FIGURE 1. Electrical Discharge Machine with an Additional Local Actuator

To realize high speed positioning of the electrode with a stroke of a few millimeters, in this paper, we focus on the development of a wide-bandwidth, high-precision, millimeter-stroke, 5-DOF maglev local actuator to realize high-speed micro EDM. First, the principle of the maglev local actuator is described and its positioning performance is evaluated. Then, using this actuator, multi directional holes are machined and the machining speed is verified.

5-DOF CONTROLLED MAGLEV ACTUATOR
Fig. 2 shows the proposed 5-DOF controlled maglev local actuator. It primarily consists of a voice coil motor type of thrust magnetic bearing with a positioning stroke of a few millimeters, a pair of reluctance type radial magnetic bearings, an air motor and brushes for the voltage supply. Using the thrust and radial magnetic bearings, the spindle shaft can be levitated and positioned

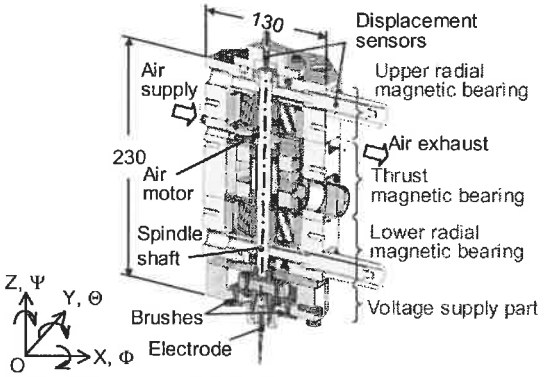

FIGURE 2. 5-DOF Controlled Maglev Local Actuator

in 5-DOF (X, Y, Z, Θ and Φ), while, using the air motor, the spindle shaft can be rotated around the Z-axis without generating heat. The voltage for EDM is applied to the electrode via four brushes. The length of the actuator without an electrode and its attachment is 230mm and the width is 130mm. The total mass is about 26Kg.

POSITIONING PERFORMANCE

The positioning performances of the maglev local actuator are shown in Table 1. The actuator exhibits a submicron and micro-radian positioning resolution, bandwidths greater than 100Hz in the 5-DOF directions, and a positioning stroke of 2mm in the thrust direction. During EDM of holes with high aspect ratio, the rapid retraction of the electrode can be realized to introduce fresh machining fluid into the hole and wash away debris.

TABLE 1: Positioning Performances of the Maglev Local Actuator

	X direction	Θ direction	Z direction
Bandwidth	200Hz	150Hz	110Hz
Positioning resolution	0.25μm	4.0μrad	0.5μm
Full stroke	±100μm	±1.0mrad	±1mm

EDM EXPERIMENTS

EDM System

In order to improve the machining speed of EDM, the maglev local actuator was attached to an electrical discharge machine (EA12E, Mitsubishi Electric Corp.). In the experiments, the electrical discharge machine was used only to move the electrode to the initial position and to supply the voltage to the electrode. The electrode was controlled solely by the local actuator.

A cylindrical shaped copper electrode with a diameter of 1mm was used and was not rotated or retracted during EDM in this experiment. The machining fluid was EDF-K (Nippon Oil Corp.), and the workpiece was age-hardened mold steel, which has a hardness of 40HRc (NAK80, Daido Steel Corp., Ltd.). The discharge circuit was an RC circuit with a resistance and capacitance of 1.1KΩ and 0.01μF, respectively, and the open-circuit voltage was 120V. These were the conditions used for finish machining.

During EDM, the voltage between the electrode and the workpiece was controlled. A block diagram of the EDM system is shown in Fig. 3.

The gap voltage, V, is amplified and averaged by a low-pass filter, and the average voltage, V_{fb}, is used as a feedback signal. The gain of the amplifier is -0.03 and the cutoff frequency of the low-pass filter is 500Hz. The deviation between the reference voltage, V_r, and the feedback voltage, V_{fb}, is sent to a PI controller to calculate the value, V_{ar}, which is used to position the electrode with respect to the workpiece. The reference $\boldsymbol{R}$ is the motion path of the electrode. To give a stable electrical discharge, the reference voltage, V_r, was set to 2.2V, and the values of P and I were set to 1.3×10^{-6} and 1.5×10^{-4}, respectively, by trial and error.

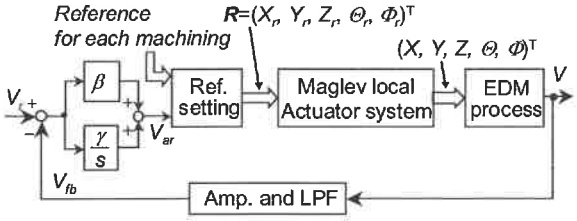

FIGURE 3. Block Diagram of the EDM System

EDM Method

Machining in the Thrust Direction

For machine small holes in the Z direction, the Z_r of the input reference $\boldsymbol{R}$ of the actuator system was set to V_{ar}, and X_r, Y_r Θ_r and Φ_r were set to zero. That is,

$$R=(X_r\ Y_r\ Z_r\ \Theta_r\ \Phi_r)^T=(0\ 0\ V_{ar}\ 0\ 0)^T \qquad (1)$$

The machining time was set to 300s. The bandwidths of actuator were set to 180Hz in the X and Y directions, and 100Hz in the other directions.

Moreover, an EDM experiment using a conventional electrical discharge machine only was carried out for comparison. In using conventional EDM, the EDM control system, the parameters of the PI controller and the machining conditions were set identically to those used for the maglev local actuator.

Machining in the Radial Direction

For machining in the radial direction, an L-shaped electrode was attached to the actuator, and the gap between the tip of the electrode and the workpiece in the X direction was controlled. Therefore, X_r of $\boldsymbol{R}$ was set to V_{ar}, and Y_r, Z_r Θ_r and Φ_r were set to zero, as given by Eq. (2).

$$R=(X_r\ Y_r\ Z_r\ \Theta_r\ \Phi_r)^T=(V_{ar}\ 0\ 0\ 0\ 0)^T \qquad (2)$$

The machining time was set to 60s and the bandwidths in all directions were set to 100Hz.

Planetary Machining

Small holes were machined in the Z direction while the electrode was driven in a circular path in the XOY plane. The diameter of the holes could be adjusted by changing the radius of the circular path. We call this technique planetary machining.

In planetary machining, ***R*** is given by Eq. (3).

$$R = (X_r\ Y_r\ Z_r\ \Theta_r\ \Phi_r)^T = (A\cos 2\pi ft\ \ A\sin 2\pi ft\ \ V_{ar}\ \ 0\ \ 0)^T \quad (3)$$

Where A and f are the radius and frequency of the circular path, respectively. The frequency of the circular path was set to 10Hz, and the radius was set to 30μm.

For a stable electrical discharge, the bandwidths of the actuator were experimentally tuned to 150Hz in the X and Y directions, 75Hz in the Z direction and 100Hz in the Θ and Φ directions. The machining time was set to 300s. Before machining holes, several trial EDM processes were carried out to increase the stability of the electrical discharge and the repeatability of the EDM.

Machining Results

Machining in the Thrust Direction

XY surface and XZ cross-section profiles of the machined holes are shown in Fig. 4. These were measured with a confocal microscope (HD100D, Lasertec Corp., 1.6mm×1.6mm region with 900×900pixels, 0.01μm resolution in terms of height). Using the maglev local actuator, the diameter and depth of the hole were 1.047mm and 0.283mm, respectively. On the other hand, using conventional EDM only, the diameter and depth of the hole were 1.041mm and 0.229mm, respectively.

For each EDM experiment, several holes were machined under the same conditions. Five holes except the holes influenced by large abnormal electrical discharge, were used for the sample data. The standard deviations of the diameter and depth of the five holes were 1.30μm and 1.69μm. Using conventional EDM only, the standard deviations of the diameter and depth were 4.42μm and 3.30μm, respectively. From these results, it can be seen that the variation in the hole profile was reduced by using the maglev local actuator. Thus, we consider the EDM with a local actuator to have better repeatability than a conventional EDM.

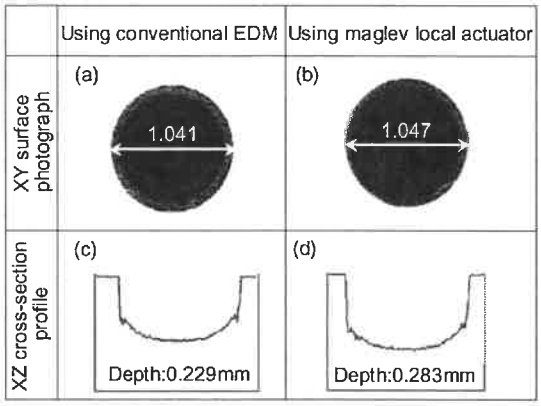

FIGURE 4. Machined Holes in the Z Direction

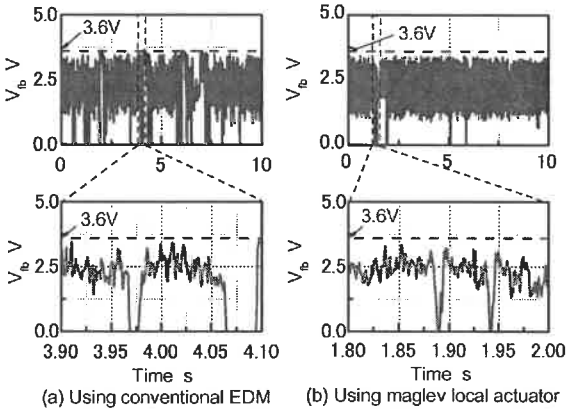

FIGURE 5. Feedback Voltage (V_{fb}) for Z Direction Machining

Defining the average machining speed as the ratio of averaged depth of five machined holes to machining time, the average machining speeds using the maglev local actuator and using only the conventional EDM were 0.95μm/s and 0.78μm/s, respectively. Thus, the average machining speed was improved by 21.8%.

To monitor the electrical discharge conditions, the feedback voltage, V_{fb}, was measured with a data recorder (EZ7510, NF Corp., resolution, 16bit) at a sampling frequency of 10 kHz, as shown in Fig. 5. A feedback voltage, V_{fb}, of 0V implies that the electrical discharge circuit is shorted. On the contrary, when the feedback voltage, V_{fb}, is equal to 3.6V, the electrical discharge circuit is open. i.e., the gap voltage is equal to the power supply voltage (120V) at this time. Comparing Fig. 5(a) with Fig. 5(b), it can be seen that the rate of incidence of short and open circuits decreases and the response of the electrode to these conditions is enhanced when using the maglev local actuator.

Machining in the Radial Direction

The YZ surface and XY cross-section profiles of the holes machined from the X direction are shown in Fig. 6. With a machining time of 60s, the depth of the holes using the maglev local actuator and using only a conventional EDM were 0.082mm and 0.021mm, respectively. Thus, the machining speed was improved by a factor of four.

From the results, it can be seen that the improvement made in the machining speed in the radial direction when using the maglev local actuator is much larger than that in the thrust direction. The reason is as follows. In a conventional electrical discharge machine, the X (radial direction), Y (radial direction) and Z (thrust direction) motions are realized by stacked one-DOF actuators as shown in Fig. 1. Due to the structure of the positioning mechanism, the mass of the moving parts in each direction increases in the following order Z, Y, then X. This makes high speed positioning more difficult, particularly in the X-direction. Since the maglev local actuator drives a small mass with nine distributed electromagnets, it is comparatively easy to have a wide bandwidth for each axis.

Planetary Machining

A planetary machining experiment to adjust the diameter of the holes was attempted. The machined hole is shown in Fig. 7. The diameter of the hole is 1.109mm. As the diameter of the circular path in the XOY plane was set to 60μm, the diameter of the machined hole increased by 62μm compared with the thrust direction machined hole shown in Fig. 4(b). This result, demonstrates that the diameter of the hole can be adjusted by the planetary motion of the electrode.

CONCLUSIONS

This paper describes a 5-DOF controlled maglev local actuator for micro EDM. The actuator is sufficiently compact to be attached to conventional electrical discharge machines. The actuator has a submicron and micro-radian positioning resolution, bandwidths greater than 100Hz in the 5-DOF directions, and a positioning stroke of 2mm in the thrust direction. Using this actuator, holes could be machined both in the thrust and radial directions, and the machining speed was improved compared with conventional EDM. Moreover, the diameter of the machined hole could be adjusted by using a planetary motion of the electrode.

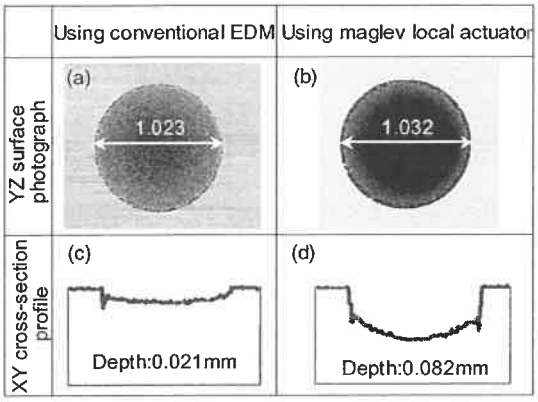

FIGURE 6. Machined Holes in the X Direction

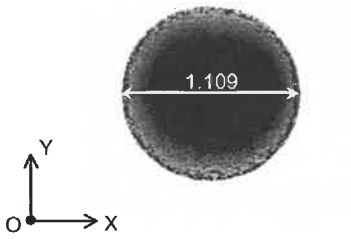

FIGURE 7. Hole Produced with Planetary Machining with a Circular Diameter of 60 μm

In future work we plan to evaluate the relationship between the machining speed and the bandwidth of the maglev local actuator, and investigate the machining of 3D microstructures.

ACKNOWLEDGMENT

This research was supported in part by Grants-in-Aid for Scientific Research (KAKENHI) from the Japan Society for Promotion of Science. The authors gratefully acknowledge the contributions of Mr. H. Morita for their support concerning the experiments.

REFERENCES

[1] Imai Y, Satake A, Taneda A, Kobayashi K. Improvement of EDM Machining Speed by Using High Frequency Response Actuator. International Journal Electrical Machining, 1996; 1: 21–26.

[2] Masuzawa T, Tanaka K, Fujino M. Study on the High Speed Machining by EDM Using a Moving Coil Head Type Feed Control. Proceedings of the 19th International MTDR Conference. 1978: 543-549.

[3] Imai T, Nakagawa T, Miyake H, Hidai H, Tokura H. Local Actuator Module for Highly Accurate Micro-EDM. Journal of Materials Processing Technology. 2004; 149: 328-333.

STUDY OF GAP CONTROL AND ELECTROSTATIC FORCE IN NANO ELECTRO MACHINING

Abdallah H. Alkhaleel[1], Murali M. Sundaram[1*], Kamlakar P. Rajurkar[1], and Ajay P. Malshe[2]
[1]Center for Nontraditional Manufacturing Research
University of Nebraska-Lincoln
Lincoln, NE 68588, USA
[2]Department of Mechanical Engineering
University of Arkansas
Fayetteville, AR 72701, USA

ABSTRACT

The potential of nanotechnology depends on the controllable fabrication, integration, and stability of nanoscale devices. The creation of nanoscale features is essential for the fabrication of these devices. This paper describes the use of the atomic force microscope (AFM) to electro-machine nano-cavities on copper samples. Using known interelectrode gap, cavities as small as 200 nm in diameter were machined. A study was conducted to check the stability of the machined cavities. The results showed that cavities were stable within the period of time of the study (48 hours) in both air and deionized water environments. Feature destruction when occurred was found to be due to mechanical forces exerted on the sample by the scanning tip during the repeated scanning of the sample. The effect of electrostatic forces on the machining process was examined as well. It was found that the application of low frequency excitations (KHz range) resulted in undesirable cantilever oscillations and hence high frequency excitations (MHz range) are prefered.

INTRODUCTION

Machining of nanoscale features has been of great importance in fabricating nanodevices. The ability to fabricate these features in a repeatable manner and the stability of the machined features are prerequisite for the manufacturing of functional devices. Many different processes have been developed for this purpose such as nano-imprinting, femto-second laser, and focused ion beam machining. These processes have limitations regarding the workmaterial and/or the cost. So there has been a growing interest in using scanning probe microscopes (SPMs) as cost effective alternative tools and they have been used in many different ways to perform sophisticated lithography [1, 2].

Nano-electromachining processes utilizing SPMs have been investigated and can be used to machine conductive materials regardless of their hardness. Scanning tunnelling microscope (STM) was used to generate nano-cavities on gold samples by electromachining [3]. Few attempts have used the AFM as a tool to directly electromachine nano-features. In previous work it was shown that electromachining of nano-cavities using the AFM is possible, and arrays of cavities as well as grooves were generated [4]. However, the gap distance between the tool and the workpiece during machining was not precisely controlled. Moreover, there was no consideration of electrostatic forces between the two electrodes. A well defined gap distance is necessary to have a reliable and repeatable machining process, and electrostatic forces tend to alter this distance. These two issues have been addressed in this work.

Electromachining involves the application of a voltage bias between two electrically conductive electrodes; a tool and a workpiece. This results in the creation of electrostatic forces between the two electrodes. In the case of AFM, this force tends to bend the cantilever leading to a change in the gap distance between the tool and the workpiece [5]. This change in gap distance is undesirable for the process repeatability. In electromachining it is necessary to avoid mechanical contact between the electrodes. This contact, if occurred, results in short circuits and may lead to destruction of both electrodes. In electromachining using AFM it is necessary to assure that the electrostatic forces do not pull the cantilever with distances more than the gap distance. In other words, it is necessary to minimize cantilever movement during machining.

* murali@ unl.edu

Stability of nanoscale features/devices is of major concern in nanotechnology [6]. It was necessary in this work to investigate the stability of the machined nano-cavities. These cavities will be of no use if they vanish after they are machined. In this stability study the investigation was conducted at room temperature.

This study aims to develop a better understanding of different aspects of using the AFM to directly electromachine nano-cavities. These machining aspects are: controlling gap distance, stability of the machined features, and the effect of electrostatic forces.

SYSTEM SETUP

Electromachining process requires electrically conductive workpiece, electrically conductive tool, machining media, and a power supply. Deionized water was used as the machining media. A copper film of about 100 nm thick was sputtered on a silicon substrate and used as the sample. The roughness of the sample was measured to be 0.26 nm (RMS). A MultiMode AFM was used as a platform to conduct experiments and for in-situ scanning. The AFM was set on a vibration isolation platform to reduce vibration. A pulse generator (Agilent Technologies # 81130A) with a maximum frequency of 600 MHz and a maximum voltage of 2.5 Volts was utilized as power supply.

The probe holder used was a fluid cell for the MultiMode AFM. The fluid cell was connected to the power supply through a plunger (a pin coiled with a spring located above the fluid cell and is in touch with the probe). The tip has a conical shape with a 30° angle and a tip radius of curvature less than 40 nm. The whole probe was coated with Ti-Pt coating which consists of a 10-nm Pt layer on a 20-nm Ti sub-layer (these coated probes are commercially available). A schematic diagram of the system setup is shown in Figure 1.

CONTROLLING GAP DISTANCE

Controlling gap distance between scanning tunneling microscope (STM) tip and the sample is a relatively easy method where a certain current can define the gap of zero level. The tip is then drawn the desired distance away from the sample even within the range of the effect of capillary forces. The case in AFM is different due to the difficulty of setting the gap to zero level because the capillary forces tend to bend the cantilever. So controlling this gap within the

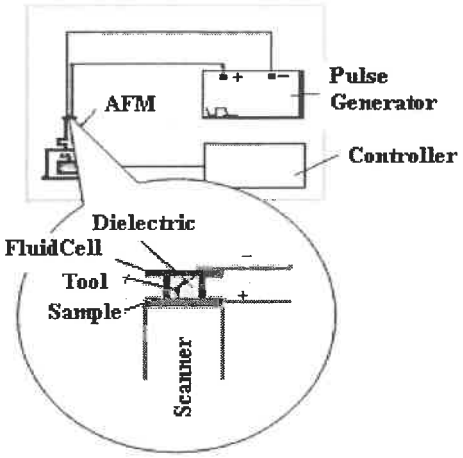

FIGURE 1. Schematic diagram of nano electromachining setup.

range of the capillary forces, which is a small range in liquid, is difficult. There are three suggested methods to control the gap distance outside the range of these capillary forces:

1. By activating the force mode, the ramping parameters can be adjusted so that the horizontal line which represents the gap distance is set to the desired value then the tool is ramped one more time to keep the tool steady at the specified height (Figure 2).

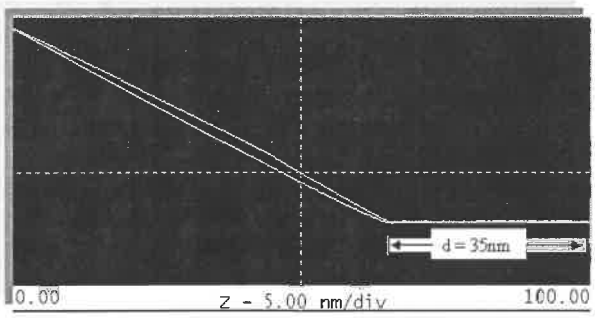

FIGURE 2. Force-distance curve utilized to control gap distance.

2. NanoScript™ macro Litho functions can be used to manipulate the tool. The vertical deflection of laser is first set to 0 V, and after engaging the tip, the NanoScript™ functions are utilized to set the set-point to 0 V resulting in minimal cantilever deflection, and this position defines the zero gap level. The tip is then withdrawn to the desired distance using an appropriate function.

3. By activating the force mode, the deflection sensitivity (nm/V) and the set-point (V) are recorded. Once the tip is engaged the NanoScript™ functions are utilized to withdraw the tip a distance equal the sensitivity times the set-point. This position defines the zero gap level, and then the tip is withdrawn the desired distance as mentioned before.

EXPERIMENTS

In order to machine cavities, the sample was scanned first in deionized water and an image was captured assuring clean and flat surface. The scan size was then changed to zero in case one cavity is to be machined. The gap distance was then set to the desired value and the voltage was applied between the tool and the workpiece. The scan size was brought back to its initial value and a new image was captured using the same tip. The image was then analyzed off-line to measure the dimensions of the machined cavity. The following discussion focuses on the stability study and the effect of electrostatic forces on machining.

Stability Study

Seven cavities were machined using a single tip as shown in figure 3 (a) where the scan size is 5 μm. These cavities were machined consequently from 1 through 7 and had depths of 53, 51, 36, 36, 31, 27, 17 nm in the same sequence. The same tip was then used to scan the machined area once every ten minutes for two hours to check their stability. It was found that the more the sample was scanned the more destruction occurred to the machined cavities. The force exerted on the sample during scanning was around 0.75 μN, which is high for typical contact mode scanning, but having a stiff cantilever was necessary to overcome the effects of the capillary forces. Figure 3 (b) shows the machined cavities two hours after the machining. It is clear that the cavities got wider, deeper, and distorted in shape. These cavities had new depths of 79, 65, 51, 53, 43, 43, 30 nm in the same sequence as before.

In order to check whether the friction force during scanning is responsible for features destruction or not, the experiment was repeated with a new tip and new cavities were machined. Scanning the sample was then performed as before but with one third of the scanning force. It was found that cavities dimensions had changed less than 1 %. This suggests that scanning itself is responsible for the destruction of cavities machined in the previous experiment.

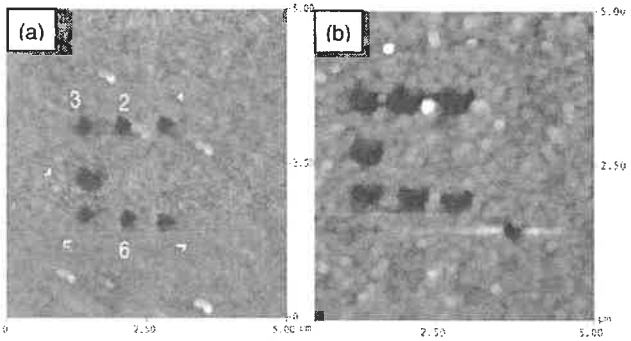

FIGURE 3. (a) Seven cavities machined using a single tip, (b) cavities after 2 hours.

In another experiment, a new tip was used to create a cavity and an image was taken immediately after machining. The sample was then left in deionized water for 24 hour and scanned again, and the cavity dimensions showed insignificant changes. The sample was then left in air for another 24 hours, and was scanned again and the dimensions of the cavity showed insignificant changes as well. The stability of the machined features is attributed to the oxidation layer formed on the copper surface which protects the cavity from possible chemical reactions.

To observe the effect of scanning on sample destruction, the sample was scanned ~ 100 times with a scan force of 0.5 μN. It was found that pitting occurred all over the scanned area and these pits propagated in size till finally the whole copper layer was removed from the scanned area exposing the Si base. Scanning another area with a force of 0.3 μN few times then increasing the scan size and scanning again with a force of 0.5 μN resulted in destruction and layer removal from the scanned area except the one that was first scanned with 0.3 μN force. The reason for this could be that the 0.3 μN force resulted in plastic deformation of the thin film and lead to an increase in the internal stresses leading to an increase in wear resistance of the thin film. It can be concluded from this work that electromachined nano-cavities are stable at least within the experiments time (48 hrs). It is to be noted that experiments that involve the use of contact mode AFM should use minimal scanning force to avoid destruction of the machined features.

Electrostatic Forces

At tip-sample separations of the order of several tens of angstrom the major interaction between the tip and the sample is the intermolecular interaction, i.e. the Van der Waals force. In the presence of liquid films, the interaction is influenced much by capillary forces. At larger separations the electrostatic interaction starts to dominate. Since machining requires a defined gap distance, studying the effect of the electrostatic forces is a necessity.

The cantilever can be modeled as system of a mass, spring, and a viscous damper. The application of 2 ms single pulse resulted in tip oscillation at the end of the pulse duration suggesting that the system is underdamped. The cantilever was subjected to periodic excitations/voltage pulses with 50 ns pulse duration (20 MHz). The applied force can be resolved into its components in terms of its Fourier series. This results in a DC component and harmonic components that have frequencies above 60MHz. Since the natural frequency of the cantilever was measured to be about 300 KHz, the application of forces of very large frequency makes the system unaffected by the applied harmonic force, because the period of excitation is very small so the system does not effectively sense the excitation of large enough forcing frequencies.

The force component left that affects the system is the DC component which is equivalent of the average of the pulsed force. The quantitative analysis of the electrostatic force between conductive sample and tip has been studied by researchers where DC volts were applied and the resulted electrostatic forces were measured by detecting the change in the amplitude of the oscillating tip [7], or by recording force-distance curves [8]. In the present work it was found that when an experiment was conducted with a gap distance set to 20 nm, and voltage pulses of 2.5 V of 50 ns pulse duration were applied, the tip deflection is less than 20 nm. This assures non-contact machining. Increasing the duty cycle from 10% to above 60% resulted in bubbles formation that interfered with the machining and the scanning processes. More research is needed to optimize the machining process in order to get faster machining by increasing the on-time pulse duration, at the same time working under electrostatic forces that don't change the gap distance significantly during machining.

SUMMARY

This work included methods to control the gap distance between the AFM tip and the sample. It also showed that electromachined cavities are stable within the period of the study and that feature destruction occurred when large scanning forces were used. Electrostatic forces were found to be of concern in maintaining a certain gap distance during electromachining. The use of ultrashort voltage pulses is suggested to minimize these forces. Further research is needed to quantify these forces and to optimize the machining process.

ACKNOWLEDGEMENTS

Authors acknowledge the support from NSF (awards numbers: DMI – 0331830 and DMI - 0423697).

REFERENCES

[1] Kim Y, Lieber C. Machining Oxide Thin Films with an Atomic Force Microscope: Pattern and Object Formation on the Nanometer Scale. Science. 1992; 257: 375-377.

[2] Xia Y, Rogers J, Paul K, Whitesides G. Unconventional Methods for Fabricating and Patterning Nanostructures.Chemical Reviews. 1999; 99: 1823-1848.

[3] Malshe A, Virwani K, Rajurkar K, Deshpande D. Investigation of Nanoscale Electro machining (nano-EM) in Dielectric Oil. Annals of the CIRP. 2005; 54: 175-78.

[4] Alkhaleel A, Yu Z, Sundaram M, Rajurkar K, Malshe A. Nanoscale Features by Electro-Machining Using Atomic Force Microscope. Transactions of NAMRI/SME. 2005; 34: 437-444.

[5] Foster A, Kantorovich L, Shluger A. Tip and Surface Properties from the Distance Dependence of Tip–Surface Interactions. Applied Physics A: Materials Science & Processing. 2001; 72: S59-S62.

[6] Bharat B. Springer Handbook of Nanotechnology. Springer. New York: 2003.

[7] Patil S, Dharmadhikari C. Investigation of the Electrostatic Forces in Scanning Probe Microscopy at Low Bias Voltages. Surface and Interface Analysis. 2002; 33: 155-158.

[8] Patil S, Kulkarni A, Dharmadhikari C. Study of the Electrostatic Force between a Conducting Tip in Proximity with a Metallic Surface: Theory and Experiment. Journal of Applied Physics. 2000; 88.

NIST STANDARD BULLETS AND CASINGS PROJECT

J. Song, T. Vorburger, S. Ballou, B. Renegar, L. Ma*,
E. Whitenton, D. Kelley, R. Clary and A. Zheng
National Institute of Standards and Technology (NIST)
Gaithersburg, MD 20899
*** Guest Researcher, Kent State University, Kent, OH 44242**
M. Ols
Bureau of Alcohol, Tobacco, Firearms and Explosives (ATF)
Ammendale, MD 20705

1. INTRODUCTION

Bullets and casings when fired or ejected from guns, pick up characteristic signatures which are unique to the weapon. Striations on the bullet are caused by its passage through the gun barrel. Marks on the casing are caused by impact with the firing pin, breech face and ejector. By analyzing these ballistics signatures, firearm examiners can connect a firearm to criminal acts. The National Institute of Standards and Technology (NIST) Standard Reference Material (SRM) 2460/2461 Standard Bullets and Casings are intended for use as check standards for crime laboratories to help verify that their computerized optical imaging equipment for ballistics image acquisitions and correlations is operating properly. These SRM Bullets and Casings aim to support the National Integrated Ballistics Information Network (NIBIN) as tools for nationwide ballistics measurement quality control and measurement unification, and to establish ballistics measurement traceability to NIST and the National Laboratory Center (NLC) of the Bureau of Alcohol, Tobacco, Firearms and Explosives (ATF).

From this project, a Virtual / Physical Bullet Signature Standard has been established that includes 35 SRM Bullets (physical standard) delivered in 2006. Twenty-six prototype Standard Casings were produced and have completed tests; 256 SRM 2461 Standard Casings are currently under production and scheduled for delivery in 2007. A NIST 2D and 3D Ballistics Signature Measurement System was established using a NIST proposed parameter for ballistics signature measurements. This system has demonstrated a great potential for 2D and 3D topography measurements in other areas. A Ballistics Measurement Traceability System was also proposed to establish measurement traceability for nationwide ballistics signature measurements to NIST and ATF.

2. SRM 2460 STANDARD BULLETS

The SRM Bullet is designed as both a virtual and a physical bullet signature standard [1]. The virtual standard is a set of six digitized bullet profile signatures that provides the profiles for machining the bullet signatures on the physical standard, the SRM Bullets. The virtual standard also provides reference profiles for the measurements of the machined bullet signatures on the SRM Bullets [1]. The virtual bullet signature standard was originally obtained from topographic profiles traced by a stylus instrument on six master bullets. Each bullet was fired by a different gun at the National Laboratory Center of ATF and the Federal Bureau of Investigation (FBI) under standardized shooting procedures [1]. The virtual bullet signature standard was stored in a computer and used for control of the tool path of a numerically controlled (NC) diamond turning machine at the NIST Instrument Shop to machine the bullet signatures on the SRM bullets [2]. Twenty SRM Bullets were manufactured at the same time with each setup. Forty SRM Bullets have been produced so far.

A SRM Bullet is shown in Fig. 1, left. It contains six land engraved areas, each having a unique bullet signature manufactured by the NC diamond turning machine. The material was OFHC copper rod with about a 1 mm thick pure-copper coating. After machining, a specially designed chemical etching process was used for roughening the surface of the bullet to improve its diffuse reflection, and make the SRM bullet appear like a real bullet when observed under an optical microscope. Then, a commercial corrosion protection was applied to the surface of the SRM bullets.

3. SRM 2461 STANDARD CASINGS

The electro-forming technique has a long history for replication of surface specimens [3]. A master specimen is put into an electrolytic tank

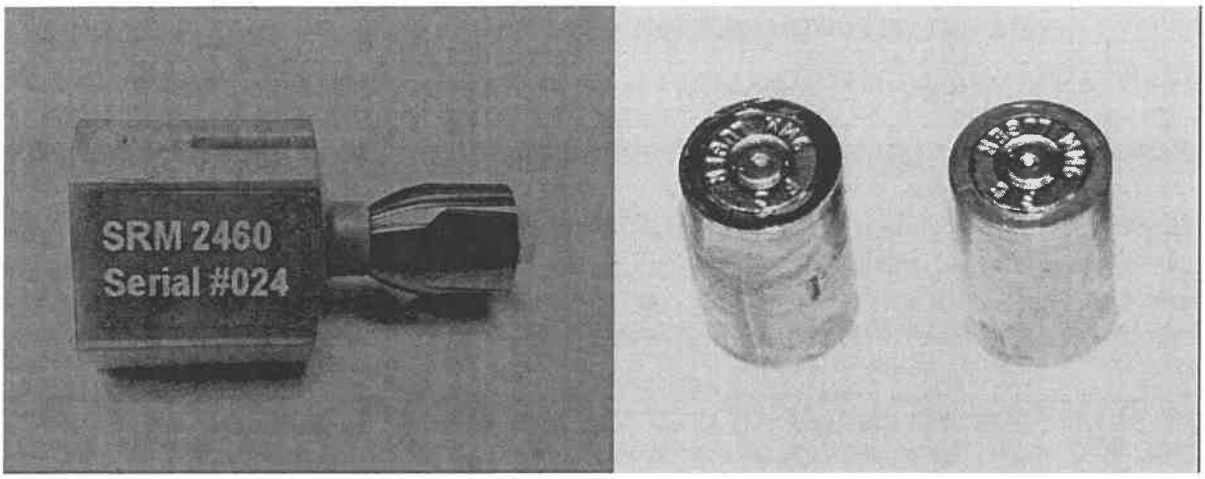

FIGURE 1. A SRM 2460 standard bullet (left) and SRM 2461 prototype standard casings (right).

to produce a negative replica on the surface of the master. By repeating the same process on the negative replica, a positive replica is produced with the same surface topography as the master specimen [3]. In order to ensure that the SRM Casings are produced with virtually the same surface topography, it is necessary to test the "decay factors" of the replication process [4]. Twenty-six prototype standard casings were replicated from the same ATF master for tests of the decay factors, two of them are shown in Fig. 1, right. Test results showed that the decay factors are very small; this can ensure the topography uniformity of 256 SRM Casings replicated from the same ATF master will be higher than 95 % in CCF_{max} (see below) [4]. Production is in progress, and 256 SRM Casings are scheduled for delivery in 2007.

4. NIST 2D and 3D Topography Measurement System

In order to test the topography reproducibility of the ballistics signatures of the SRM Bullets and Casings, a NIST proposed parameter called the topography difference D_s, combined with the cross correlation function maximum CCF_{max}, is used for 2D and 3D ballistics signature measurements [5]. CCF_{max} is the maximum value of the cross correlation function (CCF), which occurs when the two correlated surface topographies, the measured topography $Z_{(B)}$ and the reference topography $Z_{(A)}$, are registered at their maximum correlation position. At this position, a topography difference $Z_{(B\ -\ A)}$ is calculated which equals the difference between topography $Z_{(B)}$ and $Z_{(A)}$. The second parameter, the topography difference, D_s, is defined as a ratio of the mean-square roughness Rq^2 [6] of the topography difference $Z_{(B\ -\ A)}$ and the mean-square roughness of the reference topography $Z_{(A)}$:

$$D_s = Rq^2_{(B-A)} / Rq^2_{(A)}. \qquad (1)$$

When the measured topography $Z_{(B)}$ is exactly the same as the reference topography $Z_{(A)}$ (point by point), CCF_{max} is equal to 100 %, and D_s is equal to 0. Both parameters are given here because the value of CCF_{max} is not sensitive to a difference in scale height between two topographies with similar shape, whereas the value of D_s is sensitive to a scale difference.

A NIST 2D and 3D Topography Measurement System was established that includes data acquisition stations using stylus instruments and a confocal microscope, and a correlation program using the proposed topography difference parameter D_s and CCF_{max} [7]. A screen output of the 2D measurement program is shown in Fig. 2. These modified profiles result after curvature removal, resampling, and bandpass filtering (2.5 μm to 250 μm) of the measured profiles [7]. The top one is the virtual bullet signature standard, or "Signature A", which is one of the modified profile signatures from the master bullets provided by ATF and FBI. The second one shows the measured bullet profile signature, or "Signature B", which in this case is a profile from a bullet land impression of the SRM 2460-001 bullet. The cross correlation function maximum CCF_{max} is calculated to be 99.55 %. At this position, a new profile signature (B – A) is calculated (see bottom in Fig. 2), which is equal to the difference between the two compared signature profiles. The signature

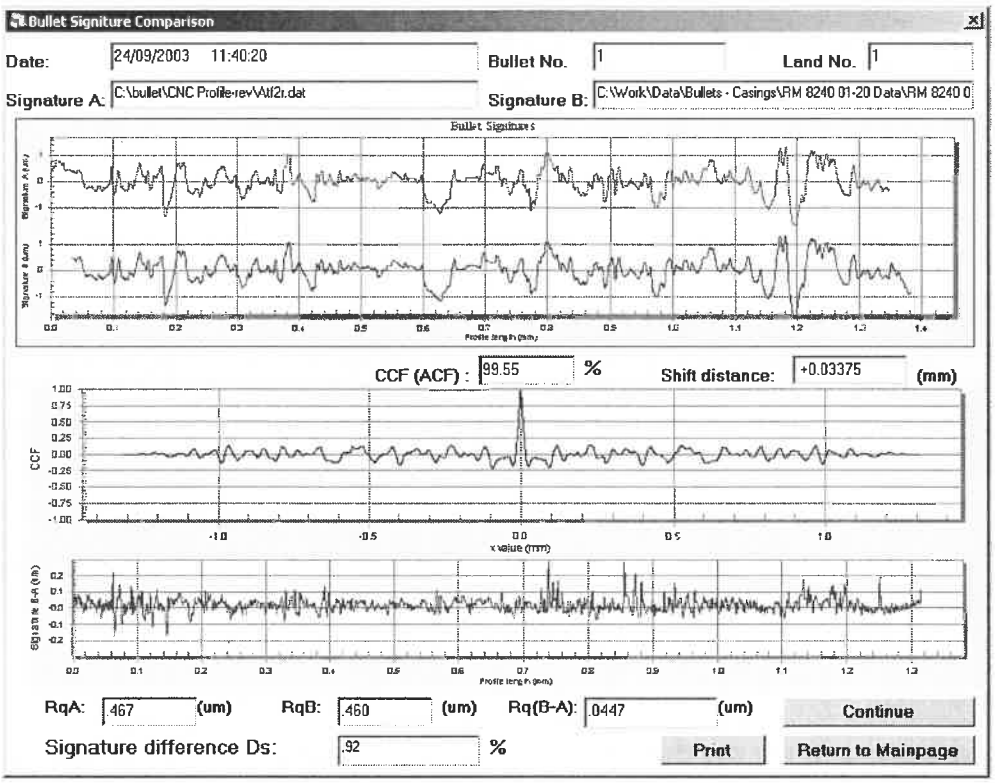

FIGURE 2. User screen for a bullet profile signature correlation of S/N SRM 2460-001 standard bullet (Signature B, shown as the second profile from the top) and the virtual standard (Signature A, shown on the top), CCF_{max} = 99.55 %. The signature difference, (B – A), is shown in the bottom, D_s = 0.92 %.

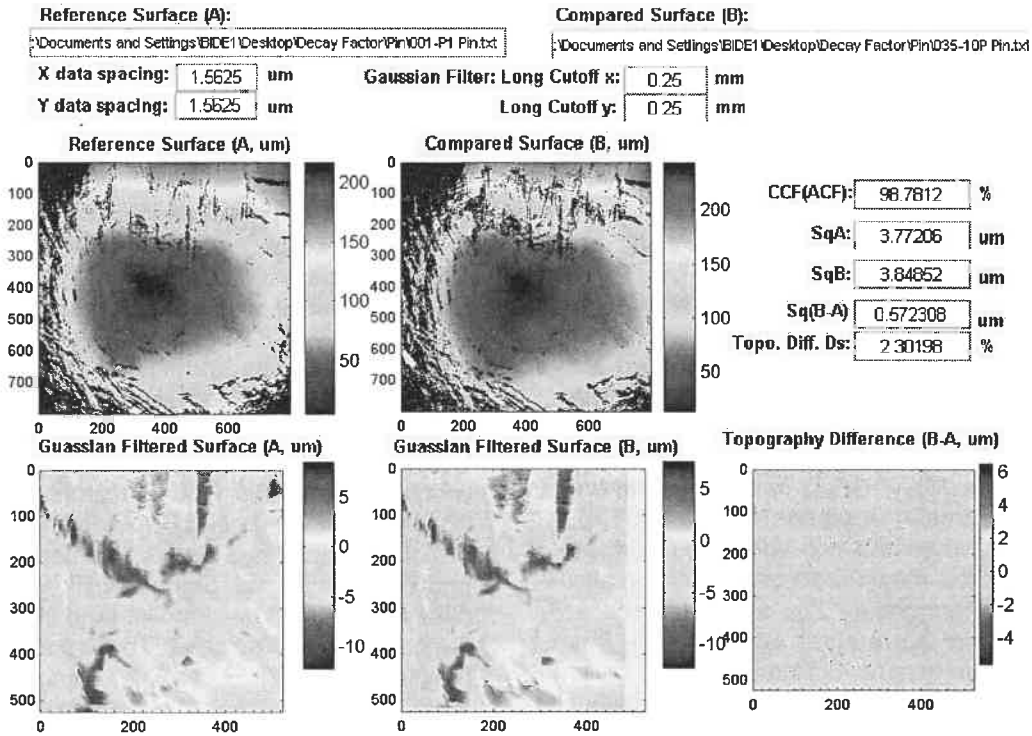
Reference Surface (A):
Compared Surface (B):
X data spacing: 1.5625 um
Y data spacing: 1.5625 um
Gaussian Filter: Long Cutoff x: 0.25 mm
Long Cutoff y: 0.25 mm
Reference Surface (A, um)
Compared Surface (B, um)
CCF(ACF): 98.7812 %
SqA: 3.77206 um
SqB: 3.84852 um
Sq(B-A) 0.572308 um
Topo. Diff. Ds: 2.30198 %
Guassian Filtered Surface (A, um)
Guassian Filtered Surface (B, um)
Topography Difference (B-A, um)

FIGURE 3. User screen for a topography correlation of firing pin images between replica casings 001 (top, left, used here as a reference) and 035 (top, right), the bottom row shows filtered images for 001 (left) and 035 (middle) casing and the topography difference (right). CCF_{max} = 98.78 %, D_s =2.30 %.

difference D_s is calculated from Eq. 1 as 0.92 %. Considering CCF_{max} = 100 % and D_s = 0 mean that the two compared profiles are exactly the same (point by point), this result shows a high agreement between the profile signature on the SRM bullet (B) and the virtual standard (A).

So far 240 bullet profiles on 40 SRM Bullets have been measured by that system. The measurement results show high reproducibility for both the measurement system and the manufacturing process for SRM bullets [2, 7].

By using the same parameters and similar algorithms, the 2D correlation program has been upgraded for 3D topography measurements. Fig. 3 shows a screen output of a firing pin signature comparison between two prototype SRM Casings 001 and 035, both were imaged by a confocal microscope. The resulting 3D surface topographies are shown on the top of Fig. 3. These two surface topographies are filtered by a 0.25 mm long wavelength cutoff [6] and registered along the *X*- and *Y*-directions and rotated around the *Z*-axis until the maximum correlation position is found, see bottom images, left and center. Once registered, the area cross correlation function maximum $ACCF_{max}$ is calculated to be 98.78 %. Meanwhile, a topography difference $Z_{B\_A}(X, Y)$ is calculated at this position and shown in the bottom right in Fig. 3. The signature difference between the two 3D topographies is calculated from Eq. 1 to be D_s = 2.30 %.

Besides 2D and 3D ballistics signature measurements, the NIST Topography Measurement System has demonstrated a great potential of use for 2D and 3D surface topography measurements in surface and nano-metrology, manufacturing quality control, and probably in tribology and other areas [8].

5. A PROPOSED NATIONAL BALLISTICS MEASUREMENT TRACEABILITY SYSTEM

The SRM bullets are used for forensic laboratories to verify that their bullet signature acquisitions and correlations using computerized optical imaging equipment are under control and traceable to the National Laboratory Center (NLC) of ATF. The SRM bullets were imaged at NLC under standardized imaging conditions. A set of images were developed as a reference standard against which the images of SRM bullets acquired at local forensic laboratories are correlated. If the correlation scores are within a control limit, one can ensure that the bullet signature acquisitions and correlations are under control and traceable to NLC [2]. The virtual standard can also provide a reference standard for the profile measurements of the SRM bullets, and can enable profile measurements at local laboratories to be traceable to the virtual bullet signature standard and to NIST surface standards.

ACKNOWLEDGEMENT

The funding for this research was provided by the National Institute of Justice (NIJ) through the Office of Law Enforcement Standards (OLES) at NIST.

REFERENCES

[1] Song, J., Vorburger, T. and Ols, M., "Establishment of A Virtual / Physical Standard for Bullet Signature Measurements," *Proc. 2001 NCSL*, Washington, D.C., August 2001.

[2] Song, J., Whitenton, E., Kelley, D., Clary, R., Ma, L., Ballou, S. and Ols, M., "SRM 2460 / 2461 Standard Bullets and Casings Project", *J. Res. Natl. Inst. Stand. Technol.* **109,** 6, 2004. pp 533-541.

[3] Song, J., Vorburger, T. and Rubert, P., "Comparison between Precision Roughness Master Specimens and Their Electroformed Replicas," *Precision Engineering* **14**, 2, 1992, pp 84-90.

[4] Song, J., Rubert, P., Zheng, A and Vorburger, "Topography Measurements for Determining the Decay Factors in Surface Replication," *Proc. of the 8th ISMTII*, Sendai, Japan, September 2007.

[5] Song, J. and Vorburger, T., "Proposed Bullet Signature Comparisons Using Autocorrelation Functions," *Proc. 2000 NCSL*, Toronto, Canada, July 2000.

[6] ASME B46.1-2002, *Surface Texture – Roughness, Waviness and Lay,* ASME, New York, 2003.

[7] Ma, L., Song, J., Whitenton, E., Zheng, A., Vorburger, V. and Zhou, J., "NIST Bullet Signature Measurement System for SRM 2460 Standard Bullets", *J. Forensic Sci.*, **49**, 4, July 2004, pp 649-659.

[8] Song, J. and Vorburger, T., "A Novel Parameter Proposed for 2D and 3D Topography Measurements and Comparisons," *Proc. of 2007 SPIE Optics & Photonics,* San Diego, August 2007.

CMM DYNAMIC ERROR ANALYSIS, CONTROL AND COMPENSATION

David W. Chang[1], Allan D. Spence[1]
[1]Department of Mechanical Engineering
McMaster University
Hamilton, Ontario, Canada

ABSTRACT

Many Coordinate Measuring Machines (CMMs) were originally designed for only quasi-static touch trigger probe based operation, and hence dynamic performance was a secondary consideration. With the emergence of analog scanning touch probes and non-contact laser digitizers, analysis, control and compensation of CMM dynamic errors must be re-examined. This paper discusses design improvements and experiments for an open architecture motion controller equipped 3-axis bridge CMM. To correct for yaw error, a parallel drive system, including cross-coupling control and continuous error compensation, is implemented. Position Sensing Detectors (PSDs) are used to confirm the yaw correction and, additionally, to correct for air bearing compliance based pitch error. Real-time laser interferometer data further confirms the faithfulness of the PSD signal.

INTRODUCTION

The touch trigger probe facilitated automation in coordinate metrology, and contributed profoundly to CMM structure design. Low measuring speeds and accelerations where anticipated, and software error compensation was not initially provided. To attain intrinsic accuracy, a rigid but massive steel structure was adopted, with compressed air bearings used to avoid stick/slip friction. Field adjustment of squareness, etc., further increased compliance. To avoid kinematic redundancy, the common 3-axis bridge style design was motorized on only one side. This choice adversely affects dynamic accuracy above low accelerations.

As the manufacturing community moved away from inspection based quality towards process control strategies, the need to measure more frequently lead to the need to measure more quickly. This requires accelerations that soon compromise accuracies achievable with conventional CMM structures and motion control systems. Analog scanning touch probes and laser digitizers collect data at much higher rates, but, particularly for analog probes, require that dynamic accuracy be maintained throughout changes in measuring speeds and directions.

Analysis of CMM dynamics errors has previously been reported by Weekers and Schellekens [1], who used displacement sensors near the major machine joints, with separate laser interferometer correlation. For a bridge style CMM, using a speed of 100 mm/s, and acceleration of 170 mm/s^2. Mu and Ngoi [2] observed angular errors of up to 5 arcseconds. A Finite Element Analysis (FEA) model was proposed, but it was acknowledged that parameter uncertainties require inclusion of real-time sensing. Dong et al. [3,4] made similar observations, and noted the influence of air bearing design on bridge pitch error (Figure 1). The CMM bridge dynamic yaw error is usually the most significant factor. A center driven approach has been developed [5], but is not widely adopted. Alternatively, the bridge can simultaneously be driven from both sides [6], with risk of damage should a malfunction occur.

The remainder of this paper presents experimental observation of dynamic errors for a typical bridge style CMM, and describes improvements achieved by adding a slave scale and slave drive motor. A new real-time compensation strategy based on Position Sensing Detectors (PSDs) is presented, with results confirmed by comparison to high speed laser interferometer data. Dynamic error effects on measurement accuracy, and improvements achieved with the proposed strategies, are presented.

OPEN ARCHITECTURE CONTROLLER CMM

The CMM motion controller used for the research is based on an Intel® Pentium® III processor, Servo-To-Go [7] interface card, and Phar Lap ETS [8] real time operating system. The loop closing frequency is 1250 Hz. Renishaw® RGH22 linear scales are used for position sensing. Pulse width modulated amplifiers, DC motors, rack and pinion gearing,

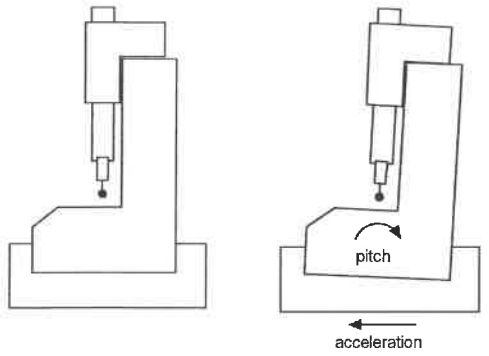

(a) (b)

FIGURE 1. Bridge style CMM pitch error illustration. (a) stationary or constant speed. (b) while accelerating.

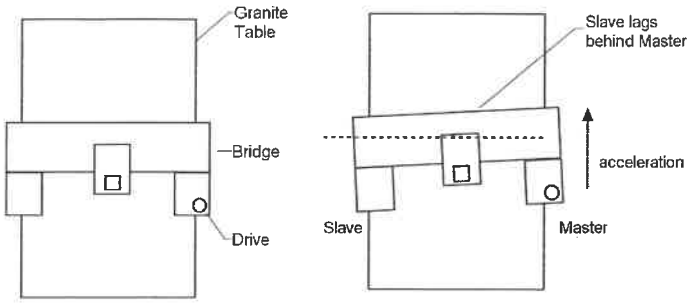

(a) (b)

FIGURE 2. Bridge style CMM yaw error illustration. (a) stationary or constant speed. (b) while accelerating.

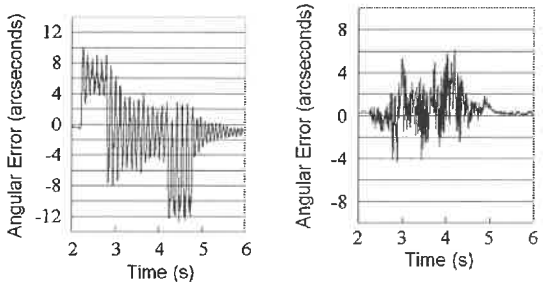

(a) (b)

FIGURE 3. Bridge style CMM yaw error observation. Speed 100 mm/s, Acceleration 170 mm/s^2. (a) 3-axis. (b) 4-axis with cross-coupling control.

and air bearings are used for all axes. Details were presented in an earlier paper [9].

PARALLEL SCALE AND DRIVE

For a bridge style CMM, oscillating yaw errors arise during acceleration. This can be measured by adding a second linear scale at the slave side, and executing a trapezoidal velocity profile. As observed in Figure 3(a), there is first a positive error of 10 arcseconds during acceleration, oscillation from 4 to -6 arcseconds during constant speed motion, and then an error of -12 arcseconds during deceleration.

To reduce this error, a parallel slave drive was added (Figure 4) together with a cross-coupling control algorithm [10] (Figure 5). Continuous geometric error compensation within the feedback loop is essential to maintain bridge squareness.

Within the Cross-Coupling Controller, the formula for calculating the reference signal offset M_n for period n is:

TABLE 1. Ring gauge measurement results. Nominal size 71.1213 mm. 100 samples.

3-axis	Master	Slave
Mean	71.1220	71.1259
Std Dev	8.9E-4	13.0E-4
Min	71.118	71.123
Max	71.124	71.135
4-axis	**Master**	**Slave**
Mean	71.1217	71.1223
Std Dev	0.8E-4	0.7E-4
Min	71.1199	71.1202
Max	71.1243	71.1250

$$M_n = K^R \left(K_p \varepsilon_{\text{sync}} + K_i S_n + K_d D_{\text{smooth}} + K_v V_{ff} \right)$$

where

K^R	overall scale factor
K_p	proportional gain
K_i	integral gain
K_d	derivative gain
K_v	velocity feed forward gain
$\varepsilon_{\text{sync}}$	master/slave synchronize error
S_n	integral error
D_{smooth}	(smoothed) derivative error
V_{ff}	modified velocity feed forward term

The synchronize error at period n is

$$\varepsilon_{\text{sync}} = enc_{\text{master}} - enc_{\text{slave}}$$

where

enc_{master}	(compensated) master encoder
enc_{slave}	(compensated) slave encoder

To reduce the aggressiveness of the derivative term in the presence of quantization noise, smoothing through a moving average of N $\varepsilon_{\text{sync}}$

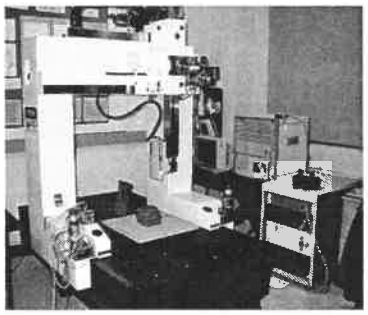

FIGURE 4. Parallel slave drive implementation.

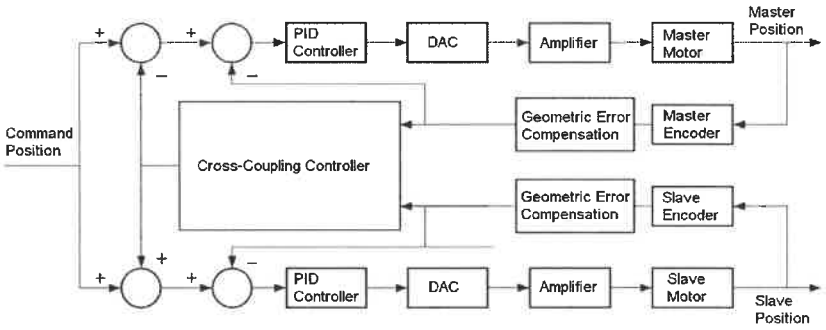

FIGURE 5. Cross-coupling control algorithm block diagram.

samples is used. Integral error $S_n = S_{n-1} + \varepsilon_{\text{sync},n}$ is limited to $\pm S_{\max}$.

Velocity feed forward is used to anticipate increases in synchronize error as the command velocity increases, and is incorporated using the formula

$$V_{ff} = |V_n| \cdot \text{sgn}(\varepsilon_{\text{sync}})$$

where V_n is the command velocity and $\text{sgn}(\ )$ is the sign function.

Individual axes are tuned using a conventional Proportional-Integral-Derivative (PID) control law

$$O_n = K^R \left(K_p (E_n - E_{n-1}) + K_i S_n + K_d D_{\text{smooth}} + K_v V_n + 64 K_a A_n \right)$$

where, in addition to the terms define above,

O_n	output to motor amplifier
E_n	position error
K_a	acceleration feed forward gain
A_n	command velocity

With this improvement enabled, there is much less oscillation, and the observed yaw error is reduced by approximately 50 percent (Figure 3(b)).

This directly affects measurement accuracy. To illustrate this for touch trigger probing, opposing points inside a 71.1213 mm ring gauge were measured near both the master and slave sides (Table 1). Each measurement was repeated 100 times. The improvement in the 4-axis case is clear, and results from the combination of parallel drive correction combined with parallel scale compensation.

POSITION SENSING DETECTORS

Pitch errors are smaller in magnitude, and more difficult to correct. Affordable real time measurement and compensation has been difficult to achieve. To address this, a novel solution based on Position Sensing Detectors (PSDs) (Lateral Effect Photodiodes) was investigated. The Edmund Optics [11] NT53-228 laser light sources were mounted on the CMM moving bridge, and the Hamamatsu [12] S5991-01 PSDs were mounted on the granite table (Figure 6). Output signals were sampled within the position control loop. At rest (Figure 7(a)), reference PSD signals were recorded. As the CMM accelerates, the laser beam position on the PSDs (Figure 7(b)) was recorded.

For verification, several trapezoidal velocity profiles experiments were conducted. Yaw errors were measured using the slave scale, PSD, and with a Renishaw ML10 laser interferometer and QuickView™ software. Results from all three sources were indistinguishable. For pitch error, the PSD and laser interferometer results are shown in Figure 7(c). The PSD captures the prominent features, and additionally is capable of measuring any vertical translation. Some of the laser interferometer signal may be due to dynamic motion of the remaining axes, and this could be measured with additional PSDs.

SUMMARY

With the introduction of new scanning sensors, CMM dynamic errors are of increased concern. This paper presents dynamic error analysis and design improvements including parallel drive with cross-coupling control and Position Sensing Detector (PSD) based real-time correction of air bearing compliance caused pitch error. The methods are implemented on an open

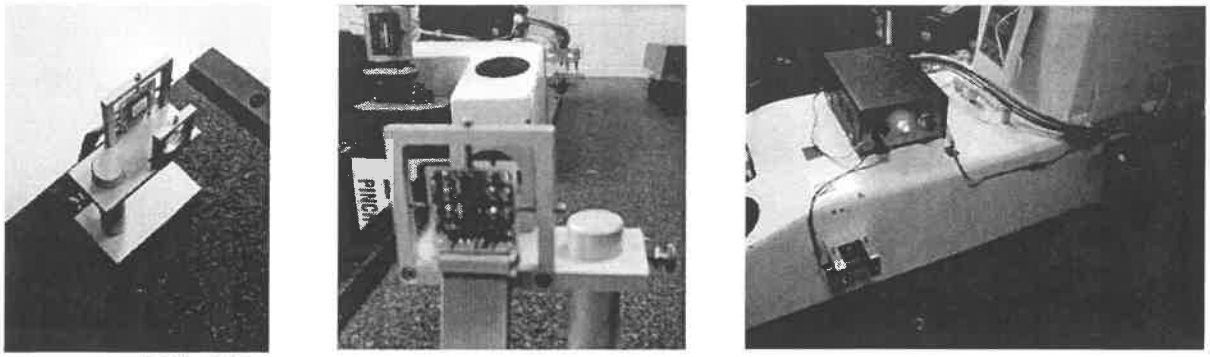

FIGURE 6. Laser sources and Position Sensing Detectors mounted on CMM.

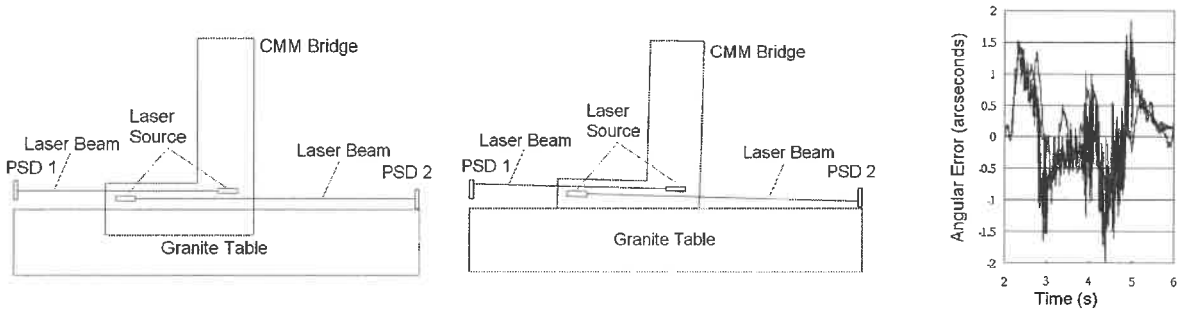

(a) (b) (c)

FIGURE 7. PSD pitch error detection. (a) stationary or constant speed (b) accelerating (c) laser interferometer (thick line) and PSD measurement (thin line) results.

architecture motion controller equipped bridge style machine, and are practical to implement in industrial practice.

ACKNOWLEDGEMENTS

This work was supported by that Natural Sciences and Engineering Research Council of Canada.

REFERENCES

[1] Weekers W.G., Schellekens P.H.J. Compensation for Dynamic Errors of Coordinate Measuring Machines. Measurement: Journal of the International Measurement Confederation, 1997; 20(3): 197-209.

[2] Mu YH, Ngoi BKA. Dynamic Error Compensation of Coordinate Measuring Machines for High-Speed Measurement. Int. J. Advanced Manufact. Tech. 1999; 15(11): 810-814.

[3] Dong C, Zhang C, Wang B, Zhang GX. Prediction and Compensation of Dynamic Error for Coordinate Measuring Machines, ASME J. Manufact. Sci. Eng., 2002; 124(3): 509-514.

[4] Dong C, Zhang C, Wang B, Zhang GX. Reducing the Dynamic Errors of Coordinate Measuring Machines. ASME J. Mech. Design. 2003; 125(4): 831-839.

[5] Carl Zeiss IMT Corp. UPMC Ultra Coordinate Measuring Machine, Maple Grove, MN.

[6] Park HK, Kim SS, Park JM, Cho TY, Hong D. Dynamics of Dual-Drive Servo Mechanism. IEEE Int. Symp. Industrial Electronics. 2001; 3:1996–2000.

[7] Servo-To-Go, Inc. Indianapolis, IN. www.servotogo.com.

[8] Ardence. Phar Lap ETS. Waltham, MA. www.ardence.com.

[9] Chang DW, Wu P, Harris JO, Peterson JE, Heslip J, Spence AD, A Modular, Multiple Sensor Embedded System CMM Motion Controller. ASPE Summer 2003 Topical Meeting - Coordinate Measuring Machines. 2003; 43-48.

[10] Feng L, Koren Y, Borenstein J. Cross-Coupling Motion Controller for Mobile Robots. IEEE Control Systems Magazine. 1993; 13(6):35-43.

[11] Edmund Optics. Barrington, NJ, 2005. www.edmundoptics.com.

[12] Hamamatsu Photonics Co. Hamamatsu City, Japan. 2005. www.hamamatsu.com.

DIRECT MEASUREMENT OF SPINDLE ERROR MOTION WITH 10-PICOMETER RESOLUTION USING REGULAR CRYSTALLINE LATTICE AND SCANNING TUNNELING MICROSCOPE

Masato Aketagawa [1], Patamaporn Chaikool [1] and Eiki Okuyama [2]
[1] Department of Mechanical Engineering
Nagaoka University of Technology
Nagaoka, Niigata, Japan
[2] Department of Mechanical Engineering
Akita University
Akita, Japan

INTRODUCTION

As the nanotechnology and the ultra precision engineering have progressed rapidly, a reduction of the rotating error of a spindle for the metrology or manufacturing field is required. A conventional spindle measurement includes the contribution from a spindle error motion and a form error of a target artifact. Therefore, methods for separating the spindle error motion from the artifact error are necessary [1].

A lattice spacing of approximately 0.2 - 0.3 nm for some regular crystalline lattice is uniform and stable over a long range when the crystals are stress free. The scanning tunneling microscope (STM) [2] is capable to observe an atomic image of the crystalline surface. We have proposed the 2-dimensional (2-D) displacement encoder with 10-picometer resolution using the graphite (highly oriented pyrolytic graphite: HOPG) crystal and the multi-tunneling-probes STM (MTP-STM) [3].

If the HOPG crystal, which is used as a 2-D reference scale, is placed on a top of the spindle and observed by the MTP-STM, a spindle error motion can be measured with 10-picometer resolution directly without any separation method.

MEASUREMENT PRINCIPLE

Figure 1 shows the principle and measuring system for the spindle error motion. The measuring system consists of a fixed *XYZ* tip scanner, an STM tip, an ultra precise spindle, the HOPG crystal, an encoder, an STM controller, a digital signal processor (DSP) with AD and DA converters, a piezoelectric (PZT) amplifier, a reference cylinder and capacitive displacement sensors. In the system, the HOPG is utilized as a 2-dimensional reference scale and installed at a top surface of the center of the spindle of interest. The fixed-STM scanner and the dithered STM tip are set upon the HOPG crystal. The high-speed lateral-circular-dither modulation is applied to the STM tip for positioning it on proper points of the HOPG crystalline surface in semi-real-time way.

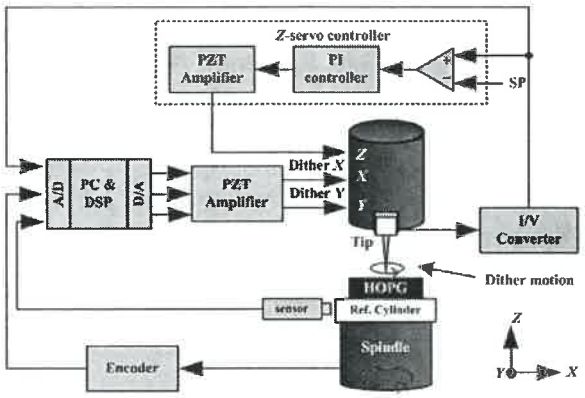

FIGURE 1. Spindle error motion measurement system.

A relative 2-D lateral displacement between the STM scanner and the top surface of the spindle can be determined from multi-current-signals of the proper multi-points, when the spindle rotates. The 2-D lateral displacement of the top surface of the spindle can be calculated from a linear sum of the two unit lattice vectors $\boldsymbol{a}_1$ and $\boldsymbol{a}_2$ of the HOPG crystalline surface using the multi-current-signals. (On the HOPG crystal, the lattice spacing of $|\boldsymbol{a}_1|$ or $|\boldsymbol{a}_2|$ is 0.246 nm [4], and the intersectional angle between $\boldsymbol{a}_1$ and $\boldsymbol{a}_2$ is 60°.) A displacement interpolation less than the HOPG lattice spacing of 0.246 nm can also be performed. To compare the proposed method with the conventional methods, in the system,

capacitive displacement sensors are also installed.

To achieve the lateral-circular-dither motion, two sinusoidal signals with 90° phase differences and proper amplitudes are applied to the tip *XY* scanner. Figure 2 shows an ideal surface structure of the HOPG crystal. The tip moves circularly along the specific points *A-F* on the crystalline surface, as shown in figure 2. The tunneling currents at the specific points *A-F* in figure 2 are obtained in semi-real-time way.

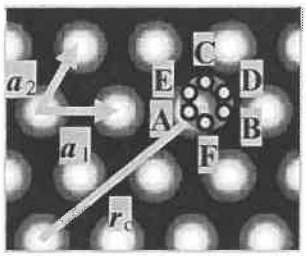

FIGURE 2. An ideal surface structure of the HOPG crystal and the specific points for the MTP-STM method ($\overline{AB}=\frac{1}{2}\boldsymbol{a}_1$ *and* $\overline{AC}=\frac{1}{2}\boldsymbol{a}_2$).

In the system, we assume that the coordinate system on the top surface of the spindle (the HOPG surface) is *o-xyz*, and the fixed coordinate system outside the spindle is *o'-x'y'z'*. The relationship of the lateral vectors $\boldsymbol{r}' = (x', y')$ and $\boldsymbol{r} = (x, y)$ in the *o'-x'y'z'* and *o-xyz* system are shown as:

$$\boldsymbol{r}' = R(\theta)\boldsymbol{r} + \boldsymbol{d}(\theta),$$

$$\text{or} \quad \boldsymbol{r} = R(-\theta)\{\boldsymbol{r}' - \boldsymbol{d}(\theta)\}, \tag{1}$$

where $\boldsymbol{d}(\theta)$ is the lateral displacement vector of the rotating center (a radial error motion), and $R(\theta)$ is the rotation matrix. The *o-xyz* system rotates with $R(\theta)$ against the *o'-x'y'z'* system. Vector $\boldsymbol{r}'_{od}$ of the center of dither motion is assumed as the origin point of the *o'-x'y'z'* system. When the center of dither motion is locked ($\boldsymbol{r}'_{od} = 0$), vector $\boldsymbol{r}_{od}$ of the *o-xyz* system is shown as:

$$\boldsymbol{r}_{od} = R(-\theta)\{\boldsymbol{r}'_{od} - \boldsymbol{d}(\theta)\} = -R(-\theta)\boldsymbol{d}(\theta), \tag{2}$$

where $\boldsymbol{r}_{od}$ should be the linear sum of the unit vectors $\boldsymbol{a}_1$ and $\boldsymbol{a}_2$ on the HOPG crystalline surface. On the other hand, $\boldsymbol{r}_{od}$ can be represented using

$$\boldsymbol{r}_{od} = m(\theta)\boldsymbol{a}_1 + n(\theta)\boldsymbol{a}_2. \tag{3}$$

Therefore,

$$\boldsymbol{d}(\theta) = -R(\theta)\{m(\theta)\boldsymbol{a}_1 + n(\theta)\boldsymbol{a}_2\}. \tag{4}$$

This equation shows a possibility to determine the lateral displacement vector $\boldsymbol{d}(\theta)$, if $m(\theta)$ and $n(\theta)$ can be determined. In order to determine $m(\theta)$ and $n(\theta)$, the high-speed lateral dither modulation is applied to the STM tip for collecting the tunneling current signals from the specific points *A-F*. The lateral displacement vectors at points *A'–F'* in the *o'-x'y'z'* system are shown as:

$$\boldsymbol{r}'_A = R(\theta)\left(-\frac{1}{6}\boldsymbol{a}_1 - \frac{1}{6}\boldsymbol{a}_2\right), \tag{5-A}$$

$$\boldsymbol{r}'_B = R(\theta)\left(\frac{1}{3}\boldsymbol{a}_1 - \frac{1}{6}\boldsymbol{a}_2\right), \tag{5-B}$$

$$\boldsymbol{r}'_C = R(\theta)\left(-\frac{1}{6}\boldsymbol{a}_1 + \frac{1}{3}\boldsymbol{a}_2\right), \tag{5-C}$$

$$\boldsymbol{r}'_D = R(\theta)\left(\frac{1}{6}\boldsymbol{a}_1 + \frac{1}{6}\boldsymbol{a}_2\right), \tag{5-D}$$

$$\boldsymbol{r}'_E = R(\theta)\left(-\frac{1}{3}\boldsymbol{a}_1 + \frac{1}{6}\boldsymbol{a}_2\right), \tag{5-E}$$

$$\boldsymbol{r}'_F = R(\theta)\left(\frac{1}{6}\boldsymbol{a}_1 - \frac{1}{3}\boldsymbol{a}_2\right). \tag{5-F}$$

Equations (5) means that points *A'–F'* rotate along spindle axis. From the above equations (1)-(5), the lateral displacement vectors in the *o-xyz* system at points *A–F* are shown as:

$$\boldsymbol{r}_A = \left\{m(\theta) - \frac{1}{6}\right\}\boldsymbol{a}_1 + \left\{n(\theta) - \frac{1}{6}\right\}\boldsymbol{a}_2, \tag{6-A}$$

$$\boldsymbol{r}_B = \left\{m(\theta) + \frac{1}{3}\right\}\boldsymbol{a}_1 + \left\{n(\theta) - \frac{1}{6}\right\}\boldsymbol{a}_2, \tag{6-B}$$

$$\boldsymbol{r}_C = \left\{m(\theta) - \frac{1}{6}\right\}\boldsymbol{a}_1 + \left\{n(\theta) + \frac{1}{3}\right\}\boldsymbol{a}_2, \tag{6-C}$$

$$\boldsymbol{r}_D = \left\{m(\theta) + \frac{1}{6}\right\}\boldsymbol{a}_1 + \left\{n(\theta) + \frac{1}{6}\right\}\boldsymbol{a}_2, \tag{6-D}$$

$$\boldsymbol{r}_E = \left\{m(\theta) - \frac{1}{3}\right\}\boldsymbol{a}_1 + \left\{n(\theta) + \frac{1}{6}\right\}\boldsymbol{a}_2, \tag{6-E}$$

$$\boldsymbol{r}_F = \left\{m(\theta) + \frac{1}{6}\right\}\boldsymbol{a}_1 + \left\{n(\theta) - \frac{1}{3}\right\}\boldsymbol{a}_2. \tag{6-F}$$

The topographical height $Z(r)$ of the HOPG crystal can be represented approximately as:

$$Z(\boldsymbol{r}) = \sum_{i=1}^{3} A_i \cos(2\pi \boldsymbol{k}_i \cdot \boldsymbol{r}), \quad (7)$$

where $\boldsymbol{r}$ is the lateral displacement vector and $\boldsymbol{k}_i$ is the reciprocal vector. The relationships between the reciprocal vector $\boldsymbol{k}_i$ and the unit lattice vectors $\boldsymbol{a}_i$ are shown as:

$$\boldsymbol{k}_i \cdot \boldsymbol{a}_j = \delta_{ij}, \quad (8)$$

$$\boldsymbol{k}_3 = \boldsymbol{k}_1 - \boldsymbol{k}_2, \quad (9)$$

where δ_{ij} is Kronecker's δ. From equations (6)-(9), the followings are obtained:

$$Z(\boldsymbol{r}_A) + Z(\boldsymbol{r}_B) = 2A_2 \cos\left\{2\pi\left(n(\theta) - \frac{1}{6}\right)\right\}, \quad (10\text{-A})$$

$$Z(\boldsymbol{r}_D) + Z(\boldsymbol{r}_E) = 2A_2 \cos\left\{2\pi\left(n(\theta) + \frac{1}{6}\right)\right\}, \quad (10\text{-B})$$

$$Z(\boldsymbol{r}_A) + Z(\boldsymbol{r}_C) = 2A_1 \cos\left\{2\pi\left(m(\theta) - \frac{1}{6}\right)\right\}, \quad (10\text{-C})$$

$$Z(\boldsymbol{r}_D) + Z(\boldsymbol{r}_F) = 2A_1 \cos\left\{2\pi\left(m(\theta) + \frac{1}{6}\right)\right\}. \quad (10\text{-D})$$

Equations (10) show the possibility to determine $m(\theta)$ and $n(\theta)$ with an integer and fractional parts. The lateral displacement vector $\boldsymbol{d}(\theta)$ can be measured with the two unit lattice vectors of the HOPG using the tunneling currents on points *A-F (A'-F')*. This method is called as the 6-points method.

The measurement procedure for the spindle error motion can be summarized as follows.

1. Fix the spindle and observe the HOPG surface with the STM, in order to determine the crystalline orientations of the HOPG crystal at the initial axial position. Determine the amplitude of the lateral-circular- dither modulation, and data collecting points for the specific points *A-F* shown in figure 2.
2. Apply the lateral-circular-dither modulation to the STM tip. Rotate the spindle and measure a rotating angle θ with the encoder. Collect the tunneling current signals from point *A-F*, then calculate the quantities of the equation (10-A) - (10-D), then determine the $m(\theta)$ and $n(\theta)$. Determine the radial error motion $\boldsymbol{d}(\theta)$ using the equation (4).
3. Rotate to next angle and repeat the 2nd procedure.
4. Integrate $\boldsymbol{d}(\theta)$ up to 1 or several revolutions.

PRELIMINARY EXPERIMENTAL RESULTS OF THE 6-POINTS METHOD

Figure 3 shows the preliminary experimental system for the assessment of the 6-points method. The circular dither modulation signals are fed into the STM tip, and, at the same time, the raster signals are fed into the sample scanner. A verification of the 6-points method is achieved.

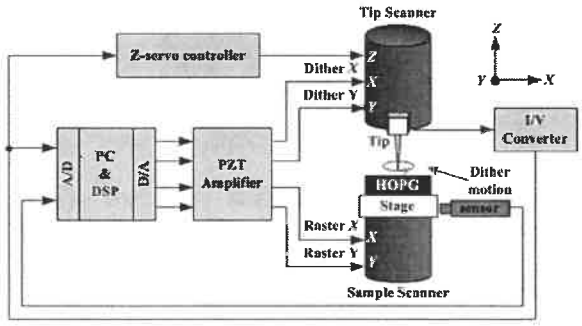

FIGURE 3. Preliminary experimental system for the 6-points method.

Figure 4 shows results of the separation of crystalline orientations. Figures 4(a) - 4(f) are the atomic images of the HOPG crystal based on the tunneling current signals from the specific points *A-F*, respectively. Figure 4(g) and 4(h) are the summed images of 4(a) + 4(b) and 4(a) + 4(c), as shown in (10-A) and (10-C), respectively. In the same way, figure 4(i) and 4(j) are the summed images of 4(d) + 4(e) and 4(d) + 4(f), as shown in (10-B) and (10-D), respectively. Figure 4(g) and 4(i) represent the $\boldsymbol{k}_1$'s sinusoidal wave signals. Figure 4(h) and 4(j) also show the $\boldsymbol{k}_2$'s sinusoidal wave signals.

The phase difference of $\pi/3$ radian between figure 4(g), 4(i) and figure 4(h), 4(j) is clearly seen in the results, that is, the results confirmed equations (10). These results show the feasibility of equations (10) to determine the number of $m(\theta)$ and $n(\theta)$. Furthermore, the displacement measured by this method and the capacitive displacement sensor will be compared in the presentation.

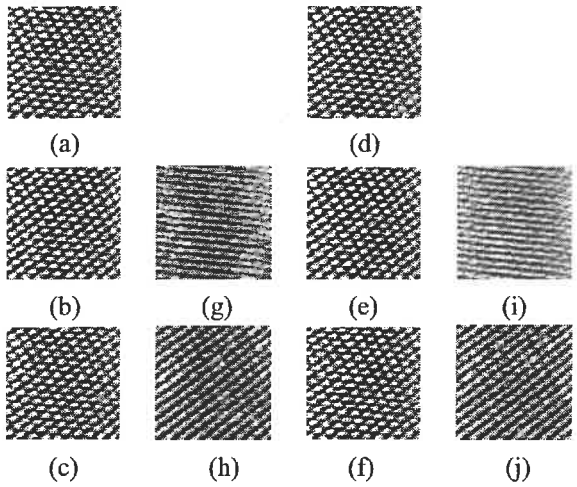

FIGURE 4. Separation of crystalline orientations of the HOPG crystal using the 6-points method.

CONCLUSION

The new method for measuring the rotating error of the ultra precision spindle using the MTP-STM method and the regular crystalline lattice is proposed. From the result of the 6-point method, the proposed method has a possibility to determine the lateral displacement with 10 picometer resolution.

ACKNOWLEDGMENT

The financial supports of the Electro-Mechanic Technology Advancing Foundation and Research Found of the Japan Society for the Promotion of Science are gratefully acknowledged.

REFERENCES

[1] E. Marsh, J. Couey and R. Vallance. Nanometer-Level Comparison of Three Spindle Error Motion Separation Techniques. J Manuf Sci Eng. 2006; 128: 180-187.

[2] G. Binnig, H. Rohrer, Ch. Gerber and E.Weibel. Tunneling through a Controllable Vacuum Gap. Appl Phys Lett. 1982; 40: 178-180.

[3] M. Aketagawa, H. Honda, M. Ishige and P. Chaikool. Two-Dimensional Encoder with Picometre Resolution using Lattice Spacing on Regular Crystalline Surface as Standard. Meas Sci Technol. 2007; 18: 342-349.

[4] P. Rerkkumsup, M. Aketagawa, K. Takada, T. Watanabe and S. Sadakata. Direct Measurement Instrument for Lattice Spacing on Regular Crystalline Surfaces using a Scanning Tunneling Microscope and Laser Interferometry. Rev Sci Instrum. 2003; 74: 1205-1210.

HIGH RESOLUTION COMPUTED TOMOGRAPHY FOR METROLOGY

David K. Lehmann[1], Kathleen Brockdorf[1] and Dirk Neuber[2]
[1]phoenix|x-ray Systems + Services Inc.
St. Petersburg, FL, USA
[2]phoenix|x-ray Systems + Services GmbH
Wunstorf, Germany

ABSTRACT

High-resolution Computed Tomography (CT) widely expands the spectrum of detectable internal micro-structures as well as the possibilities for non destructive measurements of hidden internal surfaces of complex objects which are currently inaccessible with conventional Co-ordinate Measurement Machines. The new nanotom® is the first 180 kV nanoCT® system with the capability to analyse samples with the exceptional voxel-resolution of less than 0.5 microns per volume pixel (voxel). Thus object surfaces of – for example – microsystem parts, moulded plastics, small light metal parts and any internal details related to a variation in material, density or porosity can be visualised and precisely measured.

The volume data set is visualised by slices or compiled in a three-dimensional view which can be displayed in various ways. By means of volume visualisation software, the three-dimensional structure of the reconstructed volume can be easily analysed for pores, cracks, and density and distribution of materials with the highest magnification and image quality available.

The 3D-volume of the object can also be used to extract surfaces. The generated data is measured by fitting of geometrical primitives or by variance analysis against CAD-data. It may also be used for reverse engineering. In order to ensure outstanding ease-of-use and geom.-etrically correct surfaces, innovative extraction methods have been added to the surface|extraction-module of the nanotom® software. The accuracy of metrology with CT depends on the voxel size. The smaller the object, the higher the resolution. For a 20 x 20 mm Zerodur® sphere plate, designed and calibrated by the German Metrology Institute PTB and scanned with the nanotom, the "Error of Indication for Size Measurement" is as small as ≈ 3µm.

High resolution CT opens a new dimension of 3D-micromeasurement and will partially substitute traditional destructive methods as well as the many times slower acquisition of three-dimensional metrology by conventional Co-ordinate Measurement Machines.

INTRODUCTION

For many years, the only way to determine the interior structure of a sample with resolution in the sub-micron range was to section the part. This technique was not only time-consuming, but in this destructive process a valuable sample was lost. With advances in x-ray technology, however, this is no longer necessary. In the fields of biology, geology, and engineering, nanoCT® allows the researcher to explore a sample's structures into the sub-micron level as never before. An example application for nanoCT® is shown in Fig. 2. It represents a virtual slice of a dried fern (Fig.1) with details smaller than one micron visible. X-ray computed tomography provides 3D volume data of workpieces including internal and hidden characteristics as shown in Fig. 3.

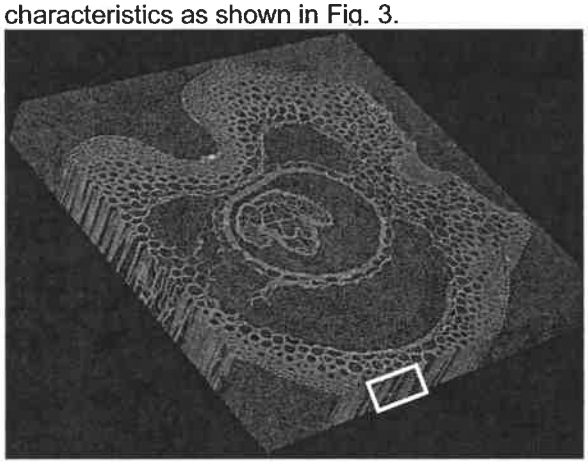

Fig. 1: nanoCT® of a dried fern sample showing the stems microstructure. The focal spot size used for the CT was 0.8 microns, the voxel size is 0.5 microns.

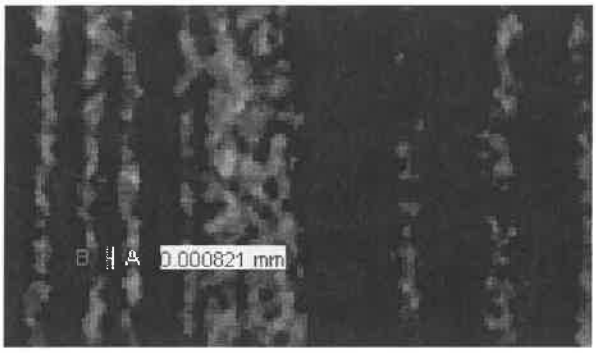

Fig 2: Magnified section of the area marked in Fig 1. The detail measured in the image has a size of 0.000821 mm.

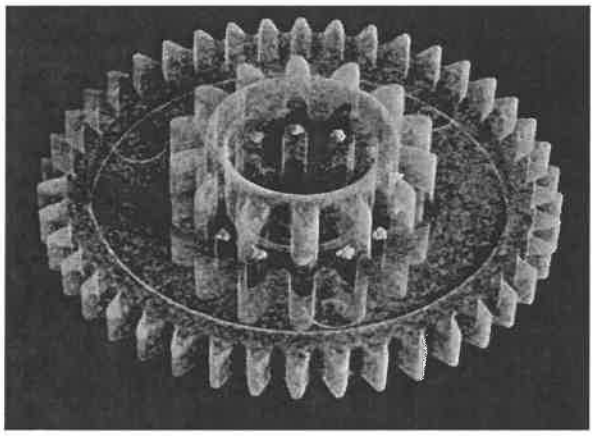

Fig. 3: Transparent 3D Visualization of a small moulded plastic gear wheel. Without any mechanical slicing the size and position of the internal shrinkage cavities may be analysed. The colour indicates the size.

The basis of precise metrology using CT is the high quality tomogram from which the surface is extracted. The measuring uncertainty mainly is determined by voxel size and focal spot size. For a spot size larger than the voxel size the penumbra is limiting the image quality. A smaller X-ray spot will reduce this effect and result in a sharper image on the detector. Due to the submicron focal spot size of the high power nanofocus tube, the nanotom® can resolve image features as small as 200-300 nm by measuring small samples with highest resolution.

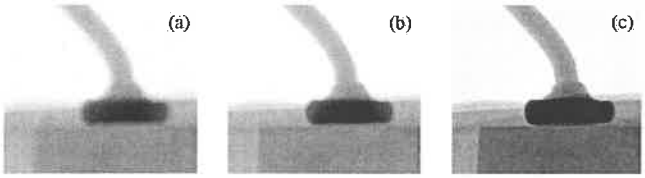

Fig. 4: nanofocus-X-ray technique: The smaller the focal spot, the higher the sharpness of the bond wire: a = 10 microns, b = 5 microns. A spot size <1 µm (c) allows a detail recognition of 200 to 300 nm.

THE NANOTOM

The new nanotom® of phoenix|x-ray is an ultra-precise high-resolution CT system (see fig 5). It is designed specifically for laboratory applications, scanning samples of up to 1 kg and 120 mm diameter with unique voxel-resolutions down to <500 nm (0,5 microns). The nanotom® is the first 180kV nanofocus CT system in the world, set up for the highest resolution applications in a variety of fields such as injection moulding, materials science, micro mechanics, electronics and geology to name a few.

Fig. 5: With its small footprint of only 163 x 143 x 74 cm, the nanotom® is uniquely suited for laboratory applications.

Computed Tomography at such exceptionally high spatial resolutions requires careful design, taking into account any features which might influence the resulting resolution. These special needs for highest precision require special

manipulation systems, detectors and X-ray tubes. For example, the nanotom uses a unique 180 kV/ 15 W high power nanofocus tube which can penetrate even high-absorption samples like copper or steel alloys. A 5-megapixel flat panel detector with an active area of 120 x 120 mm (2300 x 2300 pixels, 50 µm pixel size) and a 3-position virtual detector (up to 360 mm detector width) give rise to a wide variety of experimental possibilities. To avoid any negative influence of vibrations or thermal expansion, tube, detector and rotation unit are implemented in a high precision granite based manipulation system. Furthermore, special materials and construction details are used to guarantee a high stability for long term measurements. In addition, minimal vibrations of the system are suppressed by air bearings of the rotation unit. The precision of this system setup determines the high resolution and accuracy of the measurement results.

Further the system includes phoenix|x-rays easy to use proprietary reconstruction software datos|x which includes innovative tools for geometry calibration, detector calibration, noise and beam hardening reduction and region-of-interest-CT.

The resulting volume data set is visualised in one 3D view window and three 2D image viewing windows according to the three orthogonal cross sections. This technique is capable of substituting destructive mechanical slicing and cutting in many applications. The virtual slices may be used for easy measurement of distances just by mouse click (see figure 12). The extracted surface data of the scanned object depicts the whole workpiece geometry for examination by element fits (see figure 11) and CAD variance analysis or reverse engineering (see figure 13).

The main interface to the metrology software is the extracted surface data. The accuracy of the surface extraction may be affected by residual inevitable imperfections in the volume data set caused by physical effects like beam-hardening and scattering. The nanotom eliminates these errors by using a specifically designed surface extraction algorithm for much higher precision than common threshold gradient algorithms (ISO). This generates geometrically correct surfaces even if there are some beam-hardening artefacts which can principally not totally be avoided at industrial CT. Based on the precise surface data of all internal and external surfaces of the object, the user may now proceed with further evaluation such as variance analysis, element fits, reverse engineering etc.

METROLOGY RESULTS

To verify the precision of measurements provided by high resolution CT, a 20 x 20 mm Zerodur® sphere plate (figure 6), designed and calibrated by the National German Metrology Institute PTB was measured with the nanotom. The 3D-calibration of the PTB included uncertainties of 1.5µm (positional) and 2µm for the form.

As in the variance-analysis in figures 6 and 7 demonstrated, the deviation of the extracted surface from the ideal form can be significantly reduced by using image correction techniques like advanced beam hardening correction.

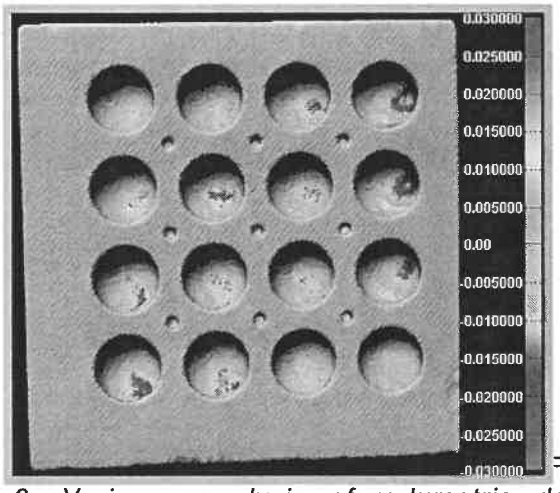

Fig. 6: Variance analysis of volumetric data reconstructed without beam hardening reduction showing a position-dependent deviation from the ideal form.

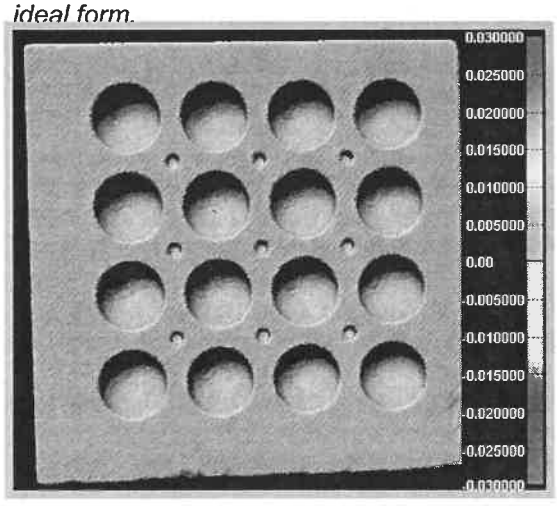

Fig 7: Using the advanced beam hardening module of phoenix|x-ray provides significant better comparison results.

To determine the "Error of Indication for Size Measurement", all 120 distances between the central points of the 16 sphere shaped calottes have been evaluated. The generation of surface data was performed with the ISO grey value method as well as with phoenix|x-rays advanced surface extraction. As Fig 8+9 demonstrates, using a phoenix surface instead of an ISO surface provides a significant reduction of the size measurement error.

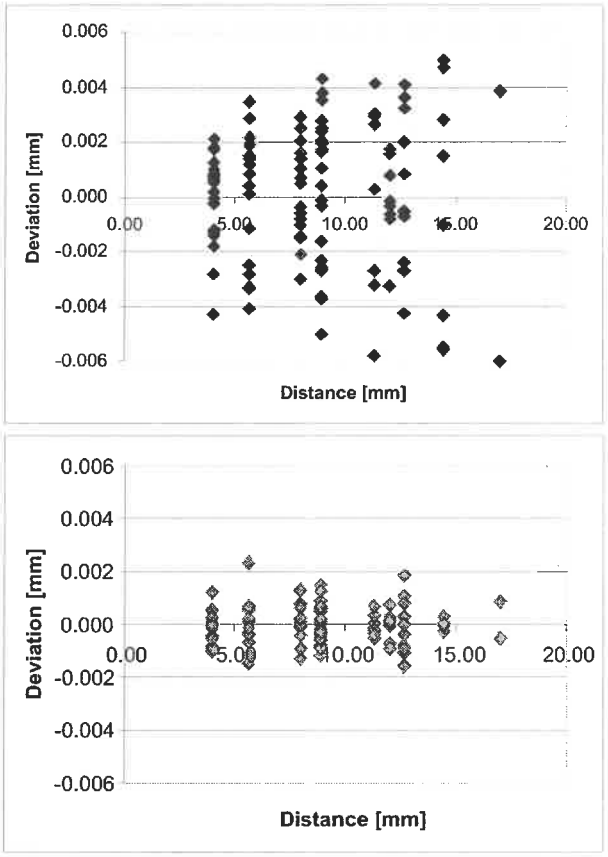

Fig. 8+9: Extracting the surface data of the PTB sphere plate by the ISO-method provides an error of indication for size measurement of ≈ 6µm (fig. 9a). By using the phoenix|x-ray surface extraction, the size measurement error is as small as ≈ 3µm (fig. 9b)

EXAMPLE APPLICATIONS

The CT results obtained with the nanotom allow the analysis of the spatial microstructure of small samples with submicrometer resolution as well as high precision metrology. Nearly any internal detail that corresponds to a contrast in material, density or porosity can be visualized and internal distances can be measured. Highly accurate extractions of the surface data facilitate 3D metrology and reverse engineering processes.

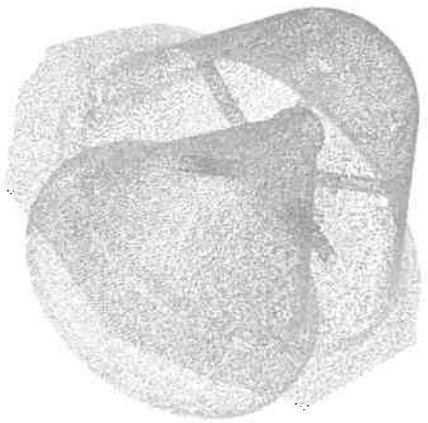

Fig. 10: Point cloud representation of an injection nozzle performed with the surface|-extraction module of phoenix|x-ray. Due to its innovative algorithm the module is independent of beam-hardening artefacts.

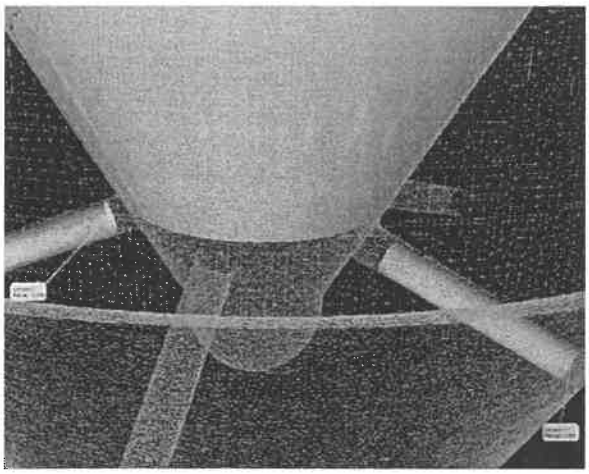

Fig. 11: Cone and cylinders fit to the polygon representation of a scanned injection nozzle. The channel diameter is 150 microns.

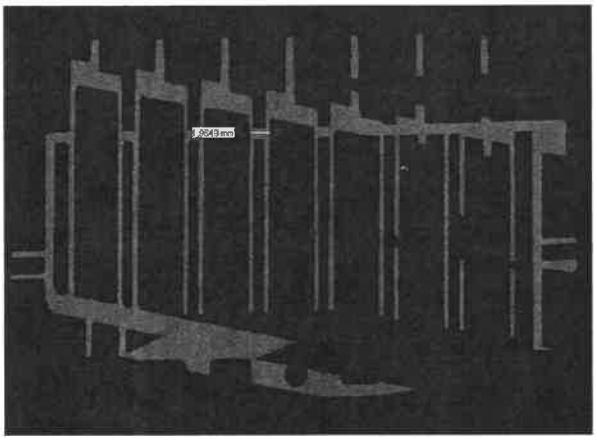

Fig. 12: Distance measurement of internal geometries of a plastic connector using a tomographic slice. The measured distance is 1.965 mm.

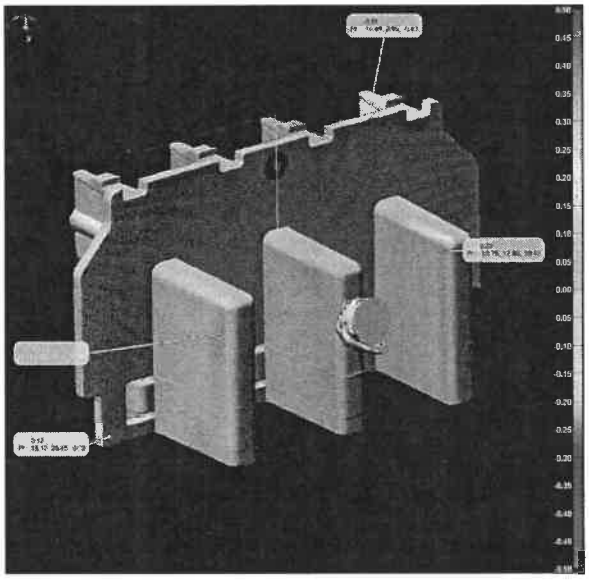

Fig. 13: Variance analysis between the extracted surface of the measured volumetric CT data and the CAD data of a connector. Deviations are displayed using pseudo-colours and may also be virtually sectioned. (Courtesy by Phoenix Contact)

OPTICAL EFFECT OF SURFACE FINISH BY SINGLE POINT DIAMOND MACHINING

Lei Li[1], Stuart A. Collins, Jr.[2], and Allen Y. Yi[1]
[1]Department of Industrial, Welding and Systems Engineering
[2]Electroscience Laboratory
The Ohio State University
Columbus, Ohio, USA

INTRODUCTION

Ultraprecision diamond turning process has been used as a direct optical surface generation method since the 1960s' [1-2]. With this process, high quality optical surfaces can be fabricated without post machining polishing.

Although ultraprecision diamond turned optics can have surface roughness down to tens of nanometers or even lower, they may still contain defects due to machining process variations. Diamond turned surfaces have been carefully studied before [3-12]. The previous research however was mainly focused on the causes of the surface texture and one of the main goals of these studies was to improve the surface roughness (R_a). For many of the diamond turned surfaces used in optical applications, surface roughness R_a or surface power spectrum density (PSD) analysis alone is not adequate.

Analyses of diffraction and scattering off diamond machined optical surfaces were also performed before [13-22]. These analyses have resulted in several methods for analyzing and measuring scattering. However, since these studies were often based on simplified surface models, they are not a full representation of actual machined surfaces. Furthermore the influence of the machining process parameters on optical performance was not evaluated.

The scope of this research can be summarized as follows:
1. Establish the relationship between the process parameters and the optical performance of diamond turned surface and identify the proper process conditions for optical surfaces that meet certain design requirements.
2. Investigate optical effects of the diamond machined surfaces using diamond tools with small tool nose radius (~ 2 μm). These tools are specifically designed for fabricating diffractive optical elements.
3. Study optical effects of surfaces that were machined using different processes, i.e., diamond turning, broaching and slow tool servo. This study is much more important in slow tool servo process since the cycle time can be extremely long and the step size has a much higher impact on surface quality.

THEORETICAL ANALYSIS

Diamond Machining Process

Diamond tools have sharp cutting edges (50 nm to 300 nm). Therefore the machining process always involves in very small depth of cuts (from sub-micron to several microns [23]) and very small cutting forces (about 0.1 to several Newtons [24]). Due to the small depth of cutting, which is close to or even less than engineering materials' crystal lattice size, the material properties will have a large effect on the cutting force and machined surface [3,4]. Since there are no effective methods available to monitor the machining process directly due to small depth of cut and cutting force, ultraprecision diamond machining process is not well understood yet.

Generally speaking, ultraprecision diamond machined surfaces have these characteristics:
1. Periodic tool marks along the radial direction.
2. Surface roughness caused by tool-workpiece vibration.
3. Surface roughness due to materials induced variation.
4. Surface roughness due to spindle error motion.
5. Other factors, such as machine tool servo performance, tool wear, environmental variation, chip scratches, and center alignment error, all are directly related to surface quality.

Scattering Calculation

Scalar Method:

The distribution of light diffracted off a diamond machined surface can be calculated using 2D

Discrete Fourier Transform (DFT), which is based on the scalar diffraction theory.

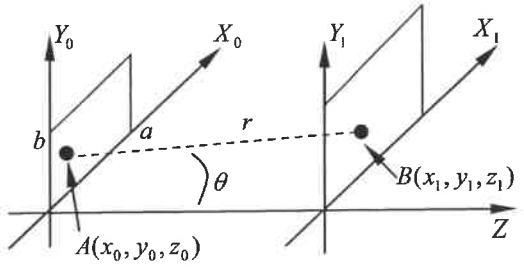

FIGURE 1. Diffraction from sample surface.

In figure 1, Electrical field $E_1(x_1, y_1, z_1)$ at point $B(x_1, y_1, z_1)$ on the observation plane $X_1 - Y_1$ is the result of light diffracting from the object plane $X_0 - Y_0$ and can be expressed as [25]:

$$E_1(x_1, y_1, z_1) = \frac{jk}{2\pi} \int_{-\infty}^{\infty} \int_{-\infty}^{\infty} E_0(x_0, y_0, z_0) \cos\theta \frac{e^{-jkr}}{r} dx_0 dy_0$$

Where r is the length of line AB, θ is the included angle between line AB and Z axis.

Under the far field diffraction condition, electrical field on the observation plane can be written as:

$$E_1(u_1 \frac{\lambda\sqrt{x_1^2 + y_1^2 + z_1^2}}{a}, v_1 \frac{\lambda\sqrt{x_1^2 + y_1^2 + z_1^2}}{b}, z_1)$$

$$= \frac{jk}{2\pi} \frac{A}{MN} \sum_{n=0}^{N-1} \sum_{m=0}^{M-1} E_0(\frac{n}{N}a, \frac{m}{M}b, z_0) e^{j\frac{2\pi}{N}(nu_1 + mv_1)}$$

where $A = \frac{z}{(x_1^2 + y_1^2 + z_1^2)} e^{-jk\sqrt{(x_1^2 + y_1^2 + z_1^2)}}$,

$u_1 = \frac{x_1}{\sqrt{(x_1^2 + y_1^2 + z_1^2)}} \frac{a}{\lambda}, v_1 = \frac{x_1}{\sqrt{(x_1^2 + y_1^2 + z_1^2)}} \frac{b}{\lambda}$,

and $E_0(\frac{n}{N}a, \frac{m}{M}b, z_0)$ is the output electrical field on the object plane. $\frac{n}{N}a, \frac{m}{M}b$ are descrete x and y coordinates for points on the object plane, and n = 1,2,...N, m = 1,2,...M. If the surface profile of the sample is known as $d = d(x_0, y_0)$, then electrical field E_0 reflected off the object plane can be calculated from $E_0 = Ee^{-j2\pi\frac{2d}{\lambda}}$ for normal incident plane wave light.

Figure 2(a) is an example of a diamond turned surface profile that was measured on a Veeco optical profilometer, and figure 2 (b) is the calculated diffraction pattern. In figure 2(a), the 10 μm spacing tool marks can be clearly identified. These tool marks are responsible for several diffraction orders as well as random scattering when light is reflected off the surface. In figure 2(b), the spot in the center (indicated by the arrow) is the specular reflection beam. The spots around it are ±1 and ±2 order diffraction, which were caused by the periodic tool marks. The scattered light around the center was produced by random surface roughness.

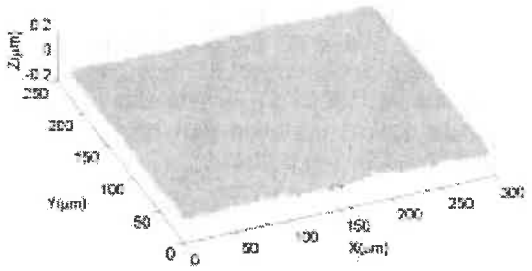

FIGURE 2(a). Surface profile of the sample,

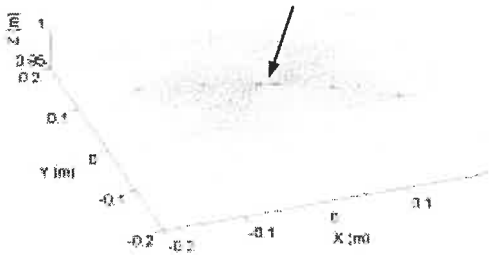

FIGURE 2(b). Spatial distribution of diffraction from the sample surface in (a).

Vector Method:

One of the popular vector scattering analysis methods is the Rayleigh-Rice perturbation theory, which was originally used in radar scattering analysis [26]. Church [14], Elson and Bennett [21] applied the Rayleigh-Rice theory in optical scattering and obtained the following expression [22]:

$$\frac{(dP/d\Omega_S)d\Omega_S}{P_i} = \left(\frac{16\pi^2}{\lambda^4}\right)\cos\theta_i \cos^2\theta_S Q S(f_x, f_y) d\Omega_S$$

where $S(f_x, f_y)$ is the PSD of the optical surface. Q is a function related to the linear polarization state of incident light. P_i is the incident light power. $dP/d\Omega_S$ is the scattering light power in direction s, and $d\Omega_S = \sin\theta_S d\phi_S d\theta_S$ is differential solid angle.

Although the Rayleigh-Rice theory can provide a precise relationship between the surface PSD function and the scattered light, it has stricter surface roughness requirements.

EXPERIMENTS

Machining Conditions:

To establish the relationship between process parameters and optical performance of a machined surface, a number of experiments were designed and performed. The machining experiments were all performed on the 350FG Freeform Generator (www.nanotechsys.com), a diamond turning machine that is capable of performing slow tool servo and broaching. Sample material was Al 6061.

Experiment one (Table 1) and two are designed to study the regular diamond turning process with regular diamond tool (tool radius ~ 3mm). In experiment one, the spindle speed was kept constant and feed rates were varied. As a result, the tool mark spacing was reduced from 15 μm to 0.8 μm. In experiment two, the spindle speed and feed rate were changed at the same time so the tool mark spacing was kept constant. Experiment three was designed to study the efficiency and quality of the devices that were fabricated with diffractive tools. To simplify analysis, the diffractive tools were used only on flat surfaces. Experiment four and five were particularly aimed at investigating the slow tool servo and broaching processes.

Table 1. Diamond turning experiment one with regular tool

No.	Feed rate (mm/min)	Spindle speed (rpm)
1.1	15	1,000
1.2	10	1,000
1.3	8	1,000
1.4	5	1,000
1.5	4	1,000
1.6	2	1,000
1.7	1	1,000
1.8	0.8	1,000

Measurement

Both surface profile and surface scattering measurements were taken on the machined surface. The surface profiles of the samples were measured on NT 3300 Veeco White Light Profilometer. The scattering from the sample surface was measured by a home built device shown in figure 3. A light detector which is connected with an Aerotech ADRT-200 rotary stage rotates around the sample surface and records the intensity of the scattering light from the machined surface. The surface scattering was calculated by both scalar and vector methods using the surface profile data from Veeco white light profilometer. The analytical and experiment results were compared to each other to identify the influence of machining processes on the optical performance.

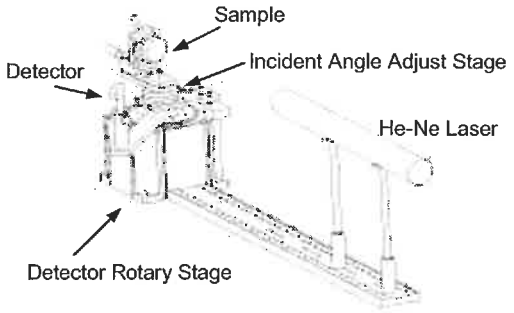

FIGURE 3. Scattering measurement device.

RESULTS AND DISCUSSIONS

The measured scattering in experiment one was shown in figure 4. The scattering of each sample consists of three parts: specular reflection, high order diffraction and random scattering. As the tool mark spacing decrease from 15 μm to 0.8 μm, the high order diffraction energy rapidly faded out, while the random scatterings of these samples were similar.

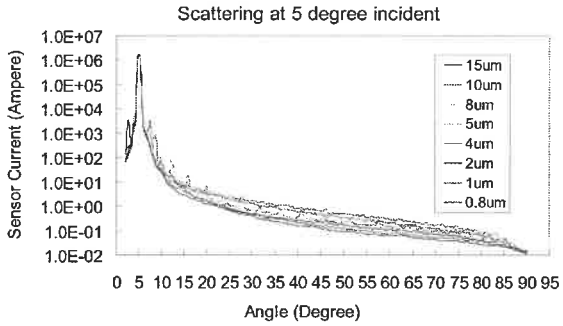

FIGURE 4. Scattering measurement results of experiment one.

REFERENCES

[1] Ikawa N, Donaldson RR, Komanduri R, König W, McKeown PA, Moriwaki T, Stowers IF. Ultraprecision metal cutting — the past, the present and the future. Annals of the CIRP. 1991; 40: 587-594.

[2] Chiu M, Lee WB. Development of ultra-precision machining technology. Fifth International Conference on FACTORY 2000. 1997; 486-490.
[3] Furukawa Y, Moronuki N. Effect of material properties on ultra precise cutting processes. Annals of the CIRP.1988; 37:113-116.
[4] Cheung CF, Lee WB. A multi-spectrum analysis of surface roughness formation in ultra-precision machining. Precision Engineering. 2000; 24: 77-87.
[5] Revel P, Khanfir H, Fillit RY. Surface characterization of aluminum alloys after diamond turning. Journal of Materials Processing Technology. 2006; 178: 154-161.
[6] Khanfir H, Bonis M, Revel P. Improving waviness in ultra precision turning by optimizing the dynamic behavior of a spindle with magnetic bearings. International Journal of Machine Tools & Manufacture. 2005; 45: 841-848.
[7] Hocheng H, Hsieh ML. Signal analysis of surface roughness in diamond turning of lens molds. International Journal of Machine Tools & Manufacture. 2004; 44: 1607-1618.
[8] Kim JD, Kim DS. Surface characteristics of magnetic-disk cutting using a single-crystal diamond tool in an ultraprecision lathe. Journal of materials Processing Technology. 1996; 59: 303-308.
[9] Ogloza AA, Decker DL, Archibald PC, O'Connor DA, Bueltmann ER. Optical properties and thermal stability of single-point diamond-machined aluminum alloys. In: Armold JB, Parks RE, editors, Advances in Fabrication and Metrology for Optics and Large Optics: Proc. Soc. Photo-Opt. Instrum. Eng.; 198; 966: p. 228-251.
[10] Cheung CF, Lee WB. Surface Generation in Ultra-precision Diamond Turning: Modelling and Practices. Professional Engineering publishing; 2003.
[11] Fawcett SC. Small amplitude vibration compensation for precision diamond turning. Precision Engineering. 1990; 12: 91-96.
[12] Roblee J. Factors Affecting Surface Finish in Diamond Turning. Available from: http://www.precitech.com/FactorsAffectingSurfFinish.pdf
[13] Bennett JM, Mattson L. Introduction to Surface Roughness and Scattering. 2nd ed. Optical Society of America; 1999.
[14] Church EL, Zavada JM. Residual surface roughness of diamond-turned optics. Applied Optics. 1975; 14: 1788-1795.
[15] Church EL, Howells MR, Vorburger TV. Spectral analysis of the finish of diamond-turned mirror surfaces. In: Howells MR editor, Reflecting Optics for Synchrotron Radiation: Proc. of SPIE; 1981; 315: p. 202-218.
[16] Myler JK, Kelsall D, Hall PR. Effect of surface texures on reliability of IRMTF measurements. In: Williams TL, editor, Image Assessment: Infrared and Visible: Proc. of SPIE; 1983; 467: 105-114.
[17] Brodmann R, Gerstorfer O, Thum G. Optical roughness measuring instrument for fine-machined surfaces. Optical Engineering. 1985; 243: 408-413.
[18] Church EL, Jenkinson HA, Zavada JM. Measurement of the Finish of Diamond-Turned Metal Surface by Differential Light Scattering. Optical Engineering. 1977; 16: 360-374.
[19] Lu R, Tian GY. On-line measurement of surface roughness by laser light scattering. Measurement Science and Technology. 2006; 17: 1496-1502.
[20] Kotha A, Harvey JE. Scattering Effects of Machined Optical Surfaces. In: Stover JC, editor, Optical Scattering in the Optics, Semiconductor, and Computer Disk Industries: Proceeding of SPIE; 1995; 2541: p. 54-65.
[21] Elson JM, Bennett HE, Bennett JM. Scattering from optical surfaces. In: Shannon RR, Wyant JC, editors. Applied Optics and Optical Engineering. Vol. 7, Academic Press; 1979. p.191-244.
[22] Stover JC, Optical Scattering-Measurement and Analysis. 2nd ed. SPIE; 1995.
[23] Yuan ZJ, Zhou M, Dong S. Effect of diamond tool sharpness on minimum cutting thickness and cutting surface integrity in ultraprecision machining. Journal of Materials Processing Technology. 1996; 62: 327-333.
[24] Arcona C, Dow TA. An Empirical Tool Force Model for Precision Machining. Journal of Manufacturing Science and Engineering. 1998; 120: 700-707.
[25] Collins SA Jr. Optics With Laser Light, Class Notes, Ohio State University; 2002
[26] Rice SO. Reflection of Electromagnetic Waves from slightly Rough Surface. Commun. Pure Appl. Math. 1951; 4: 351-378.

DEVELOPMENT OF LARGE ULTRA-PRECISION DIAMOND TURNING MACHINE FOR MAKING NEXT GENERATION HARD X-RAY TELESCOPES

Yoshiharu Namba[1], Takuji Shimomura[1], Toshiyuki Shimizu[1], Hideyo Kunieda[2], Yasushi Ogasaka[2] and Koujun Yamashita[2]
[1]Department of Mechanical Engineering
Chubu University
Kasugai, Aichi 487-8501, Japan
[2]Department of Physics
Nagoya University
Nagoya, Aichi 464-8602, Japan

INTRODUCTION

Now we have three soft X-ray telescope satellites such as Chandra [1], XMM-Newton [2] and Suzaku [3] launched in 1999 and 2005. All three telescopes were constructed by nested multiple grazing incidence reflecting mirrors consisted by a paraboloid and hyperboloid of revolution, as shown in Fig.1. The mirror surfaces were coated with Ir or gold. The surface roughness specification for the coated film was less than 0.5 nm rms.

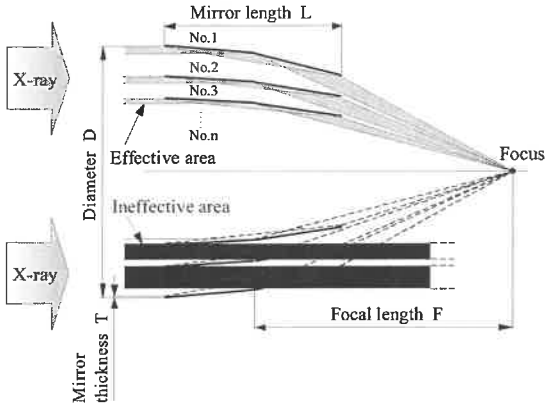

FIGURE 1. Structure of a grazing incidence X-ray telescope [4].

Focusing optics in hard X-ray region above 10 keV will open a new window of the universe, where extremely hot astrophysical phenomena or non-thermal high energy phenomena like jet occur in unknown way. There is a new proposal called NeXT to make a next-generation hard X-ray telescope having replicated Pt/C multilayer mirrors of aspheric shapes and to launch it after 2013. The specifications of such mirrors of 600 mm or 500 mm in maximum diameter are as follows; the shape accuracy of aspheric mirrors is less than 100 nm and surface roughness is also less than 0.3 nm rms. The mirror length is 400 mm and the thickness of mirror substrate is around 0.2 mm. The focal length is estimated 12 m. In the case of a grazing incidence hard X-ray telescope, hundreds of Pt/C multilayer mirrors of aspheric shape in high precision are needed for collecting X-ray from the galaxy. The weight of the telescope has to be light due to the space application, and the mirror surface area has to be larger for collecting power, so that the next-generation X-ray telescope consists of nested mirrors having Pt/C multilayer. For obtaining light-weight mirrors, replication technology is essential.

Figure 2 shows a manufacturing process of replicated Pt/C multilayer mirrors. Only amorphous material such as glass and electroless nickel can be polished into the aspheric shape down to less than 0.3 nm rms. We decided to use aluminum alloy covered with electroless nickel plating as a molding die material, because of higher machinability rather than glass. The electroless nickel is diamond-turned into aspheric shapes in high precision and polished into less than 0.3 nm rms of surface roughness. Then, Pt/C multilayers are deposited on the electroless nickel die and glued a mirror substrate over the die. The last process is separation of the mirror substrate from the molding die.

This paper deals with a large ultra-precision diamond turning machine to make various ultra-precision molding dies up to 600 mm in diameter and 400 mm in mirror length, and some experimental results on the machine and dies.

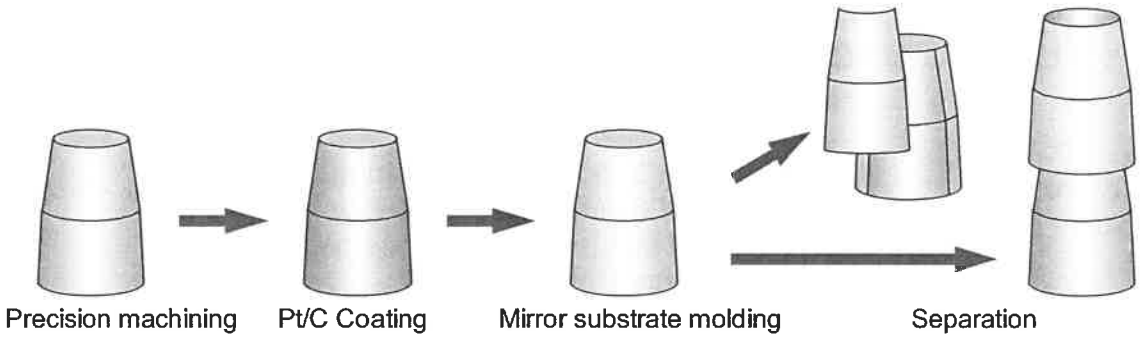

FIGURE 2. Manufacturing process of replicated mirrors for next generation hard X-ray telescopes.

LARGE ULTRA-PRECISION DIAMOND TURNING MACHINE

Figure 3 shows the large ultra-precision diamond turning, polishing and measuring machine that was newly developed for making aspheric electroless nickel molding dies of 600 mm in diameter. The machine has a large rotary table supported by a precise air bearing, and horizontal and vertical axes are moved by linear slides in 1 nm resolution. The machine was installed on a vibration proof foundation in a temperature controlled clean room. The machine was designed for water proof for polishing and washing processes. Four axes are controlled by FANUC numerical controller.

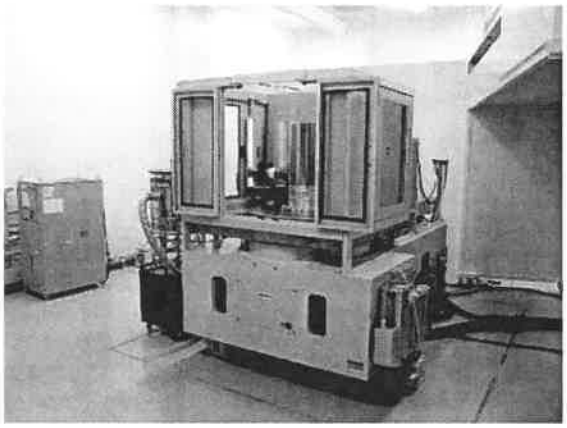

FIGURE 3. Newly developed large ultra-precision diamond turning machine of vertical spindle on a vibration proof foundation in a clean room.

Figure 4 shows an example of shape accuracy measurement of a machined aspheric molding die on the machine. Various high resolution sensors are prepared from 10 nm up to pico meter resolution.

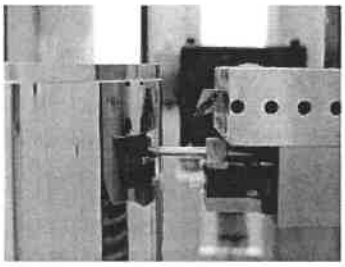

FIGURE 4. Non contact ultra-precision shape measurement on the diamond-turned molding die.

MEASUREMENT OF ACCURACY ON MACHINE

The machine was covered by an enclosure as shown in Fig. 5 for keeping better temperature stability less than 0.1 K. Figure 6 shows the temperature variation in the clean room, in the enclosure and in the machining area on the machine. The temperature variation in the

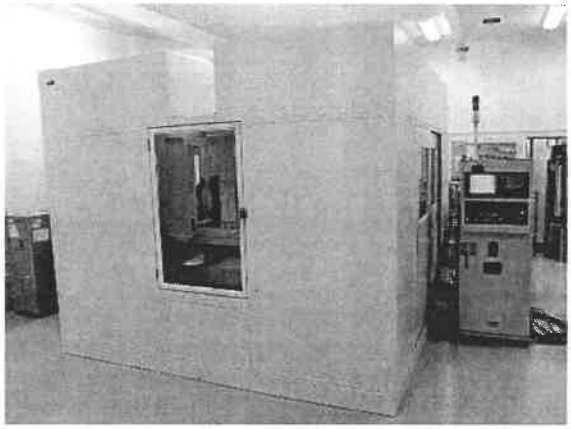

FIGURE 5. Newly developed large ultra-precision diamond turning machine covered with an enclosure for keeping the precise temperature control less than 0.1 K.

enclosure is less than ± 0.1 K, though the temperature variation in the clean room is high. The temperature variation in the machining box is rarely low, that is less than ±0.07 K. The machine is operated by a PC and numerical controller outside of the enclosure.

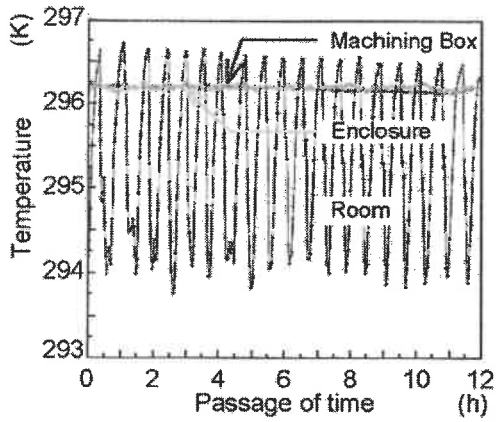

FIGURE 6. Temperature variation in the clean room, enclosure and machining box for 12 hours.

We made an optical flat gauge of 450 mm length and 50 mm width, and measured the straightness of the optical gauge with a laser interferometer in the ILE of Osaka University. The straightness of the zero expansion glass-ceramic gauge is less than ±7 nm/400 mm. The movement of each axis was measured by measuring the straightness of this gauge with a high resolution sensor on each axis.

Figure 7 shows the straightness of y-axis during +y and –y movements using the above mentioned method. The maximum straightness error is 208 nm over 400 mm y-axis traverse. The difference of straightness error between forward or +y movement and backward or –y movement is just ±7 nm/400 mm. These data are the average of several traverses.

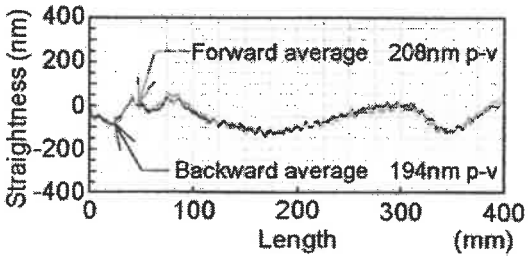

FIGURE 7. Straightness of y-axis movement, measured with a high resolution sensor and optical straightness gauge.

Then the machine was moved along the y-axis by controlling with the modified NC data obtained in Fig. 7. Figure 8 shows the y-axis straightness error of ± 34 nm/400 mm after compensation.

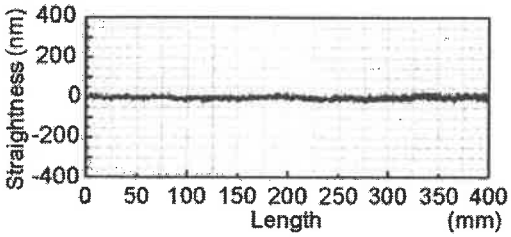

FIGURE 8. Straightness of y-axis movement after compensation.

MACHINING OF MOLDING DIES

Diamond turning metal dies

More than hundreds of molding dies are requested by astronomers for making replicated hard X-ray telescope mirrors, so productivity is also essential for making molding dies as well as shape accuracy in this purpose.

Electroless nickel and aluminum alloy dies of 300 mm in diameter and 400 mm in mirror length were machined for making a Wolter type I mirror of 12 m in focal length as shown in Fig. 9. The outer shape of dies was composed by a paraboloid and hyperboloid of revolution.

FIGURE 9. Diamond turning of electroless nickel die.

Figure 10 shows a photograph of single-point diamond turned aspheric molding dies. The sample on the left hand is of electroless nickel and the other one on the right hand is of aluminum alloy. The latter one looks a perfect mirror and no defect can be seen. We can see an inflection point at the center of both dies. At the first stage, the shape accuracy of ±475 nm on an electroless nickel sample and ±90 nm on an aluminum sample after compensation. These numbers will be improved by further experiments.

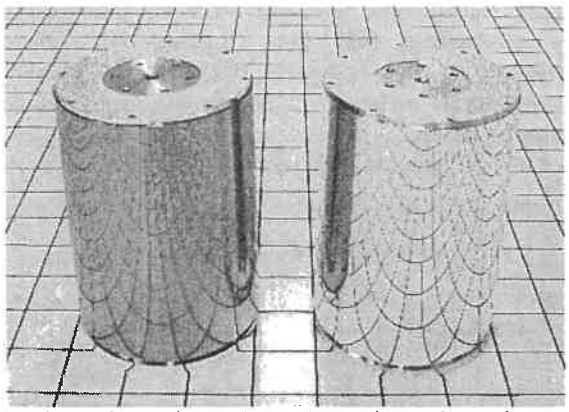

FIGURE 10. Photograph of diamond turned electroless nickel (on the left) and aluminum alloy (on the right) dies of 300 mm in diameter and 450 mm in length.

Trial polishing of aspheric mirrors

For perform simple-point diamond turning, polishing, coating, molding and separation tests, we made some small scale molding die samples of 300 mm in diameter and 210 mm in mirror length.

Figure 11 shows two electroless nickel molding dies of 300 mm in diameter and 210 mm in mirror length. The upper part of 10 mm in length is hyperboloid and the lower part of 200 mm in length is paraboloid. The sample on the left hand was diamond turned, and the other on the right hand was optically-polished after diamond turning. The former one is not so luster and we could not see any defect on the latter case.

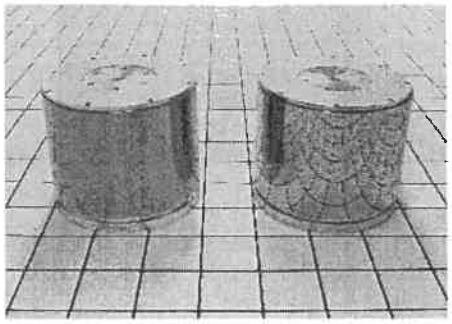

FIGURE 11. Diamond-turned (on the left) and polished (on the right) electroless nickel paraboloid die of 300 mm diameter.

Figure 12 shows surface roughness of polished paraboloid die of 300 mm in diameter, measured with ZYGO Newview 200, and the surface roughness was 0.228 nm rms, better than 0.3 nm rms. So, the specification for the surface roughness on aspheric molding die was satisfied.

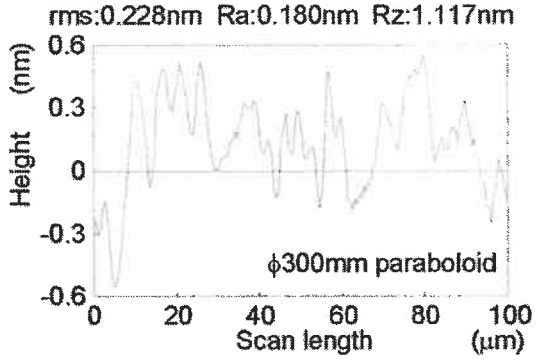

FIGURE 12. Surface roughness of polished electroless nickel paraboloid die of 300 mm diameter.

SUMMARY

A large ultra-precision diamond turning, polishing and measuring machine has been designed and developed for making electroless nickel molding dies of up to 600 mm in diameter. We proposed a method of compensating the straightness error of y and z axis movements of the machine. The specification for the surface roughness on aspheric molding dies of the next generation hard X-ray telescope was satisfied.

ACKNOWLEDGEMENTS

The authors would like to thank Toshiba Machine Machinery Co., Ltd. for designing and manufacturing the special diamond turning machine, and ILE of Osaka University for flatness measurement. This study was supported in part by the Grants-in-Aid for Scientific Research (B) No. 18360073 from the Japan Society for the Promotion of Science, and also the Grants-in-Aid for Scientific Research on Specially Promoted Research No. 15001002 from the Ministry of Education, Culture, Sports, Science and Technology, Japan.

REFERENCES

[1] http://chandra.harvard.edu/

[2] http://xmm.vilspa.esa.es/

[3] http://www.astro.isas.ac.jp/suzaku/index.html.en

[4] Namba, Y., Fushiki, A., Kunieda, H., Ogasaka, Y., Tawara, Y. and Yamashita, K., 2006, Manufacturing of Replicated Pt/C Multilayer Mirrors for Hard X-Ray Telescope, Proc. ASPE 2006 Annual Meeting, Monterey: 407-410.

RAPID MANUFACTURING OF FAST ASPHERES

PRADEEP SUBRAHMANYAN and GEORGE GARDOPEE
RAPT Industries, Inc.
46535 Fremont Blvd.
Fremont, CA 94538

ABSTRACT

An integrated manufacturing process for the processing of optics has been developed. This involves generation of the optic by conventional CNC grinding. Following this, the optic is figured using an atmospheric pressure, sub-aperture plasma tool. High material removal rates and excellent determinism have been demonstrated even for very lightweight mirrors (< 5 Kg/m^2). Conformal polishing is then used to recover the surface roughness. The resulting damage-free surfaces are figured to less than a tenth wave P-V, and Ra roughness less than 4 Angstroms. Results are demonstrated on SiC substrates and the process is shown to be considerably faster than conventional approaches. Swing-arm profilometry is used for metrology to guide the manufacturing process and to generate the error maps given that the surfaces being processed can be either specular or diffuse.

INTEGRATED MANUFACTURING PROCESS

The conventional approach to the manufacture

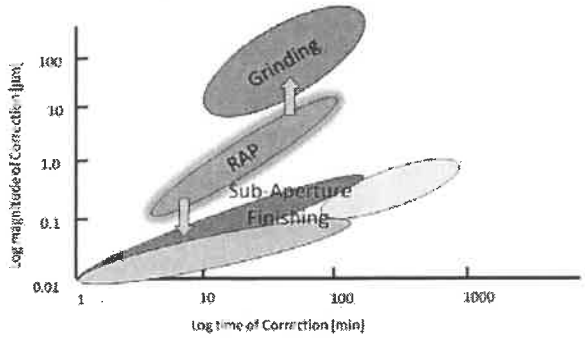

FIGURE 1. Processes flow for optics manufacturing

of precision optics relies on mechanical removal of unwanted material. Figure 1***FIGURE 1*** is a notional cartoon that illustrates the regimes of operation of the various processes involved in the fabrication of precision optics, primarily aspheres as a function of material removal rate (MRR). A near net shape substrate or a best fit sphere is first generated to the appropriate figure using fixed grinding wheels. Advances in precision grinding have allowed ground substrates to have figure errors on the order of a few microns. Typically, this has been followed by full and sub-aperture polishing iterations. These iterations involve sequentially smaller and smaller grits of abrasives and eventually converge on the desired figure. Full aperture laps and handwork by trained opticians have given way to sub-aperture techniques in final finishing. Such sub-aperture finishing techniques typically deconvolve the tool footprint from the figure error to yield a dwell time. This dwell-time is then implemented in a tool-path algorithm and the process is implemented in an iterative fashion to yield the desired figure. Commercial offerings are available from a number of manufacturers and the technologies involved include

1. Computer Controlled Polishing
2. Magneto-Rheological Fluid polishing
3. Single Point Diamond Turning
4. Ion-Beam Figuring

The removal mechanism can be chemical mechanical polishing, single point diamond turning or even the kinetics of an ion-beam figuring process. These processes typically have low MRR and as such a gap (from an economic point of view) exists between a ground substrate and one that is suitable for final figuring using the sub-aperture techniques mentioned. To illustrate the point, consider the manufacturing of mirror segments for the OverWhelmingly Large (OWL) Telescope illustrated in Figure 2.

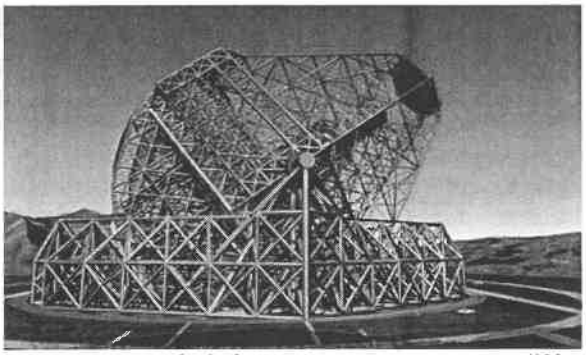

FIGURE 2. Artist's impression of the OWL telescope

Even with advances in precision grinding and the various sub-aperture finishing steps, it would typically take on the order of 6 months for finishing a single mirror segment and for the 2000 or more mirror segments involved in making the telescope, this requires a significant capital outlay or a few lifetimes.

The other issue at hand with conventional processing is that of sub-surface damage. Material removal rates for the processes discussed so far are almost invariably tied to the severity of the mechanical removal mechanism. As such, a relatively gentle process such as ion-beam figuring process has a much lower material removal rate than that of grinding for example as illustrated in Figure 1. One description of polishing that is widely prevalent in industry is that each successive polishing iteration is meant to remove damage from the previous iteration while putting in less damage than that from the previous iteration. Opticians often use rules of thumb such as removing 3x the depth of material corresponding to the previous grid size used.

When mechanical processes are applied to a substrate, a layer of microcracks is left behind. A considerable amount of stress and strain energy is stored in this layer of sub-surface damage (SSD). Typically, when progressing from one iteration to the next, the state of SSD and the associated strain energy changes. This change

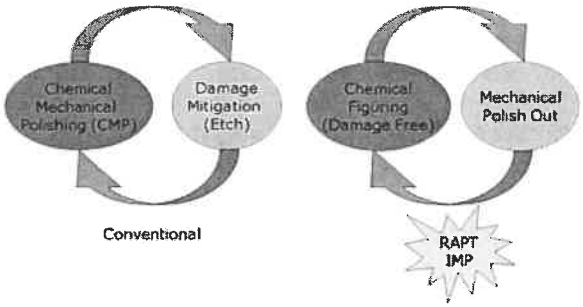

FIGURE 3. Comparison of RAP and conventional polishing approaches[5]

in strain energy can cause a change in figure of the optic depending on how drastic the change is, and unfortunately is never measured or compensated for in traditional sub-aperture polishing approaches. As the thickness of the face sheet of such lightweight optics decreases, the contribution to figure change due to change in strain energy increases dramatically. This causes conventional sub-aperture approaches to be somewhat non-deterministic unless a separate etch step is used to relieve all the damage from the previous polishing step.

RAPT Industries, Inc. has developed a process using which the bulk of the material removal in a figuring step is done in a non-contact, atmospheric pressure, dry chemical etch. This allows one to simultaneously figure without adding SSD while removing SSD from previous (grinding) operations and leads to true deterministic figuring for high aspect ratio (small facesheet thickness) lightweight mirrors.

Another issue that compounds the problem even more is the use of advanced ceramic materials such as silicon carbide (SiC). The various operating regimes in Figure 1 change dramatically when a material such as SiC is considered. SiC can be abraded only with diamond, and even then, to obtain acceptable material removal rates, a significant amount of normal pressure has to be applied according to Preston's law[1]. For a lightweight mirror, this causes serious problems as is illustrated in Figure 4.

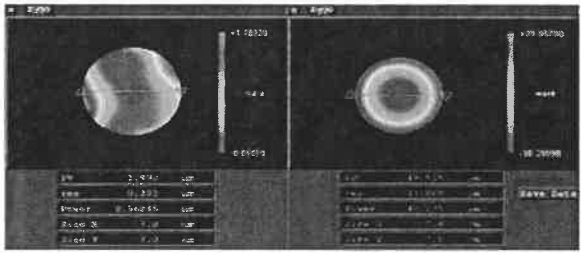

FIGURE 4. Figure error prior (1.4 um PV) to and post (49.5 um PV) milling on a 3" sample representing the inscribed circle on a lightweighted optic. Notice the convex bow indicative of the compressive stress on the damage layer.

For the experiment above, a 3" disk of CVD SiC was fine polished on both surfaces to leave them "damage-free". One surface was used for metrology while the other was milled using a process proprietary to a SiC manufacturer. The aspect ratio of the disk was selected to represent the inscribed circle on a lightweighted mirror so the deformation due to machining would be representative of that of the pockets of a lightweighted mirror during a similar operation. A peak deflection of almost 50 μm was observed after the milling operation illustrating the sensitivity of figure error to sub-surface damage.

A series of RAP etching steps were then performed to both relieve the stress and return it to the original damage-free state and to calibrate the depth of the damage layer (this was done by carefully measuring the thickness of the material etched away during each iteration until the substrate was returned to its original state). The

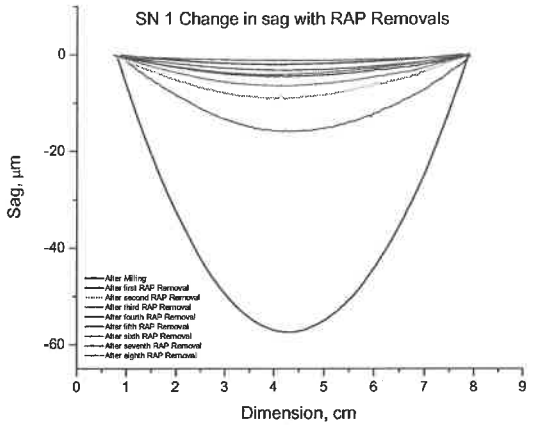

FIGURE 5. Change in sag with RAP removal steps

change in sag is illustrated in Figure 5. Using an approach prevalent in determining thin film coating stresses, the Stoney equation was used to correlate the change in sag to the amount of surface stress present[2,6].

$$\sigma = \frac{4\delta E d^2}{3(1-\upsilon)t_{ssd}D^2}$$

where

σ = Twyman stress (MPa)
ν = Poisson's ratio
E = Young's Modulus (MPa)
t_{ssd} = Damage layer thickness (nm)
δ = Circular plate deflection (nm)
d = Substrate thickness (mm)
D = Substrate diameter (mm)

Using the above equation which is conservative at best since it models a uniform state of stress across the entire damage layer, a peak stress of 0.9 GPa was observed in the substrate. Damage layer thickness for SiC typically range between 15-25 µm in thickness. These numbers confirm the big issue with change in figure between polishing iterations using conventional approaches.

The integrated manufacturing process developed at RAPT removes this layer of damage (around 15-25 µm) left by prior grinding steps and then iteratively figures and buffs (conformally) the optic to reach the final specification on both figure and roughness of the optic. As an example, consider the manufacturing of an on-axis parabola with the following specifications.

Clear aperture: 200mm
Conic constant: -1 (parabola)
f/#: 2.25
Figure Error < 0.050 λ RMS
Roughness < 1 nm RMS

Such an optic was figured using the integrated manufacturing process achieving a final roughness of about 0.33nm RMS in less than 3 weeks. Further improvements in processing will allow the extension of the process to figure errors as low as 0.010 λ RMS.

FIGURE 6. On-axis parabola for Ball Aerospace

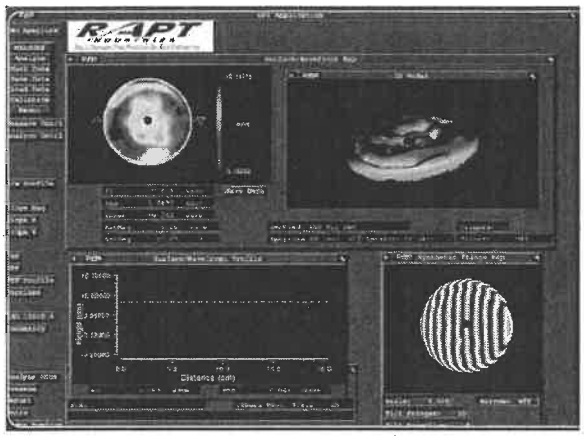

FIGURE 7. Interferometric data for figure error

CONCLUSIONS

Conventional approaches to the fabrication of high-aspect ratio precision surfaces are limited due to the damage imparted to the substrates

and the resulting stress. An Integrated Manufacturing Process has been demonstrated to provide rapid and predetermined convergence to the desired shape. This IMP is being deployed to manufacture optics to about 0.25 waves P-V at which point in time, existing final finishing approaches can take over to obtain a surface with relatively little damage and with minimal mid-spatial frequency errors.

ACKNOWLEDGEMENTS

The authors are grateful to Dr. Jeffrey Carr for some of the early work on RAP™. This work was supported under US. Army contracts DAAD19-03-2-0003 and W911NF-04-2-0001 and U.S. MDA contract W9113M-06-C-0067. RAP™ is a trademark of RAPT Industries, Inc.

REFERENCES

[1] Preston, F. W., 1921, The structure of abraded glass surfaces, Trans. Opt. Soc. v. 23, 141-164.

[2] Dalladay, A. J., 1922, Some measurement of the stress produced at the surfaces of glass by grinding with loose abrasives, Trans. Opt. Soc. London v. 23, 170-173.

[3] Randi, J. A., Lambropolous, J. C., and Jacobs, S. D., 2005, Subsurface damage in some single crystalline optical materials, Appl. Optics v. 44, 2241-2249

[4] Johnson, J. S., Grobsky, K., and Bray, D. J., 2002, Rapid fabrication of lightweight silicon carbide mirrors, in Optomechanical Design and Engineering 2002 (A. E. Hathaway, ed.), Proceedings of SPIE v. 4771, p. 243-253.

[5] Subrahmanyan, P.K., Gardopee, G., Fiske, P.S., and Chang, A., Reactive Atom Plasma (RAP) Processing of Optical Surfaces *in Annual Proceedings of the American Society for Precision Engineering, 2006*

[6] Verma, Y., Fiske, P.S., Subrahmanyan, P.K., and Gardopee, G., Damage-free Processing of Silicon Carbide Optics, *in Annual Proceedings of the American Society for Precision Engineering, 2006*

MANUFACTURE AND METROLOGY OF 300 mm SILICON WAFERS WITH ULTRA-LOW THICKNESS VARIATION

Chris Hall[1], Marc Tricard[1], Paul Dumas[1]
[1]QED Technologies, International
1040 University Ave, Rochester, NY 14607

INTRODUCTION

The recently-released December 2006 edition of the International Technology Roadmap for Semiconductors (ITRS-2006) [1] states that the site flatness of a 300 mm diameter silicon wafer (measured using a Site Flatness Least Squares (SFQR) [2] metric over 26 mm x 8 mm site size) will gradually decrease from 80 nm in 2005 to less than 32 nm in 2013, or even less than 14 nm in 2020. This trend will be combined with increasingly tight edge exclusions (going down to 1.5 mm), improved nanotopography (evolving from 20 nm peak-to-valley, or PV, on 2 mm diameter analysis area to less than 8 nm in 2013 or even 4 nm PV in 2020), and a potential (and controversial) conversion to 450 mm wafer size. These requirements are likely to exceed the capabilities of existing finishing processes, typically consisting of a combination of single and double-sided conventional (i.e., full aperture) polishing processes [3], as well as existing metrology approaches. If technology trends from the optics industry are any indication, sub-aperture polishing processes will therefore be required, along with metrology processes used not only for quality control purposes, but to "feed" these novel polishing approaches.

This paper reports on a collaboration between the National Institute of Standards and Technology (NIST) and QED Technologies®, which combined a wafer thickness metrology using infrared interferometry and polishing using Magnetorheological Finishing (MRF®) to successfully finish 300 mm wafers to unprecedented levels of flatness.

METROLOGY

Optical Wafer Thickness Metrology

In a wafer exposure tool, the wafer is held on a wafer chuck. The wafer flatness at the exposure site is determined by the chuck flatness and the thickness variation of the wafer.

Silicon with sufficiently low dopant concentrations is transparent to light at wavelengths larger than 1100 nm. At infrared wavelengths, the thickness variation of silicon wafers, or wafers made from other infrared optical materials, can be characterized using well established optical interferometry methods, that achieve low measurement uncertainties. NIST's Improved Infrared Interferometer (IR^3) is a multi-configuration interferometer, which can be used either with collimated test wave-fronts as a Twyman-Green interferometer, or as a Fizeau interferometer. Figure 1 shows a solid model of the interferometer.

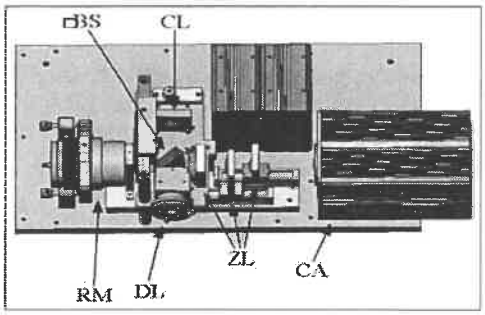

FIGURE 1: NIST Improved Infrared Interferometer (IR^3). The main components of the interferometer are: collimator lens (CL), polarizing beam splitter (PBS), phase-shifting reference mirror mount (RM) for the Twyman-Green configuration, diverger lens (DL), zoom lens system (ZL), and camera (CA).

Measurement set-up

IR^3 was used in Fizeau configuration for the measurements of wafer thickness variation described in this paper. The wafer was inserted into the test beam of the interferometer as the Fizeau cavity of the interferometer. Reflected light from both wafer surfaces returned to the interferometer's camera where interferograms were measured. Phase shifting interferometry was accomplished by varying the laser wavelength and the resulting height-maps directly represented the optical thickness variation of the test wafer. The physical thickness variation of the wafer was obtained by

dividing the optical thickness variation by the refractive index of the wafer material. The Fizeau configuration has many advantages for thickness variation measurements. The interferometer cavity is the wafer, a solid, making turbulence absent, and it is unaffected by vibration. In addition, the coherence length of the laser source can be reduced because the distance between the wafer surfaces is small. This completely eliminates coherent reflections from optical surfaces in the interferometer which would otherwise lead to measurement errors.

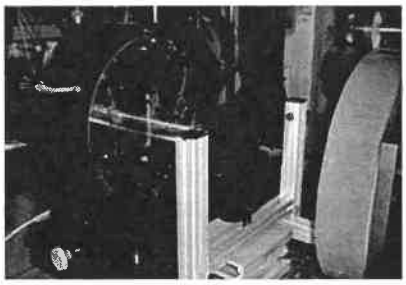

FIGURE 2: Test end of the IR^3 setup for thickness variation measurements of 300 mm wafers. Shown are the collimator lens together with a silicon wafer and a return flat.

MAGNETORHEOLOGICAL FINISHING (MRF®)

MRF is a precision polishing method developed to overcome many of the fundamental limitations of traditional finishing. It is a deterministic finishing process that has the demonstrated ability to produce optical surfaces with an accuracy better than 30 nm peak to valley (PV) and surface micro-roughness less than 1 nm rms on optical glasses, single crystals (such as calcium fluoride and silicon), and glass-ceramics [4,5].

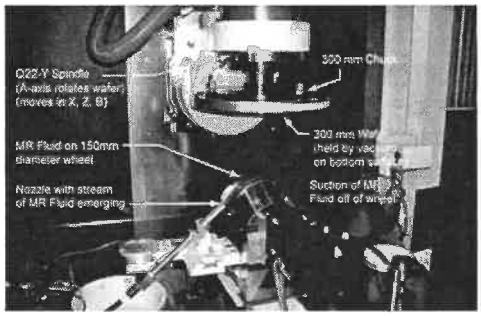

FIGURE 3 Wafer surface is polished in a ribbon of MR fluid.

The stable, sub-aperture nature of the MRF process enables high-precision figure correction. The shear-mode of removal enables the MRF process to improve micro-roughness, remove sub-surface damage, and reduce residual stress [6,7], which is typically introduced in previous manufacturing steps. The forces acting on the surface are predominantly tangential. The normal forces on the individual abrasive particles are very small (limited to hydrostatic). This is in contrast to conventional polishing techniques where an abrasive is forced into the surface through the action of a lap (either bound or loose). [8] With the conventional lapping process, normal forces can dominate, creating scratches, sub-surface damage, and stress.

MRF is most effective at removing micrometer or sub-micrometer material thickness. There are typically more efficient ways (e.g., grinding, turning, etc.) to remove many tens or hundreds of micrometers of materials. MRF excels at improving surfaces from a few micrometers PV to the limits of what is "measurable" (e.g., 30 nm PV or beyond)—a regime where other commercially available technologies bottom out [9].

MRF integration with existing polishing systems

MRF has the potential to work well with today's wafer manufacturing processes by using it to replace the existing intermediate polishing step in a conventional 3-step finishing process. It can be used to control global total thickness variation on silicon wafers as well as improve the thickness uniformity of the top silicon layer in thick or thin silicon-on-insulator (SOI) wafers[10]. This allows manufacturers to maximize their investments in their conventional equipment while introducing MRF (Figure 4).

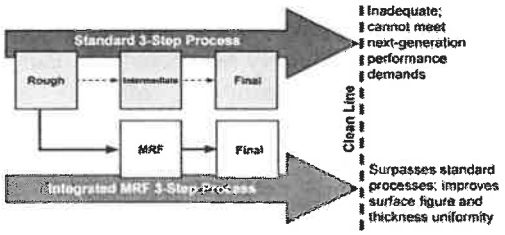

FIGURE 4: MRF can be easily integrated into existing manufacturing processes.

RESULTS

Following measurement by NIST, the 300 mm silicon wafers were delivered to QED

Technologies for polishing. All polishing was performed with a standard MRF polishing machine, diamond-based fluid, a 150 mm wheel, and vacuum fixturing (Figure 5).

MRF is based on a magneto-rheological fluid (one whose viscosity varies in the presence of a magnetic field). This process creates an extremely stable and conformable polishing tool. Since the tool is fluid-based, it conforms to any surface shape and eliminates the need for dedicated tooling. One of the benefits of MRF is its insensitivity to moderate (e.g., micrometers of error) part distortion on the mount during polishing [9]. Unlike other technologies where a tool-to-part distance error can result in a one-to-one print-through error, a plunge error into the fluid typically leads to a negligible removal error. Hence, a pin-chucking solution was not required to hold the part. A circular base with vacuum channels cut into the 5 μm flat surface held the part during polishing. As expected, the mounting scheme did cause some distortion of the wafer surface once the vacuum was applied. As seen in Figure 5, the reflection from the wafer surface of a regularly spaced grid highlights the distortion. However, MRF is insensitive to this level of part deformation and no print-through error was measured following polishing.

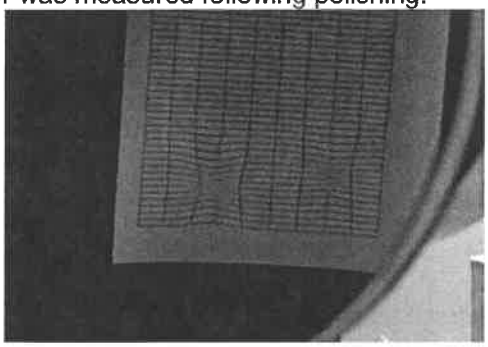

FIGURE 5a: Vacuum distortion.

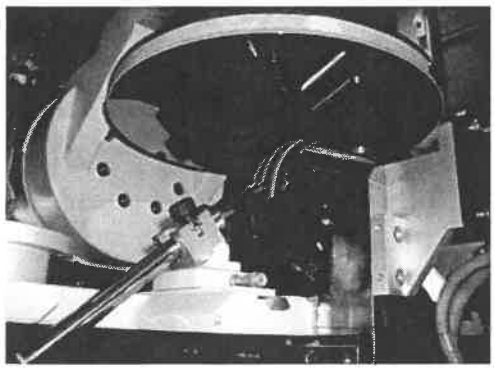

FIGURE 5b: Polishing a 300 mm wafer.

The wafer was measured in transmission by NIST using the IR^3 interferometer, which yields optical path length difference (OPD) information. To obtain the correct wafer thickness variation, as opposed to OPD variation, the data needed to be divided by two times the index of refraction of silicon. The appropriately scaled thickness maps for a sample wafer are displayed in Figure 7, given that n_{Si} = 3.48 at the operating wavelength of 1552 nm [11,12]. As shown in Figure 6, the total thickness variation (TTV) was improved from 449 nm to 95 nm. This global TTV improvement of almost 5x was achieved over a 297 mm diameter. The size and rate of the MRF removal function can be optimized to achieve a desired result, such as minimum edge exclusion, minimum cycle time, or minimum flatness.

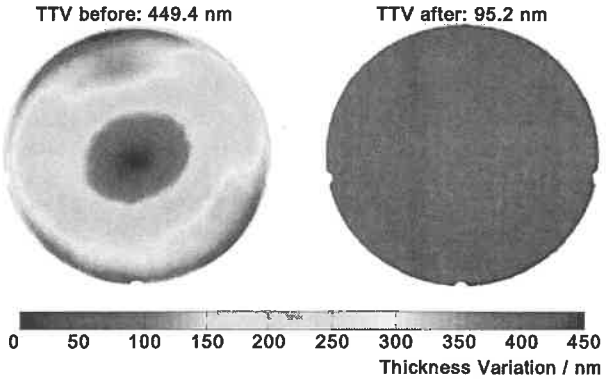

FIGURE 6: Wafer thickness variation before and after MRF correction. TTV was reduced from 449 nm to 95 nm over 297 mm aperture (1.5 mm edge exclusion).

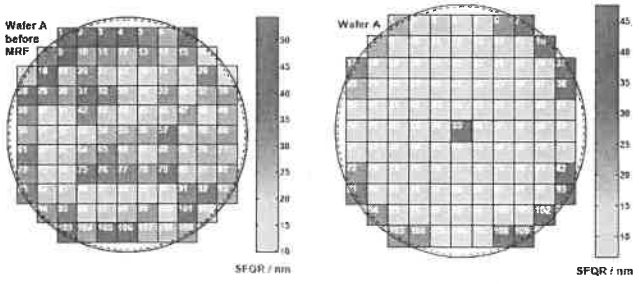

FIGURE 7: SFQR Measurement before and after MRF over 25 x 25mm sites. The site flatness improved to better than 20nm over most of the wafer.

Additionally, the site flatness improved to better than 30 nm as shown in Figure 7. As a potential next step, the outliers at the edge and center of the wafer may be eliminated by further process optimization. This is a promising result in light of

the 32 nm site flatness ITRS specification for 2013.

CONCLUSION

This paper has demonstrated that combining advanced metrology, such as the IR³ interferometer from NIST, with a state-of-the-art sub-aperture polishing process, such as MRF, can successfully address the wafer flatness requirements of many future ITRS technology nodes. It currently appears unlikely that conventional single- or double-sided polishing processes will be able to achieve similar tolerances.

Although the technologies described in this paper represent a technical path forward, a significant challenge remains in creating a cost-effective, commercially viable process. The very low total thickness variation achieved here was demonstrated with several 300 mm wafers, which were MRF polished and measured with the IR^3 interferometer at NIST. Cycle times must now be improved to achieve throughput levels consistent with the expectations of the semiconductor industry. This will require not only further development of the polishing process, but specific integration activities with wafer manufacturers to determine where to "stop" the standard (full aperture) polishing process and where to insert MRF (sub-aperture) polishing. Ultimately, the successful integration of these types of novel processes in a very cost-conscious silicon wafer manufacturing industry will indeed depend on the respective economics of this approach versus incumbent technologies.

REFERENCES

[1] The International Technology Roadmap for Semiconductors 2006 *www.itrs.net/links/2006update/2006updatefinal.htm),* Section "Front end processes", Table 67a and 67b.

[2] Tonshoff, H.K.; Schmieden, W.V.; Inasaki, I.; Konig, W., Spur, G. 1990, Abrasive Machining of Silicon. Annals of the CIRP, 39(2):621-635.

[3] SEMI Draft Document 3882, www.semi.org, 2004.

[4] Golini, D., Kordonski, W.I., Dumas, P., Hogan, S., 1999, Magnetorheological Finishing (MRF) In Commercial Precision Optics Manufacturing, Proc. SPIE, 3782:80-91

[5] Golini, D., Jacobs, S., Kordonski, W., Dumas, P., 1997, Precision Optics Fabrication Using Magneto-rheological Finishing, Proc. SPIE, CR67:251-274.

[6] Arrasmith, S.R., Jacobs, S.D., Lambropoulos, J.C., Maltsev, A., Golini, D., Kordonski, W.I., 2001, The Use of Magnetorheological Finishing (MRF) to Relieve Residual Stress and Subsurface Damage on Lapped Semiconductor Silicon Wafers, Proc. SPIE 4451:286-294

[7] Tricard, M. and Golini, D., 2002, Improving Surface Geometry and Surface Integrity Using Magneto-Rheological Finishing (MRF), Proc. euspen 3rd International Conference, 1:373-376

[8] Evans, C.J., Paul, E., Dornfeld, D., Lucca, D.A., Byrne, G., Tricard, M., Klocke, F., Dambon, O., Mullany, B.A., 2003, Material Removal Mechanisms in Lapping and Polishing, Annals of the CIRP, 52/2:611-633.

[9] Tricard, M., Golini, D., 2002, High Precision Photomask Polishing with Magnetorheological Finishing (MRF), *Proc. ASPE 17th Annual Meeting*, 27:120-125.

[10]Tricard, M., Dumas, P.R., Golini, D., Mooney, J.T., 2003, Prime Silicon and Silicon-on-insulator (SOI) Wafer Polishing with Magnetorheological Finishing (MRF), Proceedings of IMECE '03, ASME International Mechanical Engineering Congress & Exposition, MED14/MH7.

[11] Primak, W., 1971, Refractive Index of Silicon, App. Opt., 10:759-763.

[12] Villa, J.J., 1972, Additional Data on the Refractive Index of Silicon, App. Opt., 11:2102-2103.

TRIBOLOGY AND CORROSION EVALUATION USING WHITE-LIGHT INTERFEROMETRY

Erik L. Novak, Nelson R. Blewett and Tom Stout
Veeco Instruments
Tucson, AZ, USA

INTRODUCTION

Interference microscopes remain one of the most accurate, repeatable, and versatile metrology systems for precision surface measurements. Such systems successfully measure material in both research labs and production lines in the micro-optics, MEMS, data storage, medical device, and precision machining industries to sub-nanometer vertical resolution. Increasingly, however, these systems are finding uses outside of traditional surface-measurement applications, including film thickness determination, environmental responses of material, and determination of behavior under actuation.

Most recently, these systems are enabling users to examine behavior of materials over varying time-scales as they are used in cutting, grinding, or other high-stress environments. In particular, quantification of wear of surfaces with varying coatings and under different conditions is of increasing value as tolerances decrease and consistency in final products is more valuable. Also, . response of materials to corrosive environments allows users to quantify the gains of varying surface treatments against the cost of those treatments. Such quantification requires novel hardware and software for the system to ensure results are fast, accurate, and relevant.

In this paper we explore three typical applications in tribology and corrosion. First, deterioration of the cutting surfaces on several multi-blade razors is explored, with quantification of key surface features, under different use conditions. Next, corrosion of several metal surfaces is analyzed. The surfaces are analyzed for rate of deterioration over time and to examine how initial surface conditions affect corrosion. Pitting, roughness changes, and other surface parameters are evaluated and their rates of change during the corrosion process are plotted. Finally, wear of multiple drill bits of different materials and coatings is quantified.

BACKGROUND

White-light optical interferometry has been one of the preferred methods of nondestructive, precision surface characterization for more than fifteen years[1]. This non-contact, three-dimensional metrology provides vertical ranges of up to 10mm, vertical scan speeds of over 100 µm/sec and single fields of view from 60 µm to over 10mm makes this one of the fastest and most versatile techniques available. Lateral resolution is sub-µm and vertical resolution is sub-nm. Further, these instruments are available in configurations which support any environment from the research laboratory to the production floor.

For this paper measurements were performed using a Wyko NT9800 optical profiler. Vertical calibration of the instrument is via an internal HeNe reference laser which monitors the scan rather than against discrete step heights, giving the system enhanced accuracy over large ranges[2]. Lateral calibration of the instrument is via a certified pitch standard used to calibrate each objective. Measurement times ranged from approximately 4 seconds to 20 seconds on the samples studied. All analyses were performed by the Veeco's Vision software which controls the instrument. The paper is designed to illustrate key analyses and considerations used by industry when quantifying changes over time. In these studies, for each surface measurement typically twenty to forty different surface parameters were logged of the several thousand available in the software. Only a few of key results are presented in this abstract.

CUTTING SURFACE METROLOGY

Among the more common types of machined components examined in tribological studies are blades, other cutting surfaces and grinding components. Critical parameters include the roughness, width, height, and alignment variations within each surface and between them. All of these help characterize the quality

of the cutting surface and changes in these parameters with time can identify key failure points and areas for process improvement.

For this study several commercial multi-blade manual razors were examined in their new state and again over time under two conditions: in a true use case (parts used for shaving), and in a more controlled setting where they were used to shave a fibrous material over a set distance a set number of times. Low magnification measurements were first taken to examine the relative geometry between the blades in a single field of view.

Automatic region finding analysis was used to examine the relative geometries of the surface designed to contact the skin, with the right of the two blade surfaces used as the reference. In Figure 1, the left contact surface is nearly 520μm higher and tilted at an angle of 30mrads with respect to the other. Relative angles and heights between the surfaces did varied by up to 50mdeg and 200 microns.

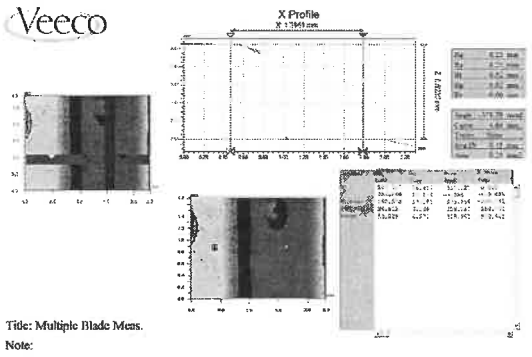

Figure 1: Roughness, height, and relative tilt information of two skin-contacting surfaces of a razor blade.

High magnification measurements were then taken to characterize both the skin-contacting surface and the actual cutting surface at high resolutions. Figure 2 below shows the surface new and after 100 and 200 cycles of use. Surface roughness of the contacting surface increases by nearly a factor of three; the process is also nonlinear, with dramatic degradation between 100 and 200 cycles. For this study no lubrication was used with the blade. There was no statistically significant surface degradation for surfaces at different angles or vertical heights with respect to one another on the four separate blades examined.

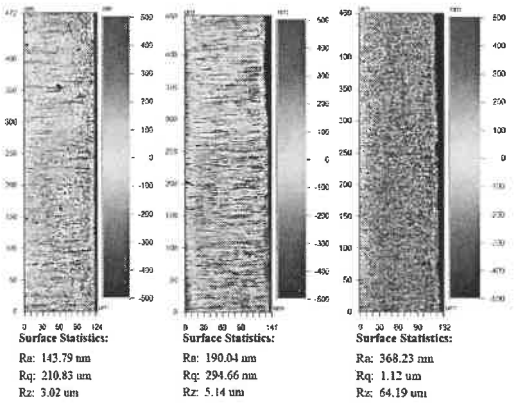

Figure 2: Skin-contacting surface measured new (left) after 100 wear cycles (center) and after 200 wear cycles (right).

The cutting surfaces of the blades were also measured throughout the study. Key measures were surface roughness, the width of the cutting surface and its variation. Significant roll-off of the worn cutting blade, and increase in the variation of the width of the cutting surface was observed.

CORROSION MEASUREMENTS

Yet another area where optical profilers are commonly used to study dynamic processes involves the study of corrosion. Often different materials and coatings are studied to determine if they are more or less resistant to degradation in a given environment. Optical profilers have been used to study corrosion processes associated with medical implants, wires and other electronics, metals, and glass[3,4,5]. In some cases surface wear is studied in conjunction with corrosion to determine how different frictive processes affect the tendency of the surface to degrade. The effect of surface finish parameters on the durability of a given material is also of high interest. It is this aspect of corrosion that will be studied below. Key parameters involving corrosion when examining a single surface include surface roughness, number of pits, their volumes, and the spatial distribution of surface features.

In this study a microfinish comparator strip from Gar Electroforming was corroded using a mildly acidic solution. The comparator strip is nickel, but had different processes used to create surface finish and different target roughnesses (lapped, ground, and milled surfaces examined here) in different regions. The goal was to examine the corrosion process for each region,

to see if there were preferential areas for the start of corrosion and how surface finish affected the overall result.

Figure 5 below shows a sub-region of a high magnification measurement of the 8G surface throughout the corrosion process. Even visually the changes in surface finish are notable. Figure 6 plots the power spectral density (PSD) of this surface against time in the corrosive environment, showing an increase in higher spatial frequency content.

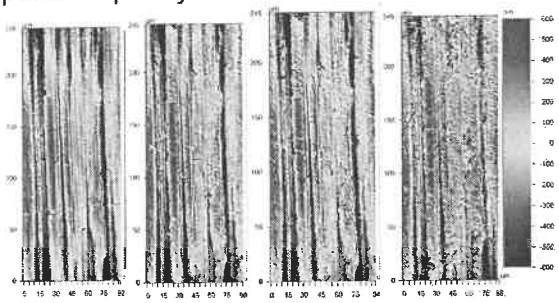

Figure 5: 50X subregions of the 8G region of the comparator strip uncorroded (left) and after 7,14, and 21 hours in the corrosive liquid.

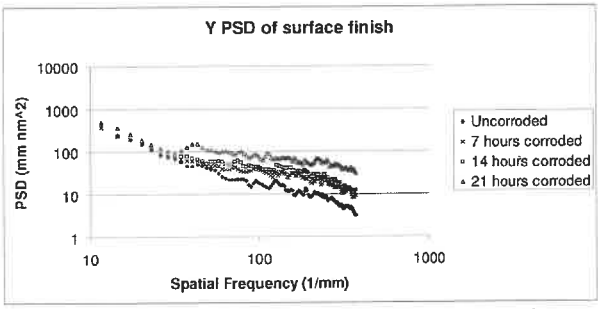

Figure 6: Power spectral density plot for the surfaces of Figure 5.

Another highly useful tool for examining surface corrosion is to directly compare the differences in surfaces across time. Through use of fiducial alignment capability in the software one is able to subtract two datasets even with translation or rotation between them. Figure 7 below shows the subtraction of the uncorroded 8G surface from the same surface after corrosion for 7 and 14 hours. One can readily see the spread and deepening of the corrosion on the left portion of the image, while the rest of the image remains fairly random in its appearance.

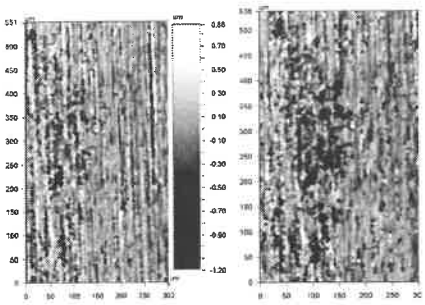

Figure 7: 8G seven hour corroded (left) and fourteen hour corroded (right) surface subtracted from the original uncorroded surface.

DRILL BIT METROLOGY

The last application examined here is tribology associated with various drill bits. Such measurements are becoming increasingly common as process control moves earlier into the machining cycle. Rather than continuous testing of final machined parts, many manufacturers are testing the tooling used for part creation. This can save significant costs as often the tooling can be replaced before many, if any, bad parts are produced.

Four ¼" drill bits were purchased and used to drill holes in a 10mm anodized aluminum plate. One bit was solid high speed stainless steel), one was solid SiC, one was TiN coated steel and the last was TiCN coated steel. After some initial studies to determine at what point noticeable wear could be observed, 10 holes each were drilled in the material. Measurements were performed on the head of the drill bit, along the inside of the bit, and along the leading edge of the bit, as illustrated by the boxes in Figure 8 below. The bits were fixtured such that measurements were performed on the same areas of the bit each time. Ultimately 30 holes drilled with each bit was shown to achieve significant changes in topology, which was noticeable as well in the ability of the bits to drill into the aluminum surface.

Figure 8: Drill bit showing boxes around the areas for measurement: head (left), inside surface (center) and leading edge (right).

As the drilling process progresses large peaks and valleys become evident as seen in Figure 9. Results from five separate locations were used to create a stable set of data for analysis; results

varied too much across the surface to employ a single location.

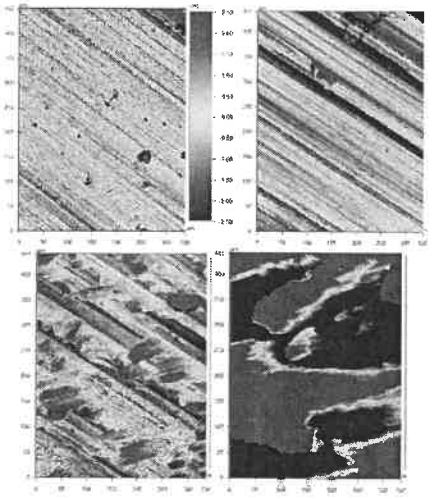

Figure 9: High speed steel inside surface measured for 0, 10, 20, and 30 times drilled and reflecting the changes in surface structure.

The S Parameter functions and bearing ratio proved most capable of quantifying the surface feature variations. These variations are obvious to the eye but often do not reflect themselves in many common analyses, particularly in areas such as average surface roughness and peak-to-valley calculations. The S parameter analyses are a set of analyses developed to characterize three dimensional surfaces.[6] In Figure 10 below the Str parameter, which is the length of fastest decay of the autocorrelation function of a surface divided by. the length of slowest decay, shows the dramatic increase in randomness of the surface as drilling progresses. The other parameter plotted is the height between the 10% and 90% points of the bearing ratio curve, showing that the surface is greatly varying from uniform as the drilling progresses.

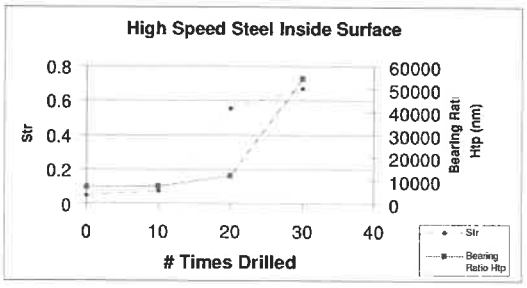

Figure 11: Str and Bearing ratio of drill bit surface.

CONCLUSIONS

White light optical profilers provide highly accurate, non-destructive metrology for precision machined surfaces. Such surface characterizations are increasingly being performed over time and under a variety of stress conditions on the sample being measured. The ability to both rapidly measure such surface and analyze them for changes with time across a large number of potential metrics enables timely and accurate feedback into the processes being examined. Increasingly metrology is moving away from the produced parts and into the tooling which makes them. Metrology needs for tribology and corrosion will continue to drive different mechanical fixturing capability, software analyses, and the ability to measure components in situ in interference microscopy so that it can remain the most versatile instrumentation for such measurements.

REFERENCES

[1] P. Caber, "Interferometric profiler for rough surfaces," Appl. Opt. 32, pp 3438-3441, 1993.

[2] Schmit, A. Olszak, "High-precision shape measurement by white-light interferometery with real-time scanner error correction," Appl. Opt. 41, pp 5943-5950, 2002

[3] Biotribocorrosion—an appraisal of the time dependence of wear and corrosion interactions: I. The role of corrosion Y Yan et al 2006 J. Phys. D: Appl. Phys. 39 3200-3205

[4] Correlation of residual fatigue life with quantified NDE measurements; E.B shell, R.G. Buchheit and B. Zoofan; International Journal of Fatigue Vol 27 Issue 2, Feb 2005, pp 105-112

[5] Inhomogeneous glass surfaces resulting from rapid forming operations – evidence from differential corrosion; Joseph O. Carnali, Guillermo M. Lugo, Anju Sharma and Himanshu Jain; Journal of Non-Crystalline Solids,Volume 341, Issues 1-3, 1 August 2004, Pages 101-109

[6] **Development of Methods for the Characterisation of Roughnes in Three Dimensions**; K. J. Stout editor, University of Huddersfield, Penton Press, 2000

INTELLIGENT SHAPE SENSOR

John H. Merritt [1], Mohammad Sayeh [2], M. Taghi Mostafavi [1]
[1]College of Computing and Informatics
University of North Carolina at Charlotte
Charlotte, NC, USA
[2]Electrical and Computer Engineering
Southern Illinois University Carbondale
Carbondale, IL, USA

Abstract
We extend the bend sensor research by applying it along the entire length of a fiber. The speckle pattern emerging from the end of a fiber cable encodes it shape. Those patterns tell us where, and by how much, the fiber bends. Shining a HeNe laser down a multi-mode fiber produces a speckle pattern that may map one-to-one and on-to (for real cables), for a particular shape of the fiber. Movement sensitivity, down to microns, is easily detected.

To calibrate the fiber, it is bent at known locations. Shining a HeNe laser down the multi-mode fiber, each bend produces a new speckle image. The output speckle pattern is the result of interference patterns as the light waves propagate down the fiber. If we know at which points, along the fiber, cause particular patterns, in the speckle image, then we can use the patterns as a lookup for fiber shape. We take the images with known bend points and construct a database. Then, for each unseen image, we determine which two images it falls between. Weighting the values appropriately, we can calculate a new set of bend points.

Our results are encouraging, with just a few images in the database, we are able to compute the bend locations and magnitude of the fiber using our image interpolation technique. Analysis that is performed on hardware, or on a chip, would facilitate the real-time readout from the shape sensor.

INTRODUCTION

Shine a laser down a multi-mode fiber and the cross-sectional output at the other end is a speckle pattern. Move the cable, put it it in the vicinity of an electomagnetic current, or change its temperature and the speckle pattern changes. These pattern changes provide information as to the shape of the fiber cable. It is the goal of this paper to illustrate that such changes can be tracked and associated with specific fiber shape.

A simple sensor system, where a buried fiber cable that can detects intruders, because their weight moves the cable and thus changes the speckle pattern, is patented in 1981 [1]. This is quite a while after speckle images were first recognized as the effect of "waveguide modes", at American Optical in early 1959[2]. Nevertheless, it is clear that speckle patterns can provide valuable information about the fiber environment.

It is normally desirable to reduce the number of modes within a fiber, down to one, to improve communication bandwidth, but that is not the case here. It is the complexity of the modal interactions that create the speckle pattern, in a multi-mode fiber, that permit the extraction of shape information. Everywhere the fiber is bent, stretched and twisted, contributes to a new speckle pattern. The goal is to associate physical fiber changes with particular speckle patterns. Even if those associations are transient, due to quantum fluctuations, or intractable effects, over time.

The goal is to construct an intelligent shape sensor. For the case of fiber optic cables, the readout is the shape of the fiber.

PREVIOUS WORK

See [3] for a comprehensive overview of fiber optic sensors. In particular chapter 6 discusses speckle-gram sensors and the spatial analysis of the modal patterns that are produced. The approach, herein, also analyzes the spatial modal relationships adding temporal analysis.

METHODOLOGY

The following descrbes our experimental setup and approach.

Experimental setup

A HeNe laser, 633nm, is focused into one end of a 120um multi-mode fiber. The other end is clamped and extruded to shine on a diffusing lens. A microscope video camera is focused onto a small portion of the speckle image, to adequately discern the modes. A stage micrometer with a cylindrical rod attached is placed such that the rod moves the fiber which is suspended across two rounded platforms. All other locations of the fiber are taped down, to ensure that the micrometer moves the fiber in one location. As the micrometer is moved the video is captured. See Figure 1 and Figure 2.

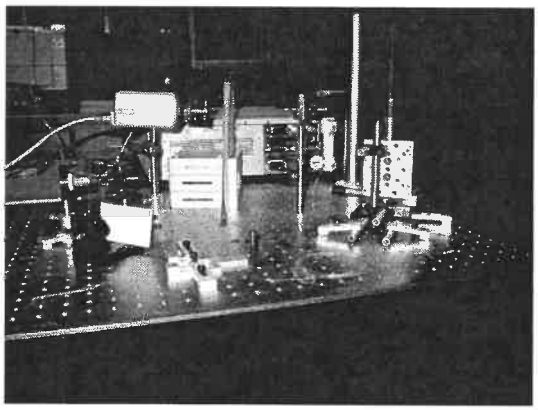

FIGURE 1. Experiment setup

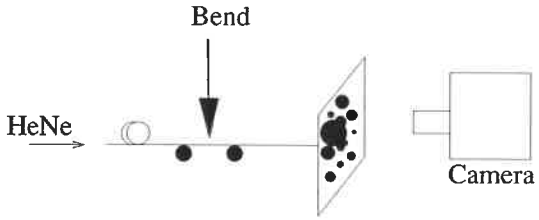

FIGURE 2. Experiment schematic

Calibration and extraction of the training set of images occurs at known micrometer settings.

Empirical experimentation

We set up a simple experiment to illustrate that there may be information in a speckle pattern that could be used to determine the shape of the fiber. As the fiber is moved and twisted, just by hitting it with our fingers, the speckle pattern changes and twists. There are, of course, many degrees of freedom: temperature, air current, initial laser alignment, fiber stretching, friction, camera field of view, etc., that may limit reproducibility, but, if our final measurement resolution is coarse, (and tenths of mm may be coarse), then those variables may not be that important.

Any motion in the fiber, due to touching, squeezing, or twisting, yields gross movement of the speckle pattern. The fidelity is high, meaning that very small movements of the fiber are easily visible as movement of the speckle pattern. Additionally, the faster the fiber shape is modified, the faster the speckle image changes. Visually, the speckle change is directly proportional to the rate of shape change. The same seems true for twisting rates.

In general, when the fiber was twisted, the speckle pattern also twisted. And when the fiber was bent, the speckle pattern showed changes, but did not twist, in general. That is, the pattern seemed to change in-place. Of course, a combination of twisting and bending produced visible twisting and in-place pattern changes in the speckle pattern.

The neural network

The speckle pattern is analyzed using a feed-forward-back-propagation neural network. Intuitively, there are two things we want to track, as the speckle pattern changes:

1. The clusters. These are the modal points of the light waves.
2. The cluster motion due to fiber motion.

The input images are 640x480 pixel video images. They are converted from color to black and white, because the speckle pattern is gradations of red. When the fiber is moved, slightly, small changes in the speckle pattern occur, and it looks like the clusters, of the modal patterns, move as if it were fluid. For small movements of the fiber, the speckle movement seems to have continuity. Thus, in order to train the neural network to track these motions, it is necessary to provide a sufficiently high density of images that this continuity is not lost.

Clustering

To construct a neural network that performs clustering is trivial. Simply, provide the number of output neurons to represent the number of clusters desired. We started with 10 output neurons or clusters, and discovered that the results were pretty good. Using 20, or even 100, gave us better results. Using raw, input images, scaled to 1/2 or 1/4 of their original size, we could train a neural network reasonably well, but, if we first apply a Gaussian blur (5x5) and then training times improved and the results were more consistent. Basically, we are increasing the signal-to-noise (SNR) which reduces the error of the neural network. For a discussion of evaluating modal noise see [4]. We are not too concerned with noise, except that it impacts the neural network training time.

Tracking clusters

As the speckle pattern moves, so do the modal patterns. The clustering neural network is fed into a second neural network to track the motion of the cluster and associate them with known fiber displacements (movements). Instead of using two separate neural networks, we use a single neural network containing 4 layers.

1. $320x240 = 76800$ neurons. The input layer.
2. 500 neurons. The clustering and noise filtering layer.
3. 100 neurons. The cluster tracking layer. It classifies unseen images into one of these neurons.
4. 1 SIGMOID neuron. Convert the 100 classifications in layer 3 into a floating point number along a SIGMOID continuous function.

The neural network is really an image database

More practically, though, the neural network is really functioning as an image database. The 20 images use to train the neural network are encoded in the neural network itself. Encoded with the images, is the set of bend points. Then, for all unseen images, the neural network determines which two images it is between, and computes a new set of bend points. Essentially, the new bend points are a weighted average of the position of the unseen image in the database. Figure 3 shows the speckle pattern arising from bending the fiber. Then Figure 4 shows the image database and the calculation of bend points for an unseen image.

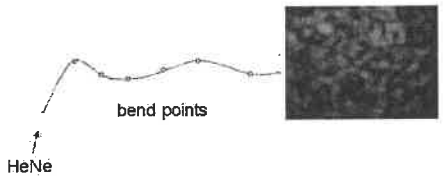

FIGURE 3. Speckle pattern and bend points.

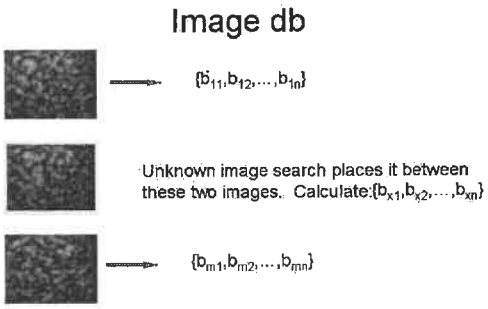

FIGURE 4. Image database interpolation.

RESULTS

From a database of 20 images culled from a video sequence of approximately 600 images, the neural network was able to determine the bend distances for the entire video sequence. There is some binning of bend distances and this is, in part, due to the limited sampling for the training set and, in part, due to the limited complexity of the neural network; only 100 output neurons to classify distances.

The neural network was trained with very few epochs. For a simple 76800, 100, 10, 1 layer neural network, just under 40 epoch would give reasonable results, but with more severe binning. The graph in Figure 5 shows the fit for 600 unseen speckle images. The training set are the green points and the unseen images are the red points. The number of epochs to train this 76800, 500, 100, 1 layer neural network was 268. Attempts to reduce the error, while training, failed as the neural network became stuck in a local minimum.

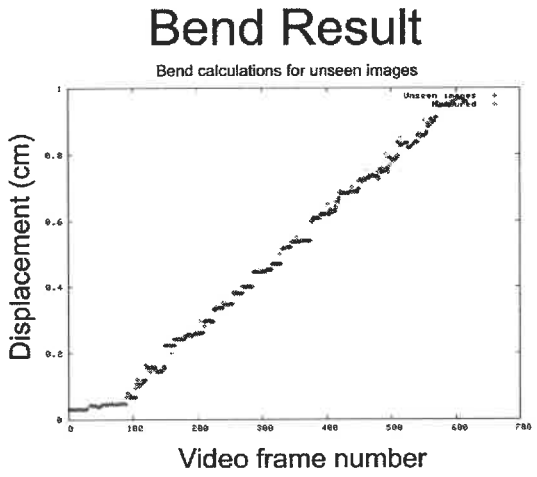

FIGURE 5. neural network with 76800, 500, 200, 1 layers. Training error < 0.0002.

CONCLUSIONS

A simple neural network consisting of 4 layers was sufficient to store a small image database that encoded the shape information of the fiber optic cable. Twenty images was sufficient to give good results. The neural network provided a direct readout of the fiber displacement for one bend location. Thus, we have created an intelligent shape sensor using a fiber cable and a neural network.

Additionally, fiber construction techniques may provide benefit. It is intractable to calibrate a fiber bend sensor continuously along its length for infinite bend points. But, if a fiber is constructed to have a finite number of bend points, then calibration seems possible.

A shape sensor catheter is a natural application of this research. The location and orientation of the catheter tip, in 3D, is a direct readout for a shape sensor. Currently, catheter tip tracking is done with stereo sensor analysis (stereo floroscope or radio triangulation). With a fiber shape sensor, all the dangers of EM radiation would be eliminated and we could generate 3D imagery, in real time. Finally, weaving, or integrating, together, many of these fiber shape sensors, would yield a surface shape sensor.

REFERENCES

[1] Butter CD. Fiber optic intruder alarm system. Google Patents; 1981. US Patent 4,297,684.

[2] Hecht J. City of Light - The Story of Fiber Optics. Oxford University Press; 1999.

[3] Yu FTS, Yin S. Fiber Optic Sensors. Marcel Dekker; 2002.

[4] Kanada T. Evaluation of modal noise in multimode fiber-optic systems. Lightwave Technology. 1984;2(1):11–18.

FIRST AND SECOND ORDER PERIODIC ERROR MEASUREMENT UNDER NON-CONSTANT VELOCITY CONDITIONS

Hyo Soo Kim[1], Tony L. Schmitz[1], David Chu[2], and Hakchu Lee[2]
[1]Department of Mechanical and Aerospace Engineering
University of Florida, Gainesville, FL, USA
[2]Agilent Technologies, Inc., Santa Clara, CA, USA

INTRODUCTION

Differential-path interferometry is often applied in situations requiring accurate displacement measurement, such as lithographic stages for semiconductor fabrication, transducer calibration, and axis position feedback for precision cutting and measuring machines. In many instances, a two frequency (or heterodyne) Michelson-type interferometer with single, double, or multiple passes of the optical paths is selected. These systems infer changes in displacement of a selected optical path by monitoring the optically-induced variation in a photodetector current. The phase measuring electronics convert this photodetector current to displacement by digitizing the phase progression of the photodetector signal. Due to non-ideal performance, mixing between the two heterodyne frequencies may occur, which results in periodic errors superimposed on the desired displacement data. First or second order periodic errors, with amplitudes that vary cyclically with the target position, are commonly observed. First order periodic error, which appears as single sideband modulation on the data at a spatial frequency of one cycle per displacement fringe, often dominates. However, second order periodic error, with a spatial frequency of two cycles per displacement fringe, is also typically present.

Although modifications to traditional optical setups may be implemented to reduce periodic error, a digital correction scheme [1-2] offers the advantage that no changes to the existing optical configuration are required. This paper describes experiments used to: 1) compare the first and second order periodic error levels determined from frequency domain [e.g., 3-4] and time domain [1-2] techniques under constant velocity conditions; and 2) identify error levels for non-constant velocity conditions using the time domain approach.

The results described here were obtained using a single pass, heterodyne Michelson-type interferometer that enabled: 1) isolation of periodic error as the primary uncertainty source in displacement measuring interferometry; and 2) variation of the frequency mixing that leads to periodic error so that the error amplitude could be changed. Target motion was achieved using an air bearing stage. Various frequency mixing levels were realized by adjustment of the setup optics.

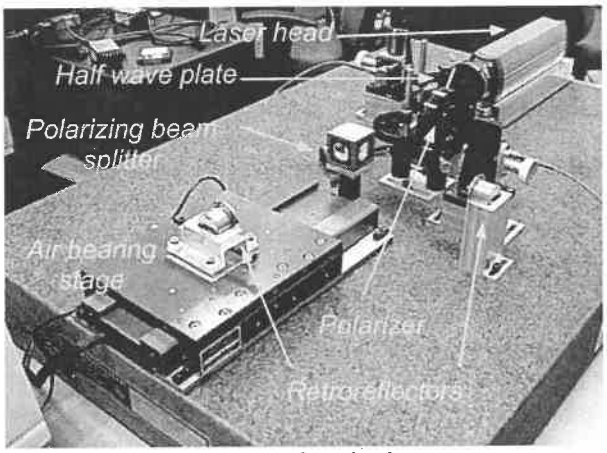

Figure 1: Components for single pass, heterodyne interferometer experimental setup.

EXPERIMENTAL SETUP

A photograph of the setup is provided in Fig. 1. The orthogonal, linearly polarized beams with a split frequency of approximately 3.65 MHz (Helium-Neon laser source) first pass through a half wave plate. Rotation of the half wave plate enables variation in the apparent angular alignment (about the beam axis) between the polarization axes and polarizing beam splitter; deviations in this alignment lead to frequency mixing in the interferometer. The light is then incident on a non-polarizing beam splitter (80% transmission) that directs a portion of the beam to a fiber optic pickup after passing through a fixed angle sheet polarizer (oriented at 45 deg to the nominal laser orthogonal polarizations). The pickup is mounted on a two rotational degree-of-

freedom flexure which enables efficient coupling of the light into the multi-mode fiber optic. This signal is used as the phase reference in the measurement electronics.

The remainder of the light continues to the polarizing beam splitter where it is (ideally) separated into its two frequency components that travel separately to the moving and fixed retroreflectors. In this design, motion of the moving retroreflector is achieved using an air bearing stage. After the beams are recombined in the polarizing beam splitter, they are directed by a 90 deg prism through a polarizer with a variable rotation angle. Finally, the light is launched into a fiber optic pickup. This serves as the measurement signal in the measurement electronics (0.3 nm resolution for single pass configuration).

The intent of the setup design was to minimize other well-known error contributors and enable variation in the periodic error nature, first or second order, and amplitude. To isolate periodic error, the setup was designed with zero Abbe offset (i.e., the measurement axis was collinear with the motion axis) and zero dead path difference (i.e., the distance between the polarization beam splitter and the moving retroreflector was equal to the distance between the polarization beam splitter and the fixed retroreflector at initialization). The measurement time (~100 ms) and motion amplitude were kept small to minimize the contribution of air refractive index variations due to the environmental changes. Additionally, careful alignment of the air bearing stage axis with the optical axis resulted in small beam shear.

EXPERIMENTAL RESULTS

In this section, we describe the analysis procedures and provide experimental results for two primary scenarios: 1) constant velocity tests with variable half wave plate and polarizer orientations; and 2) non-constant velocity tests with fixed polarizer and half wave plate angles.

Variable polarizer angle

In these tests the half wave plate angle was held fixed at its nominal orientation and the polarizer angle was systematically varied about its nominal value (normalized to 0 deg in Fig. 2). The velocity for the air bearing stage (and moving retroreflector) was 100 mm/min. The measurement and reference signal data from the interferometer were sampled at 312.5 kHz by the phase measuring hardware; displacement was then determined from these signals. For the single pass Helium-Neon interferometer setup used here, first order error repeats every 633/2 = 316.5 nm, while second order completes a full cycle in 633/4 = 158.3 nm. To identify the first and second order error amplitudes for the various polarizer angles under constant velocity conditions, two methods were compared. First, the discrete Fourier transform (DFT) of the error was computed [3-4] after performing a least squares linear regression to subtract the best fit line from the displacement data. Second, the Chu and Ray algorithm [1-2] was applied. This real time, digital method functions by modeling periodic error as periodic functions of the ideal position and continually estimating the periodic error amplitude from best fit regressions, where macroscopic motion up to constant acceleration is removed. In the implementation applied here, the fit and error estimates were updated every 1.024 ms and used to fit the next 1.024 ms of data in a leapfrog manner. In this way, the error amplitudes were continuously available (which is exploited in the non-constant velocity tests).

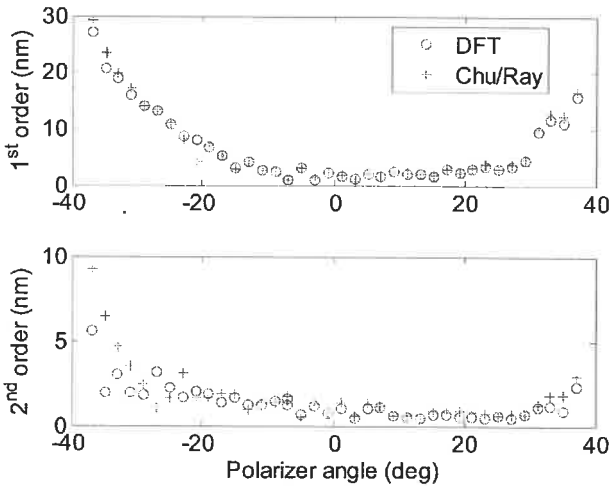

Figure 2: Error comparison for frequency (DFT) and time domain (Chu/Ray) approaches with variable polarizer angle.

The first and second order periodic errors for the two methods with polarizer angle variation are displayed in Fig. 2. The top panel shows the first order error comparison, while the bottom panel displays the second order error.

Variable half wave plate angle

In this case the half wave plate angle was varied while the polarizer angle was held fixed at its

nominal orientation. The stage velocity was again 100 mm/min. The first and second order periodic errors identified by the two methods with half wave plate angle variation are displayed in Fig. 3. The reader may note that a θ half wave plate (HWP) angle change results in a 2θ linear polarization rotation.

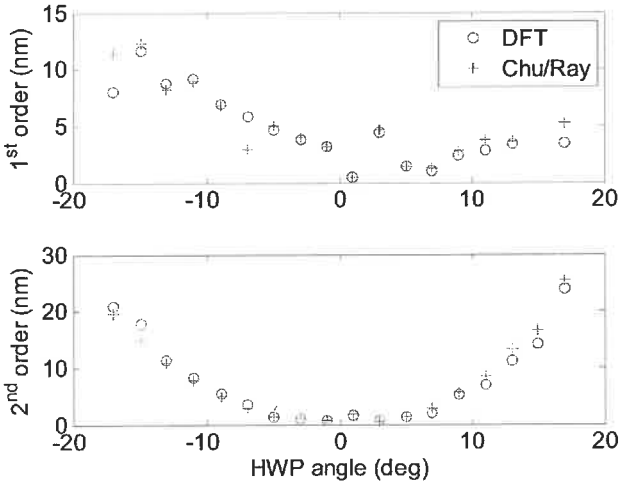

Figure 3: Error comparison for frequency (DFT) and time domain (Chu/Ray) approaches with variable HWP angle.

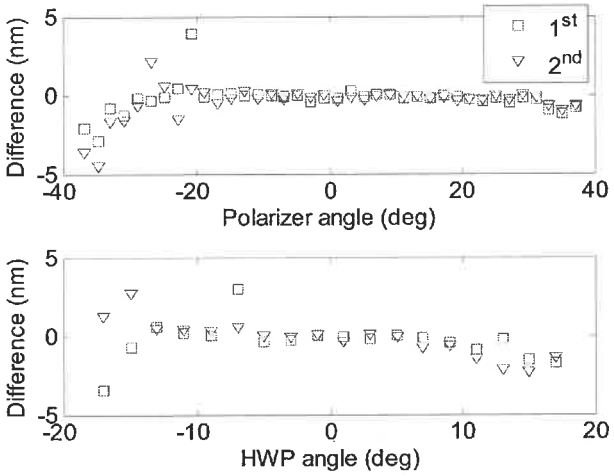

Figure 4: Difference between Fourier and Chu/Ray periodic error levels for (top) variable polarizer angle and (bottom) HWP angle.

Constant velocity comparison

To aid in comparing the frequency and time domain analysis results, the difference between the first and second order periodic errors for the variable polarizer and half wave plate angle tests was calculated. The results are shown in Fig. 4. It is seen that larger deviations occur for the extreme misalignment conditions. To better represent actual setups (which would not generally suffer from such large misalignments), Fig. 5 presents results for polarizer misalignment within 10 deg of the nominal and half wave plate misalignment within 5 deg of nominal (±10 deg linear polarization misalignment). It is observed that the agreement between the two methods is within the interferometer resolution (0.3 nm).

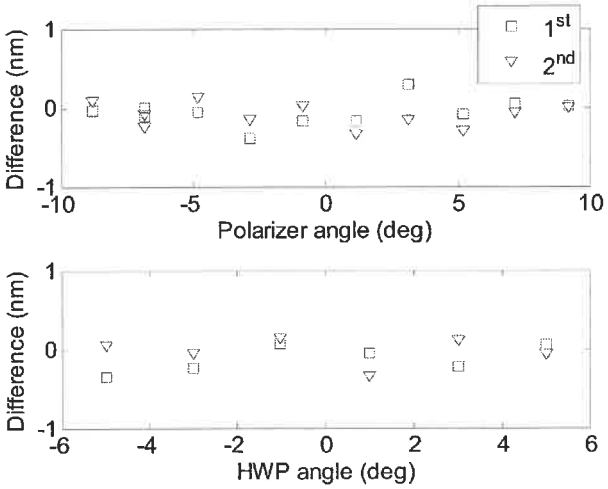

Figure 5: Difference between Fourier and Chu/Ray periodic error levels for realistic misalignment ranges.

Non-constant velocity

Here, data was collected during non-constant velocity profiles. In this case, the frequency domain approach cannot be applied because it requires signals with constant time periods, which is not true for non-constant velocity motions (i.e., although the periodic error spatial period is constant, the time period is not).

An example motion profile for non-constant velocity conditions is provided in Fig. 6. The top panel shows the overall motion, x, for the $30x10^3$ samples, while the bottom panel shows the velocity, v. Note the direction reversal which occurs near 41 ms. The periodic error was determined about this reversal over the 32 to 50 ms range using the time domain algorithm. Figure 7 shows the displacement (top panel) and periodic error (bottom panel), which was visually isolated by subtracting a least squares fit polynomial, x_{fit}, for this range (the low frequency mean drift is due to an imperfect

polynomial fit). The variation in the periodic error time period with velocity is observed.

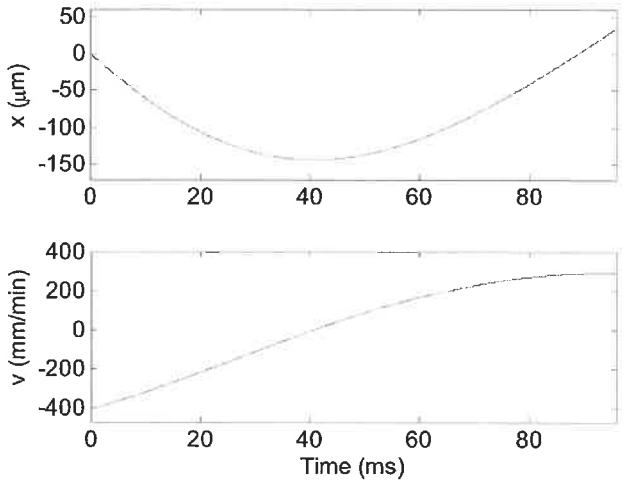

Figure 6: Displacement (top) and velocity (bottom) profiles for non-constant velocity test.

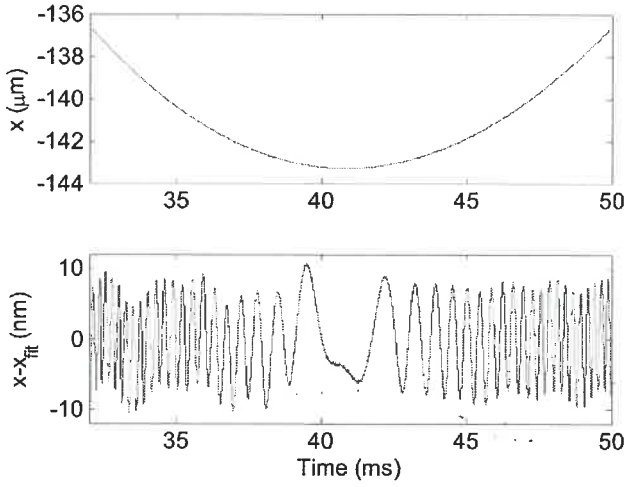

Figure 7: Displacement (top) and periodic error (bottom) near motion reversal.

Figure 8 shows the first and second order periodic error levels which were measured using the time domain algorithm (top panel). As noted, a new value is available every 1.024 ms, although updates cannot be calculated for very low velocities (points 7-10). The bottom panel of Fig. 8 shows the periodic error waveform generated from the measured error levels.

CONCLUSIONS

The tests reported in this study validated the periodic error level estimates computed using the digital, time domain Chu and Ray algorithm [1-2] by comparison with the well-known frequency domain approach [3-4]. Further, it was demonstrated that the time domain approach was capable of continuous estimates of the first and second order periodic error for non-constant velocity motion. The ability to diagnose periodic error at non-constant velocities and reconstruct the wave shape for error compensation makes the algorithm particularly well-suited to real-time implementation for precision motion systems.

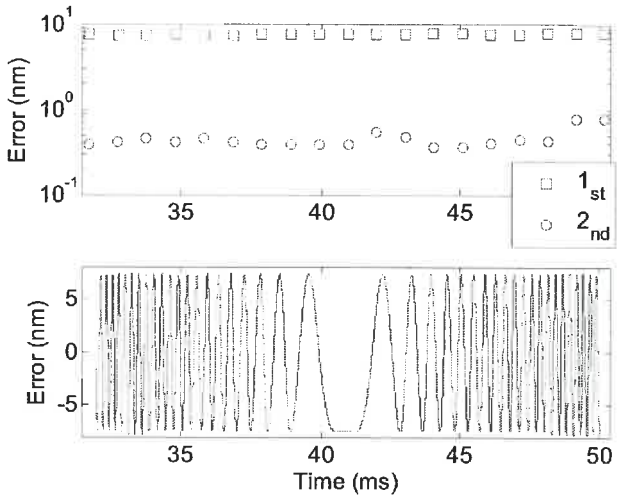

Figure 8: Measured periodic error (top) and compensation waveform (bottom).

ACKNOWLEGEMENTS

This work was supported by Agilent Technologies, Inc., the National Science Foundation (DMI- 0555645), and Aerotech, Inc.

REFERENCES

1. Chu D. and Ray, A., 2004, Nonlinearity Measurement and Correction of Metrology Data from an Interferometer System, Proceedings of 4th euspen International Conference, Glasgow, Scotland (UK), May-June, 300-301.
2. Schmitz, T., Houck III, L., Chu, D., and Kalem, L., 2006, Bench-top Setup for Validation of Real Time, Digital Periodic Error Correction, *Precision Engineering*, 30: 306-313.
3. Patterson, S. and Beckwith, J., 1995, Reduction of Systematic Errors in Heterodyne Interferometric Displacement Measurement, Proceedings of the 8th International Precision Engineering Seminar (IPES), Compiegne, France, 101-104.
4. Badami, V. and Patterson, S., 2000, A Frequency Domain Method for the Measurement of Nonlinearity in Heterodyne Interferometry, *Precision Engineering*, 24: 41-49.

ROUNDNESS MEASUREMENTS USING THE NIST FIBER PROBE

Bala Muralikrishnan, Jack Stone and John Stoup
Precision Engineering Division
National Institute of Standards and Technology
Gaithersburg, MD 20899

INTRODUCTION

We have previously described [1] a fiber probe for dimensional measurement of micro-holes on a Coordinate Measuring Machine (CMM). In this paper, we discuss the adaptation of this probe for measuring roundness in a configuration similar to that of a more traditional roundness measuring instrument with the part mounted on a precision spindle and the probe sensing radial deviations. We have measured roundness of knife-edge apertures using this method. These apertures are used as standards in radiometry and currently measured using optical techniques only [2, 3].

THE NIST FIBER PROBE

The fiber probe developed at the National Institute of Standards and Technology (NIST) was originally designed as a CMM probe to operate in point-to-point mode. The probe is capable of measuring holes as small as 125 μm diameter to depths of 10 mm, with an expanded uncertainty in diameter of 70 nm (k = 2). The probe is sensitive not only in X and Y, but also in Z; Z measurements are achieved by observing the magnitude of buckling of the fiber while measurements in the XY plane are achieved by observing the deflection (bending) of the fiber. Deflections and/or buckling are detected by optically measuring from two orthogonal directions, the stem position at a point about 10 mm from the tip of the fiber

SURFACE ADHESION

A primary limitation of slender fiber based probing systems is the adhesion of the fiber to the test surface due to water layers, contamination, etc. These adhesive forces can be significant, of the order of several micronewtons. In order to overcome these forces, the fiber has to be drawn away from the surface by several hundred micrometers before it can be located at the next sampling point. To eliminate this problem, we excite the fiber into resonance between measurements; vibrating the fiber provides necessary energy to break free from the adhesive bonds. We have demonstrated this method for profile measurement of gage blocks [4]. Here we describe the adaptation of this technique for roundness measurement of circular features.

ROUNDNESS MEASUREMENT SETUP

A schematic of the setup is shown in Fig. 1. The probe is brought in contact with the test artifact (for instance, along X), and deflections along the sensitive direction of the stem are monitored while the spindle is rotated.

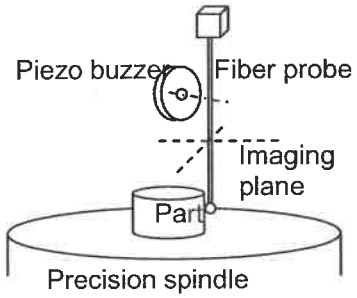

FIGURE 1. Schematic of the setup showing part mounted on a precision spindle, and the fiber excited acoustically. A piezo buzzer (which does not physically contact the fiber) generates the acoustic excitation.

The fiber is excited into resonance as the spindle is rotated to present the next sampling location on the part. However, because there is no available node on the stem, we are unable to image the stem when it is vibrating. Therefore, the spindle operates in a start-stop mode, where images are gathered when there is no spindle motion. Vibrating the fiber does not adversely impact repeatability if sufficient time is allowed (2 s) to damp out the vibrations prior to imaging.

While the technique is slower than traditional roundness instrumentation where the spindle is in constant motion, our technique does pose an advantage in that by being able to monitor the stem bending along the tangential direction in addition to the radial direction, we can quantitatively assess if the fiber displays any adhesion with the surface.

RESULTS

We have measured the roundness of precision spheres and knife-edge apertures using the above described technique. The measurements were performed using a 125 μm diameter fiber with the stem directly in contact with the test artifacts (not the ball on the end) to avoid any errors from a tilted knife-edge hole contacting the probe ball at different planes. Any variations in the stem diameter will contribute to errors; we discuss this in the later section on uncertainty.

Knife-edge aperture area is currently measured optically. However, an inter-comparison conducted by NIST [5] shows the disagreement between the different optical techniques is larger than the quoted uncertainties. A contact probe measurement of the same apertures is desirable. Traditional probes would damage the delicate knife edge but a fiber probe operating at forces ranging from about 10 nN up to several hundred nN should not damage the aperture. While we have not yet measured diameter (or area), we report on form measurements of these knife-edge apertures using a contact probe method. Poor form can be a large contributor to diameter (and area) uncertainty. The results reported here are probably the first roundness traces of such knife-edge artifacts using an ultra-low force touch probe.

Radial Form of Known Spheres

Fig. 2 shows radial form data from a 3 mm nominal diameter, ruby sphere. 180 sampling points were acquired per trace, and 10 traces were measured. The repeatability (one standard deviation) over 10 runs is under 20 nm at any angular position. While the repeatability is excellent, a systematic form component of 80 nm amplitude is clearly identifiable in Fig. 2.

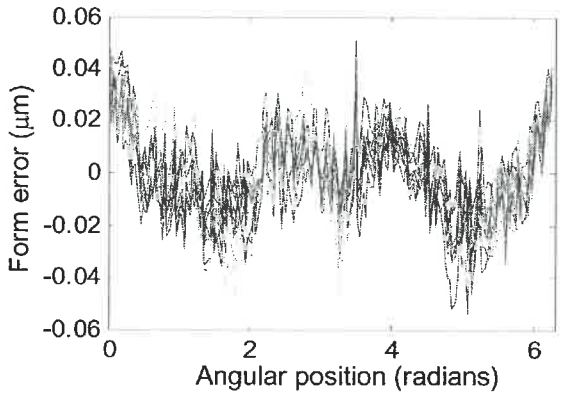

FIGURE 2 Radial form data from 3 mm sphere

Upon performing a full reversal (profiles after reversal shown in Fig.3), we were able to show that the observed form in Fig. 2 is in fact mostly due to the spindle and not the part, see Fig. 4 and 5. This was independently verified using a traditional roundness instrument available at NIST; the radial out-of-roundness of the ball was measured using this instrument as 15 nm (with an uncertainty of 6.4 nm, $k = 2$).

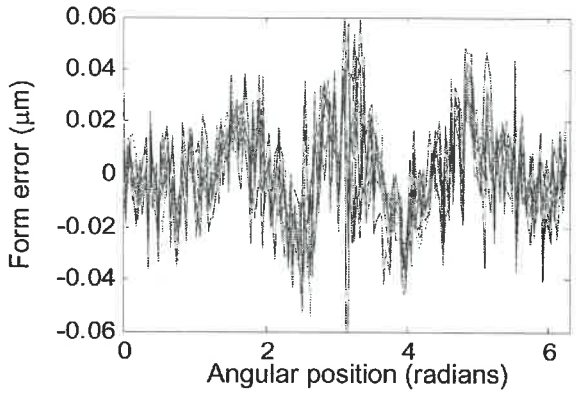

FIGURE 3 Radial form data from 3 mm sphere at the 180° position of a full Donaldson reversal, with 180 sampling points per trace and 10 traces

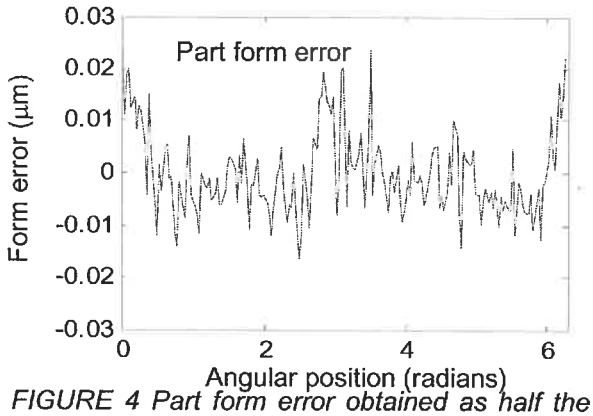

FIGURE 4 Part form error obtained as half the sum of the mean of 10 runs in Fig 2 and Fig. 3

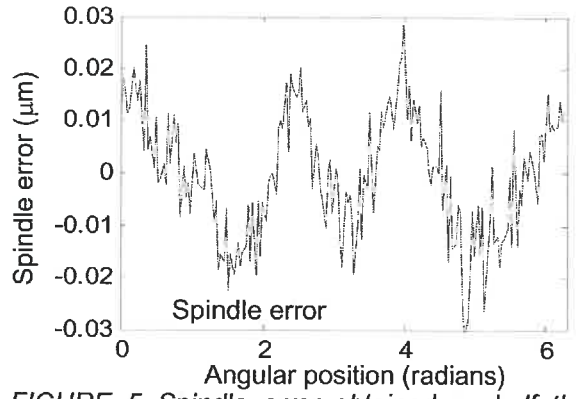

FIGURE 5 Spindle error obtained as half the difference of the mean of 10 runs in Fig 2 and Fig. 3

Radial Form of Knife Edge Apertures
We measured radial form of several knife-edge apertures using the vibration assisted fiber probe technique. In Fig. 6, we plot the radial deviations of a knife-edge aperture (nominal diameter 6 mm). 180 sampling points were acquired around the circumference per trace, and this was repeated 10 times. The one standard deviation repeatability is only 62 nm at any radial location.

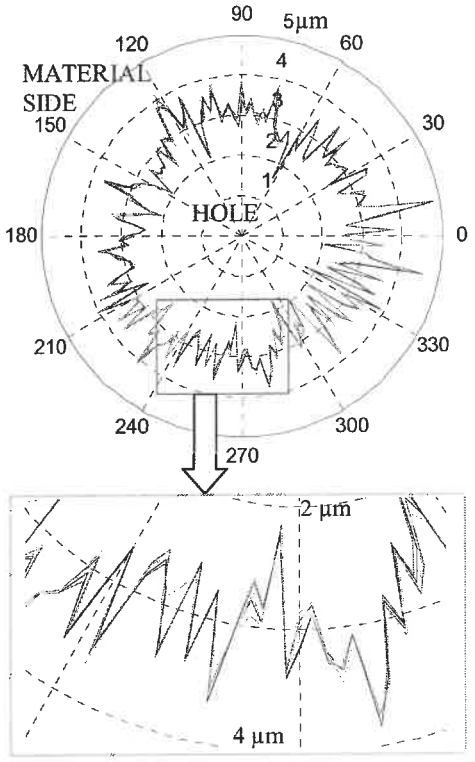

FIGURE 6 Radial form data from a knife-edge aperture. 180 sampling points per trace, 10 traces are shown. The repeatability at any location is only of the order of 62 nm. *The out-of-roundness of this artifact is approximately 2* µm.

In Fig. 7, we show the radial deviations of another knife-edge aperture (5 mm nominal diameter). This aperture was part of a round-robin comparison [5] conducted by NIST earlier. Again, we measured 180 sampling points per trace and acquired 10 traces; the average of the 10 traces is shown as the solid line in Fig. 7.

In addition to roundness measurements made using the vibration-assisted pseudo-scanning technique, we have also measured the form using our probe on a CMM in point-to-point mode. Two dimensional (2D) point coordinates were measured at each sampling location, and the residuals from the Least Squares best fit circle are plotted in Fig. 7. Form measurement on a CMM requires that the probe be retracted from the surface each time to overcome surface adhesion as described earlier. Therefore, fewer sampling points (16 points shown in Fig. 7) can only be acquired to reduce the effect of any drift in the system. Fig. 7 shows that there is good agreement in form data between the two configurations the probe can be used in: as a 1D roundness probe with the part on a precision spindle, and as a 2D CMM probe with the part on the CMM table.

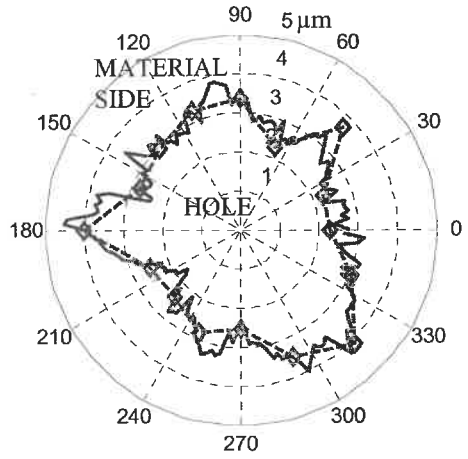

FIGURE 7 Radial form data from a knife-edge aperture used in NIST round robin comparison. 180 sampling points per trace, average of 10 traces shown in solid line. Additionally, the dashed-diamond line represents 16 sampling points measured with the probe on a CMM. 2D point coordinates were determined at each sampling location. The residuals from a Least Squares best fit circle are shown here.

The measurements we have performed indicate that these knife-edge apertures have poor form; the radial out-of-roundness is of the order of 2 µm. Therefore, part form error can be expected to have a substantial contribution to the overall uncertainty in diameter measurements and therefore the area of apertures used in radiometry.

ERROR SOURCES
Imaging errors, spindle errors, scale errors, fiber diameter non-uniformity and taper, part misalignment and surface finish contribute to uncertainty in radial form measurement.

Imaging errors (errors in determination of fiber position in camera coordinates) are extremely

small (of the order of 5 nm [1]) primarily due to the large number of pixels that are available, and the result of averaging many images. Manufacturer specified spindle radial error is 25 nm. Our measurements indicate radial error of the order of 50 nm. Taking this more conservative value, and assuming a rectangular distribution, the contribution to radial form is 29 nm. The nominal scale factor is approximately 0.4 μm/pixel with an uncertainty of 0.001 μm/pixel [1]. Although the fiber may have a starting deflection of 50 pixels, we are only concerned about changes from one sampling point to the next. Assuming part form error of 4 μm (10 pixels) based on the apertures described previously, the uncertainty in radial form is about 10 nm. We have experimentally verified that vibration does not impact repeatability in any significant manner if sufficient time is allowed (about 2 s) for the vibrations to damp out before commencing the imaging process and is therefore not a major component in the uncertainty budget.

The tilt of the top face of knife-edge apertures is aligned to within a few micrometers using a dial indicator. Any residual tilt in the part will manifest itself as ovality in the form data. It is critical to align micro-holes to within a few micrometers. For the 5 mm and 6 mm diameter apertures we have measured, a 5 μm tilt across the aperture will have negligible impact on form, of the order of 1 nm. In addition, because we use the fiber stem for these measurements, and not the ball at the end of the fiber, any non-uniformity in the fiber coupled with tilt in the part will directly manifest itself as a radial form error. We have experimentally seen that over 5 μm along the stem axis, the fiber radius can change by 10 nm. We assign this value, 10 nm, as the contribution to radial form error due to this term assuming the part can be tilted/warped by as much 5 μm across the aperture. A similar effect is obtained when both the part and a uniform fiber are tilted. Assuming a fiber tilt of 0.1° (10 nm tilt over 5 μm), and a part tilt of 5 μm across the aperture, the radial form error is 5 nm.

The above mentioned terms contribute about 30 nm to radial form uncertainty when combined in root-sum-squared manner. Experimentally, we have determined repeatability of the order of 60 nm for apertures. We believe that surface finish could be a large contributor, accounting for most of this discrepancy. For a 6 mm diameter aperture, the spacing along the circumferential direction between sampling points (2°) is 105 μm. The spindle has 94,400 counts over 360°. Assuming an uncertainty of 10 counts in positioning (0.05°), the uncertainty in circumferential position is 2.5 μm. We have noticed a radial form of 2 μm for these apertures and assuming a worst case 2 μm radial height variation occurring between two consecutive sampling points spaced 105 μm apart, and interpolating this value for a spacing of 2.5 μm yields a radial variation of 50 nm. A denser sampling with a thin stem will provide better estimates of this term. It should be noted that both roughness of the surface we are measuring and our probe diameter are sufficiently large that tip convolution (mechanical filtering) is a distinct possibility. If there is a "V" shaped indentation in the knife edge artifact where the radius increases by 2 μm at one sampling point located between two points which are at the nominal radius, then the depth of the "V" would be underestimated by 11 nm. This error is small in comparison to our overall uncertainty.

The standard uncertainty in radial out-of-roundness based on two farthest points from the mean circle, each determined with a 62 nm uncertainty, is of the order of 88 nm.

CONCLUSIONS

We have described a technique for roundness measurement using the NIST fiber probe. With this technique, we have measured roundness of precision spheres and knife-edge apertures. The estimated expanded uncertainty in radial out-of-roundness is under 200 nm (k = 2) for knife-edge apertures and under 100 nm (k = 2) for precision spheres. We plan on measuring radial form of 100 μm diameter holes in the near future with our technique.

REFERENCES

[1] B. Muralikrishnan, Jack Stone and John Stoup, Precision Engineering, 30/2, 2006

[2] J. Fowler and M. Litorja, Metrologia 40 No 1, 2003

[3] Joel B Fowler, R D Saunders and A C Parr, Metrologia 37 No 5, 2000

[4] B. Muralikrishnan, Jack Stone and John Stoup, Proceedings of the annual meeting of the ASPE 2006, Monterey CA

[5] Litorja M et al, Metrologia 44 No 1A (Technical Supplement 2007)

SPATIAL AND TEMPORAL MEASUREMENTS OF THE FIELD OF A MAGNETIC RECORDING HEAD USING A CONTACT READ/WRITE TESTER

Nils J. Gokemeijer, Shehzaad Kaka, and Anthony K. Langzettel
Seagate Technology, LLC
Pittsburgh, PA

INTRODUCTION

Nano-scale technologies are commonplace in today's magnetic recording hard drives. The hard drive industry shipped 434.2 million hard drives in 2006[1]. In these drives, a magnetic recording head flies as low as 7nm above a disk spinning at up to 15K revolutions per minute[2]. An advanced magnetic recording head consists of a tunneling magnetic reader with a width as narrow as 55nm and a perpendicular magnetic writer that is somewhat wider[3]. At these dimensions, characterization has become very difficult. Scanning Electron Microscopes (SEM) and Transmission Electron Microscopes (TEM) are used commonly to measure physical dimensions of both the reader and the writer. However, measurement of the magnetic properties of the writer is significantly more challenging. In a previous publication we demonstrated the ability to measure the spatial extent of the writer field using a contact read/write tester[4]. The major difference between ours and a similar footprint method on the spin stand[5] is the absence of media in our system. In this paper we will show how the spatial measurement of the magnetic field has been extended to measure the temporal behavior of the write field as well.

MEASUREMENT TECHNIQUE

In recent years, the magnetic recording industry has switched from longitudinal recording to perpendicular recording. Whereas in longitudinal recording the magnetization lies in the plane of the media, in perpendicular recording the magnetization is perpendicular to the plane of the media. One advantage of this configuration is that a soft magnetic layer underneath the storage layer enhances the field of the writer. We set out to measure this field with the soft magnetic under layer (SUL) in place. In order to do so we built a magnetic field sensor on top of an SUL using standard thin-film wafer processing techniques. The wafer was subsequently cut into small squares, such that the sensing device could be placed on the contact write/read tester[6]. The recording head can then be brought into contact with the device, and scanned in the cross-track and down-track direction (See Fig. 1.) An excitation current (pulse) in the write coil creates a magnetic field (pulse) in the write pole, and magnetic flux is guided through the SUL back into the return pole. When the magnetic field sensor is under the write pole, a voltage proportional to the write field is induced in the sensor and measured using a lock-in amplifier or a 20 GHz sampling oscilloscope. Similarly, because we are scanning the writer in the cross-track and the down-track direction over the sensor, when the magnetic field sensor is under the return pole a voltage proportional to the magnetic field present under the return pole is created and measured. It is in this manner that we can obtain a spatial map of the magnetic field of the writer.

A second measurement of interest is the saturation curve of the magnetic field of the writer. The sensor was first calibrated with a

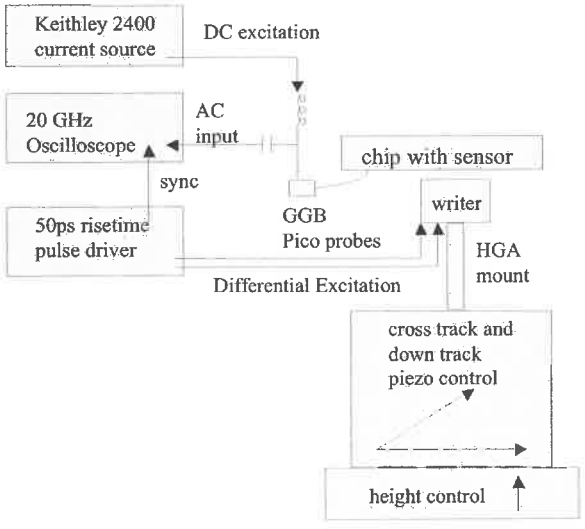

FIGURE 1. Schematic of the system design with the magnetic recording head writer aligned with the sensor.

known external field, and was assumed to have isotropic sensitivity. Because the sensor is essentially cubic (50x50nm in the plane by 42nm tall), this first approximation isn't entirely unreasonable. After placing the sensor and the writer in contact on the tester, X-Y scans of the sensor response were collected at various currents through the writer coil. The calibration of the sensor allows for the conversion of the measured voltage into the field at the sensor for each current applied to the coil. After the scan, the size of the pole was measured on a SEM and using a simple surface charge model, the spacing loss was calculated[4]. The saturation curve as shown in Fig. 2. takes this spacing loss factor into account and shows the estimated field at a distance of 20nm (i.e. in the media if it were present), even though we measured the field at a distance of 200nm.

A third measurement of interest is the rise time of the magnetic field of the writer and how it relates to the rise-time and amplitude of the applied current pulse. This measurement nicely complements two other measurement techniques: Using time-resolved Kerr microscopy, the magnetization of the writer can be measured to sub-ps timescales although the spatial resolution is diffraction limited[7]. Using a spin stand, the effect of the field rise-time can be observed in the non-linear transition shift of the recorded data-bits and the measured transition noise power[8]. To measure the field rise time, we place the writer over the sensor, and the coil current is subsequently pulsed. The sensor senses the pulse of the magnetic field, and a corresponding voltage output is generated. The sensor circuitry also has a capacitive response, which is subtracted before the final signal is obtained. This can be done because the capacitive signal does not depend on the bias current in the sensor, whereas the magnetic signal does.

DEVICE FABRICATION

The magnetic sensor used is a current-perpendicular-to-the-plane (CPP) giant magneto-resistive (GMR) sensor[5] deposited on top of a SUL. For the sensor circuitry to have good frequency characteristics, a high-resistivity silicon substrate was used. The bottom contacts and leads are made of copper, about 1 micrometer thick, and configured as a co-planar waveguide. The copper leads are back-filled with SiO2 and chemical-mechanically polished

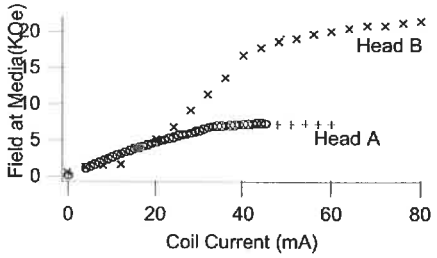

FIGURE 2. Saturation curves (magnetic field vs. current applied in the write coil (mA)) for a production longitudinal writer (Head A) (+) and for an experimental perpendicular writer (Head B) (x) with a SUL in place. The saturation curve measurement for head A was repeated a second time to verify repeatability (circles).

flat with a roughness of less than 0.4 nm. The SUL and GMR sensor are then deposited on top of the bottom contact. The 200 nm thick SUL is made of CoFeB with a cross track uniaxial anisotropy. The SUL is then patterned and back-filled with Al2O3. The sensor itself, patterned next, consists of 15 repeats of 18 Å Cu and 10 Å CoFe sandwiched between top and bottom layers of Au (~40 nm each) to ensure good contact. The fabrication method is similar to what we published previously[5]. The sensor is back-filled with an oxide and after opening a via to the copper leads, the top contact is deposited. The top contact is made of 30 nm thick Ruthenium. The device is then protected with a 30 nm thick diamond-like Carbon (DLC) coating. The coating protects the sensor when scanning the recording head over it. Finally, vias and gold pads are created so that electrical contact can be made. The gold pads are positioned such that they do not interfere with the recording head that is scanning over the sensor. Pico probes on the contact write/read tester ensure that we have a high frequency connection to the sensor. Etch recipes and CMP steps during the build were chosen to keep step

heights to a minimum, resulting in low surface topography to keep the sensor to recording head spacing small. The roughness over a one-mm area was approximately 5 nm, but surface topography caused the sensor to be recessed about 80 nm lower than we expected. The spacing from the midpoint of the sensor to the recording head is therefore approximately 200 nm, consisting of 21 nm sensor, 40 nm Au cap, 30 nm top contact, 30 nm DLC, and 80 nm due to topography. After the fabrication was completed, the wafer was diced into chips of approximately 1 cm x 1 cm. Each chip contained 80 devices of various sizes down to 50nm in diameter.

TEST CONFIGURATION

The contact write/read tester works by placing the magnetic recording head on a vertical lift stage (z-stage) and raising it into contact with a magnetic disc or coupon of magnetic media such that the recording head, mounted on a conventional Head-Gimbal-Assembly (HGA), is within the flying height of the disc[9]. The head or disc is subsequently scanned using a nm-resolution piezoelectric stage with a scan range of 100 μm in both the cross-track and down-track directions. For these experiments, the disc is replaced with a chip carrier for holding the device described above. Eliminating the media in the measurement process reduces the complexity of the measurement, allowing for a more direct measurement of the magnetic properties of the writer. Pico probes with a 40GHz bandwidth were used to connect to the sensor allowing for high frequency characterization. A bias-Tee was used to bias the sensor with a 3 mA DC current. The recording head was subsequently brought into contact with the chip, and scanned over the sensor in the cross-track and down-track direction until the writer and sensor were aligned. The writer is then parked over the sensor, and left there while pulsing the coil current (Fig. 3a). Using a 20 GHz sampling scope, the sensor response is captured both with and without the 3mA DC bias current through the sensor. After subtracting and averaging these signals, a response as shown in Fig 3b is obtained. Thermal drift was low enough such that realignment was only occasionally necessary.

RESULTS

The writer was driven with 2ns pulses with a rise time of approximately 50ps. Various drive currents were used as shown in Fig. 3a. The response for each drive current is shown in Fig. 3b. Three separate regions can clearly be identified in the response. The first fast rise is believed to be indicative of the writer response. We have used this region to characterize the writer. The second slow rise time may be attributable to the sensor response, although we have yet to confirm this. The third region, where

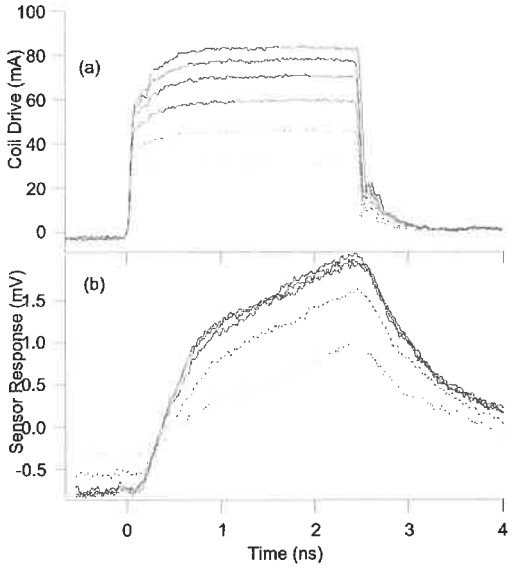

FIGURE 3. Various coil drive pulses (a) and the corresponding sensor response (b)

there is a slow decay in the observed response, is a combination of the sensor response and the decay in the writer field after the drive current has been turned off.

It can be seen from Fig. 3b that the writer saturates at a sufficiently high drive current. If we plot the sensor response at 761ps (the maximum value of the first region) versus the drive current (Fig. 4) it is clear that the writer saturates at a coil drive current of approximately 62mA. This can now be compared with saturation of the media measured on the spin stand to give an idea how much tolerance there is for increasing the media anisotropy.

The slope of the first region of the sensor response also provides valuable information. For

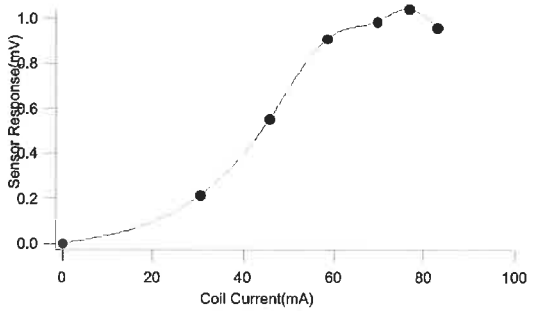

FIGURE 4. Sensor response after 761ps versus the coil drive current.

this particular writer, a slope of 3.1mV/ns was measured. A writer of a different design measures 2.82 mV/ns, and is thus a little slower. It should be noted that these values are a convolution of the head dynamics, the sensor dynamics and the SUL dynamics. If the second part of the slope is indeed the sensor response, its slope (0.64 mV/ns) should be taken into account when calculating the head rise-time. Deconvolving the writer response from the sensor response is something we plan to do in the near future.

CONCLUSION

A method to measure the magnetic field of a writer was developed. The method provides at least three interesting measurements of the magnetic field of the writer: 1) the spatial profile, 2) the saturation curve, and 3) the temporal profile. These measurements provide valuable information in discerning different writer designs. Challenges remain because 1) the spacing between the sensor and the writer is larger than the spacing between the recording head and media in a hard drive and 2) the sensors response is symmetric around zero, resulting in very peculiar responses when pulsing the coil drive current from negative peak to positive peak current. For this reason, only results for zero to peak pulses have been reported here.

REFERENCES

[1] Mah E. Seagate still king as hard drive shipments up 15.5% in 2006, says iSuppli. DIGITIMES 2007 March 8, 2007.

[2] Raman V, Pit R, Conard K, Bach N. Lubricant-Slider Interactions in Near-Contact Head-Disk Interfaces. Asia-Pacific Magnetic Recording Conference 2006:1-3.

[3] Kagami T, Kuwashima T, Miura S, Uesugi T, Barada K, Ohta N, et al. A Performance Study of Next Generation's TMR Heads Beyond 200 Gb/in2. IEEE Transactions on Magnetics 2006;42(2):93-96.

[4] Gokemeijer NJ, Langzettel A, Covington M. Write Field Measurements of a Perpendicular Head on a Soft Underlayer Film. Magnetics, IEEE Transactions on 2006;42(2):163-.

[5] Taratorin AM, Klaassen KB. Media saturation and overwrite in perpendicular recording. Magnetics, IEEE Transactions on 2006;42(2):157-162.

[6] Yamamoto SY, Shultz S. Scanning magnetoresistance microscopy (SMRM): Imaging with a MR head. J. Appl. Phys. 1997;81(8):4696.

[7] Choi BC, Krichevsky A, Freeman MR. Ultrafast magnetization imaging. Proceedings of the IEEE 2003;91(5):781-788.

[8] Taratorin AM, Klaassen KB. Write Current Rise Time in Perpendicular Recording: An Experimental Study. Magnetics, IEEE Transactions on 2007;43(2):750-755.

[9] You D, Zheng Y, Qiu J, Guo Z, Wu Y. Head-to-disk spacing control in contact recording studies. J. Appl. Phys. 2002;91(10):8703.

PLASMON RESONANCE ENHANCED SCANNING NEAR-FIELD OPTICAL MICROSCOPE PROBES FOR SINGLE FLUORESCENT MOLECULE OBSERVATIONS

Shuntaro Sugimoto[1], Hiroshi Morii[1], Keisuke Nagato[1], Kensuke Tsuchiya[2], Tetsuya Hamaguchi [1]and Masayuki Nakao[1]
[1] Department of Engineering Synthesis, The University of Tokyo
Bunkyo-ku, Tokyo, Japan
[2] Institute of Industrial Science, The University of Tokyo
Meguro-ku, Tokyo, Japan

INTRODUCTION

In the last decade, complete DNA sequences of many living animals and organisms have been uncovered. This is largely owing to the rapid advancements in mass-sequencing technologies, which were developed with the lead of the Human Genome Project [1]. Meanwhile, analysis of the huge amount of data acquired from sequencing still relies on conventional microscopy techniques, and fluorescent molecular probes are often used to mark and observe specific DNA sequences. However, the optical resolution is limited to the diffraction limit of the fluorescent emission, which is much larger than the size of a single fluorescent molecule. Therefore, it is expected that technologies that improve the optical resolution limit for observing single fluorescent molecules will greatly contribute to the field of gene analysis.

In this study, we aim to observe single fluorescent molecules using a scanning near-field optical microscope (SNOM) by introducing a probe with a plasmon-resonance-enhanced nanowire and an aperture. The nanowire is an electron-beam-deposited (EBD) wire coated with a thin layer of gold (Au), fabricated in the immediate vicinity of a subwavelength aperture, that only allows the near-field light of the incident probe laser to pass through. This design allows near-field light passing through the aperture to be guided along the nanowire by surface plasmon polaritons [2]-[4] and enhances the intensity of the local field at the apex of the probe. The advantages of both aperture and apertureless SNOMs [5]-[7] are combined in this probe: a high optical resolution due to a small tip, a high signal-to-noise ratio, and the minimal photobleaching of fluorescent molecules because light is emitted only from the small aperture.

In this paper, we provide calculated and experimental results that show the enhanced intensity of the local field at the apex obtained using our proposed SNOM probe. Additionally, the optical and topological measurements of fluorescent polystyrene nanospheres using the probe are demonstrated.

EXPERIMENTAL SETUP

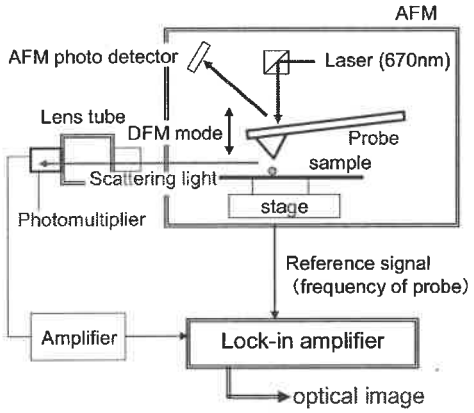

FIGURE 1: Schematic of the experimental SNOM system.

A schematic of our experimental SNOM system is shown in Figure 1. An atomic force microscope (AFM, Seiko Instruments Inc. SPA400) is operated in dynamic force mode (DFM i.e. tapping mode) and the probe is oscillated at resonance frequency. A continuous-wave laser with a wavelength of 670nm (power 52.6μW) is used as a light source for the optical lever method and also as an incident light of our proposed SNOM probe. A lens tube is focused to the apex of the probe from the broadside. The formation of the apparatus is designed to enable observations of both transparent and opaque materials. The light scattered from the probe tip is measured using a photomultiplier (Hamamatsu Photonics K.K. R1463) and a lock-in amplifier (NF Corporation LI5630), which is synchronized with the frequency

of the probe oscillation. It creates a band-pass filter that filters the scattering signals from the near-field light at the probe tip against the frequency of the oscillation.

DESIGN AND FABRICATION OF THE NANOWIRE PROBE

Our nanowire probe is based on a commercial AFM cantilever probe (OlympusTR800PSA, material: SiN_3, resonance frequency: 86kHz).

First, thin layers of aluminum (Al) and Au (thicknesses 150nm and 50nm, respectively) are evaporated onto the surface of the probe side of the SiN_3 cantilever. The metal layers are sufficiently thicker than the skin depth (approx. 14nm) to prevent the incident laser (wavelength 670nm) from passing through the cantilever [8][9]. The Au layer additionally acts as an oxidation-resistant coating of the Al layer.

Second, an aperture (200nm square) is opened at the tip of the cantilever probe by simply grinding the tip of the probe against a rough surface. The subwavelength size of the aperture causes the propagating light of the incident laser to rapidly decay, resulting in the formation of only near-field light at the opening.

Third, an amorphous carbon nanowire (diameter 50nm, length 150nm) is fabricated in the immediate vicinity of the aperture by electron-beam-deposition (EBD).

Finally, the EBD wire is sputtered with a thin layer of Au (thickness 10nm), which acts as a waveguide to convey the near-field light formed at the aperture to the apex of the wire by surface plasmon polaritons. The EBD wire is carefully sputtered so that only the side facing the aperture is coated with Au. Since the local field is concentrated at the Au layer, this design allows the apex of the SNOM probe, in respect to the optical signal source, to become virtually smaller in size than the overall tip of the EBD wire. Therefore, the optical resolution limit is potentially better than an EBD wire entirely coated with Au.

Three types of SNOM probes were fabricated. An aperture-only probe, a probe with an aperture and an EBD wire, and a probe with an aperture and a Au-coated EBD wire. The fabricated probes are shown in Figure 2.

To evaluate the design of our nanowire probe, simulations based on the finite-difference-time-domain (FDTD) method were carried out before fabrication. Comparisons between the aforementioned three types of probes were made. Figure 3 shows the basic model of the probe used for the simulations. The SiN_3 cantilever and amorphous carbon EBD wire were substituted with SiN for simplification since this does not affect relative comparisons between the probes. Results are shown in Figure 4 and clearly show the concentration of the local field at the surface of the Au-coated EBD wire while there is little difference between the local fields for the other two probes. Figure 5 shows the local field intensity plotted as a function of the distance orthogonal to the probe aperture. A strong enhancement of the local field intensity can be seen at the apex of (c) a probe with an aperture and a Au-coated EBD wire, resulting in a more than 2-fold increase compared to (a) an aperture-only probe and (b) a probe with an aperture and an EBD wire.

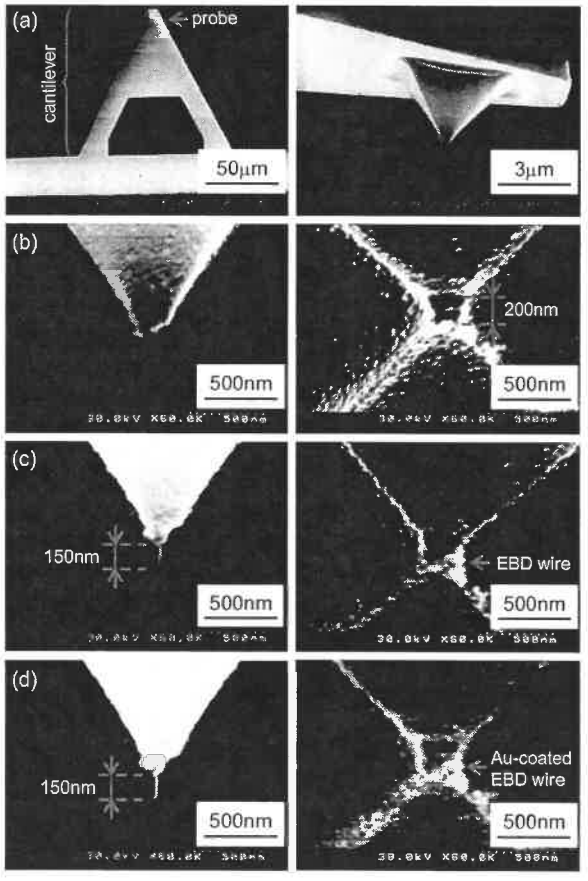

FIGURE 2: Scanning electron micrographs of the SNOM cantilever and probes. (a) Bottom (left figure) and side (right figure) views of the cantilever and probe. (b)-(d) Side (left figures) and bottom (right figures) views of the fabricated probes. (b) An aperture-only probe. (c) A probe with an aperture and an EBD wire. (d) A probe with an aperture and a Au-coated EBD wire.

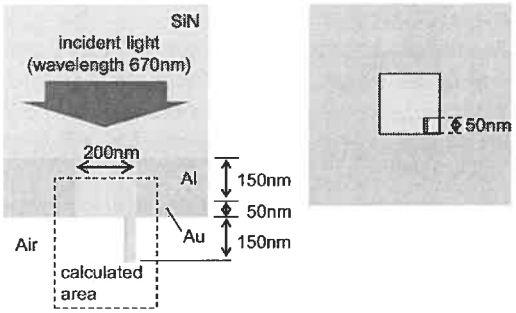

FIGURE 3: The basic model of the nanowire probe used for FDTD simulations. The left and right figures are the cross sectional side and bottom views, respectively.

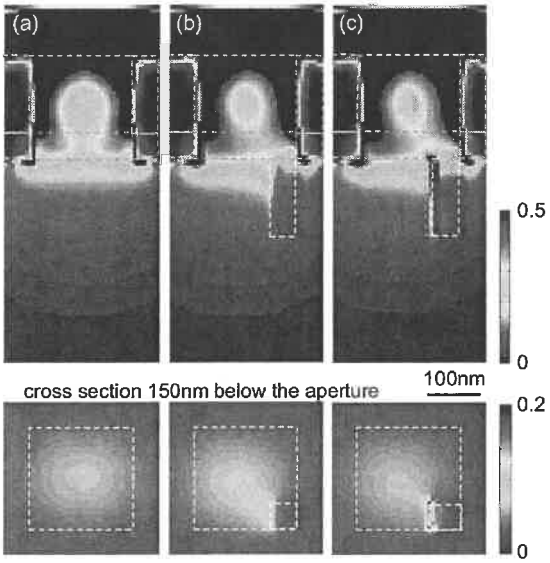

FIGURE 4: FDTD simulation results of the area inside the dotted line in Figure 3. (a) An aperture only probe. (b) A probe with an aperture and an EBD wire. (c) A probe with an aperture and a Au-coated EBD wire. The probe structure is represented in dotted lines.

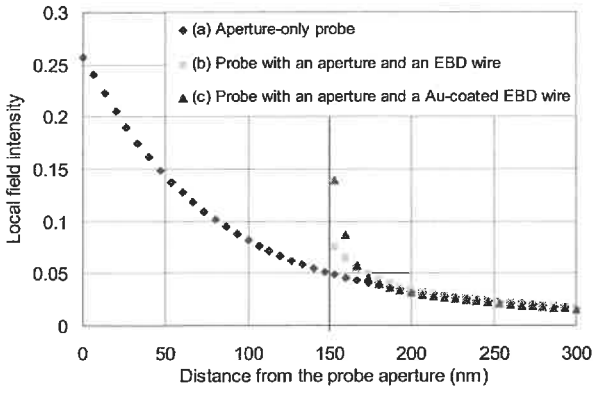

FIGURE 5: Calculated local field intensity at locations orthogonal to the probe aperture. The red vertical line at 150nm is the position of the apex of the EBD wire.

EXPERIMENTAL METHODS AND RESULTS

First, to compare the intensity of the local field at the apex of the probe, scattering intensities were measured by placing the probe above a mica substrate at varying distances. The mica substrate was cleaved and pretreated with a light-absorbent coating (Tasco Japan Corp. THI-1B) to suppress internal reflections in order to detect only scattering from the tip of the probe. The time average of the scattering intensity was taken at each distance.

The results are shown in Figure 6. The horizontal axis shows the distance between the probe aperture and the mica substrate, and the vertical axis shows the output voltage of the lock-in-amplifier. The following probes were measured, (a) an aperture-only probe, (b) a probe with an aperture and an EBD wire, and (c) a probe with an aperture and a Au-coated EBD wire. The data for probes (b) and (c) are plotted from 150nm because the EBD wire (w/o Au-coating), fabricated at the immediate vicinity of the aperture, is 150nm long and the probe aperture cannot be placed any closer to the mica substrate. An exponential increase of the scattering intensity can be seen as the probe tip approaches the mica substrate, which indicates the formation of near-field light at the apex of the probe. Moreover, no notable enhancement of the scattering intensity can be observed using probe (b) relative to probe (a), while probe (c) shows more than 2-fold enhancement. This is in agreement with our previous FDTD simulation results.

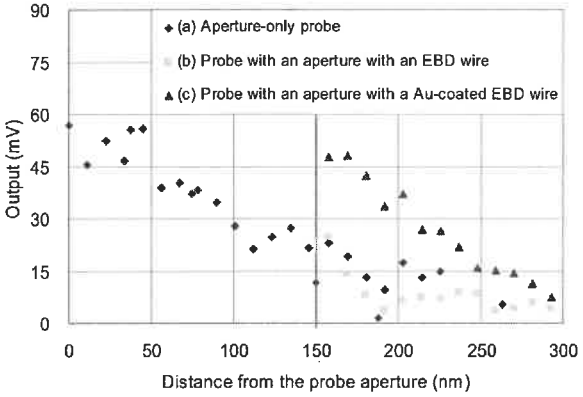

FIGURE 6: The measured scattering intensity from the apex of the fabricated probes at various distances from the mica substrate. The horizontal axis is the distance between the probe aperture and mica substrate and the vertical axis is the output voltage of the lock-in-amplifier. The red vertical line at 150nm is the position of the apex of the EBD wire.

To demonstrate the applicability of our nanowire probe, optical and topological images were obtained using our experimental SNOM system. Nonfluorescent (Polybead Polystyrene Microspheres) and fluorescent (Molecular Probes FluoreSpheres F8807) polystyrene spheres (diameter 200nm) were used as samples and were prepared as follows. Polystyrene beads were diluted to 0.02% solids with distilled water, and approximately 15μl of the sample was added dropwise to a precleaned silicon substrate. Each sample was placed on a hot plate for 10min at 90C° to evaporate the water. Silicon substrates were precleaned by sonicating with acetone and then ethanol for 5min each, then dried in ambient air, and baked in oxygen plasma for 10min.

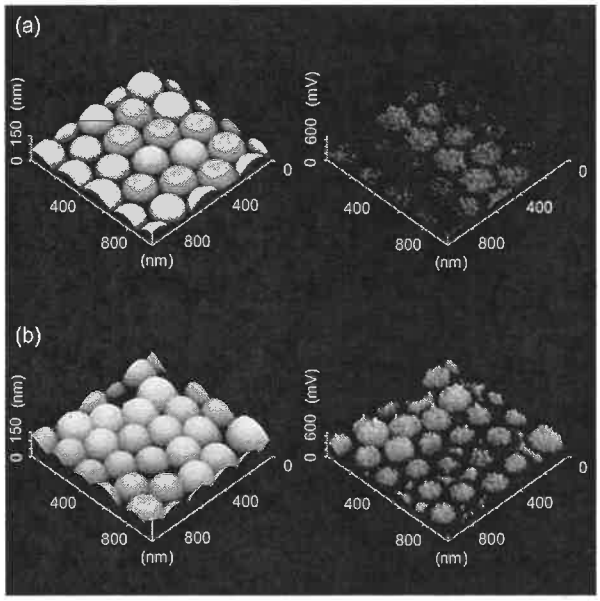

FIGURE 7: Topological (left figures) and optical (right figures) images of (a) nonfluorescent and (b) fluorescent polystyrene spheres (diameter 200nm) obtained using the experimental SNOM system with the proposed nanowire probe.

Figure 7 shows topological and optical images of the samples obtained using the experimental SNOM system with the proposed nanowire probe. The overall measured signal from the fluorescent spheres, as shown in the optical image, is stronger than that from the nonfluorescent spheres, which suggests that the fluorescent emission added to the scattering intensity. This indicates that the fluorescent molecules are excited by the enhanced local field formed at the apex of the Au-coated EBD wire.

CONCLUSION

In this study, we proposed a SNOM probe with a plasmon-resonance-enhanced nanowire and an aperture. A probe with an aperture of 200nm square and a 150-nm-long Au-coated EBD wire was designed and fabricated. We measured the intensity of the local field using our proposed SNOM probe and confirmed the enhancement of the intensity. The intensity at the apex of a probe with a plasmon-resonance-enhanced nanowire showed a more than 2-fold increase than probes without one, which is in agreement with results from FDTD simulations. Optical and topological measurements of fluorescent and nonfluorescent polystyrene spheres (diameter 200nm) using our probe were demonstrated. It was demonstrated that fluorescent molecules are excited and can be detected using the probe.

REFERENCES

[1] International Human Genome Sequencing Consortium, Finishing the euchromatic sequence of the human genome, Nature, 431, 931-945 (2004).

[2] U. Ch. Fischer and D. W. Pohl, Observation of single-particle plasmons by near-field optical microscopy, Phys. Rev. Lett., 64 (4), 458-461 (1989).

[3] F. Keilmann, Surface-polariton propagation for scanning near-field optical microscopy application, J. Microscopy, 194, 567-570 (1999).

[4] W. L. Barnes, A. Dereux and T. W. Ebbesen, Surface plasmon subwavelength optics, nature, 424, 824-830 (2003).

[5] L. Novotny, D. W. Pohl, and B. Hecht, Light confinement in scanning near-field optical microscopy, Ultramicroscopy, 61, 1-9 (1995).

[6] R. Laddada, S. Benrezzak, P. M. Adam, G. Viardot, J. L. Bijeon, and P. Royer, Detection of an evanescent field scattered by silicon tips in an apertureless scanning near-field optical microscope, Eur. Phys. J., AP 6, 171-178 (1999).

[7] D. W. Pohl, W. Denk, and M. Lanz, Optical stethoscopy: Image recording with resolution λ/20, Appl. Phys. Lett., 44 (7), 651-653 (1984).

[8] R. P. Feynman, R. B. Leighton, and M. L. Sands, The Feynman Lectures on Physics Vol. II (1965).

[9] H. J. Hagemann, W. Gudat, and C. Kunz, Optical constants from the far infrared to the x-ray region, Deutsches Elektronen-Synchrotron, SR-74/7 (1974).

AUTHOR CONTRIBUTIONS

S.S. designed the samples, carried out the experiments, and wrote the paper with support. H.M. planned the project, designed the experiments, carried out numerical simulations, and co-wrote the paper. K.N., K.T., T.H., and M.N. provided technical expertise. All of the authors participated in the analysis of the results.

DESIGN OF AN INJECTION-MOLDED IMPEDANCE CELL FOR MEASURING THE DIELECTRIC CONSTANT AND CONDUCTIVITY OF LIQUIDS AND GASES ACROSS ADJUSTABLE NANOMETER ELECTRODE GAPS

Hongshen Ma[1] and Alexander H. Slocum[2]
[1]Department of Electrical Engineering and Computer Science
[2]Department of Mechanical Engineering
Massachusetts Institute of Technology
Cambridge, MA, USA

INTRODUCTION

Accurate measurement of dielectric constant and conductivity, also known as, Electrochemical Impedance Spectroscopy (EIS) is a simple, yet powerful technique for analyzing the properties of liquids and gases. EIS is currently used in a wide range of industrial applications including monitoring the purity of boiler water in power plants [1], as well as, the health of lubricants in heavy machinery [2]. Conductivity measurements can also be used as a chemical detector by using a conductivity assay to gain selectivity over specific ions or compounds.

Recently, the idea of portable chemical analysis systems has gathered considerable attention as a way to reduce cost and expand access of laboratory technologies [3]. EIS is very attractive chemical detection technology for such systems because it is inherently electrical and therefore, can be easily integrated within microelectronic systems. Moreover, unlike many optical detection techniques, EIS does not require the use of lasers or spectrometers which can be expensive and bulky.

The apparatus used for measuring dielectric constant and conductivity, known as an impedance cell, is a geometrical arrangement of electrodes that allow a sample liquid or gas to be measured using an impedance analyzer. Existing conductivity cells, however, are not practical for use with portable devices because in order carry out measurements of desirable accuracy, typically 1% or better [4], these impedance cells require extensive cleaning and calibration, which are difficult to apply outside of a laboratory environment.

This paper explores the vision of creating disposable impedance cells that enable accurate measurements of dielectric constant and conductivity without calibration. The single-use nature of such devices would eliminate problems with contamination and the need for cleaning.

THEORY

A key problem in many EIS measurement systems is the extraction of the intrinsic values of dielectric constant and conductivity, ε and κ, from measurable quantities of capacitance and conductance, C and G. These quantities are related by the geometrical factor of the cell constant, or K_{cell}, and the fringing field capacitance and conductance, C_0 and G_0, according to the following equations,

$$C = \frac{\varepsilon}{K_{cell}} + C_0$$

$$G = \frac{\kappa}{K_{cell}} + G_0$$

Since the values of C_0 and G_0 are artifacts of electrode geometry and manufacturing process, contributions from these terms cannot be easily predicted. As a result, it is very difficult to determine ε and κ from geometrical calculations of K_{cell}. This problem is exacerbated by absorption on electrode surface which tend to change the effective size of the impedance cell. Existing conductivity meters typically address this problem by periodically calibrating the measurement apparatus using standard solutions with known values of ε and κ. This correction is of limited value since the contribution from C_0 and G_0 are typically dependent on the value of ε and κ. As a result, this calibration is valid only if the ε and κ of the sample and calibration liquids are similar. Furthermore, as discuss in the introduction, the use of calibration liquids is undesirable since the

calibration liquid may irreversibly contaminate the impedance cell.

The need for calibration liquids can be avoided using differential measurements of an array of impedance cells where the cell constant is varied in a predictable way. Such designs confront a fundamental tradeoff between varying the cell constant over a sufficient range in order to make an accurate estimate of ε and κ and minimizing the variation of C_0 and G_0. For impedance cell arrays that vary the electrode separation, this tradeoff is optimized when electrode gap is minimized, since small modulations on the electrode gap results in large variations of the cell constant.

Small electrode gap structures between planar electrodes can be difficult to fabricate since small parallelism errors between the electrodes can produce large errors in the measured results. These types of errors could be avoided using spherical electrodes since the nearest points between two spheres are by definition tangent with one another.

The cell constant between closely spaced spherical electrodes can be obtained from the expression for capacitance [5],

$$C = \pi r \varepsilon_r \varepsilon_0 \log\left(\frac{2r}{x}\right) + C_0 ,$$

where x is the electrode separation, r is the radius of the electrode, C_0 is a constant, ε_0 is the vacuum permittivity, and ε_r is the relative dielectric constant. This expression has the convenient property that the spatial derivative of C is inversely proportional to the electrode separation such that,

$$\frac{x}{\varepsilon_r} = -\pi r \varepsilon_0 \left(\frac{dx}{dC}\right) = y .$$

Thus, the value of the relative dielectric constant can be determined from a linear regression of y versus x, where the value of dx/dC can be obtained using the secant approximation.

DESIGN OF THE TEST APPARATUS

A test apparatus that approximate the geometry of the molded cell with adjustable electrode has been designed in order to validate the concept of an impedance cell using closely spaced spherical electrodes and to determine parameter such as range and tolerance of the electrode separation. The test apparatus consists of a spherical electrode, mounting shafts, sample chamber, and a mechanism for adjusting the electrode separation.

The spherical electrodes are fabricated by depositing a thin platinum film on one hemisphere of a silicon-nitride sphere. The silicon-nitride spheres have a diameter of 9.52564 ±0.00013 mm (Cerbec Saint Gobain Ceramics: Grade 5 spheres). The electrode film consists of a 50 nm platinum film with a 5 nm chromium adhesion layer.

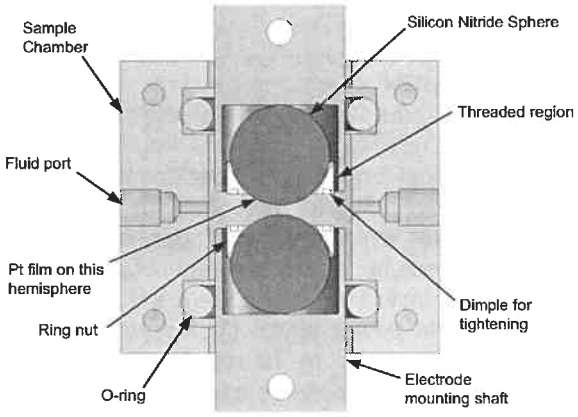

FIGURE 1. Cross section of the test impedance cell

The electrode spheres are mechanically constrained in the tip of a mounting shaft using a ring nut as shown in Figure 1. Dimples on the face of the ring nut allow it to be tightened. In doing so, the ring nut preloads the sphere against the shaft and makes electrical contact with the platinum film. Measurement probes from the impedance analyzer are connected the electrodes via the mounting shaft.

The sample chamber is designed to constrain the sample liquid between the electrodes while allowing small modulations of the electrode separation. The sample chamber is a cube with a central bore. The mounting shaft slides through the bore and the sample liquid is sealed via Kalrez (Dupont) o-rings, which offers similar solvent resistance as Teflon, but with significantly greater flexibility.

The sample chamber is electrically isolated from the mounting shafts. The chamber, made of ANSI 316 stainless steel, is connected to ground and act as a guard electrode. The sample liquid is sealed within the sample chamber and electrode shaft.

The electrode separation is modulated by precise adjustment of the mounting shaft using a monolithic flexural stage, shown in Figure 2. Both mounting shafts are clamped to the flexure mechanism, and are electrically isolated via a 50 µm layer of polyimid film. The displacement of both mounting shaft along its axial direction is measured using a capacitance probe (Lion Precision).

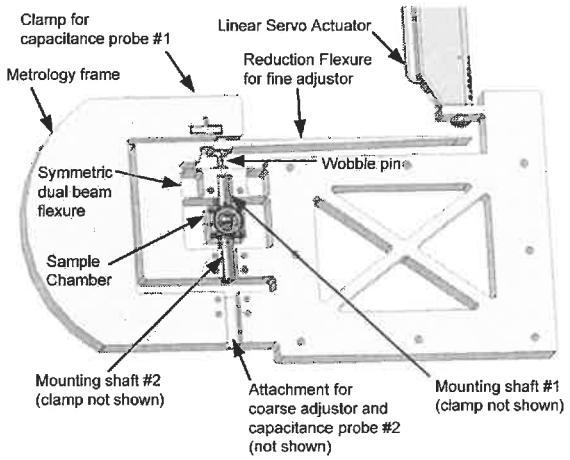
Clamp for capacitance probe #1
Linear Servo Actuator
Reduction Flexure for fine adjustor
Metrology frame
Wobble pin
Symmetric dual beam flexure
Sample Chamber
Mounting shaft #2 (clamp not shown)
Attachment for coarse adjustor and capacitance probe #2 (not shown)
Mounting shaft #1 (clamp not shown)

FIGURE 2. Mechanism for Adjusting the Electrode Separation

The monolithic flexural stage consists of three functional blocks: a coarse adjustor, a fine adjustor, and a metrology frame. The coarse adjustor is a manual lead screw that displaces the bottom mounting shaft. Assuming this screw can be adjusted in 1° increments, the resolution of the coarse adjustor is 0.9 µm.

The fine adjustor consists of an actuator and a flexural transmission. The actuator is a servo motor and lead screw assembly with 50 nm linear resolution (Newport: LTA-HL). The flexural transmission is a cantilever flexure that reduces the travel of the actuator by a factor of 190:1, thereby improving the actuator resolution from 50 nm to 0.25 nm. The overall range of the fine adjustor is 50 µm. The fine adjustor design is also optimized to minimize parasitic motion along axes perpendicular to the axis of measurement. This is done by using a symmetric dual beam flexure to constrain motion along a single axis while using a flexure wobble pin to transfer displacement from the cantilever beam to the symmetric dual beam flexure.

The electrode mounting shafts are clamped to the adjustment mechanism between two half cylinders surfaces. During installation, the top shaft is rigidly clamped first while the bottom shaft is adjusted by the coarse actuator. After the desired coarse position has been reached, the bottom shaft is then clamped and further adjustment of the electrode spacing is accomplished through the fine adjustor.

The metrology frame include two capacitance probes for measuring the position of the electrode mounting shafts. As shown in Figure 2, the bottom capacitance probe uses the same attachment with the coarse adjustor. This probe is designed to be added only after completing the coarse adjustment.

EXAMPLE RESULTS

The feasibility of this impedance cell has been confirmed via dielectric constant measurements of air and methanol. Figure 3 shows the capacitance data from air where the horizontal axis is the position of the electrode and the vertical axis is y as defined previously. The relative dielectric constant is the inverse of the slope. The data points are more distributed at larger electrode gaps since the differential value of C is smaller at larger gaps. The slope is determined using a weighted least squares (WLS) fit. The measured dielectric constant of air is within 1% of the known value of 1.00.

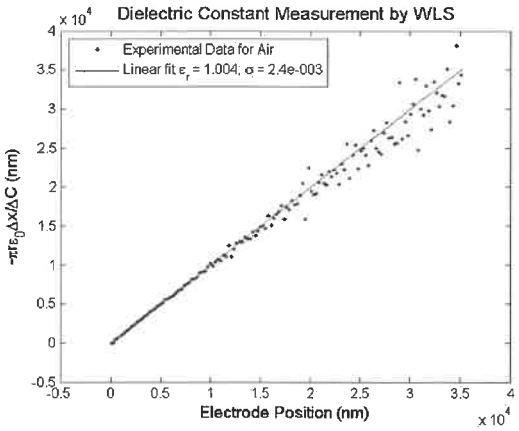

FIGURE 3. Measurement of the ε_r of air; slope determined by WLS fitting

Figure 4 shows the measurement of the dielectric constant of methanol at 21.6°C. This data show considerably less noise than the air data because of the larger dielectric constant therefore, larger capacitance signal. Figure 5 shows the spread of results from 20 repeated measurements of the relative dielectric constant for methanol. The results fall well within a ±1% range of the known value of 33.26 for this temperature. The correct determination of the

relative dielectric constant for two drastically different media confirms that calibration is not necessary in this impedance cell design.

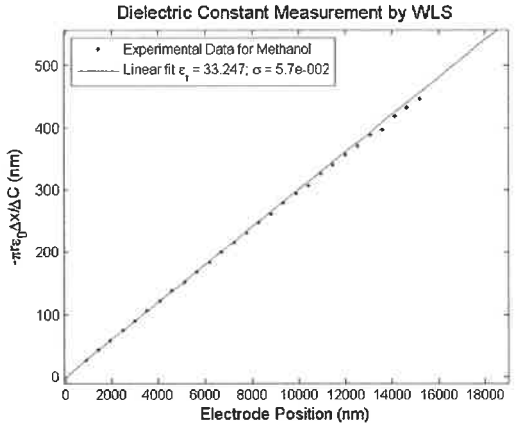
Dielectric Constant Measurement by WLS
Experimental Data for Methanol
Linear fit ε_r = 33.247; σ = 5.7e-002
$-\pi\varepsilon_0\Delta x/\Delta C$ (nm)
Electrode Position (nm)

FIGURE 4. Measurement of the ε_r of methanol; slope determined by WLS fitting

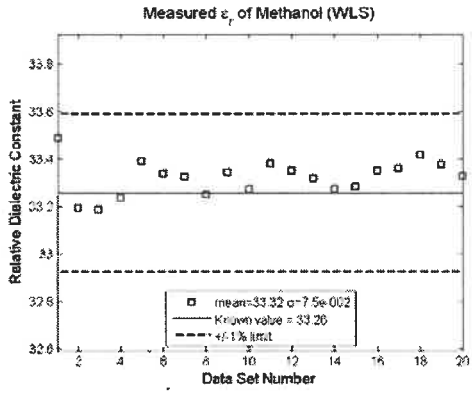

FIGURE 5. The spread of ε_r measurements for methanol

INJECTION-MOLDED IMPEDANCE CELL

After the concept of the design was verified using the test apparatus, the design of the injection molded impedance cell was been developed. As shown in Figure 6, the impedance cell consists of a planar substrate and molded plastic cover. The planar substrate is a silicon or glass wafer with a thin metal electrode layer. The metal film is patterned via standard photolithography techniques using a transparency mask. The molded plastic cover contains partial spheres that are offset from the bottom electrode at several depths. The mold surfaces of the partial spheres are diamond turned to obtain nanometer smooth surfaces. The plastic cover is made from a rigid, solvent resistant plastic, such as Teflon. The metal film is deposited by electron-beam deposition which covers the inside of the molded plastic cover almost entirely except for a few places where the top electrodes need to avoid the metal traces on the bottom substrate. Electrical contact to the top electrode film is accomplished via metal-metal contact with the traces on the bottom of the substrate. The molded plastic cover and bottom substrate is assembled together by wicking in a cyanoacrylate adhesive. Finally, the bottom substrate can be mounted on a standard printed circuit board to interface with impedance measurement circuitry.

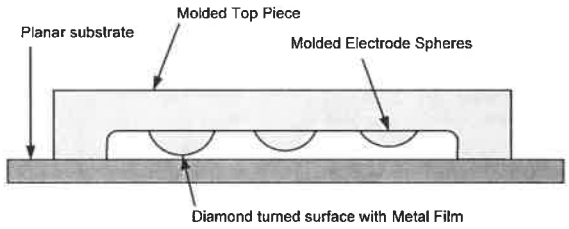

FIGURE 6. Design of the injection-molded impedance cell.

CONCLUSIONS

The design of a disposable impedance cell for measuring dielectric constant and conductivity of liquids and gases without requiring the use of calibration standards has been developed. Preliminary experiments show 1% absolute accuracy can be achieved using this design. A patent is currently pending on this device.

REFERENCES

[1] Wu Y.C., Berezansky P.A., Low Electrolyte Conductivity Standards. J. Res. of NIST, 1995; 100; 521-527.

[2] Lvovich V.F., Liu C.C., Smiechowski M.F., Optimization and Fabrication of Planar Interdigitated Impedance Sensors for Highly Resistive Non-Aquieous Industrial fluids. Sensors and Actuators B. 2006; 119; 490-496.

[3] Dittrich P.S., Tachikawa K., Manz A., Micro Total Analysis Systems. Latest Advancements and Trends. Analytical Chemistry. 2006; 78; 12; 3887-3907.

[4] Shiefelbein S.L., Fried N.A., Rhoads K.G., Sadoway D.R., A High-Accuracy Calibration-Free Technique for Measuring the Electrical Conductivity of Liquids. Rev. Sci. Instrum. 1998; 69.

[5] Boyer L., Houze F., Tonck A., Loubet J.L., Georges J.M., The Influence of Surface Roughness on the Capacitance between a Sphere and a Plane. Journal of Physics D – Applied Physics. 1994; 27; 1504-1508.

PINPOINT SYNTHESIS OF TUNGSTEN OXIDE NANOWIRES USING HEAT CONTROLLING LAYER

Yusuke Kojima[1], Keisuke Nagato[1], Keigo Kasuya[2], Hiroki Moritani[1], and Masayuki Nakao[1],
[1]Department of Engineering Synthesis, The University of Tokyo, Tokyo, Japan
[2] Central Research Laboratory, Hitachi Ltd., Tokyo, Japan

INTRODUCTION

Tungsten oxide nanowires are one-dimensional nanostructures, which have diameters of 10-100 nm and a length of 100 nm-1 μm (Figure 1)[1,2]. The nanowires spontaneously grow through the simple annealing of pure tungsten materials at temperatures of 700-800 °C. Since the nanowires have high aspect ratios and are easily fabricated, they have attracted much attention as promising materials for field emitters of field emission displays (FEDs)[3-5]. To utilize the nanowires as field emitters for FEDs, it is necessary to control the growth spot because randomly arranged emitters make the field emission no uniform. Moreover, heating the entire system for the synthesis of the nanowires may damage the system. With the need to resolve these problems, pinpoint heating has attracted much attention. It has been reported that pinpoint heating using a laser enables the synthesis of carbon nanotubes on the desired points[6]. However, this method needs a large laser system, and it takes much time to heat numerous spots because the laser system can heat only one spot at a time. In this study, we propose a new pinpoint heating process that uses a heat controlling layer (HCL) and joule heat.

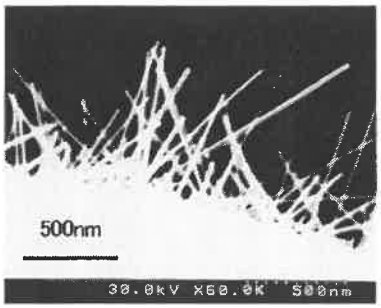

FIGURE 1. SEM images of tungsten oxide nanowires.

OPTINUM CONDITIONS FOR SYNTHESIS OF TUNGSTEN OXIDE NANOWIRES

Tungsten oxide nanowires grow only when the tungsten materials are moderately oxidized[3]. As a preliminary experiment, we studied the oxygen pressure during the synthesis of the nanowires.

We used W/Cr films sputtered on Si substrates with thicknesses of 200/50 nm as samples. These films were deposited by standard radio frequency magnetron sputtering. The Cr film prevented the W film from detaching from the Si substrates. Ar was used as sputtering gas. The base pressure of the sputtering chamber was 1 × 10^{-2} Pa and the sputtering pressure was 5 × 10^{-1} Pa. The deposition rate of tungsten was

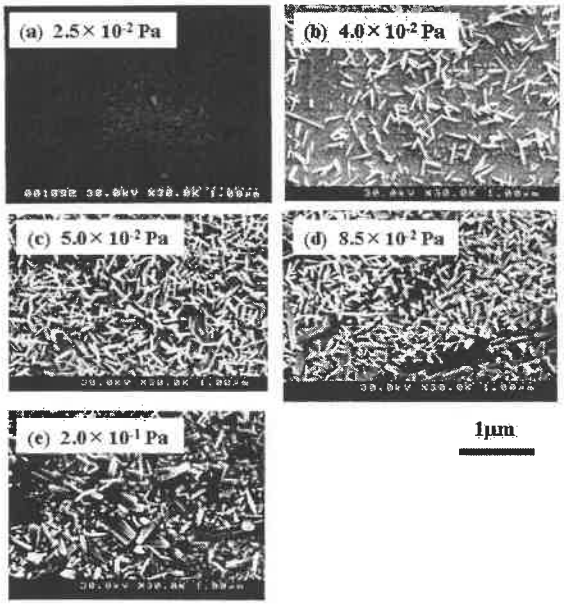

FIGURE 2. SEM images of the surfaces of the samples annealed with various oxygen pressures.

13 nm/min. After the deposition, the samples were annealed in the vacuum furnace at temperature of 800°C by infrared heating, while controlling the oxygen pressure by introducing oxygen gas. The oxygen pressure was varied from 2.5 $\times 10^{-2}$ Pa to 2.0 $\times 10^{-1}$ Pa. The base pressure of the vacuum furnace was 2.5 $\times 10^{-3}$ Pa. Figures 2(a-e) show scanning electron microscopy (SEM, Hitachi S-4160) images of the surfaces of the various samples. When the sample was heated with the oxygen pressure of 2.5 $\times 10^{-2}$ Pa, no nanowires were synthesized. When the oxygen pressure was 2.0 $\times 10^{-1}$ Pa, thick beltlike structures were synthesized. Thin nanowires were synthesized when the sample was annealed with oxygen pressures of 4.0 $\times 10^{-2}$ - 8.5 $\times 10^{-2}$ Pa.

PINPOINT HEATING USING HEAT CONTROLLING LAYER

We used a heat controlling layer (HCL) in order to synthesize the nanowires with pinpoint accuracy. Figure 3 shows a schematic of the HCL. In our study, we used a tungsten materials for the HCL and controlled where the nanowires were synthesized. The SiO_2 layer on the substrate was used as an insulation layer. When an electric current flows through the HCL, joule heat is generated on the HCL. The HCL has both narrow and broad areas. The joule heat generated per unit volume is $I^2\rho / S^2$, where I is the electric current flowing, ρ is electric resistivity, and S is the cross-sectional area of the material. Therefore, when the electric current flows through the HCL, only the narrow areas are heated. Figures 4(a,b) show distributions of temperature in the HCL calculated by finite element method (FEM) simulation. In this simulation, the width and length of the narrow areas of the HCL were both 1 μm. The width and length of the broad areas between narrow areas were 100 μm and 10 μm, respectively, and those of other areas were both 100 μm. The electric current was 0.60 A. The joule heat generated in the narrow area was 0.1 W/μm^3. The narrow areas of the HCL are heated up

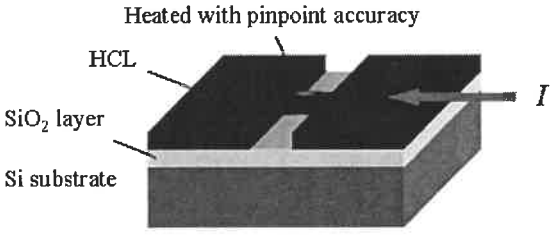

FIGURE 3. Schematic of HCL.

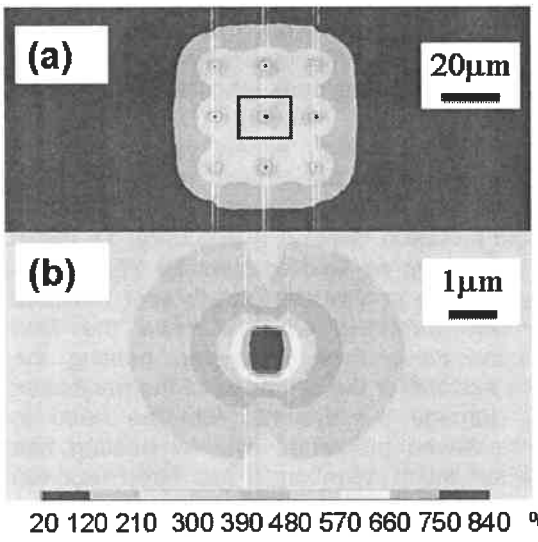

FIGURE 4. Distributions of temperature in HCL calculated by simulation.

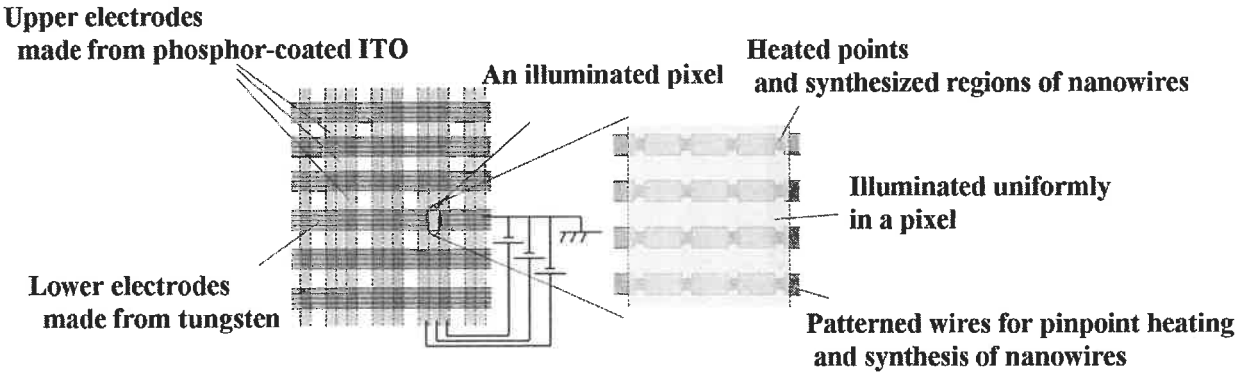

FIGURE 5. Schematic of application of pinpoint synthesis of tungsten oxide nanowires for FEDs.

to 800 °C. On the other hand, temperatures at a distance of 5 μm from the narrow areas are no more than 300 °C. Therefore, the nanowires are synthesized only on the narrow areas of the HCL without damaging other systems by heating. Moreover, the HCL with many narrow areas enables us to synthesize the nanowires on many spots simultaneously.

Figure 5 shows a schematic of the application of the pinpoint synthesis of tungsten oxide nanowires for FEDs. The spots of nanowires are controlled in a pixel by the HCL. Moreover, by using the HCL as lower electrodes of a display, no other system for heating is needed.

In this study, we showed that tungsten oxide nanowires were synthesized with pinpoint accuracy using the HCL. We also showed that the nanowires were synthesized on many areas unifromly and simultaneously with the HCL.

EXPERIMENTAL

We used W/Cr films sputtered on Si substrates covered with an oxide layer (SiO_2) as samples. The thickness of the SiO_2 layer was 1 μm. The sputtering conditions were the same as those in the experiment for studying the oxygen pressure during nanowire synthesis. After deposition, we covered each sample with a positive-type photoresist (AZ-P4903) using a spin coater. The thickness of the photoresist was 7 μm. Each sample was exposed to ultraviolet light through a photomask with the pattern of the HCL. The photoresist exposed was removed using a photoresist developer and the W/Cr film was etched using etchants. The etchant for W consisted of 3.1 % KH_2PO_4, 1.2 % KOH, 3.1 % $K_3Fe(CN)_6$, and 92.6 % H_2O. The etchant for Cr consisted of 17 % $Ce(NH_4)_2(NO_3)_6$, 6 % $HClO_4$, and 77 % H_2O. After etching, the photoresist that remained on the pattern was removed using a photoresist remover.

We made two patterns in this experiment. Figures 6 show SEM images of (a) HCL-1 and (b) HCL-2 before heating. The width and length of the narrow area of HCL-1 were 5 μm and 30 μm, and those of the broad areas were 2 mm and 10 mm, respectively. HCL-2 had three narrow areas whose width and length were 20 μm and 50 μm. The width and length of the broad areas between narrow areas were 500 μm and 50 μm, and those of other areas were 2 mm and 10 mm, respectively. The samples were set in a vacuum chamber and connected with a direct current power supply. HCL-1 was subjected to electric currents of 0.14 A at an oxygen pressure of 4.0×10^{-2} Pa. HCL-2 was subjected to electric currents of 0.37 A in the oxygen pressure of 5.0×10^{-2} Pa. The current was maintained for 10 min. After applying current, the samples were cooled to room temperature and taken out of the chamber. The surfaces of the samples were observed by SEM.

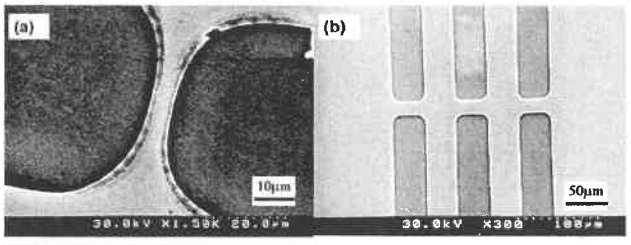

FIGURE 6. SEM image of (a) HCL-1 and (b) HCL-2 before heating.

RESULTS AND DISCUSSION

Figures 7(a-e) show SEM images of the narrow area of HCL-1 after heating. The nanowires were synthesized on the narrow area of HCL-1. The size of the area where the nanowires were synthesized was about 3 μm × 3 μm. This result shows that only the narrow area was heated at a temperatures of 700-800 °C to obtain nanowires. The reason there were no nanowire at the center of the narrow area is that the sample in this area was heated at a temperature of more than 800 °C and the nanowires melted. We can control the nanowire area at the center of the narrow area by controlling the electric current flowing through the HCL. The reason there were no nanowires at the edge of the HCL is that the tungsten material was damaged by etching for photolithography.

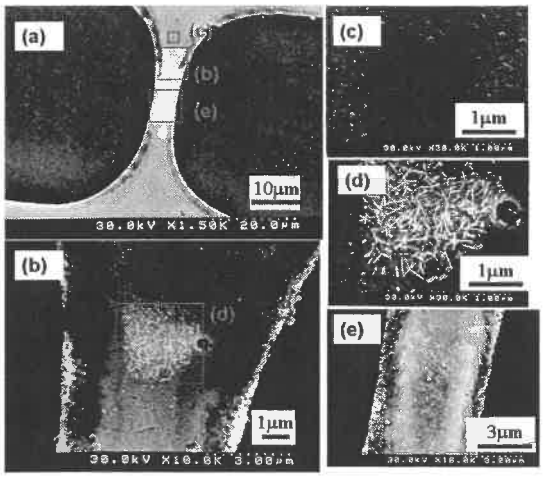

FIGURE 7. SEM images of the narrow area of HCL-1 after heating.

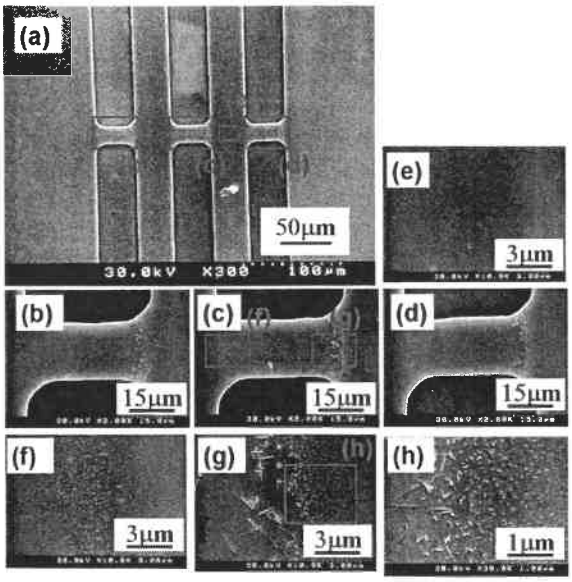

FIGURE 8. SEM images of the narrow areas of HCL-2 after heating.

Figures 8(a-h) show SEM images of HCL-2 after heating. The nanowires were synthesized at the end of each narrow area. This result shows that the narrow area of each HCL was heated uniformly to obtain the nanowires. We can synthesize the nanowires on many spots uniformly and simultaneously by flowing current though the HCL with the narrow areas. As shown in Figures 8(f,g), the nanowires synthesized at the right ends of narrow areas were longer than those at the left ends. The current direction may affect the length of the nanowires. We are now studying this phenomenon.

We have shown that we can control where the nanowires are synthesized in a 3 μm × 3 μm area and synthesize the nanowires on many areas uniformly and simultaneously with the HCL. To utilize the nanowires as field emitters of FEDs, it is necessary to control the heated spot where each nanowire synthesized. We are studying the use of HCL with narrower areas to achieve this goal in the future.

CONCLUSION

We proposed a new pinpoint heating process that uses a heat controlling layer. We used tungsten materials for the HCL and controlled the heated area where tungsten oxide nanowires were synthesized. By controlling electric current flowing through the HCL, which had broad and narrow areas, only the narrow areas of the HCL were heated to obtain the nanowires. We used the HCL whose narrow area was 5 μm and synthesized nanowires in a 3 μm × 3 μm area. We showed that we can synthesize nanowires on many spots uniformly and simultaneously using a HCL with three narrow areas.

ACKNOWLEDGEMENT

The photomasks for patterning of the HCL were made using the University of Tokyo VLSI Design and Education Center (VDEC)'s EB writer (F5112+VD01) donated by ADVANTEST Corporation. We would like to thank Dr. Kan of the University of Tokyo for his technical lecture on EB lithography and patterning.

REFERENCES

[1] Liu Z, Bando Y, and Tang C. Synthesis of Tungsten Oxide Nanowires. Chemical Physics Letters. 2003; 372: 179-182.

[2] Liu K, David T Foord, and Scipioni L. Easy Growth of Undoped and Doped Tungsten Oxide Nanowires with High Purity and Orientation. Nanotechnology. 2005; 16: 10-14.

[3] Kojima Y, Kasuya K, Ooi T, Nagato K, Takayama K, and Nakao M. Effects of Oxidation during Synthesis on Structure and Field-Emission Property of Tungsten Oxide Nanowires. Japanese Journal of Applied Physics, in press.

[4] Zhou J, Gong L, Shao Z. Deng, Chen J, Jun C. She, Ning S. Xu, Yang R, and Zhong L. Wang. Growth and Field-Emission Property of Tungsten Oxide Nanotip Arrays. Applied Physics Letters. 2005; 87: 223108-1-3.

[5] Li Y, Bando Y, and Golberg F. Quasi-Aligned Single-Crystalline $W_{18}O_{49}$ Nanotubes and Nanowires. Advanced Materals. 2003; 15: 1294-1296.

[6] Kasuya K, Nagato K, Jin Y, Morii H, Ooi T, and Nakao M. Rapid and Localized Synthesis of Single-Walled Carbon Nanotubes on Flat Surface by Laser-Assisted Chemical Vapor Deposition. Japanese Journal of Applied Physics. 2007; 46: L333-335.

SQUIRT-GUNS, SYRINGES AND SCIENCE: PRECISE JET DELIVERY OF LIQUID DRUG USING SERVO-CONTROLLED LINEAR LORENTZ-FORCE ACTUATORS

Andrew J. Taberner, N. Cathy Hogan, and Ian W. Hunter
BioInstrumentation Laboratory,
Department of Mechanical Engineering,
Massachusetts Institute of Technology
Cambridge, Massachusetts, USA
http://bioinstrumentation.mit.edu

INTRODUCTION

Transdermal delivery of a liquid drug can be effected without the use of needles by pressurizing the drug and passing it through a narrow orifice, thereby creating a high velocity jet that is capable of penetrating through the outer layers of skin into underlying tissues. Conventional jet injection devices employ energy storage and release techniques (compressed springs and gases) that offer very limited control over the rate and extent of energy delivery, thereby restricting the accuracy and repeatability of drug penetration depth and injected volume.

The BioInstrumentation Laboratory at Massachusetts Institute of Technology has developed a suite of precisely controllable jet drug delivery devices based on novel linear Lorentz force actuator technology (Figure 1).

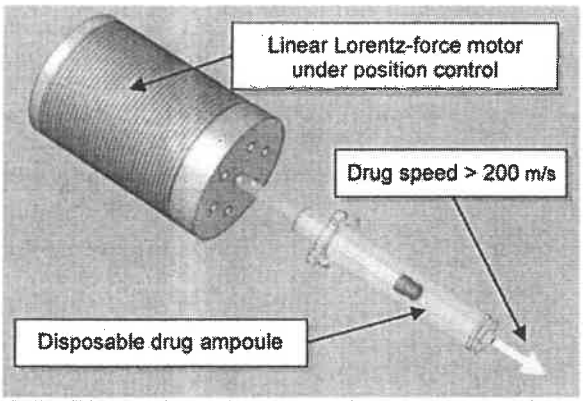

FIGURE 1. Jet injection using a Lorentz-force actuator

Through a combination of careful modeling, measurement, analysis, design and construction we have developed portable and bench-based jet injectors (Figure 2) that are powerful, compact and adaptable to a wide range of injection requirements. The inherent reversibility and controllability of our Lorentz force motors allow the speed of jet ejection together with the delivered volume to be monitored and regulated throughout the time-course of injection, offering an unprecedented level of flexibility and control over jet injection performance.

FIGURE 2. Portable jet injectors

We have used our jet injection devices to successfully deliver a range of different drugs, including a blend of relatively high molecular weight enzymes to the dermis of a live animal. Physical, biochemical, histological and/or immunological analyses have demonstrated that

drugs when delivered using our devices had activity comparable to, if not better than, drug delivered via needle using a conventional syringe.

We will discuss the challenges and advantages presented by this new form of jet injector, and the methodologies employed to develop our devices and monitor and enhance their performance.

THE DESIGN AND DYNAMIC CHARACTERIZATION OF A PRECISION THREE-AXIS, MICRO-SCALE FAST SCANNING STAGE FOR TWO-PHOTON ENDOMICROSCOPY

Shih-Chi Chen[1], Martin L. Culpepper[1], Heejin Choi[1], and Peter T. So[1]
[1]Department of Mechanical Engineering
Massachusetts Institute of Technology
Cambridge, MA

ABSTRACT

This paper presents the design and characterization of a high-speed, precision 3-axis optical scanner that is driven by contoured thermomechanical actuators (TMAs). This device is to be integrated within a two-photon excitation (TPE) endomicroscope that will perform optical biopsies. The scanner consists of a two-axis, silicon optical bench and a mm-scale fiber resonator. These components were assembled to create a 3 axis raster scanner. The scanner is driven by pulsed command signals that improve the scanning speed of the silicon optical bench, by 10X over conventional signals. The scanner (a) fits within a 7mmx55mm endoscope tip and (b) can scan its axes at 3000, 30 and 2 Hz. The alpha prototype has a measured work volume of 200x200x200 μm^3.

INTRODUCTIONS

Excisional biopsy is the only practical clinical procedure that allows early and accurate cancer diagnosis. This technique requires tissues to be excised, fixated, sectioned, stained and then examined via microscopy. The invasive nature of this approach encourages the development of a less invasive approach. TPE microscopy provides a means to obtain real-time, sub-cellular volumetric images within tissues [1]. A conventional, i.e. macro-scale, TPE microscope exhibits several advantageous characteristics: (1) 3D resolution at the micron level, (2) the ability to identify a tissue's biochemical signatures through fluorescence contrast, (3) deep (e.g. 100s of microns) image penetration into highly turbid tissues, and (4) relatively low photodamage as compared to competing methods [1]. The application of TPE within an endoscope requires the construction of precision electromechanical and optical systems that fit within the endoscope's distal end. In combination, these systems must be capable of high-speed, 3-axis raster scanning of a focal point with micron resolution. The scanner must also satisfy the functional requirements in Table 1 [2].

TABLE 1. Scanner's functional requirements

	x-axis (fiber)	y-axis (prism)	z-axis (GRIN)
Stroke	100μm	100 μm	100 μm
Speed	3 kHz	30 Hz	2 Hz
Envelope	Within a 7mm Ø tube.		

The TPE endomicroscope was designed to enable optical biopsy procedures that medical staff may use to acquire real-time images of tissue and thereby minimize the need for minor/major surgery. This change in tools/methods will help to expedite examination, reduce equipment/material costs, and mitigate the risks that are associated with excision/surgery. This in turn will improve access to, and the inclination to perform, preventive cancer screenings and pre- and post-surgical diagnostics of cancerous sites.

The lasting impact is to affect survival rates among the cancers that are shown in Table 2. Note the third column in Table 2 lists the (1) current U.S. overall death rates (OA), (2) death rates that occur even after early detection of a cancer (ED), and (3) the percentage of patients that have cancer detected at early stages (DE).

TABLE 2. Internal cancers that would be impacted via TPE endomicroscopy

Type	Case/year CY	Death rates (%) OA	ED	DE
- Cervical	12,000	36	05	N/A
- Colorectal	150,000	53	10	39
- Esophageal	15,000	90	52	01

Table 2 shows that (a) there is room to increase the percentage of patients that have their conditions detected early and (b) early detection prevents mortality in a significant percentage of those afflicted (e.g. OA-ED). The combination of

items (a), (b), and the number of new cases per year indicates the potential impact that tools for early cancer screening may have on human health and well-being.

SILICON OPTICAL BENCH DESIGN

Figure 1 contains the layout of the optical system as mounted upon the silicon optical bench. The system is comprised of a graded index (GRIN) lens, a prism and an optical fiber. The bench contains flexure bearings and micro-TMAs that control the z motion of the GRIN lens and the angular motion, θ_x, of the prism.

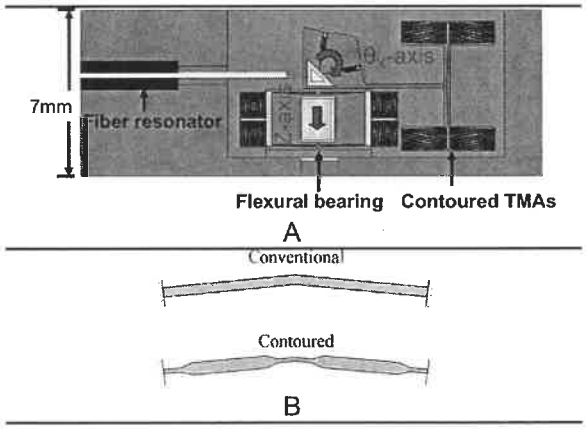

FIGURE 1: Scanner and optical systems (A) and comparison of chevron micro-TMAs with constant vs. contoured cross sections (B)

In this design, the GRIN lens and prism are mounted on the bench. They are actuated in-plane by TMAs [3] such that they provide sub-micron/milliradian positioning/rotation of the optics. The micro-TMAs possessed a contoured geometry shown in Fig 1B that enables them to achieve force (2.5X) and stroke (4X) characteristics that are better than conventional micro-TMAs [4]. Additional details regarding the system design – and system modeling – may be found in [2,3,4].

Dynamic Performance

This section compares the bench's simulated and predicted performance. Figure 2 shows the step response of the GRIN lens shuttle. This data was obtained via measurements that were conducted upon MIT's Micro-Motion Analyzer. The rise and fall times for the GRIN lens shuttle are 0.46 and 0.38 seconds respectively. This matches our modeling results with less than 6% error.

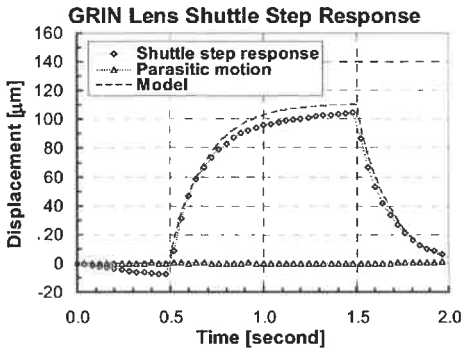

FIGURE 2: GRIN lens shuttle step response.

Our model's are at present unable to capture the effect of temperature-dependant material properties. As such, the errors in rise and fall times are due to changes in the material properties of silicon – resistivity, thermal conductivity, and coefficient of thermal expansion – with changes in temperature. Temperature variable material properties are also the primary source of errors between predicted and measure performance in the remainder of this paper. The GRIN lens shuttle is designed to scan at up to 20Hz. A comparison of predicted and measured performance characteristics is provided in Table 3.

TABLE 3. GRIN lens axis performance

	Measured	Simulated	% error
Frequency test			
1st mode	1,508 Hz	1,527 Hz	1.26
2nd mode	N/A	7,121 Hz	N/A
Step response			
Rise time	0.46 sec	0.43 sec	6.5
Fall time	0.38 sec	0.37 sec	2.6

Figure 3 and Table 4 contain results from the measured step response of the prism shuttle.

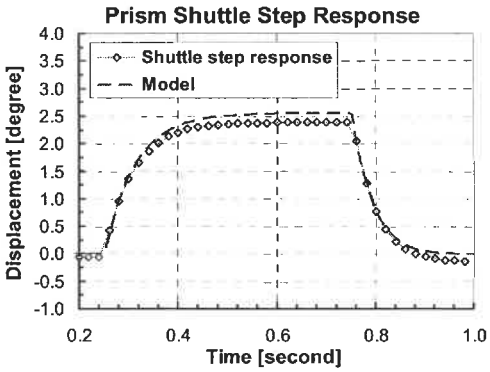

FIGURE 3: Prism shuttle step response.

The rise time and fall time for the shuttle are 0.13s and 0.09s respectively. These results match the predicted performance within 8%.

TABLE 4. Prism axis performance			
	Measured	Simulated	% error
Frequency test			
1st mode	3,124 Hz	3,205 Hz	2.59
2nd mode	7,320 Hz	7,096 Hz	3.06
Step response			
Rise time	0.13 sec	0.14 sec	7.7
Fall time	0.09 sec	0.095 sec	5.5

Pulsed command signals

In order to achieve the desired scan rates, it is necessary to employ a new control technique that is based upon pulsed command signals. In the following, we provide an overview of the technique and show that this technique makes it possible to image with the frame rates, e.g. 20 fps, that are necessary to acquire volumetric scans between heartbeats. This is important because registration of the endoscope to the area of interest is adversely affected by the shifting of the tissues that occurs during heart beats.

The concept of the pulsing technique is to supply contoured μTMAs with pulsed command signals. It is well-known that contoured beams yield a flatter steady-state temperature profile in comparison to those of constant cross section beams. This characteristic creates the transient heating process, shown in Figure 4A, that yields a "flatter" temperature profile when the beam is subject to pulsed signals.

The pulse characteristics, shown in Figure 4B, may be set so as to manipulate the "flatness" of the temperature profile at any specified temperature and time during an actuation cycle, e.g. Figure 4C. The overall effect of this method is to yield a "flatter" temperature profile that enables the scanner's actuators to possess: (1) a high temperature gradient at the beam ends which decreases the cooling time and therefore cycle time; (2) a flat temperature profile which increases the maximum achievable strain/stroke; (3) a decrease in the power per unit displacement.

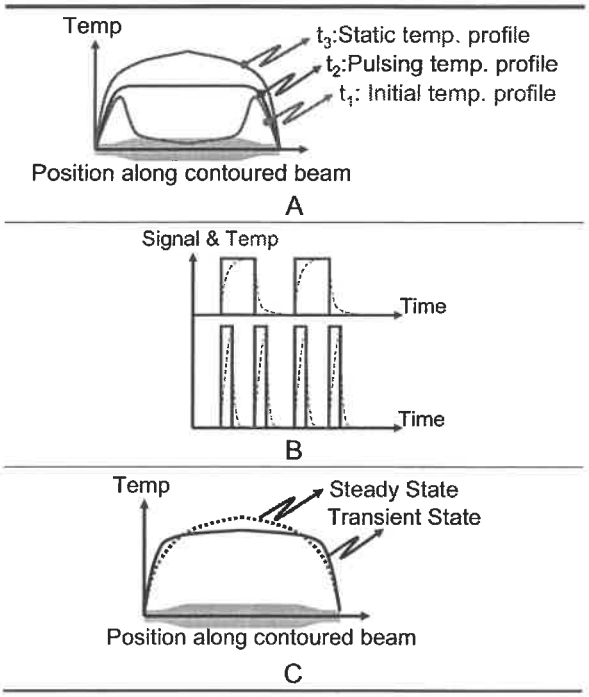

FIGURE 4: Temperature profile evolution during heating process of a contoured beam (A), Temperature response (dashed) of a micro-TMA in response to conventional (top) and pulsed (bottom) signals (B) and two temperature profiles for a contoured TMA that result from driving signals shown in (B) that yield identical displacements

Experimental Results

Figure 5 shows the experimental results obtained via the pulsing technique.

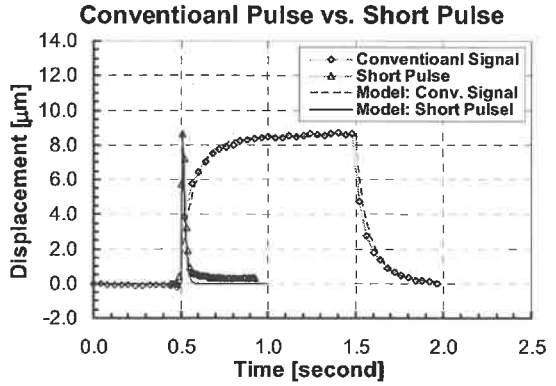

FIGURE 5: GRIN shuttle response to driving signal

The important parameters and the results of the pulsing experiment are summarized in Table 5.

TABLE 5. Summary of the high-speed pulsing technique applied to the GRIN lens shuttle.			
	Measured	Simulated	% error
Pulsed signal: Square wave, 0.5Hz, 125mA, 50% duty cycle.			
Rise time	~0.01 sec	0.009 sec	~10%
Fall time	~0.02 sec	0.022 sec	~10%
Conventional signal: Square wave, 2Hz, 250mA, 5% duty cycle.			
Rise time	0.20 sec	0.19 sec	5.00%
Fall time	0.18 sec	0.185 sec	2.78%

In this experiment, the GRIN lens shuttle was driven by a square wave signal and then driven by a pulsed signal. In each case, the signal was constructed to yield identical displacements. The shorter rise and fall times for the pulsed response yield 20X and 9X faster forward and return speeds for the GRIN lens shuttle.

FIBER RESONATOR DESIGN

A fiber resonator (6.8x5x55 mm^3) was used to provide the third, high-speed, axis of scanning. The resonator, shown in Fig. 6, was driven by a Physik Instrumente piezo-ceramic actuator.

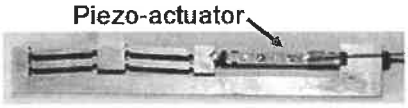

FIGURE 6: Fiber resonator prototype

The resonator is designed to resonate a fiber that is attached to the top, middle portion of the flexure chevron such that the fiber lies in a direction from left to right. The characteristics of the resonator are listed in Table 6. The fiber's transmission ratio, i.e. the displacement of its end relative to the input displacement of the resonator, is 370 at 1 kHz. This makes it possible to achieve a 200 micron scanning range with a driving signal that has a 3V amplitude. The low voltage signal is important for *in vivo* procedures as high voltage signals have the potential to damage tissues and to interfere with cardiac function.

SCANNING

The beam from a femtosecond laser was directed through the scanner as shown in Figure 7. Fluorescein samples were placed between the fiber tip and a CCD. The CCD captured the fluorescence that occurred as the focal point of the laser beam was raster scanned through the fluorescein. An infrared filter was placed in front of the CCD lens so that the two-photon signals could be, collected, differentiated and imaged.

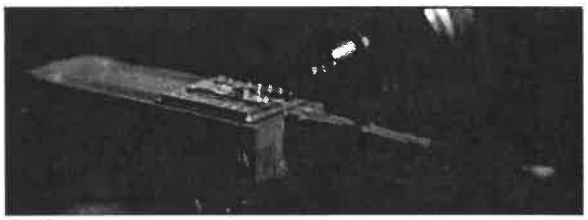

FIGURE 7: Resonator (lower-right) and silicon optical bench (middle-left) that are assembled and aligned in front of the CCD objective (back).

Figure 8 contains a compilation of screen shots that show 2D scanning at 0.07 second intervals. The vertical line is the scan line of the fiber that is resonating. The GRIN lens, which provides the out-of-plane scanning axis in Fig. 8, is capable of 200µm range. The scanner is therefore able to scan 8X more volume, 200x200x200$µm^3$, than listed in the functional requirements.

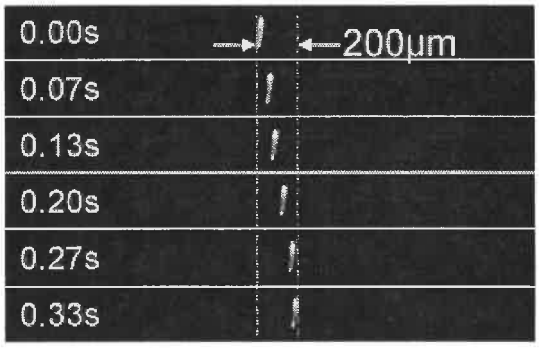

FIGURE 8: Screenshots of X-Y scan.

REFERENCES

[1] So P T, et al. Two-photon Excitation Fluorescence Microscopy. Annu. Rev. Biomed. Eng. 2:399–429, 2000.

[2] Choi H, et al. Design of a Non-linear Endomicroscope Biopsy Probe. OSA Biomed. Optics Topical Meeting and Tabletop Exhibit. 2006. FL.

[3] Chen S, et al. Design of a High-speed, Micro-scale Fast Scanning Stage for Two-Photon Endomicroscopy. Proc. of ASPE. 2006. CA. pp. 279 – 282.

[4] Chen S, Culpepper M L. Design of Contoured Microscale Thermomechanical Actuators. J. of MEMS. 2006; Vol. 15, Issue 5, pp.1226 – 34.

A COMBINED SCANNED PROBE AND CONFOCAL MICROSCOPE SYSTEM FOR LIVE CELL SPECTROSCOPIC IMAGING

Kevin E. Elliott[1,2], Stuart T. Smith[1,2,3], Gloria Elliott[2], and Patrick Moyer[3]
[1]Center for Precision Metrology
University Of North Carolina at Charlotte
Charlotte, NC, USA
[2]Center for Biomedical Engineering Systems
University Of North Carolina at Charlotte
Charlotte, NC, USA
[3]Center for Optoelectronics and Optical Communication
University Of North Carolina at Charlotte
Charlotte, NC, USA

ABSTRACT

Currently there is an interest in preserving mammalian cells in the dry state. Researchers believe that a key element to achieving this goal is the creation of a glassy state within the cell by adding sugars (disaccharides such at sucrose and trehalose) to the cell. This state is characterized by a significant increase in cytoplasm viscosity. The challenge has been to determine experimentally whether or not the cell has formed this glassy state during processing. The goal of the instrument development presented in this paper is to be able to determine the mechanical properties of cells in an environment that is non-destructive and which also enables the simultaneous use of optical methods of analysis. Knowing where and how the glass forms inside the cell would potentially lead to new techniques and the refinement of existing techniques which would direct research toward more economical and versatile cell preservation. Current work is focused on macroscopic metrics to characterize cell drying and anhydrous preservation success. To facilitate further research an instrument capable of combined intracellular probing of microviscosity and confocal microscopy incorporating fluorescence-based diagnostics is being implemented.

1 MOTIVATION

The storage life of biological samples used for transplant, such as organs or blood, is limited to a relatively short time span. For instance, organs such as the kidneys have a storage time of 48 to 72 hours, the liver 30 hours and the heart and lungs are only viable for a transplant for up to 6 hours [1]. This poses an obvious challenge to medical teams to perform transplants quickly after the death of the donor. One path towards extending the storage life of biological samples may be through the development of techniques to preserve these organisms through drying.

2 GLASSY STATE

To understand the particular mechanisms that allow samples to be dried, researchers are first working toward treatments that enable the preservation of individual cells. It is believed that the creation of a glassy state within a cell makes successful preservation possible. This glassy state is formed when most of the moisture has left the cell and only the loaded sugars remain. These sugars then form a glass which is by definition, an amorphous solid and exhibits a viscosity on the order of 10^{14} Pa-s [2]. This glass offers rigidity to the cellular structure and reduces the mobility of reactants thus offering protection to the cell while it is in this dry state. The formation of this intercellular glass causes little stress to the cells as apposed to if ice were to form in the cell, since there is no phase change in this creation. The challenge is that little is known about this glass on the cellular level. Information describing where and how this glass forms within the cells is lacking and needed to understand how to preserve larger samples. Currently, only single cells or small tissue samples are able to be preserved using drying techniques that result in viable cells after rehydration. For this reason, there is an interest in biological instrumentation capable of intracellular imaging and mechanical probing to detect the areas within the cell where these extreme viscosities exist.

3 MEASUREMENT SYSTEM

In order to accomplish the task of intercellular measurement a scanning stage is being developed which allows the simultaneous imaging of different techniques in the same location. For instance, scanned probe microscopy (SPM) and confocal microscopy can be used in conjunction to image the same individual part of a cell with one image collecting optical information and the other interrogating the cell mechanically [3]. This is accomplished through a scanning approach that moves the sample as while the probes maintain a stationary position releative to the instrument frame. In this case, the tip of the AFM and the focus of the confocal microscope are adjusted to be coincident as the sample is moved in a predefined scanning pattern thus yielding two views of the sample (optical and mechanical) taken simultaneously and with probe points being at the same location. Figure 1 shows both a block diagram indicating the major components of the scanning system and a three dimensional solid model of the system.

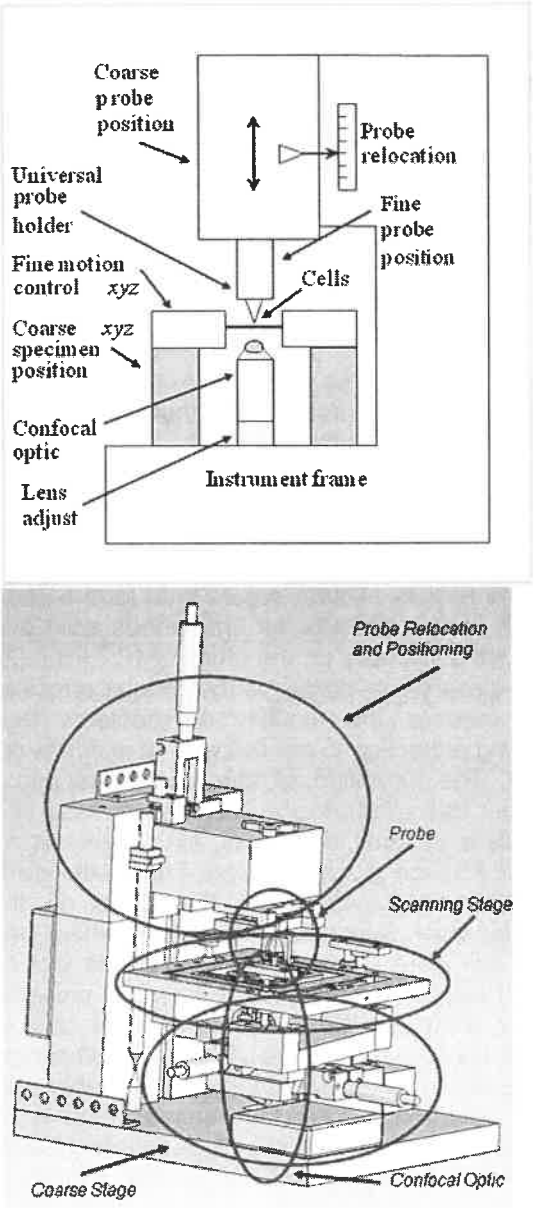

FIGURE 1: Block diagram indicating major features of the instrument (above) and 3-D conceptual image (below).

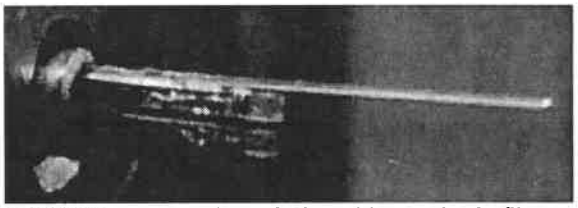

FIGURE 2: Tuning fork with optical fiber attached. Fiber extends approx. 5 mm from free end of tuning fork tine as indicated by double arrow.

4 VISCOSITY MEASUREMENT

As mentioned above the measurement system will also have to the ability to measure microviscosity of the cell in order to determine information about glass formation. This will be achieved using a probe comprised of a quartz tuning fork with an etched optical fiber attached. Quartz tuning forks have been established as force sensors partly due to their high quality factor on the order of Q (10^3-10^5) when operated near resonance [4]. The optical fiber is attached to one leg of the tuning fork and is not used for its optical properties but as a cantilever to act as a probe tip. A photograph of a typical quartz tuning fork probe with attached fiber is shown in figure 2.

The tuning fork is resonated using a driving circuit and the corresponding oscillation is monitored and controlled using a lock-in amplifier. As the probe tip (optical fiber) comes into contact with the sample, the resonant characteristic of the probe will change as a function of the viscosity of the sample, in our case biological samples at different stages of the drying process. Using the lock-in amplifier, the output voltage can be associated with the viscosity of the sample in that region, leading to

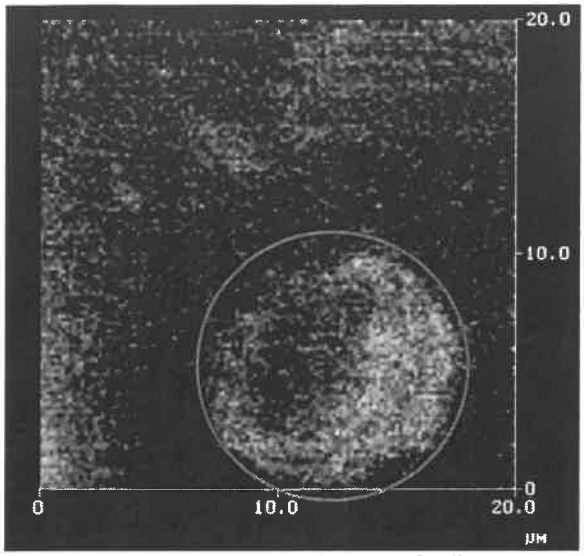

FIGURE 3. Fluorescence image of a live mouse macrophage cell (red circle) using our home-built confocal microscope.

the possibility of force, compliance or viscosity mapping over the surface of an entire cell. This should be the first step in understanding the mechanics and metrics needed in order to progress toward larger scale biological preservation. Simultaneous measurement of

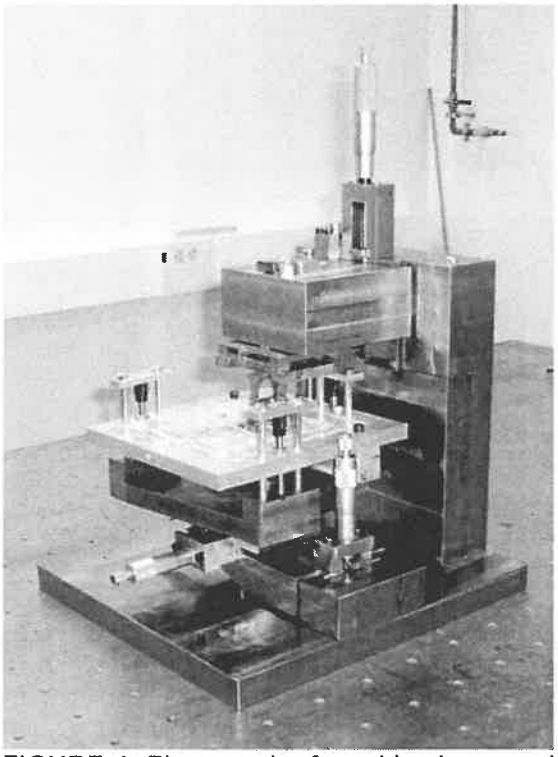
FIGURE 4: Photograph of combined scanned probe and confocal microscope SPCM system

fluorescent markers will also enable complementary information about the intracellular processes. Bulk or single molecule flourecsence measurements of effects such as anisotropy, spectroscopy of fluorescent rotors and resonant energy transfer mechanisms represent exciting methods for determination of the presence and properties of the intracellular state that may be correlated with the mechanical measurements. Figure 3 shows preliminary flourescence imaging data of a live mouse macrophage cell (red circle) incubated with the mitochondrial stain rhodamine 6G and measured with an earlier prototype scanning system. This shows a slice of the cell slightly above the plane of attachment. The dark region in the center of the cell is the nucleus, which, in the absence of mitchondria, exhibits no fluorescence.

CURRENT STATUS

As of writing the mechanical and electrical

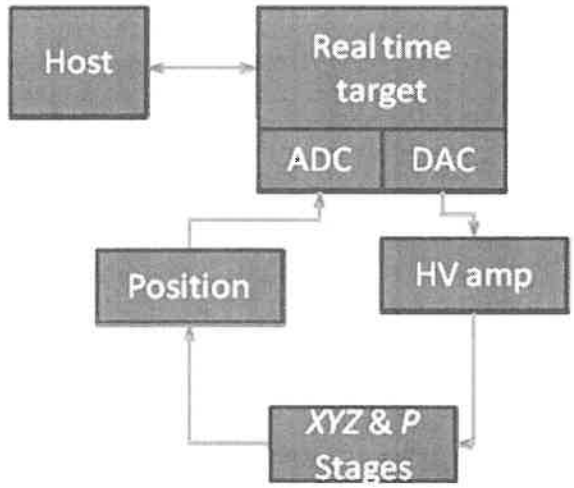

FIGURE 5: Block diagram indicating major components of the instrument controller.

systems have been manufactured and assembled. A photograph of the completed instrument is shown in figure 4.

Control of this instrument is achieved using a Labview™ desktop real time hardware interface. A simplified block diagram of the system is shown in figure 5. The hardware interfaces of this system use two NI MIO16XE data acquisition cards mounted into a Pentium 4 computer. This is configured as a realtime desktop controller dedicated to hardware interfacing and data flow control. Programming

of this desktop system is carried out using a host computer with compiled code being transferred to the target using an Ethernet data bus. This bus is also used during operation to transfer data to and from the two computers.

Four DAC channels are used to control the piezo electric actuators of the scanning stages via Insitutec Inc. IT-150V-AMP-B high voltage amplifiers tuned to a settling time of 0.1 ms. Linear displacements in all axes are measured using Insitutec Inc. IT-A01 capacitance gage electronics with probes and targets being manufactured in-house. A simple digital PID control is implemented in software.

The three piezo-electrically actuated, linear translation stages and the probe actuator have been assembled and are now operational. Range and first mode natural frequencies of these four drives are given in table 1. In general, it is known that increasing range reduces the dynamics of these systems and this is apparent. Damping by filling available cavities in the flexures with Sylgard 184 elastomer mixed to a 20:1 ratio. This considerably attenuated the *Q* of the translation stages with the *z* axis stage being over-damped in this instrument.

TABLE 1: Range and dynamic response of the scanning system

Axis	Range (μm)	First mode frequency (Hz)
X	50	228
Y	50	360
Z	30	520
Probe	17	2280

It is envisaged that preliminary measurements of live cells will be completed and presented at the annual meeting.

REFERENCES:

[1] Bumsoo, H., and Bischof, J. C., 2004, Engineering challenges in tissue preservation, *Cell Preservation Technology*, **2**(2), 91-112.

[2] Buitink, J. and Leprince O., 2004, Glass formation in plant anhydrobiotes: survival in the dry state, *Cryobiology*, **48**,. 215-228.

[3] Lim C.T., Zhou E.H. amnd Quek S.T., 2006, Mechanical models for living cells – a review, *J. Biomech.*, **39**, 195 – 216.

[4] Grober, R. D., Acimovic, J., Schuck, J., Hessman, D., Kindlemann, P. J., Hespanha J., Morss, S., Karrai, K., Tiemann, I. and Manus, S., 2000, Fundamental limits to force detection using quartz tuning forks, *Rev. Sci. Instrum.*, **71**(7), 2776-2780.

FABRICATION METHODS FOR POLYMER MEMS

Nicholas Ferrell, Daniel Gallego, James Woodard, and Derek Hansford[1]
[1]Department of Biomedical Engineering
Ohio State University
Columbus, OH, USA

ABSTRACT

Several soft lithography-based polymer microfabrication techniques are described. These processes are capable of producing polymer microstructures from various materials including piezoelectric and conducting polymers. Two of the methods described are also capable of producing freely suspended microstructures, an important step in the implementation of polymers as functional mechanical structures in MEMS devices.

INTRODUCTION

The field of MEMS (micro-electro-mechanical systems) has grown rapidly over the past several years. As MEMS have been considered for an expanding number of applications, new materials have become important in providing the needed functionality in diverse settings. This is particularly true in biomedical applications, where additional factors such as biocompatibility have to be accounted for in the design and implementation of MEMS devices [1].

Polymeric materials have become particularly attractive to those in the BioMEMS field for several reasons. There is a long list of polymers that show relatively good interactions with biological materials both *in vitro and in vivo*. Polymers also have a broad range of properties, providing a larger materials selection pool. In addition, polymer materials themselves, as well as many of the methods used to process them at the microscale, are often considerably less expensive than traditional cleanroom silicon-based processing methods.

Several different classes of polymer materials have been considered for use in micro/nanoscale devices. Various photoresists, elastomers, electrically conductive polymers, biodegradable polymers, and piezoelectric polymers have all been used for different applications. Potential applications of these materials are as diverse as the materials themselves. Some examples include elastomeric microfluidic devices [2], biodegradable drug delivery devices [3] and tissue engineering scaffolds [4], actuators and electrochemical biosensors made from conducting polymers [5,6], and piezoelectric force sensors [7].

In order for these materials to be practically applied to microscale devices, new cost effective methods of processing the materials need to be investigated. Here we look at several new soft lithography [8] based polymer processing techniques that could find potential applications in the fabrication of new and more functional polymer MEMS devices. Each process begins by making a poly(dimethylsiloxane) (PDMS) mold cast from a photolithographically patterned master. After PDMS mold fabrication, the processing steps vary depending on the material of interest and/or the application.

Four different processing techniques will be discussed here. The first is embossing of polyvinylidene fluoride (PVDF) microstructures. The second is *in situ* polymerization and lift-off processing of conducting sulfonated polyaniline (SPAN). Two additional methods for fabricating suspended polymer microstructures, patterned substrate micromolding and sacrificial layer micromolding, will also be discussed.

MATERIAL AND METHODS

PDMS Mold Fabrication

Each of the processing techniques described here involves making a PDMS mold. A master is first patterned in a photoresist material using standard photolithography. The photoresist is then replicated in PDMS by pouring a 10:1 ratio (wt/wt) of PDMS and curing agent onto the photoresist master. The PDMS then cures and the solid PDMS replica can be removed from the master.

Micromolding of PVDF Microstructures

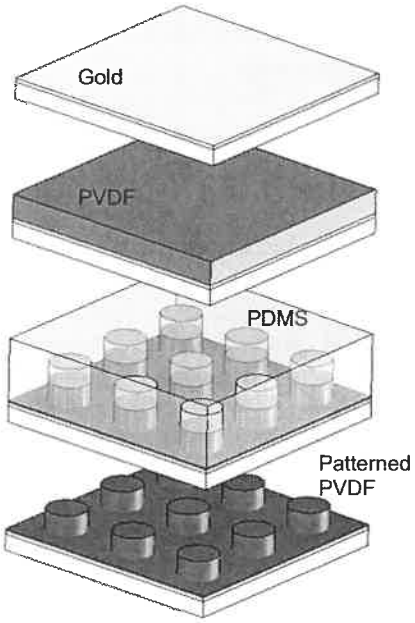

FIGURE 1. Embossing of PVDF microstructures.

PVDF microstructures were embossed using the PDMS mold as an embossing tool. The process is shown in FIGURE 1. PVDF was first dissolved in N, N - dimethylacetamide and acetone at a 1:4:5 (wt/wt/wt) ratio. The PVDF solution was spin coated onto gold coated glass substrates. The gold coating was deposited via e-beam evaporation, and served as bottom electrode for poling and actuation purposes. The PDMS mold was used to emboss the polymer microfeatures by applying 32 psi of pressure at 90 °C for 5 minutes.

A thin gold electrode was deposited onto the as-fabricated PVDF microstructures using a sputter coater. This coating served as top electrode for poling and actuation purposes. The dipoles in PVDF were aligned by applying an electric field of ~400 MV/m across the electrodes at 160 °C for 3 hours. The bias was kept for an extra hour at room temperature to sustain the orientation of the dipoles and render a piezoelectric behavior to PVDF.

Selectively Coating the Mold

The first step in the final three processes is the selective coating of the recessed features of the PDMS mold. This process is shown in FIGURE 2.

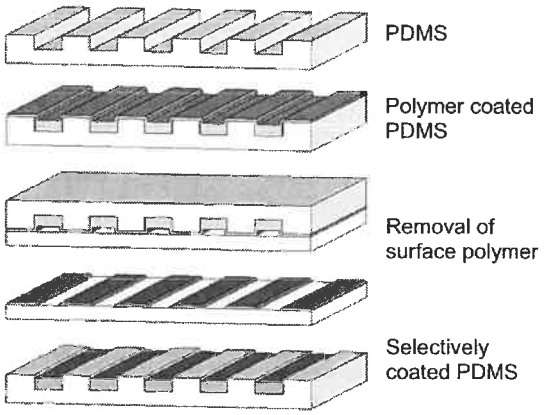

FIGURE 2. Selective filling of PDMS molds.

The PDMS mold is first spin coated with the polymer of interest. The polymer is generally an organically soluble material such as poly(methyl methacrylate) (PMMA), poly(propyl methacrylate) (PPMA), or polystyrene. The spin speed depends on the concentration of the polymer solution and the depth of the features on the mold. After coating, the polymer on the raised portions of the mold is removed by bringing the film in contact with a heated glass slide. For all of the materials mentioned previously, the substrate was heated to 200 °C.

Micropatterning of Sulfonated Polyaniline

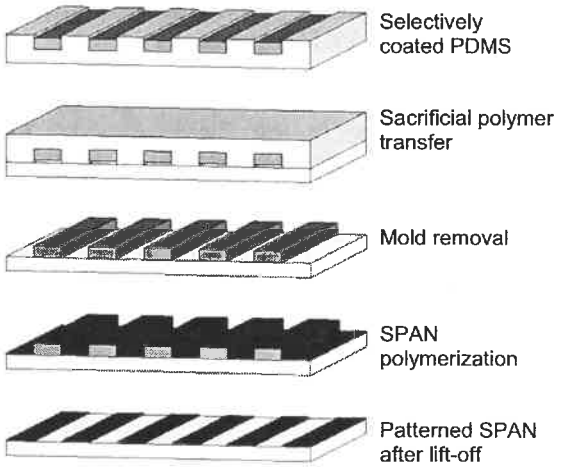

FIGURE 3. Lift-off processing of sulfonated polyaniline.

Conducting sulfonated polyaniline was patterned by lift-off processing using micromolded PPMA as a sacrificial layer. The process schematic is shown in FIGURE 3. The PDMS mold was

selectively coated with PPMA as described in the previous section. The material in the recessed portions of the mold was transferred to glass, silicon, or polyimide substrates by heating the substrates to 95 °C and applying pressure to the top side of the mold to transfer the materials from the mold onto the substrate.

The patterned substrates were then placed in a reaction vessel and the polyaniline was synthesized using the process described previously [9]. This resulted in a conformal coating of SPAN on top of the patterned substrate. The PPMA sacrificial layer was then removed by sonication in acetone. This removed the SPAN from the PPMA coated areas, leaving only the material adhered directly to the substrate.

Patterned Substrate Micromolding

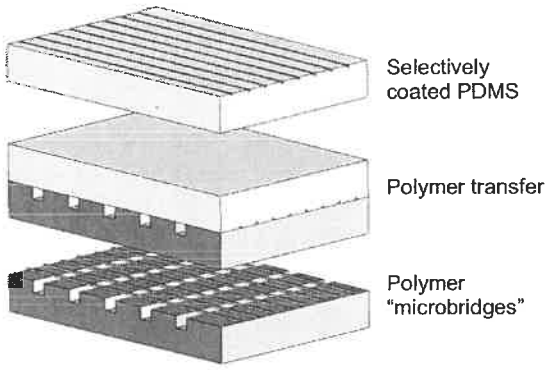

FIGURE 4. Patterned substrate micromolding.

The processes described previously have been capable of creating topographically patterned polymer films, but not suspended structures. The final two processes are able to produce microstructures that are freely suspended. The first process, patterned substrate micromolding, is shown in FIGURE 4. In this case the material in the recesses of the PDMS mold is transferred to a pre-patterned SU8 photoresist substrate. The photoresist acts as the anchor points for the polymer and the structures are suspended over the voids in the photoresist pattern. This process has been used to fabricate "microbridges" from PPMA, PMMA, and polystyrene.

Sacrificial Layer Micromolding

The final process, sacrificial layer micromolding, is also capable of producing freely suspended structures such as cantilever beams. In this case, a water soluble poly(vinyl alcohol) (PVA) sacrificial layer is first fabricated using photolithography and reactive ion etching. The coated PDMS mold is then aligned with the PVA layer and the material is transferred using heat and pressure. The suspended region of the device is placed on top of the PVA with the anchor regions attached directly to the underlying substrate. The structures can then be released by immersion in water.

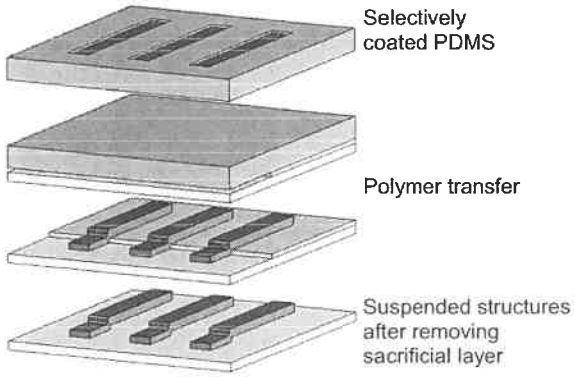

FIGURE 5. Sacrificial layer micromolding.

RESULTS AND DISCUSSION

A scanning electron micrograph of a patterned PVDF film is shown in FIGURE 6(A). The image shows that the PVDF conformed well to the shape of the PDMS mold even at the low processing temperature (90 °C). After poling, the piezoelectric activity was evaluated by applying an external voltage between 0±10 V and measuring the height of the structures using atomic force microscopy. The results showed strain of up to 7.4% during expansion of the pillars and 3.0% during contraction.

A micrograph of a patterned SPAN film is shown in FIGURE 6(B). Films ranged in thickness between around 40 nm and 180 nm depending on the duration and conditions of the polymerization reaction.

"Microbridges" fabricated using patterned substrate micromolding are shown in FIGURE 6(C). The substrate is a ~25 µm thick layer of SU8 with ~30 µm gaps. The bridges were made from PMMA, PPMA, and polystyrene. The images show that the structures remain suspended over the voids in the photoresist. These structures have been used previously as

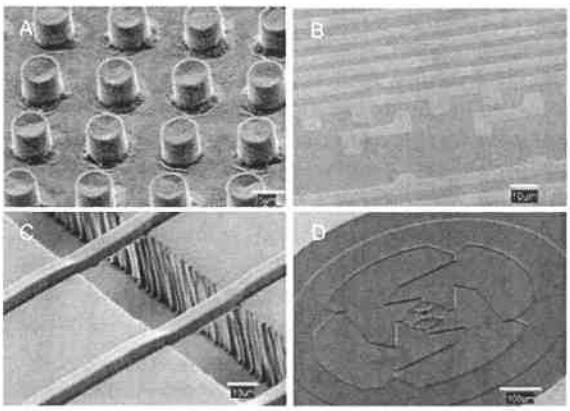

FIGURE 6. SEM micrographs of (A) PVDF micropillars fabricated by embossing (B) Micropatterned SPAN patterned by lift-off. (C) "Microbridges" made using patterned substrate micromolding and (D) Cantilevers fabricated by sacrificial layer micromolding.

test beams for evaluating mechanical properties of microscale structures [10].

Cantilever beams fabricated using the sacrificial layer micromolding process are shown in FIGURE 6(D). The beams are designed to measure forces generated by fibroblast cells as they attach and spread on the beams. Forces generated by the cell and transmitted to the beams result in deflection of the cantilevers. The deflection is measured by analyzing time lapse optical images of the beams and measuring the beam displacement over time. The displacement measurements are then used to calculate the corresponding force.

CONCLUSION

Four methods for fabricating microscale structures from various polymers have been described. Each method was based on soft lithography, thus minimizing the necessity for expensive cleanroom processing. The first method involves embossing of piezoelectric PVDF thin films. A lift-off method for micropatterning conducting SPAN films was also introduced. The unique properties of these two polymers make them strong candidates for various MEMS applications. In addition, two methods for fabricated freely suspended polymer microstructures were discussed. Currently, there are few methods available for producing freely moveable polymer microstructures. These methods could lead to wider use of polymers as mechanical components in MEMS devices.

REFERENCES

[1] Kotzar G, Treas M, Ahel P, Fleischman A, Roy S, Zorman C, Moran JM, Melzak J. Evaluation of MEMS Materials of Construction for Implantable Medical Devices. Biomaterials. 2002; 23: 2737-2750.

[2] Sia SK, Whitesides GM. Microfluidic Devices Fabricated in Poly(dimethylsiloxane) for Biological Studies. Electrophoresis. 2000; 24:3563-3576.

[3] Guan J, Ferrell N, Lee LJ, Hansford DJ. Fabrication of Polymeric Microparticle for Drug Delivery by Soft Lithography. Biomaterials. 2006; 27: 4034-4041.

[4] Yang Y, Basu S, Tomasko DL, Lee LJ, Yang S-T. Fabrication of Well-defined PLGA Scaffold Using Novel Microebmossing and Carbon Dioxide Bonding. Biomaterials. 2005; 26: 2585-2594.

[5] Tissaphern M, Madden JDW, Baughman RH. Polymer Artificial Muscles. Materials Today. 2007; 10: 30-38.

[6] Gerard M, Asha C, Malhotra BD. Application of Conducting Polymers to Biosensors. Biosensors and Bioelectronics. 2002; 17:345-359.

[7] Dargahi J, Rao NP, Sokhanvar S. Design and Microfabrication of a Hybrid Piezoelectric-capacitive Tactile Sensor. Sensor Review. 2006; 26: 186.192.

[8] Xia Y, Whitesides GM, Soft Lithography. Angewandte Chemie Int. Ed. 1998; 37: 550-575.

[9] Mac M, Žigon A, Šebenik J, Vohlidal J. Sulfonated Polyanilines Prepared by Copolymerization of 3-aminobenzenesulfonic Acid and Aniline: The Effect of Reaction Conditions on Polymer Properties. Journal of Polymer Science A: Polymer Chemistry. 2000; 38: 3390-3398.

[10] Wei G, Bhushan B, Ferrell N, Hansford DJ, Microfabrication and Nanomechanical Characterization of Microelectromechanical Systems for Biological Applications. Journal of Vacuum Science and Technology A. 2005; 23: 811-819.

HYBRID ELECTROMAGNETIC AIR BEARING SYSTEMS

Anton van Beek[1], Jo W. Spronck[1], Hans H. Langen[1], Ron A. J. van Ostayen[1], Rob Munnig Schmidt[1]
[1]Research Group Mechatronics
Department of Precision and Microsystems Engineering
Faculty of Mechanical, Maritime and Materials Engineering
Delft University of Technology, the Netherlands

ABSTRACT

In this paper a study to the challenges of air bearings with dynamic electromagnetic preloading is presented. Two configurations are compared, one in which the electromagnet is constructed into the center of the air bearing and one in which the electromagnet acts at the surface of a compliant membrane air bearing. The membrane air bearing with electromagnetic actuated membrane can also be applied with a non metallic guide surface. Active electro-magnets integrated in the bearing structure offer a promising solution of applying a dynamic preload with which a) running accuracy can be improved, b) the load capacity can be increased significantly and c) a near infinite bearing stiffness can be realized. It is studied to what extend the bearing can be adjusted vertically by varying the magnetic preload quasi static and dynamically. With knowledge of the dynamic response of the bearing system, deviations of straightness and elastic response of the guide surface to dynamic loading can be controlled by feed forward.

NOMENCLATURE

A	surface area
A_r	cross section restrictor
B	magnetic field
C_D	constriction coeff.
F	load capacity
H	field intensity
h	film thickness
h_0	flying height
M	mass flow
p_s	supply pressure
p_r	restrictor pressure
p_a	ambiant pressure
p_r	restrictor pressure
r_0	outer radius
r_1	inner radius
T_0	temperature
κ	ratio of specific heat
η	gas viscosity
μ	permeability

INTRODUCTION

Aerostatic bearings are advantageous over contact bearings in high precision motion and position stages because of their near zero friction, smooth operation and high bearing stiffness. Axial bearing stiffness is an important factor in overall performance of stages. Preloading is a method of increasing bearing stiffness. The most frequently applied method of preloading is by configuring two air bearings on opposite sides of a guide rail. This requires two parallel guide surfaces and a suitable bearing housing to keep the bearing assembly pre-stressed.

Vacuum preloading or magnetic preloading offers an elegant solution of preloading without the need of the two parallel guide surfaces and the extensive bearing assembly. Magnetic preloading requires a metallic guide surface generally a chromed steel or metal strips mounted onto a granite or ceramics base. Permanent magnets are often mounted centered between two or three air bearings. The static preload can be adjusted via the air gap between the magnet and the metal surface. In vacuum preloaded bearings the vacuum preload force is created in the center area of the bearing where a vacuum is drawn. The collar bearing around the vacuum area creates a seal preventing contaminants to be vacuumed in the bearing gap.

In this paper a study is presented to the challenges of air bearings with dynamic electromagnetic preloading. Two configurations are compared, one in which the electromagnet is provided with a flat air bearing surface (Figure 1) and one in which the electromagnet acts at the surface of a compliant membrane air bearing (Figure 2). The membrane air bearing with electromagnetic actuated membrane can also be applied with a non metallic guide surface. The analytical modeling of this configuration is further discussed in [1].

Active electro-magnets integrated in the bearing structure offers a promising solution of applying a dynamic preload with which a) running accuracy can be improved, b) the load capacity can be increased significantly and c) a near infinite bearing stiffness can be realized.

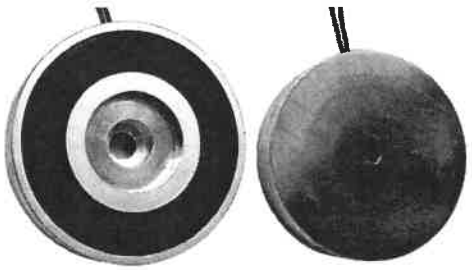

FIGURE 1. Electromagnet (left) combined with a flat air bearing surface (right). The air bearing is fed through a simple orifice which is applied in a set screw. This set screw is screwed in the center of the bearing.

FIGURE 2. Electromagnet constructed into a compliant membrane air bearing.

The flying height of the bearing shown in Figure 1 can be adjusted dynamically by varying the preload. It is studied to what extend this vertical displacement can be applied to improve running accuracy by compensating for deviations in straightness of the guide surface and for elastic distortions of the guide as a result of dynamic loading. With knowledge of the deviation of straightness and elastic response to dynamic loading running performance can be optimized by feed forward control.

A static preload improves bearing stiffness at the cost of the load capacity of the bearing. Usually up to 80% of the load capacity of a bearing is consumed in order to preload the bearing assembly. A variable preload makes it possible to compensate for additional forces and thus making the full load capacity of the bearing available for these forces.

A near infinite bearing stiffness is possible by coupling the flying height to the magnetic preload. The research is focused on the coupling of a measurable deviation of the nominal flying height to dynamic control of the magnetic preload. Important issues are the non-linearity and dynamic response of both the stiffness of the electro magnet and that of the air bearing.

HYBRID BEARING MODELLING

The bearing performance of the hybrid bearing is predicted by superposing the characteristics of the air bearing and electro magnet.

Air Bearing

Bearing stiffness is generally created by orifices, porous surfaces or groove compensation. Orifice compensation is the most widely applied in high tech applications, because of the constructive simplicity. The bearing performance can be analyzed by considering the flow resistance of the restrictor and the thin air film created between the bearing and the guide surface.

For the pure inertia flow of a compressible fluid through orifices the mass flow is equal to [2]:

$$M = C_D A \rho_0 \sqrt{\frac{2RT_0\kappa}{\kappa-1}\left[\left(\frac{p_r}{p_s}\right)^{\frac{2}{\kappa}} - \left(\frac{p_r}{p_s}\right)^{\frac{\kappa+1}{\kappa}}\right]} \qquad (1)$$

where A is the cross section area of the hole for simple orifices, C_D the coefficient of discharge and κ the ratio of specific heats. The pressure ratio p_r/p_s is limited at the lower end by the flow velocity which can only go as far as the speed of sound, for air $p_r > 0.53 p_s$.

Basic formulae for the radial flow through a long parallel film ($Re<500$ and $(r_0-R_1)/h>40$) can be written:

$$\left(\frac{p}{p_0}\right)^2 = \left(\frac{p_r}{p_a}\right)^2 - \frac{\ln(r/r_1)}{\ln(r/r_0)}\left(\left(\frac{p_r}{p_a}\right)^2 - 1\right)$$

$$F = \int_{r_1}^{r_0} 2\pi p(r)\, r dr - p_a \pi\left(r_0^2 - r_1^2\right) \qquad (2)$$

$$M = \frac{\pi h^3}{12\ln(r_0/r_1)} \frac{p_r^2 - p_a^2}{\eta RT}$$

The pressure factor β is defined as the ratio of the pressure drop over the film and the total pressure drop:

$$\beta = \frac{p_r - p_a}{p_s - p_a} \tag{3}$$

The load capacity and flow rate can now be calculated with prescribed radii of the bearing surface, properties of the gas, pressure drop over the film p_r-p_a and flying height h. The dimensions of the orifice can be calculated next, with prescribed C_D-value.

The bearing stiffness is derived from the change in flying height and load capacity as a result of an infinitesimal increase of the restrictor pressure p_r. Various configurations are analyzed in [2] and calculators of these bearing configurations are made available at www.tribology-abc.com. Figure 3 shows the calculated load capacity and stiffness of the orifice compensated circular air bearing as a function of the β-value and flying height.

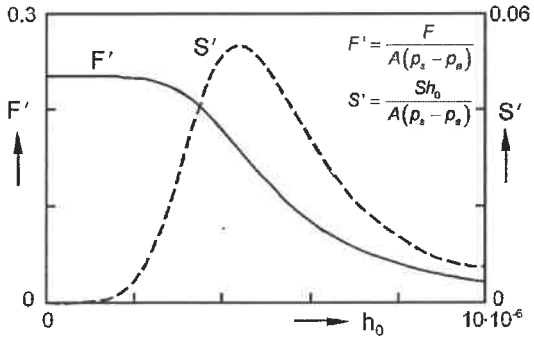

FIGURE 3. Load capacity and axial bearing stiffness of a circular orifice compensated flat air bearing.

Electromagnet

The main advantage of an electromagnet over a permanent magnet is that the magnetic field can be controlled at high frequencies. However, a continuous electric energy is required to maintain the field. A combination of a permanent magnet to supply the stationary preload and an electromagnet to compensate for dynamic loading might be an option. Since the electric energy needed to compensate for both the stationary preload and dynamic compensation was found to be very low the permanent magnet is skipped.

The magnetic force can be estimated by:

$$F = \frac{B^2 A}{2\mu_0} \qquad \mu_0 = 4\pi \cdot 10^{-7}\, H\, m^{-1} \tag{4}$$

where F [N] is the force, B [Tesla] the magnetic field, A [m^2] is the area of the pole faces, μ_o is the permeability of free space and H the field intensity. For a closed magnetic circuit can be written:

$$B = \frac{\mu N I}{L} \tag{5}$$

where μ is the permeability of the core, N is the number of turns of wire, I [A] is the current and L is the length of the magnetic circuit. Substituting (5) in (4) gives:

$$F = \frac{\mu^2 N^2 I^2 A}{2\mu_0 L^2} \tag{6}$$

A strong electromagnet requires a short magnetic circuit with large area. Most ferromagnetic materials saturate around B=1 to 2 Tesla. This occurs at a field intensity of H=787 Ampere-turn/meter. The maximum load per unit area F/A then ranges between 398 kPa (1 Tesla) and F/A=1592 kPa (2 Tesla) respectively.

Figure 4 shows the measured magnetic force of the electromagnet as a function of the air gap δ.

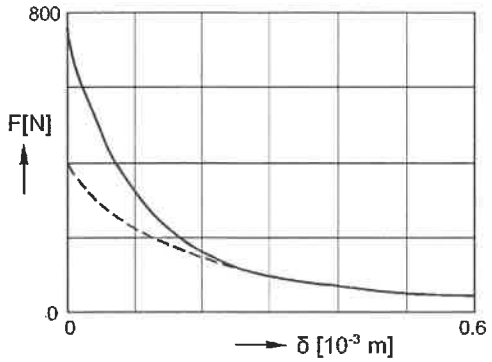

FIGURE 4. Magnetic force as a function of the air gap (90% of the nominal voltage).

The power needed (2.5 Watt) to stationary preload the air bearing was only 50% of the nominal power of the electro magnet.

Hybrid bearing system

Figure 5 shows a typical characteristic of the flying height in time as a result of a negative load step. The flying height of the orifice compensated air bearing has increased by a decreased bearing load. The slope dh/dt as a result of the load step depends on the damping in the air film.

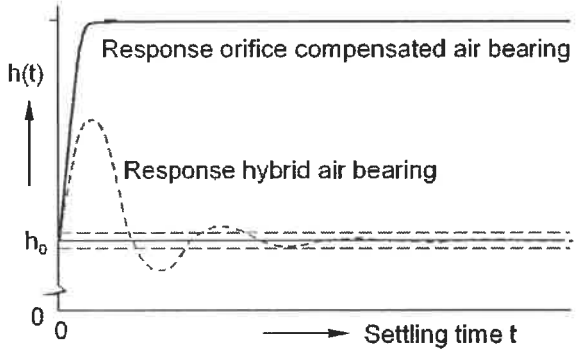

FIGURE 5. Load step response of an orifice compensated air bearing and an active controlled hybrid electromagnetic air bearing.

The recovery of the flying height in the electromagnetically controlled air bearing is obtained by adapting the electromagnetic preload. This requires a continue position measurement as input for a PID controller which determines the current through the electromagnet. The overshoot and settling time are minimized by optimal PID settings.

The stiffness of the air bearing contributes to the semi infinite stiffness realized with the help of the electromagnet. This implies the need of a restrictor. If the flying height is to be adjusted within a wide range it is preferable not to limit the flow rate by means of a restrictor. The stiffness then becomes purely dependent on the controlled magnetic field.

TEST SETUP

Figure 6 shows the actively controlled air bearing in the test setup. The flying height is measured by an inductive probe and used as input for a PID controller which is programmed in LabView. The output of the PID controller is connected to a current supply connected to the electro magnet. The bearing is loaded in the center. A load step is realized by removing a dead weight. The measured overshoot and settling time are studied for a range of PID-settings.

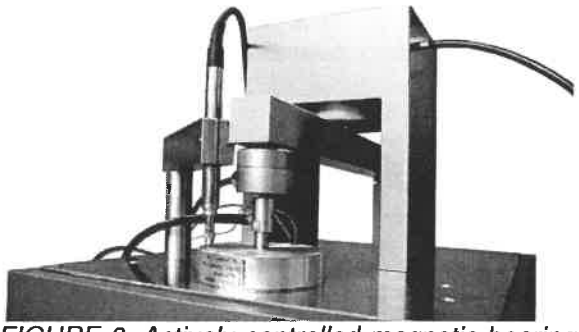

FIGURE 6. Actively controlled magnetic bearing in the test setup.

Figure 7 shows the measured overshoot and settling time as a function of the flying height and the PID-settings.

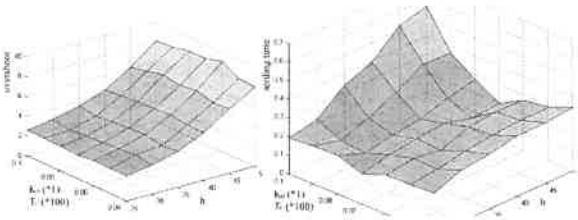

FIGURE 7. Overshoot and settling time as a function of the flying height and PID settings.

The overshoot and settling time increase with the flying height because of the lower air bearing stiffness and magnetic preload at larger flying height.

CONCLUSION

A hybrid electromagnetic air bearing has been realized. The flying height recovers after a load step and a semi infinite bearing stiffness has been realized. Further study will be focused on predictive modeling of the overshoot and settling time influenced by the PID settings, the sampling frequency of the control system and squeeze film damping of the air bearing.

ACKNOWLEDGEMENTS

Part of the research was done within the MicroNed program, subsidized by the Dutch Bsik program, a decree on the improvement of knowledge infrastructure.

REFERENCES

[1] R.A.J. van Ostayen, A. van Beek, R.H. Munnig Schmidt, "Design and Optimization of an Active Aerostatic Thrust Bearing", ASPE annual conference, October 2007.

[2] A van Beek, 2006, "Advanced Engineering Design", ISBN 90-810406-1-8, Chapter 12.

HYBRID BI-DIRECTIONAL FLEXURE JOINTS

Vincent Lee, John Ziegert
Department of Mechanical Engineering
Clemson University
Clemson, SC

INTRODUCTION

Flexures can be found in many precision machines and mechanisms, including. Micro-positioning stages, load cells, micro electromechanical systems (MEMS), and precision measuring instruments. The most typical flexure setups include notch flexures, and leaf flexures (Figure 1).

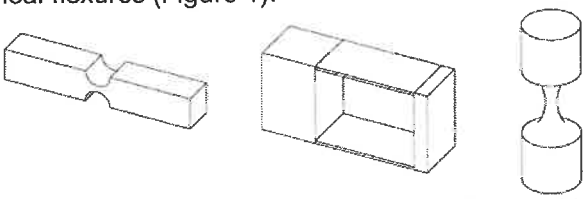

FIGURE 1: From left to right: a) Notch flexure, b) leaf flexure, c) 2 degree of freedom spherical notch flexure.

Flexural elements provide a means to allow displacement without the need for sliding mechanical interfaces such as sliding contacts or pinned connections. This is accomplished by connecting two rigid members using a thin elastic member that flexes at predefined locations or in a predictable shape, thus creating an elastic hinge [1]. The dimensions of the flexure joint determine the kinematic characteristics of the flexure, including: range of motion, in plane stiffness, out of plane stiffness, axial stiffness, pivot point location, and degrees of freedom. A typical goal of a flexure joint is to have the stiffness very high in all degrees-of-freedom except those that are intended to provide motion.

Notch and leaf-type flexures are typically intended to replace pin-type joints, providing 1 degree-of-freedom of relative motion between the rigid members. However, there are numerous applications where 2-DOF flexure joints are desirable, including micro electromechanical systems (MEMS), mirror positioning, optical mounts, multi-dof motion stages, metrology instruments, and microscopy [2, 3]. It is possible to connect 2 1-DOF flexures in series to create a 2-DOF joint (Figure 2). However, this joint does not provide intersecting axes of rotation for the 2 motions and is substantially more complex to manufacture and package since care must be taken to insure that the two notches can indeed be cut when fixtured in the cutting machine. Spherical notch flexures (FIGURE 1c) resemble thin wires connecting the rigid bodies and provide co-located 2-DOF motion. However, the very thin waisted joint has poor axial strength [3] and relatively low torsional stiffness

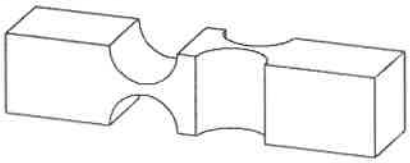

FIGURE 2: 2 DOF cross notch flexure example, axes of rotation are arranged orthogonal to each other

Two recent novel designs for multiple DOF flexural joints that attempt to address some of these issues are braided steel rope flexures, and the toroidal flexure [3, 4]. In these designs separate flexural elements are assembled between the two rigid members with the goal of providing a 2-DOF joint that is axially strong & stiff, has high out of plane stiffness, and is capable of a large range of motion. A drawback with these assembled designs is that they are not monolithic and it may be difficult to insure proper joint locations during assembly, which may affect the mechanism kinematics.

HYBRID BI-DIRECTIONAL FLEXURE JOINT

This report describes a novel 2-DOF flexure joint design that we have dubbed the Hybrid Bi-directional Flexure Joint (HBFJ) (FIGURE 3).. The HBFJ consists of two curved thin section members that form an annulus. As shown in Figure 4, the curved members that form the annulus can deform to permit rotation about both the Y and Z axes. However, this open structure is also very compliant in the X-direction which is not generally desirable. To overcome this, the annular cavity is filled with an elastomeric material. This is easily accomplished using 2-part liquid urethane compounds that fill the

cavity and cure in place. The elastomer does not significantly increase the bending stiffness of the joint about the Y and Z axes due to the low flexural modulus of the material; but does drastically increase the axial stiffness of the system due to the much higher bulk modulus of the material. Due to the planar nature of the HBJF, it can be easily manufactured monolithically using traditional manufacturing techniques such as wire electro discharge machining (WEDM), high speed milling, and rapid prototyping.

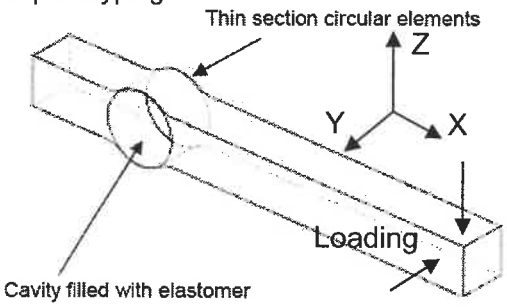

FIGURE 3: Hybrid bi-direction flexure joint

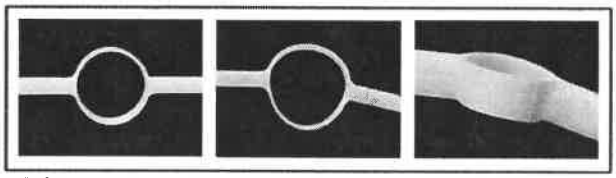

FIGURE 4: Prototype HBFJ constructed of ABS via rapid prototyping (cavity unfilled).

The geometry of the HBFJ is defined by 6 parameters, as illustrated in the following figure (FIGURE 5).

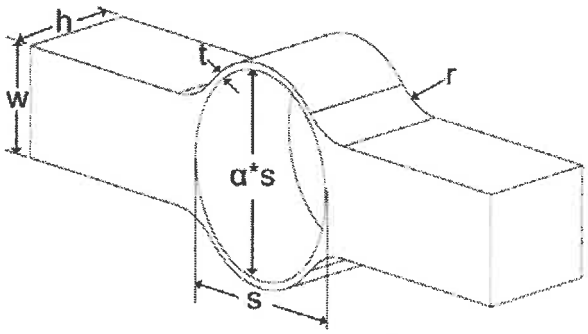

FIGURE 5: Parameters defining HBFJ

FEA MODELING OF THE *HBFJ*

In designing the HBFJ, finite element analysis (FEA) was used to determine stiffness, range of motion and stress distributions within the joint, and how utilizing different geometry and materials affect these properties. Here, the annulus is assumed to be elliptical in shape with major and minor axes *S* and *αS*. The rigid elements have height and width, *h* and *w*. The wall thickness of the annulus is *t*, and the fillet radius is *r*. A set of computational experiments was performed to show the effect of the geometric parameters on the stiffness, deflection, and load carrying properties of the HBFJ. For the FEA analyses, the structure was fixed at one end and force was applied at a distance 2.5S from the center of the joint. Figure 6 shows the free body diagram of the structural model, and a typical FEA result.

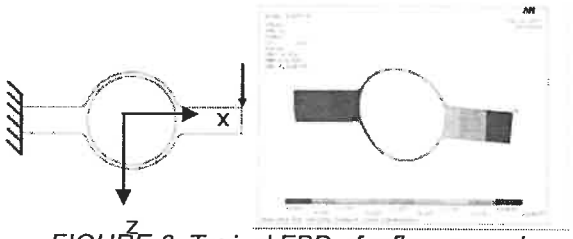

FIGURE 6: Typical FBD of a flexure and corresponding FEA results

STIFFNESS PROPERTIES OF THE *HBFJ*

The effect of joint geometry on stiffness was studied computationally by holding the material properties fixed and varying the geometric parameters shown above. A unit force was applied in the X, Y, and Z directions at a point 2.5S from the center of the annulus, and the resulting displacements were recorded. Figure 7 shows how the stiffness in the horizontal (Y), vertical (Z), and axial (X) directions are affected by variations in the parameters (Note differing scales Kx vs. Ky and Kz) . It can be seen that it is possible to obtain equal stiffness in both Y and Z directions by adjusting parameter *h* , and also to obtain axial stiffness 1 to 2 orders of magnitude higher than the transverse stiffnesses.

DEFLECTION PROPERTIES OF THE *HBFJ*

One desirable property of the HBFJ is that it can be designed to allow larger ranges of motion than notch-type flexures of the same size without sacrificing axial stiffness or load capacity. This is due to the extended length of the curved thin members which define the annulus, and function much like the leaves in a leaf-type flexure. However, when the joint is loaded axially it is not subject to the same buckling failure mode seen in the leaf flexure because the members are already curved and the embedded elastomer absorbs the load.

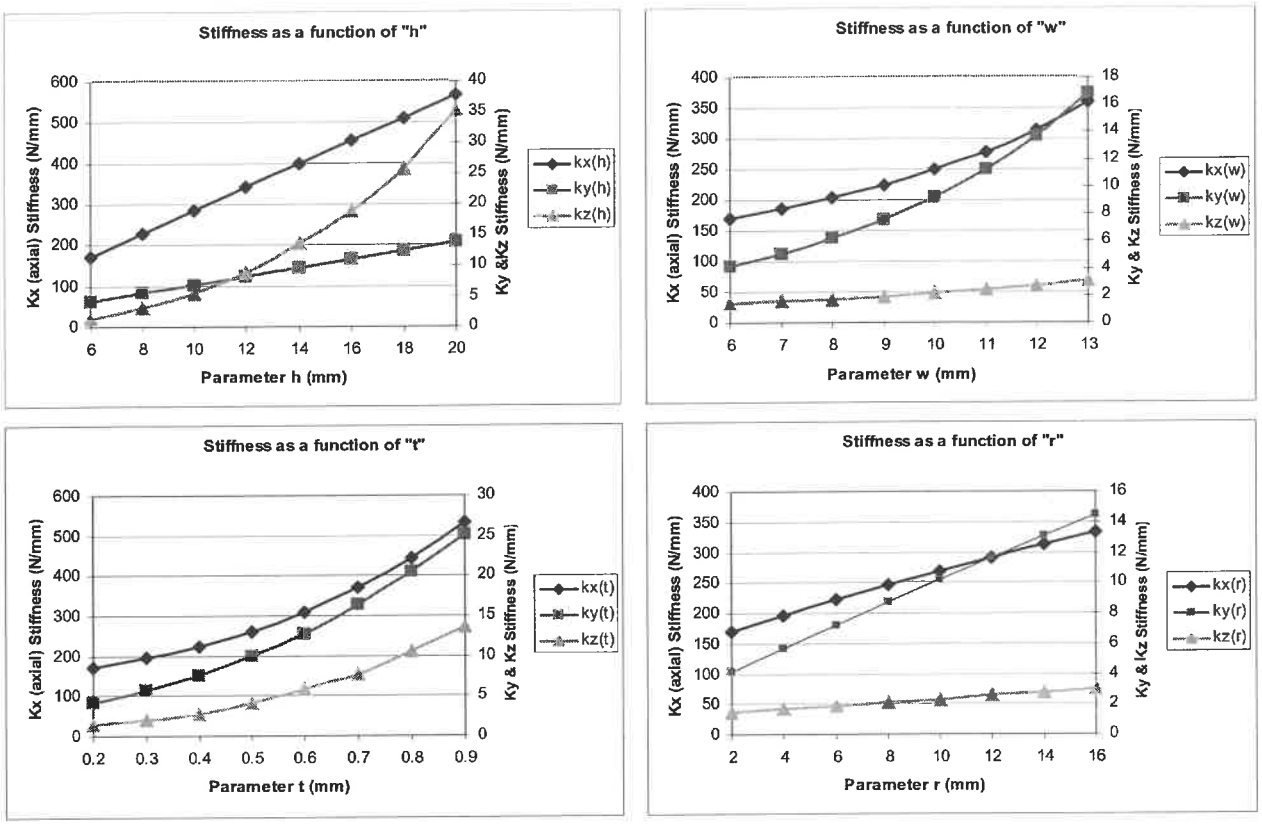

FIGURE 7: Stiffness change as a function of four different geometric parameters. Flexure material Aluminum E=70GPa, v=0.33; filler material Urethane E=30MPa, v=0.45

COMPARISON OF FLEXURE DESIGNS

The HBFJ is compared to more traditional notch-type and spherical notch-type flexures by creating designs which utilize the same material, the same minimum material thickness, and the same amount of axial space (see Figure 8). The stiffness, deflection, and load capacity properties are compared in Table 1. The range of motion for each design was computed using FEA by loading the flexures until the maximum von-Mises stress reached a target value of 200 MPa. It can be seen that it is possible to design a HBFJ of the same overall size as more traditional notch-type flexures, and with equivalent stiffness properties; but which allows significantly larger range of motion, and has higher axial load capacity.

Table 1. Comparison of flexure designs.

	Range (mm)		Stiffness (N/mm)			Max Axial Load(N)
	Y	Z	Kx	Ky	Kz	Fx
HBFJ	0.83	0.48	117	0.9	2.6	22
Circular Notch	0.48	N/A	4.5e3	2.4	N/A	800
Spherical Notch	0.77	0.77	443	0.01	0.01	3.5

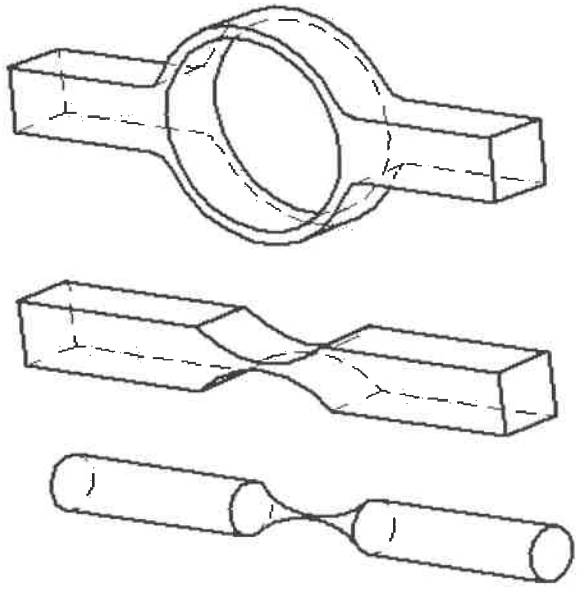

FIGURE 8. Flexure designs with comparable physical dimensions.

PHYSICAL TESTING OF THE HBFJ

Based on the FEA results, several HBFJ designs were fabricated and the stiffnesses were measured. The flexures were fabricated in ABS plastic via rapid prototyping, and the cavities were filled with a 2-part urethane. Three different grades of urethane (Shore Durometer 40, 60, and 80) were used to test their effectiveness in supporting axial loads and their effect on the bending stiffness of the joint. Also, 10 identical flexures with different heights "*h*" were tested to observe the effect of this variable on stiffness in the Y and Z directions.

Stiffness measurements were performed by clamping one end of the joint in a vise and hanging a known weight on the other, and measuring the resulting deflection with a height guage.. Figure 9 shows a comparison of the stiffness predicted by the FEA analysis, and the measured stiffness.

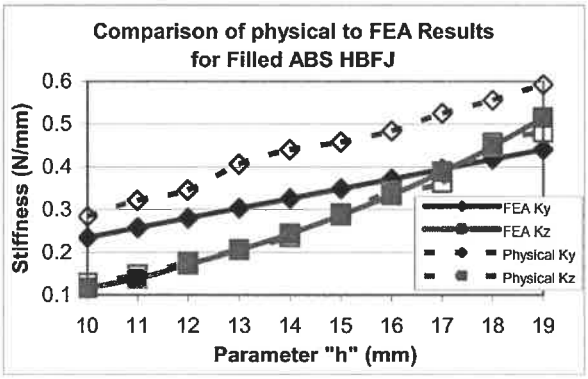

FIGURE 9. Comparison of experimental and FEA stiffness results.

APPLICATIONS OF THE HBFJ: 3-DOF FLEXURE STAGE

It is common to create planar motion stages comprised entirely of flexure joints. These typically take the form of flexural parallelogram mechanisms in a series configuration. Figure 10 shows a prototype stage with all HBFJ flexures. Because the HBFJ permits 2-DOF motion, this stage is capable of translating in 3-DOF while still capable of being fabricated as a planar structure.

CONCLUSIONS

This report describes a novel flexural joint design which can accommodate 2 degrees of freedom of motion. The joint consists of pairs of curved leaf-type elements that enclose an annulus. To increase axial stiffness of the joint,

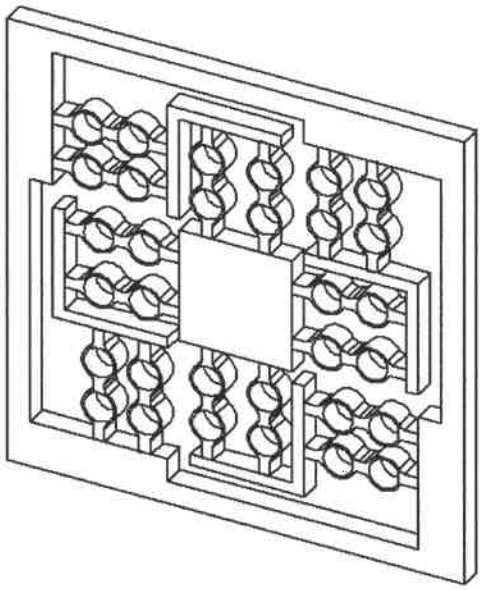

FIGURE 10. Proposed 3-DOF flexure stage.

the annulus is filled with an elastomeric material that allows relatively low stiffness bending motions due to the low flexural stiffness of the material; while providing relatively higher axial stiffness due to the large compression area and rigid constraint from the leaf elements. FEA parameter studies show that it is possible to design HBFJ with low bending stiffness in the transverse DOF, combined with high axial stiffness. The HBFJ can provide larger range of motion than spherical notch flexures, combined with much larger axial load capacity.

REFERENCES

[1] L.L Howell, "Compliant Mechanisms", John Wiley & Sons 2001 New York

[2] S.T. Smith & D.G. Chetwynd, "Foundations of Ultraprecision Mechanism Design", Overseas Publishers Association, Amsterdam, Netherlands. 1992 Pg. 95-130

[3] Noll, Tino. "Three Axis Rotational Flexure Joints of High Axial Stiffness", Precision Engineering, 2002

[4] James F. Cuttino, et Al., "Design and Development of a Toroidal Flexure for Extended Motion Applications", Precision Engineering, V.29 2005 Pg. 135-145

ACKNOWLEDGEMENTS

This work was supported in part by an endowment from the Timken Corporation.

MODEL-BASED SUBNANO-POSITIONING CONTROL

J. van Hulzen[1,2], J. van Eijk[1], P.M.J. Van den Hof[2]
[1]Precision and Microsystems Engineering Department, Mechatronics
[2]Delft Center for Systems and Control
Delft University of Technology, Delft, The Netherlands

INTRODUCTION

A common tool for inspection and manipulation in the nano and sub-nanometer range is the scanning probe microscope (SPM). Historically probe positioning is controlled in an open loop manner using piezo electric actuators (PEA). While capable of rapid scanning using fixed pre-determined trajectories there are limitations to achievable performance. Using feedback control it is possible to address problems such as thermal drift, piezo creep and non linear behavior. Here we discuss the dynamics of a stage of an existing STM prototype [2]. In the design the properties of the piezo actuator and the effective load have been balanced to improve performance. In this paper we will access this technique and discuss its application in this example.

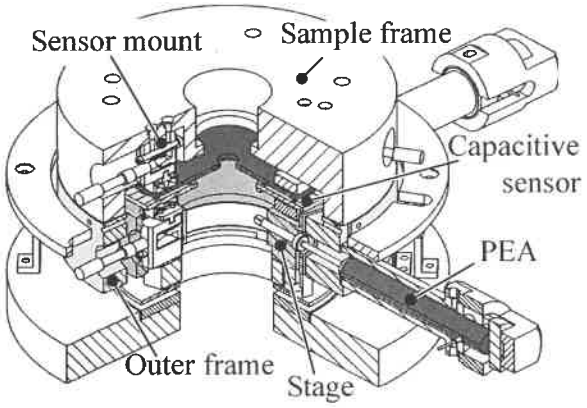

FIGURE 1. Overview of STM stage prototype.

OVERVIEW OF DESIGN

The design shown in Figure 1 features a stage capable of moving a STM probe over an area of 50x50 μm. To enable high resolution imaging a positioning resolution of 50 pm and an accuracy of 30 pm ($\pm$15 pm) over a range of 50x50 nm was required. The positioning stage shown in Figure 2 is suspended on three points using folded plate springs. The suspension restricts vertical movement and rotations around the axis of movement. In-plane rotation is further restricted using a rotation stop. In-plane motion is controlled by two piezo electric actuators (PEA), driving the stage through flexible struts. The position of the stage is measured using a large 6-DOF capacitive sensor. Distance and alignment between the two sensor plates is controlled using six adjustable flexure hinges. On top of these flexure hinges is a support structure in the form of a ring. To minimize thermal drift between sensor and stage an additional suspension between support ring and sensor plate is included. This suspension consists of a flexible (viton) ring and keeps the thermal centers of stage and sensor plate aligned using shear stress pre-load [5].

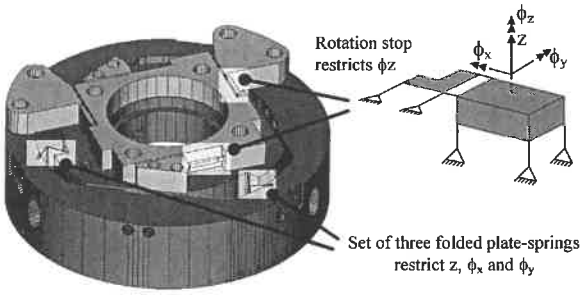

FIGURE 2. suspension of stage in frame with the rotation stop (bottom view).

BALANCING ACTUATOR AND LOAD

In devices requiring sub nanometer precision, sensor bandwidth is often an important bottleneck. In piezo actuated systems this can even lead to stability problems. These problems are caused by poorly damped high frequent resonant modes associated with a PEA. A possible solution to this problem is balancing the mechanical properties of load and actuator. The goal is to shift the closed loop resonant modes towards the anti resonances associated with the PEA [1]. An effective way of doing this is increasing the mass of the load and to a lesser extend the damping.

Model of actuator and load

In [1] a model of the mechanical behavior of a PEA has been derived. The PEA is modeled as a series connection of mass spring damper sys-

tems. The transfer function of the PEA is

$$y(s) = \frac{N_p(s)}{D_p(s)} \left(F_p(s) - F_s(s)\right) \quad (1)$$

$$N_p(s) = \prod_{i=1}^{\infty} \frac{m_p}{i^2\pi^2} + c_p s + k_p \quad (2)$$

$$D_p(s) = \prod_{i=1}^{\infty} \frac{4m_p}{(2i-1)^2\pi^2} + c_p s + k_p \quad (3)$$

Where m_p is the mass of the PEA and c_p and k_p its damping and stiffness. The mechanical system shown in figure 3 in which the PEA is embedded can be modeled as

$$y(s) = \frac{N_s(s)}{D_s(s)} F_s(s) \quad (4)$$

$$N_s = (m_1 + m_2)\, s^2 + c_1 s + k_1 \quad (5)$$

$$D_s = m_1 m_2 s^4 + (m_1 c_2 + m_2(c_1 + c_2))\, s^3 + (m_1 k_2 + m_2(k_1 + k_2) + c_1 c_2)\, s^2 + (c_2 k_1 + c_1 k_2)\, s + k_1 k_2 \quad (6)$$

Here we have frame stiffness k_1, frame mass m_1 and a pre-load spring k_2 in parallel with the PEA. The mass of the load is represented as m_2. Damping is introduced using c_1 and c_2. Combining system and PEA we get

$$y(s) = \frac{N_p(s) N_s(s)}{N_s(s) D_p(s) + N_p(s) D_s(s)} F_p \quad (7)$$

From this last expression we can conclude that the closed loop zeros associated with the PEA are invariant under feedback. In contrast, for increasing load the poles of the closed loop system shift towards the zeros. Because a PEA has low mass and high stiffness, the most effective parameter for manipulating the closed loop poles is the mass of the load. If we increase the loading of the PEA, the resonant modes will shift to lower frequencies. Under high load the high resonant peaks will decrease to such an extend that cancelations occurs and a second order system remains. The first peak of the PEA will shift to a lower frequency and has to be dealt with using additional damping.

The application of load balancing

The actuator used in this example is fairly large and has a mass m_p of 40 gr, a stiffness k_p of $1{\cdot}10^7 N/m$ and an estimated damping of c_p 3 kg/s. In Figure 4 the result of the mechanical feedback is shown. The frame mass m_1 is 3.44 kg, the stage mass m_2 is 470 gr and the frame stiffness

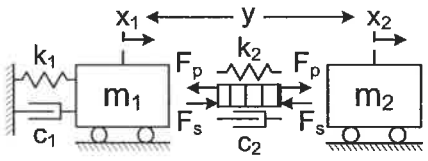

FIGURE 3. PEA in positioning system with frame m_1, stage m_2, frame stiffness/damping k_1/c_1, and pre-load spring and damping k_2/c_2

k_1 is $3.8 \cdot 10^5 N/m$ The first resonant mode of the unloaded piezo appears at 4 kHz and shifts to 760 Hz, the second from 12 kHz to 8 kHz. The low frequent resonant mode associated with the mechanical system shifts towards the zero representing the total mass oscillating against the frame stiffness and is canceled. This is due to the fact that $k_p + k_2$ is much stiffer than k_1 and that $c_1 \ll k_1$. To improve damping of the lowest flexible mode of the PEA we can include additional damping between frame and stage in the form of an eddy current damper. This was not implemented, but the blue dashed line shows an example of this for c_2 equal to 3 kg/s. With a high

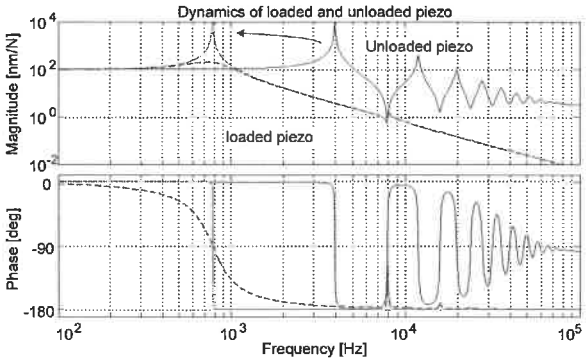

FIGURE 4. The dynamics of an unloaded piezo are canceled by increasing the mass of m_2 (solid line). Additional damping for the first resonant mode can be provided using c_2 (dashed line).

stage mass we will have canceled most of the dynamics of the PEA. We are however left with a load that is quite high compared to the stiffness of the supporting structure.

EXPERIMENTAL VERIFICATION

The Frequency response function was determined using a laser vibrometer. Displacement was measured using differential velocity measurement between frame and stage and filtering the results. The measurement setup was isolated from seismic disturbances using an air-suspended vibration isolation frame.

Sensor

Displacements are measured using a capacitive sensor in combination with a switching synchronous detector. The device used has a sensitivity of $36V/pF$. The capacitive sensor consist of two glass plates with a thin layer of gold in which the pattern shown in figure 5 is etched. The dimensions of the capacitive plates are a tradeoff between sensor range and accuracy on one hand and dimensions and mass on the other. The capacitor is placed in a bridge configuration and an AC voltage is applied on both sending electrodes on the upper (stationary) plate. The voltages are phase shifted by 180 degrees and a net current is generated if the lower plate is moved out of alignment. The amplitude of this current is measured. To enable sub-nanometer precision measurements the dimensions of the plates were chosen as large as possible (10x10 cm). With a pattern length L of 38 cm and a plate distance d of 200 μm we have a sensitivity of $\Delta C/\Delta x = 2\epsilon_r\epsilon_0 L/d$. In air or vacuum $\epsilon_r = 1$ and $\epsilon_0 = 8.8541 \cdot 10^{-12}$ giving a sensitivity of 33.6 nF/m. And thus the sensitivity of the measurement system (sensor+detector) is 1 $\mu m/V$.

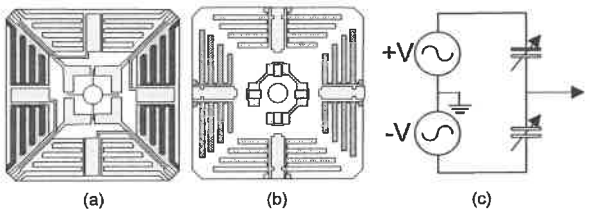

FIGURE 5. Six degrees of freedom capacitive sensor with sending electrodes (a), receiving electrode (b), and bridge circuit (c).

Experimental verification of accuracy and bandwidth of the capacitive sensor

The accuracy of the sensor was verified using a frequency analyzer and a laser vibrometer. The sensitivity of the capacitive sensor was determined to be 5.3 $\mu m/V$. To verify the relation between the accuracy and bandwidth the cumulative amplitude spectral density of the sensor noise was determined. The results are shown in Figure 6. The upper curve in the graph represents the capacitor noise with the input of the piezo amplifier shorted. The lower curve represents the achievable performance with the synchronous detector using two reference capacitors. The latter shows that to achieve subnano precision one has to improve the sensitivity of the sensor by a factor of 35. This can be achieved by bringing the capacitive plates closer together or by re-scaling the pattern. Form the upper graph it is clear that the readout of the sensor is to noisy at present. To improve signal to noise ratio, a better shielding of the sensor elements could be applied. Furthermore, improving stability and damping of the sensor may be required.

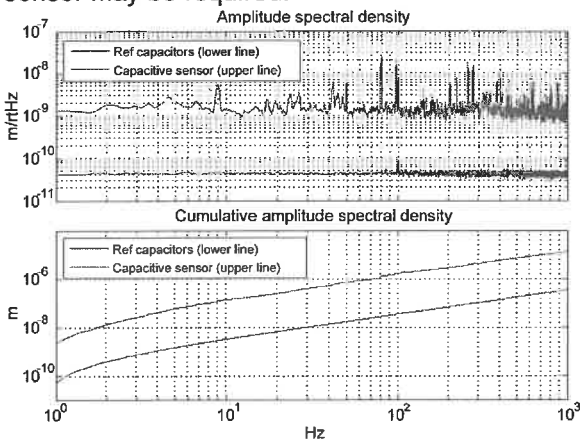

FIGURE 6. Noise level of sensor and reference capacitor. The readout of the reference capacitor measurement was scaled to m using the determined sensor sensitivity of 5.3 $\mu m/V$.

FRF measurements of stage dynamics

The FRF measurement show in figure 7 shows a lot of resonances in the lower frequency region (0-300 HZ) The first resonant modes at 138 and 155 Hz are associated with the entire structure vibrating against the flexure mount connecting frame and base. The modes around 200 Hz are associated with the rotation stop. The second pair of resonances at 294 and 308 Hz and anti resonance at 336 Hz are the stage vibrating against the frame. According to finite element studies [4] the flexible modes around 400 Hz are bending modes of the piezo and piezo tube. Finally the resonant mode at 670 Hz is caused by a rotation of the stage, probably due to imperfections of the sensor support structure. Generally the springs connecting the components of the STM are one to two orders of magnitude stiffer in vertical direction than in lateral direction. The stage is also designed to have rotation symmetry around the vertical axis. This in combination with the relatively large radius at which the springs are attached prevents rotations. Resonant modes associated with rotations are above 600 Hz. Resonant modes in the vertical direction are at 700 Hz and higher and do not play a significant role in controlling the scan stage in lateral direction.

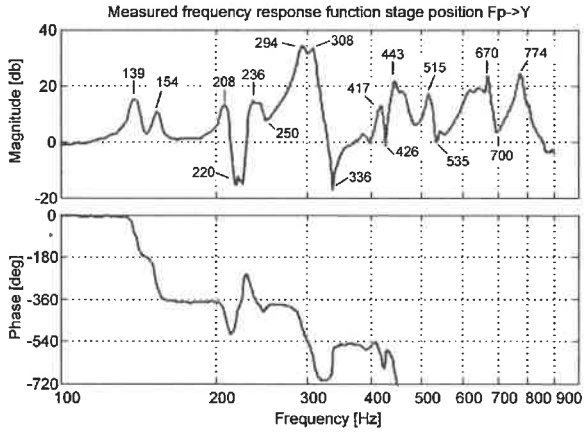

FIGURE 7. FRF measurement of piezo-stage transfer function $F_p \rightarrow y$.

CONCLUDING REMARKS

- Reducing the influence of high frequent actuator dynamics by load balancing requires an increased stage mass. This in turn requires a stiff frame and guidance. In this case the supporting frame is not stiff enough and as a result the main bottleneck is not the dynamics of the actuator but the flexible modes of the supporting structure. Because of this the bandwidth is limited to about 100 Hz.

- The low frequent dynamics of the stage and the supporting frame make it difficult to focus on the actuator dynamics. Because of this, the load balancing principle could not be verified using this setup.

- The device is very complex with many components. Reducing this complexity would reduce the level of dynamical interaction and would make the control problem more tractable.

- Judging from the FRF shown in Figure 7 we can expect that a control design will have to deal with a rapid decrease in phase while the gain remains large. In a feedback controlled system this will lead to stability problems. In order to increase achievable bandwidth we need to stiffen the frame mount by at least two orders of magnitude. In this way the first two modes at 139 and 154 Hz will shift to significant higher frequencies. In addition to this we need to improve damping of the elements having resonances between 200 and 300 Hz. With these two measures the achievable bandwidth will be improved by a factor of 3.

- Further improvements can be made by increasing the stiffness of the sensor suspension and lowering the mass of the stage, the sensor support and the sensor plate. As an alternative to this we could use three single degree of freedom capacitive sensors mounted in the frame inline with the piezo drive. This would improve vertical symmetry and reduces the mass being moved by 40%.

ACKNOWLEDGMENTS

I would like to thank dr.ir. G. Schitter for his comments and input.

REFERENCES

[1] H. J. M. T. A. Adriaens, W. L. de Koning, and R. Banning, Modeling piezoelectric actuators, IEEE/ASME Trans. Mechatron., vol. 5, no. 4, pp. 331 to 341, Dec. 2000.

[2] H. J. M. T. A. Adriaens, Modeling and Control of a Piezo-Actuated Positioning Mechanism, PhD Thesis, TU-Delft, ISBN 90-73235-68-5

[3] P.T.M. Giesen Drift arm ontwerpen - Dynamic calculations, TNO-report HOI-RPT-000009, TNO Institute of Applied Physics, Feb 2000

[4] C. Gielens FE-Analysis on a STM Stage Model to determin the Dynamic Characteristics of the System, Document 991113-CG-CR-TU-Delft, Systeem Ontwikkeling & Onderhoud, oct-1999

[5] M.P. Koster, Constructieprincipes voor het nauwkeurig bewegen en positioneren, (in dutch), Uitgeverij Universiteit Twente, 1996

A HIGH-SPEED AIR BEARING SPINDLE

Guido M.J. Delhaes[1], A. van Beek[1], R.A.J. van Ostayen[1], R.H. Munnig Schmidt[1]
[1]Research Group Mechatronics
Department of Precision and Microsystems Engineering
Faculty of Mechanical, Maritime and Materials Engineering
Delft University of Technology
Delft, the Netherlands

ABSTRACT
Spindles for micro cutting are characterised by high rotational speeds. An electric motor or an impulse air turbine is commonly used to drive spindles for micro cutting. In this paper a viscous turbine is proposed to drive the spindle. To determine the dimensions of the rotor a parameter study is carried out to achieve a maximum torque. The boundary conditions for the optimisation are a laminar and subsonic flow. The high-speed spindle is supported by aerodynamic journal bearings. To proof the concept of the viscous turbine a test-rig is designed, which is able to reach 500,000 rpm. For this working point the resonance frequencies are calculated.

INTRODUCTION
In robotics, the medical industry and many other fields there is a growing need for small parts with a complex 3D geometry. The materials used for these parts have specific properties and are complicated to manufacture. Conventionally, these parts are fabricated by cutting techniques. When maintaining conventional cutting speeds of at least 2 m/s and downscaling the tool tip to a diameter of 0.1 mm the rotational speed of the rotor must exceed 380,000 rpm. This is the reason that micro cutting is characterised by high rotational speeds. These speeds are commonly obtained by electric motors or impulse air turbines. The high-speed spindle discussed in this paper is driven by a viscous turbine and supported by aerodynamic bearings. The maximum attainable torque of the viscous turbine is very limited. Therefore, a parameter study is carried out to determine the maximum torque to be obtained. The slim rotor supported by air bearings with a relative small stiffness has lower resonance frequencies than the rotation frequency and as a consequence the spindle has to pass several critical speeds during start-up. With an analytical model the resonance frequencies of the proposed design are calculated.

NOMENCLATURE

h	film thickness [m]
R	radius of the rotor [m]
ncell	number of cells
L	total length of one cell [m] ($2\pi R$ / ncell)
_	ratio length pocket / length cell
1/_	ratio film thickness / pocket height
_	ratio width of the cell / radius rotor
U	velocity of the rotor surface [m/s]
q	air flow per width in the turbine [m^2/s]
p_{sup}	supply pressure [Pa]
p_{amb}	ambient pressure [Pa]
_p	$p_{sup} - p_{amb}$ [Pa]
_	viscosity of air [Pa s]
_	density of air [kg/m^3]
_	attitude angle [rad]
W	width of the journal air bearing [m]
_	rotational speed of the rotor [rad/s]

VISCOUS TURBINE MODELLING
The traction force of the viscous turbine is obtained by the shear stress of a laminar airflow along the surface of the rotor. The airflow is realized by inlets and outlets between the rotor and the housing. From one inlet air flows mainly across the pocket but also some air flows across the ridge. A combination of a pocket and a ridge is called a cell. Figure 1 shows the cross section of one of the cells created along the shaft surface.

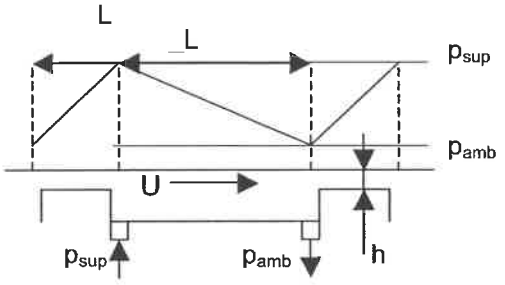

FIGURE 1. Sketch of the working principle of the viscous turbine

The pressure distribution in the pocket and over the ridge is assumed to be linear in the analytical model. The total airflow from the supply q is equal to the sum of the air flow across the ridge and in the pocket. These are calculated using the one dimensional Reynolds equation valid for incompressible mediums (1) and laminar flows.

$$q = q_{pocket} + q_{ridge}$$

$$q = \frac{h^3}{12\eta\beta^3}\frac{\Delta p}{\alpha L} + \frac{Uh}{2\beta} + \frac{h^3}{12\eta}\frac{\Delta p}{(1-\alpha)L} - \frac{Uh}{2} \quad (1)$$

The average of the traction is calculated with equation (2).

$$\tau = \tau_{pocket} + \tau_{ridge}$$

$$\tau = \alpha\left(\frac{h}{2\beta}\frac{\Delta p}{\alpha L} - \frac{\beta\eta U}{h}\right) + (1-\alpha)\left(-\frac{h}{2}\frac{\Delta p}{(1-\alpha)L} - \frac{\eta U}{h}\right)$$

$$\tau = \left(\frac{1}{\beta} - 1\right)\frac{h}{2}\frac{\Delta p}{L} - (\alpha\beta + 1 - \alpha)\frac{\eta U}{h} \quad (2)$$

The Reynolds number across the pocket and the ridge are calculated following equation (3) and (4) respectively.

$$\mathrm{Re}_{pocket} = \frac{\rho q_{pocket}}{\eta} \quad (3)$$

$$\mathrm{Re}_{ridge} = \frac{\rho q_{ridge}}{\eta} \quad (4)$$

In case the Reynolds number is less than 1000, the flow is assumed to be laminar (Re<1000).

PARAMETER STUDY VISCOUS TURBINE

A parameter study is carried out to determine the dimensions of a cell that results in the maximum average shear stress on the rotor. Two boundary condition applied in the analytical model are 1) Reynolds number less than 1000 and 2) the maximum absolute velocity below the speed of sound.

The optimisation was carried out for a configuration with 3 cells, a film thickness (h) of 10 _m and a _ of 1/3. The results are listed in table 1.

TABLE 1. Optimum geometry properties for maximum torque

Parameter	Optimum value
_	0.96
R	4.5 mm
_p	2.2 bar

The influence of the ratio of the pocket length and the total cell length (_) is small on the torque performance. Out of construction point of view _ is taken 0.9. Figure 2 shows the effect of the pocket depth where _=0.9 and _ = 25. To reach 500,000 rpm _ needs to be 1/3.

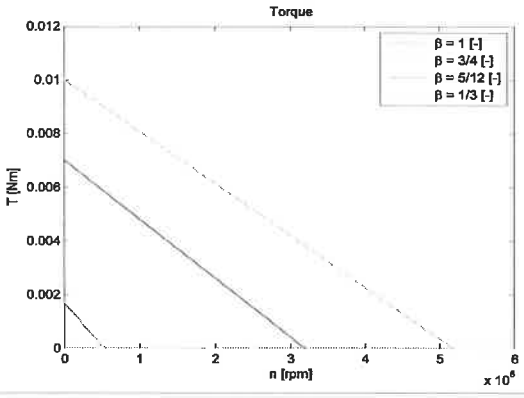

FIGURE 2. Torque of the turbine versus the rotational speed for different pocket depths

To investigate whether the assumption of incompressibility by a rotational speed of 500,000 rpm is still valid, a FEM analysis is carried out. The compressible Reynolds equation was used to calculate the pressure distribution for a turbine running 500,000 rpm and with a pressure difference (_p) of 2.2 bar. The pressure distribution is presented in figure 3 and shows an almost linear trend.

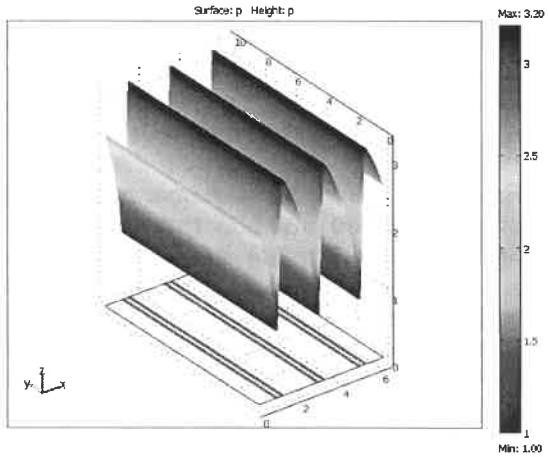

FIGURE 3. Pressure distribution of a viscous turbine running 500,000 rpm with compressibility

VISCOUS TURBINE TEST-RIG DESIGN

To proof the concept a prototype of the viscous turbine was designed with the dimensions derived from the optimisation. The housing is fabricated out of one piece. To study the effect of the pocket depth three compliant mechanisms are constructed in the housing. Screws between

the housing and the compliant mechanisms enable adjusting the depth of each individual pocket. In figure 4 the housing with the compliant mechanisms is shown.

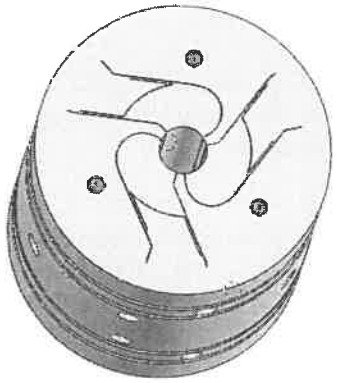

FIGURE 4. Drawing of the housing of the viscous turbine with the three compliant mechanisms

At the top and bottom of the turbine aerodynamic journal bearings are placed to support the rotor in radial direction. In figure 5 an overall picture is shown.

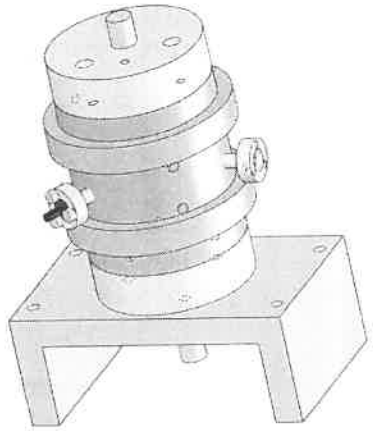

FIGURE 5. Overall figure of the viscous turbine test-rig

On top of the radial journal bearing a hybrid magnetic/air thrust bearing is placed. This bearing has to support only the weight of the rotor. The axial bearing is not shown in figure 5.

AIR BEARINGS

As mentioned above the rotor is supported in radial direction by aerodynamic journal bearings. The characteristics of these journal bearings are dependent on the rotational velocity. Not only the stiffness but also the attitude angle of an aerodynamic journal bearing changes with the rotational speed. The angle between the load vector and the displacement vector defined as the attitude angle (_) is depicted in figure 6.

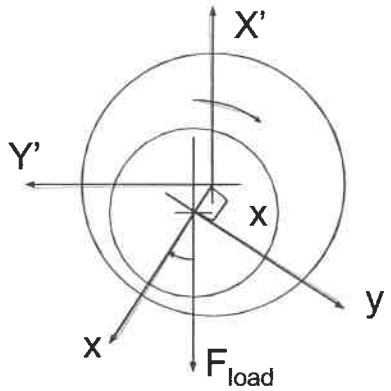

FIGURE 6. Definition of attitude angle (_)

The attitude angle is 90° for aerodynamic plain bearings with concentric shaft position running at low velocity. For an infinite rotational speed this angle is 0°. In figure 7 the attitude angle versus the angular velocity is plotted for an aerodynamic plain journal bearing with a film thickness h of 10 _m, a radius R of 4.5 mm and a W/R ratio of 2. The stiffness has a coupling term caused by the attitude angle (_). The stiffness is defined following (5) and (6).

$$K_{xx} = \frac{F_{load}}{\Delta x}\cos(\kappa) = K\cos(\kappa) \qquad (5)$$

$$K_{xy} = \frac{F_{load}}{\Delta x}\sin(\kappa) = K\sin(\kappa) \qquad (6)$$

K is the construction stiffness, which is plotted versus the angular velocity in figure 8.

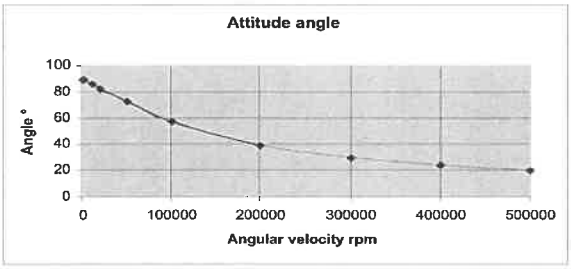

FIGURE 7. Attitude angle _ versus the angular velocity

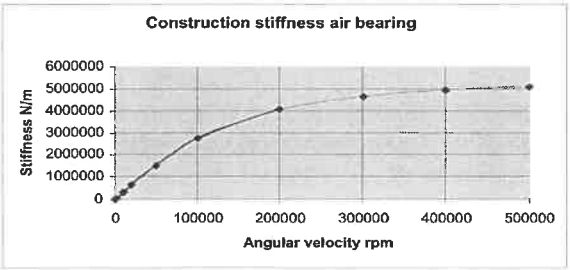

FIGURE 8. Construction stiffness K versus the angular velocity

RIGID ROTOR DYNAMIC MODEL

The dynamic behaviour of the viscous turbine with bearings has been investigated. The rotor is modelled as a rigid cylinder supported by air bearings. The bearing stiffness is represented by springs. A sketch of the model is presented in figure 9.

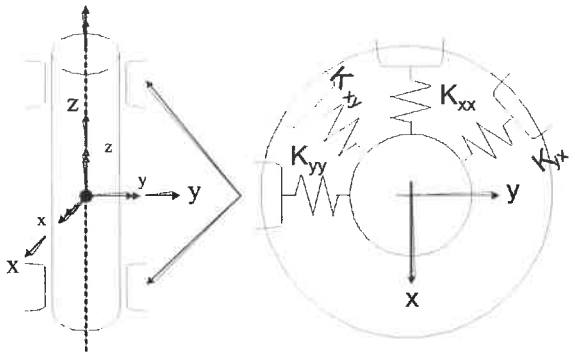

FIGURE 9. The model of the spindle

The resonance frequencies of this system are dependent on the stiffness of the bearings and the rotational speed of the rotor via the gyroscopic effect. The stiffness of the bearing varies with the rotational frequency. The resonance frequencies are calculated for the rotor of the test rig running at 500,000 rpm and supported by the aerodynamic bearings. The results are listed in table 2 and a Bode plot is presented in figure 10.

TABLE 2. Resonance frequencies

	x10^5 rad/s
_1	0.07
_2	0.11
_3	0.75
_4	1.10

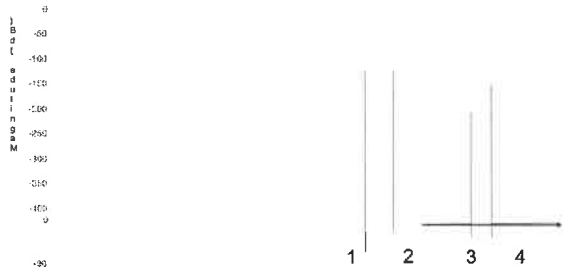

FIGURE 10. The Bode plot of the rotor running at 500,000 rpm and supported by air bearings

CONCLUSIONS

A viscous turbine is proposed and the delivered torque of the turbine is optimised to reach 500,000 rpm. With the results of the optimisation a test-rig is designed to proof the concept. The resonance frequencies of the high-speed air bearing spindle are determined with a rigid rotor model. The rotor runs with 0.5 x 10^5 rad/s and has to cross 2 resonance frequencies.

ACKNOWLEDGEMENT

This research is carried out within the MircoNed programme, subsidised by the Dutch Bsik programme, a decree on the improvement of knowledge infrastructure.

REFERENCES

[1] Tanaka S, Isomura K, Togo S, Masayoshi E. Turbo test rig with hydroinertia air bearings for a palmtop gas turbine. Journal Micromechanics Micro engineering 2004; 14: 1449-1454.

[2] Lalanne M, Ferraris G. Rotordynamics Prediction in Engineering. John Wiley & Sons, Ltd. Chichester: 1990.

[3] Matsumura F, Yoshimoto T. System Modeling and Control Design of a Horizontal-Shaft Magnetic-Bearing System. IEEE Transactions on Magnets 1986, Vol. mag-22, No.3: 196-203

[4] Park J, Ro S, Kim B, Kyung J, Shin W, Choi J. A Precision Meso Scale Machine Tools with Air Bearings for Microfactory. Proceedings 5th International Workshop on Microfactories. Besançon France. 2006

DESIGN AND FABRICATION OF AN OPERATING ROOM COMPUTER ASSISTED ORTHOPAEDIC HIP SURGERY ARTIFACT

Nicholas G. Dagalakis, Yongsik Kim, Daniel Sawyer, Craig Shakarji
Manufacturing Engineering Laboratory
National Institute of Standards and Technology
100 Bureau Dr. Stop 8230
Gaithersburg, MD 20899-8230

ABSTRACT

Hundreds of thousands of joint arthroplasty operations are performed throughout the world every year, providing life saving relief from pain and return of mobility to the majority of the individuals who have this treatment. Clinical studies have shown that improper position and orientation of the joint implants can result in accelerated rates of failure, less than satisfactory mobility and even joint dislocation or impingement. Computer Assisted Surgery (CAS) systems have been developed in order to advise the surgeon inside the operating room on the proper positioning and orientation of tools and implants during such operations. The objective of the work described in this paper was to develop a simple, lightweight, easy to use operating room high precision artifact (phantom), which can be used at the beginning of orthopaedic hip operations for a quick performance test of most CAS systems.

INTRODUCTION

Computer Assisted Orthopaedic Surgery (CAOS) systems consist of tracking sensors, tracking markers, a computer and other relevant electronics [1]. During an operation the markers are attached to bones, surgical tools and implants. The three-dimensional space position of the markers is determined with respect to a reference frame and based on that information the position and orientation of tools, bones and implants are calculated and used to generate useful surgery information. Comparison of conventional versus CAOS assisted arthroplasty operations have demonstrated that CAOS systems show significant improvement in the desired surgical result. In particular, CAOS systems help reduce the variability of the positioning of prosthetic components from the desired optimum position and orientation, thus permitting more consistent placement of the prosthetic components [2, 3].

It is therefore important that these CAOS systems function reliably and accurately during each surgical operation. We have developed a simple, lightweight, easy to use, operating room high precision artifact, called a phantom by medical professionals, which can be used at the beginning of each operation for a quick performance test of most CAOS systems. A longer and more thorough performance test can be performed early in the morning before the first surgical operation. This phantom can also be use for the calibration of CAOS systems. Calibration is of course primarily the responsibility of the manufacturer of CAOS systems and it can be performed after fabrication and during servicing operations.

Here we will describe the design and fabrication of a Horizontal Joint Operating Room Computer Assisted Orthopaedic Hip Surgery (HJ-OR-CAOHS) phantom.

TOTAL HIP ARTHROPLASTY OPERATION BASICS

Various human diseases and activities can damage the hip joint and lead to severe pain and loss of mobility. Surgery to replace the damaged joint with an artificial one, a prosthesis, is usually the last resort in order to alleviate pain and restore mobility [4]. There are two major categories of joint prostheses, the cemented and the uncemented ones. The cemented joints are attached to the bone with some kind of epoxy cement, while the uncemented joints have a porous external surface where bone can grow in order to attach the prosthesis to the skeletal bone. The hip prosthesis consists of two major parts; the femoral component and the acetabular component (see images in Figure 1 and 2). The femoral component is made of a metal stem and a metal or ceramic ball head and is intended to replace the upper part of the femur bone. The acetabular component is usually made of a concave metal shell cup and a plastic liner. After the pelvis socket is cleaned and reshaped,

usually to a hemisphere, the metal cup is attached. Then the plastic inner liner is added, and the acetabular prosthesis head is inserted into the liner socket. The initial step before the operation is to determine the coordinates of the center of rotation of the hip and ankle joints in order to calculate the length of the leg. This test must be repeated before the conclusion of the operation and adjustments must be made in order for the patient to exit the operating room with the proper length leg, since a portion of his femur bone and pelvis have been removed. Another critical step of this operation is the attachment of the acetabular component of the prosthesis. It has been found that the metal shell cup must be placed with precise angular orientation otherwise the prosthesis could fail due to dislocation, impingement and premature wear. The angles that define the correct angular orientation are defined with respect to the patient's pelvis frontal (coronal) and transverse coordinate planes, which are difficult to locate while the patient is lying on the operating table.

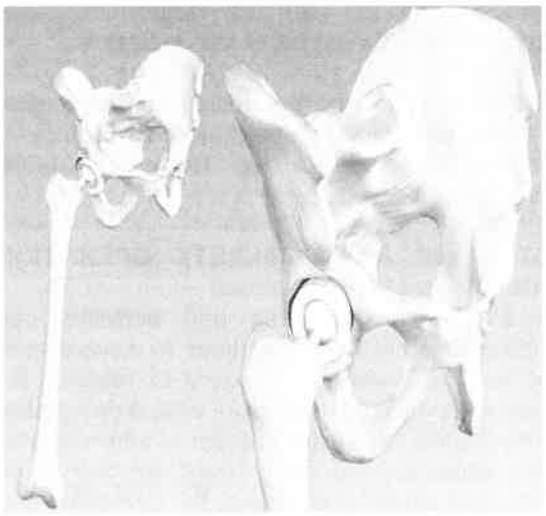

FIGURE 1. Femoral part of hip prosthesis

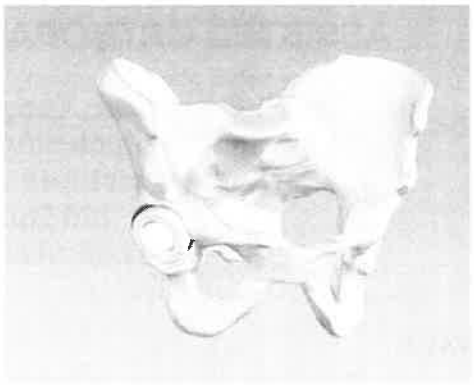

FIGURE 2. Acetabular part of hip prosthesis

THE HORIZONTAL JOINT COMPUTER ASSISTED ORTHOPAEDIC HIP SURGERY ARTIFACT

For best clinical results our phantoms are designed to resemble the skeletal joint or organ, which is the subject of the operation and the suggested performance tests resemble important tasks of the actual surgical operation. In order to reduce the fabrication and maintenance cost of these devices, we use commercially available precision engineered parts wherever possible in the phantom structure design.

The most important component of the hip joint is the ball and socket joint, which we decided to add to our artifact (phantom). Most ordinary mechanical ball and socket joints have backlash and are difficult to clean and inspect for wear because they are sealed. However, precision engineers use magnetic ball and socket joints (see Figure 3) and bars, which have none of the above mentioned drawbacks. They are commercially available for reasonable prices and are used for the calibration and testing of precision measurement machines, such as Coordinate Measuring Machines (CMM). Furthermore these joints can be fitted with various strength small size magnets, which can be selected for the proper size bar and joint orientation, so that the contact force will be sufficient to ensure that the bar will not separate from the joint socket during the test and not so large that excessive surface wear results.

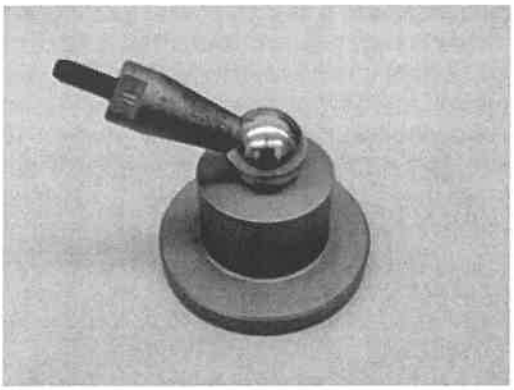

FIGURE 3. Precision magnetic ball and socket device

Our first HJ-OR-CAOHS phantom resembles a pelvis coordinate frame, as shown in Figure 4, and a femur bone connected with a precision magnetic ball and socket joint, as shown in Figure 5.

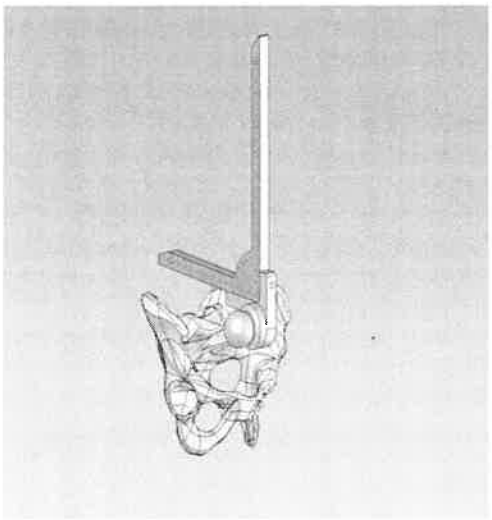

FIGURE 4. The CAOHS phantom coordinate frame superimposed on a pelvis model. The CAOHS coordinate axes, in this image, are approximately aligned with the pelvis axes (long body and sagittal) used by most medical professionals in order to locate the position and orientation of the pelvis socket (acetabulum).

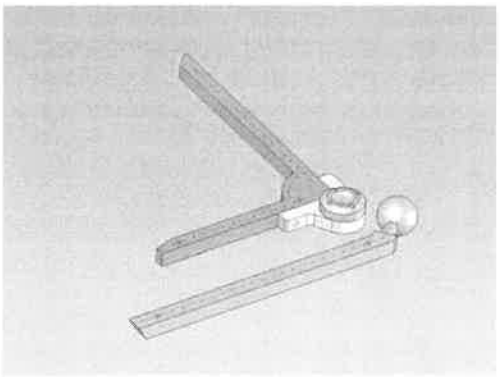

FIGURE 5. The CAOHS phantom coordinate frame and femur bar connected with a magnetic ball and socket joint

The CAOHS phantoms are designed to perform at least three performance tests relevant to hip arthroplasty operations. They are the following: 1) measure the CAOS system accuracy of determining the location of the coordinates of the center of rotation of the hip joint, represented here by the precision magnetic ball and socket joint, 2) measure the CAOS system accuracy of moving along straight lines at distances comparable to the size of human adult large bones, along two orthogonal directions, 3) measure the CAOS system accuracy of angular moves relevant to orthopaedic hip surgery. If the CAOHS phantoms prove useful for orthopaedic operations, similar devices will be developed for the human knee joint, shoulder joint, etc.

The first HJ-OR-CAOHS phantom has been fabricated (see Figure 6). It is made of an L-shaped horizontal XY orthogonal coordinate frame, a joint horizontal mount, the magnetic ball and socket joint and a femur bar. The XY coordinate frame has small target holes at regular intervals designed to fit the pointed probe tip of the CAOS systems target assemblies. These could be simple plates or Dynamic Reference Bases (DRB) with four or more active or passive markers, which can be mounted on surgical tools.

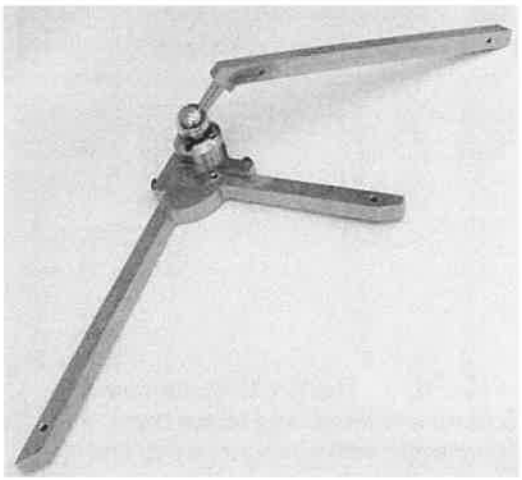

FIGURE 6. The first prototype of the HJ-OR-CAOHS phantom

The HJ-OR-CAOHS phantom also has two larger holes for the mounting of DRB target assemblies. The femur bar also has two larger holes for the mounting of DRB target assemblies, which can be used for the determination of the coordinates of the ball center of rotation. The tips of all of the HJ-OR-CAOHS phantom bars are machined to form various angles, which are useful for hip arthroplasty operations. An arc at the base of the coordinate frame has been fitted with target holes spaced at regular angular increments, which adds an additional angular calibration and testing capability. The magnetic ball and socket joint are commercially available and are made of stainless steel material, while the rest of the parts are made of Invar, for better thermal stability inside an operating room.

NIST staff has calibrated all the critical features on the HJ-OR-CAOHS using an industrial grade Coordinate Measuring Machine (CMM). These features include the target hole locations and the center of rotation. In all cases the expanded uncertainty U with k=2 in the determination of the three dimensional coordinate is less than 0.08 mm. A future publication will report on the calibration procedures and an additional publication will describe the results of industrial testing.

A new version of the OR-CAOHS, which has an angled magnetic ball and socket joint similar to that of a human pelvis, is also being designed.

CONCLUSIONS

We have designed and fabricated a horizontal joint computer assisted orthopaedic hip surgery phantom (artifact) for the performance testing of CAOS systems inside operating rooms. This device appears to be working very well and it was recently calibrated and sent to a medical research group for testing. Calibration and testing results will be reported in future publications.

KEY WORDS

computer assisted surgery, hip arthroplasty, phantom, artifact.

ACKNOWLEDGEMENTS

We would like to thank Dr. J. B. Stiehl, Dr. D. A. Heck and Dr. W. L. Bargar, for their valuable orthopaedic surgery advice and encouragement. We would also like to thank Mr. Damien Bertot for the laser scanning of several human bone models, Dr. Junhwan Kim for generating solid CAD models of individual bones and assemblies, and Mr. Marvin Kingsbury for the fabrication of the HJ-OR-CAOHS phantom.

REFERENCES

[1] Knolte LP, Langlotz F, "Basics of Computer-Assisted Orthopaedic Surgery (CAOS)," in the book "Navigation and Robotics in Total Joint and Spine Surgery," by Stiehl JB, Konermann WH, Haaker RG, Publisher Springer-Verlag, 2004.

[2] Haaker RGA, Tiedjen K, Ottersbach A, Rubenthaler F, Stockheim M, Stiehl JB, "Comparison of Conventional Versus Computer-Navigated Acetabular Component Insertion," J of Arthroplasty, Vol. 22, No. 2, 2007.

[3] Nogler M, Kessler O, Prassl A, et al. "Reduced Variability of Acetabular Cup Positioning with Use of an Imageless Navigation System," Clin Orthop , Vol. 426, pp 159-163, 2004.

[4] Thomas BJ, Stiehl JB, "Basics of Total Hip Replacement Surgery," in the book "Navigation and Robotics in Total Joint and Spine Surgery," by Stiehl JB, Konermann WH, Haaker RG, Publisher Springer-Verlag, 2004.

SINGLE-CHROMOSOME CHIP WHICH EXTENDS, FIXES DNA FIBERS AND ANALYZES THE GENE

Hisatsugu Horiuchi[1], Satoru Kaneko[2], and Masayuki Nakao[1]
[1] Department of Engineering Synthesis, The University of Tokyo
Bunkyo-ku, Tokyo, Japan
[2] Department of Obstetrics and Gynecology, Tokyo Dental College
Ichikawa city, Chiba, Japan

INTRODUCTION

Many parents want to know if their children have congenital anomaly, or chromosomal structural aberration before their birth. As a conventional diagnosis, growing babies' cells are taken from amniotic fluid, cultured till the DNA forms the chromosome structure, and checked. But even if some aberration is proved, we cannot reverse the process of pregnancy. Especially in the field of artificial insemination, obstetricians want to estimate the probability, monitoring spermatozoa before insemination. In addition to congenital anomaly, most of miscarriages are thought to be connected with spermatozoa's chromosome structural aberrations. Even after human embryo completed the insemination, the 90% of them will die. During the process of spermatogenesis, error of meiosis causes the distribution miss of chromosomes to spermatozoa (Figure 1). The embryo inseminated with such an abnormal spermatozoon will be abortion or stillbirth. We thought that evaluation of spermatozoa's chromosomal numeric aberration contributes to the evasion of congenital anomaly and decrease abortion rate,

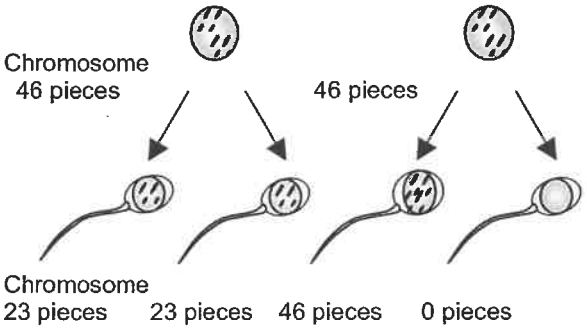

FIGURE 1: Normal meiosis (left) and abnormal meiosis (right)

We developed a single-chromosome chip that can analyze the gene of "single" chromosome. Compared with conventional DNA sequence technologies based on PCR (ex. Sanger method) [1], our chip can analyze the difference among a group composed of diverse types of genes (for example reproductive cells), using FISH method (Fluorescence In Situ Hybridization). For FISH, DNA fibers are heated, (or denature) and the double strand is separated. The base sequence is accessible (Figure 2). The fluorescence probes, which have corresponding sequence toward the target, hybridize to the intended gene sequence and show the location.

We carried out FISH for telomere region. Telomere is a gene sequence repeating (TTAGGG) by more than 10k bps, locating at the ends of each chromosome. There should be 46 telomere-signals in a normal human spermatozoon, which has 23 DNA fibers. By counting the number of signals, we can estimate the number of chromosomes. But with conventional FISH, it's difficult to recognize each probe's signal. As a specific problem of spermatozoa, the telomeres shapes dimmers [2], and we can't judge 1 FISH signal consists of 1 telomer or 2. Human's DNA is condensed in the nucleus like a "knit ball" (the diameter: 5-20um, and each extended fiber's length: 15mm-100mm.) We thought this condensation was a problem, deployment of DNA fibers could dissolve the telomere dimmers and this situation was optimistic for FISH. From a "knit ball", long DNA fibers (1-2 mm) were deployed on our chip by electric field and agarose gel, and we could recognize the DNA fibers.

Our Objective is to evaluate spermatozoa that are suspicious for chromosomal numeric aberration, using telomere FISH after extension by the single-chromosome chip. As a basic research, we prepared oral mucosa as a model of diploid and spermatozoon as haploid, and make sure that we can distinguish them by our method.

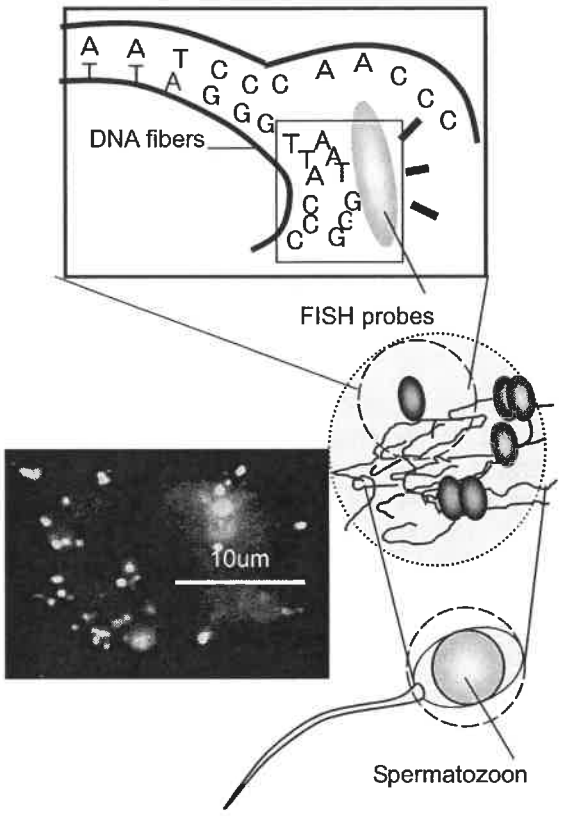

FIGURE 2: Conventional FISH for human spermatozoon

EXPERIMENTAL SETUP

Fibers extension by single-chromosome chip

The schematic of our setup is provided in Figure 3. Cells are suspended in agarose gel with protein lysis enzyme and detergents. The gel is shaped on the chemical modified glass chip by APS (AminoPropylSilane). After the cell is solved, through electric field, we extended DNA fibers that are electrically minus-charged. Changing the direction of electric field, we raveled the knit ball's tangle. The glass chip on the disk with magnetic is rotated by outside magnet on the servo motor, without touched. Compared with the method by many electric poles, continuous changing can decrease the stress for DNA fibers. Adjustment of the rotating angle and voltage controls the extending direction and strength for DNA fibers. Setting the angle, switching cycle, and voltage as the parameter, we studied the ideal condition for long extension and good arrangement.

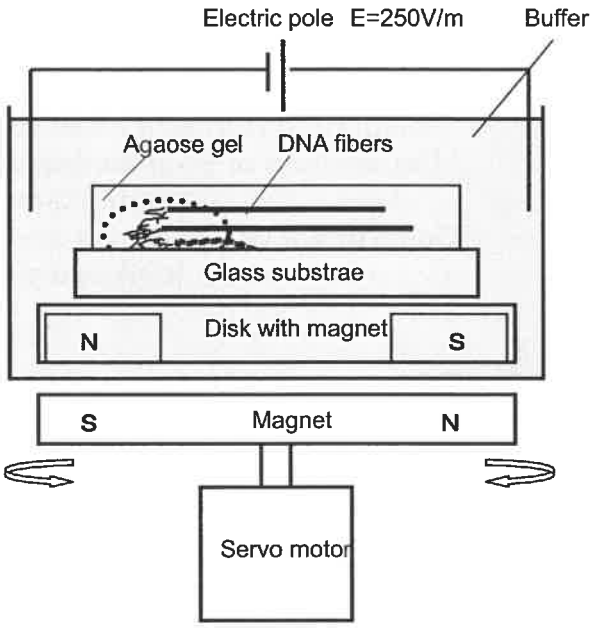

FIGURE 3: The structure of single-chromosome chip

Telomere FISH on the chip

Extended DNA fibers should bear the stress by FISH (heat, denaturing stress from flow). And at the same time, we should keep the reactivity for hybridization (flexibility for confirmation change for FISH hybridization). We realized an ideal fix that satisfies these 2 conditions.

We attached methanol-processed agarose on the. APS glass substrate (Figure 4 A). This structure keeps the accessibility of DNA fibers and PNA probes (Figure 5). On this chip, we set the agarose gel with cell (Figure 4 B), dissolve the tissues except for DNA and extend the DNA fiber by single-chromosome chip (Figure 4 C). After the extension, we dry the gel. Gel-shrink makes the fibers approach to adherent APS layer (Figure 4 D). We fixed the buoyed fibers by polymer plastic, HEMA (poly Hydroxy Ethyl MethAcrylate, Figure 4 E). After these processes, we carried out FISH for spermatozoon as models of haploid and for mucosa as diploid. We compared the signal numbers of telomere. As FISH probe, we prepared 3 repeats of anti code (CCCTAA) for telomere repeats. We used PNA probe, which has high efficiency for hybridization [3].

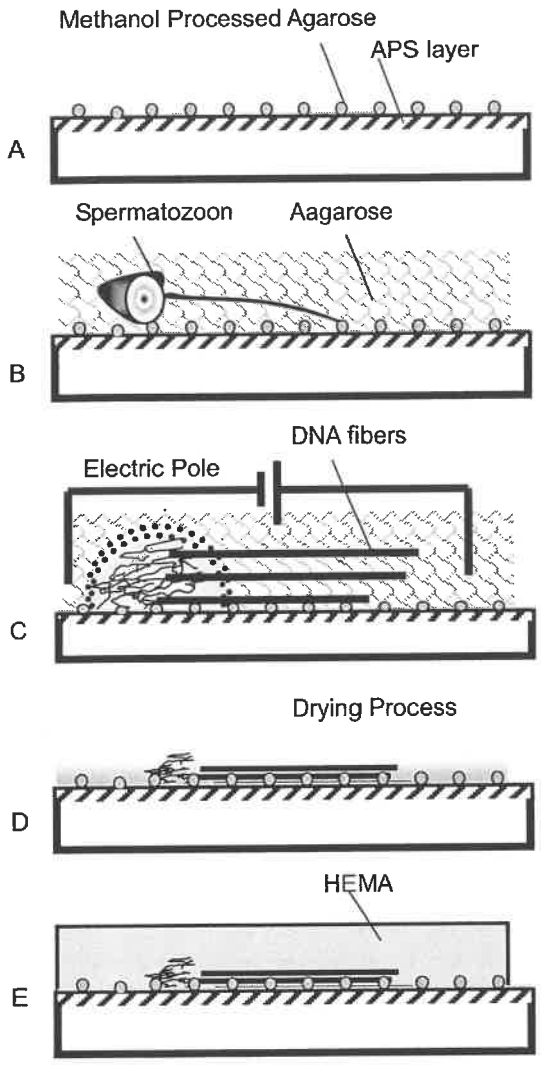

FIGURE 4: DNA fibers fix for FISH

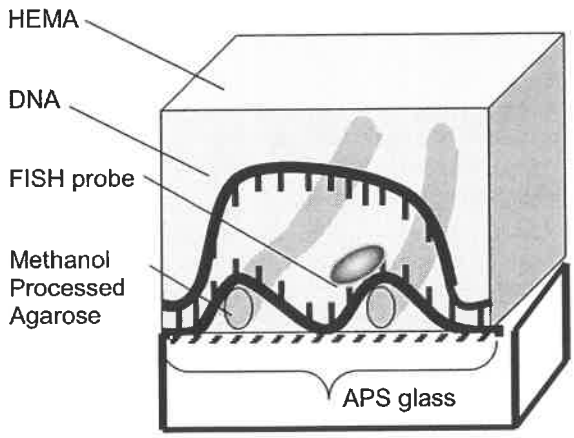

FIGURE 5: DNA fibers fix by HEMA

EXPERIMENTAL RESULTS

Arrangement of DNA fibers

Figure 6 shows the extended DNA fibers. On 1 chip, many samples can be examined. By the condition of 30 o rotating, 1 sec switching cycle, and E=250V/m electric field, we could extend fibers by maximum 2mm (Figure 7). Furthermore, changing the direction by 90 o, we executed the next 2-dimensional extension (Figure 8). This process arranged DNA fibers in good position, and improved the recognition of each fiber.

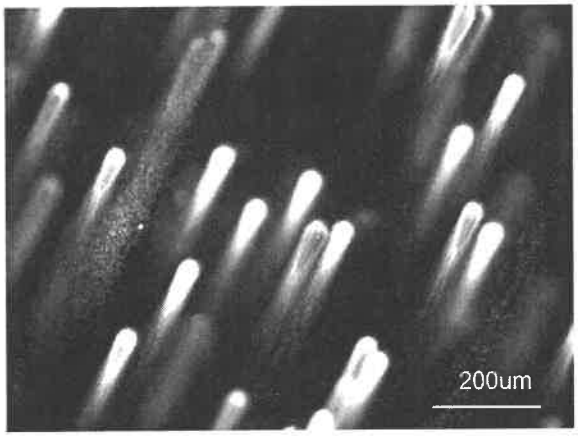

FIGURE 6: DNA fibers extension by single chromosome chip

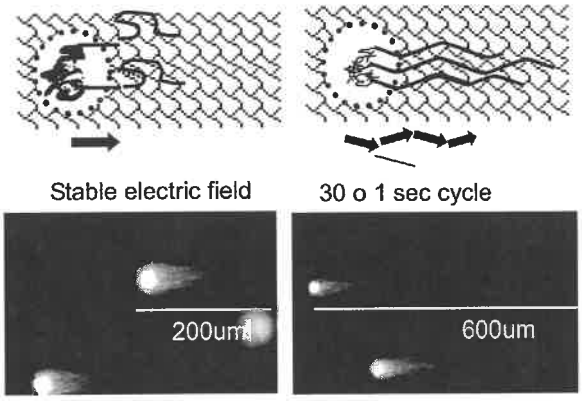

FIGURE 7: Spermatozoa's DNA fibers extending condition

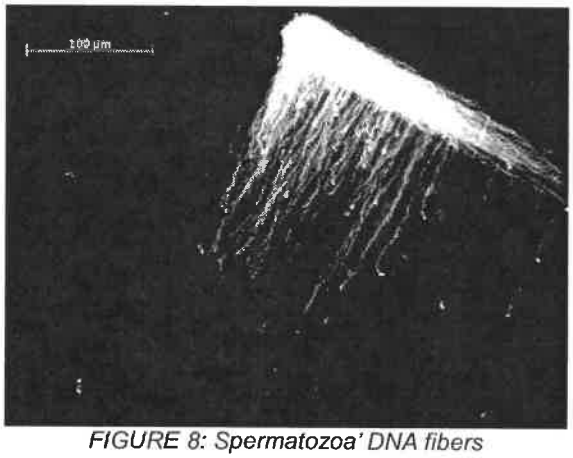

FIGURE 8: Spermatozoa' DNA fibers 2 dimensional development

The count of telomer- signals of FISH

We carried out telomere FISH for spermatozoon deployed on the chip. We counted the telomere signals and compare with the result of oral mucosa (Figure 9,10). The number of telomere signals of spermatozoa is 28.0+/-SD (18 – 41). On the other hand, one of oral mucosa is 58.5+/-SD (44 – 67). We found obvious differences between them. By this method, we can find abnormal spermatozoa of diploid, if any.

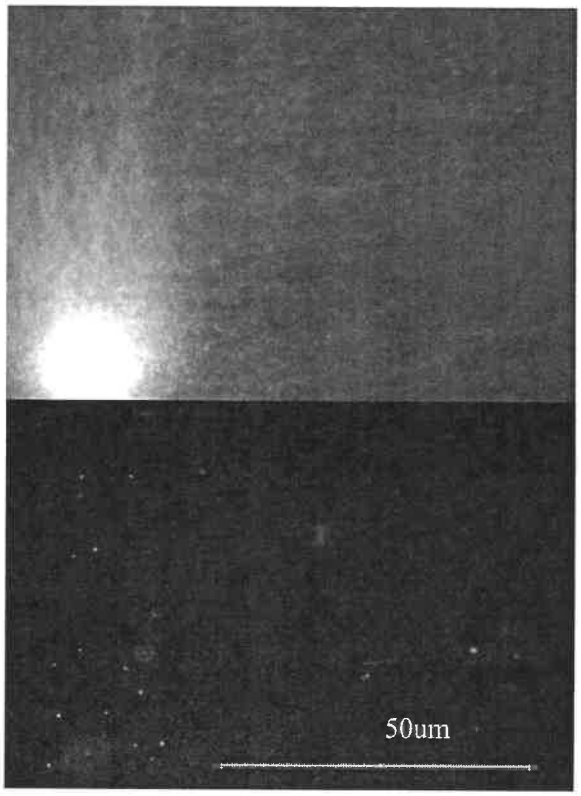

FIGURE 9: Telomere FISH for spermatozoon on single-chromosome chip

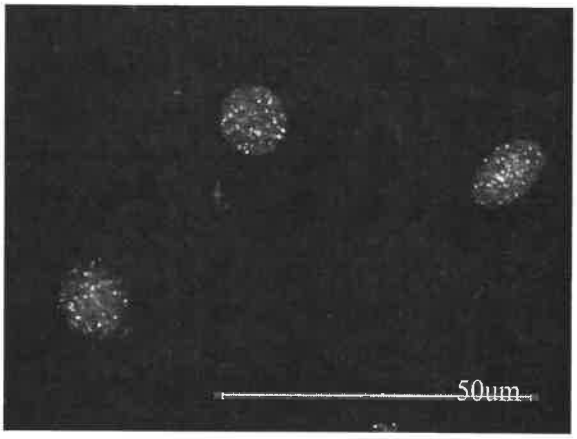

FIGURE 10: Telomere FISH for oral mucosa

CONCLUSIONS

We developed a single-chromosome chip and deployed DNA fibers of human spermatozoa. We could recognize each fiber.

We fixed DNA fiber by polymer (Hydroxy Ethyl MethAcrylate), carried out FISH for the extended DNA fibers and counted the telomere signals. We could distinguish ones of spermatozoa of haploid and oral comusa of diploid.

REFERENCES

[1.] F. Sanger and A. R. Coulson, 1975, A rapid method for determining sequences in DNA by primed synthesis with DNA polymerase, Journal of Molecular Biology, 94, 3:pp. 441-446.

[2.] Lyudmila S., et al, 2004, Nature of telomere dimmers and chromosome looping in human spermatozoa, Chromosome Research, 12:pp.817-823.

[3.] Nielsen P., et al, 1991, Sequence selective recognition of DNA by strand displacement with a thymine-substituted polyamide, Science, 254:pp.1497-1500.

COMBINATION OF MECHANICAL MICROMACHINING AND GLASS BONDING TO FABRICATE ROBUST MICRO STRUCTURES FOR PAINLESS DRUG DELIVERY

Karl-Hans Wu[1], Hans A. Adams[2], and Hans H. Gatzen[1]
[1]Institute for Microtechnology, Center for Production Technology
Leibniz Universitaet Hannover
Hannover, Lower Saxony, Germany
[2]Hannover Medical School
Hannover, Lower Saxony, Germany

ABSTRACT

This paper presents an improved process for the fabrication of a hollow microneedle array with pointed tips. The hollow needles are sufficiently long for penetrating the top skin layer, but short enough to avoid the contact with the skin layer containing the nerves. This approach guarantees a painless injection and on top, a minimum of fluid quantity. The needles are made of alumina-titanium carbide (Altic). The fabrication process includes mechanical micromachining processes like high and ultra precision dicing, profiling grinding as well as glass bonding for the assembly of the component parts. Contrary to the previous process, only a single glass bonding process is required, thus substantially reducing process complexity.

INTRODUCTION

Hollow needles play an important role in drug delivery systems. The human skin is composed of three layers. The top layer is the stratum corneum, followed by the viable epidermis, and the third layer is the dermis. The stratum corneum contains dead tissue while the viable epidermis consists of living cells, but no blood vessels, and only a few nerves. For a transdermal injection, only the stratum corneum and the epidermis have to be penetrated by needles.

The approach for a painless injection is to create hollow microneedles with a defined length to solely entering the stratum corneum and the epidermis. Due to the small size of the hollow microneedles, a large number of microneedles is required to inject a sufficient amount of fluid.

Most of the current research activities are focused on known microtechnologies. There are microneedle arrays made of silicon, polymers, or metal by means of silicon micromechanics [1][2][3], photolithography [4], or coating processes [5][6][7]. All these technologies result in needles with the necessary height, although the needle quantity of such an array is limited [3].

This paper presents an array of hollow microneedles with pointed tips, based on simplified mechanical manufacturing processes compared to an earlier version. The material applied is alumina-titanium carbide (Altic), a very hard and tough material also used for the fabrication of read/write heads for hard disk drives. The use of this ceramic provides many advantages predestining it for medical applications. Altic is a two phase polycrystalline material, mechanically robust, non-toxic, non-allergenic, and inert against most body fluids.

The presented design combines multiple mechanical microfabrication processes: ultra precision dicing, profile grinding, and lapping. For merging the component parts, a glass bonding process is used. Compared to an earlier version of the microneedle array [8], only a single glass bonding process is required.

MICRONEEDLE ARRAY DESIGN

The microneedle array has a footprint of 12 mm x 4 mm and contains 400 hollow microneedles for fluid transportation. Each microneedle has a cross section of 150 µm x 150 µm and a square cannula of 50 µm x 50 µm at the center. The front of the needle is tilted with a pointed edge at one side. The height of each needle is 600 µm. For the production of this array, a separate glass bonding process is utilized for merging the needles as well as for assembling the needle rows. As a result, a two temperature process was required, which jeopardized the needle adjustment.

By changing fabrication steps, the needle array could be fabricated with only one glass bonding

step, bonding needle rows at a separating plane adjacent to the cannulae position. This approach resulted in improved surface quality, an accurate positioning, and an increase in fabrication repeatability.

The chosen material Altic is quite hard with high fracture toughness (Table 1). Thus the risk of the needles breakage and remaining inside the skin after drug application is avoided. Dicing was done on a dicing machine with a positional accuracy of 0.2 µm, located in an air conditioned room.

TABLE 1. Mechanical properties of Altic

Altic	Al_2O_3-TiC (70/30)
Chemical composition (wt%)	70% Al_2O_3 30% TiC
Vicker's Hardness	2,000 HV
Bending strength σ_B	880 MPa
Young's modulus E	390 GPa
Density	$4.26*10^3$ kg/m^3
Average grain size	1.5 µm
Fracture toughness index	4.6 MPa m$^{-1/2}$

FABRICATION PROCESS

The first fabrication step was to create an array of grooves, which later serves as cannulae. The process flow of such an array is shown in Fig. 1.

Next, bonding glass (type SP467) was sputtered on an Altic chip. Thereby, both sides were covered with a 600 nm thick glass layer (Fig. 1a). Afterwards, size and shape of the needle cannulae were defined by cutting U-shaped grooves. The grooves were machined using a blade featuring resin binder with diamond size of 5 µm and a thickness of 45 µm. The depth of grooves was 50 µm, which resulted in square U-shaped cannulae with a size of 50 µm x 50 µm (Fig. 1b). Next, rows were sliced using a dicing blade with resin binder, 45 µm grit size, and 200 µm thickness. The cutting direction of the rows was orthogonal to the grooves. In order to obtain the needle cannulae, the rows were positioned on the cutting area and arranged as shown in Fig. 1c, so that the glass covered surface of one row was parallel to the surface of the next row. The assembled rows were positioned in a special assembly tool and heated in a soldering furnace. The fusion of the row bars and glass during the bonding process was supported by the controlling compression with a spring mechanism. A screw device outside the furnace controlled the spring force. The process temperature was 735°C. It joined the rows and provided a square array with needle cannulae (Fig. 1d).

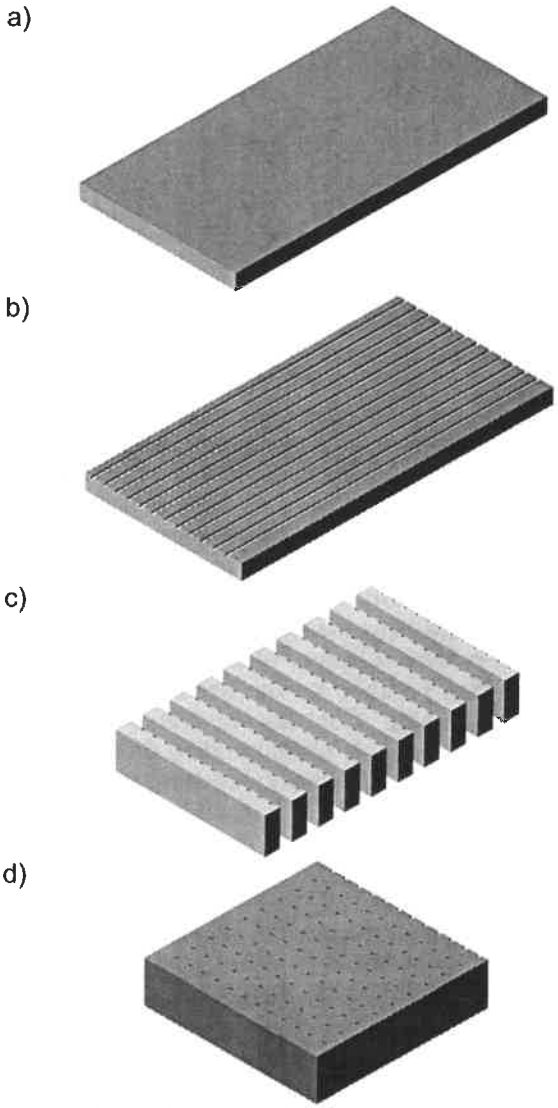

FIGURE 1. Process flow of a array with cannulae

The bonding temperature is an important factor for the quality of the array. A too high temperature causes a flow of the glass and a non-uniform adhesive area. A low temperature results in poor adhesion and undesired cavities between the rows. Therefore, the optimal adjustments of spring force and temperature control were the crucial factors for achieving optimal bonding conditions.

To provide a plane surface for the next machining step, both sides of the array were lapped. The result is shown in Fig. 2, which

depict a lapped array surface with a cannula. The cannula is clear and no glass bond blocks the hole. The bond line is homogeneous and nearly invisible.

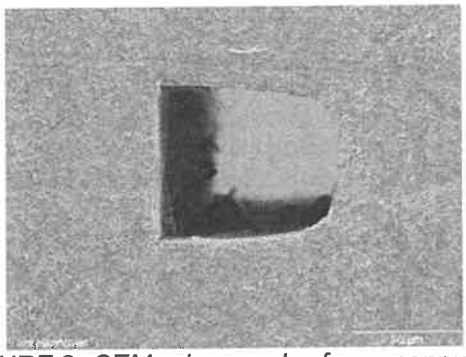

FIGURE 2. SEM micrograph of one cannula in a glass bonded array

The next fabrication step created the pointed tips of the hollow needles. They were facilitated by profile grinding. Fig. 3 shows the corresponding process flow.

a)

b)

c)

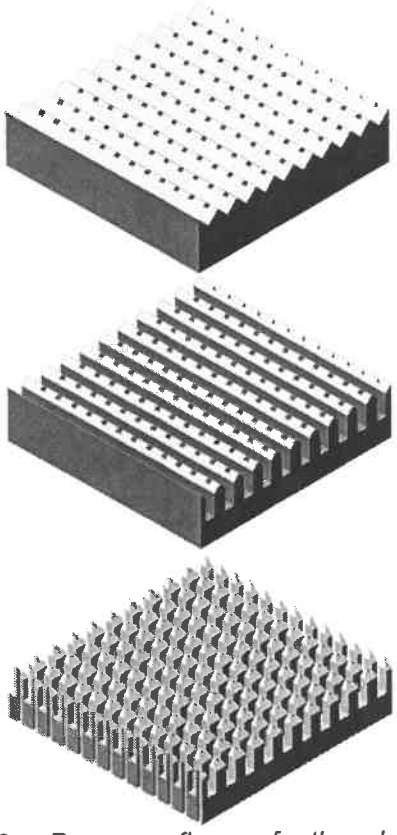

FIGURE 3. Process flow of the hollow microneedles

The process sequence started with grinding the V-grooves. The grooves were created using a dicing blade with a V-shaped profile. The angle between the diced surfaces is 90 degrees. The grooves were arranged in a way that the cannulae were located in the intersection of two parallel laying V-grooves (Fig. 3a). Afterwards, the geometry of the desired microneedles was created by grinding with a standard U-shaped blade of 200 µm thickness, which generated a square bottom profile. This results in rows with a tapered end (Fig. 3b). To create pointed pyramidal tips, further profiling was required. The sequence *is* the same as before, but the grinding was carried out in orthogonal direction to the first rows. To conclude the fabrication process, the final shape of the microneedles was generated (Fig. 3c). In comparison to Fig. 3b, the picture in Fig. 3c has been rotated 180 degrees for an improved view.
The SEM micrograph Fig. 4 depicts a section of microneedle array having cannulae in the center.

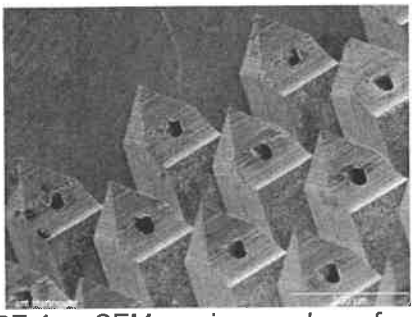

FIGURE 4. SEM micrograph of hollow microneedles

The assembled microneedle array is shown in Fig. 5.

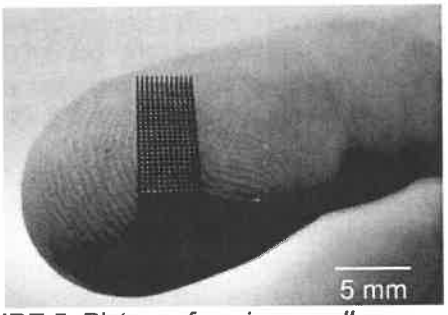

FIGURE 5. Picture of a microneedle array

EXPERIMENTAL SETUP
For evaluating the microneedle array, two tests were performed. First, the transportation capability of fluids was proved. This required a connection to an injection device. Therefore, a needle array was attached to an Altic plate with

a notch smaller than the footprint of the microneedle array (11.5 mm x 3.5 mm). For bonding, a cyanoacrylate (Dymax MEDI-CURE® 222 Series) adhesive was used, which is bio-approved and applicable for bonding ceramic and glass. Afterwards, this assembly was bonded with the same adhesive to the top of a conventional syringe. The complete setup is shown in Fig. 6.

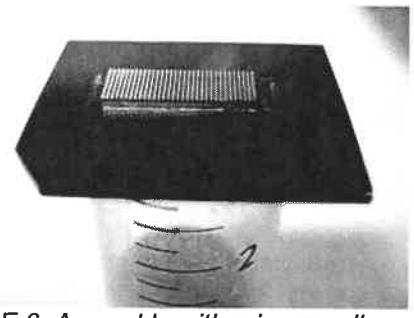

FIGURE 6. Assembly with microneedle array

The syringe was filled with water and tested. It could be observed, that a drop forms on the surface of the microneedle array (Fig. 7).

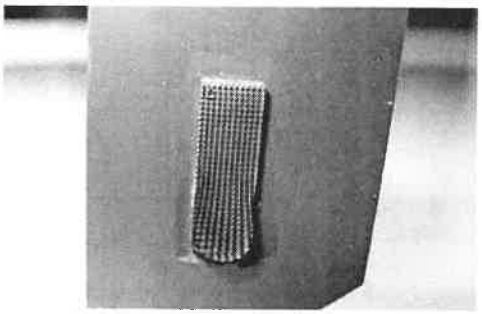

FIGURE 7. Forming of a drop

The second test made sure that the tips are sharp enough to penetrate the skin. The microneedle array bonded on the syringe was tested at the Hanover Medical School on a human hand. After the desinfection of the needle array, the syringe was filled with an anesthetic solution (Prilocain 2%). Injected into the skin, this solution caused a feeling of burn, which is typical for intradermal injection of a local anesthetic. The test persons confirmed that the injection with the microneedles was absolutely painless. After the injection test, the hand and the array were checked for injuries or damage, respectively. The injection area on the hand showed an imprint of the area, but no blood was drawn. The needles were undamaged.

CONLUSION

For fabricating a ceramic needle array for drug delivery, a new, simplified fabrication process could be developed. It requires only one glass bonding process, therefore substantially simplifying the fabrication process and the positional accuracy of the needle array component. A drug delivery test with a microneedle array showed that the needles were able to penetrate the skin painlessly and the needles were able to inject fluid below the skin. By using Altic as material for the array, very steady needles could be created which do not break off during or after the injection.

REFERENCE

[1] Gardeniers J G E, Luttge R, Berenshot E J W, de Boer M J, Yeshurun S Y, Hefetz M, van't Oever R, van den Berg A. Silicon Micromachined Hollow Microneedles for Transdermal Liquid Transport. Journal of Microelectromechanical Systems. 2003; Vol. 12, 6: 855-862

[2] Shikida M, Hasada T, Sato K. Fabrication of a hollow needle structure by dicing, wet etching and metal deposition. Journal of Micromechanics and Microengineering. 2006; 16: 2230-2239

[3] Zhang P, Jullien G A. Microneedle Arrays for Drug Delivery and Fluid Extraction. Proceedings of the 2005 Intern. Conference on MEMS. 2005

[4] Park J H; Davis S, Yoon Y-K, Prausnitz M R, Allen M G. Micromachined Biodegradable Microstructures. Proceedings of the IEEE (MEMS). 2003; 371-374

[5] Chandrasekaran S, Brazzle J D, Frazier A B. Surface Micromachined Metallic Microneedles. Journal of Microelectromechanical Systems. 2003; Vol. 12, 3: 281-288

[6] Davis S P, Martanto W, Allen M G. Hollow Metal Microneedles for Insulin Delivery to Diabetic Rats. IEEE Transactions on Biomedical Engineering. 2005; Vol. 52, 5: 909-915

[7] Kim K, Lee, J-B. High aspect ratio tapered hollow metallic microneedle arrays with microfluidic interconnector. Microsystem Technology. 2007; 13: 231-235

[8] Gatzen H.H., Halalo K. Ceramic Micro Needle Array for Painless Drug Delivery and Biological Sensing. 6th International euspen. 2006; Vol.2: 32-35

MODELING MAGNETIC FIELDS FOR PRECISION MAGNETIC ACTUATORS THAT USE NON-PERIODUC MAGNET ARRAYS

Dariusz Golda[1] and Martin L. Culpepper[1]
[1]Department of Mechanical Engineering
Massachusetts Institute of Technology
Cambridge, Massachusetts USA

ABSTRACT

In this paper we use the Fourier transform (FT) to model and simulate the 3-D magnetic field created by finite, planar permanent magnet arrays that are Fourier-transformable and possess vertical magnetization. This approach captures the three dimensional characteristic of the fields, including the field components near the ends of the array. These end effects are important in small-scale precision actuators where geometric constraints preclude the use of larger, finite arrays that emulate the behavior of infinite arrays. We demonstrate how to model and compute the field characteristics using 2-D Fast Fourier transforms (FFTs). Model predictions for a prototype magnet array are compared with measured values of a magnet array's flux density. The difference between measured and predicted values is within the expected error (5%) of the measurement system.

INTRODUCTION

Permanent magnet arrays are important to precision actuators such as linear motors that use Halbach arrays [1, 2] and multi–axis magnetic levitation machines [3-5]. These devices often consist of long, repeating coils and permanent magnet arrays. In order to design such systems, infinitely periodic magnetic field models are used in performance models [1, 5]. However, meso-scale instruments and precision machines such as probe-based data storage systems [6, 7] employ non-periodic magnetic structures due to geometric constraints, and therefore modeling them requires a departure from conventional periodic field models. Meso-scale devices often include a set of permanent magnets that interact with an energized planar coil, as shown Fig. 1. In order to predict the performance of these actuators, non-periodic field models should be employed to capture end effects. Furthermore, accurate force models of these structures must consider field effects in three dimensions. This leads to a need to develop accurate, yet computationally effective field models for the prediction of meso-scale magnetic actuator forces.

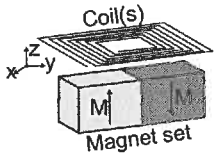

FIGURE 1: An actuator with a non-periodic array

The most commonly used method for modeling finite arrays, the superposition integral, only covers a limited number of array geometries and the equations become cumbersome for arrays of multiple magnets. In addition, the solution is unbounded along some of the magnet boundaries. For magnet-coil devices, the computation of the coil-field interactions in close proximity to the magnets requires fine discretization to ensure convergence. This is time and computationally intensive for design and optimization.

Herein, we demonstrate a new method that enables fast, accurate computation of the field components along a plane that is above or below a planar, non-periodic magnet array with vertical magnetization. This FT solution is well-suited to rapidly computing the forces on micro- or meso-scale planar coil actuators that are suspended above permanent magnet arrays. The advantages of this method over the superposition integral include:

a) FFT algorithms are computationally more efficient than standard numerical integration methods;

b) convergence is independent of distance from the pole surfaces, enabling small gaps without increased computation time;

c) the resulting Fourier Transform integral field equations provide insight into the field solutions.

MODELING

Fig. 2 shows a schematic of the model that consists of a general, planar arrangement of permanent magnets with magnetization M(x,y) that is directed in the vertical direction only. The magnitude and sign of this vector are free to vary in the x and y directions.

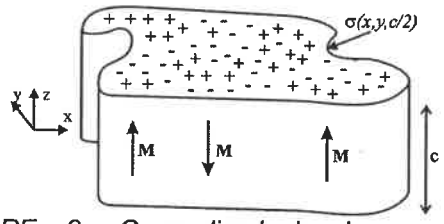

FIGURE 2: Generalized in–plane magnet arrangement with equivalent surface magnetic charge distribution σ(x,y) at z=½ c

Fig. 3 shows three regions of interest: regions 1 and 3 exist in air and extend to "infinity" above and below the array.

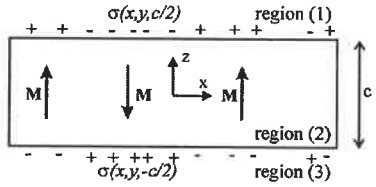

FIGURE 3: Side view of generalized charge distribution

Region 2 encompasses the magnet volume, extends to infinity in the x-y directions, and is bounded by the planes that define the upper/lower surfaces of the magnets. Under the magnetoquasistatic approximation [8] with zero current density, Maxwell's equations for the field intensity, **H**, and flux density, **B**, simplify to:

$$\nabla \times \mathbf{H} = 0 \qquad (1)$$

$$\nabla \cdot \mathbf{B} = 0 \qquad (2)$$

As a result, the magnetic field, **H**, is irrotational and may be expressed as the gradient of the scalar magnetic potential Ψ:

$$\mathbf{H} = -\nabla \Psi \qquad (3)$$

The scalar potential satisfies Laplace's equation subject to the boundary conditions imposed by the surface magnetic charge distribution [8]:

$$\sigma = -\mathbf{n} \cdot \mu_o (\mathbf{M}_1 - \mathbf{M}_2) \qquad (4)$$

In this paper, we provide an overview of the solution. For more details, see [9]. First, the charge distribution is expressed as a double inverse FT:

$$\sigma(x,y,c/2) = \frac{1}{(2\pi)^2} \int_{-\infty}^{\infty}\int_{-\infty}^{\infty} \Theta(k_x,k_y) \cdot e^{i(k_x x + k_y y)} dk_x dk_y \qquad (5)$$

where Θ is the double FT of the surface magnetic charge distribution in the frequency domain. The solution is then derived by way of separation of variables and superposition. This leads to a solution in the form of a FT. The resulting magnetic field in each direction for all (x, y) in region 1 at a height z above the mid-plane of the magnet array is given as follows:

$$H_{1x} = \mathrm{Re}\left[\frac{-i}{(2\pi)^2} \int_{-\infty}^{\infty}\int_{-\infty}^{\infty} \Theta(k_x,k_y) \frac{k_x}{k_{xy}} \cdot \sinh\left(k_{xy}\frac{c}{2}\right) e^{-k_{xy}z} e^{i(k_x x + k_y y)} dk_x dk_y \right] \qquad (6)$$

$$H_{1y} = \mathrm{Re}\left[\frac{-i}{(2\pi)^2} \int_{-\infty}^{\infty}\int_{-\infty}^{\infty} \Theta(k_x,k_y) \frac{k_y}{k_{xy}} \cdot \sinh\left(k_{xy}\frac{c}{2}\right) e^{-k_{xy}z} e^{i(k_x x + k_y y)} dk_x dk_y \right] \qquad (7)$$

$$H_{1z} = \mathrm{Re}\left[\frac{1}{(2\pi)^2} \int_{-\infty}^{\infty}\int_{-\infty}^{\infty} \Theta(k_x,k_y) \cdot \sinh\left(k_{xy}\frac{c}{2}\right) e^{-k_{xy}z} e^{i(k_x x + k_y y)} dk_x dk_y \right] \qquad (8)$$

The field is a complex–valued function and therefore we only consider the real component. As long as the magnetic charge distribution is Fourier–transformable, the field may be calculated everywhere in three dimensions. It is typically difficult to directly calculate the integrals and therefore numerical solutions are useful. Several FFT algorithms have been developed to quickly compute FTs, and they may be used to perform fast computation of the fields along horizontal planes (constant z). We have shown that this method is computationally faster and has better accuracy than the superposition integral method [9].

EXAMPLE MAGNET ARRAY

An example array is used to illustrate the use of the field equations discussed above. The array consists of three alternating–pole magnets. The

magnet arrangement and parameters are shown in Fig. 4. The uniform magnetization, **M**, is along the *z* direction, and *a*, *b* and *c* are the dimensions of the magnets. The coordinate system is located at the centroid of the center magnet, such that the charge surfaces are located at $z=\pm\frac{1}{2}c$ as in the preceding analysis.

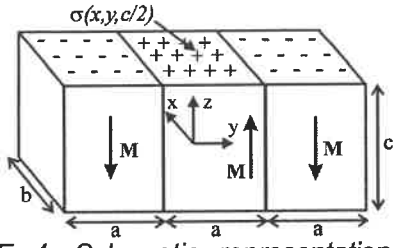

FIGURE 4: Schematic representation of the example 3–pole magnet arrangement

The arrangement of magnets in Fig. 4 has an even surface charge distribution function $\sigma(x,y, \frac{1}{2}c)$ that consists of three top–hat functions. The double FT of the distribution is:

$$\Theta(k_x,k_y)=\frac{4M}{k_xk_y}\sin\frac{1}{2}bk_y\left(2\sin\frac{1}{2}ak_x-\sin\frac{3}{2}ak_x\right) \quad (9)$$

The model in Fig. 4 was used to predict the field characteristics for the array used in the following experiment.

COMPARISON OF THE PREDICTED AND MEASURED MAGNETIC FIELDS

An experimental setup was constructed to collect magnetic flux density data in three–axes, and upon a plane that was above an array of neodymium–iron–boron magnets. Fig. 5 shows the setup.

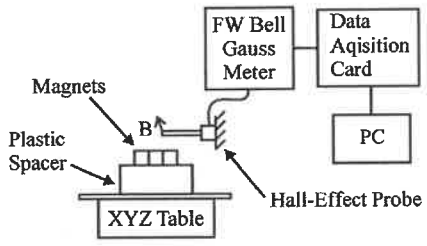

FIGURE 5: Schematic of the magnetic field measurement experiment

A set of the three permanent magnets was arranged according to Fig. 4 and then mounted on a programmable *x-y-z* translation table with positional accuracy of 12.7 micrometers. The magnet array was mounted to the table with a 100 mm plastic spacer to minimize field interaction with the steel components of the translation table. A one–axis F. W. Bell Hall–effect probe (model HTG92–0608) was fixed above the magnet array and connected to an F. W. Bell Model 9550 Gauss meter. Total field measurement linearity error was less than 2%. Data from the Gauss meter was collected via a 12–bit National Instruments DAQCard–6024E PCMCIA card and a laptop PC running LabView. The system measurement noise floor was measured in regions of zero field to be 17.43 mT (95% confidence).

Measurements of independent flux density components were made by orienting the probe and stepping through a preset grid of x-y coordinates with pitch p = 6.35 mm. Measurements were taken at a fixed height, h = 5.08 mm, above the magnet's upper surface. The location of the magnet array was registered to the probe before making measurements by locating the maximum and zero–values of the flux density. The flux density components were recorded at each x-y coordinate, and the experiment was repeated for each field component, i.e. B_x, B_y and B_z. Table 1 lists the geometric and magnetic properties of the experiment.

TABLE 1. Experiment parameters

Symbol	Description	Quantity	Units
a	Magnet width	25.4	mm
b	Magnet depth	25.4	mm
c	Magnet height	25.4	mm
h	Height	5.08	mm
Br	Remnance	1.23 ± 0.01	T
p	Pitch	6.35	mm

Nickel-plated N35-grade neodymium iron boron magnets were used in the experiment, and the catalog value for the remnance flux density was used in the calculations.

The predicted components were computed using a 2-D FFT algorithm. The *m* x *n* point FFT is computed for *m* = *n* = 200, or 40,000 total points. The corresponding truncation limits for K_x and K_y are $L=m\pi/12a\approx 2.06\ mm^{-1}$. Discretization of the magnetic charge distribution required approximately 1.5 sec, whereas calculation of all three field components along an *m* x *n* plane was approximately 0.15 sec. Figure 6A through 6C compare the measured and predicted components of the flux density.

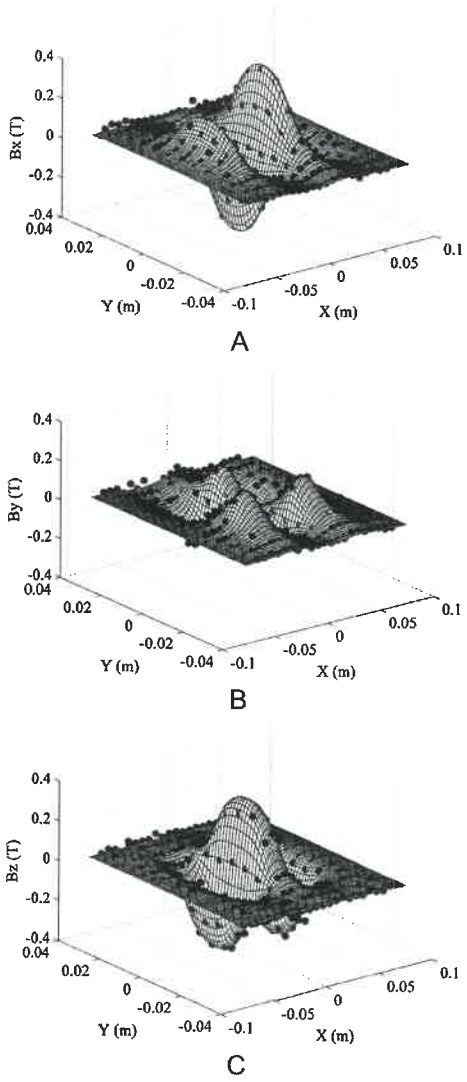

FIGURE 6: Comparison of predicted (surface) vs. measured (points) values of the x (A), y (B) and z (C) components of the magnetic flux density

The measurement error is at the system noise floor of 17.4mT, which is 4% of the maximum reading. The root-mean-square difference over the entire measurement grid is computed to be less than 5% of the maximum flux density value.

CONCLUSIONS

We use the FT to model and simulate the 3-D magnetic field created by finite, planar permanent magnet arrays that are Fourier-transformable and possess vertical magnetization. 2-D Fast FTs are used to quickly compute the fields in three-dimensions. Model predictions for a prototype magnet array are compared with measured values of a magnet array's flux density. The difference between measured and predicted values is within the error (5%) of the measurement system. The FT solution is currently being used to design meso-scale actuators for high-speed six-axis nanopositioners.

ACKNOWLEDGEMENTS

This work is supported in-part by the National Science Foundation under Grant No. 0348242. We thank Prof. Jeffrey Lang and Prof. David Trumper for their modeling advice and access to measurement equipment.

REFERENCES

[1] Trumper D L, et al. Magnet Arrays for Synchronous Machines. Proc. of the 28th IEEE Industry Applications Conf. Part 1 (of 3), Oct 3-8 1993, Toronto, Ont, Can, 1993.

[2] Zhu Z Q, Howe D. Halbach Permanent Magnet Machines and Applications: A Review. IEE Proceedings-Electric Power Applications. 2001; 148: 299-308.

[3] Compter I J C. Electro-Dynamic Planar Motor. Precision Engineering. 2004; 28:171-180.

[4] da Silveira M A, et al. Evaluation of the Normal Force of a Planar Actuator. IEEE Transactions on Magnetics. 2005; 41:4006-8.

[5] Cao J, et al. A Novel Synchronous Permanent Magnet Planar Motor and Its Model for Control Applications. IEEE Transactions on Magnetics. 2005; 41: 2156-63.

[6] Choi J-J, et al. Electromagnetic Micro X-Y Stage for Probe-Based Data Storage. Journal of Semiconductor Technology and Science. 2001: 1: 84-93.

[7] Rothuizen H, et al. Fabrication of a Micromachined Magnetic X/Y/Z Scanner for Parallel Scanning Probe Applications. Microelectronic Engineering. 2000; 53: 509-12.

[8] Haus H A, Melcher J R. Electromagnetic Fields and Energy. Prentice-Hall. Englewood Cliffs, NJ: 1989.

[9] Golda D, Culpepper M L. Modeling 3D Magnetic Fields for Precision Magnetic Actuators That Use Non–Periodic Magnet Arrays. Accepted for publication in Precision Engineering, 2007.

IN-PROCESS DIAMETER CONTROL IN PRECISION CYLINDRICAL GRINDING

Alex Moerlein[1], Ted Deakyne[1], Eric Marsh[1], and Ryan Vallance[2]
[1]Mechanical Engineering
Penn State University
University Park, PA, USA
[2]Mechanical Engineering
George Washington University
Washington, DC, USA

INTRODUCTION

This article shows the theory and implementation of a force measurement-based approach to controlling workpiece diameter in cylindrical grinding. A simple model proposed by Chen et al. is used to relate infeed velocity to grinding force. The model is extended here to accurately predict the amount of material removed in OD plunge grinding given the normal force, which may be monitored in real-time. The model gives rise to a time constant that is a function of the structural loop stiffness, the infeed velocity, and the wheel and workpiece properties. This time constant may be measured during grinding to characterize the lag between infeed and stock removal. Once determined, the removal of stock can be predicted using force feedback. This allows very accurate diameter control (0.25 μm of nominal), even in the presence of thermal drift, wheel wear, and machine error.

MODEL VERIFICATION

The theoretical model outlined above may be verified experimentally using equipment that is introduced in this section. The air bearing workpiece spindle is instrumented to measure the relative motion across the air gap between rotor and stator (Professional Instruments motorized 4R). Additional details may be found in Couey et al. [1].

In this work additional capacitance probes (Lion Precision C-23 with DMT-22 drivers) are used to measure the workpiece size reduction and machine infeed during grinding, as shown in Figure 1.

The grinding force, part size, and machine motion data are analog filtered with a Krohn-Hite Butterworth filter and digitized using a National Instruments PCI-6110E data acquisition card. All additional data processing is performed in post-processing including removal of the synchronous

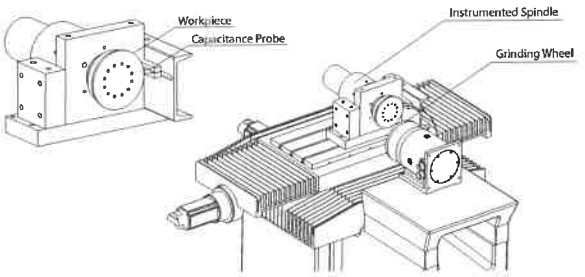

FIGURE 1. CNC base with testing configuration mounted. The instrumented spindle and workpiece are located on the table and the grinding wheel 4R BLOCK-HEAD® spindle is attached to the base. The inset showing the instrumented spindle notes the location of the rubber wiper and the external capacitance probe.

thrust plate form error and Yule-Walker low-pass filtering with a cutoff frequency of 25 undulations per revolution (upr). The software also corrects for thermal effects using a second-order curve fit.

After processing, the program converts the data to force units based upon the following experimentally-verified equation:

$$F_n = K_{eq} x \tag{1}$$

where

$$K_{eq} = \left(\frac{P_a}{P_{nom}}\right)^{0.4} \frac{K_t}{LR} \tag{2}$$

The Professional Instruments 4R spindle tilt stiffness rating is 4 lb/μin at 150 psi. During testing the air pressure is set at 110 psi. While the stiffness will decrease at a lower pressure, the relationship is not linear due to deflection of the spindle material; a spindle running at a higher pressure will have a larger air gap between rotor and stator, and a resultant diminishing return as the

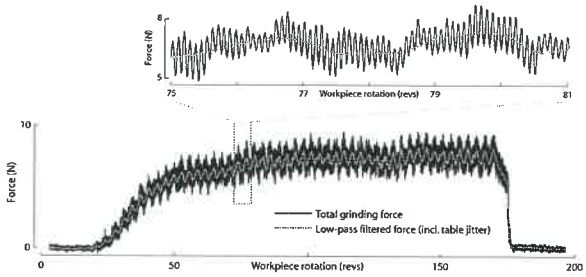

FIGURE 2. Comparison of the normal force data before and after aggressive wavelet filtering

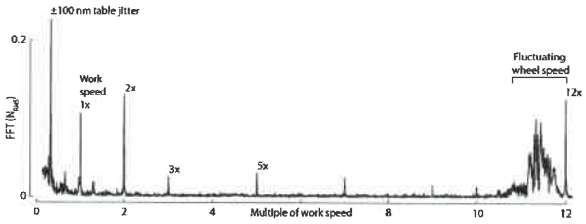

FIGURE 3. Discrete Fourier Transform of the normal force data prior to wavelet filtering with dominant grinding effects noted.

pressure goes higher. By plotting frequency response graphs for a 4R air bearing spindle under a range of air pressure settings and using a best-fit approximation to the dominant response mode, the relationship is roughly:

$$\omega_n = A \cdot {P_a}^{0.2} \tag{3}$$

where A is the natural frequency at 1 atm. This relationship leads directly to the equivalent stiffness shown in Equation 2, corrected for the nominal spindle pressure.

RESULTS

Wavelet filtering is the most appropriate choice for analyzing the grinding data because of its time-varying characteristics. Processing the normal grinding force shows several important attributes of the grinding process in Figure 2. The two effects that stand out most prominently are the overarching grinding force growth, and the higher-frequency, low-amplitude vibration superposed upon the former. The force fluctuation can be traced to machine feed axis jitter resulting from the low plunge infeed rate. In the inset plot showing a close-up of two revolutions, the repeatable higher-frequency force fluctuations that are synchronous with the grinding wheel speed are clearly visibly.

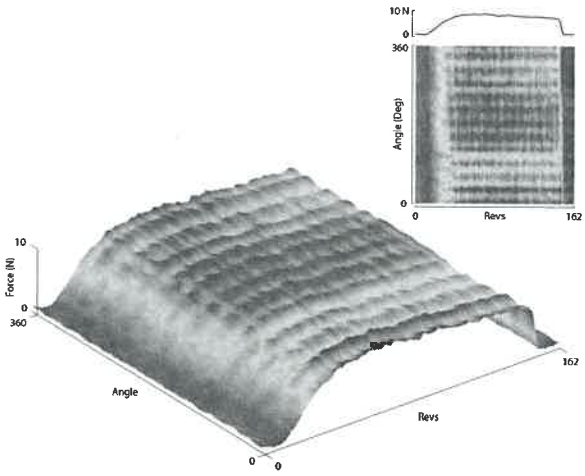

FIGURE 4. Normal grinding force F_n during one plunge cycle with 162 workpiece revolutions.

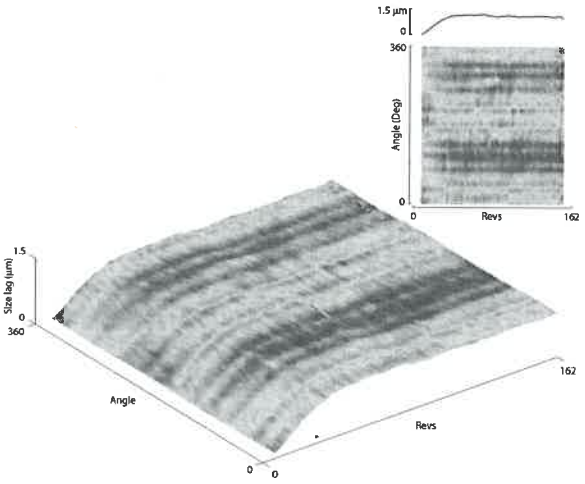

FIGURE 5. Lag between commanded infeed u and part diameter δ_w.

When plotted in the frequency domain after a fast Fourier transform, Figure 3 shows that the dominant effect (after the table jitter) occurs at approximately eleven times the workpiece speed. This represents the ratio $\frac{\omega_g}{\omega_w}$ between the wheel and workpiece rotation, with smearing from non-constant wheel rotation speed.

The force measurement alone yields very interesting conclusions, shown for one plunge cycle in Figure 4. The three-dimensional plot shows a lobed pattern throughout the grinding process. The approximately eleven-lobe pattern is caused by the relationship between the wheel and workpiece speeds. Places where the lobes appear to precess are caused by non-constant wheel and workpiece spindle motor speeds. At the begin-

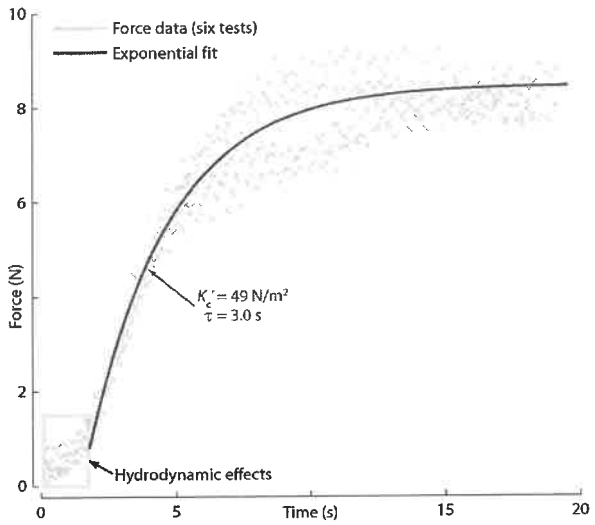

FIGURE 6. Comparison between the normal force model and the force measured during experimentation. Accuracy of the model improves with removal of the hydrodynamic effect observed just before grinding commences.

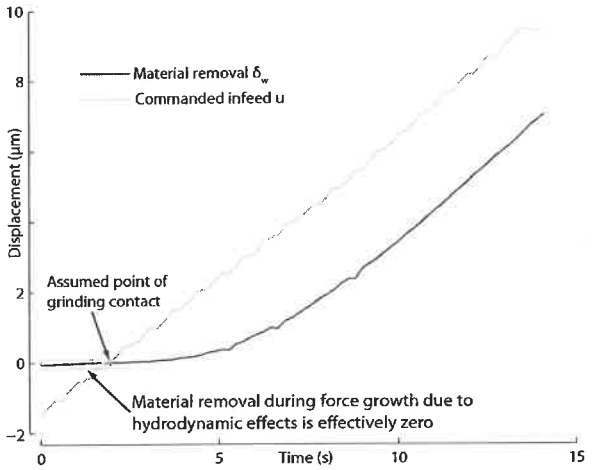

FIGURE 7. The force growth observed in Figure 6 results in no material removal, indicating that it is not a grinding effect.

ning of grinding contact, the shape of the workpiece is indirectly observable. For out-of-center parts, a single sinusoidal wave with a period equal to one revolution is apparent, while for parts that are centered but have some sort of form error, a higher-frequency wave is seen. In this case, the dominant eleven peaks show the dependence of part shape upon the relationship $\frac{\omega_g}{\omega_w}$.

Figure 5 shows a plot of the difference between the commanded infeed and the part removal during grinding, representing the amount by which the part removal lags the commanded infeed. The increasing magnitude shows the system compliance during spark-in, which eventually reaches its steady-state value. This view also validates Equation **??** by demonstrating the exponential relationship between u and δ_w. The two-lobe shape originally seen in Figure 3 as the dominant grinding frequency after the wheel-workpiece speed ratio, is seen as two darker bands on the surface of the plot.

Grinding Model Verification

The exponential force growth prediction is demonstrated with six sets of data, as shown in Figure 6. There is a slight discrepancy between the exponential force model and the measured data below approximately 0.5 N. This difference is thought to be the result of hydrodynamic effects, caused by the spinning workpiece and wheel and the slight gap (≈ 1.5 μm) just before contact, creating a pressurized air film. This theory is backed up by measurements in Figure 7, which shows material removal to be zero during the nonlinear period. When that region is neglected, the force model matches the measured values very well, with $K_c = 49$ GN/m^2 and $\tau = 3.03$ s. As a comparison, single-point turning of aluminum typically results in $K_c' = 1$ GN/m^2. K_c is directly related to the maximum force observed during grinding, while τ is a function of the system compliance. Note that these system attributes have little meaning during unstable grinding, as the force growth does not reach a constant value.

Verification of the accuracy of the assumed model then permits the application of the grinding algorithm described in the Introduction. The operator first measures the workpiece offline and determines the amount of material removal required to obtain the correct tolerance. This is only an intermediate step, since the operator does not know the moment at which grinding begins. The calculation of a threshold grinding force at which the part reaches the desired size allows easy process monitoring, so the grinding time is obtained using Equation **??** using the values of K_c and τ determined from initial system characterization. The normal force output is the point at which the operator will retract the part or begin spark-out, depending on surface finish requirements. Figure 8 shows this process graphically, comparing the grinding force model to the actual results as well as showing the error between the desired part size and the result.

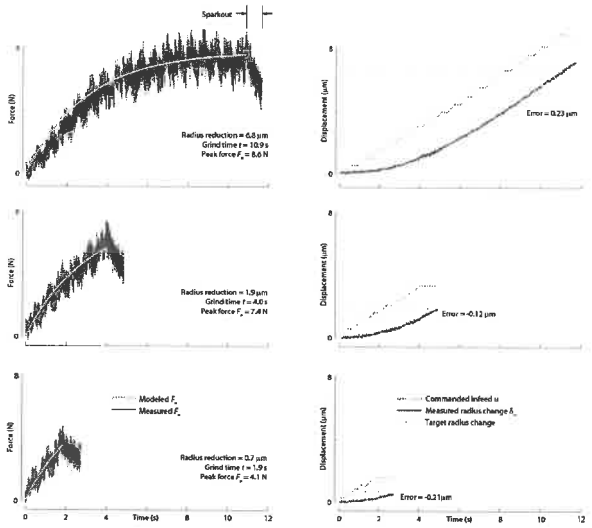

FIGURE 8. The operator determines the part radius reduction required to obtain the desired tolerance, which is then used to calculate the threshold normal force from the grinding time. Once the threshold force is reached the part can be immediately retracted. Comparison between the target radial change and the achieved are shown.

The force-dependent grinding algorithm works best for very small infeed depths. For depths which result in grinding forces approaching the steady-state value, small differences in the grinding force can result in gross part size errors. While a small force spike in the first few seconds of grinding might only result in a part error of a few tenths of a micrometer, once the force has stabilized it might cut several seconds off the process, causing several full micrometers of error. On the equipment used here, the process works best for infeed depths below 8 μm. With the accuracy and stiffness of modern machines, traditional methods can be employed to reduce the part size to within that amount, after which the finish pass can be performed.

CONCLUSION

Grinding is a complex process, and even slight changes in certain variables can drastically change the wheel-workpiece interaction. Real-time measurement of grinding forces and the part size change allow insight into the nature of the process, improving every facet of grinding technology. The grinding algorithm discussed in this paper allows repeatable creation of ground parts of the highest quality by characterizing the system with a few simple measurements and then monitoring the normal grinding force during in-process. This method reduces cost by improving yield and minimizing iterations to reach the desired part size. It works especially well for finish passes with low infeed rates. Lower-tolerance grinding applications can still get by with traditional iterative grinding methods. The point at which an operator should switch to the method described here is when the remaining material is less than the amount of machine compliance during operating conditions. As an added bonus, the instruments used to gather this data are nearly immune to the harsh environs of the industrial grinding sector.

REFERENCES

[1] J. A. Couey, E. R. Marsh, B. R. Knapp, and R. R. Vallance. Monitoring force in precision cylindrical grinding. *Precision Engineering*, 29 (3):307–314, 2005.

ANALYTICAL REPRESENTATION OF NANOSCALE PARASITIC MOTION IN FLEXURE-BASED ONE DOF TRANSLATION MECHANISM

Chinmaya B. Patil, S. V. Sreenivasan, and Raul G. Longoria
Mechanical Engineering Department
The University of Texas at Austin
Austin, Texas, USA

Abstract
Flexure-based compliant mechanisms are capable of meeting the demanding requirements of the partially constrained ultraprecision motion systems. However, the geometric errors induced by manufacturing tolerances can cause parasitic motion along the constrained directions, limiting the precision capability. Understanding parasitic motion at the nano-scale necessitates a 3-D model even for mechanisms that are designed to be planar. Analytical modeling of a flexure-based double compound rectilinear spring mechanism with one degree of freedom translation, for quantifying the nano-scale parasitic motion is presented here. A spatial kinematics based kinetostatic model, that systematically accounts for the geometric errors and enables estimation of the inherently spatial parasitic motion, is presented. A metric is defined to represent the intrinsic parasitic motion, and Monte Carlo simulation is used to estimate the standard deviation of the chosen metric. Further, the analytical model is used to investigate the influence of flexure joint compliance parameters on the parasitic motion of the mechanism. The simulation results indicate greater than 50% improvement in the precision capability of the mechanism by improved design of flexure joints, without changing the manufacturing tolerance limits.

INTRODUCTION

Flexure-based mechanisms form the foundation of motion guiding systems used for high precision positioning and scanning applications [1, 2]. Although they exhibit smooth continuous motion, are free from friction, and can be fabricated monolithically [3], their precision capability can be compromised by errors due to machining process variations. The geometric errors introduced in the mechanism by the machining tolerances can cause significant undesirable motion along the constrained directions, which is termed here as parasitic motion. Several researchers have addressed the problem of parasitic motion from the point of view of estimating the worst-case error motion for a given manufacturing tolerance limit [4, 5], or determining the probability of achieving specified precision requirement [6]. This article presents an analytical approach to characterize the parasitic motion induced by machining tolerances, and illustrates it using a one DOF notch type flexure-based double compound linear spring translation stage.

The proposed approach is based on spatial kinematics which employs 6 dimensional vectors called screws [7] to provide a minimal representation of the spatial motion of the mechanism. The modeling approach has been extensively applied in the area of robotics for compliance analysis, synthesis and control [8, 9]. The task-space compliance of the mechanism is represented by a 6×6 square matrix, and is determined in terms of the compliance of the individual flexure joints of the mechanism. The geometric errors due to tolerances are systematically incorporated into the model by treating them as normally distributed random variables. Based on the insight obtained from screw theory, the parasitic motion of the mechanism that cannot be corrected by calibration procedures is identified. A metric that quantifies this intrinsic parasitic motion of the mechanism is defined, and its statistical properties are estimated via Monte Carlo simulations of the model. The precision capability of the mechanism is compared for two different flexure joint designs, and up to 50% improvement is demonstrated without any change to the manufacturing tolerance values.

ANALYTICAL MODELING OF SPATIAL COMPLIANCE

The motion characteristic of a compliant mechanism is determined by its task-space compliance. Consider a wrench ${}^0\hat{\mathrm{f}}$ acting on the mechanism platform. The twist of motion of the platform ${}^0\hat{\mathrm{t}}$ is then given by,

$$ {}^0\hat{\mathrm{t}} = {}^0\mathbf{C} \cdot {}^0\hat{\mathrm{f}} \qquad (1) $$

where, ${}^0\mathbf{C}$ is the mechanism task space compliance matrix. The spatial quantities of the wrench

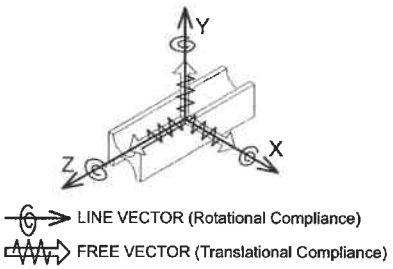

FIGURE 1. Compliance representation of a notch type flexure joint.

and twist can be represented in terms of a six dimensional, purely geometric entity called a unit screw as,

$$\begin{aligned} {}^0\hat{\mathrm{t}} &= {}^0\hat{\$} \cdot \theta = \begin{bmatrix} \underline{\theta} \\ \underline{\delta} \end{bmatrix} \rightarrow \text{twist} \\ {}^0\hat{\mathrm{f}} &= {}^0\hat{\$} \cdot f = \begin{bmatrix} \underline{\mathrm{f}} \\ \underline{\mathrm{m}} \end{bmatrix} \rightarrow \text{wrench} \end{aligned} \tag{2}$$

Here, θ and f are the scalar physical quantities representing displacement and force, respectively. The unit screw is represented by a 6×1 vector in some reference frame 0 as,

$${}^0\hat{\$} = \begin{bmatrix} \underline{\mathrm{w}} \\ \mathrm{h} \cdot \underline{\mathrm{w}} + \underline{\rho} \otimes \underline{\mathrm{w}} \end{bmatrix} \tag{3}$$

where, $\underline{\mathrm{w}}$ is a 3×1 unit vector defining the screw orientation, and $\underline{\rho}$ is a 3×1 vector defining the screw location in the reference frame 0, and h is a scalar quantity, called pitch of the screw. $\otimes$ represents the vector cross product operation.

In spatial kinematics, a spring can be completely defined by means of a unit screw describing its geometry, and a scalar compliance to quantify its elastic properties, and the joint compliance matrix **C** is defined as,

$${}^0\mathbf{C} = {}^0\hat{\$} \cdot \mathrm{c} \cdot {}^0\hat{\$}^{\mathrm{T}} \cdot \Delta \tag{4}$$

A flexure joint can be modeled as a linear combination of six springs, three rotational and three translational, located at centroidal axes of the joint [10]. Thus six unit screws, aligned with the principal coordinate frame of a flexure joint, and associated with rotational and translational scalar compliance values respectively, completely describe the compliance of the joint. This is shown in Figure 1 for a notch type flexure joint.

An expression to determine the task space compliance of the mechanism, in terms of the joint compliance matrices is presented next. Figure 2 shows schematic of the one DOF translation mechanism with the serial and parallel connection of the joints from the platform to the fixed frame. The compliance matrix of two joints in series and parallel connection respectively, in terms of the individual joint compliance matrices, is given by,

$$\begin{aligned} {}^0\mathbf{C}_{1,2} &= {}^0\mathbf{C}_1 + {}^0\mathbf{C}_2 \\ {}^0\mathbf{C}_{1-2} &= {}^0\mathbf{C}_1 \cdot \left({}^0\mathbf{C}_1 + {}^0\mathbf{C}_2\right)^{-1} \cdot {}^0\mathbf{C}_2 \end{aligned} \tag{5}$$

Therefore, the compliance of each limb is the sum of the compliance matrices of the two joints that make up the limb, i.e.,

$${}^0\mathbf{C}_1 = {}^0\mathbf{C}_{11} + {}^0\mathbf{C}_{12} \tag{6}$$

where, ${}^0\mathbf{C}_{11}$ is the inner and ${}^0\mathbf{C}_{12}$ is the outer flexure joints of limb 1. Then, the compliance of the outer and inner parallel chains, '1-2' and '3-4', respectively, are found as,

$$\begin{aligned} {}^0\mathbf{C}_{1-2} &= {}^0\mathbf{C}_1 \cdot \left({}^0\mathbf{C}_1 + {}^0\mathbf{C}_2\right)^{-1} \cdot {}^0\mathbf{C}_2 \\ {}^0\mathbf{C}_{3-4} &= {}^0\mathbf{C}_3 \cdot \left({}^0\mathbf{C}_3 + {}^0\mathbf{C}_4\right)^{-1} \cdot {}^0\mathbf{C}_4 \end{aligned} \tag{7}$$

Then, the compliance of the symmetrical chain '1-4' is simply found as,

$${}^0\mathbf{C}_{1-4} = {}^0\mathbf{C}_{1-2} + {}^0\mathbf{C}_{3-4} \tag{8}$$

Similarly, the compliance of the other three symmetrical chains, namely, ${}^0\mathbf{C}_{5-8}$, ${}^0\mathbf{C}_{9-12}$, and $\mathbf{C}_{13-16}$ can be found. Since the symmetrical chains are in parallel, the task-space compliance of the mechanism is then given by,

$$\begin{aligned} {}^0\mathbf{C}_{1-8} &= {}^0\mathbf{C}_{1-4} \cdot \left({}^0\mathbf{C}_{1-4} + {}^0\mathbf{C}_{5-8}\right)^{-1} \cdot {}^0\mathbf{C}_{5-8} \\ {}^0\mathbf{C}_{9-16} &= {}^0\mathbf{C}_{9-12} \cdot \left({}^0\mathbf{C}_{9-12} + {}^0\mathbf{C}_{13-16}\right)^{-1} \cdot {}^0\mathbf{C}_{13-16} \\ \Rightarrow {}^0\mathbf{C} &= {}^0\mathbf{C}_{1-8} \cdot \left({}^0\mathbf{C}_{1-8} + {}^0\mathbf{C}_{9-16}\right)^{-1} \cdot {}^0\mathbf{C}_{9-16} \end{aligned} \tag{9}$$

In order to analyze the influence of machining tolerances on the mechanism motion, they are systematically included into the mechanism compliance formulation as below. The geometric errors induced by the tolerances [4] introduce variation in the location and orientation of the joint screws. The geometric errors can be modeled as spatial displacement between the principal coordinate frame of the joint and an intermediate reference frame which coincides with the ideal joint position in the mechanism. In spatial kinematics,

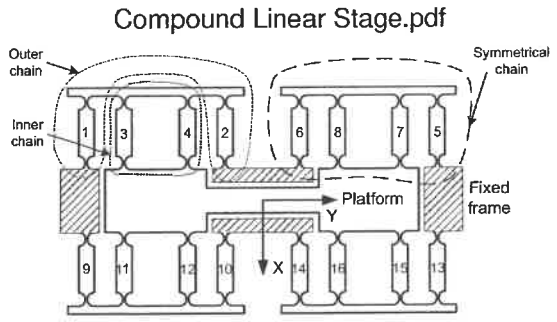

FIGURE 2. Schematic representation of one DOF translation stage.

displacement is represented by a spatial transformation matrix, which for the geometric errors is given by,

$$ {}^{1}\mathbf{X}_{\mathrm{G}} = \begin{bmatrix} \mathbf{R}\left(\underline{\phi}\right) & \mathbf{0} \\ \left(\underline{\gamma}\otimes\right)\cdot\mathbf{R}\left(\underline{\phi}\right) & \mathbf{R}\left(\underline{\phi}\right) \end{bmatrix} \qquad (10) $$

where, $\underline{\gamma} = [\gamma_{\mathrm{x}}\ \gamma_{\mathrm{y}}\ \gamma_{\mathrm{z}}]^{\mathrm{T}}$ are the location errors, and $\underline{\phi} = [\phi_{\mathrm{x}}\ \phi_{\mathrm{y}}\ \phi_{\mathrm{z}}]^{\mathrm{T}}$ the orientation errors of the joint screws.

The expression for the joint screws in the global reference frame is then given by,

$$ {}^{0}\hat{\$} = {}^{0}_{1}\mathbf{X}\cdot{}^{1}\hat{\$} = {}^{0}_{1}\mathbf{X}\cdot{}^{1}\mathbf{X}_{\mathrm{G}} \qquad (11) $$

where, ${}^{0}_{1}\mathbf{X}$ represents the spatial transform from the local joint frame '1' to the global reference frame '0'. The task-space compliance matrix of the mechanism is determined as before with this new joint screw expression.

PARASITIC MOTION ANALYSIS

The above modeling approach is applied to determine the spatial motion characteristics of the one DOF translational mechanism. The dimension L is chosen as 0.05m. An external force of 10N is applied along the Y axis. The rotational (cx, cy, cz) and translational (cX, cY, cZ) scalar compliance parameters of the flexure joint are given in Equation 12.

$$ \begin{array}{ll} \mathrm{cx} = 6.03\times10^{-4} & \mathrm{cX} = 8.81\times10^{-9} \\ \mathrm{cy} = 2.17\times10^{-5} & \mathrm{cY} = 2.45\times10^{-7} \\ \mathrm{cz} = 1.56\times10^{-1} & \mathrm{cZ} = 3.95\times10^{-8} \end{array} \qquad (12) $$

The units of the rotational and translational compliances [rad/N-m], and [m/N], respectively. It is found that, in the absence of any geometric errors, the mechanism exhibits pure translation along Y axis. However, the parameters of the twist of motion for random geometric errors with tolerance values of $\sigma_{\phi} = 3\mathrm{mrad}$, $\sigma_{\gamma} = 33\mu\mathrm{m}$ is found to be,

$$ \underline{\mathrm{w}} = \begin{bmatrix} -0.286 \\ -0.958 \\ -0.002 \end{bmatrix}, \underline{\rho} = \begin{bmatrix} 0.303 \\ -0.025 \\ -28.48 \end{bmatrix}[\mathrm{m}], \qquad (13) $$

$$ \theta = 4.34\times10^{-7}[\mathrm{rad}], \mathrm{h} = -95.45[\mathrm{m/rad}] $$

The values predicted by the model is within 5% of that obtained from finite element analysis results, carried out using COSMOSWorks Linear Solver.

From the properties of the twist of motion of the mechanism, it can be inferred that the parasitic motion of the mechanism occurs due to two reasons, firstly, the orientation of the twist vector not coinciding with the desired direction of motion (Y-axis), and secondly, the rotation θ associated with the motion. The error in the orientation of the twist vector of the platform motion can be corrected by calibration. However, the rotation associated with the motion cannot be reduced by calibration as it is linearly related to the desired mechanism translation, and therefore constitutes the intrinsic parasitic motion of the linear stage.

A metric to quantify the intrinsic parasitic motion and enable comparison of performance of the 1-DOF translation mechanisms is defined by considering the rotation of the mechanism for unit translation, as,

$$ \mathrm{m} = \frac{\|\underline{\theta}\|}{\|\underline{\delta}\|} \qquad (14) $$

Due to the statistical nature of the geometric errors induced by machining tolerances, the metric m is a random variable, and its statistical moments are estimated via Monte Carlo simulation. With 10^4 sample-size, the metric is found to be Normally distributed, having a standard deviation of 1.9907×10^{-2} rad/m. This means that, if the travel range of the 1 DOF translation stage is 50μm, the standard deviation of the rotation of the platform is $\left(1.997\times10^{-2}\right)\times\left(50\times10^{-6}\right)\approx1\mu\mathrm{rad}$. Thus a 3σ precision capability of the mechanism, measured as translation along constrained directions of X and Z axis at any point located 0.05m from the platform center, will be $3\times\left(5\times10^{-2}\right)\times\left(1\times10^{-6}\right) = 150\mathrm{nm}$.

INFLUENCE OF JOINT COMPLIANCE

The parametric compliance model can also be used to study the influence of various system parameters on the intrinsic parasitic motion of the mechanism. To investigate the influence of joint

compliance on parasitic motion, the above analysis is repeated for another notch type flexure joint with slightly modified joint compliance values, as listed in Equation 15. The compliance values of the new joint, termed design 2, are chosen such that the terms cx and cy (which are the compliance along the constrained directions for the flexure joint) are smaller than the corresponding values of joint design 1 by an order of magnitude. The compliance about the sensitive axis of the joints, cz, is kept the same as that of design 1, in order to the linear travel of the mechanism the same.

$$\begin{array}{ll} \mathrm{cx} = 7.80 \times 10^{-5} & \mathrm{cX} = 8.81 \times 10^{-9} \\ \mathrm{cy} = 7.80 \times 10^{-6} , & \mathrm{cY} = 2.45 \times 10^{-7} \\ \mathrm{cz} = 1.56 \times 10^{-1} & \mathrm{cZ} = 3.95 \times 10^{-8} \end{array} \quad (15)$$

The value of the metric for the second joint design is found to be 3.125×10^{-2} mrad/m. For a translation requirement of 50μm, a 3σ precision capability of the mechanism, measured as translation along constrained directions of X and Z axis at any point located 0.05m from the platform center, is $\approx$ 235nm. Thus, although the second joint design offers greater stiffness along constrained directions, the precision capability of the first joint design is better by $\approx$ 55%. The improvement with using joint compliance design 1 is realized without any changes to the manufacturing tolerances, and therefore at no additional cost. The two joint used in the analysis were designed in a heuristic manner. Further improvement can be expected by applying systematic robust optimization techniques to design the flexure joints.

CONCLUSIONS

Analytical modeling of flexure-based selectively compliant mechanisms for quantifying the nanoscale parasitic motion was presented. The task-space kinetostatic model based on screw systems systematically includes the geometric errors induced by manufacturing tolerances, and determines the spatial motion characteristics of the mechanism. The model was applied to a flexure based 1-DOF translation mechanism. Analysis of the mechanism parasitic motions provided the insight that the intrinsic mechanism errors cannot be minimized by calibration. A metric to quantify the intrinsic parasitic motion of the mechanism was defined, and its value was estimated using Monte Carlo simulation by propagating the variance of the geometric errors through the compliance model. Finally, the metric is determined for the mechanism with an alternative flexure joint design, to demonstrate the influence of the joint compliance values. Simulation results prove that parasitic motion can be significantly reduced by appropriate design of flexure joint compliance without requiring costly changes in manufacturing tolerance levels.

REFERENCES

[1] Choi BJ, Sreenivasan SV, Johnson S, Colburn M, Wilson CG. Design of orientation stages for step and flash imprint lithography. Precision Engineering. 2001;25(3):192–199.

[2] Choi KB, Kim DH. Monolithic parallel linear compliant mechanism for two axes ultraprecision linear motion. Review of Scientific Instruments. 2006;77(6):065106–7.

[3] Smith ST. Flexures: Elements of Elastic Mechanisms. 1st ed. CRC Press; 2000.

[4] Ryu JW, Gweon DG. Error analysis of a flexure hinge mechanism induced by machining imperfection. Precision Engineering. 1997;21:83–89.

[5] Niaritsiry TF, Fazenda N, Clavel R. Study of the sources of inaccuracy of a 3-DOF flexure hinge-based parallel manipulator. In: IEEE International Conference on Robotics and Automation. New Orleans, LA: IEEE; 2004. p. 4091–4096.

[6] Huh JS, Kim KH, Kang DW, Gweon DG, Kwak BM. Performance evaluation of precision nanopositioning devices caused by uncertainties due to tolerances using function approximation moment method. Review of Scientific Instruments. 2006;77(1):015103–1–9.

[7] Davidson JK, Hunt KH. Robots and screw theory. Oxford University Press; 2004.

[8] Huang S, Schimmels JM. The eigenscrew decomposition of spatial stiffness matrix. Ieee Transactions on Robotics and Automation. 2000;6(2):146–156.

[9] Ciblak N, Lipkin H. Synthesis of stiffnesses by springs. In: ASME Design Engineering Technical Conferences. Atlanta, Georgia; 1998. p. 1–10.

[10] Dai JS, Ding X. Compliance Analysis of a Three-Legged Rigidly-Connected Platform Device. Journal of Mechanical Design. 2006;128(4):755–764.

EVALUATION OF MACHINE TOOL CONCEPTS UNDER FRICTION INFLUENCES

Sascha Weikert[1], Sergio Bossoni[1] and Konrad Wegener[1]
[1]Institute of Machine Tools and Manufacturing
Swiss Federal Institute of Technology
Zurich, Switzerland

ABSTRACT
The fundamental effects of friction on the positioning behavior of machine tools are demonstrated and discussed. The basic nature of tilt motions due to friction is explained. A rigid body approach is used for the investigation of the frictional effects which permits the efficient evaluation of the different conceptional influences, taking into account the elastic properties of the guide-way systems, the drives and the feedback system for the investigation of the resulting positioning accuracy. Due to the dependency of frictional effects on configuration, loads, temperature and wear the standard numerical compensation may not be sufficient.

INTRODUCTION
In order to achieve the required static, dynamic and thermal behavior of a machine tool a number of optimization tools have been developed in order to optimize the future machine tool. Components and drives are optimized using FEM or simulations in the time domain [1]. The changing requirements concerning productivity and developments in the area of the tools changed the focus of the research activities towards optimization of dynamic properties. The influences due to friction nowadays therefore tend to be overlooked. For the simulation, analysis and optimization of drive systems friction is taken into account via sophisticated friction models [2, 3]. Here, the main idea is to obtain the desired positioning or contouring behavior using various compensation approaches in order to overcome the influence of the strongly non-linear friction effects [4]. These models are always one-dimensional (1D) models. In some cases contouring performance in 2D is looked at by combining two of these 1D models geometrically. For the verification of the compensation methods encoder outputs are regarded, which do not show all components of movement at the tool center point (TCP).
A wide survey on the different factors of the physical friction effect itself is given in [4]. The range is spread from surface finish over lubricant viscosity and specific load to wear effects. It shows that these factors may have a strong influence on the magnitude of friction and therefore have to be taken into account when trying to compensate for them.
This paper discusses the fundamental mechanisms of multi-dimensional effects of friction on the positioning behavior using guideway-systems.

FRICTION EFFECTS ⇔ INERTIA EFFECTS
If drive forces and friction forces or inertia do not have the same center line of action torque loads orthogonal to the direction of motion are introduced into the system. This leads to rotatory displacements due to the finite rotary stiffness of the system. If the TCP is located with an offset to the axis of rotation, significant translatory displacements can occur. These effects can be seen for inertia [5] and for frictional forces.
FIGURE 1 shows the configuration parameters for inertia (above) and for friction (below) in 2D. The basic equations for both cases in 2D are given in (1) and (2). Regarding the magnitude of translatory displacements at the TCP the following factors have to be considered:

- Tilt-stiffness $k_{rot,A}$ of the linear guideway-system orthogonal to the direction of motion => offsets of the guideway elements ΔZ_i (quadratic influence!) and stiffnesses $k_{Y,i}$ and $k_{A,i}$ of the guideway elements (bearings e.g.) is relevant
- Offset from the center of gravity of the slide of the TCP ΔZ_{TCP} in the direction of motion.
- Offset of the inertia ΔY_{Fa} / friction ΔY_{Ff} from the driving force.
- Amount of inertia F_a / friction F_f forces due to acceleration, mass and friction coefficient.

$$EYZ_{inertia} = \frac{F_a \Delta Y_{F_a} \Delta Z_{TCP}}{k_{rot,A}} = \frac{M a \Delta Y_{F_a} \Delta Z_{TCP}}{\sum_i k_{Y,i} \Delta z_i^2 + \sum_i k_{A,i}} \quad (1)$$

$$EYZ_{fr.} = \frac{F_f(div) \Delta Y_{F_f} \Delta Z_{TCP}}{k_{rot,A}} = \frac{\mu(div) F_P \Delta Y_{F_f} \Delta Z_{TCP}}{\sum_i k_{Y,i} \Delta z_i^2 + \sum_i k_{A,i}} \quad (2)$$

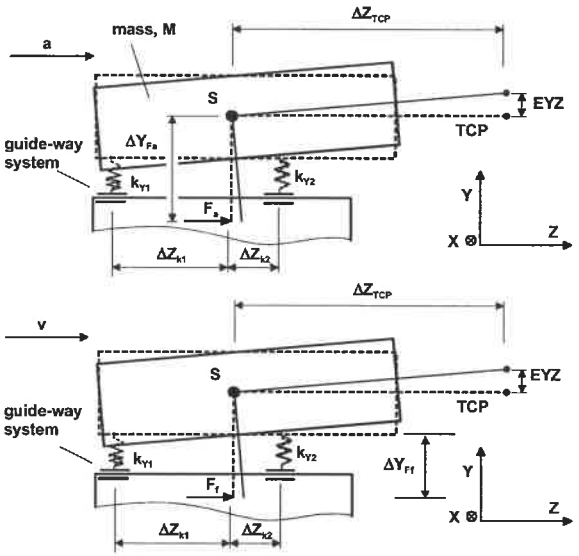

FIGURE 1. Schematic of the inertia (above) and friction (below) tilt effects on the TCP displacements

Regarding the friction case (eq. 2), the friction coefficient, depending on a diversity of factors such as preload, velocity, load, wear, viscosity of lubricant and time history of motion is the critical factor for compensational approaches.

Friction Model

For the 2D-case, as shown in Figure 1 the basic phenomenon is obvious. When a real machine has to be analyzed, a true 3D-case has to be looked at. For this, a rigid-body simulation is used which uses a multidimensional electro-mechanical model of the machine including drives and feed-back systems [6]. In order to investigate frictional effects on the TCP the following steps are carried-out:

- The deformations of the entire machine under gravity are calculated.
- Derivation of the loads on the guideway elements.
- Transforming the forces orthogonal to the direction of motion into a resulting axial force F_f in the opposite direction of the movement using the friction coefficient μ.
- Application of the force F_f on the system and calculation of resulting TCP displacements.
- If closed-loop control is used, the location of the position feedback system has to be taken into account.

The friction coefficient μ is chosen according to experience and theory [7]. When varying configuration parameters and regarding relative changes between the concepts it is shown, that the need for accurate values for μ is reduced.

MEASUREMENT EXAMPLES

The basic effects of tilt motions due to friction have been measured on a three axis machining centre being equipped with hydrodynamic guideways. The axis configuration, the measurement positions and the centers of friction are schematically shown in Figure 2. Depending on the x-position of the table the load on the y-axis guideways changes. Therefore the resulting center of friction changes depending on the actual x-position.

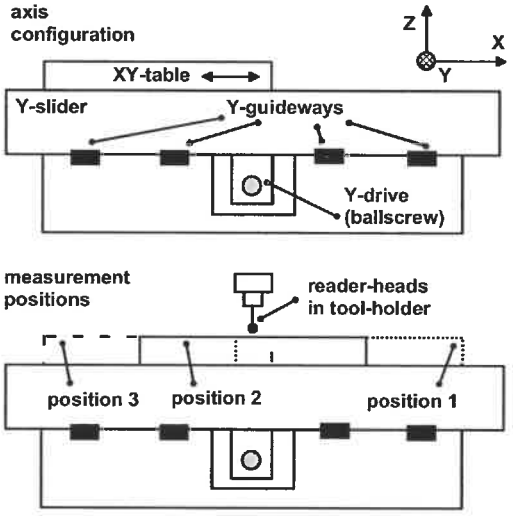

FIGURE 2. Axis configuration (above) and measurement positions (below)

MEASUREMENT SETUP

For the measurement of the displacements in x- y- and c-direction a measurement set-up consisting of a Heidenhain grid-plate and two reader-heads was used [6]. In contrast to [8] additional incremental probes for the measurement of z-, a- and b-displacements have been omitted in this case.

For the evaluation of the position dependent positioning behavior, a movement over 50mm in steps of 10mm has been carried out at the locations shown in Figure 2. As reference, the displacements at y=0 are used. The incremental movement over 50mm was repeated twice in a positive and a negative direction. Figure 3 shows the x-y-plot at a programmed speed of 50mm/min in Position 1 and the derived locations at standstill. Between the stops, systematic deviations of 2mm periodicity are visible which are caused by a mechanical periodicity in the drive.

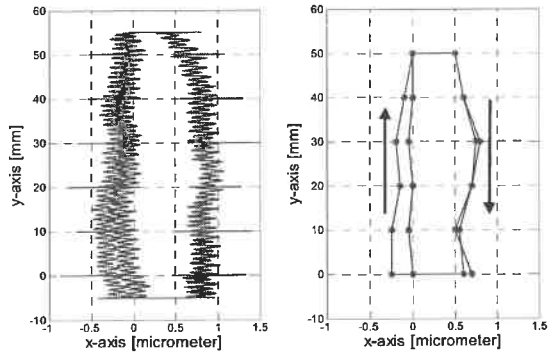

FIGURE 3. xy-plot of a positioning series, Pos.1, F 50mm/min; left: xy-plot; right: extracted positions at standstill (criterion used: y-velocity)

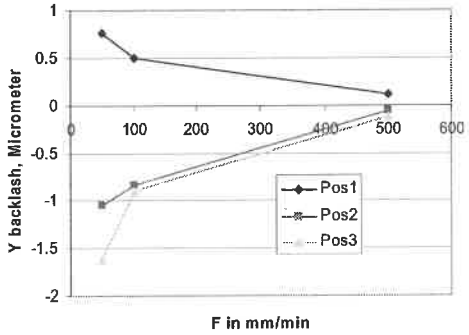

FIGURE 4. Averaged Values for backlash in y-direction for the different positions and feed rates

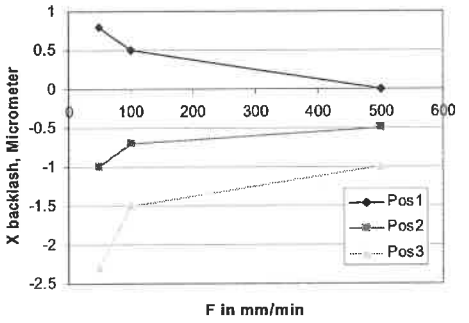

FIGURE 5. Averaged Values for backlash in x-direction for the different positions and feed rates

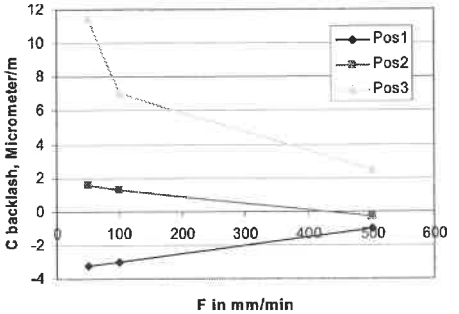

FIGURE 6. Averaged Values for backlash in c-direction for different positions and feed rates

Discussion

Depending on the measurement position significantly changing translatory motions are noticeable as shown in Figures 3 and 4. The lower the programmed feeds, the larger are the measured systematic backlash values. When changing from position 1 to 3 the direction of the effects changes. In order to distinguish inertial from frictional effects, the displacement values occurring at standstill are used (see Figure 3). Due to the low-pass behavior of the drives the actual accelerations for the measurements at 50, 100 and 500mm/min were 0.12, 0.15 and 0.4m/s^2 respectively. Therefore frictional effects should dominate at low feeds. The averaged backlash values in y- and x-direction (Figure 4 and 5) do correlate with those measured in c-direction (Figure 6). In Figure 7 the change in sign of the c-rotation depending on the measurement position is explained.

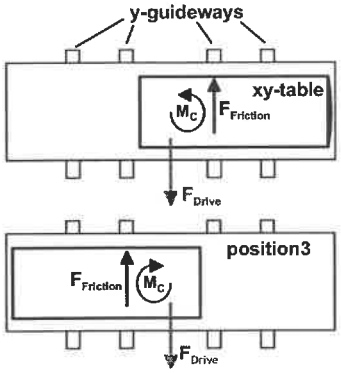

FIGURE 7. Drive and friction force and the resulting torque, pos.1 and 3, movement in positive y-direction

In the example a change in the configuration leads to a change in the friction effects. In addition to this, changing offsets in cantilever configurations may have to be taken into account, which may cause an additional position dependency.

In the case shown the basic backlash compensation based on measurements obtained close to position 2 only is obviously not capable to handle the strongly varying effects.

SIMULATION EXAMPLE

Following the procedure described above, the positioning behavior of a cantilever axis configuration is analyzed. The lateral stiffness of the guideway elements is assumed to be 600N/µm, the friction coefficient is set to 2.5%, and the moving mass is set to 1600kg. Figure 8 shows

the machine configuration. Three cases of feedback shall be compared:

- 1: closed-loop, linear scale at y=0mm
- 2: closed-loop, linear scale at y=1000mm
- 3: open-loop, no linear scale.

A set of 5 positions in X-direction is analyzed. Figure 9 shows the results for positive and negative directions of motion evaluated similar to ISO230-2 [9].

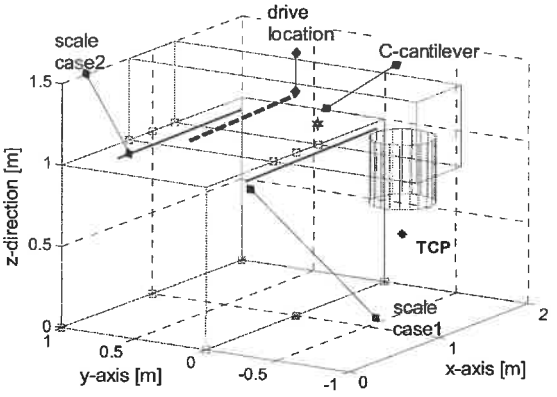

FIGURE 8. Machine configuration. The drive location and the locations of the linear scales for the closed loop cases are shown.

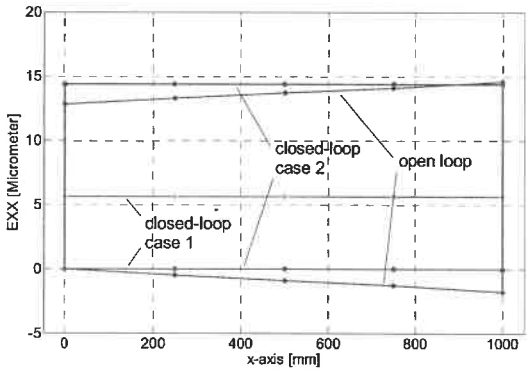

FIGURE 9. Positioning errors for open-loop and the two-closed loop cases, no compensation.

Discussion

As can be seen in Figure 9 a closed-loop configuration may be inferior to an open-loop configuration, when the location of the scale is chosen inappropriately. The positioning deviations shown are achieved without compensations. When this option is used only the changes of the TCP between the calibration and the actual values remain. These changes may be caused by temperature, load and the parameters of movement. For the general investigation of the friction influences the simulation offers an efficient possibility.

CONCLUSION

Frictional and inertial forces lead to similar effects on the TCP. Measurements show the dependency of frictional effects on the configuration and again the important role of tilt motions. Especially at very low feeds frictional effects can be large. Systematic effects could also be analyzed using rigid-body simulation. In this way, the interaction of the friction and the actual configuration on the resulting TCP-deviations can be investigated. Together with the analysis of machine tool concepts with respect to dynamic and static properties a full picture of the future machine tool is available.

REFERENCES

[1] Zirn 0, Weikert S. Modellbildung und Simulation hochdynamischer Fertigungssysteme. 2006, Springer Verlag

[2] Birchall T M, Kearney G P, Moss A J. Studies of friction and lubrification of machine tool slideways. Int. Jour. of Machine Tools Design Research. 1962, Vol.2, 317-331

[3] Tjahjowidodo T, Al-Bender F, Van Brussel H and Symens W. Friction characterization and compensation in electro-mechanical systems, Journal of Sound and Vibration (2007)

[4] Armstrong H B, Dupont P, Canudas De Wit A. A survey of models, analysis tools and compensation methods for the control of machines with friction. Automatica. 2001, 30/7. 1083-1138

[5] Rehsteiner F, Weikert S, Rak Z. Accuracy Optimization of machine tools under acceleration loads for the demands of high-speed-machining. Proc. of the 1998 Annual Meeting of ASPE, St. Louis, USA,1998, 602-605

[6] Weikert S. Beitrag zur Beurteilung des dynamischen Verhaltens von Werkzeugmachinen. 2000, PhD.-Thesis, ETH Zurich

[7] Yukeng H, Darong C, Linqing Z. Effect of surface topography of scraped machine tool guideways on their tribological behaviour. 1985, Vol.18 No.2, 125-129

[8] Knapp W, Weikert S. Six-dimensional contouring performance. Annals of the CIRP. 1999, 47/1. 363-366

[9] ISO 230-2, Test Code for machine tools - Part 2: Determination of accuracy and repeatability of positioning numerically controlled axes, Geneva, 1997

SUB-MICROKELVIN PRECISION THERMAL CONTROL SYSTEM USING MODEL PREDICTIVE ALGORITHM FOR LASER INTERFEROMETER SPACE ANTENNA GROUND VERIFICATION FACILITY

Sei Higuchi[1], Daniel B. DeBra[1], and Steve Rock[1]
[1]Department of Aeronautics and Astronautics
Stanford University
Stanford, CA, U.S.A.

INTRODUCTION

Laser Interferometer Space Antenna (LISA) aims to detect directly gravitational waves from massive black holes and galactic binaries. LISA is essentially a massive Michelson interferometer placed in space with a third spacecraft added. In Einstein's theory of general relativity, the gravity is due to curvature of spacetime, which is caused by the presence of massive objects. The gravitational waves are ripples in spacetime. As the waves reaching to the vicinity of the Earth pass through the LISA spacecraft, the fractional change in interferometer arm length can be as small as $10^{-21}\ m/m\sqrt{Hz}$ even for the powerful sources. LISA will monitor fractional changes in the light-travel times across arms of a nominally 5 million km. For this reason LISA requires gravitational reference sensors (GRS) for drag-free control [1] and will achieve the required sensitivity through minimizing spurious forces (non-gravitational-wave force), which come from both the environment and the spacecraft themselves. The total acceleration disturbance to each proof mass, which floats at the center of GRS, is required to be below $3 \times 10^{-15}\ m/s^2\sqrt{Hz}$. Optical path length variations on each optical bench must be kept below $40\ pm/\sqrt{Hz}$ [2]. The job of the spacecraft is to shield an internal proof mass that falls freely, not attached to the spacecraft, from external disturbances.

Several sources contribute to the disturbances including magnetic force, cosmic rays, temperature fluctuations, residual gas pressure, and sensor disturbance [2]. This presentation focuses on minimizing the effects of thermal disturbances to the proof-mass (PM). Thermal effects seem to be an innocent problem to manage. However, limited thermal mass of the spacecraft and relatively low frequency range, they calls for active compensation mechanism to satisfy the requirements particularly at low frequency range. P. L. Bender [3] claims that the passive thermal isolation clearly will become worse at frequencies substantially below $0.1\ mHz$ and suggests the need of active temperature control systems as well as larger gaps around the proof-mass: the current nominal gap size between PM and S/C is $2\ mm$. The modular GRS (MGRS) has been proposed by the team from Stanford University with the suggested gap size of a few cm [4].

Thermal disturbances due to, for example, solar irradiation, or temperature gradients across the proof mass housing is expected to be significant disturbance source to the LISA sensitivity requirements of $\Delta T < 30\ \mu K/\sqrt{Hz}$ over $0.1\ mHz$ to $1\ Hz$. Even a small temperature gradient can produce distortions in the housing structure, which results in a change in the mass attraction force [5]. Temperature fluctuations also cause radiometer effects with residual gas pressure as well as the net thermal radiation pressure.

Designing an active control system compensating low-frequency disturbance input is extremely challenging. First of all, the temperature stability requirement is significantly tighter compared to other types of thermal control requirements. The temperature profile of the spacecraft must be uniform to the order of $10^{-5}\ K/\sqrt{Hz}$ both temporally and spatially. Another challenging factor is the time-delay. The Smith-predictor [6] is a major control scheme that compensates time-delay. Because we are also interested in spatial temperature profile, the control system is required to manage multiple outputs as well as multiple inputs in the presence of constraints. Thus, the model predictive control (MPC) scheme is mainly discussed in this paper even though some of the experimental results were obtained through the Smith-predictor scheme.

We have developed a thermal control system for

LISA GRS. For ground testing, the LISA specification can be met fairly readily with massive amount of insulation and thermal mass. Since the ground testing facility is by extension suitable for in-flight thermal condition to compensate external forces, the test facility is designed to be analogous to the spacecraft structure. Continuing development of control algorithm and improvement of measurement resolution will extend performance to below than LISA coverage of super massive black hole mergers.

EXPERIMENTAL SYSTEM

Figure 1 shows a schematic figure of the experimental system. The various layers of insulation correspond in a rough way to the layers of thermal isolation provided by the LISA spacecraft design [7], although various adaptations were necessary to be consistent with resource availability. The

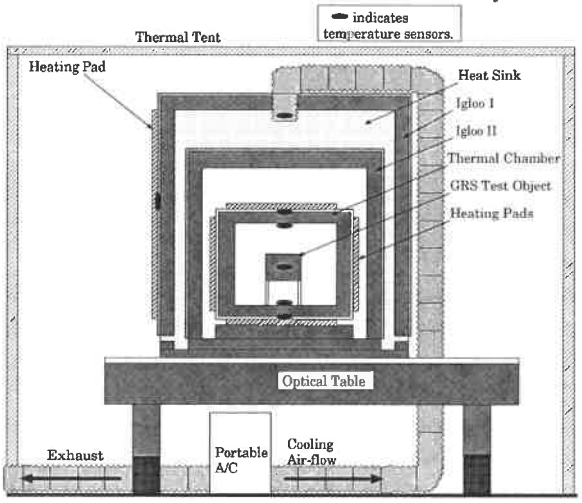

FIGURE 1. The schematic of the experimental system

GRS sensor test-object is placed in the center of a double walled thin metal thermal enclosure, analogous to the LISA internal shield. A precision thermistor monitors the test-object with ($< 100\ \mu K/\sqrt{Hz}$) noise. The enclosure is wrapped in flexible insulation, and wrapped again with copper foil. This coper foil surface corresponds roughly to the LISA Y-tube surface, and here is temperature controlled to high-precision by a heating-pad/thermocouple feedback system. Surrounding the enclosure and heater-pad apparatus is $2''$ of foil-covered polystyrene foam insulation, labeled igloo1 and igloo2, to create a sealed control volumes. The outer surface of igloo2 is maintained by a temperature regulated air-flow system which removes waste heat, simulating for space will be replaced with a cold radiator to deep space.

Six heating pads, our primary actuators, are driven with an AC power source. They are installed around the surfaces of thermal enclosure inside igloo2 and two are installed outside igloo1 to create artificial temperature disturbance inputs. Accordingly a variable controllable AC power supply is the most desired equipment. However, due to the limited availability, the experiment is being conducted utilizing a 24 Vac power source, the output level of which is fixed. Therefore, the control program first computes the numerical value of the heating pad temperature inputs (control signal) based on the desired final outputs and then sets as the value obtained as the reference track the reference of the control signal. Since the band width of the heating pad is significantly greater than that of the GRS, this scheme performs very well to emulate a smooth control input. Seven sensors are installed to measure the ambient temperature inside the thermal tent, the heating-pad temperatures, temperatures inside double-walled enclosure and the GRS test-object. Finally, the entire system is placed within a clear plastic thermal tent, primarily to cut down on air drafts.

A typical time history of the ambient and GRS test-object temperature is shown in Figure 2. The data was acquired without control authority and reveals significant coupling between the ambient and the GRS temperatures. Although the system has multiple layers of thermal insulation, the GRS test-object temperature is still varying roughly $\pm 0.2\ K$, which is obviously too large fluctuation for the LISA requirement, $30\ \mu K/\sqrt{Hz}$.

PLANT MODEL

The physical plant is modeled as a combination of a second-order system plus a single time-delay element. The model parameters are fitted empirically using least-square and MATLAB simulations. Our plant model with p inputs and q outputs is expressed in a state-space model.

$$\begin{aligned} x(k+1) &= Ax(k) + Bu(k-h) \\ y(k) &= Cx(k) + \zeta(k) \end{aligned} \qquad (1)$$

where x is the n-dimensional state vector, u is the p-dimensional control input vector, h is the time-delay, w is the disturbance vector, ζ is the q-dimensional measurement noise vector, A, B, and C are system matrices with dimensions $n \times n$, $n \times n$, $n \times p$, $n \times 1$, and $q \times n$, respectively.

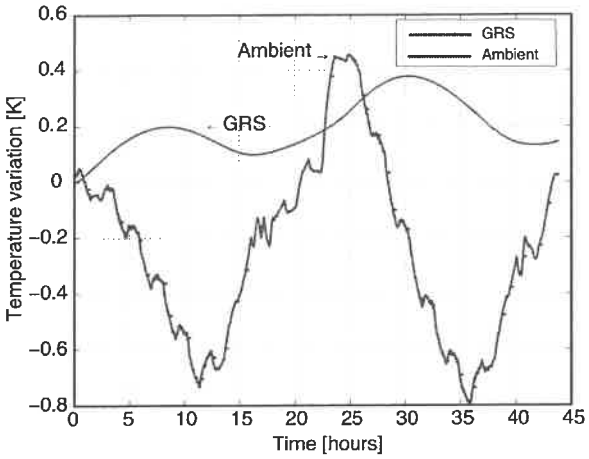

FIGURE 2. Time history of typical daily temperature variation

MODEL PREDICTIVE CONTROL

In this section, a MPC control law is developed for a general case of MIMO LTI systems. Figure 3 represents the control block diagram of the entire system. Feedback and feedforward control loops

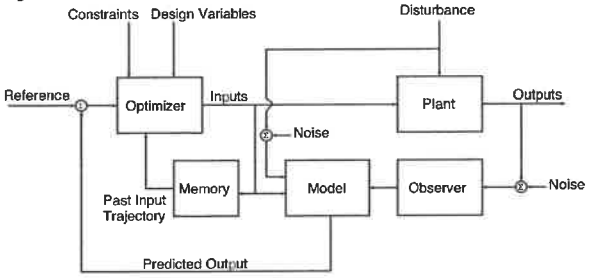

FIGURE 3. Control system block diagram

are formulated. The optimizer minimizes the cost function given by

$$J(k) = ||Y_d(k) - Y(k)||^2_{\hat{Q}} + ||\Delta U(k)||^2_{\hat{R}} \quad (2)$$

where $Y_d(k)$ is the $H_p \times q$-dimensional reference trajectory, $Y(k)$ is the predicted outputs, $\Delta U(k)$ is the $H_p \times p$-dimensional input sequence, $\hat{Q}$ and $\hat{R}$ are the weighting matrices. In order to compute the optimal control input by minimizing the cost function, predicted outputs need to be computed over the prediction horizon, H_p. The predicted outputs is given by

$$\begin{aligned} Y(k) &= G(A - KC)x(k) + GKy(k) \\ &+ F_1 U_p(k) + F_2 \Delta U(k) \end{aligned} \quad (3)$$

where, K is the observer gain, $G = [C, CA, \cdots, CA^{h+H_p}]^T$, $U_p(k) = [u(k-h), \cdots, u(k-1)]^T$ past input trajectory,

$$F_1 = \begin{bmatrix} CB & & & 0 \\ \vdots & \ddots & CB & 0 \\ CA^{h-1}B & \cdots & CAB & B \\ \vdots & & & \vdots \\ CA^{h+H_p}B & \cdots & CA^{H_p+2}B & \sum_{i=0}^{p+1} CA^iB \end{bmatrix}$$
$$\in \Re^{(h+H_p+1)q \times hp}$$

and

$$F_2 = \begin{bmatrix} 0 & \cdots & & 0 \\ \vdots & \ddots & & \vdots \\ CB & \ddots & & \vdots \\ CAB + CB & \ddots & & \vdots \\ \vdots & \ddots & 0 & 0 \\ \sum_{i=0}^{p} CA^iB & & CAB + CB & CB \end{bmatrix}$$
$$\in \Re^{(h+H_p+1)q \times (H_p+1)p}$$

Using Eq.(3), the cost function can be expressed as a function of $\Delta U(k)$.

$$J(k) = \Delta U^T(k) H \Delta U(k) + 2b\Delta U(k) \quad (4)$$

where

$$\begin{aligned} H &= F_2^T \hat{Q} F_2 + \hat{R} \\ b &= E_k^T \hat{Q} F_2 \\ E_k &= Y_d(k) - G(A - KC)x(k) - GKy(k) - F_1 U_p(k) \end{aligned}$$

Note that the constant term in Eq.(4) is omitted.

If no specific constraints is specified, the optimal input $\Delta U(k)$ is given by the least-square solution that minimizes the cost function Eq.(4).

$$\Delta U(k) = H^{-1} F_2^T \hat{Q} E_k \quad (5)$$

Otherwise, if constraints are present, the solution is given by quadratic programming. In order to add feedforward action to the controller, the internal model includes a dynamics of sinusoidal disturbance temperature, which is given by

$$\begin{aligned} x_d(k+1) &= A_d x_d(k) \\ w(k) &= C_d x_d(k) + \zeta_d(k) \end{aligned}$$

Moreover, the actual cost function account for the estimate of disturbance effect that is given by

$$d_{est}(k) = y_{plant}(k) - y_{model}(k) \quad (6)$$

and then the cost function is finally expressed by modifying the E_k:

$$E_k = Y_d(k) - G(A - KC)x(k) - GKy(k) - F_1U_p(k) - d_{est}\vec{1} \quad (7)$$

where $\vec{1} \in \Re^{(h+H_p+1)q\times 1}$. The weighting matrices $\hat{Q}$, $\hat{R}$, and the prediction horizon H_p are chosen so that the control law Eq.(5) is stabilized.

RESULTS

Figure 4 demonstrates the portion of 30-day simulation of the temperatures measured at the sensors together with the heating pad (input) and the ambient temperature (disturbance). The temperate is maintained approximately $\pm 25\ \mu K$ over 30-day observation. As the daily ambient temperature cycles in 24 hours, the GRS is still affected by such a low frequency signal ($\sim 10^{-5}\ Hz$). During the simulation, the disturbance temperature was modeled as a sum of three sinusoidal waves, $d(t) = \sum_{i=1}^{3} A_i \sin(\omega_i t + \phi_i)$. The mean squared

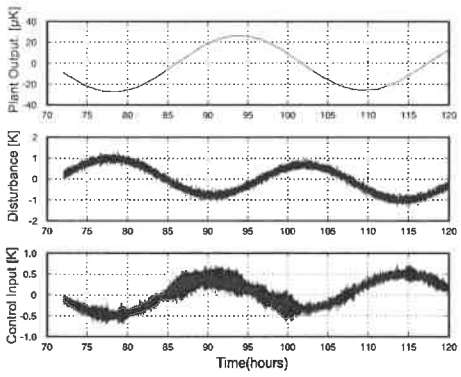

FIGURE 4. Time history of the GRS test-object, control input, and disturbance temperature

power spectral density of temperature variations of the GRS test-object as well as some experimental data is presented in Figure 5. The temperature fluctuation is almost achieved below 30 $\mu K/\sqrt{Hz}$ above $0.1\ mHz$.

CONCLUDING REMARKS

The simulation and corresponding past thermal experiment results are presented. The result implies that the control law will attenuate temperature variation as low as by a factor of $10^4 \sim 10^5$. We are expecting to implement the control system in our laboratory and demonstrate experimental results at the annual meeting. In addition to continuing development of the control system, for the better precision, less noise and more long-term stability, improved measurement will be required to fully satisfy the LISA thermal requirement.

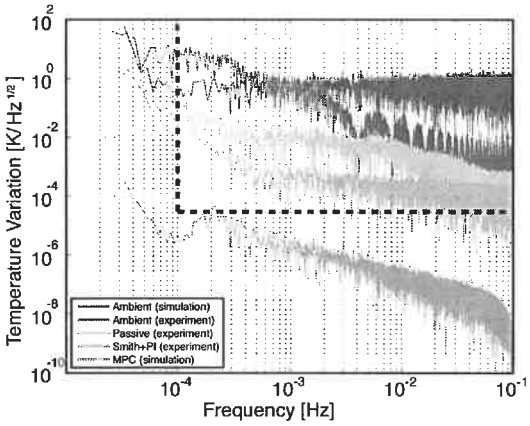

FIGURE 5. Thermal stability in the frequency domain (below of dashed lines indicates the LISA thermal requirement).

ACKNOWLEDGMENTS

This research was supported by NASA, NNX07AK65G, Modular Gravitational Reference Sensor for Space Gravitational Wave Detection.

REFERENCES

[1] DeBra DB. Drag-free spacecraft as platforms for space missions and fundamental physics. Class Quantum Grav. 1997;14:1549–1555.

[2] Schumaker BL. Disturbance reduction requirements for LISA. Classical and Quantum Gravity. 2003;20(10):S239–S253.

[3] Bender PL. LISA sensitivity below $0.1\ mHz$. Class Quantum Grav. 2001;20:S301–S310.

[4] Ke-Xun Sun ea. Advanced gravitational reference sensor for high precision space interferometers. Class Quantum Grav. 2005;22(10):S287–S294.

[5] Swank AJ. Gravitational mass attraction: properties of a right-angled parallelepiped for the LISA drag-free system. Class Quantum Grav. 2006;23:3437–3448.

[6] Smith OJM. Closer Control of Loops with Dead Time. Chemical Engineering Progress. 1957;53:217–219.

[7] Final Technical Report of the (Phase A) Study of the Laser Interferomter Space Antenna. 2000;.

INTEGRATED DESIGN OF HIGH-PERFORMANCE SERVOMECHANISMS USING A DISTURBANCE OBSERVER

Min-Seok Kim[1], Chul-Mo Sung[1] and Sung-Chong Chung[1]*
[1]Hybrid System Design & Control LABoratory
Department of Mechanical Engineering
Hanyang University, Sungdong-Gu, Seoul 133-791, KOREA

ABSTRACT
This paper proposes a systematic design methodology for high-speed/high-precision servomechanisms by using a disturbance observer. A multiplicative uncertainty model and a two degree-of-freedom controller composed of a disturbance observer (DOB) and a PD controller are considered as subsystems. The tradeoff relationship between disturbance suppression and measurement noise rejection of the DOB is studied through the design process. It is confirmed that the proposed design methodology performs excellent disturbance suppression performance.

INTRODUCTION
Accurate tracking at high speed is required in many servomechanisms used in the manufacturing, IT, and FPD (flat panel display) industries. To design a high-speed/high-precision servomechanism with smooth velocity, a disturbance rejection method suppressing effects of cutting force variation, friction, vibration, etc. is required [1]. Two degree-of-freedom controllers composed of an internal-loop controller for improving robustness and an external-loop controller for satisfying tracking performance are used to design high-performance servomechanisms. DOBs have been used as internal-loop controllers to design robust servomechanisms [1~3].

In this paper, a previously developed integrated design methodology [4~7] for high-speed/high-precision servomechanisms is applied to develop a robust servomechanism equipped with a DOB. A mechanical subsystem is modeled as a multiplicative uncertainty model. A two degree-of-freedom controller composed of a DOB and a PD controller is considered for the integrated design. Optimal parameters of the DOB and the PD controller, as well as the mechanical parameters of the servomechanism are obtained through the minimization of the multi-objective function constructed with Abbe offset, circular tracking error and bandwidth. To verify the developed design methodology, an xy-table is selected as a case study. Optimally designed results with lower Abbe offset, larger bandwidth and minimized contour error are obtained through the integrated design. It is confirmed that internal stability and excellent disturbance suppression are accomplished as well.

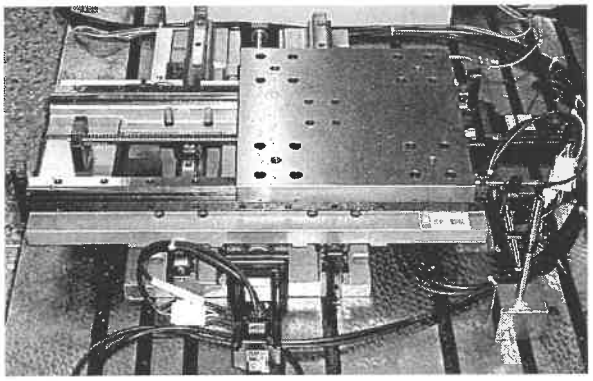

FIGURE 1. XY-table as a case study.

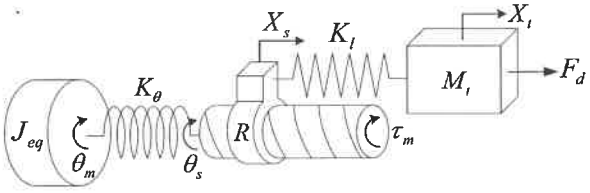

FIGURE 2. Schematic diagram of the mechanical subsystem.

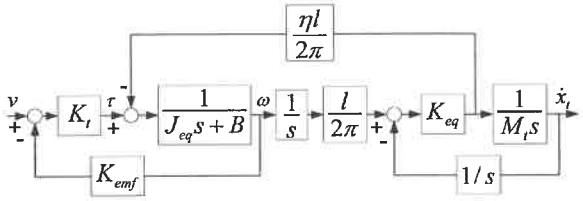

FIGURE 3. Block diagram of the mechanical subsystem.

MODELING OF SERVOMECHANISMS

Mechanical subsystem

In this paper, a precision XY-table is selected to apply the integrated design procedures and to verify the effectiveness of the design methodology. Fig. 1 shows the XY-table selected for the case study. Fig. 2 shows a schematic diagram of the mechanical subsystem of it. In this paper, it is assumed that stiffnesses of the support bearings and nut are proportional to the ball-screw diameter. Fig. 3 shows a block diagram of the mechanical subsystem between the command and actual velocities of the slide [7]. The transfer function between a motor torque and rotational speed of the motor is given by

$$G_m(s) = \frac{b_1}{s^3 + a_1 s^2 + a_2 s + a_3} \quad (1)$$

where

$$a_1 = \frac{J_m B_t + (K_t K_{emf} + B_m) M_t}{J_m M_t}$$

$$a_2 = \frac{(K_t K_{emf} + B_m) B_t}{J_m M_t} + \frac{(J_m \eta + R^2 M_t) K_{eq}}{J_m M_t \eta}$$

$$a_3 = \frac{(K_t K_{emf} + B_m) K_{eq}}{J_m M_t} + \frac{R^2 B_t K_{eq}}{J_m M_t \eta}$$

$$b_1 = R K_t K_{eq} \eta$$

$$R = \frac{l}{2\pi}$$

In order to incorporate a DOB to suppress disturbance, transfer function G_m is changed to a multiplicative uncertainty model [8] composed of nominal model G_m^n and multiplicative perturbation $W(s)$.

$$G_m(s) = \{1 + W(s)\} G_m^n(s) \quad (2)$$

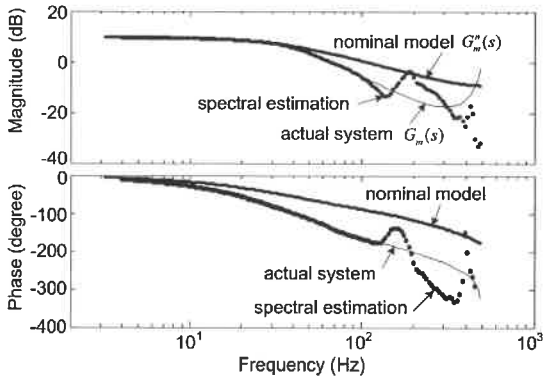

FIGURE 4. Frequency response functions of the mechanical model.

In Eq. (2), the nominal model should be simple and represent dominant characteristics of the mechanical system reliably. Using the assumption of infinite equivalent stiffness of the servomechanism, $G_m^n(s)$ is given by

$$G_m^n(s) = \frac{b_1^*}{s + a_1^*} \quad (3)$$

From Eqs. (1) ~ (3), multiplicative perturbation $W(s)$ is given by

$$W(s) = \frac{-b_1^* s^3 - b_1^* a_1 s^2 - (b_1^* a_2 - b_1) s - b_1^* a_3 + b_1 a_1^*}{b_1^* (s^3 + a_1 s^2 + a_2 s + a_3)} \quad (4)$$

In general, it is difficult to identify an accurate mechanical subsystem model of a servomechanism, because the servomechanism has nonlinear effects such as inherent frictions and backlash. To avoid these effects, a biased-square wave input signal is used for the excitation [6]. An input signal composed of a Gaussian pseudo-random binary sequence is used as the torque command, whereas the rotational motor speed is synchronously collected as an output signal. Fig. 4 shows the measured, identified and nominal frequency response functions of the mechanical subsystem. It is confirmed that the derived nominal model represent the dynamic characteristics well in the low frequency region.

Control subsystem

The two degree-of-freedom controller studied in this paper consists of two parts: An inner-loop controller, DOB, and an outer-loop controller, PD controller. The DOB is applied to compensate for disturbance and parameter variation of the servomechanism. The PD controller is applied to improve the tracking performance of the positioning loop. Q-filter is applied for designing the DOB. Fig. 5 shows the overall block diagram of the servomechanism equipped with the DOB and the PD controller. In Fig. 5, the DOB estimates disturbance and parameter variation according to the nominal plant and the designed Q-filter. Velocity output of the servomechanism V_t is represented by the control input u, disturbance d, and measured noise ζ as follows:

$$v_t = G_{uv_t}(s)u + G_{dv_t}(s)d + G_{\zeta v_t}(s)\zeta \quad (5)$$

where

$$G_{uv_t}(s)=\frac{G_m(s)G_m^n(s)}{G_m^n(s)+\{G_m(s)-G_m^n(s)\}Q(s)}$$

$$G_{dv_t}(s)=\frac{G_m(s)G_m^n(s)\{1-Q(s)\}}{G_m^n(s)+\{G_m(s)-G_m^n(s)\}Q(s)}$$

$$G_{\zeta v_t}(s)=-\frac{G_m(s)Q(s)}{G_m^n(s)+\{G_m(s)-G_m^n(s)\}Q(s)}$$

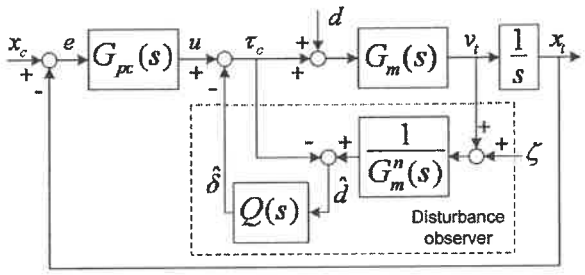

FIGURE 5. Servomechanism with the disturbance observer

As shown in Eq. (5), the Q-filter is the most important element to determine the performance of the DOB. If $|Q(j)|=1$, real system G_m acts like the nominal model G_m^n and effects of disturbance are removed completely. If $|Q(j)|=0$, however, effects of measurement noise are removed and robustness is improved. Therefore, Q-filter should be selected to account for this trade-off. Umeno, et al. [2] suggested the following Q-filter to compensate for not only the disturbance in the low-frequency range but also the measurement noise in the high-frequency range.

$$Q(s)=\frac{1+\sum_{k=1}^{N-r}a_k(\tau s)^k}{1+\sum_{k=1}^{N}a_k(\tau s)^k} \tag{6}$$

In order to determine the coefficient a_k, they proposed the following optimization problem [2].

$$\min_{a_k}\left[|W_1^{-1}(j\omega)\cdot\{1-Q(j\omega)\}|^2+|W_2^{-1}(j\omega)\cdot Q(j\omega)|^2\right] \tag{7}$$

where W_1 is the sensitivity function, and W_2 is the complementary sensitive function.

To obtain the optimum solution of Eq. (7), which accounts for the trade-off between the disturbance and noise rejections, a Q-filter having the same slope not only in the high-frequency region of $|Q(j)|$ but also in the low-frequency region of $|1-Q(j)|$ is selected in this paper [3] as follows:

$$Q(s)=\frac{3(s\tau)+1}{(s\tau)^3+3(s\tau)^2+3(s\tau)+1} \tag{8}$$

From the derived mechanical subsystem model and the two degree-of-freedom controller model including the DOB, the open-loop and closed-loop transfer functions of the servomechanism are given by

$$G_o(s)=\frac{G_m(s)G_m^n(s)G_{pc}(s)}{\left[\{1-Q(s)\}G_m^n(s)+Q(s)G_m(s)\right]s}$$

$$G_c(s)=\frac{G_m(s)G_m^n(s)G_{pc}(s)}{\left[\{1-Q(s)\}G_m^n(s)+Q(s)G_m(s)\right]s+G_m(s)G_m^n(s)G_{pc}(s)} \tag{9}$$

respectively. In Eq. (9), $G_{pc}(s)$ is the PD position controller for the outer-loop.

INTEGRATED DESIGN

In this paper, multi-object function composed of Abbe offset D_a, the contour error ratio E_r, the bandwidth of Q-filter ω_b, and the bandwidth of total closed-loop system ω_q is studied. Dimensionless variables are introduces in the optimization process. Normalization of the multi-objective function minimizes detrimental effects on design results, which are induced by round-off errors and divergence in the optimization process. Abbe offset, ball-screw lead and diameter in the mechanical subsystem are selected as the design variables. Position and velocity controller gains in the control subsystems are selected as the design variables. Since interactions between parameters of the mechanical and control subsystems are considered simultaneously through the design variables, the quality of the design process to achieve high-performance will be improved and an integrated design procedure will be realized. A nonlinear constrained optimization problem is formulated. The sequential quadratic programming (SQP) method, which is suitable for nonlinear constrained optimization problems, is employed to solve the optimization problem as follows:

Minimize

$$F(x) = C_1 D_a^* + C_2 E_r^* + C_3 \omega_b^* + C_4 \omega_q^*$$

subject to

$$g_i(x) \le 0 \quad , i = 1, \cdots, 9$$
$$x_j^L \le x_j \le x_j^U \quad , j = 1, \cdots, 6 \qquad (10)$$
$$x = \{D_a, D_{bs}, l, K_p, K_d, \tau\}^T$$

RESULTS AND DISCUSSION

In this paper, the weighting factors of the multi-objective function are set to have a uniform effect on the optimization process. In order to evaluate the performance of a servomechanism in integrated design process, the performance of this system is compared with the performance of previously design. The performance function of servomechanism after integrated design process is summarized in Table. 1. Fig. 6 shows that the integrated design with the DOB system is better than previous designs.

Table 1. Integrated design results: system performance

Perfor-mance	Unit	Initial system	Initial +DOB	Integrate d design
E_r	%	0.454	0.451	0.187
ω_b	rad/sec	44.154	45.310	63.468
ω_q	rad/sec	-	190.312	448.573
A_m	dB	32.1	41.6	41.1
ϕ_m	deg.	74.3	73.5	71.8

CONCLUSIONS

Following results are obtained:

(1) In order to design the optimal DOB, interactions between parameters of the mechanical and control subsystems should be studied simultaneously.

(2) The system and Q-filter bandwidth are increased by 30% and 2.4 times, and Abbe offset is decreased by 41% through the proposed design methodology.

(3) Validity of the proposed integrated design methodology has been confirmed through experiments. Servomechanism through the proposed method satisfies constraints and required performances.

(4) Using the proposed design methodology, both the mechanical and control subsystems are designed simultaneously. Optimal performance of the servomechanism equipped with the DOB is obtained through the integrated design.

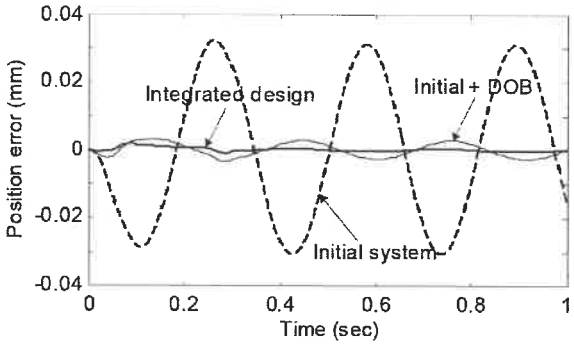

FIGURE 6.Comparisons of tracking performance.

REFERENCES

[1] White, M. T, Tomizuka, M. and Smith, C. Improved Track Following in Magnetic Disk Drives Using a Disturbance Observer. IEEE Trans. On Mechatronics. 2000; 1: 3-11.

[2] Umeno, T., Kaneko, T. and Hori, Y. Robust Servosystem Design with Two Degrees of Freedom and its Application to Novel Motion Control of Robot Manipulators. IEEE Trans. On Industrial Electronics. 1993; 5: 473-485.

[3] Lee, H. S. and Tomizuka, M. A Robust Motion Controller Design for High-Accuracy Positioning Systems. IEEE Trans. On Industrial Electronics. 1996; 1: 48-55.

[4] Kim, M. S., and Chung, S. C. Integrated Design of Feed Drive Systems using Discrete 2-D.O.F. Controllers (Ⅰ). Trans. Of KSME (A). 2004; 7: 1029-1037.

[5] Kim, M. S., and Chung, S. C. Integrated Design of Feed Drive Systems using Discrete 2-D.O.F. Controllers (Ⅱ). Trans. Of KSME (A). 2004; 7: 1038-1046.

[6] Kim, M. S. and Chung, S. C. A Systematic Approach to Design High-Performance Feed Drive Systems. International Journal of Machine Tools and Manufacture. 2005; 45: 1421-1435.

[7] Kim, M. S., and Chung, S. C. Integrated Design Methodology for High-Precision/Speed Servomechanisms. Transactions of the North American Manufacturing Research Institution of SME. 2004; 32: 487-494.

[8] Doyle, J. C., Francis, B. A. and Tannenbaum, A. R., Feedback control Treory, Macmillan Publishing Company, New York: 1992.

ADAPTIVE REPETITIVE CONTROL OF PIEZOELECTRIC ACTUATORS FOR NANO-PRECISION MOTION CONTROL

Chi-Ying Lin and Tsu-Chin Tsao
Mechanical and Aerospace Engineering
University of California, Los Angeles
Los Angeles, California, U.S.A.

INTRODUCTION

Piezoelectric actuators are used in a wide range of precision engineering applications. Nanometer level precision in static positioning has been achieved by using conventional Proportional-Integral-Differential (PID) feedback control with superior position sensors to compensate for hysteresis and creep existed in piezoelectric materials. Achieving nanometer level precision for dynamic motion is beyond the PID control capability. Earlier effort has contended that hysteresis was the main source of error and developed nonlinear hysteresis model and methods to compensate for this effect at low frequency, typically around 1 $\sim$ 10 Hz range [1, 2, 3, 4, 5]. This paper introduces linear model based high performance digital controllers and implementation results for dynamic positioning for higher frequency signals that contain both deterministic and stochastic components.

EXPERIMENTAL SYSTEM DESCRIPTION

The experimental system consists of a piezoelectric transducer (PZT) driven fast tool servo and a Pentium based PC that host analog interface to an amplifier and sensor signal conditioning electronics. Figure 1 shows the cross section of the fast tool servo. The fast tool servo includes a 20 μm stroke ceramic hollow PZT actuator and a 25 μm range capacitance sensor probe. The sensor signal conditioning electronics generate output voltage with 5 kHz. signal bandwidth, 2.4 nm r.m.s. and 25 nm peak-to-peak noise level. The PZT is driven by a voltage amplifier. The digital control schemes were implemented by xPC target (©MathWorks Simulink) computer, which host a data acquisition board with 16-bit resolution in both analog-to-digital and digital-to-analog conversions (NI 6052E). The digital control sampling frequency is 18 kHz. The sampled data of the sensor voltage output have a noise level of 3.9 nm (r.m.s. value) resulting from a combination of sensor electronics and analog-to-digital conversion noise and resolution.

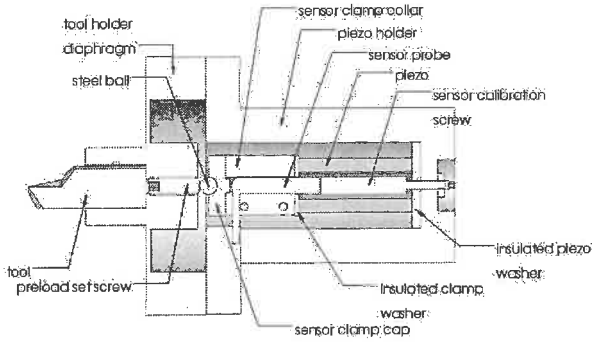

FIGURE 1. Cross section of a fast tool servo actuator system.

DIGITAL MOTION CONTROLS

To perform model based control design, system identification was performed on the system. A seventh order linear time invariant model was obtained by time-domain subspace system identification method. The frequency response of the model is shown in Figure 2, which shows a resonance frequency at 5.8 kHz. The aforementioned 18 KHz. sampling frequency was selected based on the system bandwidth shown here.

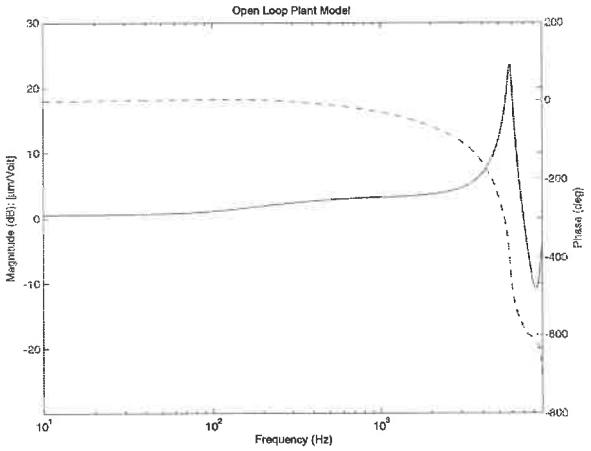

FIGURE 2. Bode plot of piezoelectric actuator model. Solid line: Magnitude; Dash line: Phase.

Figure 3 shows the overall control system block diagram, which includes robust feedback control, feedforward control, repetitive control, and disturbance cancelation compensator. The main feature of this control system structure is that the four different control blocks perform synergistically to produce superior dynamic performance while the individual controller design are generally decoupled from one another. In the block diagram shown, $\hat{G}$ is the plant model, r is the reference command input signal and w is disturbance signal appearing at the plant output. Disturbance injected at the plant input or other location can be represented as equivalent output disturbance. y is the plant output signal and e is the tracking error, the magnitude of which represents the control system performance in its capability to follow the command input r subject to disturbance input w. The control performance is thus characterized by the sensitivity functions e/r for tracking and e/w for disturbance rejection. When $\hat{G} = G$, the following can be obtained from the block diagram:

$$E(z) = S_{fb}S_{rep}S_{ff}R(z) + S_{fb}S_{rep}S_wW(z) \qquad (1)$$

As can be seen, the total error rejection transfer function is the product of the sensitivity functions of each control actions, thus the claimed synergism. This control structure has the 'add-on' or 'plug-in' feature in that each controller may be added on to existing ones and effect the total performance in a multiplicative manner. The individual error rejection (sensitivity function is as follows:

$$\begin{aligned} S_{fb} &= \frac{1}{1+\hat{G}C_{fb}} \\ S_{ff} &= z^{-L} - \hat{G}C_{ff} \\ S_{rep} &= \frac{1}{1+T_{fb}C_{rep}}, \quad T_{fb} = 1 - S_{fb} \\ S_w &= 1 - \hat{G}C_w \end{aligned} \qquad (2)$$

The absence of a particular control action simply makes the corresponding sensitivity function equal to unity.

Robust Feedback Control

A robust feedback controller [6] is designed for the plant model based on discrete-time μ-synthesis to ensure a robust performance under plant uncertainties. The feedback controller typically provides a low bandwidth performance aimed for stabilizing and linearizing the plant dynamics.

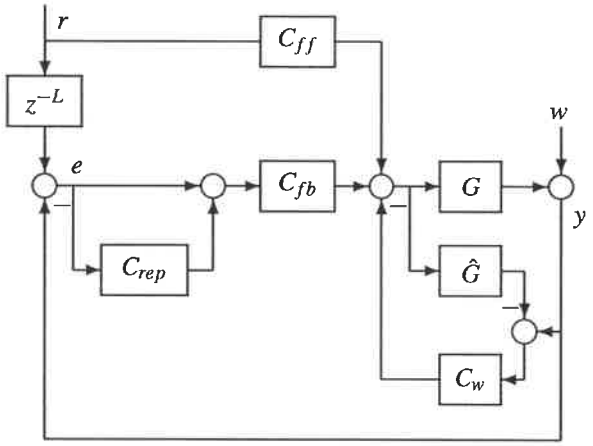

FIGURE 3. Control system block diagram.

Feedforward Tracking Control

To enhance the tracking performance, the feedforward compensator C_{ff} can be added onto the feedback controller. The delay block z^{-L} in Figure 3 is introduced to provide look-ahead or preview of the reference command signal. L represents the number of samples in previewing the reference signal. C_{ff} is a stable inversion of the plant dynamics, which can be designed in particular by zero-phase-error-tracking-control (ZPETC) method [7] or in general by optimal solution in [8], where optimal feedforward controller C_{ff} minimizes the following equation with appropriate transfer function norms:

$$\min_{C_{ff} \in RH_\infty} ||z^{-L} - \hat{G}C_{ff}||_{(\cdot)} \qquad (3)$$

Repetitive Control

The plug-in prototype repetitive controller C_rep, can be designed based on the the closed loop plant model T_{fb}

$$T_{fb} = \frac{\hat{G}C_{fb}}{1+\hat{G}C_{fb}} \qquad (4)$$

The repetitive controller includes an internal model and is in the following filter from [9]:

$$C_{REP} = \frac{q(z,z^{-1})z^{-N+l}}{1-q(z,z^{-1})z^{-N}}K_{rep}(z) \qquad (5)$$

N stands for the period of the reference signal, l is the sum of the plant delay and the controller delay which comes from the inversion of the unstable zero part in the closed loop plant T_{fb}. $q(z,z^{-1})$ is a zero phase low pass filter whose form is

$$q(z,z^{-1}) = (az^{-1} + b + az)^n \qquad (6)$$

where a & b satisfies $a + 2b = 1$ for unity d.c. gain and n is a positive integer. $K_{rep}(z)$ can be obtained from the aforementioned ZPETC as an approximate stable inversion of T_{fb}, or from robust control approaches by formulating and solving a μ-synthesis problem [10]. Although $q(z,z^{-1})$ is a non-causal filter, the controller's causality is still assured because of the cascaded long delay terms z^{-N} and z^{-N+1}.

Adaptive Disturbance Rejection

The disturbance rejection performance by the robust feedback and repetitive control is effective for low frequency and periodic disturbance respectively. A general class of disturbance can be modeled as colored noise, which is the output of sending a white noise into a filter W. The adaptive disturbance canceller C_w can be added to compensate for such type of disturbance and minimize an output measure. The minimization problem could be represented as

$$\min_{C_w \in RH_\infty} ||W(1 - C_w\hat{G})||_2 \qquad (7)$$

In general the disturbance model W is unknown or varying. In such a case adaptive scheme such as Least Mean Squares (LMS) [11] C_w may be employed to minimize the mean square value of the output y (or equivalently e with the absence of r). In the following experiments an non-adaptive C_w [8] calculated for $W = 1$ will be included to compare the performance with the adaptive LMS scheme [11].

EXPERIMENTAL RESULTS

Two sets of experiments were performed to demonstrate the effectiveness of the digital control schemes. The first one compares the tracking performance of the control action without the presence of disturbance w. The reference signal tracked is a typical step-and-move type scan trajectory traversing at 30 Hz and 300 Hz, respectively. Figure 4 shows the time domain experimental data with the reference profile for the case of 30 Hz trajectory. Table 1 shows the steady state tracking error r.m.s. values for both cases. For both trajectories adding feedforward controller to the existing feedback controller reduces at least 50% tracking error. Adding repetitive control substantially improves the tracking performance since at the multiples of fundamental frequency it provides the deep notches in the sensitivity function. For tracking 30 Hz profile case, repetitive control essentially reduces the tracking error to close to the sensor noise level.

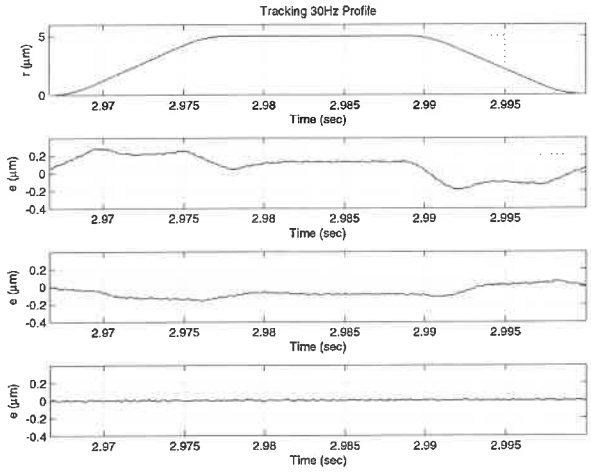

FIGURE 4. Experimental results for tracking 5 μm, 30 Hz scan profile. Top: 30Hz profile; 2nd: Feedback Control; 3rd: Feedback + Feedforward Controls; Bottom: Feedback + Feedforward + Repetitive Controls.

TABLE 1. Tracking error r.m.s.: effects of adding feedforward and repetitive controls

Controls	30Hz profile r.m.s. (μm)	300Hz profile r.m.s. (μm)
Feedback	0.12979	2.02170
Feedback + Feedforward	0.05735	0.83605
Feedback + Feedforward + Repetitive	0.00552	0.01531

In the second set of experiment disturbance w is introduced and then the disturbance canceller is added on. A sequence of color noises was generated by passing a white noise sequence through a low-pass filter of 50 Hz cut-off frequency. Injecting the disturbance to the control system significantly deteriorates the tracking performance, which is shown in Table 2. Adding non-adaptive disturbance canceller designed for $W = 1$ almost did nothing since it does not capture the disturbance dynamics. Adaptive disturbance canceller rejects disturbance inputs and shows superior performance. Figure 5 shows the magnitude of the disturbance input and the effects of adding adaptive disturbance cancellers for tracking the

30 Hz reference trajectory. Again, the adaptive control reduce the tracking error to close to the sensor noise level.

TABLE 2. Tracking error r.m.s.: effects of adding disturbance canceller

Controls	30Hz profile r.m.s. (μm)	300Hz profile r.m.s. (μm)
Feedback + Feedforward + Repetitive	0.02488	0.02235
Adding non-adaptive Disturbance Canceller	0.02427	0.02221
Adding adaptive Disturbance Canceller	0.00579	0.01805

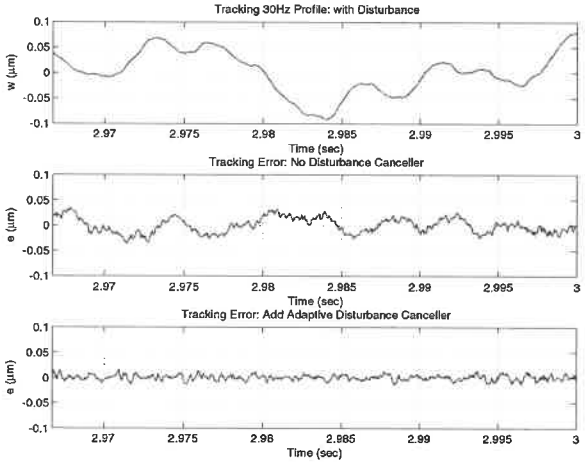

FIGURE 5. Experimental results for tracking 5 μm, 30 Hz scan profile subject to stochastic disturbance input. Top: Injected disturbance; Middle: Feedack + Feedforward + Repetitive Controls; Bottom: Feedack + Feedforward + Repetitive Controls + Adaptive Disturbance Canceller.

CONCLUSION

A digital control system that includes feedback, previewed feedforward, repetitive, and adaptive control for achieving superior performance in tracking and disturbance rejection in precision motion control is presented. Experimental results on a piezoelectric actuator driven fast tool servo demonstrate the synergistic effects of combining these linear control actions for achieving nanometer level dynamic precision.

ACKNOWLEDGMENTS

This work was supported in part by the National Science Foundation under grant no. DMI0327077, Nanoscale Science and Engineering Center for Scalable And Integrated Nanomanufacturing (SINAM).

REFERENCES

[1] Ge P, Jouaneh M. Modeling Hysteresis in Piezoceramic Actuators. Precision Engineering. 1995;17:211–221.

[2] Ge P, Jouaneh M. Tracking Control of a Piezoceramic Actuator. IEEE Transactions on Controls Technology. 1996 May;4:209–216.

[3] Schafer J, Janocha H. Compensation of Hysteresis in Solid State Actuators. Sensors and Actuators. 1995 June;49:97–102.

[4] Janocha H, K K. Real-Time Compensation of Hysteresis and Creep in Piezoelectric Actuators. Sensors and Actuators. 2000 June;79:83–89.

[5] Song G, Zhao J, Zhou X, Abreu-Garćia JAD. Real-Time Compensation of Hysteresis and Creep in Piezoelectric Actuators. Sensors and Actuators. 2000 June;79:83–89.

[6] Skogestad S, Postlethwaite I. Multivariable Feedback Control - Analysis and Design. John Wiley & Sons; 1996.

[7] Tomizuka M. Zero Phase Error Tracking Algorithm for Digital Control. ASME Journal of Dynamic Systems, Measurement, and Control. 1987 March;109:65–68.

[8] Tsao TC. Optimal Feed-Forward Digital Tracking Controller Design. ASME Journal of Dynamic Systems, Measurement, and Control. 1994 December;116:583–592.

[9] Tomizuka M, Tsao TC, Chew KK. Analysis and Synthesis of Discrete-Time Repetitive Controllers. ASME Journal of Dynamic Systems, Measurement, and Control. 1989 September;111:353–358.

[10] Li J, Tsao TC. Robust Performance Repetitive Control Systems. ASME Journal of Dynamic Systems, Measurement, and Control. 2001 sepetmber;123:330–337.

[11] Widrow B, Walach E. Adaptive Inverse Control. Upper Saddle River, NJ: Prentice-Hall; 1995.

SIMPLE AND PRACTICAL CONTROL METHOD FOR ULTRA-PRECISION POSITIONING - APPLICATION TO A BALLSCREW MECHANISM

Kaiji Sato, and Guilherme J. Maeda
Interdisciplinary Graduate School of Science and Engineering
Tokyo Institute of Technology
4259 G2-17 Nagatsuta, Midori-ku, Yokohama 226-8502, Japan

INTRODUCTION

Precision positioning systems are essential in precision industry. These positioning systems often have one or more elements that introduce friction. Friction is well known to cause steady-state errors and limit cycles, and to slow the motion of the mechanism. Thus, it is important to consider friction compensation in controller design. Simple controllers like PID controllers do not offer the best possible performance for the mechanisms. Thus the use of advanced controllers such as controllers including model based compensators and variable structure controllers is increasing. However the advanced controller design usually requires the identification of mechanism characteristics and sufficient knowledge of the control theory.

Ballscrew mechanisms have friction characteristics and are widely used in precision positioning systems. In this research, a conventional ballscrew mechanism is used as a positioning mechanism. Although some studies have achieved nanometric accuracy with a ballscrew mechanism, this research differs significantly in the ease of design and controller structure. The NCTF (nominal characteristic trajectory following) controller, has a simple structure and its design procedure does not require exact parameter identification, which makes it easy to design, understand, and adjust [1-3].

In this paper, first, the concept and the design procedure of the NCTF control method are introduced. Next, the NCTF control method is implemented to a conventional ballscrew mechanism and the positioning performance of the controller is examined. The controller is designed without any exact identification of parameters or modeling.

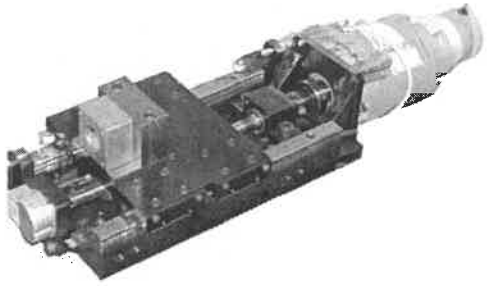

Figure 1. Experimental ballscrew mechanism

EXPERIMENTAL SETUP

Figure 1 shows a picture of the ballscrew mechanism, which is the controlled mechanism in this study. Its table mass is 3.57kg. The mechanism has several sources of friction: the DC motor, the preloaded double-nut, the linear ball guides, and the ball bearings supporting the screw shaft. Friction and damping characteristics tend to vary and depend on the warm-up condition.

The PWM power amplifier is used as a driver unit. The controller sampling frequency is 5 kHz. The feedback position is determined by a laser position sensor with resolution of 1.24 nm. The lead of the ballscrew is 2 mm/rev.

CONCEPT OF NCTF CONTROL MEHTOD

Figure 2 shows the basic structure of the NCTF

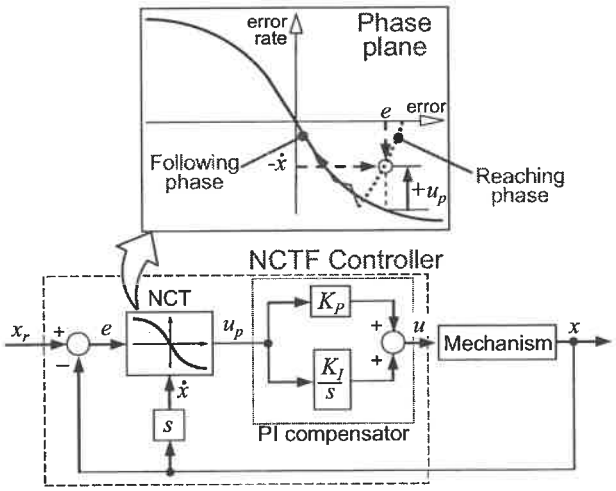

Figure 2. Basic structure of the NCTF control system

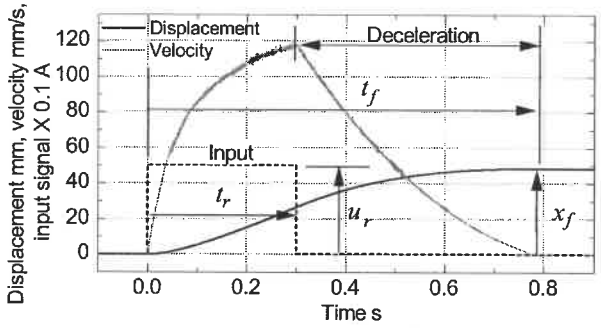

(a) Open-loop response for the NCT construction.

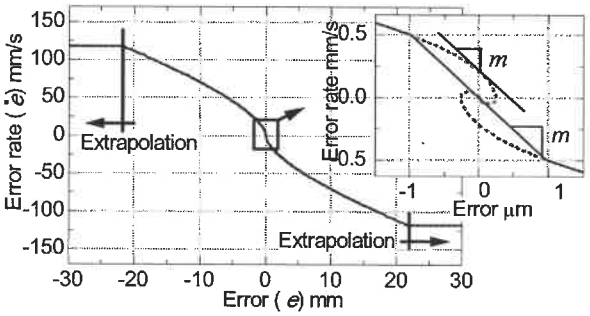

(b) NCT constructed from the open-loop response.

Figure 3. Open-loop response and construction of the NCT

control system. The controller is composed of a nominal characteristic trajectory (NCT) and a PI compensator. The objective of the PI compensator is to make the mechanism motion follow the NCT, finishing at the origin of the phase-plane. The output of the NCT is a signal, which is the difference between the actual error rate of the mechanism and the error rate of the NCT. On the phase-plane, the table motion is divided into a reaching phase and a following phase. During the reaching phase, the compensator controls the table motion to achieve the NCT. The next step is the following phase, where the PI compensator causes the mechanism motion to follow the NCT, leading it back to the origin of the phase-plane.

The design of the NCTF controller is comprised of three steps:

(i) The mechanism is driven with an open-loop step input while its displacement and velocity are measured.

(ii) The NCT is constructed on the phase-plane using the displacement and velocity of the mechanism during the deceleration.

(iii) The PI compensator is designed using simple response results and the NCT information.

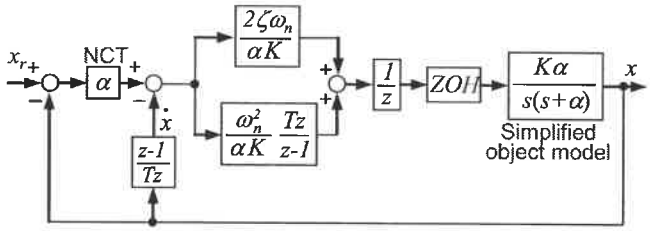

Figure 4. Digital NCTF control system

Since the NCT is constructed from the actual response of the mechanism, the actual nonlinear friction effects are included in the NCT. Thus, the actual friction characteristics are part of the control law.

DESIGN OF PI COMPENSATOR

Stability Condition Based on Linear System

When the ball screw has sufficient stiffness, the mechanism can be approximately linearized as follows;

$$\ddot{x} + \alpha\dot{x} = K\alpha \cdot i \qquad (1)$$

Where, x and i represent a table displacement and a motor current, respectively. α and K are model parameters. In this case, the nonlinear friction effects are reflected on α and the NCT.

Figure 3(a) shows the open-loop response used to construct the NCT. Figure 3(b) shows the NCT constructed from the open-loop experiment. The vertical axis is constructed from the measured velocity during the deceleration. The horizontal axis is constructed from the measured displacement during the deceleration. The inclination of the NCT near the origin m coincides with $-\alpha$. The detail shows that a spring-like behavior manifests near the origin of the NCT as a circling motion. This circling motion has negative effects on positioning and the NCT is linearized with a straight line close to the origin. The inclination of the line is chosen to be the same as the tangential line of the NCT just before the spring-like behavior begins. K is expressed as Eq. (2) using parameters in Fig.3.

$$K = \frac{x_f}{u_r t_r} \qquad (2)$$

The PI compensator gains K_P and K_I are expressed as Eq. (3), using compensator parameters ζ and ω_n.

$$K_P = \frac{2\zeta\omega_n}{K\alpha}, \quad K_I = \frac{\omega_n^2}{K\alpha} \qquad (3)$$

Figure 4 shows the block diagram of the digital NCTF control system near the origin of the NCT. T is the sampling time of the controller.

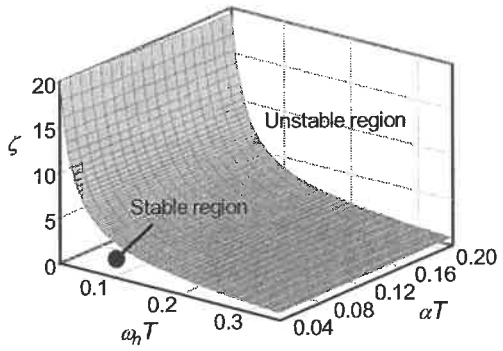

Figure 5. Stability limit of the linear digital system with PI element

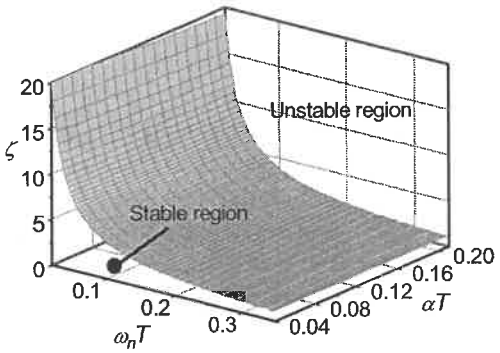

Figure 6. Stability limit of the linear digital system with P element

The stability of the linear digital NCTF control system is dependent on the parameters αT, $\omega_n T$, and ζ. Applying the Jury's test, a numerical plot of the stability limit is shown in Fig. 5. The linear stability limit has negligible variations on the αT axis. The linear stability condition is approximately expressed as:

$$\zeta > \frac{0.383}{\omega_n T} \tag{4}$$

The PI compensators determined under Eq. (4) make the control system stable. However the condition is too excessive for the mechanism with friction.

Stability Condition for Actual System

Coulomb friction is known to increase the stability of the system, allowing for the use of higher gains than those predicted by a linear analysis. This subsection introduces a simple method to find the practical stability limit of the NCTF control system.

Figure 6 shows the case in which the stability analysis is conducted with the integral gain set to zero. Comparing with the surfaces of Figs.5 and 6, it is observed that the integral gain has little effect on the linear digital stability analysis.

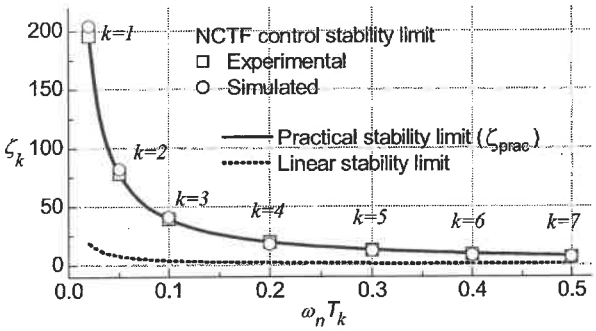

Figure 7. Practical stability limit compared to experimental and simulated results

From the comparison, it is observed that the integral element has a negligible influence on the stability of the linear system. For the following analysis, it will also be assumed that the integral element has a negligible influence on the stability of the actual system. Experiments and simulations will show that this assumption is valid.

The practical stability limit is found by driving the mechanism with the NCTF controller using only the proportional element. The value of the proportional gain is increased until continuous oscillations are generated. The determined proportional gain K_{Pu} represents the actual ultimate proportional gain. Using Eq. (3), the practical stability limit ζ_{prac} is given as

$$\zeta_{prac} = K_{Pu} \frac{K\alpha}{2\omega_n} \tag{5}$$

Equation (5) represents the maximum values allowed for a given ζ, before the control system becomes unstable. In order to prove the suitability of ζ_{prac}, the NCTF controller (using the proportional and integral elements), is designed as follows: for a fixed value of $\omega_n T_k$ (where k = 1...7), the compensator gains are calculated from Eq. (3). The parameter ζ_k is increased until the system achieves instability. The points defined by ζ_k and $\omega_n T_k$ are plotted in Fig. 7. The procedure performed both experimentally and by simulations using the mechanism model which is similar to that in [4]. As the results show, ζ_{prac} fits closely to all the points representing the NCTF control stability limit. In addition, it is observed that ζ_k represented by the linear stability limit curve is much smaller than the ζ_k determined by the practical stability limit.

Based on the above discussion, the step (iii) in the NCTF controller design is carried out as follows:

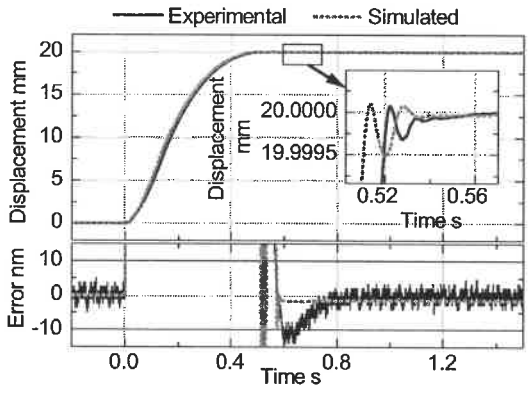

Figure 8. Response of the NCTF control system to a 20mm step input

(iii-1) The mechanism is driven with the NCTF controller using only the proportional element. The value of the proportional gain is increased in order to determine the ultimate proportional gain (K_{Pu}).

(iii-2) ζ_{prac} is obtained by using K_{Pu} with Eq. (5).

(iii-3) $\omega_n T$ and ζ are chosen within the stable region delimited by ζ_{prac}.

(iii-4) The compensator gains are calculated using parameters $\omega_n T$ and ζ with Eq. (3).

It should be noted that this procedure can be completed without any previous information about the model parameters.

EXPERIMENTS

Figure 8 shows the positioning performance for a step input of 20 mm. The compensator used in this figure is chosen to have 40% of the values of ζ_{prac}, so that the margin of safety of the design is 60%. The controller also includes the conditional freeze integrator. The achieved positioning accuracy is less than 10 nm.

Figure 9 details the positioning resolution of the control system. Stepwise inputs of 5 nm are used as reference, and the experiment is repeated for two different frictional conditions: before and after warming up. The warm-up condition is achieved by driving the mechanism with a sinusoidal reference of 20 mm in amplitude at a frequency of 0.6 Hz over 40 seconds. After the warm-up, the Coulomb friction and viscous friction were reduced by 13% and 24%, respectively. In spite of the changes in friction, a positioning resolution of 5 nm is still maintained, proving that the designed NCTF controller is robust against friction variations.

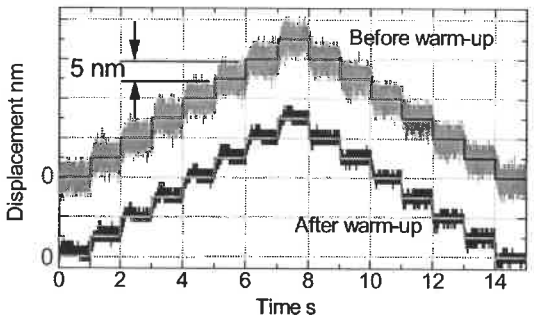

Figure 9. Positioning resolution under two frictional conditions

CONCLUSIONS

In order to clarify a simple method for ultra-precision positioning with a ballscrew mechanism, the NCTF control was introduced and improved more practically. The NCTF controller was designed without any exact identification of parameters or modeling. The practical stability limit was used to restrict the choice of two kinds of design parameters within the stable area. The designed control system achieved a positioning accuracy on the order of nanometers. The positioning resolution of the control system is 5 nm even when friction changes.

REFERENCES

[1] Wahyudi, Sato K., Shimokohbe A., Characteristics of practical control for point-to-point (PTP) positioning systems effect of design parameters and actuator saturation on positioning performance, Precision Engineering. 2003; 27: 157−169.

[2] Sato K., Nakamoto K., Shimokohbe A., Practical control of precision positioning mechanism with friction, Precision Engineering. 2004; 28: 426−434.

[3] Sato K., Robust and practical control for PTP positioning," The 1st International Conference on Positioning Technology. 2004;: 394−395.

[4] Sato K., Shinshi T., Abidin Z. and Shimokohbe A., Positioning Performance of a Leadscrew System with Six Kinds of Control Methods -Basic Positioning Performance and Effect of Coulomb Friction on the Performance-, Proceedings of China-Japan Bilateral Symposium on Advanced Manufacturing Engineering. 1998 ;: 39-44.

INTEGRATED TUNING OF BI-AXIAL SERVOMECHANISMS FOR PRECISE MOTION CONTROL

Chul-Mo Sung[1], Kyung-Don Kim[2] and Sung-Chong Chung[1]*
[1]Hybrid System Design & Control LABoratory
Department of Mechanical Design
Hanyang University, SungdongGu, Seoul 133-791, KOREA
[2]Small Business Corporation, Gyeonggi Regional Headquarter, Suwon, KOREA

ABSTRACT
In order to ensure high-speed and high-precision specifications in servomechanisms, tracking and contour errors should be minimized through optimal selection of servo parameters. In this paper, integrated tuning procedure based on the integrated design concept is performed to derive the optimal tuning method. Control parameters are optimally selected through a nonlinear constrained optimization problem of the integrated design process, while parameters of the mechanical subsystem are specified according to the identified mechanical subsystem model. Experimental results show that both tracking and contouring errors are significantly reduced by applying the proposed integrated tuning method.

INTRODUCTION
Precision servomechanisms are used widely in the manufacturing, IT, machine tool, FPD (flat panel display) and aerospace industries. It is important to improve contouring and tracking accuracy in high-speed manufacturing systems. To improve contouring accuracy in the multi-axis control, cross-coupled control (CCC) systems have been applied so far [1]. However, it is difficult to select the controller parameters optimally because the cross-coupled control system is a multivariable, nonlinear, and time-varying control system. To improve tracking performance of servos with servo lag, friction and external load, etc., ZPETC [2] and optimal ZPETC [3] have been applied in motion control systems. However, tuning of these inverse model-based feedforward controllers is difficult in practical environments due to many tuning parameters. Modeling error and nonlinearity of the servomechanisms have hindered perfect tracking as well.

In this paper, an optimal tuning method of cross-coupled controller linked with the feedforward controller is studied to reduce both the contouring and tracking errors of a biaxial servomechanism through the previously developed integrated design [4,5] and tuning [6] methods. The integrated tuning is an optimal tuning method based on the integrated design concept [4,5]. Its control parameters are optimally selected through a nonlinear constrained optimization procedure of the integrated design process, while parameters of the mechanical subsystem are specified according to the identified mechanical subsystem model. Linear and circular motion experiments are performed on a bi-axial servo to verify the effectiveness of the developed optimal tuning procedure.

CONTOUR ERROR
A cross-coupled controller is a effective control structure to reduce contour errors directly by coupling multiple axes. In order to design the cross-coupled controller, it is required that contour error, difference of normal direction between the required and active positions, should be calculated correctly. In case of linear motion, contour error is given by

$$\varepsilon_l = -e_x \sin\theta + e_y \cos\theta \qquad (1)$$

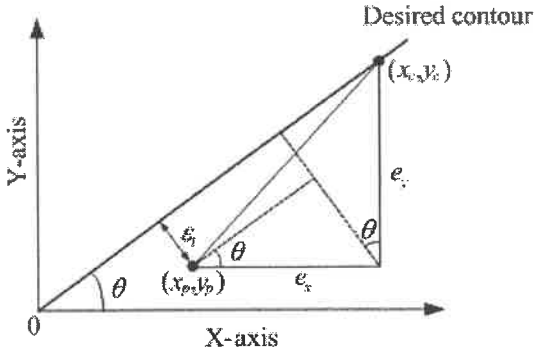

FIGURE 1. Contour error in a linear motion.

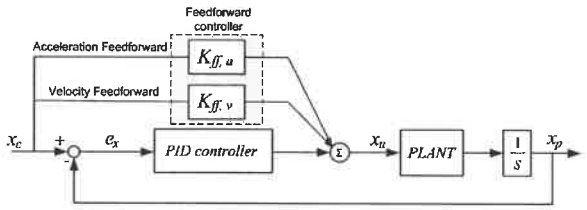

FIGURE 2. Feedforward control structure.

In Fig. 1, (x_c, y_c) is the desired coordinate and (x_p, y_p) is the actual coordinate at the same time of (x_c, y_c).

FEEDFORWARD CONTROL

Fig.2 shows a block diagram of a feedforward controller combined with velocity and acceleration effects. It is necessary to reduce tracking errors due to servo lag, friction and external load, and so on. Typical type of the controller equipped with the velocity and acceleration feedforward terms is given by

$$Feedforward\ Controller = K_{VF}\dot{x} + K_{AF}\ddot{x} \tag{2}$$

Feedforward refers to the addition of open-loop information to modify the profile generator. By injecting feedforward velocity and acceleration signals to the servo system, it is possible to improve bandwidth of the feedback control loop and tracking performance of the servo.

SYSTEM STRUCTURE

Fig. 3 shows an overall system composed of the cross-coupled and feedforward controllers. $P_{x,y}$ are position controllers, and $FF_{vx,vy}, FF_{ax,ay}$ are velocity and acceleration feedforward controllers for each axis. C_c is a cross-coupled controller and $C_{x,y}$ are cross-coupling gains defined as follows:

$$P_{x,y}(s) = K_{px,py} + K_{ix,iy}\frac{1}{S} + \frac{K_{dx,dy}s}{\tau_{dx,dy}s+1} \tag{3}$$

$$FF_{vx,vy}(s) = K_{ffvx,ffvy}\frac{s}{\tau_{fvx,fvy}s+1} \tag{4}$$

$$FF_{ax,ay}(s) = K_{ffax,ffay}\left(\frac{s}{\tau_{fax,fay}s+1}\right)^2 \tag{5}$$

$$C_c(s) = K_{pc} + K_{ic}\frac{1}{s} + \frac{K_{dc}s}{\tau_{dc}s+1} \tag{6}$$

$$C_x = \sin\theta\ ,\ C_y = \cos\theta \tag{7}$$

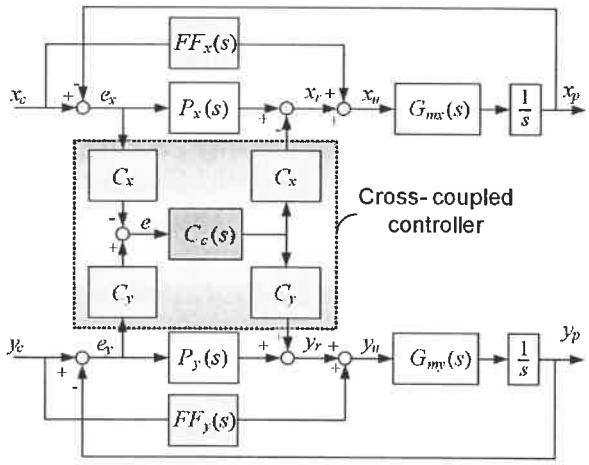

FIGURE 3. Block diagram of the overall system.

MATHEMATICAL MODELING

In order to apply the previously developed integrated design concept [4, 5] to the integrated tuning procedure, identification of the mechanical subsystem model is required first. To derive an accurate dynamic model of the mechanical subsystem of a bi-axial servomechanism, xy-table, shown in Fig. 4, an input signal composed of Gaussian pseudo-random binary sequence is used as the torque command, whereas the rotational motor speed is synchronously collected as an output signal. Fig. 5 shows the measured and mathematically identified frequency response functions of the mechanical subsystem. Second order models of x and y axes are given by

$$G_{mx}(s) = \frac{206500}{s^2 + 696.9s + 238300} \tag{8}$$

$$G_{my}(s) = \frac{154800}{s^2 + 574s + 173400} \tag{9}$$

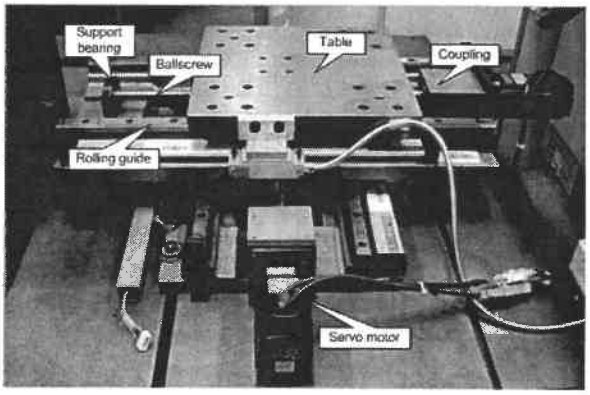

FIGURE 4 Configuration of the xy-table.

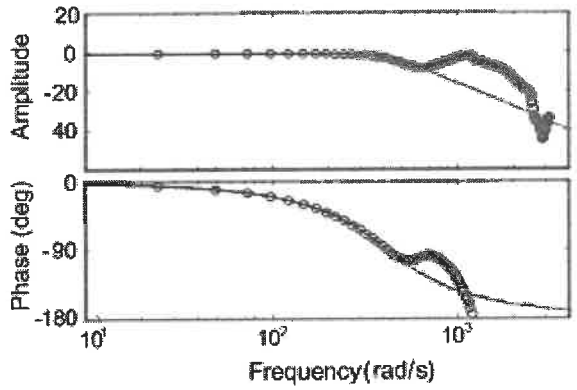

FIGURE 5 Frequency response functions of the mechanical subsystem.

The overall system including the mechanical subsystem is formulated as a state space equation which is applicable to MIMO (Multi-input, multi-output) system. Contrary to a cross-coupled control system for the linear motion, cross-coupling gains for a circular motion are time-varying parameters. It is difficult to represent the system through the state-space formulation. However, as all curves are converted to a sequence of micro straight lines, the cross-coupled control system for an arbitrary curve is formulated as a state-space equation based on a series of linear motion trajectories [6].

OPTIMAL TUNING PROBLEM

In this paper, objectives of the optimal tuning are fast response and higher contour accuracy. Optimal tuning of the multi-objective function is performed to minimize both the contour error and the settling time. To exclude excessive overshoot, it is bounded as constraints. In addition, to secure stability of the designed system although there are uncertainties due to modeling errors and variation of cross-coupling gains, relative stability is considered in the design process. Kharitonov's polynomials [7] are applied to investigate the relative stability as constrains.

Using the modeling procedure described above, the optimal tuning problem is formulated as a nonlinear constrained optimization problem. Design variables $\mathbf{X}$, a multi-object function $F(\mathbf{X})$ and constrained conditions $g(\mathbf{X})$ are defined in this procedure. All control parameters K_{px}, K_{dx}, K_{ix}, K_{py}, K_{dy}, K_{iy}, K_{pc}, K_{dc}, K_{ic}, K_{ffvx}, K_{ffvy}, K_{ffax}, K_{ffay} are selected as design variables. Consequently, the optimal tuning problem is given by

Minimize

$$F(\mathbf{x}) = w_1\varepsilon_l + w_2 t_s$$

subject to

$$g_i(\mathbf{x}) \le 0 \qquad ,i = 1 \sim 6 \tag{10}$$

$$x_j^L \le x_j \le x_j^U \qquad ,j = 1 \sim 13$$

$$\mathbf{x} = [K_{px}, K_{dx}, K_{ix}, K_{py}, K_{dy}, K_{iy}, K_{pc}, K_{dc}, K_{ic}, K_{ffvx}, K_{ffvy}, K_{ffax}, K_{ffay}]$$

TUNING RESULTS AND EXPERIMENTS

Sequential Quadratic Programming (SQP) algorithm is applied for optimal tuning. Applying plant uncertainty = ±1%, feedrate of the servo =1m/min, and equal weighting factors of the objective function, $w_{1,2}$ =0.5, optimal tuning results are obtained as listed in Table 1.

To verify effectiveness of the integrated tuning procedure, experiments are performed on the xy-table shown in Fig. 4. Linear and circular motions are performed with the feedrate of 1m/min. Fig. 6 shows comparisons of linear motion results. Previous result [6], CCC+PID, is shown as optimal tuning. Integrated tuning result obtained from combination of CCC, feedforward and PID controllers show better contouring accuracy. It is confirmed that the contour error is lower than 0.5 μm in the linear motion.

TABLE 1. Integrated tuning results.

Design variable	Unit	Initial design	Integrated tuning
$x_1(K_{px})$	V/V	100.000	153.68
$x_2(K_{dx})$	V/V	0.100	0.32783
$x_3(K_{ix})$	V/V	0.100	0.00259
$x_4(K_{py})$	V/V	80.000	151.46
$x_5(K_{dy})$	V/V	0.020	0.35974
$x_6(K_{iy})$	V/V	0.001	0.00384
$x_7(K_{pc})$	V/V	0.000	85.112
$x_8(K_{dc})$	V/V	0.000	0.4983
$x_9(K_{ic})$	V/V	0.000	0.00025
$x_{10}(K_{ffvx})$	V/V	0.000	0.0059
$x_{11}(K_{ffvy})$	V/V	0.000	0.0198
$x_{12}(K_{ffax})$	V/V	0.000	0.0002
$x_{13}(K_{ffay})$	V/V	0.000	0.0005

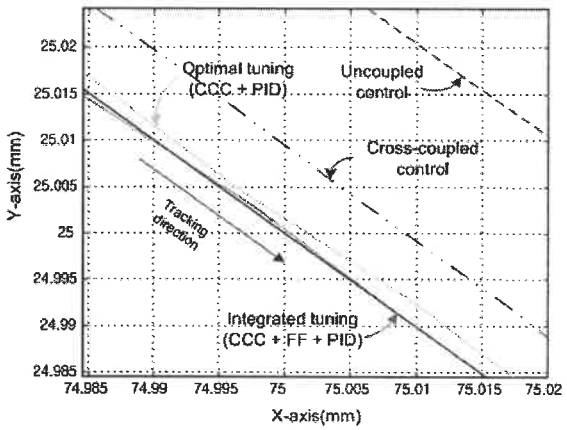

FIGURE 6 Errors of the linear motion.

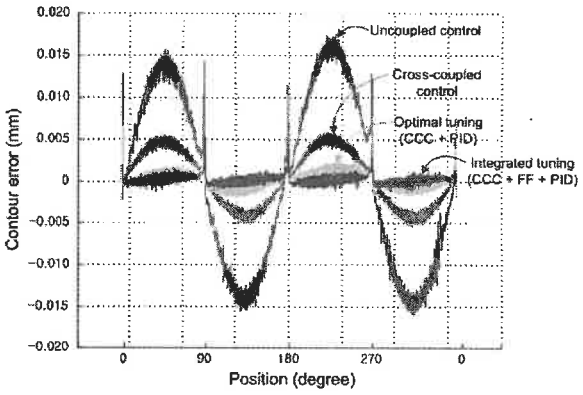

FIGURE 7 Errors of the circular motion.

Fig. 7 shows tracking and contouring performance of various controllers in the circular motion. The integrated tuning result obtained from CCC+FF+PID show the best performance. Contour errors are measured within 1 μm for $50mm$ radius and speed of $1m/min$. However, the peaks are around 5 μm generated every 90 degrees due to friction and backlash of the mechanical system. They are rejected by using a feedforward friction compensator [8].

CONCLUSIONS

The optimal tuning of a cross-coupled control system equipped with the velocity and acceleration feedforward controllers is proposed to improve contouring accuracy and tracking performance of a biaxial servomechanism by using the integrated design concept. The mathematical modeling of the overall system including the mechanical subsystem identified through an accurate identification process is formulated as a state-space equation based on linear motion trajectories. Using Kharitonov's theorem, robustness of the system is secured. Optimal parameters minimizing the contour error and the settling time while satisfying relative stability conditions are obtained through the integrated tuning procedure.

Experimental results of the circular motion show that contour error of the system tuned optimally is reduced by 94%, 83% than those of the uncoupled and cross-coupled control systems, respectively. Developed CCC+FF+PID control system is 50% better performance than that of previously developed CCC+PID [6]. It is confirmed that the contour error is lower than 0.5 μm in the linear motion.

REFERENCES

[1] Koren, Y, Cross-Coupled Biaxial Computer Control for Manufacturing Systems. ASME Journal of Dynamic Systems, Measurement and Control. 1980, 102. 265-272.

[2] Tomizuka, M, Zero Phase Error Tracking Algorithm for Digital Control. ASME journal of Dynamic systems, Measurement and Control. 1987, 109. 65-68.

[3] Yeh, S. S. and Hsu, P. L, Analysis and Design of the Integrated Controller for Precise Motion System. IEEE Transactions on Control System Technology, 1999, 7. 706-717.

[4] Chang, H., D. and Chung, S. C., Integrated Design of Radial Active Magnetic Bearing Systems Using Genetic Algorithms. Mechatronics, 2002, 12. 19-36.

[5] Kim, M. S. and Chung, S. C., A Systematic Approach to Design High-Performance Feed Drive Systems. International Journal of Machine Tools and Manufacture, 2005, 45. 1421-1435.

[6] Bae, H. K. and Chung, S. C., Optimal Tuning of Biaxial Servomechanisms using a Cross-Coupled Contoller. Transactions of NAMRI/SME, 2006, 34. 603-610.

[7] Ackermann, J., A. Bartlett, D. Kaesbauer, W. Sienel, and R. Steinhauser, Robust Control Systems with Uncertain Physical Parameters, 1993, Springer-Verlag, London.

[8] Kim, M. S. and Chung, S. C., Friction Identification of Ball-screw Driven Servomechanisms through the Limit Cycle Analysis. Mechatronics, 2006, 16. 131-140.

A VERSATILE, LONG-RANGE, POSITIONING SYSTEM FOR MECHANICAL PROBE STUDIES

Eric S. Buice[1], Stuart T. Smith[1], Robert J. Hocken[1], David L. Trumper[2] and David Otten[2]
[1]Center for Precision Metrology
The University of North Carolina at Charlotte
Charlotte, NC USA
[2]Department of Mechanical Engineering
Massachusetts Institute of Technology
Cambridge, MA USA

INTRODUCTION

This abstract presents an overview of the assembly and interface developments for the implementation of an ultra-precision motion controlled positioning stage for nanometer positioning over a working volume of 50 mm × 50 mm × 4 μm with a maximum speed of 5 mm·s^{-1}. The stage is to achieve positioning accuracies of better than 10 nm that are traceable to national standards while operating in a vacuum environment (below 1 x 10^{-3} Torr). The vacuum chamber can also act as an environmental chamber where different gases can be used depending on the measurement task. The positioning stage is designed to use various probing systems to perform "pick and place" manipulations and scanning of large specimens. The positioning stage is comprised of a 2 DOF long-range stage, for achieving traverses of up to 50 mm, and a 6 DOF short-range stage, to correct for positioning and angular errors generated by the long-range stage to achieve nanometer level positioning accuracies. A brief overview of the design, assembly and alignment of the positioning stage along with measurement results will be presented at the conference.

POSITIONING STAGE

This section provides an overview of a 2 degree-of-freedom (DOF) long-range stage for traverses up to 50 mm in each axis, while utilizing a 6 DOF short-range stage to correct for any motion errors generated by the long-range stage and therefore providing nanometer positioning capabilities.

2 DOF long-range stage

The 2 DOF long-range stage is comprised of two single DOF stacked slideways for traverses of up to 50 mm. Each slideway is comprised of 6 kinematically positioned, ultra-high molecular weight polyethylene (UHMWPE) bearings [1] mounted onto the bottom of the carriage, and contacted against two Zerodur optical flats. To generate the sliding motion of the carriage a feedscrew (pitch of 0.4 mm per revolution) driven by an Aerotech frameless motor translates a polymeric nut [2] that is attached to the carriage through a decoupling mechanism. The decoupling mechanism is comprised of a thin rod (1 mm in diameter) in tension to attenuate parasitic motions generated by the drive mechanisms from being transferred to the carriage. This design concept was initially tested in a separate single DOF slideway that was capable of maintaining controller errors of 100 nm rms over a 5 mm traverse [3]. The completed 2 DOF long-range stage is shown in figure 1.

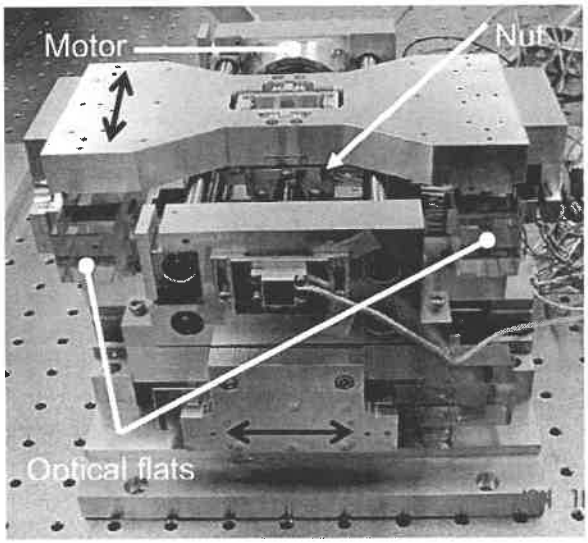

FIGURE 1. Image of the completed 2 DOF long-range stage.

6 DOF short-range stage

To achieve nanometer positioning a third generation 6 DOF short-range stage, see figure 2, is mounted on top of the 2 DOF long-range stage, and is utilized to correct for any motion errors generated by the long-range stage.

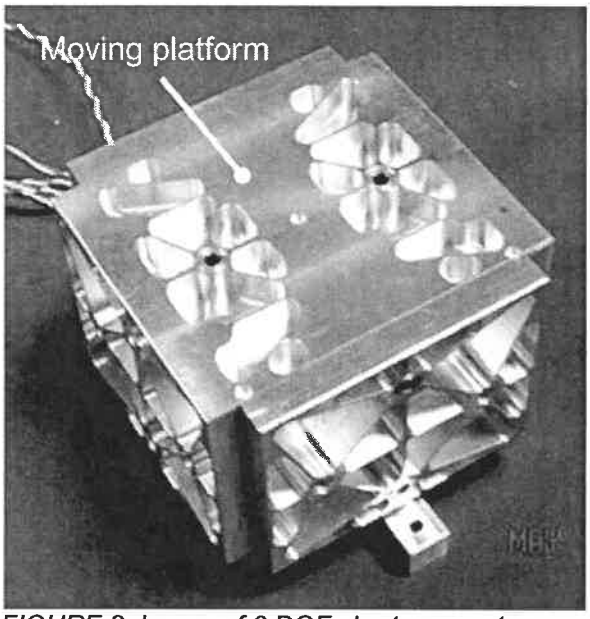

FIGURE 2. Image of 6 DOF short-range stage.

The 6 DOF short-range stage is comprised of a moving platform (rigid body), base structure, and 6 actuators (2 for each axis). The actuator is mounted, at one end, to the base structure by a v-groove clamp and, at the other end, to the moving platform using a collet. These are indicated by the flexures in figure 3 and provide a coupling having 5 DOF or a single axial constraint between the base and moving platform. Each actuator pair has a translation capability of 4 μm while being able to generate a rotation of 160 μRad.

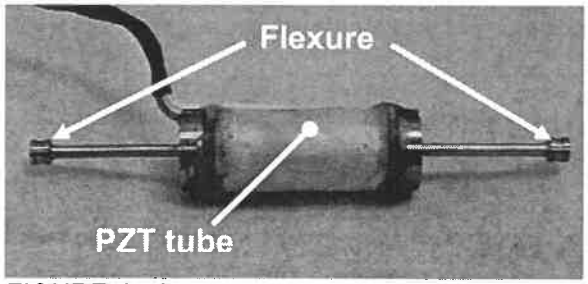

FIGURE 3. Actuator used in the 6 DOF short-range stage.

Table 1 shows the dynamic response of the 6 DOF short-range stage with a ~360 gram load on top of the moving platform. The resonant frequencies between 200 and 300 Hz are mainly due to the large mass of the capacitance target electrodes used to measure the three dimensional response. This mass center was also a long distance from the line of action of the actuators, thereby contributing a considerable second moment of mass about these axes. Whereas, the *z*-axis actuates directly through the center of mass, resulting in a higher first resonant frequency in both linear and angular coordinates.

TABLE 1: Dynamic responses of the 6 DOF short-range stage for each individual DOF.

Coordinate	First resonant frequency (Hz)
x	208
y	301
z	524
θ_x	280
θ_y	208
θ_z	588

POSITION FEEDBACK

To measure or monitor the displacement of the positioning system a laser interferometer is used in all 6 DOF. The laser interferometer system is comprised of a Zygo 7722 HeNe laser, 4-pass optic, 4 DOF fiber optic coupler (see figure 4), and two Zygo 4004 measurement boards.

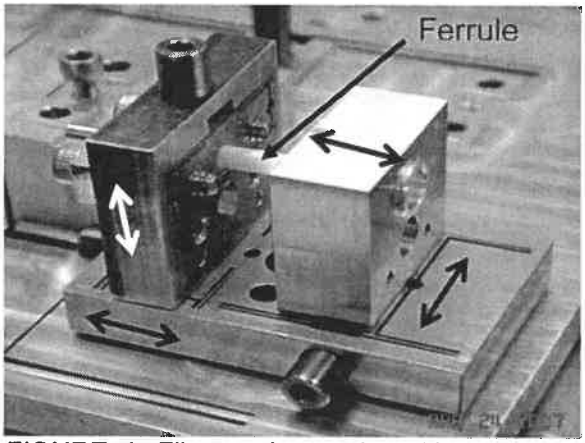

FIGURE 4. Fiber optic coupler with 4 DOF to launch the laser beam into a fiber and carry the beam to the Zygo 4004 measurement boards.

PROBING

One of the main objectives of this work is to be able to perform studies on a variety of mechanical probing schemes with nanometer positioning capabilities. This study will initially be performed on commercially available probes and

then later on probing schemes developed within the Center for Precision Metrology. One of the initial probes, from Insitutec Inc., to be used in this positioning system is a tuning fork with an attached fiber, as developed by Bauza *et.al* [4]. The operating principle is based on the tuning fork shaking an optical fiber or shank to generate standing waves in the fiber and producing a virtual tip, see figure 5.

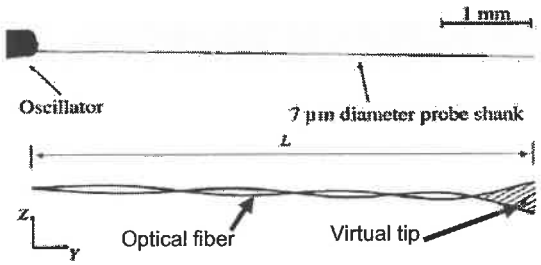

Figure 5: Operating principle of the fiber tuning fork probe, taken from Bauza et.al. [4].

In order to maintain a constant force during probing with the fiber tuning fork probe a single DOF translation stage was fabricated, see figure 6 and figure 7. The translation stage generated a translation of approximately 5 μm and a first resonant frequency of approximately 6176 Hz. Position feedback is provided by a capacitance gage.

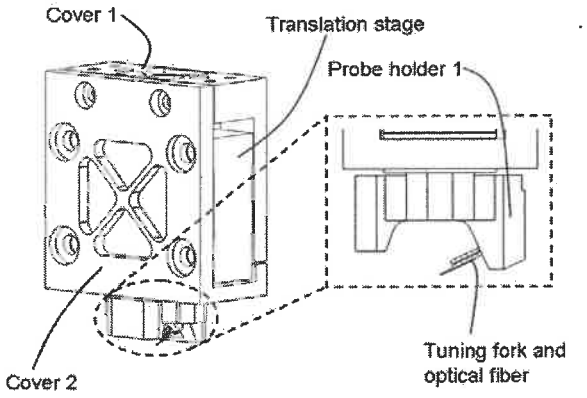

FIGURE 6. Line diagram of the translation stage used to maintain a constant probing force.

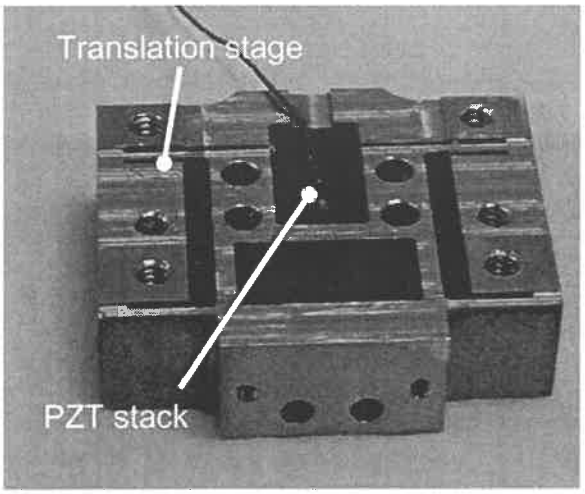

FIGURE 7. Image of the translation stage.

ASSEMBLED POSITIONING SYSTEM

The completed positioning system is shown in figure 8, with major components highlighted. Currently the laser interferometer is being incorporated into the system. The current status of the positioning stage is depicted in figure 9.

An overview of the design, assembly and alignment of the positioning stage along with measurement results will be presented at the conference.

ACKNOWLEDGEMENTS

The authors would like to thank Hua Yang (UNCC) and Richard Seugling (LLNL) for their valuable contributions toward the development of the positioning system. The authors are also thankful to the Center for Precision Metrology (UNCC), the Department of Mechanical Engineering (MIT) and the National Science Foundation (DMI-0210543) for support of this work. Any opinions, findings, and conclusions or recommendations expressed in this material are those of the author(s) and do not necessarily reflect the views of the National Science Foundation.

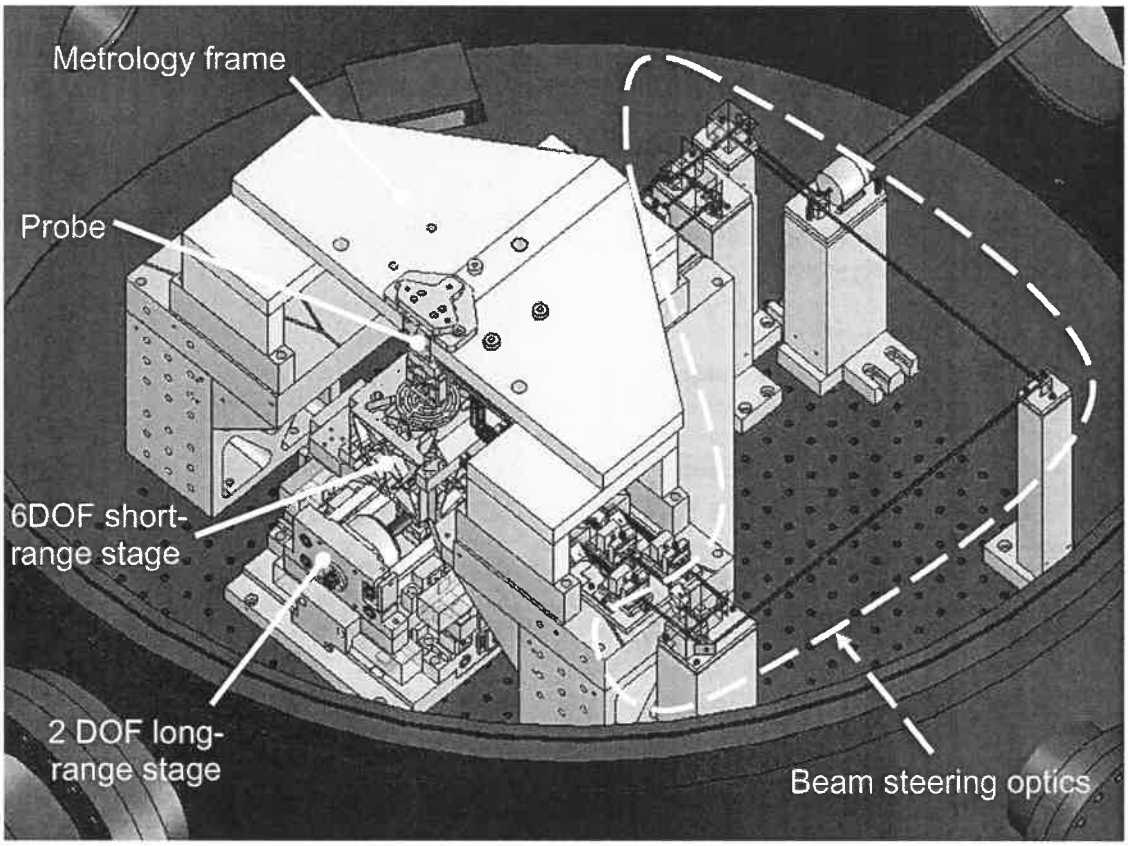

FIGURE 8. Solid model of the positioning stage in the vacuum chamber with key components highlighted.

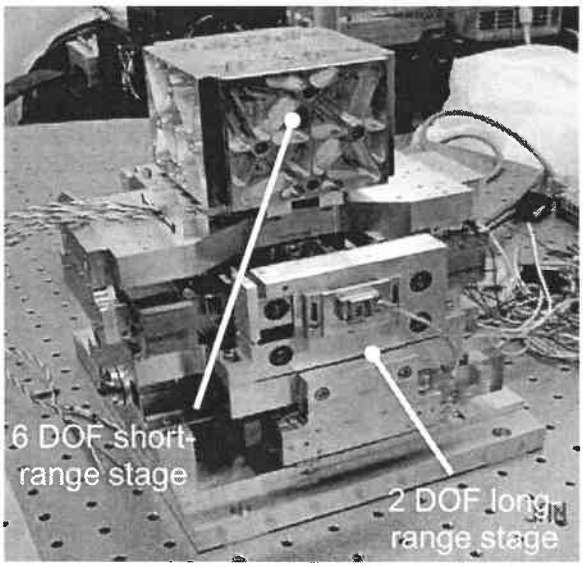

FIGURE 9. Image depicting the assembled 2 DOF long-range and 6 DOF short-range stages.

REFERENCES

[1] Buice ES, Yang H, Seugling RM, Smith ST, Hocken RJ. Evaluation of a novel UHMWPE bearing for applications in precision slideways. Precision Engineering Journal. 2006; 30 (2): 185 – 191.

[2] Buice ES, Yang H, Smith ST, Hocken RJ, Trumper DL, Otten D, Seugling RM. A comparison of drive mechanisms for precision motion controlled stages. Proceedings of the European Society of Precision Engineering and Nanotechnology. 2006; 6 (1): 321 – 324, ISBN: 0955308208.

[3] Buice ES, Otten D, Yang H, Smith ST, Hocken RJ, Trumper DL Seugling RM. Control of a 2 DOF long-range and 6 DOF short-range stages for nanometer positioning. Proceedings of the American Society of Precision Engineering. 2006; 37.

[4] Bauza MB, Hocken RJ, Smith ST, Woody SC. Development of a virtual probe tip with an application to high aspect ratio microscale features. Review of Scientific Instruments. 2005; 76: 095112-1 – 8.

SYNTHESIS OF MULTI-DEGREE-OF-FREEDOM PRECISION FLEXURE CONCEPTS VIA FREEDOM AND CONSTRAINT TOPOLOGIES

Jonathan B. Hopkins[1], Martin L. Culpepper[1]
[1]Department of Mechanical Engineering
Massachusetts Institute of Technology
Cambridge, MA, United States

ABSTRACT

In this paper we introduce a new approach – Freedom and Constraint Topology – to the conceptual design of parallel precision flexures. The import of this work is that it provides a means (a) to synthesize flexures with coupled or non-coupled degrees of freedom in a deterministic manner and (b) to rapidly generate flexure concepts with coupled or non-coupled motions. This method represents the general shape of a flexure's constraining elements (constraint topology) and the flexure's degrees of freedom (freedom topology) as 3D shapes. For a desired set of motions, there is a unique constraint topology. This geometric mapping technique makes it possible to select the proper constraint topology for a set of desired motions requirements. Several specific concepts may then be generated from the general 3D shape that represents the constraint topology

INTRODUCTION

The intent of this paper is to introduce a new method – Freedom and Constraint Topology (FACT) – that may be used to synthesize multi–degree of freedom (MDOF) flexure system concepts. Flexure systems consist of a combination of rigid and flexural elements. These elements are arranged and connected in a way such that their compliant directions permit specified motions and their stiff directions prevent motions in other directions.

Flexures are important to conventional precision applications, for instance they are commonly used within optical manipulation stages, precision motions stages, nanomanufacturing equipment and instruments that are used in nano–scale research. Many of these devices require the capability to move in several axes such that the motions achieved via some axes may be coupled and/or they may be independent of the other motions. This paper provides a means to synthesize parallel flexure systems for these types of applications.

The synthesis of multi–axis parallel flexure concepts is difficult because there are several flexural components and these components provide constraints and permit motions in orientations that are not generally parallel between the different elements. It is necessary, and difficult, for designers to keep track of (a) the relative, three dimensional orientations of the flexural constraints, (b) the orientation of the permitted motions, and (c) the three dimensional relationships between each constraint and the permissible motions. Given the preceding, it should not be surprising that parallel flexure systems with three to five degrees of freedom (DOFs) are designed via iteration and designers are fortunate if they are able to synthesize one or two new and viable concepts.

Figure 1A provides a contrast of the traditional design method used in precision engineering, constraint–based design (CBD), and FACT.

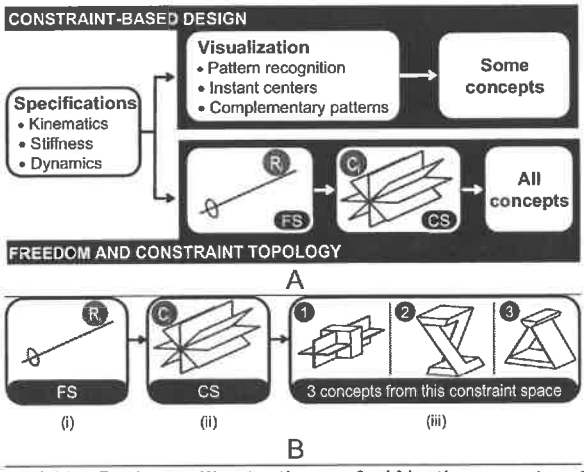

FIGURE 1. . Illustration of (A) the contrast between CBD and FACT and (B) example geometric shapes that represent the permissible motion – Ri – and the appropriate geometric shapes that contain the constraints – Ci – that are used to generate several concepts for a flexure system that permits the desired motion.

In CBD, a designer must use his visualization skills, pattern recognition and CBD's rule of complementary patterns to guide a visual iteration process until a viable flexure system concept is identified. Additional concepts are generated via more iteration. In contrast, FACT uses sets of 3D geometric shapes, for example planes and spheres, to embody quantitative information about a flexure system's shape and its DOFs. These types of geometric shapes, for instance the examples shown in Figure 1Bii, are capable of displaying the general form of a flexure system design. All possible concepts are represented within the shapes and therefore a designer may have access to all solutions for a given motion guidance problem. These shapes may also be used to determine when coupled rotations–translations exist and they may also be used to visualize coupled rotations–translations.

In the FACT method, a first set of shapes contains information about the flexure system's DOFs (its freedom topology) and a second set contains information about the flexure system's geometry (its constraint topology). If a designer wanted to generate concepts for a flexure system with one rotation DOF, they would first specify the geometric shape (freedom topology) that represents this rotation. The designer then identifies the rotation line in Figure 1Bi as the desired topology. The principle of complementary topologies is then used to find the set of geometric shapes, i.e. the intersecting planes in Figure 1Bii, that represents concepts for all parallel flexure systems that can permit the specified DOF. The designer then selects constraints that lie within the shapes that represent permissible constraints in order to form various different concepts. For instance the three concepts shown in Figure 1Biii contain flexural constraints that lie within the planes. This example demonstrates the use of FACT for a simple flexure design, however more complex, multi-DOF flexures may be designed [1,2].

Designers need to understand two main issues with respect to FACT, the:

(1) geometric shapes that are used to synthesize parallel flexures and

(2) the process one should follow to use the shapes while forming concepts.

The details on the second point are summarized in a complimentary paper within these proceedings: *A Design Process for the Creation of Precision Flexure Concepts via the use of Freedom and Constraint Topology*. The contents of that document will be best appreciated after learning about the first point, the shapes, in this document.

BACKGROUND KNOWLEDGE USED IN FACT

This section provides an overview of principles that are central to the use of FACT.

Maxwell's Principles of Constraint

A first principle of constraint–based design is that a rigid body has six DOFs and any non–redundant constraint upon the body removes a DOF. This may be expressed as:

$$R = 6 - C \qquad (1)$$

where C is the number of non–redundant constraints and R is the number of DOFs. Non–redundant constraints are mathematically equivalent to constraints that possess lines of actions, i.e. vectors, which are independent.

A constraint is idealized as providing resistance to motion along its line of action only. Maxwell augmented this equation with observations that enable one to understand some of the DOFs that are permitted given the lines of action of a system of constraints [3]. Maxwell used these principles to design many types of precision instruments and fixtures for his experiments.

Projective Geometry

In the design of multi-axis devices, i.e. as in robotics, it is useful to visualize geometric shapes that possess a mix of finite dimensions and dimensions that approach infinity. The mathematic field of projective geometry addresses these types of geometric shapes. The first principle of import from this field may be stated as lines emulate circles with a radius of curvature that approaches infinity. The relevance of this principle is demonstrated in Figure 2. For small motions, translations may be emulated by rotations about a circle whose radius approaches infinity. The circle is shown as a "hoop" in Figure 2. The rotation of the stage could occur about points on this hoop such that the rotation yields a motion that emulates a translation in a direction that is perpendicular to the plane of the hoop. This is

an important concept because CBD and FACT treat translational motions as though they are the result of a rotation about a hoop.

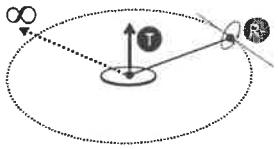

FIGURE 2. Illustration showing how a hoop represents a translation via a rotation, R_T

The second relevant principle from this field is that parallel lines may be considered to share an intersection in the limit as the lines approach infinity. These principles have been used in CBD and will also be used in FACT to identify the intersections between geometric shapes that represent constraints and DOFs.

The Rule of Complementary Patterns

Blanding [4] viewed constraints and DOFs via constraint lines and freedom lines respectively. A constraint line is the line of action of an idealized constraint. All DOFs are viewed as rotations about a freedom line. The hoop principle from the previous section is used to describe translations in terms of rotations. Blanding's Rule of Complementary Patterns [4] states that every freedom line intersects every constraint line. This is powerful because it enables a designer to visualize the relative relationships between a flexure system's constraints and the DOFs that these constraints permit. The rule of Complementary Patterns has been used to design many mechanical devices, flexures and fixtures.

Screw Theory

To this point we have only considered rotation DOFs, i.e. freedom lines. It is possible for a parallel flexure to undergo coupled translations-rotations, i.e. screw lines. CBD principles can not be used to diagnose or synthesize flexures that exhibit this type of behavior.

Screw theory may also be used to create geometric shapes that contain information about coupled DOFs. Screw theory may be used to derive the following relationship that links constraints and coupled rotations–translations:

$$p \cdot \cos(\psi_i) = r_i \cdot \sin(\psi_i) \qquad (2)$$

In Equation 2, r is the shortest distance between the constraints and the axis of the screw motion, ψ is the skew angle between the screw and the constraint lines, and p is the translation per unit rotation, or pitch. In FACT, the shapes are used to visualize all permissible motions (rotations, translations and screws). The utility of the preceding will become apparent in a moment.

PRINCIPLE OF COMPLEMENTARY TOPOLOGIES

The Rule of Complementary Patterns that is used in CBD can not address coupled degrees of freedom and so it is not possible to use this principle alone if one wishes to understand/design for translations, rotations and screws. With the Principle of Complimentary Patterns, it is possible to design a flexure that will end up possessing unwanted, coupled degrees of freedom. Given the necessity for deterministic design in precision engineering, it is desired to have a general principle that applies to coupled degrees of freedom.

The Principle of Complementary Topologies was created to map freedom and constraint topologies that are relevant when any combination of translations, rotations or screws occur. The principle states that a set of 3D shapes which contains freedom lines and a set of 3D shape that contain constraint lines are complementary when all the constraint lines are complimentary to all the freedom lines. This condition occurs when Eq. 2 is satisfied for each constraint-freedom line pair between the sets.

In practical terms, this principle (a) enables the matching of any set of desired motions (translations, rotations and screws) with shapes wherein any of the constraint lines is a valid option for use in the flexure and (b) may be used to prove [1] that there are only 26 different sets of motions (translations + rotations + screws) and 26 different types of parallel flexures that provide them. This is good news for designers as they only need to learn how to translate their motions' requirements into the shapes that represent the motions and then find the matching set of shapes that show them how to arrange a flexure's geometry to allow the desired motions. It is not possible to show them here due to size limitations. The proof of this statement, and the 26 types of parallel flexures, are available in the reference [1,2].

USING FACT TO GENERATE CONCEPTS

As an example (see [2] for more examples) suppose we desired to synthesize concepts for a parallel flexure (not a stacked set of flexure stages) that would translate and rotate an optic. The translation must be orthogonal to the axis of rotation and all other motions are to be resisted. The sets of shapes that represent the desired motions are shown in Figure 3A and the complementary set of shapes that contain permissible constraints are shown in Figure 3B.

The former consists of (1) a hoop that represents the translation and (2) a plane of parallel freedom lines that are orthogonal to the direction of the translation. The latter consists of (1) a box that represents every line that is orthogonal to the translation and (2) every line that lies on a plane that is parallel to, or coincident with, the parallel constraint lines. We use Eq. 1, which tells us to select four non-redundant constraints from the box and plane in order to achieve two degrees of freedom.

Figures 3C–3F, 3G–3J, 3K–3N show three ways to pick four independent constraints. There are many other possible solutions that may be generated using these shapes.

REFERENCES

[1] Hopkins J. Design of Parallel Flexure Systems via Freedom and Constraint Topologies. Masters Thesis. Massachusetts Institute of Technology, 2007.

[2] Hopkins, J.B. and Culpepper, M.L., "Synthesis of Multi–degree of Freedom Flexure System Concepts via Freedom and Constraint Topologies (FACT)," Submitted to Precision Engineering.

[3] Maxwell J. General Considerations Concerning Scientific Apparatus. The Scientific Papers of James Clerk Maxwell. New York: Dover Press, 1890; 2:505-21.

[4] Blanding D. Exact Constraint: Machine Design using Kinematic Principles. New York, NY: ASME Press; 1999.

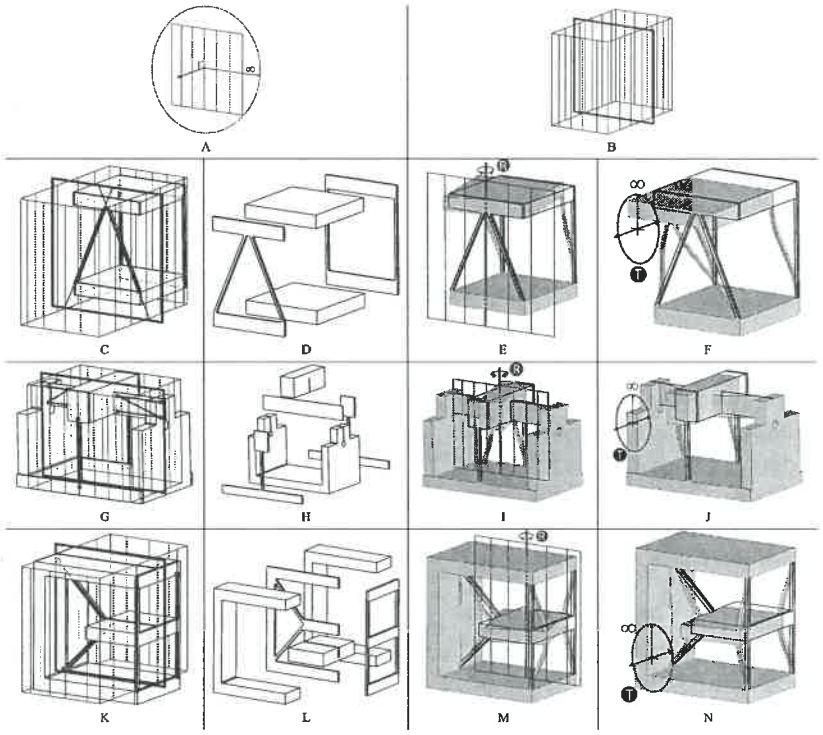

FIGURE 3. The freedom space for orthogonal rotational and translation motions (A) and the constraint space (B) that yields several viable topologies/embodiments – (C), (G), and (K). FEA post processing of the components – (D), (H), and (L) – of each embodiment contrast the respective deformed and non–deformed states for the rotational motion – (E), (I), and (M) – and the translation motion– (F), (J), and (N) – of each flexure.

A DESIGN PROCESS FOR THE CREATION OF PRECISION FLEXURE CONCEPTS VIA THE USE OF FREEDOM AND CONSTRAINT TOPOLOGY

Jonathan B. Hopkins[1], Martin L. Culpepper[1]
[1]Department of Mechanical Engineering
Massachusetts Institute of Technology
Cambridge, MA, United States

ABSTRACT

In this paper we introduce a systematic process that may be used to generate concepts for multi-degree of freedom, parallel flexure systems. The process described herein guides the designer in (a) determining if it is possible to solve their problem by using a parallel flexure, (b) selecting the right shapes to represent the flexure's motions and the flexure's geometric layout, (c) selecting the minimum number of flexure constraints for a given design and (d) selecting redundant constraints that improve a flexure's stiffness characteristics and its symmetry. This paper compliments a concurrent submission in the proceedings: *Synthesis of Multi-Degree-of-Freedom Precision Flexure Concepts Via Freedom and Constraint Topologies*.

INTRODUCTION

Freedom and Constraint Topology is a new method for use in synthesis of parallel flexure systems [1,2]. This method uses geometric shapes to represent a flexure's motions and geometry. The shapes have special characteristics that can be used to link flexure motion shapes and flexure geometry shapes. This linking enables one to use a catalog of matching motion/geometry shapes to rapidly generate flexure concepts once the desired motions are known. Designers need to understand two main issues with respect to FACT, the:

(1) The geometric shapes that are used to synthesize parallel flexures; and

(2) The process one should follow to use the shapes while forming concepts.

The details on the first point are summarized in a complimentary paper within these proceedings: *Synthesis of Multi-Degree-of-Freedom Precision Flexure Concepts Via Freedom and Constraint Topologies*. It would be helpful to read that document prior to learning about the process that is contained in this paper.

The process described herein guides the designer in (a) determining if it is possible to solve their problem by using a parallel flexure, (b) selecting the right shapes to represent the flexure's motions and the flexure's geometric layout, (c) selecting the minimum number of flexure constraints for a given design and (d) selecting redundant constraints that improve a flexure's stiffness characteristics and its symmetry.

There are other design processes that are geared toward creating new concepts for compliant machine elements/devices, such as topological synthesis and constraint-based design (CBD); however, they are not ideally suited for solving all parallel flexure problems in precision applications.

Topological synthesis is a concept synthesis method that uses computer algorithms to add/subtract material from an initial design volume/space in order to create an optimal topology for a compliant device's design requirements [3]. Unfortunately, topology synthesis is not readily applied to most precision flexure design problems. This is due to the specialized precision machine design knowledge that is required [1] and the fact that the designer is removed from the decision making process when a concept is created. The FACT design process is user-driven, therefore enabling the designer to apply their precision engineering knowledge and any custom requirements during the design process.

The fundamental premise of CBD is that all motions of a rigid body are determined by the

position and orientation, i.e. the topology of constraints, that act upon the body [4,5]. The rules/principles of CBD are used by designers to visualize the relationship between motions and constraints via the intersections of their lines of action. This method is not general in that it is only capable of use with rotations and translational motions; it can not predict coupled translations-rotations and there is no guarantee that an undesired coupling will occur even when all its design rules/principles are followed. FACT is capable of handling coupled degrees of freedom. In addition, there are many cases wherein it may be difficult to visualize the relationships between constraints and motions when multiple degrees of freedom exist. The FACT design process eliminates the need to perform complex visualization.

PROCESS FOR GENERATING CONCPETS

At this point, we are only interested in the early stage synthesis of concepts that would provide the desired kinematics. The concepts that are developed through this process may then be modeled and refined using the direct stiffness approaches or FEA. The process consists of 6 steps that are demonstrated below in the context of a practical flexure design problem. The six steps are listed below and illustrated in Figure 1:

Step 1: Determine the stage's geometry.

Step 2: Specify the desired motions, the freedom topology, of the stage.

Step 3: Select the best sets of geometric shapes that represent the desired freedoms. These shapes have matched sets of geometric shapes that describe the constraints. The matched sets are selected from a chart that contains the 26 possible ways to solve a parallel flexure problem [1]. The sets of shapes that are used to describe the freedoms and constraints are called freedom spaces and constraint spaces.

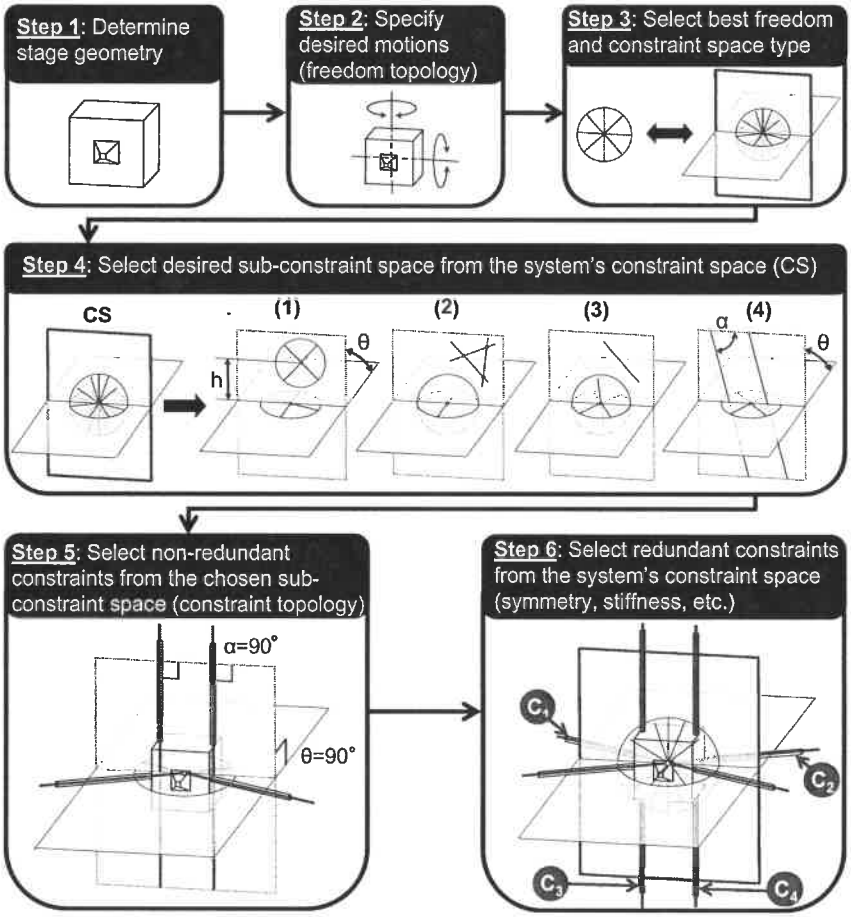

FIGURE 1. FACT synthesis process applied to the design of a two–axis, i.e. yaw-pitch, flexure system

Step 4 Select a constraint space. There are many ways to select constraints from a given set of shapes. For instance, the four different ways to select independent constraints as shown in Fig. 4 step 4. Each of the different ways is called a sub–constraint space. The goal of step 4 is to select a sub-constraint space that best addresses design constraints such as device envelope, symmetry, location of flexure attachment points, etc...

Step 5 Select the minimum number of constraints, i.e. non–redundant constraints that provide the desired motion. They are selected from a sub–constraint space.

Step 6: Select redundant constraints, if required, from the system's constraint space.

PROCESS APPLIED TO AN EXAMPLE

We wish to design a flexure system that positions a stylus during profilometry of concave, hemispherical surfaces on a wafer. This two-DOF flexure system permits only yaw and pitch rotations. Sensitivity to thermal expansion errors is to be minimized, preferentially by using a symmetric design.

Step 1: Determine the Stage's Geometry

The first step is to determine the stage's geometry. The only restrictions on the stage's geometry are determined by fabrication constraints, as well as other constraints such as compatibility with surrounding components. In Step 1 of Figure 1, a rectangular stage has been selected. It is also important to note that this geometry may later be altered if this is desired.

Step 2: Specify the Desired Motions of the Stage (Freedom Topology)

The second step requires the designer to specify the system's freedom topology, i.e. the degrees of freedom with which he/she would like the stage to move. Step 2 of Figure 1 illustrates the two desired rotations that the probe's stage is intended to move with, yaw and pitch, about the lines as indicated.

Step 3: Select the Best Freedom and Constraint Space Type

The third step is to find the freedom and constraint space type from among the complete set of 26 types [1]. If a matching case can not be found, then it is not possible to achieve the motion with a parallel flexure. Fortunately, our motion is among the listings for possible two DOF flexures.

The freedom and constraint space type for the two–axis probe example of this section is Case 4, Type 1 [1,2]. This type is shown in Step 3 of Figure 1. Its freedom space consists of a pencil of rotational freedom lines. Any two lines in this disc may be used to achieve two independent rotations, such as our two orthogonal rotations. This type's constraint space consists of two superimposed shapes (a) a plane that pierces the intersection of the pencil and (b) a sphere whose center is coincident with the intersection within the pencil. Any desired constraint lines may be selected from the plane. The sphere represents any constraint line that pierces the center of the sphere and hence the center of the pencil.

Step 4: Select the Desired Sub-Constraint Space from the System's Constraint Space

There are four ways in which to select four independent constraints from the plane and sphere. Each way is represented by a sub-constraint space in Fig. 1. Each sub–constraint space yields different types of constraint topologies and therefore different flexure design concepts. When the goal is to generate many concepts, it is prudent to synthesize concepts from each sub–constraint space. Other factors, such as symmetry, balanced stiffness and geometric constraints, affect which sub–constraints may generate concepts that provide practical solutions. For example, if the stage and ground geometries are set, it may not be possible to select constraints from a certain sub–constraint space such that they could link the stage in ground in a practical way.

For our example, we will select the fourth sub–constraint space shown in Figure 1 because it is easily used to create a symmetric design when redundant constraints are selected.

Step 5: Select Non-Redundant Constraints from the Sub-Constraint Space (Constraint Topology)

The next step is to decide where to place the stage among the constraint lines within the sub–constraint space so that the desired non–redundant constraints intersect the stage. That is, so they may be physically attached to the stage.

At this point, precision engineering principles and best practices become important. For instance, intersecting constraints provide balanced stiffness, when they are orthogonal and the rotary stiffness of parallel constraints improves as the distance between them grows. Furthermore, flexural constraints should have the proper aspect ratios to emulate ideal constraints and to avoid buckling.

In this example, we position and orient the stage body within the fourth sub–constraint space as shown in Step 5 of Figure 1. Fabrication considerations lead us to select θ and α equal to 90 degrees. Stability considerations lead us to select two constraints from the plane of parallel constraints that are as far apart as practical. We select two constraints from the pencil of constraint lines in such a way that allows space for a sample to approach the stage without interfering with the flexure constraints.

It is important to note, that once Step 5 is complete, the flexure system is "exactly" constrained and therefore the stage will move with the desired degrees of freedom. In some instances, the designer could stop here having achieved the desired motions. For this example, however, we continue on to Step 6, where we will have the opportunity to add redundant constraints that improve the flexure's symmetry and therefore its thermal stability.

Step 6: Select Redundant Constraints from the System's Constraint Space

In step six, the designer selects redundant constraints from within the system's constraint space. By adding redundant constraints, the flexure system design may be improved without affecting its kinematics. Furthermore, suppose the designer wishes to add stiffness to the system without making the existing constraints shorter or thicker. This may be realized by adding appropriate redundant constraints.

In Step 6 of Figure 1, four redundant constraints have been added to the stage from within the constraint space of Case 4, Type 1. Figure 2A and Figure 2B show this flexure system after having flexed to produce yaw and pitch. These images were generated using an FEA analysis tool. These motions would be controlled via actuators that are appropriately positioned and oriented between the stage and a ground.

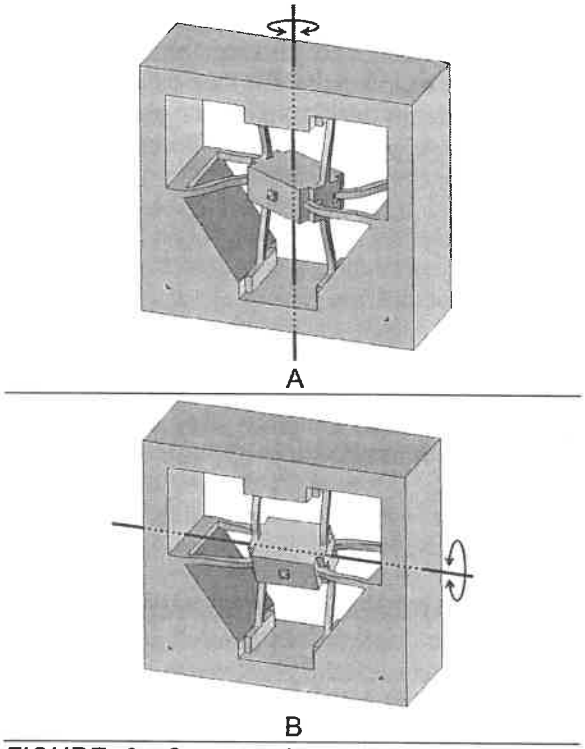

FIGURE 2. Concept for a practical two–axis flexure system that is capable of yaw and pitch rotations. Parts A and B show the independent rotations, yaw and pitch, that the flexure system is capable of guiding

REFERENCES

[1] Hopkins J. Design of Parallel Flexure Systems via Freedom and Constraint Topologies. Masters Thesis. Massachusetts Institute of Technology, 2007.

[2] Hopkins, J.B. and Culpepper, M.L., "Synthesis of Multi–degree of Freedom Flexure System Concepts via Freedom and Constraint Topologies (FACT)," Submitted to Precision Engineering.

[3] Ananthasuresh G, Kota S, Kikuchi N. Strategies for Systematic Synthesis of Compliant MEMS. Proceedings of the 1994 ASME Winter Annual Meeting, November 1994

[4] Blanding D. Exact Constraint: Machine Design using Kinematic Principles. New York, NY: ASME Press; 1999.

[5] Hale L. Principles and Techniques for Designing Precision Machines. PhD Dissertation, Massachusetts Institute of Technology, 1999.

OPTIMIZATION OF DIAMOND MICRO-DRILLING PROCESSES IN GLASS MACHINING

Hyun-Ho Kim and Sung-Chong Chung*
Hybrid System Design & Control LABoratory
Department of Mechanical Engineering
Hanyang University, Sungdong-Gu, Seoul 133-791, KOREA

ABSTRACT
Optical and medical devices require micro-drilling of holes on glass. Brittle fracture occurs during the drilling on the glass. Cone and radial cracks are generated due to impact load and walking when a drill hit a glass to make a hole. In this paper, diamond micro-drills are applied to produce accurate holes on glass. To minimize cracks developed around the hole exit, a backup panel method is introduced. To monitor micro cracks and analyze the diamond drilling mechanics, vision and force measurements are applied for experiments. Optimal selection of drilling parameters assisted by backup panels is studied through Taguchi method.

INTRODUTION
Glass and ceramic materials are widely used in construction, IT, BT, optics and manufacturing industries. Compared to metal or high molecular materials, ceramic and glass materials have better characteristics against wear and corrosion. However, as they are difficult to drill, it is hard to get accurate machining results in the ceramic and glass machining processes. Diamond micro-drills made of diamond grits are used on glass and ceramic drilling. As the glass and ceramic are isotropic, it is difficult to obtain precision micro holes though machining processes.

Swain [1] conducted the sliding indentation job by using Vickers compression against soda lime glass. Ceramic machining process by using a micro diamond drill was conducted for alumina green bodies [2]. Condition monitoring of micro-drilling processes on glass by using machine vision was conducted through twisted cutting edge micro-drills [3].

Brittle fracture occurs during the drilling on the glass. Cone and radial cracks are generated due to impact load and walking when a drill hit a glass to make a hole. In this paper, diamond micro-drilling of glass assisted with backup panels are conducted to reduce the cracks. To monitor micro cracks and analyze the diamond drilling mechanics, the machine vision [3, 4] and force measurements are applied for experiments. Selection of optimal drilling conditions to protect from cracks is conducted through Taguchi method.

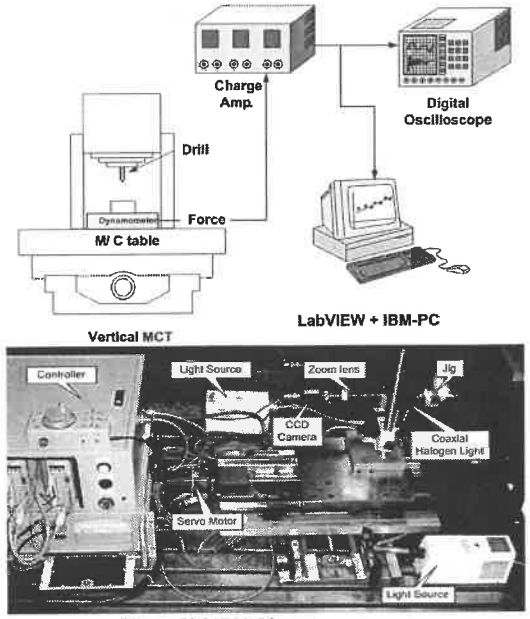

FIGURE 1. Experimental setup.

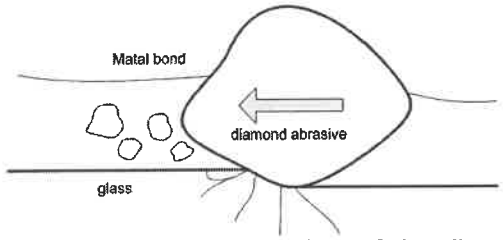

FIGURE 2. Cutting mechanism of the diamond grit on the glass.

EXPERIMENTS

Experimental setup
Fig. 1. shows the overall experimental setup. Drilling experiments of glass are conducted on the vertical milling machine with maximum spindle speed of 12,000rpm. To measure drilling force, a tool dynamometer (9257B, KISTLER Co.) is mounted on the machine tool (VX 380TD,

WIA Ltd.) Digital oscilloscope (LeCroy, 9314A) and LabVIEW 8 are used for data acquisition. To measure cracks along the exit hole boundary, a machine vision system [3] equipped with the zoom lens and illumination unit is applied for the hole quality measurement as shown in Fig. 1.

Specimens and Tools

As a workpiece, the study employed soda-lime glass. The size of soda-lime glass used as a test material and the mechanical properties are as in the Table 1. As a representative brittle material, glass requires a different type of cutting process from that of the existing metal materials. Fig. 2. shows the schematic cutting process of the diamond abrasive. For brittle material, the impact load from the diamond abrasive appears and causes a crack in the brittle material, and a chip created by successive cracks is released outside through space between the fine hole and drill. Diamond drills with diameter 0.6mm and electro deposited #325/400 diamond grits shown in Fig. 3 are used for experiments.

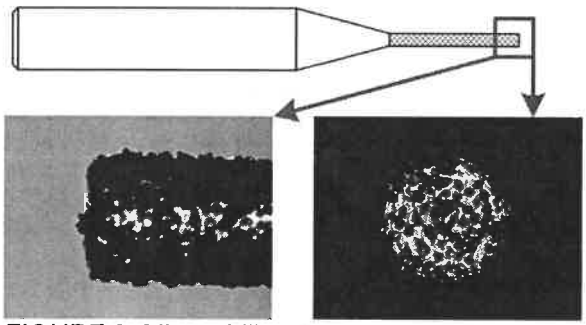

FIGURE 3. Micro-drill with diamond grits.

TABLE 1. Mechanical properties of workpiece.

Material	Soda-lime glass
Size	$21 \times 25 \times 1$ (mm)
Density	2490 (Kg/m^3)
Young's modulus	69 (GPa)
Poisson's ratio	0.22

TABLE 2. Levels of selected factors

Factor \ Level	1	2	3
Cutting fluid	No	Yes	-
Spindle rotation (rpm)	2000	2500	3000
Feed ($\mu m/rev$)	0.1	0.15	0.2
Peck feed (mm)	0.05	0.075	0.1
bond	No	Water	Oil

Experimental design and procedure

In the fine hole process of the brittle fracture, the study used the Taguchi method for determining the optimal process condition through the analysis of the size of crack by process condition and cutting force[5]. In order to identify any influence of heat generated from chip loading in the diamond micro drilling process, the test compared a dry micro drilling with a wet micro drilling by using cutting fluid [6]. As a way of minimizing any crack occurring to a fine hole of brittle material, it is necessary to use a fixation method, which can lower a drill thrust or reduce the transformation of a material [7]. Since there appears a crack to glass even by minute force, there is a limitation in the method of changing a cutting condition only as it increases a process time. Even when using a backup material, the parts around the fine hole are lifted up according to the compression level between the two glass workpieces before being penetrated by the micro drill. As a way of compressing the two glass workpieces, the study used an adhesion method with the use of water and oil (ISO 68). The factors used for the experiment and the level were designated as in the Table 2.

In order to designate the optimal process condition, the study used the Taguchi method. The study also used $L_{18}(2^1 \times 3^7)$ mixed orthogonal arrays. For accurate results, the study used the average value by measuring the crack size and cutting force after repeated processes of a couple of fine holes. Then, the study designated the optimal process conditions by comparing influential factors of crack size and cutting force, and analyzing the S/N ratio for each factor. In the meantime, the better and the smaller the crack size and the lower the cutting force. In the meantime, the better and the smaller the crack size and the lower the cutting force. Therefore, the study converted the ratio as a signal to noise ratio by applying a "smaller the better type" as in the formula below. The n represents the number of the repetition of a test, and the y is a measured data value.

$$SN = -10\log\left[\frac{1}{n}\sum_{i=1}^{n} y_i^2\right]$$

RESULTS AND DISCUSSION

Micro cracks

Values of crack factor(F_C) which represent the crack size that occurred to the entry and the exit of hole, the study measured the maximum diameter of the crack around the fine hole as in

the Fig. 4 and defined the maximum diameter(D_{max}) to the diameter(D) of the mocro-hole ratio.

$$F_C = \frac{D_{max}}{D}$$

Fig. 5. is a graph showing the results of the crack size occurring to the entry and the exit hole in each condition. As shown in the graph, there appeared a large crack more the exit than the entry. Also, there appeared smaller cracks around both the entry and the exit in the wet micro drilling when using cutting fluid. Fig. 6. is a graph showing the results of S/N ratio analysis. As also in the results of S/N ratio analysis, it was found that cutting fluid was the most influential to the crack size from the gradient of the graph.

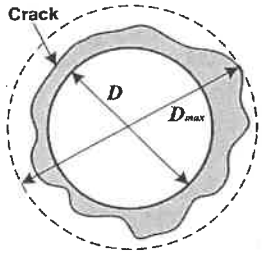

FIGURE 4. Cracks along the hole boundary

Cutting forces

The cutting force(F) appearing when processing a fine hole may be expressed as the sum of force(F_a) for removing a material as follows and the pressure(P) for removing a chip which occurred between the diamond particle of the micro drill and the fine hole.

$$F = F_a + \int PdA$$

The increase in pressure for removing a chip occurred between the diamond particle of a micro drill and the fine hall, generating the rise of heat in the process part of the fine hall as well as the change of cutting force. Heat generated from micro drilling accelerates the oxidation of the diamond particle, which is a major reason for diamond grit wear. The Fig. 7. is a graph showing the results of measuring cutting force under each test condition, and the Fig. 8 is a graph showing the results of S/N ratio analysis. Cutting fluid is shown most influential also in the change of cutting force

Optimum drilling conditions

It is possible to obtain the optimal cutting condition in cracks and cutting force, which is generated on entry and exit of micro holes. In order to designate the optimal micro-drilling condition, the study used the multiple-performance characteristics Taguchi method. In order to optimize the multiple-performance characteristics, namely, $F_{C(exit)}$ and F , the Taguchi parameter design with the utility concept has been introduced. Here both $F_{C(exit)}$ and F are to be minimized and hence "smaller the better type" quality characteristic has been selected for each of the responses. In the utility concept, the multi-response S/N ratio is

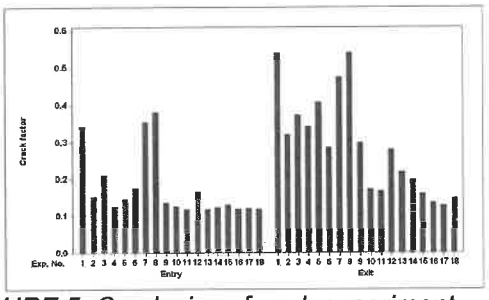

FIGURE 5. Crack size of each experiment

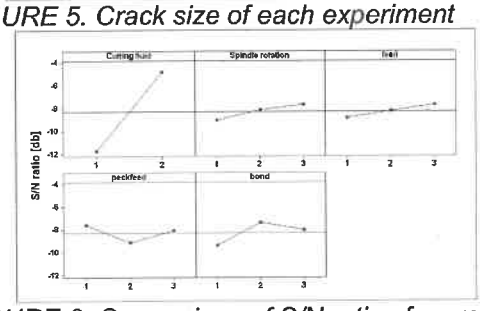

FIGURE 6. Comparison of S/N ratios for crack at exit of holes

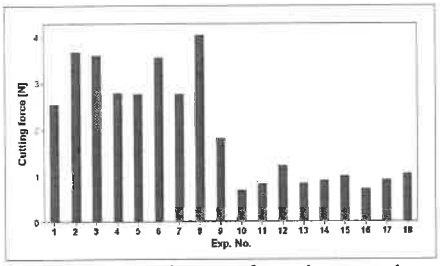

FIGURE 7. Cutting force of each experiment

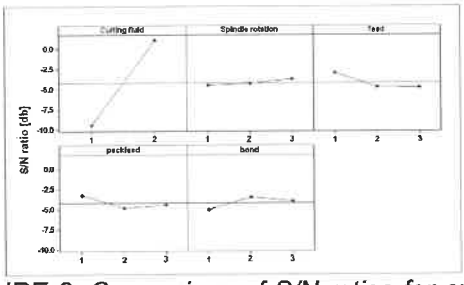

FIGURE 8. Comparison of S/N ratios for cutting force

TABLE 4. Response values and computed values of multi-response S/N ratio.

Exp. No.	$F_{C(\text{exit})}$	F	η_1	η_2	η
1	5.41	2.54	-14.66	-8.11	-12.52
2	3.20	3.68	-10.10	-11.32	-10.75
3	3.73	3.61	-11.44	-11.15	-11.30
4	3.43	2.78	-10.69	-8.89	-9.89
5	4.08	2.76	-12.22	-8.83	-10.85
6	2.85	3.56	-9.09	-11.03	-10.17
7	4.75	2.77	-13.54	-8.84	-11.80
8	5.43	4.05	-14.69	-12.15	-13.60
9	2.99	1.81	-9.50	-5.18	-7.86
10	1.74	0.68	-4.79	3.36	-2.40
11	1.67	0.82	-4.48	1.71	-2.40
12	2.79	1.22	-8.92	-1.70	-6.67
13	2.20	0.83	-6.83	1.61	-4.40
14	1.96	0.88	-5.85	1.07	-3.64
15	1.60	0.98	-4.06	0.18	-2.44
16	1.36	0.71	-2.69	2.95	-0.73
17	1.29	0.91	-2.21	0.85	-0.95
18	1.48	1.03	-3.38	-0.24	-2.09

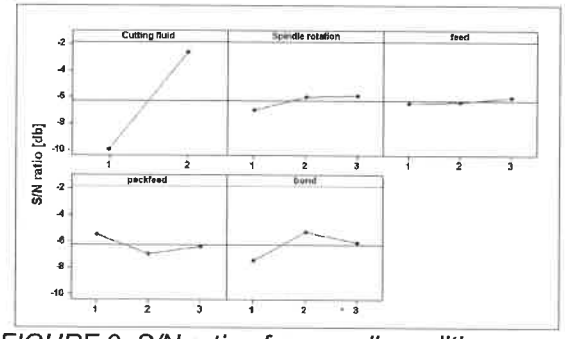

FIGURE 9. S/N ratios for overall conditions.

TABLE 5. Optimum micro-drilling conditions.

	Cutting fluid	Spindle rotation	Feed	Peck feed	bond
$F_{C(\text{entry})}$	Yes	3000	0.2	0.05	Water
F	Yes	3000	0.1	0.05	Water
Overall	Yes	3000	0.2	0.05	Water

$$\eta = \sum_{i=1}^{m} w_i \eta_i$$

where w are the weighting factors, and m are the number of the characteristic. In this study, there are same weight values for each characteristics. Reaction characteristics and multi-response S/N ratio analysis result as shown in the Table 4. Fig. 9 is a graph showing the results of optimal drilling condition through multi-response S/N ratio. Table 5 shows optimal drilling conditions for the each characteristic and overall characteristic indices.

CONCLUSIONS

In this study, the result is obtained from the experimental verification of micro-drilling of glass using diamond micro drills.

(1) The optimal drilling condition about factors affecting micro cracks and cutting force is selected using Taguchi design of experiment.

(2) In each experimental condition, the tendency of size of cracks is similar in entry and exit region.

(3) The wet drilling and compressing method of glass with water have good tendency for each characteristic.

(4) The optimum cutting conditions for each characteristic are as follow, the entrance of crack(2500 rpm ,0.2 $\mu m/rev$,0.05 mm), the exit of crack(3000 rpm ,0.1 $\mu m/rev$,0.05 mm), the result considering of multi-performance characteristics(3000 rpm ,0.2 $\mu m/rev$,0.05 mm).

REFERENCES

[1] Swian M V. Microfracture about Scratches in Brittle Solids. Proceedings of the Royal Society of London. 1979; A366: 575-597.

[2] Lee D G, Lee H G, Kim P J, Bang K G. Micro-drilling of Alumina Green Bodies with Diamond Grit Abrasive Micro-drills. International Journal of Machine Tools and Manufacture. 2003; 43: 551-558.

[3] Kim H H, Chung S, Kim S C, Jee W H, Chung S C. Condition Monitoring of Micro-Drilling Processes on Glass by using Machine Vision. Proceedings of the ASPE. 2006; 21: 535-538.

[4] Yoon H S, Chung S C. Vision Inspection of Micro-drilling Processes on the Machine Tool. Transactions of the NAMRI/SME. 2004; 32: 391-398.

[5] Tsao C C, Hocheng H. Taguchi Analysis of Delamination Associated with Various Drill Bits in Drilling of Composite Material. 2004; 44: 1085-1090.

[6] Kalidas S, DeVor R E, Kapoor S G. Experimental Investigation of the Effect of Drill Coatings on Hole Quality under Dry and Wet Drilling Conditions. Surface and Coatings Technology. 2001; 148: 117-128.

[7] Tsao C C, Hocheng H. Effects of Exit Back-up on Delamination in Drilling Composite Materials Using a Saw Drill and a Core Drill. International Journal of Machine Tools and Manufacture. 2005; 45: 1261-1270.

DEVELOPMENT OF A DESIGN TOOL SUPPORTING CONCEPTUAL DESIGN OF MACHINE TOOLS - APPLICATION TO MULTI-AXIS MACHINE TOOLS -

N. Mishima
Advanced Manufacturing Research Institute
National Institute of Advanced Industrial Science and Technology
Tsukuba, Ibaraki, JAPAN

INTRODUCTION

Since processes of machine tool design are rather experience basis, design procedures starting from conceptual to detailed design often take long time. At the same time, the variety of target products of machine tools is growing larger and larger. Conceptual design is very important to create appropriate design. In the former research [1]-[3] the author tried to develop a new design tool to support decision-making at the conceptual design stage of machine tools. The proposed design evaluation method based on robust design methodology [4] was effective in determining suitable structure of machine tools. The prediction results led by the design tool were similar to the existing knowledge. The fact proved the appropriateness of the design tool. However, to show the effectiveness of the design tool in supporting conceptual design, it is necessary to apply the tool to an actual design problem.

Recently, 5-axis machine tools that have, not only linear motion axis but also rotational axis, are becoming popular. Progress of computer power has made the multi-axis machine tools which was proposed many years ago, recent hot topics. However, when number of axis of machine tools increases, number of possible combinations and sequences of axis also increases greatly. It is impossible for a machine tool designer to prototype or to simulate the performance of all the candidates. So, this type of design tool will be useful in filtering designs, at the conceptual design stage. After decreasing the design candidates to considerable number, precise calculation based on FEM can decide the final machine tool structure. By applying the design tool to multi-axis machine tools, it is possible to make the design procedure efficient.

DESIGN EVALUATION METHOD BASED ON FORM-SHAPING THEORY

A machine tool structure can be thought of as a chain of directly linked rigid components extending from the product through the cutting tool. An orthogonal coordinate system corresponding to each element is defined. The transformation between two local coordinate systems is represented by a coordinate transformation. Form-shaping theory [4] represents these respective coordinate transformations by homogeneous transformation matrices (HTM) [5]. In an ordinary machine tool, HTM is represented by a parallel transition along the X, Y or Z axes or rotation around the axes. Each of these six coordinate transformations is assigned a distinguishing number, such as transformation along the X-axis being 1, and so on. By writing the HTM of ith element as A_i, vector represents the relative displacement between the product and the cutting tool, is given by equation (1). The equation is the definition of the form-shaping function that expresses the cutting motions of the machine tool. Actual machine tools have imperfect alignment, and experience thermal deformation, wear, and many other sources of error. In order to describe actual cutting motions, one must take these errors into account. Such errors can for convenience's sake be treated as errors in transformations between elements. Another homogeneous transformation matrices $A\varepsilon_i$ to generally represent transformation error between elements are defined. (Equation 2) By inserting the error component matrix $A\varepsilon_i$ between A_i and A_{i+1} in equation (1), the form-shaping function including errors, is written as equation (3). The form-shaping error function expressing the error as a quantitative deviation from the target value, is defined as the difference between the form-shaping function with and without errors, as equation (4). By analyzing the equation, it is possible to evaluate how each design parameter and error factor affects the overall performance. In addition, by analyzing different from-shaping functions having same design parameters and error factors value, it is

possible to compare the performance of different structure types.

$$\vec{r}_0 = A_1 A_2 \cdots A_i A_{i+1} \cdots A_n \times \vec{r}_t \quad (1)$$

$$A_{\varepsilon i} = \begin{bmatrix} 1 & -\gamma_i & \beta_i & \delta_{xi} \\ \gamma_i & 1 & -\alpha_i & \delta_{yi} \\ -\beta_i & \alpha_i & 1 & \delta_{zi} \\ 0 & 0 & 0 & 1 \end{bmatrix} \quad (2)$$

$$\vec{r}_{\varepsilon 0} = A_1 A_{\varepsilon 1} A_2 \cdots A_i A_{\varepsilon i} A_{i+1} \cdots A_n \times \vec{r}_t \quad (3)$$

$$\Delta\vec{r}_0 = \vec{r}_{\varepsilon 0} - \vec{r}_0 \quad (4)$$

$\vec{r}_0$: from-shaping function, $\vec{r}_t$: tool shape vector, $\vec{r}_{\varepsilon 0}$: form-shaping function with errors, $\Delta\vec{r}_0$: from-shaping error function

COMPARISON OF CALCULATION AND EXISTING DESIGN KNOWLEDGE

In advance to the application of the design evaluation method to 5-axis machine tools, it is necessary to show that the method has a certain validity. To prove this point, comparison of the prediction results with knowledge of skilled machine tool designers will be useful.

Expression of machine tool structure indicating motion axes and their sequence is called "structural code" of machine tool. Structures of a 3DOF(Degrees of freedom) vertical milling machine can be categorized into 4 major types. And the structural codes which correspond to those types are XYZ/, XY/Z, X/YZ and /XYZ. The question was "which of these 4 structural types has the best performance, when the characteristics of components are all the same". Figure 1 shows a 3DOF milling machine which has the structural type "XY/Z". And the type was predicted to have the best theoretical performance by the design evaluation method.

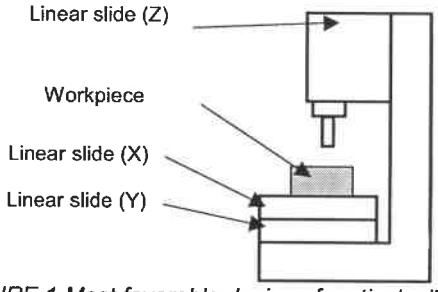

FIGURE 1 Most favorable design of vertical milling machine (based on the calculation)

Fig.2 indicates the answer of skilled designers against the aforementioned question. As it is shown in the figure, more than 3/4 of the designers choose type XY/Z as the best structure. The comparison showed that the design evaluation method is useful in determining machine tools structure in concept design stage, and it is ready to apply the method to 5-axis machine tools in which existing design knowledge is not enough.

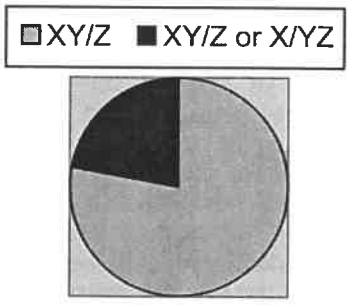

FIGURE 2 Most favorable design of vertical milling machine (designer's opinion)

DESIGN OPTIONS OF 5-AXIS MILLING MACHINE

Even for a 3DOF milling machine, there are some design options. For a 5-axis milling machines, number of design options is almost innumerable. However, it is possible to focus on some practical types and categorize structures of 5-axis milling machines. For example, since designs of workpiece are drawn under orthogonal coordinate system, a practical 5-axis milling machine should have 3 linear axes, X, Y and Z. In an existing survey from a Japanese machine tool builder [6] reported that still there are 2160 design candidates having 3 linear axes and 2 rotational axes. In addition, by eliminating structures which cannot machine 5 surfaces without re-fixture and structures which have a linear axis mounted on a rotational axis, the design options are reduced to 216. These design options can be categorized into 3 major types. Those are "tilting rotary table type", "a swivel head and a rotary table type" and "2 double pivot spindle head type". Proposing design tool can evaluate any of 216 designs. But, as the first step, the paper tries to select one design candidate each and compare the performance of those 3. The 3 structure types to be analyzed are shown in Fig. 3 to 5. Each figure corresponds to "tilting rotary table type", "a swivel head and a rotary table type" and "2 double pivot spindle head type". And using the

aforementioned structure code, each type can be written as CA/XYZ, CY/ZXB and XY/ZBA.

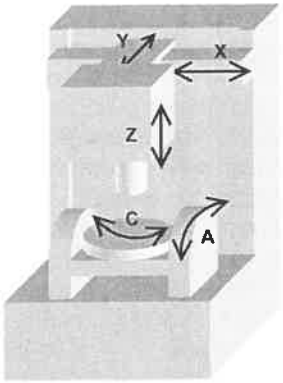

FIGURE 3 Schematic view of 5-axis milling machine (type CA/XYZ)

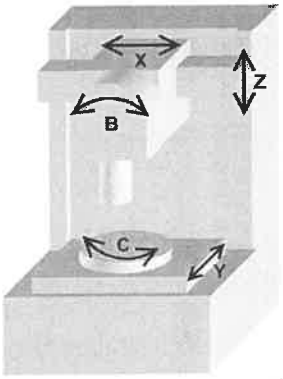

FIGURE 4 Schematic view of 5-axis milling machine (type CY/ZXB)

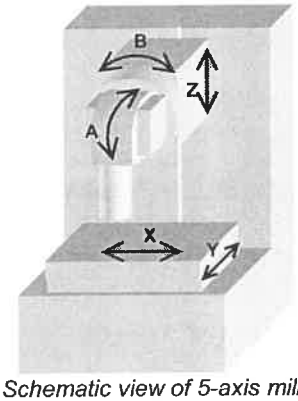

FIGURE 5 Schematic view of 5-axis milling machine (type XY/ZBA)

RESULTS OF CALCULATION

As it was mentioned in the former section, it is necessary to set same design parameters and error factors in order to compare the effect of structure. Table1 shows the design parameters commonly defined in 3 machine tool types. Especially, θ shows the rotating angle of the rotary table. It shows the rotating angle of C axis in Fig. 3 and 4, and the rotating angle of B axis in Fig.5. Similarly, ϕ shows the rotating angle of A, B and A axis corresponding to Fig.3, 4 and 5.

Table 1 Defined design parameters

Parameter	Identification	Ranges of evaluation
θ	Rotating angle of the rotary table (or spindle head tilt)	-90-90 deg.
ϕ	Rotating angle of table tilt (or tool tilt)	-60-60 deg.
Lt	Length of tool	0.16-0.64 m
Ls	Height of linear slides (or rotary table)	0.08-0.32 m
Lr	Height of tilting table	0.16-0.64 m

Table 2 shows the defined error factors. In the paper, angle errors and transitional errors (straightness errors) of each axis were defined. Values of the maximum error amounts shown in the table were assumed, based on some machine component catalogs.

Table 2 Defined error factors and assumed amount

Error factors	Maximum error amount
Angle errors of rotational axes	0.0000625 rad.
Transitional errors of rotational axes	5 μm
Angle errors of transitional axes	0.0000485 rad.
Transitional errors of rotational axes	1-5 μm

In order to compare performance of the 3 types, form-shaping error functions were calculated and a robust design method [7] were applied to clarify the effect of design parameters have on the machine performance of each machine type. Design parameters defined in Table 1 are the control factors and the error factors in Table 2 are noise factors.

The next figure (Fig.6) shows the behavior of overall error amount calculated as the distance between the ideal position of the cutting tool looking from the workpiece and the actual position of the cutting tool. The horizontal axis of the figure corresponds to the 5 design parameters. The vertical axis shows the error amount, when the design parameters vary within the defined ranges.

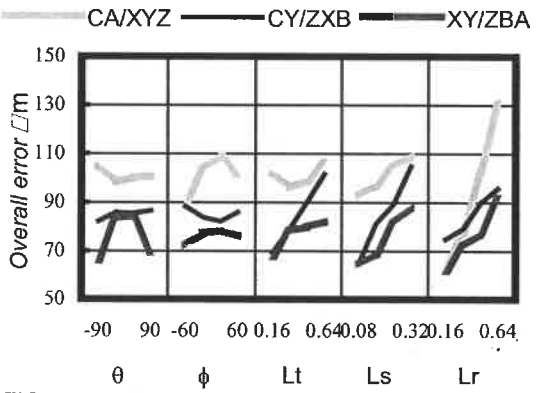

FIGURE 6 Effect of design parameters on machine performance of 3 structure types.

The information obtained from Fig.6 suggest us some basic design strategies for 5-axis machine tools. These are the calculation results.

1) Among three major categories, "2 double pivot spindle head type" has the smallest error amount.

2) On the other hand, "tilting rotary table type" has the largest theoretical error.

3) Among the design parameters, "height of tilting table (Lr)" was the critical design parameters for the "tilting rotary table type" and "2 double pivot spindle head type".

4) In "a swivel head and a rotary table type", "height of linear slides" affected the overall error amount most.

Because this is the first step of evaluation it is difficult to interpret the results. But, basically, since the assumed amount of the error factors of the rotary axis were larger than those of the transitional axes, large error sources which are located far from the cutting tool may play a role.

CONCLUSIONS

The proposed design evaluation method was effective in determining design strategies of machine tools, in its concept design stage. The predicted result showed a good agreement with design knowledge of skilled machine tool designers.

In this report, the design evaluation method was applied in analyzing structure of 5-axis machine tools. By defining common design parameters and error factors to different machine tools structures, it was possible to clarify the effect of structure on the machine performance.

As the results of the design evaluation, when all the types have the same ranges of design parameters and errors, "2 double pivot spindle head type" seemed to have the best theoretical performance.

For future work, more practical comparison of structure based on detailed definition of design parameters and error factors should be done. Other error sources such as structural deformation and thermal deformation should be considered. And other design constraints such as work area will also be important information for determining design guidelines for 5-axis machine tools.

REFERENCES

[1] Mishima, N. and Ishii K., Robustness Evaluation of a Miniaturized Machine Tool, Proc. of ASME/DETC99, Las Vegas, NV, Sept. 1999, DETC/DAC-8579(CD-ROM).

[2] Mishima, N., Design evaluation method for miniature machine tools utilizing form-shaping theory, Proc. of ASME/DETC '02, Chicago, IL, Sept. 2003, DETC/DAC-48787(CD-ROM).

[3] Mishima, N., Derivation of design guidelines for miniature machine tools, Proc. of ASME/DETC '04, Salt Lake City, UT, Sept. 2004, DETC/DAC-57091(CR-ROM).

[4] Reshtov, D.N. and Portman, V.T., Accuracy of Machine Tools, ASME Press, New York, (1988).

[5] Paul, R.P., Robot Manipulators, THE MIT press, Cambridge (1981).

[6] Sato, M, Design and Performance of 5 –Axis Machines in Japan, Proc. of The 12th International Machine Tool Engineer's Conference, Nov. 2006, pp.167-189.

[7] Taguchi, G. and Konishi, S., Quality Engineering Series, ASI Press. (1994).

MODELING AND SELF-CALIBRATION OF LASER TRACKER SYSTEM USING PLANAR CONSTRAINTS

Jianfei Ouyang[1], Wanli Liu[2], Xinghua Qu[2], Yonggang Yan[1], and Zhiyong Liang[1]

[1] Precision Engineering Institute, Henan Polytechnic University
Jiaozuo, Henan Province, China
[2] State Key Laboratory of Precision Measuring Technology and Instruments
Tianjin University, Tianjin, China

ABSTRACT

A kinematics model that describes not only the motion but also the geometric variations of LTS is developed. Through error analysis of the proposed model, it is claimed that gimbals axis misalignments and tracking mirror center offset are the key contributor to measuring errors of LTS. A self-calibration method is presented to calibrate LTS with planar constraints. Various calibration strategies utilizing plane constraints are proposed for different situations. For each calibration strategy, issues about the error parameter estimation of LTS are exploded to find out in which conditions these parameters can be uniquely estimated. These conditions reveal the applicability of the planar constraints to LTS self-calibration. Intensive experimental studies are conducted to check the validity of the theoretical results. The results show that the measuring accuracy of LTS has been increased by 5 times after using the proposed technique for calibration.

KEYWORDS: Laser tracking, Modeling, Self-Calibration, Planar constraints

INSTRUCTIONS

Establishing dimensions and relative locations of object surfaces is one of the basic tasks of geometric metrology. Coordinate measuring machines (CMM) are the most commonly used device for the dimension inspection, but they are severely restricted when measuring very large objects in workshop. Recently, laser tracking measuring technology has been demonstrated commercial success at overcoming this difficulty. Laser tracking system (LTS) is the latest portable 3D large size coordinate measuring system, which can measure three dimensional coordinates with laser beam by tracking a spherically mounted retroreflector (SMR). The LTS can track a SMR automatically in range of 35m. It can scan 1000 points per second with the accuracy of 1×10^{-6}m. Among the large-scale measuring technologies, such as measuring arms, theodolites, and total station systems, LTS possesses many advantages, such as broad range, high speed, high accuracy and real time. It has been widely used in manufacturing measurement for dimension inspection, robot calibration, machine alignment, surface contour mapping, and reverse engineering, etc[1-2].

Although LTS is very accurate instrument, the measurement accuracy is highly dominated by the geometric errors in the tracking mirror mechanism. The proper calibration of LTS is essential for a good measurement. There have not been any standard device and method with broad range for the calibration of LTS. The purpose of this paper is to develop a kinematics model that describes not only the motion but also the geometric variations of LTS, and to propose a self-calibration method to calibrate LTS with planar constraints.

WORKING PRINCIPLE

LTS is composed of laser interferometer, beam splitter, tracking mirror mechanism, retroreflector, position sensitive detectors (PSD) and control unit as shown in Figure 1.

Figure 1 shows the working principle of LTS. A laser beam emitted from laser interferometer is divided into two orthogonally polarized beams, referred to as the measuring beam having a frequency of f_1 and the reference beam having a frequency of f_2. The reference beam is diverted to the receiver by polarizing beam splitter. The measuring beam proceeds through beam splitter and is directed by the tracking mirror to a retroreflector sited on the measured objects and reflected back by the retroreflector.

The returning beam then goes back to receiver through the tracking mirror and polarizing beam splitter. If the retroreflector changes its position, a frequency shift of Δf occurs and the relative displacement can be measured. Part of the returning beam is directed to the PSD to measure possible offset of the returning beam. The beam offset got by PSD is used to control the angle of the tracking mirror to make sure that the measuring beam is always pointed at the optical center of retroreflector. The change of horizontal and vertical angles of the measuring beam is measured by two angle encoders respectively. At the same time, the moving distance of the retroreflector is measured by a laser interferometer. Thus two angular values and one linear value are good enough to do 3D coordinate measurement of the retroreflector as well as the measured objects accurately [3].

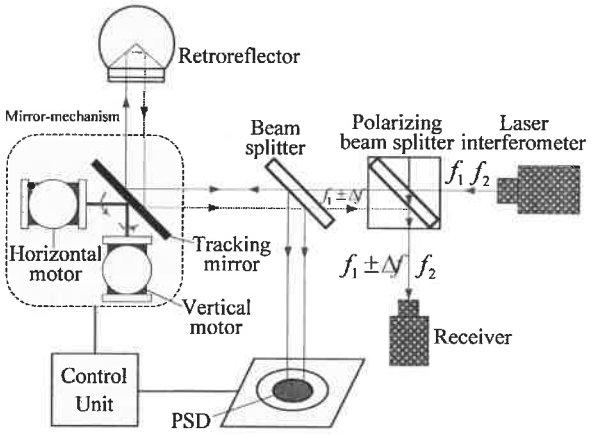

FIGURE 1. Working principle of LTS

MODELING

Modeling is a process of finding a function to best describe the real system. As shown in Figure 2, three coordinate systems are established to model a LTS. They are the base coordinate system of the gimbal $\{X_b, Y_b, Z_b\}$, the first link frame $\{X_1, Y_1, Z_1\}$, and the mirror frame $\{X_m, Y_m, Z_m\}$. O_b, O_1, and O_m denote the origins of the three coordinate systems $\{X_b, Y_b, Z_b\}$, $\{X_1, Y_1, Z_1\}$, and $\{X_m, Y_m, Z_m\}$ respectively. When the LTS is at its home position, X_b and X_1 are along the common normal directions of Z_b and Z_1. If Z_b and Z_1 intersect, X_b and X_1 are assigned perpendicular to both Z_b and Z_1. O_b and O_1 are the intersection points of the common normal of axes Z_b and Z_1 with Z_b and Z_1 respectively. Angular parameter α_1 and a_1 are used to model the misalignment of the gimbal axes. Thus, $Rot(x,\alpha_1)$ will align $\{X_b, Y_b, Z_b\}$ with $\{X_1, Y_1, Z_1\}$, and $Tran(a_1,0,0)$ will bring the resultant frame to be coincident with $\{X_1, Y_1, Z_1\}$. Z_m is parallel to the direction of the mirror surface normal and passes through O_1. O_m is the intersection point of Z_m with the mirror surface. X_m may lie arbitrarily on the mirror surface. Two angular parameters θ_2 and α_2 as well as one translation parameter e_2 are thus sufficient to model the case, in which the second rotation axis does not lie on the mirror surface. In other words, $Rot(z,\theta_2+\Delta\theta_2)Rot(x,\alpha_2)$ will align $\{X_1, Y_1, Z_1\}$ with $\{X_m, Y_m, Z_m\}$, and $Tran(0,0,e_2)$ will bring the result frame to be coincident with $\{X_m, Y_m, Z_m\}$.

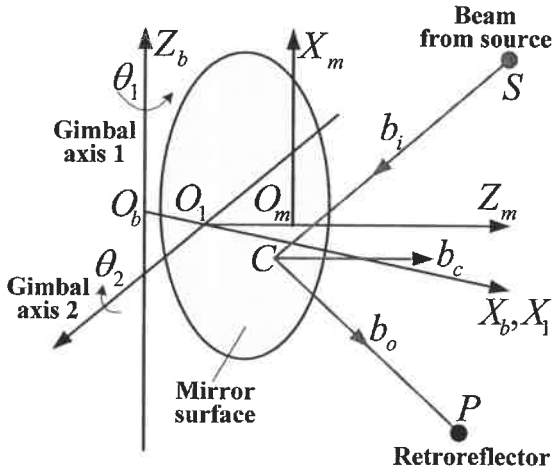

FIGURE 2. Modeling of LTS

In summary, the transformation matrix ${}^bT_m$ relating the coordinate system $\{X_m, Y_m, Z_m\}$ to $\{X_b, Y_b, Z_b\}$ is:

$$ {}^bT_m = Rot(z,\theta_1)Rot(x,\alpha_1)Tran(a_1,0,0) \\ Rot(z,\theta_2+\Delta\theta_2)Rot(x,\alpha_2)Tran(0,0,e_2) \quad (1) $$

Nominally, $\alpha_1 = 90°, \Delta\theta_2 = 90°, \alpha_2 = 90°$ and $e_2 = 0$. The target coordinates can be computed through the following formula:

$$ r_p = R_r\,{}^m c_r + t_r - (l_m + l_r - l_s)B(b_c)b_i + l_s b_i \quad (2) $$

Where, $l_s = -\vec{b}_c \cdot (R_r\,{}^m\vec{c}_r) / \vec{b}_c \cdot \vec{b}_i$,

$$B(\bar{b}_c)=\begin{bmatrix} 2b_{cx}^2-1 & 2b_{cx}b_{cy} & 2b_{cx}b_{cz} \\ 2b_{cx}b_{cy} & 2b_{cy}^2-1 & 2b_{cy}b_{cz} \\ 2b_{cx}b_{cz} & 2b_{cy}b_{cz} & 2b_{cz}^2-1 \end{bmatrix}$$

is the familiar of the mirror image reflection matrix [4].

The beam incident on the mirror represented in the base coordinate system $\{b\}$ is:

$$c = R_r + {}^m c_r + t_r + l_s b_i \tag{3}$$

SELF-CALIBRATION

LTS calibration is a process of accuracy enhancement. It encompassed compensation for absolute accuracy deficiencies using compensation software. In this paper, we develop a self-calibration method with planar constraints to calibrate LTS. Planar constraints are chosen because they are the simplest types of surfaces and still provide sufficient constraints for LTS calibration. By restricting retroreflector motion to an arbitrary surface of constraints plane, the calibration problem is reduced to an optimization problem of minimizing a cost function C of the type [5]:

$$C=\sum_{i=1}^{m}(n\times b\cdot r_i(x,\theta)-d)^2 \tag{4}$$

Where, $r_i(x,\theta)$ is the coordinates of retroreflector at ith position, which can be calculated from the forward kinematics model of LTS, n is the plane normal, b is the laser beam vector, d is the distance from the origin to the plane, x is a parameter vector to be calibrated, and θ is the angular measurement of LTS.

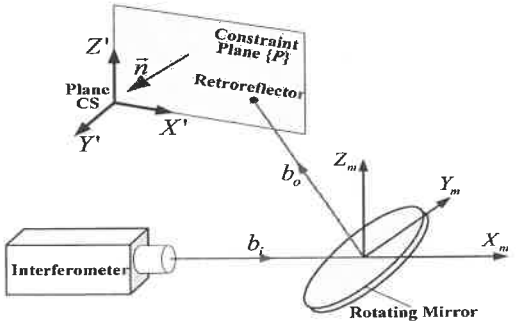

FIGURE 3. Self-calibration of LTS with plane constraint

The schematic to calibrate LTS using a plane constraint is shown in Figure 3. In the LTS, a retroreflector is moved along planar constrains, the gimbal rotation angles and the interferometer relative distance reading between the LTS and retroreflector are both recorded. The constraint plane is defined as a coordinate frame that is different from the base coordinate system. We develop a self-calibration algorithm as following. These steps are iteratively solved until the difference of two consecutive solutions is within a preset limit.

Step1. The forward kinematics model of the LTS is used to compute $r_i^0(x^0,\theta)$, $i=1,2\cdots m$, for a given initial values x^0 of the nominal parameter vector of the LTS and the measuring data θ, d .

Step2. The result of $r_i^t(x^t,\theta)$ is then used to update the geometric parameter vectors consisting of x^t, b^t, d^t , where t indicates the iteration index. The equation (4) can be computed as:

$$\begin{aligned}&(n\times b)^t\cdot r_i^t(x^t,\theta)-d^t+[(n\times b)^t]^T\nabla r_i^t(x^t,\theta)dx \\ &+r_i^t(x^t,\theta)\cdot n\times db-d(d)=0\end{aligned} \tag{5}$$

Where,

$$db=\begin{bmatrix} \cos\theta_1^t\cos\theta_2^t & -\sin\theta_1^t\sin\theta_2^t \\ -\sin\theta_1^t\cos\theta_2^t & -\cos\theta_1^t\sin\theta_2^t \\ 0 & \cos\theta_2^t \end{bmatrix}\begin{bmatrix} d\theta_1 \\ d\theta_2 \end{bmatrix}=C^t\begin{bmatrix} d\theta_1 \\ d\theta_2 \end{bmatrix} \tag{6}$$

Then, $J^t\cdot d\rho=\mathrm{Re}s^t$ (7)

Where, $\rho=[x^T,\theta_1,\theta_2,d]$, $\mathrm{Re}s^t=-\begin{bmatrix}(n\times b)^t\cdot r_1^t(x^t,\theta)-d^t \\ \vdots \\ (n\times b)^t\cdot r_m^t(x^t,\theta)-d^t\end{bmatrix}$

The Jacobean matrix of J^t can be written as:

$$J^t=\begin{bmatrix}[(n\times b)^t]^T\nabla r_1^t & (r_1^t)^T C^t & -1 \\ [(n\times b)^t]^T\nabla r_2^t & (r_2^t)^T C^t & -1 \\ \vdots & \vdots & \vdots \\ [(n\times b)^t]^T\nabla r_m^t & (r_m^t)^T C^t & -1\end{bmatrix} \tag{8}$$

The error parameters vector $d\rho$ can be solved from equation (7). If $|d\rho|<\varepsilon$ (a preset small number), the current ρ^t is the values of the parameters. If not, the parameter vector can be updated in the following formula:

$$\rho^{t+1} = \rho^t + d\rho(t = t+1) \quad (9)$$

Step3. The forward kinematics model of the LTS is used to compute $r_i^t(x^t, \theta)(i = 1, 2 \cdots m)$ for a given initial values x^t of the calibration parameter vectors and the measuring data θ, d. Go back to step2.

Two kinds of self-calibration methods are available, which uses single-plane constraint and multi-plane constraints respectively.

EXPERIMENTS

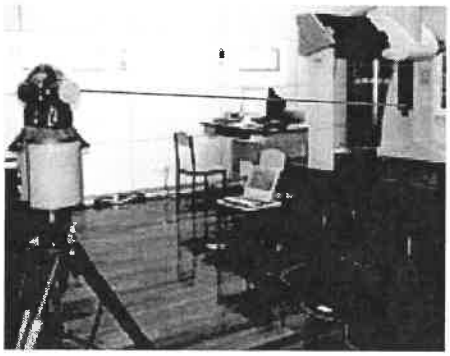

FIGURE 4. Experiment layouts

A lot of experiments are done to check validity of the theoretical results. The experiment layouts are shown in Figure 4. The retroreflector is mounted on the *Z*-axis of a CMM. The CMM that rides the retroreflector moves in space to simulate the constraint planes. The LTS then tracks the retroreflector and measures the coordinates of the retroreflector in real-time.

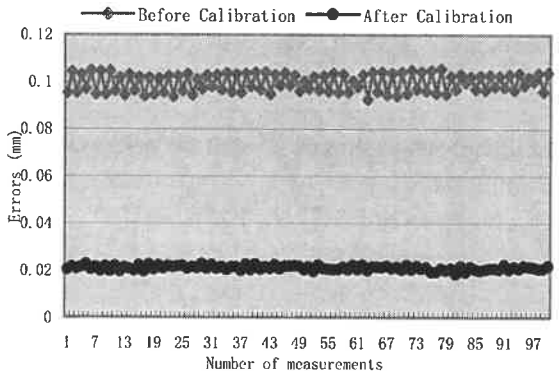

FIGURE 5. Measuring results

In the experiments, 100 points are measured on each plane. Figure 5 shows the measuring results. The horizontal axis represents the number of measurement and the vertical axis denotes the measuring accuracy. The red line is the results, in which LTS has not been calibrated by the proposed technique. At the same time, the blue line denotes the results, in which LTS has been calibrated using the proposed technique. As shown in Figure 5, after calibrated, the mean measuring error of the LTS has been decreased from 99.67μm to 21.05μm, which means that the measuring accuracy has been increased by near 5 times.

CONCLUSIONS

(1) We develop a kinematics model, which describes not only the motion but also the geometric variations of LTS.

(2) A self-calibration method to calibrate LTS with planar constraints is proposed. Various calibration strategies using plane constraints are proposed for different situations.

(3) The experimental results have proved that using the proposed technique to calibrate a LTS, the measuring accuracy of LTS has been increased by 5 times.

ACKNOWLEDGMENTS

This project is sponsored by National Natural Science Foundation of China (NSFC 50475038). The authors would like to express their sincere thanks to the NSFC.

REFERENCES

[1] Ouyang J.F, Liu W.L, Yan, Y.G. Angular error calibration of laser tracker system. Proc SPIE Int Soc Opt Eng. 2006; 6344.

[2] Ouyang Jianfei, Liang Zhiyong, Zhang Haixin, Yan Yonggang. Research of measuring accuracy of laser tracker system. Proc SPIE Int Soc Opt Eng. 2006; 6280.

[3] Liu Wanli, Ouyang Jianfei, Qu Xinghua, Yan Yonggang. Misalignment error calibration of faro retro probe for laser tracker system. Chinese Optics Letters 2007; 5(5):281-283.

[4] Zhuang H. Modeling gimbal axis misalignments and mirror center offset in a single-beam laser tracking measurement system. Int J Rob Res.1995; 14(3): 211-224.

[5] Lin Psang Dain. Modeling and sensitivity analysis of laser tracking systems by skew-ray tracing method. J Manuf Sci Eng Trans ASME. 2005; 127(3): 654-662.

RECENT DEVELOPMENTS AND UPGRADES IN-PROGRESS OF A PRECISION SIX DEGREE-OF-FREEDOM MAGNETICALLY SUSPENDED MEASURING INSTRUMENT

Jerald L. Overcash, Charles G. Stroup, Robert J. Hocken
Center for Precision Metrology
University of North Carolina at Charlotte
Charlotte, North Carolina

ABSTRACT

The Center for Precision Metrology houses a custom measuring instrument previously referred to as the Long Range Scanning Stage (LORS) and, most recently, as the Sub-Atomic Measuring Machine (SAMM) [1, 2]. This unique instrument was developed through collaboration between researchers at UNC-Charlotte and MIT. The SAMM has a 25 mm by 25 mm by 100 μm working volume and currently has a 3-sigma positioning noise of approximately 0.4 nm. Systems such as the SAMM rarely achieve their full operating capabilities immediately and in most cases require years of development to reach their potential. New technology developments, both hardware and software, have allowed the initial design goals to be surpassed. From 1997, when the SAMM was first completed, processor speeds have increased from around 200 MHz to nearly 3.8 GHz. Presented in this paper are the progress of the updates to achieve 10 pm measurement resolution and efforts to decrease the controller induced positioning noise and the measurement uncertainty.

INTRODUCTION

The long range scanning stage, developed by M. Holmes, has a neutrally buoyant platen floated in silicone oil over four linear motors; see figure 1 [1]. The motors are a novel Halbach array linear motor design that positions the stage in six degrees-of-freedom. The Zerodur target mirror and measurement sample assembly is elevated above the oil's surface by a flexure-based Kelvin clamp coupled to the platen. The metrology frame, also of Zerodur, holds three 4-pass laser interferometers and three capacitance gages which read against the target mirror / sample holder. An enclosed metrology chamber above the oil level provides increased stability and environmental isolation from the laboratory. A closed loop control system positions the stage in the travel volume with a velocity limit of 1 mm/s.

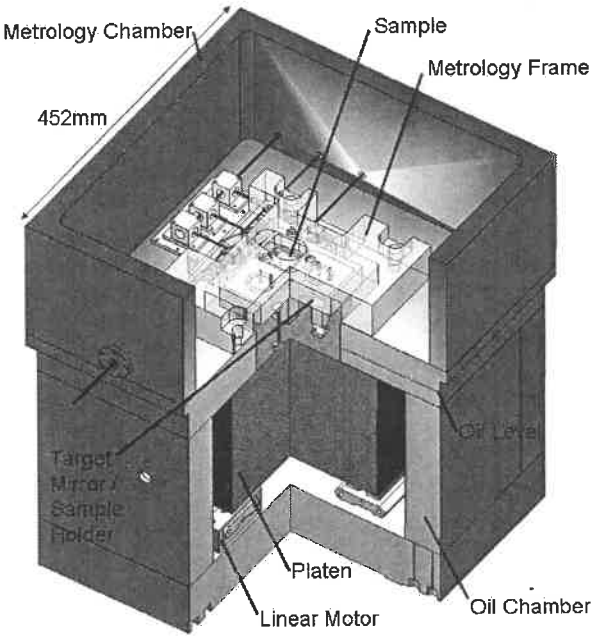

FIGURE 1. Section view of the SAMM with the top of the metrology chamber removed and no probe shown.

UPGRADES IN PROGRESS

Upgrades to the SAMM are underway to lower the positioning resolution to 10 pm. Commercially available laser interferometers do not meet the resolution requirements even with stage's 4-pass interferometer optics.[1] The original laser system, dating back to 1997, uses a ZYGO 7701 laser and remains in use. The displacement is determined from time interval measurements, therefore, the time resolution of the analyzer limits the position resolution [1]. Efforts are underway to replace the current,

[1] For clarity, let a pass be defined as a path to and from the mirror to the interferometer. Four reflections can be observed on the mirror surface for the 4 pass configuration.

20ns resolution time interval analyzers with newer units having time resolution of better than 100ps. The noise on the interferometer signals is currently about 0.4 nm, 3-sigma under servo control but the noise decreases to 0.1 nm without servo control. This confirms the controller is responsible for some portion of the noise value; therefore a real-time control system is being implemented to allow the feedback loop to be closed at a higher frequency. For increased wavelength stability, the ZYGO laser is being discarded in favor of a helium neon laser tube offset locked to an iodine stabilized laser system [3]. Other improvements include the addition of a helium atmosphere surrounding the interferometers to both stabilize and lower the uncertainty in the refractive index while also decreasing the temperature and pressure sensitivity [4].

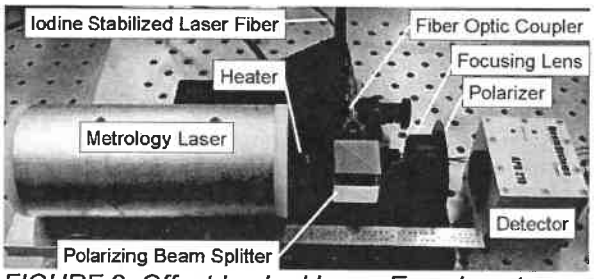

FIGURE 2. Offset Locked Laser Experiment.

LASER SYSTEM

The offset locked laser system consists of a helium neon metrology laser offset locked to an iodine stabilized laser system (ISL); see figure 2 for the experimental assembly and figure 3 for a block diagram of the entire optical system. The ISL system outputs a signal from a working, helium neon laser whose frequency is stabilized and offset from the iodine stabilized laser. An aluminum cylinder encompasses the metrology laser tube, aiding in open-loop thermal stability. The heater has a 20.9 ohm resistance and is wrapped around the cathode of the tube. When continuously applying 8 Volts to the heater, ~65 mode hops were observed over eight minutes. Conversely, ~45 mode hops occurred during the subsequent cooling of the cathode over the same amount of time, demonstrating sufficient range and bandwidth for the control of the metrology laser with this heater arrangement.

The optical layout of the SAMM is illustrated by the block diagram shown in figure 3. The fiber output of the iodine stabilized laser system is converted to free space through a fiber optic coupler (FOC) before combining with the metrology laser in the polarizing beam splitter (PBS). The metrology laser is a sealed-cavity helium neon laser type with both cavity mirrors fixed to the plasma tube. The cathode mirror is less than 100% reflective allowing approximately 15μW to escape while the anode mirror supplies the working signal at 1mW. The weaker signal from the cathode end of the laser tube is used to lock the frequency of the metrology laser to the ISL system such that the stronger, anode signal sees as few disturbances as possible. A Faraday isolator at the output of the metrology laser protects against optical feedback. A lens and polarizer are placed in the optical path between the PBS and photo detector to align the polarization axes of the two signals and focus the beams on the avalanche photo detector. The rf counter reads the frequency of the amplified signal from the detector and communicates with the laser controller via GPIB (general purpose interface bus).

A dedicated computer is used for the laser controller allowing the laser system to be autonomous and expandable to an array of offset locked metrology lasers providing support for other instruments in the Center for Precision Metrology. An error signal based on the difference between the counter reading and the defined offset value is generated by the digital controller. This error signal is the input for the digital proportional-integral-derivative (PID) controller. The output from the PID is sent to the heater through a digital-to-analog (D/A) converter and power amplifier. The heater will be controlled around a set temperature, elevated above ambient, such that the time constant for heating and cooling is roughly the same. The heater induces a length change on the tube that relates to a change in frequency. By coupling the metrology laser into optical fiber, the offset locked signal can be housed in a laboratory apart from the SAMM. The metrology laser signal is converted to a suitable source for heterodyne laser interferometry through an acousto-optic modulator (AOM) and recombining prism. The AOM driver frequency is chosen to be 20 MHz based on laser interferometer electronics available at this frequency. However, this frequency difference may be set to any convenient value and is only constrained by the physical limits of AOMs. Note frequencies below 10 or 15 MHz are most easily achieved by using an arrangement of two AOM's. To decrease the thermal load, both the

heterodyne laser source and detectors are fixed outside of the metrology chamber.

The interferometer electronics are the same for the signals from the detectors and the reference signal from the AOM rf driver. They first pass through a primary amplifier and a mixing circuit. The mixer combines the detector/driver output with a reference from a frequency synthesizer. This generates the sum and difference of the two signals. The frequency synthesizer output is selected to match the rf driver frequency, 20 MHz, plus 18 kHz. A low pass filter (LPF) is used to filter out the sum of the signals leaving the 18 kHz signal plus or minus any Doppler shifts from the target mirror displacement. By referencing the AOM driver frequency and detector output to a single reference oscillator, any instability in the reference oscillator cancels in the phase comparison. Likewise, instability in the AOM's rf driver cancels in the measurement. Zero crossing detectors convert the filtered, frequency shifted, sinusoidal, analog signal into a TTL level square wave whose period is equal to the period of the input. These TTL level inputs are read by time interval analyzers (TIA's) resident in the control system. Displacements are calculated based on the time stamps from the zero crossings of the measurement signals as compared with the zero crossings of the reference signal.

ENVIRONMENTAL EFFECTS

The metrology chamber for the SAMM is constructed with 1 inch thick aluminum walls. The walls act to decouple high frequency temperature, humidity, and pressure variations of the laboratory environment from the SAMM metrology environment. However, self-heating of the metrology environment from the linear motors is a concern and has been measured, see figure 4. The data show the temperature history over 7 hours. Control of the stage in six degrees of freedom was initiated 1 hour after data collection began. Home position was held for the duration of the experiment to investigate the temperature rise in the metrology chamber due to the linear motors. A rise of 0.05 °C over 6 hours was observed without any indication of reaching steady state. Further experiments showed that the heat from the motors is coupled to the metrology chamber through the oil.

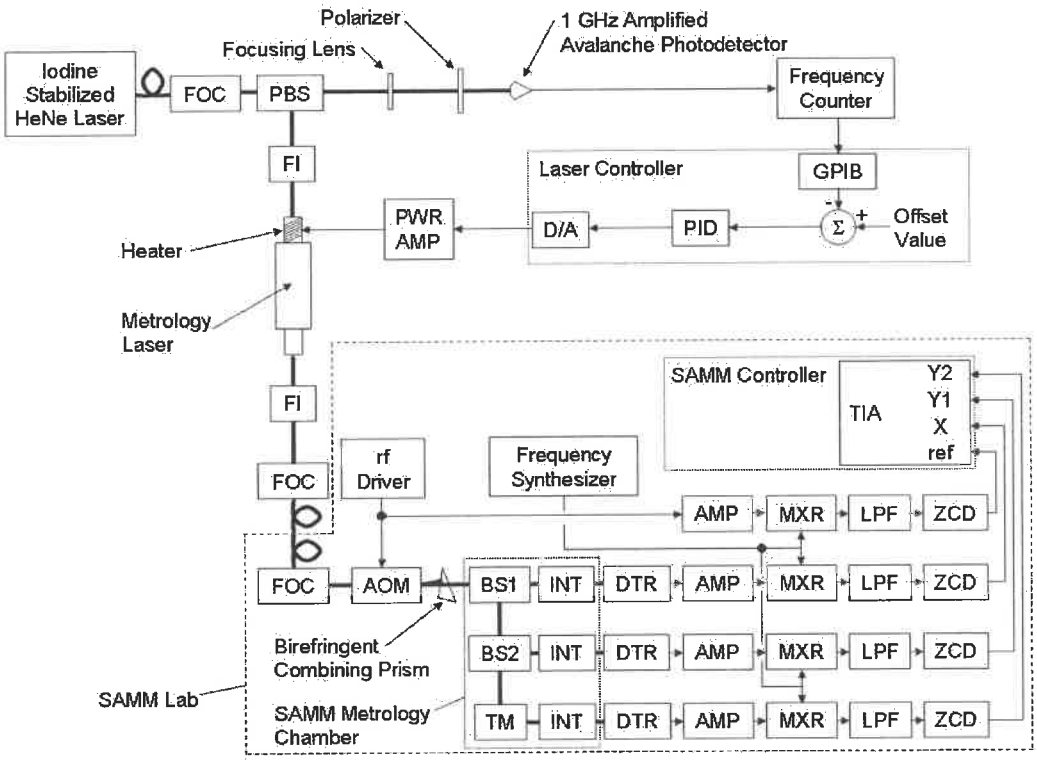

FIGURE 3. Block diagram of the offset locked laser system. Abbreviations are: FOC, fiber optic coupler, PBS, polarizing beam splitter, FI, Faraday isolator, AOM, acousto-optic modulator, BS1, 30/70 beam splitter, BS2, 50/50 beam splitter, TM, turning mirror, INT, interferometer, DTR, detector, AMP, amplifier, MXR, mixer, LPF, low pass filter, ZCD, zero crossing detector, TIA, time interval analyzer, PWR, power amplifier.

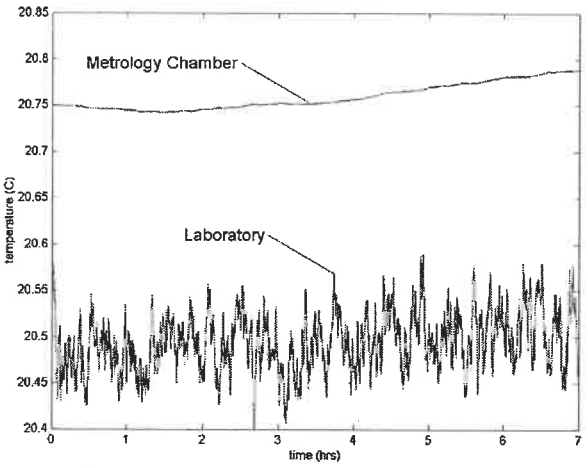

FIGURE 4. Temperature data of the SAMM.

The gradients inside the chamber have not been explored but are a concern, given no means of air circulation. Corrections for the index of refraction are easily calculable and valid for offsets from standard conditions but gradients remain uncompensated. Vacuum is often used in metrology systems for more accuracy in terms of refractive index. The design of the SAMM allows for only small pressure deviations since the platen was designed to be neutrally buoyant at atmospheric pressure. In practice, gross pressure changes are non-controllable since the gains are set from the measured model parameters at normal laboratory pressure. Additional weight along with other control strategies can be added to stabilize the platen. However, the compatibility of materials and the behavior of the oil remain concerns for vacuum operation. Helium provides the most promise for lower uncertainty and supplying a stable metrology environment for the laser interferometers. The distinct advantages to using helium as the medium for the metrology environment are the high thermal conductivity, low refractivity, and the accuracy by which the refractive index can be calculated [4]. The thermal conductivity of helium acts to reduce the gradients in the chamber and also reduces the time for the chamber to equilibrate after the purging process. The low refractive index of helium decreases the demand for accuracy of the sensors monitoring temperature and pressure by a factor of 8. Due to the small size of helium molecules, high priority will be placed on sealing the chamber such that pressure will be maintained over the duration of the sample measurement. However, pressure variation is likely considering the number of sealing interfaces on the chamber. A wavelength tracking interferometer will be added to compensate all measurements for change in the index of refraction. The Zerodur metrology frame provides a stable reference for the wavelength tracking optical arrangement, see figure 5. The metrology laser is passed through an AOM, providing a 20 MHz frequency split and small angular separation (~1 degree). A 50/50 pellicle beamsplitter divides the signal into separate paths. The zero order beam acts as the measurement arm and is directed in a path around the metrology frame by the 3 turning mirrors. The 1st order, frequency shifted beam acts as the reference arm. The alignment ensures that the two different paths overlap and interfere on the detector. Detection is completed by mixing the reference from the AOM rf driver and the detector output.

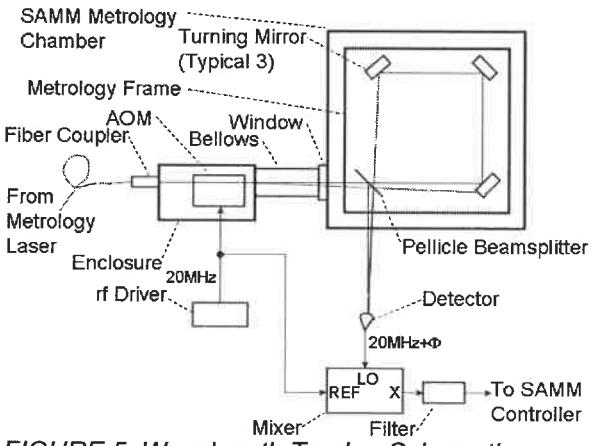

FIGURE 5. Wavelength Tracker Schematic.

ACKNOWLEDGEMENTS

This research is funded by the National Science Foundation under award number 0506898 and carried out in the Center for Precision Metrology.

REFERENCES

[1] M.L. Holmes, *Analysis and Design of a Long Range Scanning Stage*, Ph.D. Dissertation, UNC Charlotte, 1998.

[2] R.J. Hocken, D.L. Trumper, and C.H. Wang, "Dynamics and Control of the UNCC/MIT Sub-Atomic Measuring Machine," CIRP, 50/1, pg. 373, 2001.

[3] J. Lawall and J.M. Pedulla, "Ultrastable laser array at 633nm for real-time dimensional metrology," Rev. Sci. Instruments, Vol. 72, No. 7, pp. 2879-2888, July 2001.

[4] J.A. Stone and A. Stejskal, "Using helium as a standard of refractive index: correcting errors in a gas refractometer," Metrologia, 41, pp. 189-197, 2004.

DEVELOPMENT OF ULTRA-LIGHT ULTRA-FLAT ROBOT APPLYING MONOLITHIC SPIRAL JOINT MECHANISM

Roro Sai, Takeo Hiramoto, Yusuke Sakaki, and Nobuhiro Tsuda
Precision Mechanics Division, Faculty of Engineering, Tokai University
1117 Kitakaname, Hiratsuka, Kanagawa, Japan

INTRODUCTION

We propose a new method to make the robot thin and light; we try to process the joint and the link together in one thin board as a robot, and we use the elastic deformation of spring

MONOLITHIC TWO SPIRAL SPRING JOINT

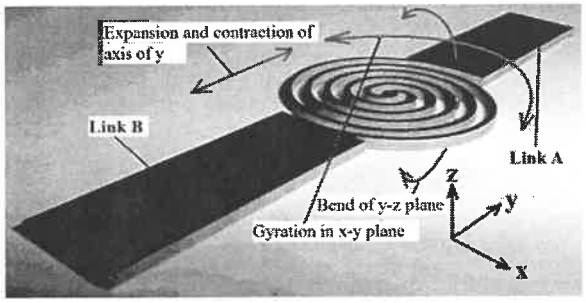

FIGURE 1. Monolithic two spiral spring joint

In Fig.1 we present new type monolithic joint consisting of two spiral springs, and one end of each springs is combined together in the center of each joints. The other end of each springs is connected with the link A and the link B. Main behavior of this joint is an elastic circular movement: the gyration in x-y plane by the link A's bending in the x-y plane, however additional behaviors, that is small amount of expansion on construction in the y direction, and big bending in the y-z direction will happen. We will try to solve this problem later using Fig.4 or Fig.5. We try to analysis the monolithic spiral joint's stress and strain when driving forces are added.

In Fig.2, both stress and strain diagram are shown, when the link A over the joint is fixed and the link B under the joint is rotated elastically by the driving force. We can understand that the stress around the joint center is almost zero and the more the spring's outside is far from the joint center, the more the stress is strong. We apply the MSC/NASTRAN for the joint stress and strain analysis.

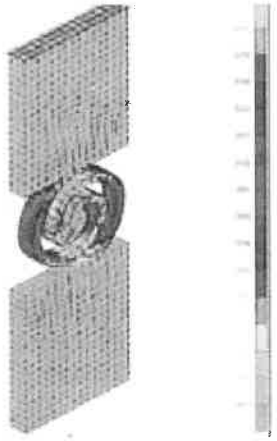

FIGURE 2. The joint stress and strain analysis by MSC/NASTSTRAN

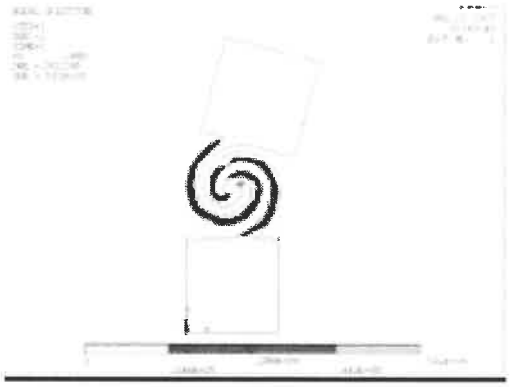

FIGURE 3. The joint expansion and constriction analysis by MSC/ANSYS

In Fig.3 we show both the monolithic spiral joint consisting of two spirals and its stresses arisen by the driving force by ANSYS. It proves that the dynamic ranges of this two spiral joint is much bigger than just one spiral form and any stresses occurred in the monolithic spiral joints is much more homogeneous; not so much sharp changed.

APPLICATIONS USING THIS MONOLITHIC TWO SPIRALS JOINT

Fig.4 shows a human robot with three monolithic joint together. The first one of this joint is used as a hip joint, the second one is done as a knee joint and the third one is done as an ankle joint. The three joints are sandwiched by two metal sheets for preventing bending in the y-z planes. This robot mechanical part's materials are made by Copper-phosphate alloys, manufactured using the wire cutting dischange machine. This robot's weight is 150g, height: 216mm, and its thickness: 3mm.

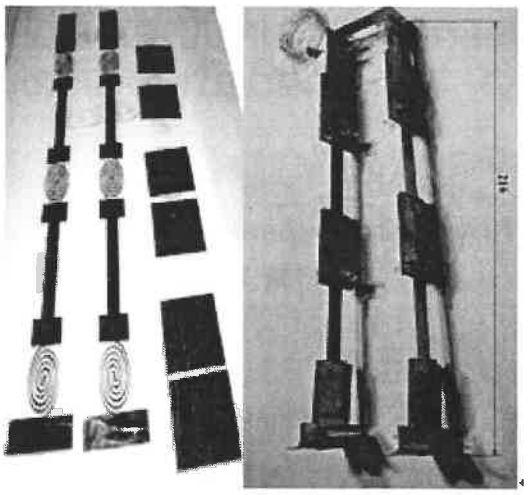

FIGURE 4. Human two leg's robot

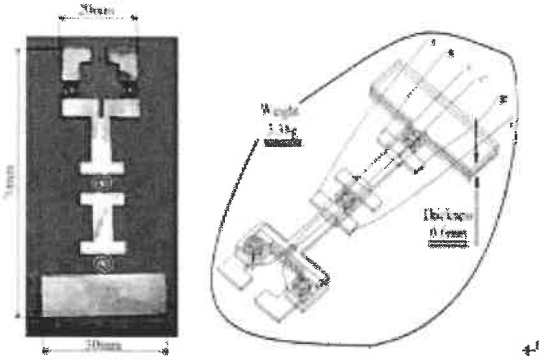

FIGURE 5. Manipulator robot

Fig.5 shows a manipulator that functions is griping something in the plane. This has 4 monolithic spiral joints, 5 links and 6 wires for making each links' move. Its weight is 3.38g; its thickness is 0.6mm.

In Fig.6 spaces between two fingers is first going to be closed, to be opened and finally opened again for catching up something, when 2 wires are driven by 6 servomotors which are controlled

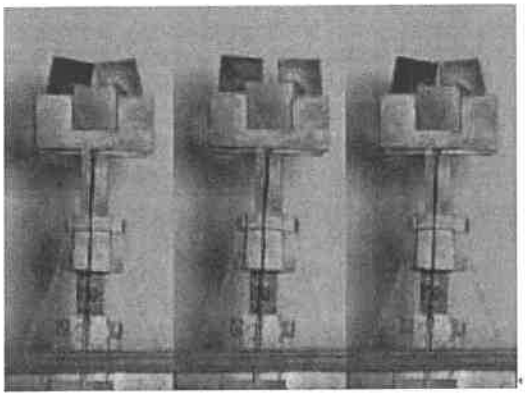

FIGURE 6. Behavior of gripping manipulator

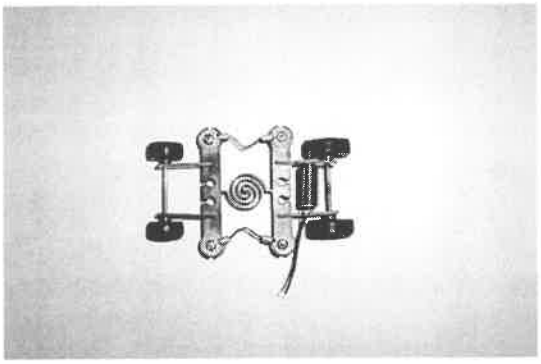

FIGURE 8. A small car applying 1 monolithic spiral joint driving by BMX

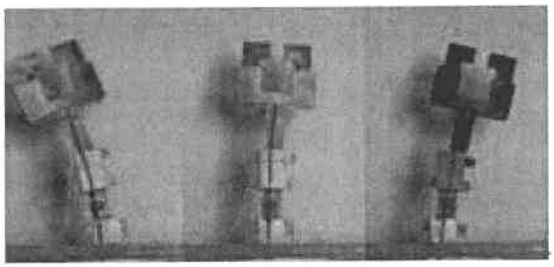

FIGURE 7. Behavior of arm manipulator

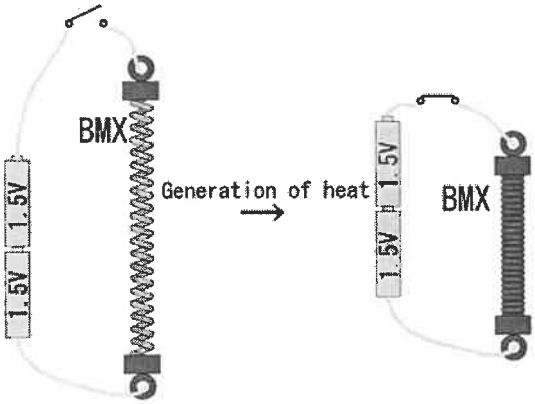

FIGURE 9. BioMetal Helix (BMX)

by microcomputers. In Fig.7 two monolithic spirals joint which are located under the fingers inclines by upper mentioned servomotors clockwise or unticlockwise, when 4 wires are driving 2 those joints again.

In Fig.8 we present a small car which consists of 1 monolithic spiral joint and 2 BMX which will be able to extend on constrict applying a voltage. The length of this car is 60mm, width is 30mm, and body part thickness is just 0.6mm
This is also made of copper-phosphate and manufactured by the wire discharge.

The exact function of BMX is shown in Fig.9.
BMX's is a spiral spring form and made from the shape memory alloy, which is possible to be constricted as small as 200% compared with normal no implied voltages condition. Two BMX makes this car drive in the left hand direction or sometimes in the right hand direction.

We manufactured the new type manipulator; we call this snake robot which has 4 monolithic spiral joints, as many as 9 BMX, and two fingers as shown in Fig.10

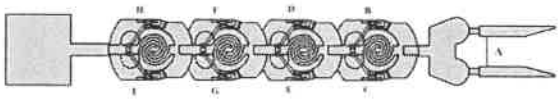

FIGURE 10. Thin and light snake robot

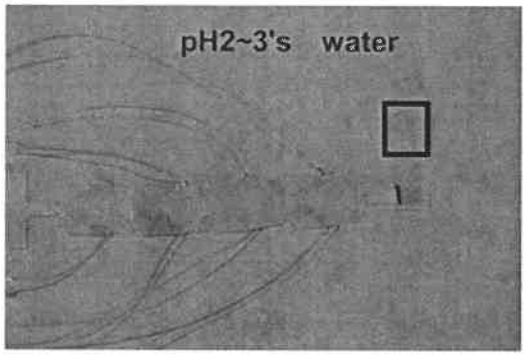

FIGURE 11. Thin and light snake robot trajectory on the desk

Fig.11 shows this robot is going to inspect whether a water drop on the desk is acid or alkali. Two fingers in this robot grips a litmus paper and carry this paper as far as the place the water drop is located. We can judge now that the water drop is acid drop because the paper is changed into pink color which means PH values are 2 or 3.

This experiment shows that this snake robot can pass through even the very narrow clearances between the floor and locked door's bottom frames and this also will be able to inspect the PH values of some liquids outside of the door which are something very dangerous.

Fig. 12 shows an insect which has 4 legs with 4 monolithic spiral springs, a human model, a water strider which floats on water and will jump up on the water surface.

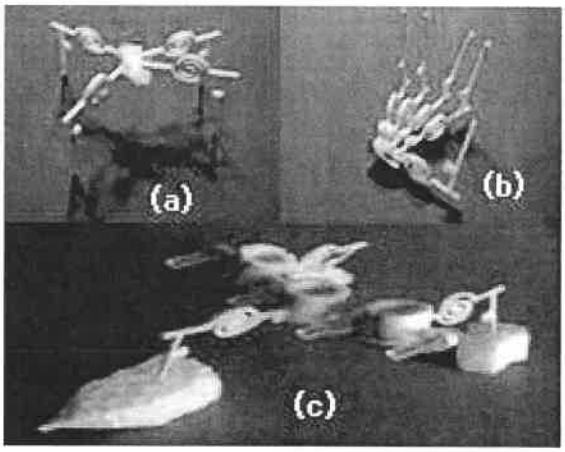

FIGURE 12. (a),(b),(c) 3 kinds of trial

CONSTRUCTION

1. We propose very thin very light monolithic spiral joint which rotates elastically around the center point combined with two spiral springs. We analysis this joint behavior using FEM, then it proves that these are almost no stresses around the spiral spring combined center point, which means this joint center is almost steady and does not rotate.

2. The monolithic spiral joints are applied for hip, knee and ankle's mechanical parts for gyration. We also manufacture very thin manipulator, a small car, PH value inspecting snake robot which passes through very narrow spaces like a locked door and floor clearance, is developed.

3. 4 leg's insect, a human hand and a floating insect are also very light since they are manufactured using a two component polyurethane resin.

REFERENCES

[1] FEM software, 2005 Riko-Gaku-sha Co.ltd.

80 mm DISPLACEMENT FLEXURE STAGE WITH SUB-MICROMETRIC DEVIATION FROM STRAIGHT LINE

François Villar[1], Jean David[2], and Gérard Genevès[1]
[1]Laboratoire national de métrologie et d'essais (LNE)
Trappes, France
[2]École Nationale Supérieure d'Arts et Métiers (ENSAM)
Lille, France

INTRODUCTION

We present a translation stage designed specifically for a watt balance experiment.

A watt balance [1] is an electromechanical apparatus used to measure the Planck constant *h* as a function of a standard mass. Several national metrology laboratories have build or are building such an apparatus. Results obtained by these experiments could be used to redefine the SI[1] unit of mass if the relative uncertainty reach at most 10^{-8}, overcoming the instabilities of the international prototype of the kilogram [2]. The design of the LNE experiment (formerly BNM experiment) is described in [3].

During the operation of a watt balance, a coil is displaced inside a magnetic field. The relative movement of the coil with respect to the field lines must be controlled. In our experiment, a magnetic circuit produces a radial field whose mean plane is aligned horizontally. The nominal movement of the coil is a 80 mm rectilinear translation perpendicular to the field plane. This movement is covered at 2 mm/s under vacuum and the total mass of the travelling objects (including the coil) is about 20 kg. To achieve the required performance on the overall experiment, the deviation of the coil trajectory from this nominal movement must be kept within 1 µm for straightness in both directions and within 5 µrad for yaw and pitch.

In addition, the perturbations produced by the translation stage on the moving coil must be as small as possible. For this reason, smoothness of motion is of prime importance and discontinuities of the movement must be avoided. The absence of wear, play and friction of flexure hinges led us to choose this type of bearing to build the stage.

PROTOTYPE

A first prototype capable of a 72 mm stroke has been built [4]. We briefly summarize the design of this prototype, measurements of the deviation from a rectilinear translation and conclusion from these results.

Arrangement of the hinges

A rectilinear translation can be achieved with a symmetrical arrangement of hinges around the axis of translation. The layout chosen is represented in figure 1.

However, symmetry leads to an over-constrained mechanism which could provoke stress exceeding the elastic limit of materials or bistable behaviour. These difficulties can be largely reduced if great care is taken when machining the different components of the stage. Then, symmetry offers the following advantages :

- transverse forces acting on the mobile body and due to the deformation of flexure hinges are cancelled;
- symmetrical gradients of temperature do not affect the geometry of movement;
- the over-constrained mechanism averages machining inaccuracies provided that there is no bistable behaviour;
- failure of a hinge do not compromise the safety of the stage.

Results

Measurements of the deviation from a rectilinear movement (straightness in X and Y directions, yaw and pitch deviations) have been carried out thanks to a set of two capacitive sensors looking at a straightedge kinematically mounted on the mobile body. Separation of the straightedge shape and stage straightness was performed by a reversal method. For a 72 mm stroke, measurements showed that straightness is smaller than 0,5 µm for both X and Y directions. For the same stroke, angular orientation is constant within 3,6 µrad around Y axis (yaw deviation) and within 80 µrad around X axis (pitch deviation).

[1] International System of Units

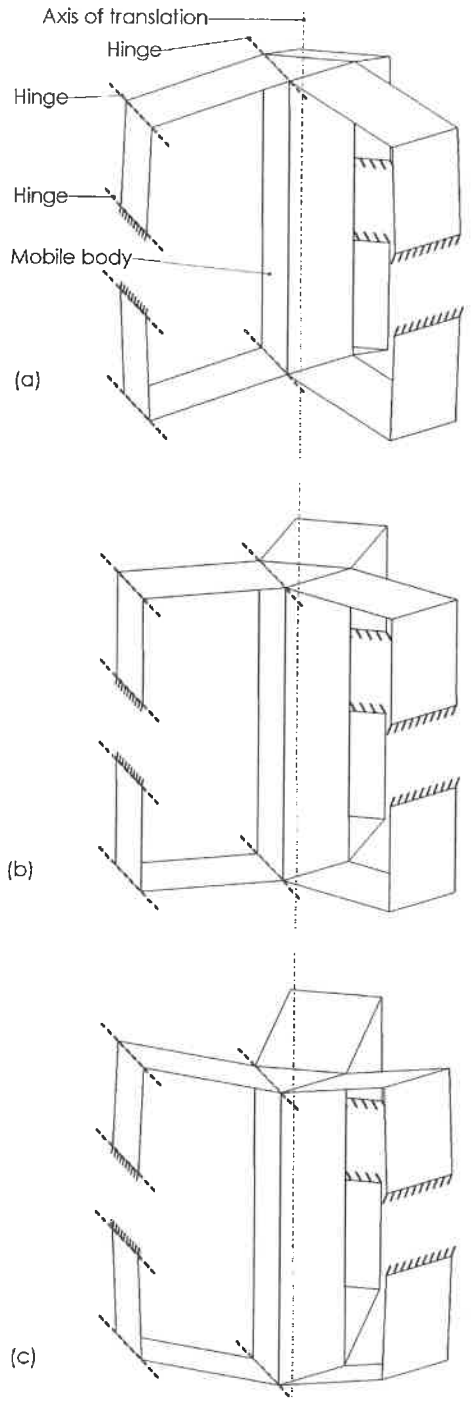

FIGURE 1. Prototype stage : arrangement of the hinges around the axis of translation. The stage is composed of 6 sets of 3 hinges each. Sets are oriented at 120° from each other. 3 positions of the stage (a, b ,c) corresponding respectively to +36 mm, 0 mm (undeformed flexure) and -36 mm are represented. Total size is about 600 mm ×600 mm × 600 mm.

Conclusion

Even if good results have been obtained for straightness of the stage, the pitch deviation exceeds our goal of 5 µrad.

Because of over-constraint there is no direct relation between construction inaccuracies (angular misalignment of hinges, unequal distance between axis of rotation, ...) and each components of the deviation from rectilinear translation. Therefore, it would be difficult to find and cure the origin of the pitch deviation even if (i) a complete measurement (via CMM for example) of the relative positions of the hinges is undertaken and (ii) a model of the stage is constructed (by finite element method for example).

For this reason and because of the number of hinges and the size of the stage, this work was not undertaken. We have rather chosen to design and build a new stage.

FINAL DESIGN

Considering the limitations found with the prototype, we have decided to reduce the number of constraints between the frame of the stage and the mobile body. Moreover, the 120° symmetry has been abandoned to gain accessibility on one side of the stage.

Flexures

A flexure arrangement, derived from one set of three hinges used in the prototype, has been designed to build a single degree of constraint (DOC) mechanism. This arrangement, referred to as a leg, is represented in figure 2. A group of three parallel flexure hinges capable of large rotation (typically, several degrees) connects the frame to the mobile body thanks to a terminal element providing two additional degrees of freedom. It provides one constraint in the X direction and five degrees of freedom, allowing large motion (typically, tens of millimetres) of the terminal element in the YZ plane.

Hinges are cross strip pivots whose geometry and arrangement have been designed to maximize stiffness of a leg in the constraint direction. Considering the arrangement chosen, this stiffness is dependent on the angular stiffness of hinges 1 and 2 around Z. Angular stiffness being proportional to the square of their width, this dimension has been increased compared to hinge 3.

The stiffness of a leg in the direction of constraint has been calculated to about 13 N/µm.

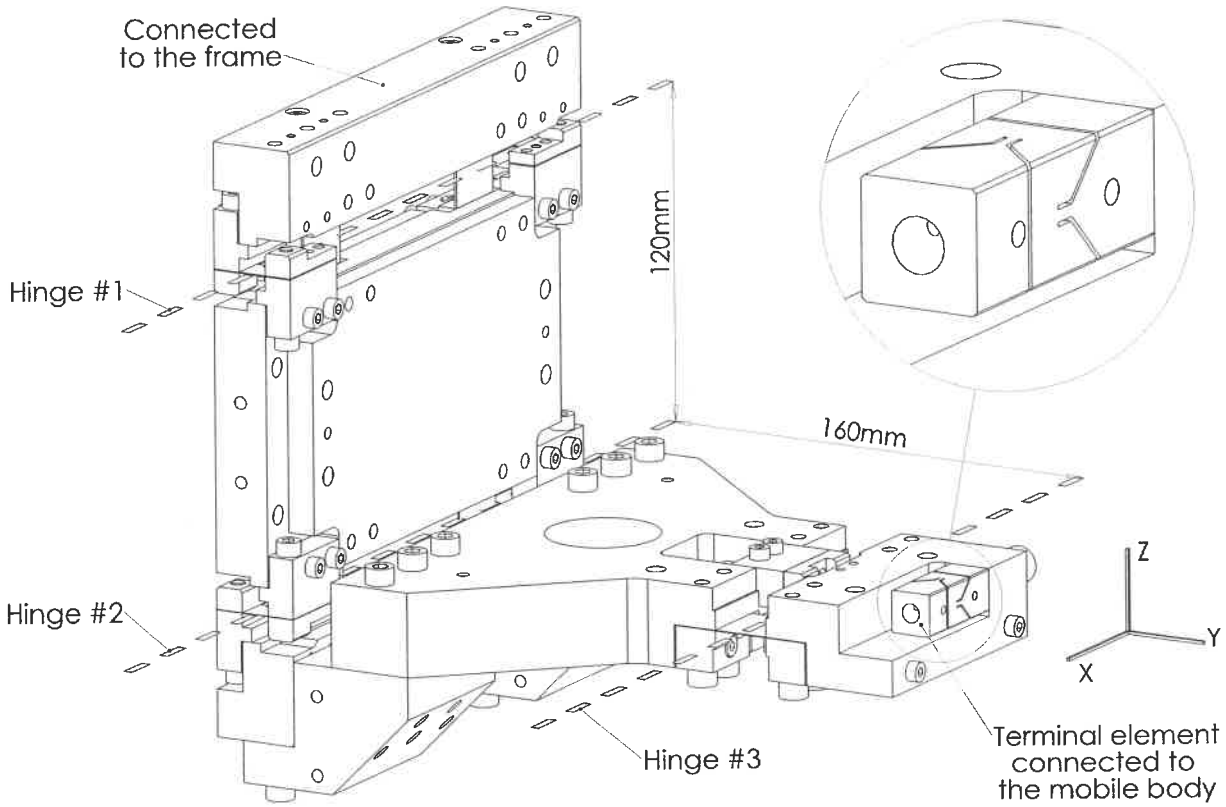

FIGURE 2. Isometric view of a set of hinges and flexure providing one constraint in X direction and five degrees of freedom. Large motion of the terminal element (typically, tens of millimetres) is possible in the YZ plane. Hinges 1, 2 and 3 are capable of 4°, 15° and 17° rotations respectively. The detailed view represents the terminal element connected to the mobile body. This set is referred to as a leg in the text.

Stage

Figure 3 presents the kinematic construction of this stage. In figure 3(a), a planar movement can be constructed using 3 parallel constraints. In figure 3(b), we have chosen to add a fourth parallel constraint to increase stiffness in X direction, and, considering the set of flexure used to build a one DOC mechanism (figure 2), to keep a symmetrical arrangement of hinges with respect to XZ plane. In figure 3(c), two other constraints limit the movement to a rectilinear translation.

Figure 4 shows the arrangement of six legs corresponding to the kinematic construction. Legs have been numbered to match the constraints of figure 3(c).

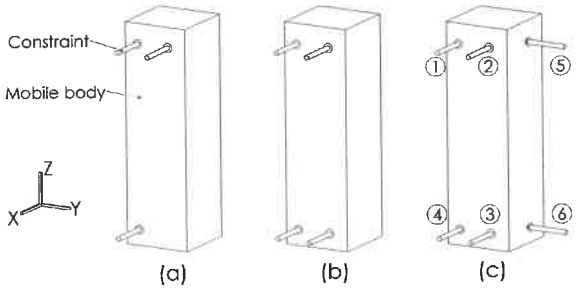

FIGURE 3. Construction of the rectilinear translation. In (a), three constraints defines a planar motion in the YZ plane. In (b), a fourth constraint is added to the planar motion to increase stiffness in X direction and symmetry with respect to XZ plane. In (c), two other constraints limit the movement to a rectilinear translation.

Sensitivity to transverse forces

The total stiffness of the stage is 52 N/µm and 26 N/µm in X and Y directions respectively. In

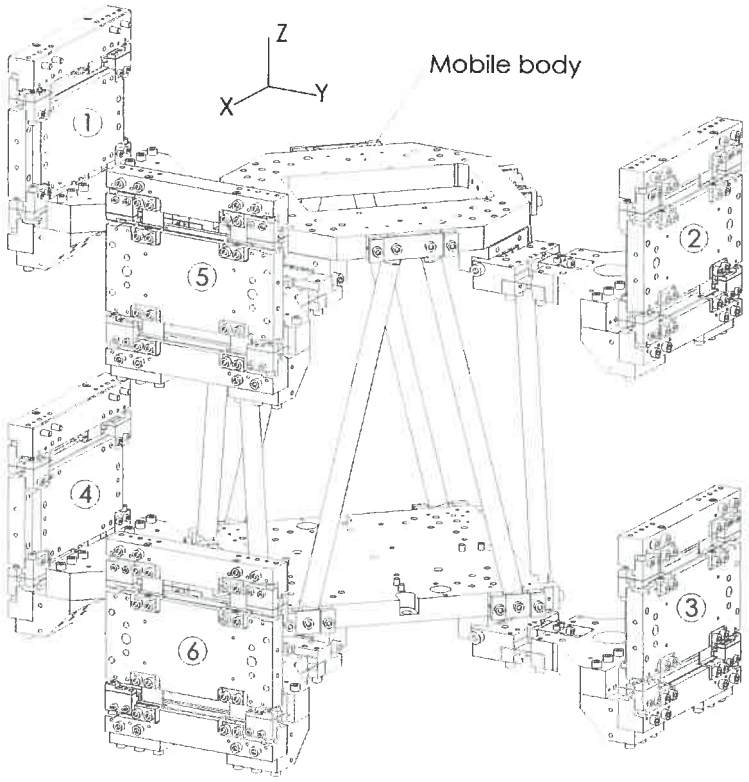

FIGURE 4. Assembly of 6 legs to construct the translation stage. Legs have been numbered to match the constraints of figure 3(c). Frame and actuator are not represented.

comparison, the transverse stiffness of the prototype stage was only 7 N/µm.

For the final stage, considering the moving mass of 20 kg, the natural frequencies of the stage are about 250 Hz and 180 Hz for X and Y directions respectively. This is well above the cut-off frequency of the concrete slab on which the experience will be conducted.

It should also be noted that, because of the asymmetry of the stage with respect to ZY plane, transverse forces in the X direction due to the deformation of flexure hinges 5 and 6 are not cancelled. This will lead to a straightness deviation in this direction of about 0,15 µm, small enough compared to our goal of 1 µm.

In addition, to limit the transverse forces created by the actuator, its motion will be transmitted to the flexure stage by a beam having a flexure pivot at each end. Moreover, thanks to an additional mechanical system, it will be possible to align the direction of movement of the actuator with respect to that of the stage.

FUTURE WORK

As of writing, the different components of the final stage have been manufactured and will be assembled soon. Measurements of the deviation of motion from rectilinear movement will be presented during the conference.

REFERENCES

[1] Kibble B P. A measurement of the gyromagnetic ratio of the proton by the strong field method. Atomic Masses and Fundamental Constants 5 (edited by J. H. Sanders and A. H. Wapstra); 1976.

[2] Girard G. The third periodic verification of national prototypes of the kilogram (1988-1992). Metrologia. 1994; 31: 317-336.

[3] Genevès G et al. The BNM watt balance experiment. IEEE Transaction on Instrumentation and Measurement. 2005; 54 2.

[4] Villar F, David J, Genevès G, Pinot P, Juncar P. Long stroke flexure stage for a watt balance experiment. Proceedings of the 6th Euspen International conference. 2006.

SUB-PICO LITER DISPENSING MECHANISM WITH PRECISE OPTICAL GAP DETECTOR

Hisauiki Aoyama[1],Tomoyuki Ekko[1], Yutaka Adachihara[1], Ohmi Fuchiwaki[1], Daigo Misaki[2] ,Yuka Irie[3], Shuichi Dejima[3],Yoshiyuki Kato[3] and Takashi Usuda[4]

[1]University of Electro-Communications, Tokyo
[2]Shizuoka Institute of Technology
[3]Applied Micro Systems Inc.
[4]National Institute of Advanced Industrial Science & Technology

1. INTRODUCTION

Micro despensing technique of very small amount of liquid less than pico liter is one of the most important issues to achieve the micro analysis system such as DNA identification and protein investigation. In this report, it is described that this unique despensing mechanism is simply composed of the thin glass pipettee and the thin rod which can be traveled in the tube. When the end of the thin rod can be contacted with the surface, then the very small amount of the liquid in the tube can be dosed and stuck onto the target surface. Generally this amount is depending on the viscosity of liquid, the hydrophilicity as well as the diameter of the thin rod end. In the primary experiment, the resolution and repeatability if the pico dsipensing were investigated under the different conditions with viscosity of liquid, rod travel speed and hydrophilicity of the target surface. Then the miminum amount of 0.1 pico liter can be succesfully distributed on the surface and measured by the optical microscopic instrument when the liquid with the viscocity of 1000cS and the diameter of 10 micrometer thin rod are used.

And the automatic optical gap detection is also develped to get the high reliability for dispensing with pico liter resolution because the mechanical contact causes the damage of the tip end and the surface. Here the collimated optical beam can be focused at the contact point then the reflected light can be changed due the small gap between the tip end and the surface. Even the liquid is

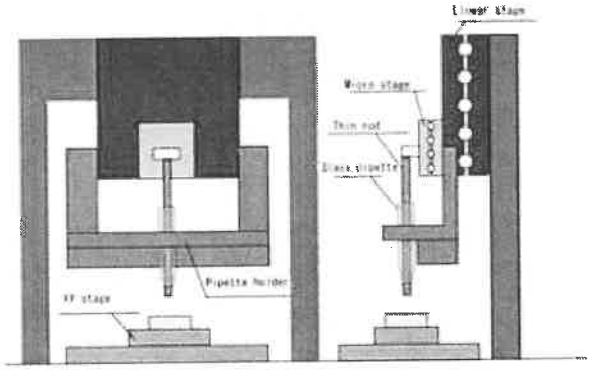

FIGURE 1. Isometric view of the pico-liter dispensing mechanism composed of the thin rod and glass pipette on XYZ stage.

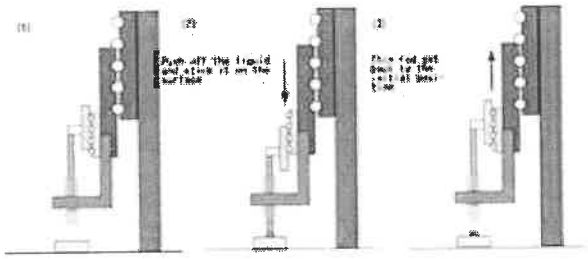

FIGURE 2. Simple principle that the thin rod can push off the liquid in the tube and put it onto the surface.

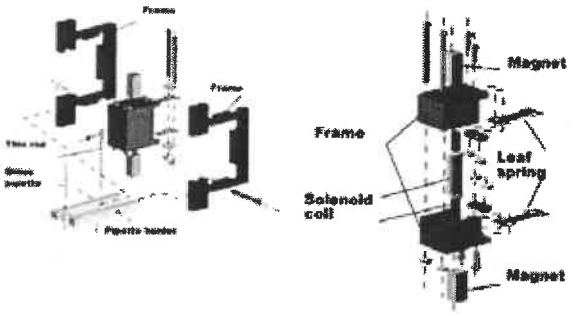

FIGURE 3. Voice coil motor driven pico-liter despensing mechanism that can be mounted on the small XY stage.

contained around the tip, then it can be detected with the optical signal deviation. In this report, the simple principle, the mechanical performance with precise position control and the actual pico liter despensed results are discussed and demonstrated.

2. EXPERIMENTAL SETUP

2.1 Pico-liter dispensing mechanism

In Fig.1, the principle of vibrating needle dispenser mechanism is illustreted. This dispenser is composed of a simple thin glass pipette and a thin needle made by tungsten which is electro-chemical machined. This thin needle can travel through this glass tube by the micro stage. When the thin needle goes through the liquid retained in the tube, the small amount of liquid can be stripped off by the penetrated thin needle. Finally the liquid at the end of needle can be stuck onto the surface and the needle can get back quickly as shown in Fig.2. In the previous experiment, the amount of the stuck liquid is smalll enough to be su -pico liter and the higher viscous liquid can be dispensed.This cycle can be repeated on the micro stage and the array of small droplet with accurate separation can be provided without any special facilities. Alternative mechanism that the thin rod can be driven by the voice coil motor is also developed as shown in Fig.3 and this mechanism can proide the compact despensing facility as well.

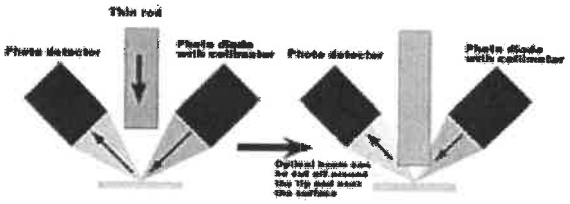

FIGURE 4. Optical gap detector that is composed of LED collimated beam and PD with lens can measure the refrected light around the focus point in which the tip can contact with the surface.

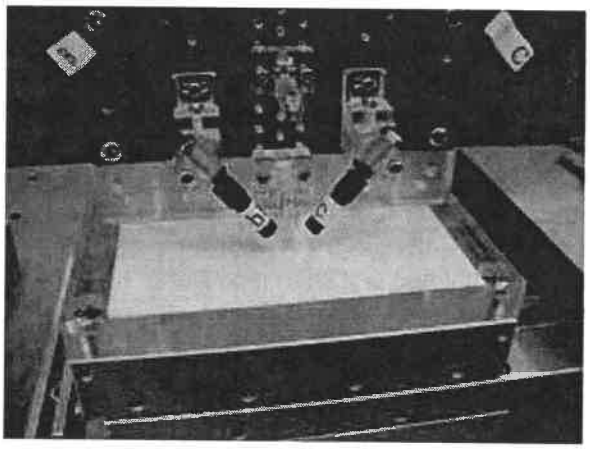

FIGURE 5. Developed optical gap detector that can measure the gap between the tip end and the surface for preventing the collision.

2.2 Optical gap detector for thin rod positioning

For preventing the tip from colliding with the surface, the optical detector with the simple layout is also developed. The LED beam can be collimated to focus around the gap between the tip end and the surface as shown in Fig.4. Then the optical beam can be interrupted and the amount of the recieved light can be monotored by the photo detector to check the tip end collision with the surface. In order to investigate the performance, the experimental set up is built up as shown in Fig.5. Here the diameter of the focus beam is approximately 0.3mm in the primaryexperiment although the sensitivity depends on the focused beam diameter.

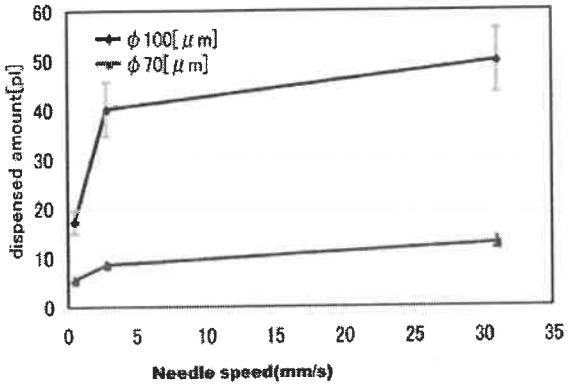

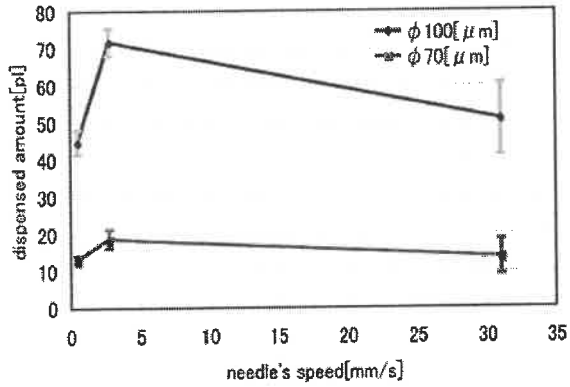

FIGURE 6. Dispensed amount with rhe thin rod with the diameter of 70 and 100 um, viscosity with 48(upper) and 975cP(bottom), thip speed with 0.52, 2.56 and 33.2 mm/s.

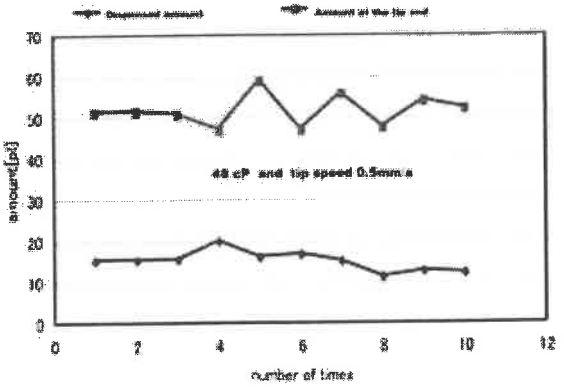

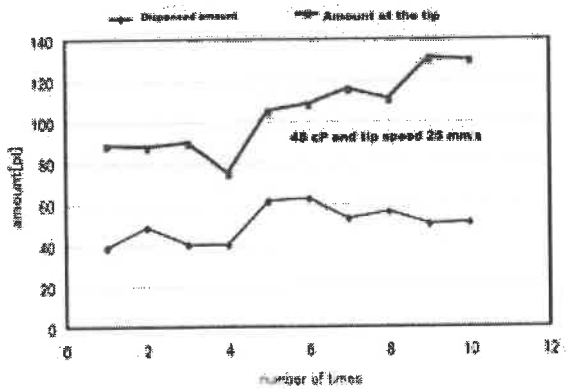

FIGURE 7. The dispensed amount and the volume of the liquid on the tip end are investigated to check the transfer rate.

3. EXPERIMENTAL RESULTS AND DISCUSSIONS

3.1 Dispensed amount

In this set up, it can be expected that the amount of the dispensed on the surface depends on the various factors such the tip diameter, the tip speed, liquid viscocity and hydrophilicity. In Fig.6, the dispensed amounts are plotted when the tip speed is .052, 2.56 and 33.2(mm/s) and the silicone oils with viscocity of 48 and 976(cP) are tested. The tip diameters of 70 and 100(um) are uesed for dispensing and the droplet are measured by the optical microscope instrument. When the viscosity is small, then the dispensed amount is increased to the tip speed, while the amount is decreased when the tip speed is more than 2.5(mm/s) with the high viscosity.

In Fig.7, the dispensed amount and the liquid volume attached on the tip end are investigated. Here approximately one fifth of the tip end droplet can be dispensed when the viscosity is 48(cP) and the tip speed is 0.5(mm/s) while one third of that can be done when the tip speed is 25 mm/s.

3.2 Gap detection

In Fig.8, the output signal from the photo detector is shown when no liquid is around the tip end and some liquid is attached the tip end. It is clear that the gap between the tip and the surface can be found by the reading of the output signal as well as the position of the tip with the liquid can also be detected by the irregular signal output.

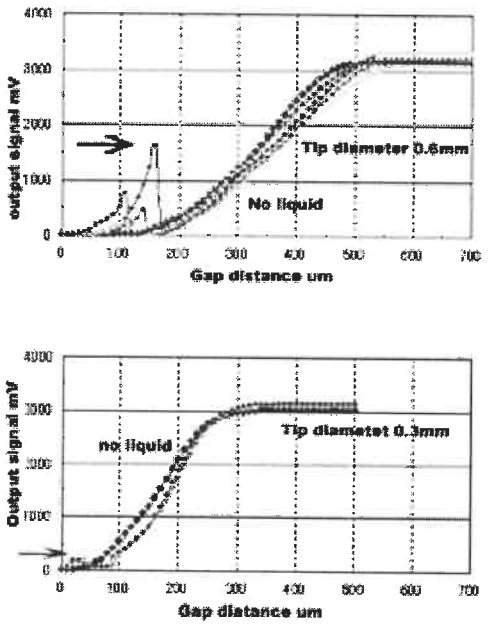

FIGURE 8. Output signal fromthe PD with the gap between the tip end and the surface.When the liquid is attached around the tip end, then the signal can indicate the irregular characteristics.

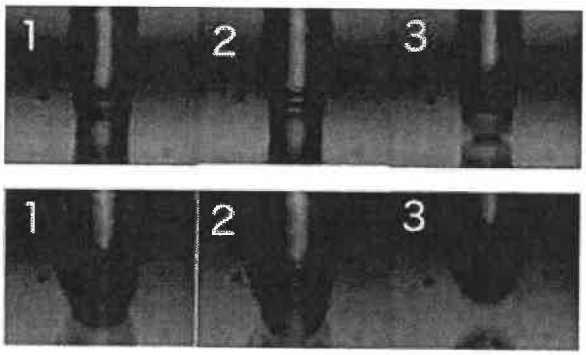

FIGURE 9. Sequential photo shows the accurate dispensing performance even with high viscos liquid

3.3 Applications

In Fig.9, the sequential photo of the precise dispending liquid is shown while the array of the pico liter dispensed liquid of Ag paste and silicone oil are demonstrated as the typical applications in Fig.10.

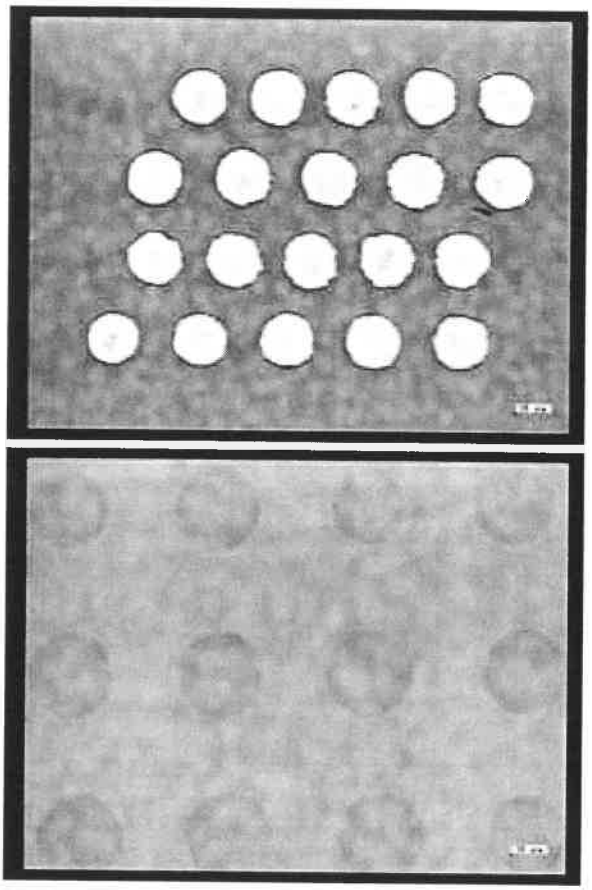

FIGURE 10. Several liquids such Ag nano paste(upper) and silicone oil(bottom) can succesfully be dispensed. The average amount is measured with 30 pico-liter.

4. CONCLUSIONS

In this report, the simple dispensing mechanism that is composed of the thin rod and glass pipette is described and the optical gap detecting is also developed for preventing from the tip collision with the surface. In the primary experiments, the relation between the dispensed amount and the tip diameter, the tip speed, liquid viscocity and hydrophilicity are investigated to check the repeatability. And the optical detector that is composed of the combinaion of the focused LED beam and PD can measure the gap between the tip and the surface for automatic sequential despensing process. A part of this research is supported financially by 2006JST Academic-Industry Partnership Seed Innovation Enterpize Potentiality Verification Stage-

CALIBRATION OF A ROBUST 2 DOF PATH MONITORING TOOL FOR INDUSTRIAL ROBOTS AND MACHINE TOOLS BASED ON PARALLEL KINEMATICS

E. Batzies[1], M. Kreutzer[1], D. Leucht[2], V. Welker[2], O. Zirn[1]
[1] Mechatronics Research Group
Giessen University of Applied Sciences
35390 Giessen, Germany
[2] Fachbereich Mathematik und Informatik
Philipps-Universität Marburg
35035 Marburg, Germany

INTRODUCTION

Up to the early 90s acceptance tests of machine tool and robot manipulators have been realized by static positioning accuracy measurements, e.g. using laser interferometers. With the increasing demand for higher manipulator performance dynamic trajectory monitoring became important. A first dynamic monitoring approach was the circular test using a touch trigger probe [1]. Speed and measurement accuracy are limited due to probe friction. The Double Ball Bar [2] measurement system avoids friction influences but is limited to large circle trajectories. The circular test elucidates static and dynamic manipulator performance and is meanwhile standardized [2] for machine tool inspection tests.

FIGURE 1. Prototype of the parallel 2 DOF inspection system in the Giessen University machine tool laboratory - arranged beside the Lattice Grid Plate [2].

The most sophisticated inspection tool for arbitrary trajectories is the Lattice Grid Plate [1]. It yields high precision (ca. 1μm) as well as high resolution (ca. 5μm) path monitoring at velocities up to 0.5 m/s. The Lattice Grid Plate consists of a steel substrate with a grid of pattern squares. A scanning unit that has no mechanical contact to the plate measures the position with two degrees of freedom (2 DOF). The air gap between plate and scanning unit is in the range of 500 to 1000μm. Inspection devices to measure three and more DOF movements are subject of further developments [3], [1]. These high precision systems require careful use, especially in the rough manufacturing environment. Operator or path errors rectangular to the measurement plane as well as falling screws, tools, etc. can cause severe damages to the inspection devices. Especially robot inspection devices require adequate robustness against path errors and end effector orientation errors. On the other hand, the measurement precision for robot acceptance tests is much smaller than the required precision for machine tools. Experiences gained with parallel manipulators show that these kinematic principles yield very high repeatability with moderate effort [4]. Based on these experiences and the growing need to inspect robot manipulators a parallel 2 DOF inspection device was developed (see Figure 1). The end effector of the robot or the tool center point of the machine tool is attached at the top joint. The foot joints are attached to legs, mounted on two high resolution rotary encoder.

REQUIREMENTS AND DESIGN

The mechanical and operational requirements for the parallel 2 DOF inspection device are:

- ▷ rectangular measurement area (200x200 mm) to achieve adequate robot velocities
- ▷ 50μm absolute precision in the measurement

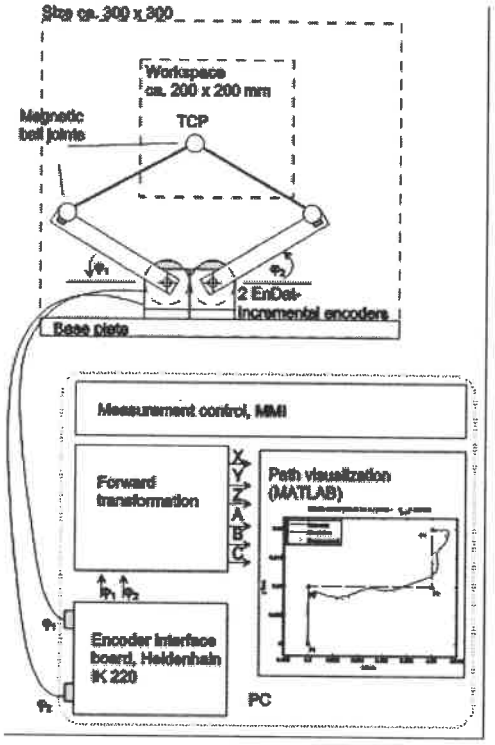

FIGURE 2. Principle sketch of the parallel 2 DOF inspection system with measurement hardware and postprocessing.

area

- ▷ 2 m/s maximum path velocity
- ▷ robustness against operator errors
- ▷ low cost design
- ▷ easy to use calibration method

For the recommended measurement area, the ratio of device size to measurement range is high. Prolongation of the measurement area in the preferred direction parallel to the linear encoder yields better ratios. Thus the system is scalable without any changements to concept presented here. Especially for large measurement ranges, the "inverse Dinosaur effect" [4] of parallel manipulators leads to increasing system performance of the concept. The mechanical design of the inspection device is based on standard components. The backlash free and stiff joints are realized with magnetic ball joints. A PC interface board captures the linear encoder positions [2] (see Figure 2). Real time measurement and data recording is implemented in C. Forward transformation and error compensation requires no real time programming. Thus it is integrated in a MATLAB postprocessor step as well as the graphical display of the inspection result.

The application of standard components reduces the costs for the parallel inspection device to a fraction of the Lattice Grid Plate system price. Scaling up the measurement range will cause minor additional costs.

CALIBRATION ISSUES

Figure 3 shows a systematic picture of the measurement device: The encoders are positioned at coordinates (x_1, y_1) and (x_2, y_2) and measure the angles α_1 and α_2. For the calculation of the TCP position from angles α_1 and α_2, that is, working out the forward-transformation, the following system parameters are needed: x_1, y_1, x_2, y_2, a_1, b_1, a_2, b_2, β_1, β_2. Here, β_1 and β_2 are the "zero-angle-positions", that is, the angles at which the encoders measure angles 0. The task of calibration is to calculate these system parameters from a set of measurements which give corresponding values for the TCP-Position and the rotary encoders.

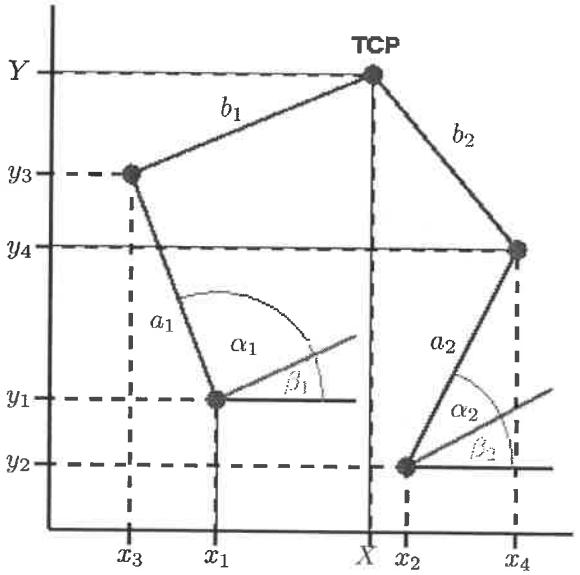

FIGURE 3. Schematic figure of measurement device Introduction of the errors (leg lengths, tolerances of the magnetic ball joints, Encoder offsets, lattice grid plate position and orientation).

NUMERICAL APPROACH TO CALIBRATION

In the previous section a mathematical model was presented that, based on known system parameters, allows the calculation of Cartesian co-

ordinates of the tool center point from the angles measured by the position monitoring system. The numerical approach to calibration is based on this forward transformation. Starting from an estimate of the system parameters the forward-transformation is calculated for each pair of α_1 and α_2 in the calibration dataset. A merit function is defined as the sum of squares of differences between the Cartesian coordinates calculated by the forward-transformation and the coordinates given by the comparison measurement system. The optimized parameter set is determined by localizing the minimum of the merit function for all given calibration positions. From the set of mathematical algorithms applicable to this situation we have chosen the Levenberg-Marquardt-Algorithm [5], known as a robust solver for least square optimization problems.

The results obtained by numerical calibration are disappointing. The measurement error of the position monitoring tool after calibration averages around 200μm. But an analysis of the mechanical construction leads to an expected measurement error $\leq 50\mu$m. In addition, it turns out that the determined system parameters differ significantly from their measured physical dimensions. Particularly, the calculated lengths of the legs b_1 and b_2 differ more than 10% from their actual lengths.

In the sequel we show that an analysis of this failure leads to a hybrid method combining the numerical with the symbolic approach from the next section. A close examination of the model leads to the conclusion that the location of minima obstructs the success of the numerical algorithm.

First, we examine the situation when only the system parameters b_1 and b_2 are considered. Figure 4 shows a 3D-plot of the merit-function. The axes labelled b_1 and b_2 are scaled by the difference of the parameter value and its physical value. Figure 4 shows that there is a unique minimum at the position where the system-parameters b_1 and b_2 equal the physical length. Thus the minimum can be easily localized by any numerical least square optimization method.

Next, we study the situation when only the system parameters b_1 and β_1 are considered. Using conventions analogous to Figure 4 in Figure 5 the reason why numerical calibration fails becomes transparent. The merit-function has numerous local minima which are distributed along a a flat valley. Therefore, optimization with numerical algorithms can only be performed by extraordinary charges of computing time or fails at all.

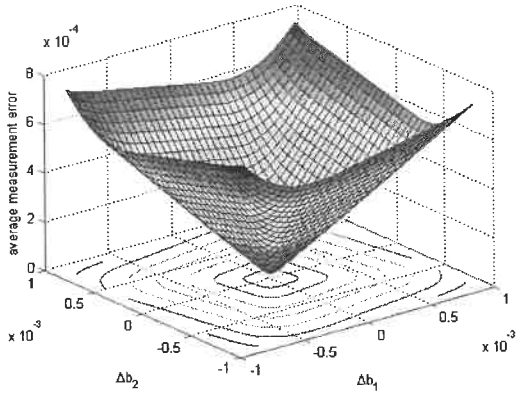

FIGURE 4. Measurement error depending on the parameters b_1 and b_2.

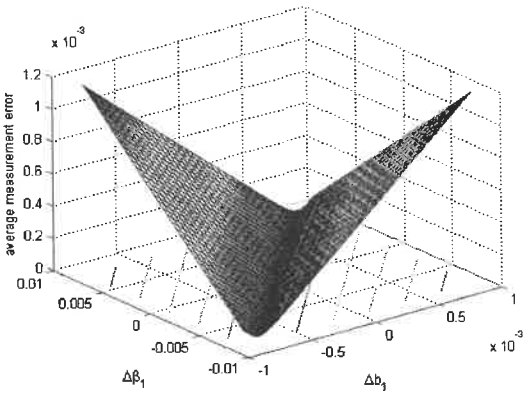

FIGURE 5. Measurement error depending on the parameters β_1 and b_1.

The situation is significantly different in case the estimates of the system parameters are very accurate. The next section describes how this can be achieved by symbolic methods. Experiments show that a numerical optimization based on very good estimates of the system parameters can further reduce the measurement error by involving additional calibration measurements. The remaining calculation complexity is small since nearly accurate system parameters guarantee fast convergence. The measurement errors of the Levenberg-Marquardt algorithm with different estimates of the system parameters are as follows:

Error	rough estimates	symbolic method estimates
Average	200μm	20μm
Maximum	1000μm	200μm

SYMBOLIC APPROACH TO CALIBRATION

The symbolic approach to calibration is based on the solution of polynomial dependencies between the measured data and the calibration values. In order to obtain polynomial dependencies, we introduce the following symbols:

$$\begin{aligned} p_1 &:= a_1\cos(\beta_1), & p_2 &:= a_2\cos(\beta_2),\\ q_1 &:= a_1\sin(\beta_1), & q_2 &:= a_2\sin(\beta_2),\\ u_1 &:= \cos(\alpha_1), & u_2 &:= \cos(\alpha_2),\\ v_1 &:= \sin(\alpha_1), & v_2 &:= \sin(\alpha_2). \end{aligned}$$

Exploiting the measurement geometry, we obtain the following equation:

$$\begin{aligned} & x_1^2 + y_1^2 + p_1^2 + q_1^2 - b_1^2 \\ & +2u_1((x_1p_1 + y_1q_1) + 2v_1(-x_1q_1 + y_1p_1) \\ & -2(u_1X + v_1Y) + 2(-v_1X + u_1Y)q_1 \\ & -2Xx_1 - 2Yy_1 + X^2 + Y^2 \;=\; 0 \end{aligned} \qquad (1)$$

This equation involves only variables which belong to the left part of the device, that is, the legs with lengths a_1 and b_1. There is an analogous equation for the right part. Therefore, the calibration problem separates into two identical problems for the two parts. These consist of a list of equations of the above type (1), one equation for each single measurement of the calibration process. Here, for all single measurements of the calibration process, the system parameters x_1, y_1, p_1, q_1 and b_1 are the same and unknown, while for each single measurement of the calibration process the values of the variables u_1, v_1, X and Y are measured. In the symbolic approach for each measurement we introduce a new set of these variables. We successfully applied two different methods for solving the system in case of 7 and 5 measurements.

7 measurements: Using appropriate transformations which successively eliminate all nonlinear terms from the equations, it is possible to deduce a system of 4 linear equations for the unknowns x_1, y_1, p_1 and q_1. Solving the system by standard methods after replacing the measurement variables by the actual values and then successively solving equation (1) for b_1 leads to a solution.

5 measurements: By calculating Gröbner bases using SINGULAR [6] for the system of 5 measurements it can be shown that the system indeed can be solved using 5 measurements only, which clearly is the best one can hope for. After some simple transformations of the system by hand it was possible to calculate another Gröbner basis using an elimination order. The resulting Gröbner bases then reduces the calibration to finding zeros of univariate polynomials of degree 4 and a simple elimination of the geometrically inconsistent roots.

Both solutions lead to an algorithm which has been implemented in MATLAB. We apply the algorithm on randomly chosen sets of 7 (resp. 5) measurement points and chose the best results with regard two maximum errors between Lattice Grid Plate TCP position measurements and TCP - positions as calculated from forward transformation based on the calibration result. Figure 6 shows a plot of these two grids of TCP positions in the case a 7 measurements. The resulting errors were as follows:

→ Average error: 50μm

→ Maximum error: 200μm

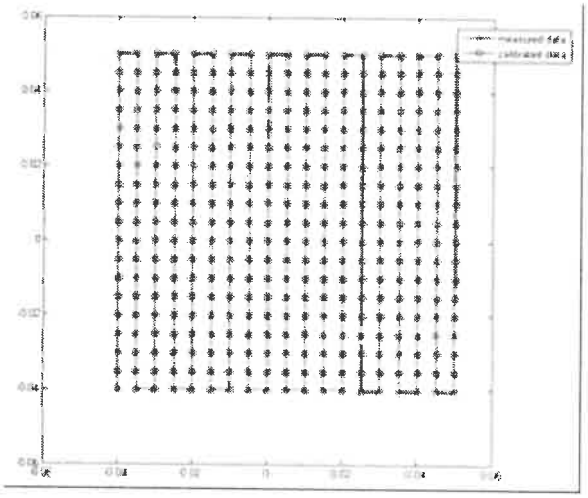

FIGURE 6. Comparison of TCP-position grids: Crosses represent measured positions, circles represent positions calculated from encoder values using forward transformation based on calibrated values.

MEASUREMENT RESULTS

The exemplary measurements at the robot shown in Figure 7 demonstrate, that dynamic path errors

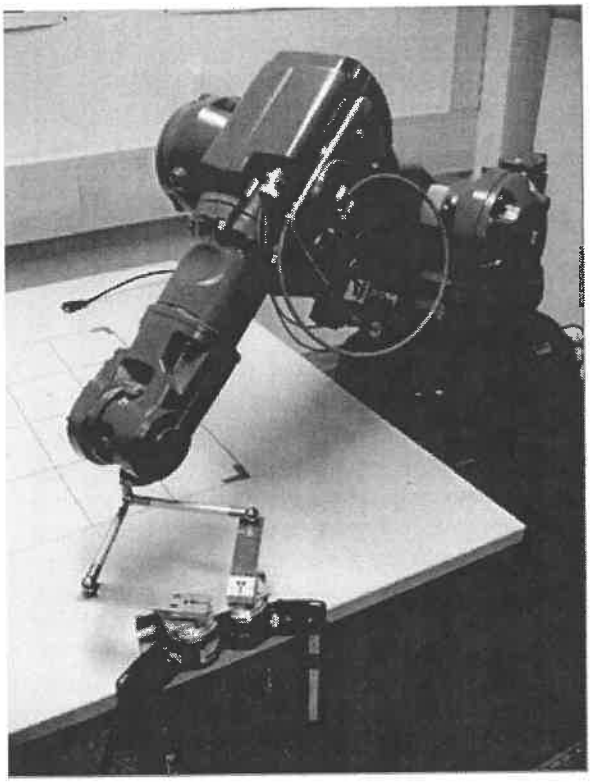

FIGURE 7. Prototype applied on the ABB-robot in the Giessen University robot laboratory.

of industrial robots are in the range of several millimeters (see Figure 8). Thus the achieved calibration accuracy of 50μm satisfies the needs of robot trajectory monitoring quite well.

CONCLUSION

The parallel 2 DOF inspection device is a easy to use trajectory monitoring tool robot manipulators. The high repeatability of parallel mechanisms and suitable error compensation yield sufficient accuracy in the range of 50μm. Here, the presented symbolic methods yield more accurate and more reliable calibration results than numerical approaches. The system has a simple and low cost mechanical design. It is robust against operator and path errors as well as manufacturing environment influences. The new inspection tool will be used for dynamic robot manipulator measurements to validate simulation models.

ACKNOWLEDGMENTS

The presented results have been worked out in the applied research project "HWP/Innovationsbudget" founded by the Hessian Ministry of Science and Art.

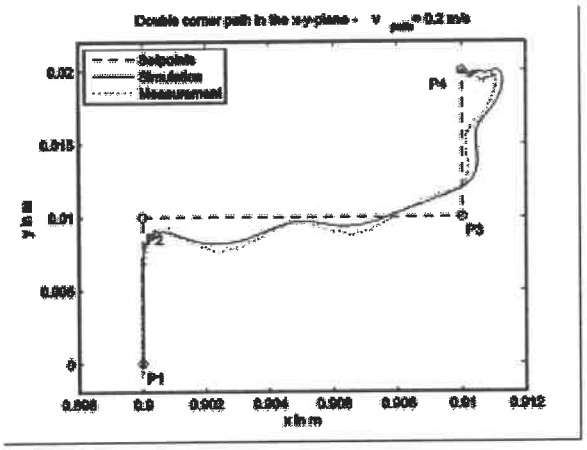

FIGURE 8. Fast double corner test path for the ABB-robot.

REFERENCES

[1] Weikert, S.: Dynamic Accuracy Monitoring. Proceedings ASPE 14th Annual Meeting, 1999.

[2] N.N.: ISO 230-1..4 Test code for machine tools. International Organization of Standardization, 1996.

[3] Zirn, O.; Weikert, S.: Dynamic Accuracy Monitoring for the Comparison and Optimization of Fast Axis Feed Drives. Proceedings ASPE 12th Annual Meeting, , Norfolk, 1997.

[4] Zirn, O.; Treib, T.: Similarity Laws of Parallel and Serial Manipulators for Machine Tools. Proceedings, MOVIC'98, IfR ETH Zürich, 1998.

[5] Mor´, J.J: The Levenberg-Marquardt algorithm: implementation and theory. in Lecture Notes in Mathematics 630: Numerical Analysis, G.A. Watson (Ed.), Springer-Verlag: Berlin, 1978, pp. 105116.

[6] Greuel, G.-M.; Pfister, G.; Schönemann H.: SINGULAR 3.0. A Computer Algebra System for Polynomial Computations. Centre for Computer Algebra, University of Kaiserslautern (2005). `http://www.singular.uni-kl.de`.

AN ADVANCED NURBS INTERPOLATOR FOR MECHANICAL-COUPLED LINEAR SERVO SYSTEMS

Chung-Wei Cheng[1], Chun-Hsien Yang[2], and Mi-Ching Tsai[2]
[1]ITRI South,
Industrial Technology Research Institute,
Tainan County, Taiwan, ROC
[2]Department of Mechanical Engineering,
National Cheng Kung University,
Tainan, Taiwan, ROC

ABSTRACT

This study presents a real-time motion control scheme for the control of mechanical-coupled linear servo systems. The scheme comprises a variable-feedrate non-uniform rational B-spline (NURBS) curve interpolator with an S-curve velocity planning function and a synchronous controller, which are implemented in real-time using a digital signal processor. In the proposed approach, acceleration/deceleration (ACC/DEC) planning on the feedrate command is performed prior to the feedrate interpolation process such that the path command errors caused by conventional schemes in which ACC/DEC planning is executed after feedrate interpolation are eliminated. The effectiveness of the proposed control structure is demonstrated experimentally using a NURBS circle for illustration purposes.

INTRODUCTION

To satisfy the requirements for higher machining speeds, the ball-screw driven mechanisms used in computer numerical control (CNC) machines have been replaced by direct-drive linear motors nowadays. Typically, such machines physically couple two linear motors in parallel so as to achieve a sufficient thrust to accomplish one-degree movements. The resulting structure is conventionally described as a mechanical-coupled linear servo system. However, such servo systems require the use of precise synchronous control techniques to optimize their performance [1][2][3].

Synchronous control techniques can be classified as either parallel or series schemes. The former regard the two coupled motors as independent units and control them separately. In such schemes, the state signals of one motor are not fed back to the other and hence external disturbances may prevent accurate synchronous movement despite the fact that the two motors receive an identical command signal. By contrast, in series-type control schemes, the motion commands of the second motor (i.e. the slave) are not given directly, but are determined by the states in the servo loop of the first motor (known as the master). As a result, any change in the response of the master is automatically reflected in a corresponding change in the command signal provided to the slave motor. However, series-type control schemes can not handle the synchronous motion error caused by external disturbance to slave motor. For coping with the above shortcoming, this paper adopted an advanced synchronous controller which is a series-type-like control scheme [3], while the synchronous errors are feedback and controlled to each motor.

The problem of improving the accuracy of mechanical-coupled linear servo systems using advanced interpolators has attracted relatively little attention in the literature. Conventionally, CNC motion controllers only provide line or arc interpolators, and motion paths are usually given by a set of lines or arc segments. However, this approach has several disadvantages, namely (1) a significant volume of data must be processed to ensure the accuracy of the motion path and (2) the practice of executing ACC/DEC planning after the feedrate has been interpolated introduces a low-pass filter effect, which causes servo lag and hence results in machining errors.

To improve the precision of the machining performance of a CNC machine actuated using mechanical-coupled linear servo systems, this study develops a real-time, variable-feedrate NURBS curve interpolator with an S-curve velocity planning function which executes prior to the feedrate interpolation process such that the precision of the motion path is enhanced.

An integrated motion control scheme is implemented using a TI TMS320C32 digital signal processor (DSP). The performance of the proposed scheme is evaluated experimentally using a prototype mechanical-coupled linear servo system. Having determined the minimum sampling period required to enable real-time interpolation, the control scheme is used to drive the motors in such a way as to describe a NURBS circle. The actual feedrate and position responses are then compared with the instructed values in order to assess the effectiveness of the proposed controller.

NURBS CURVE INTERPOLATOR

In general, a NURBS curve in 3-D space can be described as [4]

$$P(u)=\frac{\sum_{i=0}^{n}N_{i,k}(u)W_iQ_i}{\sum_{i=0}^{n}N_{i,k}(u)W_i}=\sum_{i=0}^{n}V_iR_{i,k}(u)\quad u\in[0,1]\quad(1)$$

and

$$R_{i,k}(u)=\frac{N_{i,k}(u)W_i}{\sum_{i=0}^{n}N_{i,k}(u)W_i}\qquad(2)$$

where $P(u)=(x(u)\ y(u)\ z(u))^T$, Q_i is the control point, W_i is its weighting factor, $n+1$ is the number of control points and k is the order of the NURBS. The terms $N_{i,k}(u)$ and $R_{i,k}(u)$ are referred to as the kth order basis function and the rational basis function, respectively.

The purpose of the variable-feedrate NURBS curve interpolator is to convert the NURBS curve segments into each axis's motion command so that all axis motions are coordinated with a desired feedrate. To achieve the desired variable feedrate along a NURBS curve, it is necessary to adjust the incremental distance specified for each time interval T. Accordingly, at each sampling period, a method is required to determine successive values of u such that appropriate incremental distance along the curve can be accurately generated. Applying the method proposed in [5][6], the basic procedure required to determine successive values of u can be summarized as follows.

In general, the feedrate along the NURBS curve $P(u)$ given in Eq. (1) is defined as

$$V(t)=\left\|\frac{dP(u)}{dt}\right\|\qquad(3)$$

Since the dummy variable $u(t)$ is a strictly monotone increasing function, the following chain rule can be constructed

$$V(t)=\left\|\frac{dP(u)}{du}\frac{du}{dt}\right\|=\left\|P^{(1)}(u)\right\|\frac{du}{dt}\qquad(4)$$

and therefore

$$\frac{du}{dt}=\frac{V(t)}{\left\|P^{(1)}(u)\right\|}\qquad(5)$$

Furthermore, the second derivative of $u(t)$ has the form

$$\frac{d^2u}{dt^2}=\frac{A(t)}{\left\|P^{(1)}(u)\right\|}-\frac{V^2(t)\left(P^{(1)}(u)\bullet P^{(2)}(u)\right)}{\left\|P^{(1)}(u)\right\|^4}\qquad(6)$$

where $A(t)=dV(t)/dt$, $\bullet$ denotes the inner product, and $P^{(m)}(u)$ is the mth derivative of $P(u)$.

Various methods have been proposed for solving Eq. (5) numerically. One well-known method is based on the Taylor's expansion, in which the second-order approximation of du/dt at time instant $t_k=kT$, is formulated as

$$u_{k+1}\approx u_k+T\left.\frac{du}{dt}\right|_{t=t_k}+\frac{T^2}{2}\left.\frac{d^2u}{dt^2}\right|_{t=t_k}\qquad(7)$$

where $u_k=u(t_k)$ denotes the value of u at the kth sampling time instant $t_k=kT$.

Let $V_k=V(t_k)$ and $A_k=A(t_k)$ denote the desired feedrate and acceleration commands at time t_k, respectively. From Eqs. (5)-(7), the second-order Taylor's expansion interpolator for generating u_{k+1} can be derived as

$$u_{k+1}=u_k+\frac{T\,V_k}{\left\|P^{(1)}(u)\right\|_{u=u_k}}+\frac{T^2}{2}\left(\frac{A_k}{\left\|P^{(1)}(u)\right\|_{u=u_k}}-\frac{V_k^2\left(P^{(1)}(u)\bullet P^{(2)}(u)\right)\Big|_{u=u_k}}{\left\|P^{(1)}(u)\right\|^4_{u=u_k}}\right)\qquad(8)$$

For simplicity, the first-order approximation of Eq. (8) is given by

$$u_{k+1}=u_k+\frac{T\,V_k}{\left\|P^{(1)}(u)\right\|_{u=u_k}}\qquad(9)$$

Substituting the computed value of u_{k+1} into the NURBS curve given in Eq. (1) yields the next position command at time t_{k+1}.

REAL-TIME MOTION CONTROL STRUCTURE

Figure 1 presents a flowchart of the proposed motion control structure for a mechanical-coupled linear servo system. As shown, the control tasks include both off-line and real-time tasks. In the off-line stage, the total arc length is

computed from the individual NURBS segments. The real-time stage, includes four major components, namely (1) S-curve velocity planning; (2) variable-feedrate NURBS curve interpolator; (3) NURBS curve representation, and (4) synchronous control.

The total arc length, L, can be calculated off-line from the given NURBS curve segments, $P_i(u)$, i=1,2,...,M, using a numerical integration technique such as Simpson's 1/3 rule [7]. Meanwhile, in the real-time stage, an S-curve velocity planning function (Figure 2) is employed to generate appropriate feedrate, V_k, and acceleration, A_k, commands at time t_k which minimize the acceleration jerk (J=dA/dt). Having computed the velocity and acceleration commands, a variable-feedrate NURBS curve interpolator is used to compute the position command $P_i(u_{k+1})$ for the synchronous controller at time t_{k+1}.

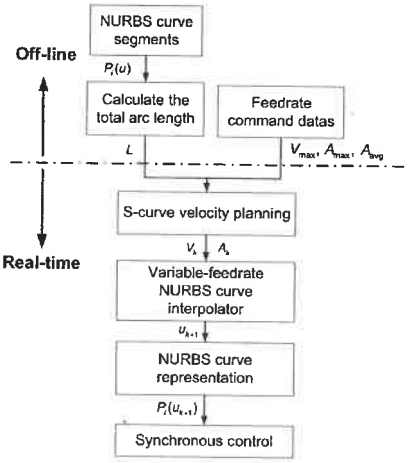

FIGURE 1. Flowchart of proposed motion control structure.

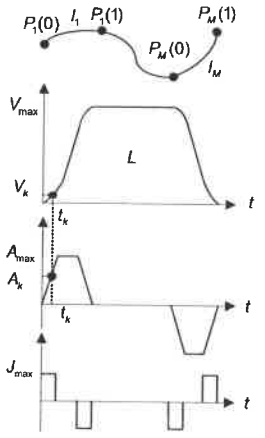

FIGURE 2. S-curve velocity planning function.

EXPERIMENTAL RESULTS

Figure 3 illustrates the layout of the experimental system. As shown, the hardware components include the mechanical-coupled linear servo system, three drivers, and a PMC32-6000 motion control card equipped with a high performance TI TMS320C32 DSP. The real-time control algorithms shown in Figure 1 are implemented using C-language and are executed using the DSP. The mechanical-coupled linear servo system comprises two parallel linear motors driving the y-axis (where Y1 is the master and Y2 the slave) and a single linear motor driving the x-axis and fixed to a saddle linking the slides of the two y-axis motors.

The applied synchronous controller is depicted as Figure 4 [3], where two PI controllers C_{mv} and C_{sv} for master and slave motors respectively are designed to achieve the same velocity loop response, proportional position controller C_{mp} of master motor is for acquiring higher stiffness, C_{syn} means the synchronous error compensator (PI controller), x denotes the position command after NURBS curve interpolation, v is the velocity command of both motors, and e shows the synchronous position error.

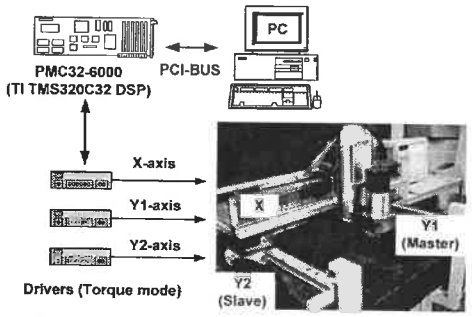

FIGURE 3. Layout of experimental system.

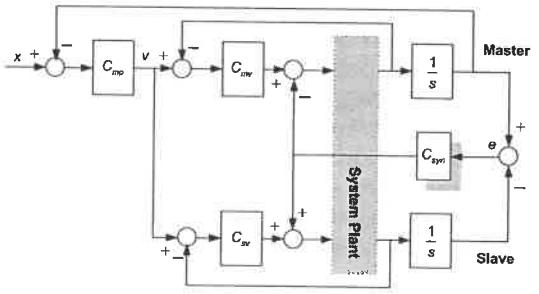

FIGURE 4. Advanced synchronous controller.

The sampling period T is of fundamental importance in implementing real-time control schemes. Therefore, prior to the current

experimental study, an investigation was performed to determine the minimum sampling period required to allow the real-time implementation of the proposed control scheme. Table 1 presents the computational times of two of the major processing operations, namely variable-feedrate NURBS curve interpolation based on S-curve velocity planning and synchronous controller, respectively. The results indicate that for real-time control, the motion control structure with a first-order NURBS interpolator requires a sampling period of $T \geq 0.64$ ms, while that with a second-order NURBS interpolator requires a sampling period of $T \geq 1.12$ ms.

The performance of the proposed controller was evaluated by considering the case of a NURBS circle with a radius of 200 mm (total arc length is 1256.6371 mm). Setting a maximum feedrate of V_{max}=200 mm/s, a maximum acceleration of A_{max}=150 mm/s^2, and an average acceleration of A_{avg}=100 mm/s^2, the total motion time is found to be 8.2832 s. Figure 5 compares the command and actual feedrate and position tracking responses achieved using a second-order variable-feedrate NURBS interpolator with a sampling period of T=2 ms. The good agreement between the two sets of results confirms the effectiveness of the proposed control scheme.

TABLE 1. Computational times of proposed interpolator and control scheme (ms).

	First-order	Second-order
Compute $P^{(1)}(u)$	Yes	Yes
Compute $P^{(2)}(u)$	No	Yes
Variable-feedrate NURBS curve interpolator	0.54	1.02
Synchronous control	0.10	0.10
Total	0.64	1.12

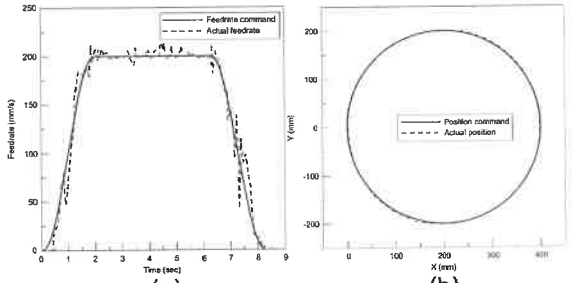

(a) (b)

FIGURE 5. Experimental results for: (a) feedrate and (b) position tracking.

CONCLUSIONS

This study has proposed an advanced motion control structure comprising an S-curve velocity planning function, a variable-feedrate NURBS curve interpolator and a synchronous controller to improve the precision of a mechanical-coupled linear servo system. The proposed control structure has been implemented in real-time using a TI TMS320C32 DSP and its performance evaluated experimentally taking the case of a NURBS circle for illustration purposes. The results of a preliminary investigation showed that when first- and second-order Taylor's expansions were employed for the variable-feedrate NURBS curve interpolator, sampling periods of 1 ms and 2 ms, respectively, were sufficient to achieve a real-time implementation. Meanwhile, the experimental evaluation results have confirmed that the proposed approach, in which ACC/DEC planning on the feedrate command is executed prior to feedrate interpolation, reduces the discrepancy between the command and actual feedrate and position tracking responses and therefore minimizes errors in the motion path.

REFERENCES

[1] FANUC Corp. Parameter Manual of α-series AC Servo Motor. FANUC user manual. 1994.

[2] Sinumerik 840D/FM-NC Description of Functions, Special Functions (Part 3). SIEMENS user manual. 1999.

[3] Yang J.X, Tsai M.C, Hsieh M.F. Identification and Control of a Linear Servo System. International Symposium on Linear Drives for Industry Applications. 2003.

[4] Piegl L, Tiller W. The NURBS Book. 2nd edition. Springer.1997.

[5] Farouki R.T, Tsai Y.F. Exact Taylor Series Coefficients for Variable-Feedrate CNC Curve Interpolators. Computer-Aided Design. 2001; 155-165.

[6] Cheng C.W, Tsai M.C. Real-time Variable Veedrate NURBS Curve Interpolator for CNC Machining. International Journal of Advanced Manufacturing Technology. 2004; 865-873.

[7] Nakamura S. Applied Numerical Methods in C. Prentice-Hall International Inc. USA: 1993.

DEVELOPMENT OF SMALL VIBRATORY CRUSHER FOR SAMPLE-RETURN MISSION

Katsushi Furutani and Yasutake Tagata
Department of Advanced Science and Technology
Toyota Technological Institute
Nagoya 468-8511 Japan

INTRODUCTION

Collecting samples from various planets or asteroids is demanded to investigate the age of the event and the phenomena in the primitive solar system. Japan Aerospace Exploration Agency (JAXA), National Aeronautics and Space Administration (NASA) and European Space Agency (ESA) execute and plan many unmanned exploration missions. A small and light drilling machine is preferable to decrease the energy consumption in a rover and the payload in a launcher [1]. Though the machining accuracy is not required in the process, crushing or cracking is also usable at cryogenic and high temperatures.

Jet Propulsion Laboratory (NASA/JPL) operated Rock Abrasion Tool (RAT) with a rotating grinding wheel on Mars in January 2004 [2]. In the vacuum environment such as the moon, bearings to support the rotor will have tribrogical problems. Therefore, vibration excited with a piezoelectric actuator and simple structure are responsible for drilling in the vacuum environment. JPL has developed also an ultrasonic/sonic driller/corer (USDC) with a bolted Langevin transducer [3]. The wavelength of the ultrasonic restricts the size of the machine.

In this paper, a small drilling machine by using a piezoelectric actuator is proposed. The machine is driven at a non-resonant frequency to make its size small.

PRINCIPLE AND STRUCTURE

Figure 1 shows components and the working principle of a crusher. A hammer deforming itself is reciprocated between a stopper and a drill stem instead of the free mass of USDC [3]. When the hammer collides with the stopper or the drill stem, it extends and kicks the collided part. Then the hammer contracts before the next collision. By the repeating this cycle, the impulse can be generated and crush a rock. The reciprocating rate is independent from the resonant frequency of the movable part, the

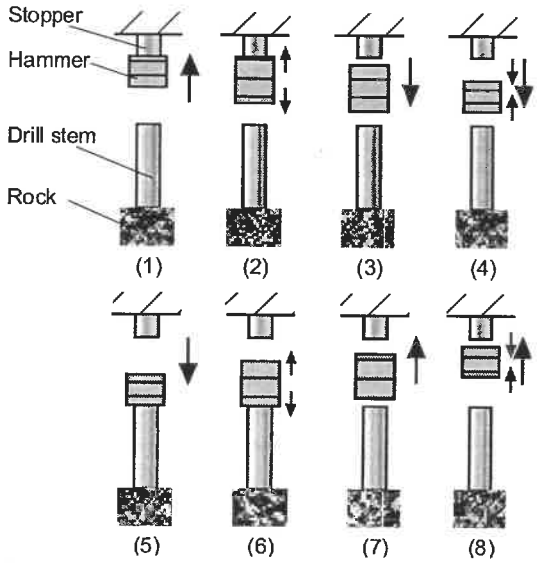

FIGURE 1. Principle of vibration generation.

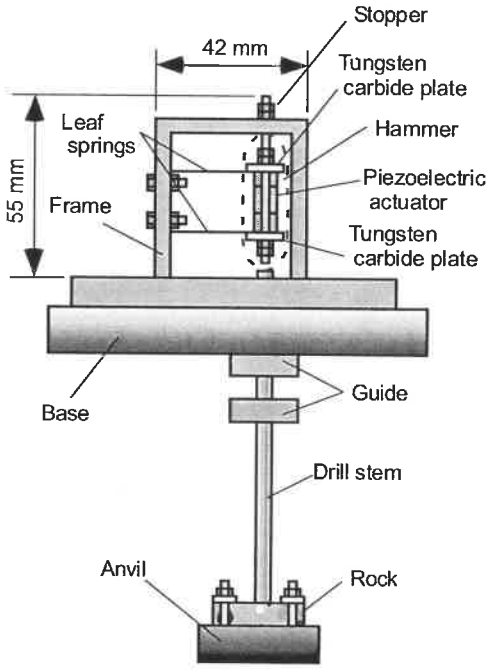

FIGURE 2. Schematic view of crusher.

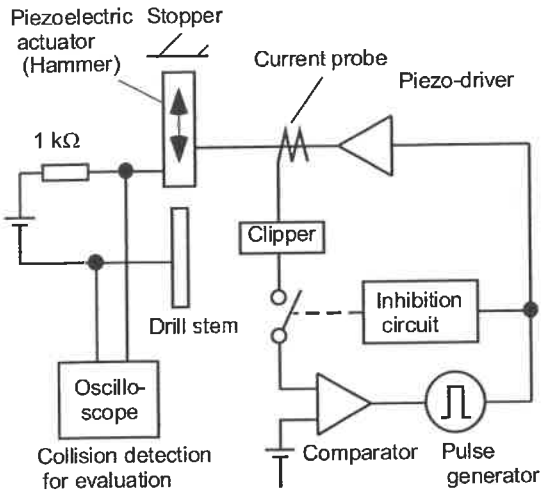

FIGURE 3. System configuration.

whole size of the device can be reduced.

Figure 2 shows a schematic view of the crusher. The crusher consists of a stacked piezoelectric actuator (hammer) supported with leaf springs, the stopper mounted on a frame and the drill stem. It measures 42 mm × 55 mm × 14 mm and weighs 67 g excluded the drill stem. The piezoelectric actuator extending 12 μm at an applied voltage of 100 V was preloaded with 2 2-mm bolts. The drill stem of 3.9 mm in diameter and 100 mm in length was made of tungsten carbide. The gap length between the hammer and the stopper is adjusted by shifting the base height.

Figure 3 shows a system configuration. A rectangular wave with a pulse duration of 167 μs and a peak voltage of 90 V is applied to the piezoelectric actuator through a piezo-amplifier. The collision of the piezoelectric actuator with the stopper or the drill stem was detected by the reverse current from the actuator due to the piezoelectric effect. The driving current of the piezoelectric actuator was neglected by an inhibition circuit. The displacement of the piezoelectric actuator is measured with an optical vibrometer with a band width of 250 kHz. The impulse for machining was measured with a piezoelectric load cell with a range of 35 kN and a resonant frequency of 100 kHz.

PERFORMANCE OF CRUSHER

Delay of Extension of piezoelectric actuator

Figure 4 shows an example of the hammer displacement and the impulse. While the hammer contacted with the stopper or the drill

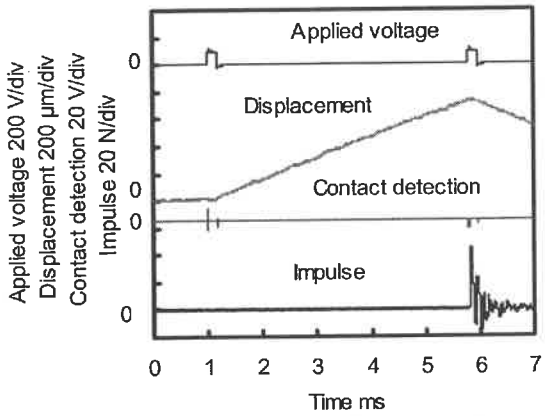

FIGURE 4. Example of hammer displacement and impulse.

TABLE 1. Influence of timing of extension.

Lapse time after collision ms	Velocity ratio	Impulse N
Without extension	0.37	32.4
0.016	1.10	87.4
0.069	1.07	53.0
0.102	1.13	46.3
0.132	1.40	43.7
0.184	1.15	33.9

stem, the detection voltage changed to zero. The delay time from the collision was set to 0.016 ms, which is the shortest delay. Table 1 shows the influence of the delay. Both the velocity and impulse were increased by the hammer extension. Because the impulse is more important for machining than the velocity, the delay was set to the shortest.

Basic Performance

The gap length was changed from 0.7 to 2.4 mm.

Figure 5 shows an example of the hammer displacement and the impulse at a gap length of 1.9 mm. The intervals of the impulse were constant. Because the drill stem hopped by the collision, the hammer displacement measured was smaller than the gap length. The device generated an impulse of 150 N with an average hit frequency of 120 Hz.

Figure 6 shows the relationship between the average of the velocity and impulse. The velocity and the impulse were the maximum around 1.7 to 1.9 mm, which depended on the stroke of the leaf springs. The dispersion of the velocity was 14%. The impulse showed the

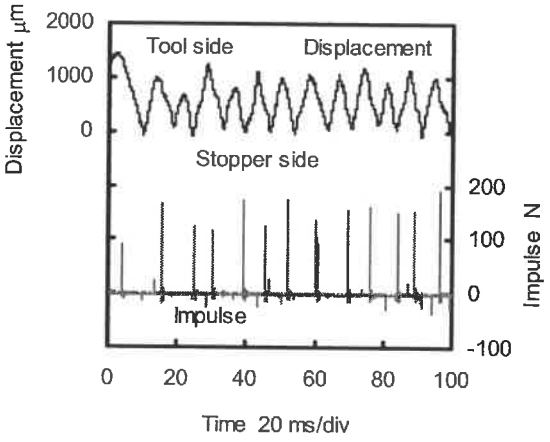

FIGURE 5. Generative force of crusher.

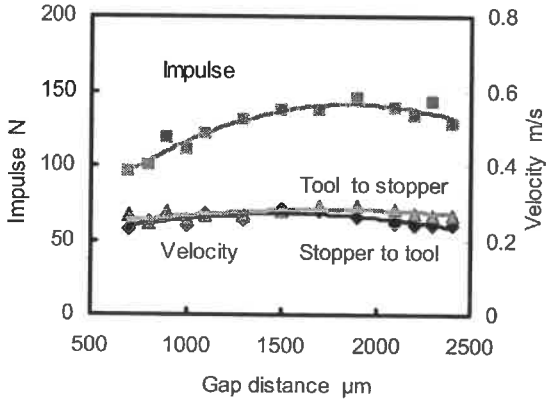

FIGURE 6. Average of impulse and hammer velocity.

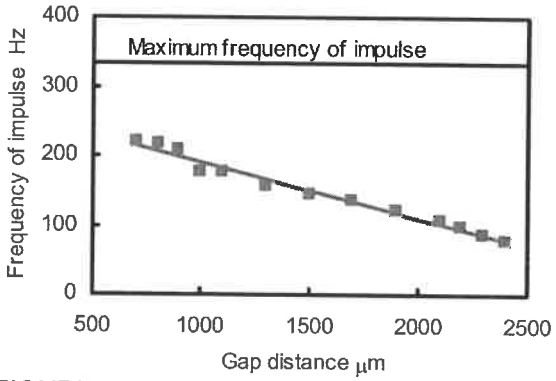

FIGURE 7. Relationship between frequency of impulse and gap length.

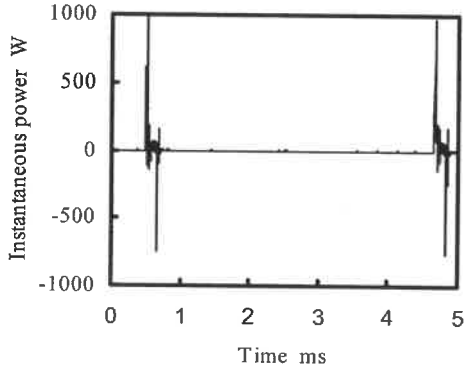

FIGURE 8. Supplied power to piezoelectric actuator.

same trend as the velocity because the impulse is proportional to the momentum.

Figure 7 shows the relationship between the frequency of the impulse and the gap length. Because the inhibition circuit neglected the current of the piezoelectric actuator for 1.5 ms, the dead time a cycle was 3 ms and the highest frequency was restricted to 330 Hz. With an increase of the gap length, the frequency was decreased.

The gap length was set to 1.7-1.9 mm to maximize the impulse in machining.

Figure 8 shows the supplied power to the piezoelectric actuator. Although the peak of the instantaneous power was 1 kW in the extension, the regenerative power was almost the same in the contraction. The cycle time was 4.2 ms at a gap length of 1.9 mm. Consequently, the average supplied power was 4 W.

Machining Demonstrations

Figure 9 shows tips of the drill stems shaped into a flat, frustum or multiple-pyramids. The top diameter of the frustum shown in Figure (b) was 2.2 mm with a point angle of 18°. The pyramids shown in Figure (c) measured 1-mm square.

Figure 10 shows examples of machining. After 5-minite machining of pumice, the hole diameter, depth and the removal amount were 4.3 and 4 mm, and 6 mg as shown in Figure (a). After 60-minute machining of gypsum, the diameter of the hole bottom, depth and the removal amount were 2.9 and 2 mm, and 20 mg as shown in Figure (b). After 60-minute machining of basalt, the maximum depth and removal amount were 0.6 mm and 30 mg as shown in Figure (c).

Therefore, brittle rocks and weathered surface of rocks can be machined.

COMPARISON WITH USDC

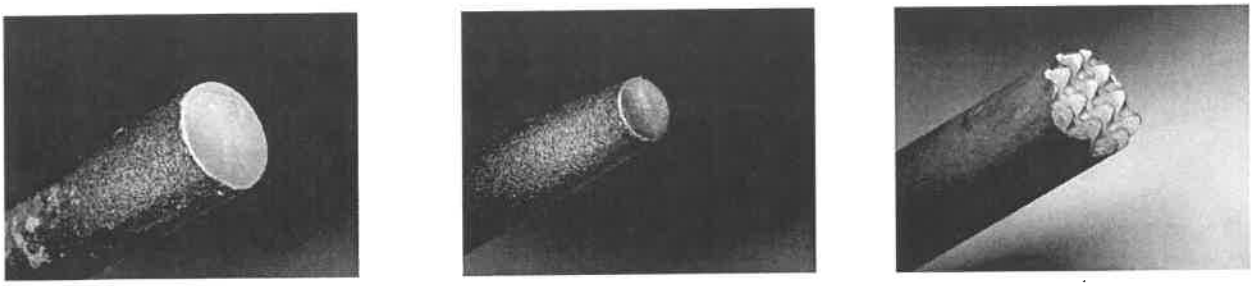

(a) Flat (For pumice). *(b)Frustum (For gypsum).* *(c) Multiple pyramids (For basalt).*

FIGURE 9. Tip shapes of drill stems made of tungsten carbide.

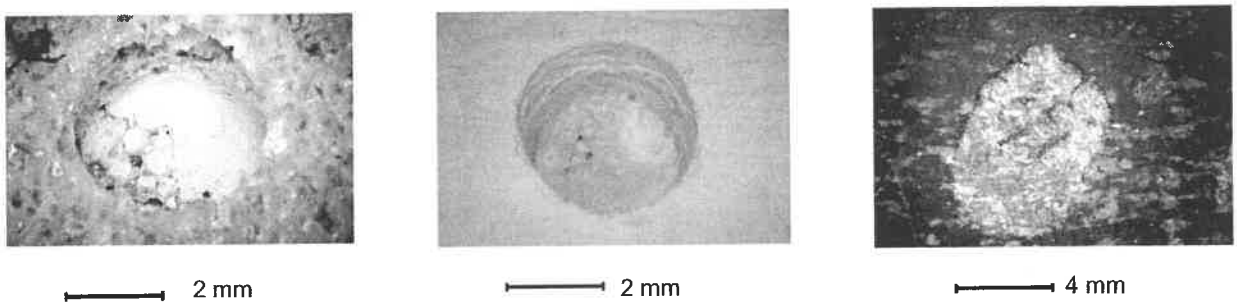

(a) Pumice. *(b) Gypsum.* *(c) Basalt.*

FIGURE 10. Results of machining.

Table 2. Comparison of developed crusher with USDC.

	Impulse N	Impulse frequency Hz	Dimensions mm	Mass g	Average power W
Developed crusher	150	120	42×55×14	67	4
USDC [3]	350	1100	ϕ36×111	450	12
Crusher/ USDC	0.43	0.11	. 0.38 in length	0.15	0.33

Table 2 shows the comparisons of the crusher with USDC [3]. The impulse and frequency were 0.43 and 0.11 times, the device size in length and the weight are 0.38 and 0.15 times, and the supplied electric power is 0.33 times.

CONCLUSIONS

In this paper, the small vibratory crusher with the piezoelectric actuator working as the hammer was proposed. Conclusions can be drawn as follows.

(1) The relationship between the gap length, impulse and frequency was described.
(2) Pumice and gypsum were drilled and the surface of basalt was removed.

For the future work, the control method should be improved to increase the impulse.

ACKNOWLEDGEMENTS

The authors wish to thank Prof. Takashi Kubota of JAXA/ISAS and Prof. Yasuharu Kunii of Chuo University. This work was financially supported by High-Tech Research Center Project for Private Universities, "Space Robotics Research Center": matching fund subsidy, 2003-2007 by Ministry of Education, Culture, Sports, Science and Technology, Japan.

REFERENCES

[1] Kubota T, Kuroda Y, Kunii Y, Nakatani I. Lunar exploration rover: Micro5. Adv. Rob. 2000; 14(5): 443-444.
[2] http://mars.jpl.nasa.gov/mer/mission/spacecraft_instru_rat.html
[3] Bao X, Bar-Cohen Y, Chang Z, Dolgin B P, Sherrit S, Pal D S, Du S, Peterson T. Modeling and Computer Simulation of Ultrasonic/ Sonic Driller/ Corer (USDC). IEEE Trans. Ultrasonics, Sonics and Frequency Control. 2003; 50(9) 1147-1160.

FABRICATION OF A NEW POSITION SURVEYING SYSTEM FOR THE UNDERGROUND PIPES USING TWO PAIRS OF ROTARY ENCODERS

Toshiaki HAMANO[1], Manabu ONO[2], Akira SHINO[1], and Shigeo KATO[1]
[1]Nippon Institute of Technology, Saitama, Japan
[2]Tokyo Metropolitan College of Industrial Technology, Tokyo, Japan

1. INTRODUCTION

Optical fiber cable for high-speed and large-capacity communication is usually covered by plastic pipe and buried under the ground. Then, we are required to grasp its real buried position before digging at the construction or the maintenance in order to prevent from the cutting of the optical fiber. However, once the optical fiber cable is buried under the ground, it is very difficult to confirm the buried position of the pipe, because the optical fiber cable and plastic cover pipe are not the metal.

A former way to confirm the buried position of the optical fiber cable is the ground penetrating radar method.[1], [2] The ground penetrating radar method is very useful for the metal. However, the optical fiber cable in plastic cover pipe is not metal. Another method is the elastic wave method.[3] In this method, a vibrator is put on the ground. The wave from the vibrator is detected by many in-lined receivers that are arrayed on the ground. However, the detection is only done at the place where the ground is covered by soil and the accuracy of the surveying is not good at the place where the position of the plastic cover pipe is so deep in the ground or in the different soils.

If we can detect directly the information of the buried position of the pipe by a new position surveying system that can move itself in the pipe, the problem of the former way to confirm the buried position of the optical fiber cable is solved.

This research aims to identify easily the buried position of the pipe, using the information of the buried position from the pipe. We use two pairs of rotary encoders that have pulleys contacting right and left walls of the buried pipe in order to detect directly the information of the buried position of the pipe. Output of rotary encoder contacting the wall shows the length of the wall. Average of summation of the outputs of the one pair of right and the left rotary encoder shows moving distance of a surveying mechanism of the position surveying system. The curvature of the buried pipe is obtained by difference of the outputs of the one pair of right and the left rotary encoder. Another one pair of rotary encoders is used to correct of irregular data of the one pair of rotary encoder.

The position of buried pipe is identified by the moving distance and the curvature of the pipe. It is confirmed that the new position surveying system can identify the buried position of a pipe that is 12 m long and has loose curvature in the error of 5.5 mm.

2. PRINCIPLE OF POSITION SURVEYING

Length of walls of both side of a pipe is same if the pipe is straight. If the pipe curves toward right, the length of the right wall is shorter than the length of the left wall. We use two pairs of rotary encoders that have pulleys contacting right and left walls of the buried pipe in order to detect directly the information of the buried position of the pipe. The principle of position surveying using one pair of rotary encoders is

shown in Fig. 1. Inner diameter of the pipe that has loose curvature is D. The original point is P_0 (x_0, y_0). Present position of the surveying mechanism is P_n (x_n, y_n). Angle between the tangential line and the x-axis is . It is assumed that a difference is made by the both side rotary encoders when the surveying mechanism moves a small distance of s. This moved point is $P_{n+1}(x_{n+1}, y_{n+1})$. The normal lines that cross points P_n (x_n, y_n) and P_{n+1} (x_{n+1}, y_{n+1}) make an angle . The radius of the curvature is assumed as R. The surveying mechanism may incline by some rolling force. The rolling angle is assumed as . Projection of the pulley is D_1 and is shown as

$$D_1 = D\cos\phi \tag{1}$$

The difference of the right and left rotary encoders is shown as

$$\varepsilon = \left(s+\frac{\varepsilon}{2}\right)-\left(s-\frac{\varepsilon}{2}\right) = \left(R+\frac{D_1}{2}\right)\theta-\left(R-\frac{D_1}{2}\right)\theta = D_1\theta \tag{2}$$

Then, the small angle is obtained as

$$\theta = \frac{\varepsilon}{D_1} \tag{3}$$

The x-coordinates and the y-coordinates of P_{n+1} are calculated from the x-coordinates and the y-coordinates of P_n as

$$x_{n+1} = x_n + s\cdot\cos(\Theta+\theta) \tag{4}$$

$$y_{n+1} = y_n + s\cdot\sin(\Theta+\theta) \tag{5}$$

The tangential angle is the summation of the small angle and shown as

$$\Theta = \Sigma\theta \tag{6}$$

3. POSITION SURVEYING SYSTEM

A new position surveying system for underground pipes is shown in Fig. 2. The system consists of a surveying mechanism that carries the two pairs of rotary encoders, a signal processor, an I/O interface and a computer. The surveying mechanism that is 375 mm long is held to the inside of the pipe by eight small rollers and can move in the pipe. A weight is attached under chassis in order to prevent rolling of the surveying mechanism. However, rolling of the mechanism can not be prevented perfectly. So, rolling angle is measured by an another rotary encoder that is attached the chassis. The right and left encoders are held by arms that have pin joints and are attached the chassis of the surveying mechanism. The pulley is pushed to the wall of the pipe by force of 1 N and vibration of the rotary encoder is severely damped, because the arm is suspended by a spring and a dash pod. The circumference of a pulley is 64.7mm. The signal processor consists of a detecting circuit of clockwise or counter clockwise and a mechanical chattering circuit. The rotary encoder makes 1440 pulses per one rotation. Resolution of the rotary encoder is 44 μm. The signal from the signal processor is introduced into the computer through the I/O interface. Software in the computer calculates locus of the surveying mechanism every 64.7

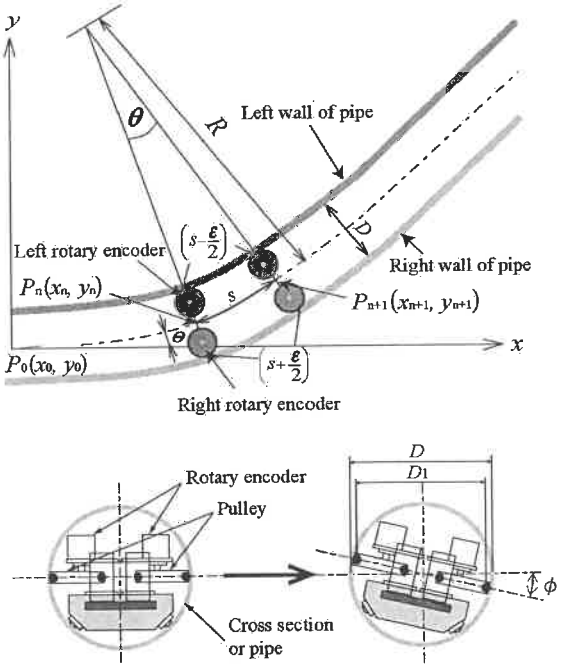

FIGURE 1. The principle of the position surveying in the underground pipe by in-pipe surveyor using rotary encoders

mm. This method decreases an error by the distortion of the pulley. Consequently, Small distance *s* is 64.7 mm of the same length as the circumference of a pulley. The result of the position surveying is displayed on the screen of the computer.

4. PIPE FOR SURVEYING EXPERIMENT

4.1 Coordinates of the pipe for surveying experiment

Pipe for surveying experiment is shown in Fig. 3. The pipe consists of two straight pipes and a curved pipe.The first straight pipe is 4000 mm long.The second curved pipe has a curvature radius of 74000 mm and is 4000 mm long. The third straight pipe that is attached the second pipe and is 4000 mm long.The x-axis of the pipe for surveying experiment is standardized by a fishing line that is 0.05 mm in diameter and is intensely tightened. Distance from the original point that is the x-coordinates is measured by a tape measure.The y-coordinates is measured by steel measure from the standard line of the fishing line.The y-coordinates at 11700 mm of the x-axis is 302.5 mm.

4.2 Decreasing of errors

We use two pairs of rotary encoders that have pulleys contacting right and left walls of the buried pipe in order to detect directly the information of the buried position of the pipe. The curvature of the buried pipe is obtained by difference of the outputs of the one pair of right and the left rotary encoder. Another one pair of rotary encoders is used to correct of irregular data of the one pair of rotary encoder. When the small angle calculated from a front pair of rotary encoders exceeds a threshold, the small angle is transposed to the small angle calculated from a back pair of rotary encoders. Optimal threshold is confirmed to be ±0.18 degrees. The angle calculated from a front pair of rotary is

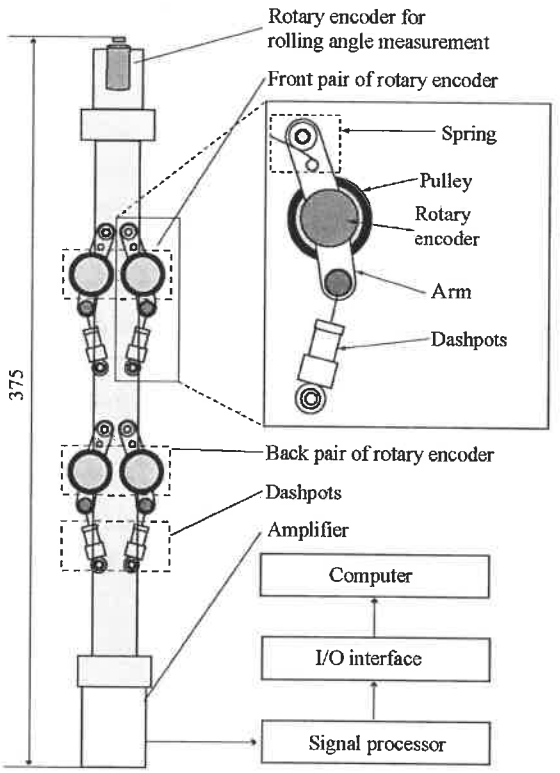

FIGURE 2. Structure of the position surveying system

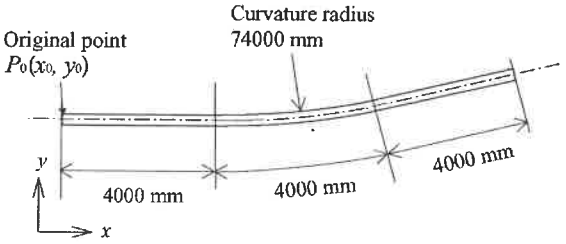

FIGURE 3. Pipe for surveying experiment

shown in Fig. 4. The small angle after using transposition processing is shown in Fig. 5. The small angle of 0.36 degrees at 4000 mm of the x-coordinates is transposed to 0.08 degrees.

4.3 Result of position surveying

The position coordinate by the rotary encoders is obtained from the small angles shown in Fig. 5. The position coordinate by the rotary

encoders and the position coordinate by the steel measure are shown in Fig. 6. Maximum of the difference occurs at the curved pipe and is 5.5 mm.

5. CONCLUSIONS

1. We fabricated a position surveying system for underground pipes using two pairs of rotary encoders. Two pairs of rotary encoders measure distance of right and left walls of the pipe.
2. Another one pair of rotary encoders is used to correct of irregular data of the one pair of rotary encoder. Transposition processing can decrease the measured error.
3. It was confirmed that the fabricated position surveying system can survey the position of the experimental underground pipe that consists of two 4000 mm straight pipes and 4000 mm curved pipe that has the curvature radius of 74000 mm in the error of 5.5 mm.

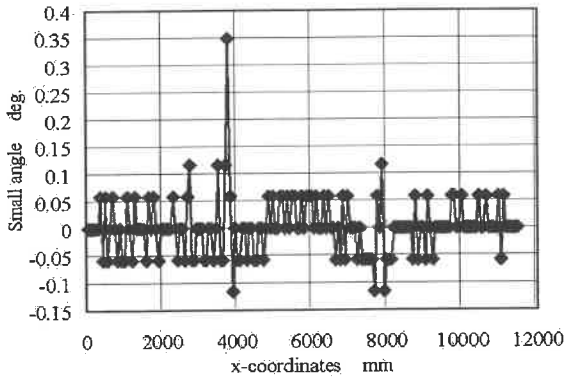

FIGURE 4. The small angle by front pair of rotary encoders of the position surveying system

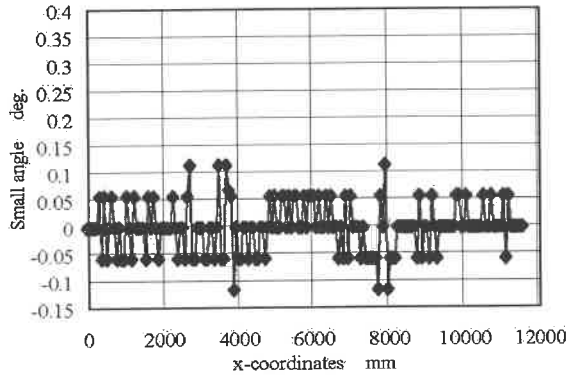

FIGURE 5. The small angle after using transposition processing

REFERENCES

[1] M. Sato, Subsurface Imaging by Ground Penetrating Radar, Society of The Institute of Electronice Information and Communication Engineers Trans. , Vol. J85-C No. 7 (2002), pp. 520-530.

[2] M. Tanaka, J. Takayama, S. Ohyama Imaging Process Based on Bistatic Scanning for Subsurface Radar, Trans. on Society of Instrument and Control Engineering, Vol. 39 No. 4 (2003), pp. 325-331.

[3] Y. Kokubo, Y. Igarashi and K. Ozaki, Development of an Elastic Wave type Position Surveying System for Underground Pipe, EXTEC No. 64 pp. 57-60.

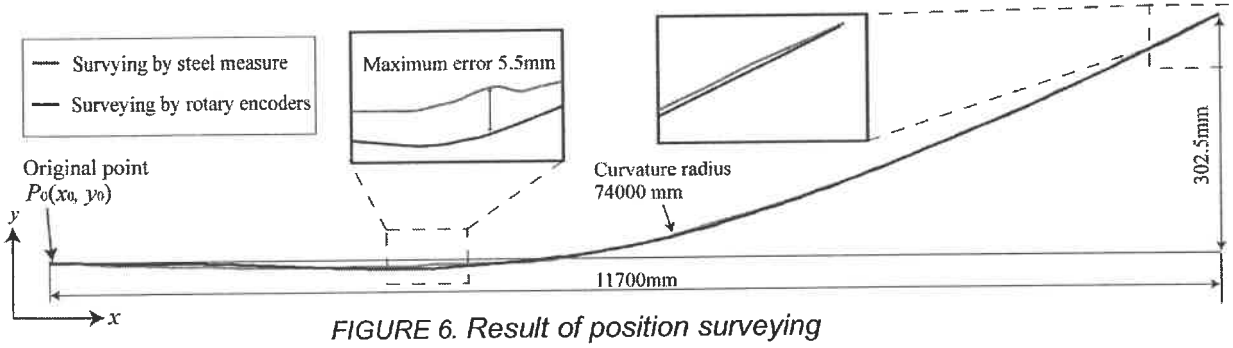

FIGURE 6. Result of position surveying

FABRICATION OF A MICROROBOT MOVABLE IN FREELY HELD PIG'S SMALL INTESTINE

Shigeo KATO[1], Manabu ONO[2], Akihiro GAKUHARI[1], Yuji KUNIYOSHI[2],and Toshiaki HAMANO[1]
[1]Nippon Institute of Technology, Saitama, Japan
[2]Tokyo Metropolitan College of Industrial Technology, Tokyo, Japan

1. INTRODUCTION

An inspection of the large intestine is very effective in order to prevent the large intestine cancer. A fiberscope is excellent for the inspection of the large intestine. However, the inspection by the fiberscope often attends many pains and injuring of the intestine. We are hoping the inspecting method for the intestine with no pain and no injuring of the intestine before the operation by the fiberscope. Many microrobots which can move in the large intestine have been proposed by several research groups [1], [2]. However, the sure moving in the large intestine has not been confirmed, because the actual large intestine in our human body is especially very flexible to the radius direction and the mobile moving in the flexible pipes is very difficult.

Now, we propose a new microrobot that can surely move in the large intestine in the human body. We need a holding work to the radius direction of the flexible intestine and a driving work to the longitudinal direction of the microrobot using the friction force by the holding of the intestine, in order to move surely in the flexible and severely curved intestine, for example, that is a sigmoid. We use six rubber bellows in series. Two outer rubber bellows are provided bulging rubber sheets. These are called as friction braking mechanisms. So, the friction braking mechanisms works as a brake of the microrobot. The center four rubber bellows are arranged as a matrix and is called a driving mechanism. The driving mechanism drives the microrobot by its stretching, shrinking and bending motion. When the rubber bellows of the friction braking mechanism shrinks, six bulging rubber sheets spread to the radius direction and touch the intestine. Then the spread bulging rubber sheets surely hold the intestine. When the rubber bellows of the friction braking mechanism stretches, spreading to the radius direction of the six bulging rubber sheets and touching to the intestine are canceled.

The microrobot was confirmed to move at the speed of 9.5 mm/s in the freely held and severely bended pig's raw small intestine. In this experiment, it was also confirmed that the microrobot is able to generate the traction force of 3.7 N. The pig's small intestine is very similar to the human's large intestine. If the microrobot can move at the speed of 9.5 mm/s in the human's large intestine, it can move at only five minutes in the round trip of the large intestine.

2. STRUCTURE OF THE FABRICATED MICROROBOT

Structure of the fabricated microrobot is shown in Fig. 1. The microrobot consists of two friction braking mechanisms and a driving mechanism. The two friction braking mechanisms are driven by bellows which are 16 mm in outer diameter,

25 mm long and made of nytrile butyl rubber (NBR). The driving mechanism is driven by four bellows which are arranged as matrix and are 8 mm in outer diameter, 67 mm long and made of NBR. Each bellows is an independent vessel. Six air feeding tubes which are 2.0 mm in outer diameter, 1.2 mm in inner diameter and 1 m long are connected to the two friction braking mechanisms and the moving mechanism. The bulging rubber sheets for two friction braking mechanisms are 5 mm wide, 1.5 mm thick, 25 mm long and made of NBR. The rubber bellows are stretched by pneumatic pressure (positive pressure) and shrank by vacuum pressure (negative pressure). The stretching, shrinking and bending of the rubber bellows are controlled by a computer and electromagnetic valves.

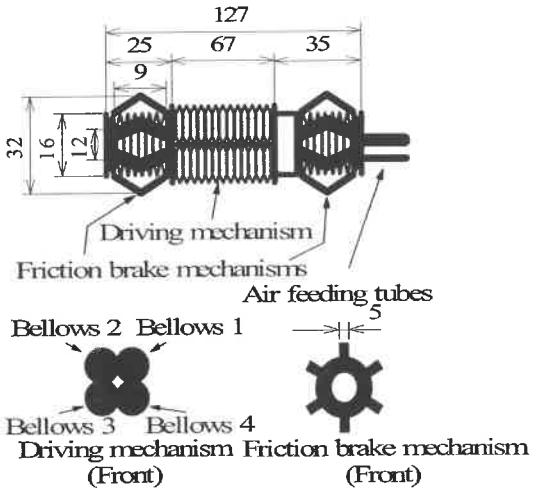

FIGURE 1. Structure of the fabricated microrobot

3. ACTION OF THE DRIVING MECHANISM

An action of the driving mechanism is shown in Fig. 2. In the Figure, a straight moving and a moving with the bending are shown. At the case of the straight moving, all four bellows are supplied the negative pressure and the positive pressure in the same timing. At the moving with the bending, two bellows are supplied the positive pressure and two bellows are supplied the negative pressure in the same timing. The driving mechanism can stretch and shrink with the bending as like a bimetal. If three bellows are supplied the positive pressure and a bellows is supplied the negative pressure, the driving mechanism can stretch and shrink with the bending of 45 degrees.

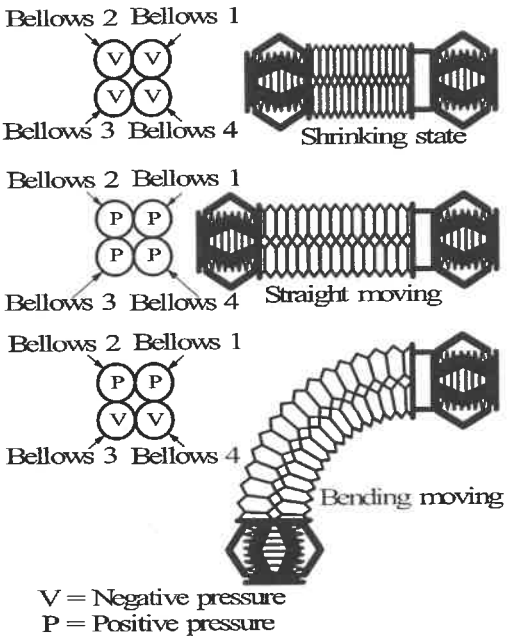

FIGURE 2. The action of the driving mechanism feeds the positive pressure in order to stretch the bellows.

4. EXPERIMENTAL APPARATUS

An experimental apparatus for measuring the characteristics of the microrobot is shown in Fig. 3. A conputer controls six electromagnetic valves through a valve conroller. Six air feeding tubes are connected from the electromagnetic

valves to the two friction braking mechanisms and the moving mechanism of the microrobot.

An air compressor is connected to the entrance ports of the electromagnetic valves and A vacuum pump is connected to the exit ports of the electromagnetic valves and feeds the negative pressure in order to shrink the bellows.

5. EXPERIMENTS

5.1 Measurement of friction force

The relationship between the number of the bulging rubber sheets for friction braking mechanisms and the friction force is shown in Fig. 4.The experiment was done using the pig's small intestine. The pressure in the bellows was -80 kPa. The friction force was measured by the force gage. The friction force is confirmed to increase in the proportion of the number of the bulging rubber sheets. In the case of six sheets, the friction force of 3.7 N is obtained.

5.2 Measurement of bending angle of the moving mechanism

The relationship between the positive pressure in the bellows and bending angle of the moving mechanism is shown in Fig. 5. The positive pressure is supplied to two bellows and zero pressure is supplied to another two bellows. The bending angle is confirmed to increase in the proportion of the positive pressure in the bellows. In the case of the positive pressure of 30 kPa, the bending angle of 180 degrees is obtained.

5.3 Measurement diameter of the bulging braking sheets

The relationship between the pressure in the bellows and diameter of the bulging braking sheets is shown in Fig. 6. The diameter of the bulging braking sheets is less than 26 mm at the pressure more than 20 kPa. Then, the braking

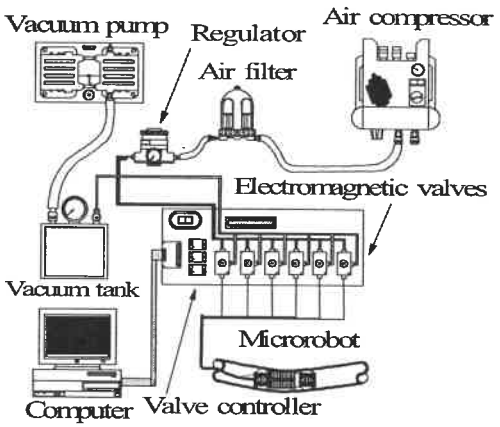

FIGURE 3. Experimental apparatus

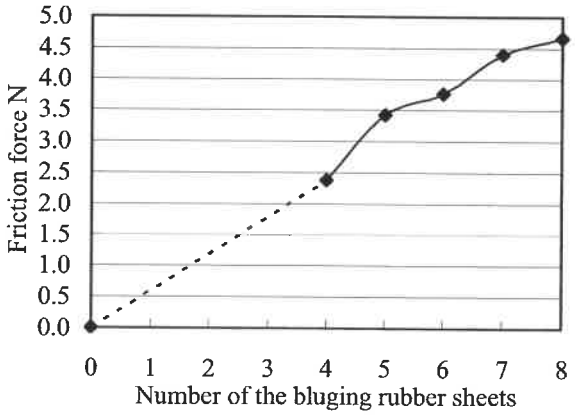

FIGURE 4. The relationship between the number of the bulging rubber sheets for friction braking mechanisms and the friction force

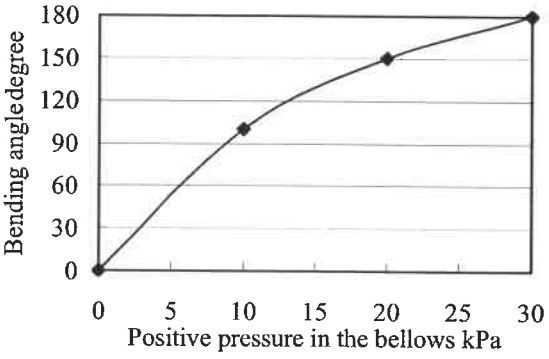

FIGURE 5. The relationship between the positive pressure in the bellows and bending angle of the moving mechanism

action of the bulging braking sheets is canceled at the pressure more than 20 kPa, because the average diameter of the pig's small intestine.

5.4 Moving experiment in the freely held pig's small intestine

The freely held pig's small intestine for moving experiment is shown in Fig. 7.

The microrobot was confirmed to move at the speed of 9.5 mm/s in the freely held and severely bended pig's raw small intestine.

6. CONCLUSIONS

1. We fabricated a new microrobot that can move in the freely held and severely bended pig's raw small intestine. The microrobot consists of two friction braking mechanisms and a moving mechanism. The friction braking mechanism has bulging friction sheets.
2. The driving mechanism, in which four rubber bellows are arranged as a matrix, drives the microrobot by its stretching, shrinking and bending motion.
3. We confirmed by the experiment that the microrobot can move in the freely held and severely bended pig's raw small intestine. The moving speed is 9.5 mm/s.
4. The microrobot may be used to the inspection mobile microrobot for the human large intestine, because the pig's small intestine is very similar to the human large intestine. If the microrobot can move at the speed of 9.5 mm/s in the human's large intestine, it can move at only five minutes in the round trip of the large intestine.

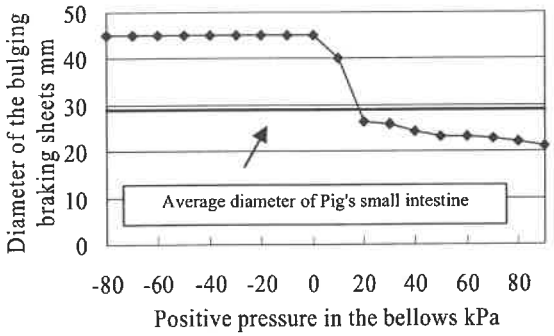

FIGURE 6. The relationship between the pressure in the bellows and diameter of the bulging braking sheets

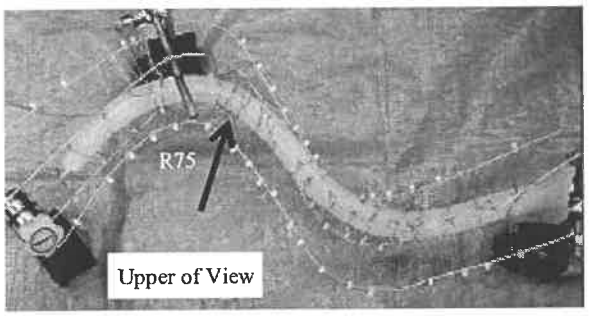

FIGURE 7. The freely held pig's small intestine for moving experiment

REFERENCES

[1] L. Phee, C. Stefanini, A. Arena, D. Accoto, A. Menciassi, G. Pernorio, M. Boccadore, P. Dario: "Mechanical Clamping Mechanism for Locomotion in the Gastrointestinal Tract", Proceedings of the 2nd International Conference of EUSPEN, pp. 770- 773.

[2] M. Ono, E. Arakawa, S. Kyoumine, S. Kato: " Fabrication of a Microrobot Movable in a Freely Held Pig's Small Intestine", Proceedings of the 2nd International Conference of EUSPEN, pp. 806- 809.

DEVELOPMENT OF A LASER-GUIDED DEEP-HOLE GRINDING TOOL: PERFORMANCE TEST

A. Katsuki[1], H. K. Park[2], H. Onikura[1], T. Sajima[1], T.Nakanishi[2], and H. Murakami[3]
[1] Department of Intelligent Machinery and Systems, Faculty of Engineering, Kyushu University 36, 744 Motooka, Nishi-ku, Fukuoka, 819-0395, JAPAN
[2] Graduate School of Kyushu University
[3] Fukuoka Industrial Technology Center, Kitakyushu, 837-0901, JAPAN

INSTRUCTIONS

Axial hole deviation in deep hole drilling results in the degradation of the quality and a decrease in the yield rate of products. A prototype laser-guided deep-hole boring tool with a diameter of 110 mm, whose attitude was controlled by piezoelectric actuators, was developed to prevent hole deviation. Counter-boring of duralumin workpieces (JIS-type A2017-T4) was performed with a straightness of $\pm 10\mu m$ over 700 mm, the maximum machinable length of the machine tool [1]. Even in the machining of the steel (JIS-type S45C) workpieces with abnormally prebored holes, which are disturbances while boring, the tool can be guided to bore a straight hole [2].

After boring, internal grinding is conducted to obtain hole accuracy. However it is very difficult to grind a deep hole accurately with a large length to diameter ratio. Hence the laser-guided deep-hole grinding tool with a diameter of 110 mm is designed and produced to improve hole accuracy [3].
The working characteristics of the components of the grinding tool are examined via experiments on a milling machine with respect to grinding forces. Further the guiding test is conducted on the deep-hole boring machine using steel (JIS-type S45C) workpieces [4]. As a result, it is clarified that the tool can be guided and that the accurate hole can be produced.

In this study, the performance of the tool has been examined by using prebored holes, which are inclined on one side and both sides of the hole wall.

EXPERIMENTAL PROCEDURE

Experimental Apparatus

A laser-guided deep-hole internal grinding system is constructed to produce deep holes accurately (Fig.1) [3, 4]. The tool consists of a grinding head, front and rear actuators mounted on an actuator holder, and a laser diode set at the back end of the holder. The tool attitude is detected by the laser diode (**7**) and two PSD (Position-Sensitive detector), located behind the tool. An optical device in front of the tool is used to set the guiding axis. The tool head eccentrically holds an air motor (**11**) driving a CBN wheel with a diameter of 82 mm (Figs.2 and 3). Air compressed to 0.5 MPa for driving air motor is supplied from the air filter to the air motor through a flexible hose. In order to supply compressed air to the air motor and cutting fluid to the grinding wheel, a rotary joint (**15**) is used

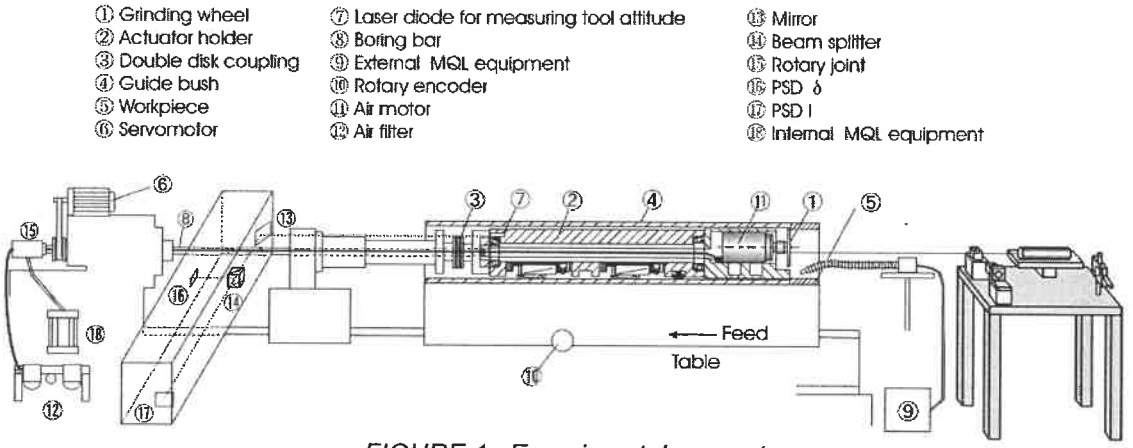

FIGURE 1. Experimental apparatus.

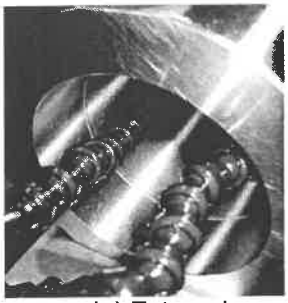

(a) External

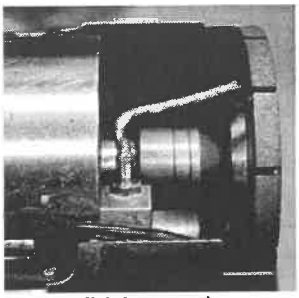

(b) Internal

FIGURE 2. MQL equipment.

(Fig.4). The air exhausted from the air motor is used to remove the chips.

The external and internal MQL (Minimum Quantity lubrication) equipment (**9** and **18**) are used to supply the cutting fluid continuously. Figure 2(a) shows the two nozzles for external MQL inserted into the prebored hole of the workpiece (**5** in Fig.1). The external MQL equipment is used to supply the cutting fluid to decrease the burnishing force between the guide pads and hole wall, while the internal MQL equipment is used to supply the cutting fluid to the grinding wheel (Fig. 2(b)). At a supply pressure of 0.5 MPa, cutting fluids are supplied at rates of 244 cc/h (per nozzle) and 34 cc/h in case of the external and internal MQLs, respectively.

Experimental Conditions

The grinding conditions are shown in Table 3. Vegetable oil is used as the cutting fluid.

Figure 5 shows the shapes of the workpieces. Workpiece A has a tapered prebored hole, which reduces the large force at the entrance, and the prebored hole is ground even if the dimensions of the workpiece are not accurate (Fig.5 (a)). Till a depth of 10 mm from the entrance, the prebored hole has a diameter of 110 mm for setting of the tool. Workpiece B has a prebored hole with an inclination on one side of the hole wall (Fig.5 (b)). The inclination is at 60 μm over a length of 120 mm. Workpiece C has an inclined prebored hole (Fig.5 (c)). The prebored hole is inclined at 5 μm over a depth of 120 mm.

EXPERIMENTAL RESULTS

The grinding performance improves when the wheel is not loaded using the MQL and segment grinding wheel; this results in good guiding performance of the tool.

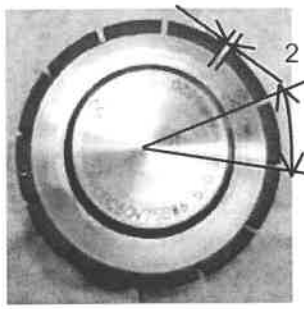

Dia.82mm
Width 6mm

FIGURE 3. Segment grinding wheel.

Hose of air filter

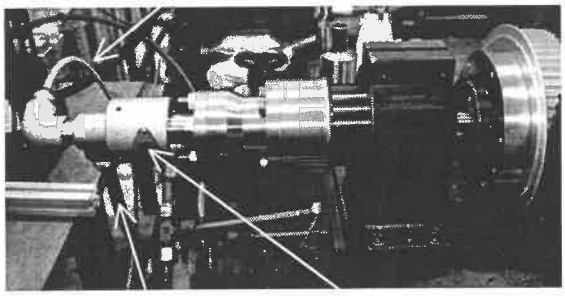

Hose of MQL equip. Rotary joint

FIGURE 4. Rotary joint.

TABLE 3. Grinding conditions.

Rotational speed of grinding wheel min^{-1}	2132
Revolutionary speed of tool min^{-1}	270
Feed mm/rev	0.125
Cutting fluid	Vegetable oil
Tool diameter mm	109.980
Workpiece	Carbon steel (JIS-type S45C, HRC 40)
Grinding wheel	CBN wheel (CBC80V75BW6)

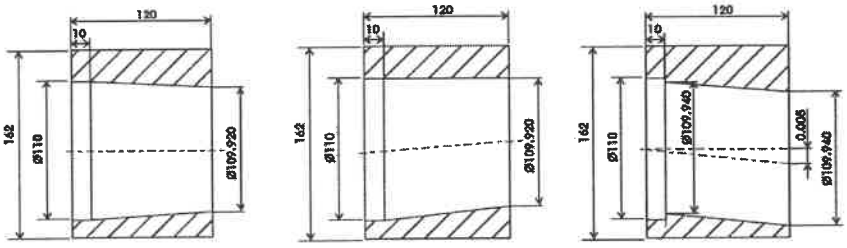

(a) Workpiece A (b) Workpiece B (c) Workpiece C

FIGURE 5. Shapes of the workpieces.

Tapered Prebored Hole

Figure 6(a) shows the variations at the center of the front and rear ends of the tool in the *X*

direction with the hole depth. The front end is always maintained near the zero level and the rear end is manipulated so that the tool position moves to the guiding axis (X axis).
Figure 6(b) shows the hole deviation with the hole depth. A straight hole is bored. However, the tapered shape remains even after grinding. The reason for the behavior is as follows.

The hole wall cannot be ground from the entrance of the prebored hole to a hole depth of 40 mm because the diameter of the prebored hole is larger than that of the tool. From a depth of 40 mm to 80 mm, the tapered shape is maintained due to the deflection δ of the grinding wheel axis that increases with the increase in the grinding forces (Fig.7). From a depth of 80 mm, normal grinding commences.

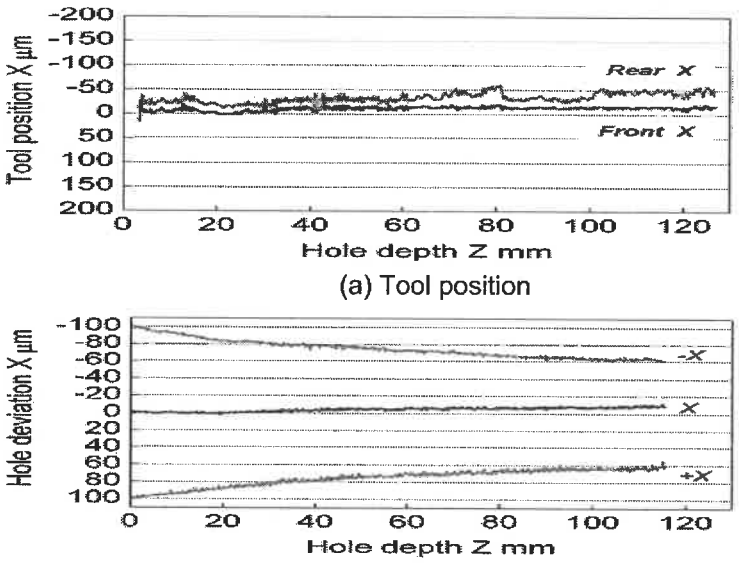

FIGURE 6. Tool position and hole deviation (Workpiece A)

Prebored Hole Inclined on One Side

Figure 8(a) shows the variations at the front and rear ends of the tool along the X direction with the hole depth. The front end (tool position) is always maintained near the zero level and the rear end is manipulated such that the tool position moves to the guiding axis (X axis).
Figure 8(b) shows the hole deviation with the hole depth. The centerline of the ground hole is inclined. Figure 9 shows the tool attitudes under the grinding conditions. The centerline of the ground hole inclines due to the unground depth. The tool is guided along the guiding axis.

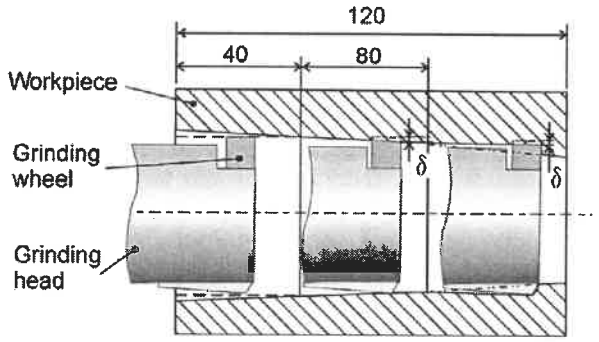

FIGURE 7. Tool attitudes while boring workpiece A.

Inclined Prebored Hole

Figure 10(a) shows the variations at the front and rear ends of the tool along the X direction with the hole depth. The front end is always maintained near the 50-μm level and the rear end is manipulated such that the tool position moves to the guiding axis (X axis). Figure 10(b) shows the hole deviation with the hole depth. A straight hole is bored. The reason why a straight hole is bored in spite of the deviation of 50 μm is as follows.

As shown in Fig. 11, the tool bends at a bearing while grinding. The centerline of the piezoelectric actuator holder, which holds a laser diode for detecting the tool position, is δ_F at the front end

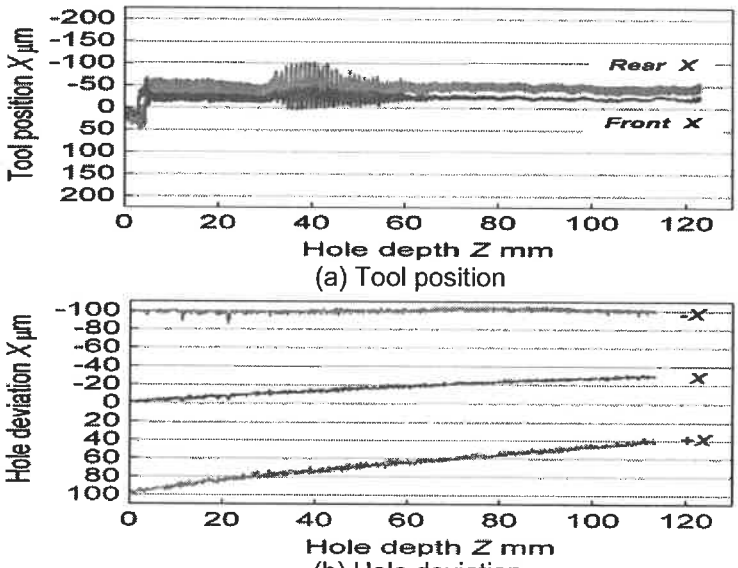

FIGURE 8. Tool position and hole deviation (Workpiece B).

of the grinding head. However, the center of the front end of the grinding head is located on the guiding axis.
If the tool is not guided, it moves along the inclination of the centerline of the prebored hole.

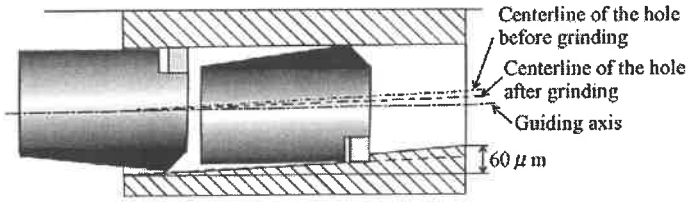

FIGURE 9. Tool attitudes while boring workpiece B.

CONCLUSIONS

A laser-guided deep-hole internal grinding tool with a diameter of 110 mm has been designed and fabricated to produce deep holes accurately. Based on the performance tests, the following conclusions were made.

- The internal grinding tool can be guided along the guiding axis.
- The guiding performance can be improved by using MQL and the segment grinding wheel, which can prevent the wheel from loading.

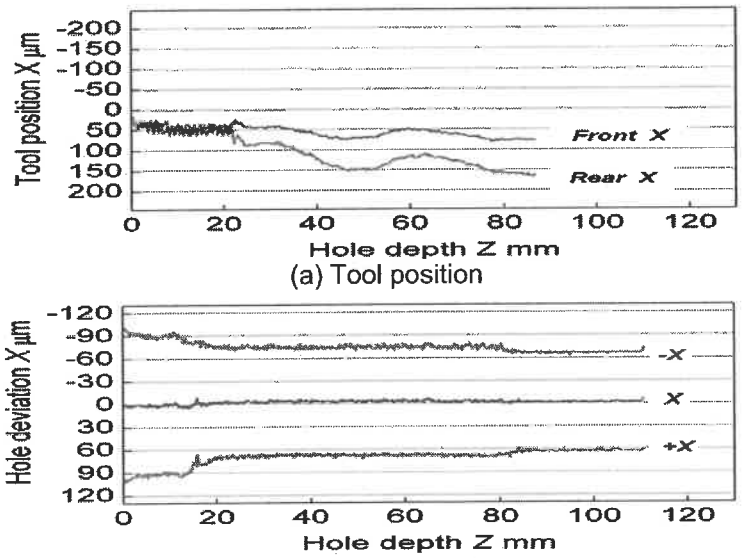

FIGURE 10. Tool position and hole deviation (Workpiece C).

ACKNOWLEDGEMENTS

We are grateful to Kyushu Industry Technology Center, Japan Science and Technology Agency (Research for Promoting Technological Seeds), and Noritake Co., Ltd. for support this study. We wish to express our gratitude to Mr. K. Tei and Mr. T. Nakanishi, graduate students, and to Mr. F. Wakabayashi, an undergraduate student, for their cooperation.

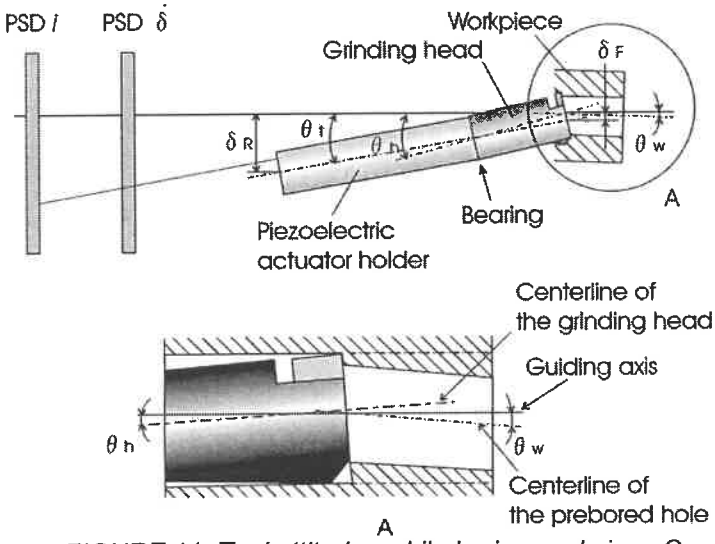

FIGURE 11. Tool attitudes while boring workpiece C.

REFERENCES

[1] Katsuki,A. et al., Development of a Practical High-performance Laser-guided Deep-hole Boring Tool: Improvement of Guiding Strategy. Proc. of **euspen** International Topical Conference on Precision Engineering, Aachen, 2003; 1, 97-100.

[2] Katsuki,A. et al., Development of a Practical High-performance Laser-guided Deep-hole Boring Tool: Boring of Steel Workpieces, Proc. of ASPE 2005 Annual Meeting-Norfolk, 2005; 415-418.

[3] Katsuki,A. et al., Development of a Laser-guided Deep-hole Grinding Tool, Proc. of. 4th **euspen** International Conference-Glasgow, 2004; 402-403.

[4] Katsuki,A. et al., Development of a Laser-guided Deep-hole Internal-grinding Tool (Series 1): Grinding Forces, Memoirs of the Faculty of Engineering, Kyushu University, 2005; 65, 4, 1-12.

DSP-BASED PRECISION MOTION CONTROLLER FOR IRON-CORE LINEAR MOTORS

Seung-Chul Kim[1], Kyung-Don Kim[2] and Sung-Chong Chung[1]*
[1]Hybrid System Design & Control LABoratory
Department of Mechanical Engineering
Hanyang University, SungdongGu, Seoul 133-791, KOREA
[2]Small Business Corporation, Gyeonggi Regional Headquarter, Suwon, KOREA

ABSTRACT
Precision motion controller using a digital signal process (DSP) is studied to apply for iron-core permanent magnet linear motor (PMLM) stages. Friction force, velocity and force ripples, and positioning errors are measured and analyzed on the linear servo according to various operating conditions. To improve transient characteristics as well as to minimize tracking error and disturbance, the perfectly matched feedback controller, feedforward controller, feedforward ripple compensator, and notch filter are combined together to make a precision motion controller for a stage equipped with iron-core linear motors. The controller is installed on the DSP, TMS320C. Experimental results verify the effectiveness of the developed system.

INTRODUCTION
Precision motion control is essentially required in the FPD (flat panel display), machine tool, robot, semiconductor, medical and packaging industries. Many processes requiring sub-micron resolution and control are applied to the measurement, manufacture and control of large, macro and/or micro components of display, optical, MEMS and/or semiconductor devices. Lithography, MEMS and FPD fabrications are three representative examples of nanofabrication processes. Precision machining such as cutting, grinding and super finishing are required to provide nano-precision surfaces such as ultra-precision bearings, spindles, memory disks, mirrors and lens for optical systems, and so on. Surface mounting, IC packaging, assembly of micro-machines, inspection of FPDs, SEM, AFM require nano-level motion control as well. In order to achieve such precision motion control, precision level of sensing and control technology is required [1, 2].

In this paper, a DSP-based precision motion controller is developed to apply for iron-core permanent magnet linear motor stages. To improve transient characteristics as well as to minimize tracking error and disturbance, the perfectly matched feedback controller, feedforward controller, feedforward ripple compensator, and notch filter are designed and installed on the DSP, TMS320C. The force ripple compensation is performed through the adaptive feedforward compensation. The feedforward controller is included to reject servo lag. The perfectly matched feedback controller is applied to improve tracking performance and robustness of the control system. The notch filter reduces the power noise and rejects unwanted vibration due to natural frequency of the servo. In order to verify the performance of the developed system, Velocity and force ripples, frictions and positioning errors are measured on the linear servo according to various operating conditions. Experimental results verify the effectiveness of the developed system.

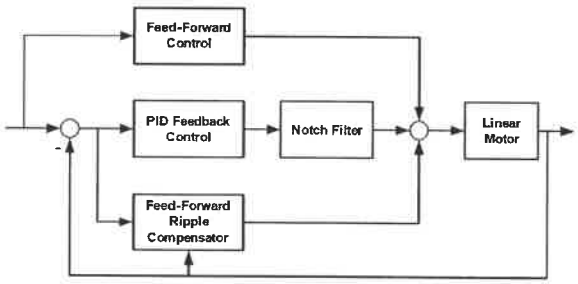

FIGURE 1 Overall structure of control system.

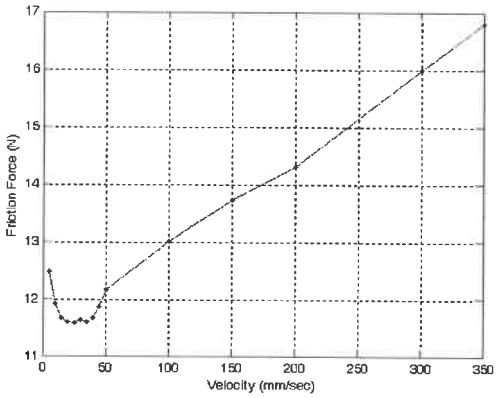

FIGURE 2 Friction force vs. velocity.

CONTROLLER DESIGN

Fig. 1 shows the overall structure of the control system. DSP controller constructed with the feedforward controller and feedforward ripple compensator are to be based on the mathematical models of PMLMs.[2,3]

Dynamics of PMLMs

Considering dominant effects of the mechanical and electrical dynamics of a PMLM, following models are given by [3]

$$F_m = K_m I_m = M\ddot{x} + B\dot{x} + F_f + F_{ripple} \qquad (1)$$
$$K_e I_m + L_m \, dI_m/dt + R_m I_m = v$$

where F_M is the motor force, K_M is the torque constant, I_M is the motor current, F_{ripple} is the force ripple, and F_f is the friction force.

From precision motion control viewpoints, force ripples are highly undesirable but yet they are predominantly present in PMLMs.

In general, the most significant friction components distorting the identification results are the stiction and the Coulomb friction [4].

$$F_{frictoin} = sgn(\dot{x}) \cdot F_c + F_s N_s(\dot{x}) \qquad (2)$$

where F_c is the Coulomb friction coefficient and N_s is a striction nonlinearity.

Friction in the linear motor is computed from average disturbance by unloading tests at 10 ~ 350 mm/s axis velocity. Fig. 2 shows observed friction force versus axis velocity to estimate the friction model.

Feedforward ripple compensator

Force ripples are described as sinusoidal functions according to position. However, as shown in Fig. 3, it is complex to make a mathematical model. The ripple consists of several sinusoidal functions with unknown frequencies and amplitudes. Fig. 4 shows velocity and force ripples according to the velocity command in the open loop system. The force ripple is described with a periodic sinusoidal signal depending upon the location, and with the amplitude depending upon the load velocity as follows:

$$F_{ripple}(x,v) = \sum_{k=1}^{N} A(x,v)\sin(\omega x + \phi) \qquad (3)$$

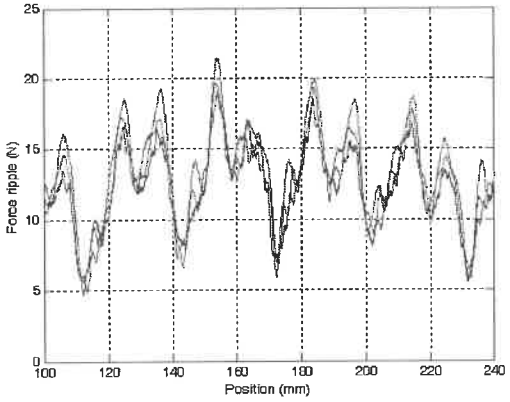

FIGURE 3 Force ripple signal via position

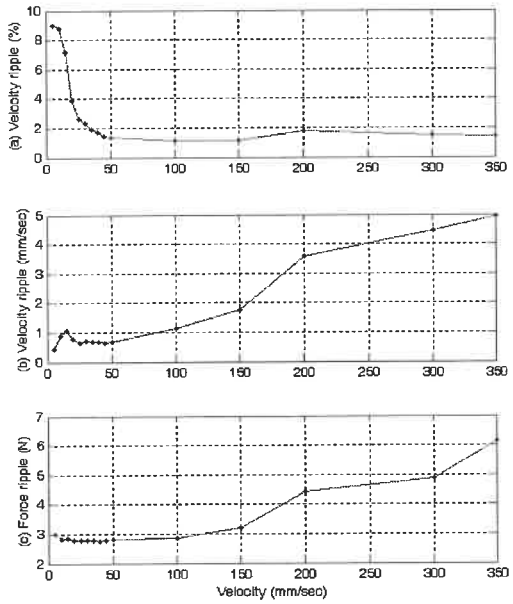

FIGURE 4 Force and velocity ripple for the open-loop system.

Feedforward controllers

Velocity, acceleration and friction feedforward controllers are designed to reduce tracking errors due to servo lag, friction and external disturbance as follows:

$$F_{FF} = K_{af}\ddot{x} + K_{vf}\dot{x} + F_{friction}(x) \qquad (4)$$

Feedforward refers to the addition of open-loop information to the profile generator. Through injecting nominal control input to the servo system, it is possible to improve the bandwidth

of the feedback control loop and the tracking performance of the servo.

PID feedback controller

The servo control loop is essentially based on a three-term PID controller. And the perfectly matched feedback controller is applied to improve tracking performance and robustness of the control system. In this paper, the PID feedback controller is designed with the integrated design methodology to obtain optimal and robust performance of the nominal system [4-6].

Notch filter

Notch filters reduce the response of the power noise and resonance frequency of the servo. And, it is applied to reject instability at stop command. Using fast Fourier transform (FFT), the instability frequency is identified and adaptively feedback to manipulate the notch frequency.

Fig. 5 shows the frequency spectrum of the control system without the notch filter. From the spectrum, undesirable frequencies are 100Hz and 120Hz, etc. A narrow-band notch filter is applied to compensate for the undesirable vibration.

EXPERIMENTAL RESULTS

Fig. 6 shows an experimental setup constructed with linear motors (Anorad, LCK-S) and servo drives (Glentek, SMA 9815). In order to install the developed controller and compensators, TMS320C6713 DSP board is developed. Experimental results are shown in Figs. 7~11. Fig. 7 and 8 show control performances of velocity ripple in the steady-state. Velocity ripples with the ripple compensator are measured less than 0.4% at both 100 and 300 mm/sec. Tracking performances with respect to sinusoidal inputs are shown in Figs 9~11. Figs. 9 and 10 show position and velocity tracking performances according to the proposed PID control system. Fig. 11 shows control performances obtained from the proposed controller composed of the PID, feedforward and force ripple controllers. Comparing Figs. 9~11, it is confirmed that the proposed control system has excellent control performance.

CONCLUSIONS

Precision motion controller using the DSP is proposed to apply for iron-core permanent magnet linear motor (PMLM) stages. Force ripple is compensated for through the developed Force ripple compensator. Perfectly matched feedback controller is developed through the previously developed integrated design methodology. The narrowband type notch filter is applied to reject unwanted vibration. Effectiveness of the proposed system is confirmed through experiments.

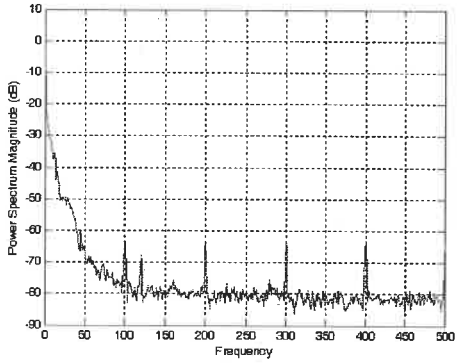

FIGURE 5 Power spectral density of the control system without the notch filter.

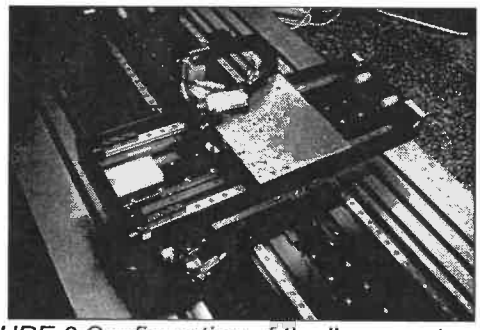

FIGURE 6 Configuration of the linear motor

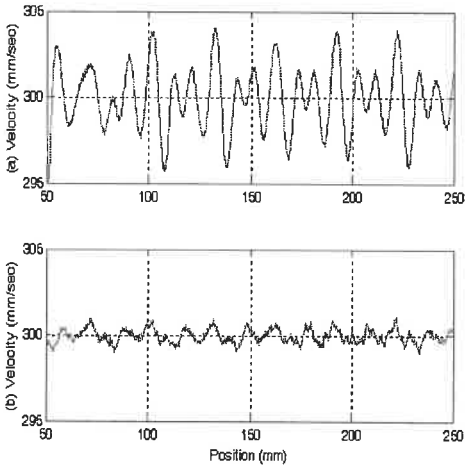

FIGURE 7 Performance of the force ripple compensator at 300mm/sec velocity: (a) without compensator; (b) with compensator.

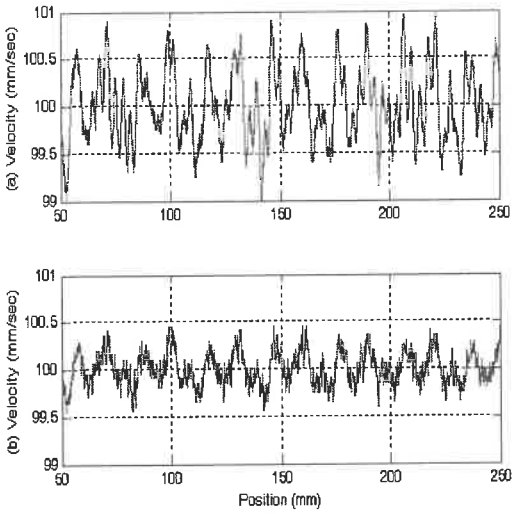

FIGURE 8 Performance of the force ripple compensator at 100mm/sec velocity: (a) without compensator; (b) with compensator.

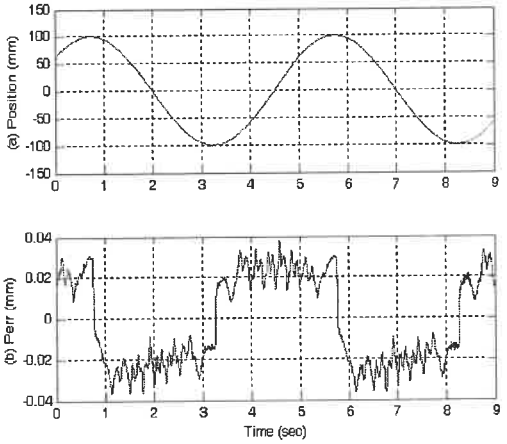

FIGURE 9 Position tracking performance of the PID control system

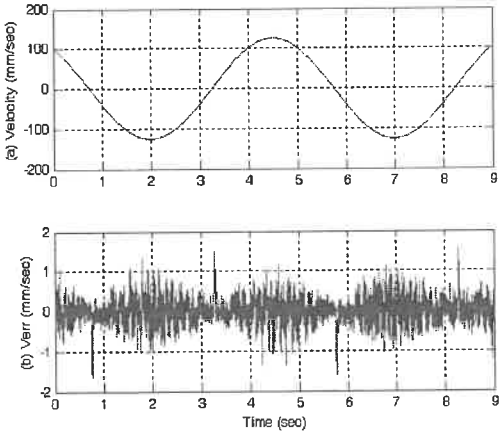

FIGURE 10 Velocity tracking performance of the PID control system.

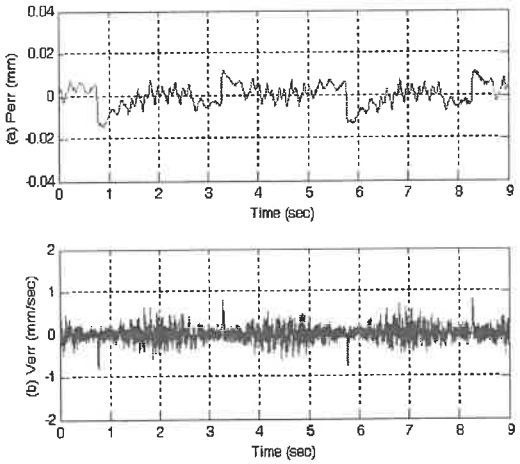

FIGURE 11 Tracking performance of the developed PID+FFC+FRC control system.

REFERENCES

[1] Bae, H. K. and Chung, S. C. Optimal Tuning of Biaxial Servomechanisms using a Cross-Coupled Controller. Transactions of the North American Manufacturing Research Institution of SME, 2006; 34: 603-610.

[2] Tan K.K., Tang K.Z., Dou H.F. and Huang S.N. Development of an Integrated and Open-Architecture Precision Motion Control System. Control Engineering Practice, 2002; 10: 757-772.

[3] S. Zhao, and Tan, K.K. Adaptive Feedforward Compensation of Force Ripples in Linear Motors. Control Engineering Practice, 2005; 13: 1081-1092.

[4] Kim, M. S. and Chung, S. C. A Systematic Approach to Design High-Performance Feed Drive Systems. International Journal of Machine Tools and Manufacture, 2005; 45: 1421-1435.

[5] Kim, M. S., and Chung, S. C. Integrated Design of Feed Drive Systems using Discrete 2-Degree of Freedom Controllers (I). Transactions of the KSME(A). 2004; 7: 1029-1037.

[6] Kim, M. S., and Chung, S. C. Integrated Design of Feed Drive Systems using Discrete 2-Degree of Freedom Controllers (II). Transactions of the KSME(A). 2004; 7: 1038-1046.

PLANAR MOTOR BASED ON THE PRINCIPLE OF ULTRASONIC WAVE USING PZT

Chang-Woo Lee[1], Jun-Yeob Song[1], Tae-Ho Ha[1]
[1]Intelligent Machine Systems Research Center,
Korea Institute of Machinery and Materials,
171, Jang-dong, Yuseong-gu, Daejeon, 305-343, S. Korea

INSTRUCTIONS

Recently manufacturing system is required to reduce producing cost and development time in response to sudden model change that demands reconfigurable factory. The micro factory has been studied to bring a solution to these requirements. The micro factory of size is so small that consuming power is reduced and also manufacturing line could be easily reconfigurable. The micro factory is required automation to satisfy high productivity. It is one of the big problems to convey goods, In case of automated reconfigurable micro factory. Planar motor that can perform linear motion in XY direction is one of solution that solves this problem. But conventional planar motor using a magnetic force has a disadvantage that planar motor base is permanent magnet. In this paper we consider new type of a planar motor based on principle of ultrasonic waves using PZT. This planar motor has several ceramic finger tips that generate driving force. The driving force is produced by elliptical motion of finger tips and friction force. The elliptical motion of finger tips is generated by electrical driver that create two dimensional ultrasonic waves. In this paper, we achieved fundamental efficiency test of new type planar motor. We investigate the static characteristic of the new type of a planar motor, such as the maximum velocity and relationship between the maximum force and the load. This paper describes features and fundamental technology of the planar motor based on the ultrasonic wave using PZT.

MOVING PRINCIPLE

We designed the new type of a planar motor using HR ultrasonic motor series from Naomotion LTD. An ultrasonic motor using PZT is one in which electrical energy is converted by the inverse piezo-effect to obtain oscillation of the PZT in ultrasonic frequency range. Figure 1 shows the schematic representation of the HR ultrasonic motor series from Nanomotion LTD. The simultaneous excitation of the longitudinal extension mode and the transverse bending mode creates a small elliptical trajectory of the ceramic edge, thus achieving the dual mode standing wave motor. HR series ultrasonic motor has the ceramic finger tip pusher is locked on the end of the piezoelectric plate.

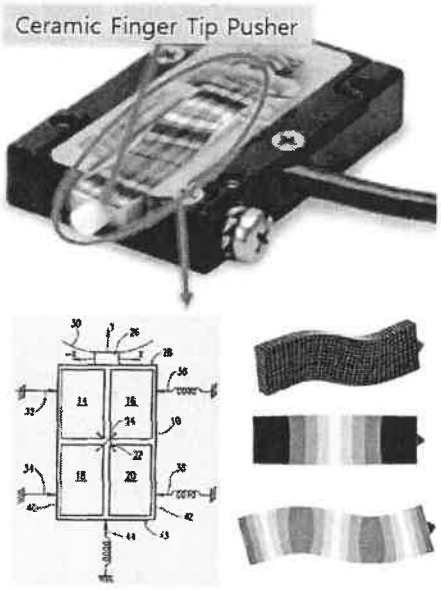

FIGURE 1 Schematic representation of the Ultrasonic motor from Nanomotion LTD.

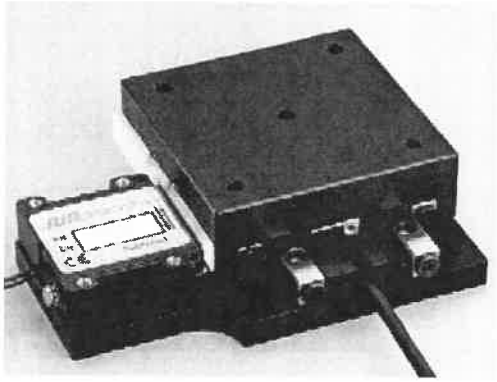

FIGURE 2 1 axis stage using HR ultrasonic motor series from Nanomotion LTD.

The motion of this pusher is elliptical trajectories that can make the object move by the friction force. HR ultrasonic motor series are classified by the number of ceramic finger tip pusher. The design of ultrasonic motor is dependent on that of the frictional components. Figure 2 shows 1 axis stage of which frictional component is ceramic bar using HR ultrasonic motor series. It would be useful to achieve better resolution, higher velocities and greater drive force for ultrasonic motors.

UTRASONIC PLANAR MOTOR DESIGN

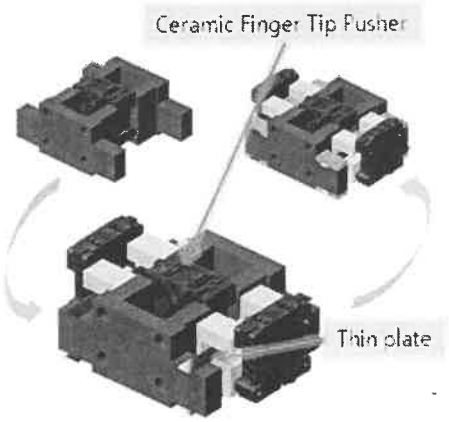

FIGURE 3 Schematic diagram of new type ultrasonic planar motor assembly

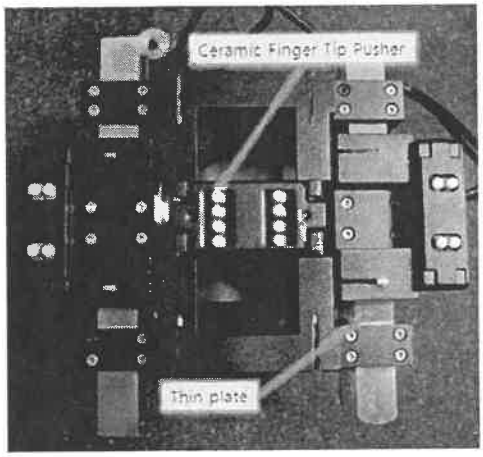

FIGURE 4 Bottom picture of new type ultrasonic planar motor

Figure 3, Figure 4 show new type of ultrasonic planar motor that we design in this paper. The new type ultrasonic planar motor is manufactured with a size of 125×95×50 (mm) and a weight of 1080 g. Two HR4s that have four ceramic finger tip pushers and one HR8 that has eight pushers are used in new type ultrasonic planar motor. X axis direction moves by the HR8. Two HR4s take charge of motion of Y1 axis and Y2 axis. The Θ axis angle is calculated from the difference between Y1-axis and Y2-axis. Two HR4s is controlled separately so that Y-axis and Θ -axis can be controlled independently. The fiction force that is the source of a driving force depends on the both of planar motor own weight and the coefficient of friction between the ceramic finger tip pusher and the surface of planar motor. There are machining error and assembly error and the ceramic finger tip pushers can't exist on plane to the principle simultaneously. The ceramic finger tip pushers that are located on the bottom of the planar motor can't be horizontality. Three HR ultrasonic motor series are linked by thin plate of which thickness is 30 μm. The mechanism connected by thin plate has strong hardness to horizontal direction but weak hardness to vertical direction relatively. The weak hardness to vertical direction makes ceramic finger tip pushers of three HR may bottom at the same time even if there are machining error and assembly error. High stiffness to horizontal direction delivers driving force generated by HR ultrasonic motors.

SYSTEM CONTROL CONFIGURATION

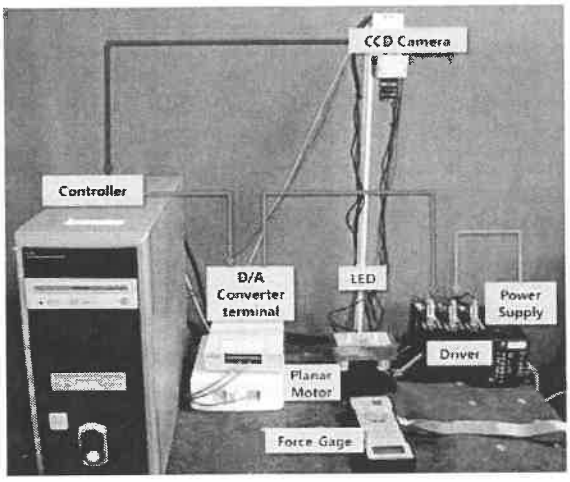

FIGURE 5 System control configuration

Figure 5 shows the system control configuration of the new type planar motor. It consists of

planar motor, HR driver, power supply, CCD camera, D/A converter and controller. HR driver drives elliptical motion and control frequency according to command input from a controller by D/A converter. The resolution of D/A converter is 12-bit. X, Y1 and Y2 motors are arranged symmetrically with respect to a point on the planar motor. There are two LEDs on the top of new type planar motor and measured by the CCD camera. The size of image sensor is 1/2 inch. Input can be configured to accept an external trigger signal. The platform of the CCD camera is IEEE-1394 bus and FPS (frame per second) is 60, so sampling rate for digital control is 60 Hz. It is very weak point for this control system that the sampling rate is slow by 60 Hz. The pixel number is 640 × 480 and view area is 320 × 240 mm so that the resolution of CCD camera is 0.5 mm. If the view area is reduced, the resolution would be better. But wide view is more profitable for basis performance evaluation of the new type planar motor. This measured value by the CCD camera represents the position of planar motor. The average of measured value of two LEDs is X Y position. The θ axis angle is calculated from the difference between two LEDs positions. The planar motor controls the position and speed on the X, Y, and θ axis independently. The controller transfers Y and θ axis error to Y1, Y2 axis error and sends command signal to each driver. This allows the control gains for X, Y and θ axis to be set individually.

EXPERIMENTAL RESULT

We measured maximum driving force and speed that is fundamental performance of servo in two circumstances. The first circumstance is not loaded and the second circumstance is loaded. The weight of load is 1580 g. In general even if load increases, driving force does not increase, so the maximum speed is lower. But because the source of driving force in this planar motor is friction force, if load increases, driving force increases.

TABLE 1. In no load condition, the relation with X axis driving force and driver input.

Input (volt)	First (N)	Second (N)	Third (N)
3	0.56	0.53	0.38
4	0.86	0.78	0.86
5	0.94	0.91	1.07
6	1.21	1.18	1.4
7	1.48	1.43	1.39
8	1.62	1.71	1.65
9	1.73	1.56	1.68

TABLE 2. In no load condition, the relation with Y axis driving force and driver input.

Input (volt)	First (N)	Second (N)	Third (N)
3	1.77	1.92	1.7
4	1.91	2.32	2.07
5	2.53	2.22	2.13
6	2.65	2.57	2.53
7	2.71	2.69	2.5
8	2.79	2.62	3.06
9	2.71	2.95	2.57

TABLE 3. In no load condition, the relation with Y axis maximum speed and driver input.

Input (volt)	First (mm/s)	Second (mm/s)	Third (mm/s)
3	24.11	26.23	26.46
4	35.47	36.39	34.94
5	48.69	49.59	47.43
6	62.06	59.37	59.21
7	71.12	70.73	71.09
8	81.93	81.48	78.35
9	83.87	84.27	83.29

Because if X axis was only controlled without angle control, the planar motor rotates, we have difficulty in speed measurement to X axis direction.

TABLE 4. In loading condition, the relation with Y axis maximum driving force and driver input.

Input (volt)	First (N)	Second (N)	Third (N)
3	1.72	1.83	1.84
4	3.13	2.62	2.76
5	3.63	3.94	4.37
6	4.35	5.06	5.37
7	5.12	5.19	4.95
8	5.18	5.53	5.97
9	6.81	7.07	6.51

TABLE 5. In loading condition, the relation with Y axis maximum speed and driver input.

Input (volt)	First (mm/s)	Second (mm/s)	Third (mm/s)
3	31.29	27.61	36.57

4	59.16	62.39	56.45
5	88.46	84.72	87.04
6	110.53	97.52	109.80
7	131.62	125.68	125.01
8	147.63	143.23	133.04
9	155.80	150.04	160.05

In loading condition the force of static friction grows than the driving force to X axis direction. Because the load is delivered only to Y axis structurally, the driving force to X axis direction is not increased but only the driving force to Y axis direction is increased. Therefore Y axis is more satisfactory result in loading condition in the driving force and the maximum speed.

CONCLUDE

We have introduced the feature of new type ultrasonic planar motor and investigated static characteristic such as the maximum velocity and relationship between the maximum force and the load. We confirmed enough possibility by servomotor to transform goods in speed and driving force. The new type ultrasonic planar motor can use general surface plate to base plate unlike existing planar motor that has to use permanent magnet to base plate. Therefore it is advantage that the stroke of planar motor can be increased easily.

FUTURE WORK

This planar motor has two weak points. First, the control sampling rate and the position sensor resolution is very low. Second, X and Y axis driving force are not equal. Especially X axis driving force is weak. The first problem happens because of CCD sensor. We have considered new type planar sensor that has fast response and good position resolution. The structure of planar motor must be changed to solve the second problem. The load is delivered only to Y axis structurally in this planar motor.

REFERENCES

[1] K. Spanner, Survey of the Various Operating Principle of Ultrasonic Piezomotors. White Paper for ACTUATOR 2006.

[2] Jona Zumeris, Nasher, Israel, US Patent Number 6,064,140

[3] K. Spanner, O. Vyshneevskyy, W. Wishnewskiy W., New Linear Ultrasonic Micromotor for Precision Mechatronic Systems. Actuator 2006. Bremen

[4] T. B. Lauwers, Z. K. Edmondson, R. L. Hollis, Free-Roaming Planar Motors: Toward Autonomous Precision Planar Mobile Robots Proc. IEEE Int'l. Conf. on Robotics and Automation, New Orleans, LA, April 26 - May 1, 2004 pp.1-6

[5] Hashida Shigeru, Kaiho Fumio, Koizumi Yutaka, Tamura Tetsuji, Planeserv Planar Servomotor. Yokogawa Technical Report English Edition, No. 32 (2001)

3D MODEL RECONSTRUCTION WITH NON-CONTACT ROTATION MECHANISM USING MICRO ROBOTS

Daigo Misaki[1], Atushi Oguri[1], Nigh Zhu[1], Ohmi Fuchiwaki[2], and Hisayuki Aoyama[2]
[1]Department of Mechanical Engineering
Shizuoka Institute of Science and Technology
Fukuroi, Shizuoka, Japan
[2]Department of Mechanical Engineering and Intelligent Systems
University of Electro-Communications
Chofu, Tokyo, Japan

INTRODUCTION

For these years, our group has successfully developed the precise micro robots system for micro industrial production. For the application toward such bio cell surgery, the cell manipulation and observation technique is one of most important issues and there it is required to handle such the small bio cell without any damages. In this report, the unique non-contact micro object manipulation mechanism and 3D model reconstruction mechanism are proposed and its mechanism was applied to precision observation of a micro object. Our small robot, which is composed of piezo elements and electromagnets, can walk with an inchworm manner to X and Y directions and rotate with the resolution of such sub micrometer in the plane under the microscope view field. The piezo driven thin glass pipette can be set on this small robot and it can be vibrated near the target bio cell which is floated in the water of schale. Then the micro non-linear flow around the vibrated pipette can be generated and the target small particle can be conveyed along the flow and rotated in the whirlpool. We can control the position of the thin glass pipette on the micro robot so that the small bio cell can move to the specified point and rotate to align the face of cell. In order to carry out the micro observation of a micro object using inverted microscope, we observe a micro object from various directions by using this non-contact rotation mechanism. In order to carry out more precise microscopic operations or to carry out detailed diagnosis of a cell, acquisition of the precise 3D information of a micro object is important. Reconstruction of 3D model is carried out combining CT and rotation observation. Although the approach proposed until now is used a contact type rotation mechanism or a laser trapping mechanism, those rotational mechanisms may have bad effect on a micro object. In order to carry out more stable observation, proposed non-contact rotation mechanism applied to 3D model reconstruction.

CONSEPT OF MICROROBOT SYSTEM

Fig.1 shows the microscopic operation system using micro robots which is ongoing development in our research group. These micro robots can be controlled using a PC in real-time analyzing of microscopic images. All micro robots are set on a steel table. In this basic setup, this system can execute flexible microscopic tasks with easy operation. All positioning facilities are given by micro robots' movement so all mechanical functions are simply divided. This unique arrangement allows the system good flexibility and high mechanical stability although sophisticated control is required. This may be a good application for micro robots practically. We can easily attach micro robots to micro processing instruments. This flexibility meets the requirements of users, and the use of small robots avoids reparation of microscopes and easily implements processing with low cost.

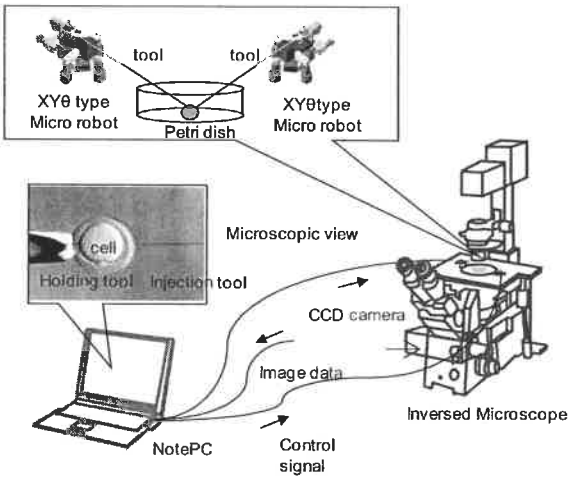

FIGURE 1. The basic set up of microscopic operations system by using micro robots.

VERSATILE MICRO ROBOTS

In microscopic operations, an operator needs to operate a tool intricately. Fig.2 shows the structure of the versatile micro robot which is proposed to satisfy the requirements above. Two u-shaped electromagnets which are arranged to cross each other are connected by four piezo elements so that the micro robot can move in any direction like an inchworm. Also we designed the special joint at one of the 4 legs to ensure all legs smooth simultaneous contact on the surface. This layout of actuators can allow it to move precisely in a holonomic locomotion manner. We use the stacked type PZT elements of 5[mm] ×5[mm] ×10[mm]. Each piezo element is connected to each electromagnet with a plastic insulator. In experiments, we confirmed that the micro robot can move in XY directions. The step length of a micro robot is 4.5 micron and velocity is 2.25[mm/s].

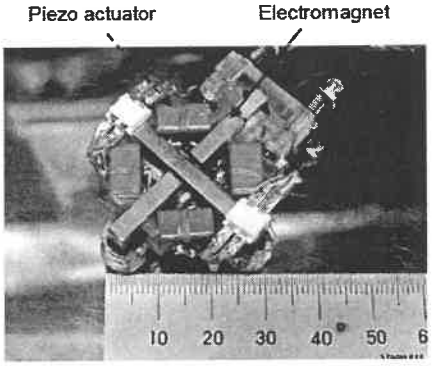

FIGURE 2 Micro robot provided for microscopic operation.

3D MODEL RECONSTRUCTION WITH NON-CONTACT ROTATION MECHANISM

In order to carry out more precise microscopic operations or to carry out detailed diagnosis of a cell, acquisition of the precise 3D information of a micro object is important. In this paper, in order to acquire the 3D information of a micro object without having a bad influence on an object, we proposed the non contact rotation positioning of a micro object using pipette vibration which makes a rotational flow and the 3D reconstruction method using this non-contact rotating mechanism.

Non-contact rotation mechanism using a micro robot

In this paper we proposed and used the non contact rotation positioning of a micro object using pipette vibration, which makes a rotational flow near the pipette. In this system, this rotational flow is generated by using the versatile micro robots. First, as shown in Fig. 3, a robot's electromagnet 1 is always adsorbed and electromagnet 2 is always not adsorbed. And the position Fig. 3 (a) and (b) is repeated by expanding and contracting the piezo-electric element between both electromagnets. By this motion, the pipette on a micro robot can be vibrated with the amplitude of tens of microns. The small mechanism as shown in Fig.3 (c) is developed for an basic experiment of non contact rotation mechanism and this has the same function of Fig.3 (a),(b). This mechanism consists of a PZT and displacement expansion mechanism. This proposed mechanism can be carried out non contact rotation operation, without using some additional actuators for a micro robot. This is a very important factor, in order to construct a simple and low cost microscopic operation system. Fig.3 (d) shows the outward appearance of the actually produced non-contact rolling mechanism.

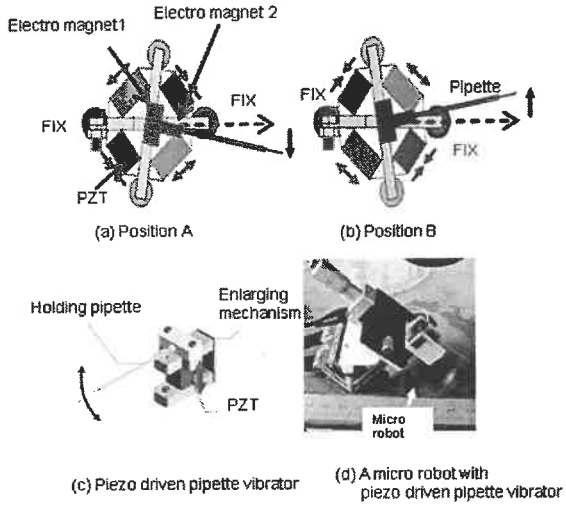

FIGURE 3. Flow generating mechanism using a micro robot.

In the basic experiment, the rotational follow in water of schale was generated using the holding pipette of the bore 15 [μm] and an outside diameter 100 [μm] at a tip of micro pipette. The pipette tip was bent to 45 [°], and it placed in parallel to the schale bottom, and observed from the schale bottom. To tracing partial flows, water mixed with black sumi ink was used. The flow pattern when vibrating a piezo-electric element by the sine wave of pitch 200 [Hz] and the seal-of-approval voltage±45 [V] is shown in Fig.4. This experimental results show that pipette vibration can generate constant flows, which

shows a fixed flow pattern near the pipette. When changing the pitch and seal-of-approval voltage of a piezo-electric element, the flow velocity changed, but this flow pattern was about fixed. Therefore, the proposed mechanism may be effective in order to control rotation of a micro object such as an egg cell for bio cell operations.

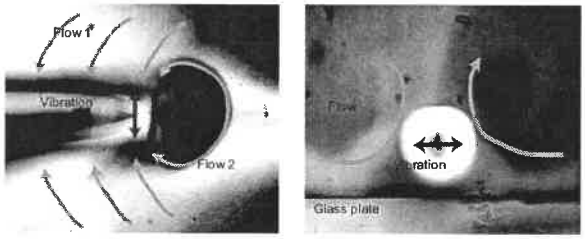

FIGURE 4. Flow pattern near a tip end of micro pipette [Scale:×200].

As shown in Fig.5, the rotational direction of a micro object is decided by the location between a object and pipette. Moreover, rotational speed changes with the frequencies of a pipette.

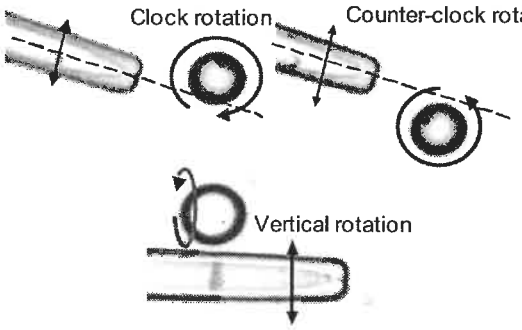

FIGURE 5. Non contact rotation positioning of the minute ball using vibration by pipette vibration [Scale:×160].

Reconstruction of 3D model using non-contact rotation and CT

Proposed non-contact rotation mechanism make microscopic observations a micro object from various directions possible. These observed microscopic image information can be used for computerized tomography (CT) is employed to establish a system for visualizing 3D model as shown in Fig.6.

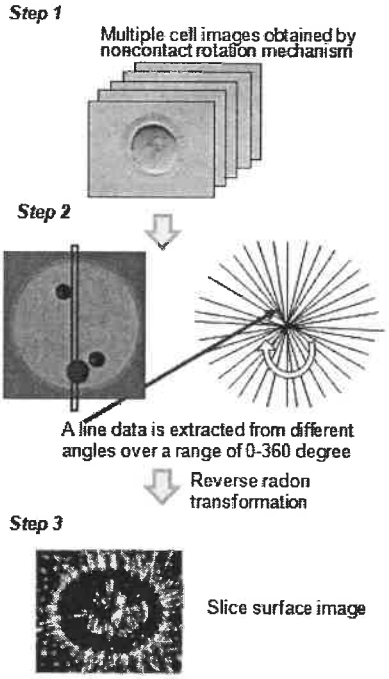
Step 1
Multiple cell images obtained by noncontact rotation mechanism
Step 2
A line data is extracted from different angles over a range of 0-360 degree
Reverse radon transformation
Step 3
Slice surface image

FIGURE 6. Concept of 3D model reconstruction using non contact rotational mechanism.

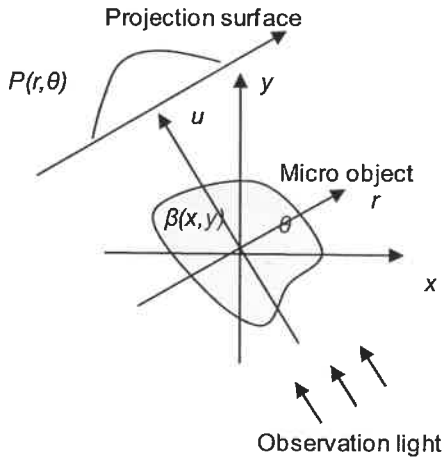

FIGURE 7. Principle of basic computerized Tomography

CT is a kind of technique that can reconstruct the cross-sectional information from projection data. The usual image-reconstruction algorithm implemented on existing CT scanners requires the collection of X-ray data representing line integrals that are evenly spaced over a 360-deg range of angles. When the light of a microscope travels through a micro object such as a cell at an angle θ toward axis x where a internal deletion exists, its optical path changes

accordingly. This fact inevitably leads to a change of phase difference of internal structure of an observation target in Fig.7. The general phase difference $\Delta\beta = p(r,\phi)$ can be expressed as the summation of the local difference.
Many methods have been proposed to obtain 2D distribution of $\beta(x,y)$ by mathematically handling the projection data from different angles over a range of 0-360 degree. Then stacking up the reconstructed 2D information will reconstruct a full 3D physical field. The 3D information of a micro object was reconstructed by applying reverse radon conversion to the image of a large number obtained by non-contact rotation observation.

BASIC EXPERIMENTS

As a basic experiment, the basic performances of proposed methods are discussed. As a basic experiment, the rotation observation experiment of the two kinds of microscopic balls (UB-67L Union Co. Ltd: Diameter 130 [μm]) shown in Fig.8 was carried out.

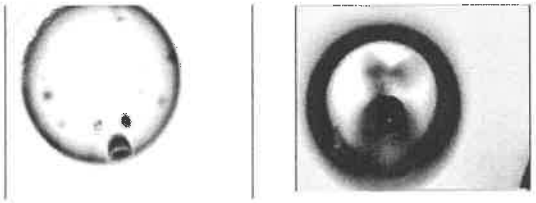

(a) A micro ball with no internal deletion (b) A micro ball with internal deletions

FIGURE 8.Microscopic glass ball for the basic experiments.

In order to reconstruct 3D model from observed 2D microscopic image, firstly, we take about 30 microscopic images of a micro object from various directions using non-contact rotation of 20HZ(s) PZT vibration. This number of image is enough for 3D model reconstruction with CT. Secondly, in order to obtain the projection data of a micro object, image de-noising and 255 gray scale conversion are carried out about each image. Fig.9 shows the central line of a micro ball of each image is picked out and displayed by one revolution. Finally, slice surface information of a micro object as shown in Fig.10 is re-constructible by applying the reverse radon transform method to each data shown in Figure 9. In order to obtain complete 3D model, it is necessary to carry out this process about all slice surface of a micro object. This process is under development now.

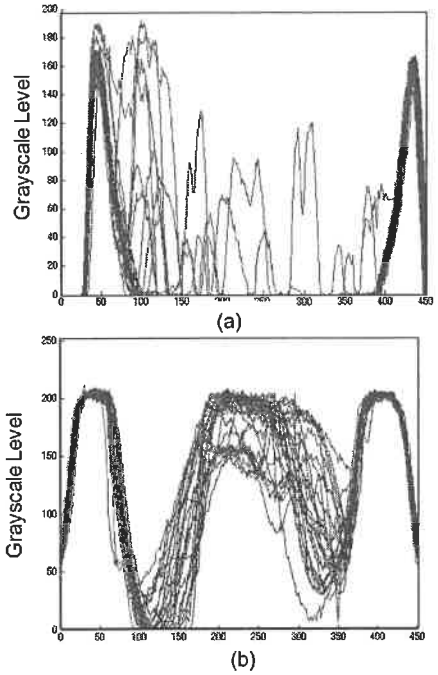

FIGURE 9 Gray-Scale distribution of a line segment of a microscopic glass ball.

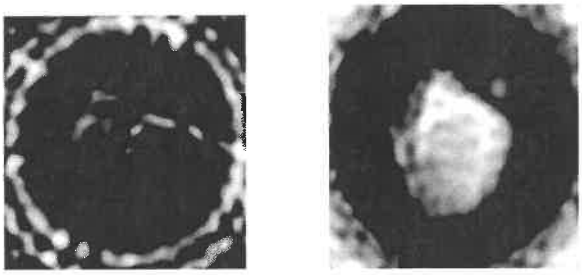

(a) (b)

FIGURE 10. The cross section surface image reconstructed by CT

CONCLUSIONS AND FUTURE WORKS

Flexible reconstruction of 3D model using non-contact rotation method was proposed and was shown demonstrated. The performance of non contact rotation mechanism is sufficient ability for the CT process of 3D observation In future work, the process which reconstructs complete 3D model is developed and the accuracy of the model is verified. And then we're going to develop a more precise bio operation system using 3D model information.

ACKNOWLEDGEMENT

This research was partially supported by the Ministry of Education, Science, Sports and Culture, Grant-in-Aid for Young Scientists (B), 2006-2007,18760201.

PROPOSAL OF A SNAKE TYPE IN-PIPE MOBILE ROBOT CORRESPONDING TO THE DIFFERENT DIAMETERS

Manabu ONO[1] , Shuzo ITO[1],
Shigeru IKEDA[1] and Shigeo KATO[2]
[1]Tokyo Metropolitan College of Industrial Technology
Shinagawa, Tokyo 140-0011
e-mail: mana@tokyo-tmct.ac.jp
[2]Nippon Institute of Technology
Miyashiro, Saitama, 345-8501
e-mail: kato@nit.ac.jp

1. INTRODUCTION

We have many small diameter pipes that are cooling pipes for atomic power stations, boiler pipes, and gas or water pipe lines. They must be periodically inspected in order to protect the accident previously. Diameters of these pipes are different at the place where pipes change from the main to the branch. The inspection robot for these pipes must move different diameter.

A step comes where the pipe changes its diameter. The in-pipe robot driven by wheels is very difficult to cross the step [1]. We have used cone-shape friction rings for the driving legs of the in-pipe robot. However, the robot driven by friction rings is also difficult to move in the pipe where diameter changes more than 3 mm [2].

Now, we propose a mobile robot that can surely move in a pipe whose diameter changes. The robot is constructed by the five rubber bellows as pneumatic actuator, five electromagnetic valves and five air feeding tubes. Outer diameter and natural length of the bellows are 16 mm and 108 mm, respectively. The bellows composes three somite by being arranged in two rows and three columns. The somite can make the arc like the bimetal by giving different pressure to each bellows. The arc somite can hold the pipe. The movement of the robot with three somite is imitating as for the accordion movement that is the movement of the snake operation.

The fabricated mobile robot was confirmed to move in different diameter pipes whose diameters are between 44 mm and 90 mm. Its moving speed was 25 mm/s.

2. STRUCTURE OF IN-PIPE MOBILE ROBOT

A structure of the fabricated robot is shown in Fig. 1 and photograph shown in Fig. 2.

The robot is constructed by the five rubber bellows as pneumatic actuator, five electromagnetic valves and five air feeding tubes. Outer diameter and natural length of the robot is 33 mm and 304 mm, respectively. The bellows composes three somite by being arranged in two rows and three columns. Outer diameter and natural length of the bellows are 16 mm and 108 mm, respectively. The somite is defined forward of the robot as first somite, second somite and third somite. Each somite can make the arc like the bimetal by giving different pressure to each bellows. The first somite and third somite are mechanisms that hold the pipe and the second somite is

mechanisms that obtain displacement.

An experimental apparatus for measuring the characteristics of the robot is shown in Fig. 3. A computer controls six electromagnetic valves through a valve controller. Three air feeding tubes are connected from the electromagnetic valves to each bellows of the robot. An air compressor is connected to the entrance ports of the electromagnetic valves and feeds pneumatic pressure to stretch the bellows. A vacuum pump is connected to the exit ports of the electromagnetic valves and feeds vacuum pressure to shrink the bellows.

3. MOVEMENT OF SNAKE IN A PIPE

We observed snake's accordion movement in pipe. Fig. 4 shows the brief movement of an snake. When the snake moves a vertical pipe,

(1) The snake bends the body like the accordion and holds the pipe by the whole body.
(2) The snake stretches oneself to the moving direction. At this time, snake's lower part of the body continues the holding of the pipe.
(3) The snake bends the upper part of the body and holds the pipe.
(4) The snake extends the lower part of the body, and releases the holding of the pipe.
(5) The snake hauled in the lower part of the body. Afterwards, the snake bends the lower part of the body and holds the pipe.

Thus, the snake can move in the vertical pipe.

4. MOVING PRINCIPLE OF THE ROBOT

The moving principle of the robot shown in Fig. 5. The moving principle of the robot referred to the accordion movement of the snake.

As for step 0, negative pressure is given to all bellows.

Step 1: The third somite is bent and it holds of pipe.

Step 2: Positive pressure is given to the first and second somite and somite are stretched.

Step 3: The first somite is bent and it holds of

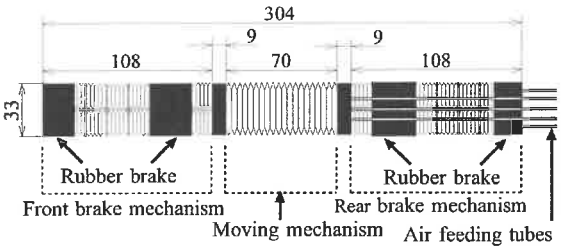

FIGURE 1. Structure of in-pipe mobile robot

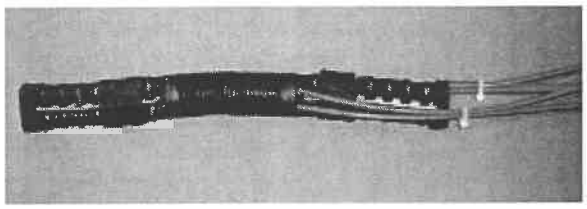

FIGURE 2. The photograph of in-pipe mobile robot

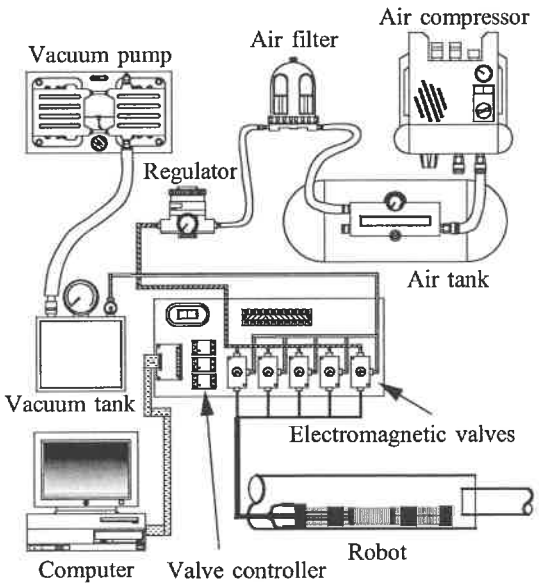

FIGURE 3. Experimental apparatus

pipe.

Step 4: Negative pressure is given to the third somite and the holding of the pipe is released.

Step 5: Negative pressure is given to the second somite. The latter half of the robot advances in this step.

Step 6: The third somite is bent and it holds of pipe.

The robot can move by repeating these steps.

5. MOVING EXPERIMENT

5.1 Moving speed of the robot

The moving speed of the robot is measured. Fig. 6 shows the experiment result. The using pipes to experiment are 44 mm, 60 mm, 70mm, 79 and 90 mm in the inner diameter. The air pressures used to experiment are 50 kPa and -80 kPa.

The robot is able to move in these pipes and a combined pipe of a different diameter. The moving speed confirmed no relation to inner diameter of pipe and average moving speed was 25 mm/s.

5.2 Brake mechanism characteristics

We measured the friction force that became brake force of a in-pipe mobile robot. Five kinds of acrylic pipes of the inside diameter 44 mm, 60 mm, 70 mm, 79 mm, and 90 mm were used in the experiment. Internal pressure of two bellows that compose the brake mechanism was changes in the experiment.

Internal pressure of an inside bellows was controlled to be constant -80 kPa and the pressure supplied to an outside bellows was changed with -50 kPa, -25 kPa, 0 kPa, + 25 kPa and + 50kPa. The frictional force that occurs for the inside diameter of the pipe in shown in Fig. 7.

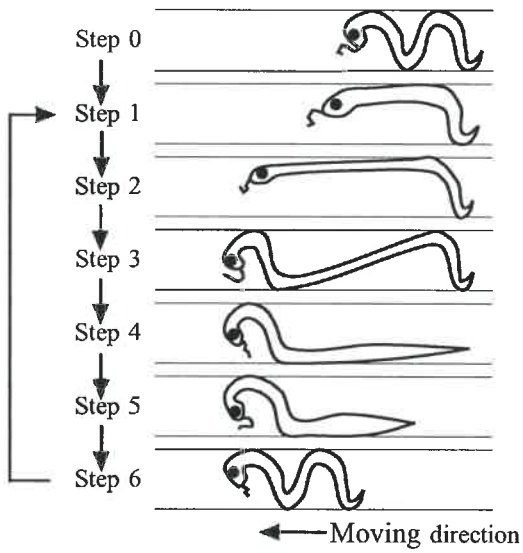

FIGURE 4. Accordion movement of a snake

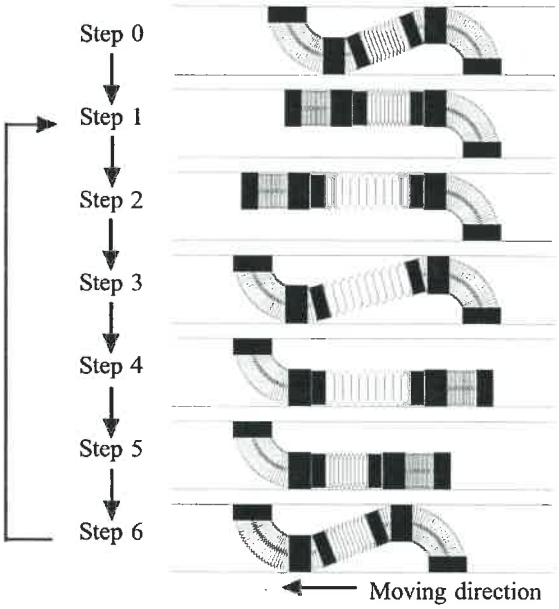

FIGURE 5. The moving principle of the robot

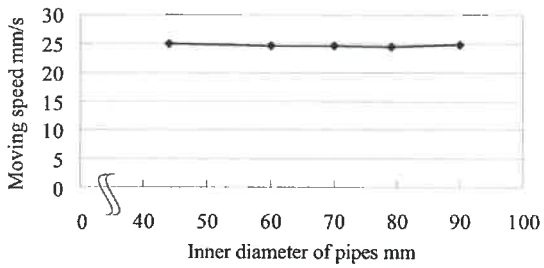

FIGURE 6. The moving speed characteristics

The measured friction force was 6.8 N in the pipe of 44 mm in the inner diameter when pressure in an outside bellows was +50 kPa, and 2.5 N in the tube of 90 mm in the inner diameter. Therefore, the friction force was confirmed to depend on the inner diameter of the pipe. When pressure in an outside bellows was -50 kPa, the measured friction force was 2.6 N in the pipe of 44 mm in the inner diameter. Therefore, it has been understood that the friction force depends also on the pressure in an outside bellows of brake mechanism.

The pressure supplied to an outside bellows was controlled and the normal force which was generated at the braking mechanism was measured. The normal force that occurs for the inside diameter of the pipe is shown in Fig. 8. When pressure in an outside bellows was +50 kPa, normal force was 1.9 N in inner diameter 90 mm. Moreover, it was 2.3 N in the pipe of 44 mm in the inner diameter. The normal force is larger in case of the pressure of +50 kPa than the case of the pressure of -50 kPa.Therefore, it has been understood that the generated normal force depends also on an internal differential pressure of two bellows of the brake mechanism.

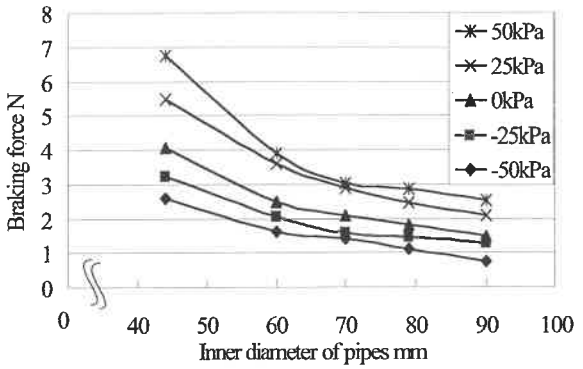

FIGURE 7. Relationship between diameter of pipe and braking force of robot

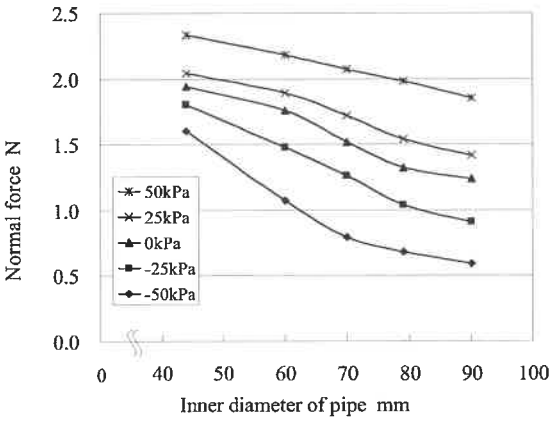

FIGURE 8. Relationship between pipe diameter and normal force

6. CONCLUSIONS

We propose the robot which is imitate the snake of accordion movement. The fabricated mobile robot is confirmed to move in different diameter pipes whose diameters are between 44 mm and 90 mm. Its speed is 25 mm/s.

REFERENCES

[1] K. Kawaguchi, O. Yoshida, K. Iwao and T. Kikuta: Control of an In-pipe Inspection Robot for Iron Pipes, Journal of the Robotics Society of Japan, Vol 15, No. 3 (1997), 387. (in Japanese)

[2] M. ONO, T. HAMANO and S. KATO: A Basic Study of Mobile Inspection Robot Movable the Long Distance in Small Diameter Pipes, Journal of the Japan Society for Precession Engineering, Vol. 69, No. 4 (2003), 564. (in Japanese)

DESIGN AND OPTIMIZATION OF AN ACTIVE AEROSTATIC THRUST BEARING

Ron A.J. van Ostayen[1], Anton van Beek[1], and Rob Munnig-Schmidt[1]
[1]Research group Mechatronics
Department of Precision and Microsystems Engineering
Faculty of Mechanical, Maritime and Materials Engineering
Delft University of Technology, the Netherlands

ABSTRACT

The properties of a circular aerostatic thrust bearing with an actively controlled flexible bearing surface are investigated. The flexible surface consists of a simply supported plate. Variation of the radius on which this plate is supported, results in a bearing with increased or reduced stiffness. In addition, in order to actively control the bearing an ideal force actuator to modify the bearing flexure is added. The static properties of the bearing are studied and furthermore it is shown that the dynamic properties of this type of bearing are primarily determined by the air film, and less by the dynamics of the flexible plate.

NOMENCLATURE

Dimensionless variables/constants

C_p	pressure constant	$= p_a R^2/Edh_{0,R}$
$\bar{d}$	bearing plate thickness	$= d/R$
D	flexural rigidity	$= 1/2(1+\nu)$
G	shear modulus	$= 1/12(1-\nu^2)$
H	film height	$= h/h_{0,R}$
$\bar{h}$, $\tilde{h}$	static, dynamic film height	
H_0	nominal film height	$= h_0/h_{0,R}$
$\bar{h}_0$, $\tilde{h}_0$	static, dynamic nominal film height	
L	bearing load	
M_r, M_θ	radial and circumferential bending moment per unit length	
P	pressure	$= p/p_a$
$\bar{p}$, $\tilde{p}$	static, dynamic pressure	
Q	transverse shear force per unit length	
r	radial coordinate	
t_f	specific time (air film)	$= \eta R^2/p_a h_{0,R}^2$
t_s	specific time (plate)	$= (\rho R^2/E)^{0.5}$
W	transverse flexure	$= w/h_{0,R}$
$\bar{w}$, $\tilde{w}$	static, dynamic transverse flexure	
Ψ	rotation of transverse normal	$= R\psi/h_{0,R}$
$\bar{\psi}$, $\tilde{\psi}$	static, dynamic rotation of transverse normal	
κ	shear correction factor	$= \pi^2/12$
ν	Poisson ratio	
τ	time	

Parameters (values in reference point)

d	plate thickness	$(0.005\ \mathrm{m})$
E	Youngs modulus	$(2.1 \cdot 10^1 1\ \mathrm{Pa})$
$h_{0,R}$	nominal film thickness	$(10 \cdot 10^{-6}\ \mathrm{m})$
p_a	ambient pressure	$(10^5\ \mathrm{Pa})$
p_s	supply pressure	$(5 \cdot 10^5\ \mathrm{Pa})$
R	bearing radius	$(0.05\ \mathrm{m})$
η	air viscosity	$(17.1 \cdot 10^{-6}\ \mathrm{Pa\,s})$
ρ	bearing density	$(7800\ \mathrm{kg/m^3})$

INTRODUCTION

The aerostatic thrust bearing is a bearing type commonly used in high precision linear and planar stages. In an aerostatic bearing a pressurized gas (usually air) is supplied between the bearing surfaces, thereby fully separating the surfaces and forming a lubricating film in between. The aerostatic bearing combines a simple design with excellent properties, i.e. low or zero friction, no stick-slip behavior, and high load capacity and stiffness. In a typical aerostatic bearing design, the air is supplied to the film via a number of supply restrictors. The load carrying capacity of the aerostatic bearing is proportional to the air pressure in the film at those supply points and the shape and height distribution of the lubricating film.

Bearing stiffness is defined as the gradient of the load carrying capacity with respect to the nominal film height. One method to ensure that an aerostatic bearing has sufficient passive bearing stiffness is to use a non-parallel film. In a bearing with a non-parallel film the pressure distribution will change as a result of a change in nominal film height, resulting in a normal stiffness. Holster e.a. [1] extended this basic idea of the non-parallel film to use the elastic flexure of the bearing as a result of the film pressure. An elastically supported, compliant plate bearing was developed, with the plate support positioned at a radius somewhere between the center and the edge of the bearing. It was shown that this bearing type exhibits a increased passive stiffness and

even an infinite stiffness for a small range in film height.

In order to further increase and in particular control the load carrying capacity and stiffness, active aerostatic bearings have been developed. In active aerostatic bearings either the supply pressure, or the resistance of the supply restrictors, or the bearing film height distribution is controlled. The third method, control of the bearing film height distribution, is less sensitive to delay times in the lubricating film and is to be preferred. Al-Bender e.a. [2] have investigated this type of actively controlled aerostatic bearing. In their design the central supply point in the compliant plate bearing surface was fixed, and the edge of the bearing is controlled using piezo-actuators.

The goal of this present study is to arrive at a bearing configuration that, depending on the actuating action, exhibits either very low stiffness, so the bearing can function as a vibration isolator, or very high stiffness, so the bearing can function to optimally support a vibrating machine. To that end, a combination of both these earlier configurations [1, 2] is presented (figure 1). The bearing geometry is similar to that of the bearing presented in [1]. A flexible plate is supported on a intermediate radius (b) and the bearing is supplied through a central supply point and recess (a). However in addition, the height distribution of the lubricating film is controlled using an ideal force actuator, positioned at the edge of the bearing (c). In contrast to [1] the central area of the bearing is not supported by the supply pressure.

In order to better explain the basic operation of this bearing a typical film height – load curve and its corresponding film height – stiffness curve are presented in figure 2 with the (schematic) film height and pressure distributions at three different nominal film heights presented in figure 1. For high film heights (point A, see also figure 1) the flexure of the bearing is negligible compared to the nominal film height. As a result the film shape and therefore pressure distribution and load carrying capacity are largely independent of the film height. The bearing has close to zero stiffness. For intermediate film heights (point B) the variation of pressure distribution for changing film heights is at a maximum, and the bearing has maximum stiffness. Finally, for very small film heights (point C) the pressure distribution approaches its asymptotic value and again the stiffness is small.

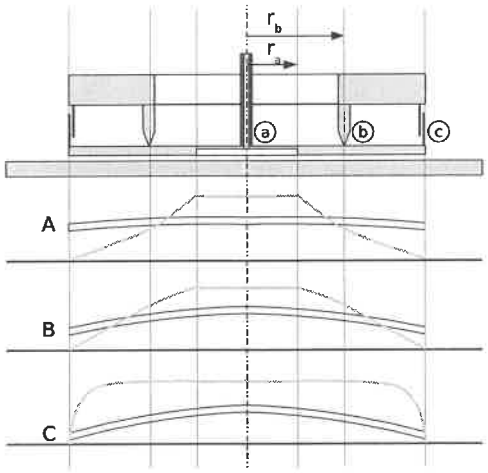

FIGURE 1. Bearing geometry and typical high (A), medium (B) and low (C) film shape (double line) and pressure distribution (blue).

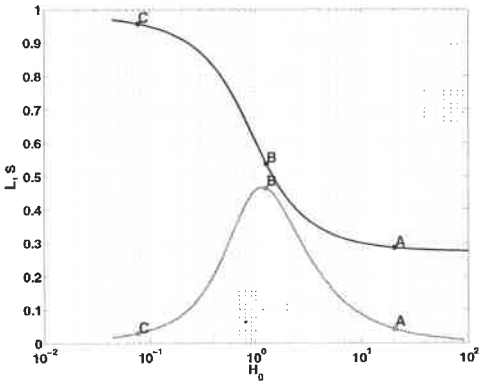

FIGURE 2. Typical film height – load (black) and film height – stiffness (gray) curves.

The properties of the bearing are determined by its geometry, in particular the position of the support point r_b, and by the action of the actuator. In the next section, a mathematical model is presented to determine these properties.

MATHEMATICAL MODEL

In order to determine the characteristics of the bearing a mathematical model has been developed. The model describes both the aerostatic pressure distribution P in the lubrication film and the deformation of the bearing surface W. The pressure distribution is calculated using the Reynolds' equation and the flexure of the bearing surface is calculated using the Mindlin thick plate

theory which describes the flexure and rotation of the neutral surface of the bearing plate.

It is assumed that the deformation of the bearing is restricted to the flexure of the plate. The support of the plate and the base of the bearing are assumed to be rigid. The support point is assumed to have no bending stiffness and the bearing plate is assumed to be simply supported. Furthermore, the bearing geometry is axisymmetric. So in our model the bearing geometry can be reduced to a one-dimensional domain: a line with coordinate r between 0 and 1. The central supply recess has a radius r_a and the bearing support is placed at a radius r_b.

The model consists of three partial differential equations and their boundary conditions. The dimensionless pressure distribution P follows from the solution of the axisymmetric Reynolds' equation:

$$\frac{\partial}{\partial r}\left(rH^3P\frac{\partial P}{\partial r}\right) = 12r\frac{\partial PH}{\partial \tau} \tag{1}$$

Reynolds' equation is valid for thin laminar lubricating films in which viscous forces dominate. The lubricating film height H is the sum of the nominal film height and the flexure of the bearing plate:

$$H = H_0 + W \tag{2}$$

The flexure of the bearing is described using the Mindlin thick plate theory (see e.g. [3]). In this case, the equations of motion for an axisymmetric loaded homogeneous circular plate are:

$$\begin{aligned}\frac{\partial}{\partial r}(rQ) &= -C_p r(P-1) + r\left(\frac{t_s}{t_f}\right)^2\frac{\partial^2 W}{\partial \tau^2}\\ \frac{\partial}{\partial r}(rM_r) &= M_\theta + \frac{rQ}{\bar{d}^2} + \frac{r}{12}\left(\frac{t_s}{t_f}\right)^2\frac{\partial^2 \Psi}{\partial \tau^2}\end{aligned} \tag{3}$$

where the force and moment resultants are given by:

$$\begin{aligned}Q &= \kappa G\left(\Psi + \frac{\partial W}{\partial r}\right)\\ M_r &= D\left(\frac{\partial \Psi}{\partial r} + \nu\frac{\Psi}{r}\right)\\ M_\theta &= D\left(\frac{\Psi}{r} + \nu\frac{\partial \Psi}{\partial r}\right)\end{aligned} \tag{4}$$

where W and Ψ denote the dimensionless transverse deflection and rotation of a transverse normal.

The relative load carrying capacity L of the bearing is found using:

$$L = \frac{2\pi}{L_{\max}}\int_{r=0}^{1} rP\,dr \tag{5}$$

where the load is given relative to the maximum obtainable load carrying capacity $L_{\max} = \pi(P_s - 1)$ and the dimensionless bearing stiffness S is defined as:

$$S = -\frac{H_0}{L}\frac{\partial L}{\partial H_0} \tag{6}$$

We are interested in both the static and dynamic properties of the bearing. To that end this model uses a two-step approach: First the stationary characteristics of the bearing are determined in a nominal operating point. Secondly, using a linearized perturbation technique the dynamic characteristics of the bearing (stiffness and damping) around this nominal point are determined. It is assumed that the solution P, W, Ψ, H is the sum of a stationary solution $\bar{p}, \bar{w}, \bar{\psi}, \bar{h}$ and a small dynamic and complex perturbation around this solution:

$$\begin{aligned}P &= \bar{p} + \tilde{p}e^{j\omega\tau}\\ W &= \bar{w} + \tilde{w}e^{j\omega\tau}\\ \Psi &= \bar{\psi} + \tilde{\psi}e^{j\omega\tau}\\ H &= \bar{h} + \tilde{h}e^{j\omega\tau} = (\bar{h}_0 + \bar{w}) + (\tilde{h}_0 + \tilde{w})e^{j\omega\tau}\end{aligned} \tag{7}$$

STATIONARY PROPERTIES

Substituting eq. 7 in the in Reynolds' equation 1 and plate flexure equations 3 and linearising around the operating point yields three coupled partial differential equations for the stationary operating solution. These equations can be solved, and the stationary properties of the bearing can be determined. To this end a commercial finite element code [4] is used. The pressure $\bar{p}$, and flexure $\bar{w}$ are approximated using cubic Lagrange elements, whereas the rotation $\bar{\psi}$ is approximated using quadratic elements.

First the influence of the position of the support point is determined (figure 3). The support radius is varied between $r_b = 0.9$ (close to the bearing edge) until $r_b = 0.3$. Starting at $r_b = 0.9$ and reducing the support radius a clear trend can be found: The stiffness decreases steadily until for $r_b = 0.5$ it is found that the stiffness is close to zero for a large range of the operating conditions and the stiffness becomes negative for even smaller values of r_b. Furthermore it is clear

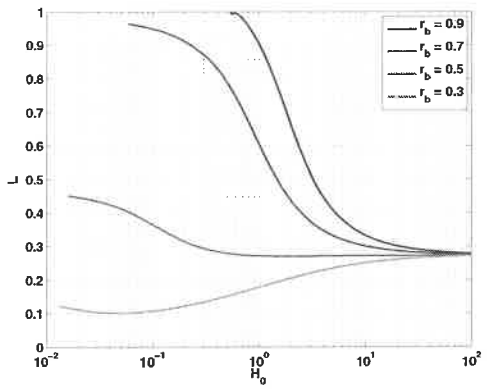

FIGURE 3. Film height – load curves for different r_b.

that the optimal film height, that is the film height where a maximum stiffness is reached, moves to higher values for an increase in r_b.

Next the properties of this bearing are studied for a prescribed actuator action. The actuator is placed at the edge of the bearing, and r_b is chosen to be equal to 0.5. In figure 4 the load carrying capacity and required actuator force are presented, both normalized with the maximum obtainable load $L_{\max}$. From this graph it is clear that

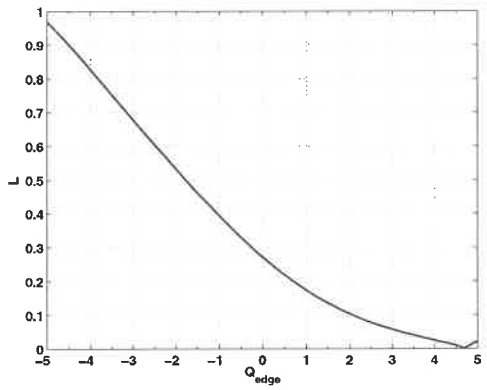

FIGURE 4. load curve vs. actuator force ($r_b = 0.5$.

any load carrying capacity within the theoretical limits is obtainable. However, the required actuator load varies between zero and five times the maximum theoretical bearing load.

DYNAMIC PROPERTIES

From the perturbed solution in eq. 7 the dynamic properties can be calculated as function of frequency. The frequency response is calculated both for a vibrating counter surface and for a vibrating bearing. From the results it is clear that only at high frequencies there is a clear difference between both responses. The dynamics of the plate bearing only come into play at these high frequencies.

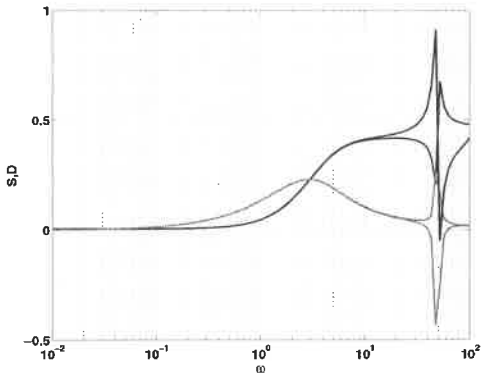

FIGURE 5. Bearing stiffness (black) and damping (gray) as a function of frequency.

CONCLUSIONS

The force actuated bearing exhibit a large variation in load around the operating film height as a function of the actuator function. Both bearing types can be controlled up to high frequencies without concern for the eigenfrequencies of the bearing plate. The next step will be to test this bearing in the laboratory and verify the characteristics as predicted in this research.

REFERENCES

[1] P.L. Holster and J.A.H. Jacobs, Theoretical Analysis and Experimental Verification on the Static Properties of Externally Pressurized Air-Bearing Pads with Load Compensation, Tribology International, 1987; 20: 276–289.

[2] F. Al-Bender, Active compensation of aerostatic bearings, `http://www.mech.kuleuven.be/micro/topics/airbearing`

[3] J.N. Reddy and C.M. Wang, Relationships Between Classical and Shear Deformation Theories of Axisymmetric Circular Plates, AIAA Journal, 1997; 12: 1862–1868

[4] Comsol AB, Comsol 3.3a User's Guide, version Februari 2007, COMSOL 3.3a, 2007

DEVELOPMENT OF MICRO MECHANICAL PARTS UTILIZED EXTRA FINE WIRES

Satoshi Honda
Department of mechanical Engineering
Tokyo Metropolitan University
Minami-osawa, Hachioji, Tokyo, Japan

INSTRUCTIONS

Research and development of the micro machine which is called MEMS (Micro Electro Mechanical System) have been done with the big expectations of many people, since a birth of the micro machine in the 1980s. In the big expectations toward the micro machine, many people have been waiting for appearing of a new machine which had not been gained in the history of man. Under the big expectations of the people, researchers and engineer developed three major methods of photolithography[1], LIGA process[2] and ultra-precise milling[3]. They are produced the micro mechanical parts such as a micro gear, a micro linkage, a micro motor. However, if we choose these methods to make the micro mechanical parts, we have to install huge and expensive facilities. Moreover, if the micro mechanical parts are designed in three dimensionally complex shapes, we can not manufacture by these methods. Therefore, many researchers and engineers wait for the forth method to developed micro mechanical parts with small facilities and simple process and high making ability and without expensive equipments. A novel method to make the micro mechanical parts utilized extra fine wires was developed and a micro screw, a micro nut, a micro helical gear, and a micro turbine impeller were manufactured by the developed method[4].

In this paper, the micro screw with smaller pitch of 40 micrometers and the micro nut with smaller pitch of 40 micrometers and a micro helical gear with smaller module of 18.1 micrometers are manufactured by a new brazing process. Additionally, the micro parallel stage driven by the helical micro gears is produced as a prompt application.

THE MICRO SCREW AND THE MICRO NUT UTILIZED EXTRA FINE WIRES

The micro screw and the micro nut utilized the extra fine wires are shown in figure 1 and figure 2. The micro screw is made by brazing an extra fine wire which is coiled around a needle pin. The micro nut is made by brazing an extra fine wire which is coiled on the inside of a small tube. The micro screw and the micro nut have following dimensions; both of major diameters are 740 micrometers, both of pitches are 40 micrometers, and threaded portion's length of the micro screw is 14 millimeters and thickness of the micro nut is 1.2 millimeters. Just for reference, major diameters of the last developed micro screw and the micro nut were 600 micrometers and those pitches were 100 micrometers. [4]

The micro screw utilized extra fine wires is made through following processes as shown in figure 3.

(1) Firstly, a needle pin to be firmly soldered is prepared as shown in figure 3(1). We used a terminal pin of a hybrid IC as the needle pin. The pin is undercoated with nickel plating and is plated with gold. Its diameter is 700 micrometers and its length is 20 millimeters.

(2) Secondly, a pair of one extra fine wire to be

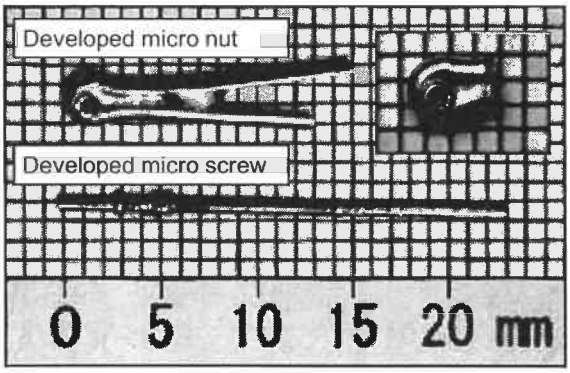

FIGURE 1. The micro-screw and the micro-nut utilized extra fine wires.

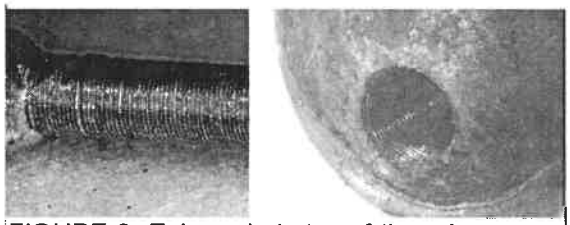

FIGURE 2. Enlarged photos of the micro-screw and the micro-nut.

firmly soldered and another extra fine wire to be hardly soldered is closely coiled each other around the needle pin as shown figure 3(2). We used a brass wire plated with gold as the extra fine wire to be firmly soldered, and used a tungsten wire plated with tin as the extra fine wire to be hardly soldered. Both wires have same diameters of 20 micrometers.

(3) Thirdly, the extra fine wire to be firmly soldered is brazed around the terminal pin by filling a spiral gap between the needle pin and the coiled wires with the melted solder as shown figure 3(3), yet the extra fine wire to be hardly soldered is not brazed around the needle pin. On this brazing process, a solder ball is attached at upper tip of the coiled needle pin, and lower tip of the coiled needle pin is put into melted solder of a solder pot as shown figure 4. Melted solder in the solder pot rises up into the spiral gap by capillarity phenomenon, and melted solder drop at the upper tip of the coiled pin flows down into the spiral gap as shown figure 5. The spiral gap is filled with melted solder without defect bubbles. This brazing process is newly developed.

(4) Finally, the wire to be hardly soldered is removed, as shown figure 3(4), and the extra fine wire to be firmly soldered is remained as a ridge of the external thread.

The micro nut utilized extra fine wires is made through following processes as shown in figure 6.

(1) Firstly, a needle pin to be hardly soldered is prepared as shown figure 6(1). We used a hypodermic needle as the needle pin. The pin is made of stainless steel and its diameter is 715 micrometers because minor diameter of internal thread of the micro nut should become slightly bigger.

(2) Secondly, a pair of one extra fine wire to be firmly soldered and another extra fine wire to be hardly soldered is closely coiled each other around the needle pin as shown in figure 6(2). We used a brass wire plated with gold as the extra fine wire to be firmly soldered, and used a tungsten wire plated with tin as the extra fine wire to be hardly soldered. Both wires have same diameters of 20 micrometers.

(3) Thirdly, the double-coiled part mentioned above is inserted in a head hole of a small split pin, and the melted solder is poured into gap between the head hole and the double-coiled part as shown in figure 6(3). The extra

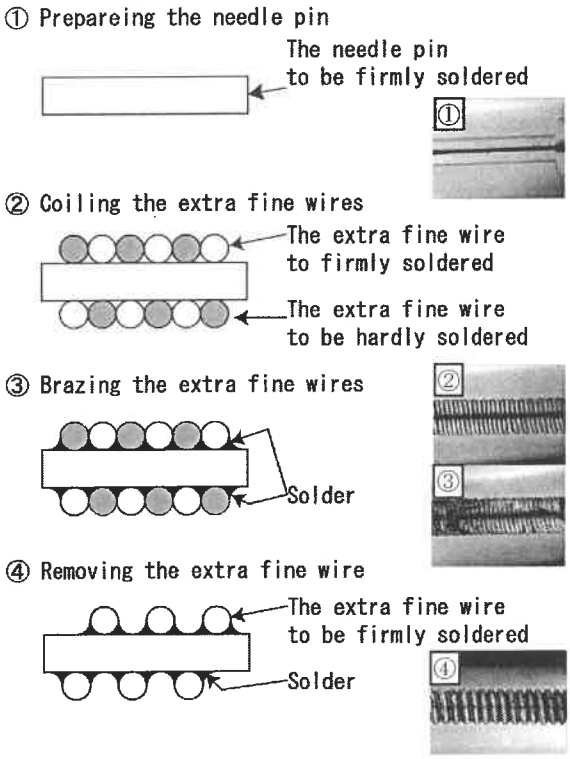

FIGURE 3. Making process for the micro screw utilized extra fine wires.

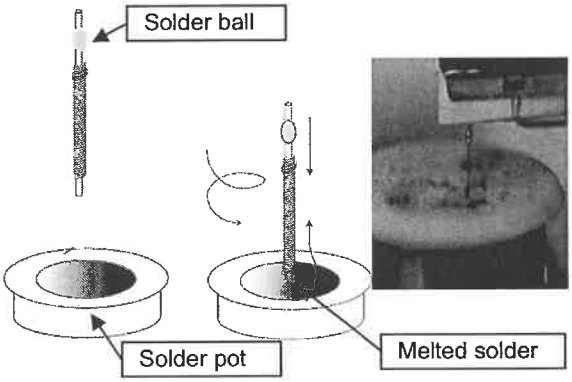

FIGURE 4. New brazing process for the micro screw.

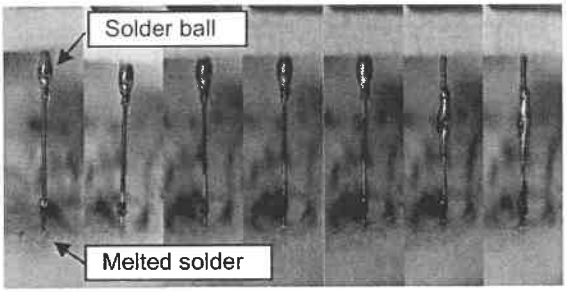

FIGURE 5. Rising up and flowing down of the melted solder.

fine wire to be firmly soldered is brazed on the inside of the head hole, yet the extra fine wire to be hardly soldered and the needle pin are not brazed.

(4) Fourthly, the needle pin is drawn out from the brazed part as shown in figure 6(4).

(5) Finally, the wire to be hardly soldered is removed through the center hole which is made by removing the needle pin as shown figure 6(5). The extra fine wire to be firmly soldered is remained as a ridge of the internal thread.

When we used the small tube instead of the split pin, minor diameter of internal thread of the micro nut became smaller than the diameter of the hypodermic needle. This production result indicates followings; residual stress of inside solder in the small tube is generated during brazing process as shown in figure 7, the residual stress is released after the needle pin is drawn out and the wire to be hardly soldered is removed, the inside solder expands toward its center. When we used the split pin, minor diameter of internal thread of the micro nut became slightly bigger than the minor diameter of the micro screw. This production result indicates followings; residual stress of inside solder in the split pin is slightly generated during brazing process because the split pin have an opening section, the residual stress is released after the needle pin is drawn out and the wire to be hardly soldered is removed, the inside solder almost expands toward its outside and the circular head of the split pin is enlarged.

By using the split pin in the brazing process, the minor diameter of internal thread of the micro nut becomes slightly bigger than the minor diameter of external thread of the micro screw, and thread overlap between the micro screw and the micro nut is guaranteed within the range from 10 to 20 micrometers. The micro screw is screwed in the micro nut as shown in figure 8.

THE MICRO HELICAL GEARS UTILIZED EXTRA FINE WIRES

The helical micro gears utilized extra fine wires are shown in figure 9. The helical micro gears are made by brazing several extra fine wires which are helically twining around a narrow pin or a narrow pipe. The micro helical gears have following dimensions; number of teeth is 18, module of the gears is 18.1 micrometers, tip diameter of the gears is 350 micrometers, and helical angle of thread is 21.4 degrees, and

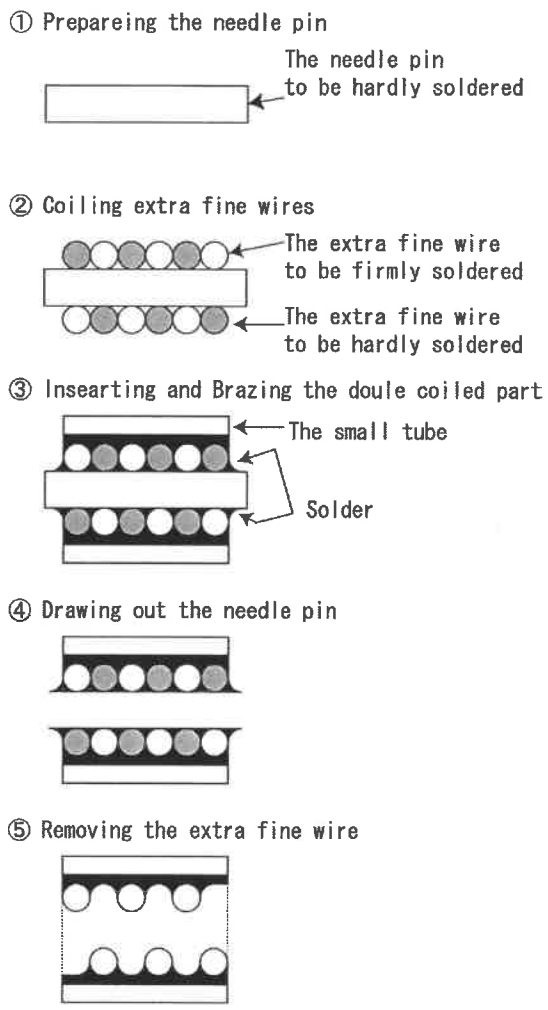
① Prepareing the needle pin
The needle pin
to be hardly soldered
② Coiling extra fine wires
The extra fine wire
to be firmly soldered
The extra fine wire
to be hardly soldered
③ Insearting and Brazing the doule coiled part
The small tube
Solder
④ Drawing out the needle pin
⑤ Removing the extra fine wire

FIGURE 6. Making process for the micro nut utilized extra fine wires.

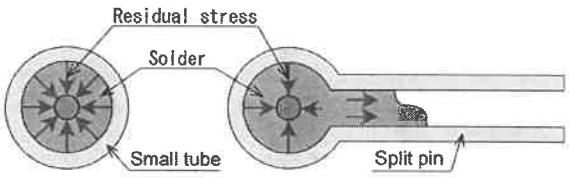

FIGURE 7. Residual stress of inside solder of the small tube and the split pin

FIGURE 8. Assembly of the micro screw and the micro nut.

diameter of the extra fine wire is 25 micrometers.

The brazing process which utilize capillarity phenomenon of melted solder is added to the developed processes[4] for producing the micro helical gear which module is several ten micrometers.

THE MICRO PARALLEL STAGE DRIVEN BY HELICAL GEARS

Figure 10 and figure 11 shows a micro parallel stage driven by three pairs of helical micro gears. The micro parallel stage consists of handle axes with the helical micro gears, wirework links with the helical micro-gears, joint links connected with narrow pipes, triangular table with three pins. The handle axes and the wirework link's axes are stood up on the base, and their axis's tops and their axis's feet are bind by the double bearings connected with narrow pipes. In the experiments, the triangular stage was positioned in X, Y, θ directions by manual rotations of the handle axes as shown in figure 12.

CONCLUSIONS

(1)The micro screw with small pitch of 40 micrometers was produced by the brazing process utilizing capillarity phenomenon of melted solder.
(2)The micro nut to be possible to assemble to the micro screw was produced by using the split pin.
(3)The micro helical gears with smaller module of 18.1 micrometers were produced by the brazing process utilizing capillarity phenomenon of melted solder.
(4)The triangular stage to be possible to position toward X, Y, θ directions was developed.

REFERENCES

[1] Y. C. Tai, et al.. IC-processed electrostatic synchronous micromotors. Sensors & Actuators. 1989; 20: 49-56.
[2] W. Menz, et al.. The LIGA Technique –a Novel Concept for Microstructures and the Combination with Si-Technologies by Injection Molding. Proc. of IEEE Workshop on MEMS, Nara, Japan, Jan.30-Feb.2. 1991: 69-73.
[3] Y. Takeuchi, K. Sawada and T. Sata. Ultra-precision 3D Micromachining of Glass. Annals of the CIRP, 1996: 45/1: 401-404.
[4] S. Honda. Development of a micro screw thread and a micro gear utilized extra fine wires. Proc. of 18th annual meeting of ASPE. 2003: 208-211.

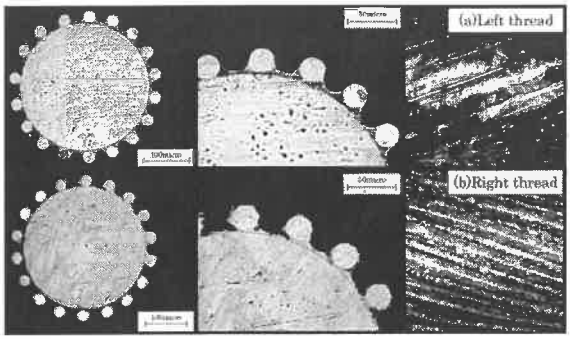

FIGURE 9. The micro helical gears utilized extra fine wires.

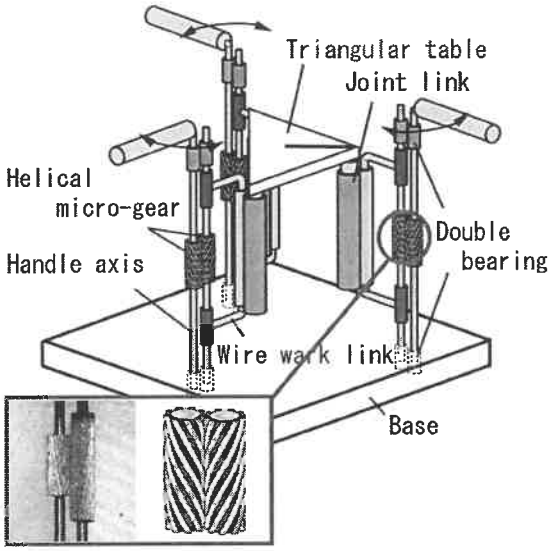

FIGURE 10. Structure of the micro parallel stage driven by the helical micro gears.

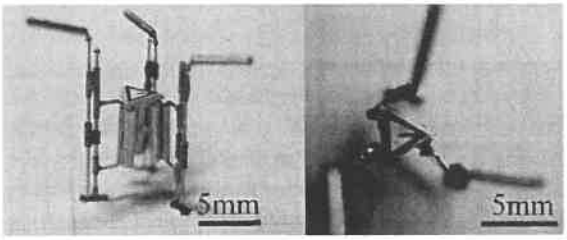

FIGURE 11. The micro parallel stage.

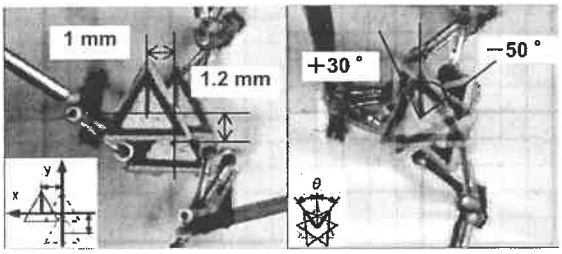

Figure 12. Motions of the micro parallel stage in X-Y directions and rotational direction.

DEVELOPMENT OF 2-DOF DEFLECTION MIRROR WITH CLOSED LOOP CONTROL

Toon A.A. Kuijpers, Diederik van Lierop, Ton A.J.M. Nellissen, Herman M.J.R. Soemers, Adrian Rankers
Mechatronics
Philips Applied Technologies
Eindhoven, The Netherlands

ABSTRACT

This paper presents the development of a 2-DOF closed loop controlled deflection mirror. A novel suspension using a Silicon-Nitride (SiN) membrane makes actuation in 2 DOF possible with large deflections at low actuation voltages. The separation between the two modes with the lowest natural frequencies (coinciding with the actuation direction) and interfering modes with higher natural frequencies can be pushed up to a ratio of 20, which is important for control stability. Furthermore, the SiN membrane is tough, durable and can withstand high strain. The mirror is actuated using four quadrant electrodes, allowing for both tilt actuation and suppression of vibrations perpendicular to the membrane. A high frequency measurement signal superposed upon a low frequency actuation signal, allows for a high bandwidth control loop.

INTRODUCTION

Almost all of the 2D deflection mirrors demonstrated up to now are either operated at their natural frequency or are open loop controlled.

The resonant type deflection mirror devices can be used in scanning applications such as displays and barcode readers. Usually these mirrors are constructed using two individual suspensions and an intermediate body. Elastic hinges provide the angular deflection of the suspensions. Such mechanisms suffer from a trade-off between a low deflection angle and a low control bandwidth, which are both related to the angular stiffness of the hinges.

The second type of deflection mirror device is open loop controlled such as the Digital Mirror Device of Texas Instruments. The deflection-angle of the mirrors is often measured externally, or is not measured at all resulting in 2 controlled positions.

Purpose

The present micromirror designed by Philips Applied Technologies is not intended for any specific application, though there are various interesting application fields close at hand, e.g. automotive, consumer products, medical, etc. This project will combine and extend the mechatronics expertise and micromachining process technology, readily available within Philips Applied Technologies. The demonstrational purposes of this micromirror request some challenging features: a high bandwidth in closed loop control, while not being operated at its eigenfrequency. The range of steady-state set-point deflections is about 3°.

Concept

An extensive literature study showed that tilting mirrors are usually constructed using torsion beams (*FIGURE 1*), which allow for smooth tilting over a large angular stroke. Their low radial stiffness though introduces an eigenmode perpendicular to the tilting axis from which the dynamics will suffer badly. These parasitic eigenmodes will have frequencies very close to the eigenfrequency of the tilting mode, which makes it difficult to excite only the desired motion.

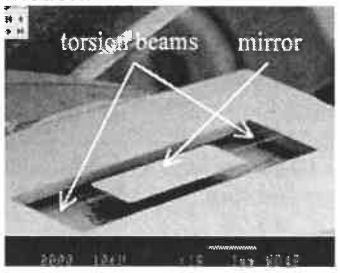

FIGURE 1. Example of torsion beams (source: CNRS)

The concept depicted in *FIGURE 2* employs a circular diaphragm or membrane, which allows for tilt of a mirror in two degrees of freedom. The eigenfrequencies of the two corresponding mode shapes (tilt), f_1 and f_2, should be kept as far away as possible from the eigenfrequencies of the other mode shapes (f_3, f_4, etc.) which are considered to be parasitic. The ratio f_3/f_1 is a suitable measure for the dynamic quality.

Calculations show that when using a small and thin diaphragm a ratio higher than 10 can be achieved easily, even an extremely high ratio of 25 should be possible. Therefore, downscaling will improve the dynamics. Another strength observed for this suspension is the robustness of the diaphragm / membrane compared to delicate torsion beams.

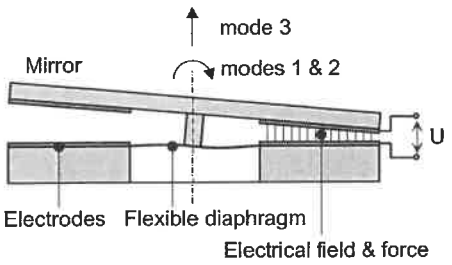

FIGURE 2. Concept of 2-DOF tilting

ACTUATION

After considering many options it was decided to include an electrostatic gap-closing actuator, as disclosed in *FIGURE 2*. This type of actuator integrates nicely with the diaphragm suspension and allows for controlling two degrees of freedom by simply dividing the electrodes in four quadrants. Furthermore, the stroke fits our requirements and processing doesn't come much easier than this. The force is limited though, due to the allowable electrical field strength E:

$$F_{es} = \tfrac{1}{2}\varepsilon_r\varepsilon_0 E^2 \mathrm{A} \quad \Rightarrow \quad P_{es} = \tfrac{1}{2}\varepsilon_0 E^2 \quad \wedge \quad E = \frac{U}{l}$$

The well-known Paschen curve describes the electrical breakdown and discharge behavior. Due to the large gap (20 µm) and operation in atmosphere, the electrical field must be kept well below 20 MV/m. The corresponding force of approximately 0.4 mN should be sufficient, but uncertainties in the achievable field strength and expected load (e.g. due to squeeze film damping) might still prove this to be wrong.

MEASUREMENT

For closed loop control a feedback signal is required. The integrated electrodes provide a capacitive sensor, which only requires some additional amplification circuitry to measure the change in capacitance as a function of deflection and displacement. The measurement signal will be superimposed on the actuation voltage. As the measurement bandwidth should preferably be at least 10x higher than the closed loop bandwidth of the MEMS device, and the carrier signal frequency should preferably be at least 10x higher than the measurement bandwidth, the amplifiers should be able to measure capacitances of the order of e.g. 10^{-13} F at 150 kHz. This is not easy to accomplish, but feasible when dedicated amplification circuitry can be integrated close to the electrodes.

DESIGN

Some important dimensions and materials selected for our design are summarized in *TABLE 1*.

TABLE 1. Geometrical properties

Mirror	Silicon	Ø 800 x 20 10^{-6} m
Pole	Silicon	Ø 50 x 20 10^{-6} m
Diaphragm	Silicon-Nitride	Ø 200 x 0.3 10^{-6} m

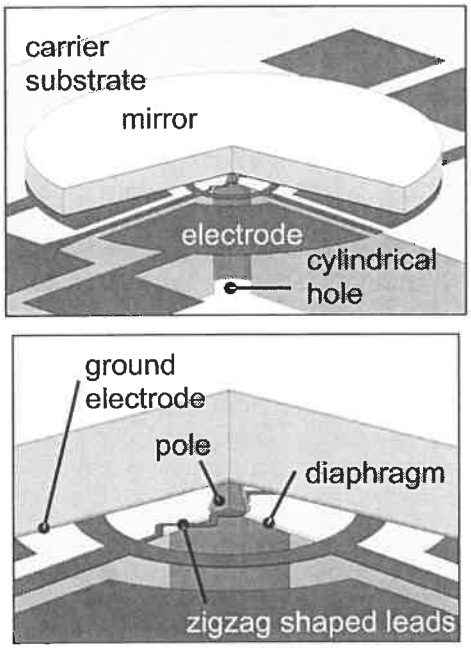

FIGURE 3. Cut out of MEMS device

A cut-out of the design is depicted in *FIGURE 3*. Please note these bodies:

- the thin Silicon-Nitride (SiN) layer spanning the hole in the carrier substrate to create a membrane,
- the leads across the diaphragm which are zigzag shaped to avoid adding stiffness to the diaphragm,
- the rigid mirror-disc and mirror-pole form one uniform body which is connected to the ground electrode at the bottom of the mirror with the ground leads on the diaphragm.

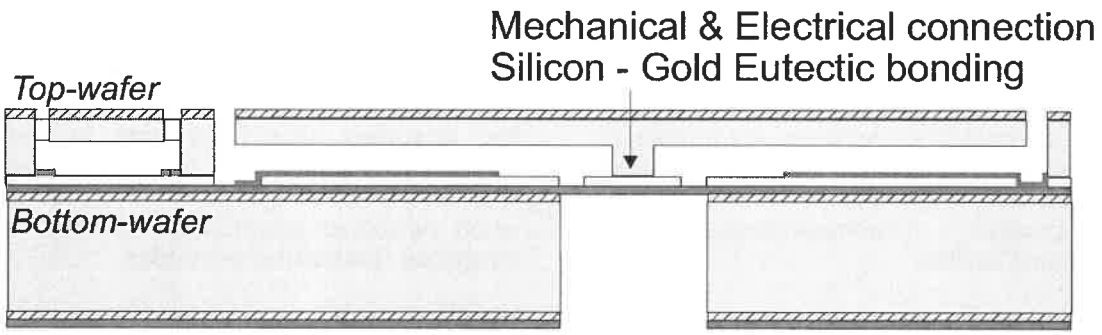

FIGURE 4. Cross view of micromirror

PROCESSING

In short, the presented micromirror consists of two silicon wafers which are structured and combined using micromachining technology. This includes photo-lithography, Reactive Ion Etching (RIE) techniques, Eutectic bonding and wafer grinding techniques.

In the top-wafer, see *FIGURE 4*, the mirror-body and pole are formed using RIE etching with an intermediate Silicon-oxide layer to stop the RIE in time.

The bottom wafer is used as a substrate or carrier for the micromirror. On the surface several layers are grown, deposited and structured to form the SiN membrane and the gold (Au) -electrodes for electrostatic actuation.

An important aspect is the formation of a ground-electrode, an Au-island with diameter of ~ 70 µm, which is to be connected mechanically and electrically with the pole of the micromirror, i.e. the Si-Au eutectic bonding. It is this Si-Au eutectic bonding process which is the most critical process in the whole process outline.

The eutectic bonding process itself is quite conventionally used among other techniques for packaging and hermetic sealing of microdevices. For our fabrication process it seems most likely to consider Si-Au eutectic bonding above bonding through e.g. conductive adhesive or thermo-compressive bonding (Au-Au). So far, the surface treatment and process parameters as temperature and time seem to be the most critical aspects to apply this process at 6"-wafer-level.

RESULTS

Our preliminary eutectic bonding results are promising. *FIGURE 5* shows an example of a silicon pole of a micromirror successfully bonded to the Au-electrode. The two wafers were mechanically separated for closer inspection of the wafer-level bonding. This result shows that the Si-Au bond at this position is stronger than the breaking strength of the monocrystalline pole.

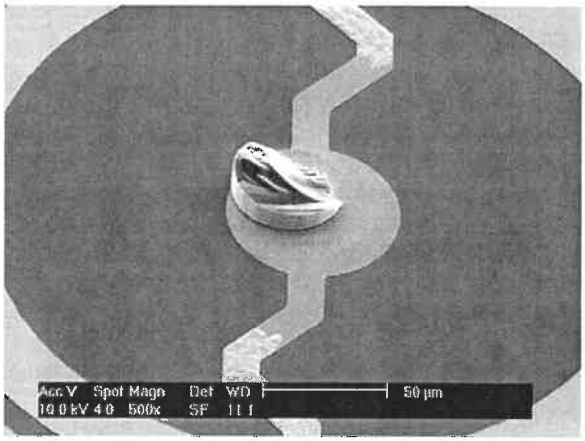

FIGURE 5. Example of a silicon pole of the micromirror bonded to the Au-electrode.

Current development is focusing on the Si-Au eutectic bonding and the appropriate bonding machines and parameters. Other bonding processes will be considered as well. However, it is expected that the results presented here will lead to the continuation of the remaining final steps of the fabrication process of the micromirror. The holes for the membrane need to be etched and the micromirrors need to be release-etched by RIE-etching to obtain movable 2-DOF deflection micromirrors.

FABRICATION OF 50nm LEVEL MASTER WITH A SPIRAL PATTERN FOR OPTICAL STORAGE MEMORY USING E-BEAM LITHOGRAPHY

Oh, S.-H.[1]; Jeong, M.-Y.[1]; Je, T.-J.[2]; Yoo, Y.-E.[2] and Choi, D.-S.[2]

[1] Department of Nano Science and Technology
Pusan national University
Korea
[2] Nano Mechanical Systems Research Center
Korea Institute of Machinery & Metals
Korea

INSTRUCTIONS

In order to satisfy the demand for increasing data capability, the further research will be focused on reducing the size pattern down to 50nm level. Recent optical storage memory pattern is fabricated using optical lithography, but it is very difficult to manufacture patterns fewer than 50nm scale because of limit of optical diffraction[1]. Therefore, electron beam lithography is required for the optical storage memory pattern with 50nm level. General patterning researches for storage memory with 50nm level using e-beam lithography were contents of orthogonal arrangement and continual circle arrangement. But, spiral pattern with repeated line will be required for optical storage memory such as DVD. However, existing study for this pattern is very rare.

We manufacture the software program to generate a discontinuous spiral pattern. Based on this program, we design the spiral pattern with line lengths of 50nm, 100nm, 150nm, 200nm and width of 100nm. And to fabricate the designed pattern using e-beam lithography, we consider the scattering effect of e-beam and the condition of development. Firstly, we perform the experiments with several parameters such as accelerating, aperture size and dose to optimize the exposure condition and minimize the scattering of e-beam and writing time. Also we find the optimum development process condition with development time and temperature to solve the swelling and bridging problems.

Through the several experiments, we acquire spiral patterns on HSQ resist for optical storage memory having small difference below 3% precision compared to the designed pattern. The fabricated ER master can be used as template for electroforming.

THE SPIRAL PATTERN DESIGN FOR OPTICAL STORAGE MEMORY

We devise the self-made program which can design the spiral patterns for original master fabrication with 50nm level. The design of a spiral pattern is stored in ASCII format and this ASCII file can be compatible with commercial program such as RAITH 150[2]. All unit lines in nanometer scale on a spiral curve are designed as the straight lines for short processing time and convenience of design.

The unit line consisting Point 1(x1, y2) and Point 2(x1, y2) is decoded as shown in Fig. 1(b). Fig. 1(c) displays the meaning of Fig. 1(b). Here, The form of "L 100 1 0" corresponds to Line, Dose percent, Layer number, Line thickness

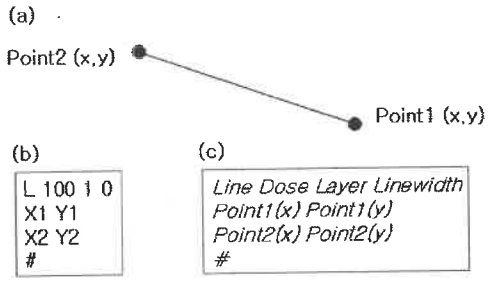

FIGURE 1. Defining a unit line for E-beam writing, (a) a unit line and (b) the corresponding codes in RAITH program and (c) the meaning.

The whole region of patterns is obtained by repeating a respective line design. Using the angle for 50nm line as unit angle for one cycle and the finely increased inner radius related with track pitch, we calculate the pattern length, pitch, starting point and ending points. Through this method, we make the spiral pattern to be made up of four discrete lines with a pitch of 100nm

and a length of 50nm, 100nm, 150nm, 200nm respectively.
Fig. 2 shows the window panel of the program to define the exposure area for a spiral pattern with the period of 4 lines. The input parameters are the inner radius and the number of cycles. The designated patterns can be created as an ASCII format by pressing the button of "create"

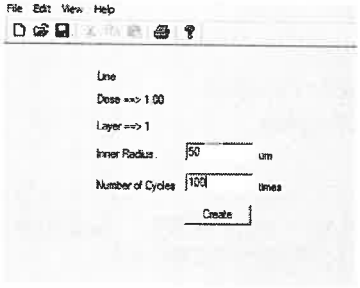

FIGURE 2. The window input panel for a spiral pattern design.

Fig.3 shows the results that display designed pattern to windows using RAITH program. There is no problem to compose the spiral pattern with designed 50nm~200nm straight lines.

(a) the whole area.

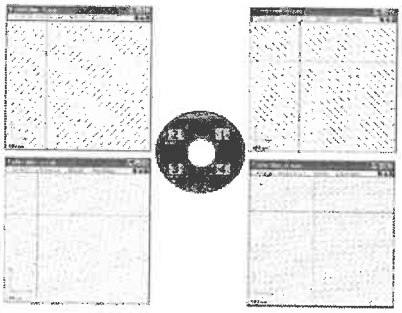

(b) the four different sections of the digitized spiral patterns.

FIGURE 3. The pattern array displayed from an ASCII design file.

EXPERIMENT

We use the commercial form of HSQ(Flowable Oxide resist-12 from Dow Coring) to fabricate positive patterns. Firstly, the HSQ layer on the silicon substrate is coated in a very thin layer of 50nm for the high contrast and the short exposure time(4000rpm/s, 45sec). Then it is pre-baked on a hotplate at 200℃ in order to eliminate the solvent excess and compact the resist. The e-beam lithograpy is performed using Raith 150. The working distance between resist and objective lens is 7mm and the step size is 3.2nm. After the exposure, HSQ resist is developed by TMAH 25% for 45sec at 21℃. Then it is rinsed by the DI water.
As the design and the size become denser and smaller, the scattering effect of e-beam comes to a barrier for clear pattern resolution[3]. To overcome the scattering of e-beam, the design of pattern is modified and optimized by applying 10 to 20 % expansion compared with the original design[3]. But, this spiral pattern by proposed program is difficult to modify the feature size in design. So we need to optimize the condition of exposure and development for desirable designed pattern without blurring. The dose to affect the feature size and uniformity is depended on beam current, dwelling time and field size. Here, the beam current is decided by EHT and aperture size; and the dwelling time is related to the step size. Therefore, the condition of exposure is optimized by controlling important parameters such as EHT, aperture size to precisely fabricate the designed spiral pattern. In order to optimize the expose condition, we perform several experiments with several parameters such as accelerating, aperture size, dose. Also, to solve problems with scum, swelling and bridging between features for development, we try to search the optimum development condition by controlling time and temperature.

THE OPTIMIZATION OF EXPOSURE AND DEVELOPMENT CONDITION

To analyze the effect of EHT, aperture size and dose in designed pattern fabrication, we performed the e-beam lithography with the properties such as aperture size, EHT and dose set as 10 or 30, 20kV or 10KV and within a range of 1500μC/cm and 3100μC/cm respectively. The experimental results are shown in Fig. 4 and Fig. 5. When the EHT is 10kV, the variation of pattern shape and scale do not appear for aperture size. Whereas, in case of the 20kV EHT and the 10 ㎛ aperture size, the exposed HSQ residual layer at the center is existed in undesirable area due to the

scattering of e beam. But, in the 30 ㎛ aperture size at the 20kV, the same problem does not arise within a range between 2500μC/cm and 2900μC/cm. Hence, we can produce an improved result in terms of uniformity and precision. The reason for the above is caused by the relationship among aperture size, the current and the dwelling time(As the aperture size increases, the current also increases and the dwelling decreases). When EHT is 10kV or 20kV and dose is 1500 μC/cm, we acquire the designed pattern with high precision. But, this process condition has the limit of throughout due to long exposure time and low beam speed.

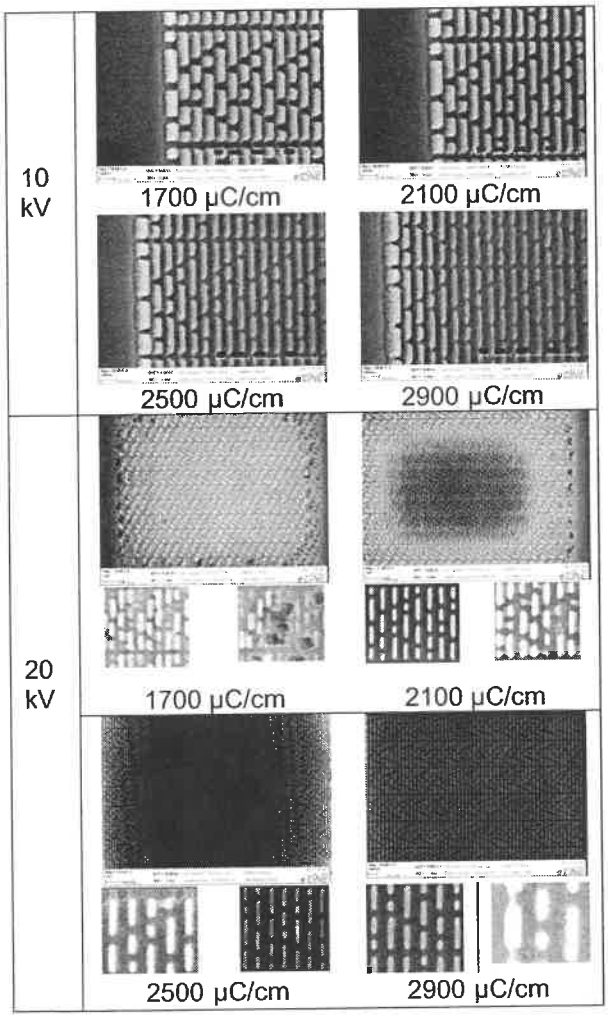

FIGURE 4. The pattern results according to EHT in the 10 ㎛ aperture size.

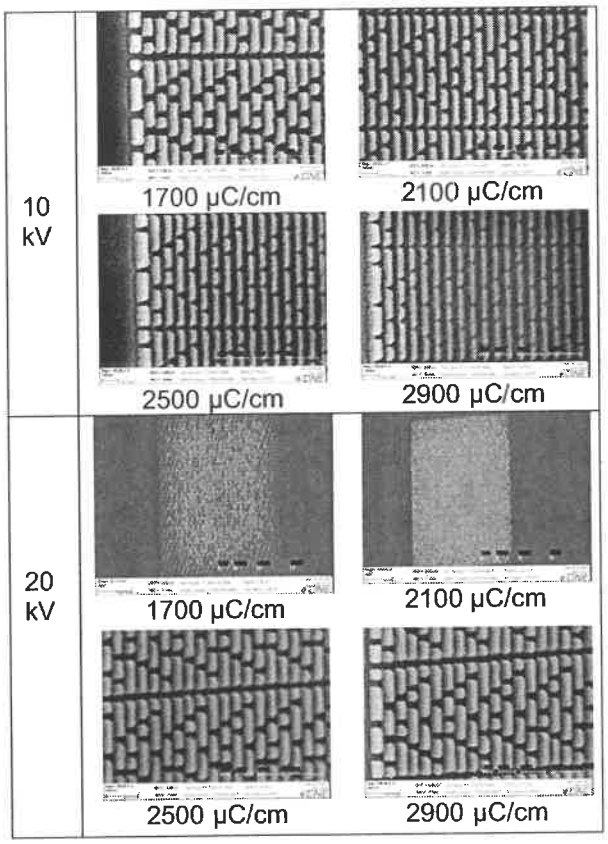

FIGURE 5. The pattern results according to EHT in the 30 ㎛ aperture size.

We study the optimum development process condition with development time and temperature to solve the swelling and bridging problem as shown in Fig. 6(a) and (b). These problems can be solved by optimizing development time and temperature such as 45 sec and 45 ℃ respectively.

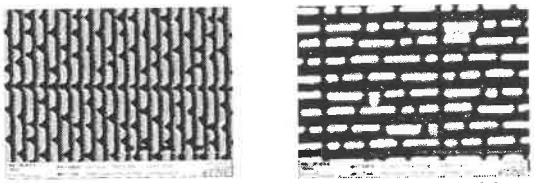

(a) swelling problem: *(b) bridging problem.*

FIGURE 6. The problem of development in HSQ negative resist.

THE FABRICATION OF DESIGNED SPIRAL PATTERN FOR STORAGEM MEMORY MEDIA

The parameter is set to the following:

Dose is 2700 μC/cm, EHT is 20kV, aperture size 30um, develop time is 45sec, development temperature is 45℃

Through the results of exposure and development condition test, we can precisely fabricate the discontinuous line pattern with orthogonal array within 3% precision as shown in Fig. 7.

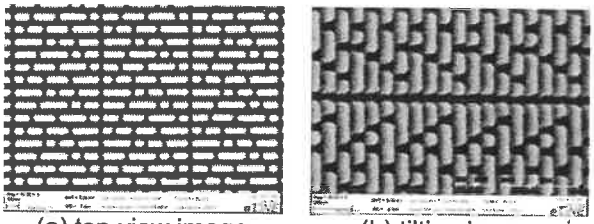

(a) top view image (b) tilting image

FIGURE 7. The optimized discontinuous line pattern with 50nm scale using the e-beam lithography.

Based on the optimized exposure and development condition, we fabricate the designed spiral pattern with inner radius 80 ㎛ and outer radius 160 ㎛. Fig. 8 shows the fabrica ted spiral patterns taken at four different sections after development. And the fabricated spiral pattern can be out of range from small difference below 3% precision compared to the designed pattern.

The fabricated ER pattern master using e-beam lithography will use as template to make a Ni stamp for injection molding.

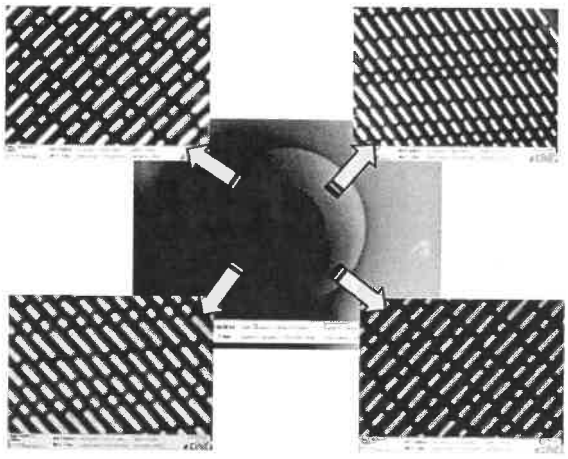

FIGURE 8. The FE-SEM image of discontinuous spiral pattern.

CONCLUSION

We develop the original master fabrication of spiral pattern with periodic array. For this, we devised self-programmed software which can design the spiral patterns to be made up of 4 discrete lines. This program can overcome the problem that is impossible in the commercial pattern design program for e-beam lithography or other CAD softwares.

Also, we fabricated the original ER master below 3% precision through the optimum process conditions for e-beam lithography and development.

REFERENCES

[1] Seo, Y. H., Choi, D. U., Lee, J. H., Yoo, Y. E., Je, T. J. and Whang, K. H., "Fabrication of Nanoscale Reusable Quartz Master for Nano Injection Molding Process," Trans of KSME(A), Vol. 29, pp. 228, 2005

[2] http://www.raith.de.

[3] Ampere A. Tseng, Kuan Chen, CHii D. Chen, and Kung J. Ma, Electron Beam Lithography in nanoscale fabrication Recent Development. IEEE 2003. VOL. 26. No. 2,

[4] M. Osawa, K. Takahashi, M. Sato, and H. Arimoto, Proximity Effect Correction Using Pattern Shape Modification and Area Density Map for electron beam projection Lithography. J. Vac. pp. 2483-2487

PRECISE MICROMOLDING OF PATTERNED SILICONE LAYERS FOR FORMATION OF PLATING INSTANT-MASKS

Gang Zhang
Echemics
Monterey Park, California, USA

1. INTRODUCTION

EFAB (Electrochemical Fabrication) is a multi-layer-based electrochemical microfabrication technology for the manufacture of truly 3-D metal microdevices [1-3]. The EFAB process flow is shown in Fig. 1 where a pattered layer of a first metal is selectively electrodeposited onto a substrate with instant-mask (IM) plating (Figs. 1a and 1b). In Fig. 1c, a second metal is blanket-electrodeposited over the first metal and the substrate to form a composite layer. The entire composite layer is planarized to achieve precise thickness and flatness (Fig. 1d). The above steps are repeated to form a multilayer structure (Fig. 1e). Then one of the two metals is etched from the multilayer structure to yield a desired 3-D microdevice shown in Fig. 1f. Fig. 2 shows a 12-layer nickel microchain made with EFAB, which has 14 independently-movable links (290 μm wide and 500 μm long) and a total thickness of ~ 100 μm.

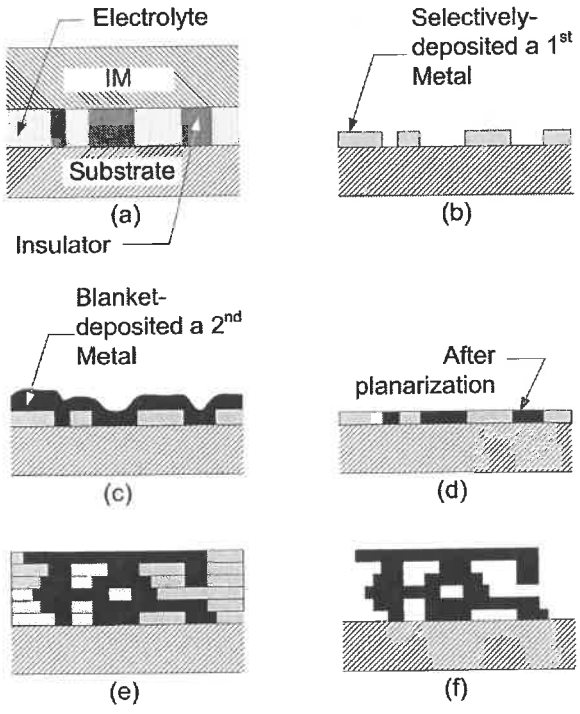

Figure 1. EFAB process flow.

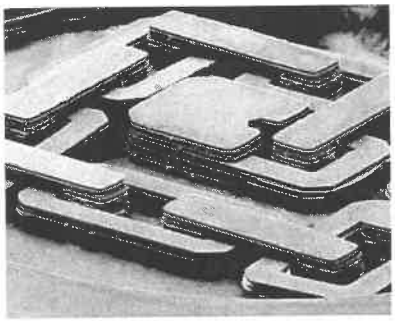

Figure 2. 12-layer nickel micro-chain made with EFAB.

In EFAB, an IM is used in IM plating to selectively electrodeposit a patterned layer of metal microstructures on a substrate (Fig. 1a-1b). An IM comprises a patterned conformable insulator layer on a supporting substrate. For example, a copper IM (Cu-IM), one type of IM, may comprise a patterned silicone layer supported by a copper substrate. The copper substrate acts as both a mechanical support for the silicone layer and an anode during IM plating. Cu-IMs can be used to produce patterned copper microstructures.

This paper presents a precise micromolding method for making the Cu-IM. The performance of the Cu-IM is also discussed.

2. COPPER INSTANT-MASK FABRICATION

The fabrication of the Cu-IM refers to the formation of a patterned conformable insulator layer on a copper substrate. In this study, Cu-IMs were fabricated by using a micromolding technique. Fig. 3 shows the Cu-IM fabrication process flow.

The first step is to fabricate a photoresist micromold on a silicon wafer by using a photolithography process (Fig. 3a). In this work, the photoresist, SU-8 (MicroChem), was applied and patterned on 3" silicon wafers. SU-8 is an epoxy-based negative photoresist that can serve as an excellent micromold material. A spin-speed of 700 rpm and a UV exposure of 70-80 mJ/cm^2 were used to apply and pattern SU-8 to

obtain 30 μm thick mold layers. Fig. 4a shows an SEM photo of part of a beehive pattern on a silicon wafer. Note that the minimum resolution of the mold in Fig. 4a is down to 12 μm.

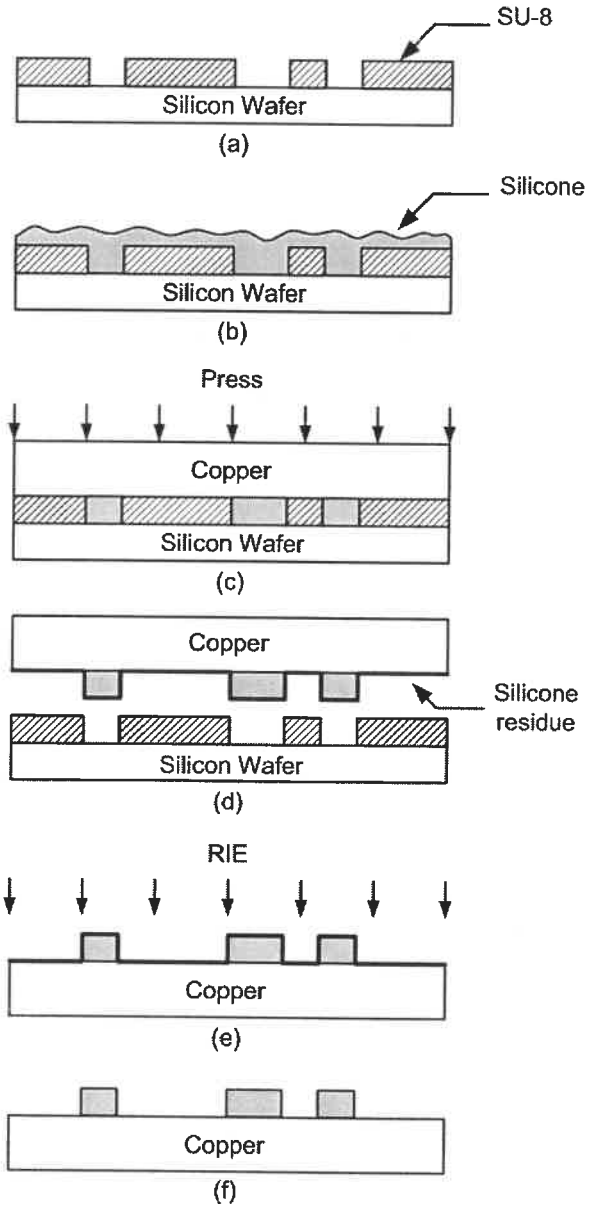

Figure 3. Cu-IM fabrication process flow.

The second step is to apply a liquid silicone over the micromold (Fig. 3b). Before applying the silicone, the SU-8 mold was first passivated with a silane, tridecafluoro-1,1,2,2-tetrahydrooctyl)-1-tri-chlorosilane, in a vacuum desiccator pumped down to 28" Hg. The passivation process took about 2 hours. The formed silane layer on the mold functions as a releasing agent for the demolding of the silicone from the mold.

The silicone used in this study was Sylgard 184 silicone elastomer (Dow Corning). It is a two-part liquid product comprised of liquid base and curing agent. The two components were first well mixed. The mixture was then degassed in a vacuum desiccator at 28" Hg until no air bubbles were seen. Finally the silicone was slowly poured over the mold and, if necessary, was degassed again.

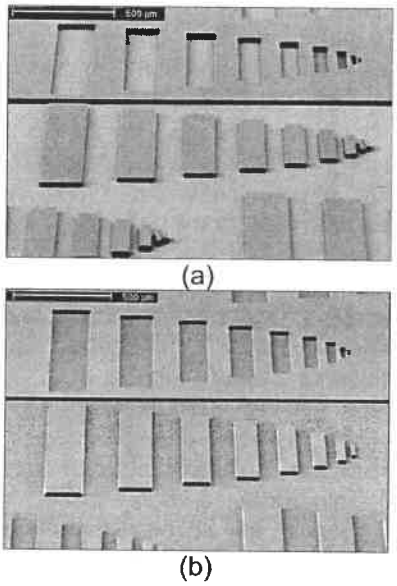

Figure 4. (a) Part of an SU-8 micromold and (b) part of a Cu-IM made from the SU-8 micromold.

The third step is to press a flat and smooth copper substrate on the micromold filled with the silicone (Fig. 3c). High purity (99.95+%) OFHC (oxygen free high conductivity) copper disks (Goodfellow) were planarized to flat and smooth with diamond lapping down to 2 μm diamond slurry. The diameter and thickness of the disks were 25.4 mm and 5.2 mm, respectively.

To increase the adhesion between copper and silicone, an adhesion promoter, Sylgard Prime Coat (Dow Corning), was spun onto the cleaned copper disk at 1000 rpm for 30 seconds. After it was exposed in the air for 1-2 hours, the copper disk was placed onto the mold and pressed down and held with a custom fixture. The silicone was cured at 65°C for 6 hours in an oven.

The fourth step is to demold the copper disk with the patterned silicone layer from the micromold after the silicone has been cured (Fig. 3d). After demolding, there is a thin layer of silicone

residue (~ 5 μm) left on the copper disk, which must be removed to expose the underneath copper.

The last step is to remove the thin silicone residue with RIE (Reactive Ion Etching), a dry plasma-assisted etching process (Fig. 3e). The RIE gases were CF_4 and O_2. Their flow rates were set at 125 mtorr. The RF power was set at 250 W. The pressure of the vacuum chamber was around 400 mtorr. The silicone etching rate was measured at ~1 μm/min. As RIE etches all exposed silicone isotropically, a 30 μm thick silicone layer will be roughly 25 μm thick after RIE if the silicone residue is around 5 μm thick. After RIE, a Cu-IM is now ready for use shown in Fig. 3f.

An SEM photo of part of a Cu-IM made from the SU-8 micromold (Fig. 4a) is shown in Fig. 4b. For the positive silicone features (islands in the picture), the minimum resolution can go down to 25 μm. The smallest 12 μm wide features were lost due to the mechanical demolding process. On the other hand, the negative silicone features can reach 12 μm resolution.

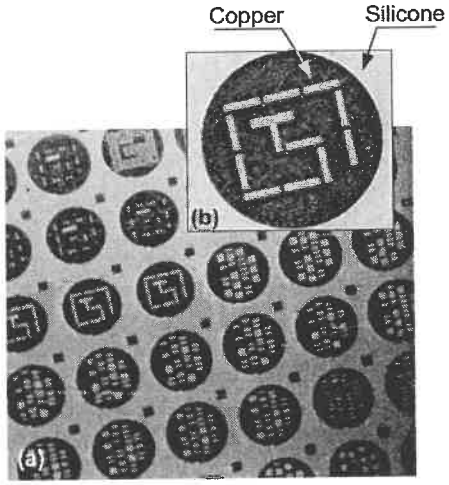

Figure 5. (a) Top view of a Cu-IM comprising a group of submasks and (b) top view of one of the submasks.

An IM usually comprises a group of submasks, each of which represents one layer of a multilayer structure such as shown in Fig. 1e. Fig. 5 shows one example of a Cu-IM with 56 submasks on a 25.4-mm diameter copper disk in which each submask has a diameter of 1.2 mm. The SU-8 micromold can be reused after cleaning and removing the silicone residue. However, the mechanical demolding process gradually weakens and damages the adhesion between SU-8 and silicon wafer with time. Therefore, the SU-8 mold has a limited service life.

3. COPPER INSTANT-MASK PERFORMANCE

In IM plating, a Cu-IM is immersed in a copper plating bath. A substrate is pressed on a mask or submask. The plating solution is trapped in the openings of the silicone layer. The experimental setup of IM plating is described in elsewhere [4]. A predetermined plating current is applied between the copper (anode) and the substrate (cathode). A patterned copper layer can be instantly realized on the substrate after unmating the substrate from the Cu-IM. Fig. 6 shows one example of a patterned copper deposit on a nickel substrate. Fig. 6a shows a close-up view of some features of a submask. The corresponding copper deposit after IM plating is shown in Fig. 6b. Fig. 6c shows the whole copper deposit from this submask. The copper deposit thickness is ~12 μm.

Some important performance of the Cu-IM was investigated and is summarized as follows.

3.1 Silicone Sealability

The role of silicone features on the Cu-IM is to mechanically mask the area of a substrate where a copper deposit is not required. If the silicone cannot seal the area very well, a extraneous copper deposit or flash would form underneath the silicone features, which could delaminate multi-layer structures during the etching of copper which serves as a sacrificial material.

The results of IM plating testing indicated that with a proper mating pressure (> 20 psi) the silicone mask can perfectly define non-copper deposit areas without copper flash.

3.2 Adhesion of Silicone on Copper

The adhesion strengths between the silicone and polished copper disks (12.7 mm diameter and average roughness R_a <0.2 μm) were measured with and without Sylgard Prime Coat The test results indicated that the tensile bonding strength with Sylgard Prime Coat was more than two times bigger than the one without the primer. The adhesion strengths were 154.7 kPa and 62 kPa, respectively [2].

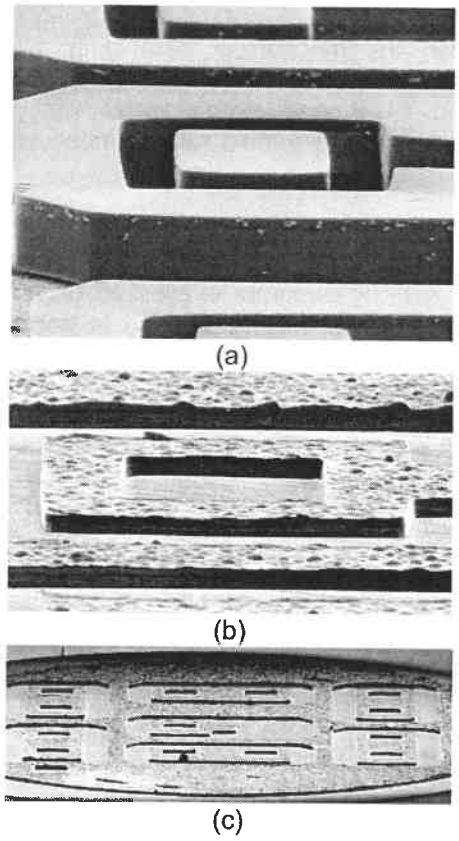

Figure 6. (a) Close-up view of some features of a submask, (b) corresponding copper deposit after IM plating, and (c) whole copper deposit from this submask.

3.3 Silicone Deformation Under Pressure

The silicone is an elastic material which can well mask a substrate without copper flash under a proper mating pressure. However, the silicone at the mating pressure must not be significantly distorted since plated copper features will exactly copy a distorted silicone mold.

The silicone deformation test indicated that the silicone compression was 1.2-1.6 μm vs. 40-45 μm thick silicone at normal operating pressure (35 psi) for a silicone area between 7.4 and 19.6 mm^2. This compression is small and acceptable. In addition, the test also indicated that the silicone is able to return to its original position after unmating, which is important for multiple use of the Cu-IM. The detailed deformation test method is described in elsewhere [2].

3.4 Silicone Delamination in Plating Bath

The interface between silicone and copper in the Cu-IM is the weakest link. The Cu-IM is used in the copper plating bath which, however, attacks the interface chemically and electrochemically. Thus, the adhesion of silicone features to the copper substrate gradually decreases and finally the silicone features are delaminated from the copper substrate due to total loss of adhesion. The Cu-IM has a limited use life even in a copper pyrophosphate plating bath which is the least corrosive bath among copper plating baths.

Proper copper surface modification can be used for extending the use life of the Cu-IM. For example, the copper substrate can be treated in a benzotriazole (BTA) solution to form a protective polymeric film on the copper substrate prior to the application of the silicone on the copper substrate [5-6]. BTA-treated Cu-IMs exhibit much better delamination resistance to the attack than untreated ones.

ACKNOWLEDGMENTS

This work was done at the University of Southern California (USC) and was primarily supported by the Defense Sciences Office of the Defense Advanced Research Projects Agency (DARPA) under the Mesoscale Machines program. The author wishes to thank the EFAB team members for their support.

REFERENCES

[1] Cohen A, Zhang G, Tseng F, Mansfeld F, Frodis U, Will P. In: Proceedings of the 12th IEEE Micro Electro Mechanical Systems Workshop. 1999. p. 244-251.

[2] Zhang G. EFAB: A Novel, High-Aspect-Ratio True 3-D Microfabrication Process for Rapid, Low-Cost Desktop Micromachining of MEMS. Ph.D. Dissertation. University of Southern California; 1999.

[3] Zhang G. Electrochemical Microfabrication for High-Aspect Ratio 3-D Microstructures. Journal of Applied Surface Finishing. 2006; 1(2): 116-126.

[4] Zhang G. Monitoring of Instant-Mask Plating for Fabrication of Patterned Copper Microstructures. ECS Transactions. 2006; 3(10): 325-335.

[5] Zhang G. Applications of Metal Surface Modification in Microdevice Fabrication. ECS Transactions. 2005; 1(3): 3-16.

[6] Zhang G. Electrochemical Deposition with Enhanced Uniform Deposition Capabilities and/or Enhanced Longevity of Contact Masks. U.S. Patent Application Number 20040065551; 2004.

FAST LONG RANGE ACTUATOR (FLORA)

Qunyi Chen, Thomas A. Dow, Kenneth Garrard and Alex Sohn
Precision Engineering Center, NC State University
Raleigh, NC

INTRODUCTION

Diamond turning (DT) has revolutionized the fabrication of optical surfaces for consumer, defense and science applications such as contact lenses, forward-looking infrared radar and infrared spectrometers. It has made this impact not only because it can accurately and rapidly fabricate diffractive, refractive and reflective optical surfaces, but also because it can create reference features tied to the optical surfaces to assist in the assembly process. An emerging trend in optical design is the use of Non-Rotational Symmetric (NRS) surfaces to reduce complexity, bulk and weight while improving optical performance. To create these so-called freeform surfaces, DT machines have been operated at very slow spindle speeds or modified with a piezoelectric Fast Tool Servo (FTS) or a flycutter. The proposed Long Range Actuator (FLORA) integrates existing technologies (air bearings, linear motors, high-resolution encoders and real-time control) into a lightweight, moving tool holder that can be retrofitted onto a conventional DT machine.

The goal of the FLORA is to create optical quality surfaces while moving the tool over a range of ± 2 mm at a frequency of 20 Hz. The technical challenges include:

Form Error Diamond turning machines can create excellent form fidelity because of their stiff, linear slides and air-bearing spindles. Reducing the moving mass will improve the bandwidth of the system but also make it more susceptible to disturbances.

Surface Finish Simple theoretical relationships between machining parameters (spindle speed, axis velocity) and tool geometry can be used to predict surface finish. However, the dynamic conditions envisioned for the FLORA may play a more significant role.

SYSTEM DEVELOPMENT

A prototype FLORA was built during 2004 and has continued with support from NSF. The FLORA has a light-weight honeycomb triangular piston, a linear motor and a high-resolution linear encoder. The total range of motion of the motor is 50 mm but the goal is a stroke of 4 mm at 20 Hz. A photograph of the actuator is shown in Figure 1.

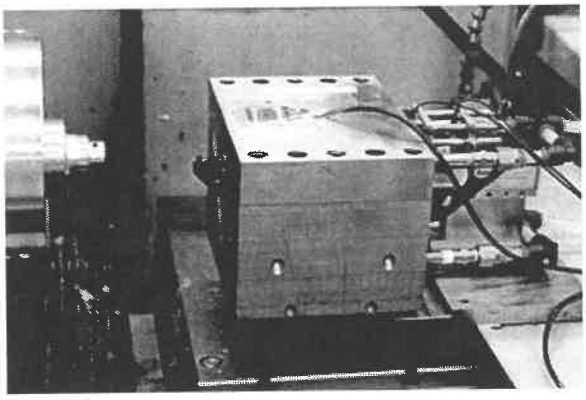

FIGURE 1. Photograph of the FLORA system mounted on the ASG 2500 DTM.

To improve the surface finish and figure error for this actuator, a number of changes to the electronic components were made over the previous design [1].

High-resolution encoder – A Sony glass scale encoder was added to provide piston position feedback with 0.25 nm resolution at speeds up to 750 mm/sec.

Linear Amplifier – An Aerotech linear amplifier BL10-80A is being used to drive the Airex linear motor. The amplifier has a maximum current output of ±10 Amps with a bandwidth of 2000 Hz. The motor can produce a peak force of 81 N.

Control platform – A PMDi controller has been installed that can provide an update time of 25 µsec or 40 Kz. This system uses an Analog Devices SHARC processor 40 MHz ADSP-21061L.

OPEN LOOP TRANSFER FUNCTION

The single DOF system shown in Figure 1 consists of moving piston in an air bearing (an undamped mass m), the actuating force $K_f I$ from the linear motor and the tool feeding position $z(t)$ from the linear encoder. Figure 2(a) shows the measured open loop system transfer function for output in mm to input in current to the amplifier. Figure 2(b) shows the result when the command

amplitude is modified to account for the mass inertia and in this case the transfer function is from mm command to mm motion. The peak in Figure 3(b) at 900 Hz is due to the analog current loop within the amplifier and motor. Additional resonance peaks above 1000 Hz are due to aerodynamic effects in the linear air-bearing.

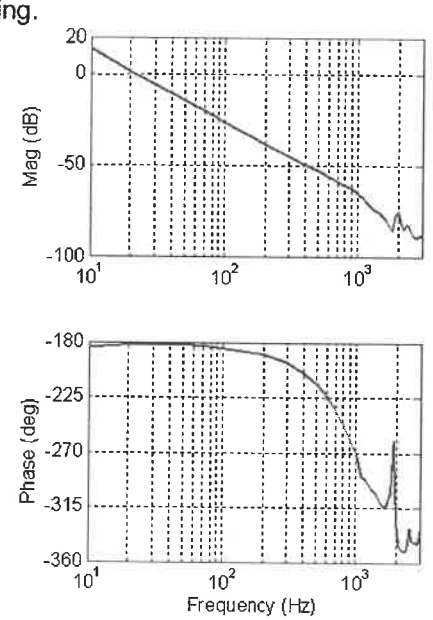

(a) from current command

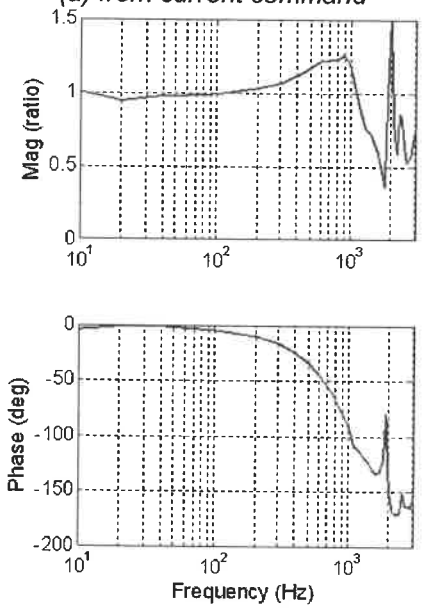

(b) Corrected for inertia

FIGURE 2. Commutated open loop system transfer functions

CONTROL SYSTEM DESIGN AND TESTING

The controller design is based on the measured open loop frequency response and desired closed-loop system performance specification. A PID controller (Equation (1)) was first designed due to its intuitive nature and the gains are determined by trial-and-error tuning process. A frequency design approach using a lag-lead controller (Equation (2)) was followed to obtain desired frequency response across the desired range of frequencies.

$$K_{PID}(z) = \frac{3321.1z^2 - 6518.9z + 3200}{z^2 - z} \quad (1)$$

$$K_{LL2}(z) = \frac{4355z^3 - 11928z^2 + 10878z - 3303}{2z^3 - 4.4197z^2 + 3.1516z - 0.73186} \quad (2)$$

A comparison of the theoretical closed-loop system frequency response is shown in Figure 3. These two controllers behave similarly in the frequency domain; that is, they increase loop gain at low frequency, add phase lead to obtain phase margin at the crossover frequency and lower the gain at high frequency. The transfer function in Figure 3(a) is for position command to the output position. It shows the closed-loop system has a bandwidth of 1122 Hz with the PID controller and 1594 Hz with the lag-lead controller. As a result, the closed-loop response for the lag-lead will be faster but with slightly larger overshoot. The sensitivity function in Figure 3(b) is a measure of the error in tracking commands at low frequencies and rejecting disturbances at high frequencies. The position error is (1-1/magnitude) in this graph and it shows results that would not be visible in Figure 3(a) especially at low frequencies. For a sine wave command using the PID controller at 20 Hz, the magnitude is -52 dB, the error is 0.25% and the amplitude ratio in Figure 3(a) is 0.9975.

It is important to make the sensitivity magnitude small and Figure 3(b) shows the typical trade-offs involved in feedback control design.

1. The lag-lead controller will minimize tracking errors and disturbance forces at frequencies lower than 1000 Hz. Below 100 Hz, the sensitivity magnitude from the lag-lead controller is about half that of the PID controller. Experiments with 60 Hz disturbance have verified this result.
2. Both controllers have nearly the same peak sensitivity magnitude but the lag-lead controller peaks at a higher frequency (1219 Hz) than the PID (875 Hz). This behavior will amplify disturbances above 1000 Hz.

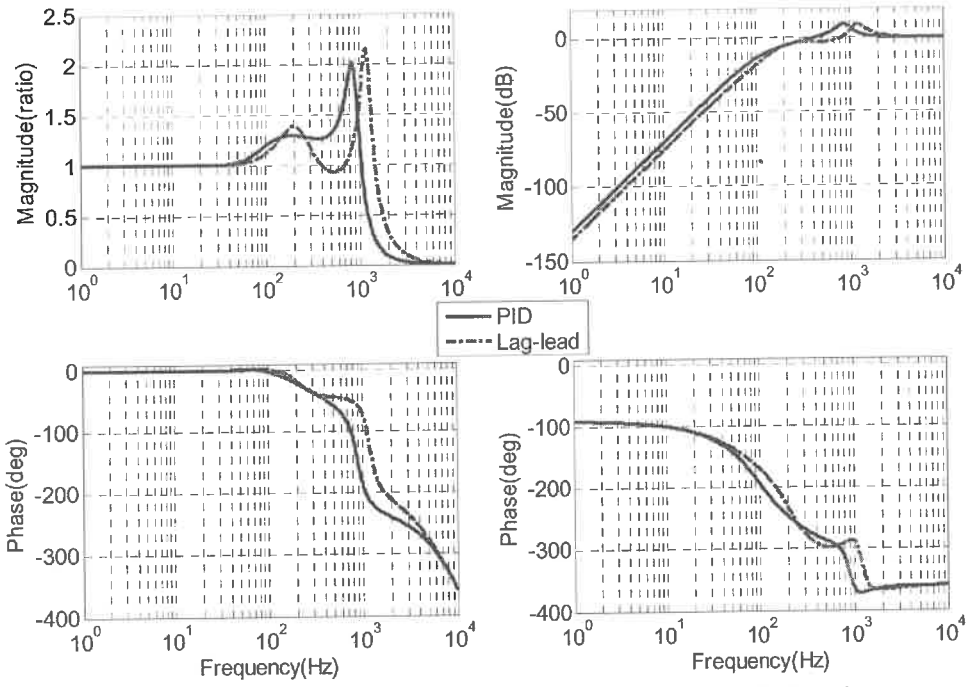

(a) Transfer function *(b) Sensitivity function*

FIGURE 3. Closed loop simulations for PID and Lag-lead controllers

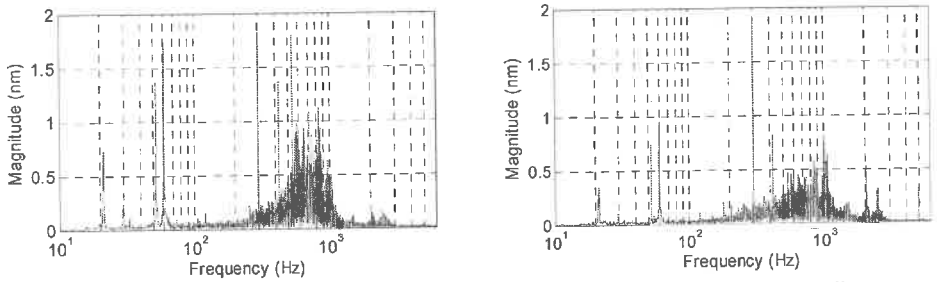

(a) PID controller *(b) Lag-lead controller*

FIGURE 4. Frequency spectrum of encoder data when holding position

The design process involves a compromise between reducing low frequency error magnitude and improving disturbance rejection at high frequency as shown in Figure 3(b). Figure 4 shows the frequency spectrum of the piston motion when holding position. Error for the PID controller is ±40 nm PP (10.8 nm RMS) and ±30 nm PP (8.0 nm RMS) for the Lag-lead. It is clear that the amplitudes are much smaller for frequencies less than 1000 Hz in the case of lag-lead controller.

With these two controllers design, additional studies on sensitivity function have been performed regarding the need for physical damping and most desirable piston mass.

1. Physical damping is not needed for FLORA designs. At high-frequency the amplitude is too small to generate useful forces and at low frequency the damping forces are high but are not needed and only lead to higher motor force.
2. When the magnitude of the sensitivity function exceeds 0 dB, the system relies totally on the mass to reject disturbances. In fact, the controller actually amplifies the disturbances at frequencies higher than crossover frequency (430 Hz for the PID controller and 830 Hz for the lag-lead controller in Figure 3(b)). As a result of the high frequency disturbance with current FLORA design and achievable controller design, the reduction of piston mass will

reduce the system disturbance rejection capability.

CUTTING PERFORMANCE

A flat surface was machined to test the ability of the FLORA piston to hold position while excited by the forces of machining. Figure 1 shows the FLORA mounted on the ASG-2500 DTM. The flat was machined with a 0.5 mm radius diamond tool at 500 rpm with a 2 mm/min feedrate (4 µm/rev) and 2 µm depth of cut on the finish pass. The theoretical finish is 4 nm PP. The Zygo NewView measurement in Figure 5 shows a 144×108 µm patch represents approximately 72 tool passes and has an average surface finish of 9 nm (RMS).

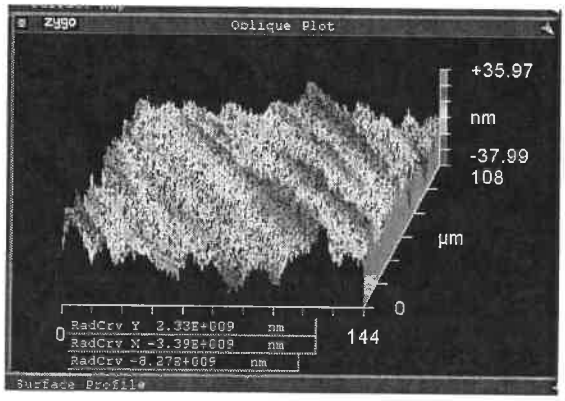

FIGURE 5. ZYGO image of surface finish (RMS=9.0 nm) on a plated copper flat

Table 1 compares the motion of the piston and the RMS finish of flat surface when the tool is locked or held in positioned by the control system. For the locked case, the air pressure was removing from the lower sides of the triangular piston but retaining the preload pressure. This is the same surface finish achieved under these conditions using a standard tool holder. Table 1 shows the piston motion as measured by the encoder. For the locked tool there is little piston motion but when the air bearing is turned on and the motor is used hold the piston, the motion is increased to 8 nm RMS for the Lag-lead controller and 13.1 nm for the PID. The surface finish is also increased when the piston is unlocked. The active closed-loop control using the Lag-lead algorithm adds 2.3 nm RMS to the surface finish and the PID adds 5.6 nm.

TABLE 1. Comparison of RMS error with a locked and position controlled tool holder

	Tool holding method		
	Piston Locked	Lag-lead controller	PID controller
Piston Motion, nm	1	8.0	13.1
RMS Surface finish, nm	6.7	9.0	12.3

CONCLUSIONS

The FLORA control system has been upgraded with a high-resolution encoder, a linear amplifier and a high-speed DSP based controller. The key conclusions are as follows:

1. High controller gain in the frequency range below 1000 Hz is needed to reduce tracking error at 20 Hz and reject cutting force disturbance at the natural frequency of the z slide of the DTM which is approximately 60 Hz. Improved performance could be achieved if the high frequency (>1000 Hz) dynamics within the FLORA can be minimized physically.
2. The feedback control design approach achieved reasonable performance over the range of frequencies of interest. It will be combined with feedforward control and other more advanced control approaches to improve the tool positioning performance.
3. The system changes discussed in this paper improved the position holding capability by 85% over the system described in 2006 [1].

ACKNOWLEDGEMENT

Principal funding for this work is by National Science Foundation grant DMI-0556209, monitored by G. Hazelrigg. PMDi assisted with the development of the control system.

REFERENCES

1) Buescher, N., Dow, T and Sohn, A., "Live Axis Turning", Proceedings of ASPE, Vol 37, 2006, pg 25-28.

ON A BEARINGLESS LINEAR MOTOR CAPABLE OF SELF–MAGNETIC LEVITATION

Woo-Yeon Kim[1], Seung-Jong Kim[1], Jong-Min LEE[1], Sung-Chong Chung[2] and Sang Jo Kim[3]
[1]Energy Mechanics Research Center, KIST,
39-1 Hawolgok, Seongbuk-gu, Seoul, 136-791, Korea
[2]Department of Mechanical Engineering, Hanyang Univ.
17 Hangdang, Seongdong-gu, Seoul, Korea
[3]Nano Motion Technology Co., Korea

ABSTRACT
In this paper, a bearingless linear motor is proposed, in which a mover can be magnetically levitated during linear movement without any magnetic bearings. In the structure of both-side linear motor, it is enabled by controlling the amplitudes of phase currents of both sides based on the variation of air gap. Thus, it is very efficient and compact. The feasibility of the proposed bearingless linear motor was experimentally investigated with the simplest controller.

KEYWORDS
Linear motor, Active magnetic bearing, Magnetic levitation, Bearingless motor

INTRODUCTIONS
Bearingless motor or self-bearing motor, which has been widely developed for artificial heart since 1990's, is a combination of electric motor and active magnetic bearing(AMB)[1,2]. It can, therefore, levitate as well as rotate its rotor by itself. Extending this concept, we propose a so-called bearingless linear motor(BLLM) in this paper. Namely, BLLM is a combination of linear motor and linear AMB, and it cannot only make a linear movement but also magnetically support the mover without mechanical contact. Thus it still possesses the well-known advantages of AMB such as no friction, no lubrication, good applicability into vacuum or clean environment, electrically controllable dynamics and so on. And further, it gets more compact and efficient, even compared with a linear motor with linear AMBs. Thus it is expected to be very useful in factories producing a semiconductor or large flat TV.
In this paper, we introduce a permanent-magnet (PM) type BLLM. After its structure and principle are explained, a simply designed control system and a prototype constructed for experimental verification are introduced. From some basic test results, it is found that the mover can successfully keep the stable levitation state even during movement.

STRUCTURE AND PRINCIPLE
Figure 1 shows a typical structure of PM-type BLLM which is similar to a conventional double-side linear motor. It consists of a stator having an elongated ferromagnetic core and a pair of PM arrays attached to the core so as to sandwich the core from upper and lower sides symmetrically, and a moving part with two sets of 3-phase windings to generate a traveling magnetic field along the lengthwise direction. When producing only the thrust force, the same phase currents flows in upper- and lower-side cores, just like the double-side linear motor[3]. Meanwhile, for levitation in vertical direction, the current amplitudes of the upper- and lower-side electromagnets should be different from each other. It is because a control current calculated depending on the variation of air gap between stator and mover is added to or subtracted from their nominal values which are corresponding to bias currents of general AMBs.
In the BLLM shown in Fig.1, 3-DOF motions are actively controlled: horizontal movement, vertical levitation and tilting(pitching) motion. For this,

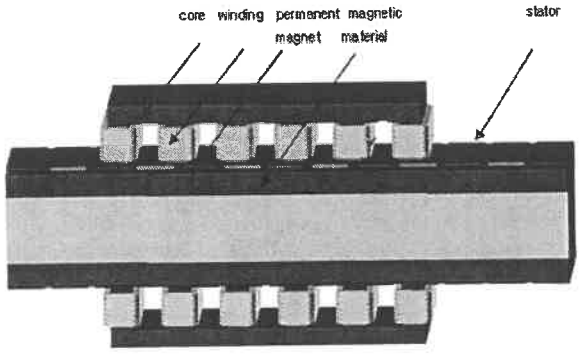

FIGURE 1. Schematic of the proposed BLLM

the windings of the mover are again divided to two groups(left and right), and thus, four winding groups comprised of three cores(i.e. a set of 3-phase winding) are independently connected with power amplifiers. When the mover is tilted in the clockwise direction in Fig.1, control current to make it return is added to the current amplitudes of upper-left and lower-right windings, and subtracted in the other windings. Or when the mover moves down, the upper two winding groups are activated to keep the levitated state. As mentioned before, there is neither linear bearing nor linear guide in this BLLM, however, at least two proximity probes and four-channel three-phase power amplifiers are newly required to supply control currents in the four groups of windings.

On the other hand, the other directional motions such as lateral movement, yawing and rolling motions are passively stable even without active control.

CONTROL SYSTEM

Although, in the real system, the thrust and levitation forces are strongly coupled with each other and nonlinear with respect to lengthwise movement or vertical displacement, we designed a simple PD-controller, ignoring such effects. It is because the purpose of this paper is to investigate the feasibility of BLLM. For this, we assume that the levitation(y-direction) force equation can be written as the following linearized form,

$$F_y = (K_y + K_{pm})y + K_{i_y} i_y \tag{1}$$

where K_{pm} and K_y are position stiffnesses defined as the variation of magnetic forces generated by PM and nominal phase currents, respectively, according to the displacement, K_{iy} is a current stiffness which is the variation of magnetic force according to the current, i_y, at nominal position(i.e. y = 0). Since Eq.(1) is widely used in the AMB analysis but for K_{pm}, the above assumption can be quite reasonable. However, it should be noted that the vertical magnetic force of Eq.(1) is a function of longitudinal position as well as y and i_y, because K_{pm} is so.

Now, the equation of vertical motion and the PD controller equation are expressed by the Laplace transformation as

$$\left\{ms^2 - (K_y + K_{pm})\right\} Y(s) = K_{i_y} I_y(s) \tag{2}$$

$$I_y(s) = -\left(\frac{K_d s}{\tau_d s + 1} + K_p\right) Y(s) \tag{3}$$

Equations (2) and (3) are also almost the same with the case of the conventional AMB using a PD-controller. However, because K_{pm} is an additive negative stiffness and the magnetic reluctance with respect to the electromagnets is relatively high due to the thickness of PMs, the

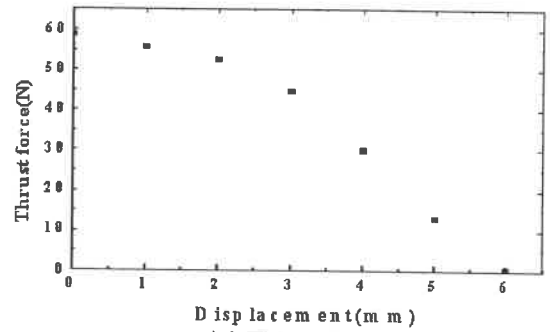

(a) Thrust force

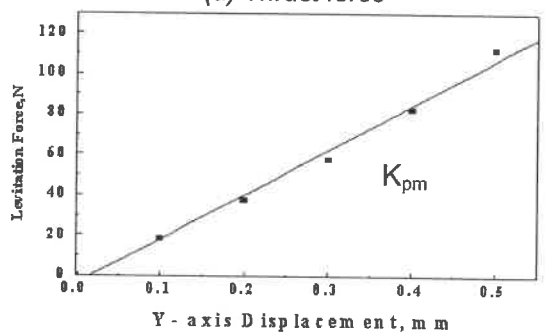

(b) Position stiffness by only PMs

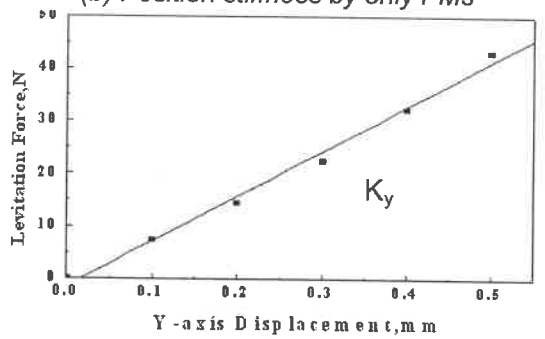

(c) Position stiffness without PMs

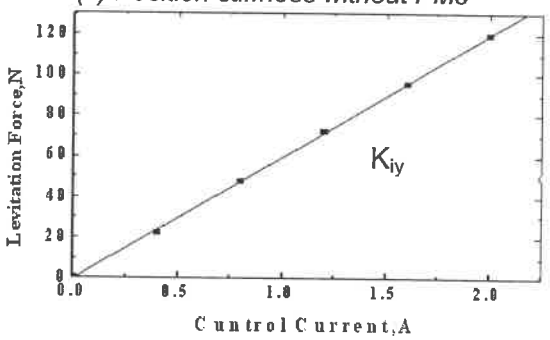

(d) Current stiffness

FIGURE 2. Results of FEM analyses

Table 1. Design specification

Parameter	Value	Parameter	Value
PM thickness	1mm	PM Residual Flux Density(Br)	0.6 T
PM Area	360mm^2	Pole Pitch	12mm
Core Area	60mm^2	Nominal Air Gap	0.6mm
No. Coil turns	200	Nominal Current Amplitude	2A

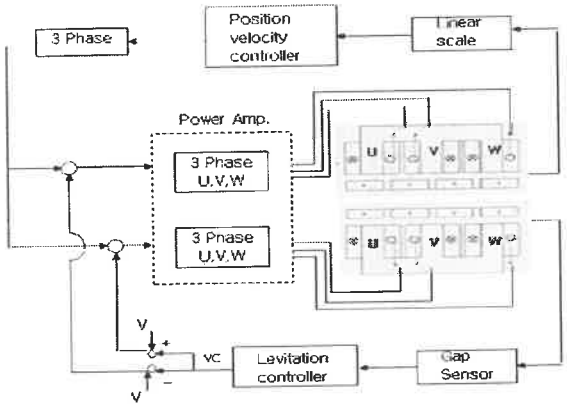

FIGURE 3. Block diagram of the system

levitation control of BLLM requires more efforts than AMB. To determine the control gains, we should first find the values of position and current stiffnesses, K_{pm}, K_y and K_{iy}. For this, FEM analysis was performed by using a commercial software, MAXWELL(2D). The parameters used in the analysis are listed in Table 1. Before finding the stiffnesses, we calculated the variation of thrust force according to the longitudinal position as shown in Fig. 2(a). When the amplitude of phase currents is 2 A, the maximum thrust force is about 60 N and as expected, the force becomes zero at 6 mm which is the half of the pole pitch. Figure 2(b) and (c) show the position stiffnesses, K_{pm} and K_y, which are defined as slopes of the approximated lines. Here, K_{pm} and K_y are about 1.54×10^5 N/m and 0.72×10^5 N/m. Since these results are for the case that the mover is in the longitudinal position where the thrust force becomes a minimum, the K_{pm} obtained above is the maximum value. Using this value in controller design is proper because it is the worst case. On the other hand, Figure 2(d) shows a current stiffness. In the figure, we can see that the relation is so linear and the slope is about 59.7 N/A.

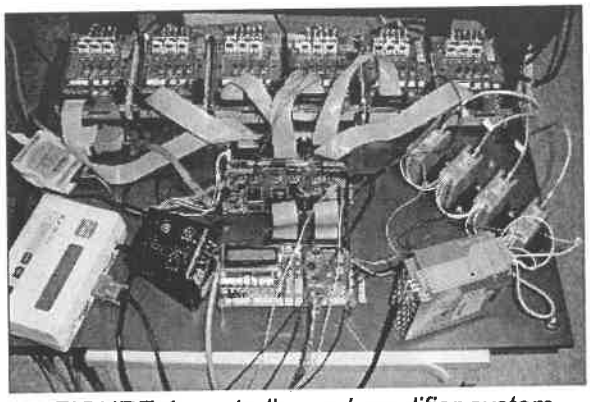

FIGURE 4. controller and amplifier system

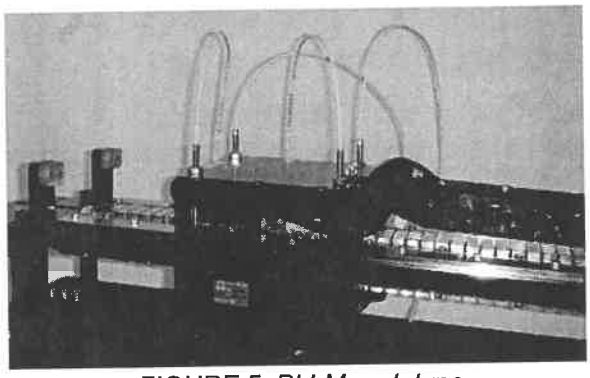

FIGURE 5. BLLM prototype

Through the stability analysis and time response simulation, the control gains, K_p and K_d, including the gains of sensor and power amplifier are determined as 8000 A/m and 23 A·sec/m.
Figure 3 shows the block diagram for levitation and linear motion control. The position signals measured by proximity probes and a linear scale go into each controller for thrust and levitation and then the controller outputs are combined and supplied to the windings of BLLM through a three-phase inverter. For this, we use the DSP board with a TMS320VC33 DSP chip and an IPM using IGBT(600V, 30A). The whole control system constructed in the laboratory is in Fig. 4. To experimentally verify the feasibility of the proposed BLLM, we made a prototype as shown in Fig. 5.

EXPERIMENT

Figure 6(a) shows the time response of the mover when the levitation controller is ON. Very quick and stable levitation is observed. Though the vibration is at that time, it is controlled for 0.25sec. And to verify stability for the outside impact, the test is carried out. In Fig. 6(b), the result is shown that it stabilized within 0.05sec. Add to this, the moving test for 1sec is represented in Fig. 6(c).

The vibration level is about 5 ~ 15μm during linear motion. It depends on the speed. Thus it is proved that the proposed BLLM can levitate and operate without any additive magnetic bearings or additive windings, although some proximity probes, a real-time controller and a multi-channel power amplifier are necessary.

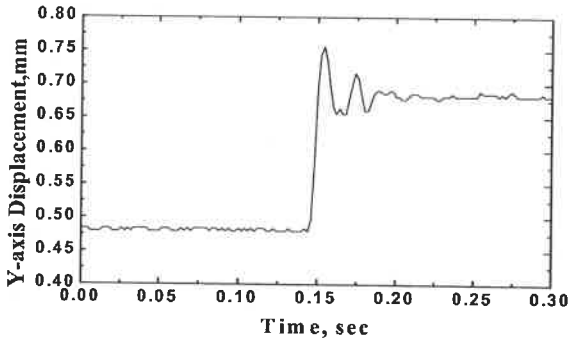

(a) Starting test

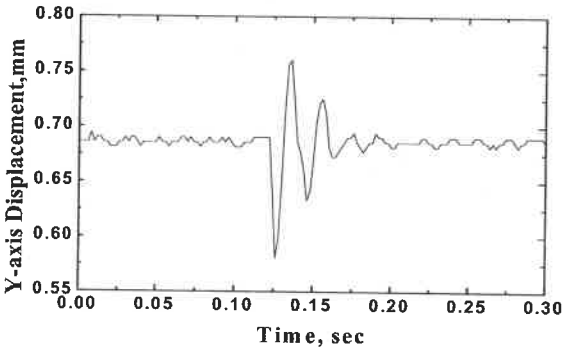

(b) Impact test

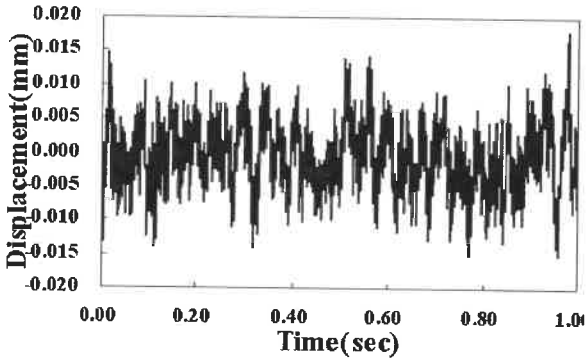

(c) Moving test

FIGURE 6. Results of the experiment

CONCLUSION

To improvement weak points of the bearing system in common linear motor, a new bearingless linear motor which is capable of self-levitation is presented in this paper. By use the concept of bearingless, it can operate non-contact without additive magnetic bearings which is certainly needed for supporting the mover in common linear motor. Thus BLLM can be high efficient and compact compared to the conventional linear motor. The mover of the prototype successfully levitated and moved by using very simple PD-controller. From experiment results, its feasibility confirmed, even though the vibration is larger than that of common linear motor. Considering that we used the simplest decoupled controller, the results demonstrate that the BLLM can work well and show that it can satisfy the conditions required to commercialize in further.

REFERENCES

[1] Seung-Jong Kim, Keisuke Abe, Hideki Kanebako, Yohji Okada and Chong-Won Lee. A Lorentz Force Type Self-bearing Motor with New 4-pole Winding Configuration. JSME International Journal (Series C). 2003; Vol. 46, No. 2, pp.349-354

[2] Seung-Jong Kim and Yohji Okada. An Axial-type Self-bearing Motor for Small Vertical Axial-flow Pump. *Journal of Sound and Vibration*. 2001; Vol. 11, No. 6, pp.223-232

[3] Sehwa Public. Linear Motor Application. vade-mecum. 1988

DESIGN OF A PRECISION SPECIMEN EXCHANGE ROBOT-ARM SYSTEM FOR A HARD X-RAY NANOPROBE INSTRUMENT

D. Shu[1], J. Maser[2,3], M. Holt[2,3], R. Winarski[2,3], C. Preissner[1], B. Lai[3], S. Vogt[3], and G. B. Stephenson[2,4]

[1]APS Engineering Support Division
[2]Center for Nanoscale Materials
[3]X-ray Sciences Division
[4]Materials Sciences Division
Argonne National Laboratory
Argonne, IL 60439, U.S.A.

INTRODUCTION

A hard x-ray nanoprobe beamline is being developed at the Advanced Photon Source (APS). The beamline will house a hard x-ray nanoprobe instrument, one of the centerpieces of the characterization facilities of the newly constructed Center for Nanoscale Materials (CNM) at Argonne National Laboratory (ANL). This new instrument will cover an energy range of 3-30 keV with 30-nm or higher spatial resolution. The instrument will combine a scanning probe mode with a full-field transmission mode. It uses x-ray fluorescence for trace-element mapping and spectroscopy, x-ray diffraction to obtain local structural information, and x-ray absorption to image internal structures of complex devices [1].

As shown in Figure 1, the optomechanical structure for the hard x-ray nanoprobe instrument consists of the following major sub-assemblies: a granite base, a nanoprobe instrument main chamber with scanning stages for x-ray focusing optics and sample stages, an industrial robot-arm-based microdiffraction detector manipulator, a stage system for an x-ray transmission imaging detector, a stage system for an x-ray fluorescence detector, and a precision specimen exchange robot-arm system to provide automated high throughput operation capability.

Inside the instrument main chamber, as shown in Fig. 2, the positioning stages for the optics are grouped into several subcomponents that are engineered to be moved in or out of the beam to allow configuration of the instrument for scanning probe mode and full-field transmission mode. These subcomponents are the condenser module (CM), the focusing optics module (FOM), the specimen module (SM), and the imaging optics module (IOM). The FOM and SM form a scanning nanoprobe instrument, and the CM, SM, and IOM form a transmission x-ray microscope (TXM). The specimen module is shared by both configurations [2].

Fast feedback for differential vibration control between the zone-plate x-ray optics and the sample holder has been implemented in this design. A specially designed, custom-built laser Doppler displacement meter (LDDM) system provides two-dimensional differential displacement measurement with subnanometer resolution between the FOM and the SM [3].

The specimen exchange system includes four positioning stages: a specimen magazine long transit stage, a magazine positioning arm, a magazine station with rotary stage, and a specimen positioning arm with gripper.

A total of six customized ceramic-motor-driven linear or rotary stages have been designed to perform the required precision motions. Table 1 summarizes the design specifications of the six ceramic-motor-driven stages.

This paper presents the mechanical design of the precision specimen exchange robot-arm system. Design specifications for the customized ceramic-motor-driven stages are also discussed in this paper.

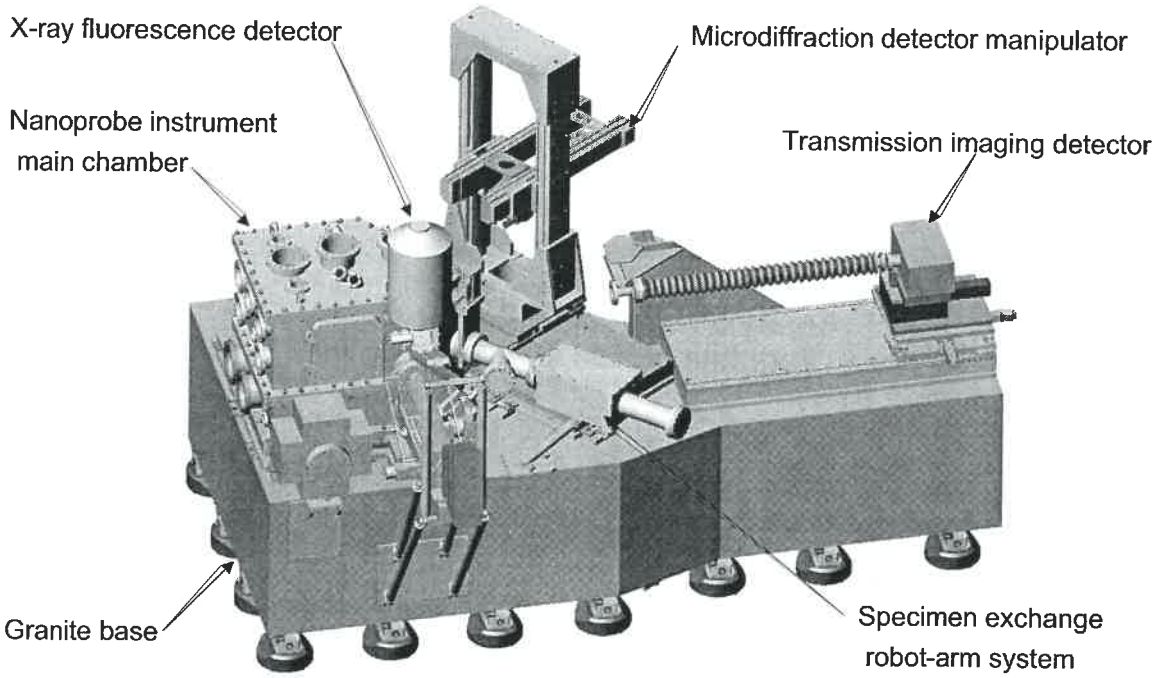

FIGURE 1. A 3-D model of the optomechanical structure for the hard x-ray nanoprobe instrument.

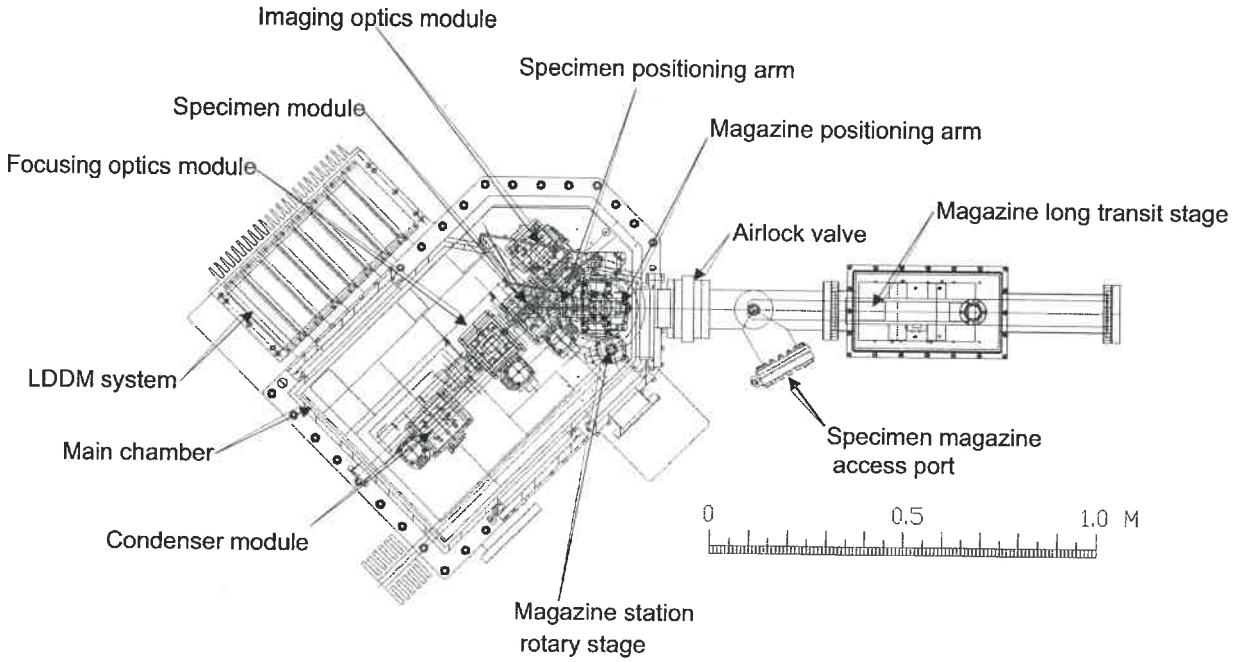

FIGURE 2. A top view of the precision specimen exchange robot-arm system for the hard x-ray nanoprobe instrument.

TABLE 1. Design specifications of the customized high-vacuum compatible Alio™ stages for the precision specimen exchange robot-arm system [4-6]

	Specimen magazine long transit stage	Magazine positioning arm linear stage
APS drawing number	Z7-232100-00	Z7-234200-00
Normal load capacity (kg)	10 kg	2 kg
Motor type	Nanomotion™ ceramic motor 2X HR-8	Nanomotion™ ceramic motor HR-2
Encoder type	Renishaw linear optical encoder	Renishaw linear optical encoder
Travel range	360 mm	96 mm
Min. incremental motion	0.2 micron	0.2 micron
Closed-loop repeatability	+/- 5 micron	+/- 5 micron
Max. speed	120 mm/sec	100 mm/sec
	Specimen positioning arm linear stage	**Specimen gripper linear stage**
APS drawing number	Z7-234100-00	Alio™ catalog item AI-ST1-2500E
Normal load capacity (kg)	0.8 kg	0.2 kg
Motor type	Nanomotion™ ceramic motor 2X HR-4	Nanomotion™ ceramic motor ST1
Encoder type	Renishaw linear optical encoder	Renishaw linear optical encoder
Travel range	50 mm	25 mm
Min. incremental motion	0.2 micron	0.02 micron
Closed-loop repeatability	+/- 5 micron	+/- 0.2 micron
Max. speed	50 mm/sec	250 mm/sec
	Magazine station rotary stage	**Magazine and specimen arm rotary stage**
APS drawing number	Z7-234400-00	Z7-234300-00
Normal load capacity (kg)	15 kg	15 kg
Motor type	Nanomotion™ ceramic motor HR-2	Nanomotion™ ceramic motor 2X HR-2
Encoder type	Renishaw optical encoder	Renishaw optical encoder
Travel range	+/- 180 degree	+/- 175 degree
Min. incremental motion	0.0014 degree	0.00014 degree
Closed-loop repeatability	+/- 0.014 degree	+/- 0.0014 degree
Max. speed	90 degree/sec	90 degree/sec

SPECIMEN HOLDER AND MAGAZINE

The specimen for the nanoprobe instrument is mounted on a silicon specimen holder. As shown on left side of Fig. 3, it is a 4 mm x 22 mm x 1 mm silicon chip with a 2-mm-diameter hole near the top for specimen mounting, and three notches for the robot gripper. The right side of the Figure 3 shows a 3-D model of the specimen holder clamped on the SM specimen base. A top view of a specimen magazine designed for holding up to 16 specimen holders is shown in Fig. 4. There are two sets of kinematic mounting structure integrated with the specimen magazine: one set fit the long transit stage and magazine station rotary stage, and the other set is for the magazine positioning arm use.

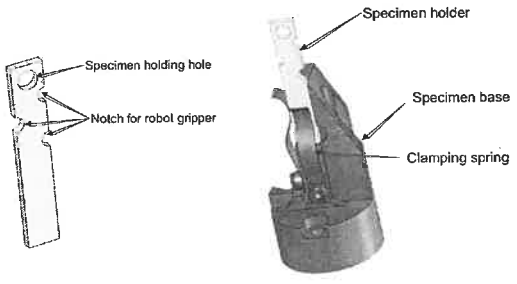

FIGURE 3. Left: A 3-D model of the specimen holder. Right: A 3-D model of the specimen holder clamped on the SM specimen base.

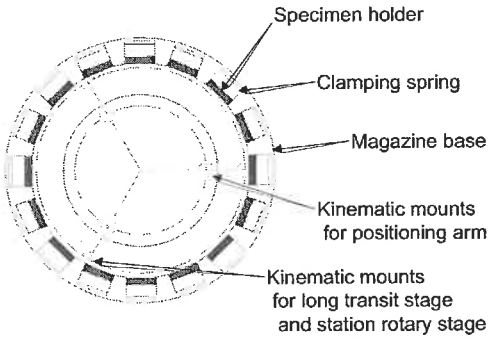

FIGURE 4. A top view of a specimen magazine designed for holding up to 16 specimen holders.

MAGAZINE LONG TRANSIT STAGE

As shown in Figure. 2, a transit stage with a travel range of 360 mm is assembled in a vacuum chamber that is connected to the nanoprobe instrument main chamber through an airlock valve and a magazine access port. During the magazine mounting process, the specimen magazine is loaded through the access port manually. After the transit chamber is pumped down, the airlock valve opens, and the transit stage delivers the magazine to a transient position inside the main chamber as shown in step 2 of Fig. 5.

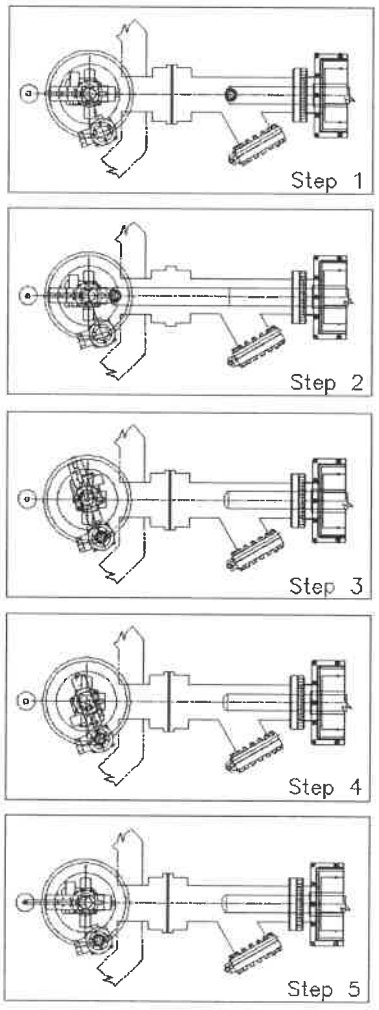

FIGURE 5. Operation steps of the precision specimen exchange robot-arm system.

MAGAZINE POSITIONING ARM

The function of the magazine positioning arm is to transport the specimen magazine from the transient position to a magazine station that has a customized ceramic-motor-driven rotary stage that positions the 16 specimen holders individually to an interface position for pickup, as shown in step 3 of Fig. 5. The magazine position arm is operated by two stages: a customized ceramic-motor-driven linear stage mounted on top of a customized ceramic-motor-driven rotary stage.

SPECIMEN POSITIONING ARM WITH GRIPPER

Once the specimen holder is located at the interface position, it is ready to be picked up by the specimen positioning arm's gripper and mounted on the SM specimen base for the experiment. The operation of this process is completed with the motions associated with three ceramic-motor-driven stages: a linear stage mounted on top of the same rotary stage that drives the magazine positioning arm, and a miniature linear stage that operates the specimen holder gripper, as shown in steps 4 and 5 of Fig. 5.

SUMMARY

This paper presents the mechanical design of the precision specimen exchange robot-arm system for a hard x-ray nanoprobe instrument. The nanoprobe instrument has been constructed and is being commissioned. The specimen exchange system will be integrated with the nanoprobe in the next six months.

ACKNOWLEDGEMENTS

The authors would like to thank M. Muscia and A. Nyman from Argonne National Laboratory for their help in the manipulator development. This work was supported by the U.S. Department of Energy, Office of Science, Office of Basic Energy Sciences, under Contract No. DE-AC02-06CH11357.

REFERENCES

[1] J. Maser, G. B. Stephenson, D. Shu, B. Lai, S. Vogt, A. Khounsary, Y. Li, C. Benson, G. Schneider, SRI 2003, AIP Conf. Proc. 705, 470 (2004).
[2] D. Shu, J. Maser, M. Holt, R. Winarski, C. Preissner, A. Smolyanitskiy, B. Lai, S. Vogt, and G. B. Stephenson, SRI 2006, AIP Conf. Proc. 879, 1321 (2007).
[3] D. Shu, J. Maser, B. Lai, S. Vogt, M. Holt, C. Preissner, A. Smolyanitskiy, B. Tieman, R. Winarski, and G. B. Stephenson, Proc. 8th Int. Conf. X-ray Microscopy, IPAP Conf. Series 7, pp. 56-58 (2006).
[4] Alio is a trademark of Alio Industries, Inc., U.S.A.
[5] Nanomotion is a trademark of Nanomotion Ltd, Israel.
[6] Renishaw is a trademark of Renishaw, Inc. U.K.

PHOTOCATALYTIC NANO-IMPRINTING USING DIRECT NEAR-FIELD OXIDATION

Yuuki Sugiue[1], Hiroshi Morii[1], Keisuke Nagato[1], Kensuke Tsuchiya[2], Tetsuya Hamaguchi[1], and Masayuki Nakao[1]
[1] Department of Engineering Synthesis, The University of Tokyo Bunkyo-ku, Tokyo, Japan
[2] Institute of Industrial Science, The University of Tokyo Meguro-ku, Tokyo, Japan

INTRODUCTION

In the field of nano-fabrication, photolithography can now be used to fabricate patterns and structures that have lines with pitches of less than 100nm and it is gradually reaching the diffraction limit of light. To compensate this limit, new approaches such as near-field, e-beam, and x-ray lithography have been proposed [1-3]. In this study, we propose a nano-fabrication method that utilizes the oxidation of a photocatalytic mold to directly imprint nanometer order patterns on a substrate. Because the oxidation is able to decompose organic matter, this method has an advantage that the exposure, development, and etching process can be accomplished in a single step. Furthermore, since the oxidation can be induced by i-line exposure, it enables us to break the diffraction limit of light with current photolithographic facilities by replacing a small part of the existing fabrication process. Additionally, our method allows the imprinting of photoresist sensitive materials, such as silane-coupling agents. Although the photocatalytic mold must be prepared by other nano-fabrication methods, it can be repeatedly used once made.

Figure 1 shows the oxidation mechanism of the photocatalyst [4]; 1) Free electrons and holes are generated by the photocatalyst when exposed to UV light. 2) Electrons and holes react to H_2O, and H_2O_2 is produced. 3) H_2O_2 diffuses into air and travels to the substrate. 4) H_2O_2 turns into hydroxyl radicals during UV light exposure. 5) Hydroxyl radicals oxidize and decompose organic matter. The diffusion of H_2O_2 reaches a distance of about 100μm. Micrometer order imprinting by oxidation has been reported by other groups [5][6].

In this paper, we propose a "near-field oxidation" method to realize nanometer order imprinting using oxidation. Experimental results demonstrating the applicability of the method are presented.

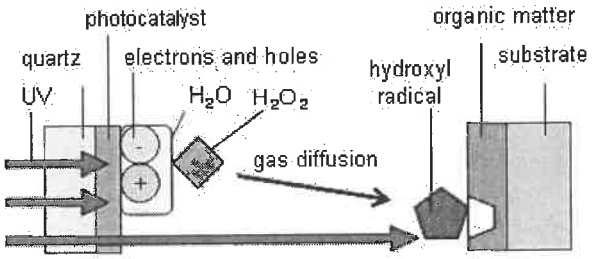

FIGURE 1: The oxidation mechanism of photocatalyst

PROPOSED NEAR-FIELDOXIDATION METHOD

To realize nano-imprinting using oxidation, the generation of hydroxyl radicals and diffusion of H_2O_2 must be controlled and confined to the vicinity of the photocatalyst. The following contact near-field oxidation method was developed;

First, to control the field of generation of hydroxyl radicals, near-field light is used. The photocatalyst is masked with a thin layer of metal. As the mold is illuminated with UV light (wavelength 365nm), nanometer order patterns on the metal layer act as subwavelength apertures that only allow near-field light to pass though. This restricts the field where the hydroxyl radicals are generated to the vicinity of the mold's surface, because the intensity of near-field light rapidly decreases as it moves away from the surface of the mold. Figure 2 shows the time-averaged intensity of light calculated by the finite-difference-time-domain method.

Second, to control the diffusion of H_2O_2, a contact method is used; pressure is applied to make the photocatalytic mold come into firm

contact with the substrate. This eliminates space for H_2O_2 to diffuse between the mold and the substrate.

To fulfill the above mentioned functions, the spacer layer must provide the following; UV shielding, allows fabrication of subwavelength apertures, adaquate flatness for the contact between the photocatalytic mold and the substrate, mechanical resistance for the contact pressure, and chemical resistance for the photocatalytic oxidation. Sputtered Au and Cr were chosen as the spacer layer. Cr also functions as an adhesion layer between the Au layer and the photocatalytic layer. Figure 3 shows a schematic of our proposed contact near-field oxidation method.

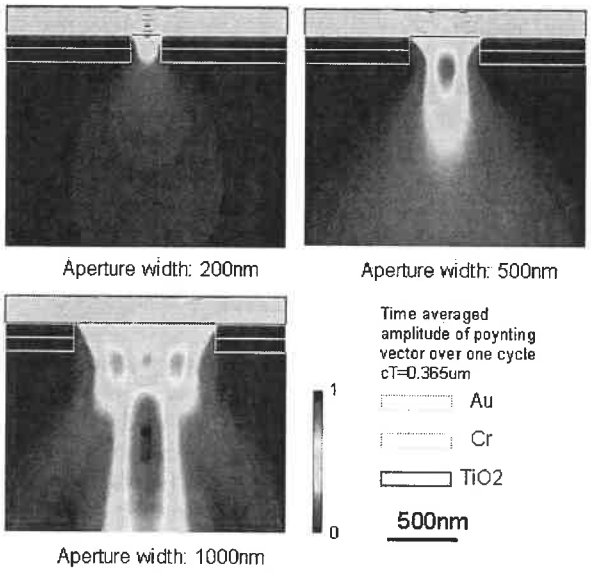

FIGURE 2: Time-averaged intensity of light

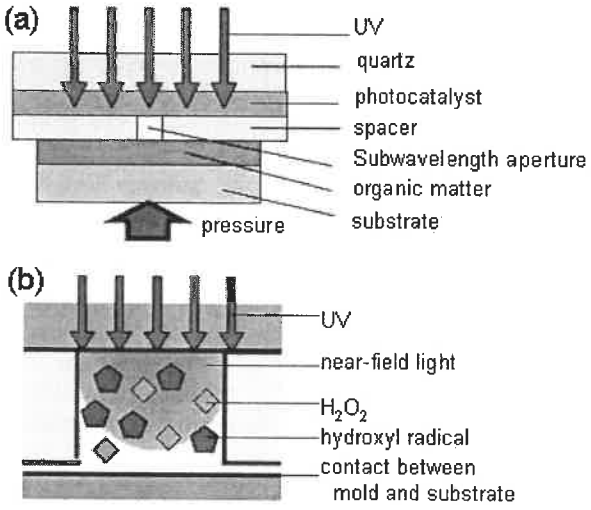

FIGURE 3: Contact near-field oxidation method; (a) overview (b) detailed view of aperture

FABRICATION OF MOLD

Photocatalytic molds were fabricated as follows; 1) Quartz plates were sonicated with acetone and then with ethanol for 5min, respectively, and placed in oxygen plasma for 10min. 2) Photocatalytic TiO_2 sol (Ishihara Sangyo, LPC-215, STS-01) was diluted with distilled water (50vol%), spin coated at 1000rpm for 10sec, and baked at 120C° for 5min. Three layers of TiO_2 sol were coated to a thickness of 1μm. 3) Cr and Au were both sputtered 100nm to mask the TiO_2 layer. 4) The metal layer was etched using a Focused Ion Beam (Hitachi, FB-2100) to fabricate apertures. It is known that TiO_2 particles inside sol agglomerate at 400C° and their photocatalytic activity decreases significantly. Therefore, the dwell time was set to 2μsec to prevent agglomeration due to heat generated from the collision of Ions.

EXPERIMENTAL METHODS

Organic substrates were prepared as follows; 1) Si substrates were sonicated with acetone and then with ethanol for 5 min respectively, and placed in oxygen plasma for 10 min. 2) The Si plates were dipped in APTMS (Shinetsu Silicone, 3-(2-Aminoethylamino) propyltrimethoxysilane) for 5min which was diluted with distilled ethanol (10vol%), washed in water, and baked at 180C° for 30min. APTMS forms an organic matter monomolecular film on Si substrate. Both APTMS and photoresist are distilled in an organic solvent where they affect each other negatively. The solvent causes APTMS patterning by photolithography difficult.

Figure 4 shows the photocatalytic oxidation of APTMS. When APTMS is decomposed by photocatalytic oxidation, N and C are oxidized, chemically change into NO_2, CO_2 and H_2O, and diffuse in air, after which a hydroxyl group binds chemically to Si.

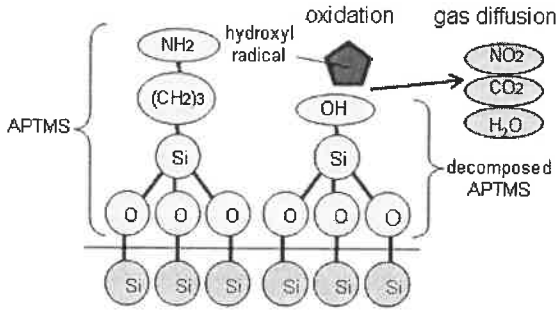

FIGURE 4: photocatalytic oxidation of APTMS

After decomposition, the substrate was dipped in water containing ø20nm Au particles (BBInternational Ltd. EM.GC20) for 2hr. Au nano-particles are trapped on the APTMS surface at a high density and form a metal colloid monolayer. We used the Au colloid monolayer to observe the patterns fabricated on the APTMS by the photocatalytic mold under a scanning electron microscope (SEM).

Two types of contact and exposure systems were devised;

1) Black light-weight system.
The light source is black light (Asone, LUV-16), and the irradiation intensity is approximately 1.8mW/cm^2 at 365nm. Pressure bringing about the contact of the mold and the substrate is applied by weight, and its value is approximately 4.0×10^{-3}atm.

2) Mask aligner system.
The light source is UV lamp (Ushio Denki, USH-250D), and the irradiation intensity is approximately 14mW/cm^2 at 365nm. Pressure bringing about the contact of the mold and the substrate is applied by air, and its value is approximately 2.5atm. A mask aligner (Nanometric Technology Inc., LA-310S) is used for the light source and air pressure.

Figure 5 shows the experimental setups of the black light-weight and mask aligner systems.

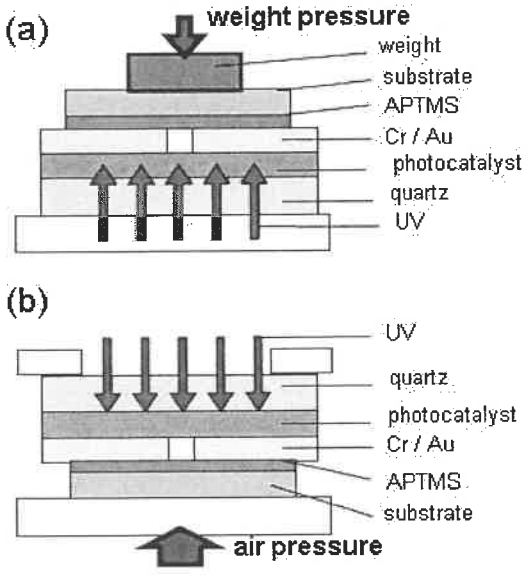

FIGURE 5: Contact and exposure systems; (a) Black light-weight system (b) Mask aligner system

EXPERIMENTAL RESULTS AND DISCUSSIONS

1) Relationship between the aperture depth of photocatalytic mold and decomposition.
The organic substrate was decomposed using the black light-weight system and photocatalytic molds with different aperture depths for 6hr. Figure 6 shows the aperture depths of molds and the decomposed substrates. This indicates that the appropriate aperture depth is about 300nm.

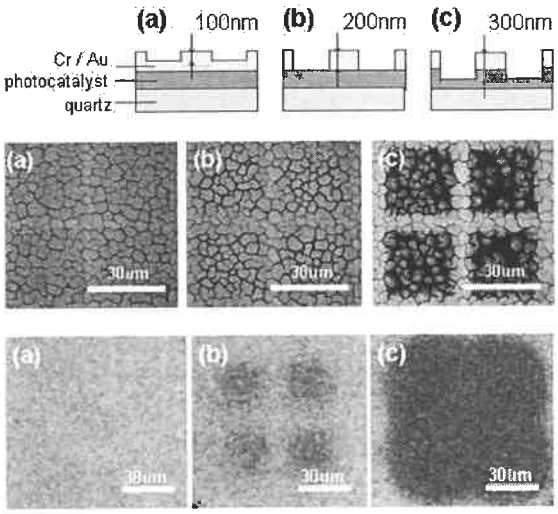

FIGURE 6: Photocatalytic molds with different aperture depths and substrates decomposed using the photocatalytic molds; (a) 100nm depth (b) 200nm depth (c) 300nm depth

2) Relationship between the aperture width of photocatalytic mold and decomposition.
The organic substrate was decomposed using the black light-weight system and photocatalytic molds with different aperture widths for 12hr. Figure 7 shows the aperture widths of the mold and the decomposed substrate.

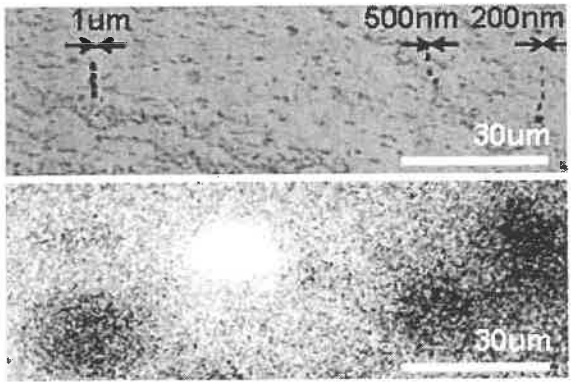

FIGURE 7: Photocatalytic mold with different aperture widths and substrate decomposed using the photocatalytic mold

The expansion of decomposed area over the apertures is about 10μm in extent regardless of aperture widths. This indicates that hydroxyl radicals diffuse outside the aperture, under the controlled generation of hydroxyl radicals by exposure of near-field light to H_2O_2 for a period of as long as 12hr. An appropriate exposure time and tighter contact are required to confine the oxidation to the vicinity of the photocatalytic mold's surface.

3) Relationship between contact of the mold and substrate and decomposition.
The organic substrate was decomposed using a photocatalytic mold that had a 10μm-wide line with the black light-weight and the mask aligner systems for 12hr. Figure 8 shows the pattern of the photocatalytic mold and substrate decomposed using the black light-weight and mask aligner systems. The extent of the expansion of the decomposed area over the apertures of the black light-weight system is beyond 5μm, and that of the mask aligner system is about 1μm. 10μm-wide line imprinting was demonstrated using the mask aligner system. This shows that the proper contact of the photocatalytic mold and the substrate reduces expansion of the decomposed area over the aperture. Figure 9 shows the topological measurement along the dotted line in Figure 8 (a).

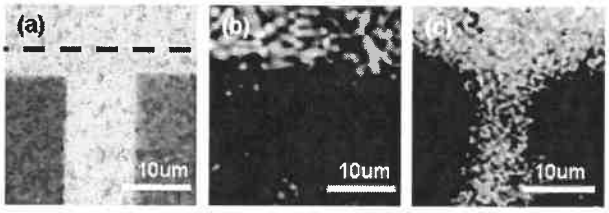

FIGURE 8: (a) Photocatalytic mold and substrate decomposed using (b) black light-weight and (c) mask aligner systems

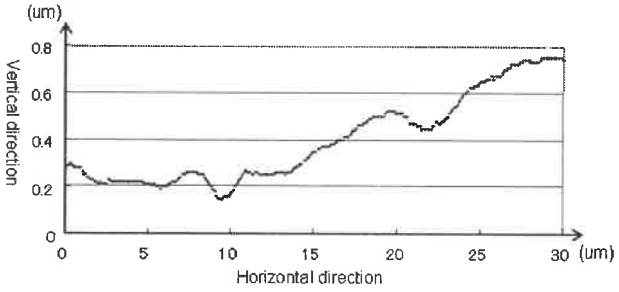

FIGURE 9: Topological measurement of the mold along the dotted line in Figure 8

Contaminations from the dust in the environment and swelling of the photocatalytic layer causes about 500nm asperity. This indicates that a cleaner environment and a mold with a flatter surface will achieve higher resolutions.

CONCLUSIONS

In this study, we have proposed a "near-field oxidation" method for nano-imprinting, and experimental results demonstrating the applicability of the method we presented. The generation of hydroxyl radicals and diffusion of H_2O_2 must be controlled and confined to the vicinity of the photocatalytic mold's surface to realize nano-imprinting. Oxidation using subwavelength apertures of 200nm width has been demonstrated. It has been indicated that not only H_2O_2 but also hydroxyl radicals diffuse outside the aperture. Therefore, the degree of contact between the mold and the substrate has a greater effect than the control of light.

ACKNOWLEDGEMENTS

We gratefully acknowledge Prof. S. Tanemura (Japan Fine Ceramics Centre) for discussions regarding the oxidation mechanism of TiO_2. TiO_2 sol was provided by Ishihara Sangyo Kaisya, Ltd.

REFERENCES

[1] T. Ono et al, 1998, Evanescent-field-controlled nano-pattern transfer and micro-manipulation, Proc. IEEE 11th Int. Workshop on MEMS, p.488.

[2] D. S. Masintyre et al, 2006, High resolution e-beam lithography using thin-titanium layer to promote resist adhesion, Microelectronic Engineering, 83: p.1128.

[3] R. Feder et al, 1977, X-ray lithography, Polymer Engineering and Science, 17: p.385.

[4] W. Kudo et al, 2004, Mechanisms and Resolution of Photocatalytic Lithography, J. Phys. Chem. B, 108:p.3005.

[5] H. Notsu et al, 2005, Super-hydrophobic/super-hydrophilic patterning of gold surfaces by photocatalytic lithography, Journal of Materials Chemistry, 15: p.1523.

[6] J. P. Lee and M. M. Sung, 2003, A new patterning method using photocatalytic lithography and selective atomic layer deposition, Journal of American chemical Society, 126: pp.28.

AUTHOR CONTRIBUTIONS

Y.S. designed the apparatus, carried out the experiments, and wrote the paper with support. H.M. planned the project, designed the experiments, carried out numerical simulations, and co-wrote the paper. K.N., K.T., T.H., and M.N. provided technical expertise. All of the authors participated in the analysis of the results.

A STUDY ON SURFACE MATERIAL MEASURES FOR AREAL SURFACE TEXTURE MEASURING INSTRUMENTS

K. Nemoto[1], K. Yanagi[1], M. Aketagawa[1], D. Kanda[1], T. Sakurai[1], I. Yoshida[2] and M. Uchidate[3]

[1]Department of Mechanical Engineering, Nagaoka University of Technology
1603-1 Kamitomioka, Nagaoka, Niigata 940-2188, Japan
[2]Japan Science and Technology Agency, Satellite Niigata, Japan
[3]Department of Mechanical Engineering, Iwate University, Japan

INTRODUCTION

Various surface texture measuring instruments such as contact stylus type, optical probing type and interferometer system have appeared on the market. Subsequently, the sampling length and evaluation length by liner profiling method can be expanded to sampling area and evaluation area by areal measuring method. However, the identical surface texture data can not always be obtained due to different measuring principle of each instrument. So, all the instruments should be calibrated properly. Needed is the areal surface texture standard to cross check the overall performances of surface texture measuring instruments. Nowadays, only the surface material measures for conventional 2D stylus instruments are standardized. As to the 3D surface texture measuring instruments, their calibration method and uncertainty analysis procedure have not been established. So the performance test of the instruments may be carried out using arbitral calibration tools at each manufacturer.

In this study, a surface material measure with the irregular surface topography which can be used for various measuring instruments is proposed. And the surface material measure was manufactured using a super 5-axis nano machine. The optimal measuring conditions are clarified under the software gauge data. The evaluation results using the manufactured surface material measure are discussed.

GENERATION OF SOFTWARE GAUGE DATA

In the ISO, the measurement standards for 2D surface texture measurement are five kinds of types, A ~ E [1]. Their dimensions and roughness parameters are defined for evaluating overall performances of stylus type surface texture measuring instruments. The measurement standard which can verify overall performances of the measuring instruments equipped with analysis software on these measurement standards is a roughness standard of Type D. The roughness standard has irregular surface topography, and is characterized by the arithmetical mean deviation (*Ra*) and the maximum height of profile (*Rz*). And measuring instruments can be evaluated by comparing measurement values with nominal values.

About areal surface texture evaluation, calibration method and measurement standards for the instrument have been discussed in ISO/TC213. There, seven kinds of measurement standards such as triangle groove, hemisphere, plane and crossed grating are proposed as measurement standards similar to the 2D measurement standards. However, *x*, *y* and *z* coordinate values for measuring instruments can be calibrated by the proposed measurement standards. Therefore, the proposal of the measurement standards for verifying overall performance of measuring instruments like the roughness measurement standard is required. Then, the surface material measure with the irregular surface topography for 3D roughness calibration is determined. So, the software gauge data for surface texture standard was generated by using the non-causal 2D auto-regressive model (2D A-R model) [2] from the following two reasons.

1. Possible to generate periodical irregular surface topography data.
2. Possible to generate surface topography data from specified feature index.

The 2D A-R model is shown by the equation (1) and equation (2).

$$z(x,y)=\sum_{(i,j)\in D}\sum \phi(i,j)\{z(x-i,y-j)+z(x+i,y+j)\}+\sigma(x,y), \quad (1)$$

$$D = \{(i, j) \mid (1 \le i \le m, j = 0) \cup (-m \le i \le m, 1 \le j \le n)\} \quad (2)$$

where, $z(x, y)$ is height at the position x and y. The weight function $\varphi(i, j)$ is AR parameter. $\alpha(x, y)$ is random noise components. D is the area of the linear weighted summation. m and n are AR orders in x and y directions. Thereby, $z(x, y)$ is related to the surrounded data in the whole directions. The software gauge generation parameters needed for generating irregular surface topography data using this 2D A-R model are 6 kinds, i.e. correlation length (βx and βy), power index w, root mean square height Sq, skewness Ssk and kurtosis Sku. βx, βy and w are auto-correlation coefficient (ACC), and Sq, Ssk and Sku are height probability density function (HPDF). The values of the generation parameters under test are calculated shown in Table 1. And generated software gauge for the unit sampling area is depicted in Fig. 1 (a).

TABLE 1. Generation parameters of software gauge data for surface texture standard.

Parameter	Symbol	Value
Correlation length	βx, βy	40μm
Power index	w	0.9
Root mean square height	Sq	1.0μm
Skewness	Ssk	0
Kurtosis	Sku	3

EVALUATION CONDITIONS

Evaluation area

In order to evaluate parameter values in 2D roughness measurement, it is necessary to measure 5 times of sampling length which is identical to the evaluation length [3]. When this method is applied to 3D roughness measurement, it is necessary to take 5 times the evaluation length in x and y directions for the sampling area corresponding to 2D sampling length. Therefore, the evaluation area will be 25 times the sampling area. Its measuring time by a conventional instrument can be too long. And the measurement data points also exceed 100,000 points. In this surface material measure, the area (768μm×768μm) of the unit sampling area shown in Fig. 1 (a) is proposed as an evaluation area. And the area of Fig. 1 (b) which combined four of the unit sampling area shown in Fig. 1 (a) is proposed as one surface material measure (1,536μm ×1,536μm). Constant roughness parameter values should be obtained by measuring the evaluation area. Here, when changing a measurement area to the evaluation area, the obtained roughness parameter values with the area are shown in Fig. 2.

As a result, when measurement area is composed of about 16 times or more on the correlation length, the difference between evaluation value and design value becomes 5% (400nm) or less.

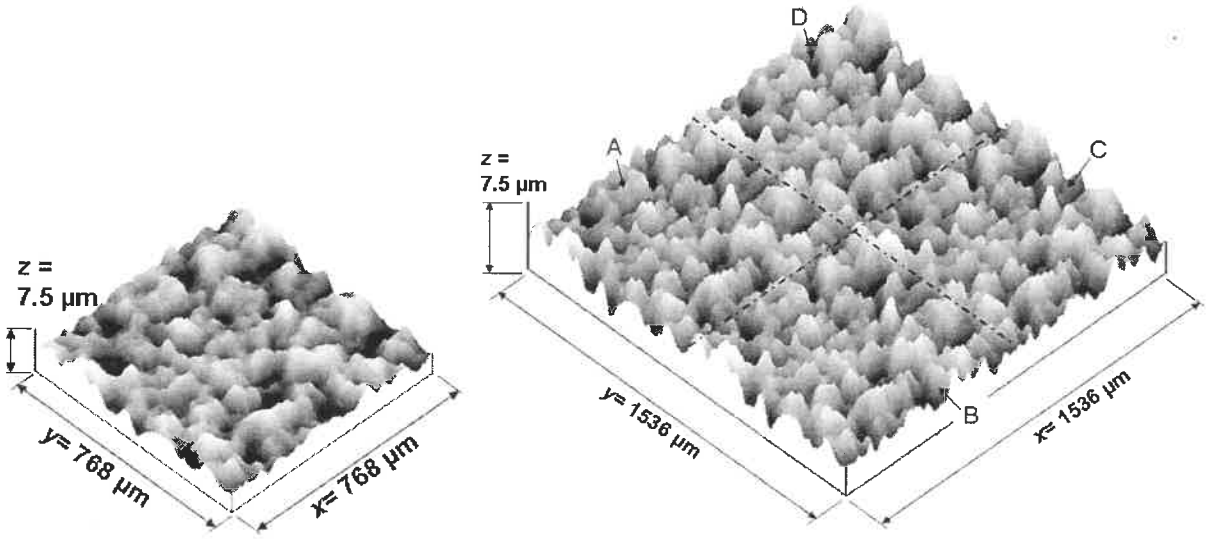

(a) (b)

FIGURE 1. Composition of software gauge data.
(a) is an unit sampling area. And (b) is multiple sampling area.

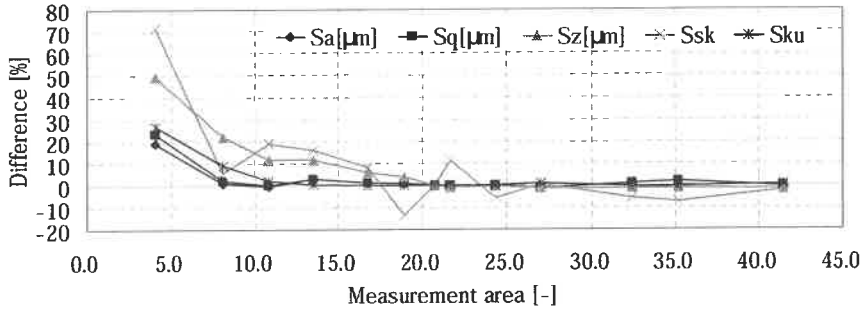

FIGURE 2. Variation of roughness parameter values against the size of measurement area. The horizontal axis shows a length of one side of the measurement area normalized by correlation length. And the vertical axis shows the difference between evaluation value and design value.

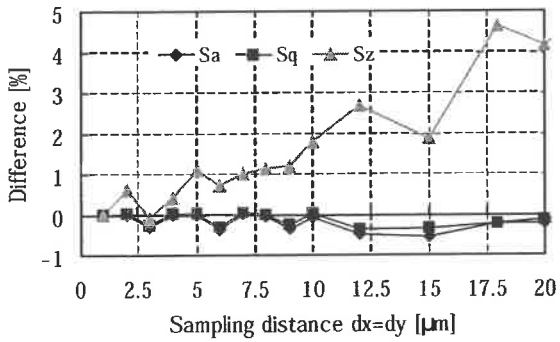

FIGURE 3. Variation of roughness parameter values against sampling distances in both directions.

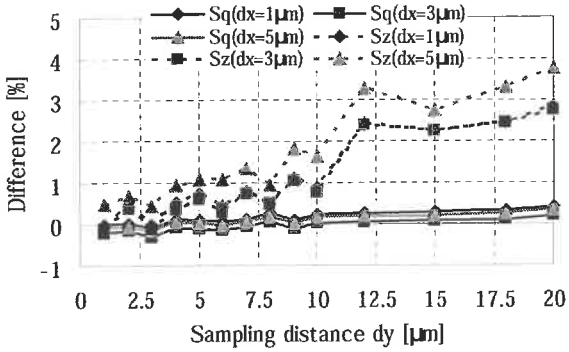

FIGURE4. Variation of roughness parameter values against sampling distance in y direction.

Sampling distance

The sampling distances in *x* and *y* directions are defined as *dx* and *dy*, respectively. The sampling distance for 2D roughness evaluation is determined by the cutoff wavelength (λs, λc) of the filter for evaluation roughness parameter values, and tip radius (R_{tip}) of stylus. From these conditions, when the sampling distance of this surface material measure is calculated, the maximum sampling distance (*dx*) is set to 0.5μm. And the data points of the evaluation area exceed 2 million points.

So, the optimal sampling distance with this surface material measure is discussed in this section. The result under constant sampling distance (*dx* = *dy*) is shown in Fig.3. And the result when changing the sampling distance in *y* direction is shown in Fig.4. When the sampling distance is 10μm, the difference between evaluation value and design value becomes 2% (about 150nm) from these results. And, when the sampling distance is 5μm, the difference between evaluation value and design value becomes 1% (about 70nm).

Generation of machining data

The machining data for manufacturing a material measure is generated from the software gauge data. The value of *w* was set to 0.9 in order to decrease the short wavelength component which is not manufacturable with a ball end-mill. However, 2D A-R model cannot remove a specific wavelength band, in order to generate the irregular surface texture. Then the Morphological filter (closing) was used for removing the short wavelength component which is not manufacturable with a ball end-mill. Since the nominal value of the tip radius of the ball end-mill used for machining was 50μm, closing processing was carried out with the ball diameter 100μm. The surface profile after this filter processing is shown in Fig. 6. As shown in Fig. 6, the short wavelength component was removed by this filter processing. And as shown in Table 2, surface texture parameter values are not changing before and after filter processing.

The filtered irregular surface topography data is converted into the NC program by using CAM system. In this study, the FUNAC super 5-axis nano machine was utilized.

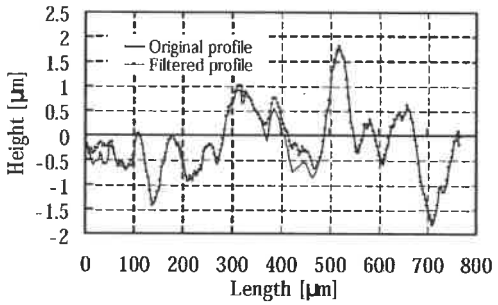

FIGURE 6. Comparison of surface profile between original data and filtered one.

TABLE 2. Comparison of roughness parameter values between original data and filtered one.

parameter	*Sa* [μm]	*Sq* [μm]	*Sz* [μm]	*Sku*
Original	0.788	1.000	7.253	3.188
Filtered	0.784	0.995	7.169	3.175

MANUFACTURING OF THE MATERIAL MEASURE

Machining conditions

Material measure has been manufactured with micro size ball end-mill. Machining conditions are shown in Table 3. Cutting edge radius of the ball end-mill is 50μm and center of rotation and knife point have 3μm offset. To prevent machining near center of rotation, where circumferential velocity 0, the tool should be leaned by about 20 degrees.

A short pick feed distance reduces the influence of the cusp on the surface form. However, a short pick feed distance makes machining time increase. Then, influence of pick feed distance on the surface texture parameter values was analyzed. As a result, influence of the cusp on the surface texture parameter values can be made smaller down to 0.5% or less by setting the pick feed distance to 3μm. Therefore, pick feed was set to 3μm.

In addition, tool rotation speed is assumed to be 37,000rpm in consideration of the resonance.

Manufactured material measure

Manufactured material measure was measured by contact stylus type and optical probing type surface texture measuring instruments. Measurement results are shown in Table 4. The sampling distance was obtained from the software gauge data. As a result, the obtained roughness parameter values are almost the same regardless of each measuring principle.

TABLE 3. Machining conditions for manufacturing material measure.

Pick feed	3 μm
Tool rotation speed	37,000 rpm
Depth of cut	Crude 4 μm
	Finish 2 μm
Feed speed	Crude 50 mm/s
	Finish 20 mm/s
Tool angle	20 degrees

TABLE 4. Measurement results of manufactured material measure (dx=1μm, dy=10μm).

parameter	*Sa* [μm]	*Sq* [μm]	*Sz* [μm]	*Sku*
Original	0.788	1.000	7.253	3.188
Contact stylus	0.761	0.968	6.787	3.221
Optical probe	0.746	0.950	6.893	3.217

CONCLUSIONS

We applied the 2D A-R model to the generation of software gauge data for the surface material measure which can be used to verify the overall performances of 3D surface texture measuring instruments. And material measure was manufactured using a super 5-axis nano machine. The following concluding remarks were obtained.

(1) The evaluation area is defined as 768μm × 768μm. And the area which combined four evaluation areas is defined as multiple sampling areas (1,536μm ×1,536μm).
(2) By measuring the area of 16 times or more on the correlation length, the influence of measurement area on the roughness parameters becomes 5% or less. And the optimal sampling distance is 10μm or less.
(3) The material measure with *Sa*:0.788μm was manufactured. This material measure can be used for various 3D surface texture measuring instruments.

REFERENCES

[1] ISO 5436-1: 2000, Geometrical Product Specifications (GPS) - Surface texture: Profile method - Measurement standards - Part 1: Material measures
[2] M. Uchidate, T. Shimizu, A. Iwabuchi and K. Yanagi, Generation of reference data of 3D surface texture using the non-causal 2D AR model, Wear, 257, (2004), 1288-1295
[3] ISO 12179: 2000, Geometrical Product Specifications (GPS) - Surface texture: Profile method - Calibration of contact (stylus) instruments

MICROLENS CHARACTERIZATION USING CONTACT PROFILOMETRY AND POINT-SPREAD FUNCTION MEASUREMENT

Craig R. Forest, Miguel A. Saez, and Ian W. Hunter
Department of Mechanical Engineering
Massachusetts Institute of Technology
Cambridge, MA, USA

ABSTRACT

As microlens fabrication technologies proliferate, accurate and accessible metrology techniques are vital to ensure quality. Oft cited interferometric techniques alone can be insufficient and their implementation can be costly. We report on combined contact profilometry and non-contact point-spread function measurement as simple, quick characterization tools for metrological feedback. Their application to quantitative metrics including figure error, roughness, and optical performance are described. Nanometer resolution figure and roughness determination are possible, as well as comparison between measured and theoretical point spread functions. These methods comprise a simple, low-cost, rapid means for characterization of refractive microlenses.

INTRODUCTION

Lens metrology is critical for manufacturing process feedback and system implementation. A variety of techniques are employed for lens metrology, such as interferometry, measurement of the point-spread function (PSF), measurement of the modulation transfer function, and surface profilometry [1]. Interferometers such as Twyman-Green, Mach-Zender and white light are discussed frequently in the literature [2]. However, interferometric techniques can be costly and limited by inadequate spatial resolution and steep angles in high numerical aperture microlenses. Oftentimes, multiple techniques are utilized to fully characterize lens quality (e.g., [3]). In this work we combined a contact metrology tool—a stylus profilometer, with a non-contact method—measurement of the point spread function, to characterize the quality of sub-1 mm injection-molded polymer microlenses, close-packed in arrays. This results in a low-cost, rapid method for evaluation of lens quality. We report on the physical and algorithmic implementation of these techniques as a readily available characterization procedure for microlenses.

MATERIALS AND METHODS

To measure the surface profile of the microlenses, we utilized a stylus profilometer (Mitutoyo SV-3000) with a 2 µm tip radius, 1 µm lateral resolution and 1 nm traverse resolution. The raw profile data was processed using various algorithms that measured figure error and surface roughness. An optical apparatus was assembled to measure the PSF response of the manufactured lenses, a seen in Figure 1.

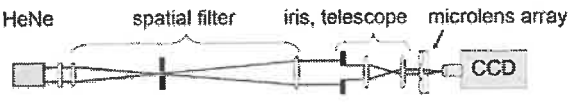

FIGURE 1. Schematic of the optical apparatus used to measure the point spread function. The laser beam was spatially filtered, collimated and subsequently contracted such that it was incident on the aperture of a single microlens.

In this apparatus, a HeNe laser (Uniphase model 106-1) with output centered at 632.8 nm was spatially filtered and collimated. The radius of the collimated beam was truncated using an iris diaphragm and then further reduced by a telescope comprised of a pair of positive lenses. Uncertainty in the diameter of the truncated beam is 250 µm, which imposes a range on the theoretical diffraction limited PSF for comparison to experimental measurement.

The microlens being tested was attached to a two-axis linear stage perpendicular to the incoming beam. Lastly, the resulting image was magnified by a 60x microscope objective mounted on a translational stage and captured with a CCD (Photometrics, Cascade 650) having 653 x 492 pixels and a pixel size of 7.4 µm x 7.4 µm.

Figure Error

Figure error was calculated by comparing the measured surface profile with the desired shape over 80% of the lens aperture. The desired shape was shifted vertically and horizontally with respect to the measured profile in order to minimize the error and determine the optimal fit. The process of fitting the measured profile to the desired geometry is shown in Figure 2.

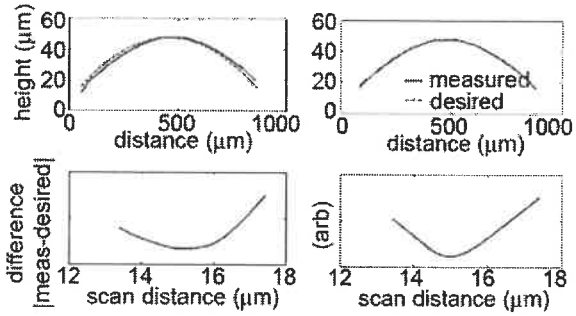

FIGURE 2. Raw mold profile slightly shifted to the right (left) and in the optimal position (right) relative to the desired circular profile. The bottom plots show how the error, or area between the profiles, changes as the measured profile is scanned axially. This measured profile has a figure error of 354 nm.

In the algorithm, the absolute difference between the measured and desired profile was calculated at each data point, and the area under the resulting curve was defined as the error. Once the optimal fit was found, at minimum error, the figure error was calculated as the average absolute difference between the measured and desired profiles.

Roughness

The surface roughness was determined by removing the low frequency information associated with the len's round shape from the measurement. This was achieved by first dividing the measured profile into segments of equal length and sequentially fitting and subtracting 2^{nd}, 1^{st} and 0^{th} order polynomials to each segment. The average roughness (R_a), defined as the average absolute deviation from the mean [4], was calculated for each individual section. The surface roughness was then calculated as the average R_a of the series of sections.

Dividing the measured profile into the correct number of sections is critical when implementing this algorithm. Using an excessive number of sections will yield a result lower than the actual R_a and vice versa. The optimal section size was determined by using the algorithm to calculate the R_a of various computer-generated spherical profiles with known roughness. The algorithm calculated the correct R_a when these simulated profiles where divided into sections with 40 data points. For our profilometer with 1 μm resolution, this corresponds to 40 μm section width. Thus a surface profile with 1000 μm aperture should be divided into 25 sections and one with 400 μm aperture into 10 sections, etc.

Point-spread function

Using the apparatus from Figure 1, we measured the PSF of microlenses manufactured using a variety of processes. One example, for a polymer lens injection-molded into a forged mold, is shown in Figure 3. The measured PSF was aligned laterally to the theoretically predicted PSF and both measurement and theory were normalized as shown.

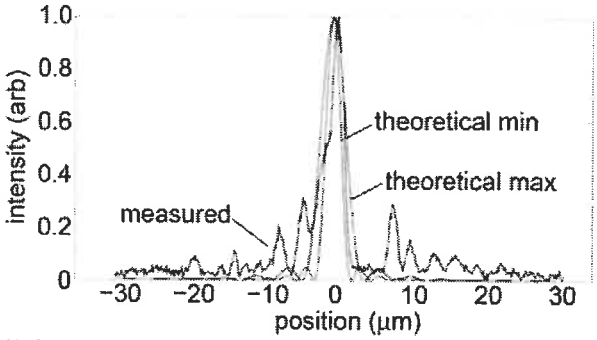

FIGURE 3. Point-spread function measured as compared to the theoretical maximum and minimum functions given the aperture uncertainty.

To evaluate the quality of the microlen's PSF, we verify that the width of the bright central peak, at full width half maximum (FWHM), falls within the range predicted for a diffraction limited system. For a more detailed description of the mathematical basis for the theoretical PSF, see Hecht [5].

CONCLUSIONS

A combination of contact metrology using a stylus profilometer and non-contact measurement of the PSF has been applied to

the characterization of microlenses. The physical and algorithmic implementation of these techniques has been detailed. Figure error measurement relies on fitting of an ideal profile in two-dimensions. Roughness measurement is achieved by dicing the profile into sections of 40 data points each, subtracting polynomials from them, and computing their mean R_a. The PSF is aligned to a theoretical function with tolerance band corresponding to uncertainty in the beam diameter measurement. Together, these tools provide a useful, rapid, and relatively low-cost means to characterize the quality of sub-mm refractive microlenses.

ACKNOWLEDGEMENTS

We gratefully acknowledge the generous support of the National Science Foundation, Sandia National Laboratories, the MIT BioInstrumentation Laboratory and the MIT Undergraduate Research Opportunities Program.

REFERENCES

[1] Mersereau K, Crisci RJ, Nijander CR, Townsend WP. Testing and measurement of microlenses. Proceedings of the SPIE 1993; 1992:210-215.

[2] Weible KJ, Volkel R, Eisner M, Hoffman S, Scharf T, Herzig H-P. Metrology of refractive microlens arrays. Proceedings of the SPIE 2004; 5458:43-51.

[3] Bardinal V, Daran E, Leichle T, Vergnenegre C, Levallois C, Camps T, Conedera V, Doucet JB, Carcenac F. Fabrication and characterization of microlens arrays using a cantilever-based spotter. Optics Express. 2007; 15:6900-6907.

[4] Kalpakjian S, Schmid S. Manufacturing Engineering and Technology. Prentice Hall, Upper Saddle River, NJ, fourth edition, 2001.

[5] Hecht E, Optics. Addison Wesley Longman, 2001.

THE USE OF MAGNETIC RECORDING FOR NANOSCALE METROLOGY

R. J. Heaton and T. M. Crawford
Department of Physics and Astronomy and USC NanoCenter
University of South Carolina
Columbia, SC

INTRODUCTION

Positioning system resolution and repeatability are critical enabling technologies for reducing the feature size possible with optical lithography. The positioning systems employed in microelectronic fabrication are mechanical stages with large travel lengths (100's of mm), which must be able to accelerate and travel rapidly, while simultaneously delivering nanoscale positioning accuracy and in-position stability. While these systems excel in travel and speed, their accuracies are limited by encoder technologies in the range of 20-40 nm. In contrast, Scanning Probe Microscopy (SPM) techniques like Atomic Force and Scanning Tunneling Microscopy (AFM/STM) employ piezoelectric materials or flexures to obtain sub-nm resolution, but are typically limited in travel to < 1 mm.

In magnetic data storage systems, dimensions have rapidly decreased to the nanoscale. Magnetic recording media have grain sizes in the 5-10 nm range, and the linear density of recorded information is determined by the bit-length, which is approaching 25 nm. Further, the recording heads are flown above the media with spacings below 10 nm [1]. Here we employ contact write/read magnetic recording metrology [2-4] to compare these two types of positioning technologies, and demonstrate the potential for applying magnetic recording to nanoscale position metrology.

CONTACT RECORDING WITH DUAL ROLLER BEARING AND PIEZO FLEXURE POSITIONING STAGES

Figure 1 shows a photograph of the tester. Along the left-right axis in Figure 1, we have two positioning stages, a 50 mm travel crossed roller bearing stage ("bearing stage", Aerotech ALS-130), and a 15 μm piezo flexure stage ("piezo stage", Insitu-Tec). Our first results from contact

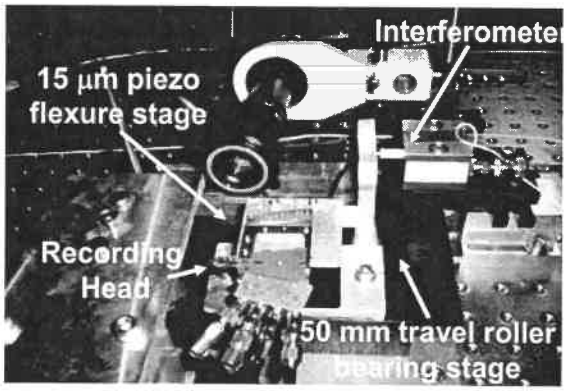

FIGURE 1. Schematic of contact write/read recording tester showing dual stage (piezo and bearing stages) along with optical fiber interferometer used for sub-nm position measurement of the bearing stage

magnetic recording were obtained without the piezo stage. The recording head is mounted on the bearing stage, and placed in contact with the media, using a manual stage with a micrometer to align the head cross-track. After many trials we read the track of bits shown in Figure 2. An optical fiber interferometer (Figure 1) is used to record the downtrack position, while the voltage

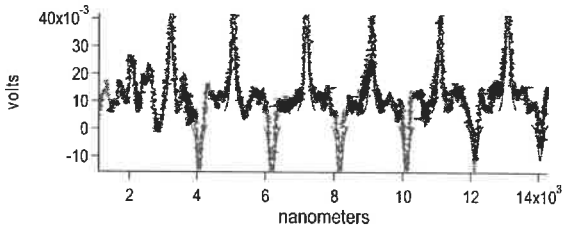

FIGURE 2. Track recorded and readback using the roller bearing stage only with no piezo stage

change from the recording head was monitored. For the data shown in Figure 2, we wrote and read back the signal with the bearing stage, and thus we could not determine the true stage jitter. We next integrated the piezo stage into our

system for writing the bits, as well as to provide an imaging capability in the cross-track direction, with the goal that the track readback signal could be used to characterize the mechanical stage performance. Figure 3 shows an image of a region of a magnetic disc obtained with the piezo stage. The upper part of the image and the top linescan show previously recorded data written on the media when it was in a disc drive. The lower part of the image was erased on our tester and then re-written as tracks of dibits. A dibit is created by pulsing the head with current, for example, while the head is stationary. This magnetizes the small region between the poles of the inductive write head. For a DC erased region on the media, this pulsing creates two closely spaced transitions, as shown in the right linescan in Figure 3.

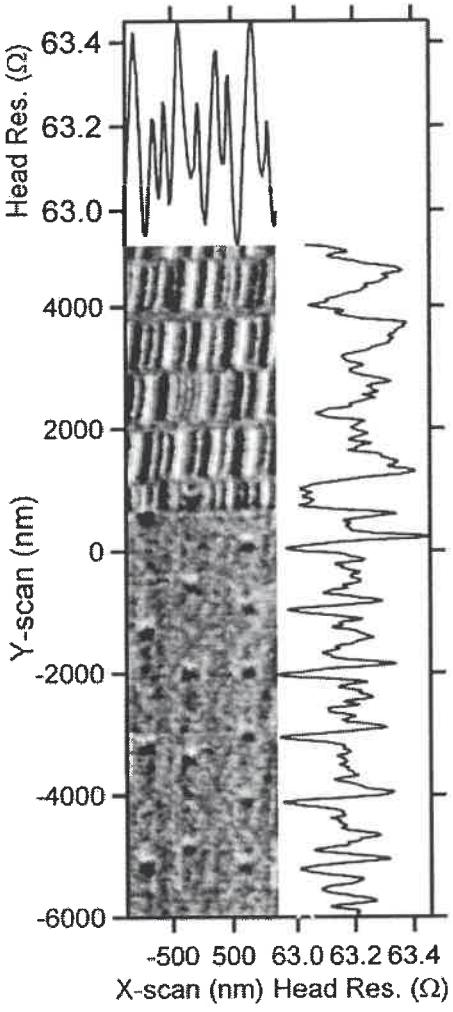

FIGURE 3. Previously recorded data read by the recording head (top) and di-bits recorded using a piezo flexure stage (15 μm travel)

READING THE SAME TRACK WITH BOTH STAGES

Figure 4a and b show dibits that were written with the piezo stage, and read using the piezo (4a) and bearing (4b) stages. We perform the write operation using the piezo stage, with the bearing stage held in place using a threaded bolt. After the write process, the bits can be read back using either stage. To read with the piezo stage, the threaded bolt remains in place with the bearing stage turned off. To read with the bearing stage, the Y axis of the piezo stage is given a constant voltage, the bearing stage is turned on and given a command to hold position. Finally, the threaded bolt is hand-loosened so that the carriage is free to move. This process proved very difficult because motion of just a few microns makes it very difficult to find the recorded track. To date we have succeeded in reading back only opposite ends of the same written track with the two stages (Figure 4).

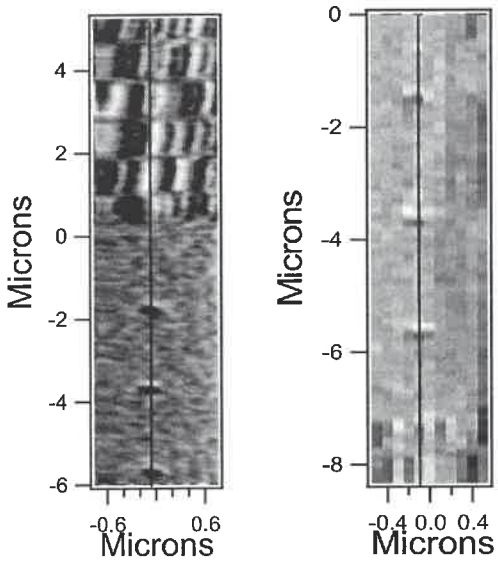

FIGURE 4. Di-bit track written with the piezo stage and top half read with the piezo stage (left) and bottom half read with the bearing stage (right).

ANALYSIS OF DOWNTRACK POSITION JITTER.

Figure 5 and 6 show linescans from the di-bit tracks shown in Figure 4a and 4b respectively. These images were acquired with 15 nm steps, and since only three di-bits are visible in each image, our jitter analysis is limited. The peak

separations in figure 5 from left to right are 1995 nm and 1935 nm respectively, yielding a 60 nm difference (4 15 nm steps). The peak separations in Figure 6 from left to right are 2002 and 2142 nm respectively, with a 140 nm difference (9 15 nm steps). Using the fiber interferometer, we obtained p-p stability (400 Hz low pass filter on a dynamic signal analyzer) of 38 nm with the bearing stage engaged, 4 nm with the bearing stage disabled (the granite table p-p stability was 2.97 nm), and 16 nm targeting the piezo stage on top of the bearing stage. Given the larger p-p jitter on the bearing stage with its motor engaged, we suggest that the 140 nm di-bit peak difference obtained with the bearing stage is more than twice as that obtained with the piezo stage because of the bearing stage's larger in-position jitter.

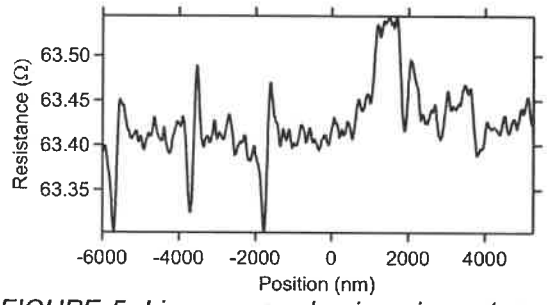

FIGURE 5. Linescan read using piezo stage (Figure 4a)

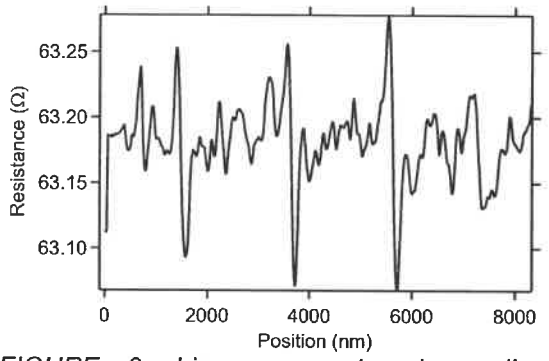

FIGURE 6. Linescan read using roller bearing stage (Figure 4b)

Supported by the interferometry measurements, the magnetic readback signal successfully detects this difference in stage stability. However, with only two di-bit separations, and the actual di-bits read being different for the two stages (even though they are part of the same track, written at the same time), some contribution due to bit-to-bit jitter is possible.

To more accurately assess the performance of the piezo stage, Figure 7 shows a track readback entirely with the piezo stage with di-bits separated by 1 μm. This linescan was obtained with a 1 nm point-point resolution, compared with the 15 nm resolution used to obtain the data in Figures 4-6. Here we have five separations, and can analyze the data using conventional magnetic recording physics. Parameters that influence the profile of the recorded signal include the physical dimensions of the recording head and the magnetic media. The gap width between the write poles depends on the specific head design, and can vary from 80-200 nm for longitudinal recording heads. The final parameter is the magnetic transition parameter, a, which describes the spatial width necessary to accommodate a magnetic transition, and depends on several factors, including the size of the magnetic grains in the media, the head field at the media, and the head to media separation. To model our dibit pattern, we simply add two Lorentzian pulses of opposite polarity, that are separated by a distance that is equal to the gap width of the write head [1,5]. Our complete model for the relative voltage as a function of downtrack spacing, relative to the peak transition voltage, is shown below, where the two terms describe two dibit peaks,

$$V_x = V_{sp}^{peak}\left[\frac{\frac{g^2+4(a+d)(a+d+\delta)}{4}}{(x-(x'+g))^2+\frac{g^2+4(a+d)(a+d+\delta)}{4}} - \frac{\frac{g^2+4(a+d)(a+d+\delta)}{4}}{(x-x')^2+\frac{g^2+4(a+d)(a+d+\delta)}{4}}\right].$$

Here x is the position down track, a is the transition parameter, g is the write gap of the head, d is the head-media spacing, and δ is the magnetic media thickness,.

Next we fit the experimental dibits in Figure 7 using this model, in order to determine the spatial jitter over the stage travel. For fitting, we employ a Levenberg-Marquardt fitting algorithm. The fitting program is written so that all of the dibits for a track of data would be fit using the same parameters. The only parameter that is not held constant for every dibit is the center position along the track of the leading Lorentzian pulse. Because the second dibit's center position is determined by the gap spacing, the separation from the first and second pulses of each dibit is constant. We note that 100% changes in the seed values have no effect on the positions

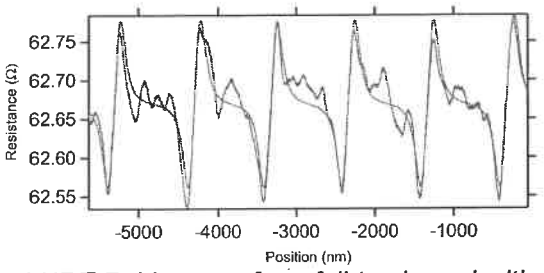

FIGURE 7. Linescan from full track read with piezo stage with 1 nm positioning stepsize, and fitting using magnetic recording physics model.

recorded for the dibits. For this experiment, the position of the recorded bits was of primary importance.

The average separation in Figure 7 is 956 nm (note that a 1 μm bit separation was commanded in the high resolution image compared with a 2 μm separation for the low resolution images in Figure 4). The standard deviation is 14 nm, and the maximum separation from the mean was 25 nm. These results further confirm the hypothesis that the 140 nm difference between the di-bits read back with the bearing stage is due largely to the stage's engaged in-position stability.

CONCLUSIONS

We have shown that, in principle, magnetic recording has sufficient spatial resolution to identify mechanical stage position jitter > 20 nm. Our statistics and number of analyzed bits are as yet insufficient to determine the ultimate limit of magnetic recording for jitter detection, but qualitatively we suggest that it is below 20 nm. Larger data samples and model refinement will allow us to pin down a more quantitative upper bound on the recording jitter. Given the low cost of magnetic recording components and their continued spatial improvement as recording densities increase, we suggest magnetic recording could play an enabling role in nanoscale mechanical positioning feedback and metrology.

REFERENCES

[1] S. X. Wang and A. Taratorin. Magnetic Information Storage Technology. Academic Press. London: 1999.

[2] Gokemeijer N J, Clinton T W, Crawford T M, Johnson M. Recording Head Metrology at sub-100 nm Device Dimensions. J. Appl. Phys. 2005; 97: 083912-16.

[3] Gokemeijer N J, Clinton T W, Crawford T M, Johnson M. Direct Measurement of the Field from a Magnetic Recording Head using an InAs Hall Sensor on a Contact Write/Read Tester. J. Magn. Magn. Mat.2005; 254: 290-291.

[4] Gokemeijer N J, Langzettel A K, Covington M. Write Field Measurements of a Perpendicular Head on a Soft Underlayer Film. IEEE Trans. Magn. 2006; 42: 163-165.

[5] Bertram H Neal. Theory of Magnetic Recording. Cambridge University Press. Cambridge: 1994.

NOVEL HIGH-BANDWIDTH ACTIVE PARASITIC MOTION COMPENSATION FOR SUB-NM PLANARITY IN AFM AND PROFILER APPLICATIONS

Scott Jordan[1] and Dr. Harry Marth[2]
[1]PI (Physik Instrumente) L.P.
San José, California, USA
[2]Physik Instrumente (PI) GmbH & Co. KG
Karlsruhe, Germany

BACKGROUND

The diminishing dimensions of lithographic and imprinted devices are characterized by Moore's familiar Law and the even-steeper disk-drive areal density curve. One consequence is that features of interest in atomic-force microscopy (AFM) and similar metrologies are becoming smaller than the parasitic (orthogonal) motion errors of even the finest nanopositioning equipment. In particular, since the X-Y motion of the scanning stage forms the datum plane for the measurement of surface topography, any deviation of the workpiece in Z risks being perceived as data or can obscure features of interest. The challenge has heightened as application needs for larger-area scans have emerged--for example to image large biological structures or meso-scale microelectronic components on the order of 1mm square--with AFM-class resolution.

Previous approaches to minimizing out-of-plane-motion (OOPM) include passive and active techniques:

-- Passive approaches have centered on flexure design improvements and implementation of ever-more-demanding tweaking of the mechanism, including fine adjustments to the guidance components and piezo actuator mount to achieve a datum plane approaching the desired nanometer-scale flatness. Since these exacting mechanical adjustments can be compromised by thermal effects, shipping vibration, attachment technique, operator error, loading and fixturing, scanning parameters and a host of similarly uncontrollable influences, the result is an un-robust solution for which the first indication of adjustment need is often a serious drop in yield for the devices-under-test.

-- Active approaches have relied on designs in which the moving workpiece is both observed and actuated in closed loop in the coordinate orthogonal to motion using conventional servo techniques. Most typically this has included interferometric or capacitive-sensor metrology of the workpiece. The datum plane in this approach is thus defined by the polished flat optic or cap-sensor surfaces. Such solutions tend to be costly, bulky or both, and the scanning speed is limited by the servo bandwidth of the Z compensation servo. Ultimately, the OOPM of such systems are limited by the metrology technique utilized, and by Z servo noise and stability.

While both approaches have been effective in meeting applications requirements, emerging needs for sub-nm surface feature extraction in XY scanners have exposed their limitations.

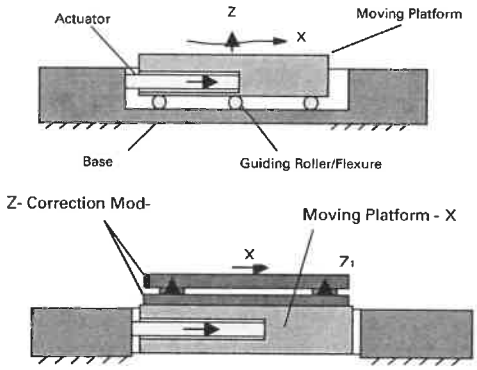

FIGURE 1. Conceptualization of the problem. Inevitable flexural or bearing imperfections of even the finest positioners result in parasitic errors (e.g., OOPM) exceeding emerging tolerances. Integration of a novel high-dynamic, limited-travel Z positioner allows compensation of OOPM, facilitating profiling datum planes surpassing 1-2nm planarity.

A NEW APPROACH

In this paper we describe a new approach (FIGURE 1), on which patents are pending, which eliminates the repetitive, meticulous tweaking required of passive approaches while avoiding the bulk and complexity of traditional active OOPM-compensation approaches. Tradenamed PicoPlane™, the technique lever-

ages one or more linearized Z-axis actuators of travel sufficient to accommodate the native OOPM of the uncompensated scanner mechanism.

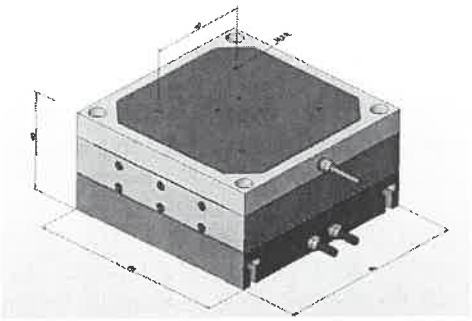

FIGURE 2. Catalog 800x800μm XY nanopositioning scanning stage with active compensator for proof-of-principle. The stage travel is sufficient to profile meso-scale microelectronic and biological specimens with <1-2nm planarity.

A fast active compensation operates to correct the mechanism's native OOPM (FIGURE 2). Importantly, the compensation may be refined in-situ by scanning a reference flat while observing Z motion through real-time external metrology, such as the AFM tool's own probe. The resulting data is then used automatically by the stage's digital controller to flatten the stage's motion.

RESULTS

The following figures demonstrate the effectiveness of the technique, which results in OOPM of a degree unachievable by previous volume-manufactured nanopositioning scanners.

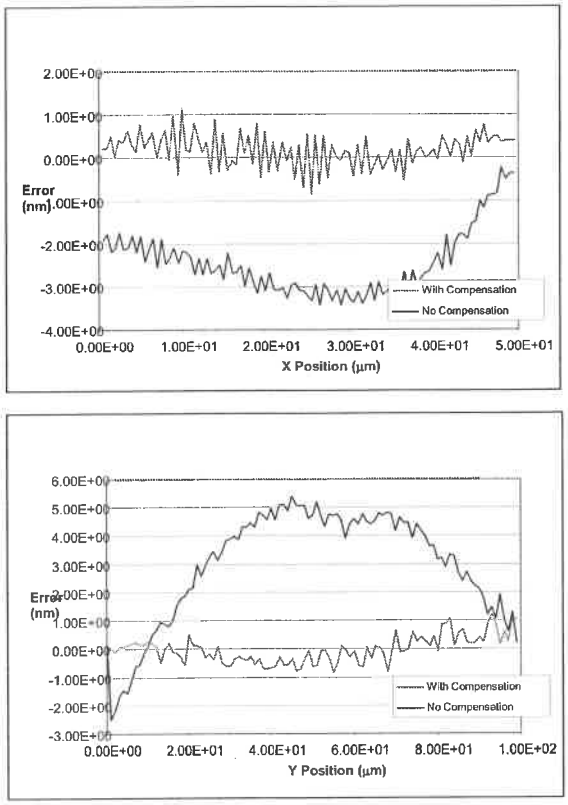

FIGURE 3. Interferometric measurement of OOPM in nm vs. stage travel in um for a 100x100μm scanner for Y axis [top] and X axis [bottom]. Blue traces are uncompensated; orange plots are compensated using the PicoPlane™ technology.

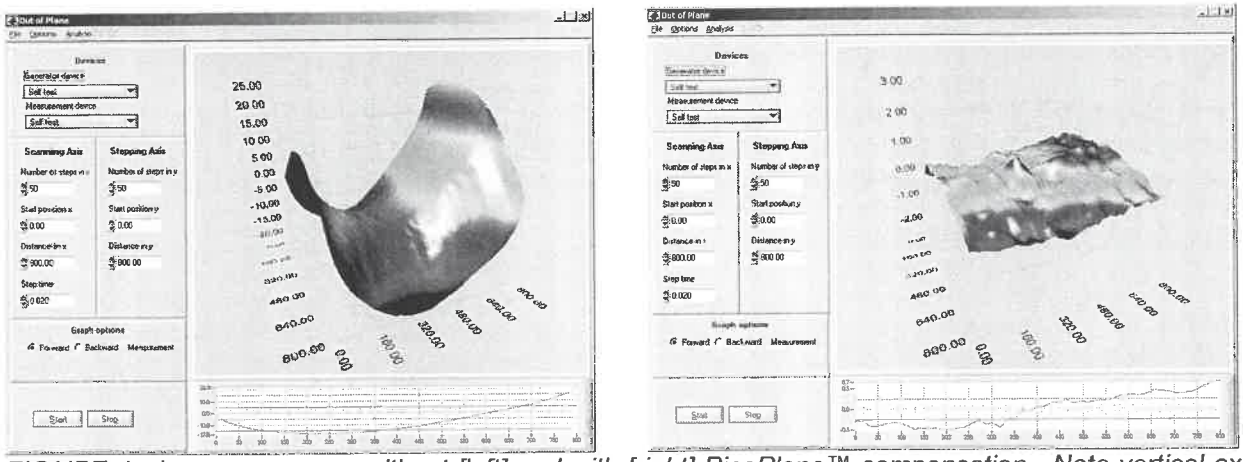

FIGURE 4. Large-area scan without [left] and with [right] PicoPlane™ compensation. Note vertical axis auto-scales and has units of nm. A mechanical constraint was applied to provide a severe nanoscale warping of the uncompensated trajectory; this is seen to be reduced to <1-2nm planarity using the new high-bandwidth/low-noise PicoPlane™ compensation approach.

The technique offers many times the bandwidth of conventional active-compensation techniques, facilitating the higher-throughput scanning critical to economic industrial applications. It eliminates the most problematic sources of datum-plane noise and nonrepeatability. Robustness is enhanced, and it is an easy, quick and automatic procedure to automatically refine the OOPM compensation after assembly, rough handling or other significant change. The nanopositioning scanning mechanisms enabled by this new approach are compact, with reduced surface area resulting in lower ambient acoustic coupling which could otherwise appear as Z noise.

In addition, for surface studies and AFM calibration, the highly accurate Z compensator can be independently commanded in controlled steps or even waveforms of known amplitude and sub-Ångstrom precision. This can illuminate subtle phenomena such as meniscus, electrostatic and capillary forces.

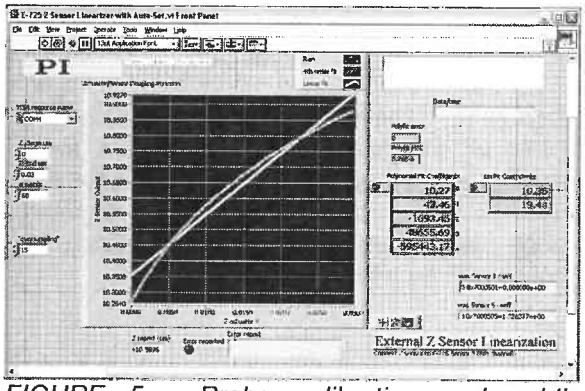

FIGURE 5. Probe calibration and subtle tip/surface interactions can be illuminated by using the compensator mechanism as a sub-Angstrom-precision nanopositioner for point-to-point or waveform actuation. Here, sixty 5 Ångstrom steps are performed while the AFM sensor is monitored by the PicoPlane™ controller and its response modeled for linear fit [yellow line] and 4th-order polynomial fit [red curve].

CONCLUSION

The new PicoPlane™ technique is an enabler in production scanned-probe metrology in semiconductor and data storage production-metrology applications, in life sciences, in nanoindentation and microlithographic mask alignment, and in "laboratory on a tip" applications. The technique addresses simultaneously emerging needs for ever-finer flatness of the scan plane, higher throughput, and large (mm-scale) scan areas.

REFERENCES

[1] Stout K, Blunt L, Three Dimensional Surface Topography, 2nd Edition. Penton Press, 2000.

[2] McClure P, Mancevski V. Calibration of a dual probe NanoCaliper™ AFM for CD metrology. Proceedings of SPIE v 5752, Metrology, Inspection, and Process Control for Microlithography XIX, Richard M. Silver, Editor, May 2005, pp. 922-936.

[3] Bernal M.-P., Marquis-Weible F., Boillat P.-Y., Lambelet P. Theoretical and experimental study of the forces between different SNOM probes and chemically treated AFM cantilevers. Proceedings of the IEEE, v. 88, Issue 9, Sep 2000, 1460 - 1470.

[4] West P, Ross A. An introduction to Atomic Force Microscopy Modes. Pacific Nanotechnology application note, http://www.pacificnanotech.com/afm-modes_principles-and-components.html.

[5] Leach R.K., Calibration, traceability and uncertainty issues in surface texture metrology, National Physics Laboratory (UK), NPL Report CLM 7.

SURFACE PROFILE MEASUREMENT
BY TANDEM TYPE SEQUENTIAL TWO-POINT METHOD
- Improvement of Spatial Resolution Without Approximation -

Kazuhide Kamiya[1], Takashi Nomura[1], Hatsuzo Tashiro[2],
[1]Department of Intelligent Systems Design Engineering
Toyama Prefectural University
Imizu, Toyama, Japan
[2] Department of Mechanical and Intellectual Systems Engineering
Toyama University
Toyama, Toyama, Japan

1. INTRODUCTION

The two-point method [1] with two displacement probes has been proposed to measure profiles of machined surfaces accurately. Since the two-point method is a kind of scanning method, it is necessary to separate the profiles from raw data with the scanning error obtained by the two probes. In the two-point method, when a sampling interval is equal to an interval of the two probes, the scanning error is canceled by simple data processing. In this case, the two-point method is called Inclination method [2]. However, the spatial resolution decreases when the sampling interval is wide, and random error accumulates when the sampling interval is narrow. On the other hand, the generalized two-point method [3] has been proposed to increase the spatial resolution. In the generalized two-point method, the sampling interval is smaller than the interval of the two probes. In this method, even if spatial resolution is increased, high frequency components of profiles are lost because the data are analyzed by integration method. To measure profiles including high-frequency components, the combined method [4] is proposed. The combined method combines merits of the inclination method and the generalized two-point method. However, results from the combined method changes according to the threshold level.

In this paper, a tandem type sequential two-point method that shares one of three probes is proposed, and a new analysis algorithm is developed for the proposed method.

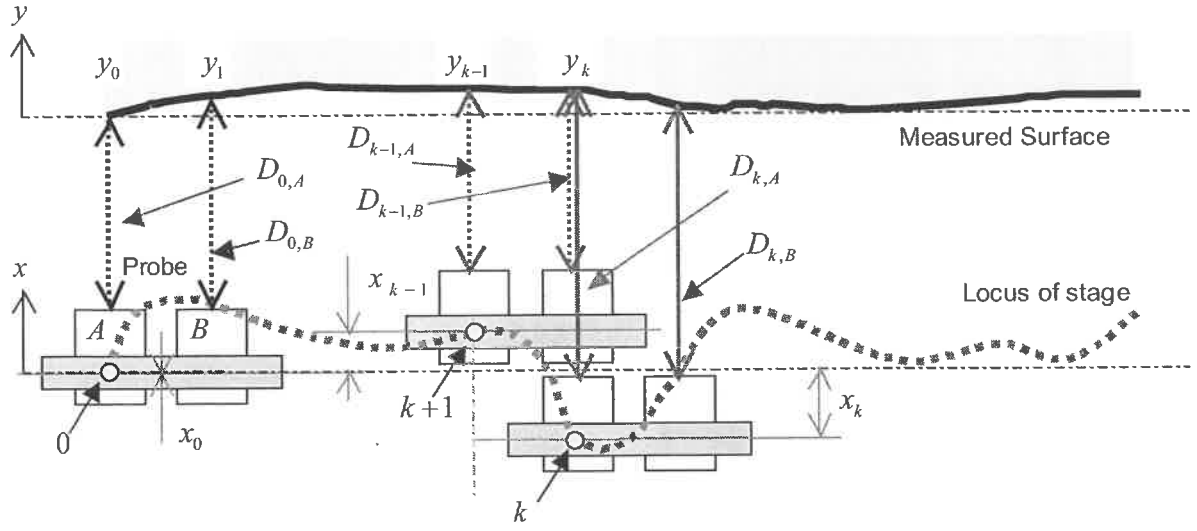

FIGURE 1. Probe setup of the 2-point method

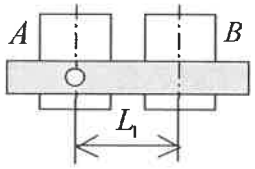

(a) Probe interval with L1

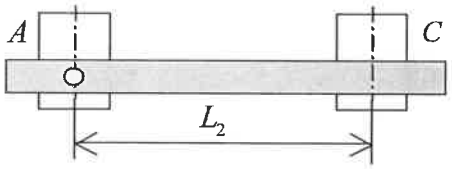

(b) Probe interval with L2

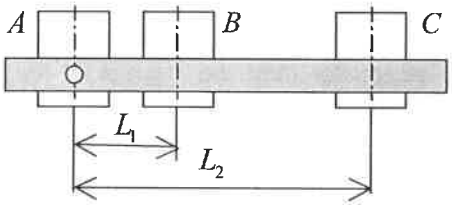

(c) Probe interval with L1 and L2

FIGURE 2. Relationship between the normal type sensor and the tandem type sensor

2. PRINCIPLE OF THE TWO-POINT METHOD

The principle of the two-point inclination method is shown in Figure 1. The sensor stage consists of two displacement probes. The interval of the two probes is equal to the sampling interval. $D_{k,A}$ denotes the output signal of probe A at point k, and $D_{k,B}$ denotes the output signal of probe B at point k. x_k and y_k are the amount of the scanning error of sensor stage and the profiles of the measured surface at point k respectively, and x_k and y_k can be expressed as follows:

$$x_k = x_{k-1} + D_{k-1,B} + D_{k,A}, \quad (1)$$

$$y_k = x_k + D_{k,A} - D_{0,A}. \quad (2)$$

Here, $k = 1,2,3,...,N-1$, $x_0 = 0$. The scanning error x_k is obtained by equation (1) and is eliminated by equation (2).

3. TANDEM TYPE TWO-POINT METHOD

3.1. SENSOR STAGE

Figure 2 shows the difference in appearance of probe setup between the normal type and the tandem type. In the tandem type, three probes are mounted on the stage. The probes A and B is a setup of the two-point method with interval L_1, and the probes A C also is a setup of another two-point method with interval L_2. Here, L_2 is not a multiple of L_1.

3.2. ANALYSIS METHOD

The operation of the tandem type two-point method is shown in Figure 3 and described in the following steps:

[1st step]

Sampling of data from probes A, B and C with stage feed interval S as shown in Figure 3 (a). Assume that $L_1 = 3$ and $L_2 = 4$ to simplify the explanation. A condition is required that L_1 and L_2 are multiples of S. Here, $S = 1$ to simplify the explanation.

[2nd step]

The data is divided into L_1 / S parts as shown in Figure 3 (b) and 3 (d). Here, $L_1 / S = 3/1 = 3$ and φ is the starting point of the data. In each data, the interval is equal to L_1 and the starting point is different. The scanning errors and profiles are obtained by equation (1) and equation (2) respectively. These profiles obtained by the inclination method are not connected to each other.

[3rd step]

The other data is selected from the data obtained by probes A and C with interval L_2 as shown in Figure 3 (e). The data and the results from step 2 are compared at points shown by vertical blue arrows. At these points, connecting information is obtained to compare the data with interval L_1 and the data with interval L_2. All data can be defined exactly and be analyzed without approximation by using the connecting information.

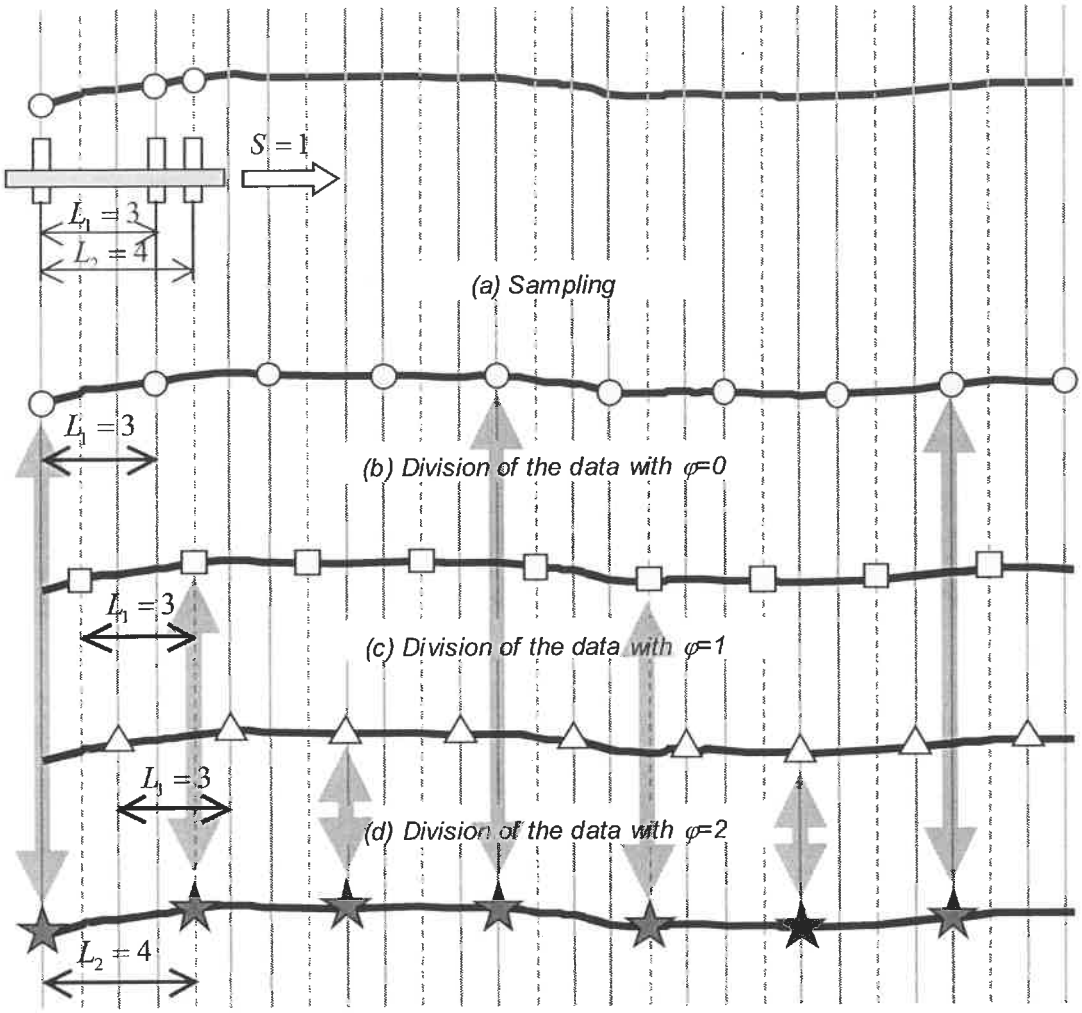
S = 1
L1 = 3
L2 = 4
(a) Sampling
L1 = 3
(b) Division of the data with φ=0
L1 = 3
(c) Division of the data with φ=1
L1 = 3
(d) Division of the data with φ=2
L2 = 4
(e) Selection from the data obtained by the probe A and C with φ=1

FIGURE 3. The tandem type two-point method

4. SIMULATION

The proposed method has the ability to measure step-wise profiles that include high frequency components because no Fourier technique is used. In this section, the validity of the proposed method is confirmed by simulation.

In the simulation, the design shape is step-wise profiles as shown in Figure 4. Here, $L_1 = 5$, $L_2 = 3$, $S = 1$ and the number of data points is equal to 20. The red, blue and yellow lines are data obtained by probes A, B, and C respectively as shown in Figure 4. Figure 5 shows the result from using the proposed method. The analyzed result agreed well with the design profile.

5. CONCLUSIONS

In this paper, a tandem type sequential two-point method that shares one of three probes was proposed, and a new analysis algorithm was developed for the proposed method. The proposed method was able to measure step-wise profiles that include high frequency components because no Fourier technique was used. In this paper, the validity of the proposed method was confirmed by simulation.

6. ACKNOWLEDGMENT

This study is financially supported in part by a special grant in aid from the Toyama Prefectural University.

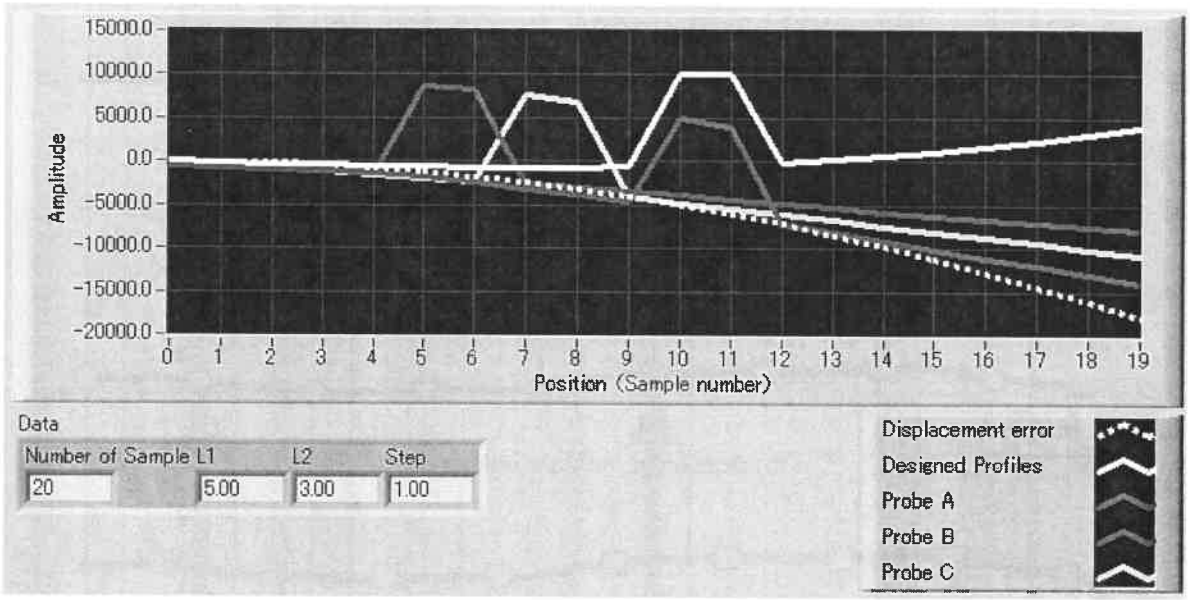

FIGURE 4. The Design profiles and data obtained by tandem type two-point method with probes A, B and C

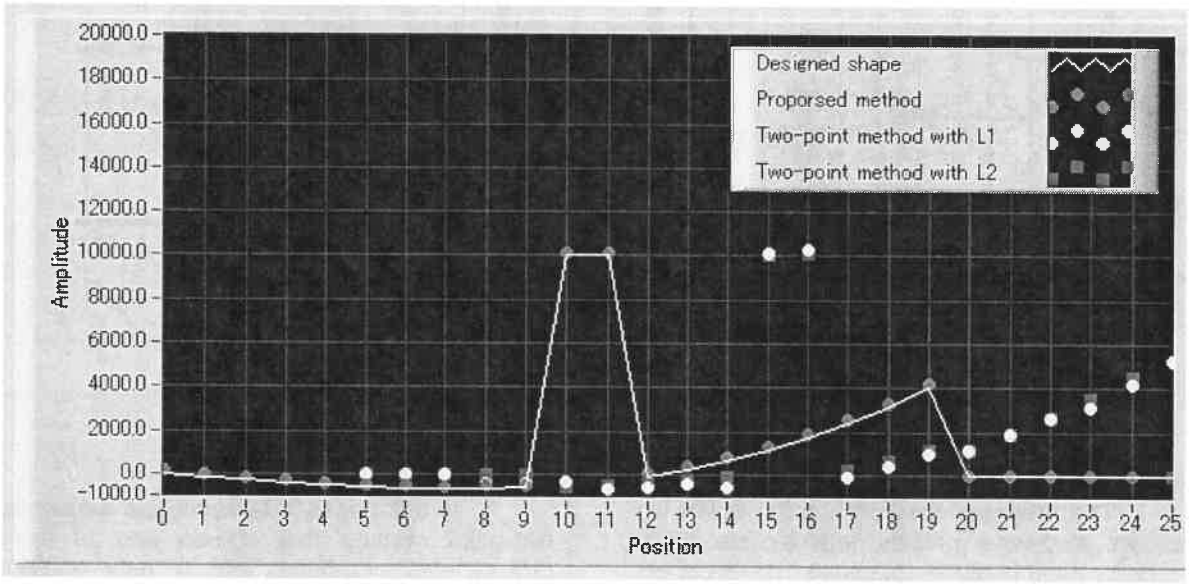

FIGURE 5. The result obtained by tandem type two-point method

REFERENCES

[1] G. Makochs, B. Scholf, Surface profiling by electro optical phase measurements, SPIE, High Resolution Soft X-Ray Optics, 1981; 316: 42-53.

[2] H. Tanaka, K. Tazawa, H. Sato, M. Ohori and H. Sekiguchi, Application of a new straightness measurement method to large machine tool, Annals CILP 1981; 30(1): 455-459.

[3] S. Kiyono, P.Huang, N. Fukaya, Datum introduced by software methods, Int. Conf. Of Advanced Mechatronics, Tokyo 1989; 467-472.

[4] W. Gao, A. Kiyono, High accuracy profile measurement of a machined surface by the combined method, Precision Engineering, Journal of ASPE 1996; 19(1): 55-64.

BASIC STUDY FOR DEVELOPMENT OF MEASUREMENT SYSTEM FOR MICRO CYLINDER

Ichiro Ogura[1], Yuichi Okazaki[1]
[1]Fine Manufacturing Systems Group
Advanced Manufacturing Research Institute
National Institute of Advanced Industrial Science and Technology (AIST)
Tsukuba Ibaraki Japan

INTRODUCTION

In order to guarantee the accuracy of products, a profile measurement evaluation process is indispensable. This study describes the development of measurement system for micro parts. The concept for micro measurement center that can measure profile, roundness, and hole profile of micro parts, is proposed. We developed a measurement system for micro cylinder that is a basic system for this measurement center. These probes measure a diameter and roundness of the micro cylinder on spindle. The contact detection results guarantee the validity of this system that measures the micro cylinders in sub-micron order.

CONCEPT OF MICRO MEASUREMENT CENTER

FIGURE 1 shows a concept of micro measurement center (MMC). The MMC system is an integrated one of micro-CMM and micro cylinder measurement system. The system can change suitable probe unit for measured object, such as general profiles (CMM), cylinder profiles (roundness), and roughness.

To realize MMC, we must develop new probe unit, and valuate rectangular between each axis strictly.

We have developed novel type of CMM probes that can measure contact and contact angle simultaneously [1][2]. This probe is an element technology integrated into the MMC system. And, the measurement system for micro cylinder that will be described in next section, is also an element technology of MMC.

MEASUREMENT SYSTEM FOR MICRO CYLINDER

We developed a measurement system for micro cylinder. FIGURE 2 shows a set-up of this system. The system has two micro-contact

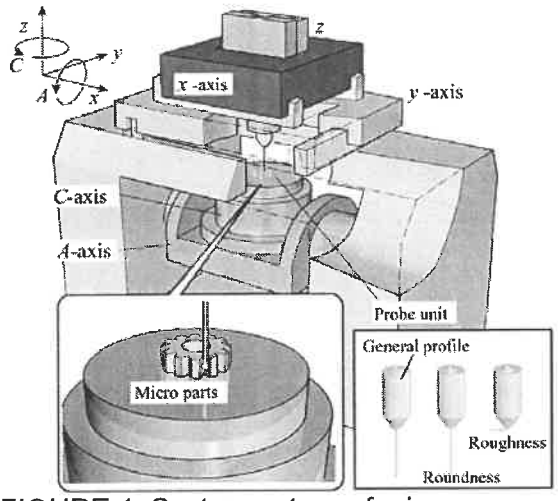

FIGURE 1. System set-up of micro measurement center

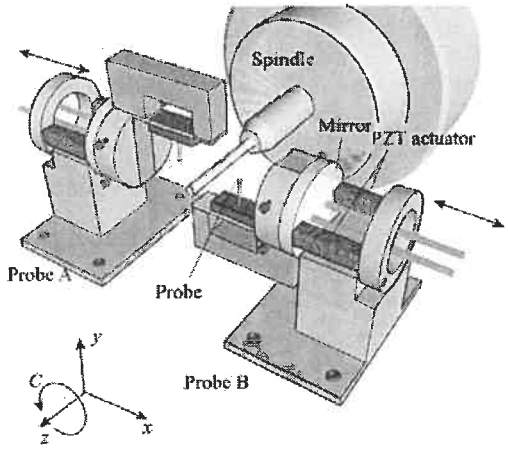

FIGURE 2. Overview of measurement system for micro cylinder

probes, which are arranged in the opposite side. Each probe motion is measured by precision displacement sensor. These probes measure a diameter and roundness of the micro cylinder on spindle. This system can also measure the straightness of micro cylinder if the probes move z direction precisely.

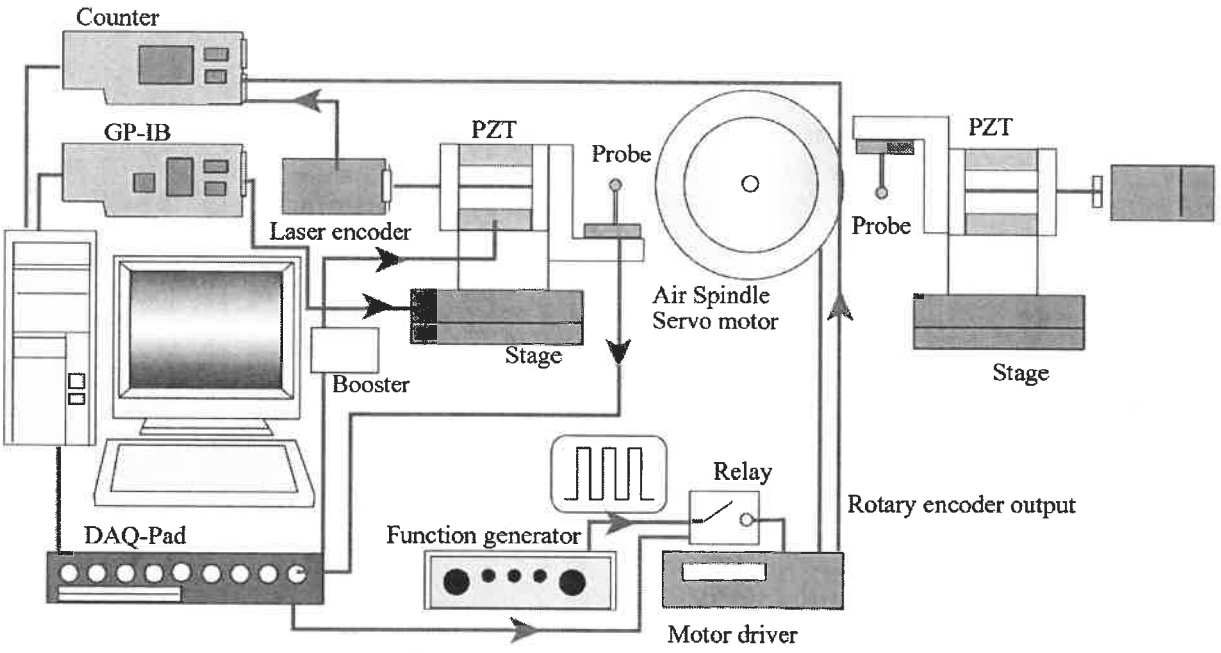

FIGURE 3. Signal configuration

The PZT actuator is set to a ring base, and the contact detection probe is arranged in the mirror installed in the edge of PZT actuators. The height of the probe is equal to the one of an optical axis of the laser encoder measured through the ring base. Therefore, in this system, the Abbe error can be avoided.

The laser encoder is the Renishow RLE10. This encoder measures the whole motion displacement of the probe that is set on the rough motion stage. The light source of RLE10 is built into the main body of this system, and the optical system consists only of the main body and the fiber that ties it with the measuring head. Therefore, the system becomes compact. The resolution of this encoder is 10nm. To get higher resolution, the analog signal of the encoder is divided into 1200 by the interpolator.

FIGURE 3 is a signal configuration of this device. The laser encoder measures the motion displacement of the rough stage and the PZT actuator in real time, and the stage is controlled while observing the contact signal on the personal computer for the measurement. The pulses of the laser encoder and the rotation encoder of air spindle are taken into the personal computer through the counter of each channel. The air spindle rotates at the speed corresponding to the frequency of TTL signal from the function generator. A relay begins and stops the rotation of the spindle. The personal computer controls this relay. In this system, a manual stage moves z-direction. Therefore, about the displacement of the z-direction, the scale of the manual stage is only observed.

EXPERIMENTAL RESULTS

Some basically experiments were performed to verify our developed system.

First of all, the zero point of two contact probes was detected. When the probes make contact, a series of signal is detected like FIGURE 4. We distinguished the contact when the mean value of signal for 100msec was 0.5V or higher. FIGURE 5 is a result of zero point detection. This figure shows the motion displacement and contact signals of right and left probes. The approach displacement was 30nm step. The contact was detected within 30nm step though this experiment. The contact detection is excellent.

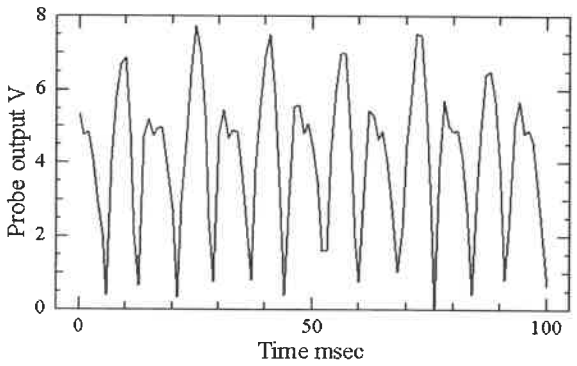

FIGURE 4. Contact signal of probe

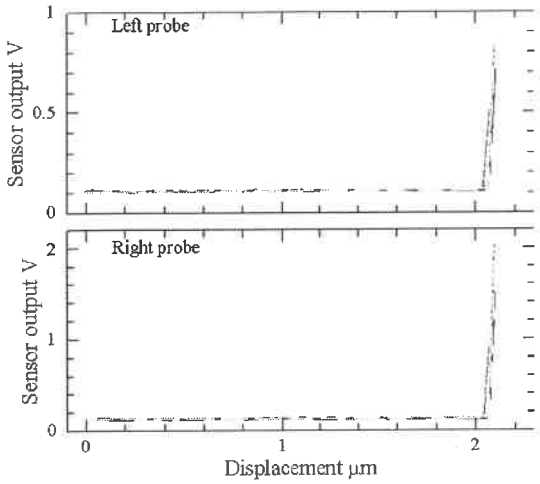

FIGURE 5. Result of zero point detection

Next, the measurement experiment for a minute cylinder was performed. The measurement procedure is as follows. The diameter of a minute cylinder is measured based on zero points. The cylinder is rotated by air spindle for next measurement point. When the rotation of the cylinder becomes 360 degrees, the diameter of a round is measured. In addition, the sample is moved over in the direction of z, and the straightness of the cylinder is measured.

FIGURE 6 is a typical result of the measurement. The sample is stainless wire of 350 microns diameter. The mean value of the diameter that measured data was 346.43 microns and it was corresponding well. The part where the diameter of 240 degrees neighborhood has become small is a place where it could be confirmed that this part is smooth also in the camera observation.

The 1st order run out error is the problem for measurement experiments. This is caused by a disagreement between center point of rotating spindle and measured cylinder. In this experiment, the cylinder was just set to the spindle chuck. Therefore, we must add an adjustment mechanism to this system.

FIGURE 7 is a straightness measurement result. The stage was feed in the step of 0.5mm, and the contact displacement of a right and left probe at that time was plotted. In this figure, the inclination element when the stage is sent is removed. The shapes of right and left probe have similar tendency. The reason is thought that the influence of the motion error of the stage is large. It is necessary to use precise stage for more accurate measurement.

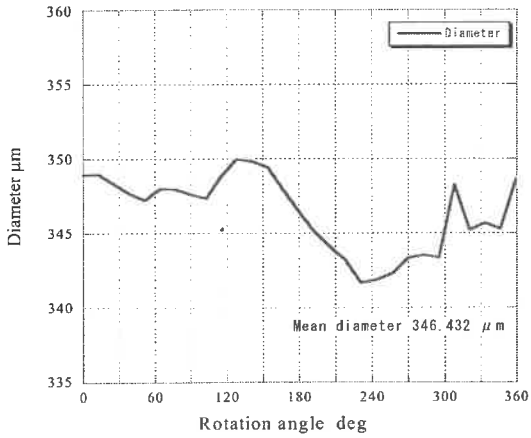

FIGURE 6. Results of diameter measurement

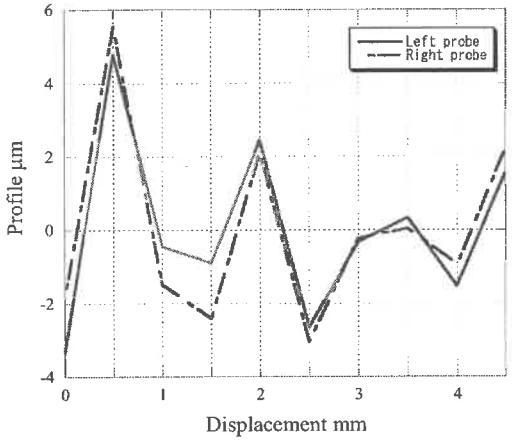

FIGURE 7. Results of straightness measurement

CONCLUSION

A concept of MMC, that can measure profile, roundness, roughness of micro parts, is proposed. We have developed the measurement system for micro cylinder. This probe is an element technology integrated into the MMC system. The contact detection results guarantee the validity of this system that measures the micro cylinders in sub-micron order. The profile measurement result for a minute cylinder showed some problem about the 1st order run out error of rotating cylinder and the motion error of the stage.

REFERENCES

[1] I. Ogura and Y. Okazaki. A Study for Development of Small-CMM Probe Detecting Contact Angle, Proc. of ASPE Summer topical meeting. 2003.

[2] I. Ogura and Y. Okazaki, Development of micro-CMM Probe detecting contact angle, Proc of ASPE annual meeting. 2004.

DEVELOPMENT OF CALIBRATION DEVICE FOR ATOMIC FORCE MICROSCAPE

Yuta Suzuki and Satoshi Honda
Department of mechanical Engineering
Tokyo Metropolitan University
Minami-osawa, Hachioji, Tokyo, Japan

INSTRUCTIONS

An atomic force microscope (AFM) is very useful for observing surface of nano-structures. However, the measured topography of the nano-structure, which is detected by a cantilever of the AFM, does not completely correspond to the true topography of the nano-structures because the cantilever is driven by some piezoelectric actuators with their undesirable properties such as non-linear expansion or hysterics displacement. Therefore, if we do not compensate motion of the cantilever during detecting of the nano-structures or we do not calibrate the measured data, the topography of the nano-structures is measured as a distorted topography.

Some compensation methods and calibration methods have been developed. One of the compensation methods is that the scanning motion of the cantilever is accurately compensated by a feedback control system with an ultra precise position sensor. The precise position sensor detects the horizontal position of the cantilever with accuracy of nanometers, and the feedback control system precisely generates the scanning motion of the cantilever without non-linear expansion and hysterics displacement. However, the vertical detecting motion in which the cantilever detects altitude of the nano-structures remains not to be compensated because it is impossible to measure the vertical position of the cantilever without including the vertical displacement error of the piezoelectric actuator and it is impossible to utilize measured vertical position as a feedback value of the compensation control system.

The calibration method utilizing a topography standards[1] and a self-calibration method[2] have been also proposed. The topography standards is precisely formed into the checked pattern which depth and width and pitch have absolute values. Therefore, scanning motion and vertical detecting motion of the cantilever are calibrated by comparing the profile detected by the AFM with the profile of the topography standards. However, many topography standards must be provided so that depth and width and pitch of the topography standards are typical of depth and width and pitch of many nano-structures, and also the topography standards must represent many three-dimensional shapes and many surface conditions.

In the self-calibration method, two piezoelectric actuators to be connected in series are attached at the cantilever. Several topographies of the nano-structure are measured by driving one piezoelectric actuator under another piezoelectric actuators are expanded by several displacement. Calibration property for the non-linear expansion and hysterics displacement of the piezoelectric actuators is calculated, and true profile of the nano-structure is measured. However, stiffness of the cantilever unit weakens by attaching two piezoelectric actuators, and also, structure and system of the AFM becomes complicated by this modification.

In this paper, a novel calibration device for the AFM is developed. The calibration device consists of an elastic hinge frame and two amplitude stoppers. A calibration surface of the calibration device always vibrates with constant amplitude and with changeable frequencies. The calibration is accomplished by comparing waveform of the calibration device with measured waveform by the cantilever of AFM. In this paper, structure of the calibration device and the principle of this calibration method are described. The fundamental performances of the calibration device are confirmed in experiments.

STRUCTURE OF THE CALIBRATION DEVICE FOR THE ATOMIC FORCE MICROSCOPE

The calibration device consists of an elastic hinge frame with six elastic hinges and two amplitude stoppers as shown in figure 1. The elastic hinge frame is fixed on the base at a

center of the frame by two bolts, and the amplitude stoppers are closely set to the left and right end of the frame. When the periodic force acts at the end of the frame, the frame vibrates with constant amplitude limited by the stoppers as shown in figure 2. If the periodic force becomes stronger or the frequency of the periodic force changes, amplitude of the vibrating frame is not changed, and amplitude of the vibrating frame is only regulated by the gap distance between the ends of the flame and the stoppers. When the calibration is executed and a tip of the cantilever is approached on a calibration surface of the calibration device, the cantilever detects horizontal vibrating waveform of the calibration surface and vertical vibrating waveform of the calibration surface. The horizontal amplitude of the calibration surface becomes constant amplitude of several micrometers, and the vertical amplitude of the calibration surface becomes constant amplitude of several nanometers because the calibration device composes a parallel linkages and amplitude of the calibration surface is reduced geometrically. The calibration is accomplished by comparing vertical and horizontal amplitude of the calibration device with vertical amplitude and horizontal repeated pitch of the vibrating waveform detected by the cantilever. The calibration device has advantages as follows; the structure of the calibration device is simple and small, the calibration surface always vibrates with constant amplitude, the amplitude of the calibration surface is geometrically reduced, vibrating frequency of the calibration surface changes by frequency of the periodic force.

Figure 3 shows the geometrical model of the calibration device. If we set the gap distance (x) between the ends of the frame and the stoppers to a several hundred micrometers, the horizontal amplitude (X) of the calibration surface becomes

$$X = (a/b)x \quad ,$$

where, b represents distance between an end hinge and a center hinge, a represents distance between the center hinge and a top hinge. The horizontal amplitude (Y) of the calibration surface becomes

$$Y = -a(1-\cos\theta) \quad ,$$

where, θ represents deformed angle of the hinge frame, and the vale of the deformed angle

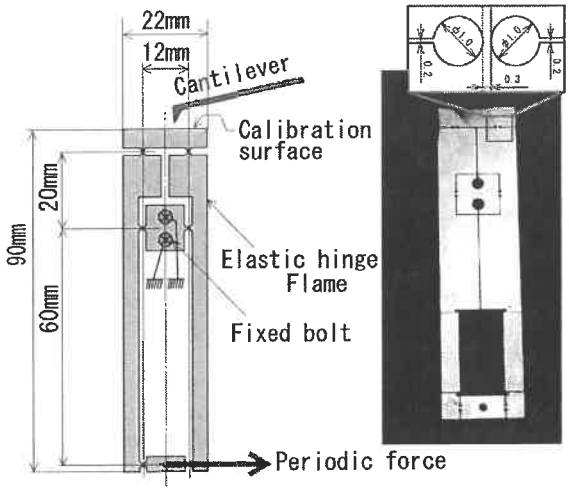

FIGURE 1. Structure of the calibration device for the atomic force microscope.

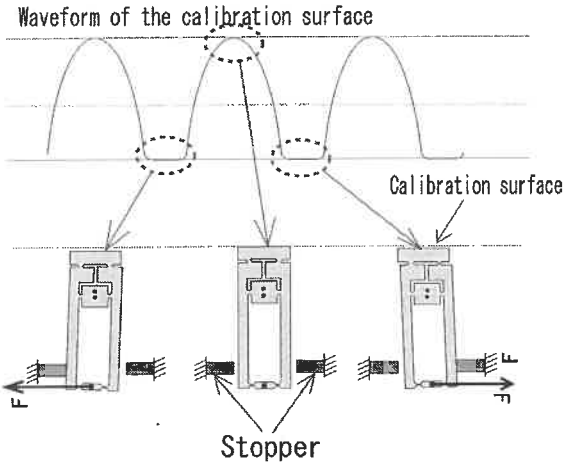

FIGURE 2. Vibrating waveform of the calibration device.

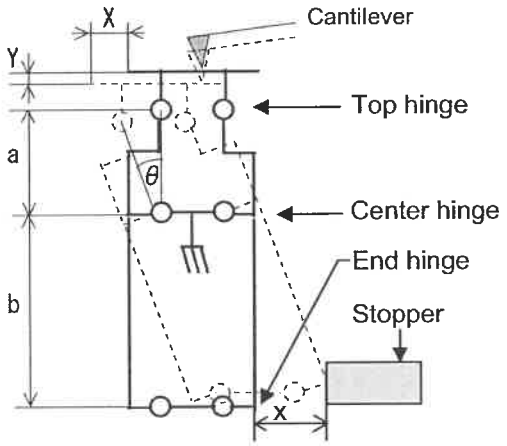

FIGURE 3. Geometrical model of the calibration device.

becomes $\theta = \sin^{-1}(x/b)$.

For examples, when we set the gap distance (x) to 200 micrometers, the horizontal amplitude (X) of the calibration surface becomes 66.6 micrometers and the horizontal amplitude (Y) of the calibration surface becomes 55.6 nanometers. We can make the calibration device with constant amplitude of several nanometers.

EXPERIMENTAL RESULTS

An experimental apparatus is shown in figure 4. The elastic hinge frame is fixed at the frame center by bolts, and the amplitude stoppers are closely set to the left and right end of the frame, and static force instead of the periodic force is acted by hanging weight on the loading system composed of wire and pulleys as shown figure 5. The displacement of the calibration surface against static force is measured by laser interferometers when the amplitude stoppers are not set to the left and right ends of the frame, or when the stoppers are closely set to the left and right end of the frame. The elastic hinge frame is made of ultra super duralumin of A7075. The elastic hinge frame is made by a wire discharge cutting method.

Figure 6 showed the horizontal displacement of the calibration surface against static force when the amplitude stoppers were not closely set to the left and right ends of the frame. The displacement of the calibration surface was proportional to the static force in the range from -0.49 N to +0.49 N, and the horizontal displacements became from -0.1 millimeters to +0.1 millimeters. The proportional displacements also indicated fine repeatability of relation between the static force and horizontal displacement.

Figure 7 showed the vertical displacement of the calibration surface against static force when the amplitude stoppers were not closely set to the left and right ends of the frame. In this figure, red square marks and yellow triangular marks were experimental displacements, and blue diamonds marks were theoretical displacements. The experimental displacements of the calibration surface symmetrically indicated a convex curve against the static forces in the range from -1.0 N to +1.0 N, and the displacements became from 0.0 micrometers to -1.4 micrometers. The experimental displacements generally

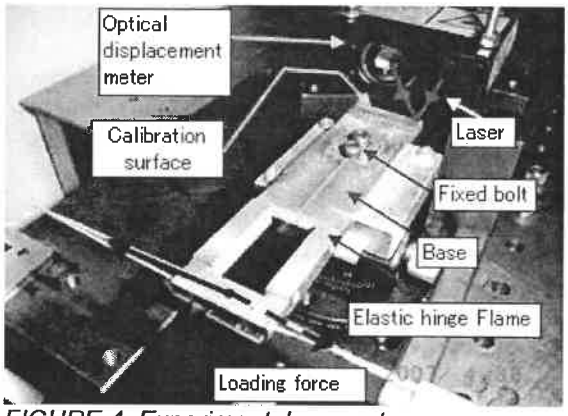

FIGURE 4. Experimental apparatus.

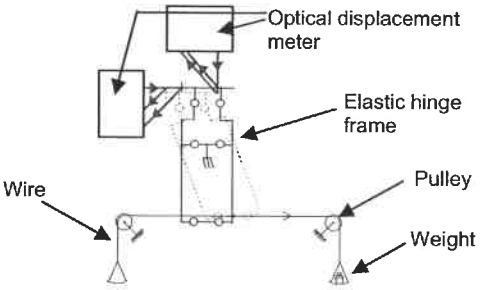

FIGURE 5. Static force loading system utilizing wire and pulleys.

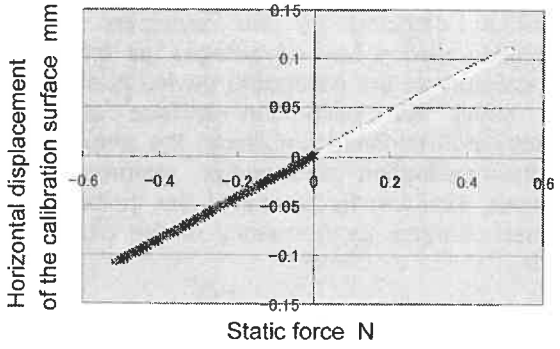

FIGURE 6. Horizontal displacement of the calibration surface without stoppers.

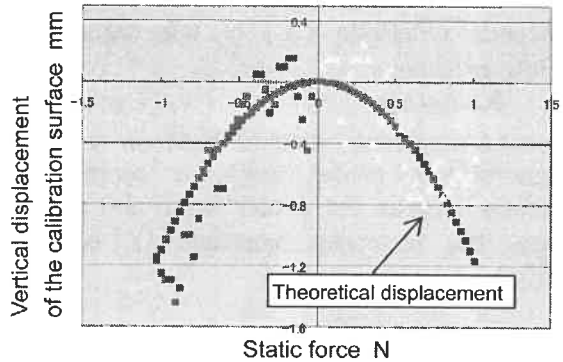

FIGURE 7. Vertical displacement of the calibration surface without stoppers.

corresponded to the theoretical displacements.

Figure 8 showed the horizontal displacement of the calibration surface against static force when the stoppers were closely set to the left and right ends of the frame. Gap distance between the stoppers and the left and right ends of the frame was regulated by micrometers. The horizontal displacement of the calibration surface was proportional to the static force until the frame contacted on the stoppers. After the frame contacted on the stoppers, the horizontal displacement of the calibration surface was kept to the limited displacement. Although the displacement of the calibration surface was increasing little by little after the frame contacted on the stopper, this drift was estimated the elastic deformations of the frame and the stoppers, and other parts.

Figure 9 showed the waveform of the horizontal displacement of the calibration surface against the periodic force when the stoppers were closely set to the left and right ends of the frame. The periodic force was generated by swing of the hanging weight of the loading system in the figure 5, and the periodic forces with same period were regulated by changing initial swing angle. In this figure, when the gap distance was set to 0.035 millimeter and initial swing angle were over 20 degrees, the calibration surface horizontally vibrated with the limited amplitude without crashed shakings.

Figure 10 showed the waveform of the vertical displacement of the calibration surface against the periodic force when the stoppers were not closely set to the left and right ends of the frame. The vertical displacement vibrated with two amplitudes of 250 nanometers or 180 nanometers. These two amplitudes indicated the elastic hinge frame did not contact on the left or right stopper. If the elastic hinge frame contacted on the both stoppers, the calibration surface vertically vibrated with same limited amplitude as shown in figure 2.

CONCLUSIONS

(1)The novel calibration device for atomic force microscopes is proposed.

(2)The fundamental performances of the calibration device are confirmed in experiments.

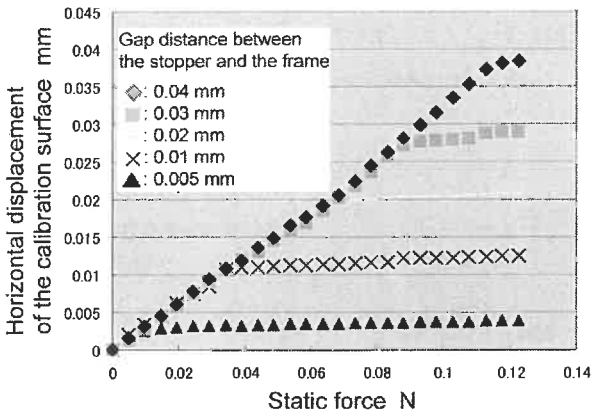

FIGURE 8. Horizontal displacement of the calibration surface with the stoppers.

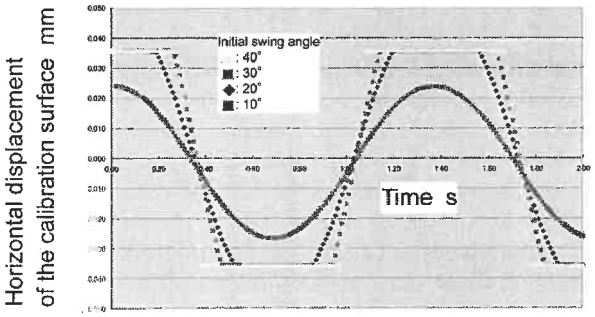

FIGURE 9. Horizontal displacement of the calibration surface for the periodic force with the stoppers.

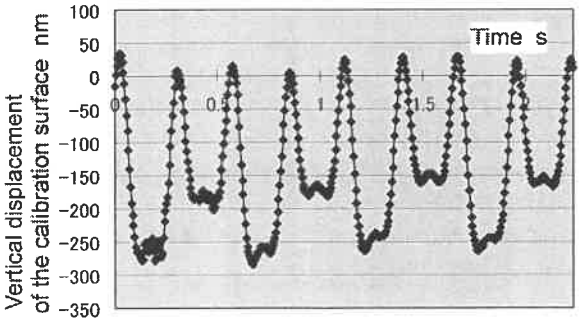

FIGURE 10. Vertical displacement of the calibration surface for periodic force without stoppers.

REFERENCES

[1] VLSI Standard Inc, http://www.vlsistandards.com.

[2] Hyun-kyu Kweon, Wei Gao and Satoshi Kiyono. In situ self-calibration of atomic force microscopy. Nanotechnology. 1998; 9: 72-76.

UNCERTAINTY ANALYSIS OF A LASER CALIBRATION SYSTEM FOR KINEMATIC ACCURACY ASSESSMENT OF MACHINE TOOLS

Heber F.F. Castro
Departamento de Engenharia Mecânica
Universidade Federal da Bahia (UFBA)
Salvador, Bahia, Brazil

INTRODUCTION

The accuracy of thread components depends on the kinematic errors of lathes and thread grinding machines. Castro and Burdekin [1] have developed a method for kinematic accuracy assessment of lathes and thread grinding machines in screw-cutting mode and free of load. Figure 1 shows a schematic layout of the measuring system to assess the kinematic error on a CNC lathe based on this method. A Hewlett Packard (nowadays, "Agilent Technologies") 5529A laser interferometer system measures the longitudinal displacement of the saddle with respect to a cube-corner affixed on the chuck of the spindle. A laser diode system (hereafter LDS), in conjunction with a precision polygon mounted on the spindle assesses the angular position of the spindle. As the spindle rotates, a string of pulses is generated by the angular trigger device (LDS and a pulse generator). These pulses are used for triggering the laser interferometer. A software package has been elaborated for on-the-fly data acquisition and data analysis. The components of the kinematic error considered are progressive pitch error, the cyclic error and spindle-free float. This paper intends to study the individual measurement uncertainties associated with this laser calibration system. As a result of this analysis, the uncertainty budget and the measurement uncertainty of this calibrator are determined.

UNCERTAINTY COMPONENTS

The uncertainty components of this calibrator can be classified into four categories as follows: 1) uncertainties due to trigger device repeatability; 2) uncertainties inherent to the laser system; 3) uncertainties caused by environmental effects; 4) uncertainties caused by the installation. These uncertainty components can be divided into proportional and fixed terms. In this analysis, the calculation of the standard uncertainties associated with this calibrator is based on Type A and Type B evaluations in accordance with GUM [2].

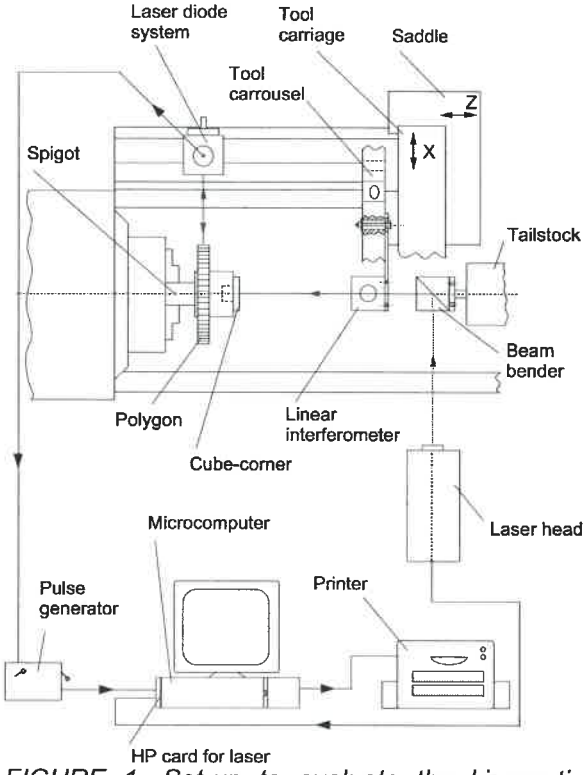

FIGURE 1. Set-up to evaluate the kinematic error on a CNC lathe [1].

Trigger Device Repeatability

The repeatability of the angular trigger device is ±0.2 arc sec with a level of confidence of 95% [1]. The standard uncertainty associated with this repeatability is computed by

$$u_D(\text{arc sec}) = \frac{Re}{t_{95}(m)\sqrt{m}} \qquad (1)$$

where, Re is the repeatability of the trigger device; m is the number of measurements; $t_{95}(m)$ is the Student factor for a given value of m with a level of confidence of 95%. In this case, Re = 0.2 arc sec, $m = 5$, $t_{95}(5) = 2.776$. Substituting these values in Eq. (1), it results u_D = 0.0322 arc sec. Therefore, the standard

uncertainty in the position of the saddle due to the repeatability of the trigger device is given by

$$u_1(\mu\text{m}) = \frac{(0.0322\text{s})\,pitch(\text{mm})10^3}{(360)(3600\text{s})} \quad (2)$$

where, $pitch(\text{mm})$ is the nominal pitch (in millimetre) that is set on the machine for the screw-cutting test.

Uncertainties Inherent to the Laser System

Some sources of uncertainty of the laser interferometer system are intrinsic to this equipment and affect the measurement accuracy. They are considered in the following sections.

Laser Wavelength Uncertainty

The principle of measuring of the laser interferometer system is based on the value of the wavelength of the laser light. If this value changes for any reason, a measurement error occurs. Lifetime wavelength uncertainty for the laser heads is ±0.02 ppm (parts-per-million) with optional calibration to MIL-STD 45662 [3]. In this analysis, the measured distance L (hereafter) is given in metres. Assuming a rectangular probability distribution for the uncertainty in the laser wavelength, its standard uncertainty is calculated by

$$u_2\ (\mu\text{m}) = \frac{L(\text{m})(\pm 0.02\ \text{x}10^{-6})}{\sqrt{3}} = \frac{0.02L}{\sqrt{3}} \quad (3)$$

Electronic Error

In the Hewlett Packard (HP) system, the electronics error is equal to the uncertainty of the least resolution count. For this set-up, the measurement resolution is 1 nm. A rectangular distribution for the resolution of the laser interferometer system' s measurement display is assumed. This gives a standard uncertainty of

$$u_3(\mu\text{m}) = \frac{0.001/2}{\sqrt{3}} \quad (4)$$

Optics Non-linearity

The interferometer can contribute to measurement uncertainty because of its inability to separate perfectly the two laser beam components (vertical and horizontal polarisation). This error is referred to as optics non-linearity. For a linear interferometer, the peak-to-peak phase error is 5.4°, corresponding to a distance of ±4.8 nm. Using a statistical model, this value is ±4.2 nm. As this error is periodic (sinusoidal), the "U"-shaped probability distribution is assumed [4]. The standard uncertainty of the optics non-linearity is computed by

$$u_4(\mu\text{m}) = \frac{0.0042}{\sqrt{2}} \quad (5)$$

Uncertainties caused by Environmental Effects

These uncertainties are related to the influence of the atmospheric conditions, thermal properties of the machine under test and temperature change of the optics on the measurement uncertainty of this calibrator.

Wavelength Compensation

Since most laser interferometer systems operate in air, it is necessary to correct for the difference between vacuum wavelength and the wavelength in air. This correction is referred to as *atmospheric or wavelength compensation*. Without this compensation, degradation in system accuracy and repeatability would occur. Assuming a standard and homogeneous air composition, a 1 ppm error results from any one of the following conditions [3]: a) a 1°C change in air temperature; b) a 2.5 mm of mercury change in air pressure; c) an 80% change in relative humidity.

The thermometer and barometer utilized in the experiments have an accuracy of ±0.2°C and ±2 mm Hg, respectively. The relative humidity was estimated at an accuracy of ±20%. Assuming a rectangular distribution, the standard uncertainties in the assessment of the air temperature, air pressure and relative humidity are, respectively, $0.2\ \text{ppm}/\sqrt{3}$, $0.8\ \text{ppm}/\sqrt{3}$ and $0.25\ \text{ppm}/\sqrt{3}$. The standard uncertainty of the wavelength compensation is given by

$$u_W(\text{ppm}) = \sqrt{(\frac{0.2}{\sqrt{3}})^2 + (\frac{0.8}{\sqrt{3}})^2 + (\frac{0.25}{\sqrt{3}})^2} = \frac{0.862}{\sqrt{3}} \quad (6a)$$

$$u_5(\mu\text{m}) = u_W L = \frac{0.862L}{\sqrt{3}} \quad (6b)$$

Material Thermal Expansion

Correction for expansion (or contraction) may be necessary due to the variation of dimensions of the machine caused by temperature changes. This correction relates the distance measurement back to a standard temperature of 20°C. The method of correction is to change the laser wavelength compensation by an amount sufficient to correct for thermal expansion. This correction is known as *material thermal compensation* (MTC) and is defined as

$$\mathrm{MTC} = \alpha(T_{\mathrm{M}} - 20) \tag{7}$$

where, α is the coefficient of material expansion (ppm/°C) and T_{M} is the temperature of the machine in Celsius (°C). MTC is given in ppm. For steel α = 11.7 ppm/°C.

The standard uncertainty of the MTC u_6 is computed in accordance with GUM [2], considering that the input quantities α and T_{M} are independent or uncorrelated. In this computation, the partial derivatives $\partial \mathrm{MTC}/\partial \alpha = T_{\mathrm{M}} - 20$ and $\partial \mathrm{MTC}/\partial T_{\mathrm{M}} = \alpha$ are employed. Besides, $u'_T = 0.2/\sqrt{3}$ is the standard uncertainty of the thermometer in °C (Celsius) and $u'_\alpha = 0.1\alpha/\sqrt{3}$ is the standard uncertainty of the coefficient of material expansion α in ppm/°C. Hence,

$$u_6(\mu\mathrm{m}) = \sqrt{\left(\frac{2.34L}{\sqrt{3}}\right)^2 + \left[\frac{|T_{\mathrm{M}} - 20|\,(1.17L)}{\sqrt{3}}\right]^2} \tag{8}$$

Optics Thermal Drift

This occurs in the linear interferometer in the form of a change in optical path length with changes in temperature. A typical value for optics thermal drift is 0.5 µm/°C [3]. This error only occurs when the temperature varies during the measurement time. As the tests were of short duration, the temperature did not change. Therefore, the correction for optics thermal drift is null. Assuming a rectangular distribution for the thermometer accuracy (±0.2°C), the standard uncertainty of the optics thermal drift is calculated as follows:

$$u_7(\mu\mathrm{m}) = \frac{0.2}{\sqrt{3}}(0.5\ \mu\mathrm{m/°C}) = \frac{0.1}{\sqrt{3}} \tag{9}$$

Uncertainties caused by the Installation

These sources of uncertainty are related to the installation of the laser interferometer system.

Deadpath Error

Deadpath error is caused by an uncompensated length of the laser beam between the interferometer and retroreflector, with the machine stage at zero position. Deadpath error can be calculated as follows [3]:

$$De = (D)(\Delta WCN) \tag{10}$$

where, De is the deadpath error, D is the deadpath distance and ΔWCN is the change in wavelength compensation number during the measurement time. As the tests were of short duration, the deadpath error is negligible due to the fact that there were no significant changes in the atmospheric conditions, i.e. $\Delta WCN = 0$.

The standard uncertainty of the deadpath correction is calculated by

$$u_8(\mu\mathrm{m}) = Du_W = (0.21)\left(\frac{0.862\ \mathrm{ppm}}{\sqrt{3}}\right) = \frac{0.1810}{\sqrt{3}} \tag{11}$$

where, $D = 0.21\,\mathrm{m}$ and u_W is given by Eq. (6a).

Cosine Error

The cosine error in ppm, when using the cube-corner reflectors, is approximately equal to $S^2/8L_{\mathrm{mm}}^2$, where L_{mm} is the measured distance in millimetre and S is the lateral offset of the returning beam in micrometer [3]. In this application, $S = 300\,\mu\mathrm{m}$ for a measured distance of 1 m. Hence, for L_{mm} =1000 mm, the cosine error is given by

$$Ce(\mu\mathrm{m}) = \frac{S^2}{8L_{\mathrm{mm}}^2}(1\,\mathrm{m}) = \frac{(300)^2}{8(1000)^2}(1\,\mathrm{m}) = 0.01125 \tag{12}$$

Assuming a rectangular distribution, the standard uncertainty of the cosine error for $L = 1\,\mathrm{m}$ is given by

$$u_9(\mu\mathrm{m}) = \frac{0.01125}{\sqrt{3}} \tag{13}$$

COMBINED AND EXPANDED UNCERTAINTY

The standard uncertainties u_5 and u_8 are a function of u_W. This means that these input

uncertainties are correlated. Assuming all of the other standard uncertainties are independent, the combined standard uncertainty u_C is calculated by [2]

$$u_C = \sqrt{u_1^2 + u_2^2 + u_3^2 + u_4^2 + u_6^2 + u_7^2 + u_9^2 + (u_5 + u_8)^2} \quad (14a)$$

For L = 1 m, T_M = 20°C and $pitch$ = 10 mm, the value of u_C is

$$u_C(\mu m) = 1.48 \quad (14b)$$

The expanded uncertainty $U_p = k_p u_C = t_p(\nu_{eff}) u_C$. t_p is the Student factor for a given value of ν_{eff} with a level of confidence p [2]. ν_{eff} is the effective degrees of freedom which is calculated by the Welch-Satterthwaite formula [2]. For this application, $\nu_{eff} = 5.03 \times 10^{15}$. As ν_{eff} has a huge value, the t-distribution (Student's distribution) approaches the normal probability distribution [2]. Thus, for a level of confidence of approximately 95%, the coverage factor $k_{95} = 2$, considering the normal distribution. Hence,

$$U_{95}(\mu m) = 2u_C = 2.96 \quad (15)$$

TABLE 1. The uncertainty budget of the kinematic error calibrator for L = 1 m, $pitch$ = 10 mm and T_M = 20°C.

Source of uncertainty	**Probability distribution**	**Standard uncertainty (μm)**
Trigger device repeatability	normal	$u_1 = 0.0002485$
Laser wavelength uncertainty	rectangular	$u_2 = 0.012$
Electronics error	rectangular	$u_3 = 0.00029$
Optics non-linearity	"U" shaped	$u_4 = 0.0030$
Wavelength compensation	rectangular	$u_5 = 0.498$
Material thermal compensation	rectangular	$u_6 = 1.351$
Optics thermal drift	rectangular	$u_7 = 0.058$
Deadpath correction	rectangular	$u_8 = 0.105$
Cosine error	rectangular	$u_9 = 0.006495$
Combined standard uncertainty	Normal	$u_C = 1.48$
Expanded uncertainty	Normal; $k_{95} = 2$ $p = 95\%$	$U_{95} = 2.96$

CONCLUSIONS

1) A study of the uncertainty components that make up the uncertainty budget of the kinematic error calibrator has been carried out. The sources of uncertainty that have been considered are the following: trigger device repeatability, laser wavelength uncertainty, electronics error, optics non-linearity, wavelength compensation, material thermal compensation, optics thermal drift, deadpath correction, cosine error;

2) The measurement uncertainty of this calibrator was computed according to GUM [2]. This uncertainty analysis was calculated when this calibrator was applied on a CNC lathe. The expanded uncertainty of this calibrator was ±2.96 μm for a measured distance of 1 m and nominal pitch of 10 mm with the machine at temperature of 20°C. This uncertainty is based on a combined standard uncertainty multiplied by a coverage factor $k_{95} = 2$, providing a level of confidence of approximately 95%.

REFERENCES

[1] Castro HFF, Burdekin M. Calibration System based on a Laser Interferometer for Kinematic Accuracy Assessment on Machine Tools. Int. J. Mach. Tools Manuf. 2006; 46(2): 89-97.

[2] Guide to the Expression of Uncertainty in Measurement, ISO (International Standardization Organization) TAG 4, corrected and reprinted, 1995.

[3] Steinmetz CR. Sub-micron Position Measurement and Control on Precision Machine Tools with Laser Interferometry. Precision Engineering 1990; 12(1): 12-24.

[4] Bendat JS, Piersol AG. Engineering Applications of Correlation and Spectral Analysis. John Wiley & Sons. California: 1980.

INCLUDING THE UNCERTAINTY OF CMM MEASUREMENTS AND STITCHING ALGORITHMS IN THE UNCERTAINTY ANALYSIS OF FIDUCIAL BASED MACHINING

Deven Chopra[1], Bethany Woody[1], and Scott Smith[1]
[1]Center for Precision Metrology
University of North Carolina
Charlotte, North Carolina, U.S.A

INTRODUCTION

Fiducial based manufacturing technique holds a great potential to help achieve long range accuracy on large scale machine tools. The technique called 'Fiducial Calibration System (FCS) was developed at UNC Charlotte. Initial work demonstrated the proof of concept and a technique for uncertainty analysis [1, 2, and 3].

Previous work on the FCS involved the development of the algorithm and proof of concept experiments. This work showed that improved accuracy when machining large scale parts was possible, even though the machine is only required to be accurate over a small work volume. The long range accuracy is derived using fiducials. Fiducials are marks on the part whose position is established using an accurate metrology system in a thermally controlled environment. A model is developed relating the original location of the fiducials to the location of the fiducials in the manufacturing environment. A mathematical transformation is then made on the NC program, altering the original programmed coordinates so that the machined features will be correct at 20°C, regardless of the manufacturing environment. The model corrects for scale errors resulting from temperature, machine squareness, and rotation of the part with respect to the machine (not restricted to a small angle).

To make this technique practically feasible several tasks still need to be accomplished. First it is desirable to implement a technique to probe on a machine tool fast enough to make this method viable in a high volume manufacturing environment. The first step in this process is to investigate different type of fiducials. The choice of fiducial type will then affect the sensor required to read the fiducials both in the manufacturing environment as well as in the metrology laboratory.

Second, there are two significant metrology issues related to this concept that need to be addressed. This concept requires measurement of fiducials on a part both in the metrology lab (to establish a reference) and also on the machine tool. These parts are large and often it is challenging to measure the entire part on a CMM in one set-up. As a result we have investigated the effects of measuring a part in stages and then stitching the measurements together into one coordinate system.

Present work is focused on implementing FCS technique involving all its components and the extension of the uncertainty analysis. Uncertainty analysis is an important criterion to measure the effectiveness of this technique. The previous work on uncertainty analysis of the FCS was based on the assumption that there is no uncertainty associated with the reference data (i.e. the measurements made in the metrology laboratory). An important goal of the present work is to present an uncertainty analysis including the major contributing factors which are, the reference data, stitching algorithm, and the machine data. Each of these uncertainties will affect the final calculated parameters and therefore they must be propagated through the FCS algorithm.

SYSTEM DESCRIPTION

FIGURE 1 presents a flow chart showing the steps involved in fiducial manufacturing technique. The components involved in fiducial manufacturing process include:

(1) Work piece marked with fiducials. In this case the raw material is a piece of ¼ inch thick plate of Al 6061 and the fiducials are different geometries like circles, diamonds and cross hairs marked using laser. However in general, the material can be different as well as

large in size. Also the fiducials need not be the same as shown here.

(2) A coordinate measuring machine in a metrology lab at a controlled temperature (i.e. 20 deg C). The fiducials measured on the CMM form the reference data. If necessary the work piece is measured on the CMM in parts and the then the measurements are stitched to get the reference data.

(3) A machine tool on which the machining is performed. In this case the machine is Monarch VMC 45 vertical spindle milling machine. In order to measure the fiducials on the machine, a vision probe has been designed using a CCD camera in such a way that it can be held in the tool holder. The measurements taken on the machine form the machine data.

The reference data and machine data are then fed into the FCS algorithm together with the CNC part program. The FCS algorithm creates a new part program which is used to machine the part and the machined features show improved dimension and position.

Choice of Fiducials

One of the goals of this project is to investigate alternative techniques for marking and measuring the fiducials. For the original proof of concept tooling balls or machined holes were used as the fiducial. Although these are sufficient for laboratory experiments they are not ideal for a manufacturing environment since the measurement time can be long. One of the techniques we investigated was laser marked geometries as fiducials. FIGURE 2 shows pictures of different fiducial shapes which were marked on the Al 6061 plate with laser.

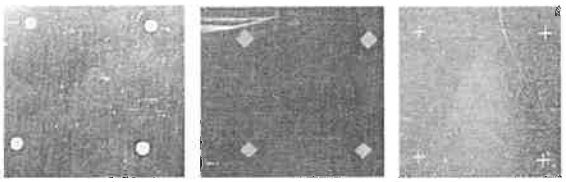

FIGURE 2. Plate with circular fiducials, diamond fiducials and cross hair fiducials.

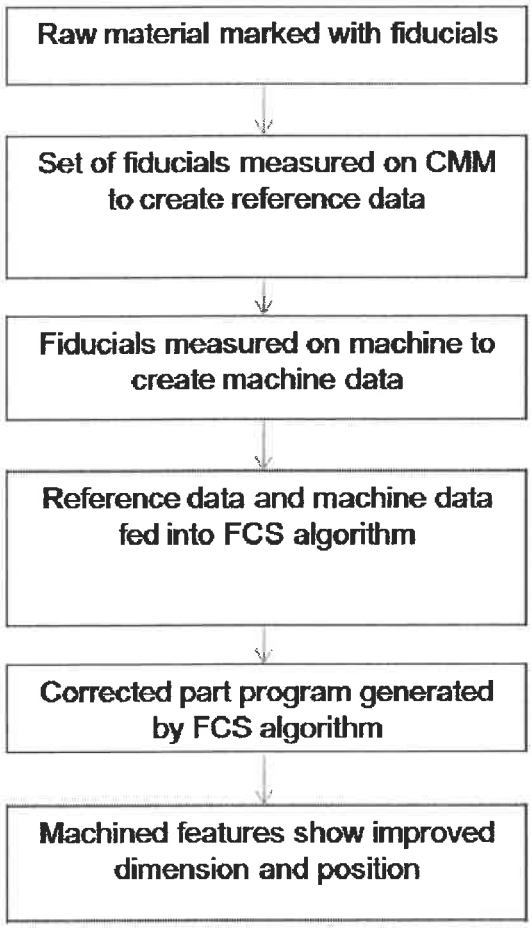
Raw material marked with fiducials
Set of fiducials measured on CMM to create reference data
Fiducials measured on machine to create machine data
Reference data and machine data fed into FCS algorithm
Corrected part program generated by FCS algorithm
Machined features show improved dimension and position

FIGURE 1. Fiducial manufacturing process.

TESTS ON VISION CMM

We used the View voyager vision CMM available at UNC Charlotte to investigate the affect of various parameters on the ability to measure the position and size of each fiducial. FIGURE 4 shows the arrangement of the fiducial marked plate being measured on vision CMM. The tests also helped to understand how well these types of fiducial marks can be measured on commercially available vision systems. This information will help us evaluate what level of performance can be expected from a vision probe that is retrofitted to a milling machine. Results from tests conducted on the vision CMM will aid in developing the measurement process for the vision system fitted on the machine tool.

It was observed that the accuracy in measurement of fiducials depends on how well the edges are formed. A greater roughness in the edges of the fiducial leads to greater edge point scatter, and therefore a higher variation in the measurement. For example the 'rough'

circular fiducials always measured undersize. Since the center of the feature will be calculated from the feature size, error introduced due to rough edges can be a considerable source of uncertainty. FIGURE 3 shows a close up view of a circular fiducial. It is clearly visible how the edges are clearly defined on some part and not so clearly defined on the rest.

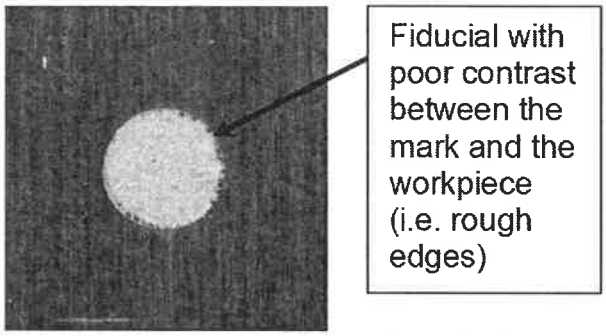

FIGURE 3. Close view of a circular fiducial as seen through the vision CMM.

Also the important role of proper lighting was evaluated during the measurement tests. For the current work, we made measurements under varying lighting conditions by changing the position of the ring light and changing its intensity. It has been observed that lighting which is lesser or greater than the optimum amount leads to edge point scatter and causes considerable error. The measurement setup can be seen in FIGURE 4.

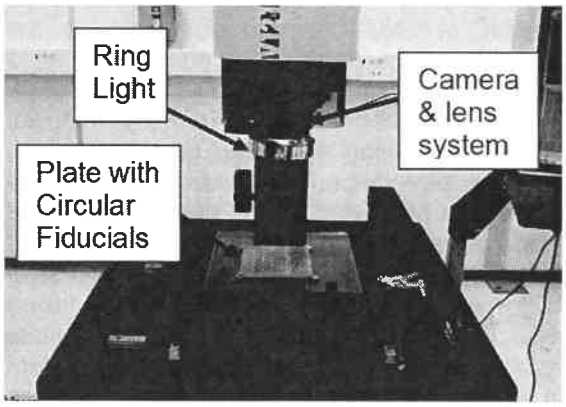

FIGURE 4. Fiducial marked plate being measured on the vision CMM.

Repeatability Tests

TABLE 1 shows the repeatability test results in the x and y coordinate measurements for the centers of fiducials having different geometries. A set of 12 fiducials was measured 10 times each and the standard deviation was calculated for each fiducial. Later a root mean square of the standard deviations from all fiducials was taken. It can also be observed how varying the lighting has affected the measurements in case of circular fiducials.

TABLE 1. Table showing repeatability test results conducted on different fiducial geometries.

Circular	X Coordinate	1.2 μm
	Y Coordinate	1.8 μm
Diamond	X Coordinate	0.77 μm
	Y Coordinate	0.44 μm
Cross Hair	X Coordinate	0.24 μm
	Y Coordinate	0.26 μm
Circular with varying light	X Coordinate	6.3 μm
	Y Coordinate	3.8 μm

STITCHING OF MEASUREMENTS

The FCS technique targets large scale components, often for aerospace applications. These parts are large and often it is challenging to measure the entire part on a CMM in one set-up. The method of choice here is to measure the part in stages using common fiducials in each stage and stitch together each measurement to obtain the map of the fiducials on the part and create the reference coordinate system.

Mathematical modeling of the uncertainty will be conducted in three areas; (1) the uncertainty of the on machine probing, (2) the uncertainty of the reference coordinate system (including CMM stitching), and (3) the propagation of these uncertainties through the fitting algorithm to obtain the uncertainty of the final feature. Steps 1 and 3 have been outlined in previous work. We are focusing on the uncertainty analysis for the creation of the reference system when stitching is required.

We performed stitching of measurements on Al6061 plate marked with circular fiducials. The methodology followed is detailed below.

A set of sixteen fiducials forming a grid of 4x4 is chosen from the set of 4x6. It is to be noted here that the fiducials need not be marked in the same pattern as used in this work. The fiducials are measured in a part coordinate system (designated PCS1). Then the part is taken off the machine table and repositioned so that next grid of fiducials is in the field of view. Then the

second set of fiducials is measured after setting up part coordinate system two (PCS2). Here it is shown that a set of eight fiducials is common between set 1 and set 2. FIGURE 5 shows how the two sets of fiducials will appear in the machine coordinate system. The fiducial shown in square shape is the one that forms the origin for PCS2. Since the fiducial which forms the origin of PCS2 has already been measured in PCS1, the coordinates of all fiducials in PCS2 are then compensated in such a way that the origin of PCS2 is brought back to its position in PCS1. As a result of this we get the position of all fiducials of set 2 in PCS1.

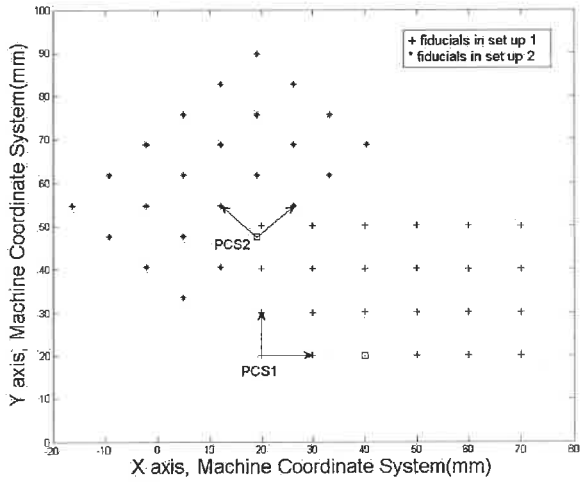
+ fiducials in set up 1
* fiducials in set up 2
PCS2
PCS1
Y axis, Machine Coordinate System(mm)
X axis, Machine Coordinate System(mm)

FIGURE 5: Figure showing the position of PCS1 and PCS2 in the machine coordinate system. We can see that the gird of fiducials has been moved to an altogether different location on the machine table.

UNCERTAINTY CONSIDERATIONS

An uncertainty analysis for FCS technique was presented in [4] which discussed a mathematical model of uncertainty taking into account the uncertainty in the machine data and the propagation of uncertainty. Since the uncertainty in the reference data was not considered in that model, present research is focused on addressing the uncertainty analysis including the reference data and stitching algorithm as well.

Following the method described in the Guide to the Expression of Uncertainty in Measurement (GUM) [5] requires calculation of sensitivity coefficients. This approach was followed in the previous work on uncertainty in [4]. However, including the reference system terms in the analytical model makes it complex to derive the sensitivity coefficients. This complexity calls for an alternative method to estimate the uncertainty for which Monte Carlo simulations will be used. Before proceeding for Monte Carlo simulations, it is important to first understand the sources which contribute towards the uncertainty.

Sources of Uncertainty

The sources of uncertainty in the present work include three major contributors - the reference data, stitching and the machine data.

Data from the tests conducted on vision CMM, stitching of measurements and measurements from the vision probe will be utilized in future to complete this task.

It is to be noted here that when stitching of measurements is performed, error associated with the measurement of the common fiducial will be added to all the measurements of set 2.

Further tests need to be conducted on stitching. Also it is required to find out a method to account for the uncertainty of the stitching process.

REFERENCES

[1] Miller, J., 2001, Utility Patent Application Number 10,007,051, Fiducial Calibration Systems and Methods for manufacturing, Inspection and assembly.

[2] Woody, B.A., Smith, S., "Fiducial Calibration System" *Transactions of NAMRI, XXXIII*, May 24-27, 2005.

[3] Smith, S., Woody, B.A., Miller, J.A., 2005, "Improving the Accuracy of Large Scale Monolithic Parts using Fiducials", Annals of CIRP. Antalya, Turkey, Aug. 21-25, 2005.

[4] Woody, B.A, Smith, K.S., Hocken, R.J., Miller, J.A., 2005, "Uncertainty Analysis for the Fiducial Calibration System", Proceedings of the IMECE2005.

[5] U.S. Guide to the Expression of Uncertainty in Measurement, ANSI/NCSL Z540-2-1997(R2002).

STUDIES ON REPRODUCIBILITY AND ACCURATE MEASUREMENT OF MOISTURE CONTENT OF WOOD SAMPLES USING AN ELECTRIC MOISTURE METER

Reynolds Okai
Department of Design and Technology Education
University of Education, Winneba
Kumasi Campus, P.O. Box 1277, Kumasi, Ghana

ABSTRACT
Studies were conducted on reproducibility, and accurate measurement of moisture content of four wood samples using an electric moisture meter. Experimental results indicated that there was no clear relationship between moisture content and grain angle within a radius of 30mm. Repeated measurements of moisture content at different locations or points on the wood surface showed similar patterns of variation. Within-point standard deviation of the moisture content was bigger than between-point standard deviation. A non-destructive method of measuring moisture content at the same location or point on the wood surfaces could not be proposed because of the high variation of moisture content when repeated measurements were taken at the same point. Instead, accurate measurements of moisture content could be obtained at random positions with a radius of 30mm.

INTRODUCTION
Lumber drying is an important phenomenon in the timber industry. Lumber that is not properly dried will result in loss in strength, susceptibility of the lumber to decay and insects attack and more importantly deformation by warping. The essence of drying is to remove the moisture in the wood to a preferred level. In the timber industry, a non-destructive method of measuring the moisture content of wood samples at different locations is normally employed using an electric moisture meter. However, because of the variation of moisture in wood, in both the radial and tangential directions, readings from the electric moisture meter at different locations on the wood surface may not show similar patterns of variation. Therefore reproducibility which refers to the consistency of the moisture meter to show repeatedly similar patterns of variation may be missing. The purpose of this study is to determine an accurate method of measuring the moisture content of wood samples within a radius of 30mm from the pins of the moisture meter, and also determine if at particular locations or points, there is reproducibility, that is, repeatedly similar patterns of variation when multiple readings are taken.

THEORETICAL CONSIDERATIONS
The standard deviation of a set of measurement is a useful parameter in precision engineering to determine accuracy and reproducibility. In wood processing, standard deviation of a board thickness is a useful parameter to determine lumber thickness variation [1]. The standard deviation of repeated readings at points on the surface of lumber using a moisture meter can be described as within-point standard deviation, S_w, which is the average of the standard deviation of moisture content repeatedly measured at individual points. The between-point standard deviation, S_b, is the standard deviation of the average moisture content repeatedly measured at individual points. Equations 1, 2, and 3 can be used to determine the standard deviation, S_J, of repeated measured moisture content at a point on the wood surface, within-point standard deviation, S_w, and between-point standard deviation, S_b, respectively [2].

$$S_j = \sqrt{\frac{\sum_{j=0}^{N_j} x_j^2 - \left(\frac{1}{N_j}\left(\sum_{j=0}^{N_j} x_j\right)^2\right)}{N_j - 1}} \quad (1)$$

$$S_w = \sqrt{\frac{\sum_{j=0}^{k} S_j^2}{k}} \quad (2)$$

$$S_b = \sqrt{\frac{\sum_{j=0}^{k} A_j^2 - \left(\frac{1}{k}\left(\sum_{j=0}^{k} A_j\right)^2\right)}{k - 1}} \quad (3)$$

The variables used in describing Equations 1 to 3 above are defined as follows:

A_j: average moisture content at point j
K: number of points
N_j: number of measurements at point j
S_j: standard deviation for point j
X_j: measurement from individual points

MATERIALS AND METHODS

Four wood samples, *Elais guineensis*, *Milicia excelsa*, *Khaya ivorensis*, and *Triplochiton scleroxylon*, of tropical origin were selected for the study. The moisture content was measured at grain angle of 0 degree to 150 degrees in step of 30 degrees using an electric moisture meter, that is, measurements were in the order of 0, 30, 60, 90, 120, and 150 degrees. Measurements in the direction of the grain orientation corresponded to 0 degree whilst measurement perpendicular to the grain orientation corresponded to 90 degrees. The wood samples were partitioned into four quadrants and measurements of moisture content were taken at a radius of 30mm from the center axis of the quadrant at six points.

FIGURE 1. Measurement of moisture content at different location (points) on the wood surface at a radius of 30 mm using an electric moisture meter.

Measurement of the moisture content at each point was repeated fifty times. Figure 1 shows a photo of the electric moisture meter and the wood samples. The moisture content recorded from each point on the wood samples was analysed statistically using Equations 1, 2, and 3. Within-point standard deviation and between-point standard deviation of moisture content were computed to determine if there was reproducibility in the readings recorded at each point. The standard deviation of moisture content at each point was determined. Thereafter within-point standard deviation was determined by computing the average standard deviation of the individual standard deviation of moisture content at each point using Equation 2. The mean moisture content recorded at each point was also determined. Thereafter the between-point standard deviation was determined by computing the standard deviation of the mean moisture content of the six points using Equation 3.

RESULTS AND DISCUSSION

MOISTURE CONTENT DISTRIBUTION

Figure 2 shows the relationship between mean moisture content and grain angle of wood samples, *Elais guineensis*, *Milicia excelsa*, *Khaya ivorensis and Triplochiton scleroxylon* measured at six locations. It can be seen from figure 2 that with the exception of *Triplochiton scleroxylon* which showed a continuous decrease of moisture content with increase in grain angle from 0 to 120 degrees, no clear relationship could be established between moisture content and grain angle. In the case of wood samples, *Elais guineensis*, *Milicia excelsa* and *Khaya ivorensis*, there were fluctuations in moisture content with increasing grain angle.

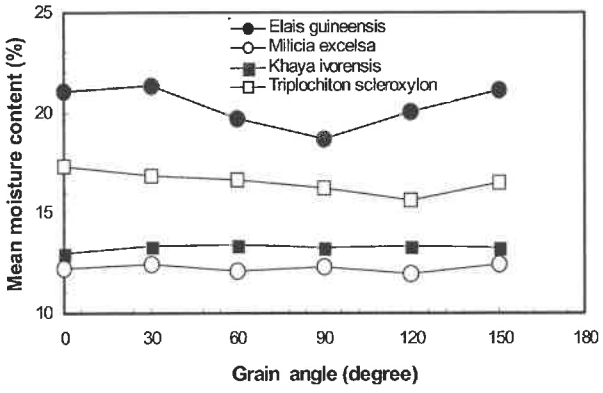

FIGURE 2. Relationship between mean moisture content and grain angle of wood samples, Elais guineensis, Milicia excelsa, Khaya ivorensis and Triplochiton scleroxylon measured at six locations.

Wood is a heterogeneous material and therefore moisture content distribution in the radial and tangential direction is not uniform. It has been

established that cutting force is influenced by grain angle [3]. This study sought to establish the relationship between moisture content and grain angle and to clarify if moisture content has an effect on the relationship between cutting force and grain angle. Experimental results shown in figure 2 indicated that moisture content distribution in wood was not influenced by grain angle due to the fluctuating effect of moisture content with increasing grain angle.

WITHIN-POINT AND BETWEEN-POINT STANDARD DEVIATION OF MOISTURE CONTENT

Table 1 shows within-point and between-point standard deviation of moisture content of the four wood samples selected for the study. It can be seen that regardless of the wood species, within-point standard deviation is always greater than between-point standard deviation. Thus the ratio of within-point standard deviation to between-point standard deviation is greater than unity. A close observation of table 1 shows a high value of within-point standard deviation for all species. The high value of within-point standard deviation is due to the high variation of moisture content for repeated readings. When repeated readings are taken at the same point, the wood cells are broken and the water in the cells is absorbed into the atmosphere thus accounting for variation of moisture content.

REPRODUCIBILITY

This section is solely devoted to reproducibility which refers to the consistency of the moisture meter to show repeatedly similar patterns of variation. Note that reproducibility forms the basis of this study and therefore attempts have been made to treat this topic in a holistic manner. As shown in table 1, similar patterns of variation are recorded, that is, within-point standard deviation is always greater than between-point standard deviation for all the species selected for the study. To address the issue of reproducibility of moisture content measurement, one needs to have a critical look at non-destructive method of moisture content measurement. Ordinarily, the best approach is to measure the moisture content of wood samples at the same location for consistent readings due to the variation of moisture content along the radial or tangential direction of wood. Table 1 clearly suggests that there will be high variation of moisture content if measurements are taken at the same location or points as indicated by higher values of within-point standard deviation. However, consistent readings can be recorded if measurements of moisture content are taken at different locations or points on the wood surface as indicated by lower values of between-point standard deviation.

TABLE 1. Within-point and between-point standard deviation of moisture content of wood samples, Elais guineensis, Milicia excelsa, Khaya ivorensis and Triplochiton scleroxylon measured at six locations.

Species	*MC(%)*	S_b	S_w	S_w/S_b
M. excelsa	12.26	0.20	1.07	5.35
T. scleroxylon	16.54	0.65	0.94	1.45
K. ivorensis	13.17	0.17	0.38	2.24
E. guineensis	20.33	1.03	1.56	1.51

CONCLUSION

Cutting force in wood machining is influenced by moisture content and grain angle. However, no clear relationship has been established between moisture content and grain angle. This study sought to determine an accurate and non-destructive method of measuring moisture content at the same point or location. Experimental results indicated that there is no clear relationship between moisture content and grain angle, that is, the moisture content in wood is not influenced by the grain angle. Repeated measurements of the moisture content at different locations or points on the wood surface showed similar patterns of variation. Within-point standard deviation of the moisture content was bigger than between-point standard deviation. Thus, a non-destructive method of measuring moisture content at the same location or point on the wood surfaces could not be proposed because of the high variation of moisture content when repeated measurements were taken at the same point. Instead, accurate measurements of moisture content could be obtained at random positions with a radius of 30mm.

REFERENCES

[1] Okai R, Mitchual J, Frimpong-Mensah K. Optimisation techniques for minimizing saw teeth deflection and lumber thickness variation. Journal of the American Society for Precision Engineering. 2006; 30:39-46

[2] Brown, TD. Performance excellence in the wood products industry. Lumber size control part 2. Size analysis consideration. 2000
[3] Tanaka C, Huang J. On-line control of bandsaw feed-speed using fuzzy logic. In Proceedings of the 12th International Wood machining Seminar.1995; 412-422

UNCERTAINTY IN MEASUREMENTS OF DIMENSIONAL CHANGES FROM AN INTERFEROMETRIC DILATOMETER

Dongmei Ren, Jimmie A. Miller, Kevin M. Lawton
Center for Precision Metrology
Department of Mechanical Engineering & Engineering Science
University of North Carolina at Charlotte
Charlotte, NC 28223, USA

INTRODUCTION

With low expansion materials finding great applications in micro-lithographic systems and other systems requiring high dimensional stability, accurate determination of the coefficients of thermal expansion of such materials becomes essential. In order to meet requirements for high accuracy determinations of the coefficients of thermal expansion (CTE) of low expansion materials and measurements of other dimensional instabilities, a nanoscale absolute interferometric dilatometer has been developed at the University of North Carolina at Charlotte. This dilatometer is to measure a variety of samples of length up to 100 mm with an uncertainty of 2 nm for the measurement of dimensional change and 1 ppb/K for CTE measurement in a temperature range of 293–373 K. A novel double-pass heterodyne interferometer has been designed for this dilatometer. In this paper, the uncertainty of the measurements of dimensional changes from the interferometer is analyzed.

INTERFEROMETER

The working principle of the interferometer is shown in Figure 1 [1]. This interferometer has a nearly balanced design, in which the nominal optical lengths of the measurement path and reference path are equal except for the paths corresponding to the sample length.

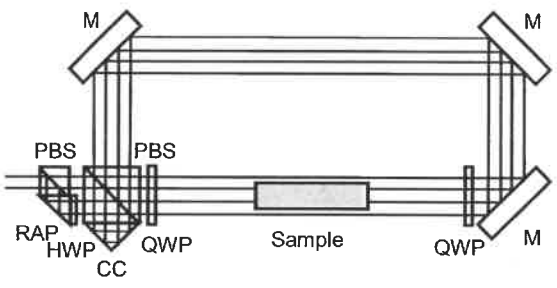

FIGURE 1. Interferometer

UNCERTAINTY ANALYSIS

The main sources of uncertainty for measurements of dimensional changes from this interferometer include the stability of the laser wavelength, nonlinearity of the system, uncertainty of the electronics, uncertainty of the sample length, and environmental changes if the measurements are conducted in air.

Measurement Equation

The heterodyne interferometer determines the dimensional change of a sample by measuring the relative phase change that occurs between the optical path lengths of the interferometer's measurement arm and reference arm. The displacement information given by the interferometer can be expressed as

$$L = k\frac{\lambda}{nK} \tag{1}$$

where λ is the wavelength of laser in vacuum, n is the refractive index of the measurement environment, λ/K is the resolution of the interferometer, and k is the electronic count. Considering the change in the unbalanced path, the dimensional change of the sample should be

$$\Delta l = k\frac{\lambda}{nK} - \Delta l_d \tag{2}$$

where Δl_d is the change of the unbalanced path. For the interferometer operated in air, the major part of Δl_d results from environmental changes. In this analysis, we use the modified Edlén equation [2] to correct the change of refractive index. The correction is given by

$$\Delta l_n = l[(0.93(t-20) - 0.36(p-760) + 0.05(f-10)]\times 10^{-6} \tag{3}$$

where l is the length under standard conditions (t = 20 °C, p = 760 mmHg, f = 10 mmHg), t, p and f are the air temperature (°C), pressure (mmHg) and humidity (water vapor pressure, in

mmHg) of air. From equation (3), the dead-path error caused by environmental changes can be expressed as

$$\Delta l_{d,n} = L_s[(0.93(t-t_0) - 0.36(p-p_0) + 0.05(f-f_0)]\times 10^{-6} \quad (4)$$

where t_0, p_0 and f_0 are the initial temperature, pressure and humidity at the beginning of the measurement, and L_s is the sample length. Another source of Δl_d is the change of laser wavelength during the measurement, which is treated as uncertainty in this analysis. So equation (2) becomes

$$\begin{aligned}\Delta l = {} & k\lambda/(n_0 K)\{1+[0.93(t-20) - 0.36(p \\ & -760) + 0.05(f-10)]\times 10^{-6}\} \\ & - L_s[(0.93(t-t_0) - 0.36(p-p_0) \\ & + 0.05(f-f_0)]\times 10^{-6}\end{aligned} \quad (5)$$

where n_0 is the refractive index of air at the standard condition.

Uncertainty budget

The uncertainty of the measurement of dimensional change can be estimated by considering the uncertainty sources individually and then combining them. According to the law of propagation of uncertainty [3], the combined standard uncertainty of the estimate of Δl in equation (5) can be determined by the positive square root of the combined variance $u_c^2(\Delta l)$, which is given by

$$\begin{aligned}u_c^2(\Delta l) = {} & (\frac{\partial \Delta l}{\partial \lambda})^2 u^2(\lambda) + (\frac{\partial \Delta l}{\partial n_0})^2 u^2(n_0) \\ & + (\frac{\partial \Delta l}{\partial k})^2 u^2(k) + (\frac{\partial \Delta l}{\partial t})^2 u^2(t) \\ & + (\frac{\partial \Delta l}{\partial p})^2 u^2(p) + (\frac{\partial \Delta l}{\partial f})^2 u^2(f) \\ & + (\frac{\partial \Delta l}{\partial t_0})^2 u^2(t_0) + (\frac{\partial \Delta l}{\partial p_0})^2 u^2(p_0) \\ & + (\frac{\partial \Delta l}{\partial f_0})^2 u^2(f_0) + (\frac{\partial \Delta l}{\partial L_s})^2 u^2(L_s) \\ = {} & \sum_{i=1}^{10} u_i^2(\Delta l)\end{aligned} \quad (6)$$

where $u(\lambda)$, $u(n_0)$, $u(t)$, $u(p)$, $u(f)$, $u(t_0)$, $u(p_0)$, $u(f_0)$, $u(L_s)$ and $u(k)$ are standard uncertainties of λ, n_0, t, p, f, t_0, p_0, f_0, L_s and k, respectively. $u_i^2(\Delta l)$ represents the ith term in the equations. In equation (6), all uncertainty components are assumed to be independent.

Uncertainty of wavelength

The variance in equation (6) associated with wavelength uncertainty is

$$u_1^2(\Delta l) = (L/\lambda)^2 u^2(\lambda)$$

The accuracy of vacuum wavelength of the laser head, Zygo ZMI 7722, is ±0.16 ppm. The stability of vacuum wavelength of the laser is ±10 ppb over the lifetime of the laser head and ±0.5 ppb over one hour. Assuming that these uncertainties have normal distributions, the standard uncertainty caused by the accuracy is

$$u_{1,a}(\Delta l) = \frac{L}{\lambda_0} u_a(\lambda_0) = 5.3\times 10^{-8} L$$

and the standard uncertainty caused by the long-term stability of wavelength, in which the influence of wavelength stability to the unbalanced path is included, is

$$u_{1,s}(\Delta l) = \frac{L - L_s}{\lambda_0} u_s(\lambda_0) \approx -3.3\times 10^{-9} L_s$$

Since the dimensional changes to be measured are typically smaller than 0.1 mm, the uncertainty due to wavelength is mainly in the form of the influence of wavelength instability to the dead-path length.

Uncertainty of refractive index of air under standard conditions

The refractive index of air under the standard condition can be calculated using the modified Edlén equation with an uncertainty of 3×10^{-8} (2σ). So the standard uncertainty associated with n_0 in equation (6) is

$$u_2(\Delta l) = L/n_0\, u(n_0) = 1.5\times 10^{-8} L$$

This uncertainty term is negligibly small for measurements of small dimensional changes.

Uncertainty of the detection electronics

The variance associated with the uncertainty of electronics in equation (6) is

$$u_3^2(\Delta l) = (\frac{\lambda}{nK})^2 u^2(k)$$

The standard uncertainty caused by electronics of the ZMI 4004 measurement system is assumed to equal the least resolution of the

interferometer, which is $\lambda/4096$ for a double-pass interferometer. So the resulting standard uncertainty is

$$u_3(\Delta l) = 0.15 \text{ nm}.$$

Uncertainties of environmental parameters

When using the modified Edlén equation to correct for environmental changes, the uncertainties in determining the air temperature, pressure and humidity cause measurement uncertainties. The variances in equation (6) associated with t, p and f are given by

$$u_4^2(\Delta l) = (L - L_s)^2 \times 0.93^2 \times 10^{-12} u^2(t)$$
$$u_5^2(\Delta l) = (L - L_s)^2 \times 0.36^2 \times 10^{-12} u^2(p)$$
$$u_6^2(\Delta l) = (L - L_s)^2 \times 0.05^2 \times 10^{-12} u^2(f)$$

Assuming that the uncertainties, which include both measurement uncertainties and non-uniformities, of the temperature, pressure and humidity are 0.05 °C, 0.1 mmHg and 0.5 mmHg, respectively, and they have normal distributions, the resulting standard uncertainties, $u_4(\Delta l)$, $u_5(\Delta l)$ and $u_6(\Delta l)$ will be $1.6\times10^{-8} L_d$, $1.2\times10^{-8} L_d$ and $8.5\times10^{-9} L_d$, respectively. Similarly, the variances associated with t_0, p_0 and f_0 are given by

$$u_7^2(\Delta l) = {L_s}^2 \times 0.93^2 \times 10^{-12} \times u^2(t_0)$$
$$u_8^2(\Delta l) = {L_s}^2 \times 0.36^2 \times 10^{-12} u^2(p_0)$$
$$u_9^2(\Delta l) = {L_s}^2 \times 0.05^2 \times 10^{-12} u^2(f_0)$$

Since the dimensional change is negligibly small compared to the sample length, the environmental-induced uncertainties mainly arise from the correction of the dead-path error. For measurements in vacuum, these uncertainties can be neglected.

Uncertainty of sample length

The variance associated with the sample length in equation (6) is

$$u_{10}^2(\Delta l) = [0.93(t - t_0) - 0.36(p - p_0) + 0.05(f - f_0)]^2 \times 10^{-12} u^2(L_s)$$

If the maximum changes in air temperature, pressure and humidity during the measurement are 1 °C, 10 mmHg and 10 mmHg, respectively, the standard uncertainty estimated by the root-sum-square of these items is

$$u_{10}(\Delta l) = 3.8\times10^{-6} u(L_s)$$

Assuming that the uncertainty of the sample length is ±0.1 mm and it has a normal distribution, this term of standard uncertainty is approximately 0.13 nm.

Nonlinearity of the interferometer

An uncertainty source that is not included in equation (6) is the nonlinearity of the interferometer, which is caused by optical mixing. The nonlinearity of the interferometer was measured using the thermal translation method [4], as shown in Figure 2. If the uncertainty is treated conservatively as having a rectangular distribution, the standard uncertainty is

$$u_{11}(\Delta l) = 0.75/\sqrt{3} \approx 0.43 \text{ (nm)}$$

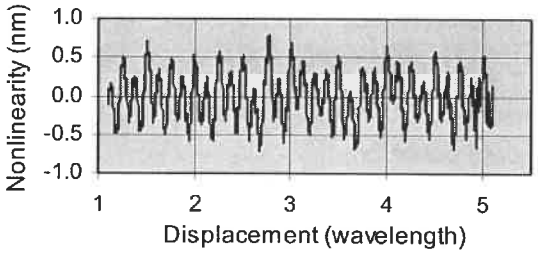

FIGURE 2. Nonlinearity of the interferometer

Other uncertainties

The correction of refractive index of air using the modified Edlén equation has a relative uncertainty of 3×10^{-8} (2σ). The resulting standard uncertainty is approximately

$$u_{12}(\Delta l) = \sqrt{2} \times 3\times10^{-8} L_s / 2 = 2.1\times10^{-8} L_s$$

Combination of the uncertainties

The sources of uncertainty and their contributions to the measurement uncertainty of the interferometer are summarized in Table 1. The combined standard uncertainty of the interferometer can be obtained by calculating the root-sum-square of the individual standard uncertainties. The combined standard uncertainty in the laboratory environment, where the temperature, pressure and humidity are 22.9 ± 0.5 °C, 747 ± 5 mmHg and 40 ± 20 %, is calculated and listed in the column of 'in air' in the table. This interferometer is designed be operated in a vacuum chamber with the temperature control of 20 ± 0.1 °C. The combined standard uncertainty under such condition is also calculated and is listed in Table 1 in the column of 'in vacuum'.

TABLE 1. Summary of standard uncertainties of the interferometer for measurements of dimensional changes

Source of uncertainty	Standard uncertainty $u(x_i)$		$\frac{\partial f}{\partial x_i}$	$u_i(\Delta l)$ (nm)	
				In air	In vacuum
Wavelength stability	$u(\lambda)$	3.3 ppb	$(L_s - L)$	0.33	0.33
Electronics	$u(k)$	1	λ_0 / K	0.15	0.15
Environment					
Temperature	$u(t)$	0.017 °C	$0.93(L_s - L)\times 10^{-6}$	1.6	
Pressure	$u(p)$	0.03 mmHg	$0.36(L_s - L)\times 10^{-6}$	1.2	
Humidity	$u(f)$	0.17 mmHg	$0.05(L_s - L)\times 10^{-6}$	0.85	
Initial temperature	$u(t_0)$	0.017 °C	$0.93L_s \times 10^{-6}$	1.6	
Initial pressure	$u(p_0)$	0.03 mmHg	$0.36L_s \times 10^{-6}$	1.2	
Initial humidity	$u(f_0)$	0.17 mmHg	$0.05L_s \times 10^{-6}$	0.85	
Edlén equation		$1.5\times 10^{-8} L_s$	$\sqrt{2}$	2.1	
Total				3.72	0
Sample length	$u(L_s)$	0.033 mm	3.8×10^{-6}	0.13	0
Nonlinearity		0.43 nm	1	0.43	0.43
Dilatation measurement $u_c(\Delta l) = \sqrt{\sum_{i=1}^{12} u_i^2(\Delta l)}$				3.8	0.6

CONCLUSIONS

The analysis of uncertainty has shown that, although the dead-path lengths have been reduced to the sample length by the balanced interferometer design, the uncertainty associated with the correction for dead-path error is the most significant source of uncertainty for measurements in air. It is necessary to operate the interferometer in a vacuum chamber in order to achieve the proposed accuracy. Two key components for further improving the measurement accuracy of the interferometer in vacuum are to reduce the nonlinearity resulting from the optical mixing and to improve the stability of laser wavelength. It can be concluded that this double-pass interferometer should be able to measure dimensional changes with an uncertainty of 2 nm (3σ), which meets the accuracy requirement of the interferometric dilatometer.

ACKNOWLEDGEMENTS

This work was supported by the National Science Foundation under Grant No. 0216420. The Center for Precision Metrology is supported as an NSF Industry/University Cooperative Center under Grant No. 0331950.

REFERENCES

[1] Ren D. Optical Measurements of Dimensional Instability. Ph.D dissertation. University of North Carolina at Charlotte. 2006.

[2] Birch K, Downs M. An Updated Edlén Equation for the Refractive Index of Air. Metrologia. 1993; 30: 155-162.

[3] Guide to the Expression of Uncertainty in Measurement. ISO. 1995.

[4] Zhang L. Fiber-coupled Heterodyne Interferometer. Ph.D dissertation. University of North Carolina at Charlotte. 2003.

DESIGN AND EVALUATION OF BULK-MICROMACHINED SILICON ARTIFACTS FOR HYBRID DIMENSIONAL CALIBRATION

Meghan Shilling, Andre A. Claudet, David L. Luck, and Hy D. Tran[1]
Sandia National Laboratories
Albuquerque, NM USA

ABSTRACT

A dimensional calibration artifact based on silicon bulk micromachining fabrication has been developed and manufactured with the intention of evaluating the artifact both on a high precision coordinate measuring machine (CMM), and on a video-probe based measuring system. A high accuracy touch-probe based CMM can achieve accuracies that are as good as the 2-D repeatability of video-probe systems. While video-probe based systems are commonly used to inspect mesoscale mechanical components, a video-probe system's certified accuracy is generally much worse than its repeatability. A hybrid artifact where the same features can be extracted by either a touch-probe or a video-probe could then be used to improve the accuracy of video-probe systems.

The hybrid dimensional artifact has been measured using several vision and touch probe systems. Measurement results from the vision and touch probe systems are compared and evaluated to determine the capability of the manufactured artifact to serve as a 2-D calibration tool for video-probe systems. A redesign of the 2-D calibration artifact is proposed based on initial observation and discussion. Additionally, the design of a 3-D hybrid artifact to improve the accuracy of the vertical dimension of a video-probe is presented and discussed. Measurement results from the first artifact are also presented.

INTRODUCTION

Mesoscale mechanical components are 10^0mm in scale with features on the order of 10^{-1}mm and tolerances from 10^{-3}mm to 10^{-4}mm. An example would be watch mechanism components[1]. Figure 1 shows a detail of a mesoscale component from a mechanical wristwatch. Inspection of these components can be difficult. Frequently, vision-based inspection equipment is used to measure these components.

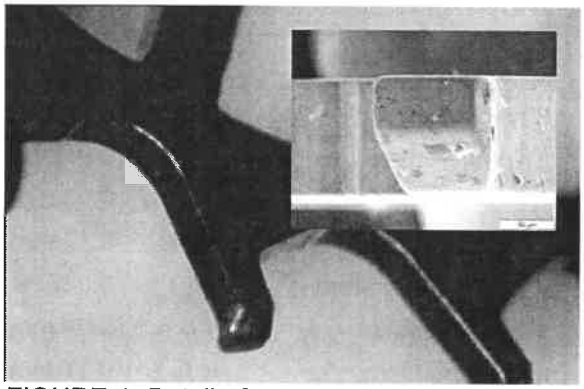

FIGURE 1. Detail of an escapement wheel from a Rolex watch. The inset is a scanning electron micrograph of the escapement. The scale bar on the SEM is 50 μm. From [1].

An example of a vision-based inspection machine is the OGP Avant, as illustrated in Figure 2. These types of machines have a workspace greater than 100mm×100mm horizontally with typical repeatability in the horizontal directions of 10^{-4}mm. Their nominal usage is on parts that have 2-D characteristics.

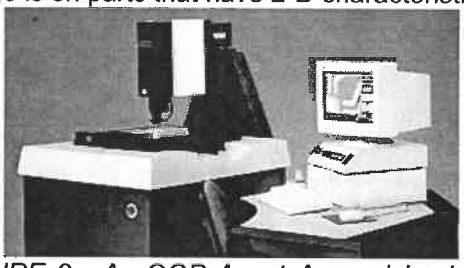

FIGURE 2. An OGP Avant Apex vision-based inspection machine.

An alternative to vision-based inspection, especially with parts that have requirements for features in three dimensions, is the use of micro CMMs [2]. Micro CMMs are CMMs which are purpose-designed to have relatively small work volumes (on the order of 100mm × 100mm × 100mm), typically with touch probe stylus tip smaller than 500μm. Hybrid measurement systems are also available, that combine a

[1] Hy D. Tran, MS-0665, Sandia National Laboratories, PO Box 5800, Albuquerque, NM 87185, hdtran@sandia.gov

vision or video probe system with a touch probe system on the same machine.
Figure 3 illustrates the workspace of a commercially available micro CMM, which combines a touch probe, a vision probing system, and a surveillance camera for setup and operation.

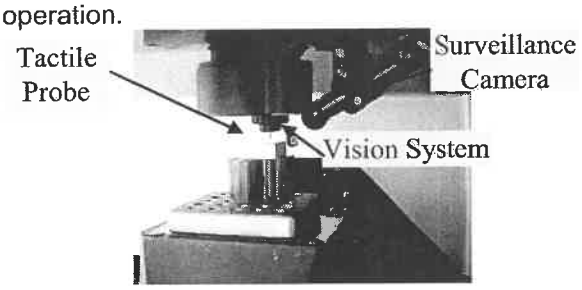

FIGURE 3. The workspace of a Micro CMM is typically 100 mm × 100 mm ×100 mm. From [2].

Calibration of these machines is an important consideration. For commercial vision-based inspection equipment, the typical calibration process uses a glass reference artifact (commonly called a grid plate), with chrome cross-hairs. Another method commonly used with optical microscopes are "stage micrometers", which are glass slides with chrome rulings. The calibration artifacts are typically the limiting factor for measurement uncertainty of vision-based equipment [3,4,5]. Additionally, these artifacts are not useful for tactile or hybrid measurement systems.

For tactile systems, one may follow the guidance of ASME/ANSI and ISO standards for evaluation of CMMs [6,7]. These standards for evaluation and performance testing require the use of calibrated length artifacts. Typically gauge blocks or step gauges are used for many of the evaluations. Unfortunately, gauge blocks and step gauges are not suited for use in vision-based systems.

The design and preliminary evaluation of calibration reference artifacts is presented. These artifacts can be either calibration standards or check standards, for use in vision-based, touch-probe based, or hybrid measurement systems for mesoscale dimensions. The design will be manufactured using bulk micromachining of silicon [8,9].

BULK MICROMACHINING OF SILICON

Bulk micromachining of silicon, also referred to as wet bulk micromachining and anisotropic wet-etch, uses single crystal silicon as a substrate. It is a well known process that uses different sensitivity of single crystal silicon to alkaline solutions along different crystal planes. Single crystal silicon wafers are readily available from semiconductor suppliers. Figure 4 shows a scanning electron micrograph of a portion of a bulk-etched wafer. The top <100> planes were originally protected by a mask. Note that while the masked <100> and the etched <111> planes appear to have a good surface finish, other surfaces are uneven.

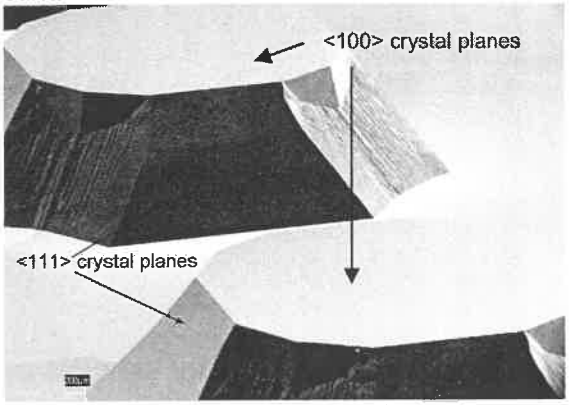

FIGURE 4. Silicon mesas on a <100> oriented silicon wafer. From [5].

Angles between <100> and <111> planes will typically be 54.74° (arccos(1/√3)). Design of bulk-micromachined structures which possess features that are not rectangular, that have convex corners, and that are not perfectly aligned with a <100> plane, can be difficult, because of the need to provide corner compensation [8].

ARTIFACT DESIGNS

We designed three artifacts. The first design was a feasibility prototype. This design was intended to establish feasibility of manufacturing a step gauge that could be probed with either vision-probe or touch probe, manufacturing methods for fabricating mesoscale ball plates, and exploring different ways of implementing step gauges. After obtaining user feedback from the first design, two additional artifacts were designed. The second design is strictly a set of step gauges, while the third design incorporates a number of artifacts designed for use in a micro CMM.

First Prototype Design

This design has been previously presented [4,5]. A photograph of the artifact is shown in Figure 5. The design was fabricated on nominal 100mm (4 inch) <100> wafers. The features included

four step bars of varying pitch and spacing, three grid patterns for mounting balls for ball plates, two grid arrays, and a small artifact that could be diced out for use as a step height artifact for z-axis focus calibration.

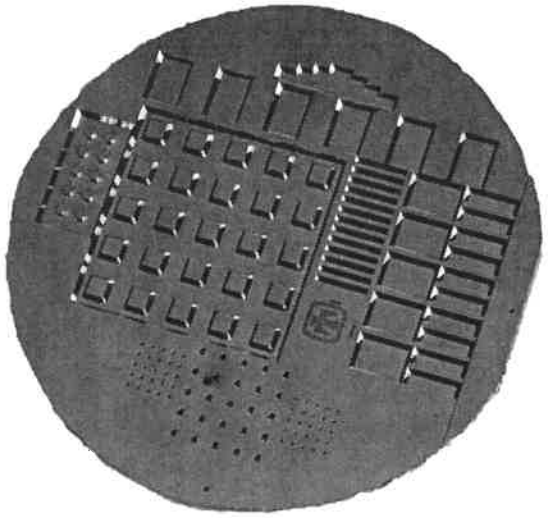

FIGURE 5. Photograph of one of the first prototype design silicon artifacts. This design incorporates 4 step bars, 3 ball holders for ball plates, two grid arrays, and a focus height calibration structure.

Discussion with potential users showed that the focus height calibration for vision systems could be adequately served with existing technologies. Users were more interested in the hybrid step gauge and the ball plate. A key advantage of using silicon bulk micromachining is the potentially sharp corner between the masked <100> surface and the <111> etched planes. With proper processing, the surface finish of <111> etched planes can be "mirror-like" [10], while the masked <100> surface is already polished. When we placed some of the first prototype artifacts in a vision-probing system using top-down illumination, the edges at the end of <100> planes were extremely sharp, and the pitch between edges was insensitive to illumination intensity [11].

2-D-only Prototype Design

Based on preliminary user feedback, the two most desired artifacts were a number of step gauges made of bulk micromachined silicon, and mesoscale ball plates. Figure 6 shows the mask design for a 2-D-only design, which consists of several step bars that can be sawn from the wafer using silicon dicing equipment, and a structure that can be diced as a monolithic "L" with each arm of the "L" containing a step gauge. This mask is designed for a 6 inch (150mm) wafer.

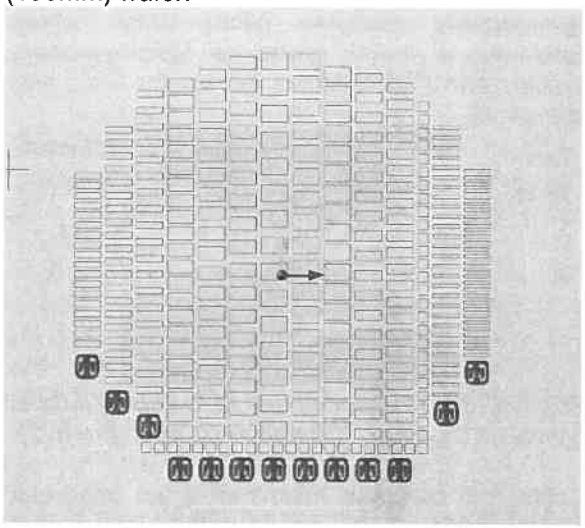

FIGURE 6. Mask layout for manufacturing a family of silicon step gauges of varying pitch, spacing, and lengths.

2-D and 3-D Prototype Design

We also designed an artifact that included holders for balls for mesoscale ball plates, again for a 6 inch mask and wafer. Because we had approximately 170000mm^2 of area on the wafer, we added several experimental features, including a more complicated "L" segment, several convex steps, and polygons without corner compensation. The mask is shown in Figure 7.

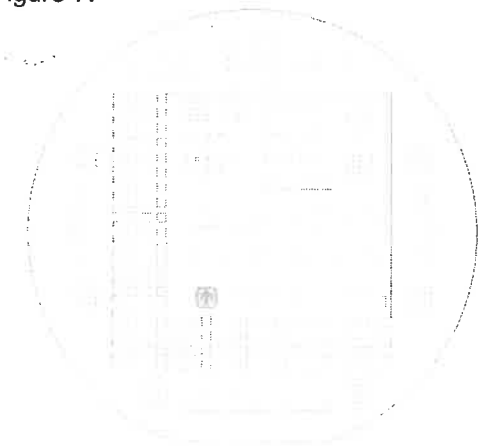

FIGURE 7. This design is intended for a 6 inch (150mm) wafer. The central portion can be diced out as a complete 100mm×100mm artifact

INITIAL MEASUREMENT RESULTS

Initial measurements are only for the first prototype built on 4 inch wafers. They are line-

to-line measurements taken on the features shown on Figure 8.

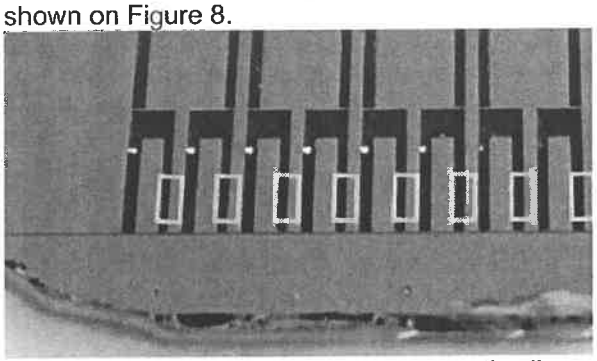

FIGURE 8. The highlighted edges are the lines which were evaluated, using a high accuracy CMM, and two different vision systems.

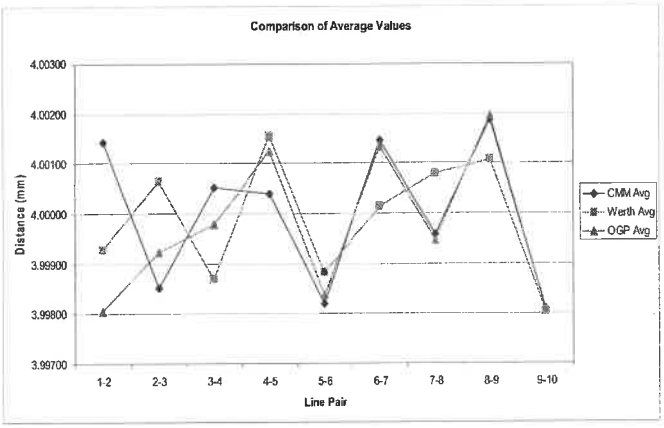

FIGURE 9. Comparison of CMM measurement versus vision systems.

Figure 9 shows a comparison of measurements taken with a CMM and measurements using two different vision systems, all on the same lines.Each of the measurement systems used had very good reproducibility, but none of the measurement systems had good agreement with each other. The worst disagreement is on the order of 3 μm. On further investigation, we found that the surface finish of the <111> planes was poor. In fact, the CMM had evaluated total deviation of nearly 600 nm from plane for some of the <111> planes used to compute the line, while the <100> planes had less than 70 nm maximum deviation from plane. We have identified several unoptimized processing parameters as the source of the poor surface finish in the <111> planes.

Once the process has been tuned to achieve the best surface finish in both <100> and <111> planes, additional batches of all three designs will be fabricated.

ACKNOWLEDGMENTS

Sandia is a multiprogram laboratory operated by Sandia Corporation, a Lockheed Martin Company, for the United States Department of Energy's National Nuclear Security Administration under contract DE-AC04-94AL85000. References made to specific commercial equipment are for identification purposes, and constitutes neither endorsement nor recommendation.

REFERENCES

[1] Lohr, C. and Benavides, G. L. "Lessons from the Watch Industry," Sandia Student Intern Symposium, August 2007.

[2] Claudet, A. A., Bryce, E. A., and Tran, H. D., "Initial Evaluation of a Micro-CMM," *Proc. of the 2007 NCSLI Workshop and Symposium*, St Paul, MN, 2007.

[3] Mason, S., "In House Capability of an Optical CMM Calibration for Any Company," *Proc. of the2007 NCSLI Workshop and Symposium,* St Paul, MN, 2007.

[4] Shilling, M., Claudet, A. A., and Tran, H. D., "Uncertainty Analysis for a Silicon Bulk Micromachined Dimensional Metrology Artifact," *Proc. of the 2006 ASPE Annual Meeting*, Monterey, CA, 2006.

[5] Oliver, A. D., Tran, H. D., and Claudet, A. A., "Design of a Silicon Micromachined Artifact for Hybrid Dimensional Measurement," *Proc. of ASME MSEC 2006,* Ypsilanti, MI, 2006.

[6] *Methods for Performance Evaluation of Coordinate Measuring Machines*, ASME B89.4.1b-2001 standard

[7] *Geometrical Product Specifications (GPS)—Acceptance and reverification tests for coordinate measuring machines (CMM)*, ISO10360 part 2, 2001.

[8] Madou, M. J. , *Fundamentals of Microfabrication*, CRC Press, 2002

[9] Kovacs, G.T.A., *Micromachined Transducers Sourcebook*, McGraw-Hill, 1998.

[10] Kovacs, G. T. A., Maluf, N. I., and Petersen, K. E., "Bulk Micromachining of Silicon," *Proceedings of IEEE* v86(8), 1998.

[11] Shilling, M., Claudet, A. A., Tran, H. D., Doiron, T., and Stoup, J., "Measurement Results for a Hybrid Dimensional Artifact," presented at 2007 NCSLI Workshop and Symposium, St Paul, MN 2007, and to appear in *Proc. 2008 NCSLI Workshop and Symposium.*

ADVANCED APPLICATIONS FOR STYLUS PROFILOMETERS

Melinda Bullaro, Erik Novak
Veeco Instruments, Inc.
Tucson, Arizona, USA

INTRODUCTION

Stylus profilers are the most commonly used surface measuring instruments due to their rugged design, ease of use, and excellent value. Different configurations of stylus systems are available to fit a variety of budget, space and performance targets. The most common uses for these systems have been in measuring steps, particularly for films in the semiconductor industry, as well as in machine shops to examine precision metal surfaces. Configurations range from manual systems, where an operator drives to the measurement sites for single-line profilers, to automated gantry based systems, where multiple sites can be programmed for measurement with minimal operator intervention.

Stylus profilometry has been serving industry for more than 50 years, but innovation continues in these metrology instruments, driven by increasing customer requirements to measure smaller features, faster, and in a greater variety of applications. Newer applications include micro structures, 3D profiling of micro-shapes of optics and other precision surfaces, determination of cutting surface angles and sharpness, among many others. In addition to new applications, the systems have to perform to tighter specifications even on traditional applications, such as semiconductor step measurements. All of these factors are driving newer, more capable generations of products, while maintaining cost targets and the ability to deploy in most any environment.

ENVIRONMENTAL INSENSITIVITY

Low-cost stylus profilers are traditionally on smaller, less stable platforms, resulting in a higher degree of susceptibility to environmental noise than their more expensive counterparts. However, other systems, such as precision microscopes and white-light optical profilers, have developed extremely rigid but low-cost platforms to allow precision measurements by those instruments. For Veeco, moving the Dektak 150 model stylus profiler to the same base as its Wyko line of optical profilers, which have a very high stiffness to weight ratio, allows low-cost stylus profilers to be deployed to measure finer features in noisier environments, such as industrial clean rooms with noisy air handlers and other industrial process equipment.

Data from the UCLA NRF lab below illustrate results from different systems in the same overall environment. To determine how well the stylus profiler operates in a noisy environment, a 1mm scan is taken on an optically flat surface, such as a silicon carbide mirror, and two items are analyzed to identify the stability of the measurement. The overall shape of the scan can be determined by analyzing the topographical difference of the highest point of the dataset to the lowest (Peak to Valley), the higher the Peak to Valley, the more shape the scan has, this is an indication of low frequency noise disturbing the system. The other analysis, Ra, is of the profile height deviations from the mean the scan is broken into 10 segments and Ra is analyzed and averaged over the entire dataset, consistently high Ra values indicates high frequencies from the environment is disturbing the stability of the measurement. Many applications require measured Ra of less than 10Å in order to achieve consistent repeatable results. Such results are easily achieved on the D150 product while other stylus systems cannot reach those levels.

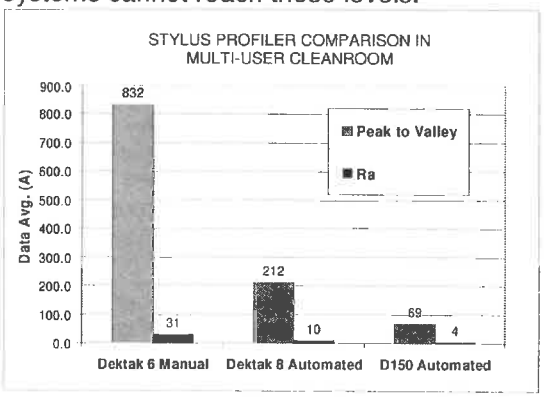

FIGURE 1)Several different stylus profilers were compared in an extreme environment. The Dektak 6M was very susceptible to the environmental noise and could not repeatably measure 1μm steps. The Dektak 150 was the

best at controlling both the high and low frequencies, resulting in the best measurement quality and allowing for angstrom-level repeatability on a 1µm step.

IMPROVING AUTOMATION

Implementation of new, smarter, higher performance motors allows for enhanced performance in a compact package, so that long travel and high precision can be achieved without increasing cost. Previous stylus profiler offerings by Veeco and other vendors achieved only +/- 5µm stage repeatability. The latest profiler, the D150, achieves +/- 1µm. Such x-y automated stages can repeatedly find precision measurement sites using feature recognition wizards. This is key to applications where not only repeatability but reproducibility of measurements are critical.

The example below is a rendering of a structure on a 4-inch semiconductor wafer. Two fiducials or alignment points were identified in opposing corners and 16 features, rendered below, were automatically located, measured and analyzed using dynamic step detection software that can be monitored with real-time databases.

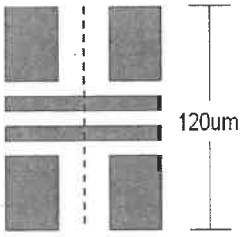

FIGURE 2) 10µm wide by 2µm step automatically located and measured on 4" wafers.

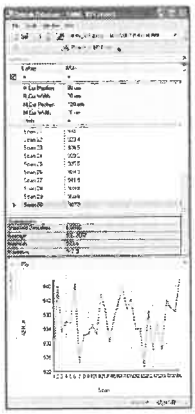

FIGURE 3) User-configurable database with real-time plotting monitors measurements as they are taken.

The newer motors also have the added benefit of enabling higher resolution stylus 3D mapping. This is enabling applications in the solar/photovoltaic industry where optical profiling is held back due to multiple layering of thin films, and AFM may not be cost effective. This next example illustrates this feature. Stylus profilers render 3D maps of surfaces by incrementing the y-axis in between taking scans in the x-axis. As the y-axis increment decreases, higher resolution is achieved and smaller features can be mapped. Typically, stylus profilers can step in 3 to 5µm increments. The D150 can step in micron increments and it is even possible to step in submicron increments. This enables stylus profilers to image surfaces that were previously out of their range of resolution.

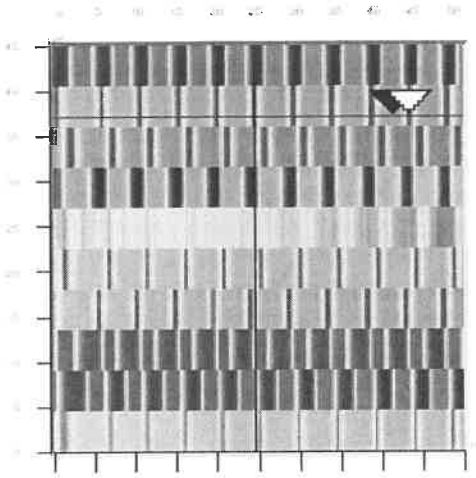

FIGURE 4) 50µm square area imaged with 5µm y-axis spacing.

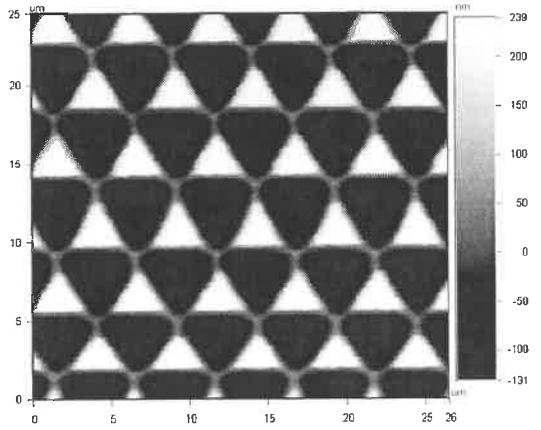

FIGURE 5) 25µm square area imaged with submicron scan spacing, the base of the triangles are 2.5µm.

MEASURING MICRO FORMS

The next generation of stylus profilers have new calibration routines that can extend accurate stylus metrology to microforms. Stylus profiling instruments commonly use a pivoted horizontal arm with a perpendicular stylus tip at the end. The stylus moves up and down along an arc, not straight up and down. The result is a horizontal shift, the run of the angle is elongated while the stylus is rising, and shrinks while descending (see Figure 6). Using a well known sample or an angle standard, it is possible to calibrate your profiler to better than 1% symmetry. For accurate angles the profiler must be calibrated vertically and horizontally, with this done and the symmetry calibrated, +/- 0.1deg of accuracy can be achieved from 1 to 60 degrees. This is ideal for measuring blades, sharps, microlenses and gratings where symmetry is crucial. Vision, the 3D analysis package for Dektak, has built-in features, such as curvature removal for in-depth surface analysis, line-width analysis for critical dimensioning and multi-region analysis for considering different regions in the same dataset individually, as well as many other analyses. Therefore, Vision is not limited to just displaying the entire map, the software allows the user to manipulate it to acquire more information about the sample.

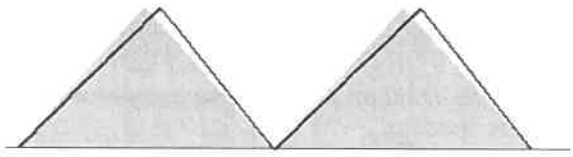

FIGURE 6) Gray area is actual surface, dark line is skewed measurement without correction.

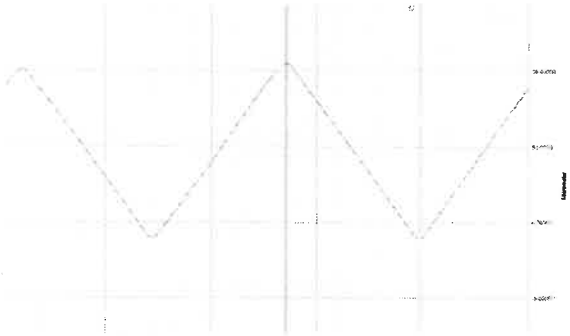

FIGURE 7) 90 degree symmetrical grating.

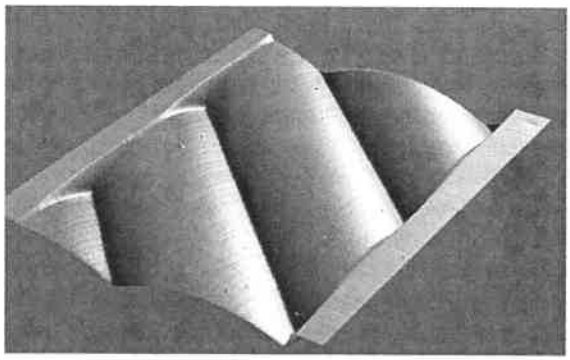

FIGURE 8) Microlens array

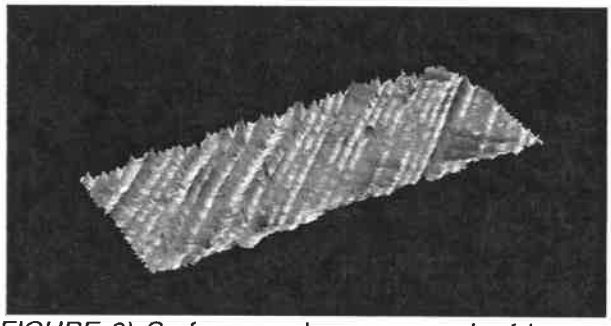

FIGURE 9) Surface roughness on peak of lens array in previous figure. A subregion of the peak with curvature removal displays the machine marks used to make the mold.

CONCLUSION

Stylus profiling technology has been in wide use for decades. Stylus profilers continue to be the metrology systems of choice for step heights, thin films, and other large shape characterization. However, innovative hardware enhancements and advanced software capabilities have continued to make large strides in fitting stylus techniques to challenging and emerging applications. Coupled with convergent software platforms, stylus users can now also confidently measure microshapes and other traditionally difficult sample features without incurring the costs of more expensive technologies.

REFERENCES

[1] J.Fruhaut, B.Hannemann, K.Lohr. Measurement of Form Profiles of Microstructures Using Stylus instruments. Meas. Sci. Technol. **9** No 3 (March 1998) 293-296

[2] "Filtering of Surface Profiles," Section 1, *Terms Related to Surface Texture,* ASME B46.1, American Society of Mechanical Engineers: New York, 2002

THE EFFECT OF 3D ANISOTROPIC ROUGH SURFACE ON FRICTION IN PRECISION HYDRAULIC ASSEMBLIES

Manesh K.Kailathuvalappil[1], Ramamoorthy B.[1], Singaperumal M.[2]
[1]Manufacturing Engineering Section
Department of Mechanical Engineering
Indian Institute of Technology Madras, Chennai, TamilNadu, India
[2]Precision Engineering and Instrumentation Lab
Department of Mechanical Engineering
Indian Institute of Technology Madras, Chennai, TamilNadu, India

1. INTRODUCTION

The functional performance of precision hydraulic assemblies is closely linked to the geometric properties of the surfaces of its components. At stringent tolerance levels, surface topography (the characteristic of the manufacturing process used to generate the same) can contribute to good fluid retention property to the components. Hence, the prediction of functional behaviour of precision hydraulic assemblies requires consideration of 3D surface roughness of its mating components.

Significance of micro geometry on friction is widely reported in literature but they were based on various 2D surface parameters. 3D surface analysis is also reported in the area of asperity level contact analysis. All these micro geometry studies are essentially meant for materials with sliding friction and do not address hydraulic systems.

Prediction of the functional behaviour of these assemblies requires input of 3D surface data, which could be obtained from profilometer. But measured profiles cannot be used to determine an optimized surface roughness, in terms of 3D surface roughness parameters, for a specified application. Therefore, a simulation procedure for the generation of arbitrarily defined rough surfaces is needed. A surface profile, being of random type, can be defined (in a statistical sense) by two characteristics: the height distribution and the autocorrelation function (ACF) [1]. Hence, random process description of engineering surfaces makes it possible to generate a rough surface by numerical simulation.

In this paper, a procedure is developed for computer simulation of 3D non-Gaussian anisotropic rough surfaces with specified anisotropy, standard deviation, skewness and kurtosis and to model 3D fluid continuum representing the fluid flowing through the clearance gap between the mating components of the precision assemblies. The procedure is then implemented to study the effect of 3D anisotropic rough surface on friction in spool-sleeve assembly of servo valve.

2. GENERATION OF ROUGH SURFACE

In this section, a computer program is developed based on 2D digital filter technique [2] for modeling 3D rough surfaces. Initially, random non-Gaussian surface data is generated with different histogram inputs to obtain specified skewness and kurtosis. Further, areal autocorrelation function (AACF) is used for establishing dependency between the consecutive data points such that the generated surface is in conformance with the machining process considered.

For a Gaussian rough surface with prescribed autocorrelation function, two surface roughness parameters are used to represent its characteristics: the standard deviation of surface heights (σ), and the correlation length (τ). Areal autocorrelation function for ground surfaces can be approximated as an ellipsoidal, which is expressed as:

$$R(\tau_x,\tau_y)=\sigma^2\exp\left\{-\left[\left(\frac{\tau_x}{\tau_x^*}\right)^2+\left(\frac{\tau_y}{\tau_y^*}\right)^2\right]^{1/2}\right\} \quad (1)$$

Where, τ_x,τ_y are the correlation distances in x and y directions, τ_x^*,τ_y^* are the correlation lengths of the surface profiles in x and y directions at which the AACF in the direction of the profile decays to a threshold *r*.

The method to generate three-dimensional surfaces can be summarized as follows:

Suppose $\eta(i,j)$ is a sequence of random number having a Gaussian distribution of known

standard deviation σ, the simulated rough heights $z(i,j)$ can be taken as:

$$z(i,j)=\sum_{k=0}^{n-1}\sum_{l=0}^{m-1}h(k,l)\eta(i+k,j+l) \qquad (2)$$

Where $h(k,l)$ is filter function which define the system. By signal process theory, $z(i,j)$ will posses the same height distribution with the input sequence $\eta(i,j)$. The Fourier transform of Equation (2) is given as:

$$Z(\omega_x,\omega_y)=H(\omega_x,\omega_y)A(\omega_x,\omega_y) \qquad (3)$$

Where A and Z are Fourier transform of η and z respectively, and H is the transfer function of the system, which can be calculated, for a linear system, as:

$$S_z(\omega_x,\omega_y)=|H(\omega_x,\omega_y)|^2\,S_\eta(\omega_x,\omega_y) \qquad (4)$$

Where S_η is the spectral density of input sequence $\eta(i,j)$, which gives a constant value for a random sequence in white noise type; S_z is the spectral density of output sequence $z(i,j)$, i.e. the Fourier transform of the expected autocorrelation function $R(\tau_x,\tau_y)$. Thus, the filter coefficient $h(i,j)$ can be obtained by applying inverse Fourier transform to $H(i,j)$.

When non-Gaussian rough surface is expected, the Gaussian input sequence $\eta(i,j)$ should be first transformed to another sequence $\eta'(i,j)$ with appropriate standard deviation (σ), skewness (S'_{sk}) and kurtosis (S'_{ku}) using Johnson translator system of frequency curves [3], then let this new sequence pass through the filter to obtain the output sequence $z(i,j)$, which possesses the specified standard deviation, autocorrelation function, skewness and kurtosis. The skewness (S'_{sk}) and kurtosis (S'_{ku}) for the modified input sequence $\eta'(i,j)$ can be obtained by the following relation:

$$S_{sk}=S'_{sk}\sum_{i=1}^{q}\theta_i^3/\left(\sum_{i=1}^{q}\theta_i^2\right)^{3/2} \qquad (5)$$

$$S_{ku}=[S'_{ku}\sum_{i=1}^{q}\theta_i^4+6\sum_{i=1}^{q-1}\sum_{j=i+1}^{q}\theta_i^2\theta_j^2]/(\sum_{i=1}^{q}\theta_i^2)^2 \qquad (6)$$

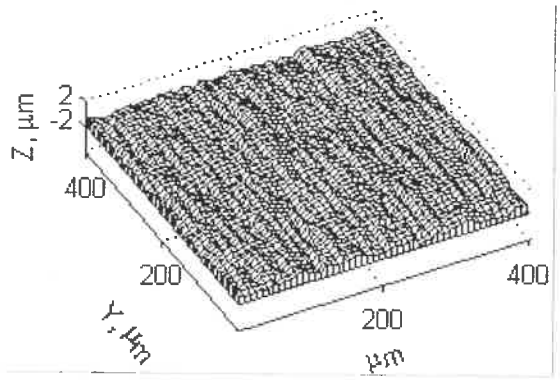

(a)

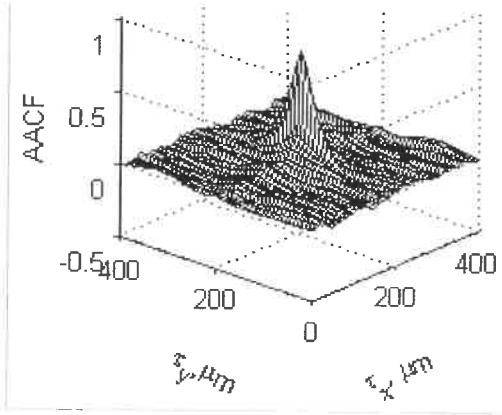

(b)

FIGURE 1. (a) Typical Anisotropic Non Gaussian Surface with $\tau_x^*=60, \tau_y^*=5$, Ssk =-0.7 & Sku=4.0
(b) Its Areal Autocorrelation Function

Where S_{sk} and S_{ku} are the present skewness and kurtosis for the rough surface to be generated ($z(i,j)$), and;

$$\theta_i=h(k,l); \qquad k=1,2,...,n; \qquad l=1,2,...,m; \quad i=(k-1)m+l \qquad (7)$$

A typical anisotropic rough surface, generated with $\tau_x^*=60$ & $\tau_y^*=5$, and its areal autocorrelation function (AACF) are presented in figure 1.
In this study, nine ground surfaces with σ =0.4, Kurtosis=4.0 and varying Skewness and correlation distances τ_x^*, τ_y^* and a similar set of another nine rough surfaces with σ =0.2 are generated. The parameters are made in conformance with the spool valve surface. One honed surface is generated, representing the sleeve, by post processing the simulated ground

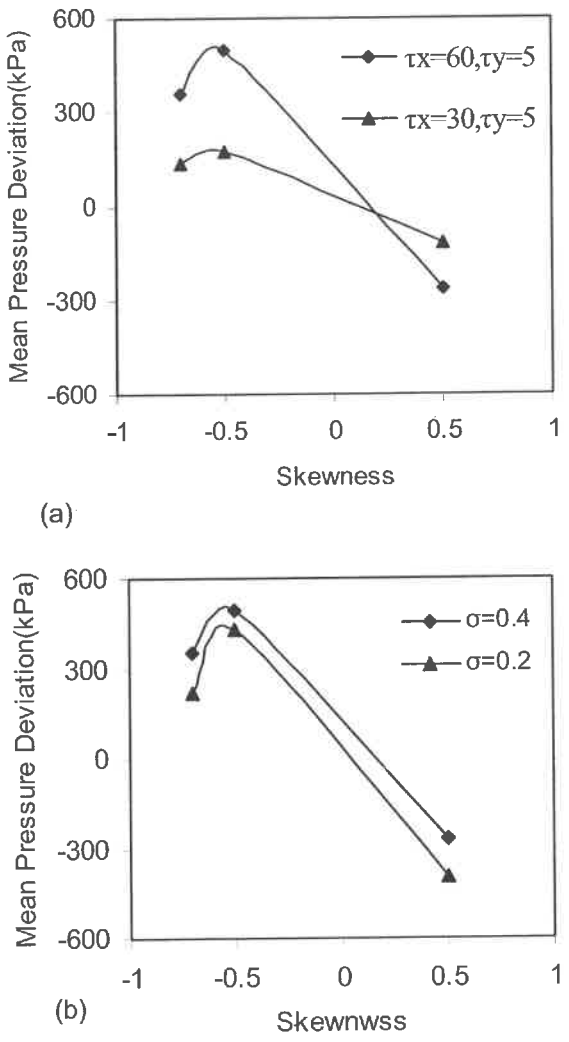

FIGURE 2. Variation of Mean Pressure Deviation as a Function of Skewness,
(a) at Two Different Anisotropic Conditions
(b) at Two 'σ' Values.

surface with σ =0.3 for generating cross hatches of 55^0 hone angle. Only spool surface topography is varied in this study.

3. MODELING AND SIMULATION

Three-dimensional CAD surface models were generated using Non Uniform Rational B-Spline (NURBS) interpolation from the generated surface maps. 3D Fluid continuums, of thickness equal to the radial clearance of the assemblies, were then modeled with the generated sleeve and spool rough surface models as envelops. A radial clearance of 4 μm is used. Surfaces were assumed to be ergodic. Hence fluid continuum of 400x400 μm^2 size only was considered, in accordance with the computation power of the computer, from a section at the centre region of the EHSS assembly. MIL-H-5606 E fluid was considered as the medium. Three dimensional, steady, laminar flow was assumed. The gap geometry is evaluated with known pressures as boundary conditions. Pressure inlet and pressure outlet for the modeled fluid continuum were calculated as 2.81 MPa and 2.60 MPa respectively by conducting similar test, but on the macro geometry of the assembly with inlet pressure of 5 MPa and outlet pressure of 0.1 MPa for the assembly. The spool surface was assumed to be moving with a uniform velocity of 1m/s and the sleeve at rest. The modeled fluid continuum was discretised and analysed by Computational Fluid Dynamics (CFD) technique, using the commercially available CFD software, Fluent. After solving, pressure and velocity data were extracted from the grid. The viscous friction force exerted on the piston/spool in the direction of gap length is,

$$F_f = \int_0^{\pi d} \int_0^{y_{max}} \mu \frac{dv_y}{dz} dx dy \qquad (8)$$

Where, μ is the coefficient of friction.

Viscous friction force of all the gap geometries were evaluated and compared.

4. RESULTS AND DISCUSSION

The pressure data of the grid in the flow direction was considered for analysis. Only a small deviation in pressure distribution was observed (of the order few kPa) between the evaluated surfaces (gap geometries). However this is significant in the first stage of EHSS assemblies. As the pressure and velocity profiles exhibits highly irregular variations with surface topography due to the irregular converging and diverging flow paths caused by the topography of surfaces, for comparison purpose, isotropic surface with $\tau_x^* = \tau_y^* = 5$ was chosen as reference to evaluate the deviation of these parameters for different surface topographies.

The variation of Mean pressure deviation as a function of skewness is presented in figure 2. The Figure shows that pressure build up in the radial clearance is more with negatively skewed surface than with a positively skewed surface. This may be because negatively skewed surfaces exhibit more material in peak zone and they have shallow valleys that can retain fluid. Hence the fluid that enters the valley is pushed against the opposite wall, which creates flow

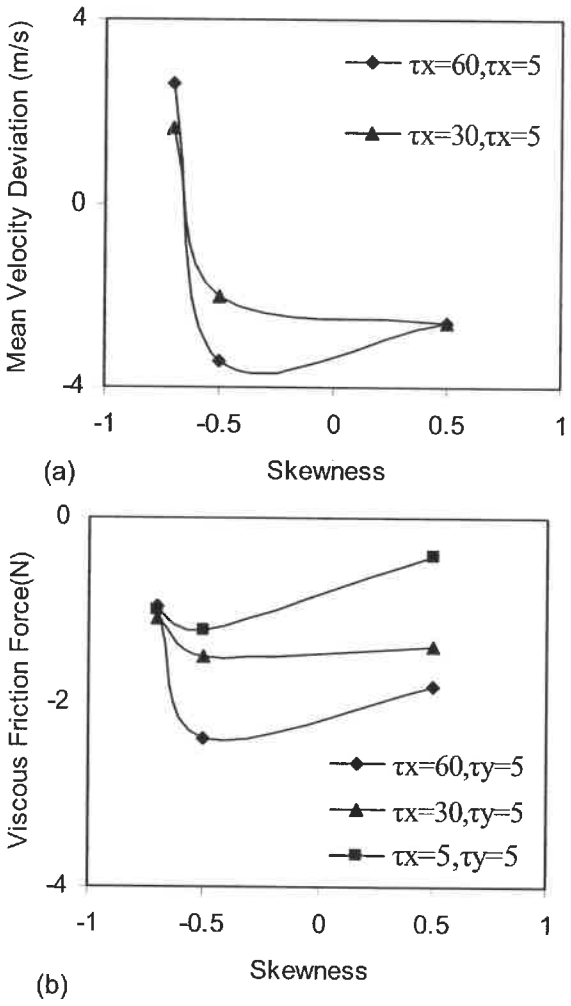

FIGURE 3. Variations of (a) Mean Velocity Deviation (b) Viscous Friction Force as a function of Skewness at Different Anisotropic conditions

resistance and hence the pressure increase. Figure 2(a) reveals that anisotropy of the surface supports this phenomena of pressure build. When the flow takes place in a direction inclined to the direction of lay, resistance to flow of fluid will be more, that also aids the pressure build up. But as skewness increases, pressure build up is getting reduced. This may be because, in the present analysis, Kurtosis kept constant.

When pressure increase, velocity of flow will decrease, hence the viscous friction force also decreases and this is well supported in figure 3. Standard deviation of surface irregularities also supports pressure build, as shown in the figure 2(b) and figure 4; but its effect is very minimal.

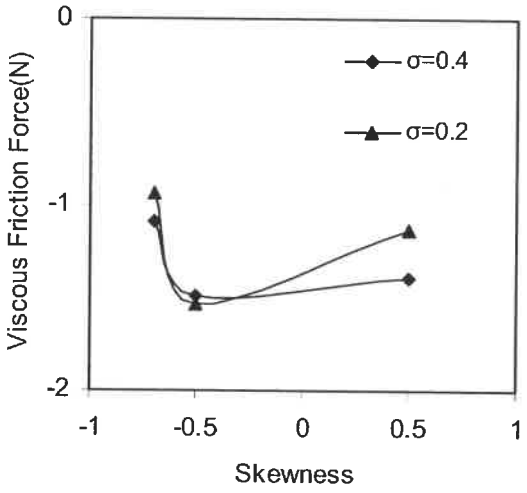

FIGURE 4. Variation of Viscous Friction Force as a Function of Skewness at different 'σ' values

It may be because, in the present study, a constant radial clearance only is considered. As surface becomes more and more smooth, for irregularities to have better role in pressure building, radial clearance should also come down.

5. CONCLUSION

In this research work, a simulation procedure is developed to study the effect of 3D anisotropic surface roughness on friction in precision hydraulic assemblies. It is found that anisotropy of the surfaces aids the assembly to develop pressure within the radial clearance. The results indicate that for better functional performance, surfaces of the assemblies need not be too smooth. Further studies have to be carried out, to determine an optimized surface roughness from the view point of functional behaviour.

6. REFERENCE

[1] Whitehouse D.J., Archard J.F. The properties of random surfaces of significance in their contact. Pro.R.Soc.(London). 1970; A316:97-121.

[2] Hu Y.Z., Tonder K. Simulation of 3-D random rough surface by 2-D digital filter and Fourier analysis.Int.J.Mach.Tools Manufacture.1992; 32: ½, 83-90.

[3] Johnson N.L. Systems of frequency curves generated by methods of translation. Biometrika. 1949; 36: 149-176.

CHARACTERIZATION AND SELECTION OF SURFACE TEXTURE MEASUREMENT INSTRUMENTS AND MANUFACTURING PROCESSES FOR A FUNCTION

Haritha Peruru, and Jayaraman Raja
Department of Mechanical Engineering
University of North Carolina at Charlotte
Charlotte, NC, USA

There is a renewed interest in quality control and measurement needs with the growing trend of off shore manufacturing. The process engineers and designers are expected to design and qualify a process or a product with little control over the actual process or manufacturing equipment. This results in engineers relying heavily on inspection data to make decisions on process development and control. Product surface data could be used to decipher machine conditions such as vibration, tool wear etc. In order to accurately measure a surface, correct instrument and filtering parameters are essential. An important tool for selecting instrument is Amplitude Wavelength graph.

AW SPACE

Stedman introduced the concept of creating limit lines in AW space for the instrument, there by creating a unique AW plot for that instrument. The height of AW space gives the amplitude range/resolution ratio and width gives bandwidth that an instrument can respond to the surface wavelengths. Each edge of the AW map is associated with a particular component or parameter and the length of this component determines the performance of any instrument [1].

Limiting factors for instruments performance

a) Horizontal range & resolution;
Rh > W > 2rh
b) Vertical range & Vertical resolution;
Rv/2 > A > rv/2
c) Slope limit lines; a1, a2, b1, b2

METHODS OF AW IMAGE CREATION

AW image can be created by two methods. First, analytical approach, based on individual instrument parameters, limit equations or conditions can be formulated. The limit lines are plotted and the intersection points are determined. The polygon based on those intersection points is represented as the AW diagram for that instrument. Second method is an image processing approach, where each limiting equation is converted to a binary image and a normalized product of all the images gives an AW image for a given instrument. Because of its simplicity, image processing approach is used over analytical approach.

AW IMAGE FOR INSTRUMENTS

AW images for stylus instruments

The factors that confine the performance of stylus instruments are given below [1] Figure 1 shows the AW space for stylus instruments.

a. Vertical range (R_v) and Vertical resolution (r_v); $R_v > 2A > r_v$
b. Horizontal range (R_h) and Horizontal resolution (r_h); $R_h > W > 2r_h$
c. Slope limit lines(Ss & Sd); $S_s > S > S_d$
d. Radius of curvature limit lines (Rs & Rd); $R_d > R > R_s$

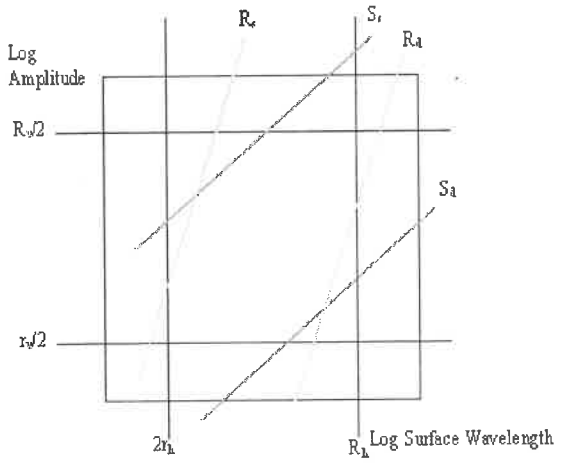

FIGURE1. A-W space for stylus instruments [1]

Table 1 shows the parameters of a stylus instrument. In order to create a generalized working window for AW space, a target space is chosen with a minimum of 0.001nm and a maximum of 1000mm for both amplitude and wavelength. This space is then converted to a log-log space to simulate the normal AW space

representation. Data from Table.1 is utilized to generate AW image of individual limiting parameter. Each image is combined and normalized to get required image representation of the instrument's A-W space as shown in Figure 2.

TABLE 1. Data for A-W Plot

Vertical Range	4mm
Horizontal Range	120mm
Vertical resolution	10nm
Horizontal Resolution	0.5μm
Radius of Stylus	2μm
Stylus Flank Angle	36°
Slope Error	0.5μ m /120mm

AW images for optical instruments

The factors that confine the performance of optical instruments are given below

a) Horizontal range; Rh = FOV
b) Horizontal resolution;
   Rh = min (LRes, Lsamp), where LRes = Lateral Resolution and Lsamp = Lateral Sampling
c) Vertical range;
   Rv = depth of field of objective
d) Vertical resolution;
   Rv = resolution of Z scanning stage
e) Slope limit lines; Ss > S > Sd
   Where Ss - (Rh /(2*WD)) ; WD = Working Distance and Sd - (rh)/(2*WD))
f) Radius of Curvature; *Rd > R > Rs*
   Where Rd = (Lsamp)^2/4*rv+rv/4;
   Lsamp = Lateral Sampling and
   Rs = (Rh)^2/4*rv+rv/4

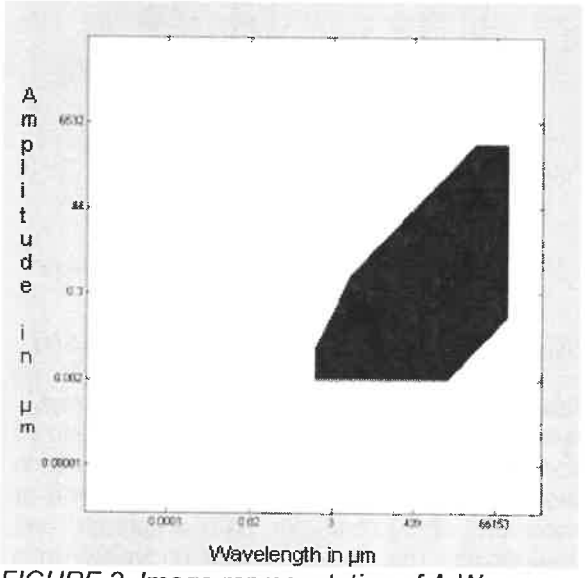

FIGURE 2. Image representation of A-W space

Each objective used in the optical instrument has its own AW space, so it is proposed that the individual objective's AW space be treated as a subspace of the total instrument. As an example, a 2.5X objective is chosen. Specifications of 2.5X objective are shown in Figure 3.

Vertical scan	150 μm
Range	15 mm
Vertical resolution	0.1 nm
Lateral resolution	0.43 μm to 11.6 μm

FIGURE 3. 2.5X objective specifications

Based on the specifications, AW sub image for the 2.5X objective is generated as shown in Figure 4.

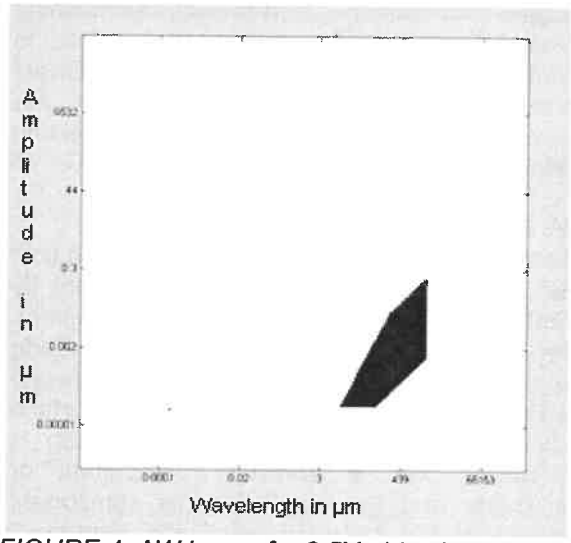

FIGURE 4. AW image for 2.5X objective

AW IMAGE FOR PROCESS

Similar to the A-W images generated for the instruments, AW images also can be generated for individual manufacturing processes. Then these images can be analyzed to pick the best suitable instrument to measure the surface generated by the selected process.

Ground surfaces are considered to explain the method of generation of AW images for a process. Those are measured using a Mitutoyo SJ400 instrument. Bounding envelope of the data cloud is analyzed, least square or polynomial fit is applied to generate the individual images of the limit lines of the process and all the images are combined and normalized

to get the AW image of the grinding process as shown in the Figure 5.

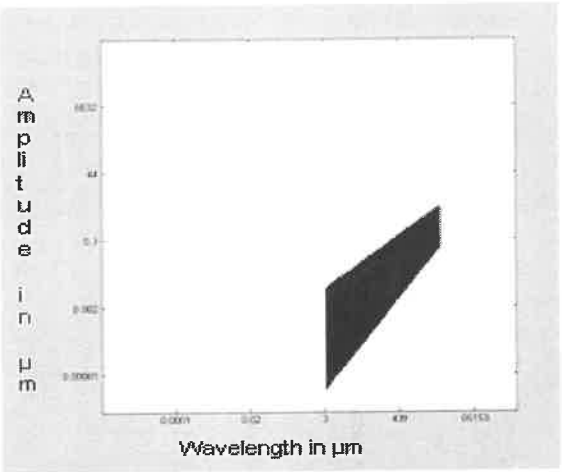

FIGURE 5. A-W Image for grinding process

AW IMAGE FOR A FUNCTION

Whitehouse D. J. gave generic approach to discuss relationship between Surface and Function. The classification chain in Figure 6 below shows the flow of function, surface, and manufacture. [2]

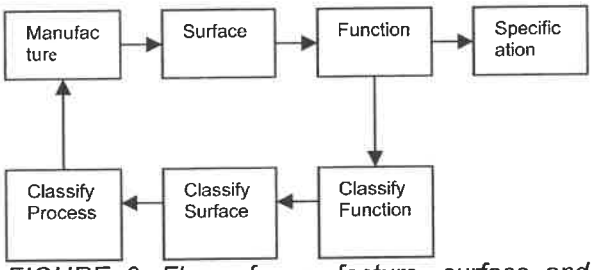

FIGURE 6. Flow of manufacture, surface and function

A gage block with poor wringing properties is measured under an interferometer and AW image is plotted as shown in Figure 7. Stoning is done on same gage block to improve the wringing properties and again measured under an interferometer. The AW image is plotted as shown in the Figure 8. Figures 7 and 8 clearly show the change in amplitudes and wavelengths which helped in improving the wringability of the gage blocks.

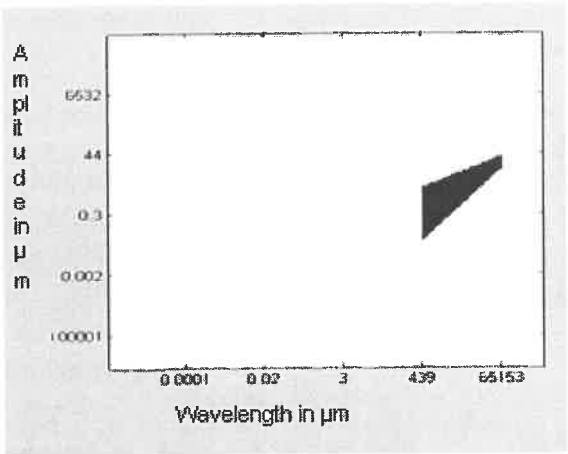

FIGURE 7. AW image of gage block before stoning

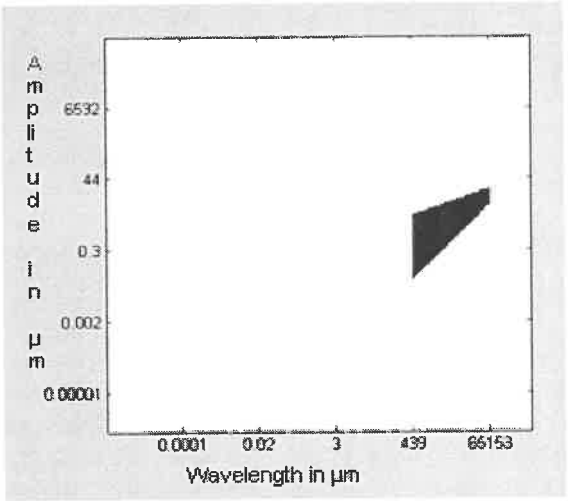

FIGURE 8. AW image of gage block after stoning

METHOD OF SELECTING MANUFACTURING PROCESS OR INSTRUMENT FOR A REQUIRED SURFACE FUNCTION

Since the A-W images for both the process and the instruments are generated with the common limits, they can be used as a means of selection of an instrument or a process for a required function. The selection of process would require creation of data management system of A-W images for instruments and processes.

To select an instrument or a process for a required function, the requirements are plotted as an AW image and compared with the instrument or process AW images in the data management system. Depending on the overlap of the images instruments can be ranked for the ease of selection. Table 2 and 3 are examples of

ranking of instruments and processes respectively for a required function

TABLE 2. Ranking of instruments for the required function

Number of common data points	Rank	Instrument
4100	1	Talysurf
3835	2	SJ400
3226	3	Talysurf Intra
1426	4	NewView6300

TABLE 3. Ranking of processes for the required function

Number of common data points	Rank	Process
2019	1	Vertical Milling
1919	2	Turning
1791	3	Horizontal Milling
1517	4	Grinding

CONCLUSIONS

By using AW maps as a common method to uniquely represent manufacturing processes, surface functions and surface measurement instruments, a uniform method to identify all these important sub sets of the design process is established. By linking all the facets of process development and control, it is easy for the engineer to identify the common thread between all the facets. This greatly enables the engineer to design the surface taking into account both the processes and instruments, similar to other designing concepts that have gained currency in the recent years – design for manufacturability, design for assembly, design for recyclability – to name a few.

AW mapping technique also helps in efficient data management by storing information on capability of the instrument/process/function in a single image.

AW images provide an efficient method to select manufacturing processes and surface texture measurement instruments to meet functional surface requirements.

REFERENCES

[1] M Stedman, Basis for comparing the performance of surface measuring machines.

[2] D. J. Whitehouse, Surfaces and their Measurement, Kogan Page Science, ISBN 1-9039-9660-0.

[3] Haritha Peruru, Characterization and Selection of Surface Texture Measurement Instruments and Manufacturing Processes for a Function, Master's thesis, University of North Carolina at Charlotte.

DEVELOPMENT OF STRAIGHTNESS MEASURING MACHINE FOR LONG PARTS USING IN-SITU SELF CALIBRATION LASER DIFFERENTIAL AUTO-COLLIMATION – INFLUENCES OF PROBE ASSEMBLE ERROR –

Yutaka Uda[1], Shoichi Shimada[1], and Yasuyuki Go[2]
[1]Department of Mechanical Engineering
Osaka Electro-communication University
Neyagawa, Osaka, Japan
[2]Machine Design Division
Nagase Integrex Co., Ltd.
Seki, Gifu, Japan

INSTRUCTIONS

Demands for long mechanical and optical parts which have high straightness or flatness are increasing. Examples are seen in a flat panel for liquid crystal display, a throttle die for thin film production and machine elements of semiconductor equipments. Although the length of the parts exceeds 1 m, the requirement for their figure accuracy is higher than 0.1μm. However, there is no useful method to evaluate precisely the figure accuracy of the long parts. The reasons are inevitable difficulties in manufacturing long tangible datum and prevention of deformation due to gravity and environment. Therefore, developing the ultra-precision measuring machine for long parts is an urgent need.

A possible method for the purpose described above is differential laser auto-collimation (DLAC). The principle of figure measuring with DLAC is the accumulation of difference angle in inclination measured by laser auto-collimation between two points along a straight line on the surface to be measured. However, the figure accuracy measured by the method is influenced by the in alignment error of the devices in the measuring system.

IN-SITU SELF CALIBRATION LASER DIFFERENTIAL AUTO-COLLIMATION

A schematic drawing of in-situ self calibration DLAC is shown in Figure1. To eliminate the alignment error of laser beams and angle detectors, the system consists of two angle detectors (AD_a, AD_b), which simultaneously detect the angles in inclination of the surface at two measuring points on the surface to be measured, two laser diodes (LD_a, LD_b) and a rotary table with two polarization beam-splitters (PBS_a, PBS_b) and two quarter-wave plate (QWP_3, QWP_4). In Figure 1, the inclination angles of the reflected laser beam $T(x_1)$ and $T(x_2)$ from the points x_1 and x_2 on the surface $S(x)$ are simultaneously detected by the angle detectors AD_a and AD_b, respectively. d is the distance between x_1 and x_2. The alignment errors of AD_a and AD_b, PBS_a and PBS_b and QWP_a and QWP_b are supposed to be E_a and E_b, M_a and M_b and P_a and P_b respectively. The parallelism between the beams from LD_a and LD_b and the total alignment error of QWP_c and QWP_d are supposed to be P and P_{cd}, respectively.

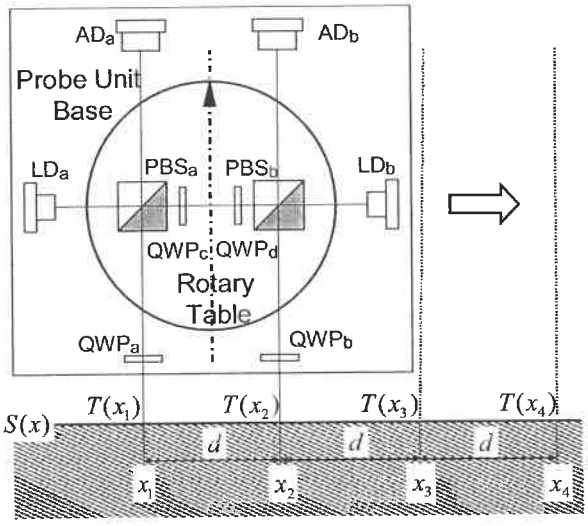

FIGURE 1. In-situ self calibration Differential Laser Auto-Collimation

The measuring procedure has four steps as shown in Figure 2 and the table 1. At each steps

the angle of rotary table and/or laser emission source are changed.

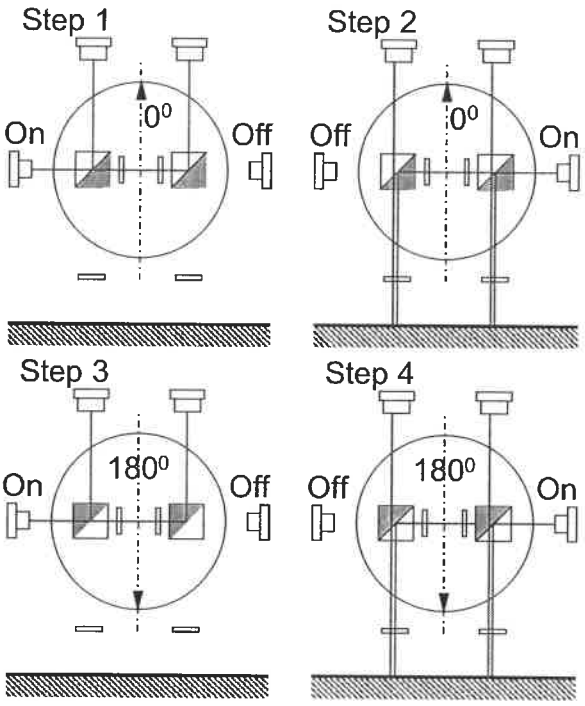

FIGURE 2. Measuring procedure of In-situ self calibration DLAC

Table 1. Measuring Procedure

Step	R.T.	LD_a	LD_b
Step 1	0^0	On	Off
Step 2	0^0	Off	On
Step 3	180^0	On	Off
Step 4	180^0	Off	On

The output signals from the angle detectors at each step are expressed by the symbols shown in Table 2.

Table 2. Output signals at each step

Procedure	AD_a	AD_b
Step 1	$S_{a1}(x_1)$	$S_{b1}(x_1)$
Step 2	$S_{a2}(x_1)$	$S_{b2}(x_1)$
Step 3	$S_{a3}(x_1)$	$S_{b3}(x_1)$
Step 4	$S_{a4}(x_1)$	$S_{b4}(x_1)$

At step 1, LD_a is turned on, LD_b is off and the angle of rotary table is 0 (original angle). The laser beam from LD_a is divided into transmitted light and reflected light by PBS_a. Reflected light are detected by AD_a. Transmitted light is detected by AD_b through QWP_c and QWP_d and PBS_b. The output signals including alignment errors of the devices are expressed by Eqs. (1) and (2).

$$S_{a1}(x_1) = M_a + E_a \quad (1)$$

$$S_{b1}(x_1) = M_b + E_b + P_{cd} \quad (2)$$

At step 2, LD_b is turned on, LD_a is off and the angle of rotary table is 0. The laser beam from LD_b is divided into transmitted light and reflected light by PBS_b. The path of reflected light is QWP_b – Surface $S(x_2)$– QWP_b - PBS_b – AD_b and the path of transmitted light is QWP_c- QWP_d – PBS_a –QWP_a – Surface $S(x_2)$ –QWP_a – PBS_a – AD_a. As the laser beams are reflected at opposite surfaces of PBS_a and PBS_b, M_a and M_b are changed to $-M_a$ and $-M_b$. The output signals including alignment errors are expressed by Eqs. (3) and (4).

$$S_{a2}(x_1) = P - M_a + P_a + T(x_1) + E_a - P_{cd} \quad (3)$$

$$S_{b2}(x_1) = P - M_b + P_b + T(x_2) + E_b \quad (4)$$

At step 3, the rotary table with PBS_a, PBS_b, QWP_a and QWP_b is turned 180degrees and LD_a is turned on. As PBS_a and PBS_b turned 180degrees, M_a and M_b are changed to M_b and M_a. The output signals are expressed by Eqs. (5) and (6).

$$S_{a3}(x_1) = M_b + E_a \quad (5)$$

$$S_{b3}(x_1) = M_a + E_b + P_{cd} \quad (6)$$

At step 4, as the laser emission source is changed, the output signals are expressed by Eqs, (7) and (8).

$$S_{a4}(x_1) = P - M_b + P_1 + T(x_1) + E_a - P_{cd} \quad (7)$$

$$S_{b4}(x_1) = P - M_a + P_2 + T(x_2) + E_b \quad (8)$$

By the calculation using the formulas shown above, the terms of alignment errors are eliminated as follows.

$$\{S_{a2}(x_1) - S_{b2}(x_1)\} - \{S_{a1}(x_1) - S_{b1}(x_1)\} = T(x_1) - T(x_2) - 2(M_a - M_b) + (P_a - P_b) \quad (9)$$

$$\{S_{a4}(x_1) - S_{b4}(x_1)\} - \{S_{a3}(x_1) - S_{b3}(x_1)\} = T(x_1) - T(x_2) + 2(M_a - M_b) + (P_a - P_b) \quad (10)$$

$$[\{S_{a2}(x_1)-S_{b2}(x_1)\}-\{S_{a1}(x_1)-S_{b1}(x_1)\}$$
$$+\{S_{a4}(x_1)-S_{b4}(x_1)\}-\{S_{a3}(x_1)-S_{b3}(x_1)\}]$$
$$=T(x_1)-T(x_2)+(P_a-P_b) \quad (11)$$

By changing QWP_c and QWP_d, P_a and P_b can be measured correctly. Therefore, $T(x_1)$-$T(x_2)$ can be calculated. The new DLAC method proposed can eliminate the alignment errors of the devices in the system. However, a new problem is coming up. It is an off-set error between the rotating center of the rotary table and the center of two phase beam splitters due to assemble error of beam-splitters on rotary table. The off-set error causes the change in distance between the measuring points. To investigate the influence of the off-set error on measuring accuracy, a numerical simulation is carried out following the Eqs.(1) ~ (11)

ERROR BUDGET SIMULATION WITH OFF-SET ERROR

An error budget simulation of measuring accuracy is carried out with three typical cases of off-set errors. The parameters of the simulations are shown in Figure 3.

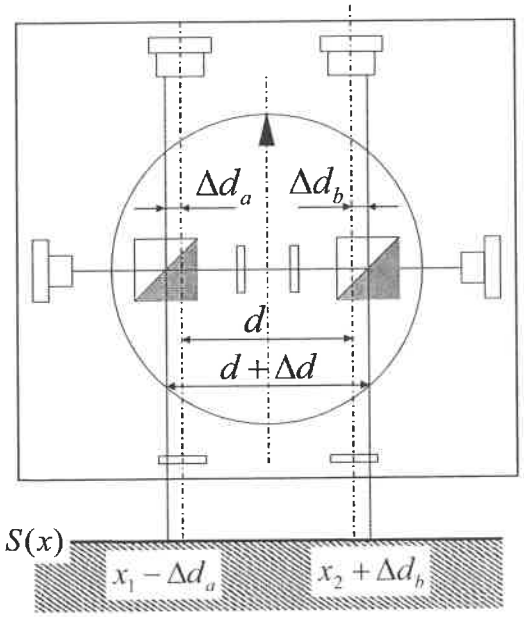

FIGURE 3. Error budget simulation model with off-set error

In the simulations, the cross sectional figure of the surface $S(x)$ along the measuring line is assumed to a sinusoidal wave the wave length and amplitude of which are λ and 1 (dimensionless). The probe unit is assumed to move on straight line without error motion and positioning error.

When the distance between two beams is not correct but the center of the beams coincides with the rotating center, the distance d changes to $d+\Delta d$ but $\Delta d_a = \Delta d_b$. A result of the simulations in the case of $d = \lambda/36$ is shown in Figure 4. The relative amplitude comparing with that without error is proportional to $\Delta d/d$. The measuring error can be estimated to be less than a few percent.

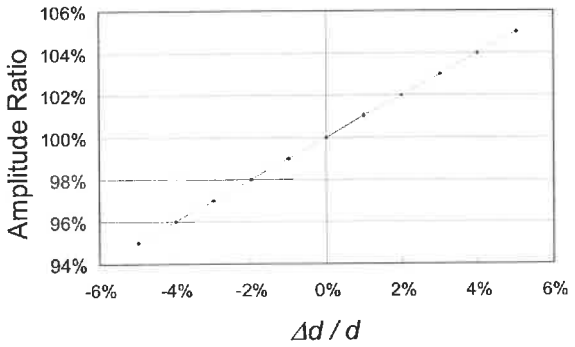

FIGURE 4. Relative amplitude vs. Δd

When the beam center is shifted from the center of rotary table with correct beam distance, Δd_a is equal to $-\Delta d_b$ in Figure 3. Figure 5 shows the result of simulation in the case of $\Delta d_a = d/100 = -\Delta d_b$. The solid line shows the amplitude difference between the measured figure by in-situ self calibration DLAC with and without off-set error. Almost no error is observed. The result suggests that the method proposed is not influenced by off-set error when the beam distance is correct. The dotted line in Figure 5 shows the amplitude difference between the measured figure by conventional DLAC method with and without off-set error. The method is influenced by off-set error.

When the beam center is shifted from the center of rotary table together with wrong beam distance, d is changed to $d + \Delta d$ and Δd_a is not equal to Δd_b. Figure 6 shows the result of the simulation in the case of $\Delta d_a = 0$ and $\Delta d_b = d/50$. Solid line shows the amplitude difference between the measured figure by in-situ self calibration DLAC with and without Δd error. Dotted line shows the amplitude difference between the measured figure by conventional DLAC method with and without Δd error. The

measuring error can be estimated to less than 2% of amplitude of surface figure. The result suggests that the off-set of two laser beam is a robust positioning by using in-situ self calibration if the distance *d* can be measured correctly.

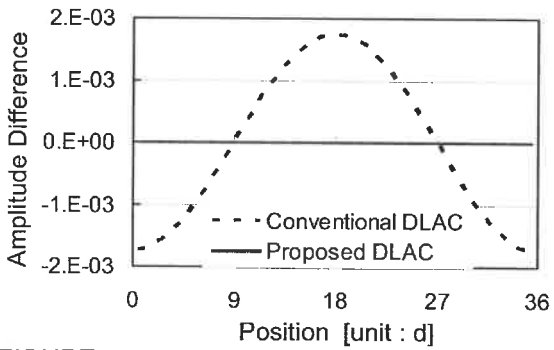

FIGURE 5. Amplitude difference between the measured figure with and without off-set error

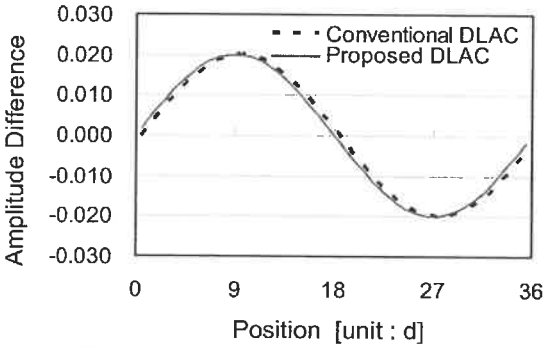

FIGURE 6. Amplitude difference between the measured figure with and without Δd error

SUMMARY

A new concept of in-situ self calibration DLAC method is proposed for straightness measuring of long parts. To confirm an effectiveness of the method proposed, an error budget simulation is carried out.

(1) The proposed new DLAC method can eliminate the parallelism problem.
(2) The error of the distance between two laser beam influences the amplitude of the measured surface and the amplitude ratio is proportional to $\Delta d/d$.
(3) Using in-situ self calibration, the off-set error between the rotating center and the center of two beams dose not influence the amplitude of the measured surface. If the distance *d* can be measured correctly.

A target of straightness measuring accuracy of the method proposed for the parts longer than 1m is 1nm. The results of this work suggest that the influence of the assemble error at the order of 0.1 mm on measuring accuracy is less than 1%.

ACKNOWLEDGMENT

This work was supported by the Grant-in-Aid for Scientific Research (Start-up), (18860079) of the Ministry of Education, Science, Sports and Culture, Japan. The authors express their thanks to Professor S. Kiyono for his useful suggestions and advices.

REFERENCES

[1] Kiyono S, Fukaya N, Kume T. Differential Laser Autocollimation Method (1st Report). J.S.P.E. 1989; Vol.55 No.2; 412-417

[2] Kiyono S, Kume T, Asakawa Y, Kamada O. Differential Laser Autocollimation Method (2nd Report). J.S.P.E. 1991; Vol.57 No.4; 652-657

MILLIMETER-SCALE REFLECTING OPTICS FABRICATED USING ELLIPTICAL VIBRATION-ASSISTED MACHINING (EVAM)

D. E. Brehl, T. A. Dow, K. Garrard, and A. Sohn
Precision Engineering Center
North Carolina State University
Raleigh, North Carolina, USA

INTRODUCTION

"Elliptical vibration-assisted machining" (EVAM) is a diamond-tool machining process that can be used to create 3-dimensional micro-structures. In EVAM, the tool tip is driven very rapidly through a small (tens of micrometers) ellipse at multi-kHz frequencies; this elliptical motion is superimposed on the normal tool feed motion. When feature tolerances of ~200 nm suffice, EVAM can be more economical than methods such as micro-electro-discharge machining, focused ion beam, or laser ablation. EVAM also avoids problems of tool deflection, chatter, runout, and vibration associated with chip-making processes like micro-milling [1]. It can achieve cut edges which are virtually burr-free. Finally, because the tool is cutting in the workpiece for only part of each elliptical cycle, average cutting forces, and tool wear from mechanical and chemical effects, are reduced compared to conventional machining [2].

The Precision Engineering Center has built an EVAM tool, the "Ultramill". In early experiments the Ultramill made geometrically simple structures in materials such as copper, aluminum, stainless steel and SiC. These parts included optical quality flats and low relief binary structures with arbitrary geometry. This work showed that the Ultramill can achieve surface finishes better than 15 nm RMS in a variety of materials and a figure error less than $\lambda/4$ [3, 4, 5, 6].

Current Ultramill research is directed toward making functional optical structures. A beam splitter project for fiber-optics is described in this article. This beam splitter improves upon existing concepts by using the Ultramill to machine complex reflecting surfaces which eliminate the need for collimating refracting elements.

PROCESS DESCRIPTION AND EQUIPMENT

Figure 1 shows how EVAM can be achieved using two parallel piezoelectric actuators to drive a diamond tool. Applying cyclic voltages to the stacks causes them to change length in a cyclical manner. The toolholder acts as a linkage to convert the linear stack motion into an elliptical path. By changing the voltage amplitude and/or phase difference between the stacks, the ellipse geometry (aspect ratio, tilt, and dimensions) can be varied through a wide range.

Figure 2 shows the tool motion in EVAM for two cutting cycles. During each cutting cycle, the work advances relative to the elliptical tool path. The overlapping toolpaths produce thin chips, resulting in greatly reduced tool forces compared to conventional cutting.

Figure 3 is a cutaway view of the Ultramill. The two piezoelectric actuators are cooled by a dielectric fluid circulating continuously through the steel chamber. The hollow lightweight ceramic toolholder rests on alumina pins on the

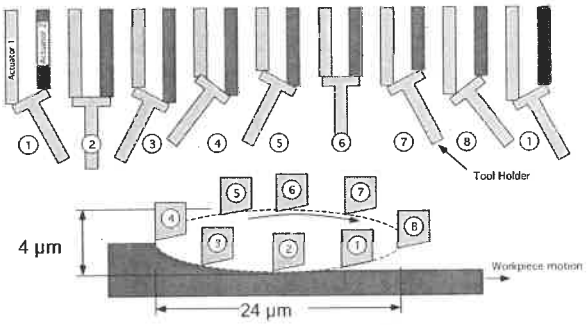

FIGURE 1. Ultramill EVAM concept

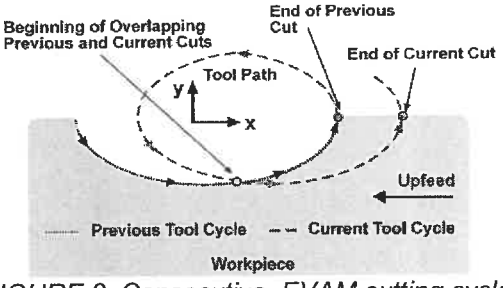

FIGURE 2. Consecutive EVAM cutting cycles

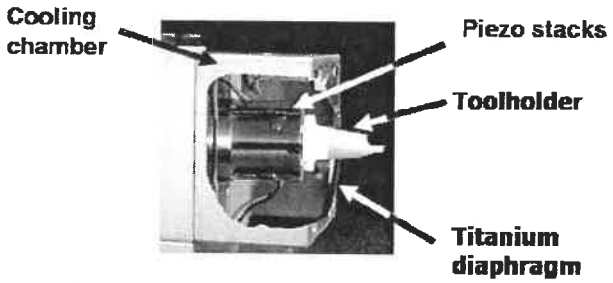

FIGURE 3. Cutaway view of Ultramill EVAM tool

tops of the piezo stacks. A diamond tool is cemented to the toolholder. The titanium diaphragm exerts the required preload force on the piezo stacks and seals the coolant chamber. The Ultramill operates at frequencies up to 4 KHz. It is installed on a diamond turning machine (DTM), which provides 3-axis X-Y-Z motion for raster machining (the spindle is locked when using the Ultramill). The DTM's three axes are supported by hydrostatic oil bearings with nanometer-scale encoder resolution.

FIBER OPTIC BEAM SPLITTER

The fiber-optic beam splitter will be used to demonstrate the ability of the Ultramill system to make a functional device that requires fabrication of optical surfaces with complex geometry. Figure 4 shows a beam splitter design that is based on refracting collimating optics. A light beam exits the source fiber in a diverging cone. The divergence angle is approximately the same as the required angle of acceptance for light entering the inlet of the receiving fibers. Light approaching at greater than the angle of acceptance is not transmitted by the fiber and is wasted. To keep coupling losses small, ball lenses are used to collimate light emanating from the source fiber before it reaches the beam splitter mirror, and then to focus the light on the entrance plane of the receiving fibers. Note that other lens geometries can be used besides ball lenses.

An alternate concept, making use of the capability of the Ultramill, is shown in Figures t and 6. The beam splitter mirror is concave and curved in three dimensions. It focuses the diverging beam from the source fiber onto the receiving fibers. This approach eliminates refracting elements such as ball lenses which must be precisely positioned relative to the fibers for maximum coupling efficiency. The number of optical components is reduced from four to just one. The semi-major axis length A and semi-minor axis length B can be selected using the relationship $B^2 = A^2 - F^2$, where F is the distance of the foci from the center of the ellipse. Once the ellipse profile is established, the corresponding three-dimensional figure is obtained by revolving it around the major axis. The maximum radius of the ellipsoid's circular cross section is B, the length of the semi-minor axis.

The concept is designed around a commercially-available multimode optical fiber with an active diameter of 0.486 mm and 61° angle of acceptance/divergence as shown in Figure 5. The reflector's elliptical cross section has semi-major axis A = 2.38 mm and semi-minor axis B = 1.40 mm. The figure shows light originating at one focus behind the exit plane of the source fiber, emanating over the entire divergence angle, and being brought to the other focus at the entrance plane of the receiving fiber. To

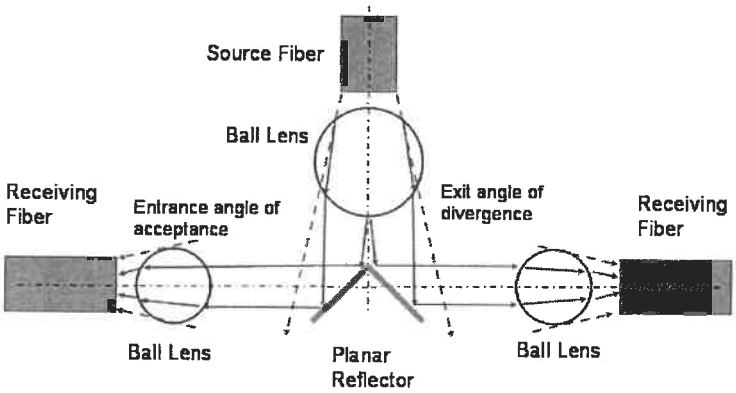

FIGURE 4. Schematic view of typical refractive-type beam splitter. Ball lenses are used to collimate the divergent light rays from the source fiber and focus them onto the receiving fibers..

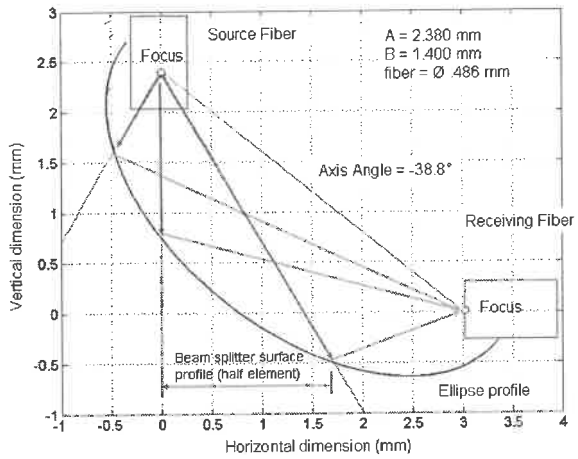

FIGURE 5. Development of reflector surface for the beam splitter, based on geometry of an ellipse with one focus located in the source fiber and the other focus on the receiving fiber.

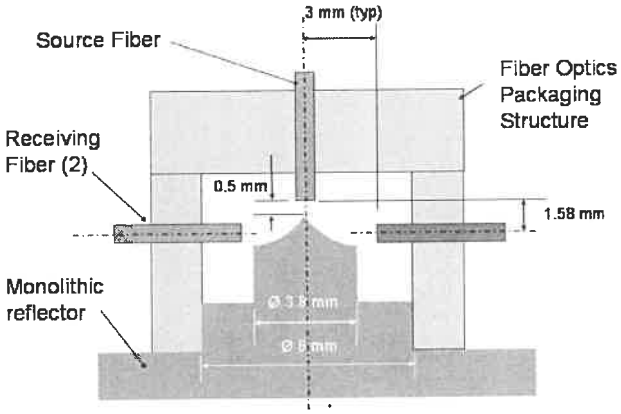

FIGURE 6. Sectional view of beam splitter. Reflector replaces planar beam splitter and refracting elements in Figure 4.

fabricate the beam splitter, only the indicated portion of the elliptical profile is needed, extending from the source fiber's centerline to the intercept point of the ray at the divergence half-angle with the ellipse. The required surface makes a circular curve into the plane of the paper, with maximum radius of 1.40 mm. Figure 6 shows a sectional view of the complete beam splitter assembly.

SPHERICAL SURFACE MACHINING TEST

Before fabricating the beam splitter, the Ultramill was used to machine concave spherical reflectors of similar size and sag. A spherical form was selected because the whole surface can be measured with a Zygo GPI interferometer rather than measuring cross-sections with a contact profilometer. The part aperture diameter is 1.5 mm and the radius of curvature (-4.5 mm) was chosen so that such that surface angle was less than the 10° clearance angle of the cutting tool.

To achieve the maximum sag of 63 µm multiple sets of cutting passes were made up to 11 µm deep . The finish pass was made at a nominal depth of 1 µm and required 150 raster passes at 10 µm crossfeed spacing. Mineral oil was used as the lubricant and the part required 70 minutes to machine.

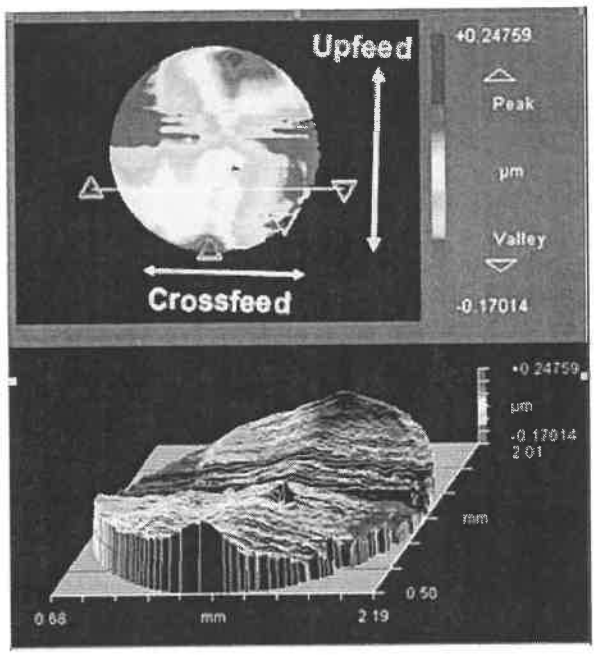

RMS = 62 nm

Power = - 0.11 wave

FIGURE 7. Interferogram of spherical copper surface machined using the Ultramill with a form error 62 nm RMS or λ/10. The errors in the surface show astigmatism and a central ridge feature.

Figure 7 shows a GPI interferogram of the spherical surface. It shows the departure of the machined surface from the intended spherical surface. The top panel is a contour plot of the error while the bottom panel is an oblique view of the error surface. There is a small valley across the middle of the part caused by non-linearity in the ballscrew drive of the Z-axis. The Z-axis has to stop and move in the

opposite direction while the X-axis moves at constant speed. This creates an error near the center of the part. In addition, there is some astigmatism (saddle shape) caused by lack of squareness between the X and Z axes. Finally there is a ridge along the upfeed centerline caused by the tool radius differering slightly from the nominal value used to generate the DTM motion program, which shows up at this high resolution. Measurements will also be made on this surface using a Talysurf profilometer to understand how these features would be represented in those 2D scans.

CONCLUSIONS

The Ultramill EVAM tool can been used to make a variety of feature geometries, including flats, binary features, trihedrons, and sculpted 3-D features. A fiber optic beam splitter been designed which features ellipsoidal reflecting surfaces to be machined using the Ultramill. This concept eliminates additional refracting elements, such as ball lenses, used by existing beam splitter concepts for collimation. Concave reflecting surfaces with spherical form have been machined by the Ultramill to see the form errors that would be present in the elliptical sections. Several surfaces were machined and errors have been removed on successive parts, reducing the figure error to 62 nm RMS.

ACKNOWLEDGMENTS

Principal funding for this work was by NSF grant DMI-433215, monitored by G. Hazelrigg. Additional funding received from Oak Ridge National Laboratory and Sandia National Laboratory. Chardon Tool provided diamond tools for machining experiments.

The reflecting beam fiber optic beam splitter was suggested as a project for the Ultramill by T. G. Bifano of the Boston University Photonics Center.

REFERENCES

[1] Benivedes G. Meso-Machining Capabilities. M^4: Workshop on Micro / Meso-Mechanical Manufacturing, Evanston, IL, May 2000.

[2] Cerniway MA. Elliptical Diamond Milling - Kinematics, Force, and Tool Wear. MS thesis, North Carolina State University, 2001

[3] Brehl DE, Dow TA. 3-D Microstructure Fabrication Using Elliptical Vibration-Assisted Machining. ASPE Proceedings, 2007:40:21-26

[4] Brehl DE, Dow TA, Garrard K., Sohn A. Micro-Structure Fabrication Using Elliptical Vibration-Assisted Machining (EVAM). ASPE Proceedings, 1999:39:511-515

[5] Negishi, N. Elliptical Vibration-Assisted Machining with Single Crystal Diamond Tools, MS thesis 2003; North Carolina State University

[6] Brocato, B. Micromachining Using Elliptical Vibration-Assisted Machining. MS thesis 2005; North Carolina State University

LASER MICROMACHINING IN SILICA GLASS WITH ABSORBENT SLURRY

Ippei Kono[1], Naohiko Sugita[1], and Mamoru Mitsuishi[1]
[1] Department of Engineering Synthesis, School of Engineering
The University of Tokyo
7-3-1, Hongo, Bunkyo-ku, Tokyo, Japan

INTRODUCTION

Laser machining is expected that it fabricate a 3D microstructure in transparent material without bonding. The microstructures in glass materials are required for optical waveguides and micro fluidic chips. In laser micromachining for glass, a specific laser which is a very short pulse laser (i.e. femto-second laser [1][2]) is often used for machining the glass without cracks. In other methods, use of absorbent materials and high processable glass materials as work pieces are also effective for non-crack machining. Especially, a method of machining by femto-second laser [3] and machining with absorbent materials are suited for micromachining in glass materials. This is because selective laser absorption in glass materials is required. In femto-second laser machining, it is possible to absorb the laser beam selectively by nonlinear absorption. In machining with absorbent materials, the laser beam is absorbed at the interface between glass and absorbent materials, and only a part of glass contacted with the absorbent is removed. It is possible to machine the glass even by nano-second laser, which is less expensive than femto-second laser. Therefore, the authors investigated the method of machining the microchannel in silica glass with absorbent materials by UV nano-second pulsed laser. In this method, the liquid-like absorbent is required for continuous supply of absorbent and evacuation of the debris. As a method of machining glass with liquid absorbent, LIBWE (Laser-Induced Backside Wet Etching) method was reported [4]. However, in LIBWE method, the high concentrated organic solution is used as the absorbent material. In this research, it is proposed the method of machining in glass materials with absorbent slurry which is water including metal-oxide nanoparticles as absorbent instead of harmful organic solution.

LASER MICROMACHINING SYSTEM

Laser micromachining system is shown in Figure 1. A Laser source is the UV nano-second pulsed laser (COHERENT AVIA355-3000) which is 355nm in wavelength and 40ns in pulse duration. The laser beam is focused by a lens, and the minimum spot size of the laser beam is 9.17μm. Laser irradiated spot is moved by moving the silica glass horizontally by XY stage, and the focal point is moved by moving the lens vertically by Z stage. The bottom of a silica glass as a work piece is contacted with the absorbent slurry, as shown in Figure 1(b). The laser beam goes through the silica glass and is absorbed by absorbent slurry at the interface between the silica glass and the absorbent slurry. The absorbent slurry is CeO_2 (average particle size: 14nm), TiO_2 (36nm) and ZnO (34nm) particles in water. These materials are generally used for UV screening. The absorbent slurry is stirred by magnet stirrer to prevent precipitation.

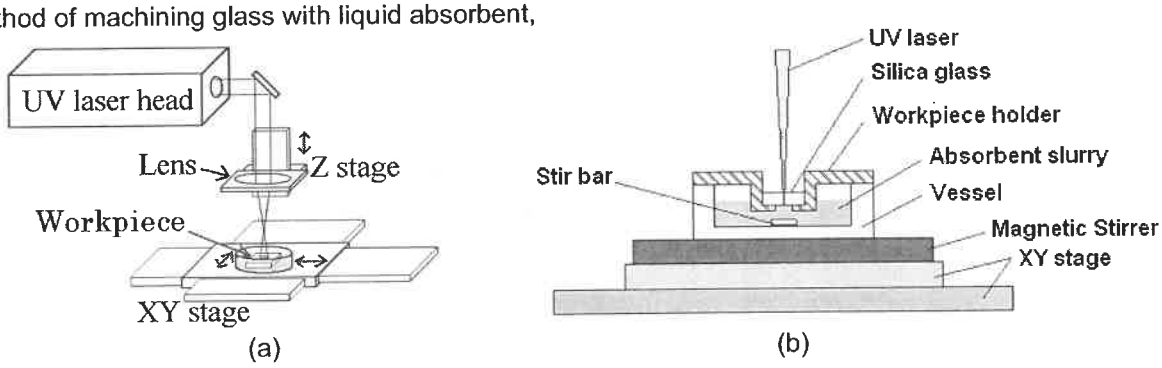

FIGURE 1. Laser micromachining system

MACHINING EXPERIMENT

Machining Grooves

Through the surface machining experiment, it was confirmed machining capability, and machining characteristics were investigated in the proposed method. A groove on the backside of the glass was machined by scanning with laser beam linearly. After ultrasonic cleaning with NaOH (1mol/l), the groove was measured by laser microscope (KEYENCE VK-9500), and it was investigated the relationship between machining conditions and the depth of the groove. Machining conditions were pulse energy: E (μJ), defocus: d (μm), concentration of absorbent: c (wt%), scan speed: v (μm/s), pulse frequency: F (kHz) and number of scan times: n.

CeO_2 was the most efficient of three for machining in proposed method. With larger pulse energy or smaller absolute value of the defocus, the radiated laser beam had higher intensity and machined the deeper grooves, in Figure 2(a) and (b). As shown in Figure 2(c), higher concentrated absorbent slurry had higher energy conversion efficiency, and the deeper groove was fabricated. As shown in Figure 2(d), (e) and (f), the depth of the groove was inversely proportional to scan speed and proportional to pulse frequency and number of scan times. These parameters determine the number of laser pulses radiated in unit area. Therefore, the depth of the groove is proportional to the number of the laser pulses.

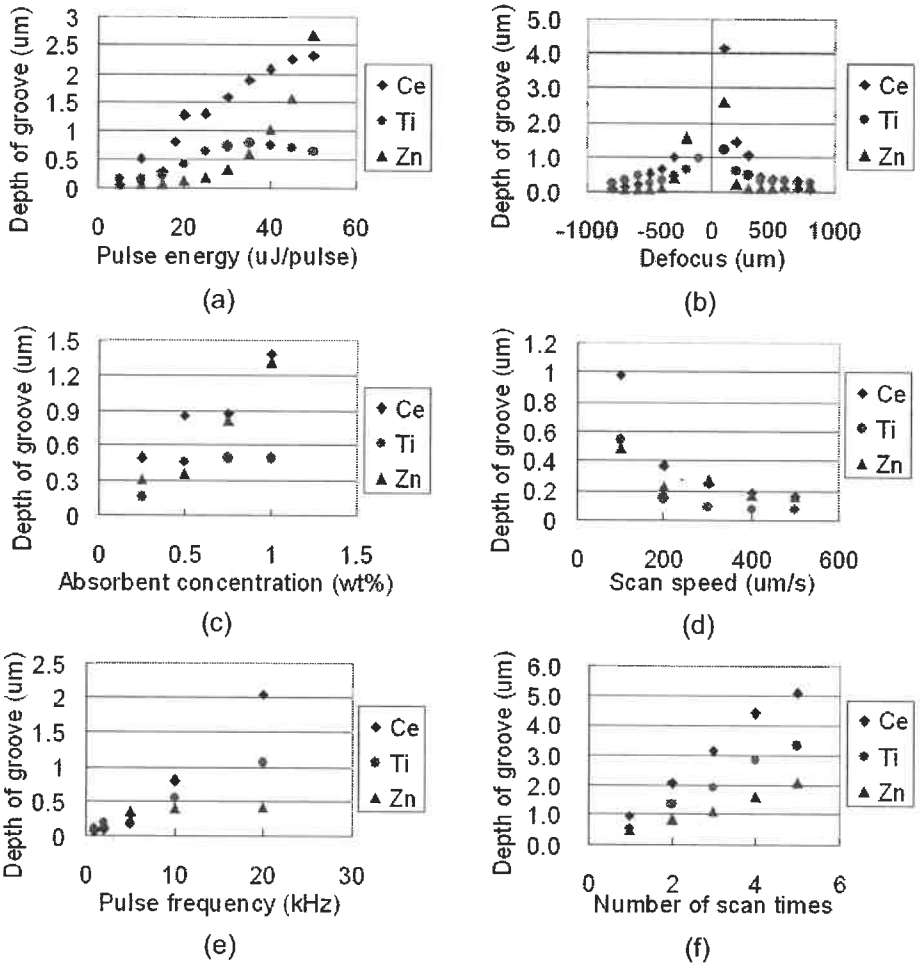

FIGURE 2. Relationship between machining conditions and depths of grooves (Machining conditions: E = 18μJ/pulse, d = -300μm (+300μm at (a)), c = 0.5wt%, v = 100μm/s, F = 10kHz, n = 1)

Machining Holes

The machining characteristics in machining in the glass were investigated through a vertical micro hole machining from the backside of the glass. The hole was fabricated by scanning with laser beam in 50μm-square area repetitively. A focal point was moved 1μm up per scanning around the area. As shown in Figure 3, machining rate was constant in machining with TiO_2 and ZnO. In the case of CeO_2, amount of machining became small when the laser scanned the machined area more than 40 times. It is caused by small laser intensity at machined surface because of a large distance between machined surface and focal spot.

Then, the holes machined by moving focal point 2 or 3 μm up per scan as compensation of defocus. The deep vertical hole with at most 1 mm in depth was fabricated, as shown in Figure 4, and its aspect ratio was over 17. However, in Figure 4(b), cracks were occurred at the end of the hole because of high laser intensity. Furthermore, it is difficult to fabricate a deeper hole than this. It is considered that this is because the bubbles generated on machining blocked up the hole and the absorbent slurry enough for machining were not supplied at the machined area.

As shown in Figure 5, a tilted micro hole was fabricated by moving the machined area horizontally by degrees. It was possible to fabricate the hole which was tilted at an angle of 30 degrees below to laser axis. In trying to machine a hole with over 30 degrees tilt, instead of the tilted hole, the groove was fabricated because the backside of the glass was machined.

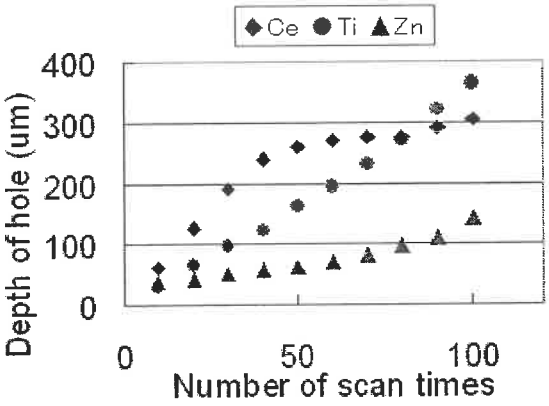

FIGURE 3. Relationship between number of scan times and depths of micro holes

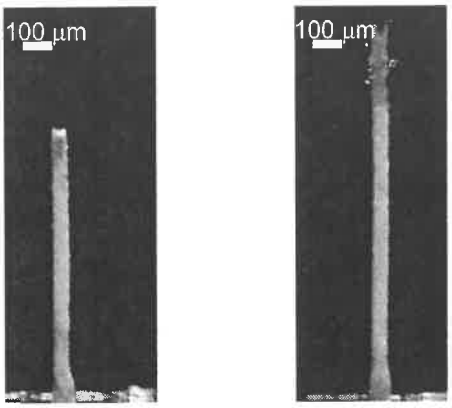

FIGURE 4. Deep hole in silica glass

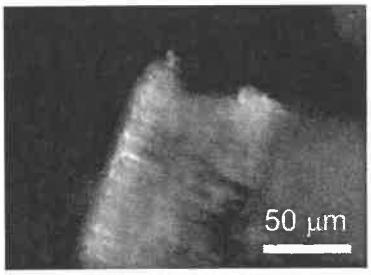

FIGURE 5. Tilted hole in silica glass

Machining Microchannels

It was investigated to machine bended microchannels in glass as an element of the 3D microchannels. The microchannels which was bended at a right angle was fabricated. In machining the bended microchanels, after fabricating a vertical hole, the glass with the hole was rotated by 90 degrees, and another hole was drilled by laser from the side wall of the hole previously fabricated. The debris was expected to disperse into the absorbent slurry.

According to this procedure, the bended microchannel with two corners was fabricated, as shown in Figure 6. This indicated it was possible to fabricate microchannels in silica glass in the proposed method. However, it was difficult to fabricate the long microchannels. As in the case of the deep vertical hole, it is considered that this is because of blocking the hole with bubbles.

DISCUSSION

Through the experiments, it was found that CeO_2 and TiO_2 were better than ZnO as absorbent particles. Absorbed fraction of ZnO is not lower than CeO_2 and TiO_2. Therefore, it is influenced by the efficiency of energy conversion

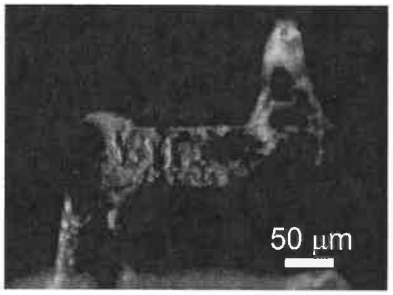

FIGURE 6. Bended microchannel in silica glass

or transfer. In machining long channels, it is required to remove the bubbles which block up the channels and prevent the supply of the absorbent slurry. Therefore, it is important to analyze components of the bubbles. The roughness of side wall also needs improvement. The roughness was submicron order in Ra, and the required roughness is less than 10 nmRa. It is considered that this is caused by micro cracks and adhesion of melted glass.

CONCLUSIONS

For 3D micro fabrication in silica glass, the method of machining by UV nano-second pulsed laser with absorbent slurry was proposed. Through the experiments, the machining characteristics in the proposed method were investigated. According to the proposed method, it was possible to fabricate following microstructures in silica glass. The deep hole with about 1 mm in depth was fabricated, and its aspect ratio was over 17. Moving machined area by degrees, the hole tilted about 30 degrees to laser axis was also fabricated. Furthermore, by rotating the glass and radiating the laser beam to the side of the machined hole, the bended microchannel with two corners was fabricated. These microstructures can be applied to constituent element of microfluidics and MEMS.

REFERENCES

[1] S. Nikumb, Q. Chen, C. Li, H. Reshef, H.Y. Zheng, H. Qiu and D. Low, 2005, Thin Solid Films, Vol.477, 216-221.

[2] C. Hnatovsky, R.S. Taylor, E. Simova, P.P. Rajeev, D.M. Rayner, V.R. Bhardwaj and P.B. Corkum, 2006, Applied Physics A, Vol.84, pp.47-61.

[3] Li, Y., Itoh, K., Watanabe, W., Yamada, K., Kuroda, D., Nishii J., and Jiang, Y., 2001, Optics Letters, Vol26, 1912-1914.

[4] Kawaguchi, Y., Sato, T., Narazaki, A., Kurosaki R., and Niino, H., 2005, Jpn. J. Appl. Phys., Vol44, no5, 176-178.

CHARACTERIZATION OF ERRORS AFFECTING SURFACE GENERATION IN FAST TOOL SERVO (FTS) MACHINING

T.C. Kwok*, C.F. Cheung, S. To, and W.B. Lee
Advanced Optics Manufacturing Centre,
Department of Industrial and Systems Engineering,
The Hong Kong Polytechnic University, Hung Hom, Hong Kong

ABSTRACT

In this paper, a study of the fabrication of optical microstructures by fast tool servo (FTS) machining technology is presented. The study started from locating the sources of error exclusively involved in ultra-precision machining with FTS, which are stroke error, spatial error, trajectory generation error and errors of cutting parameters such as spindle speed, depth of cut, feed rate, etc. Hence, a series of cutting tests and analyses have been carried out to characterize the systemic error of FTS system. The results show that stroke movement is one of the factors affecting the form accuracy of machined profile.

INTRODUCTION

Nowadays, the use of display system in photonics products is increasing; optical microstructures such as micro-lens arrays are widely used critical components in the display system. One of the supreme methods which are commonly used in the fabrication of optical microstructures is ultra-precision machining with fast tool servo (FTS). The FTS is an independently operated positioning device which is usually mounted onto ultra-precision machines for increasing the tool positioning accuracy in order to fabricate optical microstructures by the rapid actuation of tools with fine resolution, positioning accuracy, and sufficient high bandwidth [1].

Although there has been extensive research work on the design and control of tool actuators for FTS machining [2-5], relatively little work has been reported in the studies of nano-surface generation in FTS machining of optical microstructures. There is a need to study on the optimization of the cutting conditions and minimizing the errors in FTS machining of optical microstructures. As a result, this paper presents a study of the fabrication of optical microstructures by FTS.

Factors affecting surface generation

To study the fabrication of micro-lens array by FTS machining, the first step is to identify the factors affecting the surface generation. Based on the literature presented in the last decade, FTS machining is the technology which is developed based on single-point diamond turning technology. The material removal process is governed by the ultra-precision machine characteristics, tools and lubrication, environmental condition, machining parameters, surface defects and morphological characterization of samples. The machining parameters include rotational spindle speed, feed rate, depth of cut and material of samples while the morphological defects could be distinguished into four types, which are waviness due to vibration, stria or tool mark created by diamond tools, cracks due to material structure and variation of form and position.

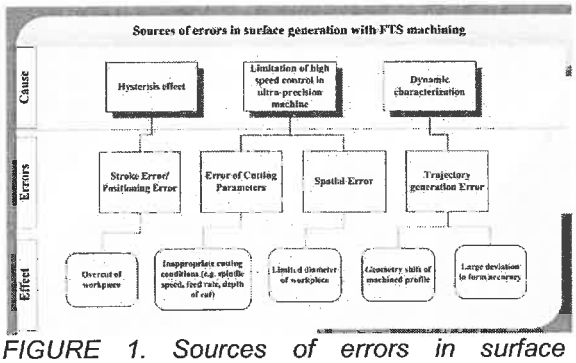
Sources of errors in surface generation with FTS machining
Cause
Errors
Effect
Hysterisis effect
Limitation of high speed control in ultra-precision machine
Dynamic characterization
Stroke Error/ Positioning Error
Error of Cutting Parameters
Spatial Error
Trajectory generation Error
Overcut of workpiece
Inappropriate cutting conditions (e.g. spindle speed, feed rate, depth of cut)
Limited diameter of workpiece
Geometry shift of machined profile
Large deviation in form accuracy

FIGURE 1. Sources of errors in surface generation with FTS machining.

Figure 1 shows the sources of errors exclusively involved in surface generation with FTS machining. It is well known that piezoelectric actuator is often used for the purpose of micro-positioning and active control. However, one of the drawbacks of the piezo actuators is the existence of hysteresis which leads to oscillation and vibration [6]. Eventually, stroke error or positioning error would happen and there exist over cut phenomenon on the fabricated profile. On the other hands, the limitation of ultra-precision machine also leads to error of cutting parameters and spatial error which limits size of the workpiece. For example, the surface roughness of fabricated profile could be

enhanced by employing spindle speed in SPDT technology. When designing the machining conditions employed in FTS machining, it could hardly simply increase the spindle speed for better surface finish because of the limitation of the bandwidth of the FTS actuator.

In FTS machining, the rotational and linear sensor feedback the real-time position of the spindle and diamond tool for DSP (digital signal processor) Kernel to calculate the location being cut in the next moment. This calculation is according to the program of the geometry of desired profile preset in SOP control system. Figure 2 shows the signal processing in FTS machining. The final source of error to be mentioned is dynamic characterization which leads to trajectory generation error. This error could also be mentioned as improper computing of the cutting position in real-time which always induces geometrical shift of machined profile and large deviation in form error.

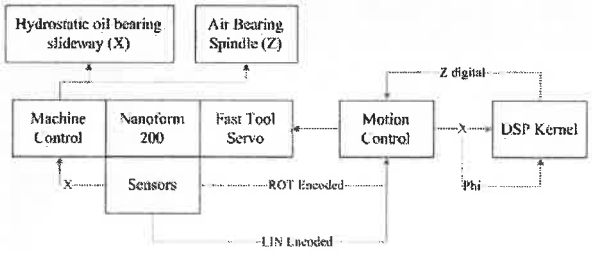

FIGURE 2. Signal processing in FTS machining

Characterization of systematic errors

To investigate the highlighted errors exclusively for FTS machining, a series of cutting tests was carried out on Nanoform 200 ultra-precision machine incorporated with a FTS system located in Advanced Optics Manufacturing Centre (AOMC) of The Hong Kong Polytechnic University (see Figure 3). FTS driven by a piezo-electric actuator is mounted on the Z-slide of the lathe, which enables the diamond tool to cut back and forth in 1000 Hz bandwidth of natural frequency. The FTS control system receives input from work spindle and slide, the tool position can be calculated in real-time and commanded in order to move the tool accordingly.

Proposed methodologies on characterization of systematic errors

The first step to investigate the fabrication process of complex regular micro-structural pattern (e.g. microlens array as shown in Figure 4), the study was proposed by starting from the fundamental level – flat surface.

(a)Nanoform 200 ultra-precison machine

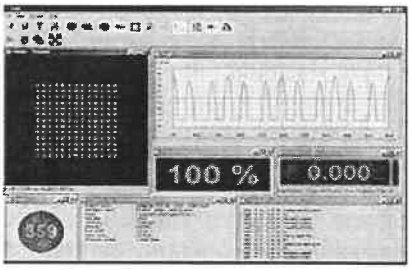

(b) User interface of FTS control system

FIGURE 3. Fast tool servo machining system

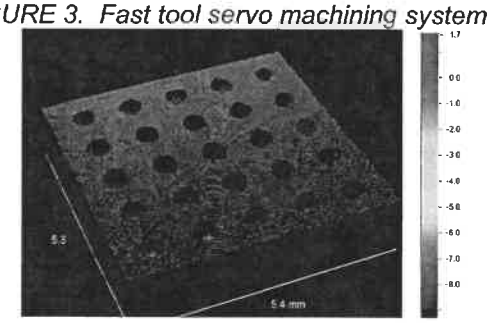

FIGURE 4. Fabricated optical microstructure

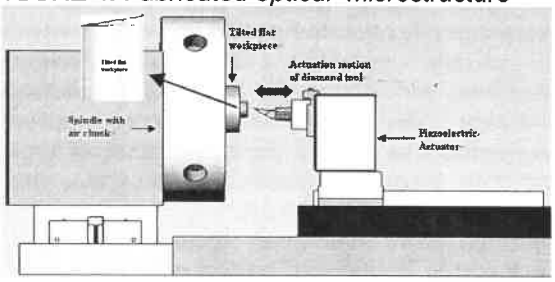

FIGURE 5. Fabrication of tilted flat surface by ultra-precision machining with FTS

To test the performance of FTS machining technology, tilted flat surface (see Figure 5) is machined since flat surface helps to minimize the geometric error involved and is easier to be measured. In cutting tilted flat surface, the FTS is required to drive the tool to move in a sinusoidal trajectory at full amplitude.

On the other hands, the effect of spatial error can be investigated by conducting cutting tests on samples with different diameters and small gradient. This can minimize effect of other

cutting conditions and help to determine the spatial error quantitatively. Hence the geometrical error is determined. Single spherical surface would be proposed as the geometry of cut. Figure 6 shows the spherical profile machined by FTS machining technology. The results would be used to further study the surface generation of optical microstructure with FTS machining.

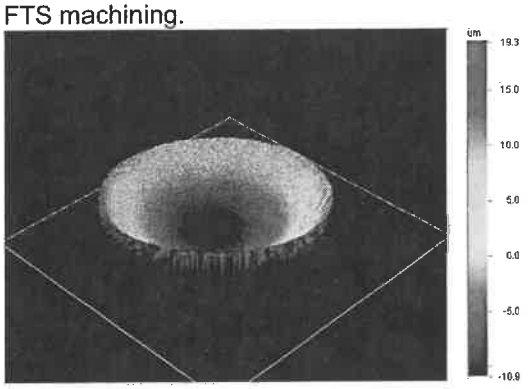

FIGURE 6. Spherical profile machined by FTS machining technology.

Determination of optimal cutting parameters

To increase machine or process efficiency, the determination of optimal cutting process parameter settings is a key factor and a number of mathematical models and techniques have been proposed and effectively used to achieve this objective. One of the most popularly adapted methodologies named Taguchi method is used in the present study for optimizing the cutting conditions of tilted flat surface with FTS machining. The selected process parameters affecting surface generation in FTS machining include radius of diamond tool, spindle speed, feed rate, and depth of cut.

Accordingly, four controllable 3-level factors and two response variables are proposed in the present study. Table 1 tabulates the four factors of spindle speed (rpm), feed rate mm/min), depth of cut rate (μm), and radius of diamond tool (mm) with three levels in this study. Namely, the experimental work is based on the orthogonal array L9(34). The two response variables include surface roughness mean and form accuracy in the fabricated tilted flat surface.

To investigate the stroke error, cutting testes were carried out by presetting range of actuation so as to determine the error from the motion of stroke or travel of actuator with 5 μm of depth of cut. To test the positioning accuracy of the FTS, full range of displacement of the actuator (i.e. 30 μm) have been used. Figure 7 shows the schematic illustration of regional analysis of stroke error. It can be seen that stepping height of each zone is 5 μm, which is also the Z-axis feed after each round of machining. This means that a total of 6 rounds of machining is needed to cut a component of 30 μm in depth. And full stroke of each zone is changing from the lowest 5 μm of zone 1 to the highest 30 μm of zone 6.

Table 1: Experimental factors and factor level

Level of experimental factor	Expermenal factors			
	A(rpm)	B(mm/min)	C(μm)	D (mm)
1	50	0.25	5	0.02
2	75	0.5	10	0.03
3	100	0.75	15	0.04

Table 2: Orthogonal array $L_9(3^4)$ of the experimental runs

L9	A	B	C	D
1	1	1	1	1
2	1	2	2	2
3	1	3	3	3
4	2	1	2	3
5	2	2	3	1
6	2	3	1	2
7	3	1	3	2
8	3	2	1	3
9	3	3	2	1

Analysis of stroke error

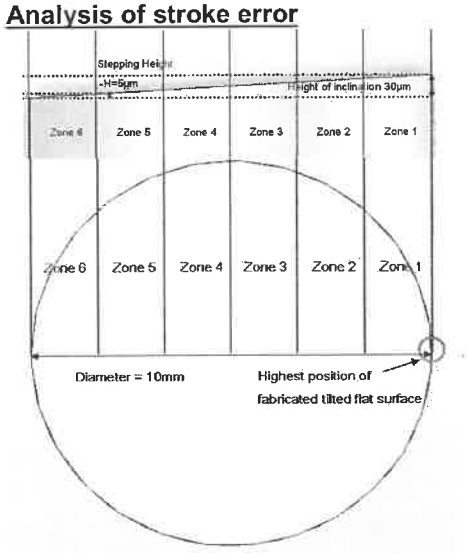

FIGURE 7. Schematic illustration of regional analysis of stroke error

To analyse the stroke error of machined profile regionally, the machined profile was measured across the diameter of fabricated tilted flat surface from the highest position to the lowest. And then the measured surface should the most

oblique ranged 30 μ m. Afterwards, the measured data of tilted flat surface would be equally divided into six zones. The depth of cut in machining is 5 μm for each round of cut. By an analysis of the form error of equally distributed zone, stroke error of different travel ranges of the FTS can be determined. Then the measured data are analysed zone by zone by removing the tilted form for determination of the form error in specific zone.

Zone	Stepping Height (μm)	Stroke of FTS (μm)	Form Error (μm)
1	5	5	0.6175
2	5	10	0.5823
3	5	15	0.5835
4	5	20	0.6073
5	5	25	0.6229
6	5	30	0.6801

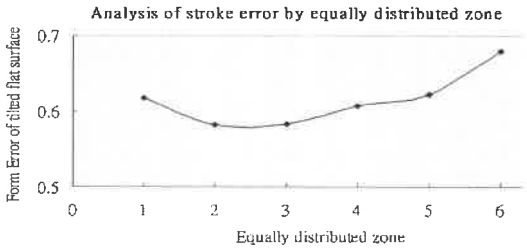

FIGURE 8. Results of form analysis in specific zone.

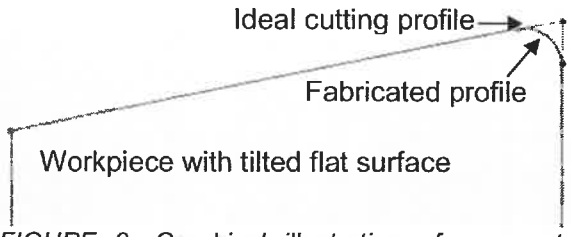

FIGURE 9. Graphical illustration of over cut phenomenon happened in FTS machining of tilted flat surface.

Figure 8 shows the results of form analysis in specific zones. In the plot of the stroke error in equally distributed zone, it is interesting to note that there exists a trend that form error increases with increasing range of travel except zone 1. Since a larger travel range of the FTS demands the actuator to drive the diamond tool forth and back, this leads to larger form error. The exception case of zone 1 can be explained by the overcut phenomenon which happens in each cut and affect the form error of zone 1 significantly when employing high stroke such as 30 μm. Figure 9 shows the graphical illustration of the over cut phenomenon happened in FTS machining of tilted flat surface.

CONCLUSION

This paper presents methodologies and experimental work for the characterization of errors affecting surface generation in FTS machining. The errors are associated with the material removal process which is governed by the ultra-precision machine characteristics, tools and lubrication, environmental condition, machining parameters, surface defects and morphological characterization of samples. A series of cutting experiments have been conducted. It is interesting to note that high stroke movement is prominence for affecting surface generation in FTS machining and this significantly affect the form accuracy of the workpiece being cut

ACKNOWLEDGEMENT

The work described in this paper was fully supported by a grant from the Research Grants Council of the Hong Kong Special Administrative Region, China (Project No. PolyU 5140/05E). Many thanks are also due to Precitech Inc. for their support of the research work.

REFERENCES

[1] T.A. Dow, M.H. Miller, P.J. Falter, Application of a fast tool servo for diamond turning of non-rotationally symmetric surfaces, Precision Engineering 13 (4) (1991) 243–250.

[2] Ludwick SJ, Chargin DA, Calzaretta JA, Trumper DL. Design of a rotary fast tool servo for ophthalmic lens fabrication. Precision Eng 1999;23:253–9.

[3] Hanson RD, Tsao T-C. Development of a fast tool servo for variable-depth-of-cut machining. ASME Dyn Syst Control 1994;2: 863–71.

[4] Rasmussen JD, Tsao T-C, Hanson RD, Kapoor SG. Dynamic variable depth of cut machining using piezoelectric actuators. Int J Machine Tools Manufact 1994;34(3):379–92.

[5] Kim J-D, Kim D-S. Waviness compensation of precision machining by piezo-electric micro cutting device. Int J Machine Tools Manufact 1998;38:1305–22.

[6] Y. Yu, N. Nagi, D. Rao, Preisach modeling of hysteresis for piezoceramic actuator system, Mechanism Machine Theory 37 (2002) 49–59.

OPTICALLY BALANCED, MULTI-PASS DISPLACEMENT INTERFEROMETRY FOR PICOMETER STABILITY TESTING

Jonathan D. Ellis[1], Justine H. Hatzigeorgopoulos[2], Jo W. Spronck[1], and Robert H. Munnig Schmidt[1]
[1]PME: Mechatronics
Delft University of Technology
2628 CD Delft, Netherlands
[2]APPE Optics
TNO Science and Industry
2628 CK Delft, Netherlands

MOTIVATION

In precision instruments, unintended motion of components in the instrument can cause significant uncertainty in the overall measurement. One of the chief causes of these motions is thermal gradients in the instrument. However, as the uncertainty of instruments is ever decreasing, another source of uncertainty is the stability of the actual materials used in the construction and the connection between these materials.

The astronomy industry is one field where the stability of the materials and the construction techniques can have an adverse effect on the resolution, and ultimately, uncertainty of the measurand. There is limited knowledge in the current literature of the long term (20+ years) stability of optical elements and their constructed joints. Many of these instruments, such as GAIA and LISA, consist of hundreds of optical surfaces, taking many years to construct. During the manufacturing process, numerous processes are performed on the optic surface, all of which will induce stress. If one optical surface is manufactured years after other surfaces in the instrument, then there will be varying drift rates in the optical elements. Additional instability sources such as the atmosphere to vacuum transitions and the data acquisition system also need to be considered. One typical method to counteract instability is to continuously adjust components to ensure proper alignment using actuators. The two most significant downfalls to this is the actuators induce more instability and they still may not be capable to account for the full amount of drift in the instrument.

On the opposite end of the size scale, there is the semiconductor industry, where material and instrument stability can significantly affect the production process. As the line width of integrated circuits becomes smaller, there is a greater importance on the stability of the lens column. The lens column consists of different materials and joints, varying from adhesives to bolted joints. If the stability of each individual element in the column is better understood, then error correction by prediction becomes possible and consequently the time between instrument calibrations can be increased.

SYSTEM SPECIFICATIONS

This work is the preliminary investigation of the uncertainty contributors of an instrument that interferometricly measures instability. The target relative displacement resolution for this instrument is 1 pm (picometer). Because this research is of interest to both the semiconductor and astronomy sectors, the samples will be investigated for various lengths of time, ranging from 100 seconds to 3 weeks. The target relative displacement uncertainty is 10 pm ($\pm 2\sigma$) for the short term measurements and 100 pm ($\pm 2\sigma$) for the long term measurements. The geometry of the samples is restricted to cubic shapes, approximately 25 mm on each side, with reflective surfaces that are "flat" and "parallel". The first generation instrument focuses on a single, linear degree of freedom (DOF) measurement. Future generations of the instrument will focus on measuring multiple degrees of freedom, from 3 DOF to 6 DOF.

CURRENT LIMITATIONS

Commercial interferometers typically are not able to measure with overall uncertainties much less than 1 nm because they are predominately optimized for measuring moving stages at high speeds. Many operate with a Zeeman split frequency, which requires sampling rates at least

in the MHz regime which significantly increases the quantum noise at the detector. The other dominant factor increasing the overall uncertainty in typical interferometers is temperature control of the surrounding environment, which also increases the uncertainty due to the refractive index of air. This is further compounded by the fact that displacement interferometry is a relative measurement, thus the two separate beams which make up the interferometer inherently have separate paths in the instrument. A promising double pass interferometer design by Lawton and Ren has an optical path difference (OPD) equal to the length of the sample. [1] Their concept is the basis for this new instrument and research.

INSTRUMENT DESIGN

To achieve a resolution of 1 pm, there are two overriding concerns in the instrument design. The first is reducing or eliminating the uncertainty due to drift in the interferometer and the second is obtaining enough phase resolution to interpolate to 1 pm. Although the interferometer by Lawton and Ren has an OPD equal to the length of the sample, the component order for transmitting/reflecting the light changes between the measurement and reference beams. Because each component can be represented by a 2x2 Jones matrix and the matrices do not commute, the drift in an individual component has different effects on the measurement and reference beams. [2] To counteract this, we measure the deadpath in the interferometer continuously during the measurement. Figure 1 shows a schematic of the new interferometer that measures both sides of the sample while the OPD is equal only to the sample length and while the deadpath of the instrument is simultaneously measured.

A major obstacle to achieving the required resolution is the phase interpolation. Previous instruments have shown meaningful phase interpolation on the order of 0.01°. [3, 4] Applying those techniques to this research is still inadequate because that would require the resolution of the interferometer (before phase interpolation) to be $\lambda/18$. The initial design (Figure 1) has a resolution of $\lambda/4$. However, this interferometer is easily adapted to achieve a resolution of $\lambda/8$ by moving the right angle prism (RAP) and adding either a retroreflector, as shown in 2, or a vertically oriented RAP. In this configuration, the deadpath in the interferometer is also measured simultaneously. While this interferometer has resolution of

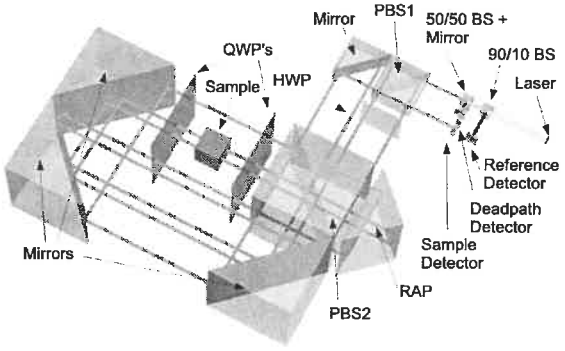

FIGURE 1. Schematic of the interferometer which measures both sides of the sample and the instrument deadpath at the same time with a resolution of $\lambda/4$. The OPD difference is the length of the sample and the deadpath measurement allows for continuous correction of instrument instability. Only one of four beam paths is shown.

$\lambda/8$, the required phase interpolation will need to be 0.005°, which is still an area of ongoing research.

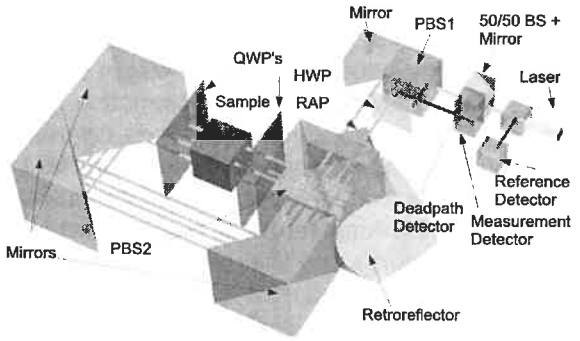

FIGURE 2. Schematic of the interferometer which measures both sides of the sample and the instrument deadpath at the same time with a resolution of $\lambda/8$. The OPD difference is the length of the sample and the deadpath measurement allows for continuous correction of instrument instability. Only one of four beam paths is shown.

In both interferometers, there are two pairs of interfering beams, for a total of four beams: a Sample Measurement Beam (SMB), a Sample Reference Beam (SRB), and two Deadpath Beams (DP1 and DP2). The measurement of the sample is determined by the phase difference between SMB and SRB, and the stability of the SRB is determined by the phase difference between DP1 and DP2. Figure 3 shows a cross sectional view of the sample along the same direction in which the beams propagate.

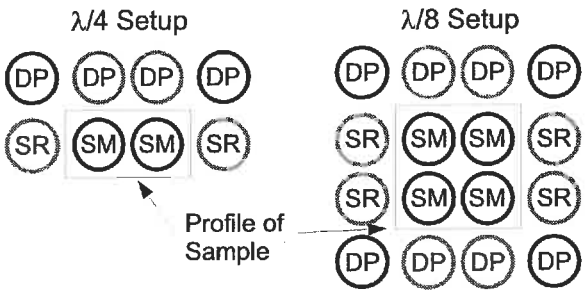

FIGURE 3. Cross sectional view of sample at the measurement surface showing the beam path arrangement.

NUMERICAL SIMULATIONS

We developed models for the λ/4 interferometer shown in Figure 1 to compare with the work previously done by Ren. [5] Further studies will show models of the interferometer in Figure 2. Because this instrument is highly sensitive to changes in polarization, the drift of individual polarizing components will effect each of the four beams differently. A model of the interferometer in Figure 1 was developed in MATLAB to determine the effects due to asimuthal angle rotational misalignments of the polarizing beam splitters (PBS), the quarter-wave plates (QWP) and the half-wave plate (HWP). This model uses Jones matrices to describe the propagation of the electric field through each component in the interferometer for each of the four beams. [2] The polarizing beam splitters were modeled as non-ideal, with reflectance and transmission coefficients of 98% for each of the polarization states. In addition, 2% power loss was assumed for all transmitting and reflecting surfaces. Lastly, phase change errors were considered due to localized surface effects for both transmitting and reflection surfaces. A beam diameter of 5 mm was used with each surface flatness modeled as λ/20 and the worst case phase change due a random, Guassian lateral change with a 1σ error being 500 nm in both directions on the surface.

Figures 4 and 5 show the average intensity error at the detector for rotations of components PBS1 and PBS2, respectively. The initial laser power was 10 mW, split equally between the four beams. The split frequency between the interfering beams was 100 Hz. Detection takes place with a sampling rate of 10 kHz. The intensity error was calculated as a difference from the ideally aligned interferometer and the error is an average of one cycle at the split frequency.

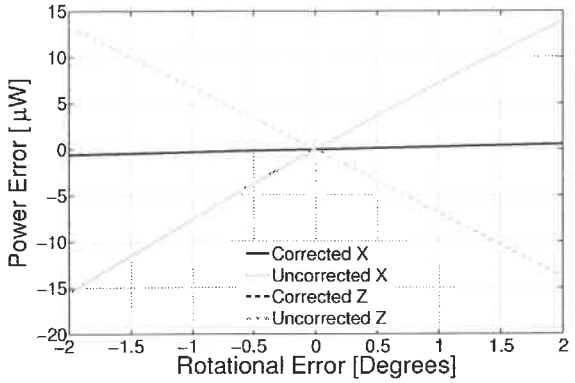

FIGURE 4. MATLAB simulations for misalignments of PBS1 about the X and Z axes. The uncorrected measurements do not account for the instrument deadpath error whereas the corrected measurements do account for deadpath errors.

The uncorrected values in Figures 4 and 5 show the average intensity difference between measurements with a perfectly aligned component and those with a misaligned component. These uncorrected values only take into account a "typical" measurement (i.e. not simultaneously measuring the deadpath). The corrected values are the difference between a "typical" measurement with the misaligned component and the deadpath measurement with the same misaligned component. In both cases, when the deadpath of the instrument is considered, the error due to misalignments is significantly reduced.

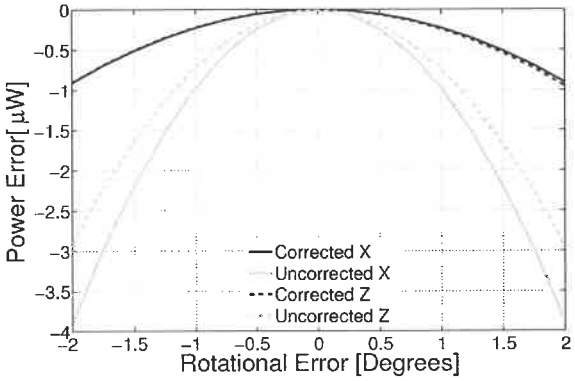

FIGURE 5. MATLAB simulations for misalignments of PBS2 about the X and Z axes. The uncorrected measurements do not account for the instrument deadpath error whereas the corrected measurements do account for deadpath errors.

To verify the MATLAB simulations, Zemax (an optical modeling software package) was used. The same polarization errors used in the MATLAB

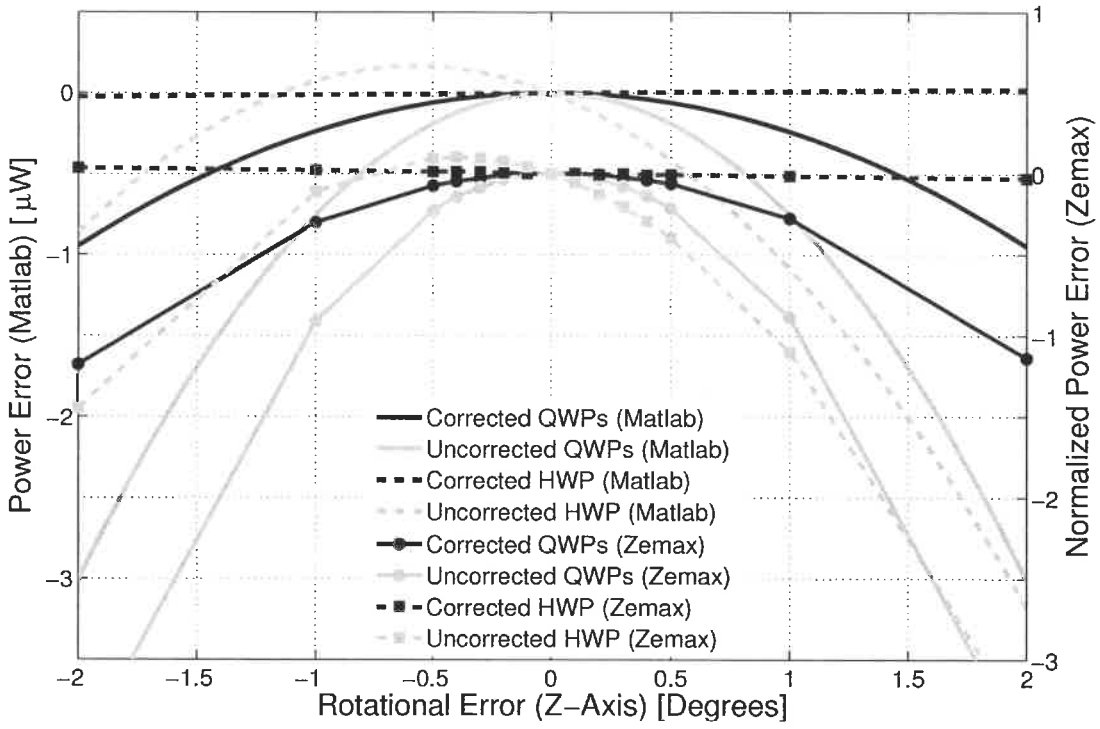

FIGURE 6. MATLAB and Zemax simulations for misalignments about the Z-axis for the QWPs and HWP. The MATLAB simulations are plotted against the left axis and the Zemax simulations are plotted against the right axis and offset for clarity.

simulations were considered, however, localized surface effects were not. Figure 6 shows the simulations from rotations about the Z-axis for the QWPs and the HWP. As before, the uncorrected terms are the measurements not considering the instrument deadpath, and the corrected measurements do consider the instrument deadpath.

It is important to note that because the Zemax simulations are normalized to the ideal interferometer alignment, the MATLAB and Zemax simulations are not equal in magnitude. However, the trends between the MATLAB and Zemax simulations are the same. Also the Zemax simulations were performed for the two PBSs and since Zemax is a full ray tracing program, the large angular misalignments caused the interfering beams not to overlap, something which is not considered in the MATLAB simulations. However, for small misalignments ($<0.1°$), the trends between the two different simulations are the same.

REFERENCES

[1] Ren D, Lawton KM, inventors; Double-pass balanced interferometer for nanoscale dilatometry. United States provisional patent US US60/881554; 2007 Jan 22.

[2] Jones RC. A new calculus for the treatment of optical systems: Part 1. J Opt Soc Am. 1941;31:488–493.

[3] Wu CM, Lawall J, Deslattes RD. Heterodyne interferometer with subatominc periodic nonlinearity. Appl Opt. 1999;38:4089–4094.

[4] Lawall J, Kessler E. Michelson interferometry with 10 pm accuracy. Rev Sci Instrum. 2000;71:2669–2676.

[5] Ren D. PhD Thesis: Optical measurements of dimensional instability. University of North Carolina at Charlotte; 2006.

ULTRA-PRECISE AND WIDE-RANGE DISPLACEMENT MEASUREMENT USING PHASE MODULATION HOMODYNE INTERFEROMETER AND TUNABLE LASER DIODES

M. Ishige[1], M. Kawasugi[1], Y. Hoshino[1], and M. Aketagawa[1]
[1] Nagaoka University of Technology
1603-1 Kamitomioka, Nagaoka, Niigata 940-2188 Japan

INTRODUCTION

As the nanotechnology has progressed rapidly, displacement measurement methods with picometer resolution will be required in the near future [1]. Currently, commercial laser interferometers are widely used as length standards in industries. However, the interferometer suffers from cyclic errors of several nanometers due to an imperfection of the fringe interpolation [2]. Therefore, it is difficult to determine an arbitrary displacement with accuracy of nanometer or better using the interferometer. On the other hand, a phase modulation homodyne interferometer (PMHI) [3] can determine an optical path difference (OPD) with picometer resolution using the lock-in detection and the null method, when the OPD equals a product of an integer and the wavelength.

In this paper, we propose a displacement measurement method using one PMHI and two tunable laser diodes (TLDs) as light sources. In the method, two beams from the two TLDs go through same optical path in the PMHI and their frequencies are controlled so that PMHI outputs of the two beams must be looked to null at adjacent interference fringes (= resonance modes). Since interference fringes must be maintained by adjusting the frequency of the TLDs, the variation of mode numbers must be null. In the proposed method, the direct OPD determination ensures the measurement-range extension. In this paper, we discuss the principle, instrumentation and measurement results.

PRINCIPLE

The former proposed system [4] is shown in Fig. 1. The system includes the PMHI, the TLD as a light source of the PMHI, a frequency stabilized laser (FSL), a servo unit to tune the TLD, and a beat-signal detection unit. The beat-signal detection unit has a high-speed photodetector (HSPD) and a frequency counter, and is used to observe the beat signals between the TLD and the FSL. At null cross-points of the PMHI, we obtain

$$L = \frac{c}{2fn} N \ , \tag{1}$$

where L, c, n, f, and N are OPD, the speed of light, the refractive index, frequency of the light, and the mode number, respectively. When the moving corner cube (CC) is displaced, the optical frequency of the TLD is controlled to maintain the same null cross-point, and the equation becomes

$$\frac{\Delta L}{L} = -\frac{\Delta f}{f} + \frac{\Delta N}{N} \ , \tag{2}$$

where ΔL, Δf, and ΔN are changes of the optical path, the frequency, and the mode number, respectively. In this case, it is assumed that $\Delta n = 0$. In the system, since one of the null cross-points must be maintained by adjusting the frequency of the TLD, the change in the mode number (= ΔN) must be null. Then ΔL, can be determined from

$$\frac{\Delta L}{L} = -\frac{\Delta f}{f} \ . \tag{3}$$

Δf can be observed from the beat signal between the TLD and the FSL.

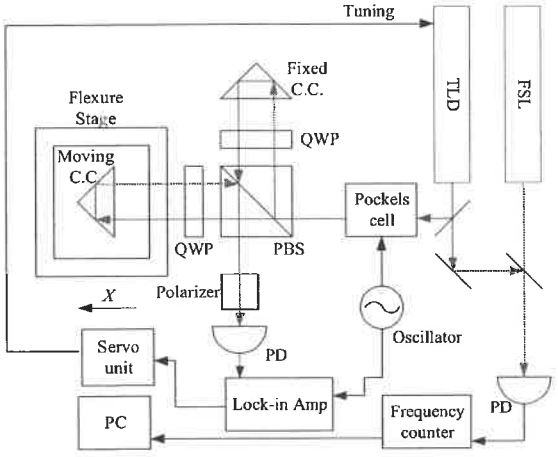

Fig.1 Configuration of former system

To measure the displacement using the configuration of fig.1, OPD (L) should be previousely known for equation (3) and is defined as below

$$L = \frac{c}{2 \times n \times FSR}. \quad (4)$$

Where FSR is free spectral range of interferometer and a frequency difference between adjacent interference fringes. The FSR can be determined by observing the PMHI output signal, when the moving CC is locked and the TLD's frequency is swept. In the determination, the frequency difference between the adjacent null points is the FSR. However, the above method has a disadvantage. The disadvantage is that a prior measurement of the FSR is required for the displacement measurement. That means that, if the OPD varies, the new FSR measurement is necessary. Since it is time consuming process, a real-time determination of FSR must be needed.

We propose a new measurement to enhance a wider measurement range and direct determination of the OPD by measuring FSR in real time way. Figure 2 shows a new measurement system. The configuration has one PMHI and two TLDs. Two laser beams from TLDs go through the same optical path. In this configuration, FSR can be measured directly by measuring the beat frequency between two TLDs when the frequency of two TLDs is locked to adjacent interference fringe. In the condition,

$$FSR = f_2 - f_1 = \frac{c}{2nL}. \quad (5)$$

Where f_1, f_2 are frequency of TLD1 and TLD2, respectively.

With the system, a measurement range can be expand. Measurement process is shown below;

(1) Frequencies of the two TLDs are controlled to maintain PMHI outputs of the two beams to null points at adjacent dark fringe modes.
(2) Displace the movable (target) mirror (CC) of the PMHI while keeping the frequency control.
(3) Determine the OPD (FSR) by measuring a beat signal frequency between the two TLDs.
(4) Measure the frequency shift of one of the TLDs by using the beat signal between it and a frequency stabilized He-Ne laser.

Measurement range could be expand to hundred of mm by repeating above procedure.

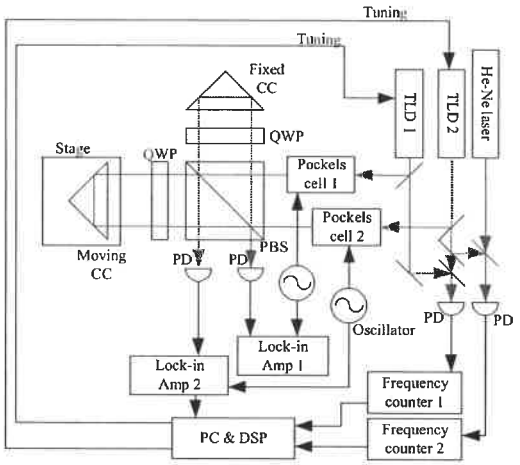

Fig.2 Configuration of proposed system

EXPERIMENTAL RESULT

Proposed method can determine the FSR directly by measuring beat signal between the two TLDs when the frequencies of two TLDs locked to adjacent interference fringes. The measured beat signal between TLDs is shown in fig.3. In this result, the FSR is equals 1.00579GHz from the frequency difference of separated 6 mode numbers. Standard deviation of the FSR measurement is 1.84MHz. This result was improved to be less than 15% of the previous measurement [4].

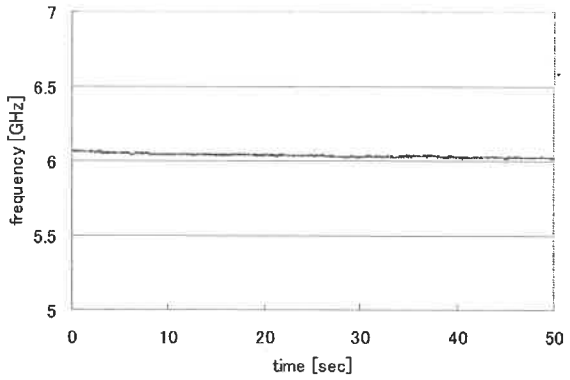

Fig.3 Result of new FSR measurement method

CONCLUSION

The new displacement measuring method with a wider measurement range and a higher accuracy is proposed. The FSR measurement is improved.

ACKNOWLEDGEMENT

The Scientific Research Fund of the Japan Society for the Promotion of Science is gratefully acknowledged. The Mitsutoyo Association for

Science and Technology (MAST), the Research Foundation for Opto-Science & Technology (RFOST) and the CASIO Science Promotion Foundation are also gratefully acknowledged.

REFERENCES

[1] International Technology Roadmap for Semiconductor: http://public.itrs.net/

[2] N. Bobroff. Recent advances in displacement measuring interferometer. Measurement Science and Technology. 1993; 4: 907-926.

[3] G. Basile, A. Bergamin, G. Cavagnero, G. Mana. Phase modulation in high-resolution optical interferometry. Metrologia. 1991; 28: 455-461.

[4] M. Ishige, F. Matsuura, M. Kawasugi, M. Aketagawa. Phase modulation Homodyne interferometer with 10-pm resolution using a tunable laser diode. International Journal of Precision Enginnering and Manufacturing. 2007; 8: 80-84.

DEVELOPMENT AND SLICING PERFORMANCE OF HIGH ACCURACY MULTI-WIRE SAW: EFFECT OF TABLE FEED ACCURACY AND THERMAL DEFORMATION OF FRAME ON SLICING ACCURACY

Yoshinori Abe[1], Tatsumi Hamasaki[1], Ken-ichi Ishikawa[2], and Hitoshi Suwabe[2]
[1]Business Incubation Office
Toyo Advanced Technologies Co., Ltd.
Hiroshima, Japan
[2]Department of Mechanical Engineering
Kanazawa Institute of Technology
Nonoichi, Ishikawa, Japan

INTRODUCTION

Requirements for greater flatness and enhanced warp accuracy of silicon wafers have reached a high level in order to respond to the highly detailed design rules that have resulted from the high integration of micro devices. Also, wafer area is steadily increasing in order to raise the yield of devices per wafer, in response to requirements for greater chip sizes and cost-cutting measures. Further, the recent multilayering of ICs is connected with generation of uniform insulating films, so that for reasons of quality, emphasis is now placed on the nanotopography of wafers [1,2].

As a result, improving the accuracy of the warp that occurs during slicing, and the nanotopography, in the slicing process is viewed as an important task because of the large influence that these have on the final quality of wafers.

The factors that affect the accuracy of slicing by a multi-wire saw employed in a slicing process include: (1) mechanical kinematic performance (including static accuracy), (2) thermal deformation in prolonged slicing (20 hours or so is required with diameter 300 mm), and (3) dynamic characteristics of the wires and uncertainty of the slurry. This report describes the measures implemented as regards (1) table feed accuracy, and (2) thermal deformation of the frame, together with their efficacy.

FEATURES AND HIGH ACCURACY TECHNOLOGY OF NEWLY DEVELOPED MACHINE

Basic specifications and features of newly developed machine

The basic specifications of the wire saw that we have newly developed are shown in Table 1, the basic structure in Figure 1, and a diagram of the wire system in Figure 2. The machine's main features are as follows:

(1) Enhanced accuracy of table feed, thanks to development of high accuracy guides
(2) Curbed thermal deformation during slicing, thanks to use of low thermal expansion materials for structural members
(3) Curbed thermal deformation, thanks to circulation of temperature-regulating coolant to each unit
(4) High-load slicing capability, thanks to 2-spindle drive, high-rigidity large-diameter wire guides
(5) High-load slicing capability, thanks to integrated-structure high-rigidity cutting head

Table 1. Basic specifications of newly developed wire saw

Item	Specfication
Workpiece maximum dimensions	305 mm dia. × 450 mm
Wire travel speed	max 15 m/sec
Wire guides (diameter × length)	350 mm dia. × 470 mm
Wire diameter	0.12 mm dia. × 0.20 mm dia.
Wire tension	max. 40 N/wire
Wire storage capacity	500km
Control system	TOYOMATIC-WS
Slurry tank capacity	240 L
Installed dimensions	W1860 × L3580 × H3000 mm
Machine weight	11 ton

Enhancement of table feed accuracy

For the table guides shown in Figure 3, the use of pressure-adding opposed V-V needle guides has long been customary practice in order to assure rigidity and high accuracy. Figure 4 shows data on table straightness in the conventional and newly developed machines. With the conventional machine, there occur undulations at pitches of 14 mm and 100 mm that result from the needle pitch and the guide installation pitch, and the full stroke straightness is 1.6 μm.

With the newly-developed machine, the difference in the needles' diameters is reduced to no more than 0.5 μm (conventionally it is 1.0 μm), and by rubbing the guide installation surfaces against each other, the flatness is raised to 1.0 μm (conventionally 5.0 μm). Via these measures, the 14 and 100 mm pitch undulations were drastically curbed and the straightness was improved to 1.1 μm.

Anti thermal deformation measures for structural members (frame)

Temperature variation of frame

To curb thermal deformation of the frame, coolant whose temperature is regulated to the ±0.2°C level is circulated through the interior. Temperature variation during slicing was measured at the points shown in Figure 5 by means of thermocouples. The slicing conditions at this time are given in Table 2. These measurements were performed on the newly developed machine, which uses low thermal expansion materials, but similar results are obtained with the regular cast steel.

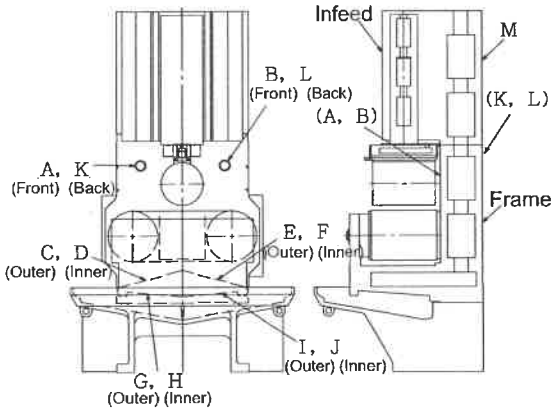

Figure 5. Temperature measurement points

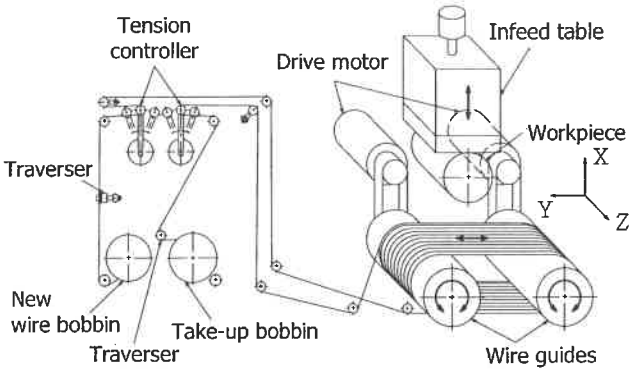

Figure 1. Basic structure of newly developed wire saw

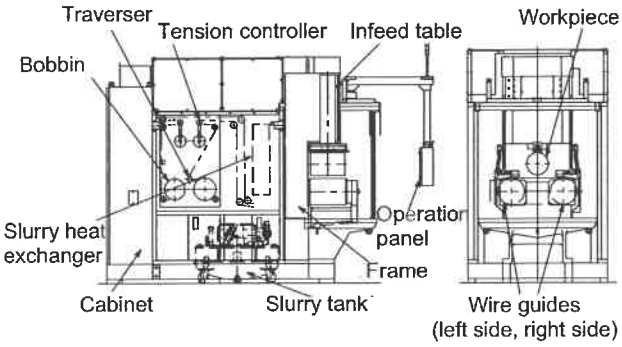

Figure 2. Wire system diagram

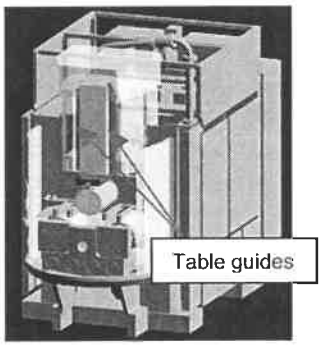

Figure 3. Table guides

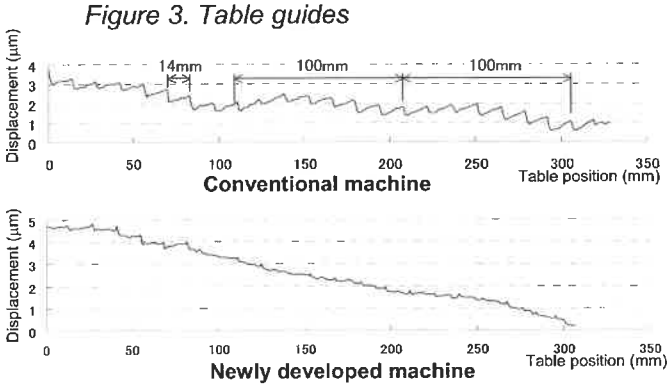

Figure 4. Table straightness (Z-direction)

The temperature variation measurement result under slicing is shown in Table 3. The frame's upper front (A, B) and bottom (C to J) are the parts where the slurry splashes, and where the temperature variation was largest, varying from 2.1 to 3.3°C. The next largest temperature variation was at the frame's upper back (K, L), where temperature varied in the range 1.3 to 1.7°C. This was due to the influence of the spindle drive motors which are installed near by. The temperature variation at the infeed section (M) was a low 0.1°C. This was because slurry does not splash at this part, and it is distant from the motors, so that there is little influence from them. That such stable results were obtained is probably due to the ambient temperature variation being 0.7°C, plus the beneficial effects of the temperature-regulated coolant.

Thermal deformation of column

It is difficult to measure the displacement between the workpiece and the wires during slicing. Accordingly, with the machine in the stopped state, we measured the relative displacement of the workpiece installation portion and the wire guides when the temperature of the coolant circulated to regulate temperature was varied. As shown in Figure 6, we measured the wire guide end portion with a displacement sensor, taking the workpiece installation portion as the reference point. The "+" displacement direction was taken to be the direction in which the workpiece emerges toward the front.

We conducted experiments using a machine that employs the regular cast steel (linear expansion coefficient 11 to 12 × 10^{-6} /°C) for the frame material, and using the newly developed machine, which employs low thermal expansion material (linear expansion coefficient 2 to 3 × 10^{-6} /°C). When the circulating coolant's temperature was raised 10°C as shown in Figure 7, displacement was around 129 μm in the + direction with the regular casting, whereas with the newly developed machine it was 36 μm. In other words, the thermal deformation characteristic is 12.9 μm /°C with the regular casting, but 3.6 μm /°C with the newly developed machine, so that the characteristic is improved by a factor of 3.

POST-COUNTERMEASURE SLICING RESULTS

Table 2. Slicing conditions

Workpiece		Silicon ingot
Workpiece dimensions		200 mm diameter ´ 150 mm
Slurry	Abrasive	GC#1000
	Dispersant	Glycol based, w ater-soluble
	Mix ratio	1 kg abrasive : 1 L dispersant
Wires	Diameter	0.16 mm diameter
	Tension	25 N/w ire
	Speed	12 m/sec
Infeed speed		460 m/min
Cycle speed		1 cycle/min
New w ire feed speed		64 m/min

Table 3 Temperature variation measurement result

Temperature(°C)

Measurement point	Lapsed time afer a processing start(H) 0	2	4	6	8	Temperature variation
Air temperature	22.4	22.3	22.5	23.0	22.4	0.7
A	25.8	25.8	24.1	24.5	26.3	2.2
B	25.4	25.4	23.9	24.3	26.0	2.1
C	24.2	22.2	22.3	22.6	25.2	3.0
D	24.5	23.2	23.4	23.5	25.9	2.7
E	24.1	22.3	22.5	22.5	25.1	2.8
F	24.2	22.4	22.5	22.6	25.3	2.9
G	23.8	22.1	22.3	22.4	25.4	3.3
H	23.4	22.2	22.3	22.4	24.7	2.5
I	23.9	22.5	22.6	22.6	25.1	2.6
J	24.1	23.1	23.0	23.0	25.2	2.2
K	26.1	27.0	27.3	27.4	27.3	1.3
L	25.5	26.7	27.0	27.3	27.2	1.7
M	25.2	25.2	25.3	25.3	25.3	0.1

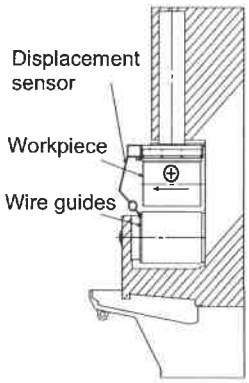

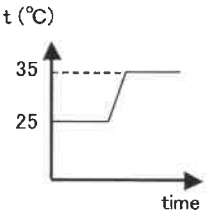

Figure 7. Temperature of coolant

Figure 6. Schematic of thermal displacement measurement

Table 4. Slicing conditions

Workpiece		Silicon ingot
Workpiece dimensions		300 mm diameter ´ 270 mm
Slurry	Abrasive	GC#1000
	Dispersant	Glycol based, w ater-soluble
	Mix ratio	1 kg abrasive : 1·L dispersant
Wires	Diameter	0.16 mm diameter
	Tension	25 N/w ire
	Speed	12 m/sec
Infeed speed		250 m/min
Cycle speed		1 cycle/min
New w ire feed speed		114m/min

The slicing result of a newly developed machine was evaluated as compared with the conventional machine. The slicing conditions are shown in Table 4. The warp accuracy of the as-cut wafer is shown in Figure 8. The warp accuracy (Warp-bf (Ave.)) of newly developed machine is 8.6 μm, a drastic improvement compared to the 15.0 μm with the conventional machine.

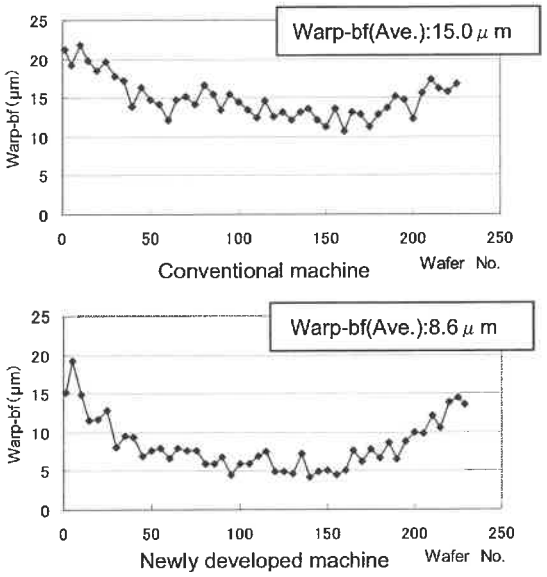

Figure 8. Slicing example (Warp-bf)

The wafer profile accuracy of the slicing direction at the ingot central part is shown in Figure 9. With the newly developed machine, the 100 mm pitch undulation component that was observed with the conventional machine is virtually eliminated.

Figure 10 shows the nanotopographies of the polished wafer surfaces sliced from 300 mm diameter workpieces using a conventional machine and the newly developed machine. The measuring instrument applies the makyo principle, and so the undulation crests and troughs of a nanometer level are portrayed in black and white. With the newly developed machine, the 100 mm pitch undulation component that was observed with the conventional machine is virtually eliminated also in the polished wafer.

CONCLUSIONS

In the development of a high accuracy wire saw capable of producing high-quality wafers, attention was focused on table straightness and frame thermal deformation, and by implementing countermeasures for these, slicing accuracy was improved.

(1) The table feed accuracy is closely connected to the warp accuracy, and by enhancing the straightness of the table guides, we improved the undulation components.

(2) We made clear the frame's thermal deformation characteristic, and by employing low thermal expansion materials, we improved the thermal deformation characteristic.

REFERENCES

[1] JEITA Semiconductor Technology Roadmap Committee of Japan: ITRS 2003 Edition, Japan Electronics and information Technology Association.

[2] Masanori YOSHISE: Measurement and Standardization of Nanotopography, J. Surface Finishing Soc. Japan Vol. 52, No. 3 (2001), pp. 40-45.

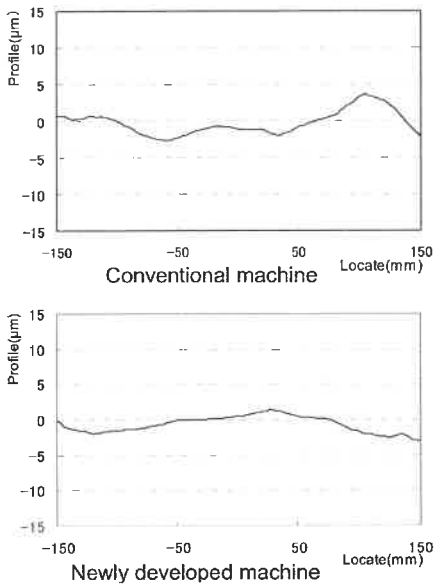

Figure 9. Slicing example (Profile)

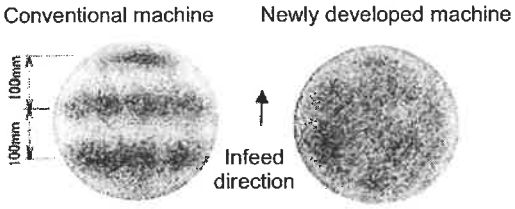

Figure 10. Slicing example (Nanotopographies)

CONCEPT FOR DISTINCTION BETWEEN THE CIRCUMFERENTIAL AND SIDEWALL EFFECTS DURING DICING OF SINGLE CRYSTAL SILICON

S. Cvetkovic and H. H. Gatzen
Institute for Microtechnology
Center for Production Technology
Leibniz Universitaet Hannover
Hanover, Lower Saxony, Germany

ABSTRACT

Dicing is a circumferential grinding process applying thin grinding wheels. Quite frequently, in Micro Electro-mechanical Systems (MEMS), the functional surface of interest generated by this process is the kerf sidewall. For a detailed understanding of the dicing process, a profound knowledge of the interactions in the contact area between the abrasive grain, the binder material, and the workpiece is required.

The cutting process may be classified into two alternative processes: outside diameter grinding performed by the wheel's circumference and surface grinding by the wheel's sidewalls. Such a separation is of particular interest when analyzing the effects occurring during the machining of a single crystal material like silicon. This paper presents a concept for distinguishing between the effect of outside diameter grinding and surface grinding by preparing the workpiece probes accordingly, to allow the wheel either to engage only at its circumference or at its sidewall. Power measurement of spindle load will enable to establish the interdependence between the cutting parameters, profile cutting, and the cutting forces.

INTRODUCTION

Dicing is a rather complex machining process combining two standard grinding processes: circumferential grinding and surface grinding. Applying these two processes with the dicing wheel, both a slicing and a precise profiling is achieved [1]. Regardless of the type of process, the dicing wheel interacts with the workpiece in two ways. For one, grinding by the wheel periphery defines the shape of the cut profile (square or rounded), and the quality of edge chipping. During grinding, the essential cutting takes place in this process, which is strongly dependent on the wheel's profile [2]. Another interaction of the dicing wheel with the workpiece is "surface" grinding by the wheel sidewall. This process primarily effects the kerf sidewall groove formation.

During abrasive grain and workpiece contact, gliding, plastic deformation, and cutting alternate. When a critical indentation depth is reached, cutting, and thus material removal take place. For this process to occur, an appropriate counterbalance of forces between the wheel and the work piece is required [3]. An important parameter for the characterization of the slicing process is the tangential force between grinding wheel and workpiece. By monitoring the spindle load, changes in the cutting condition can be detected. An approach for better understanding the dicing process parameters is investigating the interdependence of spindle load and dicing performance [4]. The complexity of the dicing process can be simplified by separating the interactions of the cutting process of wheel and workpiece in its single components. Applying such an approach, the role and amount of each single grinding effect on the total dicing result could be observed. A cutting action occurring at the dicing wheel's circumference is responsible for the circumferential grinding part, while cutting taking place at the wheel's sidewall is a surface grinding process. The latter substantially influences the kerf creation. Since circumferential as well as surface grinding occur simultaneously, it is of considerable interest to pinpoint the contribution of each individual process. This paper presents an approach in how this may be accomplished.

CONCEPT FOR DICING EFFECTS DISTINCTION

When investigating the dicing process, it is foremost necessary to understand the interactions taking place between the tool (dicing wheel) and the workpiece (monocrystal silicon). Figure 1 presents a schematic representation of the dicing process. Figure 1a depicts the process right at its start. During dicing, the grinding processes cause a stress state in the workpiece resulting in abrasive material removal; the magnitude of the stress fields is determined by the single cutting depth a_e.

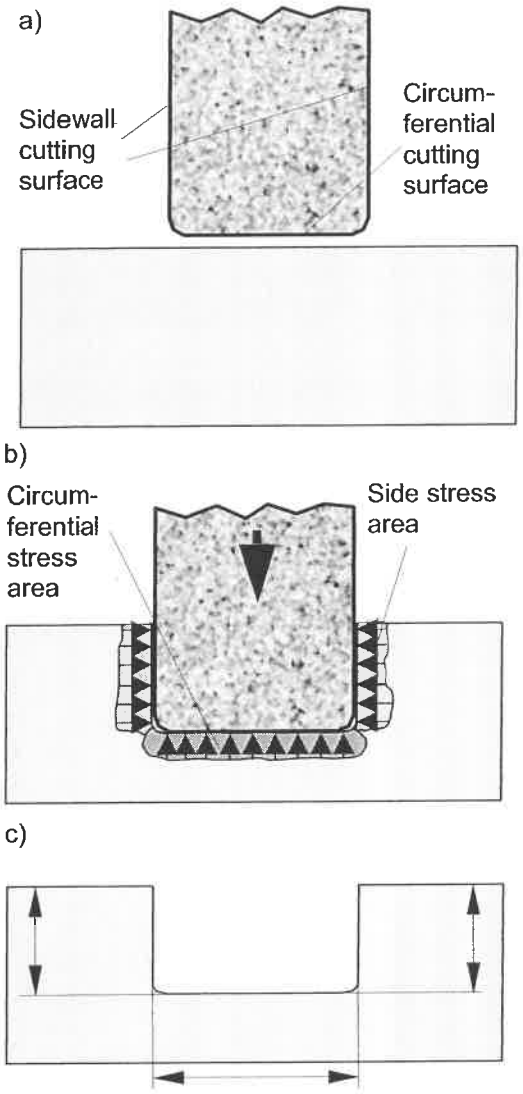

FIGURE 1. Effects of wheel topography; a) before, b) during and c) after dicing

As mentioned before, the dicing process may be considered as a combination of peripheral grinding (occurring at the dicing wheel's circumference) and surface grinding (occurring at the wheel's sidewall (Fig. 1b). The combination of both processes results in the kerf formation (Fig. 1c), again separated into the circumferential grinding area, generated by the dicing wheel's circumferential surface, and the side surface grinding area, as a result of the wheel's side wall cutting surface.
The wheel's composition at the circumferential is the same as at its sidewall. Due to the difference in cutting conditions, the wheel wear is different at the wheel's circumference and its side wall. A higher wear rate at the wheel's circumference indicates a dominance of circumferential grinding in the dicing process. To classify the respective effects, an apparent approach is to create special probes allowing either the dicing wheel's circumference to engage or the wheel's sidewall. Figure 2a presents a workpiece geometry endorsing only circumferential cutting: notching the workpiece in the area where the wheel sidewalls engage. The wheel's action is therefore restricted to circumferential cutting.

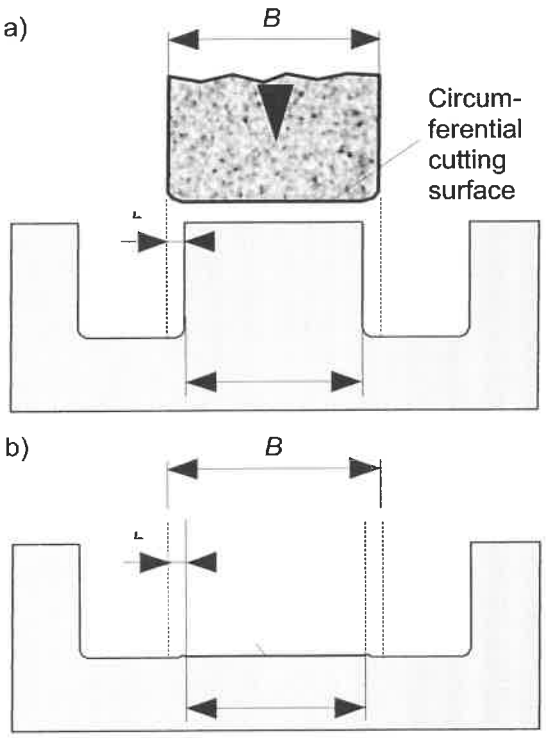

FIGURE 2. Profile for separating the front cutting area; a) before and b) after dicing

The width of the "land" area w_p was adjusted appropriately to the width of the wheel engaged in circumferential machining, and was defined as the difference between the nominal wheel width B, and edge rounding diameter b of the wheel.

$$w_p = B - b$$

The edge rounding diameter after a standard conditioning process averages 5 - 10 µm. During the machining process, only the wheel's circumference engages in the cutting action; the process does not affect the wheel's sidewalls.
Alternatively, to investigate the wheel's sidewall influence, the probe is profiled in a way, which results in a central notch slightly smaller than the wheel width (Fig. 3a). This way, circumferential cutting action is inhibited, allowing the dicing wheel to only cut in a surface grinding mode.

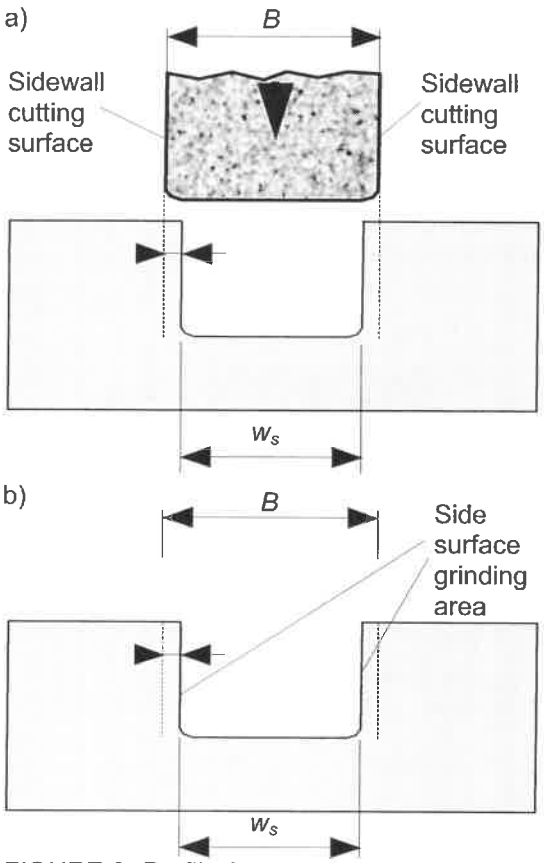

FIGURE 3. Profile for separating the side cutting area; a) before and b) after dicing

The width of the "slot" area w_s is chosen appropriately for the width of the wheel engaged in the dicing experiment in the same way as for separating the front cutting area ($w_s = w_p$). During the cutting experiment, the "real width" wheel engages at its sidewalls, widening the groove by means of surface grinding (Fig. 3b).

EXPERIMENTAL

Investigations presented in this work were carried out with a resin bonded dicing wheel for cutting monocrystalline Si wafers (Fig. 4). The wheel widths were 100 µm and 200 µm, respectively, with a diamond grit size of 5 µm. All wheels are trued and conditioned featuring a square U-shaped profile with an edge rounding less than 10 µm. Dicing was done on a DAC551 dicing machine with a positional accuracy of 0.2 µm; the machine was located in an air conditioned room.

Since monocrystalline Si is a commonly used wafer material for MEMS, achieving a better cutting quality during its separation is a very important research topic. Its high brittleness make it a perfect example for the investigation of kerf sidewall effects.

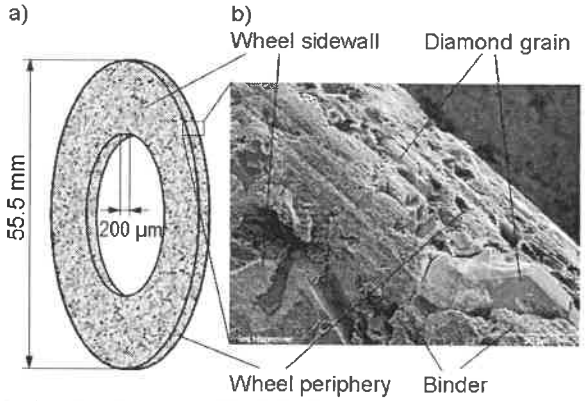

FIGURE 4. Resin dicing wheel; a) body structure and b) topography

By varying the feed rate, the effects of single grinding processes on the cut quality could be pinpointed. The transition was observed by analyzing edge chipping as well as the sidewall condition. For the fabrication of profiles for separating the effects, the silicon chips were sliced. These chips feature a footprint of 6 mm x 6 mm. The profiles are fabricated along each chip for a wheel width of 100 µm and 200 µm, respectively (Fig. 5).

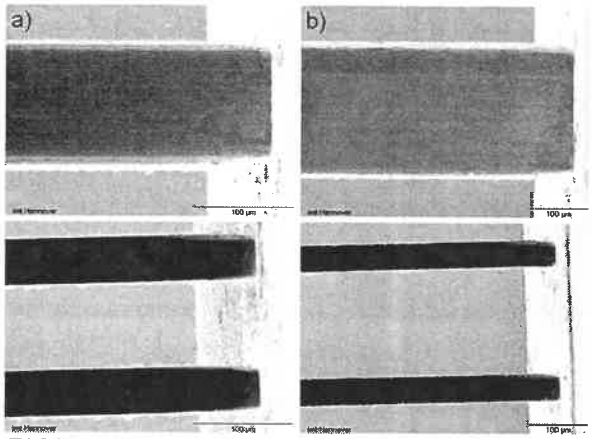

FIGURE 5. SEM micrograph of profiled structures for a) 100 µm and b) 200 µm wheel width

The width of the "land" area w_p for experiments with the 100 µm wheel was determined to be 80 µm, the same applies to the "slot" area w_s. The width of the "land" area and the "slot" area for the 200 µm wheel was analogically specified to be 180 µm. The profile height (cutting depth) was in all cases 400 µm.

For spindle load measurements, a power measurement system was used. To overcome

the substantial limitations of commercially available systems, an own system was developed and integrated in the dicing machine. The measurement principle is to simultaneously determine the power on all three phases driving the spindle motor.

RESULTS

Power is work (or energy) over time:

$$P = \frac{W}{t} \qquad (1)$$

P is power, W is work, and t is time.
The relationship between work and force is

$$W = F * s, \qquad (2)$$

where F is the force and s is the displacement of the object. Combining (1) and (2) results in a relationship between power P, force F, velocity v:

$$P = \frac{F * s}{t} = F * v \qquad (3)$$

The total velocity v is a total vector sum of cutting speed v_c and feed rate v_f.

$$v = \sqrt{v_c^2 + v_f^2} \qquad (4)$$

From this approach, an equation for the force F as a function of the two velocities dominating cutting is derived:

$$F = \frac{P}{\sqrt{v_c^2 + v_f^2}} \qquad (5)$$

For a dicing wheel with a diameter of 55.5 µm and a rotational velocity of 30,000 min^{-1}, the cutting speed v_c averages 87.2 m/s. Using the calculation shown above plus measured power data, the circumferential cutting force and the sidewall cutting force may be derived. This is due to the fact that the spindle of a dicing machine hardly exhibits and friction. To compare the force data after cuts in profiles, cuts in basic material under the same dicing conditions were made and the total cutting force was evaluated. To determine the real force contribution for a wheel cutting at the circumference, at its sidewall, or doing a full cut, force measurements were conducted. Table 1 outlines the results.
Table 2 provides a comparison between the accumulation forces at the circumferential and the sidewall cut component compared to a full cut. In most cases, there is a rather good match between the total of the cuts and the cuts separating circumferential and sidewall effects and the equivalent full cut of a dicing wheel.

TABLE 1. Force measurement results [N]

Wheel width [µm] \ Feed rate [m/s]		0.001	0.005	0.01
Circumferential cut	100	0.970	0.935	0.925
	200	1.040	1.020	1.000
Sidewall cut	100	0.960	0.940	0.900
	200	1.030	0.970	0.960
Idle running	100	0.950	0.915	0.880
	200	1.006	0.960	0.913
Total cut	100	0.980	0.960	0.930
	200	1.045	1.035	1.021

TABLE 2. Forces comparing [N]

Wheel width	100 µm			200 µm		
Feed rate v_f [m/s]	0.001	0.005	0.010	0.001	0.005	0.010
Circumferential+Sidewall force	0.021	0.045	0.065	0.058	0.070	0.134
Total cutting force	0.030	0.045	0.050	0.039	0.075	0.108

CONCLUSIONS

A new technique of analysing the cutting behaviour of a dicing wheel is based on separating the circumferential and sidewall forces by appropriated preparing test workpieces. Power measurements allow to divide the cutting force for the various cutting modes. The tests allow to separate the forces caused by circumferential and sidewall cutting and to comparate them to those occurring at a full cut.

REFERENCES

[1] Juin, H H, et. al. Effect of Laminated Wafer Toward Dicing Process and Alternative Double Pass Sawing Method to Reduce Chipping. IEEE Trans. 29 (1), 2006; 17-24.

[2] Gatzen, H H, et. al. Chipping Minimization during Dicing and Slicing. Proc. ASPE 17th Ann. Meet., St. Louis, 2002; 551-556.

[3] Gatzen, H H, et. al. Kerf Sidewall Groove Formation during Ductile Dicing of Ceramic Materials. Proc. ASPE 20th Ann. Meet. Norfolk, 2005; 387-390.

[4] Gatzen, H H, et. al. Investigations Regarding the Interdependence of Spindle Load and Machine Performance During Slicing. Proc. ASPE 18th Ann. Meet., Portland, 2003; 435-438

USE OF VARYING WORK-PIECE DISTANCE TO STUDY THE EFFECTS ON MACHINE STIFFNESS IN PLUNGE GRINDING

Theodore R Deakyne[1], Eric R. Marsh[1]
[1]Machine Dynamics Research Laboratory
The Pennsylvania State University
21 Reber Building, University Park, PA 16802, USA

ABSTRACT
This work explores the role of grinding machine structural loop stiffness on workpiece quality and the normal grinding forces. A long ductile workpiece made of steel uses three flanges at different lengths from the spindle's centerline to vary the structural loop stiffness during a cylindrical plunge grind. Specifically, the loop stiffness and grinding parameters (e.g., feeds and speeds) are mapped to the measured normal grinding forces, actual depth of cut, workpiece form and surface finish.

INTRODUCTION
There are many variables in the grinding process that can affect the quality of the finished workpiece. For these experiments only a small subset are considered, the most important one being the machine stiffness. The others are programmed depth of cut, infeed rates, and the rotational speed of the workpiece.

Many machine designers and researchers have examined both the dynamic and static stiffness of precision grinding machines, such as static stiffness with brittle materials [1, 2]. Also having spindle speeds at a system's natural frequency may be useful, since dynamic stiffness is lower at that frequency and can therefore be more tolerant to force variations [3].

Accepted practice in machine designing is to make the stiffness as high as possible. High machine stiffness does reduce the displacement variations from the normal grinding forces as seen here but also results in larger more costly machines. The future in machining seems to be starting to center around micro machining. Larger obsolete expensive machines are being replace with machines a quarter of the size, in which case reduced stiffness is acceptable as long as part tolerances can be held. To examine stiffness, tests are run on variable stiffness machines such as the one found here.

The tangential and normal grinding forces are found to increase as a result of increasing stiffness. The increase in programmed infeed rates also increase the grinding forces while lower stiffness at increased infeeds result in less material removal.

EXPERIMENTAL SETUP
The experimental setup features a Moore No. 3 machine base retro fitted with a Bosch controller and two Professional Instrument air bearing spindles as shown in Figure 1.

A model for the instrumented 4R was used for the real time grinding force calculations based on previous work with a similar type of setup [4, 5].

The benefits of having the embedded probes is that they allow the true affects of the structural loop machine stiffness to be examined on the grinding process, unlike other setups that use a measurement device built into the structural loop of the machine. These devices are not infinitely stiff and affect the structural loop.

The work spindle is a 4R twin mount, composed of a 4R air bearing spindle with DC frameless, brushless motor and mounted with a 10in 38A80-F12VBEP grinding wheel, which helped to reduce chatter during testing.

MODELING
A model was created of the workpiece and instrumented spindle with DC brushless motor rotor attached as shown in Figure 2.

The equations of motion (EOM) that describe this two degree of freedom system acquired from the model are:

$$m\ddot{x} + k_r x - k_r l_1 \theta = f \quad (1)$$

$$J\ddot{\theta} - k_r l_1 x + (k_r l_1^2 + k_t)\theta = f l_2 \quad (2)$$

To compare the output deflections of the theoretical model to that of the measured accelerometer data located at the end of the workpiece,

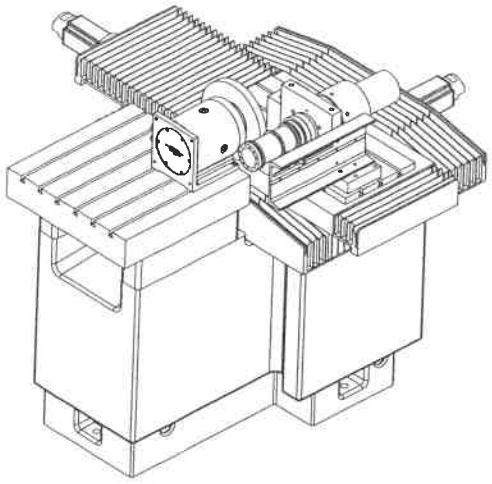

FIGURE 1. The CNC precision grinding machine with 10in grinding wheel and variable length workpiece spindles.

the Laplace transform of the EOM was taken and substituted into the equation:

$$Y(s) = X(s) + l_3\Theta(s) \tag{3}$$

The transfer function to this model becomes:

$$\frac{Y(s)}{F(s)} = \frac{(J + l_2 l_3)^2 * s^2 + (l_1 + l_2)(l_1 + l_3)k_r + k_t}{mJs^4 + (k_r J + (l_1^2 k_r + k_t)m)s^2 + k_r k_t} \tag{4}$$

The inverse of the Laplace is taken by replacing $s = i\omega$ and damping is added by assuming it is proportional to the mass and stiffness matrices.

For the static case the ω is set to zero and the static stiffness becomes:

$$K_{static} = \frac{k_r k_t}{(l_1 + l_2)(l_1 + l_3)k_r + k_t} \tag{5}$$

where k_r and k_t are the radial and tilt stiffness of the 4R, l_1 is from the center of mass (COM) to the spring locations, l_3 is the length from the COM to the accelerometer, and l_2 is the length from the COM to the input force located at one of the flanges. The stiffness of the machine decreases the further away the flange get from the centerline, ranging from 1.34E7, 0.98E7, and 0.63E7 N/m.

The dynamics of the system are examined by the frequency response functions using the equation of the transfer function and are also compared to measured data through modal analysis using a impulse hammer and the accelerometer. The results were recorded with a siglab unit processed

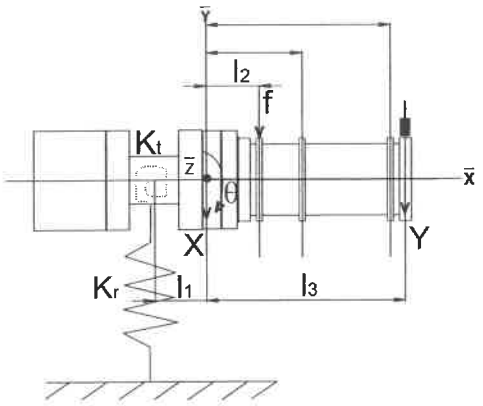

FIGURE 2. The model of the combined workpiece was created in SOLIDWORKS and is shown above. It includes the front/back adaptor plates, and the rotor of both the 4R air bearing spindle and the motor used to drive the spindle.

in MATLAB and shown in Figure 3. The dynamic stiffness is lower at the resonance peaks.

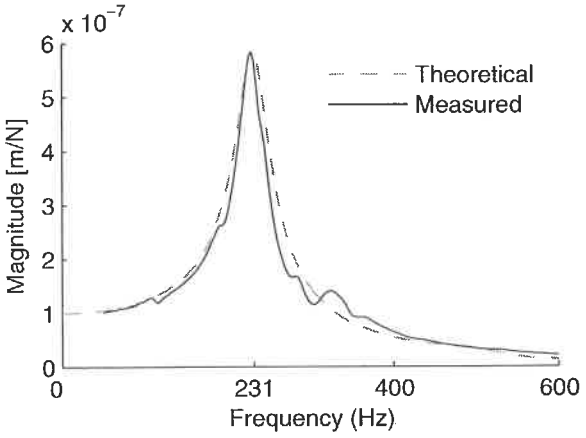

FIGURE 3. Frequency Response function(FRF) of magnitude vs. frequency comparing the measured data with solid lines to the theoretically calculated using dotted lines for flange 1.

EXPERIMENTAL TESTING AND RESULTS

Multiple tests were run varying the workpiece speed, infeed rate of cut and structural loop stiffness and measuring the grinding forces and material removed from the part. Table 1 shows all of the parameters used for the grinding tests [6].

Figure 4 shows the normal grinding force results varying workpiece speed and machine stiffness while holding the feed rate at 50 $\mu m/min$. At minimum speed while varying stiffness and at maximum stiffness while varying the speed the normal grinding force was not effected. At higher work-

TABLE 1. System Parameters set by user

Parameter	Value
Workpiece Velocity	150,200,300,&600 RPM
Wheel Velocity	1,910 RPM (5000 sf)
Coolant	Blasocut BC40SW
Dressing Depth	0.01 mm
Dressing Feedrate	177.8 mm/min
Depth of Cut	constant 0.01 mm
Spark out	0 s
Plunge infeed Rate	12.5, 25, & 50 $\mu m/min$
Length	0.375,2.675,&5.875 in

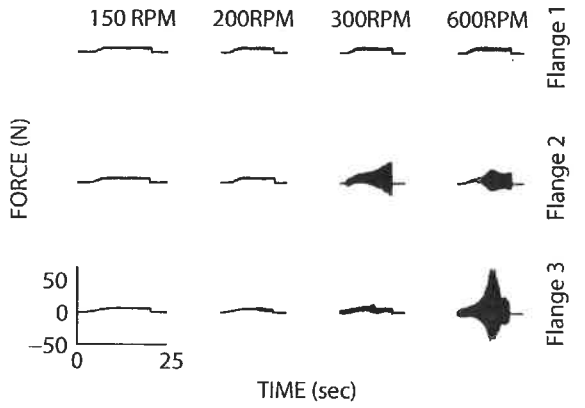

FIGURE 4. Comparing the normal grinding forces for twelve data sets varying the workpiece spindle speed and the machine stiffness at a feed rate of 50 $\mu m/min$.

piece speeds and lower stiffness chatter results and transfers to the part in the form of lobes.

Very similar results were obtained at both 25 $\mu m/min$ and 12.5 $\mu m/min$ for the force data. The only difference being a decrease in the magnitude of chatter formation.

In Figure 5 a close up of the previous force data excluding the third and fourth column set. The normal grinding force for flange 1 and 2 are the same. At flange 3 the normal grinding force has a lower growth rate as seen by the slope and lower steady state force implying there is a critical machine stiffness that until this value is reached will not impact the grinding process.

In Figure 6 a close up of the material removed off the outer diameter of each of the flanges at a feedrate of 50 $\mu m/min$ laid over the table motion

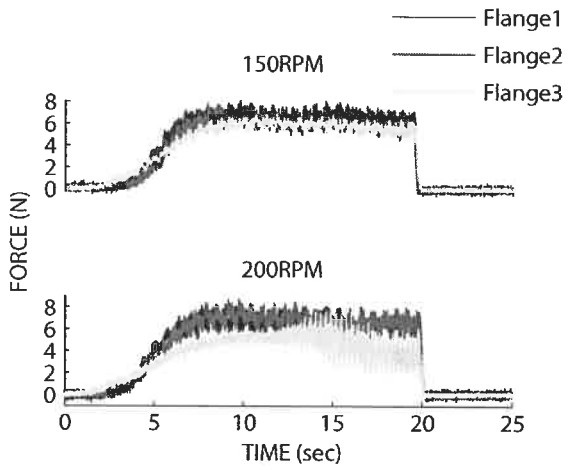

FIGURE 5. Close up of the first two columns of the normal grinding force data.

with the part as it is feed into the wheel. As can be seen in the figure the material removed from the part lags the infeed motion of the table. As a result there is an offset at the end of the grind between the actual depth of cut and programmed depth of cut from the table. As the feed rate was decreased this time lag between the part and table motion was reduced resulting in a closer tolerance part.

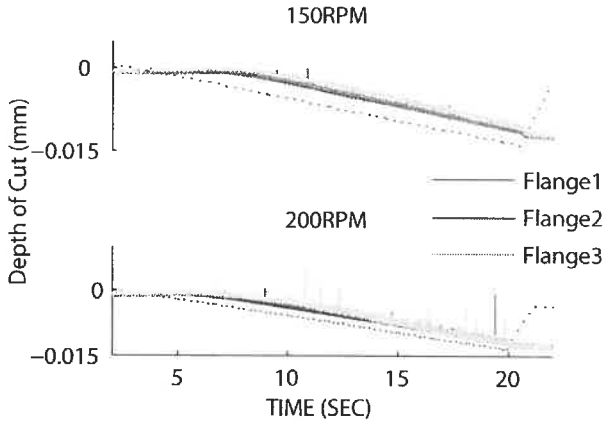

FIGURE 6. Shows the material removed from the workpiece (solid lines) overlaid with the table infeed (dotted line).

In Figure 7 a linear relationship between the steady state grinding force and the feedrate of the table with part into the wheel at a workpiece speed of 150 RPM is shown. Increasing the workpiece speed to 600 RPM did not effect this relationship.

Figure 8 shows the normal grinding force, part

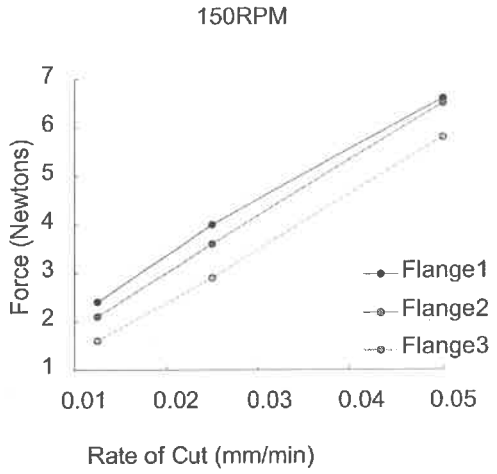

FIGURE 7. Shows the steady state grinding force vs. programmed infeed rate of the machine.

removal, and table motion. As can be seen in the plot material removal of the part does not occur until steady state normal grinding forces are reached.

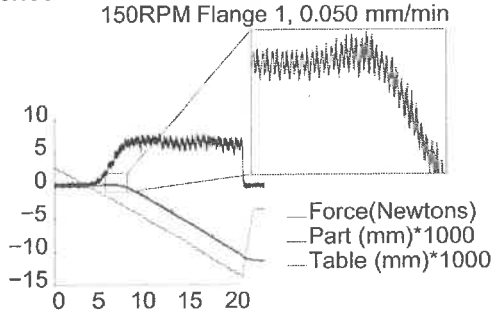

FIGURE 8. A typically grind plot of the cylindrical plunge grind process showing the normal grinding force, material removed from part and the table infeed.

CONCLUSIONS

In this work the relationship of effective machine stiffness on the grinding forces, workpiece form, and the actual depth of cut into the workpiece for a cylindrical plunge grind process is investigated. An instrumented spindle with embedded capacitance probes measured the grinding forces while a special workpiece is used to vary the effective stiffness of the structural grinding loop. A mathematical model was used to develop the spindle and workpiece setup which is compared to modal analysis experiments using MATLAB. The true beauties of the spindle and workpiece is shown as the ability to measure in-process grinding forces without adding other components such as a dynomometer. Added components such as a dynomometer is not infinitely stiff nor petite in size which would add unwanted side effects in the force measurements. The second beauty is varying the stiffness with the workpiece but without changing the natural frequencies of the system. This allows the true dynamics of the grinding process to be test, while simplifying the testing procedures.

It was shown that the steady state normal force measurements varies linearly with the feedrate. Also the cylindrical plunge grinding process is susceptible to chatter at combinations of work speed and effective spindle stiffness. Chatter leads to an unstable process which lead to deterioration of the tolerances of a part as seen by the large displacements in the part data. However, at the spindle speed of 150 RPM no matter what the effective spindle stiffness value did not result in chatter. Also at the stiffest effective stiffness no matter the velocity of the workpiece chatter did not occur. Using this information one can design a grinding machine to increase production time, save cost and be smaller in size, but if the machine is already built one may be able to save defective parts due to chatter by slowing down the workpiece speed.

REFERENCES

[1] Zhang J, Wang F, Yang Z, Zhu. The effect of machine stiffness on grinding of silicon nitride. International Journal of Machine Tools and Manufacture. 1998;39(1-2):1263–1283.

[2] Furukawa Y, Lee HS. Determination Method of Grinding Machine Stiffness. Japan Society of Precision Engineering. 1984;(5):516 – 521.

[3] Jenkins H, T K. Dynamic Stiffness Implications for Multiaxis Grinding System. Journal of Vibration and Control. 1997;3(5):297–313.

[4] Couey JA. Precision Grinding with Real-Time Force Feedback from an Instrumented Spindle. The Pennsylvania State University; 2004.

[5] Knapp BR. On the Use of and Instrumented Spindle to Determine the Effects of Machine Stiffness in Grinding Brittle Materials. The Pennsylvania State University; 2002.

[6] Krar FS. Grinding Technology. 2nd ed. Delmar Publishers Inc; 1995.

INVESTIGATION ON HIGH DEPTH OF CUT OF ULTRA-SMOOTHNESS GRINDING OF Al_2O_3-TiC CERAMIC

Yuki YAMAMOTO[1], Heiji YASUI[1], Yusuke TANAKA[1], Ryushiro SAKAMOTO[1], Kiyoshi MATSUDA[1], Takuro YOSHIMURA[1] and Kensuke MIYAMOTO[1]
[1]Graduate School of Science and Technology, Kumamoto University Kumamoto city, JAPAN

INTRODUCTION

With the increase of demand of high quality components, the ultra-smoothness grinding technique of fine ceramics with high productivity has been strongly required. In our previous research [1], the ultra-smoothness grinding method based on the new concept is devised. Using the new method, the grinding characteristics of some materials with horizontal grinder are examined [1-3]. From the results, the surface roughness of cemented carbide, glass and some fine ceramics formed by using coarse grain size of #140 diamond wheel is ascertained to attain below 50nm (R_z) in three dimensional measuring of 256 micro-meters square. Furthermore, to improve the productivity, the influence of high wheel depth of cut up to 1mm on ultra-smoothness grinding is examined by grinding of hot pressed silicon carbide ceramics (HPSC) and glass. It is found from the results that the surface roughness attains below 60 nm for HPSC ceramic ground at the high depth of cut of 1 mm [2]. As ultra-smoothness surface can be obtained by grinding the workpiece at the high depth of cut, machining time until finishing can be shortened effectively.

The present research is extended to the investigation on the ultra-smoothness grinding characteristics of Al_2O_3-TiC ceramic in high depth of cut.

ULTRA-SMOOTHNESS GRINDING METHOD

The schematic diagram of ultra-smoothness grinding method is shown in Fig.1. First of all, in the method, the contact width of workpiece-wheel is ground by feeding the workpiece toward the direction normal to grinding direction. The normal feed per a wheel revolution, f_{Gn}, must be smaller than the wear width of cutting edge normal to grinding direction. Secondly, the workpiece is slightly step-fed a small length, f_p, toward the direction parallel to grinding direction. The parallel step-feed, f_p, however, is determined so that the geometrical surface

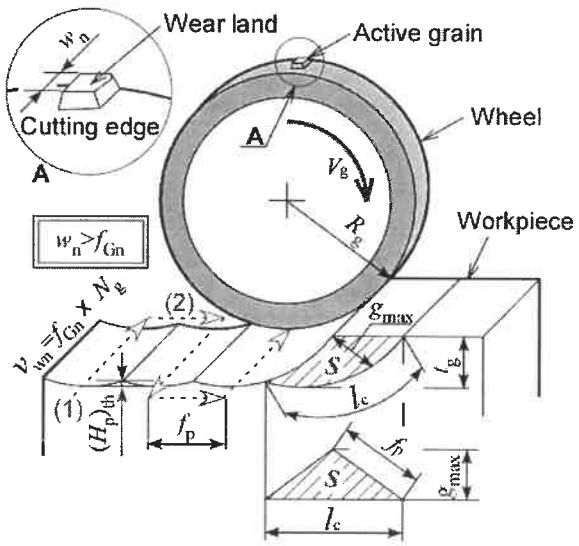

FIGURE 1 Schematic diagram of developed ultra-smoothness grinding method

roughness, H_p, which is formed by overlapping the cross-section of two wheel circles before and after step-feeding becomes smoother than the required surface roughness. After the parallel step-feed, thirdly, the workpiece-wheel contact width is ground again by feeding reversely the workpiece toward the direction normal to grinding direction. The whole surface of workpiece is finished with repeating such grinding procedure. In the newly developed ultra-smoothness grinding method, however, the depth of cut has no influence on the geometrical surface roughness.

EXPERIMENTS

The experiments are done with NC grinder as shown in Fig.2. The grinder attaches the air spindle and has accuracy of 0.1 micro-meters for each movement of X, Y and Z directions.

The main experimental conditions are listed in Table 1. The depth of cut, t_g, ranges from 5 micro-meters to 1000 micro-meters. The grain size and concentration of metal bonded grinding wheel used is #140 and 50. The workpiece and grinding fluid used are Al_2O_3-TiC ceramic and

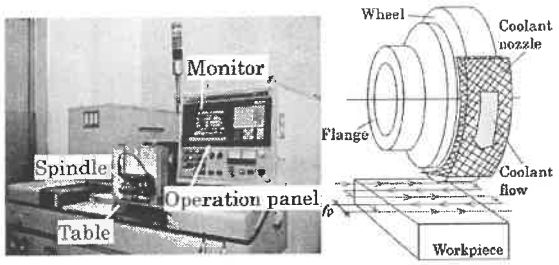

FIGURE 2 Appearance of experimental system

TABLE 1 Experimental conditions

Workpiece	Al_2O_3-TiC ceramic SiC ceramic
Wheel	SD140Q50M
Wheel speed Depth of cut Normal feed Normal table speed Parallel step feed	V_g : 12 m/s t_g : 5 - 1000 μm f_{Gn} : 10 μm/rev v_{wn}: 0.38mm/s f_p : 10 μm / pass
Grinding fluid	Type : Soluble type Dilution :1 / 10

soluble type. The workpiece surface and its surface roughness are observed with Nomarski microscope and SEM, and with surface interferometer (WYKO TOPO-3D) and AFM, respectively. The grinding force is measured by octagonal elastic ring.

RESULTS AND DISCUSSION

Figure 3 shows the Al_2O_3-TiC ceramic surface ground at the depth of cut of 5 micro-meters to 1000 micro-meters. Up to the depth of cut of 30 micro-meters, from the results, brittle mode of grinding cracks can not be observed clearly on the ground surface. It is cleared possible to obtain the high quality of ductile grinding mode of Al_2O_3-TiC ceramic surface by the ultra-smoothness grinding method using coarse wheel of #140 grain size. At the depth of cut of 300 micro-meters, on the contrary, a few brittle grinding cracks observed as the part of dark gray color occurs on the ground surface. At the depth of cut of 1000 micro-meters, brittle grinding cracks observed as the part of black color are found clearly on the ground surface. It is referred that the grinding crack begins to occur at a critical depth of cut and increases with the increase of depth of cut in the region over the critical depth of cut. However the grinding crack is considered to occur by the defection of the part of Al_2O_3 from the surface.

Figure 4 shows the surface roughness of Al_2O_3-TiC ceramic surface ground at the depth of cuts of 30 micro-meters and 1000 micro-meters

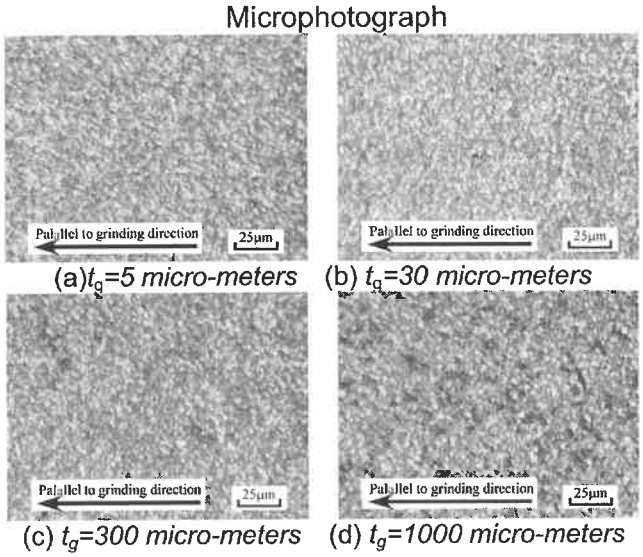

FIGURE 3 Influence of depth of cut on the ground Al_2O_3-TiC ceramic surfaces
[Al_2O_3-TiC, SD140Q50M, V_g=12m/s, f_{Gn}=10micro-meter/rev, f_p=10micro-meters/pass, Soluble type (1/10)]

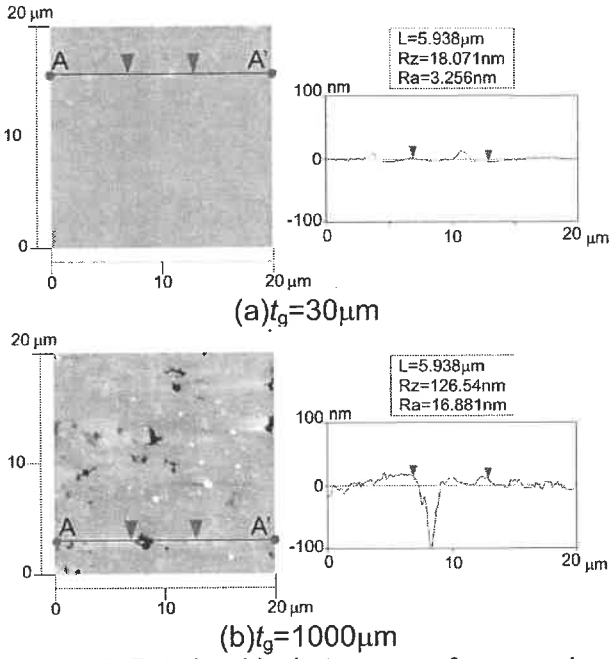

FIGURE 4 Relationship between surface roughness and depth of cut
[Al_2O_3-TiC, SD140Q50M, V_g=12m/s, f_{Gn}=10micro-meter/rev, f_p=10micro-meters/pass, Soluble type (1/10)]

measuring with AFM. The measuring area is 20 micro-meters square. In the case of the depth of cut of 30 micro-meters, from the figure, the grinding cracks can not be measured on the ground surface though the projection of about 20nm is found. The surface is ultra-smooth and its roughness is about 20 nm (Rz) or 3 nm (Ra).

In the case of the depth of cut of 1000 micro-meters, on the other hand, a few grinding cracks are measured. The crack is smaller than 3 micro-meters in the diameter and 130nm in the depth. Accordingly the surface roughness at the depth of 1000 micro-meters is referred smooth though the grinding crack occurs.

Figure 5 shows the surface roughness of Al_2O_3-TiC ceramic surface ground by the ultra-smoothness grinding method at the depth of cut of 5 micro-meters to 1000 micro-meters measuring with WYKO. In the measurement, the measuring accuracy in the longitudinal and latitudinal directions, however, is about 1 micro-meter. Thus the grinding cracks as mentioned above, which are measured in detailed with AFM are measured difficult. At the depth of cut of 5 micro-meters, the three dimensional surface roughness $(H_r)_{3D}$ attains 35.2 nm (R_z) or 1.64 nm (R_a). The surface is ultra-smooth near that obtained by lapping or polishing. The two dimensional surface roughness normal and parallel to grinding direction are H_{rn}=21.1 nm (R_z) and H_{rp}=20.3 nm (R_z), respectively. The average surface roughness in both directions is about 3.5 nm (R_a). The surface roughness in both directions is almost the same. The height of grooves formed by grinding becomes considerably low.

At the depth of cut of 30 micro-meters, the three dimensional surface roughness is about 43nm (R_z). The surface being finished to the surface roughness below 50 nm (R_z) is similar level with lapping or polishing surface. At the depth of cut of 300 micro-meters, the three dimensional surface roughness becomes rougher than that at the depth of cut of 30 micro-meters and is about 68 nm (Rz). At the highest depth of cut of 1000 micro-meters done in the experiment, the three dimensional surface roughness $(H_r)_{3D}$ becomes 86.1 nm (R_z) or 3.75 nm (R_a). However in the case of the depth of cut of 300 micro-meters, the two dimensional surface roughnesses parallel and normal to grinding direction are H_{rp}=19.3 nm (R_z) and H_{rn}=47.6 nm (R_z), respectively. And also, in the case of the depth of cut of 1000 micro-meters, those are H_{rp}=24.7 nm (R_z) and H_m=64.8 nm (R_z) , respectively. The normal surface roughness is much rougher than the parallel surface roughness. In the obtained surface roughness, as mentioned above, the depth of concave formed by the occurrence of grinding cracks is partially excluded because the measuring accuracy is rough. Thus the difference between the normal surface roughness and the parallel surface roughness is considered to be dependent on the measuring place. Namely the actual surface roughness including the concave of grinding cracks at the depth of cuts of 300 micro-meters and 1000 micro-meters is considered somewhat rougher than those measured by WYKO.

Figure 6 shows the relationship between the three dimensional surface roughness and the depth of cut. For the reference, the surface roughness of silicon carbide formed at the same

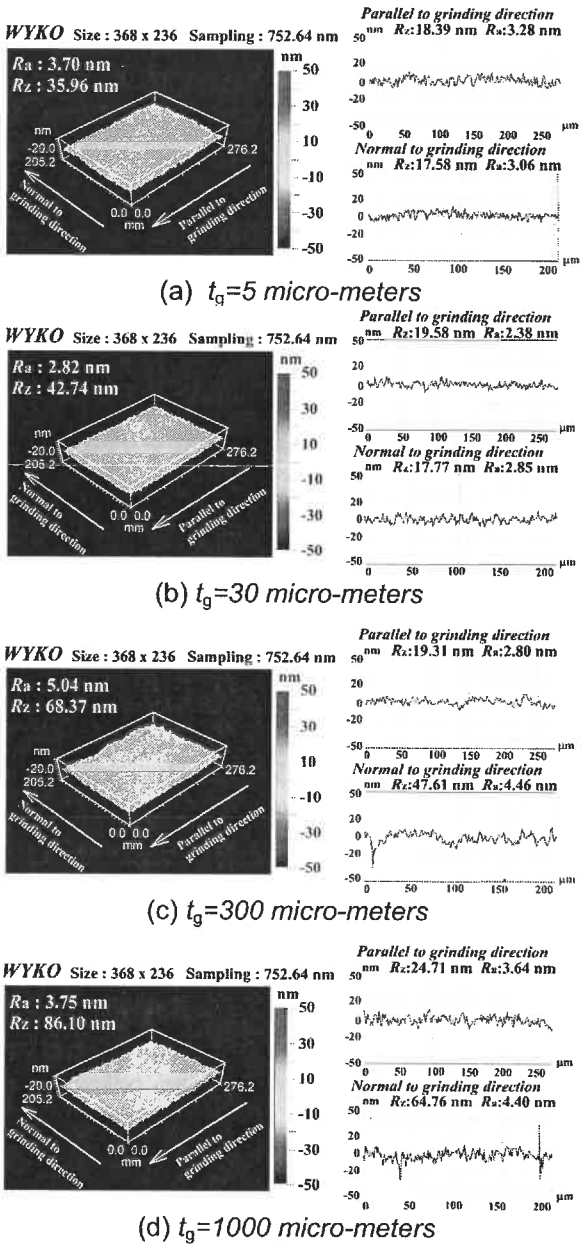
WYKO Size : 368 x 236 Sampling : 752.64 nm
Ra : 3.70 nm
Rz : 35.96 nm
Parallel to grinding direction
Rz:18.39 nm Ra:3.28 nm
Normal to grinding direction
Rz:17.58 nm Ra:3.06 nm
(a) t_g=5 micro-meters
Ra : 2.82 nm
Rz : 42.74 nm
Rz:19.58 nm Ra:2.38 nm
Rz:17.77 nm Ra:2.85 nm
(b) t_g=30 micro-meters
Ra : 5.04 nm
Rz : 68.37 nm
Rz:19.31 nm Ra:2.80 nm
Rz:47.61 nm Ra:4.46 nm
(c) t_g=300 micro-meters
Ra : 3.75 nm
Rz : 86.10 nm
Rz:24.71 nm Ra:3.64 nm
Rz:64.76 nm Ra:4.40 nm
(d) t_g=1000 micro-meters

FIGURE 5 Influence of depth of cut on the ground Al_2O_3-TiC ceramic surfaces roughness [Al_2O_3-TiC, SD140Q50M, V_g=12m/s, f_{Gn}=10micro-meter/rev, f_p=10micro-meters/pass, Soluble type (1/10)]

grinding conditions is shown in the figure. The surface roughness of both ceramics increases as depth of cut increases. The surface roughness of Al_2O_3-TiC ceramic is larger in the range of whole depth of cut than SiC ceramic. Particularly the difference becomes remarkable at the low depth of cut below 10 micro-meters. At the depth of cut 5 micro-meters, the surface roughness of Al_2O_3-TiC ceramic is about 35 nm (Rz). On the other hand that of SiC ceramic is about 20nm (Rz). It is referred that the SiC ceramic can be finished easily to ultra-smoothness surface.

At the high depth of cut of 1000 micro-meters, on the contrary, the surface roughness of Al_2O_3-TiC ceramic and SiC ceramic are about 87 nm (Rz) and 58 nm (Rz). Both surface roughnesses are below 100 nm (Rz). Accordingly the workpiece of large allowance can be finished efficiently to ultra-smoothness surface by high depth of cut grinding.

Figure 7 shows the relationship between the grinding force and the depth of cut. The grinding force increases as depth of cut increases. At the highest depth of cut of 1000 micro-meters, the both of normal and tangential grinding forceses are below 5N/mm. The small grinding force is considered to influence effectively on the formation of ultra-smoothness surface.

From the results as mentioned above, the ultra-smoothness grinding method in which the surface roughness at even the depth of cut of 1000 micro-meters is below 100 nm (Rz) is referred useful for grinding of Al_2O_3-TiC ceramic with high smoothness and high removal rate.

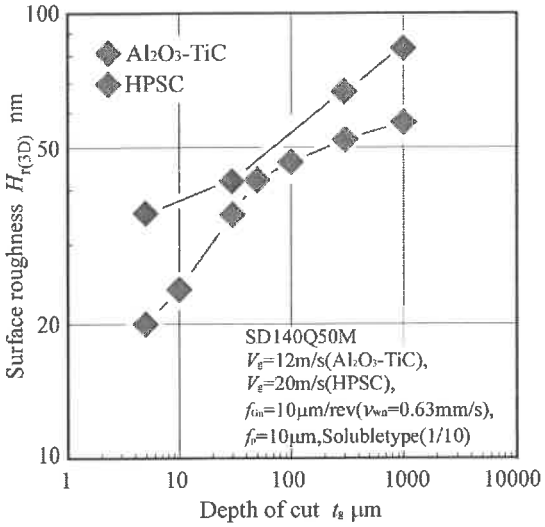

FIGURE 6 Relationship between surface roughness and depth of cut

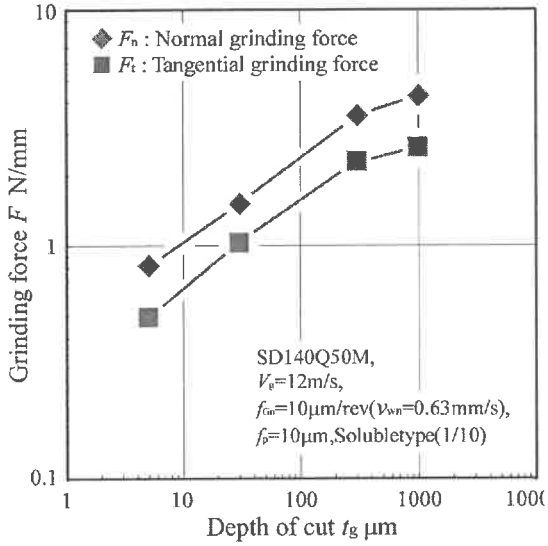

FIGURE 7 Relationship between grinding force and depth of cut

SUMMARY

The main results obtained are as followed;

[1] The high depth of cut of grinding by the new method is ascertained to be possible for the ultra-smoothness grinding of Al_2O_3-TiC ceramic.

[2] The surface roughness becomes larger for higher depth of cut.

[3] The brittle node of grinding cracks occur rarely up to the depth of cut of 30 micro-meters at least.

[4] The three dimensional surface roughness of Al_2O_3-TiC ceramic formed at the depth of cut of 5 micro-meters and 1000 micro-meters are 35.2 nm (R_z) 85.2 nm.

ACKNOWLEDGEMENT

The authors would like to thank Noritake Super Abrasive Industries Co. Ltd., Yushiro Chemical Industry Co. Ltd., and Nippon Tungsten Co. Ltd. for providing grinding wheels, grinding fluids and workpiece materials.

REFERENCES

[1] Heiji YASUI: Development of Polishingless Ultra-Smoothness Grinding Method (1st Report) ,J.Japan Society for Precision Eng., Vol.69 ,No.12,(2003)pp1713-1717

[2] Heiji YASUI et al. : Investigation on High Depth of Cut of Ultra-smoothness Grinding of a Glass by Means of Newly Developed Grinding Method, Proc. 6th euspen int. conf. (2006) pp.84-87.

[3] Heiji YASUI et al. : Ultra-smoothness Grinding of Silicon Carbide in Depth of Cut of 1mm, Proc. 5th euspen int. conf. (2005) pp. 599-602.

SELECTION OF OPTIMAL MACHINING PARAMETERS IN DIAMOND CORE DRILLING PROCESSES

Kwan-Woo Yoon and Sung-Chong Chung*
Hybrid System Design & Control LABoratory
Department of Mechanical Engineering
Hanyang University, Sungdong-Gu, Seoul 133-791, KOREA

ABSTRACT

Diamond core drills are applied to cut difficult-to-drill materials This paper intends to propose basic understanding of ceramic drilling mechanics and to enable selection of optimal machining parameters affecting tool life, material removal rate (MRR) and hole quality. In contrast to normal metal cut drilling, core drilling processes make deep grooves for removal of machining materials. One of difficulties of the core drilling process is the evacuation of chips form the drilled groove. As the drilling depth increases, an increased amount of chips tend to cluster together and clog the groove. Eventually severe wear develops and diamond grits are separated from the drill body. To relieve the chip clogging problem and to evacuate chips from the groove easily, the helical drilling process is studied. Taguchi method is applied to select optimal helical drilling conditions.

INTRODUCTION

Diamond core drills made of diamond grits brazed with nickel are widely used in IT, BT, construction and manufacturing industries. They are used to drill holes on the difficult-to-drill materials such as ceramics, wafers, glasses, tiles, tungstens, and so on. In diamond core drilling of the difficult-to-drill materials, machining parameters are main factors affecting MRR, tool life and hole quality, it is important to select optimal machining parameters. However, it is difficult to select them and to understand characteristics of them, because the diamond core drilling process has many factors acting on each other. [1-3]

In contrast to normal metal cut drilling, core drilling processes make deep grooves for removal of machining materials. One of difficulties of the core drilling process is the evacuation of chips form the drilled groove. As the drilling depth increases, an increased amount of chips tend to cluster together and clog the groove. Eventually severe wear develops and diamond grits are separated from the drill body. To relieve the chip clogging problem and to evacuate chips from the groove easily, vibration and helical drilling processes have been studied so far [4-5]. Huang and Wang [3] studied on affective machining parameters of the diamond core drilling process in rock machining. They derived mathematical models to predict the performance of drilling processes.

In this paper, diamond core drilling experiments are performed on porcelain tiles, one of difficult-to-drill materials, to select optimal drilling conditions through the helical feed motion and the Taguchi method. To analyze drilling characteristics and derive optimal drilling conditions, tool life, thrust force, and tool wear are quantified through the monitoring system equipped with a tool dynamometer and the machine vision unit. Multiple regression models are derived to estimate wear and thrust force in diamond core drilling processes.

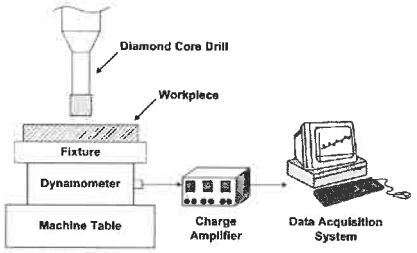

FIGURE 1. Structure of experimental setup.

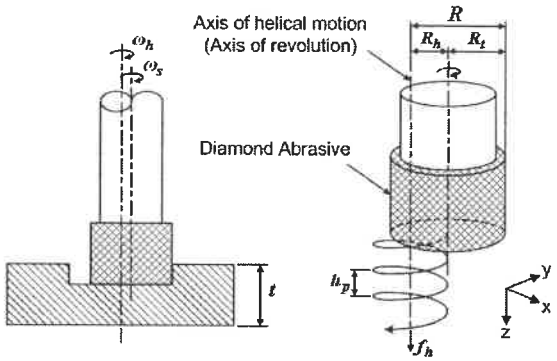

ω_s : *Spindle rotation*[*rpm*] ω_h : *Spindle revolution*[*rpm*]
f_h : *Helical feed* [*mm*/min] R : *Hole radius*[*mm*]
R_t : *Tool radius*[*mm*] R_h : *Helical radius*[*mm*]
h_p : *Helical pitch*[*mm*] t : *Hole depth*[*mm*]

FIGURE 2. Illustration of helical-feed drilling.

EXPERIMENTS

Experimental equipment

Drilling experiments are conducted on the vertical tapping center with the maximum speed of 12,000 rpm. Workpieces, porcelain tiles, are clamped on a fixture, and a dynamometer is mounted between the fixture and the machine table. Fig. 1 shows the overall experimental setup. Diamond grits are brazed to steel body to make diamond core drills with an outside diameter of 6 mm and an inside diameter of 2 mm. Kistler model 9257B dynamometer is used to measure thrust forces. Charge signals from the dynamometer are converted into voltage signals by Kistler model 5010B10 charge amplifier. Labview is used to digitize the signal with 1KHz sampling rate.

Herical drilling method

Fig. 2 illustrates a drilling method using helical motion [5]. During helical drilling motion, loading is prevented from grits since the helical motion is applied to the conventional drilling process. It enables to aid distribution of drilling temperature through a gap between tool and the groove. In helical-feed drilling method, motion of spindle consists of a rotational motion for a cutting speed and a revolution motion for generation of the helical motion. Hence, a size of machining hole is given by

$$R = R_t + R_h \quad (R_h \neq 0) \tag{1}$$

During drilling, the real feed(S) of a tool and the helical-feed angle(θ) are given by

$$S = \sqrt{(2\pi R_h)^2 + h_p}, \quad \theta = \tan^{-1}\left(\frac{p}{2\pi R_h}\right) \tag{2}$$

Total feed of tool(S_T) for machining of arbitrary drilling depth(t) is given by

$$S_T = S \times n = \frac{S \times t}{h_p} > t \quad \left(where,\ n = \frac{t}{h_p}\right) \tag{3}$$

Design of experiments

Taguchi method is a robust design method to minimize distribution due to uncontrolled conditions into the value of characteristic. The characteristic is expressed as signal and noise ratio. In this paper, tool life is applied to lager-the-better characteristics because the longer tool life is better, and thrust force and tool wear are applied to smaller-the-better characteristics because the smaller thrust force and tool wear are better. Under these application, S/N ratio is calculated as follow, Eq (4) is lager-the-better characteristics and Eq (5) is smaller-the-better characteristics.

$$\eta = -10\log\left[\frac{1}{n}\sum_{i=1}^{n} y_i^2\right] \tag{4}$$

$$\eta = -10\log\left[\frac{1}{n}\sum_{i=1}^{n} \frac{1}{y_i^2}\right] \tag{5}$$

where, η is the observe value (dB); y_i the experimental data; n is the number of observations. Through preceding experiments, the factors and levels, which affect value of characteristic, is selected and $L_9(3^4)$ orthogonal array is made. Table 1 indicates the machining parameters.

TABLE 1. Levels of control factors.

Control factor	Level 1	Level 2	Level 3
Spindle rotation (rpm) (A)	1000	1500	2000
Spindle revolution (rpm) (B)	20	40	60
Helical feed (mm/min) (C)	1	2	3

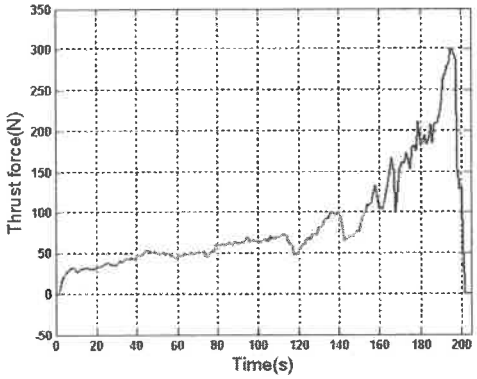

FIGURE 3. Variation of thrust force with time.

Tool life assessment

On diamond core drilling process with porcelains, the trust force according to time is shown as Fig. 3. And variation of the gradient of thrust force according to time is denotes as Fig. 4. As the trust force gradually increase with time, it is possible to know that the thrust force increases

rapidly after 150sec owing to tool wear and chip loading as shown in Fig. 3. In this paper, the criterion of tool life assessment is defined as the volume of cut with variation of the gradient of thrust force which is over 20 N/s. The volume of cut is given by

$$V_c = \pi R^2 \times D_d \quad (6)$$

where

V_c : *Volume of cut* $[mm^3]$ $\quad R$: *Hole radius* $[mm]$

D_d : *Drilling depth* $[mm]$

Thrust force and tool wear

Fig. 5 shows the average of thrust force per spindle revolution versus time. In this study, the trust force is defined as the maximum value in the steady state stage. A measurement system for tool wear consists of halogen light source, LED lights, image processing computer and machining center which is attached a CCD camera. In this paper, the tool wear is defined as the volume of cut, 684.2 mm^3, with the variation of height of diamond grit. A variation of height of diamond grit is measured by using CCD camera and image processing system [6]. Fig. 6 illustrates a variation of height of diamond grit [7].

EXPERIMENTAL RESULTS AND DISCUSSION

The statistical treatment of the data was made in two phases. The first phase was concerned with the ANOVA and the effect of the factors. The second phase allowed us to obtain the correlations between the machining parameters.

Analysis of Variance (ANOVA)

The ANOVA was used to predict the relative significance of the process factors and estimate the experimental errors. Table 2 shows the orthogonal arrays used. Tables 3-5 show the results of the ANOVA with the tool life, the thrust force and the tool wear, respectively. In table 3, the most important variable affecting the tool wear is the helical feed(P=66.35%), and the optimal machining parameters are identified, such as A_3, B_3 and C_1. In table 4, the most important variable affecting the thrust force is the helical feed(P=76.12%), and the optimal machining parameters are identified, such as A_3, B_2 and C_1. In table 5, the most important variable affecting the tool wear is the helical feed(P=96.59%), and the optimal machining parameters are identified, such as A_3, B_3 and C_1.

Multiple regression analysis

Using multiple regression analysis, mechanical properties are estimated from machining parameters as follows:

$$V_c = 1134.81 + 1.04\omega_s + 13.78\omega_h - 954 f_h \quad (7)$$

$$T_f = 56.63 - 0.02\omega_s + 0.12\omega_h + 20.58 f_h \quad (8)$$

$$h = -63.72 - 0.06\omega_s - 0.28\omega_h + 232.33 f_h \quad (9)$$

Where V_c is the volume of cut(mm^3), T_f the thrust force(N), h the tool wear(mm), ω_s the spindle rotation(rpm), ω_h the spindle revolution(rpm), f_h the helical feed(mm/min).

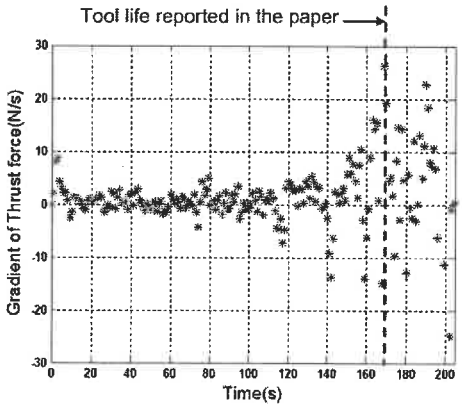

FIGURE 4. Variation of the gradient of thrust force with time.

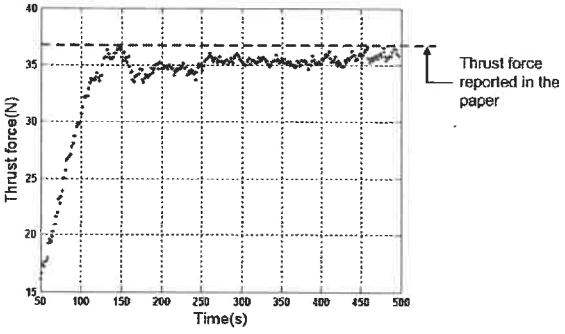

FIGURE 5. Thrust force versus time.

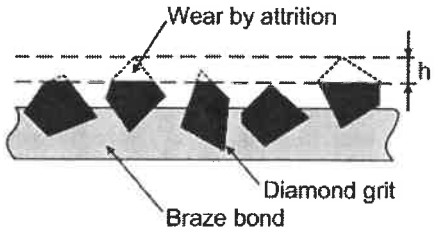

FIGURE 6. Illustration of tool wear measurement.

TABLE 2. $L_9(3^4)$ Orthogonal array.

Trial	Factor			Volume of cut (mm^3)	Thrust Force (N)	Tool wear (μm)
	A	B	C			
1	1	1	1	1479.7	57.9	92
2	1	2	2	347.2	76.3	365
3	1	3	3	342.1	112.6	492
4	2	1	2	899.8	67.1	243
5	2	2	3	722.7	80.7	652
6	2	3	1	2986.1	55.5	80
7	3	1	3	756.1	84.8	487
8	3	2	1	3079.1	41.2	65
9	3	3	2	1460.9	56.1	216

TABLE 3. ANOVA for tool life.

Factor	Level(S/N)			SS	DF	V	F_0	P(%)
	1	2	3					
A	54.97	61.92	63.54	124.59	2	62.30	20.94	32.12
B	60.02	59.25	61.16	5.52	2	2.76		
C	67.56	57.73	55.14	257.38	2	128.69	43.25	66.35
Error				6.38	2	3.19		
PE				11.90	4	2.98		1.53
Total				393.88	8			100

SS, sum of squares; DF, degree of freedom;
P, percentage of contribution; PE, pooled error.

TABLE 4. ANOVA for thrust force.

Factor	Level(S/N)			SS	DF	V	F_0	P(%)
	1	2	3					
A	-37.98	-36.52	-35.28	10.93	2	5.47	8.00	21.23
B	-36.79	-36.03	-36.97	1.48	2	0.74		
C	-34.15	-36.39	-39.25	39.20	2	19.60	28.70	76.12
Error				1.25	2	0.62		
PE				2.73	4	0.68		2.65
Total				52.86	8			100

SS, sum of squares; DF, degree of freedom;
P, percentage of contribution; PE, pooled error.

TABLE 5. ANOVA for tool wear.

Factor	Level(S/N)			SS	DF	V	F_0	P(%)
	1	2	3					
A	-48.12	-47.35	-45.57	10.31	2	5.15	2.09	2.30
B	-46.91	-47.93	-46.20	4.55	2	2.27		
C	-37.87	-48.55	-54.62	431.95	2	215.97	87.49	96.59
Error				5.32	2	2.66		
PE				9.87	4	2.47		1.10
Total				452.13	8			100

SS, sum of squares; DF, degree of freedom;
P, percentage of contribution; PE, pooled error.

CONCLUSIONS

In the diamond core drilling process, the design of experiments is applied to select the optimal machining parameters and to verify the relation of cutting conditions, tool life, thrust force, and tool wear. The results are summarized as follows:

(1) It is possible to select the optimal machining parameters about each result by using Taguchi method.
(2) By using analysis of variance, the factors, which affect diamond core drilling process, is analyzed. Helical feed is the most heedful factor for tool life, thrust force, tool wear. On the contrary, spindle rotation is a minor heedful factor.
(3) The relation of cutting condition, tool life, thrust force, tool wear is verified through multiple regression analysis.

REFERENCES

[1] Balykov, A. V. Modeling of Diamond Drilling of Holes in Brittle Nonmetallic Solid Materials. Glass and Ceramics. 2003; 60(3-4): 77-80.
[2] Zhang, Q. H., et al. Study on the Diamond Tool Drilling of Engineering Ceramics. Journal of Materials Processing Technology. 2002; 122: 232-236.
[3] Huang S L, Wang Z W. The Mechanics of Diamond Core Drilling of Rocks. Int. J. Rock Mech. & Min. Sci. 1997; 34(3-4), 612.
[4] Ishikawa K., et al. A Study on Combined Vibration Drilling by Ultrasonic and Low-frequency Vibrations for Hard and Brittle Materials. Precision Engineering. 1998; 22: 196-205.
[5] Yagishita H. Comparing Drilling and Circular Milling for Hole Making in Carbon Fiber Reinforced Plastic(CFRP) Laminates. Transactions of NAMRI/SME. 2007; 35; 153-160.
[6] Choi Y J, Chung S C. Monitoring of Micro-Drill Wear by Using the Machine Vision System. Transactions of the North American Manufacturing Research Institution of SME. 2006; 34; 143-150.
[7] Shi Z, Malkin S. Wear of Electroplated CBN Grinding Wheels. Transactions of the ASME, Vol. 128, February 2006.

CHATTER IN TURNING WITH PROCESS DAMPING

Mahdi Eynian[1], Hideaki Onozuka[2], Yusuf Altintas[1]
[1]Department of Mechanical Engineering
University of British Columbia
Vancouver, British Columbia, Canada
[2]Production Engineering Research Laboratory
Hitachi, Ltd.
Yokohama, Japan

INTRODUCTION

The dynamics of cutting process is known to be affected by the chip thickness, effective rake angle and contact between the flank face of the tool and wavy surface finish. While the effects of instantaneous chip thickness due to regeneration and angle changes caused by cutting speed and vibration velocity has been considered [1],[2],[3]), parts of cutting force changes due to the oscillation has not been explained satisfactorily in the literatures [4].

This paper describes a dynamic cutting force model with chip thickness and flank contact forces as a function of regenerative displacement, velocity and acceleration terms. The proposed dynamic model is experimentally validated in orthogonal chatter tests. The amplitude and frequency of inner and outer vibration waves are generated on the chip with the aid of a fast tool servo powered by a piezo actuator. The coefficients of dynamic cutting force components are identified and used in analyzing the effect of cutting speed, vibration frequency and wave amplitudes on the chatter stability of the process. The prediction of the chatter stability at low cutting speeds is shown to have improved with the proposed dynamic cutting process model.

DYNAMIC CUTTING PROCESS

The schematic of a simple model of orthogonal cutting is introduced in *FIGURE 1*. The traditional regenerative cutting force at time *t* is expressed as:

$$F_x(t) = K_f a\left[h_0 - x(t) + x(t-\tau)\right] = m\ddot{x}(t) + c\dot{x}(t) + kx(t) \quad (1)$$

$$F_y(t) = K_t a\left[h_0 - x(t) + x(t-\tau)\right] \quad (2)$$

where $x(t)$ and $x(t-\tau)$ are the inner and outer vibrations, respectively.

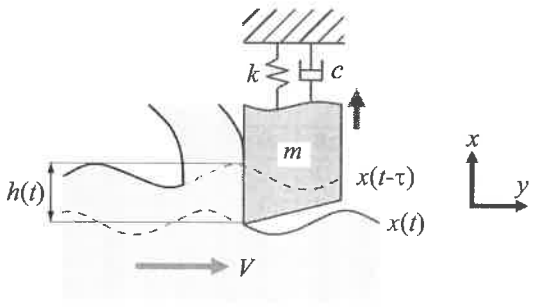

FIGURE 1: Regenerative chatter in orthogonal cutting

K_f and K_t are the static cutting force coefficients in feed and cutting speed directions, respectively. a is the width of cut, h_0 is the feed per revolution, and τ is the time delay between the inner and outer vibration waves. Stability limits for the traditional chatter model was solved by Tobias [3] Tlusty [2] , and Merit [5]. The Equation (1) is known to be sufficient at high speed where the effect of tool contact with the surface finish is negligibly small. Das and Tobias [3] included the changes in the direction of cutting force due to the vibration velocity as shown in *FIGURE 2*

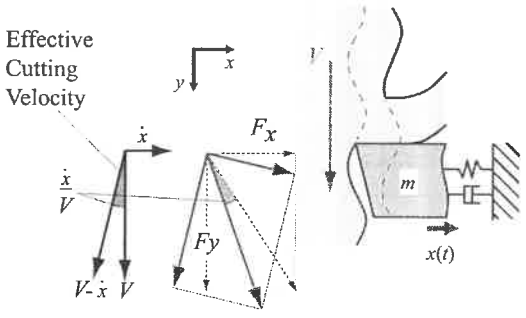

FIGURE 2. The effect of vibration velocity on dynamic cutting force

Thisleads to:

$$F_x(t) = K_f a\left[h_0 - x(t) + x(t-\tau)\right] - K_t a h_0 \frac{\dot{x}}{V} \quad (3)$$

Comparing equations (1) and (3), the velocity term ($-\dot{x}/V$) increases the damping in the system ($c + K_t a h_0 / V$ instead of c) at low cutting speeds. While Tobias's modified dynamic cutting process model leads to increased stability at the low speeds, it requires further improvements in predicting chatter stability at low speeds. It is also argued in the literature that the dynamic cutting forces depend on the shear angle oscillations caused by the vibration and cutting velocities [6]. Furthermore, Sisson and Kegg [4] and others demonstrated that the flank-wavy inner surface finish contact contribute to the dynamic cutting forces, and adds to the process damping as well.

A series of dynamic cutting tests conducted by the authors indicated that more terms are needed to model the process dynamics accurately.

In addition to the velocity effect suggested in [3]-[4], the acceleration term is also considered in order to account the influence of the wave curvature on the flank contact and the edge radius of the cutting tool, see *FIGURE 3*.

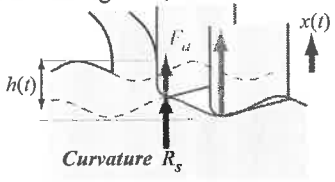

FIGURE 3. The effect of wave's curvature on the flank contact forces $\left(1/R_s = d^2x/du^2\right)$

The curvature dependant term brings the acceleration term as:

$$\frac{dx}{du} = \frac{dx}{dt}\frac{1}{du/dt} = \frac{\dot{x}}{V}$$
$$\frac{1}{R_s(t)} = \frac{d^2x}{du^2} = \frac{\ddot{x}}{V^2} \quad (4)$$

The following comprehensive dynamic cutting process model is used to assess the contribution of the regenerative term, velocity, inner and outer modulation and acceleration effects:

$$F_x(t) = a\left\{K_f\left[h_0 - x(t) + x(t-\tau)\right] - \frac{C_i\dot{x}(t)}{V} - \frac{\alpha_i\ddot{x}(t)}{V^2}\right\} \quad (5)$$

While the static cutting force coefficient K_f can be easily identified from vibration-free orthogonal cutting tests, the velocity and acceleration dependent cutting force coefficients (C_i and α_i) can only be identified from a set of dynamic cutting experiments.

When a harmonic motion ($x(t) = Xe^{j\omega t}$) is applied to the cutting tool with a frequency ω and amplitude X, the dynamic cutting force equation becomes,

$$F_x(t) = K_f a h + aXe^{j\omega t}\left\{-K_f\left[1 - e^{-j\omega\tau}\right] - \frac{C_i j\omega}{V} + \frac{\alpha_i\omega^2}{V^2}\right\} \quad (6)$$

The length of the vibration wave imprinted on the surface is $\lambda = V\frac{2\pi}{\omega}$, which leads to $\omega/V = 2\pi/\lambda$. The modified dynamic cutting force expression is,

$$F_x(t) = K_f a h_0 + aXe^{j\omega t}\left\{-K_f\left[1 - e^{-j\omega\tau}\right] - j\frac{2\pi}{\lambda}C_i + \frac{4\pi^2}{\lambda^2}\alpha_i\right\} \quad (7)$$

which correlates the damping forces to the vibration wave length or the ratio of vibration frequency over cutting speed. The effect of cutting speed can be analyzed from the dynamic cutting force equation (7). Considering that the critical vibration frequency ω remains close to the natural frequency of the structure, as the cutting speed increases, the wave length of the vibration marks becomes larger and the flank contact reduces. In other words, the effect of the velocity and acceleration terms in the dynamic cutting force model reduces at high cutting speeds. However, as the cutting speed decreases, the term ($2\pi/\lambda$) increases and the process stability is strongly affected.

EXPERIMENTAL IDENTIFICATION OF DYNAMIC CUTTING COEFFICIENTS

The dynamic cutting force coefficients are identified from a series of orthogonal plunge turning of cold rolled AISI 1045 steel bars on an instrumented CNC lathe as shown in *FIGURE 4*. The carbide grooving tool with 2.39 mm width, 0 degree rake and 7 degree clearance angles is mounted on a piezo-actuator-driven fast tool servo. The width of cut was 0.5mm and feed was 0.05mm/rev.

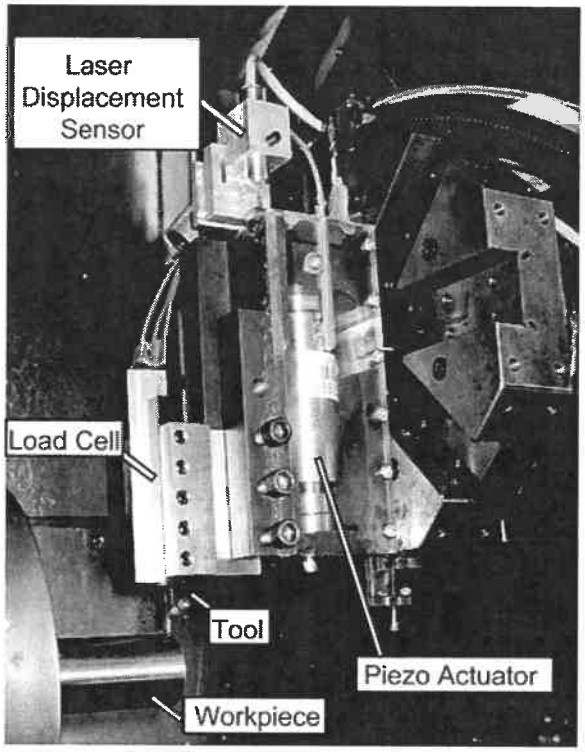

FIGURE 4. CNC lathe instrumented with fast tool servo and three component force sensor

The fast tool servo can deliver up to $50\mu m$ displacement at the frequencies up to 120 Hz. The displacement of the tool is measured with a laser sensor, and a three component load cell is integrated to the tool holder to measure the dynamic cutting forces applied at the tool [6]. The fast tool servo is mounted on the turret of the machine as rigidly as possible. While the CNC lathe provides the macro positioning and feed motion (h_0), the fast tool servo is used to generate vibrations at the desired frequency and amplitude. The tool displacement and cutting forces are measured simultaneously during dynamic cutting tests. Sample cutting force and displacement measurements are shown in *FIGURE 5.*

In the identification tests, the inner and outer waves are synchronized to be in phase ($1-e^{-j\omega\tau}=0$), therefore:

$$F_x(t)=K_r a h_0 + aXe^{j\omega t}\left\{-jC_i\frac{2\pi}{\lambda}+\frac{4\pi^2}{\lambda^2}\alpha_i\right\} \qquad (8)$$

The dynamic cutting force coefficients are extracted using the least squares method applied on the Fourier spectrum of measured forces, and given in *TABLE 1.*

FIGURE 6 illustrates the dependency of dynamic cutting force coefficients on the wave length imprinted on the finish surface. The dynamic cutting forces are reconstructed by using the predicted coefficients and compared against the measurements (a zero phase filter was employed to filter the signals); see *FIGURE 7.* The contribution of each dynamic cutting coefficient is evident from *FIGURE 7.*

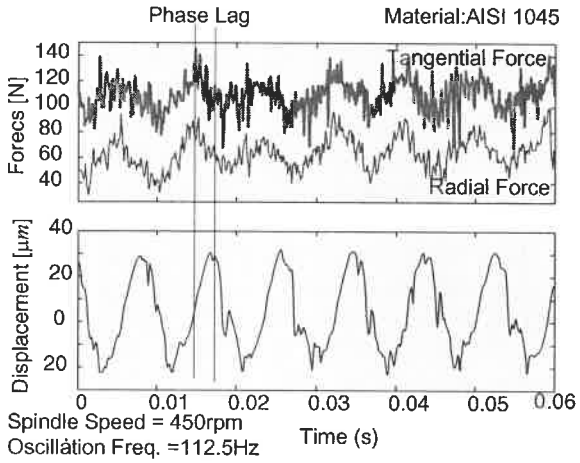

FIGURE 5. Sample cutting force and tool displacement measurements during dynamic plunge turning test

TABLE 1. Dynamic Cutting Coefficients, extracted from dynamic tests

K_t[MPa]	K_f[MPa]	$C_i[N/m]$	$\alpha_i[N]$
2580	1384	$\frac{3.84\times10^6}{2\pi}=6.11\times10^5$	$\frac{1.31\times10^4}{4\pi^2}=332$

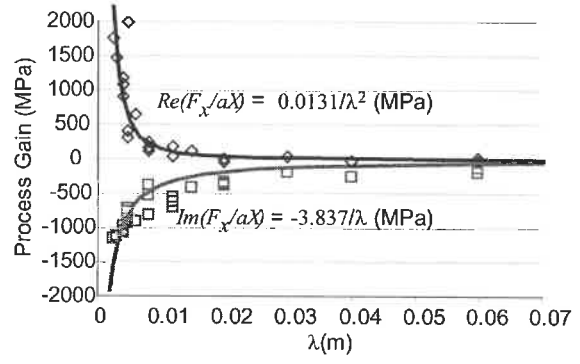

FIGURE 6. Process gain versus wavelength with zero phase shift between inner and outer oscillations

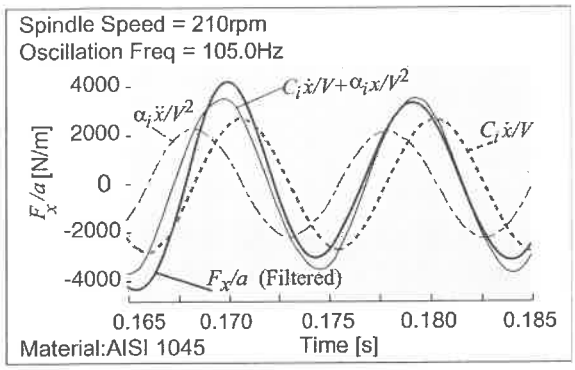

FIGURE 7. Contribution of acceleration and velocity dependent forces to the dynamic force

CHATTER TESTS

A series of chatter tests are conducted using the same orthogonal tool but in plunge turning of a AISI1045 shaft with a diameter of 38.1mm and a cantilevered length of 210mm, (see *FIGURE 8*). A 0.1mm/rev feed was employed in these tests. The shaft has a dominant mode with the experimentally identified modal parameters listed in *TABLE 2.*

TABLE 2. Dynamic parameters of 210mm shaft

$f_n[Hz]$	ζ	$K\ [\ N/\mu m\ ]$
450.7	0.038	6.48

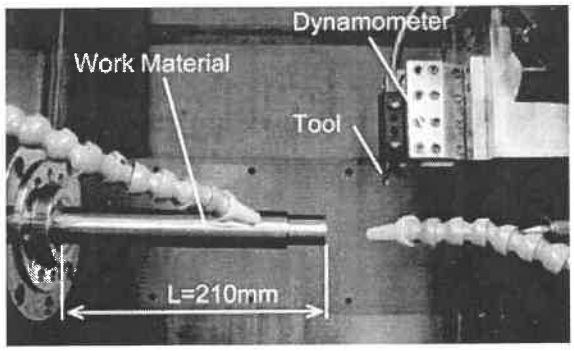

FIGURE 8. Long shaft cutting chatter test setup

The results of the chatter tests are compared against the newly introduced stability model and previous theories in *FIGURE 9.* The improvement on the prediction of the stability limit at the low speed zone is evident.

DISCUSSIONS

The low speed chatter stability prediction for orthogonal cutting is improved by adding velocity and acceleration terms to the dynamic cutting force relations. The corresponding dynamic cutting coefficients are identified from oscillatory cutting tests controlled by a fast tool servo. The prediction of stability charts at low speeds is improved considerably.

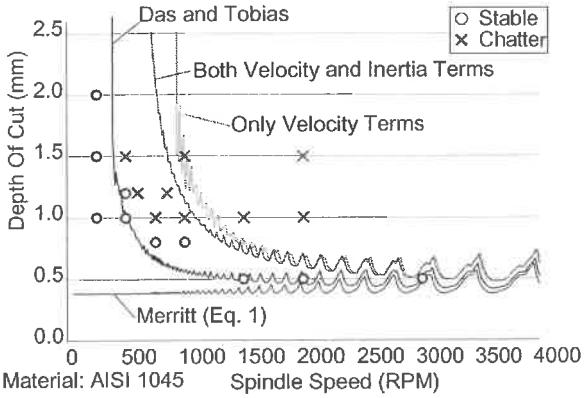

FIGURE 9. Chatter Stability Chart with process damping and inertia

AKNOWLEDGMENT

The research is sponsored by NSERC. Sandvik Coromant provided tooling for this research.

REFERENCES:

[1] Doi S, Kato S, Chatter Vibration of Lathe Tools. Transactions of ASME, 1956; 78: 1127-1134.

[2] Tlusty J, Analysis of the state of research in cutting dynamics. Annals of the CIRP, 1978, 27: 583–589.

[3] Das M K, S A Tobias, The Relation between the Static and the Dynamic Cutting of Metals. International Journal of Machine Tool Design and Research, 1967, 7:63-89.

[4] Sisson T R, Kegg R L, An Explanation of Low-speed Chatter Effects. ASME Journal of Engineering for Industry, 1969, 91: 951–558.

[5] Merritt H E, Theory of Self Excited Machine-Tool Chatter, ASME Journal of Engineering for Industry, 1965, 447-465.

[6] Nigm M M, Sadek M M, Tobias S A, Prediction of dynamic cutting coefficients from steady-state cutting data. Proceedings of the Thirteenth International Machine Tool Design and Research Conference, 1972, 1-12.

[7] Zhu, W. H. Jun, M. B. Altintas, Y. A fast tool servo design for precision turning of shafts on conventional CNC lathes, International Journal of Machine Tools and Manufacture, 2001, 953-965.

PRECISION MACHINING OF GLASS LENS MOLD WITH MINUTE STRUCTURES

Taichi Fujii[1], Minoru Hirano[2], Tetsuro Shibukawa[2], Tohru Ishida[1], Yoshimi Takeuchi[1]
[1]Dept. of Mechanical Engineering, Graduate School of Engineering
Osaka University
Yamadaoka 2-1, Suita, Osaka 560-0871, JAPAN
[2] Dept. of Machine Tool R&D, Research&Development Center
JTEKT Corporation
Asahi-machi 1-1, Kariya, Aichi 448-8652, JAPAN

INTRODUCTION

In optical devices, the demand of lenses with complicated shapes like Fresnel shape is recently growing up[1]. Fresnel shape has some sharp edges on curved surfaces. These lenses are generally composed of polymer due to the easiness of machining die with a single crystal diamond cutting tool. In recent years, it is strongly required to make these lenses by glass in terms of improving its optical performances. Brittle materials such as cemented tungsten carbide are used for glass molding. Thus, it is expected to develop a high precision machining method to fabricate minute structures on brittle materials, difficult to machine.

Concerning such a demand, the two-axes turning method with disk type resinoid bonded diamond grinding wheel or polycrystalline diamond milling tool, as shown in Fig.1, is proposed to machine glass lens mold die with Fresnel shape[2]. As these tools are composed of diamomd grains, it is difficult to form tool edge sharply. It causes the deterioration of form accuracy of sharp edges. In addition, the tool sharp edge may cause the increase in tool wear and the deterioration of surface roughness. Therefore, it is expected to apply a single crystal diamond cutting tool with a very sharp edge for high precision machining of glass molding die with Fresnel shape.

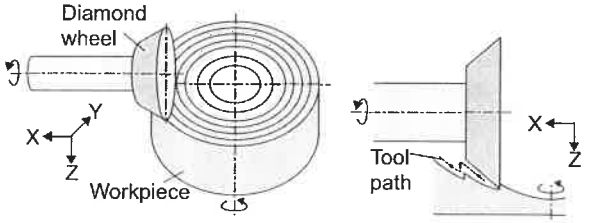

FIGURE 1. Conventional machining method.

The study proposes a new machining process for the brittle material molding die with Fresnel shape shown in Fig.2, aiming at high precision machining. In the proposed process, the curved surfaces except for sharp edges are machined by the conventional grinding method with the disk type metal bonded diamond grinding wheel. Then, ultra precision cutting with a very sharp single crystal diamond cutting tool is applied to create the sharp edges. This paper deals with the details of a newly proposed machining process and the result of fundamental cutting experiment and grinding experiment with regard to cemented tungsten carbide.

THE PROPOSED MACHINING METHOD

The proposed machining metod is shown in Fig.3.

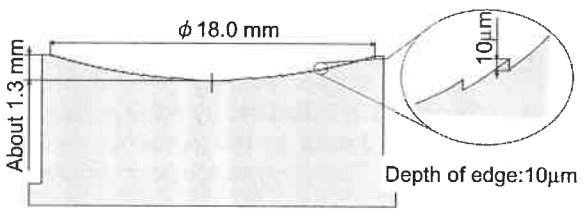

FIGURE 2. Target shape to be machined.

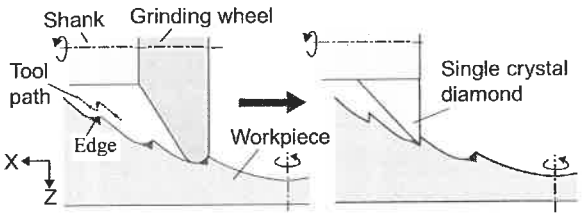

FIGURE 3. Proposed machining method

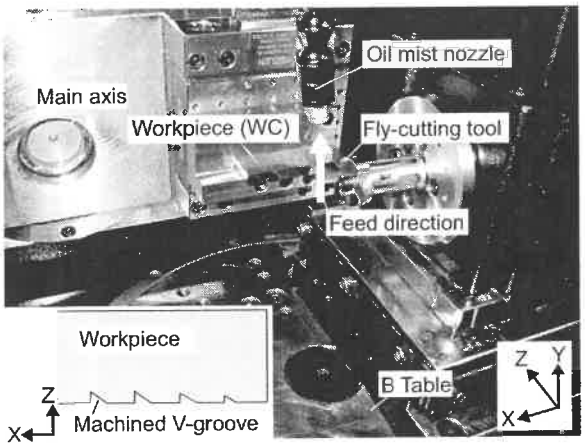

FIGURE 4. Set-up of fundamental cutting experiment.

At first, the curved surfaces except for sharp edges are machined by the grinding method with the disk type diamond grinding wheel. Resinoid bonded diamond grinding wheel is used in the usual manner. However, as the tool edge becomes sharp, a grinding wheel tends to have a large amount of tool wear. Thus, it is expected to apply metal bonded diamond grinding wheel with high bonding strength to reduce tool wear. Then, fly cutting method is applied to create the sharp edges. Fly cutting method is expected to reduce tool wear due to the intermittent machining process.

FUNDAMENTAL CUTTING EXPERIMENT OF TUNGSTEN CARBIDE

Experimental method

Fundamental cutting experiment of tungsten carbide is carried out to verify the availability of fly cutting method. The ultraprecision machining center, AHN05 by JTEKT Corporation, is used for experiments. The machine has three translational axes, X, Y, and Z and has a rotational axis, B. The resolution of translational axes are 1nm, and rotational axis is 0.0001°. Experimental set-up is shown in Fig.4. The depth of edge is 10μm, and the whole length of edges is about 625mm in the target shape. Thus, the V-shaped microgrooves, whose depth is 10μm and whose length is 5mm, are machined 130 times. The tool is fed in the Y direction, and the cutting direction is in the Z direction. Then, the extent of the tool damage is examined by observing the cross section of the machined microgrooves. Cutting condition is listed in Table 1. The single crystal diamond cutting tools with very sharp edge, whose tip angle is 60° and rake angle is -30°, are used in fly cutting and shaping.

Table 1. Cutting conditions

	Fly cutting	Shaping
Workpiece	Binderless tungsten carbide J05 (FUJI DIE Co.,Ltd.)	
Tool	Single crystal diamond	
Tip angle	60°	
Rake angle	-30°	
Relief angle	10°	
Rotational diameter	φ27mm	
Rotational rate	12000rpm (1000m/min)	
Cutting direction	Down cutting	
Depth of groove	10μm	
Depth of cut	0.05μm	0.01μm
Feed rate	200mm/min	500mm/min
Cutting fluid	Oil mist	

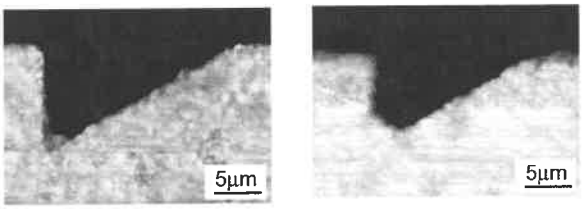

(a) Fly cutting *(b) Shaping*

FIGURE 5. Microphotographs of section view of machined V-groove (50mm).

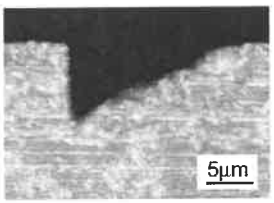

FIGURE 6. Fly cutting (650mm).

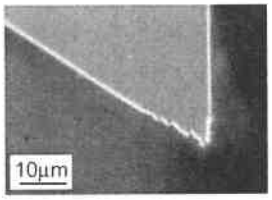

FIGURE 7. Fly cutting tool.

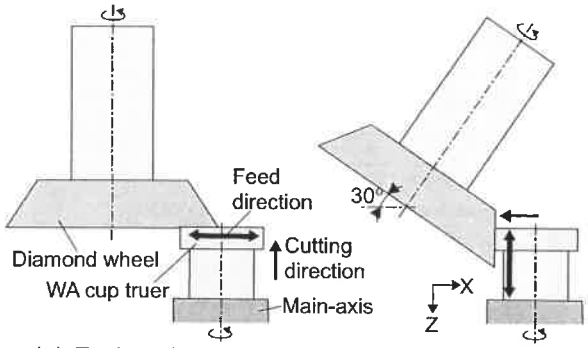

(a) End surface *(b) Side surface*

FIGURE 8. Truing method of diamond wheel.

Table 2. Truing conditions

Wheel	SD3000J75M
Rotational diameter	ϕ25mm
Rotational rate	12000rpm
Cup truer	WA4000
Rotational rate	50rpm
Depth of cut	1μm
Feed rate	10mm/min
Grinding fluid	Oil mist

Experimental result

Figure 5 shows the Nomarski microphotographs of the cross section of the machined microgrooves for 50mm. In shaping, the tool edge is intensively chipped, and machined microgroove losts its shape. In fly cutting, the V-shaped microgroove with sharp edge is machined. Figure 6 shows the microphotograph of the cross section of the fly cut microgrooves for 650mm. Figure 7 shows the microphotograph of rake surface of fly cutting tool after machining. Applying fly cutting method, the damage of cutting tool is dramatically reduced, compared to shaping, though the volume of cutting per unit time is higher than shaping. It is considered that the intermittent machining process acted effectively so that the damage of cutting tool is reduced, compared to shaping. The availability of fly cutting method is confirmed to reduce tool damage.

TRUING TEST

In the study, the disk type metal bonded diamond grinding wheel, whose diameter is 25mm and tip angle is 60°, is used. The truing of diamond grinding wheel by WA cup truer is experimented. The truing method is shown in Fig.8.The grinding wheel

Table 3. Grinding conditions

Workpiece	Binderless tungsten carbide
Rotational rate	200rpm
Wheel	SD3000J75M
Rotational diameter	ϕ25mm
Rotational rate	12000rpm
Depth of cut (Rough cut)	0.5μm
Depth of cut (Finish cut)	0.2μm × 2 0.1μm × 1 0μm × 1
Feed rate	0.2mm/min
Grinding fluid	Oil mist

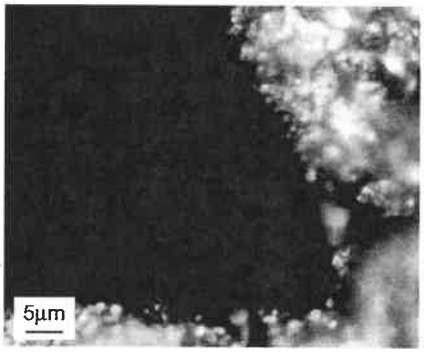

FIGURE 9. Micrograph of carbon workpiece ground by trued wheel.

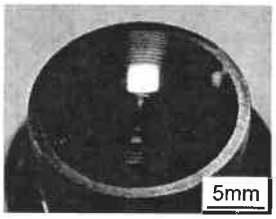

FIGURE 10. Whole view of molding die.

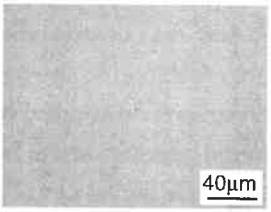

FIGURE 11. Micrograph of ground surface.

is attached to an air turbin spindle, and WA cup truer is attached to the main axis. The end surface of grinding wheel is at first trued, as shown in Fig.8(a). Then, grinding wheel is tilted 30° by rotationing B-axis, and the side surface of grinding wheel is trued, as shown in Fig.8(b). The truing condition is shown in Table 2.

The shape of trued wheel edge is observed by grinding a carbon plate. Figure 9 shows the microphotograph of ground carbon plate. The radius of wheel edge is about 5μm, which means that the edge is kept relatively sharp.

GRINDING TEST

The grinding test of glass molding die with Fresnel

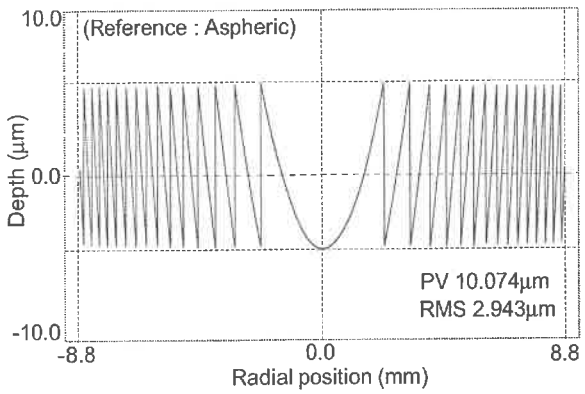

FIGURE 12. Profile of Fresnel shape.

shape is conducted by using the wheel, which is trued in truing test. The target shape to be machined is shown in Fig.2. The two-axes turning method shown in Fig.1 is applied to machining, where binderless tungsten carbide is used as the workpiece material. The grinding condition is shown in Table 3.

Figure 10 shows the whole view of machined molding die. Figure 11 shows the Nomarski microphotograph of ground surface. The ductile mode grinding mirror surface is obtained. The surface roughness of ground surface is measured with a 3D optical profiler, New View 5022 by Zygo Co.,Ltd., and obtaind about 25nmRy. The profile of machined shape is observed with a 3D profilometer, UA3P by Matsushita Electric Industrial Co.,Ltd.. Figure 12 shows the profile of Fresnel shape removing the aspheric shape from the whole machined shape. The measured depth of edge is PV10.074μm, approximately equal with design value (10μm). Figure 13 shows the deviation of machined shape except for edge sections. Figure 14 shows the enlarged view of edge section. The measured deviation of molding die is about PV0.2μm, and the width of shape error area by wheel edge radius is about 10μm. As a result, satisfactory shape accuracy is obtained as a previous stage of edge cutting process.

CONCLUSION

The study proposes a new machining process,

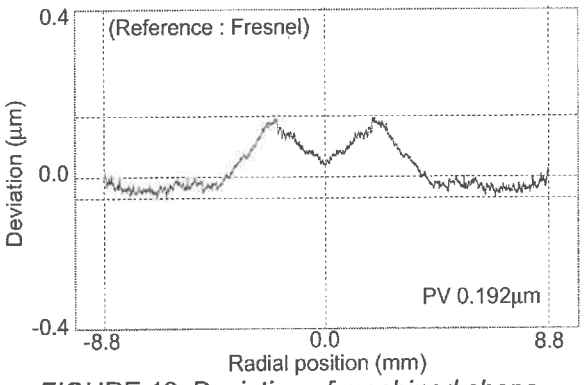

FIGURE 13. Deviation of machined shape.

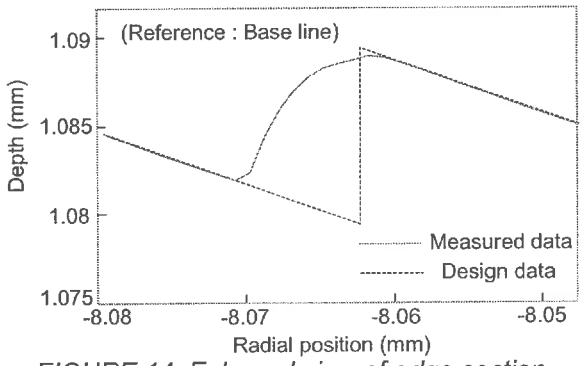

FIGURE 14. Enlarged view of edge section.

which combines grinding of curved surfaces with cutting of edge sections for cemented tungsten carbide molding die with Fresnel shape. From fundamental V-grooving experiments by fly cutting and shaping, it is clarified that the damage of cutting tool by fly cutting is reduced, compared to shaping. Grinding of Fresnel shape with metal bonded diamond wheel is conducted, and ductile mode grinding surfaces are obtained with satisfactory shape accuracy. As a result, the proposed machining method has the potential of producing a high precision glass lens mold with Fresnel shape.

REFERENCES

[1] Y. Ono. Recent Advances in Diffractive Optical Elements: From Diffractive Optics towards Periodic Structure Optics. Japanese Journal of Optics (in Japanese). 2003; 32: 468-475

[2] Y. Yamamoto, H. Suzuki, T. Moriwaki, T. Okino, T. Higuchi. Precision Grinding of Micro Fresnel Lens Molding Die (2nd Report). Journal of the Japan Society for Precision Engineering (in Japanaese). 2007; 73: 688-692

STUDY ON IMPROVEMENT OF ACCURACY IN END MILL MACHINING

Shunsuke ISO[1], Naohito TOIDA[1], Naoto IKEDA[1],
Yoshikazu KOBAYASHI[1], Kenji SHIRAI[1], Kouichi TOZAWA[2]
[1]Department of Computer Science
College of Engineering Nihon University
Koriyama 963-8642, Japan
[2]Nissan Motor Co. LTD,
Zama 228-8502, Japan

1. INTRODUCTION

Various studies are being coducted on product surface texture to enhance visual added-value and functions of parts such as automobiles and digital equipment. Such researches are drawing interest as technology for supporting manufacturing and design. In this study, machining errors were analyzed focusing on machining accuracy along the depth direction, one of the problems faced in the cutting of surface textures. A system which can predict and correct errors was also proposed.

2. MACHINING EXPERIMENTAL METHOD

Experiments were conducted using a square end mill because of its minute wear effects at the tool tip. *FIGURE 1* shows the machining method. The groove is machined from position A to B by a square end mill. The work material is S50C. After the machining, the groove center is measured using a scanning-type white light interferometer along the machining direction. The difference in the maximum and minimum values is taken as the form accuracy value.

FIGURE 2 shows the tool fluctuation during machining. The starting point of machining on the left side is taken as the machining entrance, and endpoint on the right side as the machining exit. At the entrance, the work material and tool are vertical. During machining, the tool bends in the reverse direction, resulting in shallow machining compared to the target machining amount.

At the exit, cutting amount decreases, therefore tool deflection is also reduced. Verification experiments and analysis were carried out as follows to clarify this phenomenon.

(1) Experiment for verification of form accuracy
  (a) Cutting depth
  (b) Feed rate
  (c) Tool stiffness
(2) Analysis of form accuracy in machining entrance
(3) Analysis of form accuracy in machining exit

The following shows the details.

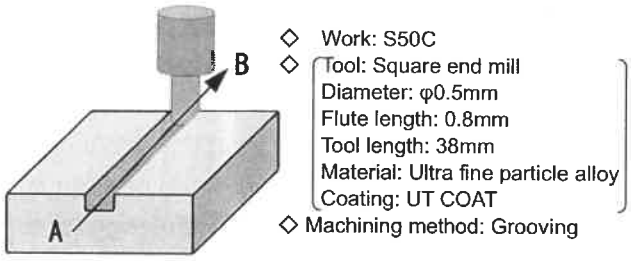

FIGURE 1 Machining method

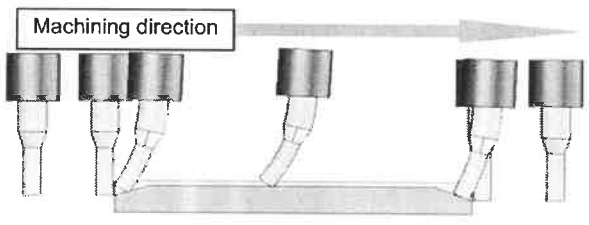

FIGURE 2 Fluctuation of tool during machining

3. EXPERIMENT FOR VERIFICATION OF FORM ACCURACY

3.1 Difference in shape according to cutting depth

The cutting depth was set at 5, 10, 15 μm, and machining was carried out using a square end mill. The feed rate was set at 500 and 1000μm/s, and the spindle rotation at 30000rpm. *FIGURE 3* shows the form accuracy by groove machining. (a) is 500μm/s and (b) is 1000μm/s. It was found that, on the whole, form accuracy fluctuates considerably with increasing feed rate and cutting depth, particularly at the machining exit.

3.2 Difference in shape according to feed rate

As a result of comparing the form accuracies of feed rates 500μm/s and 1000μm/s, fluctuation in the form accuracy was found to be great for all three cutting depths at the machining entrance for the feed rate of 1000μm/s. This tendency indicates the cause to be tool deflection. On the other hand, near the exit, the form accuracy varies according to the cutting depth, caused by reasons other than tool deflection.

3.3 Difference in shape according to tool stiffness

FIGURE 4 shows the relation between tool and deflection.

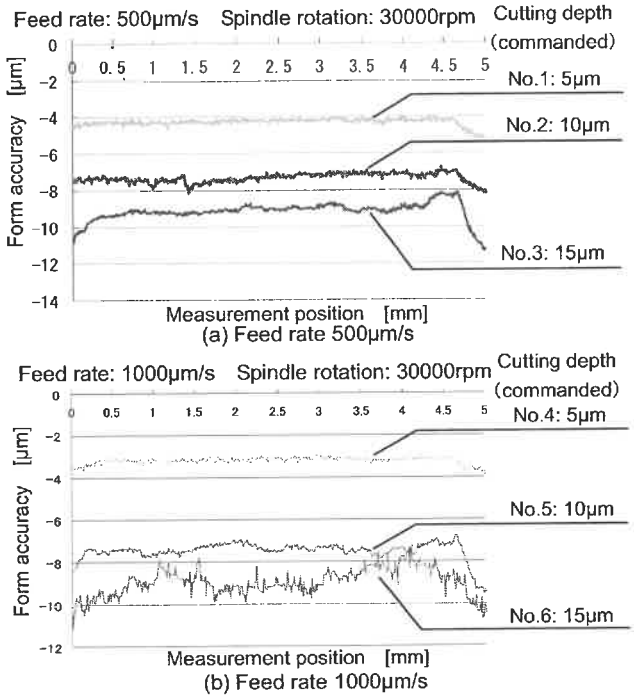

FIGURE 3 Form accuracy by groove machining

Tool deflection w is obtained by giving machining load P to the deflection equation.

$$w = \frac{64\ Pl^{3}}{3\ E\ \pi d^{4}} \qquad (1)$$

where, w :flexure (x-axis), P :machining load, l :extrusion and holder length, E :modulus of longitudinal elasticity, d :tool diameter

Fluctuation in the Z direction is obtained from the deflection in the X direction of the tool.

$$\Delta Z = \frac{w^{2}}{\sqrt{l^{2} - w^{2}}} \qquad (2)$$

The conditions for verifying the effects on form accuracy from the above two equations were set. Specifically, experiments were carried out to verify that the deflection w becomes 2.2 times when tool protrusion and holder length are increased 1.3 times. *FIGURE 5* shows verification according to difference in tool stiffness. The result is smaller than the calculated values, 1.81 times at the entrance and 1.85 times at the exit when deflection w is predicted to become double. This is because of the influence of the deflection of holders and machine main shaft, etc.

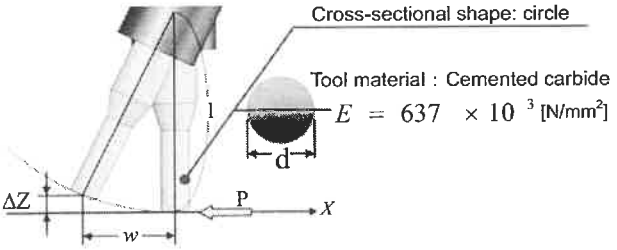

FIGURE 4 Relation of tool and deflection

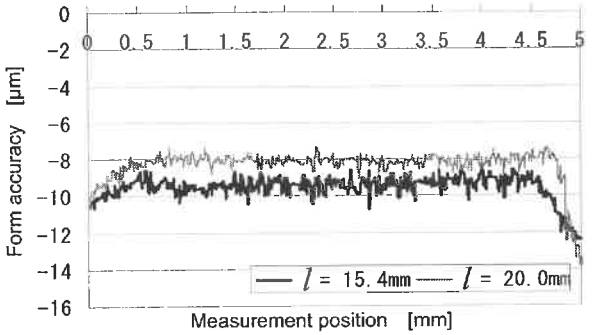

	Machining entrance	Machining exit
l =15.4mm	1.57μm	3.45μm
l =20.0mm	2.84μm	6.39μm

FIGURE 5 Verification by difference in tool stiffness

4. FLUCTUATION OF FORM ACCURACY AT MACHINING ENTRANCE

FIGURE 6(a) shows changes in the cutting width at the machining entrance. The width shown in red is the cutting width at each position. Machining load P takes the value of 0 to 1 in respect to load changes. The tool cross section has a round shape, and the feed rate is constant. The cutting width at entrance Y_{in} is predicted from Equation 3. Taking the feed direction to be x and the orthogonal direction to be y.

$$Y_{in} = 2\sqrt{r^2 - x^2} \qquad (3)$$

where, r : tool radius, x : displacement in machining direction

The cutting width is seen to become convex as shown by the changes in the cutting width at the machining entrance in *FIGURE 7(a)*. Since the cutting width rapidly increases with the advance of the tool, build-up of machining load is sudden at the machining entrance. At the same time, tool deflection occurs, and form accuracy fluctuates considerably. After this, changes in cutting width decrease, and shape fluctuation becomes gradual. This is due to cutting towards both ends from the groove center at the machining entrance as shown in *FIGURE 6(a)*.

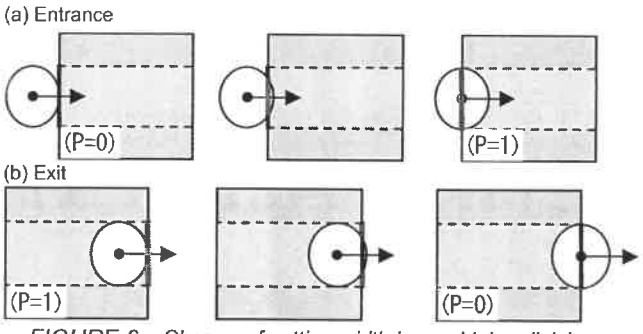

FIGURE 6 Change of cutting width in machining division

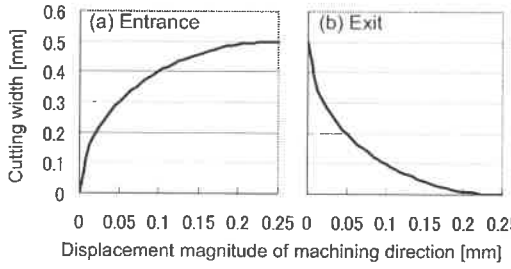

FIGURE 7 Change of cutting width at machining entrance

5. FLUCTUATION OF FORM ACCURACY AT MACHINING EXIT

5.1 Changes in cutting width at machining exit

The different form accuracy fluctuation seen at the machining exit from the machining entrance and why cutting depth is greater than the entrance were analyzed. *FIGURE 6(b)* shows changes in cutting width at the machining exit. The cutting width at the exit Y_{out} can be expressed by Equation 4.

$$Y_{out} = 2r - 2\sqrt{r^2 - x^2} \qquad (4)$$

where, r : tool radius, x : displacement in the machining direction

The cutting width is seen to become concave as shown in the changes in the cutting width at the machining exit in *FIGURE 7(b)*. Deflection rapidly decreases when the tool reaches the exit, and the shape fluctuation gradually becomes gentle. This is due to cutting, at the machining exit, towards both ends until the tool stops cutting at the tool diameter width. This results in different form accuracy fluctuation at the machining entrance and exit according to the fluctuation in cutting amount.

5.2 Verification by cross-sectional shape

The cross-sectional shape of a l =15.4mm groove was measured in order to investigate the reasons why cutting depth deepens at the machining exit. *FIGURE 8* shows the cross-sectional shape at the machining entrance and exit. At the machining entrance, as the tool approaches the work material vertically, the cross-sectional shape becomes a rectangle, thereby matching the cross-sectional shape of the tool. On the other hand, the cross section at the machining exit becomes an arc, due to tool bending which cause it to tilt.

5.3 Verification by cutter mark

FIGURE 9 shows the observation results at machining entrance and exit in heavy cutting load; where (a) is entrance, and (b) is exit. Cutter marks at the tip in the tool advance direction due to tool deflection can be seen from the machining entrance to the center. On the other hand, the cutter mark at the rear end of the tool advance

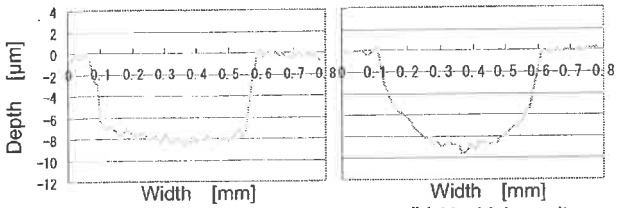

(a) Machining entrance (b) Machining exit

FIGURE 8 Cross-sectional shape at machining entrance and exit

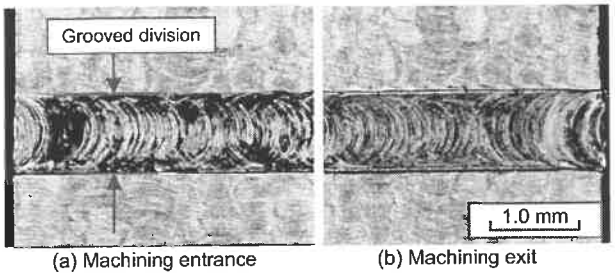

(a) Machining entrance (b) Machining exit

FIGURE 9 Observation results at machining entrance and exit in heavy cutting load machining

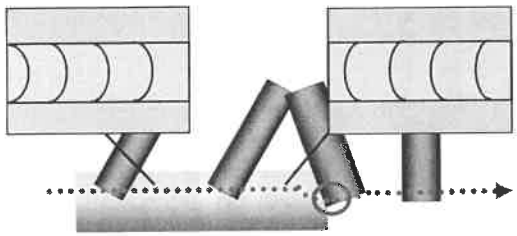

FIGURE 10 Fluctuation of tool at machining exit and cutter mark of machining form

direction gradually increases near the exit, and at the exit, there is only rear end cutter mark.

FIGURE 10 shows the fluctuation of the tool at the exit and the cutter mark at the base of the cut shape. At the exit, cutting load disappears as cutting amount decrease, and because the backlash pushes out the deflected tool, cutting is done by the rear end of the tool. The part circled in this figure is the part cut by the rear end. As a result, the groove cross- sectional shape becomes a circular arc, and in addition, the cutting depth is greater at the bottom. At the machining exit, the cutter mark gradually appears from the tip as cutting load decreases, and near the machining exit, only the cutter mark at the rear can be seen.

6. CONCLUSIONS

Groove shapes machined by a square end mill tool were analyzed. The following conclusions were obtained by verifying fluctuation in the form accuracy due to tool deflection, cross-sectional shapes at the machining entrance and exit, and cutter mark.

(1) For machining accuracy in the cutting depth direction during grooving, fluctuation in shape increases with increasing cutting depth, feed rate, and tool length. In particular, fluctuation is create at the machining exit greatly, due to reasons other than tool deflection.

(2) Fluctuation in form accuracy at the machining entrance corresponds to changes in the cutting width.

(3) Although the fluctuation in form accuracy at the machining exit increases proportionately to the changes in cutting width, fluctuation is greater at the entrance. As a result of the reaction of the tool deflection, cutting is done by the rear end of the tool in the tool advance direction.

7. FUTURE TASKS

Fluctuation of form accuracy at the machining entrance and exit caused by changes in the cutting width can be corrected by generating NC data taking into account the fluctuation along the depth direction. On the other hand, it is difficult to correct the phenomenon in which the tool is pushed out at the machining exit. This therefore requires setting of machining conditions that do not cause reaction.

REFERENCES

[1] S.Iso, N.Toida, Y.Kobayashi, K.Shirai: A Study on Accuracy Correction System of Surface Texture by End-Mill Machining, JSPE 2007 Spring Annual Meeting, Tokyo, Japan, Apr. 2007

[2] K.Tozawa, Y.Kobayashi, K.Shirai, Y.Hara, T.Kikuchi: Development of Surface Texturing System by Mechanical Machining, Journal of the Japan Society for Precision Engineering Vol.71 No.10, pp.879-884, 2005

[3] K.Tozawa, N.Toida, Y.Kobayashi, K.Shirai: Evaluation of Machining Accuracy by Measurement of Surface Texture Pattern, ASPE 2005 Annual Meeting, America Norfolk, Oct. 2005

TEMPERATURE AND STRESS ANALYSIS IN MICRO-CUTTING OF TI-6AL-4V AND AL7050-T6 WITH ADVANTEDGE

D. Lu[1,2], J.F. Li[1], Y. Rong[2], A. Grevstad[3], S. Usui[3]
[1]School of Mechanical Engineering
Shandong University
Jinan, China
[2]Department of Mechanical Engineering
Worcester Polytechnic Institute
Worcester, USA
[3]Third Wave Systems,
Minneapolis, USA

INTRODUCTION

High-precision miniaturized components are increasingly demanded in various industries, such as aerospace, biomedical, electronics, communications, and automotive. Mechanical micro-cutting is a fabrication method for creating miniature devices with high profile accuracy, surface finish quality at reasonably low cost. Therefore it is widely used to manufacture micro components. Compared with conventional cutting, some unique characterizes can be identified in micro-cutting. For example, the nose radius of the cutting tool plays critical role in chip formation. In micro scale, the nose radius could be the same as the grain size and the workpiece material property cannot be looked as uniformity. In order to analyze the difference between the conventional cutting and micro-cutting the fundamental mechanics of micro-cutting should be studied.

Experimental method has been used to investigate the mechanics of micro-cutting. The effects of cutting conditions on the machining forces, chip geometry, surface roughness, specific energy, shear angle and mean friction coefficient have been studied in orthogonal micro- and nano-scale cutting of Al7075-T6 [1]. The results indicate that when the uncut chip thickness is greater than the cutting edge radius of the tool (60~100 nm) the cutting force exhibits an approximately linear relationship with the uncut chip thickness. But when the uncut chip thickness is smaller than the edge radius of the tool, a non-linear variation in the cutting forces is observed and the size effect in the specific cutting energy is also non-linear. The feasibility of manufacturing annealed steel molds for micro component production using ultra fine grain tungsten carbide end mills are investigated and it was reported that the cutting tools represented the present bottleneck in the ongoing development of micro cutting technology [2]. A static chip formation model has been developed for micro-cutting of brass [3]. This model is able to account for the coupled minimum chip thickness and edge-radius effects.

At the same time, the finite element method was used to investigate the mechanics of micro-cutting. A finite element model was developed to predict the stress and temperature distribution in micro cutting of oxygen-free-high-conductivity copper [4]. The results indicated that the temperature was an important factor in micro cutting due to its influence on the flow stress. A train gradient plasticity-based finite element model was presented to predict the size effect in orthogonal cutting of aluminum alloy Al5083-H116 [5]. The analysis indicated that the strain gradient plasticity based model of orthogonal micro-cutting was able to capture the size effect in specific cutting energy. The finite element method was also used to analyze the orthogonal micro-cutting with the effect of the tool edge radius [6]. The results showed a good agreement with experimental cutting of copper with a sharp diamond tool. The minimum chip thickness of steel was determined by using the finite element method and it was reported the critical chip thickness was 0.2 and 0.3 times of the edge radius for pearlite and ferrite respectively.

However, these studies involved only the workpiece materials that are soft, ductile and easy to be machined. There is a need for investigations of micro-cutting of difficult-to-machine materials. Titanium and its alloys are considered as difficult-to-machine materials because of their low thermal conductivity, high

chemical reactivity, and low modulus of elasticity. The workpiece material chosen for this study is Ti-6Al-4V, which is often used in aerospace and biomedical industries. To make a compare the micro-cutting of Al-7075-T6 is also studied. The simulations were carried out with Third Wave Systems AdvantEdge machining simulation software.

MATERIAL MODELING

The flow stress is mostly influenced by temperature, strain, strain rate, and other factors. An accurate and reliable flow stress model is necessary to represent workpiece constitutive behavior during the cutting process. The material behavior is modeled by using the constitutive equation [7],

$$\left(1+\frac{\dot{\varepsilon}^p}{\dot{\varepsilon}_0^p}\right)=\left(\frac{\bar{\sigma}}{g\left(\varepsilon^p\right)}\right)^{m_1}, \text{ if } \dot{\varepsilon}^p \le \dot{\varepsilon}_t \quad (1)$$

$$\left(1+\frac{\dot{\varepsilon}^p}{\dot{\varepsilon}_0^p}\right)\left(1+\frac{\dot{\varepsilon}_t}{\dot{\varepsilon}_0^p}\right)^{m_1/m_2-1}=\left(\frac{\bar{\sigma}}{g\left(\varepsilon^p\right)}\right)^{m_2}, \text{ if } \dot{\varepsilon}^p > \dot{\varepsilon}_t \quad (2)$$

where $\bar{\sigma}$ is the effective Mises stress, g is the flow stress, ε^p is the accumulated plastic strain, $\dot{\varepsilon}_0^p$ is a reference plastic strain rate, m_1 and m_2 are low and high strain rate sensitivity exponents, respectively, and $\dot{\varepsilon}_t$ is the threshold strain rate which separates the two regimes.

And a power hardening law with linear thermal softening is given [7],

$$g=\left[1-\alpha\left(T-T_r\right)\right]\sigma_0\left(1+\frac{\varepsilon^p}{\varepsilon_0^p}\right)^{\frac{1}{n}} \quad (3)$$

where n is the hardening exponent, T is the current temperature, T_r is a reference temperature, α is a softening coefficient, and σ_0 is the yield stress at T_r.

FRICTION FORCE ON THE CHIP-TOOL INTERFACE

To obtain a reliable and realistic simulation result of metal cutting, it is essential to investigate the interaction between the cutting tool and the chip. The friction force is strongly influenced by cutting speed, contact pressure, and cutting temperature. Zorev's model [8] reveals two distinct regions on the chip-tool interface sliding region and sticking region. The normal and frictional shear stress distribution at the chip-tool interface is shown in Fig.1 [8].

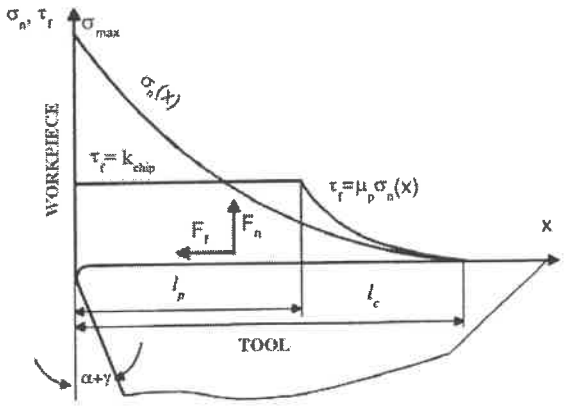

FIGURE.1 Curves representing normal (σ_n) and frictional stress (τ_f) distribution on the to rake face [8]

From the tip of the tool up to a point, frictional stress is considered constant in a sticking region. After this point, frictional stress decreases on the tool rake face in a sliding region where Coulomb's friction law can be used. This can be represented as follows.

$$\tau_f = \mu\sigma_n, \text{ when } \mu\sigma_n < k_{chip} \text{ (sliding)} \quad (4)$$

$$\tau_f = k, \text{ when } \mu\sigma_n \ge k_{chip} \text{ (sticking)} \quad (5)$$

where τ_f is the frictional stress, σ_n is the normal stress, μ is the coefficient of friction, and k_{chip} is the shear stress of the chip material.

FINITE ELEMENT MODEL DEVELOPMENT

When the cutting width is at least five times greater than the uncut chip thickness, the two – dimensional finite element model under plane strain assumptions can be applied. In this study the cutting width (1mm) is much greater than the uncut chip thickness (2 μm), so the plain strain assumption can be used. A schematic of the tool-workpiece configuration is shown in Fig.2. Simulations were performed with Third Wave Systems's machining simulation software AdvantEdge. AdvantEdge[9] is an explicit dynamic, thermo-mechanically coupled finite element model specialized for metal cutting. The element topology used is a six-node quadratic triangle element with three corner and three midsize nodes. In the simulation, the length of

the workpiece is 5mm, the height of the workpiece is 2mm, and width of cut is 1mm. The cutting tool material is single point diamond. The tool rake angle is 5^0, and the clearance angle is10^0, and tool edge radius is 1 μm .

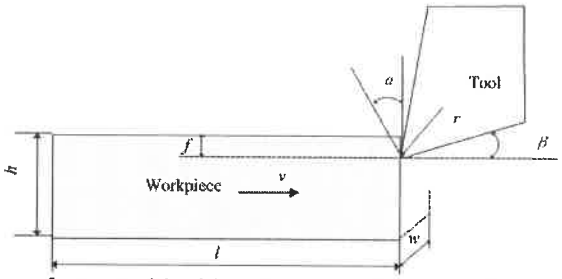

f: uncut chip thickness; *v*: cutting velocity;
w: width of cut; *h*: height of workpiece;
l: length of workpiece; *r*: tool edge radius;
α: relative rake angle;*β*: clearance angle.

FIGURE.2 Schematic of orthogonal cutting model

TEMPERATURE AND STRESS ANALYSIS

The cutting speed is 150m/min. The uncut chip thickness is 2 μm . The temperature and stress distribution were predicted for both Ti-6Al-4V and Al-7075-T7451.

Fig.3 and Fig.4 show the temperature distribution in micro-cutting of Ti-6Al-4V and Al-7075-T7451. In conventional cutting, the maximum temperature is located on the chip-tool contact surface. However, in micro-cutting of Ti-6Al-4V and Al-7075-T7451 the maximum temperature is located on the shear plane. In micro-cutting, the contact area between the chip and tool is small and the conductivity of the cutting tool is larger than the workpiece. The majority heat on the chip-tool contact surface is taken away by the cutting tool.

It is shown that with the same cutting tool and cutting parameters the cutting temperature of Ti-6Al-4V is much higher than the cutting temperature of Al-7050-T6. This is because that Ti-6Al-4V has low thermal conductivity, about 6 to 7 W/m.K (vs. 167W/m.K of aluminum alloys and 1600 W/m.K of diamond).The low thermal conductivity makes the heat difficult to transfer outside the deformation zone during the chip formation.

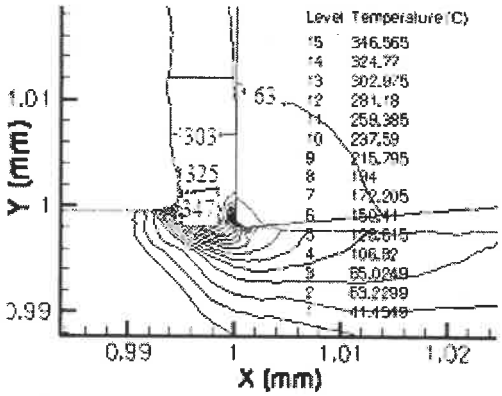

FIGURE.3 Temperature distribution of Ti-6Al-4V

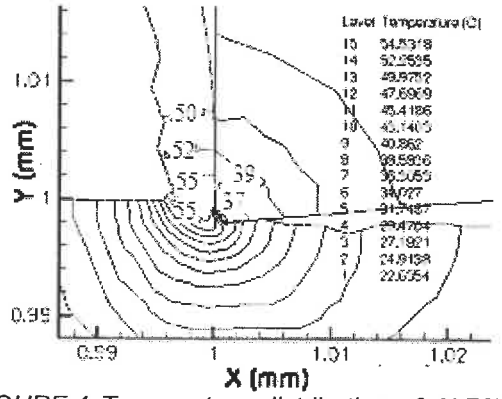

FIGURE.4 Temperature distribution of Al-7075-T6

Fig.5 and Fig.6 show distribution of the Mises stress distribution in micro-cutting of Ti-6Al-4V and Al-7050-T6 In conventional cutting, the maximum shear stress locations on the shear plan. The maximum Mises stress of workpiece exhibits in the region ahead of tool-chip contact surface. And in micro-cutting of Ti-6Al-4V the maximum Mises stress is much higher than in micro-cutting or Al-7050-T6. This is because that Ti-6Al-4V has low modulus of elasticity.

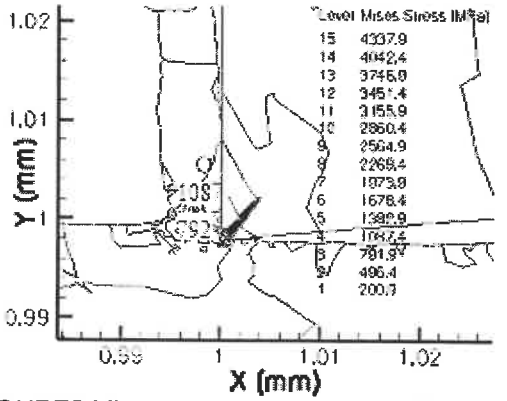

FIGURE5 Mises stress distribution of Ti-6Al-4V

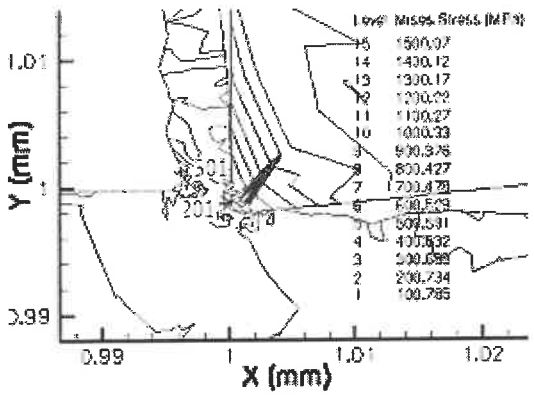

FIGURE.6 Mises stress distribution of Al-7075

CONCLUSION

In this paper, the temperature and the stress distribution in micro-cutting of Ti-6Al-4V and Al-7050-T6 are analyzed by finite element method. The following conclusions can be drawn from the simulation:

1. The simulation results show the difference of micro-cutting from conventional cutting in both cases of Al7050-T6 and Ti-6Al-4V materials. The maximum temperature location is on the shear plane in stead of on the chip-tool contact zone as in conventional cutting.
2. The location of the Mises stress is in the region ahead of tool-chip contact surface, which is also different from in conventional cutting maximum where the maximum shear stress location is on the shear plan.
3. The material property can affect the cutting temperature and the Mises stress observably. Because of Ti-6Al-4V is a difficult of machine material with low thermal conductivity, high chemical reactivity, and low modulus of elasticity, with the same cutting conditions the cutting temperature and Mises stress is much larger in micro-cutting of Ti-6Al-4V than in micro-cutting of Al-7050-T6.

REFERENCES

[1] Chee Keong Ng, Melkote, S.N., Rahman, M., 2006, "Experimental study of micro- and nano-scale cutting of aluminum 7075-T6," International Journal of Machine Tools & Manufacture, 46 (9), pp. 929-936.

[2] Schmidt, J., Tritschler, H., 2004, "Micro cutting of steel," Microsystem Technologies, 10 (3) pp. 167-174.

[3] Kim, Chang-Ju, Mayor, J., Ni, Jun, 2004, "A static model of chip formation in microscale milling," Transactions of the ASME, Journal of Manufacturing Science and Engineering, 126,(2), pp.710-718.

[4] Kim, K.W., Lee, W.Y., Sin, H.-C., 1999, "A finite element analysis for the characteristics of temperature and stress in micro-machining considering the size effect," Journal of Machine Tool and Manufacture, 39, pp.1507-1524.

[5] Liu, K., 2005, "Process modelling of micro-cutting including strain gradient effect," Ph. D thesis, Mechanical Engineering, Georgia Institute of Technology.

[6] Moriwaki, T., Sugimura, N., Luan S., 1993, "Combined stress material flow and heat analysis of orthogonal micromachining of copper," Annals of CIRP 42, pp. 75-78.

[7] Marusich, T.D., Ortiz, M., 1995, "Modelling and simulation of high-speed machining", International Journal for Numerical Methods in Engineering,126, (4),pp. 3675-3694.

[8] Zorev, N.N., 1963, "Interrelationship Between Shear Processes Occurring Along Tool Face and Shear Plane in Metal Cutting," International Research in Production Engineering, pp. 42-49.

[9] Third Wave Systems, Inc., 2006, "AdvantEdge v4.72 Machining Simulation Software," Minneapolis, MN

FIXTURING FOR ULTRAPRECISION MACHINING OF SPHERICAL PARTS

Richard L. Rhorer
Manufacturing Process Metrology Group
Manufacturing Metrology Division
National Institute of Standards and Technology
Gaithersburg, Maryland, USA

INTRODUCTION

Ultraprecision machine tools can generate very high quality spherical surfaces. For example, a cylinder with a spherical end is often used to evaluate the performance of a diamond turning lathe. The spherical surface is sometimes specified slightly past the equator to test how well the control system and machine handle the x-axis reversal (producing what is sometimes referred to as a "trailer-hitch ball" test part). A good machine can produce a spherical hemisphere (half of a full sphere) true to less than one μm, and if a diamond tool is used on an aluminum blank, a very shinny half sphere can be produced. A significant challenge arises when it is necessary to generate a full sphere—how do you hold on to one hemispherical surface while generating the other half? The two hemispheres must align very precisely to produce a true full sphere. The same problem arises when making spherical shells—if you first machine the outer radius, how do you hold on to the shell to make the inner radius and produce a uniform wall thickness?

This paper discusses the effects of the holding fixture precision on the overall part precision when machining a full-sphere or a hemispherical shell. Even if the machine tool generates a perfect hemisphere, a small error in the size of the spherical fixture (referred to as a pot chuck) holding the part for the second machining operation can produce a significant error in the alignment of the two hemispheres.

PROCESS STEPS

There are different procedures that can be used to produce spherical parts. A common process using an ultraprecision computer numerically controlled (CNC) lathe is described here. This process has many advantages; however, it is not the only process that can be used. Spheres can be produced by lapping and polishing, for example, but even then it is sometimes desirable to generate a very accurate full spherical blank before lapping. Also, a CNC lathe can generate thin walled hemispherical shells that can not be produced by lapping processes. The lathe process described in this paper involves generating a spherical end on a cylindrical blank and then turning the blank around and holding the spherical end in a chuck while machining the second half of the sphere. This process is illustrated in Fig.1, Fig. 2, and Fig.3.

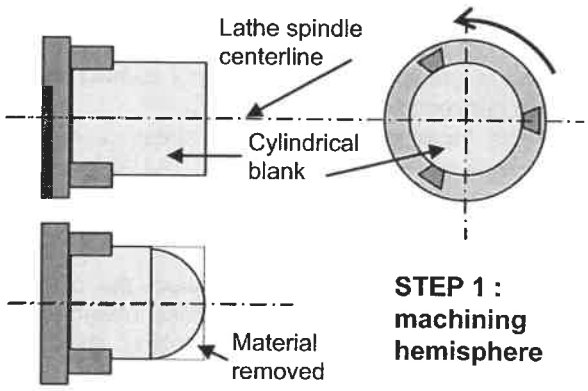

FIGURE 1. Step one of a full sphere machining process.

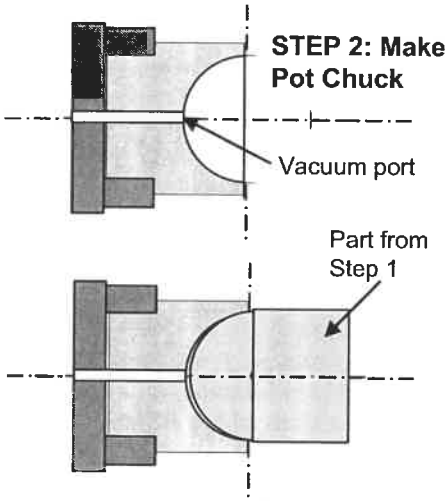

FIGURE 2. Vacuum Pot Chuck.

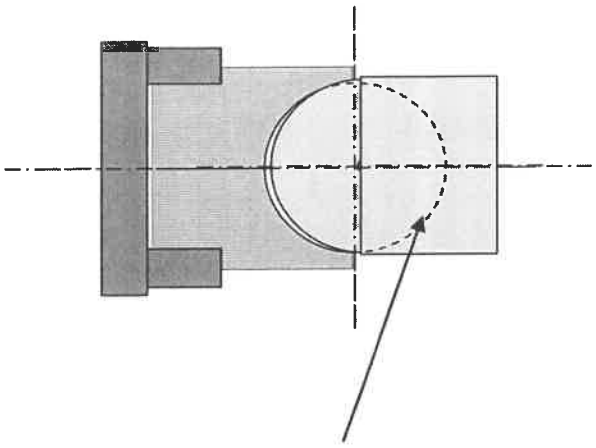

FIGURE 3. Machining second hemispherical surface.

Machine errors in producing spheres

The hemi-spherical surface is generated by programming a radius tipped tool to pass through a circular path in the x-z plane while the blank is turning about the spindle axis (usually referred to as the z-axis). The quality of the sphere in a pole-to-equator path depends on how precise the machine tool can generate a circular path. The truth of rotation of the spindle axis determines how precisely the resulting hemisphere is about any latitude sweep. How accurate a circular path the lathe can generate in the x–z plane determines how accurate the hemisphere is in the polar direction. The machine tool parameters and measuring methods used for machining the vacuum pot chuck are the same that are used for making the hemispherical part.

The case considered in this paper is for a lathe that can produce a near perfect circular path in the pole to equator direction, and has a near perfect spindle error motion. (That is to say that the machine tool can generate a hemispherical part far better than the sphericity requirement.) The case considered here is when, even though the lathe can produce a near perfect hemispherical surface, there is an uncertainty in the size of both the first hemispherical surface and the spherical cavity in the pot chuck—both can be perfect spheres but differ slightly in actual spherical radius.

In some cases the pot chuck can be made to fit almost perfectly to the hemispherical surface of Step 1 by special in-process measurements and carefully fitting each pot chuck to its unique hemisphere. However, the case considered here is the challenge when controlling or automating the process. How accurate does the process (machine tool positioning, tool set, etc.) need to be to make the part within tolerance without special fitting of the pot chuck to the first hemisphere?

If the pot chuck is slightly smaller than the part, a final "full sphere" will have a slight difference between the pole-to-pole height than twice the equator diameter as illustrated in Fig. 4.

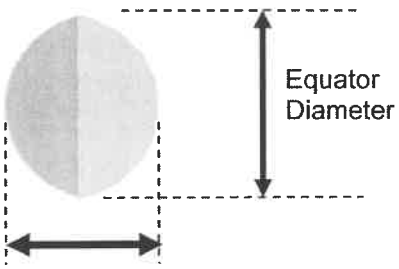

FIGURE 4. Full sphere machined as two hemispheres—some misalignment possible.

There are some process changes that would impact the final shape. For example, the process could be set up to ensure that the part be slightly smaller than the pot and always bottom in the pot; however, then the uncertainty of the size might allow the part to shift to one side during the machining that would produce a mismatch in center line between the two hemispheres. Also the case where the part is ensured to hit bottom can produce a situation where the part is not held tightly enough and can slip in the pot chuck during machining.

CONCLUSIONS

The case where the pot chuck is slightly smaller than the first operation hemispherical surface is important in many spherical part manufacturing situations. The discussion presented here suggests that the accuracy requirements for the machine tool and associated process is driven more by the match of the fixture to the part than by the sphericity tolerances of the part itself.

SHRINKING LEAD TIMES WITH MICRO TECHNOLOGY

Lee Richmond
Makino, Auburn Hills, MI 48326

Improving lead time continues to be the constant driver in business today. It's even more challenging trying to improve quality at the same time. Selecting the proper processes and machining strategies is critical to achieving success in mold building and other manufacturing industries. When to direct machine versus EDM continues to be in question as technologies change. Now, utilizing a .10mm diameter end mill is realistic in hardened tool steel. It does have limitations and specific requirements pertaining to tool-holding, programming techniques, and cutter technology. It also taxes the ability of the machine tool itself – spindle technology, servo control and tool length measuring capabilities are all critical to achieving success. See lead time comparisons and learn about the technologies and challenges in micro milling during the build of a medical staple mold. We'll show when the elimination of process steps reduce lead time and part quality, where that threshold is and when EDM is again the more economical approach. We will also discuss machine design characteristics necessary to achieve the high accuracy and surface finishes required in such processes.

PRECISION DRILLING OF CFRP (CARBON FIBER REINFORCED PLASTICS) WITH COATED TOOLS

Shigehiko SAKAMOTO[1], Yusuke KAJIWARA[1], Heiji YASUI[1]
[1]Department of Advanced Mechanical Systems
Kumamoto University
2-39-1, Kurokami, Kumamoto, JAPAN

INSTRUCTIONS

CFRP (Carbon Fiber Reinforced Plastics) is well known as a difficult-to-cut material which has very strong physical and mechanical characteristics. When the CFRP is machined by cutting technique, cemented-carbide tool is widely used. Furthermore, diamond cutting tools and PCD (Polycrystalline diamond) tools are also used in these days instead of cemented-carbide tools in order to improve the accuracy of high precision drilled holes. However the tool life of diamond tools is too short to use as a normal cutting tool for CFRP products because tool costs are too expensive. Cutting tools for CFRP which have long tool life are required by several kinds of industries such as aviation industry, automobile factories and so on [1], [2]. On the other hand, cutting tools are remarkably developed for many kinds of difficult-to-cut materials by the coating technology of cutting tool which are Chemical Vapor Deposition (CVD) coatings, Physical Vapor Deposition (PVD) coatings and so on. In our research, it is investigated that the various twist drill bits and ball nose end mills are examined for precision drill-out techniques of CFRP plates.

EXPERIMENTAL SETUP

The experiments are executed by drilling tests of 120 holes on CFRP plates with common twist drills which are set on the vertical type of machining centers "V33" or "SV-400" as shown in Fig. 1. Each drilled holes on the CFRP panel of 2.78 mm are investigated in terms of cutting forces which are measured with dynamometer system. The main experimental conditions are summarized in Table 1. Drilling tests with the various kinds of twist drills which are made by cemented-carbide, high-speed steel, TiAlN PVD-coated-cemented-carbide, DLC (Diamond-Like Carbon) coated-cemented-carbide are carried out in dry condition without cutting fluid. The high-precision drilled holes are evaluated by diameter of holes and quality of drilled exit side. The drill-out holes are observed with the digital fine scope camera. Then tool wear of every drill used in our experiments which are affected from micro fiber of composite materials is also observed.

EFFECT OF DRILLING TOOLS

In the experiments cutting speed and feed rate are set to 100 m/min and 0.05 mm/rev, respectively, which are common values for CFRP drilling process. Exit sides of holes drilled

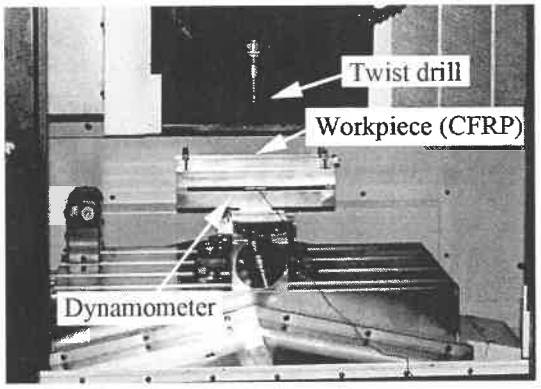

FIGURE 1. Experimental setup on V33

TABLE 1. Experimental conditions

Machine tools:	Vertical type of machining Center V33 (Makino), SV-400 (Mori seiki)
Cutting tools:	Twist drill, Ball nose end mill: Cemented-carbide, High speed steel, TiAlN PVD-coated, DLC coated Diameter: d = 6.0 mm Number of cutting edge: 2
Workpiece material:	Carbon Fiber Reinforced Plastics 8 Layers Thickness: h = 2.78 mm
Cutting fluid:	Dry
Cutting conditions:	Cutting speed: Vc = 100, 300 m/min Feed rate: f = 0.05 mm/rev

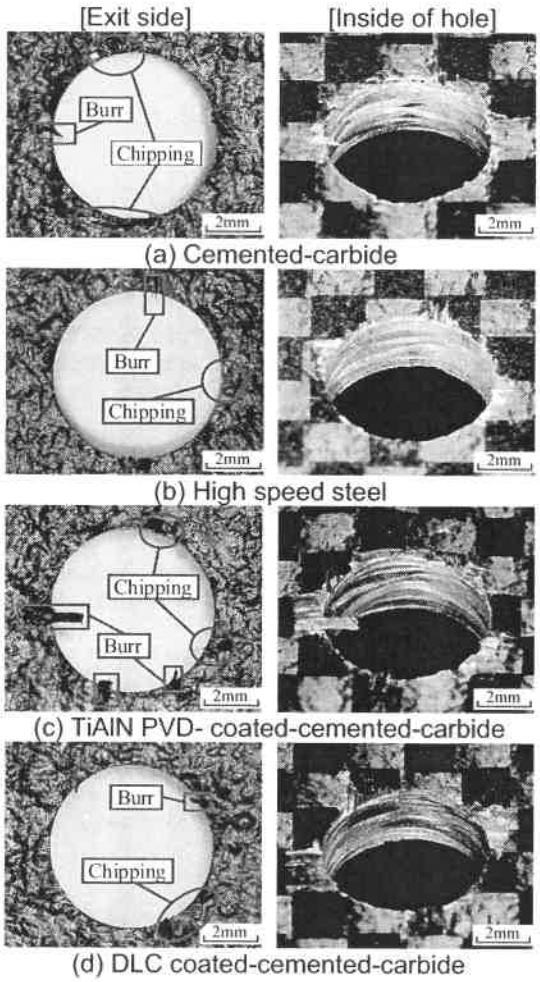

FIGURE 2. Microphotographs of exit side on the drilled CFRP plate by using various twist drills [Vc = 100 m/min]

by using the 4 kinds of brand-new twist drills are observed by microscope in Fig. 2. There are some burrs and chipping on the exit side of drilled holes in spite of first machined drilling hole. In case of cemented-carbide tool and high speed steel twist drills, burrs and chippings are very small size as shown in Fig. 1 (a), (b). When TiAlN PVD-coated-cemented-carbide twist drill bit was used, drilled holes in Fig. 1 (c) have huge burrs which are over 1.0 mm in length. The inside of drilled hole, however, has very good quality which is most clearly to see every layer of CFRP plate. Drilled hole by using the DLC coated-cemented-carbide twist drill also has small burrs and chippings. Inside of drilled hole with DLC coated tool is similar to results by normal cemented-carbide tool as shown in Fig. 1

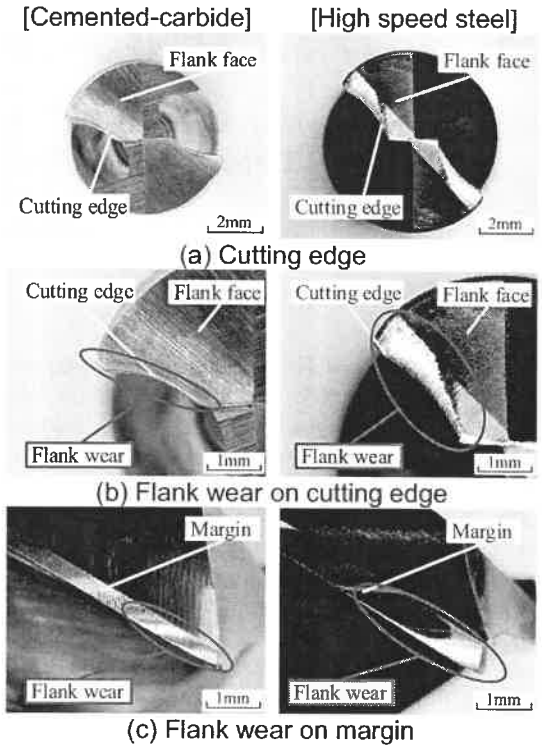

FIGURE 3. Microphotographs of Twist drill bits cutting edges after 120 drilling processes

(a)-right and (c)-right. Boundary lines of each CFRP layer inside the both drilled holes are not clear.

EFFECT OF SHARPNESS ON CUTTING EDGES

Tool wears of twist drill bits are observed after the 120 drilling processes. Flank wears of cemented-carbide and high speed steel twist drills are shown in Fig. 3. Flank wear of cutting edge on the top of cemented-carbide twist drill bit is smaller than that of high speed steel. There are huge flank wears on the cutting edge and margin of high speed steel twist drill bit. The bigger wears exist on the outer side of twist drill bit. In case of high speed steel twist drill, the quality of drilled holes is remarkably downgrade after very short drilling processes which are about only 10 drilling holes. It is declared that cemented-carbide tool is more suitable for CFRP drilling. Cemented-carbide tool can be used for CFRP drilling processes without cutting fluid at least 100 drilling holes. Sharp cutting edge of brand-new high speed steel twist drill is more effective for CFRP drilling because good result of drilled hole is obtained

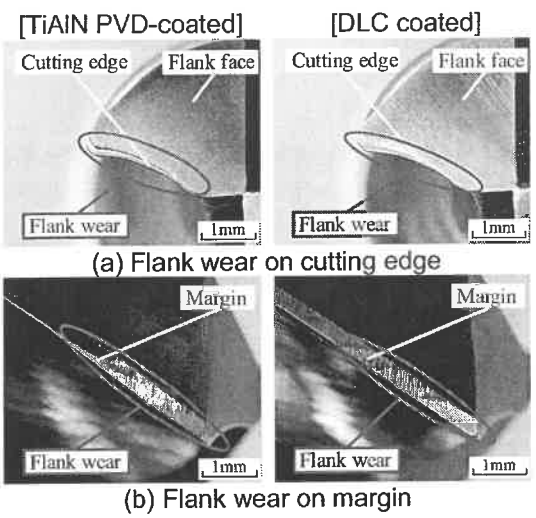

FIGURE 4. Microphotographs of Twist drill bits cutting edges after 120 drilling processes [Vc = 100 m/min]

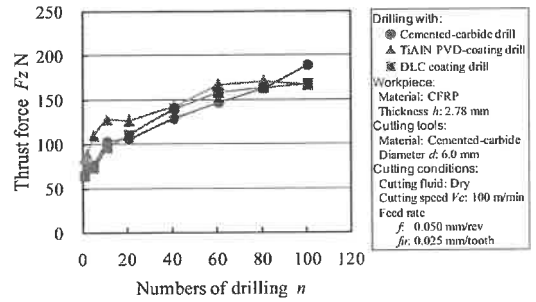

FIGURE 5. Effect of drilling numbers on thrust force of CFRP drilling processes with twist drills at Vc of 100 m/min

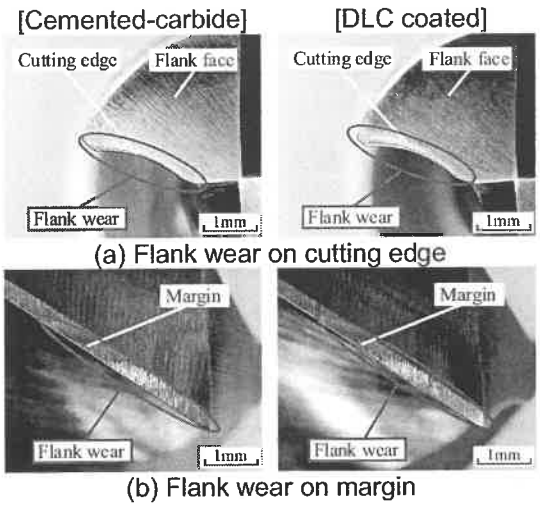

FIGURE 6. Microphotographs of Twist drill bits cutting edges after 120 drilling processes [Vc = 300 m/min]

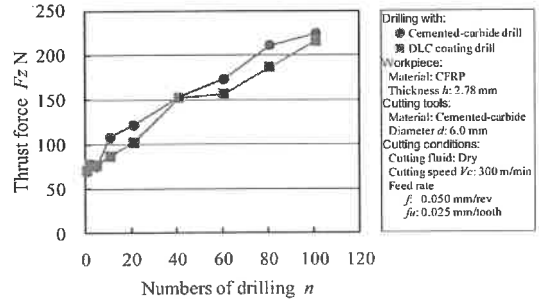

FIGURE 7. Effect of drilling numbers on thrust force of CFRP drilling processes with twist drills at Vc of 300 m/min

until 10 drilling processes. High speed steel, however, has not enough hardness to cut composite materials like CFRP.

Due to find out the effects of coated materials TiAlN PVD and DLC coated-cemented-carbide twist drills which are used for 120 drilling processes of CFRP plates are also observed by microscope as shown in Fig. 4. Both of the coated tools have obviously worn the coating material on the cutting edge and margin. Width of flank wear on the cutting edge and length of worn area on the margin are almost same. Thrust forces in drilling processes with every kind of twist drill bits are summarized in Fig. 5. Every thrust force is increasing slowly with the number of drilling holes. But there are great differences on the trend of thrust forces. Until the 20 drilling holes the thrust forces used with TiAlN coated twist drill bit are slightly bigger than other two kinds of drills which are cemented-carbide and DLC coated-cemented-carbide twist drill bits. The thickness of coating layer on the twist drill bit affects on the quality of drilled holes and thrust forces in the drilling time. DLC coat is very thin below 1 micro-meter. TiAlN PVD-coat is, on the other hand, almost 5 micro-meters. TiAlN coated tool lose sharpness on the cutting edge because of thickness of coating layer. When the cutting edges on the every twist drill are roundly worn after the 20 drilling processes, the thrust forces are close to same levels. DLC coating is very thin and efficient for keeping the sharpness of cutting edges.

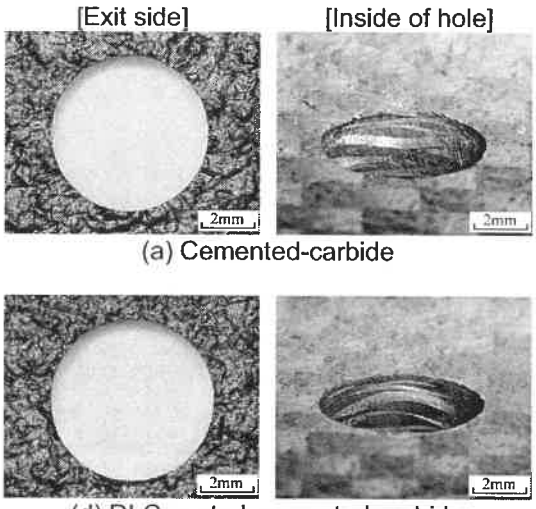

FIGURE 8. Microphotographs of exit side on the drilled CFRP plate by using two kinds of ball nose end mills [Vc = 300 m/min]

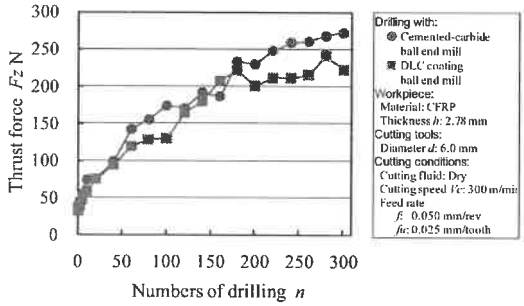

FIGURE 9. Effect of drilling numbers on thrust force of CFRP drilling processes with ball end mill at Vc of 300 m/min

EFFECT OF CUTTING SPEED

When cutting speed is changed to 300 m/min, flank wears are obtained similarly as shown in Fig. 6. Thrust forces are almost same level by comparison with difference in cutting speeds *Vc* of 100 and 300 m/min in Fig. 7.

Furthermore, ball nose end mills are applied at the high speed cutting of 300 m/min. The best quality of drilled holes without burrs and chippings is obtained by using both of cemented-carbide and DLC coated-cemented-carbide ball end mills as shown in Fig. 8. The layers of CFRP are also clearly machined inside the drilled holes. Thrust forces are measured until the 301 drilling holes as shown in Fig. 9. Thrust forces with DLC coating ball end mill are lower than that with cemented-carbide ball end mill. By using ball end mill the thrust force is below 200 N until the 150 drilling processes. The ball nose end mill is useful for precision drilling techniques of CFRP. At high cutting speed the ball end mill is also suitable to drill-out process of CFRP panel. DLC coating ball end mill is better tool than solid one because thrust forces are stable and drilled holes have better quality. Tool life of DLC coated tool is, however, as same as that of cemented-carbide tool.

CONCLUSIONS

It is evaluated that the various twist drill bits and ball end mills affect to the precision drilled holes of CFRP plates. The main conclusions are summarized as follows:

1. The sharp cutting edge of brand-new high speed steel is effective for CFRP drilling until the depth of 27.8 mm when the tool wear is not huge on the cutting edges.

2. The thickness of coating layer on the twist drill affects on the quality of drilled holes and thrust forces in the drilling time because the coating has made the roundness of cutting edge. DLC coating is very thin and efficient for keeping the sharpness of cutting edges.

3. Ball nose end mills are suitable for CFRP drilling at the high cutting speed of 300 m/min. DLC coating ball end mill is also useful to drilling technique of composite materials like CFRP panels.

ACKNOWLEDGEMENT

The authors would like to thank Sumitomo Electric Industries, Ltd., Sumitomo Electric Hardmetal Corp., Makino Milling Machine Co., Ltd., TOHO TENAX Co., Ltd and Alexander von Humboldt Foundation in Germany.

REFERENCES

[1] Tönshoff, H.K.; Friemuth, T.; Groppe, M.: High efficient circular milling – A solution for an economical machining of bore holes in composite materials (CFK, Aluminium), Proceedings of 3rd international conference on metal cutting and high speed machining, Metz, France, 2001, 287-296.

[2] Brinksmeier, E.; Koch, T.; Kube, D.; Walter, A.: Orbital milling of multi-layer composite materials consisting of aluminium alloy, carbon fiber reinforced plastics (CFRP) and titanium alloys, Production Engineering Vol. XI/1, Annals of WGP, 2004.

EFFECT OF DRILL SHAPES ON THE DRILL-OUT OF CFRP (CARBON FIBER REINFORCED PLASTICS)

Shigehiko SAKAMOTO[1], Yusuke KAJIWARA[1], Heiji YASUI[1]
[1]Department of Advanced Mechanical Systems
Kumamoto University
2-39-1, Kurokami, Kumamoto, JAPAN

INTRODUCTION

CFRP (Carbon Fiber Reinforced Plastics) has higher specific strength, modulus of elasticity and so on. In the application for aviation industries, CFRP are remarkably used for many parts of airplane structures. It will be also widely applied for automobile parts in the future. However, CFRP is well known as difficult-to-cut material which has very strong physical and mechanical characteristics. Drilling technique of CFRP which is one of the most important cutting operations is currently carried out in industrial factories. These manufactured parts have containing many precision holes for various purposes such as rivet holes. There are many typical problems in the precision drilling processes of CFRP plates which are burrs, chippings and delamination of composite materials, rapid wear of drilling tools and so on [1]. In this research, it is considered that the effect of drilling tools which have different shapes on the machining accuracy of drilling holes on CFRP plates.

EXPERIMENTAL SETUP

The experimental conditions are summarized in Table 1. CFRP drilling tests are executed without cutting fluid on the vertical type of machining center "SV-400". The workpiece material used in the experiments is 8 cross-ply laminates of CFRP which thickness h is 2.78 mm. Drilling tools used are cemented-carbide twist drill, cemented-carbide square end mill and cemented-carbide ball end mill with diameter d of 6.0 mm. Cutting speed Vc and feed rate f are 100 m/min and 0.05 mm/rev, respectively. Experimental setup of machining center is shown in Figure 1. In order to keep drilling environment clean because chips of CFRP which are very small are scattered around the machining points, the hood which are connected with dust collection machine is attached to the spindle head. Due to development of drilling techniques on CFRP plates, thrust forces in the drilling processes are measured with dynamometer system which is set load cell on the jig. Drilled holes are evaluated by accuracy of diameter. Qualities of drilled inside and exit side on CFRP plate are observed with the digital fine scope camera. Abrasive tool wear on the top and side of cutting edges are also observed.

TABLE 1. Experimental conditions

Machine tool:	Machining Center SV-400
Cutting tools:	Cemented-carbide twist drill Cemented-carbide square end mill Cemented-carbide ball end mill Diameter: d = 6.0 mm Number of cutting edge: 2
Workpiece material:	Carbon Fiber Reinforced Plastics Thickness (8 layers): h = 2.78 mm
Cutting fluid:	Dry
Cutting conditions:	Cutting speed: Vc = 100 m/min Feed rate: f = 0.05 mm/rev

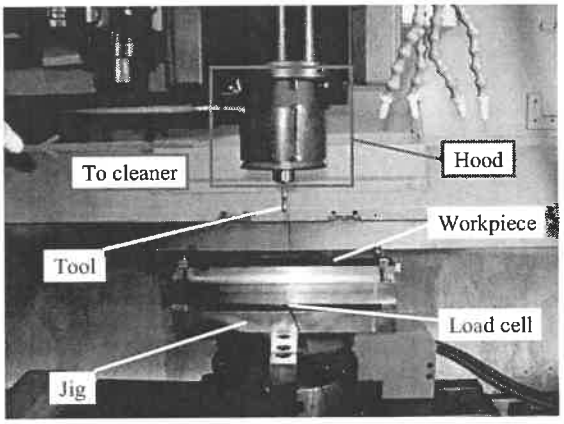

FIGURE 1. Experimental setup

RESULTS AND DISCUSSIONS

Figure 2 shows microphotographs of drilled holes at the 1st drilling process. In case of twist drill, small burrs and chippings are observed on the exit side of drilled holes on the CFRP plates.

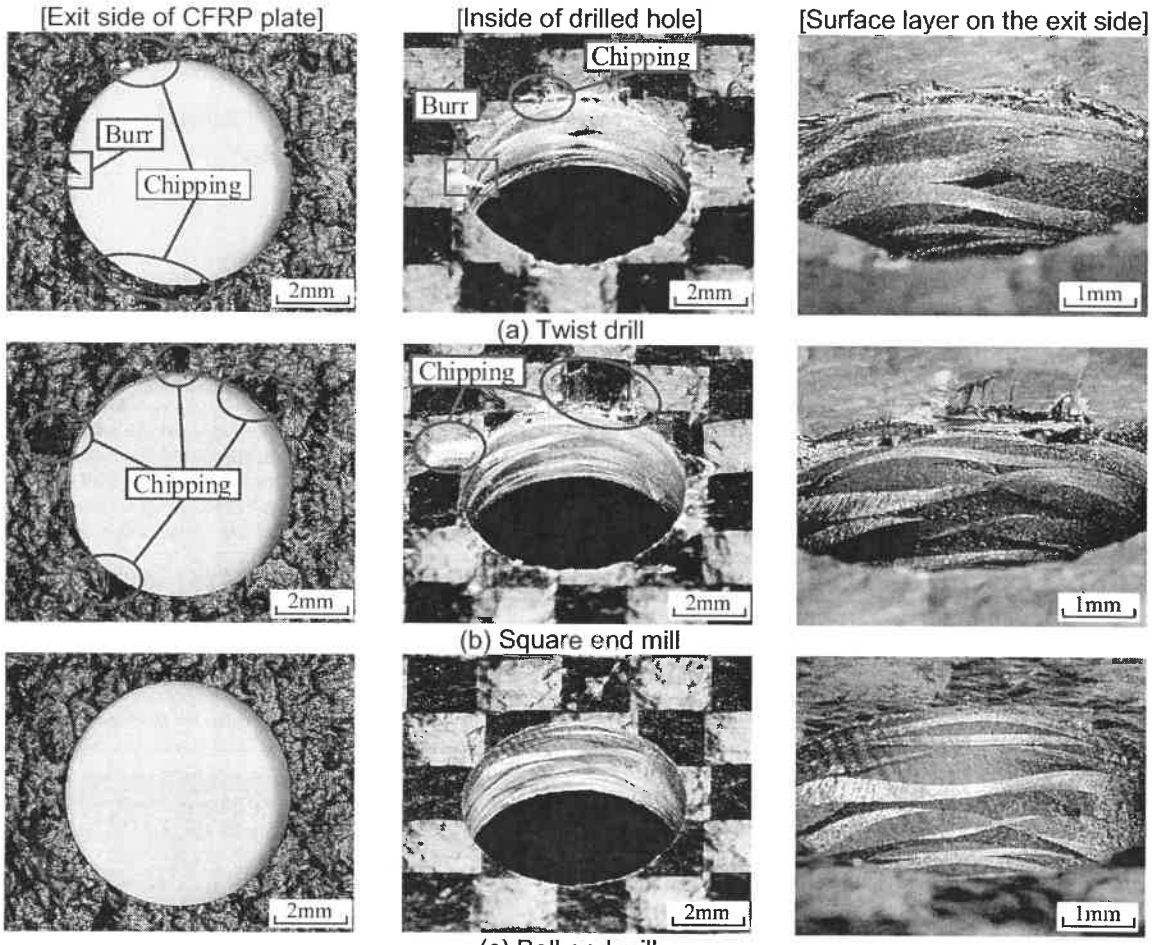

[*Vc* = 100 m/min, *f* = 0.05 mm/rev, Dry]

FIGURE 2. Microphotographs of drilled holes on the 1st drilling process

Length of burrs and chippings are less than 0.5 mm. Delamination which causes layers to separate is occurred on the exit side layer in spite of 1st drilling process as shown in Fig. 2 (a). Thrust force *Fz* during the drilling processes with twist drill is about 66 N. In case of square end mill, large chippings which sizes are over 1.0 mm are existed on the exit side of CFRP plate. Thrust force *Fz* with square end mill is, however, reduced to 49 N. The quality of inside the drilled hole by using the square end mill is much better than that by using twist drill. Boundary line of CFRP laminates is observed clearly as shown in Fig. 2 (b)-right. The best quality of drilled holes without any defections is obtained by using the ball end mill. Thrust force *Fz* in drill-out processes with ball end mill is only 21 N that is smallest value against other drilling tools. In addition, the best quality of inside the drilled holes without delamination is also observed in Fig. 2 (c)-right. When the twist drill and square end mill are used for drill-out of CFRP panel, good quality of drilled holes are kept until 20 drilling processes which are depth of only 55.6 mm. High quality precision drilled holes are, on the other hand, obtained by using ball nose end mill until 80 drill-out processes which are useful as drilling technique of CFRP.

Microphotographs of tool wear after 120 drilling processes are shown in Figure 3. Flank wears appear on the outer corner of all drilling tools. Area of tool wears on the margin of twist drill bit is widely observed as large as the drilled depth of CFRP plate used in the experiments. Flank wears on the peripheral cutting edges of square and ball nose end mills, on the other hand, have narrow width and long length because both end mill has clearance angel on the side cutting edges. Thrust forces *Fz* during the drill-out

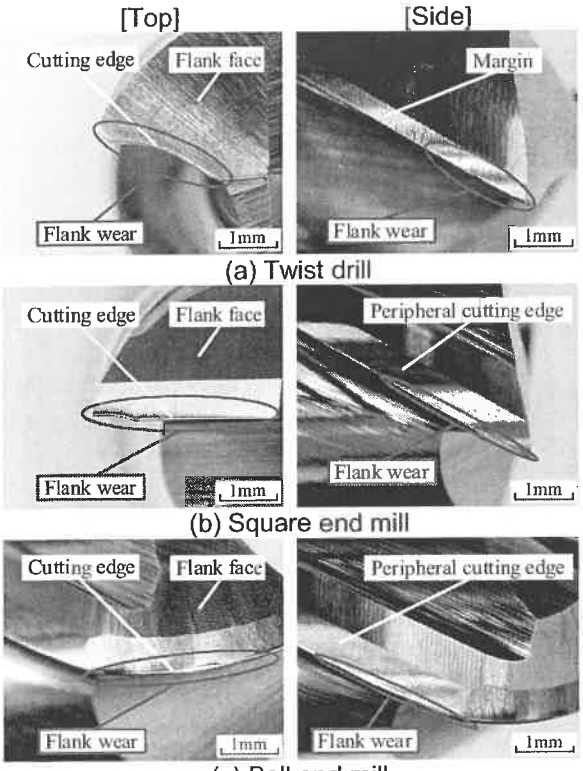

[*Vc* = 100 m/min, *f* = 0.05 mm/rev, Dry]

FIGURE 3. Microphotographs of tool wear on the cutting edges after 120 drilling processes

processes are affected by drilling numbers on the CFRP plates as shown in Fig.4. Cutting edges are rounded step-by-step by increasing the drilling values of CFRP. Thrust forces *Fz* during the drilling processes with ball nose end mill increase from 21 N to 107 N at the 1st to 101st drilling processes. Thrust forces *Fz* with ball end mill is a half level against other two tools. Furthermore, drilling tests with twist drill and ball end mill are extended until 1,000 drilling processes as shown in Fig. 5. Thrust forces *Fz* continue to increase with the numbers of drilling processes. Thrust forces are depends on the tool wear of cutting edge on the drilling tool.

Diameters of drilled holes which are measured by caliper type of inside micrometer are summarized in Fig. 6. In case of twist drill, the diameters are slowly decreasing with drilling numbers of CFRP plates. The diameters by using ball end mill is rapidly changed to small at the early phase of drilling processes which are until 200 drilling processes. Tool wears on the side cutting edges of twist drill and ball end mill after the 1,000 drill-out processes are shown in

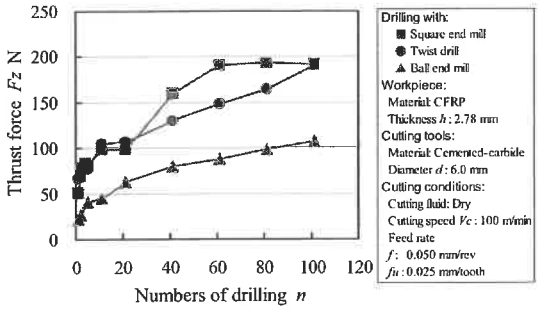

FIGURE 4. Effect of drill numbers on the thrust force of CFRP during the 120 drillings

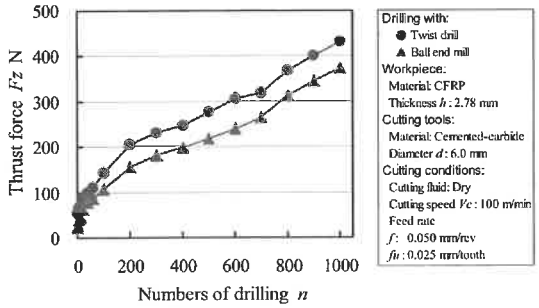

FIGURE 5. Effect of drill numbers on the thrust force of CFRP during the 1,000 drillings

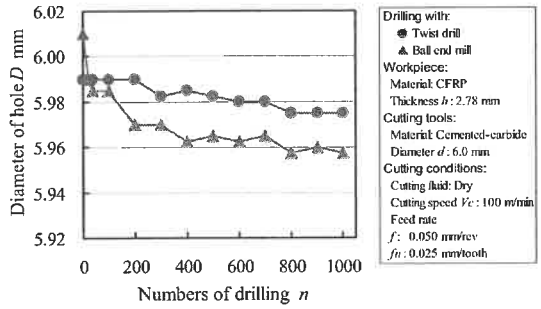

FIGURE 6. Effect of drill numbers on the diameter of drilled holes

Fig. 7. Tool wear of margin on the twist drill is grown wide area which is about 3 mm along the depth direction for drill-out processing. Tool wear of peripheral cutting edges on the ball end mill which is as same size as that of twist drill bit is expanded width in the direction of clearance face. Margin of side cutting edges on the twist drill is observed in Fig. 8. (a). Width of margin is about 300 micro-meter and have no clearance angle. Clearance face of peripheral cutting edge on the ball end mill has sharp cutting edge and about 9 degree of clearance angel as shown in Fig. 8. (b). When the peripheral cutting edge is worn, the diameter of ball end mill becomes small along the radial direction. The margin has,

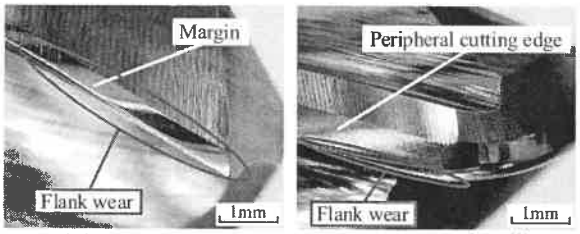

(a) Twist dril (b) Ball end mill

[*Vc* = 100 m/min, *f* = 0.05 mm/rev, Dry]

FIGURE 7. Microphotographs of tools after 1,000 drilling processes

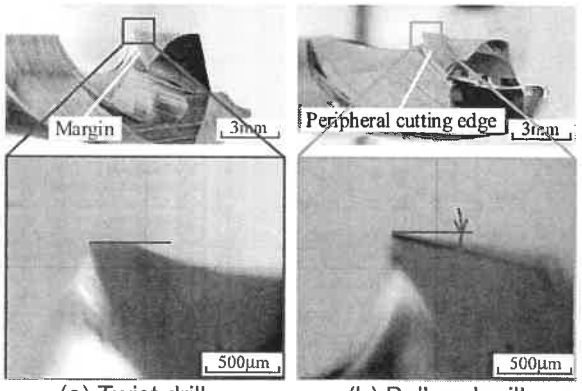

(a) Twist drill (b) Ball end mill

Figure 8. Microphotographs of peripheral relief angle

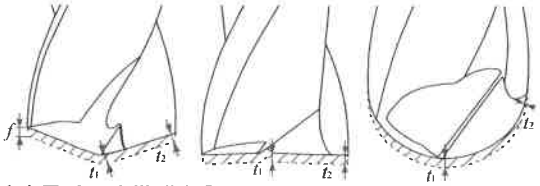

(a) Twist drill (b) Square end mill(c) Ball end mill

FIGURE 9. Schematic of removal rate by feed of drilling tools

on the other hand, a role of the guide in drilling processes and there is no peripheral relief angle. Therefore, margin of twist drill is always contacted to the inside of drilled hole. Margins are worn off wide along the drilling direction, but wear rate of drill diameter is very small.

Schematics of cutting volumes by feed rate of drilling tool which have 6 mm in diameter are shown in Fig.9. It is defined as t_1 and t_2 at the position from the center i = 0.1 and 2.9 mm, respectively. Relationship between t_1 and feed rate f are almost equal in all of three tools. In addition, in case of twist drill and square end mill, $t_1 = t_2 = f$ is also true because of their straight shape of cutting edge. The removal rate at outer corner edge becomes much larger than that of center edge. Therefore, it is considered that outer corner edge is damaged and quality of

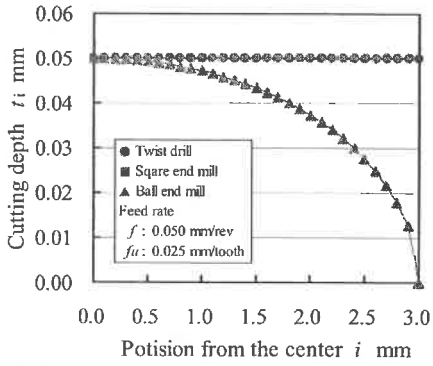

FIGURE 10. Relationship between radical position of tool edge and cutting depth

drilled holes become worse. When ball nose end mill is used by feed rate of 0.050 mm/rev, on the other hand, outer cutting volume t_2 = 0.013 mm is smaller than center cutting volume t_1 = 0.050 mm as shown in Figure 10. Then It is possible to obtain high-precision drilled holes by using ball end mill.

CONCLUSIONS

The main conclusions obtained are as follows:

1. Thrust forces *Fz* with twist drill increase from 66 N to 190 N at the 1st to 101st drilling processes. In case of ball end mill, thrust forces are similarly increasing from 21 N to 107 N which are smaller than other tools.
2. High-precision inside of drilled holes are obtained by the end mill and ball end mill. In order to improve the quality of drilled holes of CFRP plate, it is significant factor that peripheral cutting edges have clearance angle.
3. Cutting depth of outer corner edge on the ball end mill is smaller than that of other drilling tools. Shape of ball end mill is efficient for composite materials like CFRP plate. Drilled holes by ball end mill have good quality without any burrs, chippings and delaminations.

ACKNOWLEGEMENTS

The authors would like to thank SUMITOMO ELECTRIC INDUSTRIES, Ltd, MAKINO MILLING MACHINE Co., Ltd, TOHO TENAX Co., Ltd

REFERENCES

[1] S. Sakamoto, Y. Kajiwara, H. Yasui: Study on drilling process of CFRP (Carbon Fiber Reinforced Plastics), -Influence of cutting tools on machining accuracy- (in Japanese), Proceedings of autumn conference of JSPE, Utsunomiya, 2006.

RAKE ANGLE VARIATION IN DIAMOND TURNING

Alex Sohn
Precision Engineering Center
North Carolina State University
Raleigh, North Carolina

INTRODUCTION

When turning non-rotationally symmetric (NRS) surfaces using a fast-tool servo (FTS), the rake angle of the tool effectively changes as a function of the surface slope. As fast tool servos find ever more applications and are pushed to ever larger strokes and higher operating frequencies, the diamond tools used on them tend to encounter larger variations in rake angle. Recent experiments at the Precision Engineering Center (PEC) have pushed this envelope to variations in rake angle of up to 90 degrees. The effect on figure, finish and tool life is substantial, so a quantization of the errors is needed. The varying tool forces are the main contributor to rapidly changing cutting conditions. These tool forces have been measured in various cutting experiments with the goal of determining optimum rake angles for machining. Large negative rake angles produce large thrust forces whereas large positive rake angles require large clearance angles and, hence, fragile tools. With advance knowledge of the tool forces and the material being cut, an optimum initial rake angle may be found.

The example case studied here involves a 6 mm diameter cylinder with sine waves machined around the periphery. This part was machined at the PEC with a piezoelectric fast tool servo of 20 µm range and 1 kHz bandwidth. A magnified cross-section is shown in Figure 1. Two observations in making these parts led to this investigation of tool forces: 1) significant distortion in the shape of the sine waves and 2) abnormally high tool wear given the short cutting distances and small depths of cut.

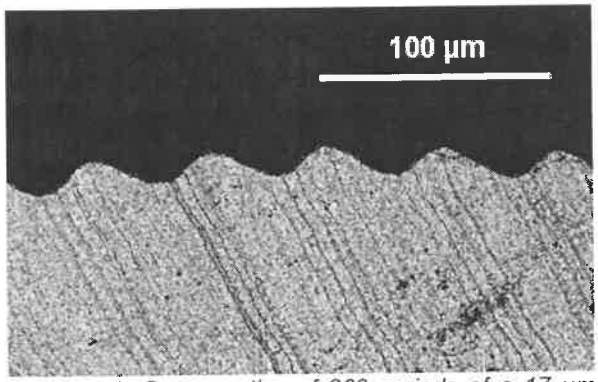

FIGURE 1. *Cross-section of 360 periods of a 17 µm sine waves on a 6 mm dia cylinder*

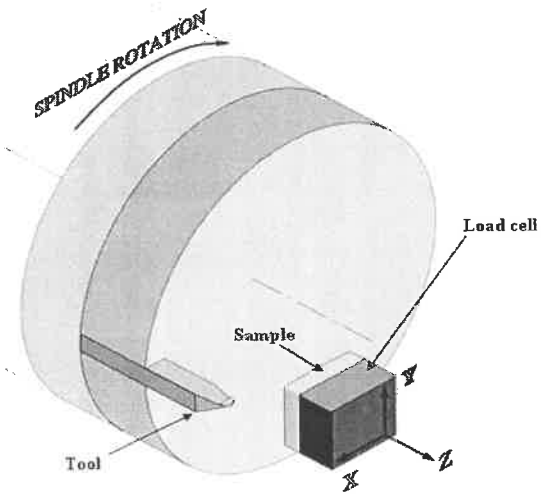

FIGURE 2. *Schematic showing setup for tool force measurements.*

TOOL FORCE MEASUREMENTS AS A FUNCTION OF RAKE ANGLE

To get an idea of the force variation involved in cutting these sinusoidally figured parts, the forces had to be measured. Previous investigations into tool forces at the PEC [1, 2] by Arcona and Drescher did not measure the effect of varying rake angles, though efforts to assess tool forces at normal (0° rake) incidence were successful.

The experimental setup used for measuring forces (Figure 2) involved placing a sample on a Kistler 9251A piezoelectric load cell and collecting force data while the sample was flycut. The interrupted cut avoided the problem of charge loss in the piezoelectric load cell, though some ringing at the beginning of each cut had to be truncated from the data. The sample was electroless nickel plated copper and was fixed while the rotating tool could be repositioned at varying rake angles. The tool clearance angle of 12°, however, limited positive rake angle

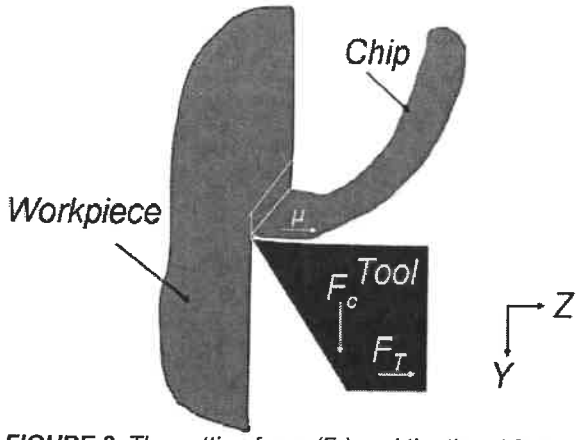

FIGURE 3. *The cutting force (F_c) and the thrust force (F_t) are measured with respect to the shown axis orientations of the machine*

measurements to 10°. The measured cutting and thrust force orientations are shown in Figure 3. The force directions are fixed with respect to the surface of. the workpiece as the tool is rotated through different rake angles. A sample measurement is shown in Figure 4. The plot shows one pass over the sample at 0° rake angle. Data was collected at 5 kHz. Cuts were made with the tool positioned at 0°, 10°, -10°, -20° and finally 0° again. The freshly lapped tool had a conical nose radius of 0.5 mm. Each cut was performed with a 20 µm upfeed and a 10 µm depth of cut at 120 rpm spindle rotation. The final results for force measurements are tabulated in Figure 5. Each data point represents an average of 20 passes over the workpiece.

A least-squares 2nd-order polynomial curve fit allows extrapolation to larger rake angles. Future experiments using large-clearance tools and a larger adjustment range of tool angle will actually allow data collection at rake angles larger than 20°.

IMPACT ON FIGURE ERROR

While tool forces are always present in machining, constant forces usually have little impact on figure error, particularly in ordinary turning applications when stiff toolposts are used. Fast-tool servos typically are limited in their static stiffness, however, and varying forces can cause them and the workpiece to deflect. Particularly on small parts, compliance in the material can be significant, causing a figure error. Test parts were structured with a 16µm sine wave with ±45° rake angle variation. The

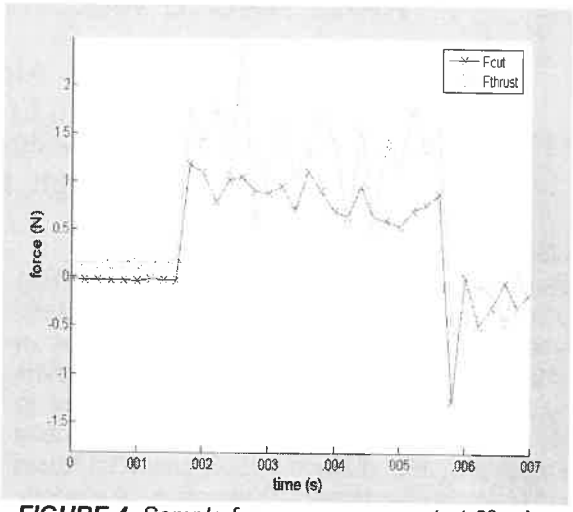

FIGURE 4. *Sample force measurement at 0° rake angle.*

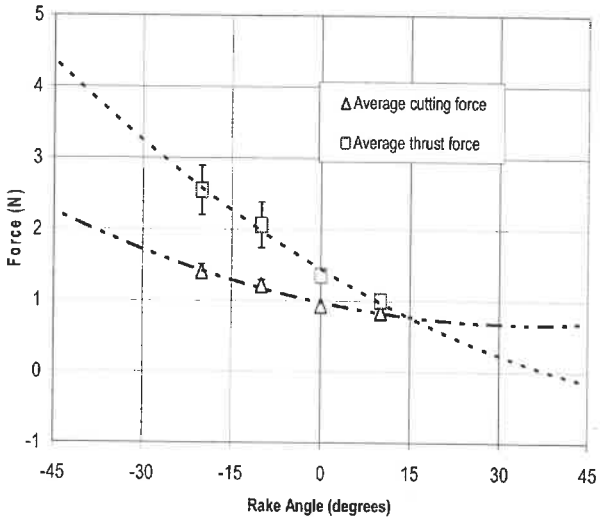

FIGURE 5. *Force variation as a function of rake angle. The dashed lines are least-squares polynomial fits to the data and are extrapolated to ±45 °.*

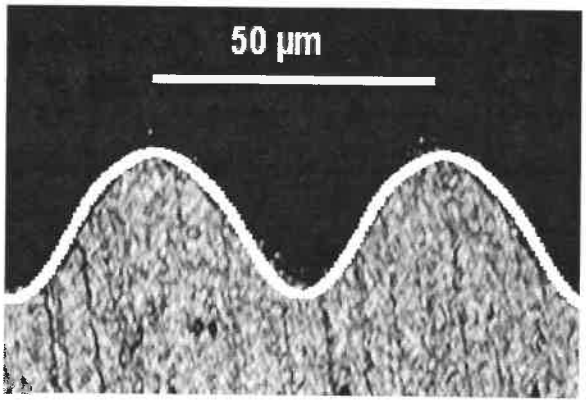

FIGURE 6. *The calculated perturbed tool path from Figure 7 superimposed on a section of Figure 1*

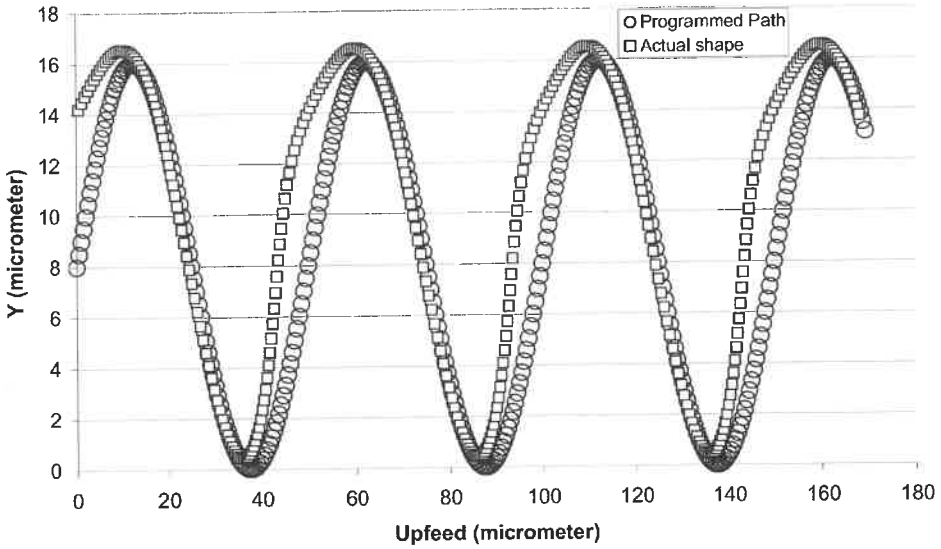

FIGURE 7. *Preturbed shape of the sine waves machined on a 6 mm diameter, 20 mm long brass cylinder. The programmed ideal path is shown for reference.*

part was a 6 mm dia electroless Nickel plated brass cylinder. Modeling the cylinder as a cantilever beam with a length of 20 mm, the deflection can be calculated from the experimentally obtained tool forces. Calculating deflection from this and correlating to the measured forces yields a perturbed sine wave as shown in Figure 7. This distorted sinusoidal shape is very similar to that shown in Figure 1 and when superimposed onto the measured data follows the shape of the actual part. This is illustrated in Figure 6.

TOOL LIFE

Significant wear was noted on the tool used to machine the sine wave parts. The distance cut was less than 500 m, surface roughness was impacted significantly. Ordinarily, this sort of cutting distance in nickel would not lead to appreciable wear or chipping of the tool, but with the extreme clearance angle of 50° used, the edge becomes quite fragile. This geometry was based on the conventional non-ferrous metal turning practice of using a 0° rake angle tool. Hence, the included angle on the tool is only 40° whereas most conventional tools have included angles around 80°. Taking another

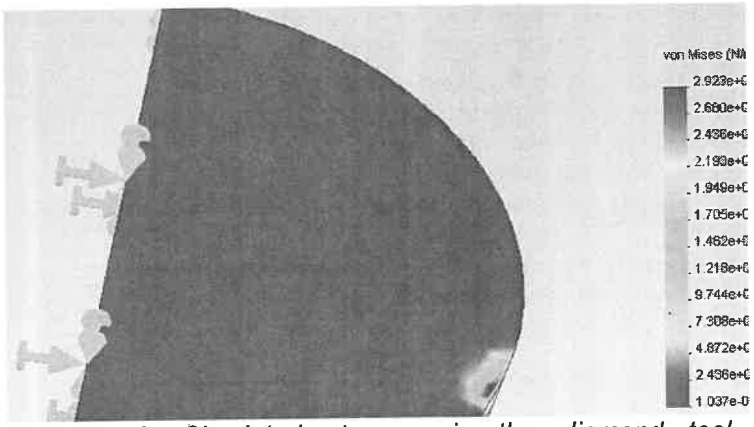

FIGURE 8. *Simulated stresses in the diamond tool calculated using FEA and measured forces. Maximum stress at 0° is 2.9 GPa*

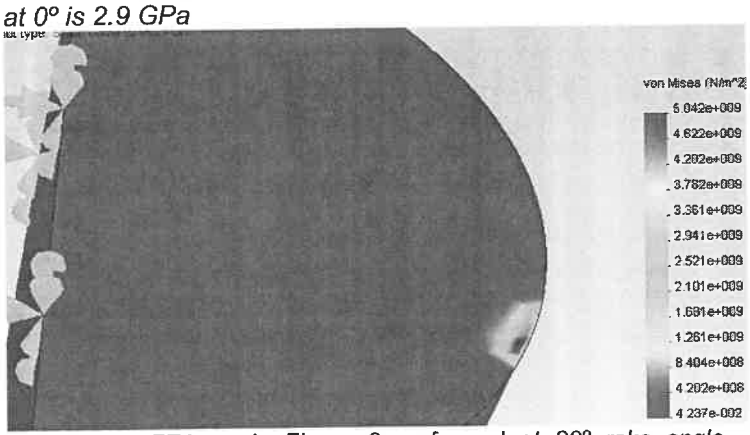

FIGURE 9. *FEA as in Figure 8 performed at 20° rake angle. Maximum stress is 5 GPa.*

look at this practice, however, say we have a requirement of ±45° as in the described part. While the clearance angle must be at least 45°, the initial rake angle could be anywhere from 0 to –45°. While increasing the rake angle increases the cutting forces substantially, it also decreases stress in the part. Finding an optimum geometry will be based on applying tool force data to different tool geometries and evaluating the internal stresses in the diamond. Initial assessments using COSMOS Finite element modeling software and the experimental force results shown in Figure 5 show that, while tool forces may decrease for more positive rake angles, the internal stresses in the tool actually increase as shown in Figures 8 and 9. Additionally, internal shear stress increases significantly as the clearance angle is increased.

CONCLUSIONS

The role of rake angle variation in machining free-form optics is rarely addressed. As tool excursions and, hence, surface slopes increase, however, the impact of rake angle variation cannot be ignored. Both static deflection of the workpiece and tool as well as the life of the tool can be be impacted significantly. The preliminary results presented here represent merely the first step in an effort to understand the impact of varying rake angles in diamond turning. The resulting knowledge will lead to methods for combating the negative effects of this phenomenon, ultimately, better more cost effective free-form optics.

REFERENCES

[1] Arcona, C., "Chip Formation and Surface Finish in Diamond Turning". PhD Dissertation 1996.

[2] Drescher, J. P, "Tool Force, Tool Edge and Surface Finish Relationships in Diamond Turning", PhD Dissertation 1992.

MICRO DRILLING FOR PRINTED CIRCUIT BOARDS –INFLUENCE OF RUN-OUT OF MICRO DRILLING ON HOLE QUALITY–

Hidehito WATANABE[1], Hideo TSUZAKA[1], Masami MASUDA[2]
[1]Sales Engineering Department
Union Tool Co.
Settaya-cho, Nagaoka-shi, Niigata, Japan
[2] Graduate School of Technology Management, Niigata University
Ikarashi 2-no-cho, Nishi-ku, Niigata-shi, Niigata, Japan

INTRODUCTION

Nowadays, many printed circuit boards (PCB) are used in electronic appliances. Smaller diameter holes are required for the PCB to be applied to more dense and compact electronic appliances. Micro drills of 0.1-0.3 mm in diameter are used in commercial production lines, and smaller drills are in tentative production lines [1]. However, it is concerned about lower stiffness, more frequent breakage, lower hole quality or higher production cost for micro drills.

Therefore, manufactures use spindles rotating as high as 3 x 10^5 /min, because higher rotational drilling is effective to reduce cutting torque and increase a drill life. On the other hand, the high rotation increases run-out of micro drills with low stiffness [2]. The run-out might cause hole quality, such as hole location accuracy, to be deteriorated. However, there are few studies about micro drills for PCBs [3]. Furthermore, the influence of run-out on the quality of drilled holes is obscure [4].

This study investigates the relationship between run-out and the hole quality drilled by 0.1mm diameter drills at 3 x 10^5 /min rotational speed.

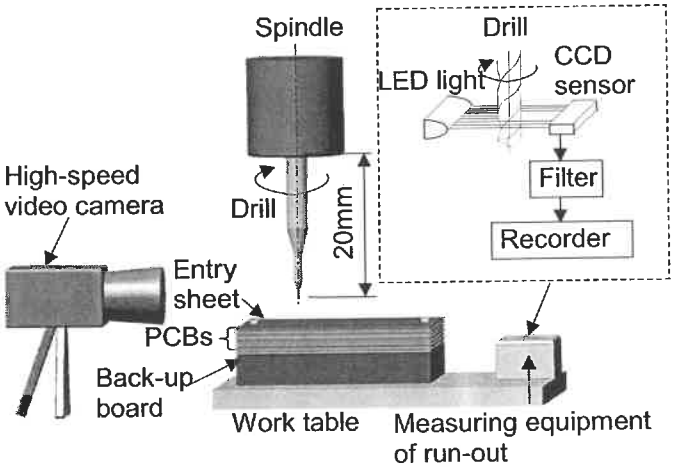

FIGURE 1. Experimental setup

In addition, the influence of run-out on hole location accuracy is revealed.

EXPERIMENTAL METHOD AND CONDITIONS

Experimental setup

The illustration of experimental setup is shown in figure 1. A NC drilling machine (Hitachi Via Mechanics, ND-1V212) for PCB is used. It has an air-bearing spindle driven by an AC motor of maximum rotational speed 3x10^5/min. A high-speed camera (Nac Image Technologies, Memrecam fx-K4) is set to observe the behavior of a drill bit during drilling from a side view of it. Frame rate of the camera is 6x10^4 fps (12 frames per a rotation at 3 x 10^5 /min). Run-out is measured by a non-contact measuring equipment (Union Tool Co., TP-FA). Run-out is estimated as the maximum TIR (Total indicator readout) during a revolution in air cut.

Drilling conditions

Table 1 shows drilling conditions. Micro drills used for drilling tests are 0.1mm diameter twist drills with 2.0mm diameter shank. It is made of ultra-fine tungsten carbide. A workpiece is PCB with 0.1 mm thick, laminated by glass cloth base polyimide. Both sides are clad with a layer of copper 6 μm in thickness. ①an entry sheet, ②4-stacked PCBs and ③a back-up board are placed orderly, fixed by stud pins at the both ends of the set on the work table.

Entry sheet is generally used for improvement of the initial hole location and reduction of burrs. The entry sheet used in drilling tests is resin matrix clad with aluminum thin film, which is popular in commercial micro drilling process for PCB. Run-out is voluntarily set up from 0 to 100μm by changing the chucking condition in a collet. According to preliminary experiment, the orbital revolution of run-out synchronized with spindle rotation, and it coincided with the rotatory direction of a drill.

EXPERIMENTAL RESULTS AND DISCUSSION

Influence of run-out on hole location accuracy

Figure 2 shows the relationship between run-out and hole location accuracy. Hole location accuracy was measured on the top and the bottom sides of PCB using a position analyzer (Hitachi Via Mechanics, HT-1AM), which consists of CCD camera and an image processor. Measurement accuracy is ± 5 μm. It is measured as the deviation of hole location from ideal drilling coordinated on the drilling machine, and the average values were analyzed. The pitch errors peculiar to the drilling machine were compensated [5].

It can be observed in the figure that hole location accuracy is constant on the top and the bottom side of the PCBs, without any correlation with run-out.

Within these experimental conditions, there is almost no influence of run-out on hole location accuracy. During the drilling of PCBs, it is presumed that run-out is almost reduced to the normal drilling after contact with a workpiece.

Centripetal behavior

Figure 3 shows the photographs of drilling behavior taken by a high-speed camera when drill bit penetrates just into an entry sheet. Their four photos were taken in very short time; a photo during air cut, one at 0.1ms (1/2 rev.) after a), one just after contact with the entry sheet and one at 0.1ms (1/2 rev.) after c) respectively. Homogeneous deviation is observed along the drill axis during air cut. On the other hand, while penetrating the entry sheet, it is observed that the drill bit is located near the center of the deviation, although the deviation is kept at the end part of flute consistently. Hence, it can be presumed that the drill is deformed elastically through long flute and the run-out is dumped at the drill bit.

Figure 4 shows eight continuous photographs taken at interval of 0.3ms (1.5 rev.), when the drill bit starts contacting with an entry sheet. From the comparison among the serial photographs, it is recognized that;

1. The deviation at the drill bit gradually decreases as penetrating gets deeper to converge to the rotating center of the spindle, although it is large before the contact with the entry sheet.
2. As the drill bit contacts with the entry sheet, it takes only around 1.5ms until the run-out at the drill bit to be dumped. Feed 37.5 μm ± 7.5 μm

TABLE 1. Drilling conditions

Drill	ϕ0.1 x 1.5mm
Rotational speed	3 x 10^5 /min
Feed rate	1500 mm/min
Work material (PCB)	Glass cloth base copper clad laminate (Mitsubishi : HL832HS)
Stack height	t0.1mm x 4 panel
Tool duration	4 000 hits
Drilling pitch	0.25 mm
Run-out	0 – 100 μmTIR
Entry sheet	Resin clad with Aluminum (t0.11 mm)
Back-up board	Bakelite (t0.15 mm)

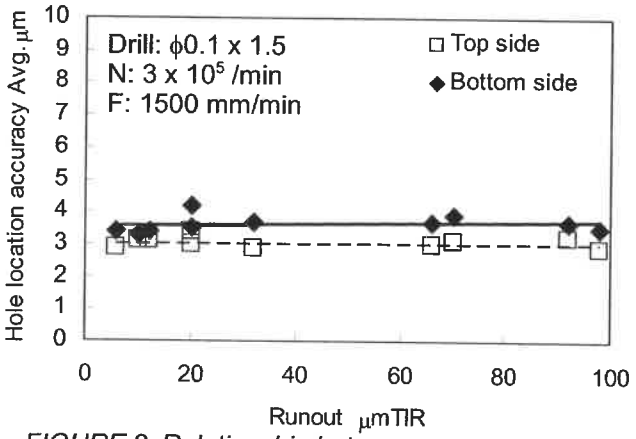

FIGURE 2. Relationship between run-out and hole location accuracy using entry sheet

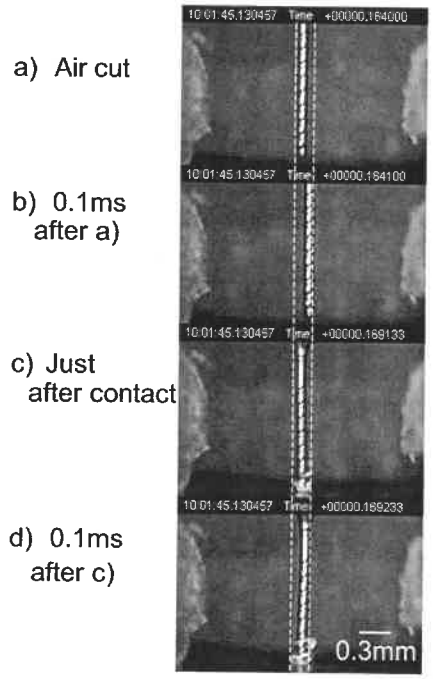

FIGURE 3. Comparison of deviation at air cut and penetrating into entry sheet

for drilling time 1.5 ms is slightly larger than the point of drill bit 23.9 μm.

According to the above-mentioned results of hole location accuracy and the dynamic mode around the drill bit, it can be concluded that centripetal action substantially occurs on the contact zone between a drill bit and an entry sheet. Run-out of the drill bit gets to be dumped soon after the initial contact with the entry sheet, and finally run-out converges to the center of rotating spindle by centripetal action. Hence, it is presumed that vibration-free drilling of PCBs is realized, after penetrating through the entry sheet.

Effect of centripetal action on entry sheet

Figure 5 shows the relationship between run-out and hole location accuracy in drilling without an entry sheet. It indicates hole location accuracy becomes worse in proportion to run-out. In especial, it depends more significantly upon run-out at the bottom side than one at the top side of PCBs. A drill bit skews in PCBs. However, centripetal action is observed even without an entry sheet, because of some correlation with run-out, significantly at larger run-out. An example is discussed in the following. The center of drill bit is located at its rotating center of drill bit, which deviates from the center of rotating spindle, when the drill bit starts to contact with the entry surface. If run-out is 80μmTIR, the center of drill bit would be at a location of 40 μm deviated from the center of rotating spindle. Therefore, the hole location error would result in 40 μm. According to Figure 5, however, hole location accuracy on the top side is about 12 μm even though run-out is 80 μmTIR. Thus, the centripetal action of run-out occurs more or less in the copper clad layer or glass cloth resin.

When drilling within these experimental conditions, it can be concluded that the drill bit primarily moves toward the centripetal direction. Using the entry sheet enhances the centripetal action, and then the drill bit is dumped from an orbital revolving position to the center of rotating spindle. Therefore, an entry sheet effectively helps the centripetal action to reduce the deviation of hole location, even though there is run-out beyond 80 μmTIR or more.

Influence of run-out on drill wear

The photographs of the drill point after drilling 4000 hits at run-out of 6 μm and 98 μm are shown in Figure 6. In order to clarify the influence on drill

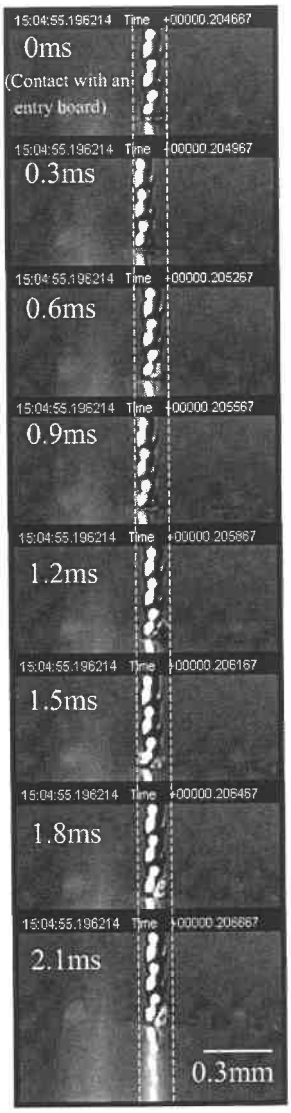

FIGURE 4. Serial photographs of micro drilling

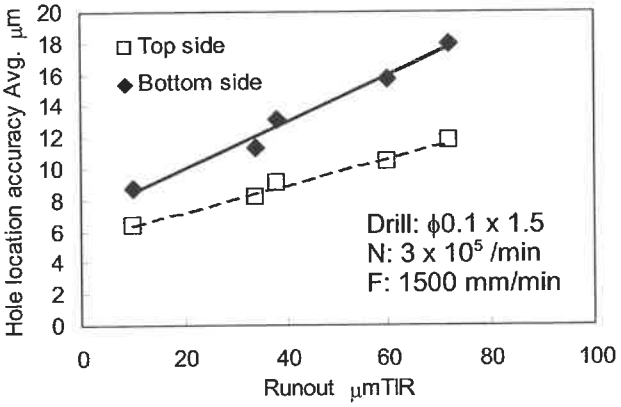

FIGURE 5. Relationship between run-out and hole location accuracy without entry sheet

wear, a white dotted circle indicates the circle circumscribed the new top of drill before the drilling test. Each photograph shows normal wear as the flank at corner cutting edges is remarkably worn. Any abnormal wear triggered by run-out can't be found.

In general, hole quality has a strong correlation with tool wear. So, wear on a chisel edge and cutting edges would lead to reduce cutting ability and to deteriorate hole location accuracy. However, any abnormal wear was not observed even with large run-out herein, and any run-out hardly affected hole quality either.

It results that any run-out hardly affects the drilling behavior as drill wear or hole location accuracy.

Influences of drill wear on centripetal action

The relationship between run-out and accumulative hits is shown in Figure 7. Run-out is measured during air cut and at every 500 hits until 2000 hits. Three drilling tests start at initial run-out 56, 80, and 98 μmTIR respectively. According to the figure, the run-out is almost independent of accumulative hits, although drill wear is gradually increasing.

It should be noted that the centripetal action is maintained during drilling, and run-out is not influential in hole quality nor drill wear for micro drilling by the use of optimal entry sheets.

CONCLUSIONS

In order to improve the productivity and breakage life which are controversial in micro drilling for PCB, this paper deals with the correlation between run-out and the hole quality in drilling tests using 0.1mm diameter drills at $3x10^5$/min rotational speed. The conclusions obtained within the experimental conditions are in the following;

1. The run-out which is below 100μm hardly affects the hole location accuracy.
2. Orbital revolving drills primarily move in the centripetal direction just after contacting with a work surface. An entry sheet effectively enhances the centripetal action.
3. The run-out is hardly influential on drill wear, because of the centripetal behavior.
4. The centripetal behavior makes drill wear insensitive to the run-out.

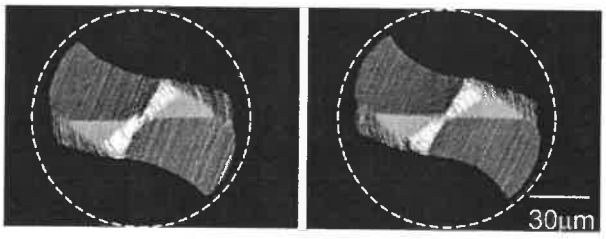

(a) Run-out : 6 μm (b) Run-out : 98 μm

FIGURE 6. Comparison of wear on the top of drill with different run-out

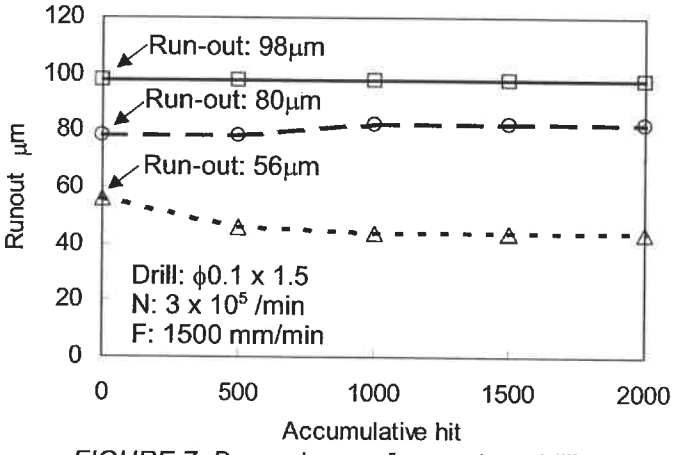

FIGURE 7. Dependence of run-out on drilling time

REFERENCES

[1] S.Kobayashi, H.Watanabe; Drilling Technology on Micro drill, Proc. of the 20th JIEP Annual Meeting, 2006, 173 [in Japanese]

[2] F.Okumara, M.Tsutsumi; Reduction of run-out and vibration of high speed spindle for machining centers (1st Report) –Effectiveness of 3-plane balancing–, JSPE 2003, 69(9): 1327 [in Japanese]

[3] Y.Daikoh, T.Terabayashi, M.Masuda; Micro Drilling of Printed Circuit Boards (1st Report) – Cutting Force and Chip Flow Mechanism–, JSPE 1994, 60(12): 1796 [in Jpananese]

[4] T.Otsuka, T.Hirogaki, E.Aoyama; Quality Evaluation of Minimum Diameter Hole Drilled by Super-high-speed Spindle in PWB's Processing, Proc. of JSPE 2006 Annual Meeting: 767 [in Japanese]

[5] M.Hiranaka, H.Yokouchi, Li Xifeng, K.Kaito, H.Tsuzaka; Studies on Bending at Small Hole Drilling of Printed Wiring Boards, JSPE 1993, 59(1): 119 [in Japanese]

QUANTIFYING THE STABILITY UNCERTAINTY IN A MILLING MODEL

Raúl E. Zapata[1], Tony L. Schmitz[1], Ali E. Abbas[2], and Liu Yang[2]
[1]Department of Mechanical and Aerospace Engineering
University of Florida, Gainesville, FL, USA
[2]Department of Industrial and Enterprise Systems Engineering,
University of Illinois at Urbana-Champaign, Urbana, IL, USA

INTRODUCTION

Our recent efforts in applying decision analytic methodologies to milling optimization [1] have provided us with a basis for including uncertainties in the milling process. By optimizing profit and including the influence of the process dynamics as constraints rather than objectives, it is now possible to create a comprehensive approach to milling optimization. Our recent work concentrated on observing the encoded uncertainties in force model coefficients (FMCs) and tool life in profit calculation [1].

Although previous studies in milling optimization have explored the use of multiple objectives and various optimization methods, much of the prior work has focused on a single aspect of milling productivity, such as tool wear or material removal rate and the influence of the process dynamics has not typically been considered. However, the approach used in [1] adopts a more holistic view that can consider multiple constraints, including stability, surface location error, and surface roughness, which depend on the process dynamics, and tool life, while maximizing what we believe to be the most appropriate single objective function, profit.

Current research involves improving our knowledge of the uncertain system through experimentation. This requires a new approach to describing the process stability. Previously, we regarded stability as a discrete quality of the milling system. The operating point was compared to the simulation stability boundary, which was represented in a step function manner, and was declared either stable or unstable. Due to the uncertainties in the FMCs and the tool-holder-spindle-machine frequency response function, however, an infinite set of boundaries is available. Therefore, we have defined the probability that a selected operating point will be stable using a subsection of that set. The following sections present the method for quantifying the stability uncertainty and the corresponding effects on the calculation of profit. The benefits that this procedure provides when performing experiments is also explored.

QUANTIFYING STABILITY UNCERTAINTY

Determining the milling stability uncertainty is notably different from obtaining the uncertainties for the analysis inputs, including the force model coefficients (FMCs) and frequency response function (FRF) of the tool-holder-spindle-machine assembly as reflected at the tool point. For our purposes, we assume that the estimates of the FMCs are based on experience or tabulated values, while the FRF is measured. The stability limit, on the other hand, is obtained from calculations based on the inputs (and the milling model). The stability uncertainty therefore depends on the input values (FMCs and FRF), their propagation through the stability model, and the selected operating point.

In this research, we apply the frequency-domain, analytical stability analysis described in [2] to determine the stability limit. Inputs to this algorithm include the radial depth of cut and number of cutter teeth (deterministic decisions), the FRF (uncertain), and the FMCs (uncertain). The output is the well-known stability lobe diagram, which identifies the stability boundary (i.e., the allowable axial depth of cut in peripheral end milling) as a function of spindle speed. The traditional first order Taylor series expansion method for evaluating measurement uncertainty [3-4] is not conveniently applied in this instance. Therefore, a Monte Carlo approach was used.

In the Monte Carlo simulation, the FMC and FRF uncertainties are quantified using appropriate mean and standard deviation values for the selected distributions (Table 1). The FMCs are scalar coefficients and the uncertainty could be evaluated by a number of methods. In this case, the FMC uncertainty is determined through encoding, a decision analysis approach based on the user's experience and beliefs. The frequency-dependent, complex-valued FRF is determined by measurement. Due to its bivariate

(complex-valued) nature, its uncertainty evaluation is complicated. A separate study [5] determined that the primary uncertainty contributors for impact testing, which is commonly applied to measure the tool point FRF, are the calibration coefficients of the measurement transducers, typically an impact hammer and accelerometer. For the purposes of this demonstration the FRF uncertainty will be neglected because the prior study [5] indicated that a measured FRF's uncertainty is small compared to FMCs in general.

In most of the previous work, assuming normal distributions for the uncertainties is reasonable unless other information is available. When conducting a decision analysis, however, the uncertainty distributions must accurately reflect the users' beliefs, which may be different from Gaussian. In this regard, beta distributions may provide significant flexibility due to their various shapes and forms. Similarly, due to the nature of the stability analysis [2], there is no guarantee that the output will be Gaussian, so a beta distribution was selected to better describe the output. Beta distributions are defined on a domain of a to b, and two parameters r and k as shown in the probability density function in Eq. 1 [6]:

$$f(x \mid a,b,r,k) = B(x-a)^{r-1}(b-x)^{k-1}, a < x < b, \quad (1)$$

Where B is a scaled Beta function with parameters a, b, r, and k.

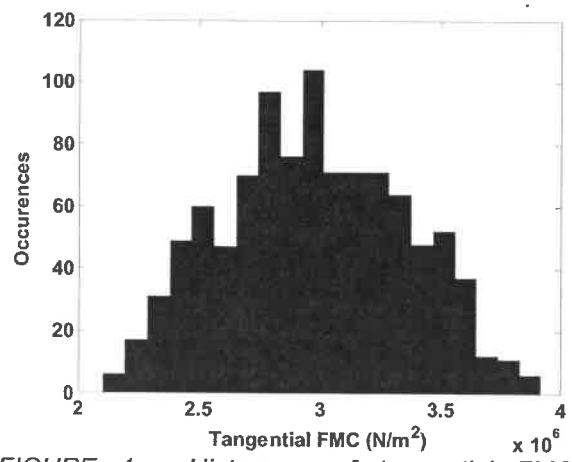

FIGURE 1. Histogram of tangential FMC values.

Using the beta distribution it is possible to quantify the stability behavior given uncertain inputs. For example, using an appropriately scaled beta distribution on the domain (2 to 4×10^6 N/m^2) with beta function parameters (r, k) of (3, 3) for the force model coefficients, we randomly sampled 1000 values of the FMCs to obtain the histogram shown in Fig. 1.

In this study, we assumed perfect correlation between the tangential and radial FMCs. Therefore, only the tangential value was sampled in the Monte Carlo simulation and the radial value was taken to be proportional (equal to 0.3 times the tangential coefficient). Table 1 shows the additional simulation input data. The 1000 paired values of the FMCs were propagated through the stability model to obtain 1000 stability boundaries (Fig. 2). The Monte Carlo output provided a distribution of stability boundaries at every spindle speed. The histogram of the distribution at 18000 rpm is shown in Fig. 3. In this example, the distributions were the same at each spindle speed, but this is not necessarily the case if FRF uncertainty is included. Fitting the Fig. 3 histogram (once normalized) to a beta distribution using maximum likelihood estimates of the parameters revealed the closest approximation was a beta distribution with parameters (a = 2 mm, b = 3.8 mm, r = 1.76, k = 2.56).

TABLE 1: Inputs to the Monte Carlo stability simulation.

Parameter	Value	Units
Stiffness	1.6×10^7	N/m
Damping ratio	0.05	-
Natural frequency	2400	Hz
Number of teeth	4	Teeth
Radial immersion	50%	-
FMC tangential	3000±1000	N/mm^2
FMC radial	600±300	N/mm^2

The value of the cumulative distribution at any combination of axial depth and spindle speed within the axial depth range of the 1000 stability boundaries obtained from simulation provides the probability that the "true" stability boundary is at a lower axial depth (i.e., the likelihood that the selected parameter combination is unstable). The likelihood that the parameter set is stable, or the probability of stability, p_{stab}, is determined by subtracting the probability of instability from one. Given that the beta distribution is a bounded distribution and the parameter space is infinite, the remainder of the parameter space must be composed of valid probability values. Therefore, everything below the minimum of the beta distribution fit to the stability boundaries at each spindle speed is

designated stable (i.e., has a p_{stab} value of 1) and everything above the maximum is unstable (p_{stab} value of 0). The results of these probability of stability calculations are provided in Fig. 4. The probability of stability is finally used to calculate profit by multiplying this probability by the unconstrained value of profit at each parameters set.

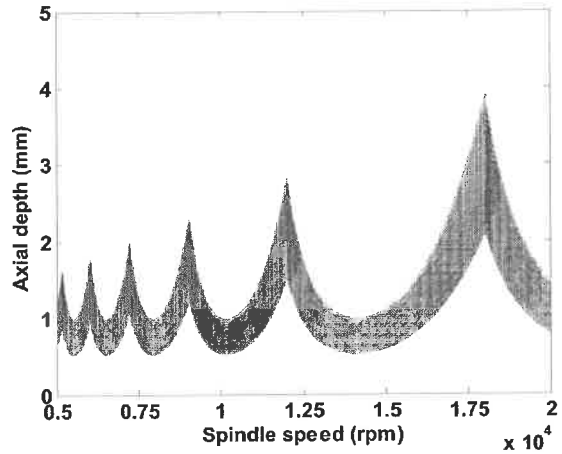

FIGURE 2: Collection of 1000 stability boundaries from Monte Carlo simulation.

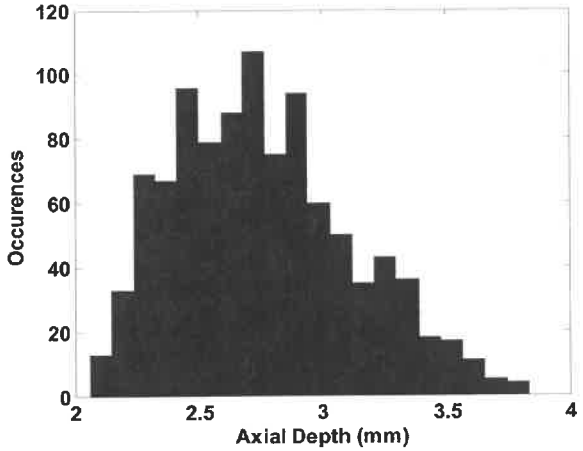

FIGURE 3: Histogram of the distribution of the stability boundaries at 18000 rpm.

CALCULATING PROFIT

The discretized method used in [1] required the user to perform an encoding exercise on the FMCs. In this exercise, the user defines a distribution to represent his beliefs about the FMCs and selects the values for 0.1, 0.50, and 0.9 probability in the distribution as the low, base, and high levels of the FMCs.

The low and high values are each assigned a rate of occurrence, or probability, of 0.25 and the base value is assigned a probability of 0.5. At each of these levels a stability boundary is calculated and it also carries the probability of occurrence from the force model coefficients (assuming there are no other relevant uncertainties).

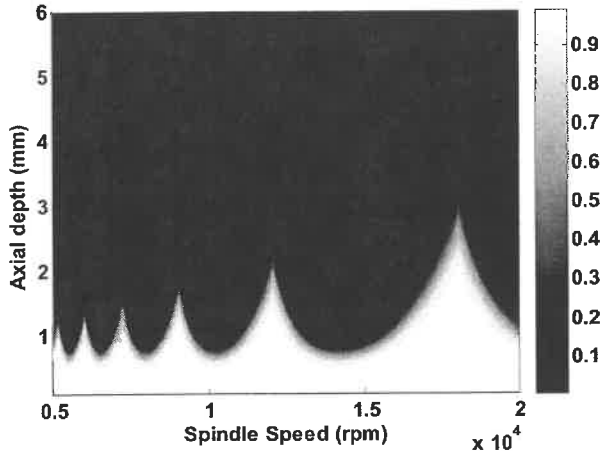

FIGURE 4: Contour plot of probability of stability in the parameter space.

Due to the nature of the stability boundary calculations, a higher level of FMCs causes the stability boundary to be lower (smaller axial depth) than the lower levels of FMCs. Therefore, the method in [1] presented the probability of stability in discrete steps (0, 0.25, 0.75 and 1) as part of the encoding exercise. This occurs because, if an operating point is stable when compared to the stability boundary with high FMC conditions, then it will also be stable for the base and low conditions giving it a p_{stab} of 1. If it is unstable in the high level, but stable in the base level, the probability is 0.75 and so on. The resulting formula for the expected value of profit using this method is provided in Eq. 2, where *P* is profit, *T* is the tool life, *F* are the FMC settings, *S* is the operating point and *M* is the multiplier that determines if the operating point is feasible (1) or infeasible (0). The multiplier can represent stability alone or a combination of constraints.

$$E[P(T,S)] = \begin{bmatrix} 0.25\times M(FMC_{low},S)+ \\ 0.5\times M(FMC_{base},S)+ \\ 0.25\times M(FMC_{high},S) \end{bmatrix} \times \begin{bmatrix} 0.25\times P(T_{low},S)+ \\ 0.5\times P(T_{base},S)+ \\ 0.25\times P(T_{high},S) \end{bmatrix} \quad (2)$$

Profit for a single part is calculated by subtracting the cost of machining that part, C_m, from the revenue generated by its sale, *R* (Eq. 3). This revenue can be selected by the user.

$$P = R - C_m \quad (3)$$

The cost of machining is obtained using Eq. 4, where t_m is the machining time, t_c is the cutting time, r_m is the cost of machining per unit

time, t_{ch} is the time it takes for a tool change, C_t is the cost of a tool, and T is the tool life. The machining and cutting times depend on the selected tool path, while the tool life is typically approximated using an empirical model.

$$C_m = t_m r_m + (t_{ch} r_m + C_t)\frac{t_c}{T} \quad (4)$$

By considering the effect of uncertainty in the FMCs as a continuous distribution, the stability boundary also becomes a continuous distribution. Stability at each combination of spindle speed and axial depth is given a probability value, p_{stab}, from the distribution of the stability boundary at that particular spindle speed. The expected value of profit is then:

$$E[P(T,S)] = p_{stab} \times \begin{bmatrix} 0.25 \times P(T_{Low}, S) + \\ 0.5 \times P(T_{Base}, S) + \\ 0.25 \times P(T_{High}, S) \end{bmatrix} \quad (6)$$

The first part of Eq. 2 is condensed to p_{stab} because it is now a continuous quantity and does not require the use of multipliers in its description.

VALUE OF INFORMATION AND VALUE OF EXPERIMENTATION

Given our stability uncertainty, p_{stab}, we can now consider: 1) value of information; and 2) value of experimentation. Value of information (or perfect information) describes the maximum amount of money we would be willing to pay to know the exact value of an uncertainty of interest. In this case, this uncertainty pertains to the FMCs (simulation inputs). In some cases, it may not be possible to obtain complete information about an uncertainty of interest, but incomplete information can be obtained through experimentation. The value of an experiment can also be calculated. The value of an experiment is the amount of money we would be willing to pay to receive information on the results of the experiment. In this case, an experiment would be a cutting test, or set of cutting tests, that would enable the user to decrease the uncertainty of one or more input quantities and, therefore, increase the expected value of profit by adjusting the milling settings. Note that value of experiment can never be larger than the value of information since it does not provide the exact value of the parameters.

When calculating the value of experiment, we first calculate the expected profit from milling without knowing the results of the experiment and then we calculate the expected profit after updating our information from the results of the experiment. This formulation assumes that the decision maker is risk-neutral and values uncertain deals at their expected value.

CONCLUSIONS

Quantifying the uncertainty of the stability property provides an opportunity to optimize the experimental process. It modifies the profit calculation to additionally enable calculation of the value of information and the value of experiment. Comparison of the value of experiment to the value of information for a set of operating conditions gives the user a measure of the possible benefit of the particular experiment. By selecting the operating conditions with the greatest value of experimentation, the user can choose an experiment that will provide the greatest amount of information about the process.

ACKNOWLEDGMENTS

The authors gratefully acknowledge financial support for this work from the National Science Foundation (DMI-0642569 and DMI-0641827). They also wish to thank G. Hazelrigg for numerous helpful discussions.

REFERENCES

1. Abbas, A., Yang, L., Zapata, R., and Schmitz, T. (2007) 'Application of decision analysis to milling profit maximization: An introduction', *Int. J. Materials and Product Technology*, Vol. x, No. x., pp. xxxx.
2. Altintas, Y. and Budak, E., 1995, Analytical Prediction of Stability Lobes in Milling, *Annals of the CIRP*, **44**/1: 357-362.
3. International Standards Organization (ISO), 1993, *Guide to the Expression of Uncertainty in Measurement* (Corrected and Reprinted 1995).
4. Taylor, B.N. and C.E. Kuyatt, 1994, Guidelines for Evaluating and Expressing the Uncertainty of NIST Measurement Results, *NIST Technical Note 1297 1994 Edition*.
5. Kim, H.S. and Schmitz, T., 2007, Frequency Response Function Uncertainty for Impact Tests, *Transactions of NAMRI/SME*, **35**: 319-326.
6. Bernardo, J.M., Smith, A.F.M., *Bayesian Theory*. John Wiley & Sons, Ltd., 2000. pp.116, 460-461.

THE CRITICAL SPEEDS OF A MACHINE TOOL SPINDLE-BEARING SYSTEM WITH THE HIGH STIFFNESS HYDROSTATIC JOURNAL BEARINGS

Y. S. Chen, Y. D. Cheng, and C. C. Chiou
Department of Mechanical Engineering
Yuan-Ze University
Chungli, Taoyuan, Taiwan

INTRODUCTION

The ordinary hydrodynamic bearings have been replaced by the hydrostatic bearings in the application of machine tools in recent years. For the hydrodynamic bearings, the journal and the bearing surface are separated by the sliding action with a wedge pressure-generating mechanism to develop a pressure within the bearing. It has advantages of simple structure and cheap cost. However, the fluid film lubrication may break down if the system is at the low rotating speed, or during the startup and shutdown processes.

On the contrary, for the hydrostatic bearings, the journal and bearing surface are separated by a fluid film maintained by a pressure source outside the bearing. The hydrostatic bearings avoid the disadvantages of the hydrodynamic bearings so that they have characteristics of high revolution and high precision, high load capacity, uniform thermal expansion, good working life and predictable performances. With proper design, the bearing stiffness of the hydrostatic bearings even surpasses the typical roller bearings [1]. As a result, the introduction of the hydrostatic bearings in the machine tool can significantly improve the surface finish and quality of the workpiece especially under the high machining speeds and feeds.

One of the key concerns to ensure the reliability of the machinery is to control the distribution of the critical speeds of the spindle system. The regenerative chatter problem that always appears near one of the critical speeds of the system is normally seen during the machining processes. Consequently, the distribution of the critical speeds is a very critical factor that dominates the dynamic properties of the system. With the goal to provide the best performance of the machine tool, this investigation is then intended to predict the critical speeds of the system with the spindle equipped with the high stiffness hydrostatic journal bearings. Those parameters such as the radial clearance, supply pressure, feeding parameter and ratio of bearing length/diameter will be adopted for examining their effects on the bearing stiffness. A realistic spindle model is represented by a number of divided beam elements at the beginning of the study when solving the problem with the self-written finite element method (FEM) program. Later, the modal testing is performed to verify the correctness of the model. Finally, with the verified FEM model, all the trends of the critical speeds of the system are explored by varying the number of feeding rows in the hydrostatic bearings.

CRITICAL SPEEDS ESTIMATION

As addressed above, the FEM model is utilized to represent a real machine tool spindle-bearing system. A Timoshenko beam element involving the shear and rotary inertia effects is formulated in the model as referred to the theoretical background in [2, 3]. Each of the nodes on the element has four degrees of freedom, i.e., the translation and rotation both in the horizontal and vertical directions. By ignoring the external force, the equation of motion of the system can be shown as:

$$[M]\{\ddot{q}\}+[G]\{\dot{q}\}+[K]\{q\}=\{0\} \tag{1}$$

To solve the critical speeds of system, the eigen-value matrix can be established by substituting $\{q\}=\{h_0\}e^{\alpha t}$ into the system equation:

$$\begin{bmatrix} [0] & [I] \\ -[K]^{-1}[M] & -[K]^{-1}[G] \end{bmatrix} \begin{Bmatrix} \alpha\{h_0\} \\ \{h_0\} \end{Bmatrix} = \frac{1}{\alpha} \begin{Bmatrix} \alpha\{h_0\} \\ \{h_0\} \end{Bmatrix} \tag{2}$$

Here, the bearing damping coefficients are ignored, hence, the so-called undamped critical speeds are then obtained from the above equation.

MULTI-ARRAY FEEDING BEARINGS

The schematic of the typical 3-row multi-array feeding hydrostatic journal bearings are shown at left in Fig. 1. As illustrated in the figure at right, there are 1-row, 2-row and 3-row of feeding holes design on the spindle. Under the conditions of thin, incompressible lubricant film and lower journal eccentricity ratios, the Reynolds equation can be simplified as [4]:

$$\frac{\partial^2 P}{\partial y^2}+\frac{\partial^2 P}{\partial z^2}=0 \tag{3}$$

The method of separating variables is then introduced here to solve the motion equation. The boundary conditions both at the feeding holes and the bearing sides are set following [5]. The dimensionless load capacity for the 1-, 2- and 3-row feeding journal bearing can be obtained as shown below respectively:

$$\begin{aligned} W_1 &= W_1(\varepsilon, \lambda, P_s, L/D) \\ W_2 &= W_2(\varepsilon, P_s, 4\lambda/3, 2L/3D) \\ W_3 &= W_3(\varepsilon, P_s, \lambda/2, \lambda(3+\lambda)/2(2+\lambda), L/D, L/2D) \end{aligned} \tag{4}$$

where $\varepsilon=e/C$, is the journal eccentricity ratio which is defined as the ratio of the journal eccentricity (e) to the radial clearance of the bearing (C). P_s =ps/pa, is the ratio of the supply pressure designated as "*ps*" to the ambient pressure "*pa*", L is the bearing length and D is the bearing diameter. The feeding parameter λ is defined as:

$$\lambda=\frac{3a^4N}{8C^3l_t}\left(\frac{L}{D}\right) \tag{5}$$

where N is the number of feeding tubes in each of the feeding row, a is the radius of the feeding tube and l_t is length of the feeding tube. Besides, throughout the study, the dimensionless bearing stiffness K is defined as the variations of the dimensionless load capacity W to the journal eccentricity ratio ε. It can be shown as:

$$K=\frac{dW}{d\varepsilon} \tag{6}$$

MODAL TESTING OF THE SPINDLE

The configuration of the machine tool spindle for this study is shown in Fig. 2. The spindle is designed with the multi-array feeding hydrostatic journal bearings for satisfying the demands of the high speed and high precision machining processes. It is also shown in the figure that there is a total of 33 elements in the FEM model of the spindle. In reality, the spindle has a total length of 151.3 mm and its outside diameter is 25.25 mm. The rear and front bearings are connected to the spindle with the isotropic bearing stiffness designated as K_b both at node 8 and node 26 respectively.

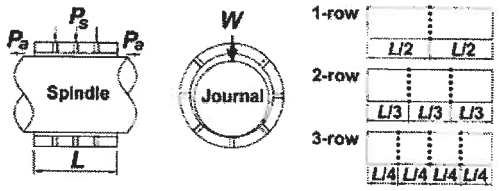

FIGURE 1. The multi-array feeding hydrostatic journal bearing.

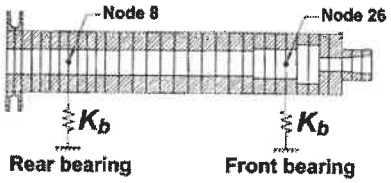

FIGURE 2. Schematic of the finite element model of the spindle-bearing system.

For the correctness verification of the spindle model, an experimental modal testing is conducted right after. During the test, the spindle is suspended with the rubber bands at both ends to simulate the free-free boundary conditions. The results of the FEM model show that the frequencies of the first and second bending modes are at 5,310 Hz and 12,670 Hz respectively. The corresponding modal testing results are at 5,356 Hz and 12,993 Hz respectively. The error percentages of those frequencies based on the experimental results are -0.86% and -2.49% respectively. This indicate that the accuracy of the data resulted from the FEM model is acceptable since all the error percentages are within ±5%

BEARING STIFFNESS WITH DIFFERENT DESIGN PARAMETERS

In this study, a pair of hydrostatic bearings each with multi-array feeding is built to support the spindle that can provide the system stiffness during the machining process. In the parametric analyses for the effects of various designs on the spindle stiffness, some of the typical values as listed below are chosen for each of the

following bearing parameters. Such as the radial clearance of C=15 μm, bearing diameter D=25.6 mm, supply pressure ps=3.5 MPa, feeding parameter λ =0.73 (i.e., for the case of eight feeding tubes in one feeding row, N=8) and the number of feeding rows are all considered initially in the analysis. Among them, one is varied while the others are kept intact with the above mentioned values during each of the analysis process. Some of the effects on the bearing stiffness of these combined parameter variations are illustrated in Fig. 3-Fig. 5 respectively.

Fig. 3 shows the bearing stiffness versus the bearing load and the bearing radial clearance. As indicated in Fig. 3(a), it is obvious that the bearing stiffness is independent of the low bearing load under 2 kg no matter for 1-, 2- or 3-row feeding designs. In other words, this condition is equivalent to the situation of lower journal eccentricity ratios. In Fig. 3(b), the stiffness decreases dramatically with the increase of the bearing radial clearance. For the larger radial clearance of 20-30 μm, the stiffness variations tend to smooth down gradually. As a result, the radial clearance should be designed as small as possible to obtain the largest stiffness.

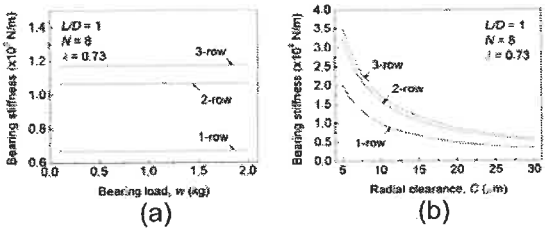

FIGURE 3. Bearing stiffness versus (a) bearing load, and (b) radial clearance.

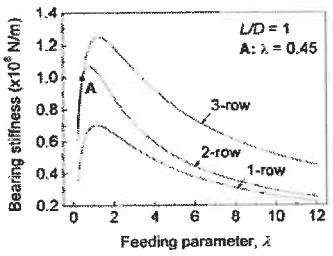

FIGURE 4. Bearing stiffness versus feeding parameter.

The effects of the feeding parameter (i.e. λ) to the bearing stiffness are shown in Fig. 4. There exists an optimum feeding parameter to maximize the bearing stiffness. From the peaks of the curves in the figure, it can be seen the feeding parameters should be limited between λ=0.5-1.5 to obtain the optimum stiffness. However, if λ <0.45 (point A), the stiffness between the 2- and 3-row feeding are fairly identical.

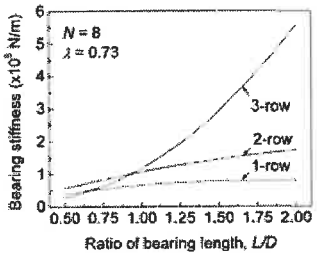

FIGURE 5. Bearing stiffness versus the length/diameter (L/D) ratio of the bearing.

The variation of the bearing stiffness versus the length/diameter (L/D) ratio of bearing is shown in Fig. 5. As can be seen in the figure, the bearing stiffness is highly sensitive to the L/D ratio for the 3-row feeding bearings but is quite insensitive to the 1- and 2-row feeding bearings. For the case of L/D<1, the 2-row feeding bearing is recommended as the best choice to retain the sufficient stiffness. Conversely, the excellent stiffness is resulted for L/D>1 with the design of the 3-row feeding bearing.

VARIATIONS OF SYSTEM CRITICAL SPEEDS

The stiffness as resulted from the bearing is introduced to the system when proceeds to the critical speeds analysis. Fig. 6 shows the variations of the critical speeds with the multi-array feeding design at the front and rear bearings correspondingly. As can be seen in the Fig. 6(a), the first critical speeds Ω_1 are insensitive to the front or rear bearing when the 1-row feeding is adopted. However, the first critical speeds are raised obviously if the 2- or 3-row feeding is considered at both bearings. Fig. 6(b) shows the variations of the second critical speeds Ω_2 of the system. It indicates that the second critical speed has increased so rapidly when the rear bearing is switched from 1-row to 2- or 3-row feedings while the front bearing has just 1-row feeding. On the other hand, when the front bearing has 2- or 3-row feeding, the second critical speeds won't have too much change no matter with 1-, 2-, or 3-row feeding in the rear bearing.

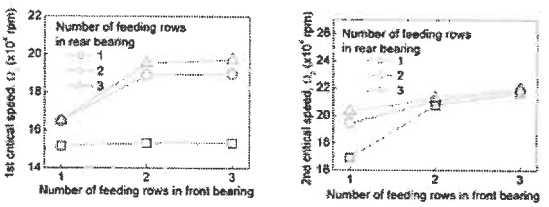

FIGURE 6. (a) The first critical speed, and (b) the second critical speed of spindle-bearing system.

Fig.7 shows the percentage differences between the first and the second critical speeds of the system. These differences actually reflect the fact about how close or apart the first and second critical speeds are located in the spectrum of the frequency domain. As shown in the figure, when the 1-row feeding is designed on the rear bearing, the differences between the first and second critical speeds are all increased regardless 1-, 2-, or 3-rwo feeding on the front bearing. Similar differences will be observed vice versa. In the mean time, the difference will be reduced for all the cases when both the front and rear bearings has more than 1-row feeding. Finally, it is also noted in the figure that the smallest percentage difference of 9.1% is achieved with the 3-row feeding in the rear bearing and the 2-row feeding in the front bearing.

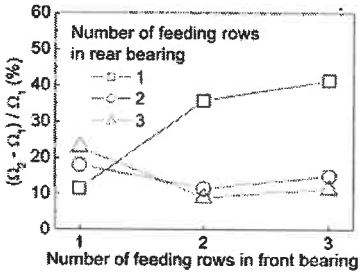

FIGURE 7. The percentage differences between the first and second critical speeds.

CONCLUSIONS

This study has investigated the stiffness characteristics of the multi-array feeding journal bearing with various bearing design parameters. The essential results for the distribution of the system critical speeds have been demonstrated visually to define the proper working speed. All the meaningful results obtained can be summarized as follows:

The bearing stiffness is independent of the bearing load for the low journal eccentricity ratios (i.e. at low bearing load). The stiffness decreases dramatically only if the radial clearance is increased.

There exists the optimum feeding parameters to make the bearing stiffness the highest. To obtain the optimum bearing stiffness, the feeding parameters should be limited to be in the range of λ=0.5-1.5.

The bearing stiffness is the most sensitive to the bearing length/diameter ratio for the 3-row feeding bearing but is insensitive to the 1- and 2-row feeding bearings.

In terms of the variations of the critical speeds, the first critical speeds are insensitive to the front or rear bearing when the 1-row feeding is adopted in either one of the front or rear bearings. The second critical speed increases rapidly by 2- or 3-row feeding either in the rear or front bearings.

The differences between the second and first critical increases steadily when only 1-row feeding is adopted in either the front or rear bearings. The minimum percentage differences can be achieved with the 3-row feeding in the rear bearing and the 2-row feeding in the front bearing.

REFERENCES

[1] Weck M, Koch A. Spindle-Bearings Systems for High-Speed Applications in Machine Tools. Annals of the CIRP. 1993; 42: 445-448.

[2] Nelson HD. A Finite Rotating Shaft Element Using Timoshenko Beam Theory. Journal of Mechanical Design. 1980; 102: 793-803.

[3] Edney SL, Fox CHJ, Williams EJ. Tapered Timoshenko Finite Elements for Rotor Dynamics Analysis. Journal of Sound and Vibration. 1990; 137: 463-481.

[4] Pinkus O, Sternlicht B. Theory of Hydrodynamic Lubrication. McGraw-Hill. New York: 1961.

[5] Su JCT, Lie KN. Approximate Solutions for Hydrostatic Journal Bearings with Multi-Array of Hole-Entry. Lubrication Engineering. 2002; 58: 19-28.

COST-EFFECTIVE WIRE-CUT EDM SYSTEM FOR PRECISION MOLD MANUFACTURING

Hyun-Goo Kim[1], In-Ho Song[2], Hyun-Ho Kim[1], Kwan-Woo Yoon[1] and Sung-Chong Chung[1]*
[1]Hybrid System Design & Control LABoratory
Department of Mechanical Engineering
Hanyang University, Sungdong-Gu, Seoul 133-791, KOREA
[2]Division of Mechanical Engineering
Ajou University, Yeongtong-Gu, Suwon 443-749, KOREA

ABSTRACT
Automatic toolpath generation system of the wire electrical discharge machining (EDM) process is proposed through the CADviewer. The visualization data of it are optimally transformed lightweight CAD files designed for collaborative works. NC toolpath of the wire-cut EDM process is generated from dimensional and sectional informations extracted from the visualization data. Using the developed system, short lead-time is accomplished without an extra design job for the wire-cut EDM NC code generation. This system is applied for 2-axis cutting for precision manufacture. In addition, verification of the generated NC code is performed on the viewer.

INTRODUTION
Wire-cut EDM(Electrical Discharge Machining) is widely used for precision machining of complex parts. Most mold manufacturers use AutoCAD to generate wire-cut EDM NC codes instead of pre-designed native 3D CAD files. Though some wire-cut EDM CAM softwares use native 3D CAD files, they only support a few CAD files. In addition, they are expensive to be introduced to small mold manufacturers.

In previous studies, during wire-cut EDM machining, Ivano et al. [1] proposed a method to reduce cutting error. The method remedies for workpiece of cutting error caused from wire bending by the real-time optical wire position sensor. Yang et al. [2] studied a minimization method of cutting error due to the circular interpolation by using R-map. In study of toolpath generation, Daniel et al. [3] studied to generate an appropriate toolpath of CNC machining, they studied creation of it from a CAD file. Wang et al.[4] proposed a method of toolpath generation using the centerline of the wire without considering thickness of wire. In this like, during EDM machining, it continuously studied for upgrading product quality through CAM system and for optimizing CNC machining. But, NC toopath generation system, using lightweight CAD file that is developed for sharing design information among collaborators, is not studied. The developed viewer system offer only dimensional verification function.

In this paper, an integrated wire-cut EDM CAM system is proposed as an extra module of the previously developed CAD viewer. This is an exclusive viewing system, which is developed for mold manufacturing, enabling dimensional inspection, draft check, and interference examination. By combining the two systems, short lead-time is accomplished without an extra design job for the wire-cut EDM NC code generation. This system is applied for 2-axis cutting for precision manufacture. In addition, verification of the generated NC code is performed on the viewer. Generation procedure of the NC code is as follows: First, visualize a CAD file including same or different shape of top and bottom planes on the viewer. Secondly, gather information of both top and bottom plane shapes of the translated data on the basis of Z-axis. Thirdly, sort out the entity information of the gathered plane shapes. Fourthly, generate cutting toolpath of X and Y 2-axis based on the sorted entity information. Fifthly, equalize each number of X, Y points, and then match each point for the smooth cutting. Sixthly, generate optimal NC toolpath code dependent on several types of wire-cut EDM machines by constructing a database of machining conditions. Seventhly, display a feature of wire in the developed CAD viewer, and combine the simulation module for the verification of the generated NC code. By using the proposed system, NC codes for 2-axis wire cutting are generated from the CAD viewer without an expensive CAM system, and short

lead-time is achieved. The efficiency of the system is confirmed on the CADviewer.

CAD DATA INTERFACE

Fig. 1 shows the structure of the translation server. Fig. 1 shows lightweight files produced from several CAD systems. Fig. 1(b) represents the InterOp Reader of Spatial Inc., which converts the ACIS kernel data into lightweight files. Fig. 1(c) shows the 3D modeling ACIS kernel. Finally, Fig. 1(c) represents the developed data extractor module, which generates lightweight files through the ACIS kernel API. All the processes described so far are automatically managed through the translation server. Various commercial CAD files (Fig. 1(a)) are converted into lightweight files through the proposed system. The CAD entities are mapped to the ACIS kernel entities and then to the lightweight entities [5, 6].

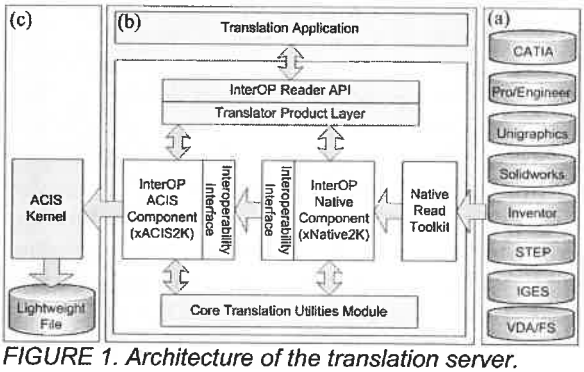

FIGURE 1. Architecture of the translation server.

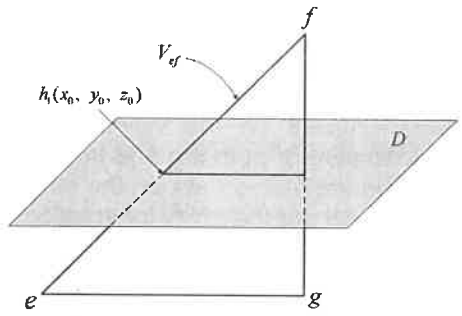

FIGURE 2. A triangle and a section plane.

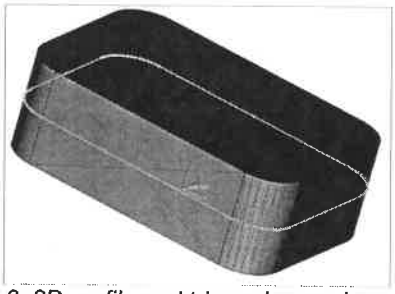

FIGURE 3. 2D profile and triangular meshes.

NC CODES FOR 3D GEOMETRIC SHAPE

Wire-cut EDM is a process of metal machining, it machine a workpiece using a thin wire has tension and through electrical erosion by generating between workpiece and the traveling wire. Among the wire-cut EDM machine, 2D machining type that vertical type machine most widely is used, is for machining a workpiece which is same shapes of upper and lower. Coordinate of workpiece surface is defined a local position in X and Y axes, it generates NC code through circular interpolation. During linear and circular interpolation, G-code is used mainly as follows:

G01: linear interpolation, X, Y

G02: circular interpolation CW [clockwise direction], X, Y, I, J

G03: circular CCW [counterclockwise direction], X, Y, I, J

I, J: The signed distance from start point to center

As above, 2D machining is consist of G-code of G01, G02 and G03 etc. Usually, NC programming method of EDM obtains a profile of 2D shape by inputting DXF file of AutoCAD, and is a type converting to G-code through it. The commercial CAM system generates profile of 2D shape using offered design module from each commercial system without using AutoCAD, and uses a generating method of corrected NC code through machining parameter and post-process.

GENERATION OF 2D PROFILE

2D profile will be generated toolpath, is determined by a polyline which is connecting line with each points after calculating the intersection point between the inputted section from user and the triangle mesh of visualization data. Computing the intersection point between plane and triangle for generating a polyline, be able to obtain the vector V_{ef}, using two points e, f of Fig. 2 and Eq. 1. The plane equation of plane D inputted from user is Eq. 2. If it substitutes the vector V_{ef} and coordinate of the intersection point $h_1(x_0, y_0, z_0)$ of section D for Eq. 1, Eq. 3 about parameter t_0 is able to be obtained. The plane D also satisfies because through the intersection point h_1. The parameter t_0 is able to be obtained using Eq. 2, 3. The coordinate of the intersection point is computed substituting the parameter t_0 for Eq. 3.

$$V_{ef} = x_f + k_1 t, y_f + k_2 t, z_f + k_3 t \quad (1)$$

$$ax_0 + by_0 + cz_0 = d \quad (2)$$

$$x_0 = x_f + t_0,\ y_0 = y_f + t_0,\ z_0 = z_f + t_0 \quad (3)$$

If the calculated intersection points be connected, the polyline is generated. Fig. 3 illustrates the intersection point between triangle and section with CAD visualization data. Fig. 3 illustrates to generate the section that based on XY plane after converted visualization data of injection molding CAD file is imported the proposed viewer system. In the proposed system, we can generate the section that based on XY, YZ, ZX plane, arbitrary three points, and perpendicular about a straight line.

NC CODE GENERATION

In this paper, the method of generating a NC code is that generated polyline in previous chapter is defined a toolpath of wire-cut. Toolpath is generated by G01 linear interpolation. If CAD file that is same shape of upper and lower is generated the section which based on XY plane, YZ plane and ZX plane, using an proposed viewer system in Fig. 4, the section automatically is located in centre position of CAD file by the perpendicular direction to the section. 2D profile in the Fig. 5 is consist of the linear interpolation that includes the circular part. After determine a point that based on this, wire-cut EDM toolpath is generated to G code computing local coordinate about a global center point. Local coordinate of each dimension be able to be computed using a coordinate is obtained from the commercial CAD data.

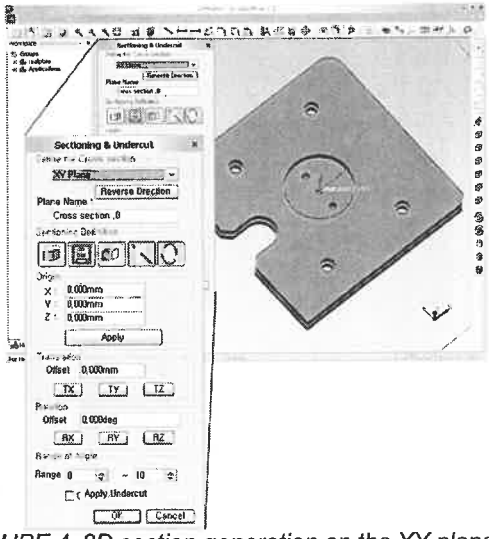

FIGURE 4. 2D section generation on the XY plane.

INSIDE-OUTSIDE CHECKING

Using a method introduced in the previous section, inner profiles of a workpiece such as a pocket or hole is generated together. However, shape of EDM in this paper needs to determine the inside-outside of a 2D profile through the odd-even test as shown in Fig. 5. The odd-even test is the most widely used test for making inside-outside decisions. When p is a point inside a polygon, any ray emanating from p and going off to infinity must cross an odd number of edges. Any ray emanating a point outside the polygon and entering the polygon crosses an even number of edges before reaching infinity. Hence, a point can be defined as being inside if we draw a line through it and if following this line, starting on the outside, we cross an odd number of edges before reaching it. Usually, we replace rays through points with scanlines, and we count the crossing of polygon edges to determine inside and outside. In this system, the odd-even number is determined through the checking of the polyline. Fig. 6 illustrates a result to keep only a required outside profile through test of the inside-outside [7].

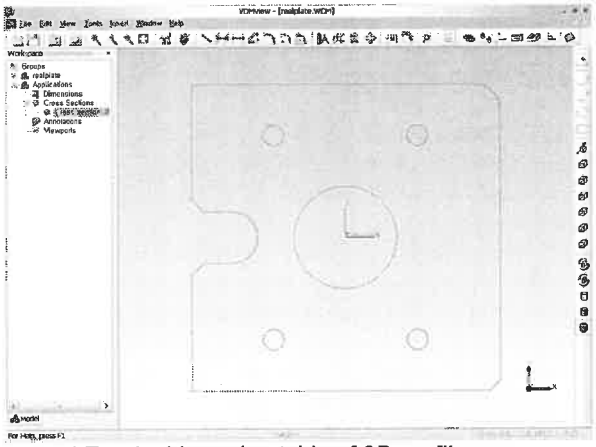

FIGURE 5. Inside and outside of 2D profile.

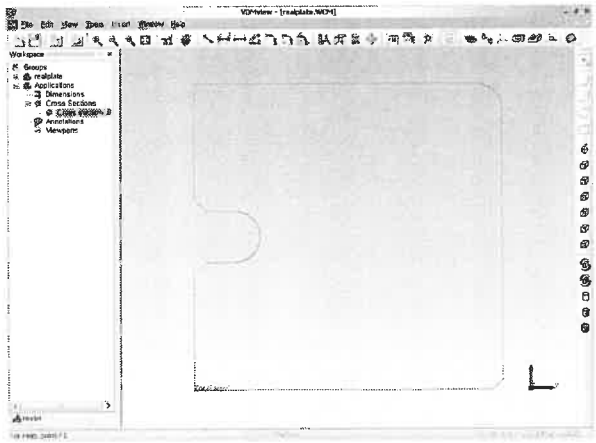

FIGURE 6. 2D profile which only has an outer.

To generate toolpath of wire-cut EDM has not only to consider a starting point of machining but also radius of wire, cutting speed, oversize and material of workpiece etc [7]. In this paper, the toolpath is generated by using lightweight CAD data, it is applied computing local location of the toolpath to the G code. Fig. 8 shows a part of the G code generated from the toolpath of wire-cut EDM using 2D profile in Fig. 7.

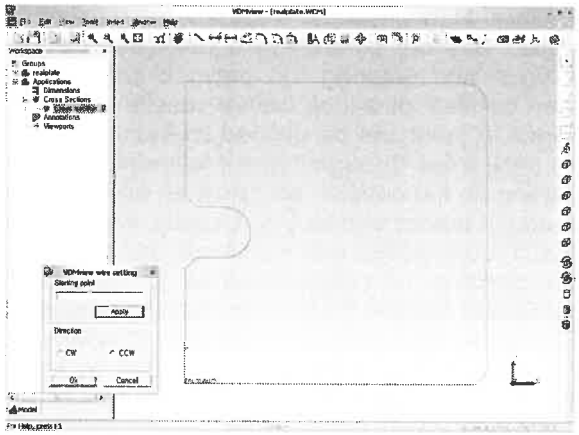

FIGURE 7. A dialog of direction selecting and the 2D profile.

```
...
N120 X-82.0575
N122 Y0.
N124 Y-49.9
N126 X-82.0455 Y-49.912
N128 G40 X-81.9955
N130 M50
N132 G0 X0. Y0.
N134 M60
N136 S0 D2
N138 G41 G1 X-82.0695 Y-49.988
N140 X-82.0575 Y-50.
N142 X67.9425
N144 Y50.
N146 X-82.0575
N148 Y0.
N150 Y-49.9
N152 X-82.0455 Y-49.912
N154 G40 X-81.9955
N156 M50
N158 G0 X0. Y0.
N160 M60
N162 S3151 D1
N164 G42 G1 X-82.0575 Y-49.988
N166 X-81.9825
N168 Y-50.
N170 X-82.0575
N172 M01
N174 Y-49.9
N176 Y-49.825
N178 X-82.0455
N180 Y-49.9
...
```

FIGURE 8. Generated G code of Wire EDM by proposed system.

CONCLUSIONS

By designing a cost-effective wire-cut EDM system for precision mold manufacturing, following conclusions are obtained:

(1) Using triangular meshes and section curves of a CAD file, NC toolpath generation of the wire-cut EDM process is performed.

(2) Using the proposed integrated system, it is possible to generate a toolpath of wire-cut EDM without using extra CAD/CAM modules.

(3) An integrated CAD viewer system for injection mold design and manufacture is developed through the NC wire-cut EDM module.

(4) The validity and effectiveness of the developed system have been verified through case studies on the CADviewer.

For the further study, 4-axis toolpath generation, material DB, machining parameter DB, etc. should be studied.

REFERENCES

[1] Ivano B, Axel B, Dirk D. A Simplified Post Process for Wire Cut EDM. Journal of Materials Processing Technology. 1996; 4: 385-389.

[2] Yang M, Lee E. NC Verification for Wire-EDM using an R-map. Computer-Aided Design. 1998; 28: 733-740.

[3] Daniel C H, Yang J J, Chuang Z, Han Z, Ding S. Boundary-conformed Toolpath Generation for Trimmed Free-form Surfaces via Coons Reparametrization. Journal of Materials Processing Technology. 2003; 138: 138-144.

[4] Wang J, Ravani B. Computer Aided Contouring Operation for Traveling Wire Electric Discharge Machining (EDM). Computer-Aided Design. 2003; 35: 925-934.

[5] Song I H, Chung S, Chung S C. Precision Design Verification System of Injection Molds using Web-based 3D Viewing Technology. Proceeding of the ASPE. 2006; 21: 451-454.

[6] Song I H, Chung S C. Geometric Kernel Design of the Web-Viewer for the PDM Based Assembly DMU. Transactions of the KSME(A). 2007; 31: 260-268.

[7] Edward A. Interactive Computer Graphics : A Top-Down Approach Using OpenGL 3rd Edition. Addison-Wesley: 2003.

SELECTION OF OPTIMAL CUTTING CONDITIONS IN MICRO-ENDMILLING PROCESSES

Kwang-jo Lee[1], Won-seck Lee[1], Kyung-Don Kim[2] and Sung-Chong Chung[1]*
[1]Hybrid System Design & Control LABoratory
Department of Mechanical Engineering
Hanyang University, Sungdong-Gu, Seoul 133-791, KOREA
[2]Small Business Corporation, Gyeonggi Regional Headquarter, Suwon, KOREA

ABSTRACT
Micro-endmillng process is applied to fabricate precision mechanical parts cost-effectively. It is a complex and time-consuming job to select optimal cutting conditions with high productivity and quality. In this paper, high speed machining(HSM) experiments of heat-treated die steel (H-13, HRc 51) are studied for optimum selection of micro-ball endmilling conditions. Tool life and wear characteristics under various cutting conditions are investigated through a monitoring system. It is equipped with the machine vision and cutting force measurement systems. Optimal cutting conditions are obtained through the Taguchi method.

INTRODUCTION
The Micro-endmilling process has been widely used to produce micro components, such as micro dies and molds, micro machines, watches, bearings, etc. [1,2] Micro-endmill wear deteriorates machining accuracy and productivity, and increases cutting force. It causes tool breakage and drops productivity. By correctly measuring the wear of micro-endmills, it is possible to understand the wear characteristics and to predict the optimal change time of endmills. Using the cutting force information, endmills are protected form tool breakage. To improve productivity and quality of cutting condition for maximizing material removal rate, condition monitoring linked with optimal selection of cutting conditions is indispensable.

Tool wear measurements are divided into direct and indirect methods. The indirect methods, such as cutting trust force, torque signal and cutting temperature measurements have been used for conventional machining processes [3]. These methods deduce tool life or wear from change of measuring signals. However, it is impossible to observe the wear of complex shaped endmills by using the indirect methods. For direct methods, measurements using SEMs, confocol microscopes, and lasers have been used. However, these measurement systems are expensive and difficult to use in the rugged work space.

It this paper, a novel machine vision system equipped with a precision servo stage is applied for wear measurement of micro-endmills directly [4,5]. Cutting force measurement system using a tool dynamometer is proposed to estimate wear during micro-endmilling processes. Micro-endmill wear is measured by the image processing and edge detection methods [6]. Gradient of cutting force signal is derived from the tool dynamometer system. Optimal cutting conditions with better tool life and MRR are obtained from the Taguchi method with the same weight values on the gradient of cutting forces and the direct wear measurement.

FIGURE 1. Experimental set up.

EXPERIMENTAL SET UP
As the high spindle speed with high accuracy is required in the micro-endmilling process, a high-precision CNC milling machine equipped with a 150,000rpm air-spindle is applied for

experiments. Fig. 1 shows the overall experimental set up. The high speed spindle is actuated by 0.5 MPa air pressure. The rotational speed of the spindle is fixed 150,000rpm. The workpiece is heat treatment mold and tool steel, H-13(HRc51), and the shape is a rectangular block($100\times100\times30mm^3$). TiAlN coated Φ 0.5 (0.0197 in) ball nose endmills are used in all experiments. The Micro-endmills are attached to the spindle of the HTS-1501S.

Wear Meaurement

Three types of wear are commonly observed in Micro-endmills: flank wear, margin wear, and crater wear. In this study, the flank wear is observed according to the milling process and quantized from the area and the average length of wear region. When flank wear occurs at the cutting lips, precision of workpiece surface is decreased and micro-endmill may cease to cut by breakage. To measure flank wear V_{BArea} shown in Fig. 2 , machine vision system shown in Fig. 3 and Eq. (1) is applied [5].

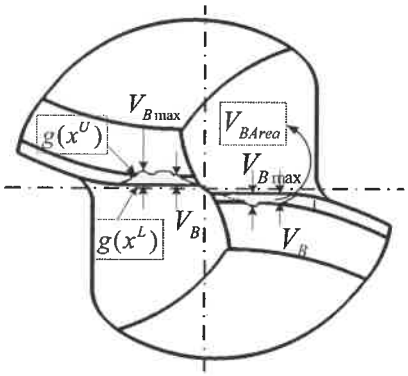

FIGURE 2. Flank wear geometry of endmills.

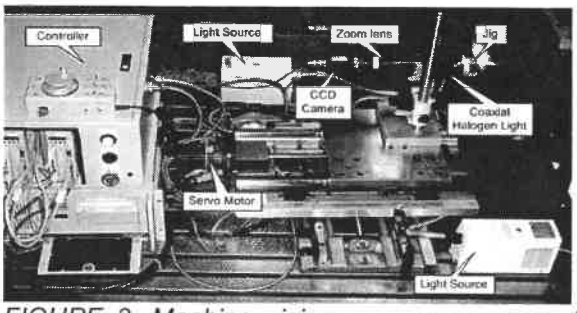

FIGURE 3. Machine vision wear measurement system.

$$V_{BArea} = \int_{SP}^{EP} [g(x^U) - g(x^L)]dx \qquad (1)$$

where, $f(x^u)$ = upper value of $f(x)$ at x

$f(x^L)$ = lower value of $f(x)$ at x

SP = x value of the start point

EP = x value of the end point

Measured images from the machine vision system are processed by three steps of digital image processing for measurement of flank wear: preprocessing, section thresholding, and extraction of wear area. In preprocessing, median filter is used to reduce the noise of the acquired images. The median filter replaces the value of a pixel by the median of the gray levels in the neighborhood of that pixel. It provide excellent noise-reduction capabilities, with considerably less blurring [6]. The section thresholding method is employed to obtain the binary image with preserving the shape of mirco endmills. The areas of the flank wear are assigned a value of '1' and others '0', with a suitable threshold value. In extraction of wear area, edge detection is used to measure the boundary of worn region of the flank surfaces from the binary image. In this paper, Sobel method calculating the horizontal and vertical gradients at a random point(x, y) is used to detect the edges [5,6].

Gradient of Cutting Force

In micro-cutting process, cutting lips remove chips along an incline plane of a tool as those reach a workpiece. At this time, cutting force is generated. In this study, cutting force is considered for evaluation of cutting force. The cutting force is defined as the gradient of cutting force which is generated against workpiece. The gradient of cutting force is defined as average of resultant force(F_{xy}) which is the sum of F_x and F_y between a region of 1m and 30m. By using dynamometer installed on jig, the signal of cutting force generated from a workpiece is measured on the NC milling process, and this signal is amplified through a dynamometer amplifier. The amplified signal of cutting forces is sampled by using an oscilloscope (LeCroy, 9314A) and NI PXI-1042Q(DAQ board equipped) based on Labview 8.0. The section average is calculated and graphed to analyze data by using Matlab program. The average of cutting force is used as relative data.

EXPERIMENTS

Preceding experiments are conducted to derive proper range of feed, radial depth of cut, axial depth of cut, and rotational speed. The rotational

speed is fixed at 150,000rpm, and experiential values are used in axial and radial depth of cut. Feed is applied at 2500mm/min in consideration of specification of NC machining center. Following the suggested condition, the radial and axial depth of cuts are determined as 0.125mm and 0.05mm, respectively.

Selection of Facts and Levels

Each factor, Level and arrangement is selected based on the result of preceding experiments. Feeds are divided into 2000, 2500, 3000 mm/min proportionally to consider specification of NC machining center. The bounds of axial and radial depth of cut are selected on consideration of progress of wear and cutting force. Axial depth of cut is determined from 0.05 to 0.10, and radial depth of cut is determined from 0.1 to 0.15. Each interval of level is increased per 0.025mm equally for estimation of tendency according to conditions. Table 1 indicates the milling test parameters.

TABLE 1. Selected factors and levels

Condition \ Level	1	2	3
Feed(mm/min) (A)	2000	2500	3000
Axial depth(mm) (B)	0.050	0.075	0.100
Radial depth(mm) (C)	0.100	0.125	0.150

Experimental Method

Taguchi method, which combines the experimental design and the quality loss function, has been applied to the robust design and some complex problems in manufacturing. Taguchi used the signal-to-noise(S/N) ratio to evaluate the quality characteristics and preserve it from interaction and disturbances. S/N ratio is defined by the objective function, the characteristics. Therefore, considering the cutting force and the flank wear of micro-endmill, the smaller-the-better is applied. In this case, S/N is used to minimize the expected value of loss function, $L(y) = kE(y^2)$, and obtaining into repeated measurement data, mean squared deviation is estimate of $E(y^2)$ to be expressed as follows;

$$MSD = \frac{1}{n}\sum_{i=1}^{n} y_i^2 \qquad (2)$$

The S/N ratio characteristic for the smaller-the-better in Taguchi method can be expressed as follows:

$$\mathrm{S/N} = -10\log\left[\frac{1}{n}\sum_{i=1}^{n} y_i^2\right] \qquad (3)$$

Where S/N is the observe value (dB); n is the number of observations; y_i the experimental data. In this study, a $L_9 3^3$ orthogonal array is employed. Addtionally, repetition experiment is arranged as outer array considering the processing errors.

RESULTS AND DISCUSSION

Throughout repeated experiments with combined conditions, the S/N ratios in Table 2 show the smaller-the-better characteristic with application of the cutting force and the wear quantity. Taguchi method is applied for selection of the optimal cutting conditions with the same weight values about cutting force and quantity of wear,

TABLE 2. Orthogonal array and values of cutting force and flank wear

No	Factors			S/N_1	S/N_2	S/N_0
	A	B	C			
1	2000	0.050	0.100	-38.720	-27.924	-36.057
2	2000	0.075	0.125	-30.400	-22.671	-28.064
3	2000	0.100	0.150	-33.141	-21.438	-30.415
4	2500	0.050	0.125	-31.754	-24.270	-29.461
5	2500	0.075	0.150	-30.553	-22.671	-28.198
6	2500	0.10	0.100	-32.908	-24.910	-30.537
7	3000	0.050	0.150	-33.198	-23.405	-30.621
8	3000	0.075	0.100	-31.198	-26.486	-29.452
9	3000	0.100	0.125	-30.423	-26.150	-28.792

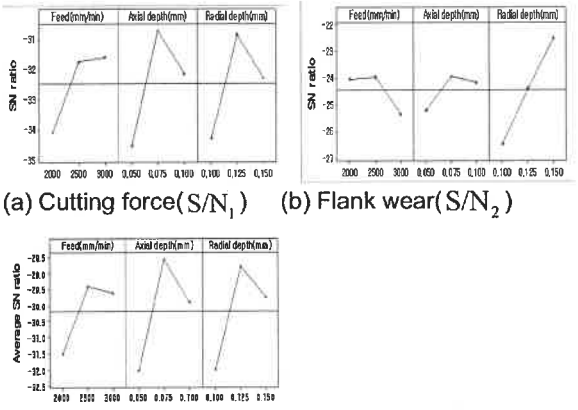

(a) Cutting force(S/N_1) (b) Flank wear(S/N_2)

(c) Overall(S/N_0)

FIGURE 4. Comparison of S/N ratios

The driven optimal conditions about the cutting force, the flank wear and the overall are shown as Fig. 4. The predicted optimal parameters

are $A_2B_2C_2$. The S/N ratio value(S/N =-26.426) of the predicted optimal condition, which is obtained from Taguchi method is better than others. Two verification experiments are conducted to prove the selected optimal cutting conditions. The gradient of cutting force is reduced comparing to the other conditions (Fig. 5.), and the quantity of flank wear is decreased considerably (Fig. 6.). Though the S/N ratio of the optimal cutting conditions, -27.380, is smaller than the predicted, it is better than others (Table 3).

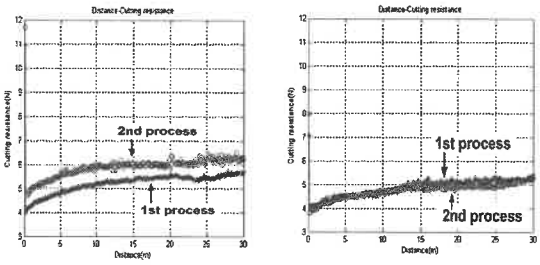

FIGURE 5. Assessment of cutting force.

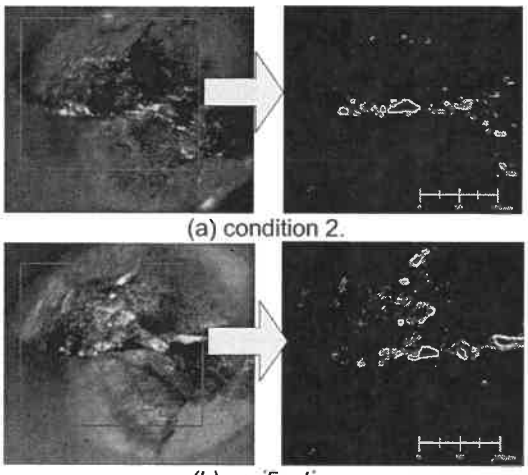

(a) condition 2.

(b) verification

FIGURE 6. The formation of flank wear for different conditions

TABLE 3. Comparison of best and optimal conditions.

No.	Factors			SN_1	SN_2	SN_0
	A	B	C			
2	2000	0.075	0.125	-30.400	-22.671	-28.064
Veri	2500	0.75	0.125	-30.049	-19.181	-27.380 (-26.424)

( ) is predicted S/N ratio

In the comparison of the optimal condition and the best condition in the orthogonal array, we are able to confirm the improvement as follow, $10^{0.068}$=1.169 is applied the low of multiple proportions. This value implies improvement of tool life.

CONCLUSIONS

Performed HSM with micro ball nose endmill, TiAlN coated Φ 0.5 (0.0197 in) and workpiece, the heat treatment mold and tool steel, with $100\times100\times30mm^3$.

An experimental approach with Taguchi methods is presented to evaluate the flank wear and the cutting force in HSM using micro-endmill. Also, the optimal condition is driven by analyzing experimental results of main cutting parameters. The results are summarized as follows:

(1) Using orthogonal array of 3factors and 3levels, the number of experiments is minimized and the change of cutting forces and the behavior of flank wear are observed in each condition.

(2) The optimal condition is derived by experimental result using Taguchi method within interested ranges. The condition Indicates what is able to extend the tool life quantitatively.

(3) The wear of micro-endmill is quantized by using the machine vision system and the image processing procedures.

(4) Suggested cutting force measurement system verifies that the behavior of resistance changes is observable and the condition of tools in predictable.

REFERENCES

[1] Uhlmann, E. and Schauer, K. Dynamic Load and Strain Analysis for the Optimization of Micro End Mills. CIRP Annals-Manufacturing Technology, 2005; 54(1): 75-78.

[2] Bissacco, G., Hansen, H. N. and De Chiffre, L. Micromilling of Hardened Tool Steel for Mould Making Applications. Journal of Materials Processing Technology, 2005; 167: 201-207.

[3] Tlusty, J. and Andrews, G. C. A Critical Review of Sensors for Unmanned Machining. CIRP Annals, 1983; 32(2): 563-572.

[4] Yoon H. S, Chung S. C. Vision Inspection of Micro-drilling Processes on the Machine Tool. Transactions of the NAMRI/SME, 2004; 32: 391-398.

[5] Choi, Y. J. and Chung, S. C. Monitoring of Micro-drill Wear by Using the Machine Vision System. Transactions of the NAMRI/SME. 2006; 34: 143-150.

[6] Gonzalez R C, R E Woods. Digital Image Processing. Prentice, Hall Inc. New Jersey; 2002.

SELF-UNBALANCE-CORRECTION TECHNIQUE FOR PRODUCTION PROCESS OF PRECISION HIGH-SPEED ROTORS

Keisuke Nagato[1], Tetsuya Hamaguchi[1], Toyoka Ide[1], Naohiro Ohno[2], Kensuke Tsuchiya[1], and Masayuki Nakao[1]
[1]Department of Engineering Synthesis, The University of Tokyo, Tokyo, Japan
[2]Industrial Technology Center, Konicaminolta Business Technologies, Ltd., Tokyo, Japan

INTRODUCTION

The unbalances of precision high-speed rotors, such as polygon scanner motors (FIGURE 1), optical disk drives, or hard disk drives, must be precisely corrected during their production. Although the precise correction of the rotors leads to higher rotation speed and low rotation noise, cost reduction of the unbalance correction process is essential.

Various passive balancing systems for suppression of the axial runout of the rotors around the whirling speeds have been applied to various rotors [1][2]. However, these techniques cannot be used for precision high-speed rotors. The polygon scanner motor shown in FIGURE 1 (by Konicaminolta, Ltd.) is precisely corrected to under 1 mg·cm (the mass of the rotor is 35 g). And now, the automatic balancing system is known a passive balancing technique, particularly for removable unbalanced weights. Washing machines are balanced using fluid balancer [3], and optical disk drives are balanced using ball balancers [4]. In this study, we applied the automatic balancing systems to the production process for high-speed rotors. We named this technique, "self-unbalance-correction (SUC)", and we carried out an experiment to confirm the principle using rotors of the size used in polygon scanner motors.

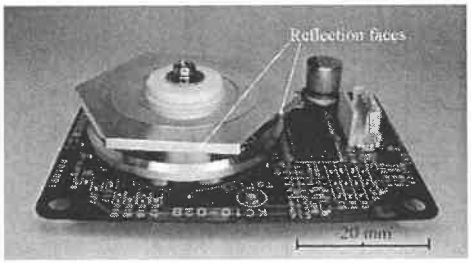

FIGURE 1. Polygon scanner motor (maximum rotation speed: 70,000 rpm).

SELF-UNBALANCE-CORRECTION (SUC)

We propose two variations of the SUC technique and demonstrate experiments to confirm the principles. One of them uses ultraviolet (UV) -cured resin (FIGURE 2), and the other uses ball balancers and adhesive (FIGURE 3). In both techniques, a rotor of unbalanced weight is set on a rotational translation oscillation system. When the phase of the rotor is inversed after achieving oscillation resonance, the balancers (UV-cured resin or ball balancers) diagonally opposite the unbalanced weight are fixed to the rotor. Therefore, the unbalance of the rotor is automatically corrected.

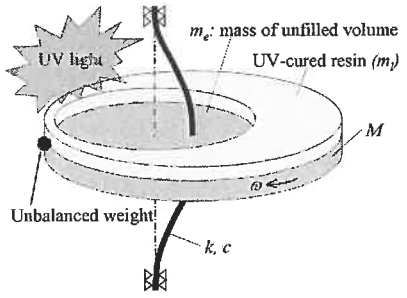

FIGURE 2. Self-unbalance-correction using UV-cured resin.

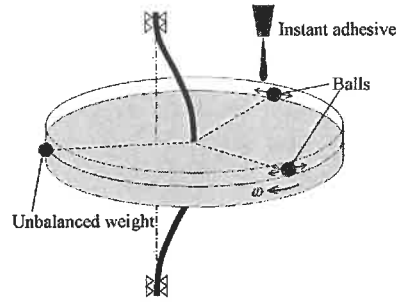

FIGURE 3. Self-unbalance-correction using ball balancers.

PRINCIPLE OF SUC USING UV-CURED RESIN

Here, we explain the principle of SUC using UV-cured resin. The equation of the basic oscillation model (FIGURE 4, left) is

$$M\ddot{r} + c\dot{r} + kr = M\varepsilon\omega^2 \cos\omega t \quad (1).$$

The mass of the rotor is M, the rotation speed (angular frequency) is ω, the spring constant and damping constant of the rod spring are k and c, respectively, the runout of the rotor is r (vector), the unbalanced weight (moment) is $M\varepsilon$?(ε?: vector). That is, ε is the relative position of the center of gravity of the rotor (G) from the rotation center (S).

When the liquid (mass: m_l) is added to the rotor, as shown in FIGURE 4, right, the inside wall of the liquid is concentric with the oscillation center. The amount of liquid is sufficient for the inside wall not to interfere with the outside wall. When the relative position of the rotation center S from the oscillation center O' is r' (vector), the moment change caused by the slanted liquid is $-m_e r'$ (m_e: mass corresponding to the unfilled liquid). Therefore, the changed unbalance position ε' (relative position of the new center of gravity of rotor G' from rotation center S) is expressed as

$$\varepsilon' = \frac{M\varepsilon - m_e r'}{M + m_l} \quad (2).$$

Also, the length from the oscillation center to the rotation center is expressed as

$$|r'| = \frac{\Omega^2}{\sqrt{(\Omega^2 - 1)^2 + (2\zeta\Omega)^2}}|\varepsilon'| \quad (3),$$

where

$$\zeta \equiv \frac{c}{2\sqrt{(M + m_l)k}} \quad (4),$$

$$\Omega \equiv \frac{\omega}{\omega_n} \quad (5),$$

$$\omega_n = \sqrt{\frac{k}{M + m_l}} \quad (6).$$

ζ is the damping ratio, Ω is the rotation speed ratio, and ω_n is the oscillation rotation speed. Then, the correction factor (CF) η (unbalanced weight after correction / unbalanced weight before correction = $(M+m_l)|\varepsilon'| / M|\varepsilon|$) is expressed as

$$\eta = \sqrt{\frac{1 + \left(\frac{2\zeta\Omega}{\Omega^2 - 1}\right)^2}{\left(1 + \frac{m_e}{M + m_l}\frac{\Omega^2}{\Omega^2 - 1}\right)^2 + \left(\frac{2\zeta\Omega}{\Omega^2 - 1}\right)^2}} \quad (7).$$

From this equation, the rotation speed ratio for the smallest CF is determined by the oscillation system (M and k, i.e., ω_n). Therefore, only two design parameters need to be considered for a better (lower) CF; mass ratio (m_e / $M + m_l$) and damping ratio ζ. In other words, the volume of the unfilled part should be maximized and the total mass of the rotor (including mount and motor, etc.) should be as small as possible. The damping of the oscillation system should also be as small as possible. Quantitative values will be given later.

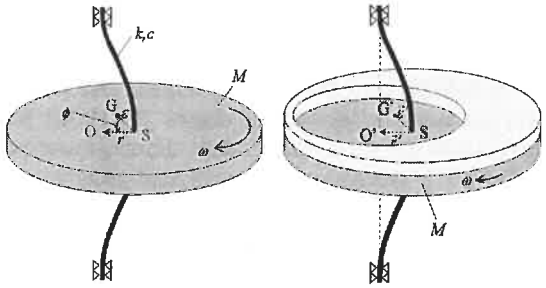

FIGURE 4. Oscillation models without and with liquid.

PRINCIPLE OF SUC USING BALL BALANCERS AND ADHESIVE

In the second technique, balls that balance the unbalanced weight are fixed to the rotor. The rotor is mounted on an oscillation translation system similar to the SUC using UV-cured resin. FIGURE 5 shows a schematic of SUC using two ball balancers. If there was no friction between the balls and the wall, the balls would be positioned at certain positions above the oscillation resonance and the unbalanced weight would be perfectly corrected. At this time, instant adhesive, with mass significantly smaller than that of the ball balancers, could be used to fix the balls.

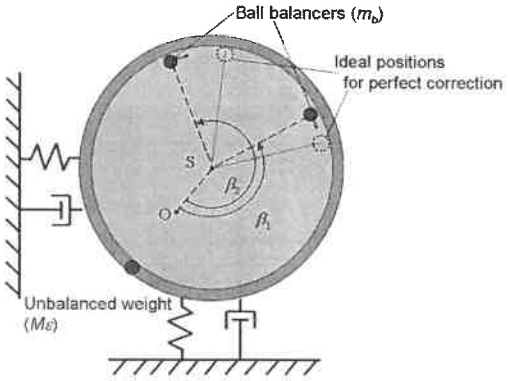

FIGURE 5. Oscillation model of ball balancers (in the case of two balls).

However, in an actual system, balls encounter friction from the guide wall. This is because CF has a limit. FIGURE 6 shows the forces applied to the ball and their values.

According to the sine and cosine laws,

$$\frac{\varepsilon}{\sin\alpha} = \frac{l}{\sin\beta} \quad (8),$$

$$l = \sqrt{R^2 + \varepsilon^2 - 2R\varepsilon\cos\beta} \quad (9).$$

The counterforce from the oscillation center is

$$F_c = m_b l\omega^2 \quad (10).$$

From Eqs. (8)-(10), the driving force F_D and the friction force from the wall f are expressed as

$$F_D = F_c \sin\alpha = m_b \varepsilon\omega^2 \sin\beta \quad (11),$$

$$f = \mu F_r = \mu F_c \cos\alpha \cong \mu m_b R\omega^2 \quad (12),$$

where $(\varepsilon / l), (\varepsilon / R) << 1$.

The ball balancers are fixed when the driving force F_D balances the friction force f. Then, the stable position of the ball balancers is independent of the mass and the rotation speed. However, the rotation speed must be selected to be above the oscillation resonance. Therefore, the only method of obtaining better CF is to reduce the friction. The effect of friction on balancing has been reported in studies on the automatic ball-balancing system for optical disk drives [5][6].

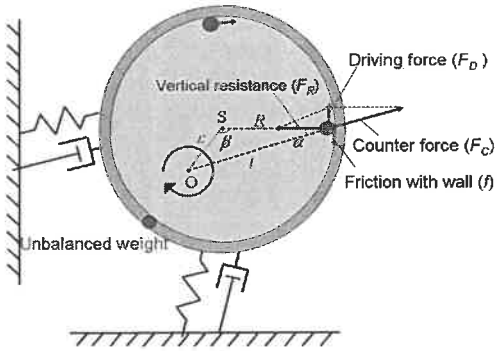

FIGURE 6. Actual forces applied to ball balancers.

EXPERIMENT ON SUC USING UV-CURED RESIN

We carried out an experiment to demonstrate SUC using UV-cured resin. FIGURE 7 shows the experimental setup and TABLE 1 shows the values used in the experiment. We used NOA81 by NORAND, Ltd., as the UV-cured resin. The viscosity is 300 cps and the density is 1.1. The precuring time is 10 sec and completion time is shorter than 60 sec when UV of over 2 W/cm^2 is applied. The initial unbalanced weight was set at 80 mg·cm.

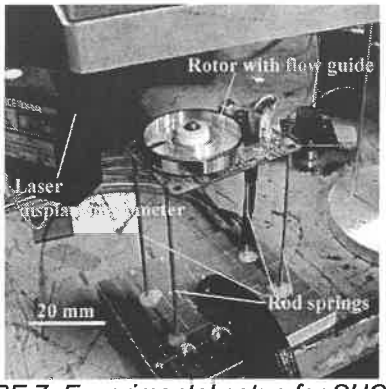

FIGURE 7. Experimental setup for SUC using UV-cured resin.

TABLE 1. Designated values in experiment to demonstrate SUC using UV-cured resin.

Symbol	Value
M	60 [g]
K	6400 [N/m]
C	0.94 [Ns/m]
ζ	0.024
ω_n	3120 [rpm]
M_l	0.5 [g]
M_e	16 [g]

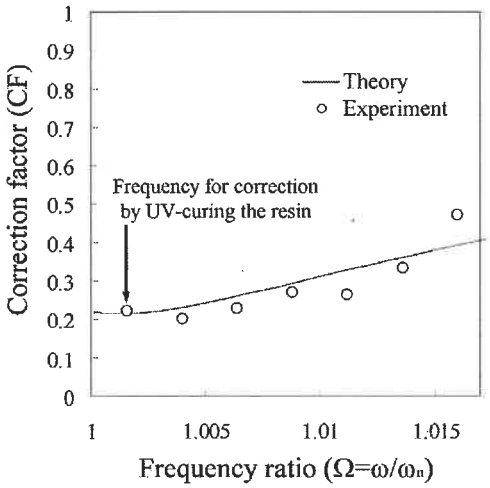

FIGURE 8. Experimental result of SUC using UV-cured resin.

FIGURE 8 shows the experimental result of SUC using UV-cured resin. The experimental CF has good agreement with theoretical values. The rotor unbalance was actually corrected by the UV-curing, and the runout was reduced to 20% of the original runout at all frequencies. A lower damping ratio of the spring and a greater mass ratio of the rotor will result in better CF.

EXPERIMENT ON SUC WITH BALL BALANCERS AND ADHESIVE

We demonstrated SUC using ball balancers and adhesive. The experimental setup is shown in FIGURE 9. TABLE 2 shows the values used in the experimental system. Again, we obtained unbalance correction, as shown by the blue bars in FIGURE 10. However, there is some scatter around the displacement peak of 400 μm (CF = 27%). We applied vibration (1.8 G) to reduce the friction between the balls and the wall. Then we confirmed the improvement of CF, as shown by the red bars in FIGURE 10 (average CF = 15%). Uncorrected samples (CF = 100%) are caused by undesirable stable situations, where the two balls are positioned at opposite sides to each other.

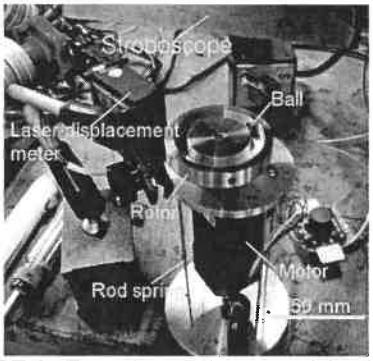

FIGURE 9. Experimental setup of SUC using two ball balancers.

TABLE 2. Designated values for experiment to demonstrate SUC using ball balancers.

Symbol	Value
M	500 [g]
K	2050 [N/m]
ω_n	510 [rpm]
m_b	1.14 [g]
R	22 [mm]

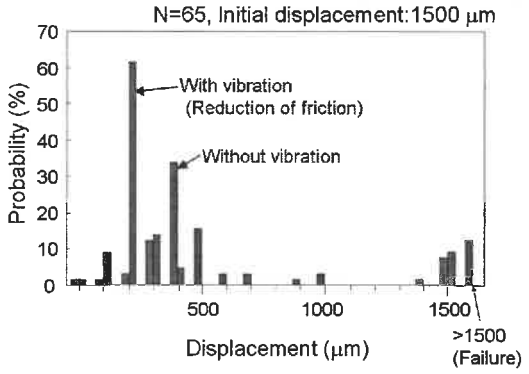

FIGURE 10. Experimental result of SUC using two ball balancers.

ADVANCED SUC BY MULTISTEP PROCESS

We also briefly mention multistep SUC for obtaining superior CF. FIGURE 11 shows a rotor with multiple balancer guides. Repetitive correction and fixation using balancers will realize near-perfect correction.

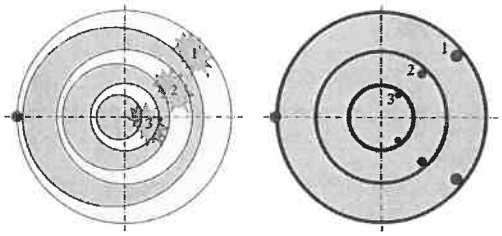

FIGURE 11. Multistep process.

CONCLUSION

We proposed a self-unbalance-correction (SUC) technique for precision high-speed rotors. We demonstrated SUC using UV-cured resin and ball balancers. The best correction factor, obtained using UV-cured resin, was 20%, and the average correction factor obtained using ball balancers was 27%. Furthermore, the addition of vibration reduced the friction of the balls and further improved the correction factor to 15% on average.

REFERENCES

[1] Tllian, T.E., Gustafsson, O.G., Progress in rolling bearing vibration research and control, ASLE-Trans 1965; 8: 195-207.

[2] Kirk, R.G., Gunter, E.J., The effect of support flexibility and damping on the synchronous response of a single-mass flexible rotor, Trans ASME, J Eng Ind 1972; 94: 221-322.

[3] Bae, S., Lee, J.M., Kang, Y.J., Kang, J.S., Yun, J.R., Dynamic analysis of an automatic washing machine with a hydraulic balancer. J Sound Vib 2002; 257: 3-18.

[4] Rajalingham, C., Bhat, R.B., Rakheja, S. Automatic balancing of flexible vertical rotors using a guided ball. Int Mech Sci 1998; 40: 825-834.

[5] Kim, W., Lee, D-.J., Chung, J., Three-dimensional modeling and dynamic analysis of an automatic ball balancer in an optical disk drive. J Sound Vib 2005; 285: 547-569.

[6] Wouw, N.V.D., Heuvel, M.N.V.D., Nijmeijer, H., Rooij, J.A.V., Performance of an automatic ball balancer with dry friction. Int J Bifurcation Chaos 2005; 15: 65-82.

SHARING OF CAE DATA TO FABRICATE PRECISION PARTS IN INJECTION MOLDING AND DIE CASTING PROCESSES

In-Ho Song[1], Hyun-Goo Kim[2] and Sung-Chong Chung[2]*
[1]Department of Mechanical Engineering
Ajou University, Yeongtong-Gu, Suwon 443-749, KOREA
[2]Hybrid System Design & Control LABoratory
Department of Mechanical Engineering
Hanyang University, Sungdong-Gu, Seoul 133-791, KOREA

ABSTRACT
Injection molded and die casted products are widely used in the auto, IT, appliance, and tool industries. Accurate molds and short lead-time are critical requirements for the mold industry. To make precision molds rapidly, a collaborative design tool with simulated injection or casting capability is required in the design process. This paper proposes the developmental procedure of a web-based 3D CAD verification system equipped with a CAE visualization module of injection molding and die casting processes. A CAE visualization module linked with previously developed CAD viewer is developed through the XML file converter. An open data translator is constructed through the CAD-CAE kernel to interface various CAE data with the CAE visualization system. Performance of the developed system is confirmed through various case studies.

INTRODUCTION
Injection-molded and die-casted products are widely used in various industries such as auto, IT, optics, appliance, etc. The molding processes consist of four stages such as filling, packing, cooling and ejection. Warpage, misrun, weldlines, blow holes, etc. degrade product quality. Mold design and determination of injection parameters are important to fabricate defect-free parts in the injection molding and die casting processes. To design a good mold or die, many design factors, such as mold size, number of cavity, cavity layouts, runners and gates systems, shrinkage and ejection system, should be considered. Molding conditions such as melt temperature, mold temperature and injection time are important operating parameters in the injection processes. Several CAE tools for filling, cooling, warpage and stress analyses have been used to the design and the determination of these process parameters. However, these processes are highly skilled jobs and have significantly depended upon engineers' experience and intuitiveness. To complete the design and the selection of the process parameters, a lot of collaboration between many engineers and the product development supervisors are required. These procedures delay the lead-time to produce molds and dies, and products. False collaboration degrades the quality of products as well.

STEP has been used for CAE data conversion. FEA(finite element analysis) uses STEP AP104 [1] and hybrid material structure uses STEP AP209 [2]. However, STEP AP209 has problems to support various CAE solvers. Deng et al. [3] proposed a CAE-CAD Integration system for developing an injection molding design system. It used an integrated data model for both design and analysis. As the system was built on top of existing CAD and CAE systems, it made full use of the strong functionality of commercial computer aided systems. However, it was not applicable to data sharing between CAD and CAE systems. Integration requires a feature-based integration model and an interactive design-analysis tool based on the model. To reduce CAD and CAE investment, but to review and discuss the analysis results without CAD and CAE systems on the Internet, a CAE verification tool over a CAD viewer is required.

This paper describes developmental procedure of a web-based 3D CAD verification system equipped with a CAE verification function. The developed system does not require expensive commercial CAD and CAE systems for collaborators. They review and discuss CAD and CAE results on the Web through the CAD viewer with the CAE review function. As the usage of the viewer is simple, collaboration between many engineers and supervisors in the design and manufacturing of molds, dies and products

is conducted efficiently. Developed CAE verification tool based on the ActiveX technology expedites the fabrication process of molds and dies. It reduces the lead-time to produce injection molded or die casted products. Performance of the system is confirmed through case studies.

TRANSLATION OF CAE ELEMENTS

Six geometric elements of CAE data are described in Fig. 1. They are comprised of two type elements: One is a face mesh composed of a triangle and quad models shown in Fig. 1(a), the other is a volume mesh composed of a hexahedron, pyramid, tetrahedron and pentahedron models shown in Fig. 1(b). The volume meshes are visualized through tessellated triangle meshes.

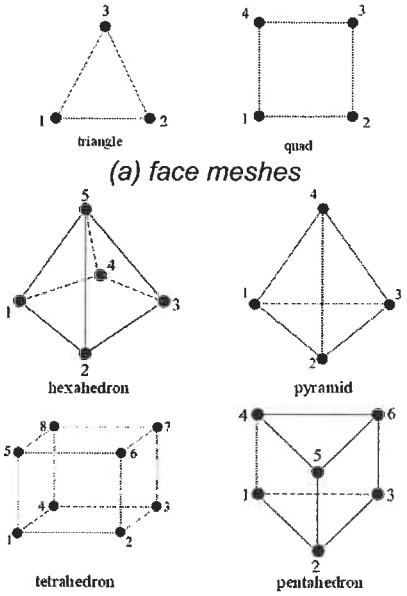

(a) face meshes

(b) volume meshes

FIGURE 1. Elements of the CAE mesh.

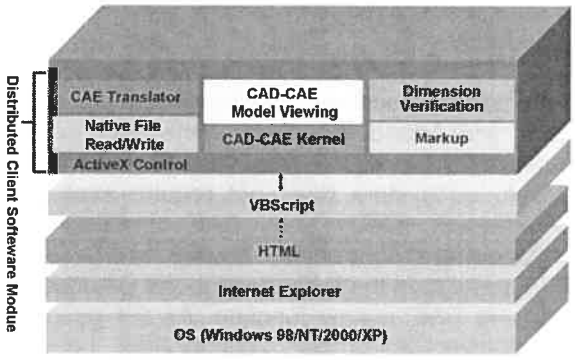

FIGURE 2. Structure of the CAE collaboration system.

SYSTEM ARCHITECTURE

Fig. 2 shows the architecture of the CAD-CAE collaboration system. The distributed client software, the ActiveX control, is executed on the platforms of Windows and Internet Explorer. HTML is used to notify the ActiveX controls on the Web. VBScript is utilized for the ActiveX plug-in [4]. The ActiveX control is realized by using OpenGL and Visual C++. OpenGL is a 3D graphic library produced by Silicon Graphics and is used for handling 3D CAE data. In order to construct a CAE Visualization system, developed ActiveX controls are made of following functional modules: i) CAE data translator module reads CAE post-processing data. ii) Native file accessing module reads or writes native files including verification results related to the CAE data. iii) CAD-CAE model viewing module visualizes triangulation data on the Web. iv) CAD-CAE kernel contains CAE results on the verification system. v) Dimension verification module offers various tools for examining dimensions of the visualized point data. vi) Markup module enables users to exchange collaborators' opinions with other collaborators by using various tools.

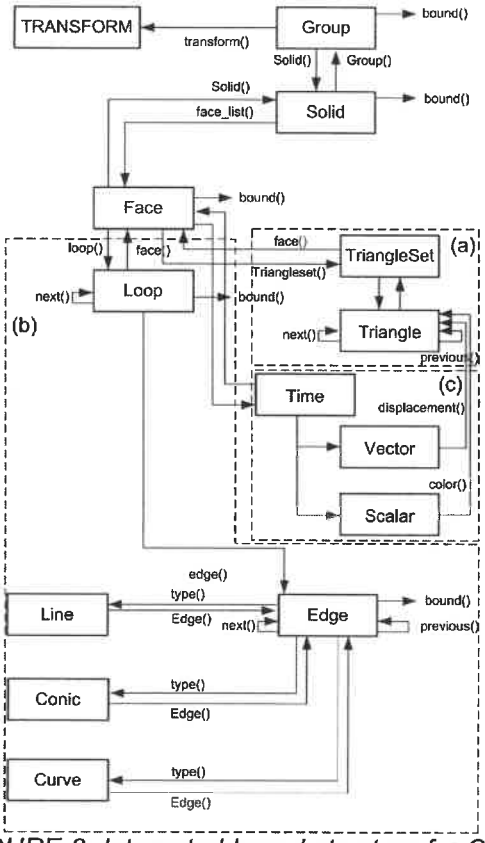

FIGURE 3. Integrated kernel structure for CAD-CAE.

CAD-CAE KERNEL

In this paper, a CAD-CAE kernel is devised by using the data structure of the previously developed lightweight CAD kernel [5, 6]. Integrated kernel structure shown in Fig. 3 is used to construct a CAE kernel structure and the structure of the lightweight CAD kernel. The lightweight CAD-CAE kernel structure discussed in this paper is designed in three parts shown in Fig. 3. One is the triangle mesh data part (Fig. 3(a)) and the second is the edge data part (Fig. 3(b)). Details of the proposed file are as follows: "Group" is the top entity for managing the combined structure of several solids and sub groups. "TRANSFORM" is the matrix for translation and rotation of each "Group". "Solid" is applicable to the solid of the CAD entity, which consists of faces. "Face" is located under the "Solid". "Face" consists of tessellated triangle data for visualization of the CAD model (Fig. 3(a)), and edge information for the dimensional verification (Fig. 3(b)). "Edge" is saved with a separator to be classified into "Line", " Conic" and "Curve". "Line", "Conic" and "Curve" consist of linear lines, conic curves and spline curves, respectively. "Time" is the time step for dynamic visualization of CAE analysis results. "Time" consists of "Vector" and "scalar" data of the CAE results (Fig. 3(c)). Using these data structures, group, solids, faces and triangle meshes are visualized successively for CAD-CAE verification.

CASE STUDIES

Mobile phone

Injection molding process of a mobile phone designed on CATIA is selected as an example. Nonuniform pressure distribution in the filling process is analyzed on Moldflow as shown in Fig. 4. Near portion of the gate is under higher injection pressure. Overflow region is under lower pressure. It is distributed between 0 to 24.6MPa. Fig. 5 shows the visualization result of the filling pressure on the developed CAE verification system.

Not only difference of between upper and lower surface temperature of mold but difference of surface temperature of mold must be within ± 10℃. And a surface temperature of mold need to lower above 10~20℃ more than temperature of coolant inlet. CAE simulation analyzes out to reduce the partial hot spot and cold spot before practical injection molding. It leads in optimal injection molding by relocating coolant circuit. Fig. 6 shows temperature distribution result of the product. It is between 50℃ to 74.22℃ at the ejection cycle. Fig. 7 shows the CAE visualization result of temperature distribution using the proposed system.

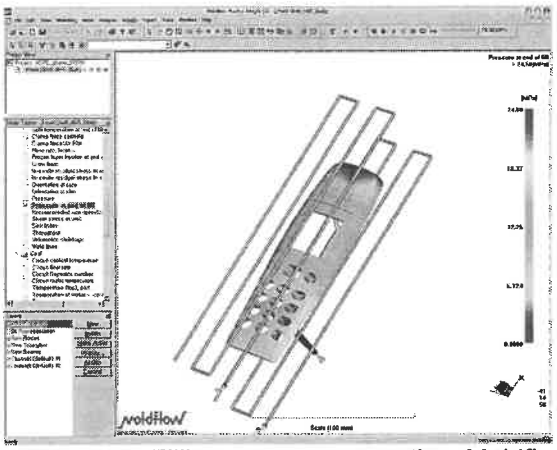

FIGURE 4. Filling pressure on the Moldflow system.

FIGURE 5. Verification of filling pressure on the developed system.

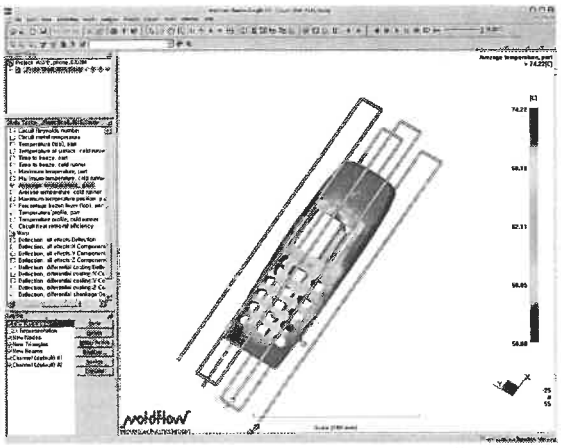

FIGURE 6. Analysis of temperature distribution on the Moldflow system.

FIGURE 7. Verification of temperature distribution on the developed system.

Automobile part

This case study verifies warpage rate of a bezel through the Moldflow system. Warpage rate of the product is described as the total warpage shown in Fig. 8. It is generated due to shrinkage variation, deflection variation and cooling variation. Fig. 9 shows a verification result of the warpage on the developed system.

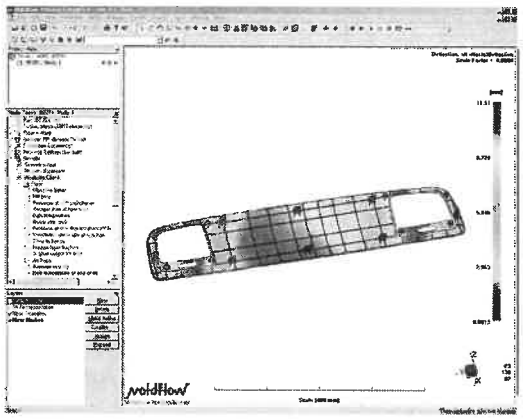

FIGURE 8. Analysis of warpage on the Moldflow system.

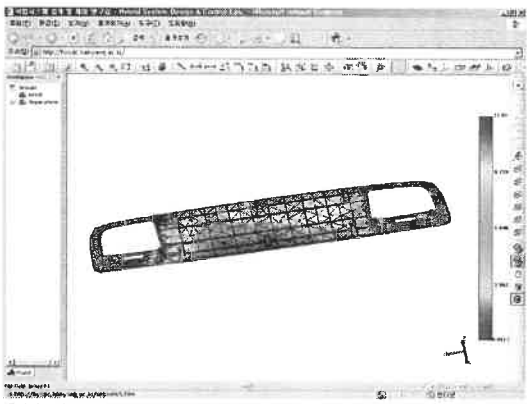

FIGURE 9. Verification of warpage on the developed system.

CONCLUSIONS

By designing a sharing method of CAE data in injection molding and die casting processes, following conclusions are obtained:

(1) Using the proposed CAD-CAE kernel, verification of CAD and CAE data constructed on various CAD/CAE systems are possible on the Internet.

(2) Using the developed viewing system, collaborators are able to verify CAE results without using expensive commercial CAE systems.

(3) Using the ActiveX control, collaborators are able to download the developed system on the Internet. System updates are accomplished through the server.

(4) The validity and effectiveness of the developed system have been verified through case studies.

REFERENCES

[1] ISO 10303-104. Part 104: Integrated Resources: FEA Reference Model. 1991.

[2] ISO 10303-209. Industrial Automation Systems and Integration Product Data Representation and Exchange Part 209: Application Protocol: Composite and Metallic Structural Analysis and Related Design. 2001.

[3] Deng Y M, Lam Y C, Tor S B, Britten G A. A CAD-CAE Integrated Injection Molding Design System. Engineering with Computers. 2002; 18: 80-92.

[4] Song I H, Chung S, Chung S C. Precision Design Verification System of Injection Molds using Web-based 3D Viewing Technology. Proceeding of the ASPE. 2006; 21: 451-454.

[5] Song I H, Chung S C. Geometric Kernel Design of the Web-Viewer for the PDM Based Assembly DMU. Transactions of the KSME(A). 2007; 31: 260-268.

[6] Song I H, Chung S C. Synthesis of the Digital Mock-Up System for Heterogeneous CAD Assembly. Transactions of the North American Manufacturing Research Institution of SME. 2007; 35: 777-785.

NEW LASER MICRO-FABRICATION FOR CREATING SURFACE FUNCTIONS

Masaki Wakabayashi[1], Junichi Ikeno[1], Hideo Shibutani[1], and Akihiko Suzuki[1]
[1] Graduate School of Science and Engineering
Saitama University
Saitama-shi, Saitama, Japan

INSTRUCTION

Recently, flat panel display (FPD), such as liquid crystal display (LCD), plasma display (PDP), and organic EL, has been widespread. FPD is requested to develop better quality on screen resolution, lightness contrast, luminosity, and so on[(1)]. Improving functions of the anti-reflection has especially been focused today. It is also hoped to manufacture anti-reflection sheets for blocking lighting and sun light reflections with a low price[1].

There are 2 types of anti-reflection sheets today; anti-reflection coating(AR) and non-glare(NG). AR may deny the reflected light by using the light interference, so that the reflected light is hardly scattered and a clear image can be obtained[2]. However, AR is costly because of its multi layer coating for high-quality anti-reflection. NG scatters reflected lights by minute ruggedness shape on the surface. Although NG is inferior to AR in the anti-reflection performance, NG cost is about 1/3 of AR with the metal mold. Therefore, NG is expected to develop higher quality. The anti-reflection sheets are requested to scatter lights from the external world and to penetrate lights from the backlight in high efficiency. To obtain above expectations, dimples of 10-30μm in diameter and 0.1-0.3μm in depth are formed on the glass substrate like an array for lower rate of clear reflective image and higher rate of clear penetrative image.

Metal molds of NG anti-reflection sheets are usually manufactured by sandblast. This method has a problem; the quality depends on the capability of craftsmen, so that it is difficult to finish sandblasting with even precision. There is also low reproducibility and stability of obtaining the best shape for anti-reflection because of randomness of its processing. Recently, it seems that a number of high-quality metal molds will decrease because many skillful engineers have been retiring.

Thus, this study proposed a new laser processing method to make minute shapes with better stability. Moreover, after NG anti-reflection shape is made by this method, an optical characteristic was evaluated.

PROPOSAL OF SPECULAR PROCESSING METHOD THAT USES LASER AND ETCHING

This research was focused more on the laser beam machining. Laser beam machining method enables to irradiate the exact spots with high precision by the precision stage or the galvano-mirror system. Moreover, because the laser irradiation position is treated and preserved as NC data, it is excellent in reproducibility and craftsmanship.

However, the laser beam machining makes the surface rougher by an influence of thermal and debris. Authors fond a technique that made specular and spherical dimples by etching with hydrofluoric acid solution[3]. The original dimples were made by irradiation of the laser on glass.

EXPERIMENT OF CREATING NG ANTI-REFLECTION SHAPES

Experimental Setup

To make the dimple shapes of diameter 10-30μm and 0.1-0.3μm in depth on the surface of the glass, the laser light was absorbed very slightly by using Nd:YVO_4 laser (λ=532nm) with high permeability for the glass, and we made shallow dimples. The relation between the oscillation frequency and the laser output of the Nd:YVO_4 laser used was the maximum output of 5.3W at the Q-SW frequency of 33kHz. This processing device enables to scan laser lights with high-speed (range of 50mm x 50mm) by galvano-mirror as shown in Figure 1.

Experiment of Laser Irradiation

When the laser was irradiated to the crown glass, the laser light was hardly absorbed, so that it was impossible to process it at all.

Thus, a material that absorbed the laser light was given to the surface of the glass, and shallow dimples were created in this research. Because the laser absorbing material had to obtain a uniform film thickness on the surface of

the glass, Au spatter film was used. The laser was used to irradiate the area of 10mm×10mm of the surface of crown glass that was spattered by Au, and arraying of dimples was tried. Because Au cannot be melted in hydrofluoric acid solution, the spatter film thickness was set 0.8nm with consideration of etching influence.

Table 1 shows the processing conditions. The laser output was 5.3W and the scanning speeds were set for dimple to line up in the lattice in 20μm pitch.

As a result, a dimple was able to be processed on the crown glass by 20μm pitch with lattice arrangement. It took about ten seconds from the beginning of processing to the end. A SEM image and three dimension measurement image of the processed dimple are shown in Figure 2 a). The super-depth surface shape measurement microscope (VK-8500) made by KEYENCE was used for the shape measurement. The processed Dimple's diameter was about 15μm and the depth was 0.2-0.3μm.

Experiment of Etching

The processed crown glass was etched with hydrofluoric acid solution (1wt%) under the conditions of 40 degrees C, 300 rpm in stirring, and 120 minutes for etching time. A SEM image and three dimension measurement image after 120 minutes etching are shown in Figure 2 b). The section shapes before and after etching is shown in Figure 3. Although debris were seen on the surface before etching, the debris were removed. Roughness was changed from 33nmRa to 13nmRa after etching for 120min. Thus, it was proven that etching achieves the mirror surface.

On the other hand, the depths of dimples hardly changed before and after etching, and the depth was 0.2-0.3μm.

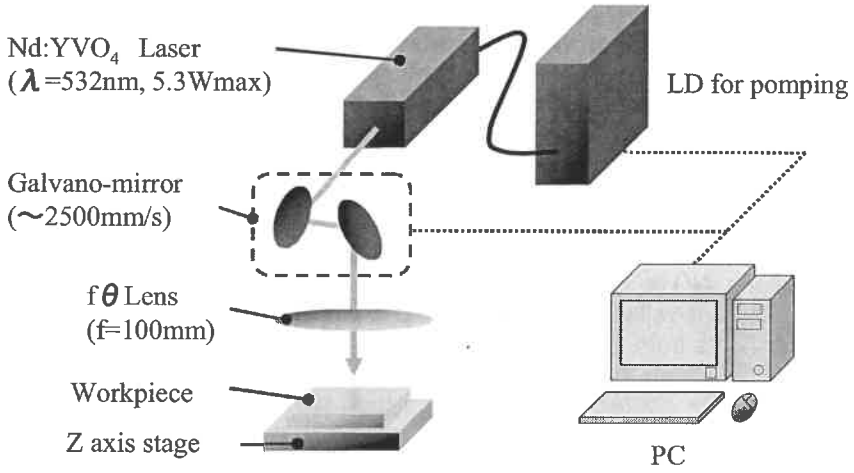

FIGURE 1 Experimental setup for laser micro-fabrication

TABLE 1 Experimental conditions

Laser power W	5.3
Q -SW frequency kHz	33
Scanning rate mm/s	825
Scanning pitch μm	20
Scanning range mm	10 × 10
Type of glass plate	Crown glass
Spattered thickness nm	0.8

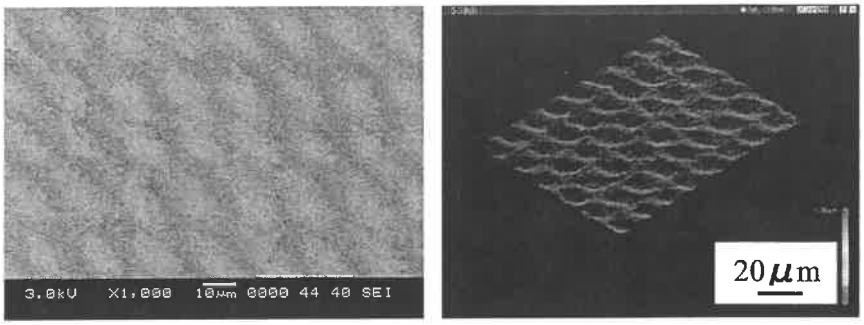

a) Before etching

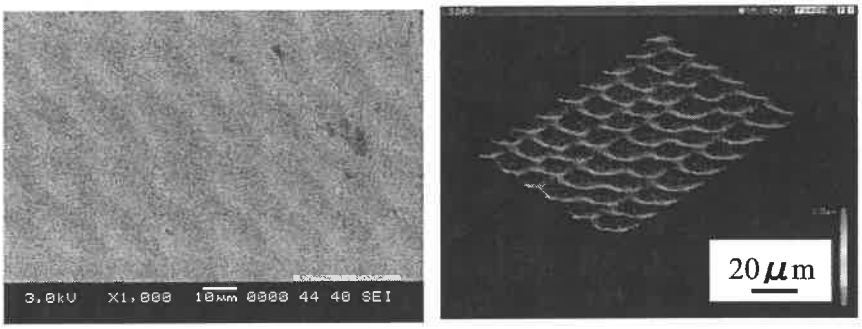

b) After etching for 120min

FIGURE 2 SEM image and 3D-Image of surface by laser machining

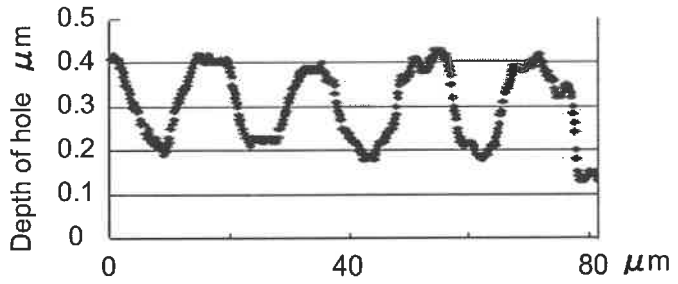

a) Before etching

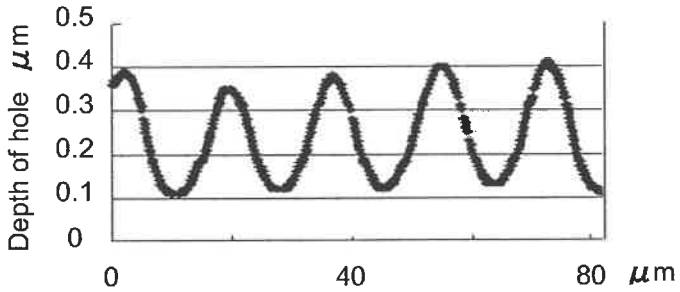

b) After etching for 120min

FIGURE 3 Image of cross sections of glass

OPTICAL EVALUATION

Rates of clear penetrative image and rates of clear reflective image were measured by the image clarity measurement (SUGA Test Instruments Co., Ltd., ICM-IDP) for optical evaluation.

The results of optical measurement of several NG anti-reflection sheets were marked as white dots in Figure 4. These results pointed out that as clear reflective images got lower, anti-reflection performance got higher, and that as clear penetrative images got higher, pictures got more clear. This study targeted the area of over 70% in penetration image distinction and under 50% in reflection image distinction as high quality.

The optical measurement results of the anti-reflection shape were marked as black dots in Figure 4. As etching time was longer, the rates of clear reflective image decreased and high effects of anti-reflection were seen. The rate of clear reflective image became 38% and the rate of penetrative image became 88% after etching for 120 min. These results were expected as high-quality anti-reflection performance.

In conclusion, etching achieved the following effects. High rates of clear penetrative image can be maintained if the debris on the surface of the glass are removed. The rates of clear reflective image decrease as dimples diameter becomes larger. It is because that a smooth part on the surface gets smaller and the slope increases.

CONCLUSIONS

In this study, the laser micro-fabrication of the crown glass that has high permeability was tried to Nd:YVO_4 laser (λ=532nm). As a result, it succeeded in making shallow dimple as 0.2-0.6μm in depth if Au spatter was given to the surface of the crown glass (0.8nm) as a laser absorbing material.

Moreover, we tried to create NG anti-reflection shapes on the crown glass by using the specular processing method that combined laser and etching.

As a result, a high-quality anti-reflection performance of the penetration image distinction of 88% and the reflection image distinction of 38% were obtained after etching for 120 minutes.

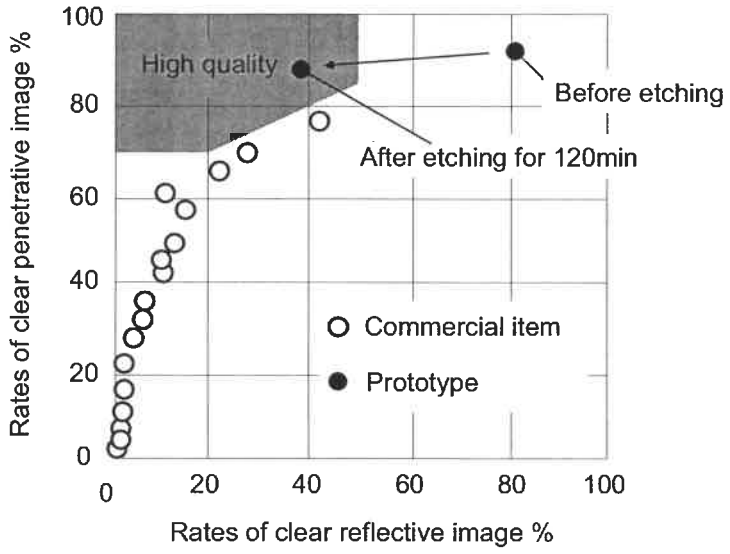

FIGURE 4 Optical evaluation

REFERENCES

[1] Liquid crystal display techniques 2001, DENSHIZAIRYO additional volume 2001 Jun., Kogyo Chosakai Publishing, 2001:1-5.

[2] Norigata N., EKISHO, Vol.9, No.4, 2004:219-226.

[3] Tomofumi Nakamura, Junichi Ikeno, Study on creating micro-lens by laser machining, The Japan Society of Precision Engineering, 2003:186.

A PIEZOACTUATED TOOL FEED MECHANISM FOR MICRO EDM

Muralidhara[1], Nilesh Jayanthilal Vasa[2], Singaperumal M.[1]
[1]Precision Engineering and Instrumentation Lab
Department of Mechanical Engineering
Indian Institute of Technology Madras, Chennai, Tamilnadu, India
[2] Department of Engineering Design
Indian Institute of Technology Madras, Chennai, Tamilnadu, India

1. INTRODUCTION

Increased demand for Micro Electro Mechanical Systems (MEMS) demands a micromachining technology that can produce the required three dimensional (3-D) shapes on silicon and other conducting materials at a lower cost. Micro Electro Discharge Machining (Micro EDM) is one of the promising micromachining technique where a tool of few tens of micrometer in size is used to fabricate 3-D microstructures on any electrically conducting materials. In Micro EDM, the tool and workpiece which are immersed in the dielectric medium forms the two electrodes of different polarity. A sufficiently small gap is maintained between them and with application of a pulsed voltage, a spark is produced resulting into melting and evaporation of some portion of the tool and the workpiece material.
Tool feed control is a critical requirement in Micro EDM as both workpiece and tool materials are being eroded during machining. Also since the pulse energy provided during machining is of the order of few hundreds of micro joules, a very small gap of the order of few microns has to be maintained between the tool and workpiece to sustain the spark discharges. These requirements of Micro EDM demand for an actuator which can feed the tool at the desired rate as well as can control the tool movement which will avoid the sparks occurring with longer delay time and which can also avoid short circuiting of tool and workpiece. Micro EDM with an inchworm type of tool feed mechanism was developed by Yong L. et al. [1]. This approach involves two clamping mechanisms along with two piezoactuators. Direct mounting of Micro EDM tool on piezoactuator have not been reported. An accurate tool feed control either by modeling the piezoactuator or by incorporating the feed back control is also necessary.
In this research work, a piezoactuated tool feed mechanism is considered for a home made Micro EDM equipment. An advantage of using piezoelectric actuator is that the voltage applied to the actuator can provide the information about its displacement by accurately modeling the Voltage-Displacement characteristics. One of the difficulties in using the piezoelectric actuators is their hysteresis behavior between the applied voltage and the displacement. In order to reduce the complexity and to reduce the costs involved in implementing the feed back control system, modeling of the piezoactuator is considered to overcome the hysteresis effect.
In Section 2, Micro EDM with piezoactuated tool feed mechanism is described. Hysteresis behavior of the piezoactuator is presented in section 3 and modeling of the piezoactuator is presented in Section 4. Simulation and experimental results are discussed in section 5, followed by the conclusion in Section 6.

2. DETAILS OF IN HOUSE DEVELOPED MICRO EDM SET-UP

A prototype Micro EDM is developed in-house incorporating piezoactuated tool feed mechanism as shown in Fig. 1. It consists of a motorized rotary table with an accuracy of 0.1° and two motorized linear stages having positional accuracy of 1µm. This arrangement is capable of fabricating micro channels with

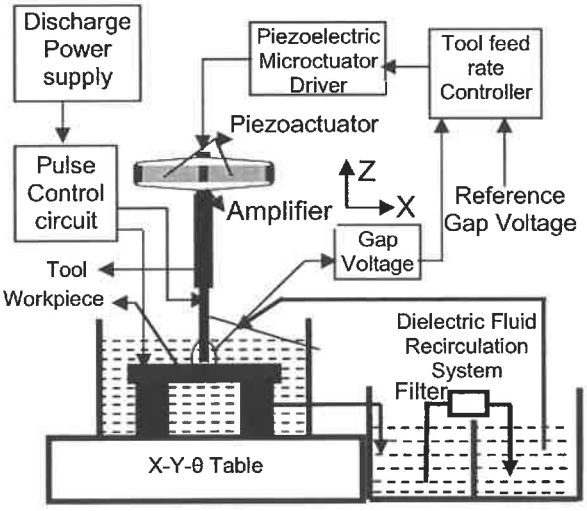

FIGURE 1. Micro EDM Set-up

shapes such as a linear, circular and spiral and fabricating either blind or through micro holes. An in situ measurement technique is used to measure the depth of the blind hole, depth of tool material removed and the total displacement given to the tool by sensing the tool and workpiece electrical contact without disturbing the tool and workpiece set-up.

A piezoelectric micro actuator (Cedrat Technologies, APA400M) is used for feeding and controlling the tool in Z-direction. Two piezostacks are arranged in series and a flexural link is used to amplify the displacement of these two piezo stacks. The maximum displacement of the piezoactuator was measured as 445µm at 150V. The displacement of piezoelectric micro-actuator is controlled by monitoring the gap voltage between the tool and the workpiece. The voltage drops as the spark occurs and correspondingly some amount of material is removed making it an open circuit. Also when it is short circuited, the potential drops to zero. This signal goes from feed back circuit to the piezo amplifier. In this path, the signal is amplified in the feed back circuit by the operational amplifier to make it fall between -1V and 7.5V. The piezoactuator driver further amplifies the signal to 20 times. This amplified signal is directly sent to the piezoactuator which feeds the tool. The tool is fed towards the workpiece until the electric discharge takes place between tool and workpiece. Microstructures with a depth up to 400µm can be machined via the displacement of the piezoactuator.

3. HYSTERESIS BEHAVIOR OF THE PIEZOACTUATOR

Piezoactuators exhibit hysteresis behavior between the applied voltage and the corresponding displacement. Experiments were carried out by varying the input voltage to the piezoactuator. A green light interferometer was used to measure the horizontal (X) displacement and a dial gauge (least count = 1µm) was used to measure an amplified vertical (Z) displacement. Fig. 2 shows the piezoactuator displacement along the Z-direction, indicating the hysteresis behavior when the voltage varied in steps in both forward and reverse directions. The input voltage was varied between 0V to 150V. Fig. 3 shows the amplified displacement in the Z direction by the flexural link for the variation in the piezostack displacement in the X-direction. Since the plot is not linear, a polynomial curve of 3rd order is fitted to get mathematical relationship between the X and Z displacements.

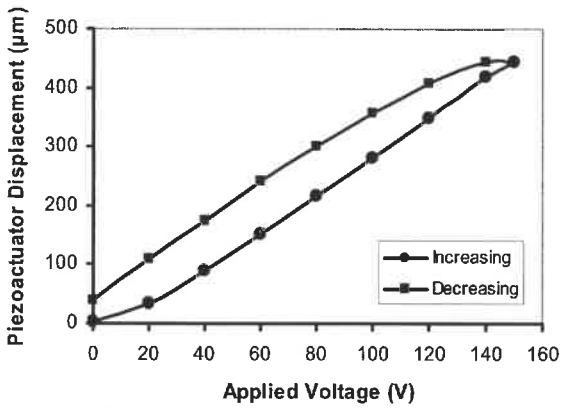

FIGURE 2. Hysteresis Behavior of the Piezoactuator

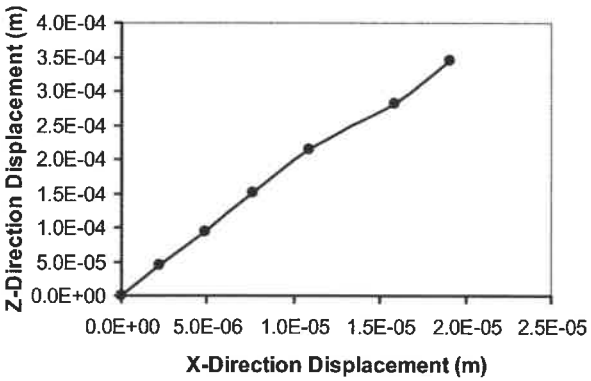

FIGURE 3. Displacement Amplification by Flexural Mechanism

4. MODELING OF PIEZOCTUATOR

In the present study, electromechanical model for the piezoelectric microactuator is proposed based on [2]. Mechanical and electrical properties of the piezostacks are tabulated in Table 1. The equations (1) and (2) represents hysteresis voltage which is responsible for the hysteresis behavior between the applied voltage and the displacement of the piezoelectric actuator.

$$V_i = \begin{cases} \dfrac{(q - q_{b_i})}{C_i} \; if \left| \dfrac{(q - q_{b_i})}{C_i} \right| < v_i \\ \left[\begin{array}{l} V_i \, sgn(q_j - q_{j-1}) \; and \\ q_{b_i} = q - C_i v_i \, sgn(q_j - q_{j-1}) \; else \end{array} \right] \end{cases} \quad \text{---(1)}$$

$$V_H = \sum_{i=1}^{n} V_i \quad \text{- - - - - - - - - (2)}$$

TABLE1. Parameters Considered For Piezostack Model

Parameter	Symbol	Value
No. of Wafers	n	200
Thickness of Wafers	t	0.1mm
C/S area of Wafers	A	25mm^2
Relative Permitivity	K_{33}^T	2900
Electromechanical Coupling Factor	K_{33}	0.7
Elastic Constant	S_{33}^E	2.22e-11 m^2/N
Mass	m_p	0.00481kg
Stiffness	K_p	6×10^6 N/m
Damping	c_p	150 N-s/m
Capacitance	C	4×10^{-6} F
Transformer Ratio	T	14C/m

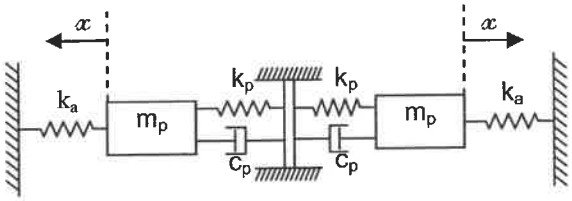

FIGURE 4. Mechanical Model of the Piezoactuator

The piezoactuator has two piezostacks which are modeled as a spring-mass-damper system as shown in Fig. 4. Flexural amplifier is modeled as a spring element and the force generated by this spring element is considered as it opposes the displacement of piezoactuator. Equations (3) to (7) are used for electromechanical modeling of the piezoelectric actuator [2].

$$m_p\ddot{x}+c_p\dot{x}+k_px=F_t-F_a \quad --(3)$$

$$q=Tx+C_pV_t \quad ----(4)$$

$$V_{in}=V_H+V_t \quad -----(5)$$

$$V_H=H(q) \quad -----(6)$$

$$F_t=TV_t \quad -----(7)$$

Where

q = electric charge (C);
x = piezo displacement (m);
T = Transformer Ratio (C/m);
C_p = Capacitance of Piezoactuator (μF);
C_i = Capacitance of i^{th} Maxwell Capacitor (μF);
V_t = Voltage across Piezoactuator (V);
V_{in} = Applied voltage (V);
V_i = Voltage across i^{th} Maxwel Capacitor
V_H = Voltage across Maxwell Capacitor (V);
$H(q)$ = Hysteresis Function;
F_t = Transduced force from electrical Domain; (N)
F_a = Force applied by the flexural amplifier (N)
m_p = mass of piezoactuator (kg);
c_p = damping coefficient of piezomaterial (N-s/m);
k_p = stiffness of the piezoactuator (N/m)

5. SIMULATION AND EXPERIMENT

A Matlab-Simulink model is developed for the piezoactuator to obtain the stack displacement for the applied voltage. The stack displacement is converted into the amplifier displacement using the 3rd order polynomial equation. Simulations are carried out at different input signals and at different frequencies to investigate the behavior of the developed model. To verify the simulation results, experiments are carried out at various input signals to the piezoactuator. A signal generator (HP 33120A) is used to generate different signal at different frequencies and amplitude of the signal is maintained between 0-6V. This input signal is amplified 20 times by the piezoactuator driver. An inductive pickup is used to sense the displacement of the piezoactuator and the signal generated by this pickup is connected to NI-DAQCard-AI-16E-4 PCMCI through a NI-DAQ signal accessory. This signal is filtered to reject noise component and is stored into the memory by using NI LabVIEW software. The voltage signal obtained from inductive pickup is calibrated by using the readings obtained from dial gauge with 1μm least count.

Fig. 5 shows the simulated and experimental piezoactuator displacements for 1mHz, 0-120V sinusoidal input. It is observed that the maximum actual displacement reached is very near to the simulated result, but there is an error of about 50μm at valley points. Fig. 6 shows the experimental and simulated displacement readings for 1mHz, 0-120V triangular input signal. This shows an error of 30μm at maximum and minimum point.

Simulation results show an error at zero input voltage which may be due to errors in hysteresis modeling of the piezoactuator. Accurate displacements may be obtained by taking more number of slopes for the initial rising curve in the

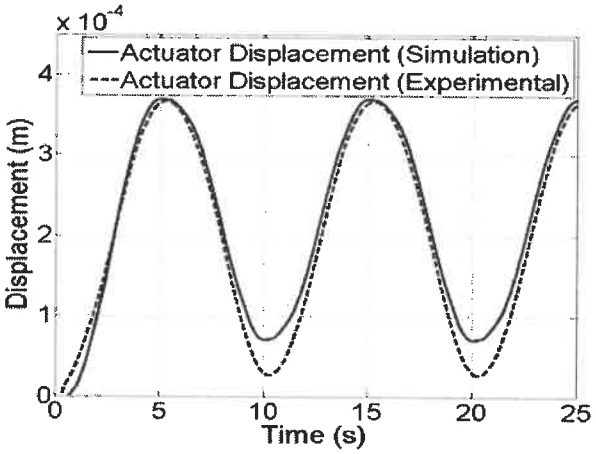

FIGURE 5. Actuator Displacement at 0.1Hz Sinusoidal Voltage Input (0-120V)

hysteresis model. Sinusoidal input voltage signal exhibits better tracking control at peak voltage which may be due to gradual variation of the signal compared to triangular signal input. The errors may also be due to the creep behavior present in the piezometerial which has not been considered in the model. Errors in calibration of inductive pick-up readings is another source of error for experimental displacement readings.

To investigate the position control of the piezoactuator, a Matlab-Simulink model is developed to calculate the input voltage required for the piezoactuator for the given reference displacement. Fig. 7 shows the reference displacement signal given to Matlab-Simulink model and actual displacement obtained by piezoactuator for the input Voltage signal which is generated by the model. The developed model shows good tracking control at the valley points but it indicates an error of about 50μm at

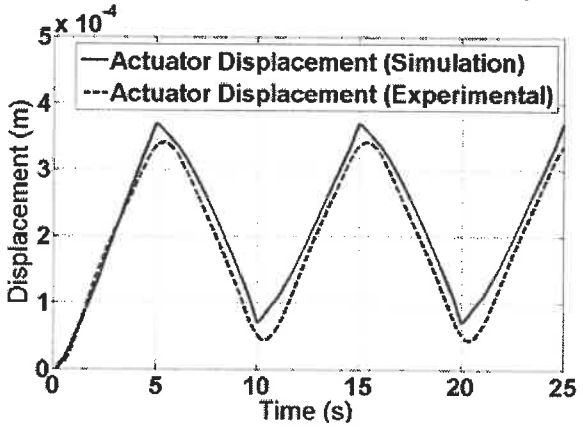

FIGURE 6. Actuator Displacement at 0.1Hz Triangular Voltage Input (0-120V)

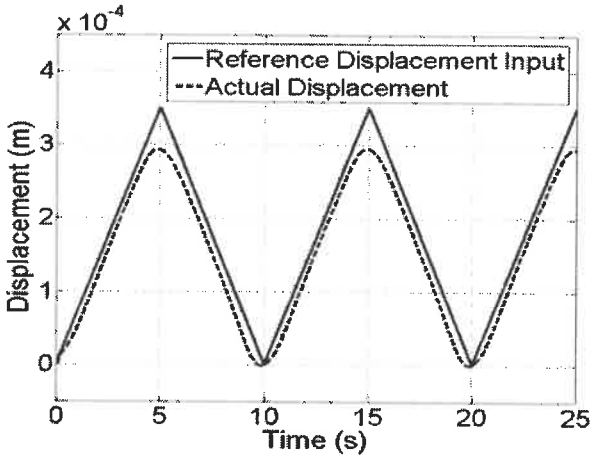

FIGURE.7 Variations in Reference and Experimental Piezoactuator Displacement

the peak points. These errors may be due to the reasons stated earlier.

6. CONCLUSION

In this research work, a piezoactuated tool feed mechanism is considered for a prototype Micro EDM equipment. For the tool feed control, a piezoactuator with flexural displacement amplifier is considered and an electromechanical model for this actuator is developed considering hysteresis effect. Simulations for piezoactuator displacement are carried out in Matlab-Simulink and compared with the experimental results. It is observed that, the simulation and experimental results are matching with an error of about 30μm to 50μm at peak and valley points for different types of input signals. These are to be corrected by incorporating creep behavior and by taking more number of slopes in hysteresis modeling of the piezoactuator.

REFERENCE

[1] Yong L, Min G, Zhaoying Z, Min H. Micro Electro Discharge Machine with an Inchworm Type of Micro Feed Mechanism. Precision Engineering, Journal of International Societies for Precision Engineering and Nanotechnology. 2002; 26: 7-14.

[2] Michael G, Nikola C. Modeling piezoelectric stack actuators for control of micromanipulation. IEEE Control Systems. 1997; 17; 3: 69-79.

INVESTIGATION ON THE IMPACT ON PROCESS QUALITY WHEN UTILIZING DIFFERENT PADS DURING CHEMICAL MECHANICAL POLISHING OF MEMS

S. Cvetkovic and H. H. Gatzen
Institute for Microtechnology
Center for Production Technology
Leibniz Universitaet Hannover
Hanover, Lower Saxony, Germany

ABSTRACT

The hardness of the Chemical Mechanical Polishing (CMP) pad strongly influences the CMP process. The most widely used material for CMP pads is polyurethane. Typically, a polyurethane pad is stacked on a softer sub pad. Recently, alternate CMP pads based on the single pad manufacturing process have been developed, where the whole pad is formed in a single process step.

The former standard type of such two layer pads is an IC1400, a pad with an IC1000 polyurethane upper pad and a gray foam sub pad. A new generation of these pads consists of an IC1000 upper and the felt-based sub pad SP, carrying the name of the upper pad. A new approach for fabricating CMP pads is the injection molded single layer pad. An example for such a pad is RimPad PnP1400.

This paper presents the results for a comparison investigation of the two layer pads (IC1400 and IC1000/SP) and the one layer pads (RimPad) using typical materials for Micro Electro Mechanical Systems (MEMS) in a MEMS typical CMP process. It provides data for the removal rate, as well a local and global planarization. Two typical MEMS materials were utilized in the tests: NiFe81/19 (permalloy) and the epoxy based photoresist SU-8™. The removal rate and the global planarization were investigated on a wafer patterned with only one material each, while the local planarization was tested on a wafer containing both materials.

INTRODUCTION

When fabricating High Aspect Ratio Micro System Technology (HARMST) devices, Chemical Mechanical Polishing (CMP) is an enabling technology required for wafer planarization [1, 2]. The complexity of CMP expresses itself in the multitude of parameters to be considered regarding the quality of the process [3, 4]. Important properties of a CMP pad besides hardness and uniformity are compressibility and durability. Depending on these attributes, the process and quality criteria of CMP like the material removal rate, local planarization (or "Within Die Non-uniformity"-WIDNU), and global planarization (or "Within Wafer Non-uniformity" - WIWNU) are determined [5]. Local planarization is the dimension describing the local height difference between two materials on the micro part level. It is an important characteristic for the CMP result, determining the quality of the planarization and functionality of the single micro part. The value of global planarization defines the uniformity of layer thickness and the number of the functional micro parts on one wafer. To adapt and optimize the hardness and uniformity with compressibility and durability of standard polyurethane pads, these pads are fabricated as two layer sandwich structures. A typical example for such a combination is a hard upper pad and a soft sub pad. A new family of polishing pads is represented by a single layer RimPAD CMP Pad, a polymeric CMP Pad based on the reaction injection molding technique [6]. The main advantages of such pads are the consistent performance and the process stability as well as longer pad life and form flexibility.

PAD EVALUATION

Two IC stacked pads and one single layer pad were subjected to experimental investigations. IC1400 is an earlier version of an IC CMP pad, consisting of an IC1000 upper pad and a gray foam sub pad. IC1000/SP is the newest type featuring a felt-based sub pad instead of the gray foam. Contrary to standard two layer pads, a RimPAD CMP-pad is a single pad manufactured in an injection molding process. The typical characteristics of all three pads are listed in Table 1.

IC pads feature the same hard polyurethane upper pad, but different sub pads. The IC1000 pad is the industry-standard upper polishing pad for CMP. It is made of a rigid, micro-porous polyurethane material. Because of its hardness and rigidity, this pad is used only as a two layer

structure in combination with a softer sub pad. A compressible sub pad improves the global non-uniformity performance of the IC1000 pad. Such a stacked two layer structure improves the pad consistency, the reliability, and the performance [7].

TABLE 1. Characteristics of CMP-pads

Pad	Stacking	Hardness	Topology
IC1000/ SP	IC1000/ SP2310	Shore D 57	K1-groo-ving
IC1400	IC1000/ foam	Shore D 57	K-groo-ving
RimPad	PnP1400 single pad	Shore D 60	K-groo-ving

All pads are equipped with U-profiled concentric grooves called K-grooves exhibiting a depth of 381 µm, a width of 254 µm, and a pitch of 1,525 µm.
The first pad subjected to the investigation is an IC1000 pad with an SP sub pad and serves as a reference. The SP sub pad is a next generation sub pad based on the SUBA IV technology, which is a felt-based. The new IC1000/SP sub pad claims to feature an improved consistency, a lower slurry adsorption, and better polishing performance. Due to the advantage of a stacked structure, the pad thickness averages 2 mm. Figure 1 depicts the cross-section of the IC1000/SP pad combination.

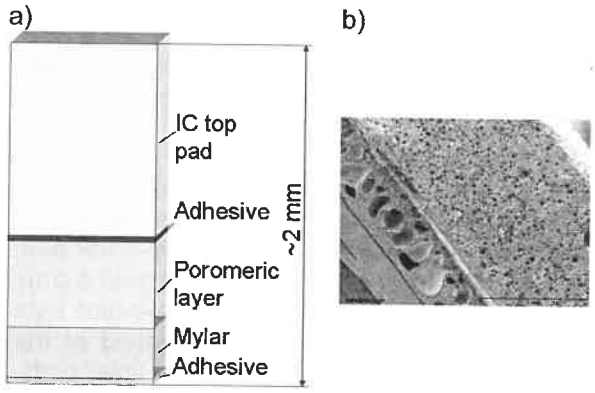

FIGURE 1. a) Schematic sandwich structure and b) SEM micrograph of IC1000/SP pad

The IC1000/SP pad has K1-grooves, which are the improved version of K-grooves: with respect to a higher accuracy of width and height, whereas the overall dimensions are the same. Grooving the pads decreases the suction power of wafers during the process but also supports slurry flow and abrasive grain distribution (Fig. 2a). Besides the grooving, the cell size is yet another important pad characteristic since it acts as a vehicle for absorbing and transporting slurry and slurry abrasives. While such pores are susceptible to plastic deformation and glazing, an efficient replenishment of the surface can be achieved through abrasion of the surface material to yield new cells. With smaller cells, this replenishment can occur more frequently and efficiently, thus providing a more stable CMP process and longer pad life. The average cell size of IC1000 pads is typically 50 µm diameter and above (Fig. 2b).

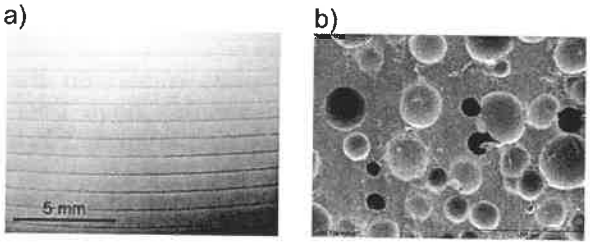

FIGURE 2. a) Micrograph of IC1000 grooving and b) surface microtexture

The second pad being investigated is an IC1400 pad, composed of an IC1000 top pad and a gray foam base, designed to find the right proportion of rigidity and compressibility, and to improve the consistency of performance [7]. The thickness of the sandwich averages 2.5 mm. Figure 3 shows a cross section of this pad.

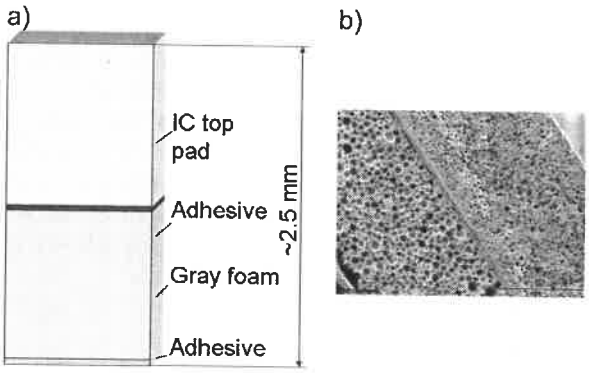

FIGURE 3. a) Schematic of sandwich structure and b) SEM micrograph of IC1400 pad

Because of the same upper pad (IC1000), the grooving and cell size is the same as the one shown in Fig. 2. The cross section of both IC pads exhibits quite uniform top pad structures with constant cell distribution through depth

(Fig. 1b and Fig. 3b). The surface material of the pads has a low coefficient of friction (COF) averaging from 0.38 to 0.55 [8].
The third pad is a representative of the advanced pad technology mentioned earlier, consisting of a single layer, which is fabricated by a single step reaction injection molding (RIM) method. Using the RIM process, the gas is mixed with a polymeric resin component prior to adding an isocyanate component [9]. Fabrication by a single pad manufacturing process provides wide flexibility for emerging forms and performances. The thickness of a single pad averages 2.5 mm, the same as for IC1400. Figure 4 depicts the cross section of a RimPad with the marking PnP1400.

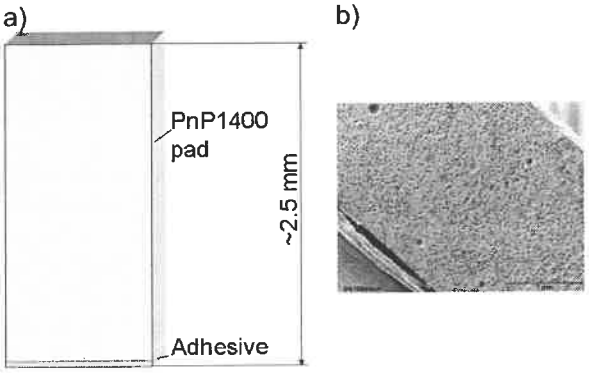

FIGURE 4. a) Schematic sandwich structure and b) SEM micrograph of RimPad PnP1400

The width of RimPad K-grooves averages 500 µm (Fig. 5a). The surface texture of the RimPad stems from an intrinsic microtexture (mold) as a result of its manufacturing method with an average cell size of 30 µm. This is smaller than for the IC pads (Fig. 5b).

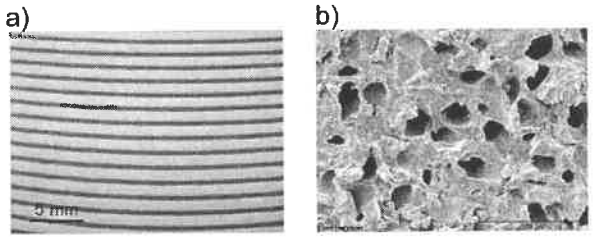

FIGURE 5. Micrograph of RimPad PnP1400 grooving (a) and (b) surface microtexture

On the other hand, the global surface non-uniformity and roughness is higher. Comparing the pad uniformity over the pad's cross section, some larger cells are found (Fig. 4b). This can be attributed to gas bubbles forming during the new unique manufacturing process. The COF of the RimPad is less than 0.4 [10].

EXPERIMENTAL

For the CMP tests, a P. Wolters 3R40 dual-axis polishing machine (adapted for CMP) was used. The plate diameter was 400 mm and the load was applied through weights. The slurry used was MSW1500, a tungsten slurry applied for the standard CMP process for this material combination [1].
The slurry supply was 1.5 ml/min. A pressure of 1.5 kPa was applied and the rotation speed of wafer and pad was 20 RPM. Every polishing step required 10 min and was repeated three times.
In preparing the experimental investigations, three types of 4 in Al_2O_3 ceramic wafers were prepared. On the first two types of wafers, rectangular patterns with a footprint of 5 mm x 12 mm and a high of 10 µm were deposited on the wafer surface.
For the first group, the material was permalloy, for the second photosensitive epoxy SU-8™. The third wafer featured the same type of pattern, but this time with permalloy rectangles embedded in SU-8™. The wafer was first polished to remove unevenness in the electroplated permalloy.
The removal rate for the two materials was measured on the wafers with single material patterns. Measurements were conducted at five wafer locations before and after each process execution. For the height measurements, a stylus profiler type DekTak^{3st} was used.
The local planarization was investigated on the wafer with both materials, measuring the local height difference between two neighboring materials. This time, an Atomic Force Microscope (AFM) was used for the characterization.
For investigating global planarization, two wafers with single materials were used. The evaluation was performed measuring the wafer thickness with a length gauge.

RESULTS

The average values of removal rates for all three pads are shown in Table 2. The highest removal rate for SU-8™ was achieved by IC1400 (179 nm/min), the highest for permalloy by RimPAD (80 nm/min).

TABLE 2. Average removal rates for CMP-pads

Material / Pad	NiFe81/19 wafer	SU-8™ wafer
IC1000/SP	33 nm/min	80 nm/min
IC1400	74 nm/min	179 nm/min
RimPad	80 nm/min	169 nm/min

For the investigation of the local planarization, two values were measured. One was the difference in height by measuring the local difference after all three polishing steps. The second value was the change of difference in height, where the signs "-" or "+"indicate if the polishing results either in lower or higher local difference in height. The average local differences in height for all three pads are shown in Table 3.

TABLE 3. Average local difference in height for CMP-pads

Pad	Final stage difference in height	Change of difference in height
IC1000/SP	186 nm	- 176 nm
IC1400	75 nm	- 85 nm
RimPad	70 nm	+ 22 nm

The best local planarization result was achieved by RimPAD (70 nm) with the lowest change in difference (+22 nm). On the other hand, IC1000/SP showed the most change in difference.

The best adequately balanced pad for global planarization of a wafer with both materials is IC1400, as depicted in Table 4, although IC1000 shows a little better result for SU-8™. The lowest flatness by IC1400 was 1.4 µm for permalloy and the highest 3.45 µm for SU-8™ (Table 4).

TABLE 4. Average global difference in height for CMP-pads

Material / Pad	NiFe81/19 wafer	SU-8™ wafer
IC1000/SP	2.46 µm	1.50 µm
IC1400	2.11 µm	1.70 µm
RimPad	3.13 µm	3.24 µm

CONCLUSIONS

The results show that RimPad is the best suitable pad concerning the removal rate of permalloy as well as for local planarization, although the longer polishing times increase the height difference. The best global planarization (wafer level flatness) could be achieved with IC1400, which also features the highest removal rate for photoresist. IC1000/SP shows a strong potential for minimizing the step height through local planarization. A combination of IC1000/SP and RimPad in a two step process yielded optimal local planarization results. Utilizing the results of the investigations performed a qualitatively superior as well as more efficient CMP process for MEMS can be realized.

ACKNOWLEDGMENT

The authors would like to thank the EURIS GmbH for providing RimPads for tests.

REFERENCES

[1] Kourouklis, C., et. al. The Application of CMP for Planarizing a SU-8/Permalloy Combination Used in MEMS Devices. Sensors & Actuators A: Physical, 106, 2003, 268-271

[2] Philipossian, A., et. al. Fundamental Tribological and Removal Rate Studies of Inter-Layer Dielectric CMP. Jpn. J. Appl. Phys., 42, 2003, 6371–6379

[3] Gatzen, H. H., et. al. Modeling CMP-Investigation of the Mechanical Removal Mechanism. Proc. ASPE 20th Ann. Meet., Norfolk, Virginia, 2005, 500-503

[4] Gatzen, H. H., et. al. Modeling CMP-Investigation of the Chemical Attack on the Mechanical Properties of Bulk Material, 6th euspen Int. Conf., Baden, 2006, 623-626

[5] Deshpande, S., et. al. Surface-Modified Polymeric Pads for Enhanced Performance During CMP. Thin Solid Films 483, 2005, 261–269.

[6] RimPad Tech/Products http://www.rimpadtech.com

[7] Rohm and Haas Electronic Materials. IC1000/IC1400, Technical Data Sheet

[8] Sorooshian, J., et. al. Effect of Process Temperature on COF during CMP. Electrochem. and Solid-State Letters, 7 (10), 2004, 222-224

[9] Polishing Pad and Method of Making Same. US patent, 2006, http://www.patentstorm.us/patents/6986705-description.html

DEVELOPMENT OF SUPERABRASIVE STONE FOR MECHANOCHEMICAL SUPERFINISHING

Masahiro Higuchi[1], Tomomi Yamaguchi[1], Takashi Sugimoto[1], Shoichi Shimada[2], Noboru Matsumori[3], and Hidekazu Ogura[3]
[1]Kansai University
Suita, Osaka, Japan
[2]Osaka Electro-Communication University
Osaka, Japan
[3]Mizuho Co. Ltd.
Jyoyo, Kyoto, Japan

1. INTRODUCTION

The roughness of rolling bearings operating under a mixed or boundary lubrication region is detrimental to the fatigue life of the bearings. Thus, their surfaces are finished to increase the elastohydrodynamic lubrication (EHL) oil film parameter. But, the current view gaining support is that smooth surfaces with negative skewness, i.e., ones with valleys, lengthen the bearing life [1]. However, such a surface morphology cannot be produced by ordinary superfinishing because a chemical action would be required. By combining the rubbing action by soft and reactive abrasives with the scratching action by hard abrasives, it is possible to produce a smooth surface with valleys. In order to realize this process in a vitrified-bonded superabrasive stone, some fundamental and practical questions were examined, as follows.

First, the soft abrasive reaction with the steel was examined by considering the degree of chemical equilibrium. Second, basic experiments were performed to check whether the selected abrasive reacts with the steel in actual practice. And last, in order to examine whether the expected surface morphology could be produced, superfinishing experiments were conducted using superabrasive stones made by mixing the reactive abrasive with the superabrasive.

2. SELECTED REACTIVE ABRASIVE AND ITS CHEMICAL REACTION

Cerium oxide (CeO_2) has the property of storing oxygen, and releasing and uptaking oxygen due to the following reversible reaction [2]:

$$2CeO_2=Ce_2O_3+1/2O_2 \quad (1)$$

Taking this reaction into consideration, it is expected that the reduction of CeO_2 to Ce_2O_3 and oxidation of Fe to FeO, Fe_3O_4 or Fe_2O_3 occur simultaneously when CeO_2 is in contact with Fe under the oxygen-lean condition. Hence, both thermodynamic simulations and experimental observations were carried out.

Figure 1 shows the Gibbs free energy change ΔG^0_T in the oxidation of iron by CeO_2 as a function of the atmospheric temperature. Since ΔG^0_T <0 in this figure, it can be predicted that CeO_2 forms various iron oxides in association with O_2. Moreover, since ΔG^0_T <0 at temperatures higher than 450 K or 800 K, it can be predicted that CeO_2 together with H_2O produces the iron oxide. Thus, it is confirmed in principle that CeO_2 oxidizes Fe in conditions in

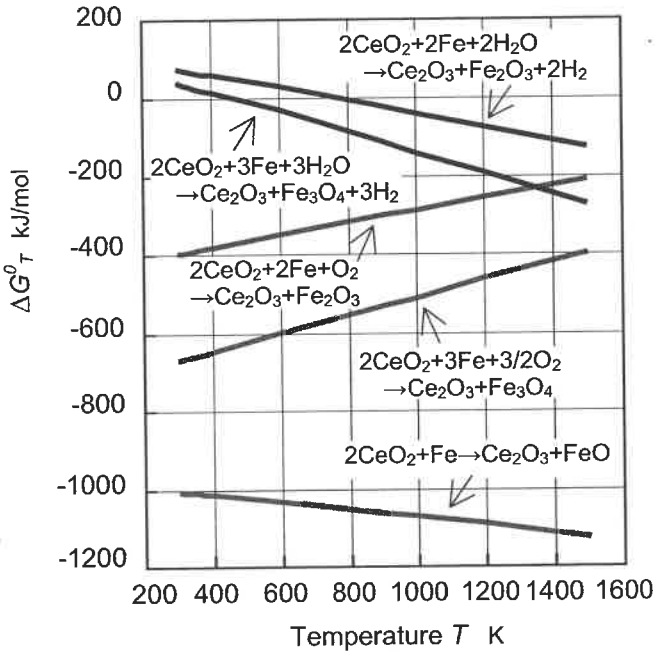

FIGURE 1. Change in Gibbs free energy in reduction of CeO_2 and oxidation of Fe.

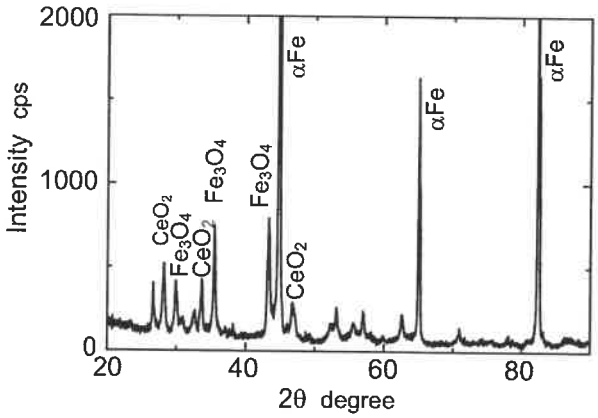

FIGURE 2. X-ray diffraction pattern on surface of SUJ-2 specimen embedded in CeO_2 and heated in a vacuum.

which oxygen is in short supply. Nevertheless, it is necessary to confirm whether such chemical reactions occur in practice; therefore, simple experiments were performed.

Two Fe specimens were heated at 773 K for 6 h in a high vacuum of 4.2×10^{-3} Pa; one specimen was embedded in CeO_2 powder, but the other was not. Although the specimen surface with heat only was hardly damaged, the one inside CeO_2 powder with heat cracked and came off in scales. From this finding, it is obvious that the scales that formed under the reducing condition resulted from CeO_2. The scales were analyzed by X-ray diffractmetry to determine the type of ferric oxide.

Figure 2 shows the X-ray diffraction pattern of the scale. In the diffraction pattern, peaks of Fe_3O_4 together with α-Fe are seen, so it is concluded that CeO_2 powder in contact with the steel forms an oxide layer of Fe_3O_4 under the oxygen-lean condition. The diffraction pattern also gives vital information about the chemical change of CeO_2. Three diffraction peaks are seen at the diffraction angles 2θ=28.20°, 32.68° and 46.80°, which relate to the interplanar spacings d=3.162 Å, 2.738 Å and 1.940 Å, respectively. These interplanar spacings differ from those of Ce_2O_3 [3] and are slightly larger than those of the unused CeO_2 powder. Therefore, the peaks are thought to be an oxide of cerium in the range of CeO_2-$CeO_{1.714}$, i.e., the oxygen-deficient non-stoichiometric oxide [2]. Many predictions have been made as to the formation of Fe_3O_4 by CeO_2, as depicted in Fig. 1. The process can be represented in the following equation:

$$4CeO_2+3xFe\rightarrow4CeO_{2-x}+xFe_3O_4 \quad (2)$$

3. SUPERFINISHING CHARACTERISTICS

3.1 Experimental Procedures

Mechanochemical superabrasive stones were made experimentally by mixing CeO_2 powder, called CeO_2 abrasive in this paper, with CBN abrasive. Since the CeO_2 abrasive is thermally unstable, the special vitreous bond of a low melting point less than 1000 K was developed. In addition to the above CBN/CeO_2 stone, a conventional vitrified CBN stone and a vitrified CeO_2 stone that consists of only bonded CeO_2 abrasive were prepared in order to investigate the effect of the CeO_2 abrasive on the superfinishing characteristics.

Figure 3 shows SEM micrographs of the structure of the CeO_2, CBN/CeO_2 and CBN stones. In the CBN stone, it seems that CBN grit with sharp edges and smooth faces is anchored by bond posts, while in the CBN/CeO_2 stone, it seems that CBN grit attaching CeO_2 grits is retained by bond posts. In contrast with these two stones, the CeO_2 stone is different in the structure. It seems that agglomerate CeO_2 grits are dispersed into the bond posts.

All tests were performed on a flat superfinishing machine. The end of the workpiece was secured to the work spindle, then face-finished by the rotating cup-shaped abrasive stone without

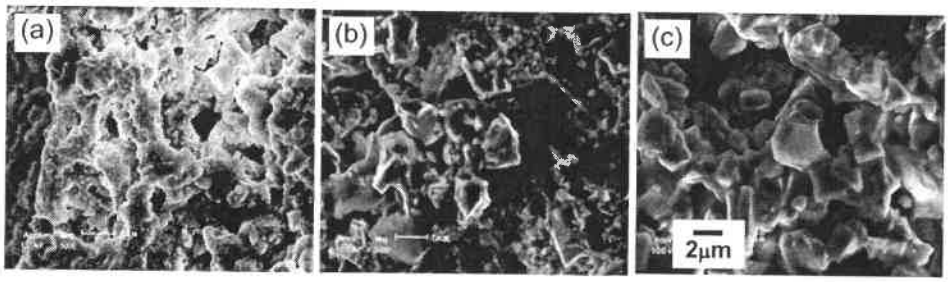

FIGURE 3. SEM micrographs of vitrified-bonded superabrasive stone. (a) CeO_2 stone (20000 grit, 56 concentration), (b) CBN/CeO_2 stone (4000/20000 grit, 82 concentration) and (c) CBN stone (4000 grit, 117 concentration).

Table 1. Superfinishing conditions.

Superfinishing pressure	0.36-1.42 MPa
Stone speed	56.5-113 m/min
Workpiece speed	21.3-84.8 m/min
Oscilation	Unused
Superfinishing time	2 min
Superfinishing fluid	Super fatted emulsifiable oil, 100×dilution
Workpiece material	SUJ 2, HRC60

oscillating motion. During the superfinishing process, water-based superfinishing fluid was used as a coolant that would exclude any chemical reaction. Table 1 tabulates the superfinishing conditions that were used.

3.2 Results and Discussions

In general, the chemical reaction rate tends to increase with a temperature rise, and this temperature dependence is described by an Arrhenius equation of the following form [4]:

$$\kappa = A\exp\left(-\frac{E}{RT}\right) \qquad (3)$$

where κ is the reaction rate, A is the frequency factor, E is the activation energy, T is the absolute temperature and R is the gas constant.

If the reaction rate is taken into account, the material removal rate of stones containing CeO_2 abrasive is presumed to depend on the temperature of the superfinishing fluid. Therefore, the removal rate of CeO_2 stone was examined over the temperature range from 298 K to 333 K, then compared to that of CBN stone. Figure 4 shows the Arrhenius plot of the removal rate versus the temperature of the superfinishing fluid. In the CBN stone, there is almost no change in removal rate. In contrast, in the CeO_2 stone, the increase in removal rate is almost linear with increasing temperature, so that the apparent activation energy can be calculated to be 32.8 kJ/mol. This means obviously that the CeO_2 stone has the ability to chemically remove a steel workpiece during the superfinishing process.

Figure 5 shows the roughness profiles of the superfinished surfaces and the corresponding height distribution functions. The interaction of CBN abrasive cutting points with the workpiece leaves overlapping scratches on the workpiece surface, so that the roughness profile is very rugged and generally has a symmetrical height distribution. On the other hand, since the CeO_2 abrasive exerts the combined action of a chemical attack and mechanical abrasion on the workpiece surface, the roughness profile is truncated and has clearly an asymmetrical height distribution.

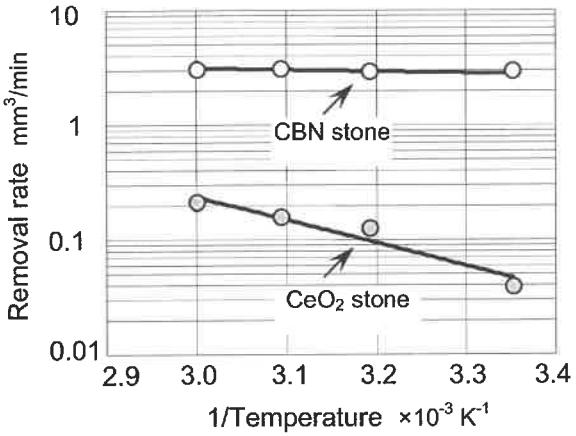

FIGURE 4. Dependence of removal rate on temperature of the superfinishing fluid.

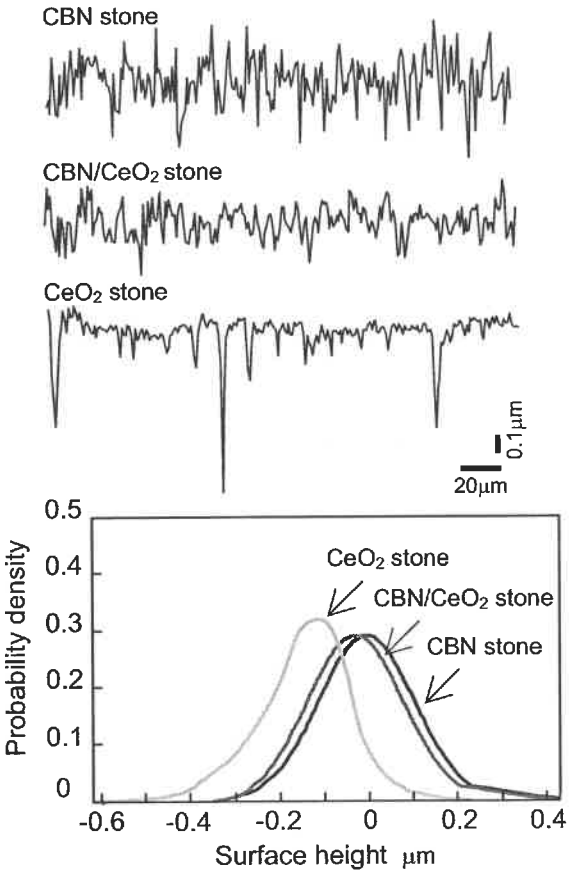

FIGURE 5. Roughness profiles and height distribution functions for steel surfaces superfinished with CeO_2, CBN/CeO_2 and CBN stones.

The skewness, which is a third-order measure of the symmetry of a profile, offers a convenient way to illustrate the feature of the profile shapes and height distribution functions. Therefore, the profiles generated by three different stones were evaluated in terms of the skewness, as shown in Fig. 6. It is found that the valley-covered surface generated by the CeO_2 stone gives a negative skewness, whereas the bump-covered surface generated by the CBN stone gives a slightly positive skewness. In comparison with these two stones, the CBN/CeO_2 stone is found to generate a normal surface, i.e., it is neither a valley-covered surface nor a bump-covered surface, and gives a zero skewness. Therefore, an appropriate CeO_2 abrasive content will result in the generation of a smooth surface with negative skewness that is suitable for bearings.

The feature of the superfinished surfaces generated by the stones of different kinds is also reflected in the roughness, as seen in Fig. 7. The CBN stone has Ra surface roughness values in the range of 0.02-0.03 μm, whereas the CeO_2 stone has values in the range of 0.05-0.1 μm because of the persistence of the valleys of the roughness profile. However, the CBN/CeO_2 stone with the scratching and chemical actions seems better for the surface roughness than the other stones. The CBN/CeO_2 stone has roughness values in the range of 0.015-0.02 μm. Hence, it can be understood that the addition of CeO_2 abrasive to a superabrasive stone is effective in smoothing the steel workpiece surface.

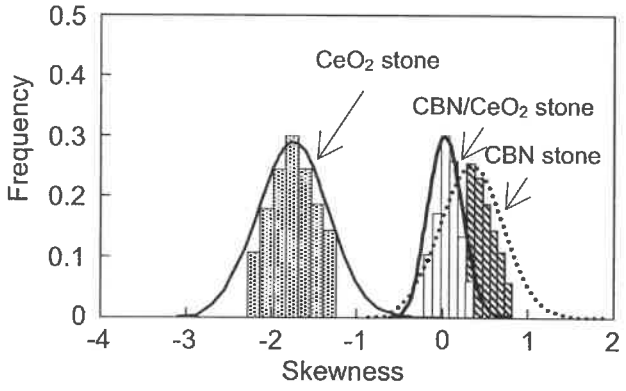

FIGURE 6. Histogram of skewness for steel surfaces superfinished with CeO_2, CBN/CeO_2 and CBN stones.

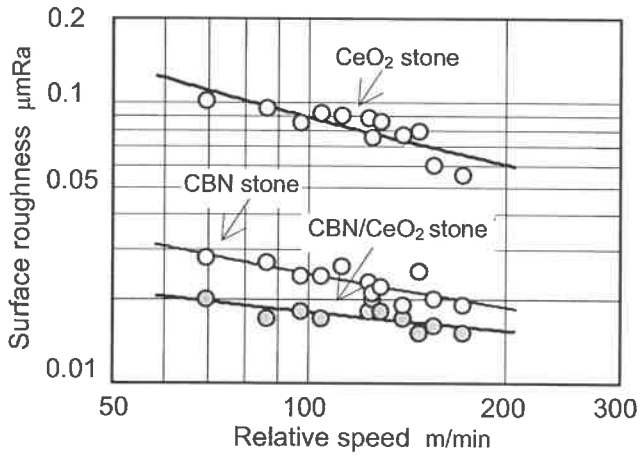

FIGURE 7. Comparison of surface roughnesses of steel workpiece superfinished with three different stones.

4. CONCLUSIONS

The present study was an attempt to develop a vitrified-bonded superabrasive stone for mechanochemical superfinishing of bearing steels. Cerium oxide CeO_2, when in contact with steel under the oxygen-lean condition, forms an oxide layer of Fe_3O_4 on the steel surface. On the basis of this interesting point, a vitrified CeO_2 stone and a superabrasive stone containing CeO_2 abrasive, i.e., CBN/CeO_2 stone, were made experimentally and their performance was evaluated with respect to the superfinishing characteristics of bearing steel. As a result, it was found that the CeO_2 abrasive can react chemically on a steel workpiece in the superfinishing process because of the temperature dependence of the removal rate of CeO_2 stone, as described by the Arrhenius equation. Moreover, it was disclosed that the rubbing action by the friable CeO_2 abrasive can produce a smooth surface with negative skewness. Hence, it is concluded that the CBN/CeO_2 stone, which made the best use of the synergistic effect of the mechanical action of the CBN abrasive and the chemical action of the CeO_2 abrasive, is superior in surface finishing in comparison with conventional CBN stone.

REFERENCES

[1] Akamatsu Y, Tsushima N, Goto T, Hibi K. Influence of Surface Roughness Skewness on Rolling Contact Fatigue Life. STLE Trib. Trans. 1992; 35: 745-750.

[2] Trovarelli A. Catalysis by Ceria and Related Materials. Imperial College Press: 2002.

[3] McClune W.F. JCPDS, Powder Diffraction File. 1999; 19-629.

[4] Taniguchi N. Nanotechnology. Integrated Processing Systems for Ultra-precision and Ultra-fine Products. Oxford University Press: 1996.

DEVELOPMENT OF POLISHING SIMULATOR FOR OPTICAL ELEMENTS

Haruki Ishibashi, Tohru Ishida, Yoshimi Takeuchi
Dept. of Mechanical Engineering, Graduate School of Engineering
Osaka University
Yamadaoka 2-1, Suita, Osaka 560-0871, JAPAN

INTRODUCTION

Semi-conductors installed in a variety of electronic goods are produced by use of steppers. Lenses in the optical system of steppers should have high performance to manufacture the good semi-conductors. Polishing is one of the processing technologies to finish lenses with high accuracy and performance. It enables to finish workpieces up to the accuracy of nanometer order with the relatively simple process.Therefore, the importance of polishing technology is strongly drawn attention.

In polishing process, however, neither the process mechanism has neither been clarified, nor the amount of material removal has been estimated accurately. One reason for it is the comlicated mechanism. Workpiece is removed by the chemical and physical operations. The amount of material removal is so small that the chemical operations must not be neglected. Another reason for it is that the amount of material removal is changeable by the surrounding condition in machining. Consequently, it is difficult to accurately estimate the amount of material removal. Therefore, some lenses are fabricated by modifying the polishing condition and repeating polishing process or measurement until the accuracy of the lenses meets the predefined precision. This way of polishing takes much time to fabricate precise lenses.

The study investigates the change in the removal shape by the variable process parameters in polishing process so as to estimate it. It is expected that the fabrication time of lenses with high performance becomes shorter, and that the surface roughness becomes better according to the accurate estimation of the amount of removal in polishing process. Therefore, firstly, the simulator to polish flat surface has developed. Secondly, the study investigates the influence of process parameters on the removal shape in polishing flat surface.

THE DEVELOPED POLISHING SIMULATOR

Outline

The simulator in the study can calculate the amount of removal by using the unit removal shape and the dwell time distribution. The unit removal shape means a removal shape obtained by traveling tools in the unit time. The dwell time distribution means a time when a tool stays in a predetermined position. This way has been proposed as the convolution model. Figure1 shows the concept of the convolution, which is used in order to calculate the amount of removal[1]. In the study, Hertz theory is

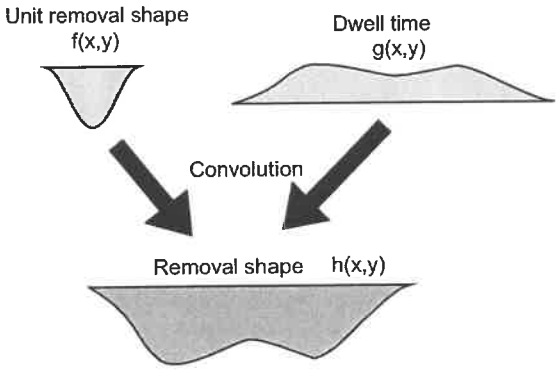

FIGURE1. Convolution model.

introduced into the simulator to deal with the influence of process parameters.

Convolution model

Preston Equation states that the amount of removal on a workpiece is propotional to the force and the relative velocity between a workpiece and a tool. The convolution model, based on Preston Equation, forms the basis of the simulator and is signified by the following equation (1).

$$h(x,y)=\iint_A g(x,y)f(u-x,v-y)dudv \quad (1)$$

,where h is the shape of removal, A is the polishing area, g is the dwell time distribution and f is the unit removal shape.

Responce to process parameter

The simulator in the study deals with the variation in the force by introdusing Hertz theory. It represents that two objects make contact with each other. When the force varies, the variation in the contact area and the magnitude of the maximum contact stress are calculated with the following equations (2), (3) in this theory. They are the equation about the contact between a sphere object and a flat object.

$$a^3=\frac{3}{4}R_1P\left(\frac{1-\nu_1^2}{E_1}+\frac{1-\nu_2^2}{E2}\right) \quad (2)$$

$$p_{\max}=\frac{3}{2\pi}P^{\frac{1}{3}}\left\{\frac{4}{3}\frac{1}{R_1}\frac{1}{\frac{1-\nu_1^2}{E_1}+\frac{1-\nu_2^2}{E2}}\right\}^{\frac{2}{3}} \quad (3)$$

,where a is an contact area, R_1 is radius of a sphere, E_1 and E_2 are longitudinal elastic modulus of a tool and a workpiece, ν_1 and ν_2 are Poisson's ratio, p_{max} is the maximum contact stress and P is the force added.

Evaluation

The simulated result was compared with the experimental one in order to evaluate the simulator. The force and the velocity of tool in the experiment was used in the simulation. Figure 2 shows the unit removal shape used in the simulation, the tool path and the force change. Figure 3 and Figure 4 show the results by the simulator and the experiment respectively. The long stay of the tool brings deeper area, as shown with thick curve line in Fig.3. The peak in the low-frequency in Fig.4(a) is seems to be due to the influence of the measured result in the experiment. The simulated depth is close to

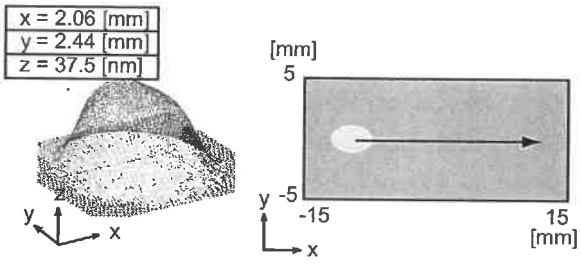

(a) Unit removal shape for estimation (b) Tool path

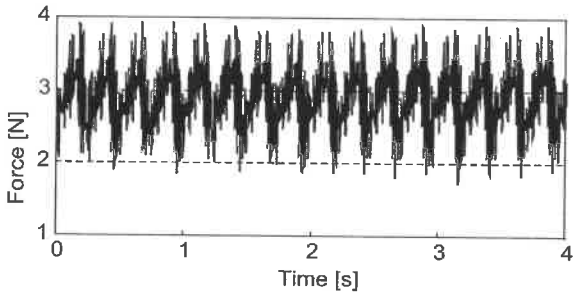

(C) Force data

FIGURE 2. Condition of the simulation.

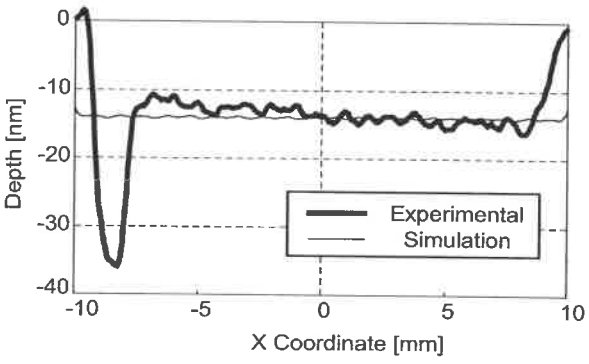

FIGURE 3. Results of the experiment and simulation for estimation.

the experimental one, as shown in Fig.3. The simulated result doesnit represent the magnitude of the surface roughness well. According to Fig.4, the two peaks are shown in Fig.4(a) and Fig.4(b) when the space frequency is about 0.5mm^{-1} and 1.0mm^{-1}. Judging from Fig.3 and Fig.4, it is not enough to represent the actual phenomenon, but the simulator seems to be effective since the both tendencies are similar.

SIMULATION WITH THE CHANGE OF LOAD

The change in the moving velocity of tool

The amount of removal was calculated without changing the condition except for the traveling velocity of the tool and the frequency of the force. Figure 5 shows the unit removal shape used in this simulation, the toolis path and the variation in force for one period. Concerning the force, the average is 3N, the amplitude is 0.5N and it was changed by 1Hz every simulation from 1Hz to 20Hz. The unit removal shape is made so that the curve is cosine function. The base area is a circle. The velocity was changed by 1.0mm/s every simulation from 1.0mm/s to 10.0mm/s in the same frequency of the force.

Figure 6 shows a part of the results from these simulations. The vertical axis represents the PV value and the horizontal axis represents the frequency of the force. There seems to be no relationship between three graphs. However, if the vertical axis is replaced by the PV value multiplied by *d/V*, and the horizontal axis is replaced by the frequency of the force multiplied by *V/d*, as shown in Fig.7, a kind of tendency comes out.

The change in the unit removal shape

The amount of removal was calculated without changing the condition except for the size of the tool and the frequency of the force. According to Hertz theory, the base area of the unit removal shape changes in changing the size of the tool.

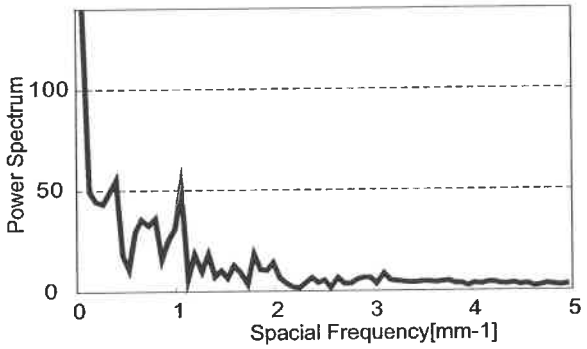

(a)Experiment

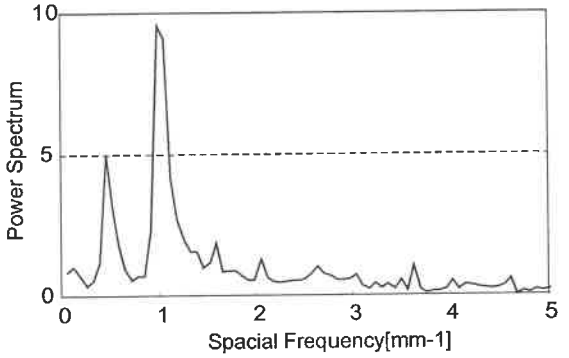

(b)Simulation

FIGURE 4. Spatial frequency analyses for the result of the experiment and the simulation

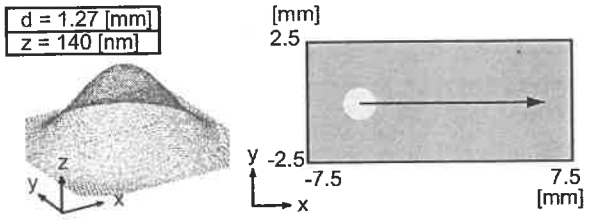

(a) Unit removal shape for estimation

(b) Tool path

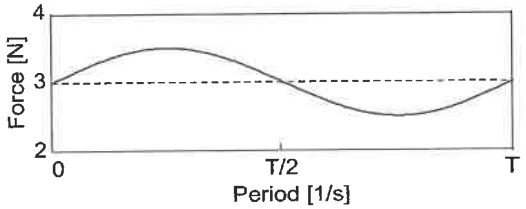

(C) Force data for one period

FIGURE 5. Condition of the simulation for the influence of process parameter.

The tool path and the force for one period are as same as in Fig.5, however, only the differences about the contact area of the unit removal shape in each simulation, the diameter 1.27mm, 1.60mm, and 1.83mm. The tool velocity is 3.5mm/s and the force is changed by 1Hz every simulation with the same diameter. Figure 8 shows the results. The vertical axis represents the PV value and the horizontal axis represents the frequency of the force respectively. Figure 8(b), the modified graph by multiplying *d/V* and *V/d* to Fig.8(a) in the same manner, shows the close relationship with Fig.7.

CONCLUSION

In the study, the polishing simulator is developed, which is based on the convolution model and utilizes the unit removal shape and the dwell time to calculate the amount of material removal. It is clarified that the simulator is effective by comparing the result of the simulator with that of the experiment. The simulated results under two different condition show that the velocity of a tool and the size of the tool make influence on the surface roughness after machining and, that the relationship between each process parameters and the surface roughness.

REFERENCE

[1] M.Negishi, M.Ando, M.Takimoto, A.Deguchi, N.Nakamura Studies on Super-Smooth Polishing(2nd Report), The Japan Society For Precision Engineering(in Japanese), 1996; 62: 408-412

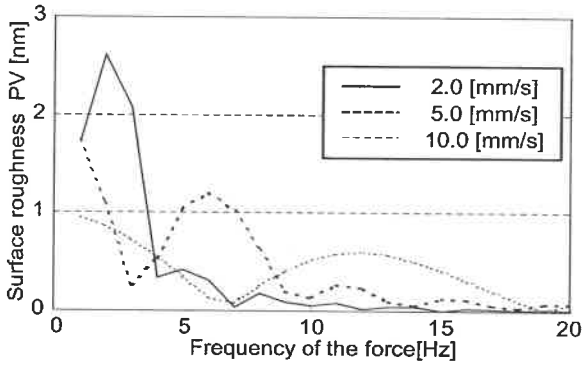

FIGURE 6. Results of the simulation with three kinds of velocity.

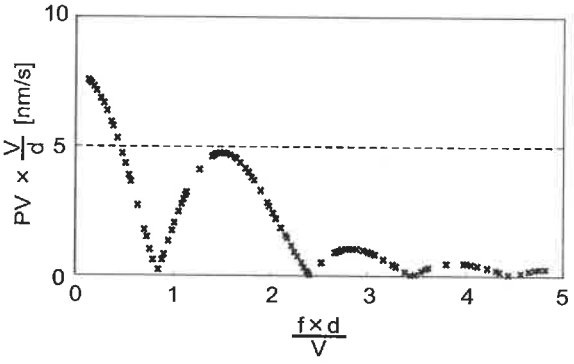

FIGURE 7. Results of the simulation with ten kinds of velocity.

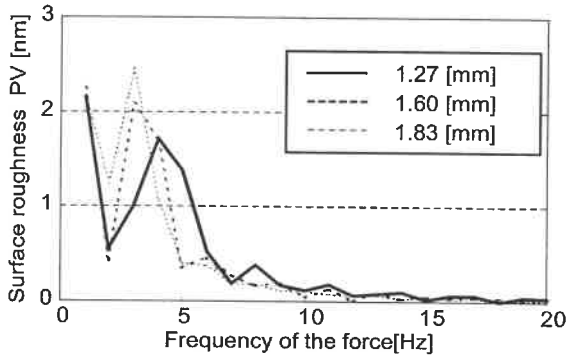

(a) Data before process

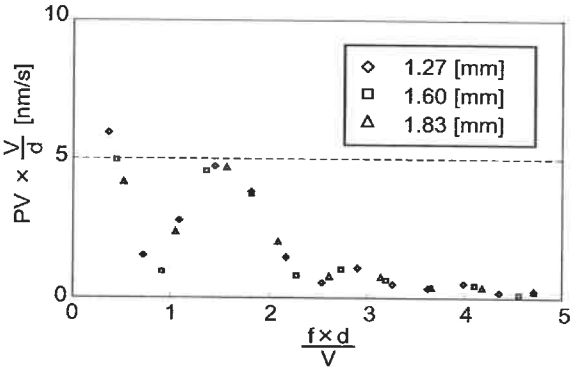

(b) Data after process

FIGURE 8. Results of the simulation for each diameters of the unit removal shape.

INFLUENCE OF POLISHER SURFACE STRUCTURE ON POLISHER LIFE IN ULTRA-SMOOTHNESS POLISHING OF NiP PLATED ALUMINUM MAGNETIC DISK SUBSTRATE

Kanta YAMAGUCHI[1],Heiji YASUI[1], Shingo OTSUKA[1], Tomohiko NAGATA[1], Kouhei KUSABA[1]

[1] Graduate School of Science and Technology, Kumamoto University, Kumamoto city, JAPAN

INTRODUCTION

To produce the low cost compact magnetic disk of high storage capacity, the high removal rate and ultra-smoothness polishing technique of the magnetic disk substrate has been strongly required. In our previous researches[1], ultra-high pressure and ultra-high speed polishing is effective for getting high removal rate in polishing of electroless nickel phosphorus (NiP) plated aluminum substrate. The polisher life in ultra-high pressure and ultra-high speed polishing, however, has not been adequately examined yet although it is one of the most important factors from the standpoint of the manufacturing cost. In the previous research, the polisher life is examined by pursuing the change of the removal rate with the polishing process using the suede type of polisher of the single layer in the surface structure.

The present report is extended to the investigation of the change of the removal rate in polishing process for the polisher surface structure of double layer. From the results, the remarkable difference between the polishers of single and double layer structure is found for the change of removal rate with polishing process.

EXPERIMENTS

The appearance of the polishing machine is shown in Fig. 1. The machine is available for polishing speed up to 9.0m/s and polishing pressure up to 60kPa. However, the maximum polishing pressure and speed generally used in the present polishing operations, are about 10kPa and 1.5m/s. The main experimental conditions are listed in Table 1. The aluminum substrate used is 3.5inch type. Supply flux is 20ml/min. The polisher surface is observed with a differential interference microscope and SEM. Surface structure of single layer and double layer polisher is shown Fig.2. From the figure polisher surfaces consist of large macroscopic holes and wall films having a lot of micro-pores.

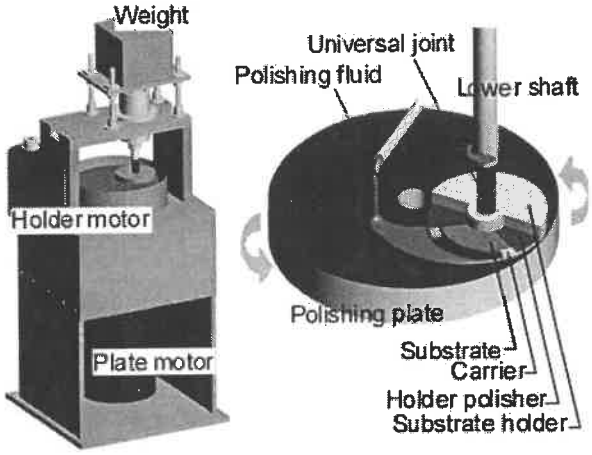

FIGURE 1. Schematic view of the polishing machine

TABLE 1. Experimental conditions

Work piece	NiP plated aluminum magnetic disk substrate (3.5inch type: ϕ95×ϕ25×1.27mm)
Polisher	Suede type
Polishing fluid	Abrasives : Colloidal silica Content of abrasives *Cg*:5wt% Supply flux *Lg* : 20ml/min
Polishing conditions	Polishing pressure *P* :10,60kPa Polishing speed *Va* :1.5m/s

Moreover, the top of films consists of projecting nap part. The substrate smoothness is evaluated from the standpoint of the slight undulation *Hwa*(Ra), and the surface roughness *Hra*(Ra), which are obtained from the surface profiles of 4mm length and 256μm length measured with a interferometric surface profiler (WYKO), respectively. The data are obtained by averaging the values of two-dimensional profiles at five random positions on the three-dimensional WYKO images measured at four locations of substrate surface.

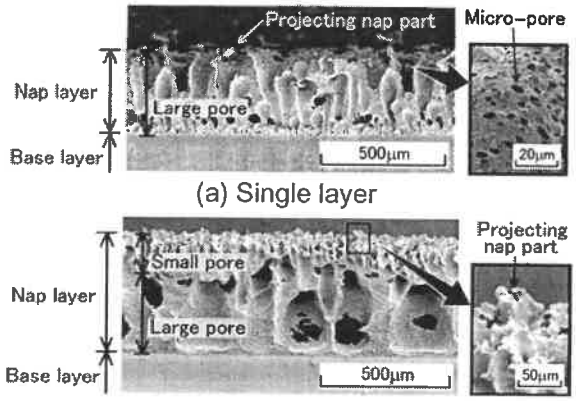

FIGURE 2. *Comparison of surface structure of single layer with double layer in the polisher surface*

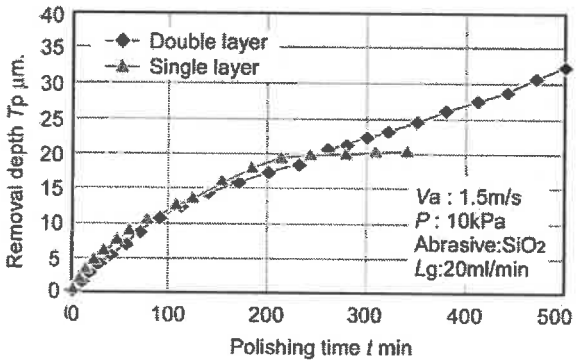

FIGURE 3. Comparison of the change of removal depth with polishing time using the single layer polisher and double layer polisher

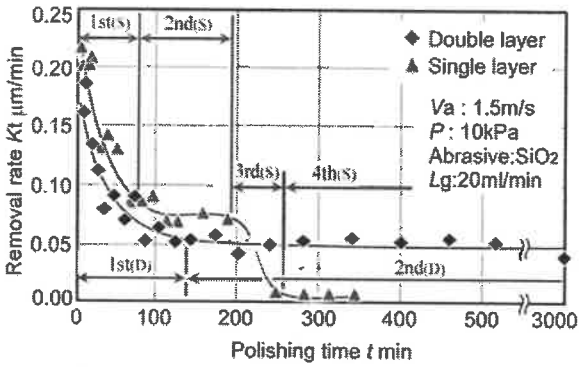

FIGURE 4. Comparison of the change of removal rate with polishing time using the single layer polisher and double layer polisher

EXPERIMENTAL RESULTS AND DISSCUTIONS

Change of removal rate with polishing time

Figure 3 shows the comparison of the change of removal depth with polishing time using the single layer polisher and the double layer polisher. Polishing pressure and speed used are 10kPa and 1.5m/s, respectively. In the case of the single layer polisher, the removal depth increases steeply in the initial polishing process. Afterward the increasing rate of the removal depth increases linearly. From the polishing time of 220 minutes, the increasing rate of removal depth begins to become small again and finally converge to a extremely small value. In the case of the double layer polisher, on the contrary, removal depth still increases linearly up to the polishing time of 500 minutes.

Figure 4 shows the change of removal rate with polishing time for both polishers. Using the single layer polisher, reported in the previous report, the removal rate in the polishing process is found from the figure to be classified by four steps. The first polishing step is the former transient process in which the removal rate changes from the extremely high removal rate at the beginning polishing process to steady removal rate at the second polishing step. The third polishing step is the latter transient process in which the removal rate changes from the

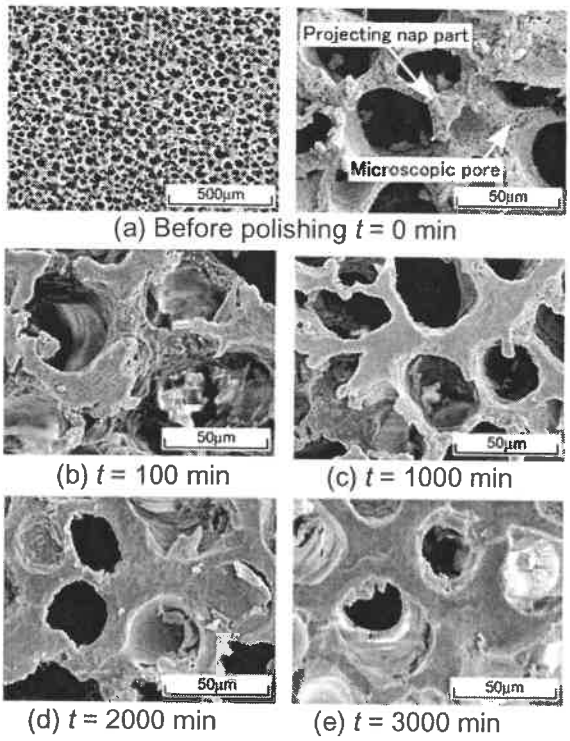

FIGURE 5. Change of polisher surface with polishing time in the double layer type polisher

[Polisher: Suede type , Abrasive :SiO2, Lg=20ml/min , P=10kPa , Va=1.5m/s]

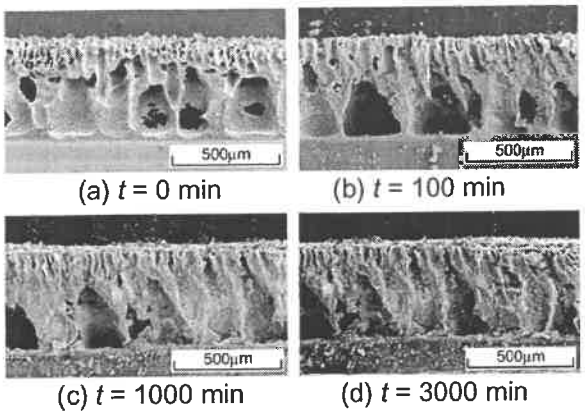

(a) t = 0 min (b) t = 100 min

(c) t = 1000 min (d) t = 3000 min

FIGURE 6. Change of polisher section with polishing time in the double layer type polisher

[Polisher: Suede type , Abrasive: SiO_2, Lg=20ml/min , P=10kPa , Va=1.5m/s]

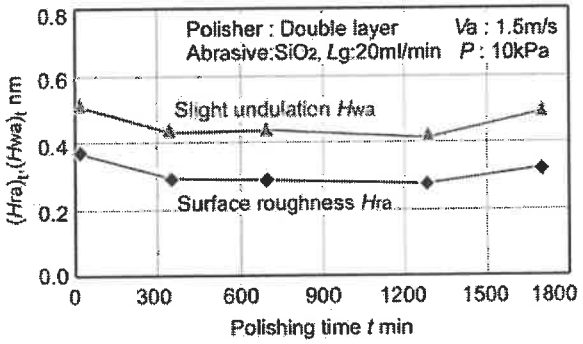

FIGURE 7. Change of the terminal surface smoothness with polishing time

steady removal rate to the extremely low removal rate at the fourth polishing step, that is, the lifetime. At the lifetime, the polisher surface layer is embedded mostly with colloidal silica abrasives. On the other hand, using the double layer polisher, it is found that only the first two steps, that is the former transient polishing step and the steady polishing step are ascertained and polisher life is not found until long polishing time.

FIGURE 5 and FIGURE 6 show the change of surface and section of polisher with polishing time for the double layer polisher, respectively. Compared with the new polisher surface, the polisher surface at t=100 min becomes flat because the projecting nap part is scrapped off. The polisher surface at t=3000 min, is not embedded with colloidal silica abrasives. The result is large different from the case of the single layer polisher. As the result, the same removal rate is kept until long polishing process.

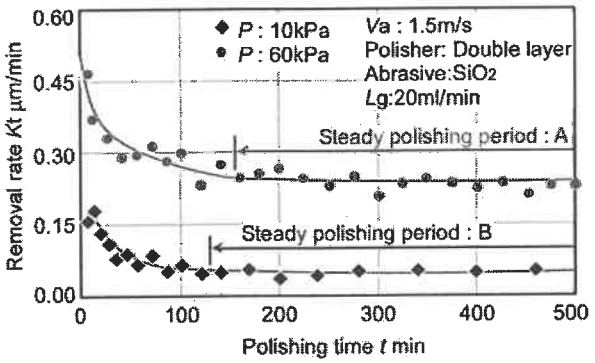

FIGURE 8. Influence of polishing pressure on the change of removal rate with polishing time

FIGURE 7 shows the change of terminal surface smoothness with polishing time for the double layer polisher. However the terminal surface roughness means that the substrate smoothness converges finally to a value related to a given polishing condition after being improved by polishing. From the figure, both of slight undulation and surface roughness are somewhat worse in the former transient polishing step and attains the smallest in the second stage. After the polishing time of 1500 min, the surface smoothness tends to increase slight with the increase of polishing time again. It is inferred why the colloidal silica abrasives, which are piled up in the shallow cave found partially on the flat surface of polisher, groove somewhat deep on the substrate. Thus the polisher surface condition is referred to influence a little on polished substrate surface smoothness.

Influence of polishing pressure

FIGURE 8 shows the Influence of polishing pressure on the change of removal rate with polishing time. From the result, the change of removal rate with polishing time is similar for both polishing pressure. It is found that the removal rate in polishing process is classified by two steps. In the second steady step, the removal rate at P=60kPa is about four times larger than that at P=15kPa.

FIGURE 9 and FIGURE 10 show the change of surface and section of polisher with polishing time in the double layer polisher for the polishing pressure of 60kPa. From the figure, it is found that the polisher surface is flattened out quickly by the short polishing time of 5min. The thickness of the polisher decreases several 10 microns. After the long polishing time of 500 min, however, the large pore on the bottom part of polisher surface is not embedded with colloidal

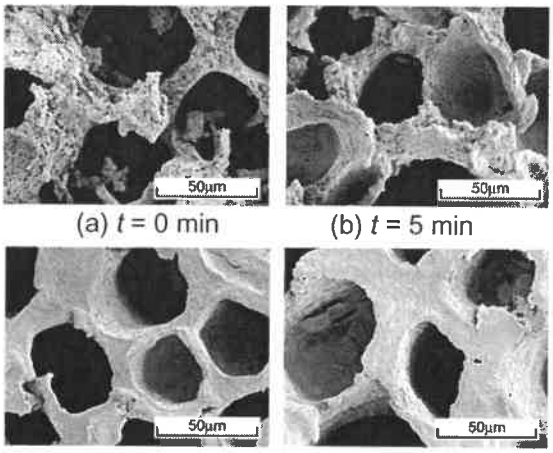

(a) t = 0 min (b) t = 5 min

(c) t = 100 min (d) t = 500 min

FIGURE 9. Change of polisher surface with polishing time in ultra-high pressure polishing condition

[Polisher: Double layer type, Abrasive:SiO_2, Lg=20ml/min, P=60kPa, Va=1.5m/s]

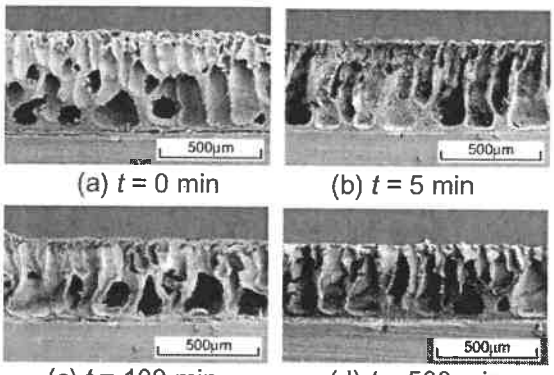

(a) t = 0 min (b) t = 5 min

(c) t = 100 min (d) t = 500 min

FIGURE 10. Change of polisher section with polishing time in ultra-high pressure polishing condition

[Polisher: Double layer type, Abrasive:SiO_2, Lg=20ml/min, P=60kPa, Va=1.5m/s]

silica abrasives. At that time, the large pore is left in the situation near the polisher before polishing.

FIGURE 11 shows the Influence of ultra-high polishing pressure on surface smoothness of polished substrate for the double layer polisher. The polishing time is found to have a little influence on the surface smoothness.

CONCLUSIONS

The main conclusions obtained are as follows:

(1) In the case of the double layer polisher, only the first two steps, that is, the former transitional polishing process and the steady polishing process among the four steps which are found in the change of removal rate with polishing process for the single layer polisher are ascertained.

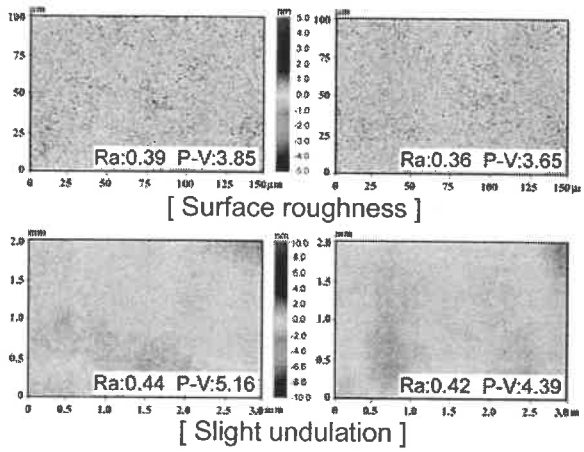

(a) t = 10 min (b) t = 500 min

FIGURE 11. Influence of ultra-high polishing pressure on surface smoothness of polished substrate

[Polisher: Double layer type, Abrasive:SiO_2, Lg=20ml/min, P=60kPa, Va=1.5m/s]

(2) The surface structure of the double layer polisher is embedded difficult with colloidal silica abrasives.

(3) In the case of the double layer polisher, the removal rate at ultra-high pressure of 60kPa is about four times larger than the maximum rate in the usual polishing pressure of 10kPa under the polishing speed of 1.5m/s.

(4) The polishing pressure has little influence on surface smoothness.

ACKNOWLEGEMENTS

The authors would like to thank TOYO KOHAN Co. Ltd, FUJIBO EHIME Co. Ltd and KAO Co. Ltd for providing magnetic disk substrate, polisher and polishing fluid. A part of the research is supported by GRNT-IN-AID for Scientific Research (2005) [Project No. 17360065] in Japan

REFERENCES

1. H.YASUI, S.KURIBAYASHI, S.MATSUKAWA, Y.YAMASAKI, K.YAMAGUCHI: Polisher Life in High Speed Ultra-Smoothness Polishing of NiP Plated Aluminum Magnetic Disk Substrate, Proc. ASPE 19th Annual Meeting, pp.737-740

NANO-SCALE MECHANICS OF FRONT-SIDE CONTAMINATION IN PHOTONIC DEVICE FABRICATION USING IMPRINT LITHOGRAPHY

Shrawan Singhal and S.V. Sreenivasan
Department of Mechanical Engineering
The University of Texas, Austin, TX 78712

ABSTRACT

Nanoimprint lithography is a cost effective technique for replicating nanoscale features with high resolution. Step and Flash Imprint Lithography (S-FIL®) is one such process based on liquid dispense and subsequent UV curing, and has potential applications in photonics, displays, patterned magnetic media, IC fabrication, etc. However, the yield of the process can be affected by particulate contamination and other surface asperities on the wafer substrate. An example of such an asperity encountered during the fabrication of structures for high brightness LEDs is the presence of GaN epitaxial defects. Typically, these defects lead to a loss in printed area on the substrate, which translates directly into a loss in yield, due to the starvation of the fluid or excessive residual material in the vicinity of the contaminant. This paper aims to estimate this area lost in the S-FIL process for templates with varying mechanical properties.

INTRODUCTION

Nanoimprint lithography has been shown to be a viable technique for patterning nano-scale features with remarkable resolution. Nanoimprint lithography techniques are essentially molding techniques where patterns etched into a template (master mold) are replicated into a polymeric resist deposited on a substrate. These techniques come in three basic flavors: (i) Thermal imprinting [2]; (ii) Spin on UV imprinting [3]; and (iii) Liquid dispense based UV imprinting [4]. A liquid dispense based UV imprinting – known as Step and Flash Imprint Lithography (S-FIL™) (Figure 1)– is the process discussed in this paper, with a focus towards the fabrication of photonic devices.

Due to its ability to print whole wafers at a time, S-FIL offers significant cost advantages over conventional lithography techniques without compromising on throughput [5]. However, nanoimprint processes are proximity lithography processes, and the end yield is sensitive to high spatial frequency perturbations like fall-on particles, both on the front and back side of the wafer [6]. In the fabrication of high brightness LED devices using GaN epitaxial layers on sapphire substrates, these perturbations are often encountered in the form of columnar defects, that are essentially, microstructure imperfections in the GaN layer. These hard front-side defects can be responsible for a remarkable loss in the imprint area (Figure 2), thereby translating into a

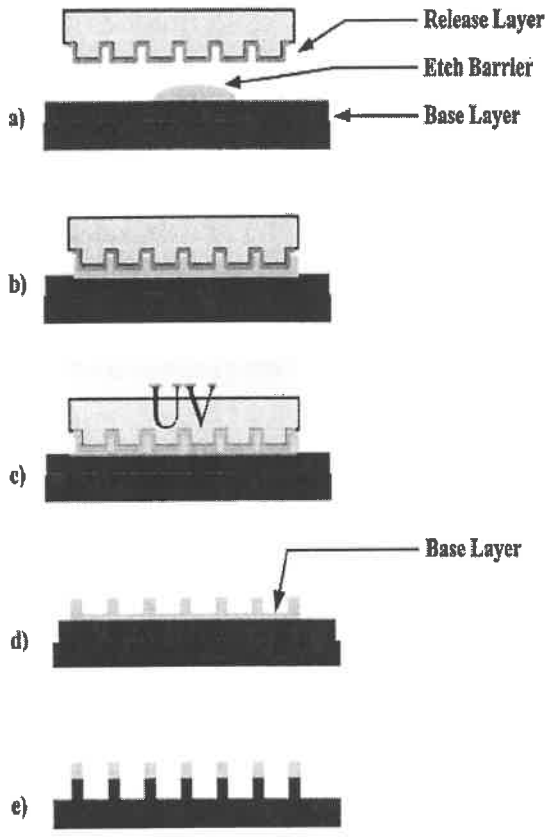

FIGURE 1. Process schematic of S-FIL [1]. The liquid is dispensed on the base layer (a) and the patterned template placed on to the fluid (b), filling the features. After UV curing in step (c), the template is removed (d).The base layer is then etched and stripped, and the pattern is replicated on the substrate (e).

loss in yield due to a disruption of the continuity of the template-fluid-substrate interface. The lost area is categorized as (i) an exclusion zone around the defect, where there is a complete starvation of the imprint fluid between the template and the substrate, and (ii) a transition zone, where the thickness of the fluid film is different from the nominal value, required for successful pattern transfer of the replicated polymer features into the substrate.

This paper attempts to estimate the size of the exclusion zone based upon a finite element

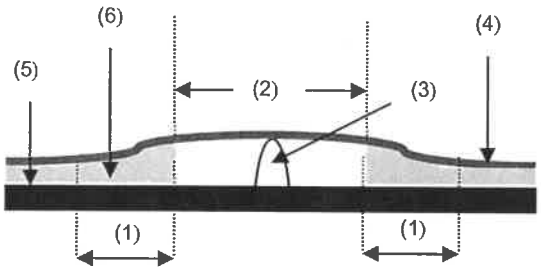

FIGURE 2. Diagram illustrating effect of the GaN defect. The transition region and exclusion zone are marked as (1) and (2) respectively, whereas the defect, soft template, GaN epitaxial layer, and imprint fluid layer are marked as (3), (4), (5) and (6) respectively.

model, using ABAQUS 6.6. For the purpose of this study, two pure monolithic featureless templates, made of fused silica and a soft elastomer each, have been analyzed. While a fused silica 'rigid' template yields an upper bound to the value of the exclusion zone, the soft template presents the lower bound due to its higher flexibility. However, the lower bound solution is not feasible practically, as a soft template may cause feature distortions affecting quality of lithography. Hence, this work serves as a preliminary step to develop bilayer systems [7], composed of a fused silica template coated with the soft elastomer layer. As the layer is made thicker, the influence of the elastomer is increased. An optimal thickness based on overlay requirements and tolerable loss in print area can then be determined, from within the bounds calculated.

MECHANICS

Fluid-Template Interaction

S-FIL works as a nano-molding process whereby the template with the desired pattern is placed onto a low viscosity monomer. The desired nominal thickness of the fluid film is typically at or less than 100 nm, whereas the diameter of the substrates used in high brightness LED applications is typically 3 or 4 inches. These disparate length scales permit the use of Reynold's transport equation used for hydrodynamic lubrication [8], for determining the flow conditions:

$$\frac{1}{r}\frac{\partial}{\partial r}\left(rw^3\frac{\partial p}{\partial r}\right)=12\mu V \qquad \ldots(1)$$

where, w represents the vertical displacement of the template with velocity V, r is the radial co-ordinate, p is the pressure in the liquid and μ is the viscosity of the liquid (1 cp). The boundary condition for this equation is given by the capillary pressure at the liquid-air meniscus:

$$p_{gauge}=-\frac{\gamma}{H}\left(\cos\theta_t+\cos\theta_s\right) \qquad \ldots(2)$$

where p_{gauge} is the gauge pressure at the meniscus, γ represents the surface tension of the liquid (0.03 N-m), and θ_t and θ_s are the contact angles at the template and substrate (45 and 10 degrees respectively). A non-dimensional number, called the capillary number [9], serves as a useful metric to identify the flow regime:

$$Ca\sim\frac{\mu VR^2}{\gamma H^2}$$

where R and H are relevant length scales in the radial and normal directions respectively. Typically, R can be represented as the radius of the wafer and H as the desired fluid film thickness. If Ca >> 1, the flow is viscous dominated, and if Ca << 1, the flow is primarily governed by the capillary pressure.

Near the end of the process, the template velocities are extremely small, such that Ca << 1, thereby indicating that the process is dominated by capillary flow. The small value of the desired film thickness, results in an equally small meniscus at the fluid-air interface. This in turn, gives rise to high capillary pressures, as given by equation (2) which drive the flow of the liquid on the substrate and in the features, and at the same time, cause the template to deform. The template deformation then has an effect on the pressure distribution as well, as can be seen in equation (1). In the ideal case, without any structural perturbations, the capillary pressure acts uniformly throughout the template. However, this uniformity gets disturbed in the vicinity of a defect, due to the presence of the exclusion zone (where the pressure is zero) and

the transition region (where the pressure is different from the bulk volume, but non-zero).

Defect-Template Interaction

The mechanics of contact between the defect and the template are governed by the mechanical properties of the template and the defect, as well as the morphology of the defect [9]. The defects are primarily observed as columnar structures and because of their sharper tips, they can cause significant, but highly local contact deformation on the template. In equilibrium, the contact forces are essentially the same as the reaction forces obtained at the defect location, due to bending of the template. Hence, the greater the bending in the template, the higher would be the contact forces, leading to a greater local deformation.

MODELING

Assumptions

The coupled nature of the problem requires a combined model to capture the physics of the fluid-template and defect-template interactions. This has been achieved using a commercial finite element analysis package, ABAQUS 6.6, with some simplifying assumptions to keep the computational effort reasonable. The materials are assumed to be linear and perfectly elastic, since damage and failure is not under the purview of this work. The template is also assumed to be completely featureless.

As a first approximation, the capillary pressure is assumed to be constant throughout, even in the transition region, but zero in the exclusion zone. This assumption is based on the hypothesis that the area of the transition region is smaller than the imprint area. Hence, a variation in pressure over the transition region will not influence the results strongly, as a major portion of the template is subject to the constant capillary pressures. The model is built for a single defect at the wafer center. This allows for the use of a 2D axisymmetric formulation (Figure 3), avoiding the use of a more expensive 3D one, without compromising on the validity or efficacy of the model. Also, the defect is approximated as a hemisphere of radius 500 nm rather than the commonly observed tall 'spike', to avoid any computational instability while modeling sharp indentations. The template is also clamped at the outer edge and constrained to not bend further below the fluid film of 100 nm.

Procedure

Since the exclusion zone is not known a priori, the region over which the capillary pressure acts is also not known. Hence, an iterative procedure is used to estimate the size of the transition and exclusion zone. In the first iteration, the capillary pressure is applied throughout the length of the template.

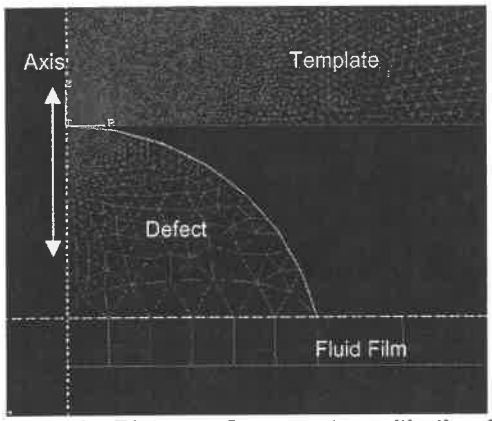

FIGURE 3. Picture of geometry with the FEA mesh

The transition region is then obtained as the radial location of the point where the template loses contact with the 'rigid' fluid film. The exclusion zone is a result of strict conservation of liquid volume, and, after knowing the transition region radius, is evaluated as:

$$2\pi \int_{R_2}^{R_1} wrdr = \pi R_1^2 H \qquad \ldots(3)$$

where R_1 and R_2 are the radial locations where the transition and exclusion zones begin, respectively, and H is the desired fluid film thickness. The integration can be performed approximately using the area under the (w^*r) plot to estimate the value of R_2. In the subsequent iteration, a new value of the exclusion zone is guessed, similar to the one obtained in the previous iteration. Now, the capillary pressure is removed from that region, and the new transition region and exclusion zone radii are obtained as before. This process is repeated till the values of the exclusion and transition regions converge.

RESULTS

The above mentioned scheme for the monolithic templates is solved using finite elements with ABAQUS 6.6. Table 1 gives the structural properties of the materials used. The thickness

of the template in both cases is taken as 0.7 mm.

TABLE 1. Structural Properties of the Materials

Material	Young's Modulus	Poisson's Ratio
Fused Silica	73 GPa	0.17
Elastomer	2 GPa	0.48
GaN	350 GPa	0.25

TABLE 2. Monolithic Template Results. The radial location where the template loses contact with the 100 nm fluid film is measured as the transition zone radius.

	Fused Silica	Elastomer
Exclusion Zone	~ 72 μm	~ 12 μm
Transition Zone	~ 240 μm	~ 43 μm

The results for the monolithic templates have been summarized in Table 2. Interestingly, the values of the exclusion zone are quite small, when compared against the radius of the wafer. As a matter of fact, these values for both, the fused silica and elastomer template, have been obtained after the first iteration itself, i.e., when the entire template was subject to the capillary pressure, and do not change to any appreciable extent in subsequent iterations, due to the small exclusion zone radius. It can also be seen that the transition region for the fused silica template is significantly higher than that for the pure elastomer template, thereby indicating a significant loss in printed area. As mentioned earlier, a pure elastomer template is not feasible practically from a process point of view.

The in-plane distortions present an interesting picture. For the fused silica template, the distortions are confined to the vicinity of the defect and drop to a value of 3 nm and less after 8.6 microns. But, for the elastomer template significant distortions are observed all the way to the outer radial edge of the template, with an average value of about 20 nm. Overall, the results do suggest that bilayer designs would be a feasible solution, as the soft elastomer serves to absorb contact while the rigid backing in the form of fused silica tries to minimize the in-plane distortions.

REFERENCES

[1] Bailey T., Smith B., Choi J., Colburn M., Meissl M., Sreenivasan S.V., Ekerdt J.G., Willson C.G., Step and Flash Imprint Lithography: Defect Analysis, Journal of Vacuum Science and Technology B: 2001: 19 (6): 2806

[2] Chou S.Y., Krauss P.R., Renstrom P.J., Nanoimprint Lithography, Journal of Vacuum Science and Technology B: 1996: 14 (6): 4129

[3] Otto M., Bender M., Richter F., Hadam B., Kliem T., Jede R., Spangenberg B., Kurz H., Reproducibility and Homogeneity in Step and Repeat UV-Nanoimprint Lithography: Microelectronic Engineering: 2004: 73-74 (1)

[4] Resnick D.J., Sreenivasan S.V., Willson C.G., Step & Flash Imprint Lithography, Materials Today: 2005: 8 (2): 34–42

[5] Hershey R., Miller M., Jones C., Subramanian M.G., Xiaoming L., Doyle G., d Lentz D., LaBrake D., 2D Photonic Crystal Patterning for High Volume LED Manufacturing, Proceedings of SPIE: 2006: 6337: 63370M-1 – 63370M-10

[6] Nimmakyala P.K., Sreenivasan S.V., Compliant Pin Chuck for minimizing the effect of Backside Particles on Wafer Planarity, Journal of Vacuum Science and Tenchnology B: 2004: 22 (6): 3147-3150

[7] Watts M.P.C., Voisin R.D., Sreenivasan S.V., Compliant Hard Template for UV Imprinting, US Patent # 7140861: 2006

[8] Colburn M., Choi B.J., Sreenivasan S.V., Bonnecaze R.T., Willson C.G., Ramifications of Lubrication Theory on Imprint Lithography, Microelectronic Engineering: 2004: 75 (3): 321-329

[9] Reddy S., Bonnecaze R.T., Simulation of Fluid Flow in the Step and Flash Imprint Lithography Process, Microelectronic Engineering: 2005: 82 (1): 60-70

[10] Johnson K.L., Contact Mechanics, Cambridge University Press: 1985

ACKNOWLEDGMENTS

The authors would like to thank Molecular Imprints, Inc. in Austin, Texas for partially funding this research. Thanks also goes to Robert Hershey and Doug Resnick of Molecular Imprints for providing constructive feedback during the course of this research.

MICRO MOLDING OF METALLIC GLASS STRUCTURED COMPONENTS

Hirofumi Suzuki[1], Takeshi Kawano[1], Daisuke Mukohata[1], Yuji Yamamoto[1], Keiichi Nakamoto[1], Toshiroh Shibasaka[1] and Toshimichi Moriwaki[2]
[1]Department of Mechanical Engineering
Kobe University
Kobe, Hyogo, Japan
[2]Department of Mechanical Engineering
Setsunan University
Neyagawa, Osaka, Japan

INTRODUCTIONS

Recently, more miniaturization and higher integration are required in the LSI circuits to be installed in the mobile devices like cellular phones and PDAs. Therefore the pitch of electrode pads on the LSI circuits has become narrower. In the manufacturing process of LSI circuits, IC probes contact with the pads to check the electric property as shown in figure 1. Their size and pitch are similarly required to be small. The material of the IC probe should have electric conductivity, a high elastic limit, and should be able to be manufactured into 3D microstructures. However, the crystal grain size of conventional materials is too large to realize the micron order pitch. In this experiment, a new method for press molding of metallic glass that satisfies these requirements is proposed. In this method, the shape of probe is created with press molding of the metallic glass, and the unnecessary part of the molded component is removed by machining.

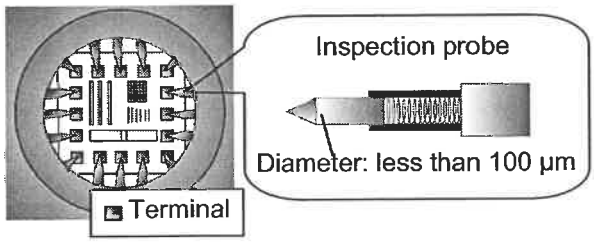

FIGURE 1. Wafer inspection

CHARACTERISTICS OF METALLIC GLASS

The metallic glass is a material with an amorphous structure without regular atom arrangement. Therefore, it is a material having excellent character for the spring material with high strength and high elasticity limit. Moreover, the size effect of metallic glass is small because it is an isotropic and a homogeneous material. In addition, it has the super-plasticity in the temperature region called super-cooled liquid state and returns to amorphous structure after cooling. Figure 2 is a transformation diagram of metallic glass. Accordingly, these characters enable producing the micro structured components.

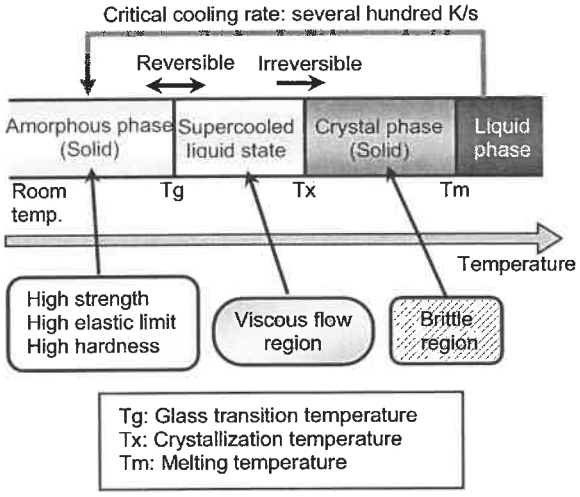

FIGURE 2. Transformation diagram of metallic glass

EXPERIMENTAL SETUP

In this study, Zr based metallic glass; $Zr_{55}Cu_{30}Al_{10}Ni_5$ (atomic %) was molded. The Zr based metallic glass is suitable for molding process, because its super-cooled liquid state is wider than that of other materials. Tungsten carbide was used for mold material polished. Three types of micro grooves as shown in figure 3 were ground on mold at 100 μm pitch. The simultaneous 4-axes controlled grinding machine (ULG-100D (H3), Toshiba Machine) was used for grinding. Figure 4 shows a view of

the high precision glass-molding machine (GMP-311V-SS, Toshiba Machine), which was used for the experiments. This machine is mainly composed of a chamber covered with a silica tube, a heating unit using infrared lamps, and driving shafts that move the lower mold up and down. A schematic illustration of one cycle of the press molding is shown in figure 5. At first, nitrogen gas is filled in the chamber and metallic glass is heated to the molding temperature. Next, the molds are driven to the pressing position and metallic glass is pressed during molding time. At last, metallic glass and molds are cooled with flowing nitrogen gas and the molded component is ejected. Molding conditions are shown in table 1. In this paper, a metallic glass was pressed on different molding temperatures and at different molding time to investigate the influence on the transcription.

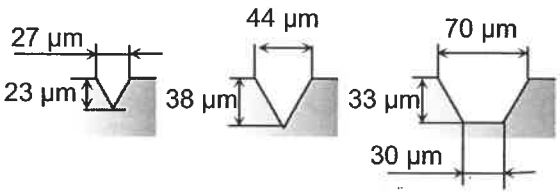

(a) V (small) *(b) V (large)* *(c) Trapezoid*

FIGURE 3. Shape of grooves

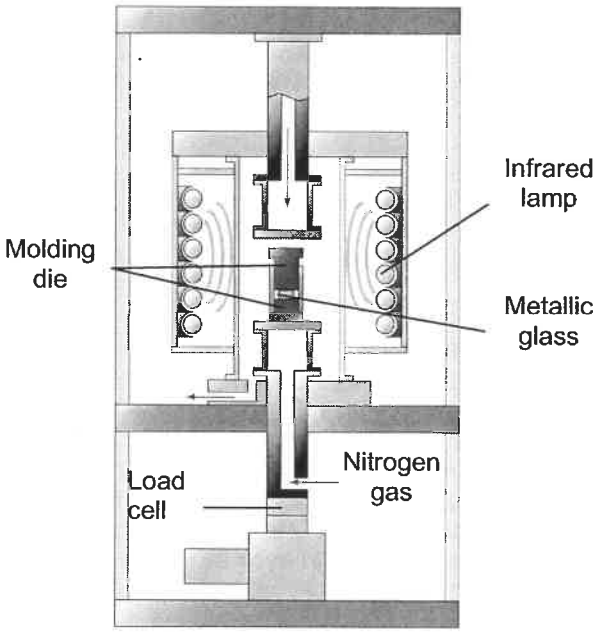

FIGURE 4. Schematic illustration of metallic glass molding machine

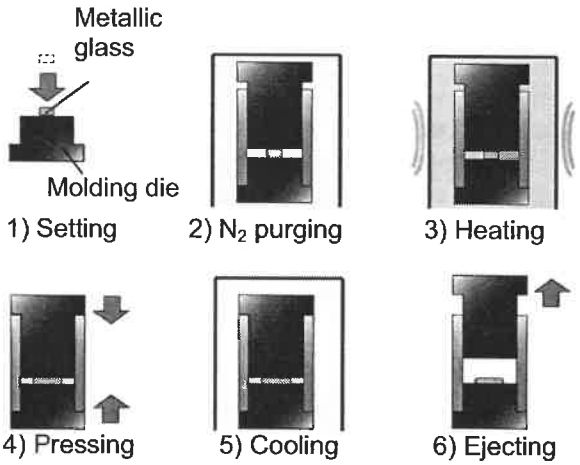

FIGURE 5. Molding process

TABLE 1. Molding conditions

Molding material	Zr based metallic glass
Size	Φ3 mm×0.55 mm
Tg	418 °C
Tx	504 °C
ΔT (Tx-Tg)	86 °C
Mold material	Tungsten carbide
Molding temperature	430-460 °C
Molding load	1, 1.5 kN
Molding time	30-120 s

EXPERIMENTAL RESULTS

Three types of microstructures shown in figure 6 were molded. Figure 7 is scanning electron microscope image of molded metallic glass components. It was confirmed that micro groove of molding die were well transcribed the molded components, V (large), V (small), Trapezoid. The molded shapes are measured with a non-contact measuring system (NH-3SP, Mitaka Kohki) and the deviation of molded component as shown in figure 8 was evaluated in order to discuss the performance of transcription. Figure 9 shows effects of molding temperature on molding deviations with different shape of groove. Because the viscosity of metallic glass decreases at high temperature, the deviation became smaller as the temperature becomes higher. At 440 °C, little deviation remained in case of V-shaped molding while there was no deviation of trapezoidal molding. Therefore, the transcription rate of trapezoidal groove is higher than that of V-shaped groove. Next, figure 10 shows effects of molding time on molding deviation. The deviation of V-shaped groove was decrease as molding time longer, however there were deviations in all conditions. There

was very little deviation of trapezoidal groove in all conditions, however the edges of molded workpiece were rounded when molding time is shorter. It is necessary to mold with enough time to transcribe microstructure precisely.

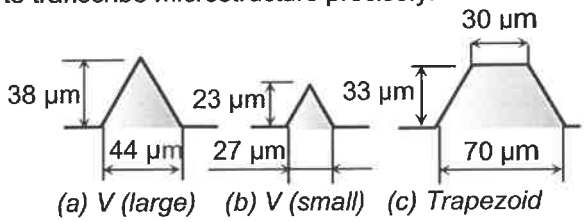

FIGURE 6. Shape of molded components

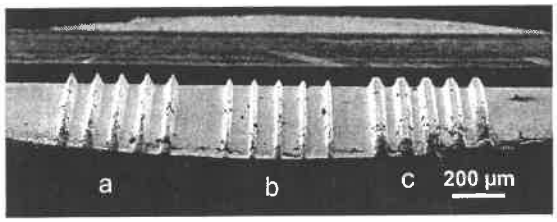

FIGURE 7. SEM image of molded components

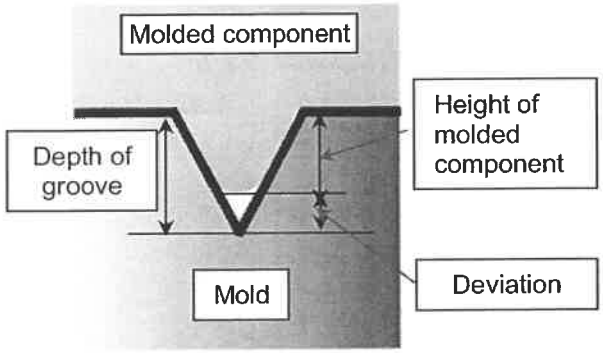

FIGURE 8. Definition of molding deviation

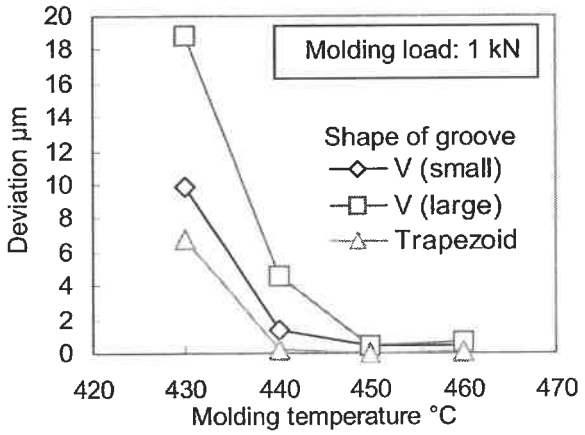

FIGURE 9. Effects of molding temperature on molding deviations

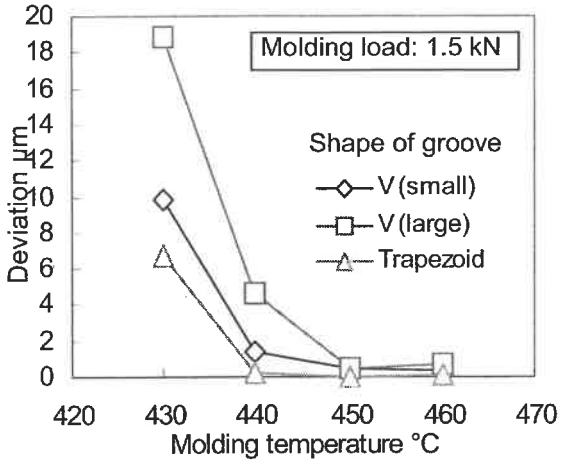

FIGURE 10. Effects of molding time on molding deviations

REMOVING UNNECESSARY PART OF MOLDED COMPONENT

The molded component includes unnecessary parts, so removing process is needed to obtain a probe as shown in figure 11. In this paper, the unnecessary part was removed with grinding using a micro diamond wheel. The high precision vertical grinding machine (UVM-350B, Toshiba Machine) was used for removing process. A schematic illustration of grinding process is shown in figure 12. The molded component was fixed on the jig with heat-resistant and impact-resistant adhesive. Grinding conditions are shown in table 2. SEM images of probe manufactured are shown in figure 13. The width of probes is less than 100 μm and their pitch is 100μm. Micro probes made of metallic glass with narrow pitch were obtained by molding and grinding process.

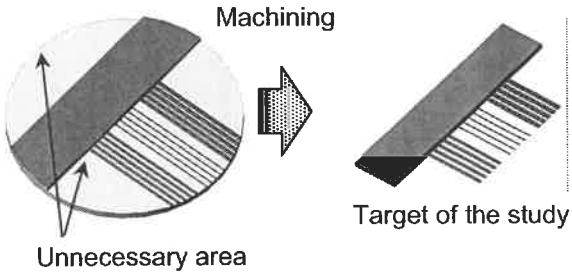

FIGURE 11. Manufacturing process of micro probes

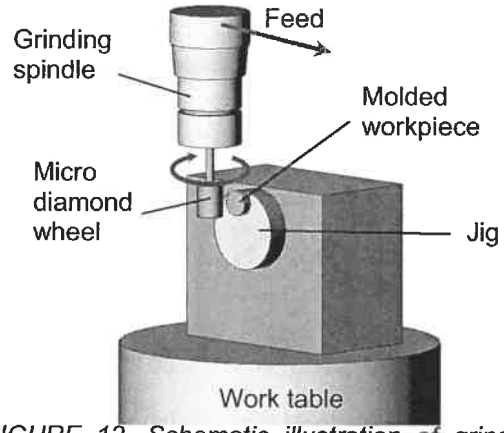

FIGURE 12. Schematic illustration of grinding process

TABLE 2. Grinding conditions

Grinding wheel Grain size Diameter Rotational rate	Resinoid bonded diamond #400 Φ10 mm 2×10^4 min^{-1}
Depth of cut	5 μm/pass
Feed rate	2 mm/min
Coolant	Solution type

CONCLUSIONS

In this research, a metallic glass molding experiment was carried out at various temperatures and molding time. As a result, successful transcription of microstructure on metallic glass was confirmed. The transcript rate was increased with increasing temperature and molding time. The transcription rate of trapezoidal probe was better than that of V-shaped probe. The final micro probe was obtained by removing unnecessary parts by grinding.

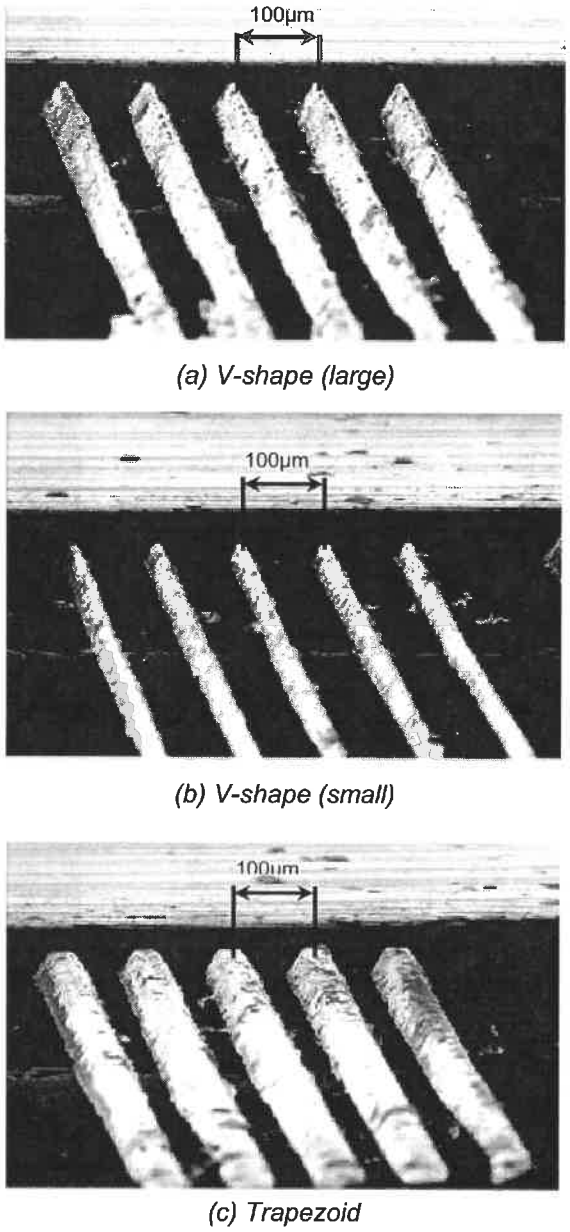

(a) V-shape (large)

(b) V-shape (small)

(c) Trapezoid

FIGURE 13. SEM images of micro probes

REFERENCES

[1] Seiichi Hata, et al. Precision and Micro Machining of Metallic Glasses, (In Japanese), Journal of the JSME (Series C), 65, 633, (1999-5) pp.346-352.

[2] Akihisa Inoue. Bulk Metallic Glasses as New Precision Engineering Materials, (In Japanese), Int. JSPE, 2004, 70(9) pp.1154-1158.

[3] Mamoru Ishida, et al. Precision Die-Casting of Bulk Metallic Glasses and its Applications, (In Japanese), Materia Japan, 2003, 42(8) pp.585-589.

[4] Hirofumi Suzuki, Akira Muramatsu, et al. Precision Molding of Micro Aspherical Glass Lenses, Proceeding of 5th euspen International Conference, Montpellier, France (2005.5) pp.41-44.

[5] Yuji Yamamoto, Hirofumi Suzuki, et al. Ultra Precision Grinding of Micro Aspherical Surface -Development of a Three-Axes Controlled Single Point Inclined Grinding Method-, Annals of the ASPE, (2004.10) pp.558-561.

Authors Index

Abbas, Ali E. . . . 437
Abe, Yoshinori . . . 382
Adachihara, Yutaka . . . 223
Adams, Hans-Anton . . . 147
Aketagawa, Masato . . . 52, 303, 379
Alkhaleel, Abdallah H. . . . 40
Altintas, Yusuf . . . 402
Aoyama, Hisayuki . . . 223, 260
Ballou, Susan . . . 44
Bamberg, Eberhard . . . 28
Batzies, Ekkehard . . . 227
Blewett, Nelson R. . . . 77
Bossoni, Sergio . . . 163
Brehl, David E. . . . 363
Brockdorf, Kathleen . . . 56
Buice, Eric S. . . . 187
Bullaro, Melinda . . . 348
Castro, Heber F. F. . . . 328
Chang, David W. . . . 48
Chen, Qunyi . . . 287
Chen, Shih-Chi . . . 111
Chen, Y. S. . . . 441
Cheng, Chung-Wei . . . 232
Cheng, Y. D. . . . 441
Cheung, Chi-Fai . . . 371
Chiou, C. C. . . . 441
Choi, Doo-sun . . . 279
Choi, Heejin . . . 111
Chopra, Deven . . . 332
Chu, David C. K. . . . 85
Chung, Sung-Chong . . . 171, 183, 199, 252, 291, 398, 445, 449, 457
Clary, Robert . . . 44
Claudet, Andre A. . . . 344
Collins Jr., Stuart A. . . . 61
Crawford, Thomas M. . . . 310
Culpepper, Martin L. . . . 111, 151, 191, 195
Cvetkovic, Srecko . . . 386, 469
Dagalakis, Nicholas G. . . . 139
David, Jean . . . 219
Deakyne, Theodore R. . . . 155, 390
DeBra, Daniel B. . . . 167
Dejima, Shuichi . . . 223
Delhaes, Guido M. J. . . . 135
Dow, Thomas A. . . . 287, 363
Dumas, Paul R. . . . 73
Ekko, Toshiyuki . . . 223
Elliott, Gloria . . . 115
Elliott, Kevin E. . . . 115
Ellis, Jonathan D. . . . 375
Endo, H. . . . 36
Eynian, Mahdi . . . 402
Ferrell, Nicholas J. . . . 119
Forest, Craig R. . . . 307
Fuchiwaki, Ohmi . . . 223, 260
Fujii, Taichi . . . 406
Furutani, Katsushi . . . 236
Gakuhari, Akihiro . . . 244
Gallego, Daniel . . . 119
Gardopee, George . . . 69
Garrard, Kenneth P. . . . 287, 363
Gatzen, Hans H. . . . 147, 386, 469
Geneves, Gerard . . . 219
Gill, David D. . . . 32
Go, Yasuyuki . . . 359
Gokemeijer, Nils . . . 93
Golda, Dariusz . . . 151
Grevstad, Andy . . . 414
Ha, Tae-Ho . . . 256
Hall, Christopher . . . 73
Hamaguchi, Tetsuya . . . 97, 299, 453
Hamano, Toshiaki . . . 240, 244
Hamasaki, Tatsumi . . . 382
Hansford, Derek J. . . . 119
Hatzigeorgopoulos, Justine H. . . . 375
Heamawatanachai, Sumet . . . 28
Heaton, Robert J. . . . 310
Higuchi, Masahiro . . . 473
Higuchi, Sei . . . 167
Hiramoto, Takeo . . . 215
Hirano, Minoru . . . 406
Hocken, Robert J. . . . 187, 211
Hogan, N. Catherine . . . 109
Holt, Martin . . . 295
Honda, Satoshi . . . 272, 324
Hopkins, Jonathan B. . . . 191, 195
Horiuchi, Hisatsugu . . . 143
Hoshino, Yuuta . . . 379
Hsu, Alan . . . 32
Hunter, Ian W. . . . 109, 307
Ide, Toyoka . . . 453
Ikeda, Naoto . . . 410
Ikeda, Shigeru . . . 264
Ikeno, Jun-ichi . . . 461
Imai, Y. . . . 36
Irie, Yuka . . . 223
Ishibashi, Haruki . . . 477
Ishida, Tohru . . . 406, 477
Ishige, Masashi . . . 379
Ishikawa, Ken-ichi . . . 382
Iso, Shunsuke . . . 410
Ito, Shuzo . . . 264

Je, Tae-Jin 279
Jeong, M.-Y. 279
Jordan, Scott 314
Kajiwara, Yusuke 421, 425
Kaka, Shehzaad 93
Kamiya, Kazuhide 317
Kanda, Daichi 303
Kaneko, Satoru 143
Kasuya, Keigo 105
Kato, Shigeo 240, 244, 264
Kato, Yoshiyuki 223
Katsuki, Akio 248
Kawano, Takeshi 489
Kawasugi, Masaaki 379
Keeler, Gordon A. 32
Kelley, D. 44
Kim, Hyo Soo 85
Kim, Hyun-Goo 445, 457
Kim, Hyun-Ho 199, 445
Kim, Kyung-Don 183, 252, 449
Kim, Min-Seok 171
Kim, Nam-Ho 21
Kim, Sang Jo 291
Kim, Seung-Chul 252
Kim, Seung-Jong 291
Kim, Woo-Yeon 291
Kim, Yongsik 139
Kobayashi, Yoshikazu 410
Kojima, Yusuke 105
Kono, Ippei 367
Kreutzer, Michael 227
Kuijpers, Toon A. A. 276
Kunieda, Hideyo 65
Kuniyoshi, Yuji 244
Kusaba, Kouhei 481
Kwok, T. C. Michael 371
Lai, Barry 295
Langen, Hans 123
Langzettel, Anthony K. 93
Lawton, Kevin M. 340
Lee, Chang-Woo 256
Lee, Hakchu 85
Lee, Jong-Min 291
Lee, Kwang-Jo 449
Lee, Vincent 127
Lee, Wing-Bun 371
Lee, Won-Seck 449
Lehmann, David K. 56
Leucht, Dennis 227
Li, Jianfeng 414
Li, Lei 61
Liang, Zhiyong 207
Lin, Chi-Ying 175
Liu, Wanli 207
Longoria, Raul G. 159
Lu, Dong 414
Luck, David L. 344
Ma, Hongshen 101
Ma, Li 44
Maeda, Guilherme J. 179
Malshe, Ajay 40
Manesh, Kochunny K. 351
Marsh, Eric R. 155, 390
Marth, Harry 314
Maser, Jorg 295
Masuda, Masami 433
Matsuda, Kiyoshi 394
Matsumori, Noboru 473
Mauntler, Nathan A. 21
Mayr, Josef 17
Merritt, John 81
Miller, Jimmie A. 340
Misaki, Daigo 223, 260
Mishima, Nozomu 203
Mitsuishi, Mamoru 367
Miyake, H. 36
Miyamoto, Kensuke 394
Moerlein, Alex 155
Morii, Hiroshi 97, 299
Moritani, Hiroki 105
Moriwaki, Toshimichi 489
Mostafavi, M. Taghi 81
Moyer, Patrick J. 115
Mukohata, Daisuke 489
Munnig-Schmidt, Robert-Han 123, 135, 268, 375
Murakami, Hiroshi 248
Muralikrishnan, Bala 89
Nagata, Tomohiko 481
Nagato, Keisuke 97, 105, 299, 453
Nakagawa, T. 36
Nakamoto, Keiichi 489
Nakanishi, Takahiro 248
Nakao, Masayuki 97, 105, 143, 299, 453
Namba, Yoshiharu 65
Nellissen, Ton A. J. M. 276
Nemoto, Kentaro 303
Neuber, Dirk 56
Nomura, Takashi 317
Novak, Erik L. 77, 348
Ogasaka, Yasushi 65
Ogura, Hidekazu 473
Ogura, Ichiro 321
Oguri, Atushi 260
Oh, S.-H. 279
Ohno, Naohiro 453
Okai, Reynolds 336
Okazaki, Yuichi 321
Okuyama, Eiki 52
Ols, M. 44
Onikura, Hiromichi 248

Ono, Manabu 240, 244, 264
Onozuka, Hideaki 402
Otsuka, Shingo 481
Otten, David 187
Ouyang, Jianfei 207
Overcash, Jerald L. 211
Park, Hyun Koo 248
Patamaporn, Chaikool 52
Patil, Chinmaya B. 159
Peruru, Haritha 355
Preissner, Curt 295
Qu, Xinghua 207
Raja, Jayaraman 355
Rajurkar, Kamlakar P. 40
Ramamoorthy, B. 351
Rankers, Adrian M. 276
Rao, Muralidhara 465
Ren, Dongmei 340
Renegar, Thomas Brian 44
Rhorer, Richard L. 418
Richmond, Lee A. 420*
Rock, Steve 167
Rong, Yiming 414
Roozen, N. Bert 24
Saez, Miguel A 307
Sai, Roro 215
Sajima, Takao 248
Sakaki, Yusuke 215
Sakamoto, Ryushiro 394
Sakamoto, Shigehiko 421, 425
Sakurai, Takafumi 303
Sato, Kaiji 179
Sawyer, Daniel S. 139
Sawyer, W. Gregory 21
Sayeh, Mohammed 81
Schmitz, Tony L. 21, 85, 437
Shakarji, Craig M. 139
Shibasaka, Toshiroh 489
Shibukawa, Tetsuro 406
Shibutani, Hideo 461
Shilling, K. Meghan 344
Shimada, Shoichi 359, 473
Shimizu, Toshiyuki 65
Shimokohbe, Akira 36
Shimomura, Takuji 65
Shino, Akira 240
Shinshi, Tadahiko 36
Shirai, Kenji 410
Shu, Deming 295
Singaperumal, Makaram 351, 465
Singhal, Shrawan 485
Slocum, Alexander H. 13, 101
Smith, K. Scott 332
Smith, Stuart T. 115, 187
So, Peter T. 111
Soemers, Herman M. J. R. 276
Sohn, Alex 287, 363, 429
Song, In-Ho 445, 457
Song, Jun-Feng John 44
Song, Jun-Yeob 256
Spence, Allan D. 48
Spronck, Jo W. 123, 375
Sreenivasan, S. V. 159, 485
Stephenson, Gregory B. 295
Stone Jr., Jack A. 89
Stoup, John R. 89
Stout, Tom 77
Stroup, Charles G. 211
Subrahmanyan, Pradeep K. 69
Sugimoto, Shuntaro 97
Sugimoto, Takashi 473
Sugita, Naohiko 367
Sugiue, Yuuki 299
Sundaram, Murali M. 40
Sung, Chul-Mo 171, 183
Suwabe, Hitoshi 382
Suzuki, Akihiko 461
Suzuki, Hirofumi 489
Suzuki, Yuta 324
Sweatt, William C. 32
Taberner, Andrew J. 109
Tagata, Yasutake 236
Takeuchi, Yoshimi 406, 477
Tanaka, Yusuke 394
Tashiro, Hatsuzo 317
To, Suet S. 371
Toida, Naohito 410
Tozawa, Koichi 410
Tran, Hy D. 344
Tricard, Marc 73
Trumper, David L. 187
Tsai, Mi-Ching 232
Tsao, Tsu-Chin 175
Tsuchiya, Kensuke 97, 299, 453
Tsuda, Nobuhiro 215
Tsuzaka, Hideo 433
Uchidate, Michimasa 303
Uda, Yutaka 359
Usuda, Takashi 223
Usui, Shuji 414
Vallance, R. Ryan 155
van Beek, Anton 123, 135, 268
Van den Hof, P. M. J. 131
van Eijk, Jan 131
van Hulzen, Jan 131
van Lierop, Diederik 276
van Ostayen, Ronald A. J. 123, 135, 268
Vasa, Nilesh Jayantilal 465
Vervoordeldonk, Michiel J. 24
Villar, Francois 219

*Extended abstract unavailable at press time.

Vogt, Stefan 295
Vorburger, Theodore V. 44
Wakabayashi, Masaki 461
Watanabe, Hidehito 433
Wegener, Konrad 17, 163
Weikert, Sascha 17, 163
Welker, Volkmar 227
Whitenton, Eric P. 44
Winarski, Robert 295
Woodard, James A. 119
Woody, Bethany A. 332
Wu, Karl-Hans 147
Yamaguchi, Kanta 481
Yamaguchi, Tomomi 473
Yamamoto, Yuji 489
Yamamoto, Yuki 394
Yamashita, Koujun 65
Yan, Yong-gang 207
Yanagi, Kazuhisa 303
Yang, Chun-Hsien 232
Yang, Liu 437
Yasui, Heiji 394, 421, 425, 481
Yi, Allen Y. 61
Yoo, Yeong-Eun 279
Yoon, Kwan-Woo 398, 445
Yoshida, Ichiro 303
Yoshimura, Takuro 394
Zapata-Ramos, Raúl E. 437
Zhang, Gang 283
Zhang, Xiaoyou 36
Zheng, A. 44
Zhu, Nigh 260
Ziegert, John C. 127
Zirn, Oliver 227